AD-A196 627 PROCEEDINGS OF THE AMERICAN TOWING TANK CONFERENCE (21ST) HELD IN WASHINGTON DC ON 5-7TH AUGUST 1986(U) NATIONAL RESEARCH COUNCIL WASHINGTON DC R F RESSALLE 1/6

UNCLASSIFIED AUG 87 F/G 13/10 NL

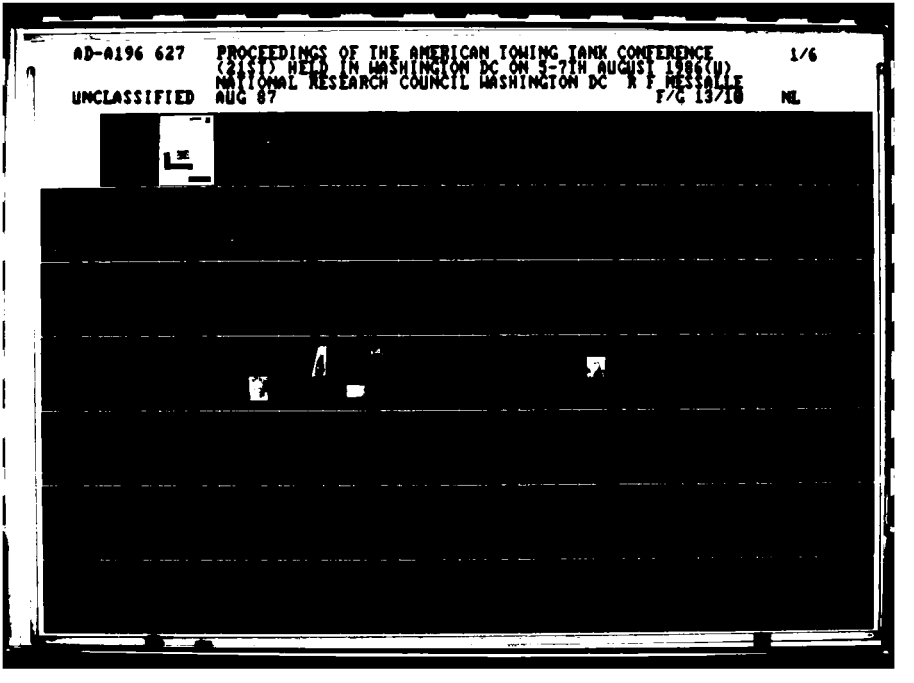

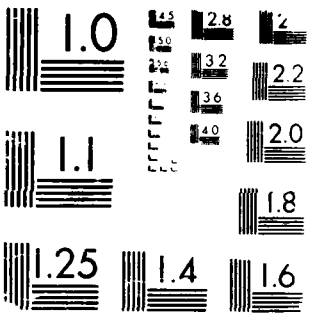

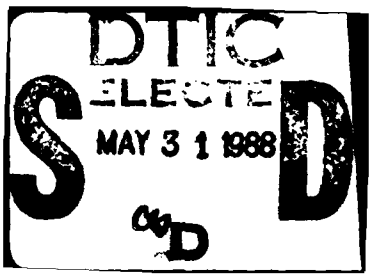
DTIC
ELECTE
MAY 3 1 1988
S
D
CCD

(2)

Proceedings of the

Twenty-First American Towing Tank Conference

edited by
Richard F. Messalle

Sponsored jointly by:
Naval Studies Board of the U.S. National Research Council
AMOCO Productions
Bird-Johnson & Company
Boeing Company
Chevron
Gibbs & Cox
M. Rosenblatt & Sons
National Steel & Shipbuilding Co.
Newport News Shipbuilding & Drydock Company
ORI, Inc.
Society of Naval Architects & Marine Engineers
TRACOR
Tracor Hydronautics, Inc.
Peterson Building, Inc.

NATIONAL ACADEMY PRESS
Washington, D.C. 1987

NOTICE: The project that is the subject of this report was approved by the Governing Board of the National Research Council, whose members are drawn from the Councils of the National Academy of Sciences, the National Academy of Engineering, and the Institute of Medicine. The members of the committee responsible for the report were chosen for their special competences and with regard for appropriate balance.

This report has been reviewed by a group other than the authors according to procedures approved by a Report Review Committee consisting of members of the National Academy of Sciences, the National Academy of Engineering, and the Institute of Medicine.

The National Research Council was established by the National Academy of Sciences in 1916 to associate the broad community of science and technology with the Academy's purposes of furthering knowledge and of advising the federal government. The Council operates in accordance with general policies determined by the Academy under the authority of its congressional charter of 1863, which establishes the Academy as a private, nonprofit, self-governing membership corporation. The Council has become the principal operating agency of both the National Academy of Sciences and the National Academy of Engineering in the conduct of their services to the government, the public, and the scientific and engineering communities. It is administered jointly by both academies and the Institute of Medicine. The National Academy of Engineering and the Institute of Medicine were established in 1964 and 1970, respectively, under the character of the National Academy of Sciences.

This work related to Department of Navy Contract N00014-85-G-0130 issued by the Office of Naval Research under contract authority NR 201-124. However, the content does not necessarily reflect the position or the policy of the Department of the Navy or the government, and no official endorsement should be inferred.

Copies available from:

The 21st American Towing Tank Conference
Mr. Frank H. Sellers (Treasurer)
MPR Associates, Inc.
1050 Connecticut Ave. N.W.
Washington, D.C. 20036

Phone: 202-659-2320

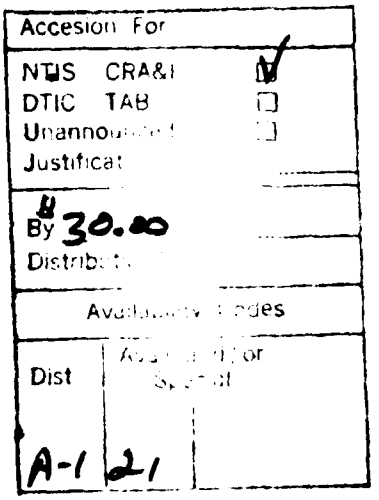

SPONSORS

The Executive Committee of the 21st American Towing Tank Conference extends its thanks to those organizations whose financial contributions made this Conference possible. Because of their generous contributions copies of the Proceedings will be distributed to all member organizations of the International Towing Tank Conference.

Naval Studies Board of the U.S. National Research Council

National Steel & Shipbuilding Co.

Newport News Shipbuilding &
Drydock Company

AMOT Productions

Bird-Johnson & Company

[illegible], Inc.

[illegible]

Society of Naval Architects &
Marine Engineers

Chevron

CRAIF

Gibbs & Cox

Tracor Hydronautics, Inc.

M. Rosenblatt & Sons

Peterson Building, Inc.

PREFACE

The twenty-first meeting of the American Towing Tank Conference (ATTC) was held at the National Academy of Sciences, Washington, D.C. from the 5th to the 7th of August 1986. The Conference was hosted by the David Taylor Naval Ship Research and Development Center and was attended by 164 delegates from North and South America representing 19 businesses, 14 government establishments and 13 universities.

Eight technical committee reports and 50 technical papers by 103 authors were presented at the Conference. The presentation of the papers was limited to a total of 16.5 hours in the three days. This restricted the discussions from the floor. The papers were not available for distribution to participants before the Conference for formal review. Because of this, it was requested that all questioners from the floor submit formal questions afterwards for inclusion in the Proceedings. Only a few did so. The Conference participants benefited from the pointed questions and exchange of experiences but the readers of the proceedings will not. The Conference was a success because it let us renew old acquaintances, exchange information, and share experiences.

The ATTC is a voluntary association of establishments and universities in the western Hemisphere that have responsibility in the prediction of hydromechanic performance of ships and waterborne craft based on experiments on small models or from theoretical calculations. The ATTC is purely a communicative body with no authority and membership is voluntary and self-supporting. Meetings are held every three years in the Western Hemisphere, in the year prior to the International Towing Tank Conference (ITTC). At the Conference, the representative to the Executive Committee of the ITTC is elected to represent the Western Hemisphere. The product of the Conference are Proceedings which are published and provided to all registered attendees and made available to others. The cost of producing and distributing the Proceedings comes from registration fees and financial contributions made by interested organizations. Because of the generous support of our sponsors, copies of the Proceedings will be distributed to all member organizations of the ITTC.

The Executive Committee of the 21st ATTC selected the nine technical areas of cavitation, high speed vehicles and sailing, ice testing, new facilities and techniques, ocean engineering, propulsion, resistance and flow, seakeeping, and steering and maneuvering for review by the Conference. The Executive Committee then formed committees for reviewing each of these areas and selected chairmen. Technical sessions were held on each of the technical areas. The chairman of each of these technical committees was responsible for choosing the papers to be presented, coordinating the written papers, presentation of the state-of-the-art report and chairing the session. The high success of the Conference was largely due to the work of these chairmen and their efforts are gratefully acknowledged. The work of the authors in sharing their research is also gratefully acknowledged, especially since writing conference papers is a task done after normal work hours and is usually not supported by the sponsor.

The Executive Committee of the 21st ATTC extends its thanks and gratitude to those organizations whose financial contributions helped make this Conference possible. They are identified on the following page of these Proceedings. We are much indebted to Vice Admiral J.H. Webber, Chief Engineer of the Navy, for giving the keynote address. His address is included in the Proceedings.

As with any Conference, there are those individuals who worked behind the scenes without whom the Conference would not have been successful. The Executive Committee would like to give special thanks to Lee Hunt, Elizabeth Locke, and Mary Gordon of the Naval Studies Board for the arrangements made at the National Academy of Sciences and to the help they gave before and during the Conference. We also thank Kay Adams, Aileen Tse, Zerlina Chen, and Sharon Sporr for handling the correspondence, collating papers, arranging the social activities, registration, etc. There are many others on the staff of the David Taylor Naval Ship Research and Development Center whose time and suggestions were invaluable and also deserve special thanks.

William B. Morgan, Chairman
Richard F. Messalle, Secretary

MEMBERS OF THE EXECUTIVE COMMITTEE
21ST AMERICAN TOWING TANK CONFERENCE

Dr. William Morgan (Chairman)
David Taylor Naval Ship Research
and Development Center
Code 1500
Bethesda, MD 20084-5000
(202-227-1578)

Mr. Richard F. Messalle (Secretary)
David Taylor Naval Ship Research
and Development Center
Code 1506
Bethesda, MD 20084-5000
(202-227-1347)

Mr. Frank DeBord, Jr.
Offshore Technology Corporation
578 Enterprise Street
Escondido, CA 92025
(619-746-5511)

Mr. David [illegible]
Institute for Marine Dynamics
Box [illegible]
St. John's, Newfoundland
A1B-3T[illegible] CANADA
(709-7[illegible]-[illegible]

Dr. Daniel [illegible]
Davidson Laboratory
Stevens Institute of Technology
Castle Point Station
Hoboken, NJ [illegible]
(201-420-[illegible]

Mr. Frank J. Sellens (Treasurer)
MPR Associates, Inc.
1050 Connecticut Avenue, NW
Washington, DC 20036
(202-659-3320)

Prof. Armin W. Troesch
Ship Hydrodynamics Laboratory
University of Michigan
North Campus
Ann Arbor, MI 48109
(313-763-6644)

Prof. Bruce Johnson
Naval Systems Engineering Dept.
U.S. Naval Academy
Annapolis, MD 21401
(301-267-3871)

TECHNICAL COMMITTEE CHAIRMEN

Propulsion Committee
Prof. William S. Vorus
214 NA&ME Bldg. North Campus
The University of Michigan
2600 Draper
Ann Arbor, MI 48109-2145
Phone: 313-764-8341

Ocean Engineering Committee
Mr. Frank W. DeBord, Jr.
Offshore Technology Corporation
575 Enterprise Street
Escondido, CA 92025
Phone: 619-746-2111

Resistance and Flow Committee
Dr. Edwin P. Rood
David Taylor Naval Ship R&d Center
Code 1542
Bethesda, MD 20084-5000
Phone: 202-227-1929

New Facilities and Techniques Committee
Mr. David C. Murdey
Institute for Marine Dynamics
National Research Council
Box 12093
St. John's, Newfoundland
A1B 3T5 CANADA
Phone: 709-772-2326

Steering and Maneuvering Committee
Mr. Thomas Waters
David Taylor Naval Ship R&D Center
Code 1562
Bethesda, MD 20084-5000
Phone: 202-227-1216

Ice Testing Committee
Dr. Steven Jones
Institute for Marine Dynamics
National Research Council
Box 12093
St. John's, Newfoundland
A1B 3T5 CANADA
Phone: 709-772-2326

Seakeeping Committee
Mr. Jeffrey T. Billingham
133 NA&ME Bldg., North Campus
The University of Michigan
2600 Draper
Ann Arbor, MI 48109-2145
Phone: 313-763-0536

Cavitation Committee
Dr. Michael L. Billet
Applied Research Laboratory
The Pennsylvania State Univ.
Box 30
State College, PA 16804
Phone: 814-865-1741

High Speed Vehicles and Sailing Committee
Mr. Peter W. Brown
Stevens Institute of Technology
Davidson Laboratory
711 Hudson Street
Hoboken, NJ 07030
Phone: 201-420-5289

CONTENTS

SESSION III: RESISTANCE AND FLOW

Chairman: Edwin P. Rood, David Taylor Naval Ship R&D Center, Bethesda, Maryland

SESSION IV: NEW FACILITIES AND TECHNIQUES

Chairman: David Murdey, National Research Council, Institute for Marine Dynamics, St. John's, Newfoundland

KEYNOTE ADDRESS
21st AMERICAN TOWING TANK CONFERENCE

The Maritime Technology Revolution 1946-1986

VADM J. WEBBER, Chief Engineer, U.S. Navy
Washington, D.C. 20362

ABSTRACT: The address covers the period 1946-1986, and touches on the tremendous achievements that have taken place in surface ships, submarines, and other marine vehicle technology: The revolutionary development of the true high speed submarine in the 50's; the order-of-magnitude increase in tanker capabilities and vast increases in cargo ship capabilities as evidenced by the 33 knot SL-7's as well as other container ships, barge carriers and roll-on/roll-off ships; the development of three totally new ship concepts: the hydrofoil, the hovercraft and the SWATH ship and the semi-submersible. Also covered are the developments necessary to operate under severe weather and sea conditions and merits of towing tanks have played a major role in these achievements.

ADDRESS: Good morning and welcome to the 21st American Towing Tank Conference.

The ATTC first met in Hoboken at the Stevens Institute of Technology in 1935. Much has happened in the interim; much that we all can be very proud of, particularly considering that many people attempt to paint the technology of ships as "old" and therefore incapable of producing vast change.

In the next 20 minutes I am going to touch upon just a little of what has happened in the marine technology business over the last 40 years or so. If you accept webster's definition of the word revolution as "a total or radical change" then you must credit those of us in the marine technology industry with creating revolutionary change in the post-war years. Virtually every one of these changes involve the towing tank community.

I am going to speak briefly about a few selected areas of marine technology that are part of this revolution and at the end I will list some others that might have been covered.

I will discuss:

- Development of the true submarine
- Cargo movement advances
- Three new surface vehicles
- Working at sea in all weather conditions
- Energy savings

By the conclusion of World War II the pressures of warfare had led to the development of some very effective submarines. These were in fact submersible surface ships; very capable ones but nevertheless submersible surface ships. Tremendous strides had been made to increase the speeds that they could achieve when submerged; some were able to make speeds well in excess of 20 knots, but only for a very short period of time before they had to surface and recharge their batteries. And when they were surfaced they became vulnerable. Even the development of the schnorkle, which permitted battery recharging from shallow depths, still left these submersible surface ships too vulnerable to ever-increasing ASW capabilities.

Navies wanted high submerged speed combined with a submarine that was capable to prolonged submerged operation. The capability for high speed submerged operation emerged from some sophisticated research and technology developments at the Center hosting this conference: The David Taylor Model Basin developed Series 58 submarine hull forms. They were proven on the ALBACORE which achieved the highest submerged speed of any submarine at that time. One half of the goal was achieved. The other half, came as a result of applying the nuclear propulsion technology that had been proven first on the conventionally configured NAUTILUS. The result was the SKIPJACK, the first true submarine configuration in a truly military sense -- a submarine capable of high speed and prolonged submerged operation (see Figure 1).

What has happened since is, in reality, only slightly less remarkable. The size of these true submarines has

Figure 1

FROM SUBMERSIBLE SURFACE SHIPS TO THE TRUE SUBMARINE

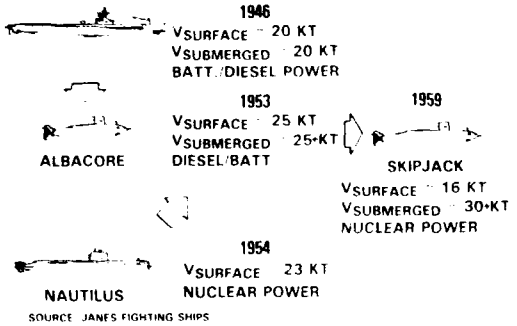

SOURCE: JANES FIGHTING SHIPS

grown tremendously (Figure 2) and their operating capabilities have increased significantly--particularly when related to quietness of operation. The technology of propeller quieting, as well as other acoustic treatments, has achieved remarkable levels of success. If classification restrictions did not prevent me from quantifying these achievements, I am sure that you would agree with me that what has been accomplished in just this one area is truly astonishing.

Towing tanks have played a large role in submarine hull form development as well as maneuvering, control and particularly propeller development. It is the latter area where, because of trends in submarine design and design requirements, facilities such as the New Large Cavitation Channel at the Model Basin, are needed.

The next area that I will touch upon in the marine technology revolution is the vast increases that have been achieved in the movement of cargo over the oceans and seas of the world.

I will first deal with the movement of bulk cargo [illegible] and then I will [illegible] "modularization." (which involves containerization, barges carried aboard ships, and what one might call multi-purpose ships).

When you look at the results after 40 years of development and application I think that you would have to agree that [illegible] the definition of "a total revolution."

The growth of tankers has been truly remarkable, as shown in Figure 3. Compared to the end of World War II, which was itself a large tanker for that era, we have seen an explosion in tanker size [illegible] from 60,000 to 80,000 tons [illegible] in the mid-50s to 200,000 deadweight tons in the 60s to, in the late 70s, the largest ship ever built--the 564,000 deadweight ton SEAWISE GIANT. This behemoth was 1,504 feet long, 226 feet wide and had a depth of 94 feet. It would take six 747 airplanes to lift that amount of cargo weight and a quite large [illegible] the requisite fuel needed [illegible] and much of the time [illegible] "marker buoy."

[illegible] have a [illegible] in carrying capacity [illegible] WW II [illegible] one of many [illegible] ships [illegible] of [illegible] mer[illegible] [illegible] of [illegible] [illegible] [illegible]

In the non-bulk cargo world an equally impressive change of events took place. Conventional break-bulk ships with their complicated masts and cargo booms have given way to the container ship, and then the different kinds of barge carriers and roll-on/roll-off ships and to what might be considered an end point in the modularity sense: the integrated tug-barge concept (which is really a multi-section ship where the propelling section is totally separable from the cargo carrying section of the ship).

The growth in size of these ships has been less than that for the tankers. But the tremendous achievement that has resulted is their increase in operating speeds from the 10 knots to 15 knots at the end of WW II to speeds of 25 knots (and, the achievements by SEA Land of the 33 knot, high capacity SL-7 container ships) (see Figure 4).

Also worthy of mention, is the increase in the unloading rates for these different kinds of ships. Tonnage unloaded per hour for these new ships is two to three ORDERS OF MAGNITUDE greater than their WW II counter-parts.

Certainly these are "radical changes!"

Between the mid- 1950s and today, three totally new marine surface vehicle concepts have been developed and exploited either commercially or by the military. These are:

- Hydrofoils
- Hovercraft, and
- Small waterplane area twin hull (SWATH) or semi-submersibles.

These three different types of marine vehicles are as different from each other (and monohulls) as fixed wing aircraft are from helicopters.

The hydrofoil concept, though worked on periodically earlier in the Century, really began its development in earnest during the 1950's.

Figure 4

BREAK BULK CARGO MOVEMENT

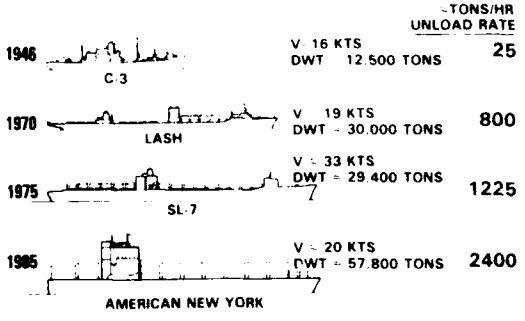

For the first six to eight years the partially-submerged foil, hydrofoil was the only type under development. Then in the early 60's the U.S. Navy, soon to be followed by other navies, began development of the fully submerged foil hydrofoil, to improve its seaway performance and to increase its speed potential (see Figure 5).

Towing tanks played very important roles in foil development, transcavitating and super-cavitating propeller development and in developing a series which permitted flexibility in the selection of hydrofoil hull forms.

The second new vehicle concept was the hovercraft- air cushion supported vehicles either with a full skirt or with two rigid side walls and a partial skirt forward and aft, as shown in Figure 6.

These types of vehicles presented the potential for very high calm water speeds and, some improvements in speed in moderate weather. The fully skirted hovercraft (or the ACV) also presented an additional important bit of potential -- the ability to be operated in an amphibious mode over both land and the sea.

The role of tanks in the development of hovercraft was substantial. In particular maneuvering and control system design as well as configuration resistance and propulsion optimization necessitated innovative, complex and comprehensive model experimental techniques to be developed.

The final new vehicle concept started its development in the late 50's when oil exploration led to offshore requirements in fairly deep waters, where weather conditions could make it difficult for drilling operations to continue with conventional types of drill ship configurations. This vehicle concept was the semi-submersible which has crude block-like lower hulls with three or more cylindrical columns extending upward to a working platform many feet above the calm water surface.

Figure 5

HYDROFOILS

Figure 6

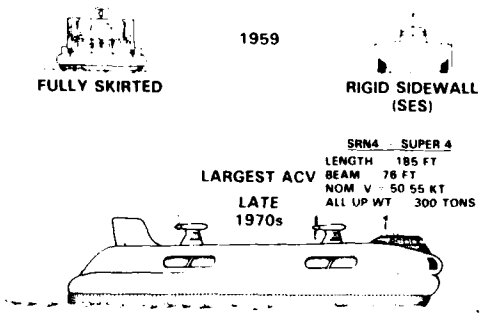

Figure 8

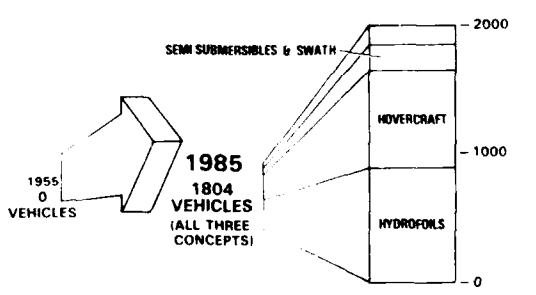

About 10 years later the U.S. Navy started the development of the Small Waterplane Area Twin Hull (or SWATH) concept. This concept embodied much more streamlined lower hulls and struts which permitted exceptional seaway performance at speeds up to 30 knots (see Figure 7).

Tanks played an immense role in the development of both semi-submerged ship and SWATH technology. Seakeeping facilities were absolutely essential not only in developing configurations but also in developing essential design tools for both semi-submersibles and SWATH ships. Additionally, SWATH technology necessitated maneuvering facilities, regular towing tank techniques and propeller and cavitation facilities.

The sum and substance of all of this is that today there are more than 1800 of these three new marine vehicle concepts that have been built for COMMERCIAL OR MILITARY use.

Oil exploration started to move offshore in the early 1950s. This led to a series of vehicle developments: the tethered barge; the so called Jack-up where the working platform would be jacked up on three legs that would rest on the bottom; modified monohull concepts with a "moon pool" - an opening in the bottom of the hull through which the drill rig could extend and, of course the semisubmersible drill rig concept that I referred to a moment ago.

These concepts have evolved to create the ability to drill for oil month in and month out - regardless of weather and sea conditions.

Competitive pressures (both commercial and military) have engendered a continuing trend towards extending the performance capabilities of many types of surface vehicles to higher and higher sea states.

The accompanying figure shows a somewhat typical northern latitude winter. Wave height is shown as a function of time for a three-month period during a nominal winter (December through February) for the

Figure 7

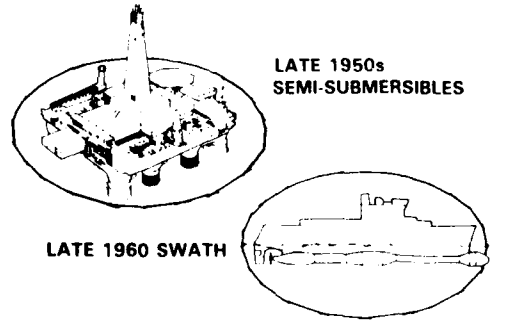

Figure 9

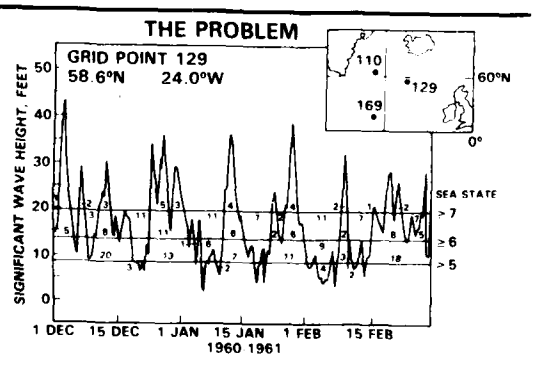

location shown. This happens to be a place of military interest but it is not all that different from what might be expected by oil drilling companies operating in the northern reaches of the North Sea or the Gulf of Alaska.

The continuing press to operate in all but the most severe of sea conditions has been the thread of the many developments over the last four decades.

In addition to the jack-up rig, the semi-submersible and SWATH configurations have inherent characteristics that permit all weather performance. Also, the hydrofoil also has this characteristic. In particular, the fully submerged foil hydrofoil has, in fact, the smallest relative waterplane area and has shown superior seaway performance when in operation foilborne. A summary of these "all weather" vehicles is shown in Figure 10.

Much work has also gone into making the hovercraft operate well at speed in heavy seas; to a point, that is in moderate seas the efforts have been successful, but more work has to be done in this area.

In the last decade, due to the drastic increase in energy prices, there has been a substantial investment in ways to reduce fuel consumption. In the marine vehicle business this investment as focused on two primary areas: machinery developments towards less energy consumption and greater efficiency, and hull form and propulsor designs to achieve greater fuel economy. I will deal today with the latter group.

Regarding hull forms, design tools and facilities have been put to work in order to develop configurations that will permit the basic functions of the ship to be performed in the most efficient manner. In addition to the use of bow bulbs to reduce wave making energy, we now see the emergence of "stern bulbs," asymmetric sterns, and coke-bottle lower hulls on SWATH ships and other schemes shown in Figure 11.

We have also encountered myriad propulsion concepts, some embodying only the propulsor itself and others involving the after part of the ship, or the addition of counterswirl devices, in addition to the propulsor.

In spite of the recent drop in fuel prices, this trend will continue.

In the past few minutes I have covered four of a larger number of areas that comprise the radical change that has taken place in marine technology in the past 40 years. In addition, the following areas deserve mention.

Undersea vehicles have gone through their own revolution, for both commercial and research purposes. The recent adventure of the submersible ALVIN, and its robotic tethered-vehicle JASON, and their exploration down into the inside of the TITANIC is truly an achievement of vast proportions. Similarly, the tethered vehicles that were used to find the Indian air liner that went down off Ireland last year are vehicles that can be very precisely controlled and which can perform useful functions while at the end of tethers miles long.

Service craft such as tug boats and the other new types of vehicles that came into being as a result of off-shore oil exploitation have changed drastically. A 1500 to 2000 horse power tug was notable in the 40's; we now have some ocean going tugs that have 25,000 horse power! And there are thousands of ships in this fleet of off-shore support craft.

Ship ice operations for primarily commercial purposes have engendered the development of vehicles and platforms which can withstand the rigors of high latitude operations as well as specialized "ice tank" developments.

During these four decades the fishing industries of the world have gone through tremendous change as evidenced by the tuna clippers which developed in this country

Figure 10

ALL WEATHER WORKING AT SEA

JACK UP SHALLOW WATER 1950s

CONV. SHIP – WITH "MOON POOL"
1960 1970s DEEP WATER
MODERATE SEA STATE LIMIT

DEEP WATER HIGH SEA STATE

HYDROFOILS – HIGH SEA STATE & HIGH SPEED

SWATH HIGH SEA STATE MOD. SPEED

Figure 11

HYDRODYNAMIC-ENERGY SAVINGS

HULL FORMS

- INCREASED EFF. HULL FORMS
- BOW BULBS
- STERN BULBS
- ASYMMETRIC STERNS
- "COKE BOTTLE" HULLS (SWATH)
- STERN TUNNELS

PROPULSION SYSTEMS

- LOW RPM PROPS
- CONTRAROTATING PROPS
- VANE WHEEL PROPULSION
- PARTIAL DUCT & PROP
- COUNTER SWIRL PROP
- OVERLAPPING PROPS
- RUDDER/BULB FIN SYSTEMS

and fishing factory ships from other countries. Even fishing trawls are now being developed in towing tanks.

This meeting would not be complete without mention of yachts; the literal explosion of the yacht business in the post-war years is obvious to anyone flying near a coast on a summer weekend. And, I should mention perhaps the largest challenge of all in the yachting world: the recovery of the America's cup.

What does all of this mean us?

In the last 40 years many new towing tank facilities have been built. In addition, new and different types of facilities have come into being such as seakeeping facilities, planar motion mechanisms, rotating arm facilities, and greatly increased capacity cavitation channels. These, as well as the traditional towing tanks and circulating water channels, have all played an absolutely vital role in the maritime revolution that has taken place.

These facilities have been used in their usual way of obtaining experimental verification of the characteristics, etc. for particular vehicle designs. They have also played an even more important role: that of developing the technical basis for exploitation of computer-aided analysis tools, computer-aided design tools based on empirical analysis of broad data bases, and validation of the development of basic computer hydrodynamic design and analysis codes.

In Figure 12 that you see before you I have tried to indicate qualitatively the role played by different kinds of towing tank facilities in the five areas that I have covered in this presentation.

The role played by you who have been involved has been innovative and productive. Much has been achieved, and there is much more to be achieved in the future.

I don't think that I have to tell any of you that the maritime industry worldwide is on hard times today, and has been for the last few years. In 1946 times were not very good either. The war had come to an end. There was a glut of available shipping. The world economy was in a state of understandable turmoil. But all of what I have covered with you this morning began to unfold as the years passed. A maritime revolution took place and I doubt that anyone could have predicted the different and multi-faceted courses that it took. But the revolution DID take place.

All of us should be proud to have been part of it and we should be confident that we will be able to contribute to its continuation in the years to come.

Thank you.

Figure 12

ROLE OF "TANKERY" IN VARIOUS AREAS OF MARITIME TECHNOLOGY

	SUBS	INCR CARGO MOVEMENT	3 NEW CONCEPTS	ALL WEATHER	ENERGY	OTHER
TOW TANKS	✓✓✓✓	✓✓✓✓	✓✓✓✓	✓✓	✓✓✓✓✓	✓✓✓
WATER (CAV.) TUNNELS	✓✓✓✓✓	✓✓✓	✓✓✓✓	✓✓	✓✓✓✓✓	✓✓✓✓
CIRC. WATER CH	✓✓	✓✓	✓✓✓	✓✓	✓✓✓	✓✓✓✓
SEAKEEPING TANKS	✓✓✓✓✓*	✓✓✓	✓✓✓✓	✓✓✓✓✓	✓✓	✓✓✓
PLANAR MOTION MECH.	✓✓✓	✓	✓✓✓	✓		✓✓
ROTATING ARM	✓✓✓	✓✓	✓✓✓			✓✓
COMP. DATA ANAL./PRED.	✓✓✓✓	✓✓✓✓	✓✓✓✓	✓✓✓	✓✓✓✓	✓✓✓✓
COMP. SHIP DES. CODES	✓✓✓	✓✓✓	✓✓✓	✓✓✓✓	✓✓✓	✓✓✓
CFD VALIDATION	✓✓✓	✓✓✓	✓✓✓	✓✓✓✓	✓✓✓	✓✓✓

*SUBMERGED OPER. ENVELOPE DEVELOPMENT

SESSION I
PROPULSION

TECHNICAL COMMITTEE MEMBERS

Prof. William S. Vorus (Chairman)	Univ. of Michigan
Prof. John P. Breslin	Stevens Inst.
Prof. Jacques B. Hadler	Webb Inst.
Dr. Robert Henderson	ARL, Penn State Univ.
Mr. Stuart D. Jessup	DTNSRDC
Prof. Justin E. Kerwin	MIT
Mr. Eugene R. Miller	Tracor Hydronautics
Mr. David Molyneux	NRC Canada
Prof. Frederick Stern	Univ. of Iowa

REPORT OF THE PROPULSION COMMITTEE TO THE 21ST AMERICAN TOWING TANK CONFERENCE

William S. Vorus
Professor
Department of Naval Architecture
and Marine Engineering
The University of Michigan
Ann Arbor, Michigan 48104

INTRODUCTION

In describing the activities of the ATTC member institutions in the ship propulsion area since the last meeting at Stevens in 1983, this report is intended primarily to reflect the recent advances made in the field. However, it seems in order to place the recent advances relative to some absolute scale by a brief statement on the existing limitations of propulsion system design technology.

There are of course many existing limitations, both analytical and experimental, that prevent precise propulsor design. The most important, however, is considered to be the continuing inability to deal as effectively as desired with cavitation, either analytically or experimentally. Whether it be from the point of view of noise generation through tip vortex cavitation in military applications, from the point of view of low frequency structural vibration excited by intermittent blade sheet cavitation with large surface ship propellers, or from the point of view of thrust breakdown associated with propeller supercavitation in high speed craft, it is safe to say that cavitation control is the most important element of the propulsor design process.

It is not clear, from the perspective of the propulsion system designer, that as much progress has been made in advancing propeller cavitation control methodology in the last three years as was made in intervening periods between some of the past ATTC meetings. Opinions of the ATTC membership on this view would be welcomed by the Propulsion Committee.

One area of ship propulsion technology that has experienced significant advancement in the last three years is that of compound propulsors, as is reflected in several of the individual member reports to follow. The primary motivation has been reduced fuel consumption. However, all of the old difficulties, both analytical and experimental, are exaggerated in designing compound propulsors. Particularly, from a standpoint of testing, the lack of Reynolds scaling is certainly more serious. This is due in part to the lower Reynolds numbers, and consequently more pronounced viscous flow effects, associated with slow moving parts, such as stators. This is exacerbated by the fact that compound propulsors generally involve greater surface areas, so that the viscous inaccuracies are amplified through proportionately larger viscous force components.

The member presentations constituting the remainder of this report take several forms, ranging from descriptions of general activities, to more detailed summaries of examples of specific research, to comprehensive technical presentations. The member presentations have been collectively arranged in order of increasing degree of detail as follows:

MEMBER PRESENTATIONS

1.0 TRACOR HYDRONAUTICS

The major portion of model testing in the Hydronautics Ship Model Basin (HSMB) has been devoted to evaluating new ship designs. Some examples are, for the U.S. Navy, a jumboized oiler, a YFRT, the T-AGOS SWATH, and a new T-AGS. For the U.S. Coast Guard, we tested a model of the 138 foot SWATH, a corvette for the Mexican Navy and a foreign submarine. We have investigated the maneuvering performance of a towboat flotilla in deep and shallow water. Various underwater vehicles have been tested for maneuvering characteristics. Different propeller designs were tested for possible use on a surface effect ship.

A great deal of study has been devoted to uncovering various hydrodynamic effects due to the launching of underwater weapons.

Over a dozen different, large-scale yacht models were tested to determine their relative merits in future races.

A patented, unusual hydrofoil configuration was model tested to assess feasibility for full-scale applications.

For commercial clients, we have model tested special towed arrays and a cable diverter.

A substantial amount of research is underway on a so-called "water piston" propulsion system. This patented device is an exciting innovation, with potential application to almost all marine vehicles. Essen-

tially, a hot slug of gas is applied to a cylinder of water. If the physics works out in practice as it does in theory, it is possible to eject the water at high efficiencies, even approaching that of a marine propeller. The potentially simple propulsive system is looking very attractive. The next phase is the construction and test of a full-scale system appropriate for propulsion of an operational small naval vehicle.

The future apparently holds more of the same, with perhaps one major addition. We have actively studied various means of quieting our model basin and carriage systems to enable certain hydroacoustic tests. These efforts have succeeded to the degree that test programs are being discussed with potential clients. A paper on this program is also being prepared for the 1986 ATTC conference.

2.0 IMD-NRC CANADA

The activities of our Institute for Marine Dynamics related to the propulsion of ships fall into 3 areas, which overlap somewhat, but can be broadly classifed as:

2.1 Commissioning New Facilities,
2.2 Research into Resistance and Propulsion,
2.3 Evaluation of Ship Hull Forms.

A summary of the activity in each group is given below.

2.1 Commissioning New Facilities

The new Institute was officially opened on November 5, 1985. The towing tank carriage was completed and accepted shortly afterwards. In order to expedite the commissioning process, as much equipment as possible was procured from commercial suppliers. Resistance and propulsion guiders, propulsion dynamometers, gear boxes and a propeller open water dynamometer were all purchased from Kempf and Remmers Gmbh, of Hamburg, W. Germany. The only major pieces of equipment which were designed and built in-house were the resistance towing post and acceleration clamp. The manufacture of all the major components for these pieces is now complete. Detailed assembly will begin very shortly, and it is hoped to have the units delivered by early fall 1986. We hope to have carried out at least one ship resistance, propulsion and propeller open water experiment by the end of the year. We intend to carefully compare the results of experiments with those carried out in our Ottawa basin, and also with models tested in other tanks. This is clearly of vital importance to establish the regulation of any new test facility.

2.2 Resistance and Propulsion

A series of analysis programs has been written to analyze the results of resistance, propulsion and propeller open water experiments. These programs will analyze the results of experiments for single and twin screw ships, with or without propeller ducts. Triple screw ships and planing hulls can also be analyzed. We have standardized our experiment methods using an overload propulsion technique since we feel this offers the most flexibility in terms of selection of correlation allowance and subsequent re-analysis to alternative scales. New areas for development will be test methods for sailing yachts, planing hulls and other unconventional marine vehicles including submersibles. We also plan to expand into methods of numerical simulation of flow around ships and the development of new measurement techniques to support the numerical modeling.

2.3 Evaluation of Ship Hull Forms

The NRC Hull Form Series for Fast Surface ships has made a lot of progress since 1983. All models have been tested for resistance (naked and appended), propulsion and head sea seakeeping. All data has been refaired for consistency and summary results were presented by Murdey and Simoes Re in October 1985, at the NSMB workshop on Ship Hull Form Design. A statistical analysis of trends in resistance with hull form has been carried out.

A new series has been developed from the above series which is more appropriate to small ships, such as fisheries patrol vessels and other similar craft. This series is designed to have the same midship section and block coefficient as the parent series, but with lower resistance in the Froude number range 0.4 to 0.5. Preliminary model tests have been completed showing the expected improvement and it is hoped that the series can be finished by March 31, 1987.

Another major project has been to develop IMD's data base for random ship forms. This work involves computerizing all IMD's existing model data, and developing a data base system which will be appropriate for modern design methods. It is hoped to have the preliminary version ready by the middle of next year.

3.0 IIHR, UNIVERSITY OF IOWA

The Iowa Institute of Hydraulic Research (IIHR) is actively involved in a number of research projects of interest to the Propulsion Committee of the 21st ATTC. The primary focus of the IIHR research concerns viscous flow effects in ship hydrodynamics. For purposes of discussion it is convenient to divide the projects into two categories: bare-hull studies and propeller-appendage-hull interaction studies. In the studies of the former category the propeller and appendages are not included whereas they are in the studies of the latter category. It should be recognized that although the bare-hull studies may not seem to be of direct relevance to the Propulsion Committee, ultimately such developments can be incorporated into the propeller-appendage-hull interaction studies.

3.1 Bare-Hull Studies

The objective of this research is the development of computational and analytical methods for predicting the detailed flow field, including resistance coefficients, for ships and submarines and the acquisition of basic experimental data to aid in validating such methods and explicate the physics. The approaches of these methods include viscous, inviscid, and viscous-inviscid interaction procedures.

One research area concerns the development of procedures for incorporating viscous effects into the calculation of ship wave-making resistance. Shahshahan (1985) and Landweber have used their measurements of the boundary layer and wake of a Wigley model at several Froude numbers in the above mentioned procedures to show that such effects are important and lead to an improvement in the wave resistance prediction. Extensions for the use of slender-body theory centerplane distributions (previously thin-ship theory centerplane distributions were used) are presently being made (Hsu, 1986).

Another research area concerns the development of procedures for calculating ship-stern and wake flows, i.e., thick-boundary-layer trailing-edge flows. The appropriate governing equations for such flows are the partially-parabolic Reynolds Equations. Chen and Patel (1985) have developed a powerful method for solving the partially-parabolic equations using body-fitted coordinates, the novel finite-analytic method, and a large solution domain so as to capture the entire zone of viscous-inviscid interaction. The results have shown very good agreement with experimental data for turbulent flat-plates, axisymmetric bodies, and three-dimensional bodies including practical ship forms.

As an alternative to a large-domain solution Stern et al. (1986b) have developed a viscous-inviscid interaction approach for solving the partially parabolic equations using body-fitted coordinates, finite-difference methods, and a small solution domain. The results thus far are for axisymmetric bodies and show good agreement with other methods and experimental data.

In support of this research, an extensive set of measurements have been made of the mean-velocities and the turbulent stresses in the stern region and in the near and intermediate wake regions for a double Wigley model (Sarda, 1986).

Lastly in this category, research is being conducted concerning free-surface effects on the hull boundary layer and wake, including the bow. Patel et al. (1985) have shown that the bow vortices originate from separation of the free-surface boundary layer. Stern (1985a and b) has performed an experimental-theoretical investigation into the more fundamental aspects of free-surface effects on the boundary layer of a surface-piercing body, including wave-induced separation.

3.2 Propeller-Appendage-Hull Interaction Studies

The objective of this research is the development of a computational method to determine the interactive and combined flow field over the stern and in the near and far wake for propeller-hull configurations, and the acquisition of experimental data to aid in validating such methods and explicate the physics. Stern et al. (1985c, 1986a) have coupled the Chen and Patel (1985) partially-parabolic method for calculating ship-stern flow with a propeller-performance program in an interactive and iterative manner. A body-force distribution is used to represent the propeller in the partially-parabolic method. Results have been obtained for applications of various levels of flow field complexity: rotationally-symmetric steady and unsteady flows, and three-dimensional steady flow. The steady-flow results for axisymmetric bodies are in excellent agreement with the available experimental data and show that the present procedures are able to predict many details of the flow field including the formation of the hub vortex and its dependence on propeller loading. The preliminary results for a three-dimensional body geometry (DTNSRDC 3:1 elliptical body) are also quite realistic; however, no experimental data is available for verification. Although much more work needs to be done, especially for three dimensional flow, in order to extend the method to realistic ship geometries, it is concluded, based on the present work, that the present procedures can accurately simulate the steady part of the combined propeller-hull flow field and can be used with some confidence for predictions of thrust deduction and effective wake as well as other flow quantities of interest. The unsteady-flow results are in reasonable agreement with the experimental data. However, they point out the limitations of the present approach for simulating the complex blade-to-blade flow. A more detailed representation of the propeller than the body force is required. Further work along these lines is also being done.

Lastly, studies are underway for body-appendage configurations (Chen, 1985). In this case, the propeller has not been included. The focus of this work concerns the appendage wakes and their influence on the nominal wake.

REFERENCES (University of Iowa)

Chen, C.J., (1985), "Finite Analytic Numerical Prediction of Turbulent Wakes Behind an Inclined Propeller Shaft and Appendages", GHR annual report.

Chen, H.C. and Patel, V.C., (April 1985), "Calculation of Trailing-Edge, Stern and Wake Flows by a Time-Marching Solution of the Partially-Parabolic Equations", Iowa Institute of Hydraulic Research, IIHR Report No. 185.

Hsu, P.P., (August 1986), "Slender-Body Centerplane Distributions for Ship

Forms", Ph.D. Thesis, M.E., Univ. of Iowa.
Patel, V.C., Landweber, L. and Tang, C.J., (October 1984), "Free-Surface Boundary Layer and the Origin of Bow Vortices", Iowa Institute of Hydraulic Research, IIHR Report No. 284. Also, Proceedings of the 2nd Int. Sym. Ship Viscous Resistance, Goteberg, Sweden.
Sarda, O.M., (August 1986), "Experimental and Numerical Study of the Flow over the Stern and in the Wake of a Wigley Hull", Pn.D. Theses, M.E., Univ. of Iowa.
Shahshahan, A., (August 1985), "Effects of Viscosity on Wavemaking Resistance of a Ship Model", Ph.D. Thesis, Mechanical Engineering, The Univ. of Iowa.
Stern, F., (May 1985a), "Effects of Waves on the Boundary Layer of a Surface-Piercing Body", Iowa Institute of Hydraulic Research, IIHR Report No. 288.
Stern, F., (September 1985b), "Influence of Waves on the Boundary Layer of a Surface-Piercing Body", Proceedings of the 4th International Symposium on Numerical Ship Hydrodynamics, Washington, D.C., 24-27.
Stern, F., Patel, V.C., Chen, H.C., and Kim, H.T., (1985c), "The Interaction Between Propeller and Ship-Stern Flow", Proc. Osaka Int. Colloq. on Ship Visc. Flow, Osaka, Japan.
Stern, F., Kim, H.T., Pate, V.C., and Chen, H.C., (1986a), "Viscous Flow Computation of Propeller-Hull Interaction", Proc. 16th ONR Sym. Naval Hydrodynamics, Berkeley.
Stern, F., Yoo, S.Y., and Patel, V.C., (June 1986b), "Viscous-Inviscid Interaction on Three-Dimensional Bodies, Including Thick Boundary Layers and Wake", Iowa Institute of Hydraulic Research, IIHR Report No.xxx.

4.0 DWTNSRDC

4.1 Propeller Research

Recent propeller research has included design method development for advanced propulsors, real blade flow effects, and new blade section design.

Design procedures are being developed for duct-propeller systems that will reduce the nonuniformity of the propeller inflow. In the past, ducted propellers have been designed using ideal linearized axisymmetric duct geometry. New procedures will use potential flow panel methods to model the duct more exactly, and allow for asymmetric duct geometries to effectively reduce the circumferential variation of the propeller inflow.

Experimental and analytical studies have been proceeding to understand real flow, viscous effects on propeller performance. Blade boundary layer characteristics have been measured model scale, and concurrently, blade boundary layer prediction codes have been developed showing good qualitative correlation with measured data. This marks a good beginning, but the complex details of propeller flows-tip vortex, hub intersection, wake modeling and the actual conditions of complex circumferential varying viscous ship wakes will make complete theoretical prediction difficult for some time.

A program has begun this year to develop blade design techniques incorporating arbitrary blade section shapes to minimize cavitation and its adverse effects. The work is an adaptation of similar two-dimensional hydrofoil section design by Shen at DTNSRDC. Arbitrary two-dimensional section shapes are incorporated into propeller geometry through lifting surface calculations of the effective three-dimensional camber from the specified two-dimensional load distributions. Two-dimensional thickness distributions are retained in the final propeller geometry. Fundamental designs of unskewed and skewed propellers will be evaluated.

4.2 Propulsion

Research and application of new hull designs has been continuing since the last ATTC conference. Ongoing research areas have included stern wedge shapes, SWATH hulls, C-P propeller performance correlation, and bulb design.

The application of wedges just forward of the transom on combatant hull forms has been investigated in recent years. The use of wedges has resulted in reduced resistance at high Froude number. Also, some benefit has been seen in improved hull efficiency by means of increased thrust identity wake fraction.

A new SWATH propulsion option has been explored with the use of contrarotating propellers. Contrarotation permits the possibility of incorporating high efficiency, contrarotating electric drive motors installed inside the SWATH hulls. Also, improved propulsion efficiency and cavitation performance are possible with contrarotating propellers. Wake scale effects have become an increased concern for the ship design community at DTNSRDC. With each new propeller design, the implications of the full scale wake are considered. For a recent SWATH design, the effect of the predicted full scale wake on the final propeller pitch was checked, using a body of revolution approach. To date, utilization of the full scale predicted flow through the complete propeller design process has not been done. There is a trade off between substantial design experience using model parameters and appropriate correlations, and the potential of improved full scale cavitation and propulsion performance with a full scale design approach that does not benefit from experience.

Recent full-scale trials of ships fitted with controllable pitch propellers have indicated the need for more accurate measurement of blade pitch angle. The ship-board blade pitch indication may have associated inaccuracies that are reflected by propeller revolutions different from those predicted by model experiments. A program is underway to precision instrument the controllable-pitch propeller hubs to more accurately measure blade pitch during sea trial installations. With the more accurate pitch measurement, better correlation is expected between model experimental predictions and full-scale trial results.

5.0 ARL, PENN STATE UNIVERSITY

An example of recent research using the ARL facilities has been the design and evaluation of a counterswirl vane assembly for improving propulsive efficiency, sponsored by the U.S. Coast Guard.

Surface vessels with engines mounted internally usually have a shafting arrangement which leads to an inclination of the rotating propulsion element relative to the fluid inflow. This, in turn leads to periodic unsteady loading of the propeller, with one side of the disc heavily loaded and the opposite side lightly loaded. In normal design practice, swirl is discharged in the exit flow which is a source of inefficiency due to a pressure drag on the propeller. A method of recovering this lost energy is to design a compound propulsor which consists of a stationary blade row either in front or behind a rotor, placing or removing the swirl induced by a rotating element. An effect of shaft inclination is to place swirl into the direction of rotor rotation on the side of the propeller which is heavily loaded, tending to increase efficiency. However, on the lightly loaded side, swirl in the direction or rotor rotation is induced, causing a doubled reduction in efficiency. A design was conducted which places a partial set of counter swirl vanes upstream of a propeller on the lightly loaded side. The vanes are mounted on the shaft bearing housing. Two effects were intended. Elimination of vanes on the heavily loaded side of the propeller eliminates skin friction and pressure drag associated with the placing of excess swirl in the inflow. The net swirl placed in the flow is equivalent to the propeller induced swirl, with the possibility of an improvement in propulsive efficiency. In addition to the above, the partial counter swirl vanes produce a positive trim force, which is beneficial in some cases.

The design philosophy described above was applied to two United States Coast Guard vessels, a 41 foot Utility Patrol boat and an 82 foot vessel. The design for the 41 foot boat was field evaluated. The design was adapted to a twin shaft configuration, with opposing direction of rotation. Each propulsor consisted of a standard propeller with a partial set of counter swirl vanes upstream. The top most vane was installed as a modification to the bearing support strut. Two high camber vanes were mounted close to the horizontal axis of the boat on the lightly loaded sides of their respective propellers. Two moderately cambered vanes were mounted near the bottom of each propeller. All of the vanes were attached to a partial ring, which was welded to the bearing housing immediately upstream of the propellers. All of the vanes were designed to impart counterswirl into the propeller. The outline of this arrangement is presented on the Figure 1.

The design described above was tested at Norfolk, Virginia, under the direction of the Naval Sea Systems Engineering Division. Shaft RPM, thrust, torque and boat speed were recorded. Fuel consumption was metered and hull vibration levels obtained utilizing an accelerometer. Data were obtained for the standard and the compound propulsor on the same hull.

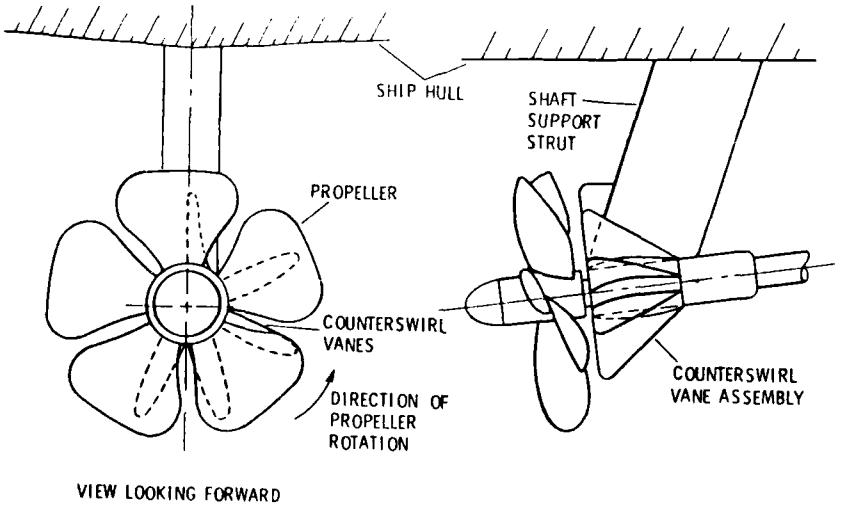

Figure 1. Counter Swirl Vane Assembly

The compound propulsor provided a gain in efficiency at all speeds, using the same propellers. The increase in speed at a given power level compensated for the increased level of preswirl and the engine power characteristic was not adversely affected. A nominal improvement of nine percent in fuel consumption was measured. Given the cost of fabricating and installing the counter swirl vanes, a payback period of one year is estimated. No adverse vibration change or effect on trim was noted. Utilizing the experience gained during this design and evaluation, additional improvements in efficiency and vibration are being considered.

6.0 STEVENS INSTITUTE OF TECHNOLOGY

Research work in areas related to propeller mean and vibratory forces conducted in part at Davidson Laboratory and mainly in the Department of Civil and Ocean Engineering has dealt with the effects of shear flow and theoretical aspects of the design of ducts to mitigate blade-rate forces and intermittent blade cavitation on ducted propellers.

The coupling of propeller induced flow with an experimentally generated axisymmetric radially sheared wake was investigated experimentally in the MIT water tunnel by Breslin and Goodman (1) with the assistance of Professor J. Kerwin and Mr. D. Lewis of MIT. Comparison was made with a theoretical model developed by Goodman (2). The abstract of Reference (1) is quoted as follows:

"A wake adapted propeller was tested behind the wake for which it was designed and also in uniform flow. Direct measurements of flow velocity near the propeller disc were obtained in both cases, as well as thrust and torque coefficients vs. advance coefficient. Comparisons are made of the flow velocity with a prediction based on a theory of a propeller in a shear flow due to Goodman. Comparison is also made of the increase in velocity due to shear from the thrust coefficient vs. advance coefficient curves based on thrust identity. It is shown that an effective wake (i.e., the nominal wake augmented by the effect of shear) as predicted by the theory agrees with the measurements to within a percent or so provided the nonlinear version of the theory is used."

The principal results of the experiments and theory are displayed in Figure 2 below. The nonlinear version of the theory was found to be necessary because the induction of the actuator disc is considerably in excess of 0.10 V_S.

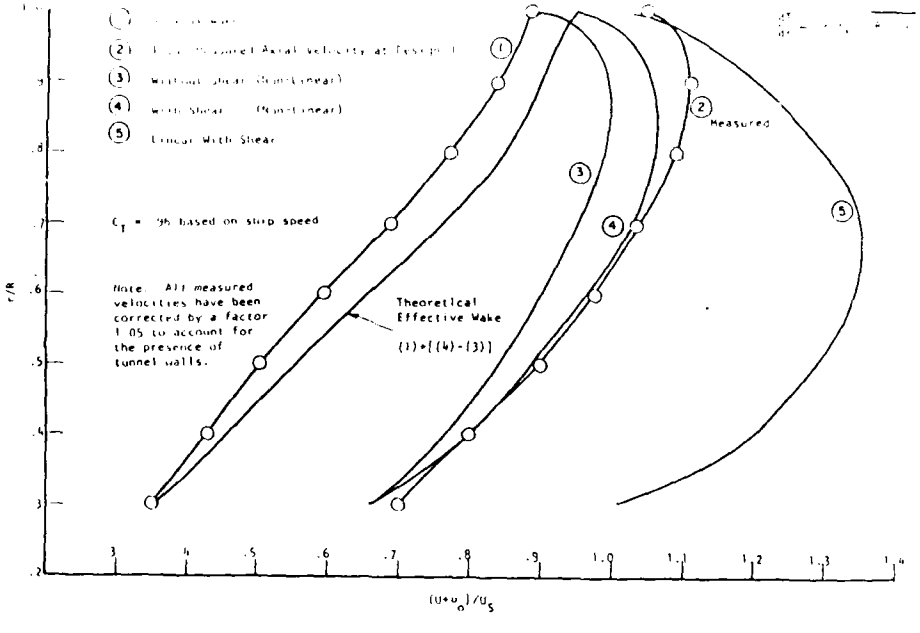

Figure 2. Theoretical and Experimental Axial Velocities Behind the Wake Screen in the Plane of the Propeller

The effect of radially shear axisymmetric inflow upon the geometry of a duct carrying a specified loading in the presence of a propeller (actuator disc) within the duct with a given loading has been studied by Dr. Hosung Lee (3) in his doctoral dissertation under the guidance of Professor J.P. Breslin. Lee's abstract is quoted as follows:

"We consider the linearized Euler equations and the continuity equation with the assumptions of large shear and small perturbation velocities of a ducted propeller.

Manipulating the Euler equations and the continuity equation in cylindrical coordinates for axisymmetric shear flow, a Poisson type equation involving the disturbance pressure can be obtained. A formal reduction of this equation yields an integral equation for the pressure which can be converted to a manageable non-homogeneous integral equation by means of a Fourier transform.

We treat the integral equation as a linear system using the far field boundary condition.

Duct and propeller are treated separately to obtain perturbation velocities of each with and without shear flow and these are then combined for the design problem of ducted propellers.

The loading on the duct is taken as the roof-top distribution and loading on the propeller disc is assumed to be an arbitrary distribution with the proviso that the combined loading can produce the designed thrust coefficient.

Each component of the induced velocities is calculated from the original Euler equations and continuity equation and the pressure distribution in the absence and presence of shear. Duct thickness effects with shear are discussed.

A design method for ducts is provided for flows with and without shear from the exact second order kinematic boundary condition on the duct surface for given propeller-thrust and duct-thrust coefficients. Duct geometry is calculated for both with-and without-shear-flow cases. Significant effects of shear are noted in the derived duct geometry.

A sample of the induced axial velocity with and without shear (the shear is derived from model wake data of a moderate V-shaped stern given by Hadler and Chang, SNAME Trans. Volume 73, 1965) is given in Figure 3. We see that the effect of shear is very pronounced.

A comparison of the duct camber t_{max} and conicity angle, α , with the NSMB 19A duct is given in Table 1.

Dr. T.R. Goodman and J.P. Breslin (4) have developed a procedure for the design of ducts to produce net flows in a nominal hull wake at the plane of the propeller which have reduced spatial harmonics at selected harmonic order numbers. The abstract of Reference 4 is as follows:

"A procedure based on inviscid flow theory is detailed for the design of propeller ducts to reduce specific spatial non-uniformities in given nominal ship wakes. The objective is to produce net flows to enclosed

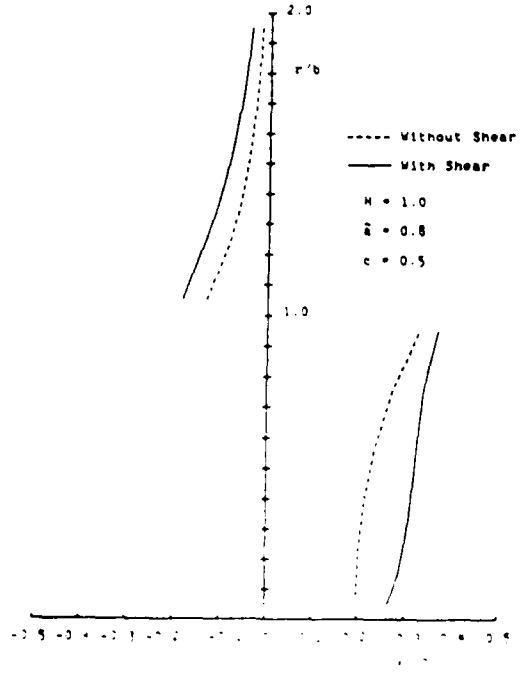

Figure 3. Axial Induced Velocity due to Duct Loading with and without Shear at x = 0

	NSMB 19A, KA4-55	Without Shear	With Shear
C_{T_P}	2.620	2.620	2.620
C_{T_D}	0.889	0.7202	0.8612
C_{T_T}	3.509	3.3402	3.4812
C_{T_D}/C_{T_T}	25.3 %	21.6 %	24.7 %
J	0.4321	-	-
2to	0.15	0.15	0.15
f_{max}	-0.07	-0.05630	-0.06431
α	10.2°	13.82°	16.0°

Table 1. Comparison of Calculated Duct Camber, f_{max}, and Conicity Angle, α , with and without Shear and the Characteristics of the NSMB 19A Duct at Comparable Loadings

propellers which will reduce cavitation and vibratory forces. The process yields perpherial variations of camber and conicity angle which will reduce the amplitude of specific wake harmonics to a maximum extent possible under the arbitrarily imposed constraint that the maximum sectional normal force coefficient must not exceed unity. Applications are made to reduce the first shaft frequency of two wakes showing resultant first harmonics reduced by factors of 4 and 1.40 in the 0.8 radius region. A 9.5-inch diameter model designed to reduce the first shaft harmonic of a screen-generated wake has been constructed for experimental verification of the efficacy of the design. Computer programs are provided."

Figure 4 shows the vertical cross-section of a duct designed to ameliorate the first harmonic of a ship model wake generated by a wake screen in a wind tunnel which turned out to have about twice the first harmonic of the series 60 (C_b = 0.6) wake which it was supposed to represent. Nevertheless, the measurements with and without the duct as displayed in Figure 5 show marked reduction in the first harmonic. The theoretical prediction is seen to compare very well when account is taken of the fact that the available mean axial velocity at the duct radius as measured was 0.79 V_0 , V_0 being the reference speed used in the theory.

In a doctoral dissertation Dr. J.K. Chen (5), under the guidance of Professor S. Tsakonas, undertook an elaboration of the Goodman-Breslin design procedure of ducts for smoothing of nominal-wakes of arbitrary harmonic orders as outlined in the following abstract from Reference 5:

"This study extends and improves the current propeller ducts design procedure, which substantially reduces selected spatial harmonics of any given ship model nominal wake and thus homogenizes the inflow field to the enshrouded propeller. This fact constitutes the most important factor in the study of the ducted-propeller problem since by controlling and homogenizing the propeller inflow field the vibratory characteristics of the system will be minimized and the intermittent blade cavitation will be reduced substantially. The duct shape is determined by means of the so-called "Penalty Function" which guarantees the minimum value of the net inflow field. Three schemes have been studied in the attempt to ameliorate the inflow field: Scheme #1, with duct of constant chord length but with varying camber, thickness distribution (keeping conicity angle and tip clearance constant). All schemes have been evaluated in terms of the existing propeller-duct interaction program and thus conclusion has been reached as for the most advantagious duct shape. Systematic calculations have been performed for two cases a) NSMB and b) SSPA ducted propeller operating in a wake of Series -60 (C_b = 0.6) equipped with three different stern configurations. Conclusions have been reached and recommendations have been made for the selection of the most effective design procedure."

These results for ducts in which the peripheral variation of camber and thickness ratios were achieved by finding the peripheral variation in chord to minimize the net harmonic amplitudes show that this method is not effective. However, Chen made unnecessary mathematical approximations in the process of his development.

For calculated values of peripheral variations in camber and thickness Chen showed a 50 percent reduction in the fourth harmonic amplitude of a particular nominal wake at 0.8 radius. However, upon use of this net harmonic as input to the Davidson Laboratory unsteady propeller force program, he found only a 15 percent reduction in blade frequency thrust for a 4 blade propeller. This result seems highly inconsistent.

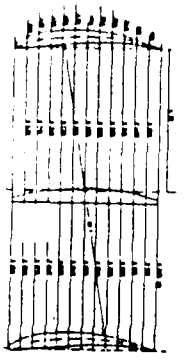

Figure 4. Cross Section of a Duct Designed by Drs. Breslin and Goodman to Ameliorate the First Harmonic of the Axial Component of a Ship Wake.

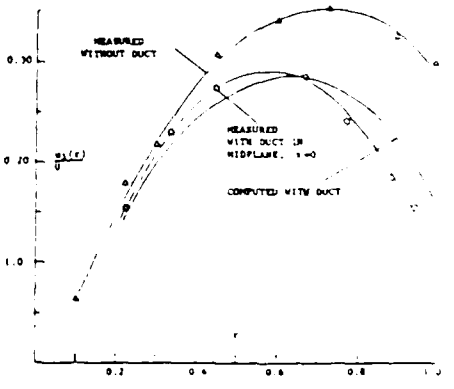

Figure 5. Radial Variation of First Harmonic of Screen-Generated Wake with and Without Duct Designed to Reduce this Harmonic Amplitude. (Tilt Angle α_1 = 0.156 rad; C_r=1.0, s=2, M=1, X_0=0.6)

REFERENCES (Stevens Institute of Technology)

Chen, J.K., "A Procedure for Design of Ducts Reduce Propeller Cavitations and Vibrations", Ph.D. Dissertation, Dept. of Civil and Ocean Engineering, Stevens Institute of Technology, August 1984.

Goodman, T.R., "Momentum Theory of a Propeller in a Shear Flow", Journal of Ship Research, Volume 23, No. 4, December 1979, pp. 242-252.

Goodman, T.R. and Breslin, J.P., "Theoretical and Experimental Induction Generated by a Propeller in an Axially Symmetric Shear Flow", Ocean Engineering Report SIT-OE-82-2, February 1982.

Goodman, T.R. and Breslin, J.P., "Design of Ducts to Reduce Cavitation and Vibration", Stevens Institute of Technology, Report SIT-DL-82-9-2298, Sept. 1982.

Lee, H., "Ducted Ship Propellers in Radially Sheared Flows", Ph.D. Dissertation, Dept. of Civil and Ocean Engineering, Stevens Institute of Technology, April 1985.

MARINE PROPULSORS FOR MINIMUM SHAFT-HORSEPOWER

T.E. Brockett and R.A. Korpus
Department of Naval Architecture and Marine Engineering
The University of Michigan
Ann Arbor, Michigan 48109

ABSTRACT

Results are presented for a non-linear constrained optimization technique applied to the selection of the circulation distribution for minimum shaft horsepower of conventional and preswirl propulsors. The non-linear mathematical model of the propulsor is a straight radial lifting line, representing the blades, with a vortex sheet trailing aft at a position that may be dependent on the solution. For the preswirl propulsor, an interaction velocity component is included and the thrust of the rotor is increased to overcome the vane drag. The major geometry variables and operating conditions are fixed in the extremum problem and the unknown circulation distribution is taken as a finite-term sine series. Several specifications of the shed-vortex sheet geometry (light, moderate, and approximately heavy loading) are included. It is demonstrated that recent investigations producing improved efficiency (relative to conventional criteria) with increased tip loads result from including a non-linear specification of the shed-vortex sheet orientation in the analysis which was not addressed in the approximate analytical optimizations. For the lightly-loaded case, Lerbs' criteria is essentially recaptured. For the conventional propeller with a non-linear specification of the shed-vortex sheet, efficiency values slightly greater than Lerbs' criteria can be produced with relatively smooth circulation distributions and significantly increased efficiency values are possible with highly-oscillatory distributions. For the preswirl propulsor, minimum shaft horsepower circulation distributions for a given upstream vane set show trends similar to the conventional propeller. For the preswirl propulsor, the shed-vortex sheet specification has a pronounced effect on the predicted efficiency.

1.0 INTRODUCTION

Recently there has been a renewed interest in increased overall propulsion efficiency. This interest is partially a result of a desire for reduced fuel consumption due to increased costs and has been further stimulated by the parametric investigations of Loukakis (1971,1981) and Khadjimikhalev (1979,1984) who showed that significant gains in efficiency (relative to conventional criteria) are possible with increased tip loading. In addition, it is known (Dyne, 1984) that compound propulsors offer a substantial increase in efficiency over the conventional propeller but procedures to define maximum hydrodynamic efficiency are unknown.

In the present work, we undertake to resolve these apparent differences in conditions for maximum efficiency and provide some insight into selection of circulation distribution for maximum efficiency of a preswirl propulsor consisting of a set of stationary vanes forward of the rotating blades. This configuration is mechanically simple and it's mathematical model is straightforward. Also it exhibits the essential feature of most compound propellers that produce efficiency gains over the isolated propeller (i.e., a significant tangential velocity component occurs at one blade row location). In subsequent paragraphs, the mathematical model of this configuration will be described.

In the present investigation, the extremum problem is simplified to the case of finding the circulation distribution that maximizes one restricted form of the propulsor efficiency:

$$\eta = C_{Th}/C_P \qquad (1)$$

for fixed thrust-loading coefficient $C_{Th} = 8T/(\rho V^2 \pi D^2)$, fixed major geometry variables (i.e., the tip and hub diameter, number of blades, chordlength distribution, thickness distribution, and blade mid-chord location) and fixed advance coefficient. That is, the power-loading coefficient, $C_P = 16\pi Qn/(\rho V^3 \pi D^2)$ is to be minimized for a given thrust. Such a formulation has an implicit assumption that the gear efficiency and the hull-propulsor interaction coefficients (thrust deduction, t, and local effective wake fraction, w_E) are unaffected by the selected circulation distribution. The assumption that the values of t and w_E are constant is only approximately valid but serves to make the problem manageable. (A more general -and more complex- hydrodynamic problem is to maximize the propulsive efficiency:

$$\eta_D = (1-t)C_{Th}/C_P \qquad (2)$$

for a fixed $(1-t)C_{Th}$ and variable C_P with major geometry and advance coefficient fixed.)

To proceed further, an algorithm relating the power-loading and thrust-loading coefficients to the circulation must be specified. One form of this relationship is the lifting-line model (Moriya, 1933; Lerbs, 1952; and summary by Morgan and Wrench, 1965). The equations resulting from this model are non-linear in two aspects: first the local velocity used to compute the load consists of the sum of a zeroth-order contribution from the onset stream plus the induced velocity, and second, the induced velocity (and hence flow angle) is a nested function of the circulation at the blades. This nesting is the explicit dependence on circulation for the induced velocity and an implicit dependence of the geometry of a filament in the shed-vortex sheet on circulation (representing the requirement that it follow a path that makes the pressure equal on both sides of the vortex surface). These non-linearities make the problem more difficult to solve relative to the linear dependence on circulation for the lift and non-linear drag dependence classically addressed for the planar wing.

Early attempts at finding a condition for the propeller maximum efficiency (e.g., Betz, 1919; Lerbs, 1952; van Manen, 1955; Burrill, 1955) were not as rigorous mathematically as more recent attempts employing calculus of variations (Courant, 1953 and Wu, 1973). The calculus of variations approach for the propeller was initiated by Moriya (1938), in an elegant numerical analysis, and picked up later by Wehausen (1964) followed by Morgan and Wrench (1965); by Yim (1976); and by Achkinadzhe (1985). The most complete of these treatments is that of Achkinadzhe, who includes a tangential preswirl component in his analysis. The recent attempts are all characterized by two approximations:

(1) simplifications in the treatment of a complicated integro-differential equation that is the optimizing condition, and

(2) explicit neglect of the implicit dependence on circulation in the nested non-linearity for induced velocity described in the preceding paragraph (i.e., for computing the induced velocity components required in the load integrals, the pitch of the shed-vortex sheet is specified rather than dependent on the circulation).

The first condition has been investigated and found to be essentially negligible, but the second aspect was not investigated. In one simple approximate form, the mathematically derived results recapture the Lerbs (1952) criteria, i.e., that the condition for maximum efficiency results when the hydrodynamic pitch is proportional to the square root of the local wake.

More recently Brockett and Korpus (1986) have used a non-linear optimizing code and include all the non-linearities in the analysis plus an ability to vary the specification of the shed-vortex sheet geometry. One result of their limited investigation is confirmation of the parametric investigation of Loukakis and Khadjimikhalev when the pitch of the shed vortex sheet depends on the circulation and agreement with the more traditional criteria when the pitch of the shed-vortex sheet is fixed. Hence it is clear that the difference in the trend of the mathematical calculus of variation analysis and the parametric trends is a consequence of including (or ignoring) the implicit non-linearity. Since it is the inclusion of this non-linearity in the analysis that is the essential feature of the trend of the results obtained relative to tip loading, it will be called a non-linear analysis when a variable position of the shed-vortex sheet is included and linear when the sheet geometry is fixed in the extremum problem.

In the present work we are concerned with the classical problem of finding the shape of the circulation distribution for maximum efficiency with a fixed thrust. In design practice, a more global problem is addressed involving additional practical constraints such as structural integrity, noise, vibration, weight, stopping and cost. A search for the maximum efficiency (or minimum cost) subject to these additional constraints is possible but it is specific to the particular problem. We do not consider this realistically-constrained optimization problem but note that it will add at least one additional constraint relative to the circulation distribution: limits on the slope in order to avoid trailing-vortex cavitation. Most of the other constraints are such that the geometry is influenced but not necessarily the circulation distribution.

In the present paper, the investigation of Brockett and Korpus (1986) is reviewed and extended for maximum propeller efficiency of both conventional and preswirl propulsors. In the following section a description of the lifting-line model of the conventional and preswirl propulsor is outlined, then the non-linear optimizing code is described, followed by definition of the parent operating conditions, the results and conclusions.

2. LIFTING-LINE MODEL

The equations selected to govern the optimization process, and which are to be solved (as part of the extremum problem), are those appropriate for a lifting line representation of the blades of a propeller. The presence of the hub is ignored and the blade becomes a straight radial line from which vortex filaments trail aft in a helicoidal path. In our previous investigation (Brockett and Korpus, 1986) these filaments were taken as quite general geometrical specifications. However, the contraction has a negligible effect on the predicted efficiency and hence we ignore that aspect in the present work. We did find (in agreement with others) that the pitch of the filaments was significant and include in our model a provision for a pitch of the sheets different than the hydrodynamic pitch at the blades. The pitch angle of the sheets is β_W and the pitch angle at the blades is β_I. The

functional to be minimized (the power-loading coefficient of the rotating blades, with subscript b denoting the blade) is given as:

$$C_P = 16\pi Qn/(\rho V^3 \pi D_b^2)$$

$$= \frac{4\pi Z_b}{J} \int_{x_{hb}}^{1} x_R \, G_b(x_R) v_{Ab} \left[1 + C_{Db}/(C_{Lb}\tan\beta_{Ib})\right] dx_R \quad (3)$$

where

$$v_{Ab} = 1 - w_{Eb}(x_R)$$

$$+ \frac{1}{2} \fint_{x_{hb}}^{1} \frac{dG_b}{dx_{Ro}} \frac{I_{Ab}(x_R, x_{Ro}; \beta_{wb})}{x_R - x_{Ro}} dx_{Ro} \quad (4)$$

which holds for either a single or preswirl propulsor. The I_A and I_T terms are calculated from the approximations developed by Wrench (see Morgan and Wrench, 1965). The functional forming the equality constraint for single propellers is the thrust-loading coefficient:

$$C_{Th} = C_{Thdesign} = 8T_b/(\rho V^2 \pi D_b^2)$$

$$= 4Z_b \int_{x_{hb}}^{1} G_b(x_R) v_{Tb} \left[1 - (C_{Db}/C_{Lb})\tan\beta_{Ib}\right] dx_R \quad (5)$$

where

$$v_{Tb} = \frac{\pi x_R}{J} - \frac{1}{2} \fint_{x_{hb}}^{1} \frac{dG_b}{dx_{Ro}} \frac{I_{Tb}(x_R, x_{Ro}; \beta_{wb})}{x_R - x_{Ro}} dx_{Ro} \quad (6)$$

The equality constraint for preswirl propulsors is given by (sub b for blades, v for vanes):

$$C_{Th} = C_{Thdesign} = 8(T_b + T_v)/(\rho V^2 \pi D_b^2)$$

$$= 4Z_b \int_{x_{hb}}^{1} G_b(x_R) v_{Tb} \left[1 - (C_{Db}/C_{Lb})\tan\beta_{Ib}\right] dx_R$$

$$+ 4Z_v \left(\frac{D_v}{D_b}\right)^2 \int_{x_{hv}}^{1} G_v(x_R) v_{Tv} \left[1 - (C_{Dv}/C_{Lv})\tan\beta_{Iv}\right] dx_R \quad (7)$$

where

$$v_{Tb} = \frac{\pi x_R}{J} - \frac{1}{2} \fint_{x_{hb}}^{1} \frac{dG_b}{dx_{Ro}} \frac{I_{Tb}(x_R, x_{Ro}; \beta_{wb})}{x_R - x_{Ro}} dx_{Ro}$$

$$+ \bar{U}_{To}(x_R) \quad (8)$$

$$v_{Tv} = -\frac{1}{2} \fint_{x_{hv}}^{1} \frac{dG_v}{dx_{Ro}} \frac{I_{Tv}(x_R, x_{Ro}; \beta_{wv})}{x_R - x_{Ro}} dx_{Ro} \quad (9)$$

The last term in the v_{Tb} equation (equation 8) constitutes the velocity field coupling between the vanes and blades and represents the circumferentially averaged tangential velocity component induced in the plane of the blades by the vanes. It can be derived by an application of Stokes law for potential flow:

$$\bar{U}_{To} = -\frac{ZG_v}{x_{Rb}} \frac{(x_{Rb} + \Delta x_R)}{} \cdot \frac{D_v}{D_b} \quad (10)$$

where $\Delta x_R(x_R)$ = x_R of filaments leaving vanes $- x_R$ of filaments at blades = $x_{Rv} - x_{Rb}$,

but must be directly computed for wake-adapted propulsors. Another coupling (which doesn't manifest itself in the above equations) is the circumferentially averaged axial velocity induced in the plane of the vanes by the blades. Provisions for these terms are included in the lifting line codes but are assumed negligible for a preswirl propulsor. Of the remaining coupling terms, the tangential induced velocity at the vanes due to the blades can be shown to be zero for potential flow; and the axial induced velocity at the blades due to the vanes is neglected as higher order. (Note that G_v is generally negative.)

The complicating aspect of equations (3-9) is that the functions I_A, I_T, β_I, β_w, and C_L all exhibit complex dependence on the functions to be minimized, G_b and G_v.

The various trailing vortex sheet geometries have been included in the above programs through the definition of β_w. The lightly and moderately loaded geometries follow the definitions set forth by Lerbs (1952) and Prandtl (see discussion of Betz, 1919). That is; the lightly loaded β_w is aligned with the local geometric advance angle β, while the moderately loaded β_w is aligned with the local hydrodynamic advance angle at the blade ($\beta_w = \beta_I$). Our heavily-loaded model takes this one step further and aligns β_w with the downstream wake velocity. This velocity is estimated as that obtained by using twice the values of the calculated induced velocities (U_A,U_T) at the lifting line (with Wrench's induction factors), the concept being that the wake is no longer semi-infinite, but infinite.

The codes developed by Brockett (1979) for single propellers, and subsequentially adapted for preswirl propulsors (Brockett and Korpus, 1986), were chosen for this work. These codes run very fast, and utilize Fourier series representations for all numerical differentiation and integration. This last attribute is believed important since it should eliminate any chances of "numerical aliasing." That is, minimize the value of a derivative or integrand at discrete integration points rather than over the whole span. Another benefit of these codes is that they have been extended to include the lightly/moderately/heavily loaded models of wake geometry (see description by Brockett and Korpus, 1986). Some data were also derived from a slight modification of the code described by Caster (1975) that is based on input values of the hydrodynamic pitch.

3. OPTIMIZATION METHOD

The procedure is essentially a Ritz method. The assumption is made that the optimum circulation distribution can be represented by a Fourier sine series:

$$G(\varphi) = \sum_{n=1}^{N} G_n \sin(n\phi) \quad . \qquad (11)$$

where N is the number of coefficients to be optimized. If one substitutes this representation for G into the equations for the load developed by the lifting line, the problem of finding G to minimize C_P for a given C_{Th} is reduced to optimizing a finite number of discrete variables. This is much like the Reyleigh-Ritz method of structural analysis, but, because of the implicit dependence of the induction factors and the β's on G, a quadratic functional does not result, and there is little chance of solving the full problem analytically.

Because of these non-linearities in the resulting systems of equations, no attempt was made to solve for the optimum G_n's analytically. Rather, the lifting-line code was treated as a "black box," where the G_n's are input and C_{Th} and C_P are returned. A systematic variation was then set up utilizing this black box to find the optimum set of G_n's.

The other half of this systematic variation was performed by a non-linear constrained optimization program called GRG2 (Lasden, et al., 1978,1980). This program uses a conjugate gradient search algorithm, coupled with a non-linear Newton-Rhapson solver for meeting the constraints, to take a new guess at the constrained optimum G_n's. Essentially, the two black boxes work in a cycle: GRG2 guesses at the G_n's, and the lifting-line code calculates C_{Th} and C_P. From the results of the last few guesses, GRG2 figures out the best direction in which to search for its next attempt.

4. PARENT PROPULSOR

The starting point for our investigations was the conditions specified in Table 1, corresponding to NSRDC model 4381 (Boswell, 1971). Most of our investigations are for operation in uniform flow but for some aspects a variable wake was selected to be a scaled version (to give a unit volume mean) of that determined by Huang (1978) for an axisymmetric body of revolution. For preswirl cases the vane chord profile was kept proportional to that of the blades, and the vane diameter was set to 1.08 times the propeller diameter. The empirical vane wake contraction data presented in the table are propeller values extrapolated by Greeley and Kerwin (1982) from Min's (1978) measurements, but were found to have a minor effect.

For the most part, blade and vane geometry such as chord length, diameter, and hub radius, are considered constant, as is the advance ratio. These parameters are most likely fixed by other practical design constraints (described previously for the realistically-constrained optimization) that need not be treated at this point. The one exception is the vane chord lengths. Arbitrary selection of the vane chords, independent of loading, can bias the results by over or under weighting the added viscous drag due to the vanes. Therefore, the magnitude of the vane chord distribution is selected to be proportional to values in Table 1 but adjusted to keep the maximum lift coefficient at 0.8 (as was described by Brockett and Korpus, 1986).

Table 1

Parent Propeller, NSRDC 4381 from Boswell (1971) and Onset Flow from Huang (1978)

C_{Th} = 0.69 J = 0.89
C_D = 0.0085 t = 0.0
Z_b = 5 Z_v = 9
D_v/D_b = 1.08

x_{Rb}	$c(x_R)/D$	$1-w_E(x_R)$	contraction ratio of vane vortex filaments*
0.200	0.174	0.605	1.060
0.250	0.202	0.667	1.052
0.300	0.229	0.725	1.045
0.400	0.275	0.821	1.032
0.500	0.312	0.899	1.020
0.600	0.337	0.959	1.011
0.700	0.347	1.012	1.005
0.800	0.334	1.056	1.004
0.900	0.280	1.100	1.014
0.950	0.218	1.123	1.032
1.000	0.000	1.145	1.080

*x_{Rv} of filaments leaving vanes/x_{Rb} of filaments at blades

Some of our parametric investigations include modifications to the diameter for the same required thrust and rpm. Hence the load coefficient and advance coefficient change with this parameter. In addition, the blade area is constrained to vary as the diameter ratio squared. This criteria is essentially one providing for equal margin against thrust breakdown. Other minor adjustments were also made to keep the hub radius fixed and adjust the radial stations proportionally.

5. DISCUSSION OF RESULTS

Our first investigation was to determine whether or not there was significant differences between the Lerbs and van Manen criteria for the relationship between hydrodynamic pitch and effective wake fraction. These criteria are both of the form

$$P_I(x_R) \sim [1 - w_E(x_R)]^A \qquad (12)$$

with Lerbs choosing A = 1/2 and van Manen proposing A = 3/4. We modified the code of Caster (1975) and performed a series of computations for various C_{Th} and J values using the geometry and wake of Table 1. One result of this investigation is shown in Figure 1 for the parent J condition (from Brockett and Korpus, 1986). Figure 2 shows the power A to produce maximum efficiency as a function of C_{Th} for J values of maximum efficiency using Lerbs' criteria. The dependence of A on C_{Th} is linear and

extrapolates to A = 1/2 at zero load but is more representative of van Manen's criteria near the parent load coefficient.

Brockett and Korpus (1986) have shown similar trends for both wake-adapted and uniform-flow propulsors and hence the rest of our investigation is concerned with only uniform flow.

In Figure 3 data (Brockett and Korpus, 1986) for the maximum efficiency as a function of number of terms in the circulation distribution (for the moderately-loaded shed-vortex-sheet representation) are given. A modest increase in efficiency is possible with a slight increase in tip loading and, as shown in Figure 4, a non-linear increase in efficiency occurs as the number of terms becomes large. Hence with a greater number of terms, significant gains are possible but the shape of the circulation becomes unrealistically oscillatory from the standpoint of real flow. In Figure 5 the results for the 5 term series are shown as a function of the shed-vortex-sheet specification. As is clear, the Lerbs' criteria is recaptured for the linear model and the non-linear models indicate tendency for increased tip loads.

The values of efficiency shown in Figure 5 have the same shed-vortex sheet location for the optimization search and the load predictions. However, it is more common to use the moderately-loaded non-linear specification of the shed-vortex sheet orientation to predict loads. In Table 2, the efficiency for each of the shapes shown in Figure 5 is presented for the various models of the shed-vortex sheet. In these calculations, the shape was specified

Table 2

Efficiency as a Function of Shed-Vortex Sheet Orientation at Parent Operating Conditions (5-Term Sine Series)

Specification of Shed-Vortex Sheet used in Optimization	SHED-VORTEX SHEET SPECIFICATION EMPLOYED IN CALCULATION		
	LIGHT	MOD	HEAVY
LIGHT	0.681	0.703	0.716
MODERATE	0.669	0.716	0.741
HEAVY	0.662	0.715	0.744

and the magnitude adjusted to produce the required C_{Th} at the given J value. These computations show minor differences for the various circulation distributions for a consistent vortex-sheet model (i.e., the columns are only a percent or two different in value).

Parametric calculations for preswirl propulsors are given by Brockett and Korpus (1986). Some of the results are that maximum efficiency results from a low vane drag and high propeller efficiency and that independent load distributions on the vanes and rotor can produce high efficiency values. Also, a difference in efficiency of over 7 points at the parent operating point was predicted for the various models of the shed-vortex sheet for a given vane configuration and fixed circulation distribution. Representative data are shown in Figure 6, repeated from that reference. This figure illustrates two features of the preswirl propulsor performance for the systematic variations described in section 4: (1) the increase in efficiency is negligible to moderate for the parent and lighter loads (i.e, increased diameter) but becomes quite significant for increased load (or reduced diameter), and (2) the maximum efficiency occurs for the case that the preswirl does not cancel the rotor swirl velocity (the speed cancellation ratio is almost equal to the torque ratio). Hence, applications with restricted diameter show most improvement when preswirl vanes are employed.

In Table 3 and Figure 7, data are given for various preswirl loads and number of terms in the circulation distribution for operation behind the vanes designed for elliptic circulation on the rotor. As can be seen, the 5-term optimum distributions are superior to the results for the propeller-alone distributions (N < 5). As shown in Figure 4 and Table 3, non-linear increases in efficiency are evident with the 7-term series.

Table 3

Net Efficiency for Various Rotor Circulations Operating behind a Set of Vanes Originally for the Elliptic Rotor with Swirl Cancellation of 0.75 at Parent Conditions (Moderately Loaded)

Rotor Circulation	η
Elliptic	0.720
Prop, 5 Terms	0.731
Tip, 9 Terms	0.735
Opt, 3 Terms	0.725
Opt, 5 Terms	0.733
Opt, 7 Terms	0.752

As a final data set, we have calculated the efficiency of a series of more heavily-loaded preswirl propulsors as a function of shed-vortex-sheet specification. These computations correspond to the reduced diameter ($0.8D_o$), and 0.75 speed ratio of Figure 6. The vanes for the elliptic-loaded rotor are used with both the elliptic-loaded rotor and the tip-loaded rotor. Data are given in Table 4 for the parent condition and a reduced diameter condition. As can be seen, the reduced diameter condition produces an even greater influence of the shed-vortex sheet orientation than occurs for the parent condition. Also, for the heavily-loaded condition, some induced velocities become so large that they exceeded the onset flow and unrealistic flow angles are predicted and hence data are not given for

those cases. In any event, as much as 10 points increase in efficiency is predicted for the tip-loaded rotor circulation distribution when the shed-vortex sheet orientation follows the moderately-loaded flow angle rather than the lightly-loaded flow angle. Hence, the specification of the vortex sheet orientation is a critical practical issue to be resolved for these highly-efficient propulsors. We suspect similar differences occur for other interacting blade rows such as contra-rotating, post-swirl and vane-wheel propulsors.

C. For preswirl propulsors, systematic variations in parameters indicates that little gain in efficiency relative to a propeller is expected for lightly-loaded rotors but a significant improvement in efficiency is possible for increased loading cases.

D. For preswirl propulsors, the maximum efficiency occurs with arbitrary distributions of circulation on the vanes and rotor, but generally

Table 4: Preswirl Propulsor Efficiency as a Function of Shed-Vortex Sheet Orientation

	Parent Conditions		0.8 Parent Diameter with same T, n		
Shed-Vortex Sheet Orientation	Elliptic Rotor	Tip-Loaded Rotor	Propeller only Elliptic G	Elliptic Rotor	Tip-Loaded Rotor
Light	0.702	0.689	0.548	0.631	0.605
Moderate	0.720	0.735	0.581	0.667	0.715
Heavy	0.731	0.759	0.604	0.689	N/A
Max $\Delta\eta$ (points)	3	7	6	6	--

6. CONCLUSIONS

A. For improved efficiency, the relationship between the hydrodynamic pitch and a power of the local effective onset speed is variable with thrust loading. In general, less than a half point increase in efficiency occurs relative to Lerbs criteria. The van Manen criteria of $A = 0.75$ in equation 12 is preferred to Lerbs value of 0.5.

B. The different trends between the conventional (Lerbs, van Manen, and Burrill) criteria and the tip-loaded criteria for improved efficiency is a result of the neglect or inclusion of non-linear specification of the shed-vortex sheet orientation. The full non-linear model of propeller performance leads to shapes of the circulation distribution that are remarkably different than for the conventional criteria. For a reduced number of terms in the sine series representation of the circulation distribution, the shape is not greatly different than the Lerbs criteria and small efficiency gains are predicted. With a large number of terms, significant increases in efficiency are possible but strong viscous effects are expected. This possibility of viscous effects must be carefully evaluated before any of the tip-loaded distributions are used.

efficient vanes and efficient rotor are necessary for superior performance.

E. The specification of the shed-vortex sheet orientation for preswirl propulsors may lead to 10 point differences in efficiency between the various sheet models. Hence there is an urgent need to quantify the actual sheet orientation in the mathematical model.

F. Numerical inconsistencies prevented the inclusion of conditions for maximum efficiency for independent vane/rotor loads.

G. Recent experience has shown the optimum circulation distribution (but not the efficiency) to be sensitive to the initial guess.

7. ACKNOWLEDGEMENTS

The work reported herein was sponsored in part by the Office of Naval Research under the Accelerated Research Initiative on Propulsor-Hull Hydrodynamics Interaction, contract N00014-86-K-0058, administered by Dr. C.M. Lee, and in part by the University of Michigan. In addition, special thanks are due to members of the 18th ITTC Propulsor Committee for enlightening discussions, especially Dr. W. van Gent and Dr. B. Biskoup.

REFERENCES

Achkinadzhe, A.S. (1985), "Generalization of the Betz Theorem for the Case of Arbitrary Induced Velocities Accounting for the Profile Losses at a Given Shape of the Free Vortices," Proceedings of the 5th National Congress on Theoretical and Applied Mechanics, Varna, Bulgaria, Vol. 2 and 3.

Betz, A. (1919), "Schraubenpropeller mit geringstem Energieverlust," Mit einem Zusatz von L. Prandtl. Nachrichten der K. Gesellschaft der Wissenschaften zu Gottingen. Math.-Phys. Klasse, pp. 193-217.

Boswell, R.J. (1971), "Design, Cavitation Performance and Open-Water Performance of a Series of Research Skewed Propellers," NSRDC Report 3339, Washington, D.C.

Brockett (1979), "A Lifting Line Computer Program Based on Circulation for Preliminary Hydrodynamic Design of Propellers," Defence Research Establishment Atlantic, Canada, Tech. Memo 79/E.

Brockett, T., and Korpus, R. (1986), "Parametric Evaluation of the Lifting Line Model for Conventional and Preswirl Propulsors," Proceedings International Symposium on Propellers and Cavitation (ISP-86), Wuxi, China.

Burrill, L.C. (1955), "The Optimum Diameter of Marine Propellers, A New Design Approach," Trans. NECIES, Vol. 72, pp. 61-73.

Caster, E.B., et al (1975), "A Lifting-Line Computer Program for Preliminary Design of Propellers," NSRDC Report No. SPD-595-01.

Courant, R. and Hilbert, D. (1953), Methods of Mathematical Physics, 2 Vols. Interscience.

Dyne, G., et al (1984), "Propeller Committee Report," Proceedings 17TH ITTC Vol. 1, Goteborg.

Greeley, D. and Kerwin, J.E. (1982), "Numerical Methods for Propeller Design and Analysis in Steady Flow," SNAME Trans., Vol. 90, pp. 415-453.

Holden, K., et al (1983), "On Optimum Skew Propeller Designs and Total Propulsive Efficiency," Int. Symp. on Ship Hydrodynamics and Energy Saving, El Pardo.

Huang, T.T., et al (1978), "Stern Boundary-Layer Flow on Axi-Symmetric Bodies," 12TH Symposium on Naval Hydrodynamics, Nat. Acad. of Sci., pp. 127-157.

Khadjimikhalev, V.H. (1979), "Theoretical and Experimental Investigations on the Influence of Load Distribution along the Screw Radius upon its Hydrodynamic Characteristics," Conference on Methods and Means for Investigation of Ship Propulsion, B.S.H.C. pp. 12-1 to 12-4.

Khadjimikhalev, V.H. (1984), "Numerical Investigation Into the Effect of Loading of the Propeller Blade Tips upon its Efficiency and Vibration," Voprosy Sudostroienija, Seria "Proektirovanie Sudov," Vyp. 39, pp. 21-26.

Lerbs, H. (1952), "Moderately Loaded Propellers with a Finite Number of Blades and an Arbitrary Distribution of Circulation," SNAME Trans., Vol. 60, pp. 73-117.

Loukakis, T. (1971), "A New Theory for the Wake of Marine Propellers," MIT Dept. of Ocean Eng. Report 71-7.

Loukakis, T. and Politis, G. (1981), "On Optimum Propeller Performance," Propellers '81, SNAME T&R Symposium S-7.

Min, K.-S. (1978), "Numerical and Experimental Methods for the Prediction of Field Point Velocities Around Propeller Blades," MIT Dept of Ocean Engineering Report 78-12, Boston, MA.

Morgan, W.B., and Wrench, J.W. Jr. (1965), "Some Computational Aspects of Propeller Design," Methods in Computational Physics, Vol. 4, Academic Press, pp. 301-331.

Moriya, T. (1933), "On the Induced Velocity and Characteristics of a Propeller," Jour. Faculty of Eng., Tokyo Imp. Univ., Vol XX, No. 7, pp. 147-162.

Moriya, T. (1938), "Formulae of Propeller Characteristics Calculation and a Method to Obtain the Best Pitch Distribution," J. Soc. Aero. Sci., Japan, Vol. 5, No. 42, pp. 995-1005.

Lasden, L.S., et al (1978), "Design and Testing of a Generalized Reduced Gradient Code for Non-Linear Programming," ACM Trans. on Math. Software, Vol. 4, No. 1, pp. 34-50.

Lasden, L.S., et al (1980), "GRG2 User's Guide," Univ. of Texas, Dept. of Mechanical Engineering.

van Manen, J.D. (1955), "Fundamentals of Ship Resistance and Propulsion; Part B: Propulsion," NSMB Publication No. 132a.

Wehausen, J.V. (1964), "Lecture Notes on Propeller Theory," NAME Dept. Univ. of California, Berkeley.

Wu, T.Y.-T. and A.K. Whitney (1973), "Variational Calculus Involving Singular Integral Equations," ZAMM Vol. 53, pp. 737-749.

Yim, B. (1976), "Optimum Propellers with Cavity-Drag and Friction-Drag Effects," Journal of Ship Research, Vol. 20, No. 2. pp. 118-123.

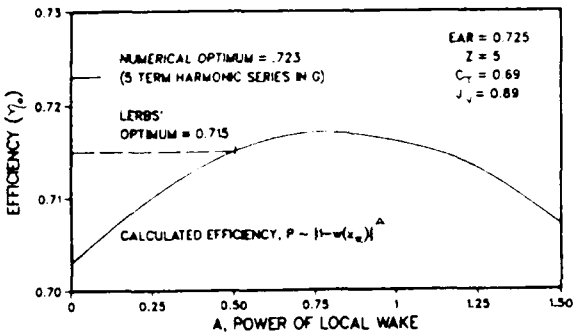

Figure 1. Efficiency vs. Exponent of Local Onset Flow

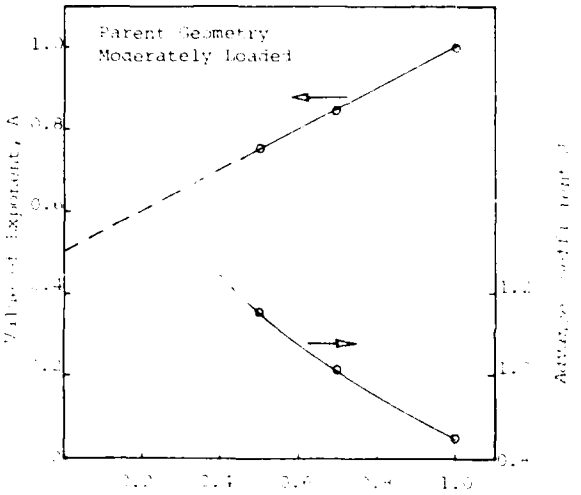

Figure 2. Exponent of Effective Onset Speed for Maximum Efficiency

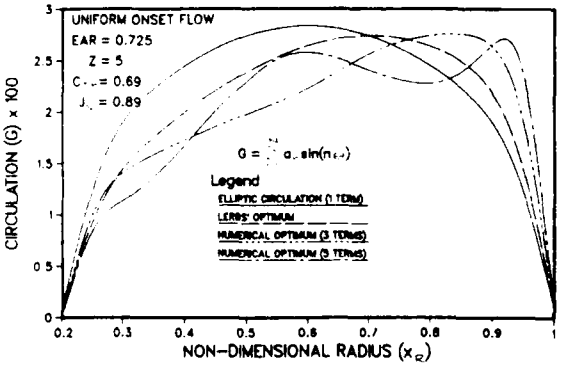

FIGURE 3 – Ciculation Distributions for Maximum Efficiency
(MODERATE LOADING MODEL)

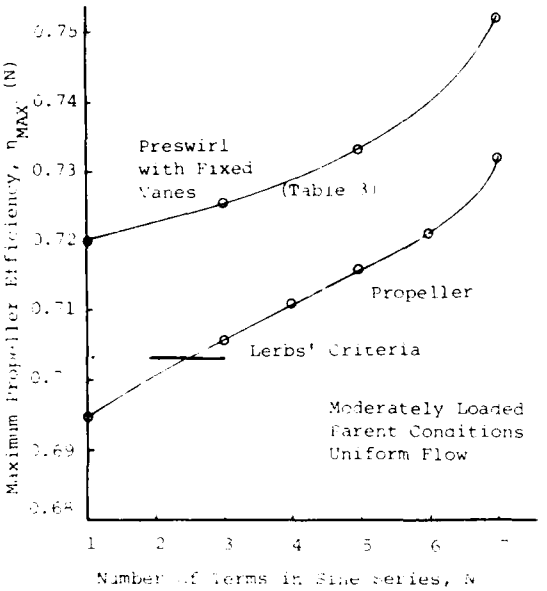

Figure 4. Maximum Efficiency as a Function of Number of Terms in Sine Series

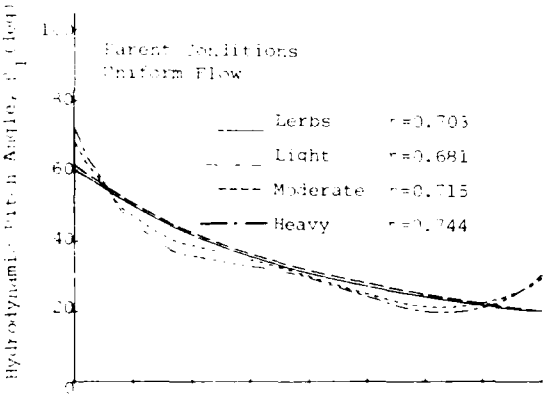

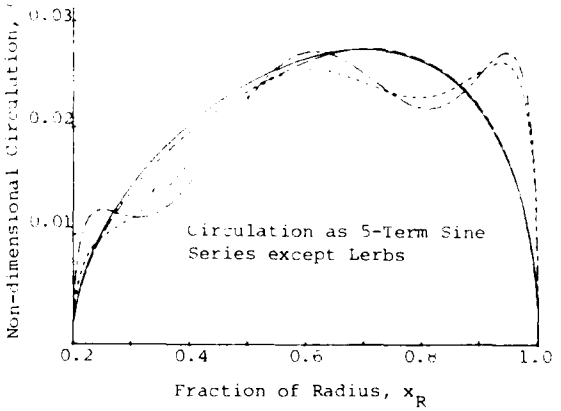

Figure 5. Propellers of Minimum SHP as a Function of Shed-Vortex Sheet Orientation

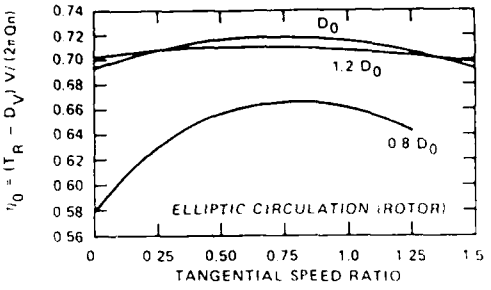

Figure 6. **Efficiency as a Function** of Diameter and Swirl Cancellation for Elliptic Circulation on Rotor

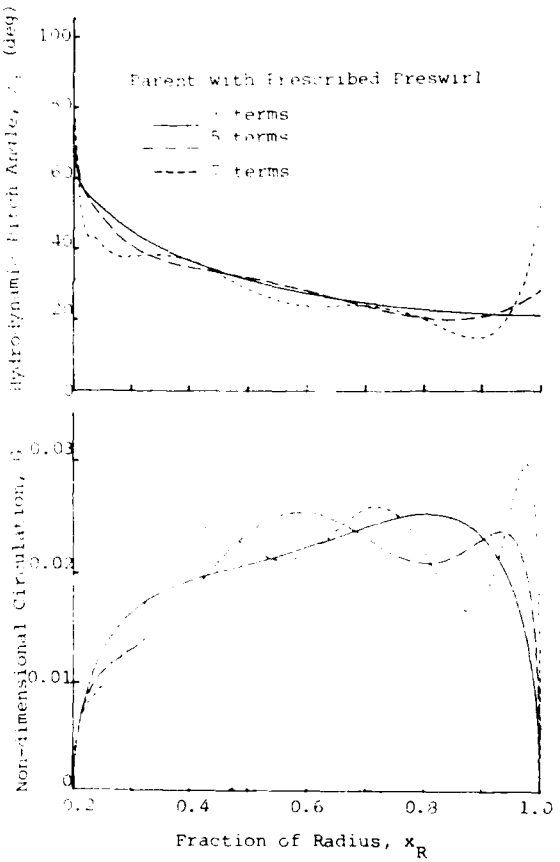

Figure 7. Preswirl Rotors of Minimum SHP for Prescribed Vanes (3,5,7 terms)

EVALUATION OF SOME PROPELLER ANALYSIS METHODS

J.L. Kennedy, D.J. Noble and C.M. Casgrain

Defence Research Establishment Atlantic
P.O. Box 1012
Dartmouth, Nova Scotia, Canada

ABSTRACT

This study examines the correlation of some current propeller analysis programs with model test data, over a wide range of operating conditions, in order to determine the suitability of the analysis methods for preliminary assessment of propeller designs. Actuator disk theory is used to define input parameters for the propeller wake geometry using two different wakes. Predictions from the lifting-surface analysis code PUF-2 developed at the Massachusetts Institute of Technology (MIT) and from a related cavitation prediction program recently developed at the Defence Research Establishment Atlantic (DREA) are compared with experimental data obtained in the depressurized towing tank of the Maritime Research Institute Netherlands (MARIN).

NOTATION

c_a dimensionless axial velocity increment

C_D drag coefficient

C_p pressure coefficient

C_p^* critical pressure coefficient

C_T thrust loading coefficient

K_T thrust coefficient

K_Q torque coefficient

R radius of the propeller tip

R_{uw} radius of the ultimate wake

V_i cavitation inception speed

V_s ship speed

V_w mean axial velocity in the wake

β_T transition wake pitch angle

β_w ultimate wake pitch angle

$\bar{\beta}_w$ mean pitch angle for the wake

η propeller open water efficiency

η_D propeller efficiency in behind condition

Ω propeller angular rotation rate

1. INTRODUCTION

The designer of naval propellers is tasked with designing propulsors to meet increasingly demanding propulsion and cavitation requirements. The approximations which are made in the design process may result in a propeller which will not completely satisfy the design objectives. Model testing of propellers is expensive; thus propeller analysis methods are routinely used to check the suitability of a design prior to embarking on a model test program. The designer needs to know the correct mix of parameters associated with theoretical design and analysis methods which will produce the most reliable results. It is also important that the ultimate accuracy of the analysis methods be defined in order that the designer knows when he must resort to model testing.

For propulsive performance it is advisable to assess the performance at off design conditions, although emphasis is usually placed on the design condition. The performance at off design conditions is required for the machinery control systems and for cases where the structural loading of the propeller is extreme. For cavitation prediction the ship's operating conditions are of most concern. Modern theoretical methods must therefore be sufficiently versatile to predict propeller performance and cavitation over a wide range of operating conditions.

The evaluation of the capabilities of propulsion and cavitation prediction methods which follows draws comparisons between results of prediction methods and model test data, not full scale data. This then leaves out the problems of model/full scale correlation.

2. MATHEMATICAL MODELS

The major part of the theoretical data reported here has been obtained using the MIT

propeller analysis code PUF-2 and an extension thereof called CAVITY. These are lifting-surface methods in which the propeller blades are represented by a distribution of vortices and sources lying on the blades' mean camber surfaces. The propeller wake is represented by vortex distributions downstream of the blades. PUF-2 can calculate propeller forces and moments for both the steady flow, open water case; and for the unsteady flow, behind case, when operating in the wake of a ship hull. A full description of the method is provided by Kerwin and Lee (1978).

Recently program CAVITY has been developed at the Defence Research Establishment Atlantic (DREA) to predict ship speed for cavitation inception and back sheet cavitation extent and thickness distributions at a given operating condition. Inception speeds are obtained by using a linear Bernoulli equation to evaluate pressure coefficients on the blade surfaces at a given operating speed and then extrapolating at the minimum pressure points for fixed advance coefficient to obtain the speed corresponding to the critical pressure coefficient at the vapour pressure of water. If V_i and V_s are the inception speed and trial ship speed and C_p and C_p^* are the minimum pressure coefficient and critical pressure coefficient corresponding to V_s, then the following relationship applies in linear, potential flow.

$$V_i = \sqrt{\frac{C_p^*}{C_p}}\, V_s \qquad (1)$$

The procedures in CAVITY for calculating back sheet cavitation development are based on methods developed by Lee (1980) and Van Houten (1982). Some modifications to Lee's method concerning chordwise singularity and control point distributions as well as downstream wake modelling are described in the paper by Noble, Sponagle and Leggat (1986).

The geometry of the trailing vortex system has a considerable influence on the induced velocities and hence on the calculated blade forces. As this geometry in turn depends on the propeller blade forces, it must be calculated by iterative procedures. In order to reduce the computational effort, it is desirable to find a model for the wake geometry which closely approximates the final solution obtained with such a procedure. This has been the objective of many researchers including Cummings (1976), and Greeley and Kerwin (1982). The latter, however, used a prescribed radial contraction of the wake coupled with a fast iterative wake alignment scheme to provide wake pitch distributions in steady flow applications.

The wake model, which is used in PUF-2, is sketched in Figure 1. It consists first of a transition wake, where the trailing vortex sheet behind a blade contracts uniformly into two roll-up points, one at the propeller axis and one downstream of the blade tip with a radial location defined by the contraction of the slipstream. Downstream of the roll-up points there is the ultimate wake which consists of a concentrated helical tip vortex and a hub vortex. The PUF-2 code must be supplied with an estimate of the roll-up radius R_{uw} and the angle in the rotation plane that the outer wake turns from the blade tip to the roll-up points. It also must be given the pitch angle at the outer edge of the transition wake, ϕ_T, and the pitch angle of the ultimate tip vortex helix, ϕ_w. The user of the program must choose suitable values for these parameters and this study examines the effects of such choices on results obtained.

Other wake models have been used by a variety of authors. For cavitation prediction, Lee uses a linear model in which the entire wake is an undeformed helical sheet of fixed pitch with no contraction. Another version described by Van Houten, Kerwin and Uhlman (1983) has no contraction of the near wake but is followed by a sudden transition to a rolled-up ultimate wake. In addition, as distinct from PUF-2, this latter version includes a gradual decay of shed vortex strengths to zero at the roll-up location, and constant values of ultimate wake tip and hub vortex strengths related to the maximum mean circulation on the blades. This model can provide faster convergence for unsteady cavitation predictions than the PUF-2 model, and some results obtained with this wake are also included here.

In selecting a slipstream contraction model, Kerwin and Lee propose that a value based on experimental data of $R_{uw}/R = 0.83$ applies to a wide variety of propellers at advance coefficients around the design point. They, however, note that some highly skewed propellers show somewhat less contraction. Kerwin and Lee also point out that the effect of variations of the transition wake pitch angle on blade thrust are quite substantial for a five-bladed propeller. They suggest that ϕ_T might best be estimated as an average of the undisturbed advance angle and the hydrodynamic advance angle from lifting-line theory.

Cummings has investigated the use of actuator disk theory to predict the wake contraction and the wake pitch angle. He concluded that this approach can lead to misleading conclusions about the geometry of the ultimate wake, due to the finite number of blades, vortex roll-up and the non-constant axial velocity increment across the slipstream. The PUF-2 wake incorporates vortex roll-up, and so the results of applying actuator disk results to this particular wake model are worth examining.

Simple actuator disk theory predicts that the inflow velocity into the propeller is increased from a value V_a far upstream of the propeller to a value $V_a\,(1 + c_a/2)$ at the propeller plane and $V_a\,(1 + c_a)$ far downstream as shown in Figure 2. Here c_a is the dimensionaless axial velocity increment which is related to the actuator disk thrust loading coefficient C_T by,

$$c_a = \sqrt{1 + C_T} - 1 \qquad (2)$$

From continuity considerations, the slipstream radial contraction is found to be,

$$\frac{R_{uw}}{R} = \sqrt{\frac{1 + (c_a/2)}{1 + c_a}} \qquad (3)$$

A single average wake pitch angle that can be applied to both the transition and ultimate wake is defined here from an estimate of the mean axial velocity near the wake's outer edge, V_w; the roll-up radius, R_{uw}; and the propeller angular rotation rate, Ω, as:

$$\bar{\beta}_w = \arctan\left(\frac{V_w}{\Omega R_{uw}}\right) \qquad (4)$$

One final variable input to PUF-2 which was briefly investigated in this study was a representative drag coefficient. While it is not reasonable to expect the drag coefficients of each blade section to be the same, it is possible that an average drag coefficient can be found to predict the propeller's overall performance characteristics.

3. PROPELLERS TESTED

The theoretical models described above have been compared with model test data on a variety of propellers. The results for five such propellers are presented here. All of these are five-bladed propellers and sketches of their projected and expanded blade outlines and pitch distributions are provided in Figures 3 to 7. Those in Figures 3, 4 and 5 are controllable pitch propellers, and those in Figures 6 and 7 are fixed pitch.

Open water propulsion, behind cavitation inception and cavitation extent tests with these propellers have all been carried out in the depressurized towing tank of MARIN, formerly the Netherlands Ship Model Basin (NSMB). Table 1 provides the full scale propeller diameters and the scale of the model propellers. With these models, open water tests were carried out at Reynolds number, based on the rpm and the chord at the 0.7 radius, of approximately 10^6 for the controllable pitch propellers, and 0.5×10^6 for the fixed pitch propellers. The cavitation data were all obtained at Froude scaled conditions.

Propeller	Full Scale Diameter(m)	Model Scale
5268	4.166	13
5733	4.318	13
5682	4.340	14
5349	3.048	10
5363	3.048	10

Table 1: Propeller Diameters and Model Scales

4. PROPELLER PERFORMANCE COMPARISONS

Studies on the influence of varying the wake roll-up radius, the wake pitch angle and the overall drag coefficient on the open water predictions of PUF-2 have been carried out for the above propellers. Kerwin and Lee have shown that changing the rotation plane angle turned by the outer wake between the tip trailing edge and the roll-up points has a negligible effect on the results. This value was fixed at 90°. Instead of abruptly changing the wake pitch angle from the transition to ultimate wake, a single average pitch angle was applied to the entire wake.

The drag coefficient was varied over a range from 0 to 0.016 with all other parameters held constant. As expected this showed a uniform decrease in K_T and a uniform increase in K_Q over the whole range of advance coefficients, as the drag coefficient was increased. The torque coefficient was the more sensitive to these changes. Based on the efficiency predictions, a value of drag coefficient of 0.008 provided the best agreement with the experimental data.

Analyses were initially carried out with the radius of the ultimate wake, R_{uw}, set at constant values between 0.6 and 0.95. Later this radius was determined by the continuity relation which, being a function of C_T, caused it to vary throughout the advance coefficient range. The value of C_T used to determine R_{uw} was obtained from preliminary model test data. The results of these procedures show that the assumption of a constant value of $R_{uw}/R = 0.83$ would give quite adequate accuracy, as does the continuity relationship which was found to be marginally better at low advance ratios.

The axial velocity in the wake, V_w, was varied from a value of V_a to $V_a\ (1 + c_a)$ to obtain estimates of wake pitch angle. The use of the value V_a resulted in divergence in the numerical procedure at advance coefficients below 0.4. The other extreme of V_w also yielded poor results at low advance coefficients. A value of $V_a\ (1 + c_a/2)$ provided the best agreement with the model test data. This corresponds to using the velocity at the propeller plane within the stream tube or the average velocity at the boundary of the stream tube and the freestream in the ultimate wake.

The best values of the input parameters based on this study are then; an overall drag coefficient of 0.008, the ultimate wake radius, average axial wake velocity and corresponding pitch angle defined above from actuator disk theory. Using these parameters, the PUF-2 wake model was changed to one with no radial contraction in the transition wake and a sudden roll-up at radius R_{uw} at the start of the ultimate wake, together with associated changes in shed and ultimate wake vortex strengths described earlier. A sample comparison of results obtained with the conventional wake model and with the model having no near wake contraction is shown in

Figure 8 for propeller model 5682. This case, as well as other cases examined, demonstrated clearly the superiority of the contraction model for propulsion predictions over the complete range of advance coefficient.

Comparisons of the best PUF-2 predictions with the model test data for the propellers of Table 1 are presented in Figures 9 to 13. The data represent quite a range of propeller types, and there is no clear trend in the correlation of model test results with theory based on any geometric factor. The trend to overpredict thrust and torque at low advance coefficients is believed to be due to the theory's inability to account for the loss of lift from viscous effects and flow separation at the high angles of attack. This may also be true for propellers 5349 and 5733 at high advance coefficients. Propeller 5349, for which the correlation between model test and theory was worst, was tested at the lowest Reynolds number which may have exaggerated the viscous problems at the extreme advance coefficients. Propeller 5682, for which the correlation was the best, was the only propeller of this set which was designed by a lifting-surface method and our limited experience to date suggests that such good correlation is a feature of propellers so designed.

The open water data obtained from PUF-2 for a particular propeller can be used in conjunction with ship model propulsion tests with stock propellers to predict the operating rpm and propulsive efficiency, η_D, of the propeller in the behind condition. Errors in the open water analysis will result in corresponding errors in rpm and η_D.

To obtain a broad picture at close to the design point, predictions of the operating RPM and efficiency were made for all the propellers of Table 1 when fitted behind ships. The preceding recommended values of C_D, R_{uw} and V_w were used to calculate open water data for these predictions. The results of this study are provided in Table 2. The rpm values from the theory were generally lower than those from the model test. The largest error being 2.6%. The propulsive efficiencies were predicted to within about 4%.

	Ship Speed	RPM		Efficiency	
Propeller	(kts)	Model	Theory	Model	Theory
5268	20	145.4	144.4	.618	.602
5733	20	122.3	119.6	.656	.630
5682	20	133.0	134.6	.599	.588
5349	15	134.2	133.5	.617	.642
5363	15	135.4	131.9	.641	.657

Table 2: Behind Efficiency and RPM Predictions

5. CAVITATION TEST RESULTS

Using the best values of input parameters obtained for the propulsion comparisons with PUF-2, the DREA code CAVITY was used to predict ship speeds for back cavitation inception and the extent of sheet cavitation development for the model propellers of Table 1. Predictions of cavitation inception speeds on the back surface of the blades using two wake models, one with and one without near wake contraction upstream of roll-up, are compared to model test results in Table 3.

Generally, calculated inception speeds are slightly closer to model test results when no contraction is applied to the near wake. Except for propeller model 5363, predicted back sheet cavitation inception speeds are high by a maximum of about 2 knots with no contraction and by almost 3 knots with contraction compared to experiment. Model 5363 has back sheet inception predicted just over 2 knots low with both wake models. Model 5682 experienced no back cavitation in tests up to the 30 knot operating speed; however, back bubble inception in the midchord region is theoretically predicted just below the 30 knot speed.

	Model	Theoretical Predictions		
Propeller	Test	No Contract.	Contraction	Type
5268	17.4	17.8	18.5	Sheet
5733	20.2	22.3	23.1	Sheet
5682	>30.0	28.1	26.2	Bubble
5349	7.7	9.9	10.3	Sheet
5363	15.2	12.8	12.9	Sheet

Table 3: Back Cavitation Inception Speeds(kts)

Figures 14 through 16 compare predictions of back sheet cavitation extents with model test observations for three of the model propellers. These figures are projected views of a blade looking downstream for selected angular positions between - 180° and 180° with 0° at the top vertical position. Model test chordwise extents are indicated by the small circles. The results show little difference in predicted extents with either the contraction or no contraction models for the near wake. However, the no contraction model can provide up to 30% saving in computation time compared to the model with contraction, due to a faster convergence of the predicted extents. Although propellers 5349 and 5268 generally correlate well with model test data, calculations for propeller 5733 fail to predict the large extents on the lower radius sections of the blade. This might be due to the larger thickness of lower radius sections for this propeller which violates the thin section assumption of lifting-surface methods.

6. CONCLUSIONS

The above study of the influence of wake parameters and drag coefficients on the predicted performance of propellers has resulted in a choice of input parameters to the programs PUF-2 and CAVITY. These require only good estimates of the thrust loading coefficient and an overall blade section drag coefficient. The program PUF-2 has good open-water prediction capabilities over a wide range of positive advance coefficients. Use

of such predictions results in estimates of operating rpm and efficiency which are within acceptable limits for determining the suitability of a propeller for a particular ship. The influence of viscous flow phenomena not being included in the theoretical methods is apparent for some propellers. It would be interesting to see how improved modelling of viscous flow separation effects included in the methods of Greeley and Kerwin (1982) performs with this range of propellers.

Predictions of back cavitation inception speeds with program CAVITY are generally within 2 or 3 knots of the model test observations, which are close enough for preliminary evaluation of the cavitation performance of new propeller designs. Extending the methods of Greeley and Kerwin to the unsteady flow problem might help to improve predictions of inception speeds on some propellers.

Cavitation extent predictions at the design points with program CAVITY generally correlate well with model test data whether or not radial contraction of the near wake is applied. However, a faster convergence of the solution procedure is obtained by suppressing the wake contraction.

Large sheet cavitation extents developing on thick root sections of a blade are not predicted well by the lifting surface meth Perhaps a surface singularity method which distributes vortices and cavity thickness sources on the actual blade surfaces is necessary to overcome this limitation.

For the propeller designer, the programs PUF 2 and CAVITY provide very useful design tools which can be used to optimize propeller designs prior to model testing. This approach is a cost effective method of arriving at a suitable propeller design within the bounds described above.

REFERENCES

Cummings, D.E. (1976): The Effect of Propeller Wake Deformation on Propeller Design, Third LIPS Propeller Symposium, Drunen, The Netherlands.

Greeley, D.S. and Kerwin, J.E. (1982): Numerical Methods for Propeller Design and Analysis in Steady Flow, SNAME Trans., Vol. 90.

Kerwin, J.E. and Lee, C.S. (1978): Prediction of Steady and Unsteady Marine Propeller Performance by Numerical Lifting-Surface Theory, SNAME Trans., Vol. 86.

Lee, C.S. (1980): Prediction of the Transient Cavitation on Marine Propellers by Numerical Lifting-Surface Theory, 13th Symposium on Naval Hydrodynamics, Tokyo, Japan.

Noble, D.J., Sponagle, N.C. and Leggat, L.J. (1986): DREA Propeller Cavitation Research, 21st American Towing Tank Conference, Washington, D.C.

Van Houten, R.J. (1982): The Numerical Prediction of Unsteady Sheet Cavitation on High Aspect Ratio Hydrofoils, 14th Symposium on Naval Hydrodynamics, Ann Arbor, Michigan.

Van Houten, R.J., Kerwin, J.E. and Uhlman, J.S. (1983): Numerical Solutions of Lifting-Surface Sheet Cavitation - A Review of Research at M.I.T., 20th American Towing Tank Conference, Hoboken, New Jersey.

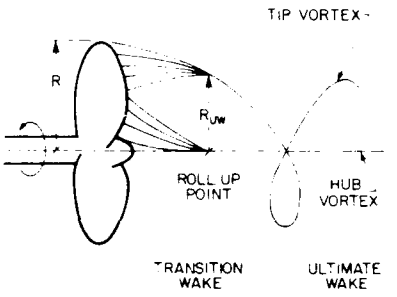

Figure 1: Roll-up and Ultimate Wake

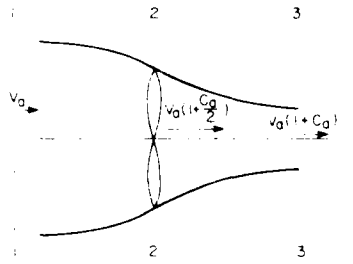

Figure 2: Stream Tube - Actuator Disk Theory

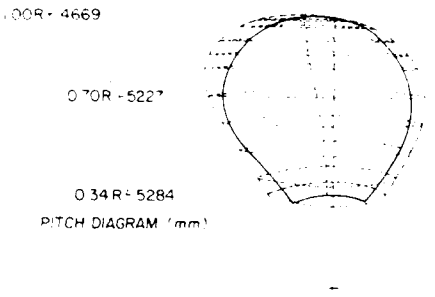

Figure 3: Propeller Model 5268

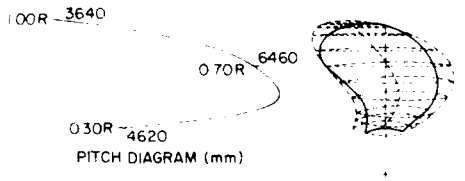

Figure 4: Propeller Model 5733

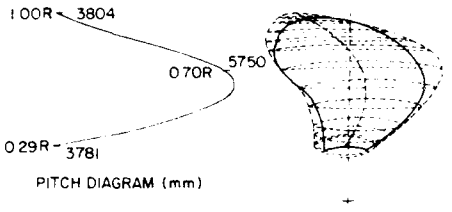

Figure 5: Propeller Model 5682

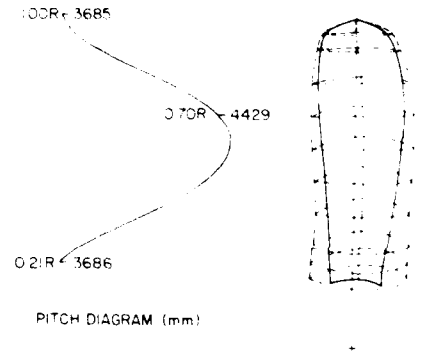

Figure 6: Propeller Model 5349

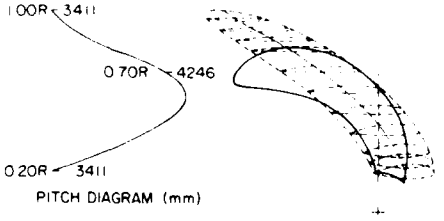

Figure 7: Propeller Model 5363

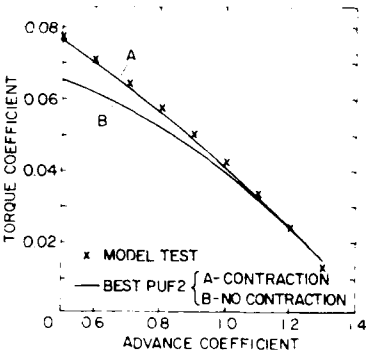

Figure 8: Effect of Different Wake Models on Torque Coefficient

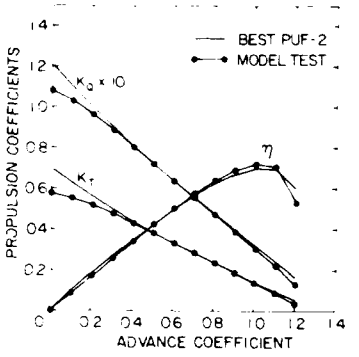

Figure 9: Open Water Performance Correlation - Model 5268

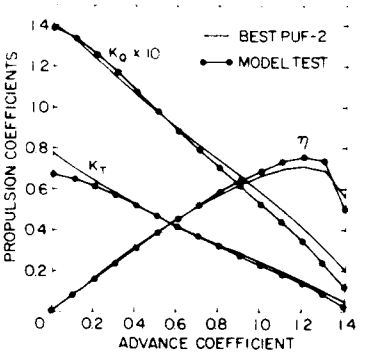

Figure 10: Open Water Performance Correlation - Model 5733

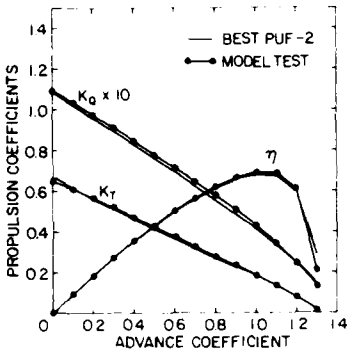

Figure 11: Open Water Performance Correlation - Model 5682

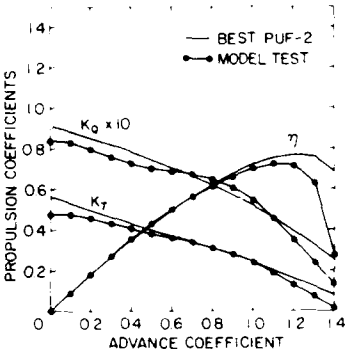

Figure 12: Open Water Performance Correlation - Model 5349

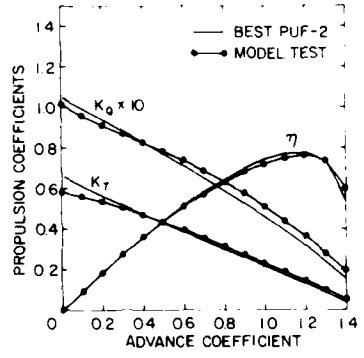

Figure 13: Open Water Performance Correlation - Model 5363

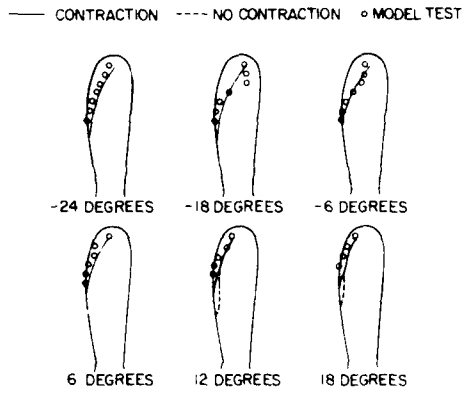

Figure 14: Cavitation Extent Correlation - Model 5349

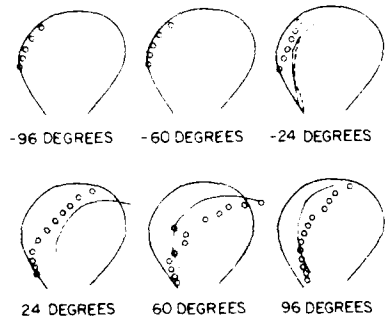

Figure 15: Cavitation Extent Correlation - Model 5268

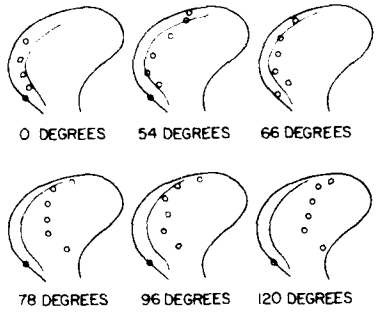

Figure 16: Cavitation Extent Correlation - Model 5733

THE WATER TUNNEL AS A TOOL IN SURFACE SHIP PROPULSION DESIGN

Robert A. Johnson, Research Engineer
Walter S. Gearhart, Senior Scientist
Allen L. Treaster, Research Associate
The Applied Research Laboratory
The Pennsylvania State University
PO Box 30
State College PA 16804

ABSTRACT

The Garfield Thomas Water Tunnel operated by the Applied Research Laboratory, The Pennsylvania State University has been used for almost forty years in the development of underwater bodies and propulsors. During the past 12 years this facility has also been used for the development and testing of surface ship propulsors. In this relatively new testing role, the free surface component associated with the ship's hull wake is neglected. Instead a shortened version of the underwater portion of the hull form is tested on a flat plate in the closed conduit test section. Measurements of the three dimensional wake made in the water tunnel in the plane of the propeller have been in excellent agreement with towing tank measurements. Recent efforts have led to the development of a reaction fin which modifies the wake swirl component from the inclined propeller shafts. Removing this velocity component creates a more favorable propeller inflow and, in turn, a higher propeller efficiency. Full scale tests have confirmed the effectiveness of such a device. In this paper the methodology, limitations, and potential future utilization of water tunnel testing for surface ship propulsor development are discussed.

INTRODUCTION

The Garfield Thomas Water Tunnel (GTWT) of the Applied Research Laboratory, The Pennsylvania State University (ARL/PSU) has been used for almost forty years in the design and testing of underwater vehicles. Use of this 48-in. diameter test section water tunnel in submerged vehicle design and development is well documented (reference (1)). However, if used in concert with towing tank measurements, a closed conduit water tunnel can be used as an effective tool in surface ship propulsor design as well.

During the past twelve years the GTWT has been used in the development of surface ship propulsors. The success of such tests, for this relatively new role, depends on towing tank measurements to establish a reference baseline of model operating parameters.

Recently, knowledge gained from water tunnel measurements at ARL/PSU, led to the development of a set of reaction fins which were manufactured and tested on a 41-ft Coast Guard boat. These full scale tests have indicated a significant improvement in the boats' stock propeller efficiency when operating with the reactions fins installed. The rationale leading to the development of the reaction fins as well as the results achieved are also addressed in this paper.

Background

The GTWT became operational in 1950. This tunnel (shown in Figure 1) is over 90-ft long and 30-ft high with a maximum diameter of 12-ft upstream of the working section (Figure 2). The cylindrical working section is 48-in. in diameter and 14-ft long. Water velocity in

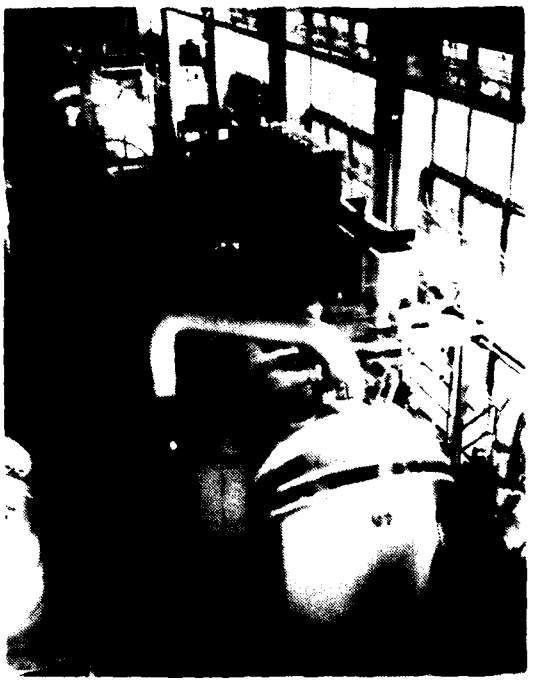

Figure 1. Top View of the Garfield Thomas Water Tunnel.

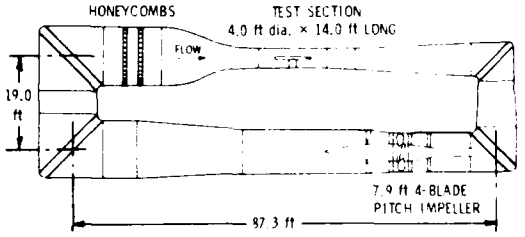

Figure 2. Diagram of Water Tunnel Showing Dimensions.

the working section is controlled by a four-bladed, adjustable-pitch impeller to a maximum speed of 60 fps. Test section pressure may be varied from 3 to 60 psia. This combination of operating parameters permits a wide range of cavitation numbers. Since the water temperature can be varied from 65 to 110°F, an 80% change in Reynolds number can be achieved through the change in water temperature alone.

By design, the closed conduit water tunnel is uniquely suited as a test tool in the development of submerged bodies and their propulsors. However, by using an innovative mounting and testing approach, the water tunnel has been used as an important tool in the development of surface ship propulsors.

Test Approach

In water tunnel testing a surface ship propeller can be mounted in an inclined position to duplicate the wake from the open drive shaft and struts, Figure 3, or with a model hull attached to a flat plate which spans the test section, Figures 4 and 5. By using a scaled model of the underwater portion of the ship's hull a good representation of the potential and viscous wake is obtained. Due to the nature of the test facility involved, there is no free surface and hence no free surface wake components. Generally, the contribution to the wake due to the free surface is small.

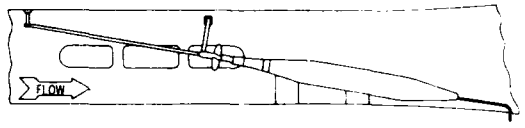

Figure 3. Model Ship Propeller in an Inclined Flow.

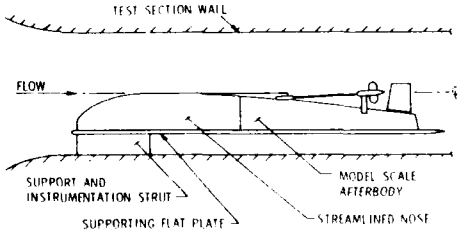

Figure 4. Diagram of Ship Model Hull and Propeller in GTWT.

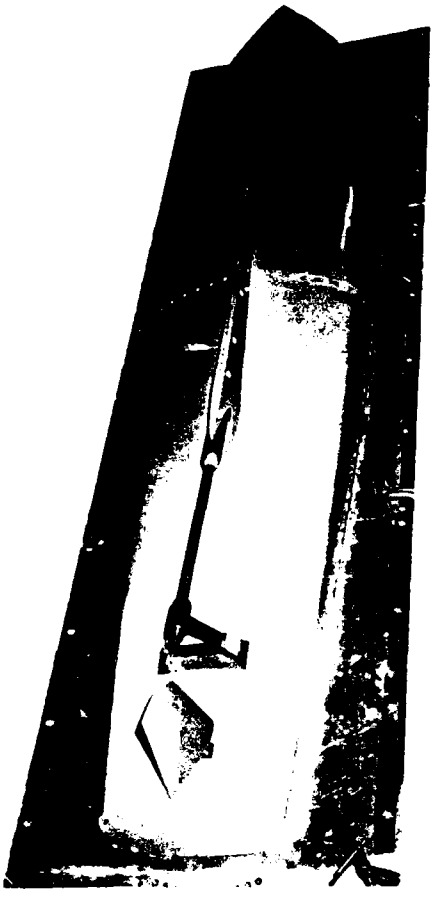

Figure 5. Actual Ship Model Hull Installation.

In order to minimize installation problems, the hull form model is mounted in an inverted position on a flat plate located in the lower portion of the tunnel test section so that the center of the propeller hub is located at the centerline of the water tunnel working section. Due to this inverted hull mounting arrangement, there is an error in hydrostatic pressure gradient of about 2% of the minimum measured cavitation indices. In general, this error is within the accepted limits of data scatter. The hull form representations used in water tunnel tests to date have been 1/19th scale, foreshortened models in which the aftmost 19% of the hull (stern section) is accurately modeled. The forward portion of the hull is simply a streamlined transitional fairing to the model-scale afterbody. The total model length used in tunnel tests is roughly 45% of the actual scaled hull form length for a cruiser type hull. By using the shortened model, higher Reynolds numbers and more realistic boundary layer thicknesses are achieved. To date, the models tested in the water tunnel concerned propellers that were located outside of the viscous boundary layer. However, when

required, accurate representations of the boundary layer can be achieved by the use of midbody screens. In either case (propeller inside or outside boundary layer), towing tank wake measurements are required to insure accurate inflow to the model propeller. Figure 6 shows a comparison of wake measurements made in a towing tank compared to those measured in the water tunnel in the plane of the propeller. Whereas, the propeller mounted on an inclined shaft simulates radial and tangential components of velocity in the plane of the propeller, the presence of the model hullform afterbody accurately simulates all three velocity components.

The three-dimensional wake survey as shown in Figure 6, is typically conducted in the propeller-disk plane. A rotating wake rake composed of six miniature five-hole, angle-tube probes (reference 3), as shown in Figures 7 and 8, is used to measure the three velocity components. The wake rake is rotated through 360° in predetermined angular increments. At each of these angular positions, data are recorded from each of the six probes located at their prescribed radial positions.

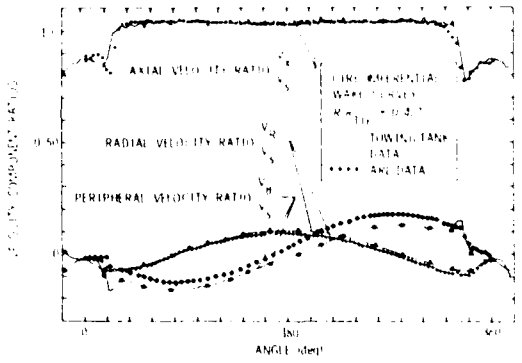

Figure 6. Typical Circumferential Wake Survey.

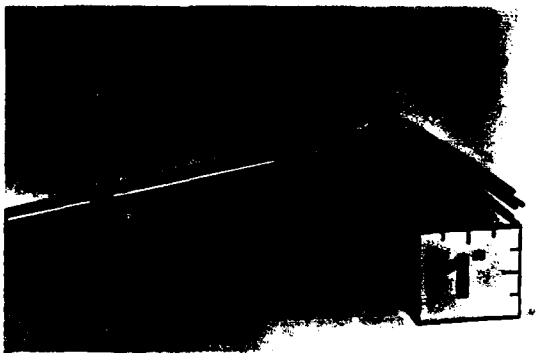

Figure 7. Five-Hole Probe for Measuring Three-Dimensional Flow Properties

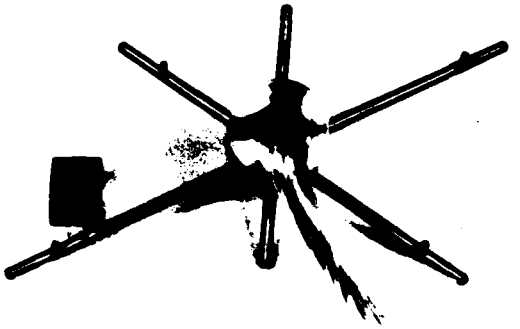

Figure 8. Five-Hole Probe Rotating Wake Rake.

Once the overall model installation has been verified by the results of wake surveys, propeller shaft thrust and torque measurements are made at selected advance ratios spanning a range of 20 percent above and below the assumed operating advance ratio. The customary coefficients are defined by the following equations:

$$\text{Advance Ratio} = J = V_\infty / nD_p$$

$$\text{Thrust Coefficient} = K_T = \frac{\text{THRUST}}{\rho n^2 D_p^4}$$

$$\text{Torque Coefficient} = K_Q = \frac{\text{TORQUE}}{\rho n^2 D_p^5}$$

where

n = the rotational speed of the propeller

D_p = the propeller diameter

ρ = the fluid mass density

A characteristic graph of K_T and K_Q versus J is presented in Figure 9. Although

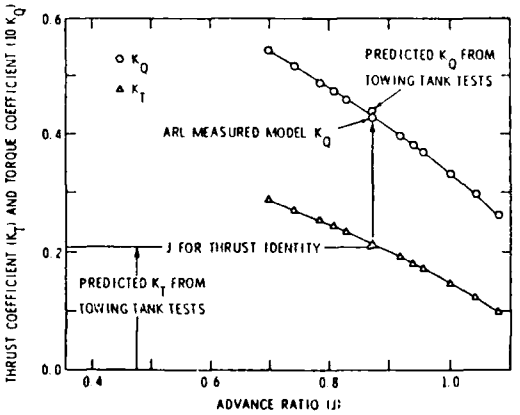

Figure 9. Typical ARL/PSU Measured Thrust and Torque Data for a Model Propeller.

these data have not been adjusted to reflect full-scale ship performance, a one point comparison with predicted full scale powering data is shown on Figure 9 and obtained as follows. For a given full scale velocity, K_T is computed from predicted (or measured) full scale data. At this value of K_T, the corresponding value of J is determined from the ARL/PSU model K_T vs J curve to give model/full scale thrust identity. At this same value of J, K_Q is determined from the ARL/PSU K_Q vs J curve. This value of K_Q is then compared with the K_Q computed from the predicted full-scale data. For all propellers tested, the agreement between the predicted full-scale and the measured model-scale value of K_Q is within 5%.

Cavitation Observations

Once the model installation is validated by the wake surveys and powering tests, the cavitation characteristics of a surface ship propeller can be evaluated. Cavitation characteristics are recorded by visually determining either the desinent or incipient cavitation condition for the various forms of cavitation as a function of advance ratio

At a given velocity, the cavitation observations are made by synchronizing a stroboscopic light source with the rotational speed of the propeller and then reducing the tunnel pressure until a particular type of cavitation has formed. The tunnel pressure is then increased until the desinent (all clear) condition is reached, at which time the pertinent parameters are recorded and the cavitation index is computed. The cavitation index σ is expressed as

$$\sigma = \frac{P_\infty - P_V}{1/2\ \rho\ V_\infty}$$

where

P_∞ = the desinent free-stream static pressure,

P_V = the vapor pressure of the water at its average temperature.

A typical graph of cavitation index versus advance ratio for various cavitation forms is shown in Figure 10. Also included on the cavitation figure is the "ship operating curve" and the corresponding inception speeds for the various cavitation forms. The ship operating curve is derived from calculated cavitation indices based on the operating depth of the propeller hub and velocities obtained from thrust identities based on full scale thrust predictions scaled from towing tank data and water tunnel thrust measurements. When the calculated ship operating curve is superimposed on the appropriately scaled cavitation inception plot, the intersection with a particular desinent cavitation curve determines a corresponding critical cavitation index for the ship. A critical or so-called inception speed can be calculated for the ship from the corresponding critical cavitation index.

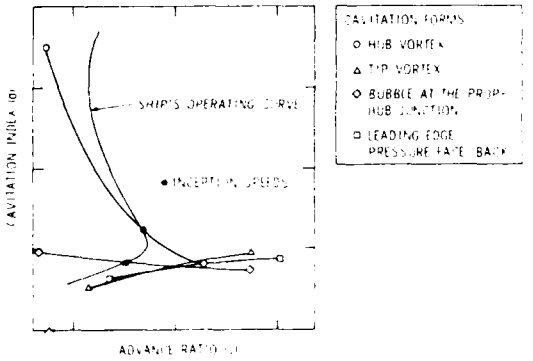

Figure 10. Typical Cavitation Data for a Model Propeller.

Past tests conducted in the GTWT determined the effects of rudder throw on propeller cavitation performance. Results of these tests indicated a marked change in cavitation characteristics due to rudder deflection, Figure 11. Such results facilitate propeller design to provide cavitation free operation at a given ship speed. Scaling model cavitation data to obtain absolute values of full scale performance still entails some risk. However, experience has shown that differences occurring in cavitation performance among various propellers at model scale provides a good representation of what will occur at full scale.

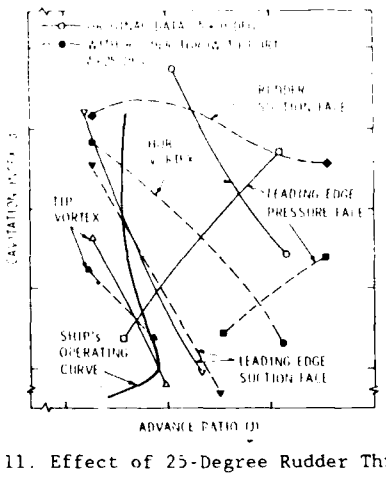

Figure 11. Effect of 25-Degree Rudder Throw on Cavitation.

Additional Measurement Capabilities

In addition to the more or less traditional measurements that can be made in a water tunnel and applied to surface ship propulsor design, there are a number of

emerging measuring techniques that can greatly enhance the propulsor design capability. These new capabilities range from the ability to map the flow field at any plane to predicting noise characteristics of new propeller designs.

Flow Field Mapping

The miniature five-hole probe mentioned previously has a maximum diameter of .066-inches and was developed at ARL/PSU. The usefulness of this probe is further demonstrated in Figure 12, where the vector sum of the radial and tangential components of the velocity downstream of a set of stationary fins is plotted. This representation clearly

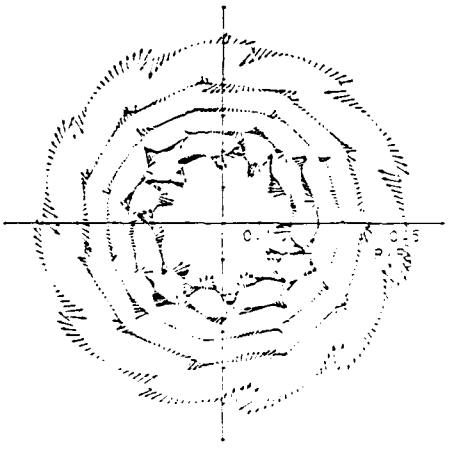

Figure 12. Radial and Tangential Velocity Vectors Measured Behind a Set of Stationary Fins.

shows the tip vortices and detailed wake structure associated with each fin. The ability of these small probes to measure accurately this flow detail provides data to compute a more exact Fourier representation of the flow field. The resulting Fourier coefficients are primary factors in the analysis of the dynamic response of a propeller.

Flow Relative to a Rotating Propeller

The hydrodynamic propeller designer is concerned with the flow field relative to the blades of a rotating propeller. In the past this information has been lacking due to the difficulty of the measurements. However, the development of the laser Doppler velocimeter provides a technique which makes these measurements possible.

The data acquisition system employed at ARL/PSU to measure the velocities relative to a rotating propeller is shown in Figure 13. The heart of this system is the data control system which was designed and built at ARL/PSU. This system receives a signal from an encoder attached to the rotating shaft,

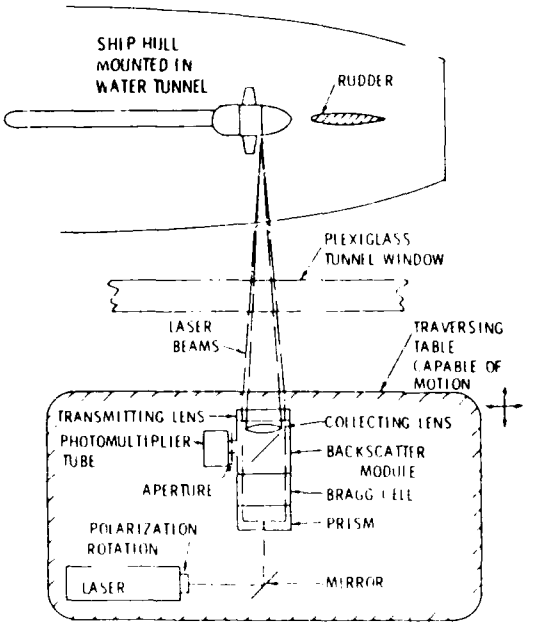

Figure 13. Laser Doppler Velocimeter Setups for Measuring Velocities Relative to a Rotating Propeller

takes this signal and chooses the correct instant when the laser beam is to be focused at a preselected position relative to the rotating propeller, accepts the scattered light at that instant and passes on to the next point. By changing the specified position it is possible to obtain a survey of the velocity field relative to the propeller. Shown in Figure 14 is an example of such a survey.

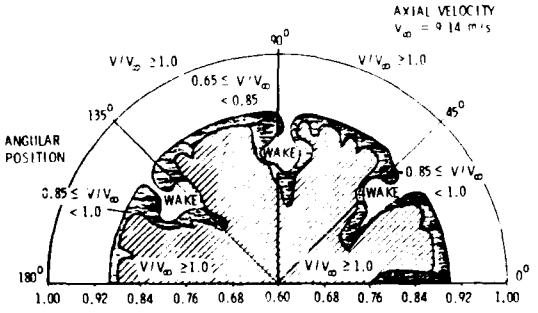

Figure 14. Axial Velocity Behind a Rotating Propeller: Relative to the Propeller.

Cavitation Noise

The GTWT was designed so that one side of its test section can be fitted with an acoustic tank in which a traversing reflector hydrophone could be mounted. With the hydrophone focused through the plexiglass window and on the centerline of the test

section the radiated noise from the model can be measured.

To overcome restrictions due to metal webs between the windows, an acoustically transparent hatch cover has been procured for the GTWT, Figure 15. This special hatch replaces the original metal access cover to

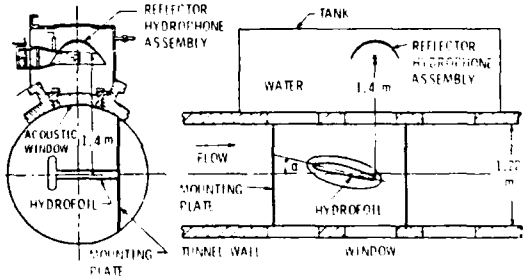

Figure 15. Acoustic Tank and Reflector Hydrophone Arrangement.

the test section with a continuous plexiglass window. A tank located over the large window is filled with water and allows the installation of additional hydrophones. This arrangement permits unobstructed acoustical scanning of the model in the test section and improved cavitation viewing.

Using these installations, and measurements, it is possible to determine the variation of propeller cavitation noise as a function of Reynolds number and to develop model-to-prototype cavitation noise scaling laws if full scale data are available.

Noncavitating Noise

In addition to cavitation noise, the GTWT can be used to study noncavitating propeller noise. This is accomplished with an array of 69 parallel-wired hydrophones in a hydrodynamic fairing which is located at the end of the tunnel diffuser in front of the first set of turning vanes, Figure 16. This sensor permits the far field radiated noise to be measured at frequencies > 300 Hz. When used in conjunction with other sensors located in the test section, dual-channel signal processing can be used to identify sources of propeller noise and paths of propagation.

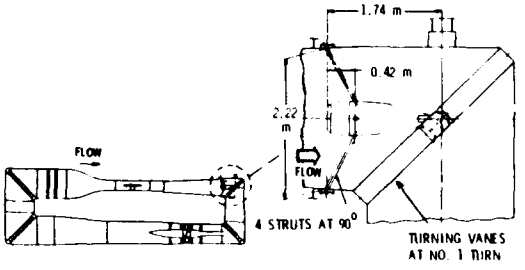

Figure 16. GTWT Downstream Array.

Recent Applications

By proper utilization of the test, evaluation, and analysis tools available through use of the water tunnel, propulsor design can be greatly enhanced. A recent example is the modification of the inflow to the stock propellers of a 41-ft Coast Guard Utility Boat (UTB). The detailed design of the reaction fins is described in reference (6).

In general, propellers operating on an inclined shaft relative to the flow experience an induced velocity in the plane of the propeller and in the direction of propeller rotation on the starboard side. Whereas, the port side of the propeller experiences the same induced velocity only counter to the propeller rotation, Figure 17. By modifying the induced radial inflow velocity to the starboard side of the propeller (Figure 18) it was rationalized that a higher efficiency

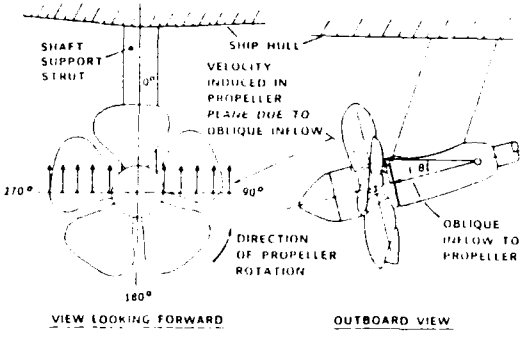

Figure 17. Schematic of Oblique Flow into a Propeller Due to an Inclined Shaft

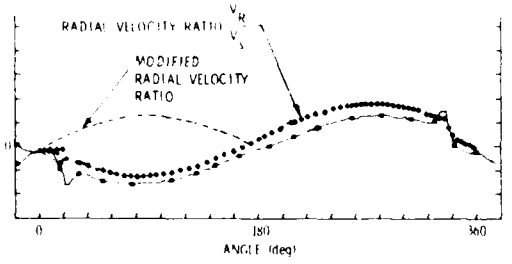

Figure 18. Modified Radial Velocity Inflow to the Propeller.

could be achieved. This improvement was attempted by installing a reaction fin assembly shown in Figure 19, forward of the propellers. Figure 20 is a photograph of the actual installation on the twin screw, 41 ft UTB. The boat displaces about 13 tons.

Full scale testing and evaluation was conducted on the James River off Newport News, Virginia. Efficiency gains of nominally 5-6 percent were obtained for a given boat speed or alternatively higher boat speeds for a

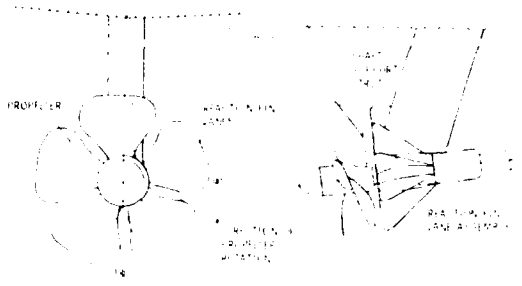

Figure 19. Reaction Fins Forward of the Propeller.

Figure 20. Actual Reaction Fin Propeller Installation

given power could be achieved with the reaction fins installed. These gains in efficiency were achieved using the reaction fins in conjunction with the existing propellers.

The potential savings in fuel costs, coupled with the advantage of using the existing propellers with the reaction fin assemblies provides an attractive propulsor arrangement which the U.S. Coast Guard is proceeding to evaluate for further application.

Other Applications

The Coast Guard application is one illustration of what can be accomplished in surface ship/boat propulsor design by using water tunnel measurements. However, by using the more extensive measurement and flow mapping techniques now available to the propulsor designer coupled with rapid computerized data analysis, modest cost trade-off studies can be accomplished to determine the effectiveness of more extensive propulsor modifications or innovative designs.

Until just recently when energy costs started to decrease, there was intense interest in designing more efficient propulsors. Modifications to the propeller inflow as well as utilizing propeller wake energy (such as installation of a vane wheel on the QE II) were explored to gain efficiency. In a recent article by Ingvason et al (reference 7), the merits of an integrated propulsor/stern design was stressed. The water tunnel could be an effective tool in evaluating design variations of such concepts at a relatively low cost However, as new concepts are developed the effect of fluctuating pressure forces on the hull is an ever present concern. By utilization of additional instrumentation, valid hull pressure force measurements can be made on a relative basis. As with all model testing more extensive comparison with full-scale field data are required to develop the model-to-full-size scaling laws.

CONCLUSIONS

The approach used in testing surface ship models in the Garfield Thomas Water Tunnel yields excellent agreement with towing tank results. A unique capability of the tunnel however is the ability to measure the cavitation characteristics of the propulsor in the presence of the hull form. New techniques recently developed at ARL/PSU will give the propulsor designer the necessary information to design and develop highly efficient, low noise propulsors. This facility has a high potential for increased use in hull pressure force measurements and or the development of integrated stern/propulsor concepts. When used in concert with towing tank measurements, the water tunnel is a highly effective tool in surface ship propulsor design.

REFERENCES

1. Lehman, A. F., "The Garfield Thomas Water Tunnel," Ordnance Research Laboratory Report Nord 16597-56, September 1959.

2. Henderson, R. E. and Parkin, B. R., "Hydrodynamic Test Facilities at ARL/PSU," ARL Technical Memorandum File No. 82-66, 12 February 1982.

3. Treaster, A. L., and Yocum, A. M., "The Calibration and Application of Five-Hole Probes," ISA Transactions, Vol. 18, No. 3.

4. Treaster, A. L., and Eisenhuth, J. J., "Surface Ship Testing at the Garfield Thomas Water Tunnel," ARL Technical Memorandum File No. TM 77-212, 30 June 1977.

5. Dyne, G., "A Study of the Scale Effect on Wake Propeller Cavitation, and Vibratory Pressure at Hull of Two Tanker Models,"

Transactions of the Society of Naval Architects and Marine Engineers, Vol. 82, 1974.

6. Gearhart, W. S., "Advanced Propulsor Design Studies," United States Department of Transportation, United States Coast Guard Report #GO-D-1-86, June 1985.

7. Ingvason, S., McCallum, D. N. and Kraine, G. L., "An Integrated Hull Design Performance and Producibility," Naval Engineers Journal, May 1986.

APPLICATION OF A CONSTANT ACCELERATION SINGLE PASS OPEN WATER PROPELLER TEST TECHNIQUE

John G. Hoyt III
Naval Architect
David W. Taylor Naval Ship Research And Development Center
Code 1562, Special Ship And Ocean Systems Dynamics Branch

Howard Fireman
Naval Architect
Naval Sea Systems Command
Code 55W1, Ship Arrangements Design Division

Michael E. Osbourne
Mechanical Engineer
Naval Sea Systems Command
Code 56X31, Engine Research / Development Branch

ABSTRACT

This paper describes a "Constant Acceleration, Single Pass, Open Water Propeller Test" as utilized during an experiment at the U.S. Naval Academy's Hydrodynamics Laboratory. This technique experimentally obtains thrust and torque coefficients for a model propeller over a broad range of advance ratios in a single run of the towing carriage. Results using this technique for a right handed wake adapted propeller are compared to those obtained by more traditional methods.

The traditional method is to measure propeller thrust and torque at both a constant advance and rotational speed. This process requires several carriage data runs to obtain a well defined set of open water curves. The control systems of many new towing carriages and propeller dynamometers are capable of very low and steady accelerations. This capability allows the measurement of thrust and torque for a propeller at a steadily increasing or decreasing advance or rotational velocity. By slowly changing either the forward velocity or the rotational speed while keeping the other constant, a complete and continuous set of open water characteristics can be obtained in a single data run.

Two sets of right and left handed propellers have been tested utilizing both methods and the correlation between the two techniques has proven to be excellent. A sample set of data for one of these propellers is presented. The traditional method required three hours of testing time for each propeller. The new method provided data for the same open water propeller curve in only 15 minutes per propeller. By reducing the total testing time involved in the collection of data, the impact of heat induced instrument drift inherent in some torque-thrust dynamometers is lessened. This extra time can be utilized to study the effect of a change in Reynolds Number that can be produced by testing at several rotational speed / forward velocity combinations. In addition, redundant data points can be aquired allowing a better definition of data repeatability.

INTRODUCTION

Time and cost are both critical factors in the design of any marine vehicle. A new technique that can potentially save these precious resources should be investigated and incorporated into the design process whenever feasible. One of the frequently used design tools available to the Naval Architect in the determination of the propulsion characteristics of his hull design is the model self-propulsion test. A phase of this test is the so called "Open Water Propeller Experiment" where the thrust and torque characteristics over a range of advance and rotational speeds are determined. The purpose of this paper is to present a new "Open Water Propeller" experimental technique that has the potential of both reducing the tank time and cost to obtain this type of propeller data.

During November of 1980 we were involved in a retest of a naval surface combatant at the U.S. Naval Academy Hydromechanics Laboratory. This project involved the performance of a model self-propulsion test utilizing both stock and wake adapted propellers. This particular ship had twin screws, thus four separate open water propeller tests were required to complete the experimentation. While involved in these experiments, we heard of a new propeller testing technique being tried in circulating water tunnels that obtained data dynamically. This new experimental technique had the promise of providing a complete open water performance curve in one data acquisition. However, in practice there appeared to be a problem with obtaining repeatable data.

This paper presents an adaptation of this technique for use in the towing basin. The results of one propeller experiment performed utilizing this new approach are compared to those obtained by the standard methods. Our modified technique significantly reduces the data repeatability problem of the original water tunnel implementation.

BACKGROUND

The dynamic propeller technique, to the best of our knowledge, has not been presented in published literature. This method was originally intended for use in a circulating water tunnel. The standard practice used to obtain open water propeller data in a tunnel is to obtain a set of thrust and torque measurements for a constant propeller rotation and advance speed. These measurements are taken over a range of advance ratios, typically in the first quadrant (forward ship motion, positive propeller rotation), and obtained by several discrete data acquisitions. The Dynamic technique obtains a complete open water performance curve for both thrust and torque in a single data acquisition. This is done by changing the angular velocity of the propeller at a slow and constant rate while holding the advance velocity steady. It was observed that, if the acceleration rate of the propellier was low enough , performance coefficients at a given advance ratio could be interpolated from the thrust, torque, angular and advance velocity time histories. This method assumes that the instantaneous values of thrust, torque, and advance ratio obtained from a constantly varying system are equivalent to those of a steady system.

The method is very tempting for two major reasons. First, the cost and time savings are significant. The reduction in total testing time will permit the acquisition of redundant points giving a better definition of data repeatability. These redundant points can be obtained at different Reynolds numbers by simply varing the fixed advance speed. The second major effect of this method will be the lessening of the impact of instrumentation drift. In fact, the impetus behind our attempt at this approach was to minimize the heat induced drift common to the thrust-torque dynamometer used in our experiment.

One of the problems associated with the dynamic technique, as implemented in the water tunnel, is that the propeller rotational speed cannot be varied independent of the tunnel velocity since the test propeller also contributes to the total tunnel mass flow. It has been purported that this effect is the major contributor to the lack of repeatabilty, most likely due to the settling time and dynamics of the water tunnel's flow system. This problem is avoided in an open water towing basin since the propeller will have negligible influence on water circulation, provided an adequate inter-run wait time is used.

In our particular case, the constant acceleration of the propeller's rotation was not possible with the dynamometer control system used. However, the control system of the U.S. Naval Academy's 360 ft towing carriage does allow for the very precise control of both advance speed and acceleration. Therefore our attempts at obtaining propeller data dynamically involved holding a constant rotational speed while slowly accelerating the advance speed.

EXPERIMENTAL SETUP

The United States Naval Academy's 360 Ft Towing Basin was utilized in performing this experiment. The major characteristics of this facility are length 360 feet,width 26 feet, and depth 16 feet. A Hydronautics water-cooled inductive pick-up type thrust-torque dynamometer was used to measure propeller performance; this unit had a stated range of 50 lbs of thrust and 100 in-lbs of torque, both capable of 100% overload. Propeller rotation was measured with a 60 tooth magnetic pick-up, while carriage speed was measured with a 100 pulse per foot optical encoder.

These experiments were performed over a period of 3 calender days. Pre and post test calibrations indicated no drift in the inherent static calibration rates over the course of the experiment. Thermal induced drift in thrust and torque were present and characterized during the measurement of the no load tares with a dummy hub. These tares have not been applied to the data used in this presentation. Little difference was found between the static and dynamic tares. In order to mask the actual numerical value of the propeller data obtained, the tares have not been reported.

All signals were amplified on board the USNA's low speed carriage, transmitted as a digital code across an optical laser communications link to shore, then stored on the Hydrodynamics Laboratory DEC PDP 11/50 computer. The acquisition system was set at a data rate of 154 samples per second per channel. All signals were filtered through Ithaco Low-Pass active filters set at a 51.2 Hertz cut-off frequency before recording and processing. Subsequent analysis used the computer records for raw data source information.

A 6 inch diameter 5 bladed propeller, model number 4755 on loan from the David Taylor Naval Ship Research and Development Center's propeller library, was used in this evaluation. The characteristics of this propeller are shown in Table 1. This propeller was tested at the tank's centerline at a depth of 22 inches.

TABLE 1: Propeller Characteristics

Model Number	4755
Number of Blades	5
Diameter	.625 FT
Pitch at .7 Radius	.800 FT
Pitch Diameter Ratio	1.28
Chord at .7 Radius	.272 FT
Blade Area Ratio	1.039

STANDARD USNA OPEN WATER PROPELLER METHOD

The standard procedure used at the U.S. Naval Academy in conducting an open water propeller test is typical of that used at most other facilities. Over a range of propeller advance ratios a discrete time average of thrust and torque over the "steady" portion of a single carriage pass is obtained. This "steady" portion of the measured propeller data is selected based upon observation of all of the recorded time histories. Each discrete time average is made only when the propeller has a fixed rotational and advance speed. The number of discrete steady runs collected in a single pass is dictated by the amount of total run time available. In our case, at the carriage speeds required for this particular test, only a single advance ratio could be obtained reliably in each carriage pass, therefore each data point required a pass of the carriage.

The step by step procedure used in collecting this data was to first check the instrumentation zeros before each carriage pass by running the propeller dynamometer at 1 rev/sec and zero advance speed and measuring thrust and torque. This was done to create a reference that would be free of static friction and sticture. Next, providing that the zero reference was within acceptable limits, the speed of the dynamometer would be increased until either the desired rotational speed for the run, or 75 percent of the dynamometer's torque rating was reached. If the desired rotational speed could not be achieved without exceeding the 75 percent torque limit, then the propeller's rotation would be increased to the desired value as the carriage accelerated. This was done to minimize dynamometer wear and hysteresis induced by overloading the dynamometer.

The propeller data obtained by the standard USNA procedure is presented for propeller number 4755 in Tables 2 and 3. This data was collected in an advance ratio range between .1 and 1.1 in the first quadrant. As mentioned before, the results of the no-load tares that were taken for this propeller have not been applied to the data.

TABLE 2: Raw Data for Propeller 4755 Obtained by Standard Method

VELOCITY (fps)	ROTATION (rps)	THRUST (lbs)	TORQUE (ft-lbs)
0.00	13.97	40.46	4.64
1.00	14.02	37.96	4.34
2.00	14.03	34.79	4.00
3.00	14.02	31.42	3.69
4.00	14.03	27.94	3.35
5.00	14.04	24.32	2.98
6.00	13.98	20.72	2.67
7.00	13.99	17.43	2.34
8.00	14.00	14.34	2.02
9.00	14.01	11.30	1.71
10.00	13.99	7.85	1.34
11.00	14.01	4.21	0.96
12.00	14.03	-0.19	0.45

TABLE 3: Normalized Data for Propeller 4755 Obtained by Standard Method

ADVANCE RATIO	THRUST COEFFICIENT	TORQUE COEFFICIENT X 10	EFFICIENCY	REYNOLDS NUMBER X 10^{-5}
0.00	0.702	1.288	0.000	2.400
0.11	0.654	1.196	0.099	2.422
0.23	0.598	1.102	0.197	2.461
0.34	0.541	1.016	0.290	2.523
0.46	0.480	0.921	0.379	2.611
0.57	0.418	0.820	0.462	2.716
0.69	0.359	0.740	0.530	2.832
0.80	0.301	0.646	0.594	2.974
1.03	0.195	0.471	0.678	3.295
1.14	0.136	0.371	0.667	3.468
1.26	0.073	0.264	0.550	3.655
1.37	-0.003	0.123	-0.058	3.849

CONSTANT ACCELERATION PROPELLER METHOD

The constant acceleration method, as applied in this investigation, consisted of accelerating the towing carriage from zero to the maximum desired speed. Acceleration rate was selected to allow the use of the entire length of the basin's run with a normal stop and still reach the maximum desired speed. The maximum desired carriage speed was selected so that the full range of advance ratios would be obtained at the propeller's fixed rotational speed. By doing this, thrust and torque over a range of advance ratios from zero to an upper limit fixed by the maximum desired carriage speed could be measured in a single pass.

The step by step procedure used to collect this constant acceleration data was, as with the standard method, to first check the instrumentation zeros by using the 1 rev/sec reference. Next the dynamometer would be set at the desired rotational speed (the 75 percent torque limit was not used). Finally, the carriage was accelerated to the desired maximum speed as data was recorded. It should be pointed out that this method could create hysteresis induced instrumentation drift in both the thrust and torque measurements if the dynamometer is undersized since the 75 percent torque limit cannot always be adhered to.

Time histories of propeller rotational and advanced speed, thrust and torque all as a function of time were obtained during each pass. An example set of time histories are given in Figures 1 - 4. In the case of this example, the carriage accelerated from zero to 10.3 ft/sec in 24 seconds at a fixed acceleration rate of 0.5 ft/sec^2. The velocity ramp shown in the example is linear and steady except for the initial 2 seconds where the USNA carriage has a preprogrammed acceleration ramp to the desired steady level. The resultant thrust and torque and angular velocity curves are also surprisingly linear. The unloading of the propeller during acceleration only slightly affected the propeller's rotational speed by 0.03 rev/sec.

Instead of steady time averages, as would be presented for the standard open water test, single point interpolations of the time histories made at one second intervals are made. These interpolations are made by fairing through the instrumentation noise with a least squares mean line to determine propeller values as a function of time. Since the noise on all of the channels was very low, little other than interpolation of the plotted time histories was required to obtain this quasi-steady data. These values for propeller 4755 are given in Tables 4 and 5.

FIGURE 1: Velocity Time History

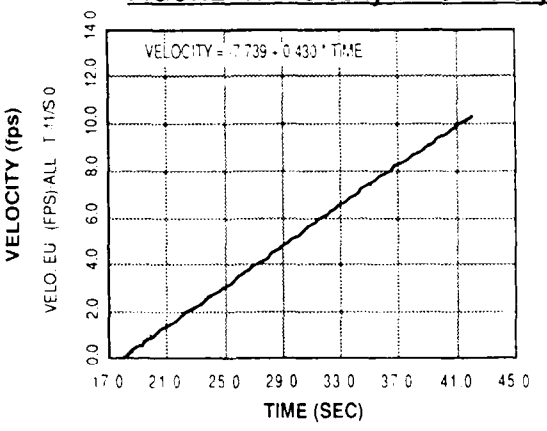

FIGURE 2: Angular Velocity Time History

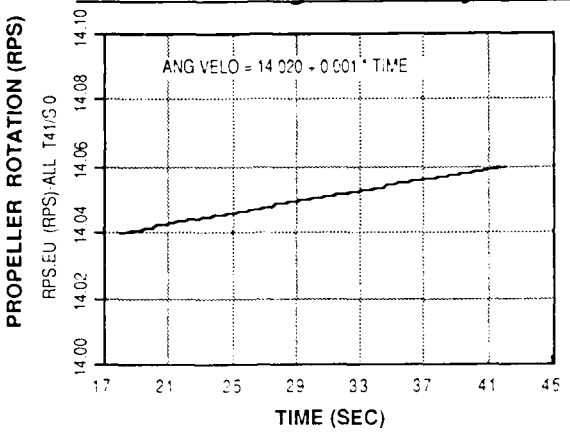

FIGURE 3: Propeller Thrust Time History

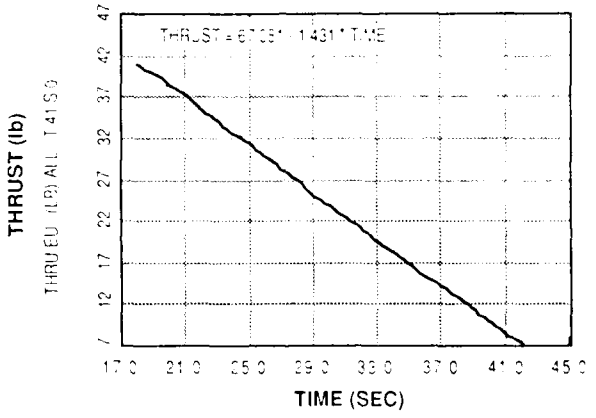

FIGURE 4: Propeller Torque Time History

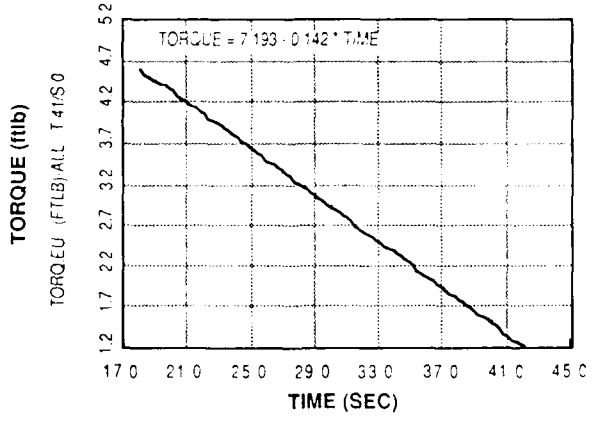

TABLE 4: Interpolated Data for Propeller 4755 Obtained by Constant Acceleration Method

TIME (sec)	VELOCITY (fps)	ROTATION (rps)	THRUST (lbs)	TORQUE (ft-lbs)
18.00	0.00	14.04	41.32	4.64
19.00	0.43	14.04	39.89	4.50
20.00	0.86	14.04	38.46	4.35
21.00	1.29	14.04	37.03	4.21
22.00	1.72	14.04	35.60	4.07
23.00	2.15	14.04	34.17	3.93
24.00	2.58	14.04	32.74	3.79
25.00	3.01	14.05	31.31	3.64
26.00	3.44	14.05	29.88	3.50
27.00	3.87	14.05	28.44	3.36
28.00	4.30	14.05	27.01	3.22
29.00	4.73	14.05	25.58	3.08
30.00	5.16	14.05	24.15	2.93
31.00	5.59	14.05	22.72	2.79
32.00	6.02	14.05	21.29	2.65
33.00	6.45	14.05	19.86	2.51
34.00	6.88	14.05	18.43	2.37
35.00	7.31	14.06	17.00	2.22
36.00	7.74	14.06	15.57	2.08
37.00	8.17	14.06	14.13	1.94
38.00	8.60	14.06	12.70	1.80
39.00	9.03	14.06	11.27	1.66
40.00	9.46	14.06	9.84	1.51
41.00	9.89	14.06	8.41	1.37
42.00	10.32	14.06	6.98	1.23

TABLE 5: Normalized Data for Propeller 4755 Obtained by Constant Acceleration Method

ADVANCE RATIO	THRUST COEFFICIENT	TORQUE COEFFICIENT X 10	EFFICIENCY	REYNOLDS NUMBER X 10^{-5}
0.00	0.710	1.274	0.000	2.412
0.05	0.685	1.235	0.043	2.415
0.10	0.660	1.196	0.086	2.422
0.15	0.636	1.156	0.129	2.434
0.20	0.611	1.117	0.171	2.451
0.25	0.586	1.078	0.212	2.472
0.29	0.562	1.039	0.253	2.498
0.34	0.537	1.000	0.293	2.528
0.39	0.513	0.961	0.333	2.562
0.44	0.488	0.922	0.371	2.600
0.49	0.463	0.883	0.409	2.642
0.54	0.439	0.844	0.446	2.688
0.59	0.414	0.804	0.482	2.737
0.64	0.390	0.765	0.516	2.790
0.69	0.365	0.726	0.548	2.845
0.73	0.340	0.687	0.579	2.904
0.78	0.316	0.648	0.607	2.965
0.83	0.291	0.609	0.633	3.029
0.88	0.267	0.570	0.656	3.095
0.93	0.242	0.531	0.675	3.163
0.98	0.218	0.492	0.689	3.234
1.03	0.193	0.453	0.696	3.307
1.08	0.169	0.414	0.697	3.381
1.13	0.144	0.375	0.687	3.457
1.17	0.119	0.337	0.664	3.535

DISCUSSION AND COMPARISON OF METHODS

A comparison of the thrust and torque coefficients obtained by both experimental methods is shown in Figure 5. The continuous lines represent the propeller characteristics obtained by the least squares fit of the constant acceleration method. The data points are the over plot of the steady state data obtained by the standard open water method. The correlation for this example is excellent; scatter of the standard discrete method about the continuous quasi-steady method is less than ±0.40 percent for torque and less than ±0.87 percent for thrust. The standard approach required two hours of testing time per propeller while a single constant acceleration pass requires 15 minutes, a factor of eight difference.

As was metioned earlier, a total of four propellers were tested by both methods, and all compared equally well. In fact, the example given represented the worst correlation in our sample. These four propellers all had very flat coefficient curves, and therefore it can be assumed that they would represent the best case for the constant acceleration method. The flatness of the thrust and torque coefficients as a function of advance ratio may contribute to the linear response found in the time histories, this allowing for just a simple least squares fit of the data. A propeller that had more curvature in its thrust and torque coefficient curve may not give a linear response during constant acceleration, and may require either a higher order fit, or more likely, a spline fit to interpolate the data.

One potential problem that must be addressed is that of thrust offset due to propeller mass during acceleration. This inertial force can be accounted for if a no-load tare is taken so that the dummy hub is equal in weight to the test propeller. The tare is then taken by running the dummy hub over the same test conditions as planned for the propeller. In this example case the inertial force at 0.5 ft/sec^2 would only be 0.03 lbs, this is assuming that the mass ahead of the thrust flexure weighed 1.7 lbs. The low value of this inertial tare accounts for the before mentioned lack of difference between the static and dynamic tares encountered during these experiments.

Another effect that should be considered is the influence of acceleration on the propeller boundary layer. Transistion is typically delayed during acceleration. This would imply that an accelerated propeller may encounter laminar flow problems at much higher Reynolds numbers than is found for the steady method. A decelerated flow, however, can trip transition and may lower the critical Reynolds number thus permiting the use of smaller models for measuring open water propeller characteristics.

CONCLUSIONS

The constant acceleration propeller technique as applied in the open water towing basin for the case of constant rotation and accelerated advance speed, does give results comparable to the standard method. This method does work in the first quadrant for propellers with flat thrust and torque curves. The technique as described here, as well as other variations, should be further investigated to establish additional correlations and limitations.

These investigations should include the use of propellers with highly nonlinear thrust and torque characteristics in order to determine the impact of nonlinear time histories on data interpolation. The correlation of these results should be made in all four quadrants, again to study nonlinear areas. The feasability of the use of spline fits for the interpolation of these time histories in order to generalize the data processing should be also considered.

In this example, constant acceleration of the carriage was used. Not all facilities may be capable of such carriage control. However, constant acceleration of propeller rotation may be more easily obtained, and should also be studied. In fact, if both advance and rotational speed can be varied so that a constant propeller Reynolds number is maintained during a pass, curves of constant Reynolds number can be obtained. This would be a useful tool for investigating the influence of transistion on model propellers and the impact of acceleration and deceleration on propeller transition.

FIGURE 5: Comparison of Methods

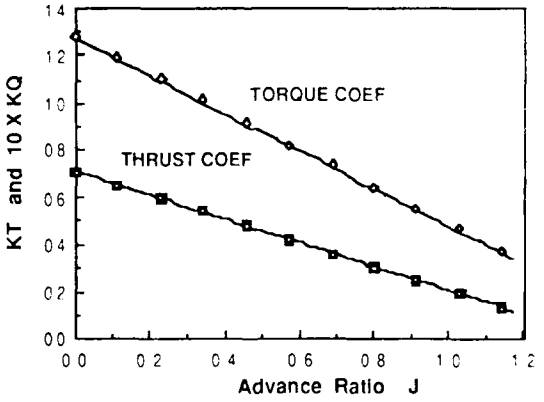

OPTIMUM CIRCULATION DISTRIBUTIONS FOR SINGLE AND MULTI-COMPONENT PROPULSORS

Justin E. Kerwin, William B. Coney and Ching-Yeh Hsin
Massachusetts Institute of Technology
Cambridge, Massachusetts

ABSTRACT

A vortex lattice lifting line theory is developed which can accomodate both single and multiple component propulsors. An optimization procedure is derived which permits the determination of the radial circulation distribution on the individual components as well as the division of loading between them. Comparison with other optimization methods for single propulsors is made. Results are given for an individual propeller, contra-rotating set, propeller with a pre-swirl stator, and a propeller with a vane wheel.

INTRODUCTION

In spite of the development of elaborate lifting surface design and analysis methods, as well as the recent introduction of surface panel codes, lifting line theory still plays an essential role in propeller design. The reason is that the most reliable prediction of the relationship between the radial distribution of circulation and the resulting thrust and torque comes from a Trefftz plane analysis, which follows directly from lifting line theory. In addition, lifting line theory provides a variety of essential inputs to the propeller design process thus permitting parametric studies to be made to determine an optimum design from the point of view of efficiency, cavitation strength and cost.

While lifting line codes for single propellers have been available for many years, their application to the problem of multi component propulsors has generally been handled by coupling single propeller codes in an iterative way. It therefore seemed worthwile to develop a new computational scheme which could handle a variety of multi component propulsors in a consistent manner. Such a code is now under development, and in its present form is able to handle single propellers, counterrotating propellers, propellers with pre or post swirl stators and propellers with vane wheels. Included in the code is an optimization procedure which enables one to determine both the division of loading between propulsor components and the radial distribution of loading on each component.

The present theory uses a vortex lattice representation of the bound and trailing vortex distributions representing each lifting line, and as a result there is no fundamental limit to the complexity of the multi component propulsor which can be analysed and/or optimized.

VORTEX LATTICE LIFTING LINE THEORY

The fundamental assumptions of the lifting line model which we have adopted are,

a. The blades of each component are represented by straight, radial lifting lines.
b. The blades of each component are considered to have equal angular spacing and identical loading.
c. The wake geometry is assumed to be purely helical, with a pitch at each radius determined either by the undisturbed inflow (linear theory) or by the induced flow at the lifting line(moderately loaded theory).

The continuous distribution of vortices along the lifting line is discretized by a lattice of concentrated straight-line elements of constant strength. The element arrangement used in the present work employs constant spacing in order to facilitate the alignment of the discretized vortex sheets shed from different components.If propulsor components have different diameters,the difference must be an integer multiple of the radial discretization.As shown by Kerwin and Lee (1978),this is not quite as accurate as "cosine" spacing,but the difference is extremely small.

As shown by James (1972), the panels at the endpoints must be inset one-quarter interval in order to properly represent the square root singularity in trailing vortex strength. The radii of the panel boundaries are therefore

$$r_{jp} = \frac{(R - r_H)(4p - 3)}{4M_j + 2} + r_H, \quad p = 1, 2, \cdots M_j + 1 \qquad (1)$$

and the induced velocity is calculated at control points located at the mid-radius of each panel. This arrangement is identical to that employed in the lifting surface design and analysis codes developed by Greely and Kerwin (1982).

Considering the interaction between two components,not only must the self-induced velocity of each component be calculated ,but also the velocity induced by each component on the other must be taken into consideration. The velocity diagrams for two components are shown in Figure 1. The axial induced velocity at the m'th panel of the j'th component can be expressed as :

$$u_{jm} + \bar{u}_{jm} = \sum_{p=1}^{M_j+1} \gamma_{jp} u^*_{jm,jp} + \sum_{p=1}^{M_l+1} \gamma_{lp} \bar{u}^*_{jm,lp} \qquad (2)$$

where

$\gamma_{jp} = \Gamma_{j(p-1)} - \Gamma_{jp}$,is the strength of the p'th trailing vortex,and Γ_{jp} is the concentrated strength of the p'th panel of the component j.

u_{jm} is the self-induced velocity at the m'th panel of component j

$\bar{u}_{jm}$ is the circumferential mean velocity at m'th panel of component j.

$u^*_{jm,jp}$ is local axial self-induced velocity at the m'th panel of component j,induced by K_j p'th trailing vortices with unit strength of the same component.

$\bar{u}^*_{jm,lp}$ is the circumferential mean velocity at the m'th panel of component j induced by K_l p'th trailing vortices with unit strength of component l.

K_j is the number of blades of component j.

M_j is the number of panels of component j.

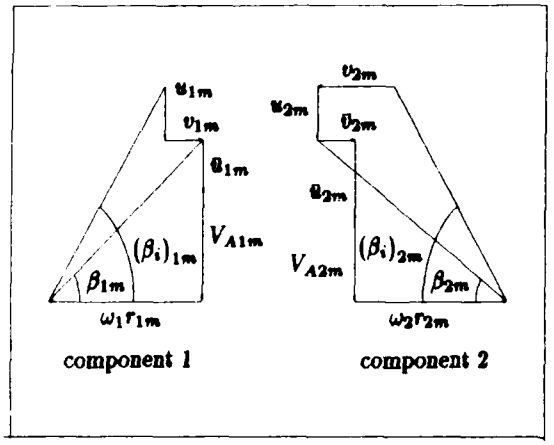

Figure 1 Velocity diagram for a contra-rotating propeller.

The tangential induced velocity, v_{jm}, can be expressed in a similar manner.

The self-induced velocities $u^*_{jm,jp}$ and $v^*_{jm,jp}$ can be computed using the very efficient asymptotic formulas developed by Wrench (1957), while the circumferential mean velocity $w^*_{jm,jp}$ can be computed from the formulas developed by Hough and Ordway (1964). Finally, the circumferential mean velocity $v^*_{jp,jm}$ may be obtained directly from Kelvin's theorem. The calculation of circumferentioal mean velocity is explained in the appendix.

An additional complication arises in the case of a stator, where the pitch angle may be close to ninety degrees. It has been determined that the formulas developed for a helical vortex will still yield accurate result up to $\tan \beta_i = 100$. For higher values, the vortices can be regarded as having infinite pitch, and the self induced velocities will be given directly by:

$$u^*_{jm,jp} = 0$$

$$v^*_{jm,jp} = \frac{1}{4\pi} \sum_{k=1}^{K_j} \frac{r_{jm} - r_{jp}\cos(\delta_k)}{r^2_{jp} + r^2_{jm} - 2r_{jm}r_{jp}\cos(\delta_k)} \qquad (3)$$

where

$$\delta_k = (k-1)\frac{2\pi}{K_j}$$

In the case of infinite pitch, the circumferential mean axial velocity induced by the stators will be zero, while the tangential component will be determined, as before, from Kelvin's theorem.

Figures 2-7 are examples of the radial distribution of induced velocity obtained for single and contra-rotating propellers with prescribed elliptical loading. It can be seen that the results obtained with 10 and 20 panels are almost identical for both the single propeller and the contra-rotating set with equal diameters. In the example shown in figures 6 and 7 the aft component of the contra-rotating set has a diameter which is 21 percent greater than that of the forward component. In this case 15 and 30 panels were used on the forward component, with additional constant spaced elements added to the aft component. Note that the tangential velocity induced at the downstream component shown in figure 7 is zero outside the radius of the forward propeller, and that the total tangential induced velocity is nearly zero at the inner radii.

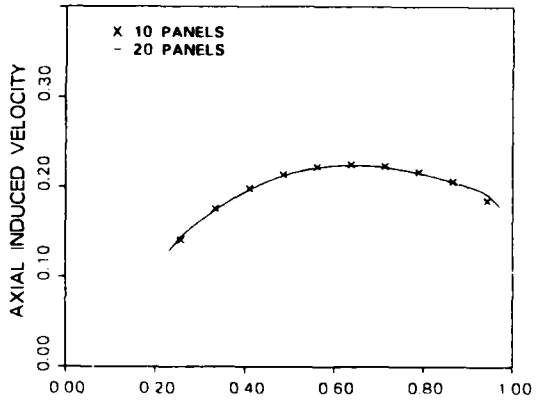

Figure 2 Axial induced velocity of a single propeller.

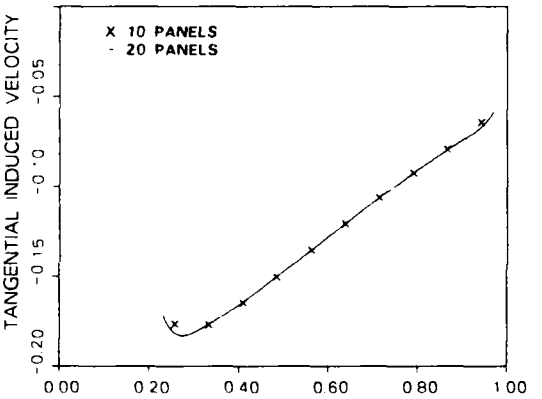

Figure 3 Tangential induced velocity of a single propeller.

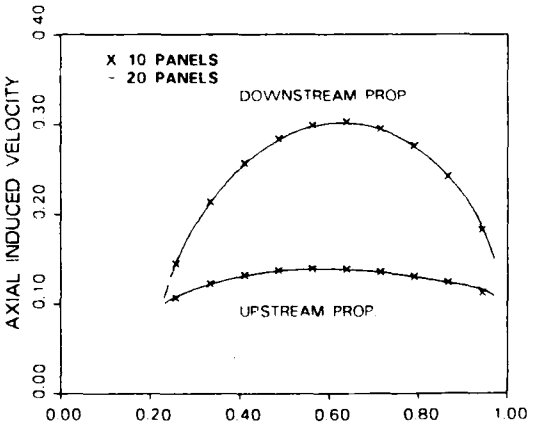

Figure 4 Total axial induced velocity on each component of contra-rotating propellers with equal diameters.

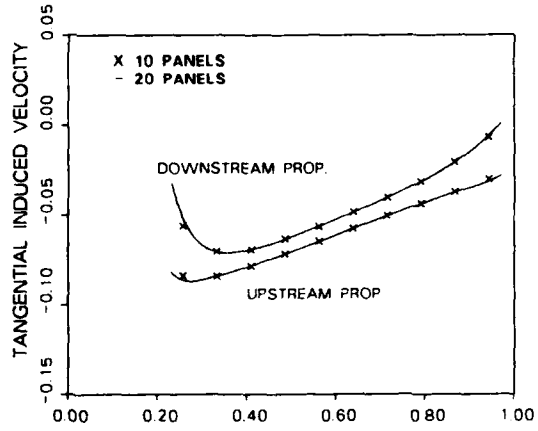

Figure 5 Total Tangential induced velocity on each component of contra-rotating propellers with equal diameters.

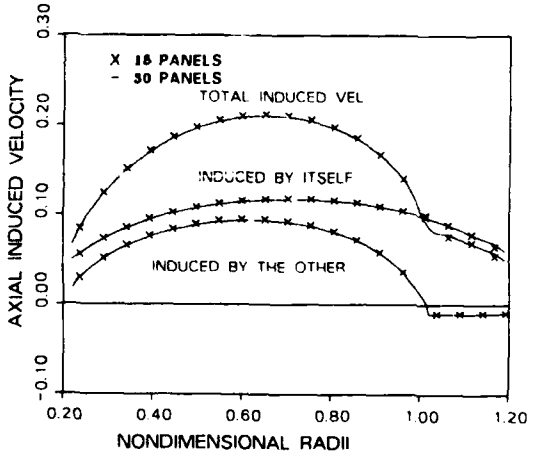

Figure 6 Axial induced velocity of the downstream propeller of a contra-rotating pair which has a larger propeller downstream.

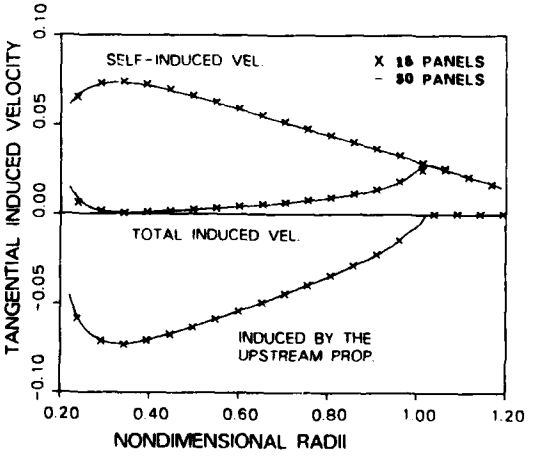

Figure 7 Tangential induced velocity of the downstream propeller of a contra-rotating pair which has a larger propeller downstream.

ON THE TIP LOADED OPTIMUM PROPELLER

The classical solution for the optimum radial circulation distribution follows from the original work of Betz (1919), who treated the case of uniform inflow, and Lerbs (1952), who considered the influence of the radial variation of the circumferential mean wake. More formal treatments of the problem were given subsequently by Wehausen (1964) and Yim (1976), who confirmed the earlier results. The solution can be stated very simply by the kinematic relationship,

$$\frac{\tan\beta_i(r)}{\tan\beta(r)} = \frac{H}{\sqrt{V_A(r)/V_S}} \qquad (5)$$

where the constant H sets the desired level of thrust or torque.

This result is correct in the limit of vanishing loading, where the propeller induced velocities are small compared to the relative onset flow and where the path of the trailing vortex sheets can be assumed to follow the streamlines of the undisturbed flow. It is generally applied, however, within the framework of the theory of the "moderately loaded propeller", in which the pitch of the trailing vortex wake is adjusted to match the induced inflow at the lifting line.

Clearly one can satisfy (5) in this case, but will the result be the optimum? Loukakis (1971) found efficiencies higher than that given by (5) by applying a systematic search procedure to the determination of the eleven term sine series approximation to the circulation. The resulting circulation distributions found by Loukakis were characterised by a high concentration of loading at the tip.

Being somewhat puzzled by Loukakis' findings, one of the present authors recomputed the efficiencies of the tip loaded circulation distributions with the same lifting line code modified to keep the trailing vortex wake at the pitch of the undisturbed flow, and found that the results were always lower than for the circulation distribution obtained by applying (5). The anomoly was therefore a direct consequence of the radial variation in trailing vortex pitch indroduced by moderately loaded theory. This, of course, did not answer the question of whether Loukakis' findings were physically correct or not, and it is perhaps sufficient to say that this issue is still controversial.

This question has come up again for two reasons. First of all, we were concerned with the question of how to optimize multi component propulsors, where it would seem desirable to use moderately loaded lifting line theory. But in addition, Brockett and Korpus (1986) have recently presented lifting line results which again show that increased loading at the tip increases efficiency. They show results for a five term sine series representation of the distribution of circulation which produces an efficiency which is higher than that obtained by applying (5).

It seemed that one possible explanation for both Loukakis' and Brockett and Korpus' results was associated with the Lerbs lifting line procedure which both employed (although in somewhat different forms). The efficiency resulting from the five term circulation series found by Brockett and Korpus was therefore computed using the present vortex lattice method with increasing numbers of panels. Calculations were also made using Lerb's induction factor method for the same set of circulation coefficients and for the Lerbs optimum distribution obtained from (5). To make the comparison as pure as possible, no viscous drag was included in this exercise. For both runs with the Lerbs induction factor program, the thrust coefficient was set equal to the value obtained with the present vortex lattice program using 160 panels. The results shown in the table below confirm the results obtained by Brockett and Korpus and lay to rest any doubts about the role of numerics in this issue. The efficiency obtained from the vortex lattice procedure has converged to five significant digits (a challenge for the experimenter!) and differs from the Lerbs result by four tenths of a percent.

Table 1 Convergence Test		
Number of Panels	η	C_T
10	0.80636	0.68467
20	0.80681	0.68636
40	0.80697	0.68679
80	0.80704	0.68690
160	0.80706	0.68693
Ind. Fact: B - K Opt.	0.81011	0.68693
Ind. Fact: Lerbs Opt.	0.79368	0.68693

Another question is whether the variational approach somehow produces a local optimum. To check this, An optimum circulation distribution for Brockett and Korpus' example was first computed using the vortex lattice optimization preocedure which will be described subsequently. For present purposes, it is sufficient to say that it is essentially equivalent to result obtained using (5). The resulting efficiency is 0.794, which agrees to three significant digits with the optimum obtained with the Lerbs induction factor code. A set of calculations were then made with circulation distributions consisting of linear combinations of the two differently obtained optima. The result is shown in Figure 8, which shows that no local optimum exists, and that the Brockett and Korpus distribution yields the highest efficiency obtainable with such a linear combination. The same excercise was repeated with the pitch of the trailing vortex wake forced to remain at the undisturbed flow angle, and these results are shown in Figure 9. Now the conclusion is opposite, with the circulation distribution derived from the present vortex lattice procedure being optimum. This confirms the earlier finding that the circulation from (5) obtained from Lerbs procedure produced higher efficiencies than those obtained by Loukakis when the trailing vortex wake was fixed.

The results given by Brockett and Korpus are therefore confirmed as the true five term optimum circulation distribution in accordance with moderately loaded lifting line theory. But what is the optimum if the circulation is allowed to be an arbitrary function of radius? This can be approached either by progressively increasing the number of terms in the sine series, or in the case of the vortex lattice method, by increasing the number of panels.

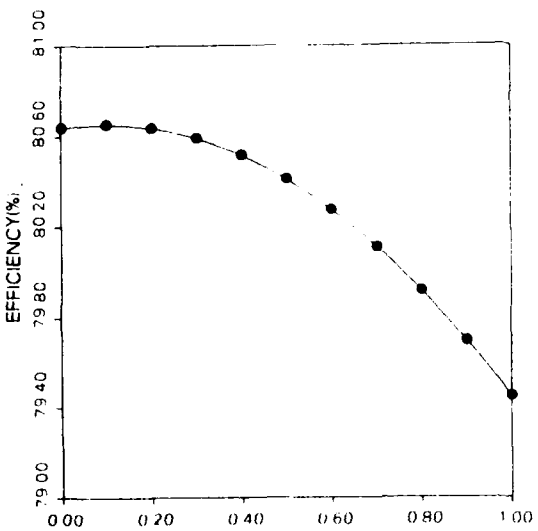

Figure 8 Efficiency as a function of circulation distribution derived from a linear combination of the present results and those of Brockett and Korpus. (0.0 = Brockett and Korpus, 1.0 = all present theory.) The wake is aligned using moderately loaded theory.

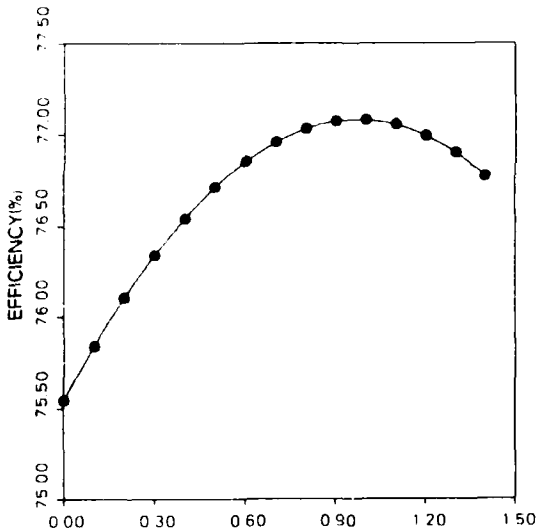

Figure 9 Efficiency as a function of the circulation distribution as in figure 8, except that the wake is constrained to follow the undisturbed flow.

To implement the latter, a crude systematic search technique was incorporated in the vortex lattice program whereby the circulation of one panel was incremented by a small amount and the entire circulation scaled to yield constant thrust. If the efficiency increased the circulation increment was kept, otherwise it was discarded. The procedure was repeated systematically moving back and forth along the radius all night on an IBM PC. The authors should emphasise that this unsophisticated optimizer (which only involved a dozen extra lines of code) was only intended to be run once!

The results were spectacular. By morning, the ideal efficiency was up to about 97 percent, and the induced velocity at the tip was almost three times the speed of advance ! In addition to demonstrating that there there is no limit to the absurdity of the optimum circulation distribution for a moderately loaded lifting line, the excercise showed clearly how the model defeats itself. A sharp increase in loading at the tip increases the pitch of the tip vortex (in this case the wake pitch angle increased from 35 degrees to 69 degrees in the last two percent of the radius) which then decreases the induced velocity everywhere inside the tip. The tip panel has high induced drag, but all the panels inside have essentially zero drag, or possibly even propulsion.

There is clearly something wrong with this physically, and the answer can be found at least qualitatively in the way a "real" vortex sheet deforms behind a wing or propeller blade tip. Perhaps it is easiest to consider the simple case of an elliptically loaded wing, where lifting line theory predicts constant downwash over the span. The equivalent of moderately loaded propeller theory would place the trailing vortex sheet on a plane inclined at a constant angle equal to the induced angle at the lifting line. Both observations and computations by a variety of "vortex chasing" methods show, on the contary, that the middle of the vortex sheet moves down at a rate faster than that given by the flow angle at the lifting line, and that the tip regions move up relative to this same reference plane. The upward movement of the tip vortices is result of the rolling up and diffusion of the viscous region in the interior of the vortex sheets. Moreover, as the wing loading is increased, the rolling up process, and hence the upward movement of the tip vortices, takes place more rapidly.

Laser-Doppler Anemometer measurements in the MIT water tunnel by Min (1978) and subsequent experimenters have shown the same behavior for marine propellers, as have numerous investigators in the area of helicopter wake trajectories, for example Murman and Stremel (1983) and Morino and Bharadwaj (1985).

A relatively simple propeller wake alignment scheme was devised by Greeley and Kerwin (1982) and found to agree well with existing water tunnel observations. This procedure was therefore used to determine the initial wake geometry for Brockett and Korpus example, both for the classical optimum and for their five term tip loaded optimum circulation distribution. This was done by running the PBD-10 lifting surface design program, which incorporates this wake model, for both circulation distributions. The axial induced velocity at the tip obtained from the wake alignment procedure was $0.185V_S$ compared with a value of $0.562V_S$ obtained from moderately loaded lifting line theory. Clearly the high axial induced velocities at the tip predicted from moderately loaded lifting line theory do not materialize with this wake model. Furthermore, the efficiency of the tip loaded propeller according to the lifting surface calculation was slightly less than for the classical optimum load distribution.

This is not condidered to be conclusive evidence that the classical optimum cannot be improved upon since the wake alignment scheme is not necessarily accurate for such an extreme load distribution. In fact, we were pleasantly surprised that it converged at all! Nevertheless, the trend is as expected.

To conclude this section, it is our opinion that the trailing vortex wake geometry associated with moderately loaded lifting line theory can only be regarded as correct in a gross sense, and cannot be relied upon as regards to the change in radial distribution of pitch of the trailing vortex sheets brought about by a change in radial load distribution. The tip loaded optimum solution succeds only as a result of a predicted local increase in pitch of the trailing vortex sheet at the tip, which probably cannot be acheived in a real fluid. Therefore, until such time as an accurate complete viscous solution of the vortex wake region becomes practical, the optimization problem should best be solved within the framework of linear theory.

It should also be emphasized that the question of whether or not high tip loading can increase efficiency should not be confused with the evaluation of the merits of adding physical boundaries such as ducts, bands or tip fins. In this case linear theory will show that increased loading at the tip will be optimum.

VARIATIONAL OPTIMIZATION

This is the classical problem of finding the optimum radial distribution of circulation given a propeller's operating conditions. Our goal is to find the circulation distribution which provides a prescribed thrust, T, for a minimum torque, Q. We begin with an inviscid vortex lattice model with a frozen wake geometry. The thrust and torque are given by:

$$T = \rho K \sum_{m=1}^{M} (V_{T_m} + \omega r_m + v_m)\Gamma_m \Delta r_m$$

$$Q = \rho K \sum_{m=1}^{M} (V_{A_m} + u_m)\Gamma_m r_m \Delta r_m \qquad (6)$$

where

$$u_m = \sum_{n=1}^{M} \Gamma_n u^*_{m,n}$$

$$v_m = \sum_{n=1}^{M} \Gamma_n v^*_{m,n} \qquad (7)$$

where Δr_m is the radial distance between the two lattice points surrounding control point m, and $u^*_{m,n}$, $v^*_{m,n}$ are the velocities induced on control point m by a unit of circulation on the complete horseshoe vortex surrounding control point n.

Using a varational approach, we form the quantity $H = Q + \lambda T$ which is to be minimized. The Lagrange multiplier, λ, is to be solved for along with the Γ_m's. Expanding H with (6) and (7) and then setting its partial derivatives with respect to the Γ_m's equal to zero, gives us M equations for the M discrete values of circulation and the Lagrange multiplier. An additional equation is provided by specifying the required thrust in (6).

$$\frac{\partial H}{\partial \Gamma_i} = 0 = \rho K \{V_{A_i} r_i \Delta r_i + \sum_{m=1}^{M} (\Gamma_m u^*_{i,m} r_m \Delta r_m + \Gamma_m u^*_{m,i} r_i \Delta r_i)$$
$$+ \lambda (V_{T_i} + \omega r_i)\Delta r_i$$
$$+ \tilde{\lambda} \sum_{m=1}^{M} (\Gamma_m v^*_{i,m} \Delta r_m + \Gamma_m v^*_{m,i} \Delta r_i)\}$$
$$(i = 1, \ldots, M)$$
$$T = \rho K \sum_{m=1}^{M} (V_{T_m} + \omega r_m + v_m)\Gamma_m \Delta r_m \qquad (8)$$

The constants, $\tilde{\lambda}$ and the v_m's, in the thrust equation are determined by (8) and (7) during a previous iteration of these optimization equations. This iterative approach allows us to unfreeze the wake and include a simple model for viscosity. At each iteration the wake geometry can be aligned by updating the pitch angle, β_i, at each control point, and then recalculating the influence functions, $u^*_{m,n}$ and $v^*_{m,n}$. The effect of viscous drag on the total thrust can be included by adding a drag computed during the previous iteration to the thrust required in the current iteration. The effects of viscous drag on the optimum circulation distribution is currently ignored.

A similiar system of equations can be derived for contra-rotating propellers. The goal in this case is to find the optimum radial distribution of circulation on each of two rotating components located at different axial locations along the propeller drive shaft. We want the circulation distribution which provides a prescribed total thrust and a prescribed torque ratio, q, between the two components for the minimum total power.

The quantity to be minimized is: $H = \omega_1 Q_1 + \omega_2 Q_2 + \lambda_1 (T_1 + T_2) + \lambda_2 (Q_2 - qQ_1)$; with the constraints: $Q_2 - qQ_1 = 0$ and $T_1 + T_2 = T$. There are now two Lagrange multipliers, λ_1 and λ_2 to be solved for, as well as M_1 values of circulatation, Γ_{1m}, on the first component and M_2 values of circulation, Γ_{2m}, on the second component. Once again we expand H with the equations for the induced velocities and set its partial derivatives with respect to the unknown circulations equal to zero. This process gives us a system of equations which we can solve for λ_1, λ_2 and the circulations at the control points.

Setting the torque ratio, q, equal to zero results in a propeller-vane wheel combination. No change to the form of the optimization equations is required.

The case of a propeller operating with a set of stator blades can be thought of as a special case of the contra-rotating optimization without the constraint $Q_2 - qQ_1 = 0$. The quantity to be minimized is: $H = \omega_1 Q_1 + \omega_2 Q_2 + \lambda (T_1 + T_2)$ with the constraint $T_1 + T_2 = T$.

ILLUSTRATIVE EXAMPLES

Presented here are some sample results from the present lifting line theory. These results are not intended as a comprehensive comparison of the propulsors examined. Rather, they demonstrate the type of results which can be obtained through the variational opimization of the vortex lattice model, which we have described.

The operating condition is that described by Brockett and Korpus (1986). A free-running ($V_A(r) = V_S$), 5 bladed propeller with an expanded area ratio of 0.725 is required to develop a thrust coefficient of 0.69 at an advance coefficient of 0.89. The chord distribution for the propeller is given in Table 2, and the local drag coefficient is considered to be a constant, 0.0065.

The results from five propulsors are shown here. Case 1 is the propeller described above with a Lerbs optimum circulation distribution. Case 2 is the same propeller with a circulation distribution from our variational optimization. These circulation distributions are shown in Figure 10. Notice the similiarity between the two distributions. In light loading the variational optimum approaches the Lerbs optimum.

The preswirl propulsor consists of a stationary blade row ahead of a rotating propeller. In case 3 a propeller with the same advance coefficient, number of blades and chord distribution as the first two cases is placed 0.25 propeller diameters downstream of a row of stator vanes. The stator has 9 blades and its diameter is 1.08 times the propeller diameter. The chord distribution is scaled to this new diameter from Table 2, however the vane blade area was adjusted to obtain a maximum local lift coefficient of 0.8. The propeller and stator vanes were together required to produce the same thrust as in the first two cases. The circulation distributions calculated for this preswirl propulsor are shown in Figure 11.

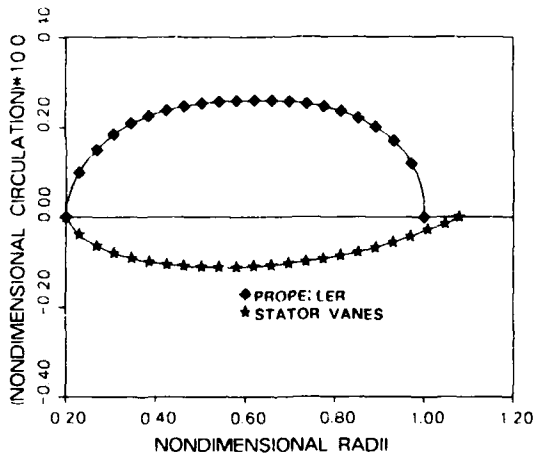

Figure 11 Optimum circulation distributions for a propeller operating behind a preswirl stator.

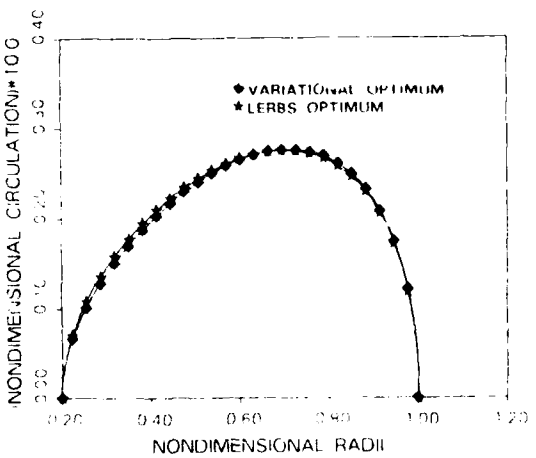

Figure 10 Comparison of optimum circulation distribution from present theory (variational optimum) and Lerbs optimum criteria.

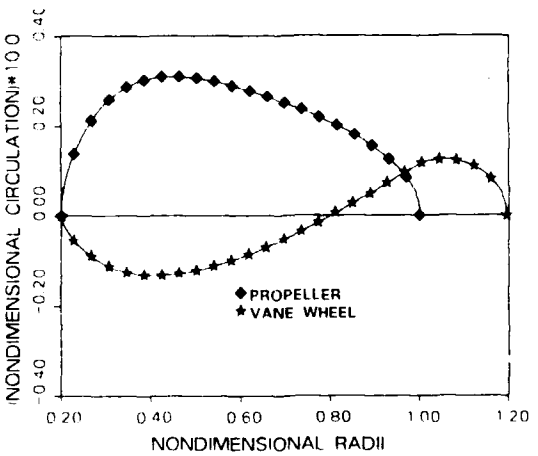

Figure 12 Optimum circulation distributions for a propeller vane wheel combination.

The vane wheel is a freely rotating set of blades installed on the propeller shaft behind the propeller. In case 4 a vane wheel is placed 0.25 propeller diameters downstream of a propeller with the same advance coefficient, number of blades and chord distribution as the previous three cases. The vane wheel has nine blades and its diameter is 1.20 times the propeller diameter. The chord distribution is again scaled to the new diameter from Table 2, however we again adjust the vane blade area so that a maximum local lift coefficient of 0.8 is obtained. The vane wheel was required to operate at a rotational speed of 23 percent of that of the propeller, this was found to be an optimum for these conditions. The propeller and vane wheel were together required to produce the thrust of the earlier cases, but an additional constraint of no total torque was imposed on the vane wheel. The circulation distributions for this propeller-vane wheel combination are shown in Figure 12. Notice that the vane wheel is being driven over its inner radii and is producing thrust over the outer.

Case 5 is a pair of contra-rotating propellers. They each have an advance coefficient of 0.89 but rotate in opposite directions. They are five bladed and of the same diameter. The chord distribution is that of Table 2, however the chord lengths have been halved so that the expanded area ratio is the same as the first two cases. We required the two propellers to produce the same total thrust as in our earlier cases. We further required them to have equal and opposite torques. The circulation distributions are shown in Figure 13. Figures 14 and 15 show the velocities induced by circulation distributions computed with varying numbers of lattice elements.

Table 3 gives the first five terms in the sine series representations of circulation for the propulsors we examined. These coefficients are nondimensionalized with the first term from the Lerbs optimum distribution. The value of this term with the standard nondimensionalization is 0.02689. Table 3 also gives the efficiency of each of the propulsors.

Table 3 Circulation Coefficients and Efficiencies						
Case	G_1	G_2	G_3	G_4	G_5	η
1	1.0000	−0.1324	0.0112	−0.0048	−0.0007	0.702
2	0.9918	−0.1525	0.0078	−0.0041	−0.0007	0.703
3						0.724
S	−0.3816	0.0338	0.0668	−0.0071	0.0086	
P	1.0004	−0.0309	0.0331	−0.0115	−0.0052	
4						0.707
P	1.0844	0.1859	0.0190	−0.0238	−0.0145	
V	−0.1071	−0.4388	0.0855	0.0190	−0.0030	
5						0.742
U	0.5058	−0.0707	0.0379	−0.0126	0.0041	
D	0.4277	−0.1149	0.0320	−0.0104	0.0060	

Table 2 Chord Distribution			
r/R	c/D	r/R	c/D
0.2	0.174	0.7	0.347
0.25	0.202	0.8	0.334
0.3	0.229	0.9	0.280
0.4	0.275	0.95	0.218
0.5	0.312	0.98	0.144
0.6	0.337	1.0	0.0

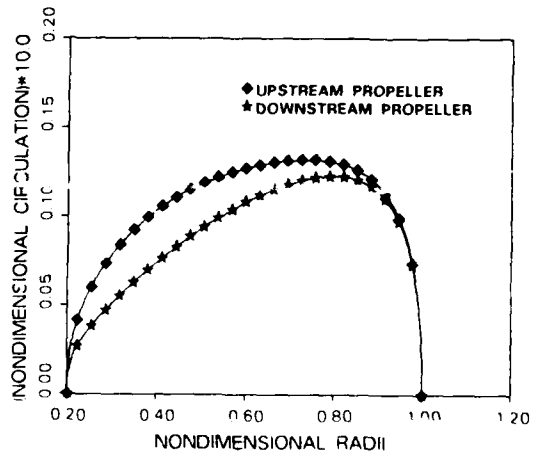

Figure 13 Optimum circulation distributions for a pair of contra-rotating propellers.

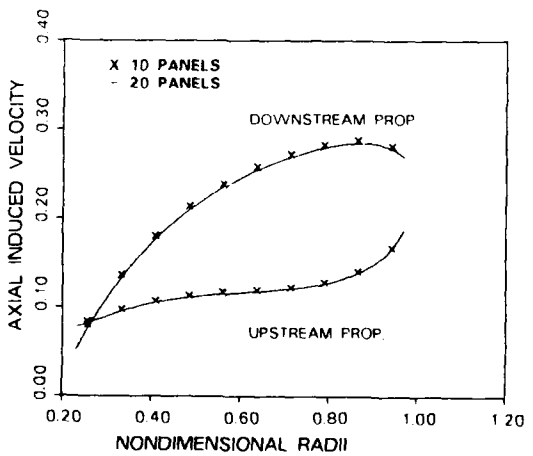

Figure 14 Axial component of velocity induced by optimum circulation distributions for a pair of contra-rotating propellers. Distributions are computed with 10 and 20 lattice elements.

$$G(r/R) = \frac{\Gamma}{\pi n D V_S}$$

$$J_S = \frac{V_S}{nD} = 0.89$$

$$C_T = \frac{8T}{\rho V_S^2 \pi D^2} = 0.69$$

$$EAR = A_E/A_o = 0.725$$

$$C_D = \frac{drag}{1/2\rho c V^{*2}} = 0.0085$$

V^* = resultant inflow velocity to a blade section

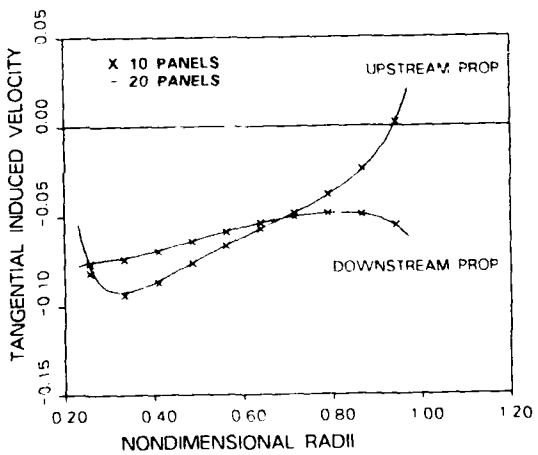

Figure 15 Tangential component of velocity induced by optimum circulation distributions for a pair of contra-rotating propellers. Distributions are computed with 10 and 20 lattice elements.

ACKNOWLEDGEMENTS

This research was supported under the U.S. Navy's Ship and Submarine Technology Program (PE 62543N) and Surface Ship Silencing Program (PE63553N).

The authors would like to acknowledge the many helpful suggestions of Dr. Arthur Reed of DTNSRDC during the development of the lifting line theory presented in this paper.

REFERENCES

Betz, A., "Schraubenpropeller mit geringstem Energieverlust," *Nachrichten der K. Gesellschaft der Wissenschaften zu Gottingen Math-Phys Klasse*, 1919.

Brockett, T. and Korpus, R., "Parametric Evaluation of the Lifting-Line Model for Conventional and Preswirl Propulsors," **Proceedings International Symposium on Propeller and Cavitation**, Wuxi, 1986.

Greeley, D. S. and Kerwin, J. E., "Numerical Methods for Propeller Design and Analysis in Steady Flow," *Trans. SNAME*, Vol. 90, 1982

Grimm, O., "Propeller and Vane Wheel," *JSR*, Vol. 24, 1980.

Hsin, C.-Y., "Efficient Computational Methods for Multi-Component Lifting Line Calculations," MIT Dept. of Ocean Engineering, S. M. Thesis, 1986.

Hough, G. R. and Ordway D.E., "The Generalized Actuator Disk," THERM Advanced Research Report No. TAR-TR6401, 1964.

James, R. M., "On the Remarkable Accuracy of the Vortex Lattice Method," *Comput. Methods Appl. Mech. Eng.*, Vol. 1, 1972

Kerwin, J. E. and Lee, C. S., "Prediction of Steady and Unsteady Marine Propeller Performance by Numerical Lifting Surface Theory," *Trans. SNAME*, Vol. 86, 1978.

Lerbs, H. W., "Moderately Loaded Propellers with a Finite Number of Blades and an Arbitrary Distribution of Circulation," *Trans. SNAME*, Vol. 60, 1952.

Loukakis, T. A., "A New Theory for the Wake of Marine Propellers," MIT Dept. of Ocean Engineering, Report 71-7, 1971.

Morino, L. and Bharaduaj, B., "Two methods for Viscous and Inviscid Free-Wake Analysis for Helicopter Rotors," Center for Computational and Applied Analysis, Boston University Report CCAD-TR-85-02, 1985.

Min, K.-S., "Numerical and Experimental Methods for the Prediction of Field Point Velocities Around Propeller Blades," MIT Dept. of Ocean Engineering, Report 78-12, 1978.

Morgan, W. B. and Wrench, J. W., "Some Computational Aspects of Propeller Design," **Methods in Computational Physics**, Vol. 4, Academic Press, 1965.

Murman, E. M. and Stremel, P. M., "A Vortex Wake Capturing Method for Potential Flow Calculations," AIAA/ASME 3rd Joint Conference, AIAA 82-0947, 1982.

Wehausen, J. V., "Lecture Notes on Propeller Theory," College of Engineering University of California, Berkeley, 1964

Wrench, J. W., "The Calculation of Propeller Induction Factors," DTMB Report 1116, Feb. 1957.

Yim, B., "Optimum Propellers with Cavity-Drag and Frictional-Drag Effects," *JSR*, Vol. 20, June 1976.

APPENDIX

THE COMPUTATION OF CIRCUMFERENTIAL MEAN VELOCITIES

The time-average velocities induced by one propulsor component on the other are equal to the circumferential mean velocities calculated in the rotating reference frame of that component.

A horseshoe vortice with lattice points at radii $r_{l(p-1)}$ and r_{lp} will, by Kelvin's theorem, induce a tangential circumferential mean velocity on a control point, at radius r_{jm} of the other component, of:

$$v^*_{jm,ln} = \begin{cases} 0, & S > 0, -\infty \le x_f \le \infty \\ & S \le 0, x_f < 0; \\ \frac{-K_l \Gamma_{l(p-1)}}{2\pi r_{jm}}, & S < 0, x_f > 0. \end{cases} \tag{9}$$

where

$$S = (r_{j(p-1)} - r_{jm})(r_{jp} - r_{jm})$$

Since the circumferential mean velocities induced on the other component by the bound vortices are only tangential, the problem now is to solve for the axial circumferential mean velocity induced by the trailing vortices. Hsin (1986) compared a variety of computation methods with respect to accuracy and computation time, and concluded that Hough and Ordway's formulas should be used for this application.

By using a Fourier analysis of the velocity field, Hough and Ordway derived formulas for the induced velocities of an actuator disk in terms of elliptical integrals. These can be thought of as the velocities induced by a propeller with an infinite number of blades. Since the circumferential mean velocities are the average of the sum of local induced velocities along a circle (with infinite points), we can just apply these formulas to calculate the circumferential mean velocities. The formulas are shown as follows:

$$C_1 = \begin{cases} \pi + \frac{x_f}{2\sqrt{r_{jm} r_{lp}}} Q_{-\frac{1}{2}}(q) + \frac{\pi}{2} \Lambda_0(s,t), & r_{jm} \le r_{lp} \\ \frac{x_f}{2\sqrt{r_{jm} r_{lp}}} Q_{-\frac{1}{2}}(q) - \frac{\pi}{2} \Lambda_0(s,t), & r_{jm} > r_{lp} \end{cases} \tag{10}$$

where

$$\begin{aligned} q &= 1 + \frac{x_f^2 + (r_{jm} - r_{lp})^2}{2 r_{jm} r_{lp}} \\ s &= \sin^{-1}\left[\frac{x_f}{\sqrt{x_f^2 + (r_{jm} - r_{lp})^2}}\right] \\ t &= \sqrt{\frac{4 r_{jm} r_{lp}}{x_f^2 + (r_{jm} + r_{lp})^2}} \end{aligned} \tag{11}$$

and

$Q_{-\frac{1}{2}}$ is the Lengendre function of the second kind and half integer order.

Λ_0 is the Heumann's Lambda function.

C_2 is the same as C_1 except the r, r inequalities are reversed.

Then we can get,

$$\begin{aligned} u^*_{jm,lp} &= \frac{K_l}{\pi r_{lp} \tan(\beta_{lp})} C_1 \\ v^*_{jm,lp} &= \frac{K_l}{\pi r_{jm}} C_2 \end{aligned} \tag{12}$$

DISCUSSION

Dr. Terry Brockett,
University of Michigan,
Ann Arbor, MI, USA

The authors have presented a solution to a problem of current great interest and importance - criteria for selecting efficient circulation distributions of compound propulsors - and warrant congratulations from all of us interested in propulsor design.

I have some minor questions about the formulation that may help clarify some of the results presented:

1) The use of the Trefftz-plane to derive load relationships seems unnecessary and somewhat misleading in the sense that somehow far-downstream flow details are related to local happenings at the lifting line. Can the authors provide some additional information on the derivations?

2) There are references to panels and lattice elements in the paper that are not clearly distinguished. In general, a lattice will correspond to a panel of constant doublet strength but with the lattice strengths as the unknowns, the concept of a panel is difficult to employ.

3) The results of the authors "overnight" run with the simple optimization scheme is an efficiency value (0.97) that is greater than the simple ideal actuator disk model will predict for this case, 0.87. Do the authors have some insight into this difference?

4) The predicted efficiency values quoted in Table 3 show that the vane-wheel propeller is within experimental accuracy of the conventional propeller but that the values for the contra rotating and preswirl propulsor are a few points increased relative to the vane wheel. I suspect that the large number of retro-fit vane wheel propellers being installed is justified on a quoted 5 point (or 10%) increase in measured efficiency for C_{Th} values nearly twice that of the authors sample (together with ease of installation). Do the authors have data to make relative comparisons at these increased loads?

5) The preswirl propulsor (Case 3 in Table 3) is similar to an example presented by Brockett and Korpus (authors second reference) for elliptic circulation on the rotor. Additional information on the loads (e.g., vane drag and torque) would be helpful to compare the two data sets.

6) Can the authors provide some information on run times of their code?

In work described by Brockett and Korpus that appears elsewhere in these proceedings, the importance of the trajectories of the vortex-sheet filaments for preswirl propulsors was such that efficiency values were as much as ±10 points different as a function of reasonable specifications. Do the authors find similar trends when they include various sheet orientations and can they present data at several radii for the predicted trajectory shapes from their lifting-surface analysis?

AUTHOR'S REPLY

1. A lifting line is a figment of the imagination used to generate a free vortex wake which matches that produced by a wing or propeller far downstream. We are therefore able to calculate total forces much more easily from momentum and energy considerations. The fact that the forces expressed in the usual way in Equation (6) look as though Kutta-Joukowski's law was being applied on the lifting lines is a convenient but dangerous concept. One can get into trouble very easily, for example, if the local force concept is applied to lifting lines which are curved or swept. We are sure that there is no disagreement about Equation (6), it is a matter of its interpretation.

2. In our terminology, a panel is a complete horseshoe vortex element, or its equivalent, a constant density dipole. A lattice element is a single discrete vortex line forming one of the boundaries of a panel.

3. Professor Brockett's observation that the efficiency which we obtained using moderately loaded propeller theory is higher than that of an actuator disk serves to emphasize that the fact that moderately loaded propeller theory is not physically consistant. Let us emphasise again that the efficiency of 97 percent that we obtained is a classical example of the theorem of "garbage in - garbage out".

4. We have subsequently tried a vane wheel for an application with a higher thrust coefficient, and find that the gain, as expected, is somewhat greater. However we have also found even greater gains if the effect of the hub is considered, which then permits finite circulation at the hub. This feature was not completed at the time the paper was prepared.

5. The thrust coefficient, C_T, for the vanes of the pre-swirl propulsor presented here is -0.022. The torque on the vanes can be expressed in terms of a torque coefficient

$$C_Q = \frac{2Q}{\rho V_s^2 A_o D}$$

which has a value -0.0685 in this example. The expanded area of the vanes is 0.385.

6. The computation of circulation distributions, velocities and forces for each of the cases presented took from a few seconds to a maximum of 30 seconds on a DEC Vaxstation II. The code which is described in part in this paper is intended to be an interactive design tool.

SESSION II
OCEAN ENGINEERING

TECHNICAL COMMITTEE MEMBERS

Mr. Frank W. DeBord, Jr. (Chairman)	Offshore Technology Corp.
Mr. Glenn McKee	Davidson Laboratory
Dr. Young Hong	DTNSRDC
Mr. Joseph Wetzel	Univ. of Minnesota
Dr. Jacek Pawlowski	Institute for Marine Dynamics/CANADA

OCEAN ENGINEERING COMMITTEE REPORT

Frank DeBord, Jr.
Vice President
Offshore Technology Corporation
578 Enterprise Street
Escondido, California 92025

Since this Twenty-First ATTC is the first ATTC to have an Ocean Engineering Committee, a report on advances in tankery related to Ocean Engineering is not really appropriate. Instead, committee members were asked to evaluate the current state-of-the-art in Ocean Engineering model testing, identify needs for improved facilities and techniques, and describe current research and development efforts and recent advances. Committee members included:

- Frank DeBord, Jr., Offshore Technology Corporation (Chairman)
- Young S. Hong, David W. Taylor Naval Ship Research and Development Center
- Glenn McKee, Davidson Laboratory
- Dr. Jacek Pawlowski, National Research Council, Institute for Marine Dynamics
- Joseph Wetzel, St Anthony Falls Hydraulic Laboratory

In the context of model testing, Ocean Engineering is a field which covers a very large variety of projects, and in certain cases overlaps exist with other standing ATTC committees. Typical uses of model basins which are considered to be within the realm of Ocean Engineering are:

- Vessel motions in a seaway (seakeeping)
- Wave and current loads on fixed and moored structures
- Offshore construction operations
- Marine transportation of offshore facilities (resistance and seakeeping)
- Mooring systems
- Dynamic positioning systems (maneuvering)
- Submersibles
- Risers, subsea pipelines and subsea cables
- Wave power generation systems
- Near-shore structures

Although tanks have been conducting experiments in most of these areas for quite a long time, only recently (since the late 1960's) have facilities been built and equipped specifically for Ocean Engineering testing. Obviously, techniques were developed based on those which existed for the most classical types of model testing, however facilities, test equipment, test techniques and data analysis techniques have evolved based on specific requirements of the above types of tests. Until recently, neither the ITTC nor ATTC have had "Ocean Engineering" committees, and therefore very little work has been done in the area of standard techniques. Due to the commercial nature of most of this work, the only standards which have developed have been those required by clients after experience with several alternate techniques.

It is beyond the scope of this committee report to even begin to describe the current state-of-the-art or attempt to identify areas where standards are needed. What we have attempted to do is to provide a description of current activities by member organizations with the intention that this will identify areas considered to be important in the future, and areas which require research into new facilities and techniques.

A review of the reports by individual committee members indicates that most facilities are involved with developments in three primary areas. These include improvement of wave generation equipment, improvement of data acquisition systems and analysis software, and development of analytic models to aid test planning and understanding of results. Work in the area of wave generation equipment includes both improvements to hardware and improvements to wave generation techniques. All facilities are becoming more sophisticated in generation of random seas, and in some cases, generation of short-crested seas is an active research area. Due to the increasing complexity of experiments,

most facilities have made major improvements to data acquisition and analysis hardware in recent years and major efforts have been made to improve techniques used for analysis of random time series data and presentation of results. Although not directly related to tankery, significant efforts are underway at most establishments to develop improved numerical models for prediction of responses of complex systems in a variety of sea conditions.

The David W. Taylor Naval Ship Research and Development Center is active in all three of the development efforts discussed in the previous paragraph. All of the pneumatic wavemakers are undergoing control system improvements and refurbishment intended to improve controllability and extend the useful frequency range. In addition, software has been developed for the determination of wave directionality based on measurements from an array of wave probes. Characterization of extreme wave events utilizing techniques such as the half cycle count method is a major effort in the area of data analysis, and research is being conducted to improve numerical models for predicting motions in extreme sea conditions. This latter project was initiated in response to the Ocean Ranger disaster and may result in the development of a new six-degree-of-freedom time domain code which would include non-linear hydrodynamic damping and exciting forces.

The National Research Council, Canada's Institute for Marine Dynamics, is currently in the process of acquisition and development of facilities which are described in several papers included in the Facilities and Techniques Session. This organization is actively engaged in an integrated development program to outfit the facilities, refine experimental techniques and assemble capable numerical models which can be used to compliment experiments. A major research effort currently underway is testing of prototype wavemaker and beach segments in the new seakeeping and maneuvering basin. In addition, a new non-contact motions measurement system has recently been tested and experimental techniques will be evaluated during a series of tests planned with a generic semisubmersible in the towing basin. Concurrently, a complete integrated system of computer models are under development to aid the facilities in providing basic and applied research services.

Recent facilities improvements at the Davidson Laboratory have included an upgrade of the Tank 3 wavemaker and replacement of the data acquisition computers for Tanks 2 and 3. Development of analysis techniques for random time series data has continued and the facility uses a unique "Peak-Trough" analysis which calculates statistics independent of zero crossings. One special project of note is the investigation of generating and maintaining a stratified fluid, with a sharp density gradient, in Tank 2. This project included design of a wavemaker to generate internal waves, a special high-frequency wavemaker, and other tools necessary to create and maintain the stratified fluid.

Ocean Engineering activities at the St Anthony Falls Hydraulic Laboratory have included extensive work on the development of instrumentation to locally measure very small water velocities. Techniques have been developed that can accurately measure velocities in the 0.1 to 8.0 cm/sec range, which is well below most available current meters. Techniques used include optical hydrogen bubble tracing for velocities above 0.5 cm/sec and tracing of an aqueous solution of thymol blue for lower velocities.

Hardware developments at Offshore Technology Corporation have included replacement of the main wavemaker in the wave and current basin to improve frequency response and wave quality, and a similar upgrade is planned for the deep water towing and seakeeping basin. Research into the generation and measurement of short-crested seas has continued and this capability has recently been used for several commercial test programs. Data acquisition computers have all been upgraded to improve on-line analysis capabilities. In the data analysis area, efforts have been focused on implementing new techniques for analysis of random time series data which provide output in a form consistent with design methods. In addition, techniques have been developed to study slowly-varying motions associated with second-order effects. Finally, like many of the other facilities, a complete set of numerical models has been acquired to aid test planning and interpretation of results.

As discussed previously, the theme throughout the ATTC member organizations active in Ocean Engineering work is continued improvement to hardware and data analysis methods, and a simultaneous integration of testing programs with more and more capable numerical models. Issues which may become important in the future include facilities and techniques for testing in very deep water (greater than 2000 ft), techniques for modeling flexible members such as risers, techniques to account for viscous effects in phenomena such as mooring line dynamics, and capabilities to model deep currents.

WAVE INDUCED ORIFICE FLOWS

M. E. McCormick and M. J. Gallet
Professor Lieutenant, USN

U.S. Naval Academy, Annapolis, MD 21402-5042

ABSTRACT

A vertical oscillating water column with orifice plates over the air chamber above the column is studied both theoretically and experimentally. The orifice plates simulate a wave energy turbine in energy conversion. Results show that the assumption of linear compressibility overestimates the spring effect of the air column, while the assumption of incompressibility underestimates the spring effect. In addition, the unsteady orifice damping is found to be far greater than the steady damping. Finally, impedence matching is approximately achieved.

1. INTRODUCTION

Of the many wave energy conversion techniques that have been both proposed and tried over the past sixty, or so, years, the pneumatic technique has been shown to be the most reliable and cost effective. A pneumatic wave energy converter is one which utilizes wave excited air motions to drive a turbine. For the purpose of analysis, the pneumatic systems can be represented by an oscillating water-air column with an orifice to simulate the effects of the air turbine, as sketched in Figure 1. This system is somewhat simplistic when compared to an actual pneumatic wave energy converter , such as that sketched in Figure 2. Despite the simplicity of the orifice system, it is believed that a study of the orifice in both theory and experiment yields most useful results.

Published accounts of the use of the pneumatic wave energy converter date back to 1920 when Palme reported that a pneumatic system had been successfully used in France. Most of the interest in the pneumatic system has occurred within the past decade due, primarily, to the efforts of Yoshio Masuda of Japan. See, for example, Masuda (1971 and 1979).

One aspect of the pneumatic technique that has received little attention is the effect of air compressibility on the water column motions. Early analyses, such as those of McCormick (1974 and 1976), neglected the compressibility of the air. More recently, Rolfes (1981) and Robinson (1980) have also studied the pneumatic system assuming incompressible air flow. A few investigators, such as Hiramoto (1978), Penney et al (1981) and Ojima et al (1984) have theoretically shown that compressibility effects might be significant, depending on the dimensions and power capacity of the pneumatic system. Orifice plates have been used in studies of front-facing pneumatic systems by Ojima et al (1984) and Malmo (1984).

In the present study, an oscillating water-air column with an orifice is theoretically and experimentally studied. The theory used is linear and includes both the linear compressibility term and the quasi-linear orifice damping term. The experimental data are obtained from tests in the 385-foot (117-meter) wave and towing tank of the U.S. Naval Academy. The purpose of this study is to determine the effects of both air compressibility and system damping on wave-induced oscillating water-air column motions.

2. WATER COLUMN MOTION ANALYSIS

An oscillating water column, such as that sketched in Figure 1, is the basic component of a Pneumatic Wave Energy Converter (PWEC), such as that sketched in Figure 2. In Figure 1 the orifice above the water column is used to simulate the presence of the turbine of Figure 2. In order to attain an understanding of the overall performance of the more complicated PWEC, one must first understand the nature of the motions of the simple orifice system. The motions of the water column in the latter system are subject to the unsteady pressures in the air chamber, influenced by the orifice losses and the losses due to both viscosity and radiation. The orifice losses are nonlinear in nature, while the other losses are well approximated by linear terms. In the analysis which follows the nonlinear terms are also

approximated by equivalent linear expressions.

The equation of motion of the water column sketched in Figure 1 is the following:

$$\left[m + a\right] \ddot{z} + b_r \dot{z} + (R_w + R_o)\, \dot{z} \left| \dot{z} \right| + (c + K_a)\, z = F(\omega,t) \qquad (1)$$

where

- m is the calm-water mass of the water column in kg,
- $a(\omega)$ is the added-mass in kg,
- $b_r(\omega)$ is the radiation resistance coefficient in N-s/m
- R_o is the nonlinear damping coefficient due orifice losses in N-s^2/m^2,
- R_w is the nonlinear damping coefficient due to both entrance and exhaust at the bottom of the water column in N-s^2/m^2,
- c is the hydrostatic restoring coef. in N/m, i.e.

$$c = \rho g \pi D_1^2/4 \qquad (2)$$

- K_a is the equivalent spring constant due to air compressibility in N/m, and,
- $F(\omega,t)$ is the wave force in N,

The wave force is represented by

$$F(\omega,t) = \rho \left[f(k,D) + 1 \right] \frac{\cosh\left[k(h-d)\right]}{\cosh(kh)} \eta(\omega,t)$$

$$= F_o(\omega) \cos(\omega t) \qquad (3)$$

where, from McCormick (1982),

$$f(kD_1) = \frac{4}{kD_1} J_1(kD_1/2) \qquad (4)$$

$J_1(kD_1/2)$ being a Bessel function of the first kind and first order. In equation (3) d is the draft of the water column, h is the water depth, k is the wave number ($2\pi/\lambda$) and $\eta(\omega,t)$ is the external free-surface displacement,

$$\eta(\omega,t) = \frac{H_o}{2} \cos(\omega,t) \qquad (5)$$

We assume that $\lambda \gg D_1$ which is the practical case of operation in a swell.

The wave number expression is

$$k = 2\pi/\lambda = \frac{\omega^2}{g \tanh(kh)} \qquad (6)$$

which is transcental. Furthermore, McCormick (1983) derives an expression for the added-mass, that expression being

$$a(\omega) = \frac{\rho D_1^3}{3} \left[1 - \frac{k^2 D_1^2}{15} + \frac{k^4 D_1^4}{525} - \ldots \right] \qquad (7)$$

which agrees well with experimental results.

The air in the chamber above the water column provides a restoring force due to compressibility. The associated "spring constant" is based on the isentropic compression of the air while having the chamber pressure being zero (gauge) when the internal free-surface displacement is zero. From Penney *et al* (1981), the equivalent spring constant is

$$K_a = \frac{P_{atm}\, \gamma A_1}{L \left(1 - \frac{z}{L}\right)^{\gamma+1}} \approx P_{atm}\, \gamma A_1/L \qquad (8)$$

assuming $z \ll L$, where L is the height of the orifice above the still-water- level. γ is the ratio of specific heats (assumed to be 1.4) in equation (8).

The damping coefficients in equation (1) are b_r, R_w and R_o. The radiation resistance coefficient, from McCormick (1982), is expressed by

$$b_r = \frac{\rho \pi D_1^2}{4k} \left[1 - \frac{2\, J(kD_1)}{kD_1} \right] \sqrt{\frac{g}{k} \tanh(kh)} \cdot e^{-2kd} \qquad (9)$$

The coefficient R_w primarily results from the entrance and exhaust of water from the bottom of the water column. If the motions of the water are, for the moment, assumed to be sinusoidal, then the damping coefficient based on the average velocity is

$$R_w = \rho\, C_v\, A_1/2 \qquad (10)$$

where ρ is the mass-density of water and C_v is a coefficient which depends on the nature of the flow. That is,

$$C_v = \begin{cases} 0.8 & \text{(entrance flow)} \\ 1.0 & \text{(exhaust flow)} \end{cases} \qquad (11)$$

The conditions correspond to the following velocity conditions of the water column:

$$\dot{z} = \begin{cases} > 0 & \text{(entrance flow)} \\ < 0 & \text{(exhaust flow)} \end{cases} \qquad (12)$$

The orifice damping coefficient R_o depends on the diameter ratio D_2/D_1. When this ratio is unity then R_o has the form of equation (10). That is,

$$R_o = \rho_a\, C_o\, A_2/2 \,, \qquad (D_2 = D_1) \qquad (13)$$

where $C_o = C_v$, defined in equation (11). The velocity conditions for equation (13), however, are reversed. Thus,

$$\dot{z} = \begin{cases} > 0 & \text{(entrance air flow)} \\ < 0 & \text{(exhaust air flow)} \end{cases} \qquad (14)$$

For the condition of $D_2/D_1 < 1$ the values of C_o are different than those of equation (11). For the experimental part of the present study the following loss coefficient values apply:

TABLE 1

D_2/D_1	C_o
0 to 1	$0.78 (A_1/A_2)^2$
0.5	12.5
0.1	7.80×10^3

from Addision (1964).

The nonlinear damping coefficients (R_v and R_o) can be replaced by equivalent linear damping coefficients (b_v and b_o). By equating the energy lost due to nonlinear damping and that due to linear damping over one cycle, equivalent linear damping coefficients are found to be

$$b_{v,o} = \frac{8}{3\pi} R_{v,o} \omega Z_o \qquad (15)$$

where Z_o is the amplitude of the water column motions. Hence, equation (1) can be approximated by

$$(m + a)\ddot{z} + b_r \dot{z} + (b_v + b_o)\dot{z} + (c + K_a) z = F(\omega,t) = F_o(\omega)\cos(\omega t) \qquad (16)$$

The solution of equation (16) is

$$z = Z_o \cos(\omega t - \varepsilon) = \frac{[F_o(\omega)/(c + K_a)] \cos(\omega t - \varepsilon)}{\sqrt{\left[1 - \frac{\omega^2}{\omega_n^2} + 1\right]^2 + \left[\frac{2(\Gamma b_j)}{b_{cr}} \frac{\omega}{\omega_n}\right]^2}} \qquad (17)$$

where the subscript j denotes the type of damping.

In equation (17), the natural frequency is

$$\omega_n = \sqrt{\frac{c + K_a}{m + a}} \qquad (18)$$

and

$$b_{cr} = 2\sqrt{(c + K_a)(m + a)} \qquad (19)$$

is the critical damping. Also in equation (17)

$$\varepsilon = \tan^{-1} \left[\frac{2\omega (\Gamma b_j)/(b_{cr}\, \omega_n)}{1 - (\frac{\omega}{\omega_n})^2}\right] \qquad (20)$$

is the phase angle between the water column displacement and the wave force, and

$$\Gamma b_j = b_r(\omega) + b_v(\omega, Z_o) + b_o(\omega, Z_o) \qquad (21)$$

where the damping coefficient b_r is obtained from equation (9), while the damping coefficients b_v and b_o are in equation (15).

Combining equations (9) and (15) with equation (17), one obtains the following biquadratic equation for the amplitude of the water column motions:

$$Z_o^4 + 2\left(\frac{b_r}{B}\right) Z_o^3 + \left[\left(1 - \frac{\omega^2}{\omega_n^2}\right)^2 \frac{b_{cr}^2}{4B^2} \left(\frac{\omega_n}{\omega}\right)^2 + \frac{b_r^2}{B^2}\right] Z_o^2 - \left(\frac{F_o}{c + K_a}\right)^2 \frac{b_{cr}^2}{4B^2} \left(\frac{\omega_n}{\omega}\right)^2 = 0 \qquad (22)$$

where

$$B = \frac{8}{3\pi} \omega [R_v + R_o] \qquad (23)$$

Equation (22) is solved numerically in the present study.

3. EXPERIMENT

The experimental part of this study was conducted in the 385-foot (117-meter) wave and towing tank at the U.S. Naval Academy. This tank is 26 feet (7.92 meters) in width and 16 feet (4.88 meters) in depth.

Referring to Figure 1 for notation, the circular cylinder has a height and diameter of

$$\ell = 1.83 \text{ meters}$$

and

$$D_1 = 0.254 \text{ meter}$$

respectively. The orifice diameters used in the study are

D_2 = 0.2540 meter
0.1270 meter and
0.0254 meter

while the draft values of the water column are

d = 0.203 meter
0.406 meter and
0.610 meter

Waves exciting the water column motions vary in frequency from 0.40 Hz to 0.80 Hz in 0.05 Hz increments. The wave height, H_o, is approximately 0.102 meter for all frequencies. The wave properties were determined using a sonic wave probe positioned two chamber diameters away from the center of the capture chamber on a line parallel to the wave front. The internal water column motions were also studied using a sonic wave probe.

Air motions at the center of the orifice were monitored using a hot-wire anemometer. Since the air velocity was measured only at the orifice center, only the time behavior of the maximum air velocity could be studied. The spacial profile of the air velocity was not determined.

4. EXPERIMENTAL RESULTS

The height ($2Z_o$) of the internal water column motions is presented in Figures 3 and 4 as a function of the circular wave frequency (ω). In Figure 3 the effects of orifice draft are shown for the three diameter values. That is, the double-amplitudde frequency response of the water column for the D_2-values studied is shown in Figures 3a, 3b and 3c for D_2-values of 0.2540 meter, 0.1270 meter and 0.0254 meter, respectively. In Figure 3 we see that the peak values occur for the draft of 0.610 meter for the three orifice diameters, while no apparent peak values occur for d = 0.203 meter in the frequency range studied. The undamped natural frequency according to the expression of equation (18) for the 0.2540-meter orifice diameter is

$$\omega_n = \sqrt{\frac{c}{m + a}} = \sqrt{\frac{g}{d + \frac{4D_1}{3\pi}}} \qquad (24)$$

Note: In equation (24) the compressibility spring constant, K_a, is omitted since $D_2 = D_1$. The natural frequencies predicted by eq. (24) are 5.62 rad/s, 4.37 rad/s and 3.70 rad/s for d = 0.203 m, 0.406 m and 0.610 m, respectively. For the 0.0254-meter orifice diameter the peak values for the three drafts all appear to occur between 3.0 and 3.5 rad/sec.

In Figure 4, the double-amplitude frequency response for the 0.610-meter draft is shown for the three orifice diameters studied. The reader can see that the peak value occurs for the 0.127 meter diameter. This is an indication of impedence-matching, which is discussed later.

The air velocity measured by a hot wire amemometer is shown in Figure 5 as a function of time, where

D_2 = 0.0254 m
d = 0.610 m
f = 0.40 Hz

in Figure 5a and for f = 0.60 Hz in Figure 5b. One can see that this velocity does not vary sinusoidally in time. The exhaust velocity at the center of the orifice is significantly higher than the intake velocity. The phase angle between the peak exhaust velocity and the maximum upward water column velocity is approximately zero. That is, the motions of the water column and the air above it are in phase. Comparing the external wave trace with that of the water column, however, shows that motions of the external and internal free-surfaces are nearly in phase for f = 0.40 Hz. For f = 0.60 Hz, however, the external wave leads the water column by approximately 90° in Figure 5b. In both Figure 5a and 5b, one can see the inception of turbulence near and at the peak of the exhaust velocity. Furthermore, the exhaust velocity trace is slightly unsymmetric; whereas, the intake velocity trace is approximately symmetrical. The double amplitude ($2Z_o$) is shown in Figure 6 with the maxima of the intake and exhaust air velocities. Note that the peak values for each occur at different wave frequencies. This indicates that the efficiency of the oscillating water column as an energy conversion system is not maximum at the peak value of $2Z_o$, but near the peaks of the velocities, since most energy is removed by the air system at the highest velocity.

5. COMPARISON of THEORY and EXPERIMENT

In this section the theoretical analysis of Section 2 is applied to the experimental conditions of 3. The purpose of the application is twofold: First, to determine the utility of the linear theory in predicting the performance of an oscillating water column with nonlinear energy extraction and, second, to determine the relative effects of air compressibility in the chamber and quadratic damping of the orifice.

The optimal condition studied, from the results of Figure 3, is that of the 0.1270-meter orifice diameter and the 0.610-meter draft. Applying the equation (22) to this condition yields the frequency response in Figure 7. In Figure 7 curves are presented for air spring constant values of both zero (incompressibility air) and $P_{atm} \gamma A_1/L$ (compressible air). The incompressible curve does have the same

behavior as the experimental data with two exceptions: First, the theoretical results are higher by a factor of approximately two and, second, the peak theoretical value occurs at a lower frequency than that of the experimental data. The compressible curve neither agrees in magnitude nor behavior with the experiment. This disagreement indicates that the theoretical air spring is far to "stiff". The theoretical curves for all of the orifice and draft conditions studied are approximately coincident with the compressible curve of Figure 7 when the spring constant of equation (8) is used. Results obtained from the application of the incompressible form of equation (22) to the 0.1270-meter orifice with the 0.406-meter and 0.203-meter drafts are presented in Figures 8a and 8b, respectively. As in Figure 7, the incompressible curves both differ from the experimental data by approximately a factor of two and predict a lower peak-frequency value (in Figure 8a).

6. DISCUSSION

The results presented in Figures 7 and 8 show that neither the assumptions of incompressibility nor linear compressibility of the air above the oscillating water column yield satisfactory comparisons with the experimental data. When the compressible theory is applied to the capped condition of Figure 4, however, the experimental and theoretical results do agree. With this knowledge, we propose the following modified spring constant formula:

$$K_a{}' = K_a \sqrt{1 - \left(\frac{A_2}{A_1}\right)^{1/N}} \qquad (25)$$

where K_a is the spring constant of equation (8), A_1 and A_2 are the respective areas of the water column and orifice and N is a dimensionless number, where

$$1 \leq N < \infty \text{ (incompressible)} \qquad (26)$$

The form of equation (25) is similar to the head-loss equation for incompressible flow in a pipe with an orifice. Combining equations (22) and (25) and applying the results to the 0.1270-meter orifice with the 0.610-meter depth yields the solid curves in Figure 9. The orifice damping coefficient value for each of the solid curves is

$$C_o = 10 \qquad (27)$$

Note: From the relative peak values in Figure 3, the condition of impedence-matching is approximated by the 0.1270-meter orifice.

The reader can see that the value of N which would yield the best peak value agreement between theory and experiment is a finite number much greater than 5,000. This fact indicates that the "spring" resulting from the air compressibility is extremely "soft", except for the capped condition.

Also presented in Figure 9 are dashed curves resulting from the use of different orifice loss coefficient values (C_o) used with the incompressible theory. The sharpness of the experimental curve shows moderate damping. Comparing the experimental data with the incompressible curvees indicates that equation (27) is not a good approximation.

Damping can be determined by measuring the half-power bandwidth. If ω_A and ω_B are the lower and upper frequencies corresponding to half the power extracted by the orifice at the peak value frequency ω_o, where

$$\omega_A < \omega_o < \omega_B$$

then the logarithmic decrement is

$$\delta = \pi (\omega_B - \omega_A)/\omega_o$$
$$= 2\pi \zeta \sqrt{1 - \zeta^2} \qquad (28)$$

(from Morse and Ingard, 1968, and elsewhere) where the damping ratio is

$$\zeta = b_a/b_{acr} = \sqrt{4\pi^2 + \delta^2} \qquad (29)$$

The critical damping for the air column is

$$b_{acr} = 2 \sqrt{c\,(m_a + a_a)} \qquad (30)$$

where, assuming incompressible air flow, the restoring coefficient is given by equation (2), the air mass in the chamber is

$$m_a = \rho_a \pi D_1{}^2 L/4 \qquad (31)$$

ρ_a being the mass-density of air, and the added mass of air is

$$\left.\begin{array}{l} 0.3\ \rho_a \pi D_1{}^3/4 \left[\text{for } D_2 = D_1\right] \\ \\ \rho_a D_2{}^3/3 \left[\text{for } D_2 < D_1\right] \end{array}\right\} = a_a \qquad (32)$$

from Kinsler and Frey (1962) and elsewhere. For the test conditions described herein

$$\rho_a = 1.20 \text{ kg/m}^3 \qquad (33)$$

Hence, the critical damping value for the 0.0254-meter orifice with a 0.610-meter draft is 12.2 N-s/m. Applying this damping analysis to the average air velocities in Figure 6, one obtains the following:

A_2 = 0.0254 m^2
d = 0.610 m
ω_o = 3.46 rad/s
ω_A = 2.25 rad/s (extrapolated)

ω_B = 4.20 rad/s (interpolated)
δ = 1.77
Δ = 0.271
b_o = 3.30 N-s/m

$$= \frac{8}{3\pi} (\rho \bar{C}_o A_2/2) \omega_o Z_o \qquad (34)$$

from the combination of equations (13) and (15). Thus,

$$\bar{C}_o = \frac{3\pi b_o}{8 (\rho A_2/2) Z_o} = 102 \times 10^3 \qquad (35)$$

Comparing this value with the corresponding value in Table 1 (D_2/D_1 = 0.1), we can see that the damping based in the averaged peak air velocity through the orifice is more than one order of magnitude greater than the steady-flow value. This observation agrees with that of Morse and Ingard (1968) for oscillating pipe flows through an orifice. Assuming that the same increase in damping applies to the 0.1270-meter orifice with a 0.610-meter draft, the modified loss coefficient value for this orifice is

$$C_o = (102 \times 10^3/7.80 \times 10^3)\, C_o$$

$$= 163$$

where C_o = 12.5 in Table 1.

CONCLUSIONS

In the present study a vertical oscillating water column with a horizontal bottom opening and an orifice above the air column is theoretically and experimentally subjected to monochromatic linear waves. The orifice diameter-to-water column diameter ratios studied (D_2/D_1) are 1.0, 0.5, 0.1 and 0.0. Using a linearized theory which includes the effects of both compressibility and quadratic orifice damping, poor agreement is obtained between the theoretical and experimental data. The inclusion of the linear compressibility term in the theory results in data that are an order of magnitude less that the experimental data and are of different character, i.e., no resonant condition is predicted. When the air compressibility is neglected, the theoretical data are approximately twice the experimental data with the resonance predicted at a lower frequency.

The measured damping of the oscillating system is found to be approximately one order of magnitude greater than that predicted for steady flow through an orifice. The predicted resonant condition occurs at lower frequencies as the damping is increased, as expected.

From these results, the following conclusions are made:

(a) The assumption of linear compressibility far overestimates the spring effect of the air above the water column except for the capped (D_1/D_2 = 0) condition.
(b) The assumption of incompressibility underestimates the air column's spring effect.
(c) The system damping for oscillatory flows is approximately one order of magnitude greater that that of steady orifice flows.
(d) The resonant condition can be effectively controlled by adjusting the water column draft, the resonant frequency decreasing with increasing draft.

REFERENCES

Addison, H. (1964), A Treatise on Applied Hydraulics, Chapman and Hall Ltd., London, 5th edition.

Hiramoto, A. (1978), "The Theoretical Analysis of an Air Turbine Generator System", Proceedings, Wave and Tidal Energy Symposium, Canterbury, England, Paper B5.

Kinsler, L. and Frey, A. (1962), Fundamentals of Acoustics, John Wiley and Sons, Inc., New York, 2nd edition.

Malmo, O. (1984), "A Study of a Multiresonant Oscillating Water Column for Wave Power Absorption", Doctoral Thesis, Univ. of Trondheim, Norway.

Masuda, Y. (1971), "Wave Activated Generator", Proceedings, International Colloquium on the Exposition of the Oceans, Bordeaux, France, March.

Masuda, Y. and Miyazaki, T. (1979), "Wave Power Electric Generation Study in Japan", Proceedings, Wave and Tidal Energy Symposium, Canterbury, England, Paper C.

McCormick, M. (1974), "An Analysis of a Wave-Energy Conversion Buoy", Jl. of Hydronautics (AIAA), Vol. 8, No. 3, July, pp. 77-82.

McCormick, M. (1976), "A Modified Linear Analysis of a Wave-Energy Conversion Buoy", Ocean Engineering, Vol. 3, No. 3, pp. 133-144.

McCormick, M. (1983), "Analysis of Optimal Wave Energy Conversion", Jl of Waterway, Port, Coastal and Ocean Engineering, ASCE, Vol. 109, No. 2, May pp. 180-198.

Ojima, R., Takahashi, S., and Goda, Y. (1984), "Hydrodynamic Aspect of PHRI Caisson Breakwater with Wave Power Extraction", Proceedings of 1st Symposium on Wave Energy Utilization in Japan, Paper I6, Nov., 1984.

Ojima, R., Suzumura, S. and Goda, Y. (1984), "Theory and Experiments on Extractable Wave Power by an Oscillating Water-Column Type Breakwater Caisson", Coastal Engineering in Japan, Vol. 27, pp. 315-326.

Palmer, A. (1920), "Wave Motion Turbine", Power, Vol. 52, No. 18, November, pp. 700-701.

Penney, T., Miles, J. and McCormick, M. (1981), "Development Program Leading to an Optimized Oscillating Water Column Wave Energy Converter Featuring a Bi-Directional Turbine", Proceedings, 2nd Terrestrial Energy Systems Conference (AIAA) Colorado Springs, December.

Robinson, R. (1980), "Analysis of a Pseudo 2-D Oscillating Water Column Duct", Queen's University, Belfast, Report WE/80/11R, July.

Rolfes, M. (1981), "Variations on the Oscillating Water Column Wave Energy Device", M.S. Thesis, Dept. of Civil Engineering, Massachusetts Institute of Technology, October.

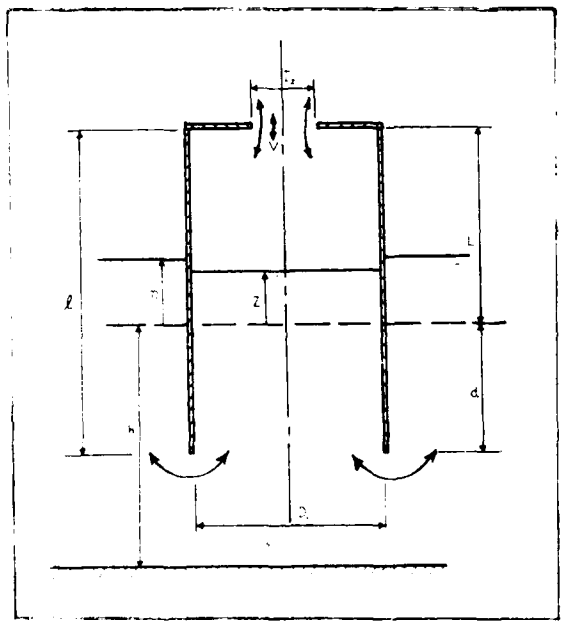

FIGURE 1. Notation for an Oscillating Water Column with an Orifice.

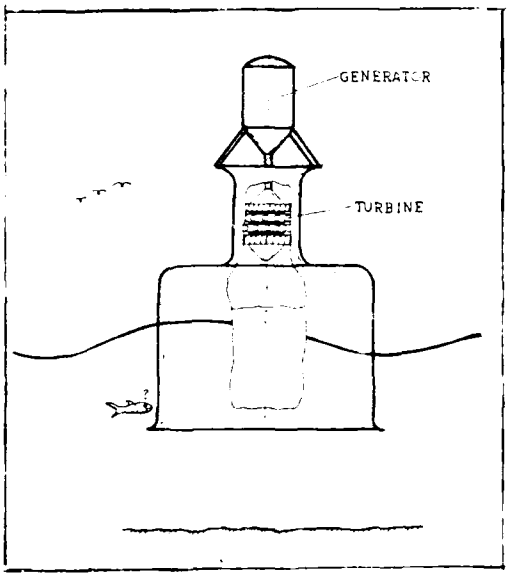

FIGURE 2. Section of a Pneumatic Wave Energy Converter with Counter-Rotating Turbine.

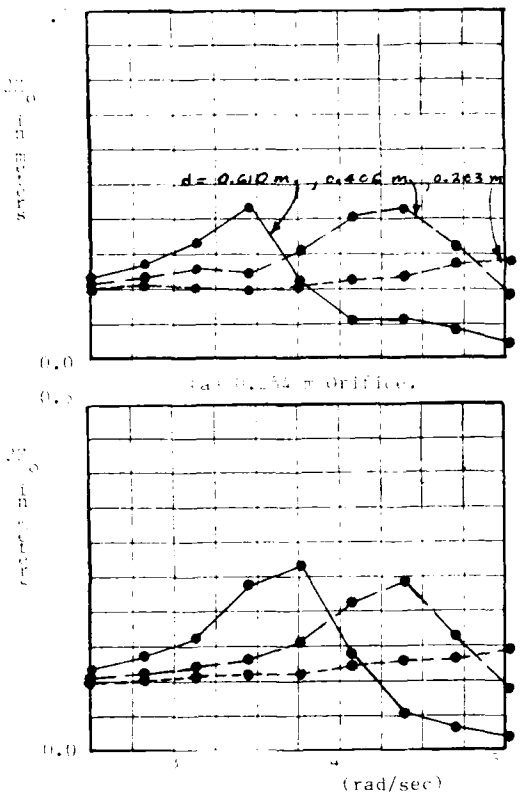

(a) 0.254 m Orifice.

(b) 0.127 m Orifice.

FIGURE 3. Water Column Wave Height as a Function of Circular Wave Frequency for Various Orifice Diameters.

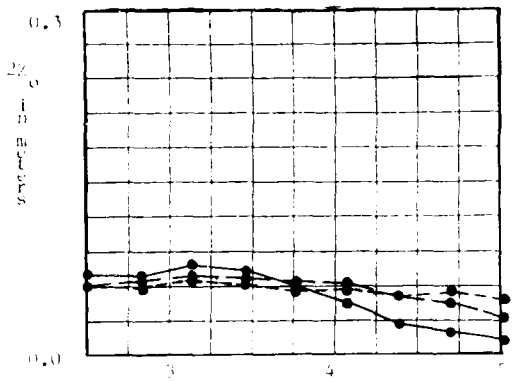

(a) D_2 = 0.0254 m Orifice

FIGURE 4. Water Column Wave Height as a Function of Circular Wave Frequency for Various Orifice Diameters.

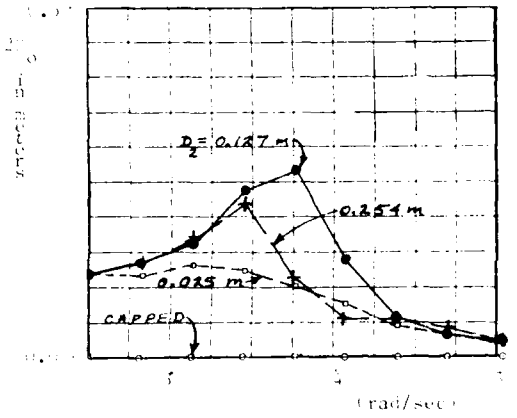

FIGURE 5. Water Column Wave Height as a Function of Circular Wave Frequency for All Orifice Diameters, d = 0.610 m.

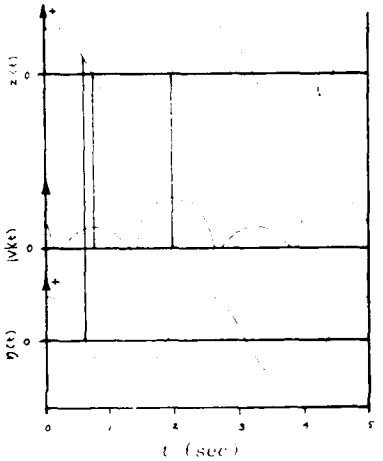

(a) f = 0.40 Hz

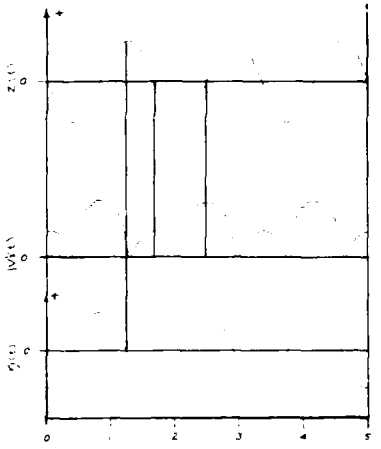

(b) f = 0.60

FIGURE 5. Internal Free-Surface, Air Velocity and External Free-Surface Variation.

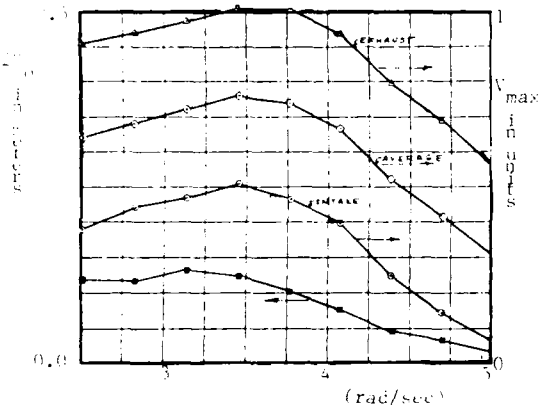

FIGURE 6. Water Column Wave Height and Maximum Air Velocity for D_2 = 0.0254 m and d = 0.610 m.

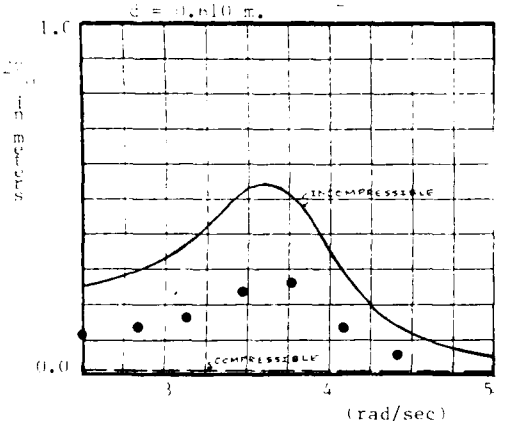

FIGURE 7. Effects of Compressibility on the Internal Wave Height for D_2 = 0.127 m and d = 0.610 m.

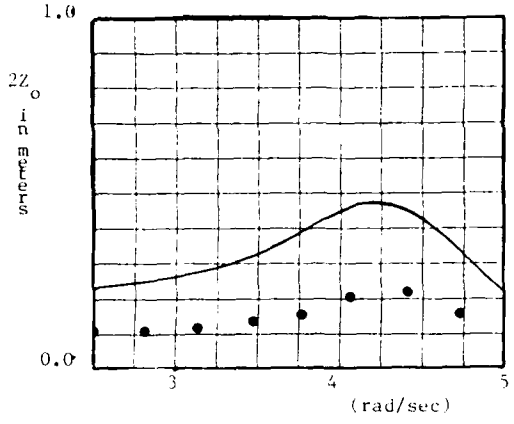

(a) 0.406 m Draft.

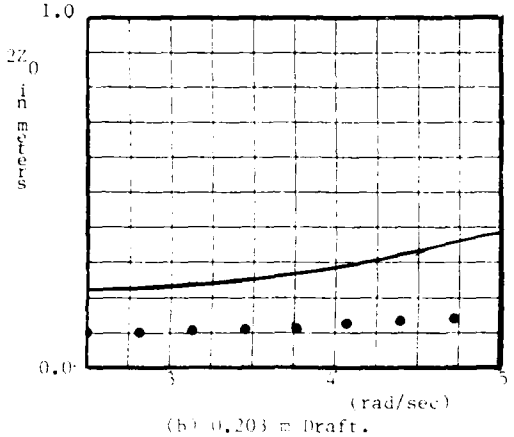

(b) 0.203 m Draft.

FIGURE 8. Theoretical and Experimental Results, Assuming Incompressible Air Flow for D_2 = 0.127 m.

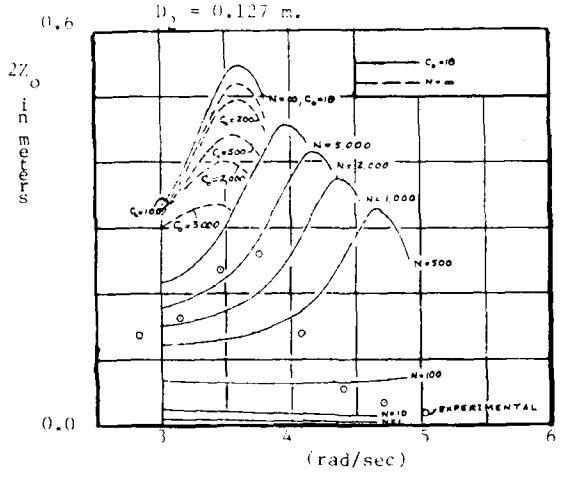

FIGURE 9. Effects of Variations in Orifice Damping (C_o) and Air Compressiblity (N) for D_2 = 0.127 m and d = 0.610 m.

DYNAMIC BEHAVIOR OF A JACK-UP PLATFORM IN WAVES

Antonio Carlos Fernandes[1]
Jose M.A. Vasconcelos[2]
Paulo T.T. Esperanca[2]
Pedro Barusco Filho[3]
Sergio H. Sphaier[2]

[1]IPT - Instituto de Pesquisas Tecnologicas do Estado de Sao Paulo
[2]COPPE/UFRJ - Coordenacao dos Programas de Pos-Graduacao de Engenharia/Uni
[3]PETROBRAS - Petroleo Brasileiro S.A.

ABSTRACT

A jack-up type platform for operation over one hundred meters depth has been studied via a comprehensive set of tests at the IPT (Technological Research Institute) towing tank in Sao Paulo. Two legs positions (fully elevated and 10 meter down) and three headings with respect to the waves. The tests were the resistance and decaying tests, the tests in waves with the model kept stationary and being towed (seakeeping). Some of the analysis was completed by a linear diffraction-theory computer program and by a full-scale instrumentation of a relative jack-up during transportation along the Brazilian coast.

NOTATION

K	wave number
A	wave amplitude
ω	wave circular frequency
ω_e	encounter wave frequency
ℓ	reference length = 70m
ρ	water density
g	acceleration of gravity
θ	pitch
ϕ	roll
z_C	heave; C is a point below the center of gravity at the depth position

1. INTRODUCTION

The jack-up is a very convenient type of platform for oil exploration. Its main characteristic is that it may work as a fixed structure and may be easily transported to different locations. It has been used since the beginning of offshore exploration and today it is common to find jack-ups which operate in 80 meters depth. Due to the increasing necessity of exploration of deeper and deeper waters PETROBRAS (Brazilian Oil Company), via its research center (CENPES) decided to design a jack-up for operation up to 100m deep waters.

In order to analyze and confirm the dynamic characteristics of this platform, a set of model tests was conducted at the IPT (Technological Research Institute) model basin in Sao Paulo, Brazil. Besides that, the monitoring of a relative jack-up has been made during transportation along the Brazilian coast and finally a linear diffraction-theory computer program has been processed.

2. THE MODEL

The jack-up has a triangular shape and triangular shaped legs. Its plan view can be seen in Figure 1. Its principal dimensions are L(length)=73,80m; B(breadth)=68,00m; D(depth=7.82m; H(draft)=3.52m and displacement=10,83ot. Based on the maximum wave height capability of IPT wave maker, the frequency range of interest, the limity of the tank walls, etc. it has been ided to build a 1:70 model.

This has led to about a 30kg model which has been made very easy to manipulate. The tests to be performed have been with the legs at most 30m down, hence there was no necessity in modeling the full legs. Therefore, only the wet parts of the jack-up were built with geometrical similarity and this includes only about one third of the legs. The inertial similarity has been reached by weights strategically placed. The latter adjustment has been made by the so-called bifilar method, taking advantage of a relatively light and compact model (Fernandes 85).

The main interest has been in the roll, pitch and heave motions. For instrumentation it has been decided to use an on-the-model set of two rate-gyros and 5 accelerometers. The former are for roll and pitch, one accelerometer for heave and the remaining for other modes and redundancy for the roll and pitch measurements.

The model has been used in the decaying tests, tests in waves, the seakeeping test and the resistance ones. As a general procedure the quantities were registered on magnetic tape and the data reduction was performed using the analog-digital capabilities of a PDP 11/23 minicomputer.

3. THE DECAYING TESTS

These kind of tests are normally made as auxiliary to the tests in waves since it helps to identify the frequency range of interest. It also yields an indication of the damping properties. However, in this case it could be used to confirm two interesting results that refer to the discontinuities in the peak period and in the damping factor as the legs were lowered from the fully elevated positions.

Tests in the roll and pitch modes have been made with five leg positions: fully elevated and the corresponding to 5,10, 20 and 30 meters down. For each leg position a pure moment was applied causing an initial angle. Suddenly the model was released and the time-history of the rate-gyros was recorded. In each case it has been possible to identify an average peak period and an exponential decay. The results for both are presented in Figures 2 and 3 respectively.

It is interesting to note that the pure moment was applied by a cable passing through two vertically aligned pulleys placed on the model legs. It also should be said that it has been difficult to obtain information for the heave mode via decaying tests. This mode is supercritical and the tests yield no complete cycles. A crude estimation was obtained by shaking the model up and down following the peak frequency.

4. THE TESTS IN WAVES

The next set has been the tests in regular waves with the model kept stationary. In this case two leg positions (fully elevated and 10 meters down) and three headings (180^{o}-head seas, 90^{o}-beam seas and 120^{o} - with a board perpendicular to the wave direction) have been considered. The model was held by two soft springs initially placed transversally to the wave propagation. As the model drifted it was easy to see that there is enough restoring moment in order to keep the correct heading.

The more significant results for the regular wave tests are presented in Figures 4, 5 and 6 for pitch, roll and heave respectively. For comparison, in these figures results from a linear diffraction - theory computer program (Vasconcellos et al 85) is also presented.

Several tests also have been performed with random waves covering the same headings and leg positions. The 10 years storm offshore Rio de Janeiro where the main Brasilian oil field is located and also the sea in the same region encountered during the transport of a relative jack-up has been simulated. The latter is similar to the one tested in the towing tank (same shape, close displacement and inertia). However, it was transported with its legs 45m down different from the fully elevated and 10m down positions which have been tested. During that transport the sea direction with respect to the platform was about 120^{o} and its spectral density is given in Figure 7. The spectral density for pitch, roll and heave are shown in Figures 8, 9 and 10 respectively.

5. THE SEAKEEPING TESTS

In the next set of tests the model was towed against head waves (simulating 6 knots towing). A similar transfer function for pitch and heave has been obtained and is shown in Figure 11 and 12 respectively. The added resistance due to waves has also been obtained and it is shown in Figure 13 and 14 for fully elevated legs and 10 meters down respectively. The latter have been confirmed to be proportional to the square of the incoming wave amplitude and it has been obtained using results from the resistance tests. The motions during these tests have been measured as before and the resistance forces have been measured with block gages. During the seakeeping tests one has oscillating resistance forces and some elasticity was given to the towing cable in order to avoid its slackness. The estimated natural frequency of the towing system was about 10 times less than the seakeeping frequency range of interest.

6. RESULTS

When someone ends up a set of tests like the ones explained here, it comes up normally the necessity of more tests. It is hard to plan in advance a research work completely. For instance, tests with other heading (0^{o}) and more leg positions would be interesting. Despite this, one may consider the work performed reasonably complete with respect to the jack-up in transport.

The results may be considered generally satisfactory for engineering purposes. For instance it is possible now to anticipate the critical frequency range for the motions that have been studied. However, looking from the researcher's point of view it is convenient to go a little deeper.

(a) From Figure 2 and 3 The discontinuity in both roll and pitch peak periods and in the damping factors is clear. The reason for the first would be the behavior of the hydrostatic restoring forces. When the legs are fully elevated they hold water and the leg holes work dynamically as on board tanks. This increases the metacentric height. When the legs are lowered by a short distance (say 5m) the holes are open to the sea decreasing the metacentric height. Maybe more important than the change in the peak period is the change in the damping factor. This is unconservative and leads to the conclusion that if one wants to decrease roll and pitch oscillations one should lower the legs by a significant amount. This is also confirmed by the experimental results as shown in Figure 4 and 5 for the tests in waves. In this respect since the potential theory calculation shows a different trend as one may see in the same

Figure 5 we may say that this is essentially a viscous effect. It seems that the leg lowering smoothed the oscillating flow leading to less viscous dissipation. It is important to say that this behavior was noticed even for [illegible] heavings. Finally the dissipation seemed to remain linear as observed by the decaying tests and tests with different amplitudes.

From Figure 6 one may observe the heave response which is lower for the legs 10m down. One must view the jack-up as at least two degrees of freedom system. From the comparison of Figure 7 with 6 it is clear that a more severe heave situation comes up when the legs are 10m down. In particular it is important to note that the experiments missed the heave resonance with the legs fully elevated [illegible] for the legs 10m down.

[illegible] refer to the random wave test. As shown in Figure 7 besides a [illegible] energy at higher frequencies [illegible]. The waves generated [illegible] the full-scale [illegible]. For roll, pitch and heave [illegible] should be seen as [illegible] should not forget that [illegible] were 10m down. Hence, [illegible] results in the heave [illegible] at least qualitatively [illegible] dissipation which is [illegible] exposed.

[illegible] and in the pitch [illegible] the seakeeping tests [illegible]. It is possible to [illegible] commented in [illegible] intensity due to the static [illegible] the flow through the hull. [illegible] for the legs down [illegible] as hydrofoils. [illegible] see the wave added [illegible] correspond to [illegible] motion. Some of [illegible] significance. The wave [illegible] increase the resistance [illegible] amplitudes of 1m.

[illegible] "[illegible] a jack-up platform," International [illegible] Engineering, [illegible], Rio de [illegible], Preprint. Rio de [illegible]. 16p.

[illegible] et al. "Mathematical [illegible] Analysis, Interference Engineering, [illegible], 1985. [illegible] ppp, 19[illegible].

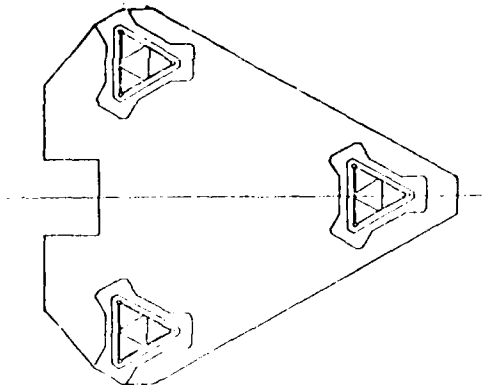

Figure 1. Plan view of the jack-up showing the position of the three legs.

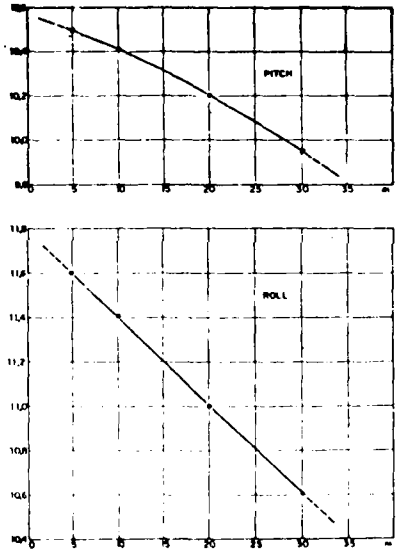

Figura 2. Roll and pitch peak period obtained from the decaying tests for several leg positions

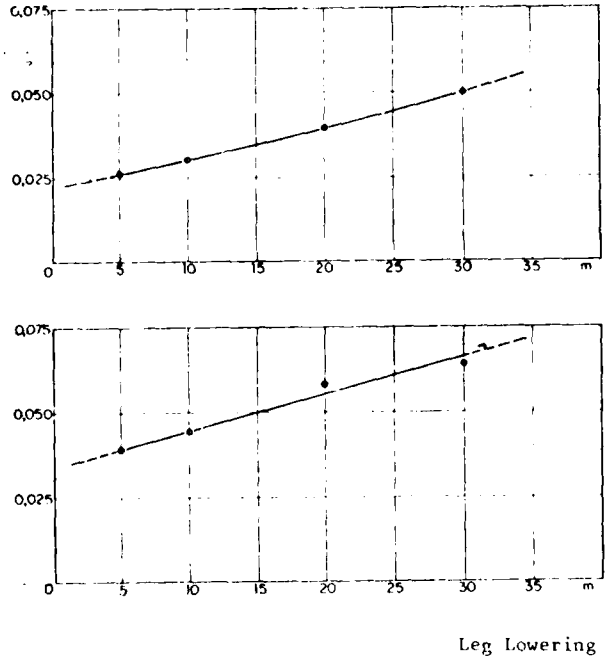

Leg Lowering

Figura 3. Roll and pitch damping factor (ζ) from the decaying tests for several leg positions ($\zeta=b/(2m\omega_n)$ with b as damping, m as inertia and ω_n as the natural frequency for an assumed constant coefficients second order system).

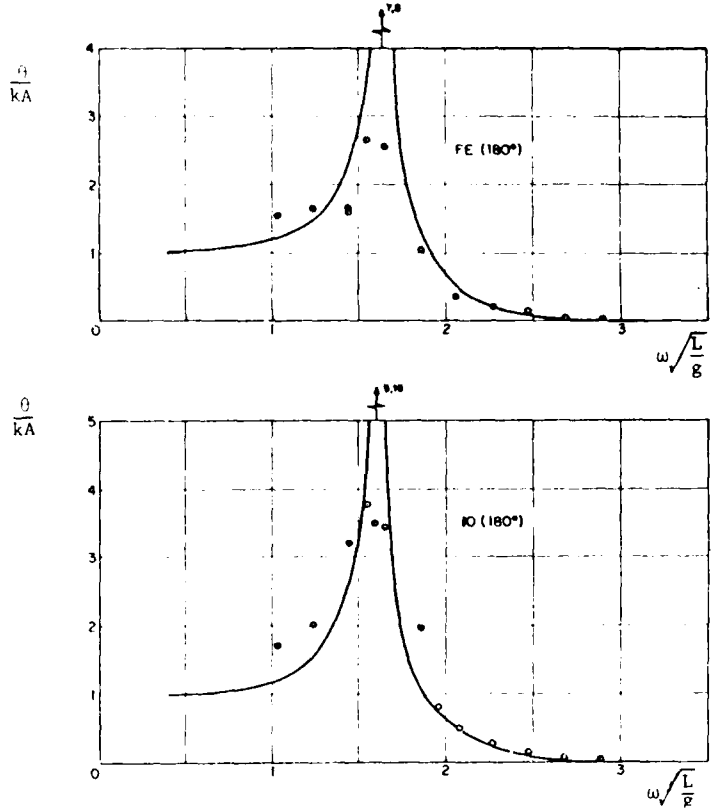

Figura 4. Pitch transfer functions for the fully elevated (FE) and 10 meters down (10) legs for head seas (180° heading). Regular waves tests. (—) potencial theory; θ experiments.

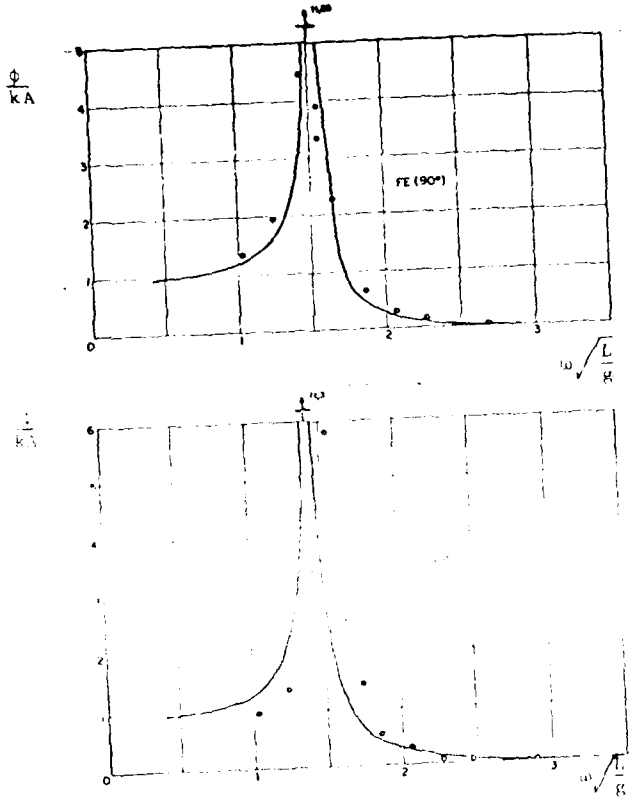

Figura 5. Roll transfer function for the fully elevated (FE) and 10 meters down (10) legs for beam seas (90° heading). Regular waves tests. (—) potencial theory; Θ experiments.

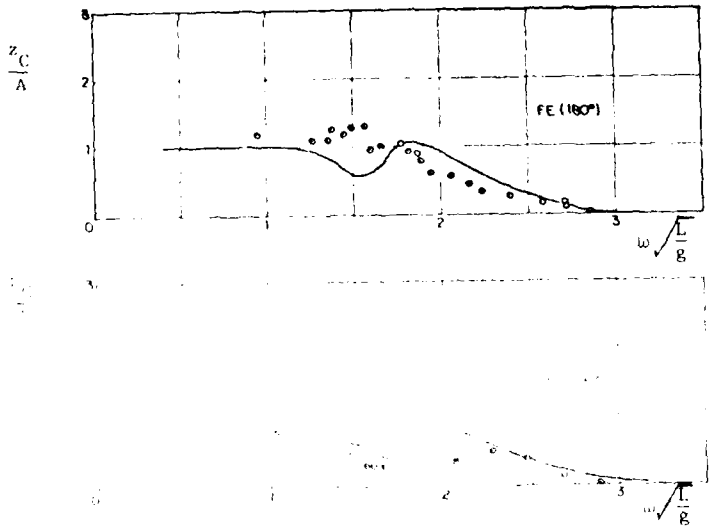

Figura 6. Heave transfer function for the fully elevated (FE) and 10 meters down (10) legs for head seas (180° heading). Regular waves tests. (—) potencial theory; Θ experiments.

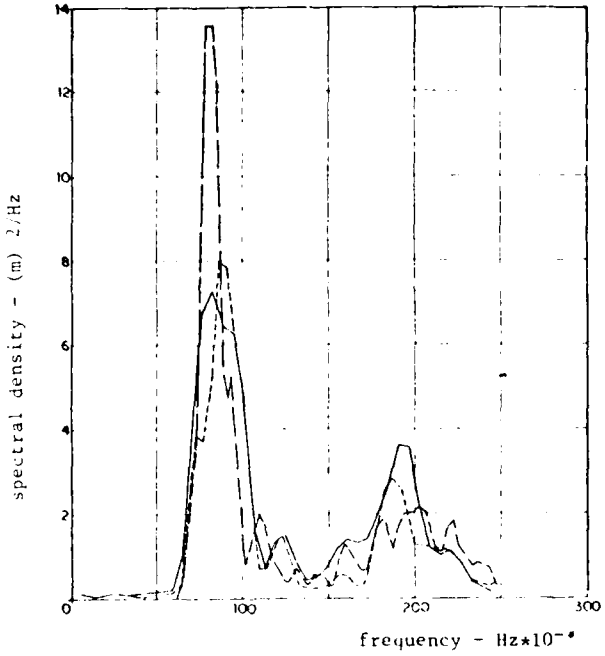

Figura 7. Wave spectral density for the sea encountered in full scale.

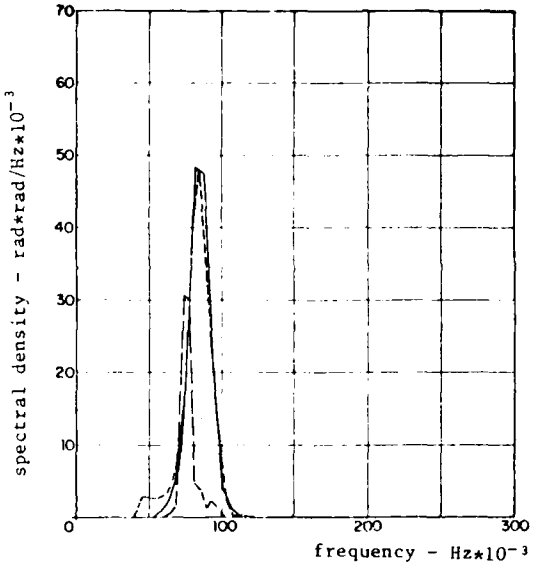

Figura 8. Roll spectral density with the sea of Figure 7.

——— fully elevated legs test
-------- 10 meters down legs test
-·-·-·-· full scale

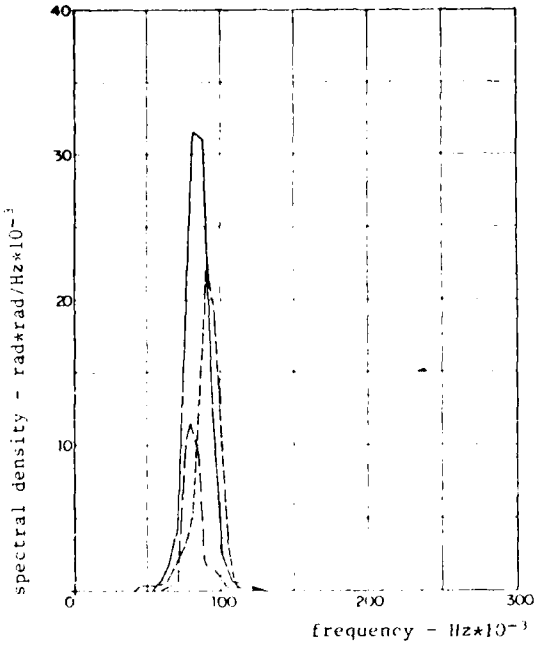

Figure 9. Pitch spectral density with the sea of Figure 7.

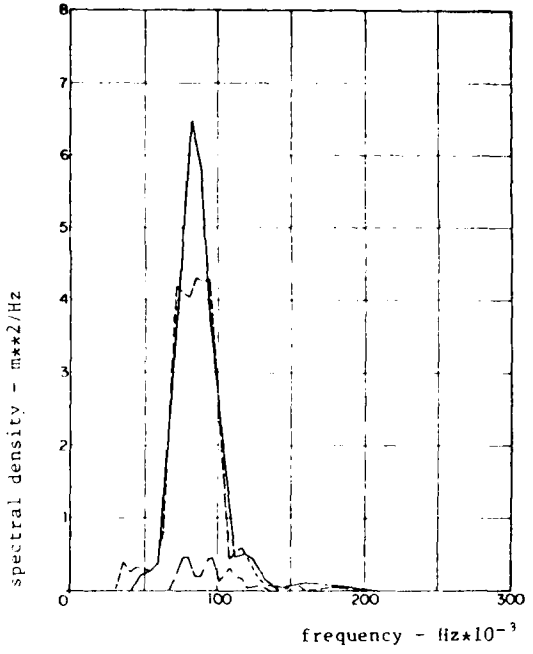

Figure 10. Heave spectral density with the sea of Figure 7.

——— fully elevated legs test
------ 10 meters down legs test
-·-·-· full scale

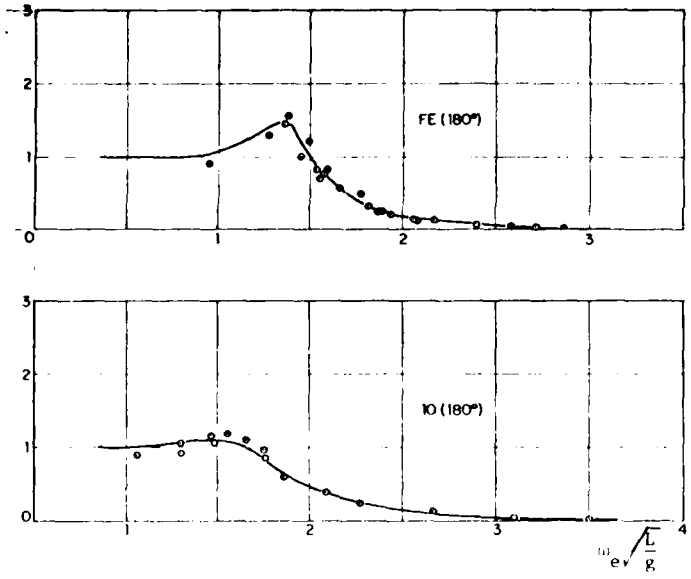

Figure 11. Pitch transfer function for the fully elevated (FE) and 10 meters down (10) legs from the seakeeping head seas tests with 6 knots. Regular waves (——) fairing curve.

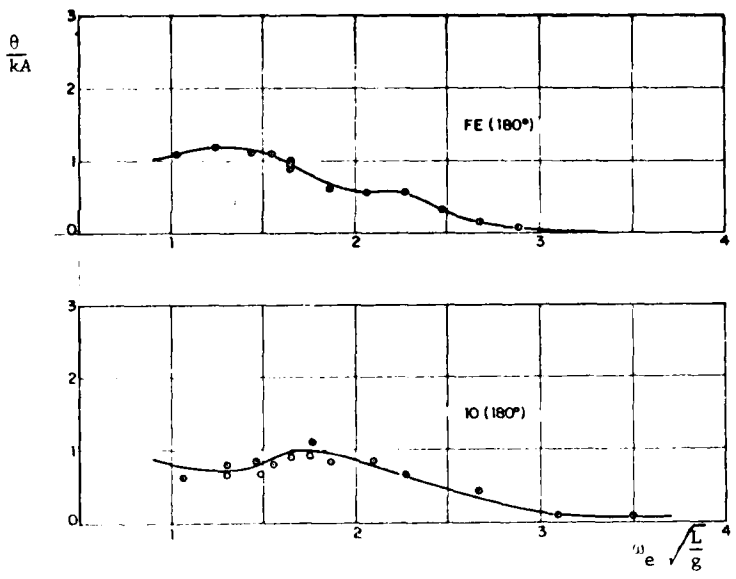

Figure 12. Heave transfer function for the fully elevated (FE) and 10 meters down (10) legs from the seakeeping head seas test with 6 knots. Regular waves. (——) fairing curve.

$$\sigma_a = \frac{R_a}{\rho g A^2 \ell}$$

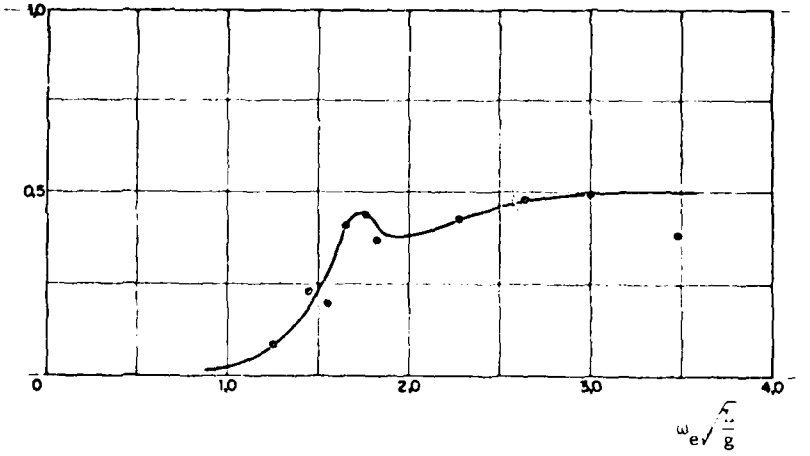

Figure 13. Wave added resistance coefficients, for the fully elevated (FE) legs from the seakeeping head seas tests with 6 knots. Regular waves. (——) fairing curve.

$$\sigma_a = \frac{R_a}{\rho g A^2 \ell}$$

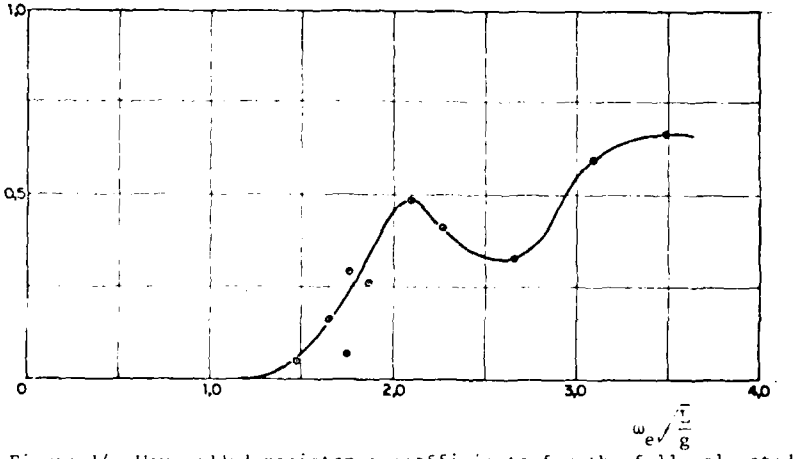

Figure 14. Wave added resistance coefficients for the fully elevated (FE) legs from the seakeeping head seas tests with 6 knots. Regular waves. (——) fairing curve.

Measurement of the Forces on a Slightly Submerged Cylinder

Stephen B. Hodges and William C. Webster
Department of Naval Architecture and Offshore Engineering
The University of California, Berkeley
Berkeley, CA 94720

Abstract

The forces on a slightly submerged rectangular cylinder undergoing vertical oscillations are investigated experimentally. This flow situation is highly nonlinear at low frequencies and at amplitudes of motion which are large compared to the gap between the top deck of the structure and the free surface. Previous experiments performed by Chung (1977) provided only sparse coverage of this interesting range. Our experiments use a new piece of test equipment, called a random motion mechanism (or RMM for short), designed to explore nonlinear phenomena such as this. The results of extensive measurements are compared with existing linear methods (the close-fit method of Frank (1967) and a matched asymptotic expansion by Newman, et al. (1984)), and with a new nonlinear theory by Yum (1985). Although Yum's theory matches best, it deviates from the experiments significantly in the very low frequency range.

1.0 Introduction

The focus of the research presented in this paper is the flow about, and the forces on, a body oscillating vertically very near the free surface. There were several motivations for this study. First, it is an important problem both for submarines (when they start to submerge or when they broach the free surface), and for semisubmersible platforms (where the twin hulls may always be only slightly submerged). Second, and perhaps more appropriate to the "tankery" aspects of the ATTC, this study gave us the opportunity to exercise our new hydraulically-operated, random-motion mechanism (which we will simply call the RMM). This piece of test equipment was designed and constructed at the University of California, Berkeley*.

The dynamic characteristics of a body floating in an otherwise undisturbed sea are an important component in the estimation of the wave induced motions of a ship, as well as in the estimation of motions arising from other effects. Much of the study of these so-called forced motion problems has been theoretical using potential theory, appropriate for the irrotational flow of an inviscid and incompressible fluid. For bodies which either pierce the water surface or are submerged deeply below it, small amplitude oscillatory motions lead to small disturbances to the flow. Thus, the free surface and body boundary conditions can be linearized and the potential flow problem solved. A variety of numerical techniques are available to compute such flows. Close-fit methods are common for two-dimensional forms (Frank (1967)). Slender-body approximations and so-called diffraction theories are available for three dimensional forms (for instance, Salvesen, Tuck and Faltinsen (1970), and Garrison, (1975)). The results from these theories compare well with experiments as long as the motion amplitudes remain small with respect to *all* of the principal dimensions of the flow situation. To apply these techniques when the body is only slightly submerged, the motions must be small relative to the gap between the top of the body and the free surface, and this restriction is severe.

A set of experiments was made by Chung (1977) for circular and square cylinders undergoing heave and sway oscillations at several submergences (as defined in figure 1), d/b = 0.25 being the shallowest. He compared the results with close-fit

* Support for this project was provided by the David W. Taylor Naval Ship Research and Developement Center under the General Hydromechanics Research (GHR) Program under contract number N00014-82-K-0007.

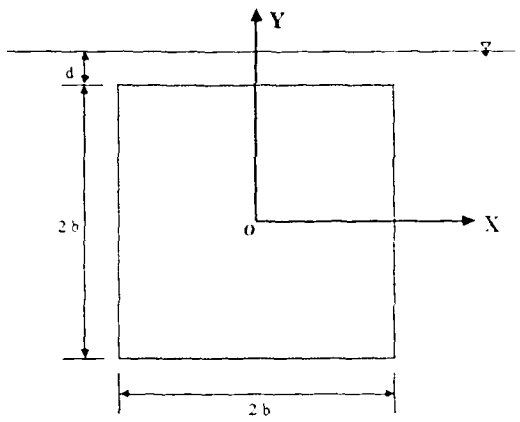

Notation: $N = \omega^2 b/g$, wave number

$\bar{d} = d/b$, submergence

$\bar{a} = a/b$, heave amplitude

Figure 1 General Configuration and notation

theory and showed that this theory breaks down as the body nears the free surface, particularly for low frequencies of oscillation. He also confirmed the existence of a negative added mass for some low frequencies which had been predicted numerically by a number of investigators. Other experimental results were recently published by Higo (1985) for a rectangular cylinder with a beam to draft ratio of 2.0. Submergences of 0.1, 0.2 and 0.5 were tested. While these results cannot be directly compared with the present experiments, the character of the results is encouragingly similar.

Newman, Sortland and Vinje (1984) presented a linear theory for this problem, based on the assumption that free surface effects are significant in the flow on top of the cylinder as well as in the fluid surrounding the cylinder, but not in a small region in the neighborhood of the corners of the cylinder. Linear solutions were found for the inner and outer regions and matched in the corner region. The results appeared to be an improvement over the close fit method and provided a simple explanation for the negative added mass at low frequencies.

The complete, large amplitude motion problem for a body floating in or near the free surface is quite difficult and has yet to be solved in any satisfactory manner. However, another approach is feasible for the special case of a body which is slightly submerged and oscillating at an amplitude which is both: (a) small compared with the body dimensions, and (b) comparable to the depth of the gap. Yum (1985) considered the flow to be composed of two domains, as did Newman, et al. The first consists of the fluid in the gap between the hull and the free surface (the inner flow); the second is all of the remaining fluid (the outer flow). The outer flow is then the flow outside of a new body which consists of the original body with sides extended upwards to the free surface. In this approach, the new body is permeable where the gap exists and impermeable otherwise. It was assumed that the solution of a linear potential problem for the outer flow is sufficient and the problem was solved using a generalized close-fit method (Wehausen, 1971). The inner flow problem was solved as a two-dimensional shallow water flow using the so-called "pressure-Poisson" method first introduced by Chorin (1968) and later refined by Chorin (1976, 1978). The two solutions were matched on their common boundary. Yum's development of this theory was the principal motivation for the present work.

Yum's predictions agreed well with Chaney's experiments for the most interesting low frequency range. Chaney's data is sparse. It was decided to repeat Chaney's experiments along the same lines as Chaney's but to collect much more data on fewer configurations. The two dimensional case of a square cylinder was therefore chosen. A set of experiments was carried out at submergences of 25% and 50% of the cylinder half-breadth, and motion amplitudes from 20% to 80% of the gap above the cylinder. The tests were concentrated in the low frequency range where nonlinear effects were expected to be most important. The results are compared with [illegible] predictions.

2.0 Experimental Apparatus

The experiments were conducted at the Ship Model Towing Tank at the University of California, Berkeley. The principal dimensions of the tank and the location of the testing apparatus are shown in figure 2. A vertical bulkhead (the wavemaker) was

Figure 2 Principal dimensions of the testing facilities

located at one end of the tank with a gently sloping beach at the other end. One criterion for selecting the model dimensions was to allow a reasonable amount of data to be taken at the lowest test frequency before the radiated waves reflected from the bulkhead reached the model.

The oscillatory heave motion was provided by a hydraulically actuated, random planar motion mechanism, hereafter referred to as the RMM. Details of the design, construction and capabilities of the RMM may be found in Hoech (1984). The RMM was mounted vertically on its steel frame which was in turn clamped to two wide flange beams spanning the tank. The beams were secured to the carriage rails on the tank walls. Figure 3 shows this arrangement. The hydraulic power supply was mounted on a small carriage adjacent to the RMM.

The RMM had been used only once prior to these experiments, for the measurement of wave drift forces on a surging cylinder (Hodges (1985)). It had never been used for vertical motions, so a secondary goal of these experiments was to evaluate the performance of the RMM in this situation. The original motivation for developing the RMM system was to provide regular as well as random oscillatory motions, unlike older cam and belt driven planar motion devices capable of only regular sinusoidal motions.

2.1 The RMM and Signal Generation System

The RMM is operated by a hydraulic servo valve actuator manufactured by MTS Systems, Inc. This choice was made after an exhaustive analysis of other alternatives, such as electric motors, stepping motors (both electric and hydraulic), etc. Although the maximum capacity of the actuator is rated at ±1100 pounds (± 4890 N), the stiffness of the current supporting structure reduces the practical limit to around 50 pounds (222 N) for horizontal motions and 250 pounds (1110 N) for vertical motions.

Most existing planar motion mechanisms of this size are either cam or belt driven, using electrical motors. However, such a system is only capable of generating regular sinusoidal motions. One motivation for designing a new planar motion mechanism driven by a hydraulic actuator was that such a device may be used to generate arbitrary motions and, in particular, may simulate motions due to a random sea state. It may also be used for prescribed sway or yaw motions for maneuvering tests of ship models.

The input signal for the RMM may be from either an analog signal generator, magnetic tape, or digital computer with a digital to analog converter.

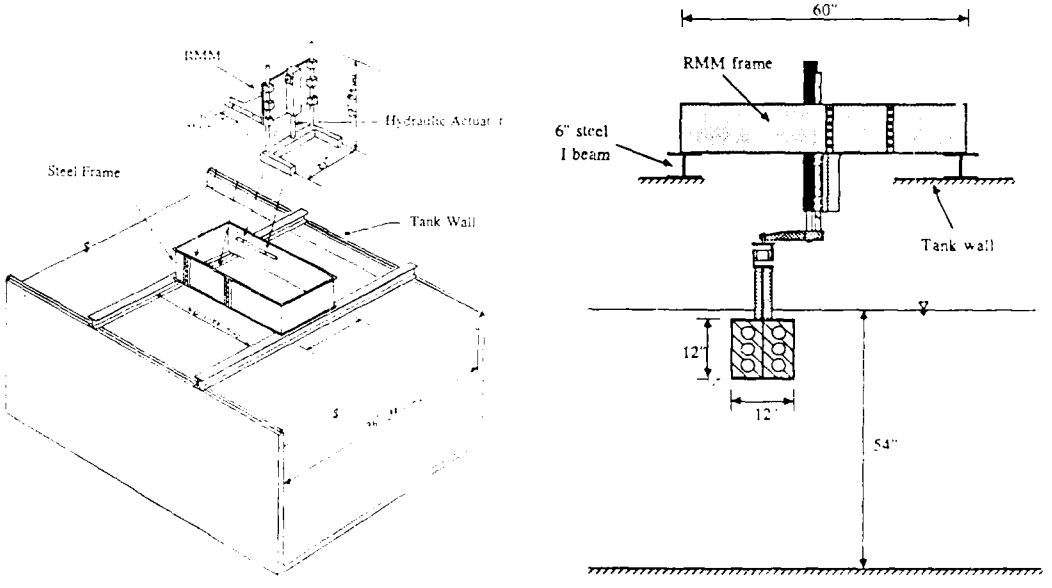

Figure 3: RMM and supporting frame

Analog filtered electronic white noise may be used, but the technique is cumbersome and the spectral shape is limited by the characteristics of the analog filters available. Alternatively, the input signal for the RMM (or the wavemaker) may be generated by a digital computer and converted to an analog signal. The advantage of the computer generated signal is that random motion spectra may be easily simulated and duplicated. The primary disadvantage of the computer generated signal is that one must be careful to generate enough data points to make the resulting analog signal smooth enough to simulate a truly analog signal.

At the University of California, Berkeley, a 16 bit microcomputer (CompuPro™ Systems Model 816) is dedicated to this purpose. A clock and a 12 bit, 4 channel digital to analog converter (Dual Systems Model AOM-12) are synchronized to generate an output signal with of a range of ± 10.0 volts. The input data may be generated by simple FORTRAN programs for sinusoidal or empirical spectra. Data may also be prepared elsewhere and transferred by modem or floppy disk. At the present, the signal is generated by another FORTRAN program which reads all of the data points from floppy disk to internal memory, and then uses the clock to control the digital to analog converter. However, during the present experiments, it was found that the actual output signal was slightly slower than prescribed by the input data. For example, a 1.0 second sine wave with 128 data points per second gives an output signal with a period of 1.0125 seconds. Apparently, computer overhead accounts for the difference. This discrepancy is easily corrected in the generation of the input data. However, it could cause problems for relatively short wave periods where more data points per second are required to achieve an adequate number of points per cycle. It could also be a problem when the input data is imported from other sources, or if the data is not sinusoidal in nature. Therefore, it is intended to rewrite in assembly language, portions of the program that drives the digital to analog converter.

It might be noted here that for purely sinusoidal oscillations, this computer-based system is not as efficient as an analog signal generator because of the time required to generate the input data and to read it from a floppy disk before running each test. However, for random motions, it is much more efficient and versatile than other approaches. The acquisition of a hard disk drive would speed up data input and output since a great deal of time is spent reading and writing to the floppy disks.

For the present experiments, only regular sinusoidal motions were used. However, other tests have been made using a random input signal with no model attached. Figure 4 shows the computer generated input signal for a Bretschneider spectrum and the corresponding motion of the RMM arm. Except for some of the high frequency components where some smoothing has occurred, the agreement is quite good. From a series of tests using the same input signal and varying the gain on the RMM controller, it was found that the high frequency response was better for smaller amplitude motions. This result is not suprising and is typical of such systems.

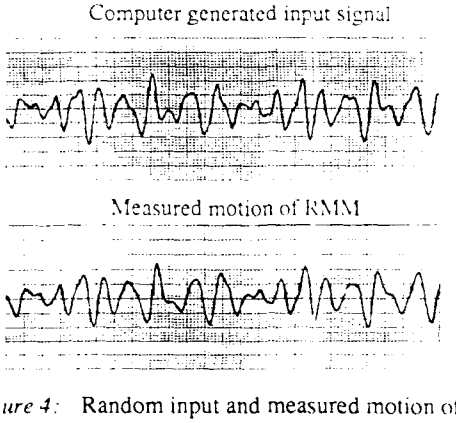

Figure 4: Random input and measured motion of RMM actuator

2.2 Details of the RMM

The model is attached to a two pronged arm that is mounted in a steel frame with three linear bushings on either side, as illustrated in figures 3 and 5. The hydraulic cylinder is mounted at the center of the frame. It is free to rotate through small angles but is laterally fixed by a pinned connection. The free end of the actuator is bolted to the arm at its center.

The actuator has a maximum peak to peak stroke of 12" (30.5 cm). The control system has the capability of specifying shorter limits that will cause the system to shut down if they are exceeded. This system works well when the RMM is used in the horizontal position, but it is not fail-safe in the vertical mode because the shutdown mechanism also cuts off the hydraulic power supply. Once the hydraulic

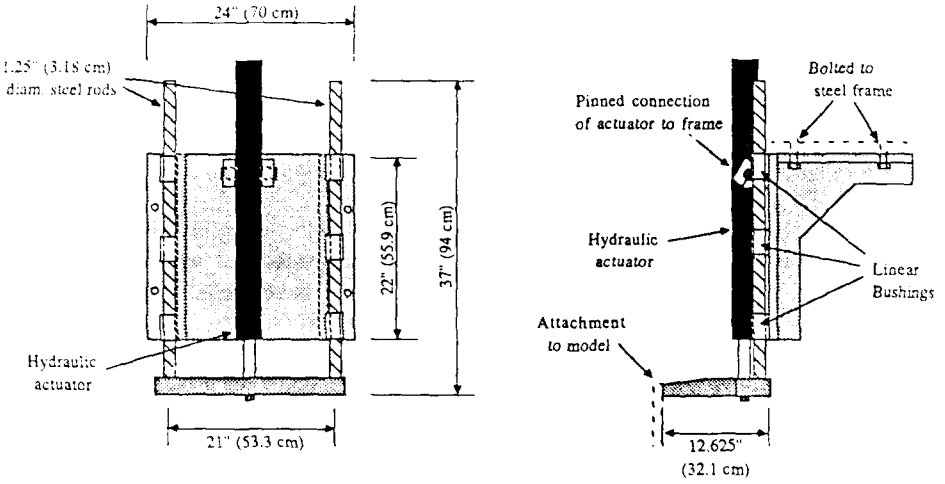

Figure 5: RMM dimensions

pressure is reduced, the actuator will slowly be extended by the weight of the model. In most cases where vertical motions are used, the RMM will be mounted with the arm on the lower side as shown in figures 3 and 5. In this configuration, the weight of the model will pull the actuator to its full extension. This will put the whole reaction on the actuator itself which may damage it. To prevent such an occurrence, a length of $\frac{1}{2}$" (1.27 cm) nylon line is secured in a loop around the support frame and the RMM arm. The line is loose enough to allow normal operation but short enough to stop the arm before the actuator reaches full extension. While originally considered an interim solution, the nylon line has proven to be advantageous in that it not only prevents full extension of the actuator, but it provides a soft stop. A more permanent mechanical device is being studied, but for the present, the line appears to be an adequate solution.

The position of the RMM arm is measured by a linear potentiometer mounted on the arm. A sheave is attached to the potentiometer and a string is wrapped around it and attached at either end to the fixed frame. The potentiometer capacity and sheave size may be easily changed to suit the resolution needs of each set of experiments. This system is simple, reliable and versatile.

Several tests were made to compare a sinusoidal input signal with the actual motion of the RMM arm. The strip chart records showed no visible discrepancies and a Fourier analysis of the output showed no significant energy at any frequency other than the input frequency.

The acceleration of the actuator was also measured with an accelerometer clamped to the arm. The measured accelerations were not nearly as smooth as the motion. At the end of each stroke, there is a small thump which can be seen in the unfiltered record of figure 6. This appears to be caused by the interaction between the actuator and the seals that prevent hydraulic fluid from leaking through the annulus between the actuator and the cylinder. These seals are rather tight, but have a small amount of play along the cylinder axis. As the actuator changes directions, the seals move a small distance before coming up against a stop. This seems to be the cause of the thump at each end of the stroke. Several different sets of seals have been used on the actuator. The original ones were quite

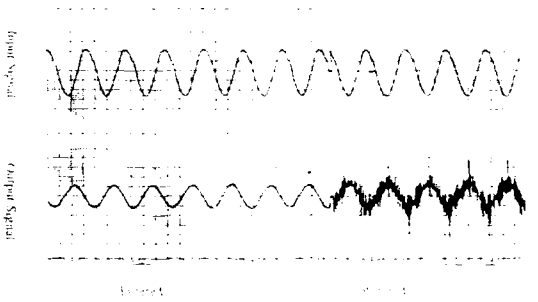

Figure 6: Measured acceleration of RMM actuator

hard and seemed to generate very large end-of-stroke accelerations. The seals we are currently using are much softer but do permit some leakage.

This impulse loading is small but may be felt by a hand holding the actuator or anything fixed in the vicinity of the RMM. It does not appear to affect the smoothness of the motion of the actuator, but it does induce a free vibration response of a model suspended from it. For most practical cases, the model attachment mechanism is quite stiff and its resonance frequency is much higher than the oscillation frequencies of interest. As long as the vibrations are not so severe as to disturb measurement of the phenomenon under study, there appears to be no problem. Most applications of such a planar motion mechanism are associated with measuring linear added mass and damping coefficients (as in this report) and these vibrations are of little consequence. However, if one is dealing with an impulsive motion, this resonance could cause difficulties.

Vibrations may also pose some problems when studying nonlinear phenomena. The RMM was used once previously to measure wave drift forces on surging cylinders (Hodges (1985)). In order to measure the drift force accurately, the force transducer attaching the model to the RMM was required to have high resolution for small forces and, consequently, had a relatively low stiffness. This induced excessive vibrations for larger motion amplitudes and it was not clear whether vibrations from the RMM adversely affected the results.

A steel frame was constructed to support the RMM which may be mounted in the vertical or horizontal direction inside the frame. The frame was designed to be mounted on the existing towing carriage in the longitudinal or transverse direction. For tests where the model is not to be towed, it may be secured to two steel wide flange sections spanning the tank as shown in figure 3.

The hydraulic power supply is mounted on a separate carriage which may be pulled behind the main carriage or secured to the tank rails for fixed tests.

2.3 The Cylindrical Model

The dimensions and structural design of the cylindrical model were based on the following criteria:

- The dimensions of the cylinder should be chosen so that the waves generated by the lowest frequency oscillation will not reflect from the bulkhead and reach the model before enough data has been collected to obtain consistent results.
- Test conditions should represent "deep" water for the radiated waves, since the theories to be compared with the results assume this.
- The maximum force induced under any test conditions should not exceed the rated strength of the force transducers of 120 pounds (533 N) each.
- The structural resonant frequency of the cantilevered ends of the cylinder should be high enough to be well out of the frequency range of interest (e.g. on the order of 10 Hz).
- The model should be ballasted to be nearly neutrally buoyant to take advantage of the full range of the force transducers.
- The internal structure of the model should be strong enough to support its own weight out of water during installation and removal. It should also be light enough to be easily handled in and out of the water.

The first two conditions limited the breadth of the model to approximately one foot. Although a smaller cylinder might have been more desirable for ease of handling, it was feared that difficulties would arise in making it structurally stiff enough to avoid excessive vibrations. For a 12" (30.5 cm) square cylinder, it was estimated that the lowest test periods would be on the order of 3.0 seconds. The time required for a wave radiating from the model to reach the bulkhead and return to the model was calculated to be around 33 seconds, allowing just enough time for a gradual start up and 20 seconds of good data.

In order to provide neutral buoyancy with the model submerged, a 12" x 12" x 96" (30.5 x 30.5 x 243.8 cm) cylinder must weigh around 500 pounds (2222 N) in air. The length of the model (96") was chosen to fit the width of the towing tank with about $1/4$" to spare. For ease and economy in construction,

AD-A196 627 PROCEEDINGS OF THE AMERICAN TOWING TANK CONFERENCE (21ST) HELD IN WASHINGTON DC ON 5-7TH AUGUST 1986(U) NATIONAL RESEARCH COUNCIL WASHINGTON DC W F MESSALLE 2/6

UNCLASSIFIED AUG 87 F/G 13/10 NL

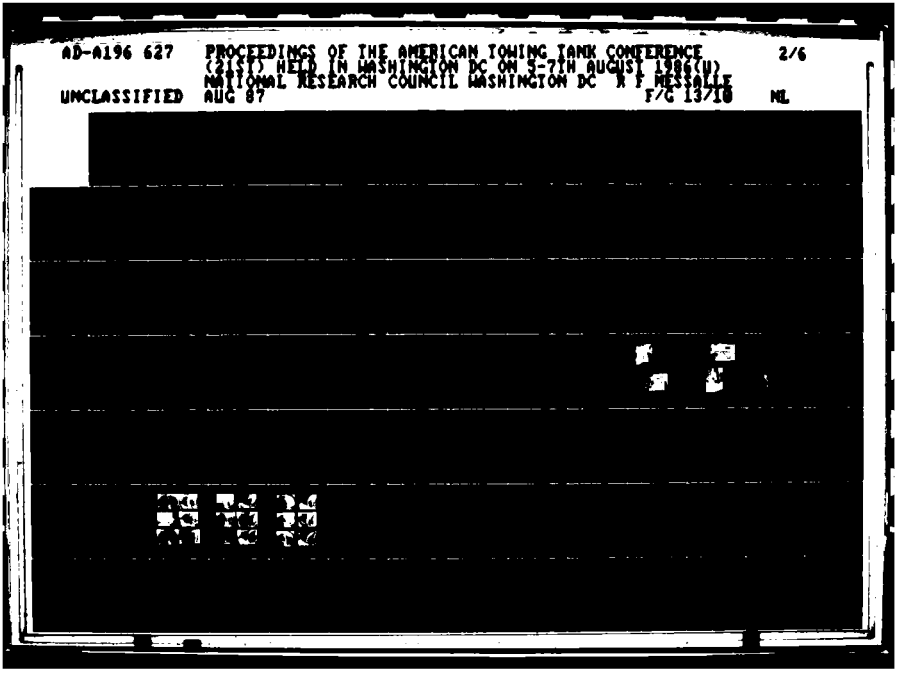

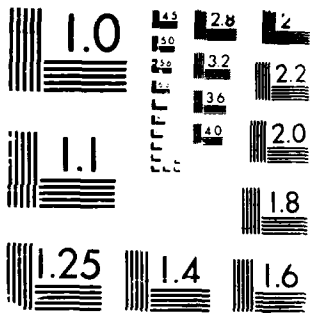

the model was to be built from Plexiglas™ sheets. Due to the relatively light weight of Plexiglas, a great deal of ballast was required to achieve the 500 pound (2222 N) weight. Various solid weight ballasting schemes were considered, but the difficulty in making all joints watertight and the unwieldiness of such a massive model made them impractical. Instead, the model was designed to be completely flooded during testing.

The model was constructed entirely from $^1/_4$" (.635 cm) thick Plexiglas sheets. Longitudinal bending strength was provided by the outer walls and a solid vertical bulkhead running the length of the model along the centerline, as illustrated in figure 7. Transverse bulkheads were placed at one foot intervals to provide shear strength and vertical load transfer. Each transverse bulkhead had six, $2^1/_2$" (6.35 cm) diameter holes drilled in it to allow free flow between compartments during flooding. Small notches were cut along the base of all transverse bulkheads as well as the central longitudinal bulkhead to facilitate drainage. During installation, all flooding was through the end bulkheads with air escaping through small holes ($^1/_4$" (.635 cm) diameter) drilled in the top panel at the corners of each compartment. None of the holes were sealed during the test. The clearance between the ends of the cylinder and the tank wall was approximately $^1/_{16}$" (.159 cm), leaving little room for any appreciable flow when the cylinder was oscillating. During some tests, a small flow was observed emanating from the air holes next to the central bulkhead, but this was considered insignificant.

Steel angle sections were bolted vertically to the bulkheads on either side of the midsection and the central bulkhead as shown in figures 7 and 8. These two transverse bulkheads were twice the thickness of the other bulkheads ($^1/_2$" (1.27 cm)) and the central bulkhead was locally reinforced near the bolts. Each angle extended approximately 10" (25.4 cm) above the top of the panel where they were connected by a horizontal aluminum T-section. The force transducers were mounted symmetrically on the flange of the T-section and secured to the RMM arm as shown in figure 8. The cylinder was lifted by a single line attached to eye hooks mounted on the outside of the angles with a wooden spreader beam to avoid interference with the transducers.

Although the model was nominally 96 inches (243.8 cm) in length, it was measured to be slightly longer after construction. The tank was measured at the top of the walls to be $96^1/_2$" (245.1 cm), but tapered slightly so that, at the level where the model was to be tested, there was only $^1/_{16}$" (.159 cm) clearance on either end. This presented considerable problems in aligning the RMM and the model so that the ends would not rub the wall at any point in the stroke of the RMM. Although the anticipated $^1/_4$" (.635 cm) clearance would have been far more convenient, it is believed that there was no interference with the wall during the tests.

It is common practice to determine the mass of such a model by oscillating it in air. Such a procedure was impossible in this case because of the ballasting method. Instead, the model was weighed before installation and the volume and mass of the Plexiglass and the submerged part of the support frame were carefully calculated. The remaining volume of water was found and the total mass estimated to be 16.27 lb·sec^2/ft (237.4 kg). The import-

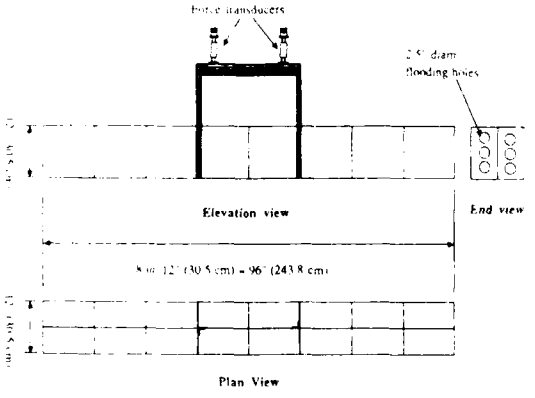

Figure 7. Model dimensions

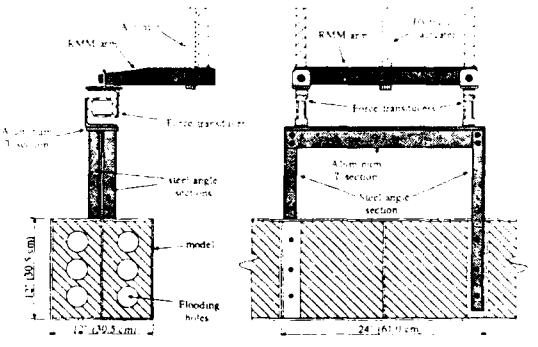

Figure 8. Attachment of RMM and model

Item	Value	
Length, L	96 in.	(243.8 cm)
Beam, 2b	12 in.	(30.5 cm)
Draft, T	12 in.	(30.5 cm)
Mass, m	16.27 lb s^2/ft	(237.4 kg)

Table 1: Model dimensions

ant dimensions and properties of the model are summarized in table 1.

The natural frequency of vibration of the free ends of the model was estimated by considering each side of the model as a cantilevered beam fixed at the midspan of the model. Using linear beam theory and hydrodynamic coefficients obtained from Yum (1985), it was found that the natural frequency was on the order of 10 Hz. This was considered acceptable, as the test frequencies were to be on the order of 0.2 to 1.0 Hz. After the model was installed in the tank, a free vibration test revealed the actual natural frequency of the system to be around 7.0 Hz.

3.0 The Experiments

3.1 Scope of Experiments

In terms of the nondimensional wave number, $N = \omega^2 b/g$, the region of $N > 1.0$ was well documented by Chung (1977) and others and consequently, was not investigated in the present study. The dimensions of the testing facilities limited the lowest frequency for the present experiments to $N = 0.07$. Tests were conducted for submergences of 0.25 and 0.10 corresponding to the available numerical results. Four motion amplitudes were tested for the deeper submergence and two were tested for the shallower case. The tested frequencies and amplitudes are summarized in table 2.

$\bar{d} = d/b$	0.25	0.10
$\bar{a} = a/b$	.05, .10, .15, .20	.10, .20
a/d (% of gap)	.20, .40, .60, .80	.40, .80
$N = \omega^2 b/g$	.071 - .80	.071 - .90

Table 2: Experimental parameters

3.2 Experimental Procedure

Prior to each test, the cylinder was aligned to the proper submergence by adjusting the zero position of the hydraulic actuator. The input signal was checked on a strip chart recorder and then the amplitude of the motion was slowly increased to the desired amplitude over a period of around five seconds. After a few cycles, when the strip chart record of the force showed an apparent steady state, data acquisition was begun. Data was taken over a period of 20 seconds at intervals of 0.05 seconds. On one or two occasions, the waves reflected from the bulkhead end of the tank were observed striking the model before data acquisition was completed so the data analysed was limited to the segment before the interference began. No noticeable lateral motion was observed during the tests.

A Fourier analysis was made of each force record, with the leading coefficients taken to be the linear hydrodynamic coefficients. Although these coefficients do not display the nonharmonic character of this nonlinear process, they form a convenient basis for comparison.

3.3 Experimental Results and Observations

The notation used in this paper follows Yum (1985). The effective added mass and damping coefficients are nondimensionalized as

$$\lambda = \frac{\lambda}{1/2\,\pi\rho b^2 L}$$

$$\mu = \frac{\mu}{1/2\,\pi\rho b^2 L}$$

Figures 9, 10, 11 and 12 show the experimental data compared with numerical results for the hydrodynamic coefficients of a square cylinder using linear theory, the theory proposed by Newman, et al. (1984)and the theory of Yum. The first two figures are for a gap between the cylinder top and the free surface of 25% of the cylinder half breadth, and the second two are for a gap of 10% of the half breadth. The results of Newman, et al were only available for the second case. The experimental data from Chung (1977) are included in the first set of figures, for which the motion amplitude was 36% of the initial gap (a/b = .089).

It should be noted that the close-fit and Newman, et al. results are from linear theories while the results of Yum are nonlinear with respect to motion amplitude. The amplitude used for these figures was quite small. Figures 13 and 14 show the amplitude dependence of this theory for d/b=0.25.

The observed flow pattern varied significantly with both frequency and motion amplitude. For relatively small amplitudes, the flow on and off of the top of the cylinder was orderly. During the downstroke, water flowed over the top like a sheet and reversed itself on the upstroke. This was particularly true for higher frequencies where the volume of the flow was restricted by the shorter time before the next half cycle. For lower frequencies, there was time for a significant volume of fluid to enter and leave the inner region on top of the cylinder during each cycle. Below a certain frequency, the sheet flow from the two sides met in the middle before the reverse flow began causing a reflection at the center line.

For higher amplitudes, the oncoming and reflected flows contained hydraulic jumps and there was often a vertical jet at the centerline as the two bores met. These phenomena were particularly pronounced for the shallow submergence case.

Chung (1977) made similar observations and noted that there was a slight discontinuity in the data at the frequency where the flows from both sides first had enough time to meet and reflect. A similar behavior may be seen in the present study for motion amplitudes of 20 and 40% of the gap in figures 9 and 11 respectively. For larger motion amplitudes, al-

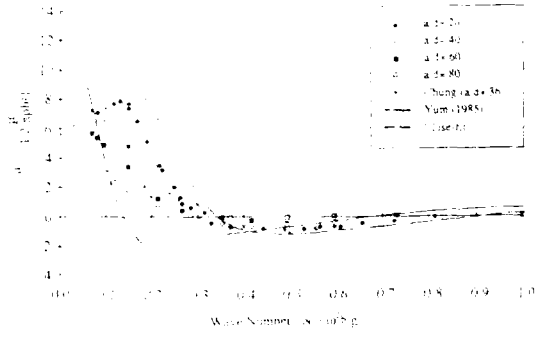

Figure 9: Added mass coefficient (d/b = .25)

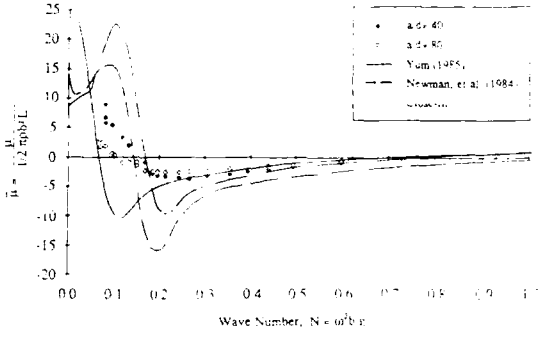

Figure 11: Added mass coefficient (d/b = .10)

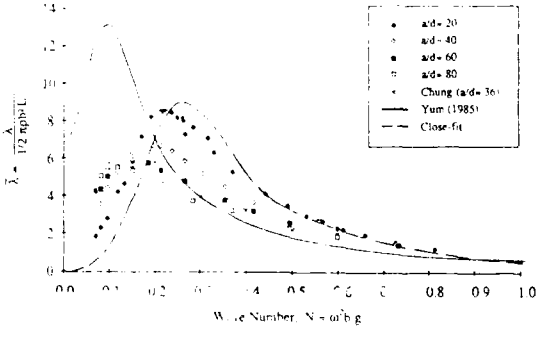

Figure 10: Damping coefficient (d/b = .25)

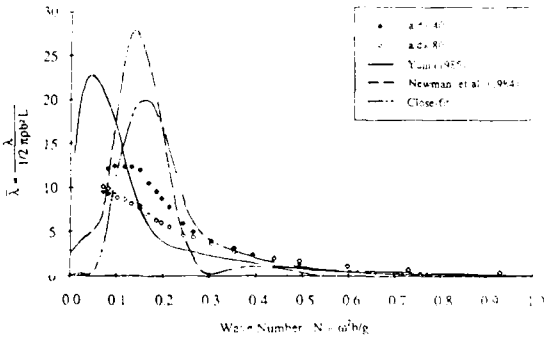

Figure 12: Damping coefficient (d/b = .10)

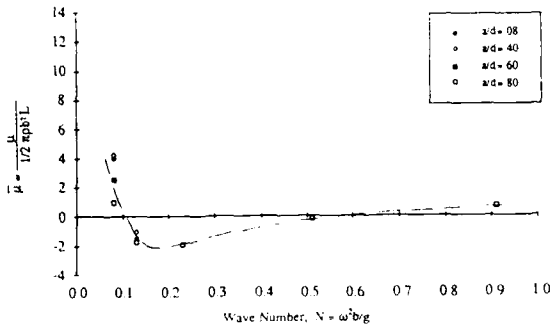

Figure 13: Amplitude dependence of added mass coefficient (d/b = .25)

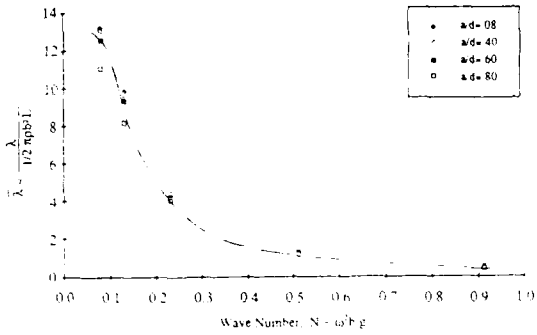

Figure 14: Amplitude dependence of damping coefficient (d/b = .25)

though the flow transition was observed, the effect on the hydrodynamic coefficients was not as pronounced. The reason for this is not clear.

The phasing between the centerline reflection and the cylinder's motion also varied with frequency. For higher frequencies, the reflection occurred later in the cycle. The sketch in figure 15 shows the approximate flow pattern observed during low frequency, high amplitude tests.

4.0 Conclusions

It is clear from these results that the hydrodynamic forces associated with the vertical oscillation of a two-dimensional cylinder very close to the free surface are strongly nonlinear with respect to motion amplitude. At the high end of the frequency range tested, as observed previously by Chung (1977), the experimental results agree well with the linear theory and show no significant amplitude dependence. However, the motion amplitude appears to be dominant at the lower frequencies. This is important because this is the region where the added mass coefficients undergo dramatic changes.

The results for the smallest motion amplitude (a/d = .20) of the deeper submergence (d/b = .25) agree reasonably well with the linear close fit solution, even for low frequencies. Results for the larger motion amplitudes diverge significantly for N < 0.5. However, these results do not follow the calculations of Yum (1985) either, particularly for the damping coefficient.

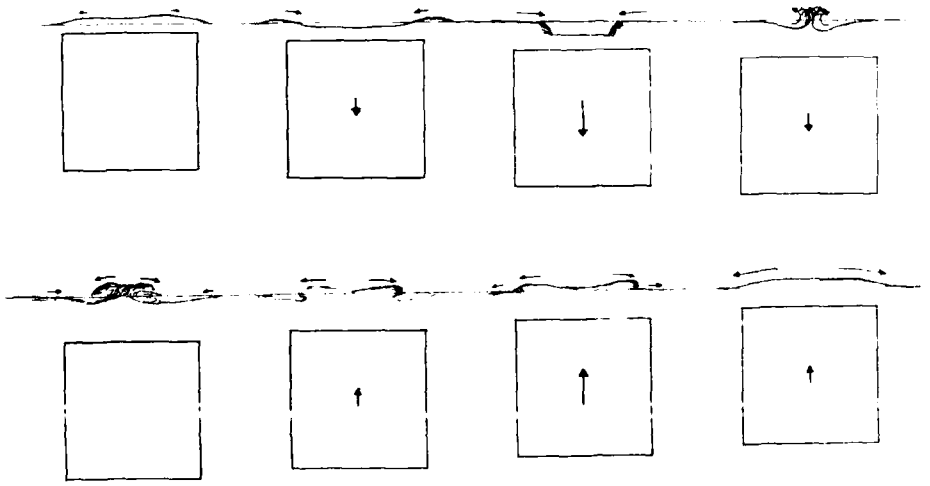

(Arrows represent approximate velocity vectors)

Figure 15: Observed flow pattern for large amplitude, low frequency oscillations

References:

Chorin, A.J. (1976): "Random Choice Solution of Hyperbolic Systems", Journal of Computational Physics, no. 22.

Chorin, A.J. (1977): "Random Choice Methods With Application to Reacting Gas Flow", Journal of Computational Physics, no. 25.

Chung, J.S. (1977): "Forces on Submerged Cylinders Oscillating Near the Free Surface", Journal of Hydronautics, vol. 11, no. 3.

Frank, W. (1967): "Oscillation of Cylinders in or Below the Free Surface", National Ship Research and Development Center report no. 2375.

Garrison, C.J. (1975): "Hydrodynamics of Large Objects in the Sea", Journal of Hydrodynamics, 1975.

Glimm, J. (1965): "Solutions in the Large for Nonlinear Hyperbolic Systems of Equations", Communications in Pure and Applied Mathematics, vol. 18.

Higo, Y. (1985): "A Study of Nonlinear Hydrodynamic Forces Acting on a Rectangular Cylinder Oscillating with a Large Amplitude" (in Japanese), Journal of the Kansai Society of Naval Architects, no. 199.

Hodges, S.B. (1985): "An Experimental Study of Surge Drift Forces on Shallow Draft Circular Cylinders", University of California, Berkeley, Department of Naval Architecture and Offshore Engineering, Master of Science thesis.

Hoech, J. (1984): "Design and Construction of a Random Motion Mechanism", University of California, Berkeley, Department of Naval Architecture and Offshore Engineering, Master of Engineering thesis.

Newman, J.N., Sortland, B., Vinje, T. (1984): "Added Mass and Damping of Rectangular Bodies Close to the Free Surface", Journal of Ship Research, vol. 28, no. 4.

Salvesen, N., Tuck, E.O. and Faltinsen, O. (1970): "Ship Motions and Sea Loads", Transactions, SNAME, vol.78, pp.250 - 279.

Webster, W.C. (1979): "Computation of the Hydrodynamic Forces Induced by the General Vibration of Cylinders", Journal of Ship Research, vol. 23, no. 1.

Yum, D.J. (1985): "Nonlinear Flow Around Slightly Submerged Two Dimensional Bodies", University of California, Berkeley, Department of Naval Architecture and Offshore Engineering, Ph.D. dissertation.

NON-LINEAR ANALYSIS OF TIME SERIES DATA

by John E. McDowall
Senior Engineer
Offshore Technology Corporation

Introduction

The problem of designing a mooring system for a ship in the ocean is a classical one that every engineer associated with the sea has to solve at least once in his career. This mooring analysis can range from either a simple static catenary analysis to a full dynamic time domain simulation. To perform such an analysis it is necessary to determine the environmental loading on the system. Due to the complexity of these forces it is often necessary to perform both physical and numerical modeling to arrive at an appropriate solution. As the response of a moored vessel is highly non-linear it has become necessary to develop techniques to interpret the data collected during physical tests to compare with numerical models. In this paper we would like to examine the application of techniques to investigate the response of moored vessels using time series analysis particularly the second order response. This is a very significant problem as the second order motions are usually greater than the first order response and can very often be the limiting design factor.

There have been published several excellent works on the subject of time series analysis (references 1, 2, and 3) and it is not intended to reiterate work already done, instead the objective of this paper is to discuss applications of these techniques as they relate to the analysis of the response of moored vessels. In the past several years Offshore Technology Corporation has invested several thousand manhours into developing a comprehensive library of time series analysis routines to interpret experimental data either at model scale or full scale. The majority of these routines are for linear input/output systems. Recently implementation of routines that determine the quadratic transfer operator has been undertaken. The primary aim of this work is to examine the slowly varying drift motions experienced by moored floating bodies in a seaway.

Background

The results of a seakeeping test usually take the form of specifying the power spectral densities of the wave and the vessel responses and the resulting vessel Response Amplitude Operators (RAOS). The power spectral density function is given in Equation (1)

$$G_{xx}(f) = \frac{1}{N_d T} \sum_{k=1}^{N_d} X_k(f)^2 \qquad (1)$$

Figure 1 gives a typical power spectral density function for a Pierson Moskowitz spectral formulation and Figure 2 gives the total horizontal restoring force in the surge direction. From figure 2 the significance of the low frequency component which is the second order response of the system can be observed.

To obtain information on both the phase and the percent random error of the ships response it is necessary to use what is termed cross spectral density analysis. Use of this technique rather than auto spectral density analysis eliminates uncorrelated signal noise and allows the determination of the true linear response of the system. The expressions for the RAO, the phase angle, and the percent random error are given in Equations (2)-(4).

$$R_{ij}(f) = \sqrt{\left[G_{xy}(f)/G_{xx}(f) \right]}$$

$$\text{RAO, } H_1(f) = \text{Modulus } (R_{ij}(f)) \qquad (2)$$

$$\text{Phase Angle} = \tan^{-1} \{ \text{Im}[R_{ij}(f)] / \text{Re}[R_{ij}(f)] \} \qquad (3)$$

$$\text{Coherence, } \nu^2_{xy}(f) = \frac{|G_{xy}(f)|^2}{G_{xx}(f)\, G_{yy}(f)}$$

$$\text{Random Error} = \frac{\sqrt{2}\,|1-\gamma_{xy}^2(f)|}{|\gamma_{xy}(f)|\sqrt{N_d}} \qquad (4)$$

where:

$G_{xx}(f)$ - auto spectral density of output

$G_{yy}(f)$ - auto spectral density of output

$G_{xy}(f)$ - cross spectral density of input with output

Examples using this technique are given in Figures 3 and 4. From this standard analysis it is possible to determine the ships response to the specified sea spectrum. If the vessel is wall sided the pitch and heave response will not vary with sea spectra and can be defined exactly by this technique over the range of input wave frequencies.

Dynamics of a Soft Moored System

The motions of a vessel in a soft moored system cannot be predicted by linear theory alone. The motions of a moored vessel are excited in two frequency ranges:

- linear wave frequency components
- components at frequencies much lower than wave frequencies

this is shown in Figure 2 which is the horizontal restoring force on a soft moored vessel. This figure shows the effects of both the wave frequency components and the low frequency components.

It has been found that the wave frequency components are proportional to the wave amplitude while the low frequency components are proportional to the wave amplitude squared. From natural period tests it is seen that the low frequency motions are at the ships surge natural period. In the example shown this period is around 0.0033Hz. At this low frequency there is very little damping. There is practically no wave damping and what little damping there is, is mainly due to hull friction and other viscous effects. This low damping and resonance effects create a highly tuned system with very little damping. The prediction of the magnitude of the low frequency motions is difficult due to the difficulty in predicting the low frequency damping. In computer models this has to be input as an empirical factor and results from model tests are difficult to scale up due to the viscous nature of the damping forces.

Description of Model Test

Recent physical model tests of a turret moored tanker have presented an opportunity to examine the low frequency response of a moored vessel in a realistic environment. The system consisted of an eight point mooring system, that was simulated with horizontal springs as shown in Figure 5. The system was tested at three different drafts and in a combination of wind, waves and current. The principal particulars of the vessel are given in Table 1 with the scaled dimensions of the other vessel used in this paper. The environmental conditions in which all three drafts were tested are given below:

Waves - Pierson Moskowitz Spectrum H_{sig} = 53.0 ft.

Wind - Uniform Wind Profile, Velocity = 100 knts.

Current - Uniform Surface Current, Velocity = 3 knts.

A detailed description of the system is given by Key, et.al. (reference 8).

The mooring line tensions for each individual mooring line were resolved into the surge and sway directions, as the turret rotation was not measured during the tests, turret rotation was not included in the analysis. As the environment was co-linear and from observations the turret breakout torque was never exceeded in the co-linear environmental tests, this assumption will produce no significant errors. The resolved tensions were checked using the measured system restoring force and the measured displacements and good agreement was shown.

Second Order Spectral Density Function

The investigation of the low frequency wave response of a moored vessel depends very heavily on the character of the input spectrum. Typically model basins compare the generated first order spectrum with the desired theoretical and iterate to achieve an acceptable spectrum. When investigating the low frequency response of it is necessary to ensure that the low frequency spectrum is also correctly modelled by the wave generator. At Offshore Technology Corporation we currently use a minimum bandwidth of 0.13Hz and a non-repeating algorithm for wave generation that can be iterated to obtain the correct spectral density function as is shown in Figure 1. The spectral density function for the low frequency response (Equation (5)) as given by Bendat and Piersol (reference 5)

$$G_{yy}(f) = 8\int_0^\infty G_{xx}(u)\,G_{xx}(f-u)\,du \qquad (5)$$

This function is shown in Figure 6 for the Pierson Moskowitz Spectrum shown in Figure 1. The figure shows both the measured data and the theoretical spectrum for the model. As can be seen for both the linear and the second order spectrum the input wave closely matches the required specifications.

Second Order Transfer Function

To properly interpret experimental data it is important to have a good measure of the error inherent in the measurements. This is a standard technique for the linear RAO's shown in Figure 3. This is also equally true for the low frequency response. As yet this has not been implemented into our system even though the theory has been published by Bendat and Piersol (reference 6). As is shown, one of the significant problems associated with the determination of the second order transfer function is the length of the record required to obtain a stable estimate of the transfer function. To investigate this problem experimentally an experiment was conducted for three hours prototype time and then analysed over the whole test and then over the first half and then the last half using second order analysis.

Cross bispectral analysis is used at Offshore Technology Corporation to analyse the steady and slowly varying forces and hence determine the second order responses of a moored system. The second order response is characterised by the quadratic transfer function (QTF) which is the second order equivalent of the Response Amplitude Operator (RAO) for linear systems. The QTF quantifies the non-linear response of a structure as a function of frequency, allowing the determination of a vessel's response to an arbitrary seaway.

In a random seaway the response of a vessel subject to a random seaway can be quantified statistically by the power spectral density. Normally the linear relationship between the input and output is expressed as the RAO. In non-linear systems this provides only part of the answer and it is necessary to quantify the quadratic RAO. The relationship between the second order spectral densities is given as follows:

$$G_{yy}(f) = |H_1(f)|^2 G_{xx}(f) + 8 \int_0^{\infty} |H_2(\mu)|^2 |H_2(f-\mu)|^2 G_{xx}(\mu) G_{xx}(f-\mu) \, d\mu$$

where $H_2(f,\mu)$ is the quadratic transfer function.

The first term on the right hand side gives the linear response and the second term gives the second order (low frequency) response. If $H_1(f)$ and $H_2(f,\mu)$ are known, the vessels linear seakeeping and slowly varying response can be determined. The second order term consists of an integral of the product of the second order transfer function and the input wave spectrum evaluated at the frequency f, and at the frequency $f-\mu$, where μ is a small delta frequency corresponding to the low frequency of interest. Note that in the integral, f is a dummy variable of integration. Therefore, what results from the integration is the value of the PSD at the delta frequency, $G_{xx}(\mu)$. We have chosen to define the quadratic transfer function $H_2(f,\mu)$ such that the relation given in the equation is exactly satisfied, consistent with our usual definitions of the wave spectrum, $G_{xx}(f)$.

In our investigation here it is the steady drift that is of interest, this implies that μ is equal to zero. This greatly simplifies the determination of the second order transfer function. By choosing the zero frequency response the Fourier transform of steady force is identically equal to the average force.

To evaluate the results of our analysis we compared the results to two similar vessels. The drift coefficients for tanker 1 come from the three dimensional diffraction program AQWA-LINE and the results for tanker 2 are from model tests reported by Huanqiu and Maoxiang (reference 7). The particulars of the two vessels are given in Table 1. The dimensions from tanker 2 were scaled using Froude scaling to be as close to the vessel tested by OTC as possible. As neither of the vessels are exactly the same as that tested by OTC the results can only be used qualitatively to determine of the results obtained are of the correct order of magnitude and of the correct general form.

Results

Comparisons of Figures 7-9 show the affect of sample length on the results, as is shown the results are in fair agreement below 0.09Hz and show differences above this. Until the error function is implemented it is not possible to accurately determine the affect of sample length on the second order transfer function. To determine if these results compared with other experimental data the quadratic transfer function for a loading condition similar to that of reference 7 was determined. Figure 10 shows this comparison. A similar comparison is made with numerical predictions in Figure 11. In both these comparisons the tankers were not identical but were sufficiently close to compare the magnitude of the results. In both cases there is fair agreement in the relative magnitude of the results but to make any further comparisons would require close agreement between the physical characteristics of the tankers used.

Computation

All the computer programs used by OTC are written in FORTRAN 77 with the exception of the Fast Fourier Transform and Inverse Fast Fourier Transform subroutines which are MACRO 11 which is Digital Equipment Corporation's assembler language for the PDP 11 series of computers. All the routines were run on a PDP-11/44 computer running the multi-tasking and multi-user operating system RSX-11M V4.0. The high efficiency of the FFT algorithm allows the computer to analyse the results and deliver the graphical output for a test with 16384 data points in

under one minute for the first order analysis and under three minutes for the second order analysis. The calculations take less time than this as much of this time is taken up by the plotting routines that are sent to a Tektronix 4052 for plotting.

Conclusions

From the results presented here it is apparent that it is now possible to quickly and efficiently obtain the second order transfer functions of moored vessels in an efficient manner using small mini computers for data analysis. It is necessary though to conduct long experiments to obtain sufficient data to have reasonable confidence in the results. To fully utilize this technique it is necessary to implement the error function estimate developed by Bendat and Piersol (reference 6) before this technique can enter regular use. From the comparisons done with other model test data and numerical models the technique shows a great deal of promise. To fully determine the value of this technique further work should include comparisons with numerical models such as AQWA to investigate any problems with either the numerical methods or the experimental techniques.

Acknowledgements

The author would like to thank Offshore Productions Systems (a division of Combustion Engineering) for permission to use the data presented in this paper. In addition, the author would like to thank Dr. Ian Collins and Mr. Dave Peterson for their assistance in developing some of the routines in the analysis.

References

1. Bendat, J.S. and A.G. Piersol, "Random Data: Analysis and Measurement Procedures," Wiley-Interscience, 1971.

2. Rice, S.O., "Mathematical Analysis of Random Noise," Selected Papers on Noise and Stochastic Processes, edited by Nelson Wax, Dover, 1954.

3. Bendat, J.S. and A.G. Piersol, "Engineering Applications of Correlation and Spectral Analysis," Wiley-Interscience, 1980.

4. Pinkster, J.A., "Mean and Low Frequency Wave Drifting Forces on Floating Structures," Ocean Engineering, Volume 6, 1979.

5. Bendat, J.S. and A.G. Piersol, "Spectral Analysis of Non-Linear Systems Involving Square-Law Operations," Journal of Sound and Vibration, Volume 82, 1982.

6. Bendat, J.S. and A.G. Piersol, "Statiscal Errors for Non-Linear Measurements Involving Square-Law Operations," Journal of Sound and Vibration, Volume 90, 1983.

7. Huanqiu, G. and G. Maoxiang, "Determination of Non-Linear Drift Force Quadratic Transfer Function and Synthesis of Drift Force Time History," Marintec Offshore China Conference, Shanghai, 1983.

8. Key, J.W., F.E. Shumaker, E.J. Theisinger, and B. Thomson, "Design and Analysis of Turret Mooring Systems for Tanker Based Storage or Production Facilities," Offshore Technology Conference, #5250, 1986.

ITEM	OTC Tanker 100% Loaded	OTC Tanker 85% Loaded	OTC Tanker 40% Loaded	AQWA 40% Loaded	Reference 7 100% Loaded
Length (feet)	1026.0	1026.0	1026.0	1002.0	964.2
Beam (feet)	161.6	161.6	161.6	148.4	152.8
Draft (feet)	62.0	53.0	28.0	29.7	64.8
B/d	2.6	3.0	5.8	5.0	2.4
L/B	6.3	6.3	6.3	6.8	6.3
Displacement (long tons)	235398.0	200565.0	96200.0	101348.0	250986.0

TABLE 1 - VESSEL PARTICULARS

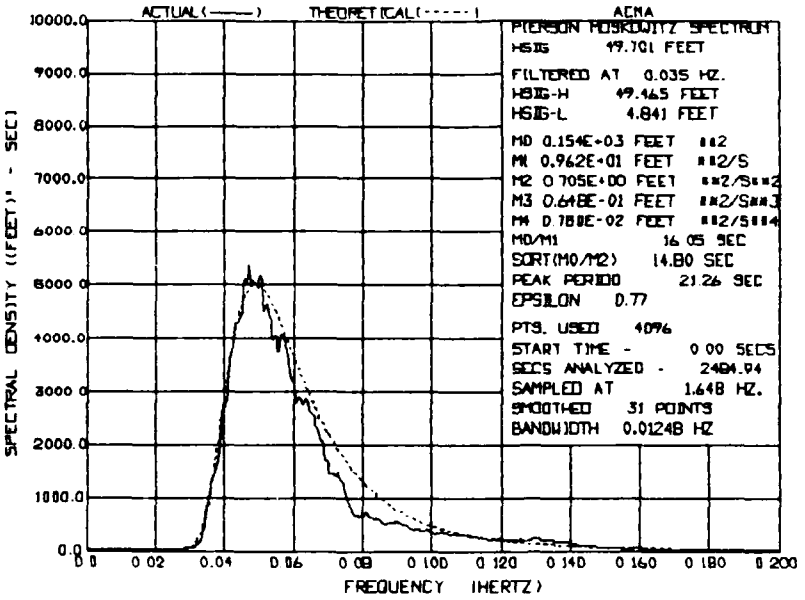

FIGURE 1 - WAVE POWER SPECTRAL DENSITY

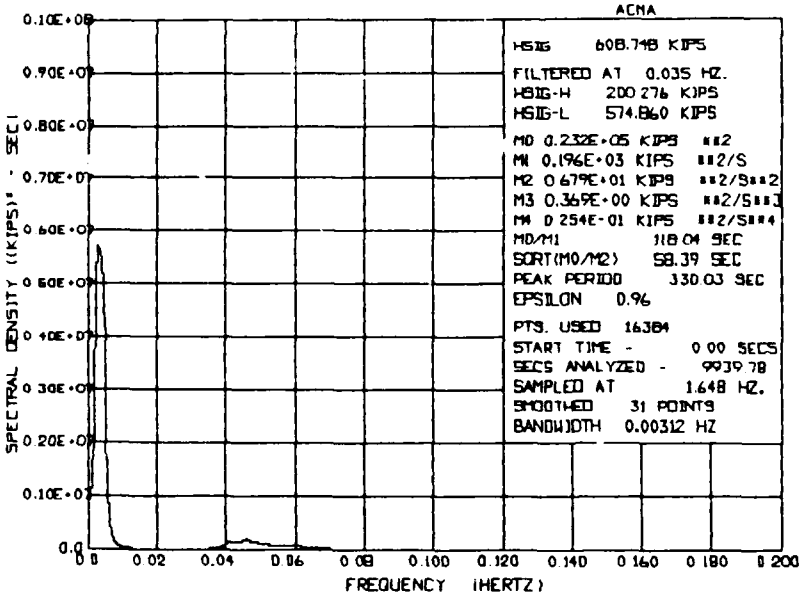

FIGURE 2 - MOORING FORCE POWER SPECTRAL DENSITY

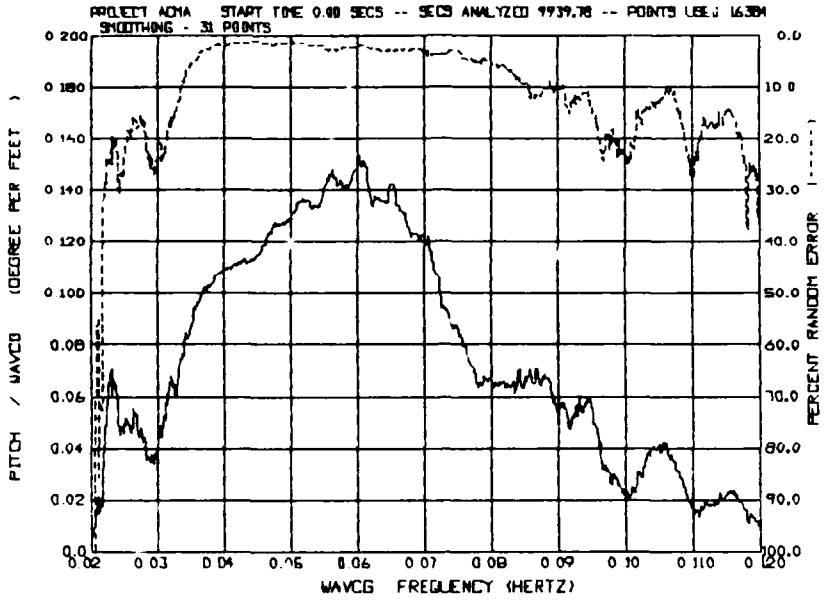

FIGURE 3 - PITCH RESPONSE AMPLITUDE OPERATOR

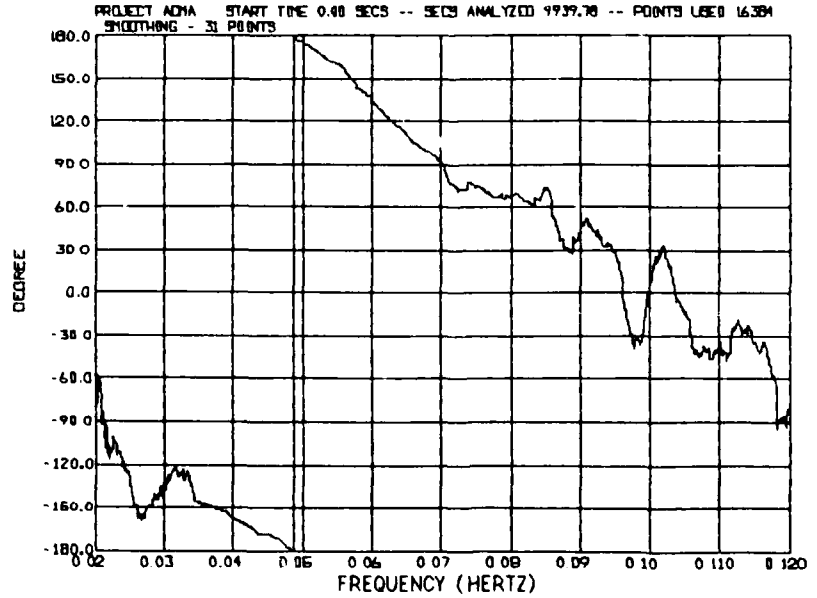

FIGURE 4 - PITCH PHASE ANGLE

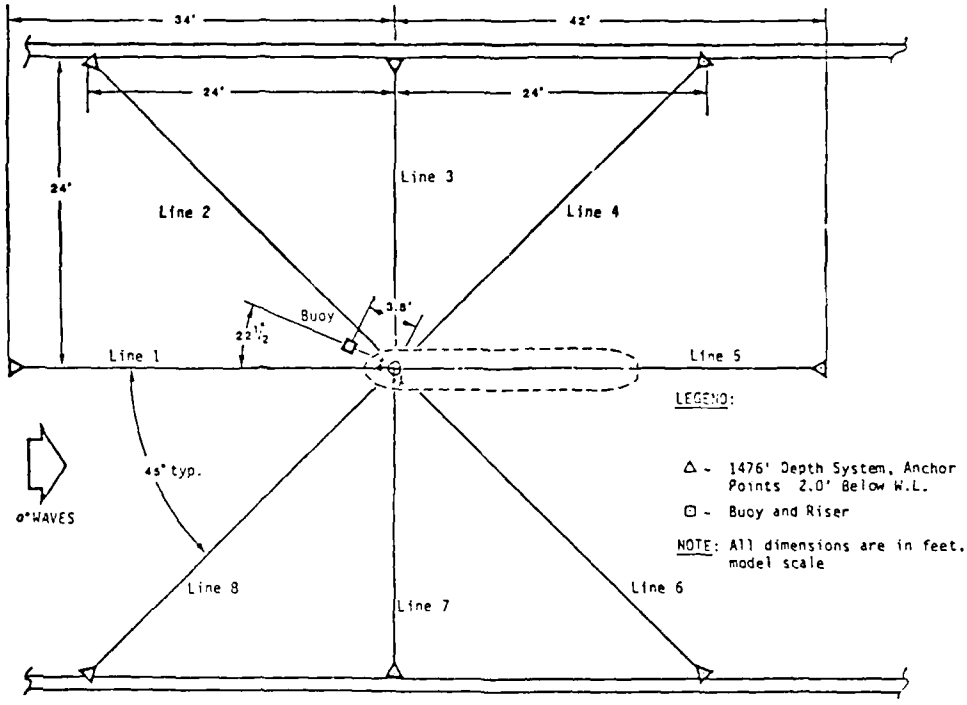

FIGURE 5 LAYOUT OF MOORING SYSTEM

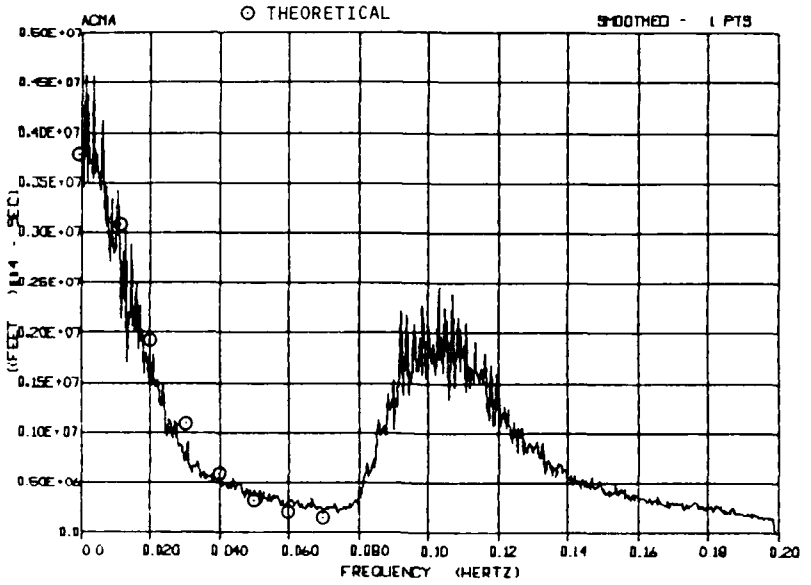

FIGURE 6 - WAVE AUTO - COVARIANCE FOR PIERSON MOSKOWITZ SPECTRUM

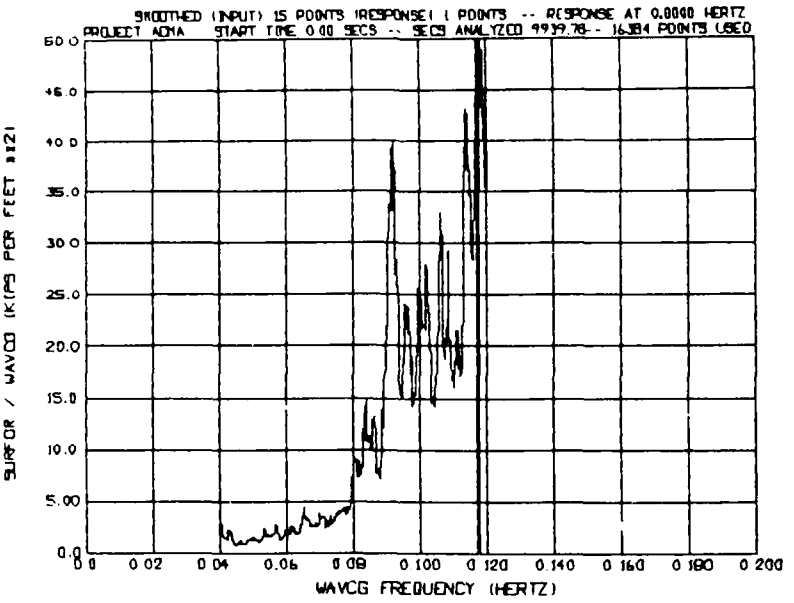

FIGURE 7 - QUADRATIC TRANSFER FUNCTION FOR COMPLETE TEST
85% LOADED CONDITION

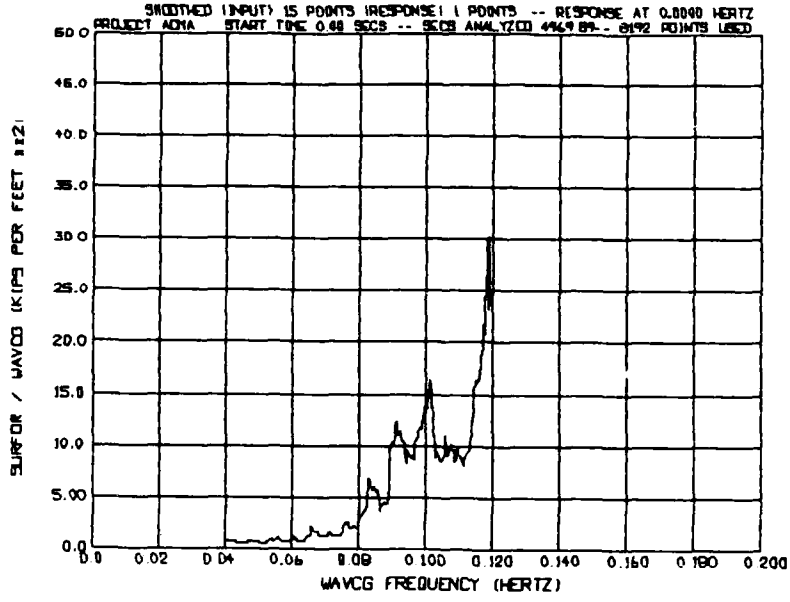

FIGURE 8 - QUADRATIC TRANSFER FUNCTION FOR FIRST 1.5 HOURS
85% LOADED CONDITION

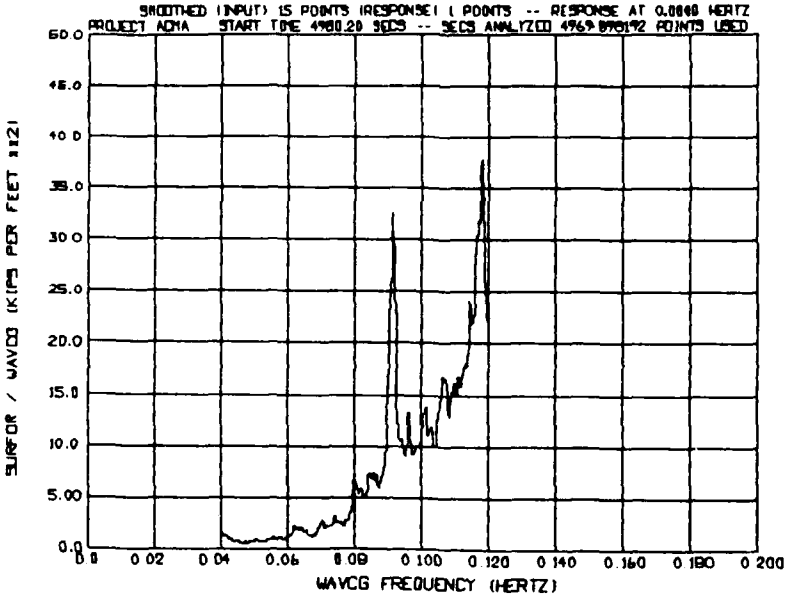

FIGURE 9 - QUADRATIC TRANSFER FUNCTION FOR LAST 1.5 HOURS
85% LOADED CONDITION

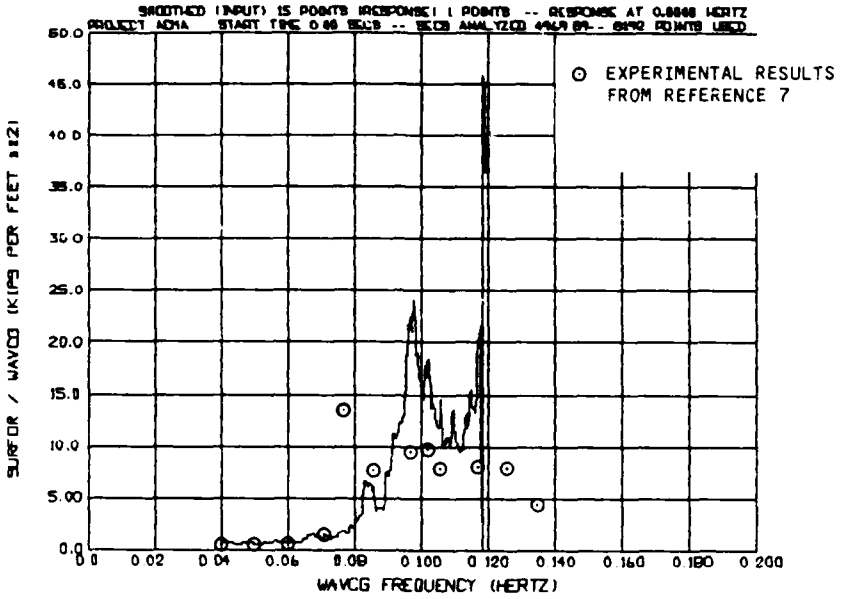

FIGURE 10 - QUADRATIC TRANSFER FUNCTION 1.5 HOUR TEST
100% LOADED

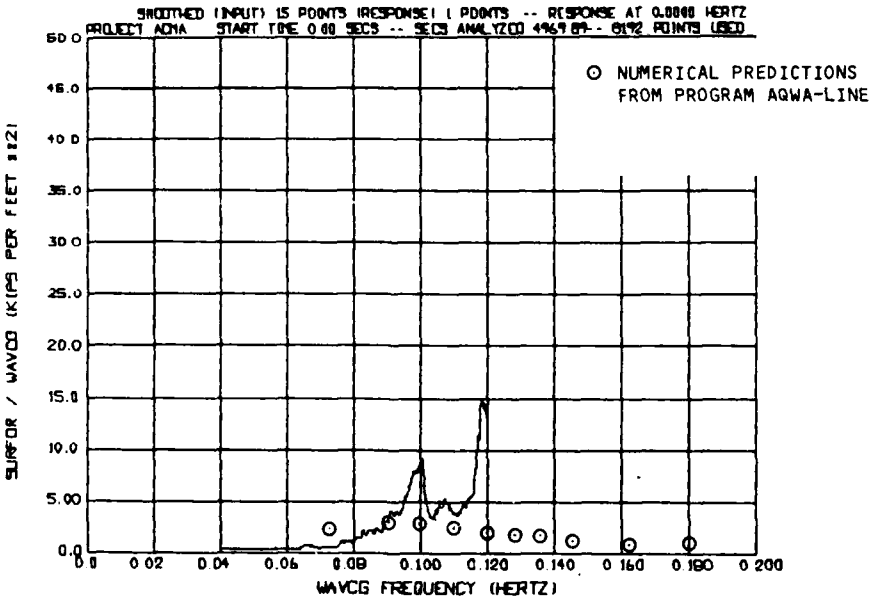

FIGURE 11 - QUADRATIC TRANSFER FUNCTION FOR 1.5 HOUR TEST
40% LOADED CONDITION

SESSION III
RESISTANCE AND FLOW

TECHNICAL COMMITTEE MEMBERS

Edwin P. Rood, Chairman	DTNSRDC
Edward M. Lewandowski	Stevens Inst.
Robert A. Kowalyshyn	Tracor Hydronautics
John R. Hill	U.S. Naval Academy
Frederick H. Ashcroft	Univ. of Michigan
John C. Kuhn	Offshore Technology Corp.

REPORT OF THE RESISTANCE AND FLOW COMMITTEE TO THE 21ST AMERICAN TOWING TANK CONFERENCE

Edwin P. Rood
Head
Special Systems Branch
David Taylor Naval Ship R&D Center
Bethesda, Maryland, 20084-5000

The three years since the last ATTC have been relatively quiet with respect to significant and major breakthroughs in the measurement and prediction of model and full scale resistance and flow. A notable exception is the intense, well-funded experimental test and evaluation work in support of competitive yacht design, especially for the 12-meter America's Cup contenders. Although it is known that the work has provided significant understanding of the consequences of complex hull geometry, and of the required quality control in measurements to effect reliable data, it is unlikely that the obtained information, regarded as proprietary for the indefinite future, will be available for open scrutiny.

This Committee notes that at least one comprehensive report was published to document comparisons of ship resistance obtained by calculation and by measurement. The report, by Shahshahan and Landweber (1986), describes measurements of total resistance, viscous resistance, pressure distribution, and boundary-layer velocities for the Wigley hull. The calculations of wave resistance were performed with and without the boundary layer and the wake. The authors point out that the data form the first complete set for the Wigley hull at zero trim and sinkage. It was observed that measured and calculated results show good agreement except at the stern, and that the inclusion of viscous effects made a marked improvement in the calculations.

That the past three years have not witnessed notable published towing tank studies such as systematic design variations or extensive comparison of analytic/experimental results is reflected in the paper contributions to this Committee for presentation at the ATTC. This Committee is, however, encouraged by the implied content of the papers and by the knowledge of work underway at the various towing tanks. The state of things is that towing tankery appears to be in an evolutionary period when new techniques, recently developed, are being applied to production measurements. It is anticipated that these methods will uncover the detailed flow around marine bodies, and the consequent effects on resistance, especially with respect to waves and wave production, that is required to close the gap between towing tank predictions and full scale observations.

This report focuses on technology development applied to systematic measurements at each of several of the leading towing tanks. It is anticipated by this Committee that the 22nd ATTC will be abundant with papers exposing new details of resistance and flow obtained as results of the current work.

UNIVERSITY OF MICHIGAN

The years 1983 - 1986 have marked a period of great change for the University of Michigan Ship Hydrodynamics Laboratory. The Laboratory is (by force of available funding as well as desire) moving from traditional areas of research and on standard type vessels (barges, tankers, etc.) into much more fundamental research. At the same time the tank facilities are undergoing extensive renovation.

In the area of flow, the Laboratory has been mainly concerned with methods of flow visualization in the global sense (flow over the entire body) rather than localized flow mapping and quantifying.

To assist in the observation of flow, it has acquired (in 1983) a Hydro Products Model TC-181 underwater video camera. This unit has remote control for focus, color balance, and the six-to-one macro/zoom lens. This unit was installed in a dedicated pod mount with side mounted lighting and remote control for both pan and tilt. It can be mounted on the towing carriage for continuous underwater observation during a test run, and has been on-line since the Fall of 1983.

The normal (and still preferred) method of observing hull flow uses yarn tufts as indicators, but in 1984 an effort was made to develop methods for indicating surface flow with oil

smears. It was found that the oil smear indicator was considerably messier than yarn tufts and also harder to document because it does not photograph well. There was also an attendant problem of oil slicks in the model basin that was not overcome. Although a good method for using oil smears as flow indicators was developed, technical reservations about the indicated flow persist because the oil dots are on the hull, deep in the boundary layer, and do not always indicate areas of possible flow problems in regions of moderate separation.

In 1985, coincident with the arrival of Terry Brockett as an Associate Professor in our Department, the Laboratory began experimenting with the use of fluorescent dyes as flow indicators on the surface of propeller blades. This technique is still under development, and a paper on progress to date is presented in the Resistance and Flow session.

The latest flow-measuring challenge is the use of lasers to define and analyze (quantitatively) the surface wake behind ship forms. This process is new to us and the techniques using off-the-shelf technology are being developed. By the 22nd ATTC, a report on both the technique and the results of our experiments should be available.

Progress has also been made on the resistance front. Although nothing has happened to smooth water tests, the Laboratory has been active in improving its ability to test models in waves. Over the past eighteen months a three degree of freedom dynamometer capable of handling models up to 6 meters in length has been designed and constructed for the Laboratory. This device allows the model to be free in heave and pitch, while applying a predefined, constant surge restraining force. The model can thus be towed with a constant force while surging under the carriage as it is influenced by wave action. This allows the performance of tests in waves (both resistance and propulsion) without the restraining spring of a rigid dynamometer set-up and will significantly improve the quality of powering predictions in waves.

Acceptance trials were run on the three degree of freedom dynamometer during the months of May and June of this year. The device performs well although it does need some refinement to make it more user friendly. From these trials it appears that new techniques will be required to make the most of this new equipment.

All in all, this has been an exciting three years for the Ship Hydromechanics Laboratory and the staff is looking forward to the next three years of improvement.

DAVID TAYLOR NAVAL SHIP R&D CENTER

Several new or improved design concepts have been tested in the towing tanks at DTNSRDC. Perhaps the most significant of these evaluations in terms of understanding results and predicting full scale performance for complex flows are for racing yacht design. Unfortunately those data are proprietary and the specific results are apparently not available for the foreseeable future. On the other hand, a considerable effort has been expended on evaluation of small waterplane area twin hull (SWATH) designs. Another design concept is the attachment of riblet material to the wetter surface of Olympic rowing shells. A short description of each of the above projects follows.

Yacht Design: Measurements have been made in the deep-water towing basin at DTNSRDC of the drag and side forces and yawing moments on models of sailing yachts. The models represented 12-meter yachts to a scale of 1:3. The towing apparatus consisted of 2 sets of force gages that could be preset at systematic variations in yaw angle. The models were also heeled systematically so that a matrix of force and moment data as functions of speed, heel, and yaw were obtained for each configuration. The measurements were made for five hull configurations including various afterbody and forebody combinations. In addition, several keel shapes were tested with three hull shapes. The data was used in parametric computer analyses of all points of sailing as decisions were made for the final geometry to build full scale.

SWATH: Seventeen SWATH models have now been tested either at or for DTNSRDC. Since it takes approximately twelve major hull form parameters to describe the form of a SWATH ship, this data base is small. Fortunately the thin-ship theory of wave making resistance applies, and there are codes by Chapman (1974) and Lin and Day (1974) that are sufficient analytic tools for early stage design. A comprehensive description of SWATH design considerations was published by Gore (1985). That paper indicates that information obtained from wake surveys is sorely missing, and that the absence of correlation model data renders the uncertainty in current allowances to be as much as 100 percent. Clearly there is much additional research needed for SWATH designs. The development state for SWATH is dependent on an evaluation of design propellers sufficiently positive to validate preliminary designs.

Shell Riblets: As part of a program described in Eilers et al. (1985) to apply riblet tape to rowing shells for the 1984 Olympics, an experiment was conducted to measure the drag reduction capabilities of riblet tape that had been developed by the 3M Corporation. Riblets are longitudinal surface groves that have been shown by Walsh (1982) and Walsh and Lindemann (1984) to give a turbulent flow skin friction coefficient reduction in air of about 8 percent for optimum riblet geometry. A single rowing shell was borrowed from the

potomac Boat Club, the outrigger oar-lock supports were removed, and the shell was ballasted with weight to represent a 180 lb person. The drag reduction was inferred by measuring the total drag with and without riblet tape applied to the hull. Preliminary analysis of the data indicate the following: The first and last sets of tests that were made without riblet tape repeated to within about 1 percent at maximum velocity. Measured total drag reduction of up to about 10 percent were recorded at the maximum velocity during the second set of data and the amount of reduction decreased thereafter during the subsequent three days of testing. Under corresponding conditions, the drag of the shell with tape never appeared to exceed the drag of the shell without tape. Possible causes for the loss of drag reduction during testing might be mechanical changes to the riblet surface, biofouling, loss of bubble adhesion, change in transition location, and surface chemistry changes. Further testing and analysis is anticipated to settle these questions.

There are some nontraditional uses for the towing tank in the near future. One example is the towing on Carriage II of a 6-ft diameter model of a submarine bow to be used to simulate three-dimensional torpedo launch hydrodynamics. This platform is expected to be available by the end of 1987.

Several new measurement techniques are currently being applied to extensive model evaluations. These include stereophotographic and laser beam measurement of surface wake details, and LDV measurements of viscous wakes and of propulsor effective wakes. Brief explanations of the techniques are given below; it is anticipated that detailed ship evaluation reports will be available by the 22nd ATTC.

Stereophotography: A stereophotogrammetric range has been installed in DTNSRDC's model towing basin, Carriage 1. Two 2.25-inch format metric cameras are mounted on the ceiling and spaced 30 feet apart along the longitudinal axis. Models are mounted behind the towing carriage beneath a slender girder to afford an unobstructed view of the near field Kelvin wake. Paper ships (computer card punchings) are distributed on the water to define the free surface in each photographic pair. The Naval Oceanographic Service (NOS) is semiautomatically digitizing the images to provide surface elevations with an accuracy of about 0.05 inch over an area 30 feet long by 20 feet wide. The Kelvin wakes of several ship models have been imaged and are presently being processed by NOS. The results will eventually be published. One shortcoming of the present method of seeding the water surface with paper chips is that the region of the ship model's viscous wake tends to be swept clear of chips by passage of the model; hence, surface elevations are not obtained in the wake along the ship centerline.

Wave Slope Meter: A new, non-intrusive instrument for measuring ship model Kelvin wake characteristics has been installed in DTNSRDC's model towing basin, adjacent to the stereophotogrammetric range, Carriage 1. A low power helium-neon (5 mW power) laser is located on the floor of the towing tank. Its light beam is passed through the surface and is projected as a spot on the ceiling of the building. The spot moves in response to perturbations of the surface slope, e.g., the Kelvin wake of a passing ship model. A video image processing system tracks the spot and generates analog signals linearly proportional to the local wave slope in two orthogonal coordinates. Frequency response of the system is higher than for traditional capacitance wire wave height probes, and wavelengths are resolved to 0.05 feet (10 Hertz). Software is presently being developed to analyze the measured two-dimensional wave-slope spectra, already obtained for several models and with ray tracing to reconstruct the distribution of the Kelvin wake virtual origins. The results will be presented in a forthcoming report.

Laser Doppler Velocimeter - Surface Ship Viscous Wake: The DTNSRDC strut-mounted 3-component LDV system has been described previously by Fry and Kim (1984). An extensive data base has been developed for three-dimensional flows in the wake of a typical high speed naval combatant, Model 5415. Mean flow and turbulence components have been measured in planes 6, 10, 16, 22, and 30 feet behind the 19-foot long model. Parameter variations include speed (20 and 30 knots, full scale) and propulsion (none, inward rotation and outward rotation). Details of the flow into the propeller plane have also been studied. Some of the more interesting aspects of the test results are changes of distribution in the developing turbulent wake for changed direction of propeller rotation and the presence of near surface velocity deficit regions arising from breaking (Kelvin) waves. Data from the 10-foot plane has been forwarded to the Naval Research Laboratory (NRL) to initialize their numerical model in order to predict the wake development downstream, free of any "optimization" of coefficients, to compare with the empirical data base. Reports documenting results are in preparation.

Laser Doppler Velocimeter - Submarine Effective Wake: DTNSRDC has made strides to incorporate the latest fiber optic technology in its Laser Doppler Velocimetry (LDV) measurement systems. Fiber optic links can conduct the laser beams to remote locations and deliver the beams to the

measurement point with a small "probe" weighing ounces. This contrasts with other implemented systems that use rigid optical platforms carrying a laser and large optics (together weighing hundreds of pounds). The instrumentation is already operating and has been matched with a measurement point traverse system. The entire unit is mounted in a small portion of a model ship hull and measures the flow about that hull. A specific application is underway to measure the inflow to a model submarine propulsor. The traverse system is mounted inside the model and the measurement point remotely varied circumferentially and radially to map the effective wake. While not the fluid velocity measurement answer in all cases, this instrumentation holds the promise of opening a whole new range of applications for the LDV technique.

As the performance requirements of ships and submarines become more stringent, there is a commensurate need to provide test and evaluation quality control sufficient to maintain measurement uncertainty within prescribed bounds. Special emphasis is being placed on implementation of measurement uncertainty procedures to ensure economically feasible and scientifically valid model tests. This renewed emphasis is in concert with guidelines being developed by ASME and is cooperation with other members of the ITTC. Although the concept of measurement error quantification is not new, the standardization of error definition and the description of "precision" and "bias" error are important steps toward a common naval architecture language.

The procedures to scale from towing tank data to predicted full scale performance are being improved. Indirect methods for drag characterization of rough surfaces are discussed in a paper by P.S. Granville, to follow in this Conference. A systematic analytic/experimental study of the proper manner to trip the flow on small appendages to duplicate, or at least to allow prediction of full scale results, is currently underway at DTNSRDC. The study will focus on appendage moments as well as forces. Accurate prediction of center of pressure is most important in submarine control surface design where powering for the controls is limited to size/weight. And, finally, an experiment is being prepared for the NASA National Transonic Facility to obtain boundary layer and resistance measurements on a flat plate with the flow at a Reynolds number of 10^9. This data will extend the current data base by two orders of magnitude, and will be useful for scaling resistance from model to full scale for large ships.

The development of numerical codes to fully exploit towing tank measurements involving ship wavemaking continued. The codes include both high order panel methods as well as sophisticated integral representations suitable for far field predictions. The intent is to use towing tank measurements first to validate the codes and second to provide input to the code that will, in turn, permit accurate evaluation of wavemaking resistance. Some of the work in this area is presented in a following paper by F. Noblesse.

OFFSHORE TECHNOLOGY CORPORATION

The offshore Technology Corporation (OTC) in Escondido, California, has been active in a great variety of types of tank testing throughout its 18 year history. While most of this work has been associated with the offshore oil industry and related fields, the Company has also been involved in many other areas of tank testing, including resistance and flow analyses. During the past few years OTC's participation in ship and yacht model testing has grown considerably, and with this growth there has been a steady development of associated equipment including dynamometers, flow measurement devices, and flow visualization apparatus. During the past year alone, for example, OTC has done over one million dollars worth of yacht testing for six syndicates in pursuit of the American's Cup.

Concerning flow measurement OTC has recently developed wake survey abilities with the addition of spherical, five hole pitot tubes. During the past year, these pitot tubes have been used to assist the United States Coast Guard in the development of a new icebreaker. There has also been interest lately in mapping pressure distribution over hulls and lifting surfaces, particularly concerning 12 meter testing. To this end, OTC has used arrays of flush-mounted pressure transducers to provide the needed information.

In addition to measuring flows, there has also been considerable activity in the area of flow visualization. One technique that has been very successful is the ejection of a very basic solution into the boundary layer of flow adjacent to a model that is painted with paint containing phenolphtalein. Large udders containing the basic compound (mounted above the model on the towing truss) feed ports in the side of the model as the model passes high speed underwater cameras. By introducing the basic solution to the flow adjacent to the paint containing phenolphthalein, the flow turns purple, thereby making the downstream flow characteristics visible. Tufted flow visualization has also been used from time to time, particularly for forebody flow visualization and flow visualization in propeller regions. For example, the use of small tufts on horned rudders recently revealed the importance of minimizing the gap between the rudder and the horn, as it was witnessed that the tufts were being "sucked" through this gap, decreasing both the effectiveness of the rudder as a lifting surface and the propulsive efficiency of the vessel.

Concerning resistance testing, OTC has developed several different types of dynamometers over the past couple of years. To accom-

modate the extensive amount of yacht testing that has been done during the past year or so, a yacht dynamometer capable of handling one-third scale 12 meters has been developed, and the towing truss in the deep Water Towing and Seakeeping Basin has been rebuilt (of OTC's three physical modeling laboratories, the Deep Water Towing and Seakeeping Basin is usually used for resistance and flow studies). There have have also been several SWATH test programs of late, and a SWATH dynamometer has been developed for these applications. In addition, a heavy duty ship dynamometer has been developed for both resistance and propulsion testing and captive maneuvering testing.

Recent involvement with a new and somewhat revolutionary planing hull design for use in ferrying people to and from Catalina Island (off Los Angeles) has led to the current development of a planing hull dynamometer. In addition to the aforementioned "towing" dynamometers, OTC has also developed a torque and thrust dynamometer for use in propulsion experiments.

Indeed, the past few years have been very busy ones for OTC concerning resistance and flow analysis. In some ways the developments made during these years represent new areas for OTC. In other ways they have simply been new applications of the same technology that has been used for years to evaluate the performance and feasibility of various offshore structures and vehicles. At any rate, the development is far from complete, and what has already been done remains to be refined further.

REFERENCES

Chapman, R.B., "Hydrodynamic Drag of Semisubmerged Ships," Journal of Basic Engineering Transactions, ASME, Vol. 94 (1972).

Eilers, R.C., C.A. Koper, J.D. McLean, and D.W. Coder, "An Application of Riblets for Turbulent-Skin-Friction Reduction," Twelfth Annual Symposium on Sailing, AIAA, and University of Washington, Seattle, Washington (Sep 1985).

Fry, D.J. and Y.H. Kim, "Bow Flow in Surface Ships," ONR Conference on Naval Hydrodynamics, Hamburg, FRG (Sep 1984).

Gore, G.L., "Modern Ships & Craft, Chapter III: SWATH Ships," Naval Engineering Journal (1985).

Lin, W.-C. and W.G. Day, "The Still-water Resistance and Propulsion Characteristics of Small Waterplane Area Twin-Hull (SWATH) Ships," AIAA/SNAME Advanced Marine Vehicles Conference, San Diego, California (1979).

Shahshahan, A. and L. Landweber, "Interactions Between Wavemaking and the Boundary Layer and Wake of a Ship Model," IIHR Report No. 302 (1986).

Walsh, M.J., "Turbulent Boundary Layer Drag Reduction Using Riblets," AIAA 20th Aerospace Sciences Meeting, Orlando, Florida (Jan 1982).

Walsh, M.J. and A.M. Lindemann, "Optimization and Application of Riblets for Turbulent drag Reduction," AIAA 22nd Aerospace Sciences Meeting, Reno, Nevada (Jan 1984).

THREE INDIRECT METHODS FOR THE DRAG CHARACTERIZATION OF ARBITRARILY ROUGH SURFACES ON FLAT PLATES

Paul S. Granville
David Taylor Naval Ship R&D Center
Code 1540.2
Bethesda, MD 20084-5000

ABSTRACT

Three indirect methods for characterizing the drag of an arbitrarily rough surface surface on a flat plate are derived or rederived from the similarity laws of turbulent shear flows. These are: (1) the well-known procedure using displacement thickness; (2) the probably not so well-known procedure using total drag and; (3) a proposed procedure using only the free-stream velocity and a local shear stress. The classical indirect procedure for pipe flow is also derived to show a commonality with the flat-plate methods.

NOTATION

A	Slope of logarithmic velocity law, Eq. (4)
a	Constant in Eq. (49)
a	Constant in Eq. (55)
B_1	Intercept of logarithmic velocity law
$B_{1,s}$	Value for B_1 for smooth surfaces
B_1'	Derivative of B_1, $B_1' = \frac{dB_1}{d(\ln k^*)} = \frac{d(\Delta B)}{d(\ln k^*)}$
B_2	Outer-law intercept, Eq. (18)
B_r	Intercept of logarithmic velocity law in relative-roughness mode, Eq. (5)
$\hat{B}_r$	Value of B_r for fully rough regime
b	Constant in Eq. (49)
b	Constant in Eq. (55)
C_F	Coefficient of total drag, Eq. (33)
c_f	Coefficient of local skin friction, $c_f = 2\tau_w/\rho U^2$
D	Total drag
f	Fanning friction factor for pipe flow, Eq. (63)
I_1, I_2, I_3	Outer-law integrals, Eqs. (12), (13), (14)
k	Primary roughness length scale
k_1, k_2, ...	Other roughness length scales
k^*	Roughness Reynolds number, $k^* = u_\tau k/\nu$
L	Length of flat plate
q	Wake modification function, Eq. (20)
R_D	Pipe Reynolds number, $R_D = 2Vr/\nu$
R_L	Length Reynolds number, $R_L = UL/\nu$
R_{δ^*}	Displacement thickness Reynolds number, $R_{\delta^*} = U\delta^*/\nu$
r	Inner radius of pipe
T	Texture of roughness, $T = \frac{k}{k_1}, \frac{k_1}{k_2}, \cdots$
U	Free-stream velocity
u	Streamwise velocity in shear layer
u_τ	Shear velocity, $u_\tau = \sqrt{\tau_w/\rho}$
V	Average velocity in pipe, Eq. (58)
w	Wake function, Eq. (19)
x	Distance from leading edge of flat plate
y	Normal distance from wall
y^*	Nondimensional y, $y^* = u_\tau y/\nu$
ΔB	Drag characterization
δ	Thickness of boundary layer
η	Nondimensional δ, $\eta = u_\tau \delta/\nu$
Θ	Momentum thickness
ν	Kinematic viscosity of fluid
ρ	Density of fluid
σ	Shear-stress coefficient, $\sigma = U/u_\tau$
τ_w	Wall shear stress

SUBSCRIPTS

L	Conditions at trailing edge of flat plate
r	Rough condition
s	Smooth condition

1. INTRODUCTION

The similarity laws of turbulent shear flows provide a drag characterization for any specified arbitrarily rough surface; regular or irregular in its geometry. Once known, the characterization may be then used to determine the drag of any body configuration covered with the specified roughness by means of a boundary-layer method. Such a drag characterization may be obtained experimentally by probing the velocity profile of the logarithmic similarity law close to the specified rough wall in a flow facility. This procedure may be termed the direct method.

However, it may be simpler or more convenient to apply an indirect determination which involves more readily attainable and

usually less costly measurements. The first reported indirect method may be attributed to Nikuradse[2] who used an indirect as well as a direct method in analyzing his classical pipe experiments on sand-grain roughness. Both the indirect and direct methods showed excellent agreement. This indirect determination used an average pipe velocity instead of a measured velocity profile required for the direct method. The value of the average velocity was easily attained from the rate of mass flow through the pipe.

Later on, indirect methods were devised for rough surfaces on flat plates (in zero longitudinal pressure gradients). The most prominent seems to be that of Hama[3] who used the wall shear stress and the displacement thickness of the whole velocity profile at a station instead of the velocity close to the wall to determine the characterization. Another innovation by Hama was to use measured values for the smooth surface which were appropriately subtracted from measured values for the rough surface. This procedure tended to minimize experimental errors due to the flow facility.

Another indirect method[4], which may not be too well known, involves measurement of the total drag and the speed of a towed rough flat plate in a basin or the total drag of a flat plate immersed in a uniform flow of a given velocity. The wall shear stress at the trailing edge is related to the total drag by a boundary layer similarity-law analysis.

More recently, experiments by Karlsson[5] using a floating element to measure the shear stress at a station on a rough flat plate in a uniform flow of given velocity seem to indicate the necessity of another indirect method. Most of the experiments involved no survey of the velocity within the boundary layer. An appropriate indirect method is now proposed which will be developed further on.

There is an alternate indirect method for rough surfaces, using rotating disks[6] instead of flat plates, which has already been adequately presented.

As a start, the elements of the similarity laws for rough surfaces are stated. Then all three indirect methods for flat plates are derived in a similar manner in order to show the common basis for the methods. It is emphasized that the characterization for the specified rough surface is obtained by comparison with appropriate measurements for a smooth surface in the same facility in order to minimize possible experimental error. It is not the purpose of this paper to investigate the relative merits of the various methods. These may involve non-hydrodynamic considerations such as availability of facilities, personnel, funding, et cetera.

2. VELOCITY SIMILARITY LAWS

2.1 Inner Law or Law of the Wall

In the close proximity of an arbitrarily rough surface defined by a sufficient number of length factors, k, k_1, k_2, ... the inner similarity law or law of the wall for turbulent shear flows may be stated in the Reynolds-number mode as

$$\frac{u}{u_\tau} = f\left[y^*, k^*, T\right] \tag{1}$$

or in the relative-roughness mode as

$$\frac{u}{u_\tau} = f\left[\frac{y}{k}, k^*, T\right] \tag{2}$$

Here $y^* = u_\tau y/\nu$, $k^* = u_\tau k/\nu$ (roughness Reynolds number), $u_\tau = \sqrt{\tau_w/\rho}$ (shear velocity) and $T = k/k_1$, k_1/k_2,... (roughness texture). Also, u is the stream-wise mean-velocity component, τ_w is the wall shear stress, ρ is the fluid density, ν is the fluid kinematic viscosity and y is the normal distance away from the rough wall (the zero position of y for $u=0$ may vary slightly with roughness geometry).

2.2 Outer Law or Velocity-Defect Law

For the outer part of the turbulent shear layer, the similarity law is stated as a velocity defect which is solely a function of relative position

$$\frac{U-u}{u_\tau} = f\left[\frac{y}{\delta}\right] \tag{3}$$

Here U is the streamwise velocity at the outer edge of a shear layer of thickness δ. The outer law has been experimentally shown to be independent of roughness. There is, however, an indirect dependence on roughness through shear velocity u_τ which varies with roughness. It should be noted that the outer law will vary at the low Reynolds number following transition from laminar to turbulent flow for either smooth or rough surfaces.

2.3 Logarithmic Velocity Laws and Roughness Characterizations

If the inner and outer laws are considered aplicable in a common overlapping region, it is easy to show that the analytical consequences are logarithmic relationships.
For the inner law in the Reynolds-number mode

$$\frac{u}{u_\tau} = A \ln y^* + B_1\left[k^*, T\right] \tag{4}$$

or in the relative-roughness mode as

$$\frac{u}{u_\tau} = A \ln \frac{y}{k} + B_r\left[k^*, T\right] \tag{5}$$

B_1 and B_r are related by

$$B_r = B_1 + A \ln k^* \tag{6}$$

For the usual roughness regimes (1) hydraulically smooth: $B_1 = \text{constant} = B_{1,s}$, (2) intermediate roughness: B_1 and B_r both vary with k^* and T, (3) fully rough: $B_r = \hat{B}_r$

is constant with respect to k^* and is only a function of T.

Either $B_1[k^*, T]$ or $B_r[k^*,T]$ may be termed a similarity-law roughness drag characterization. Another form of B_1 arises when the value for a smooth surface $B_{1,s}$ is subtracted to give

$$\Delta B\left[k^*,T\right] = B_1\left[k^*,T\right] - B_{1,s} \qquad (7)$$

ΔB as defined is always negative in value for rough surfaces. Nikuradse used the B_r characterization while Hama preferred the ΔB (actually $-\Delta B$) characterization although with a different notation.

The outer law in turn develops a logarithmic relation in the overlapping region:

$$\frac{U-u}{u_\tau} = -A \ln \frac{y}{\delta} + B_2 \qquad (8)$$

B_2 is a velocity-defect factor which does not vary with roughness but does vary with streamwise pressure gradient. $B_2/2A$ is sometimes called the Coles Wake Factor and given a symbol. It should be noted that B_2 also varies at the low Reynolds number following transition from laminar to turbulent flow for either smooth or rough surfaces.

A direct similarity-law drag characterization of a roughness with given texture T requires the determination of B_1, B_r, or ΔB as a function of roughness Reynolds number k^* from measurements of wall shear stress τ_w and velocity u in the region where the logarithmic inner law holds, i.e. Equation (4) or (5). For a thin shear layer this may not be very feasible. Hence an indirect method may be more practical.

2.4 Logarithmic Laws of Friction

The addition of the overlapping inner logarithmic relation, Equation (4) or (5), to the outer logarithmic relation, Equation (8), results in the logarithmic law of friction which in the Reynolds-number mode is

$$\sigma = \frac{U}{u_\tau} = A \ln \eta + B_1\left[k^*,T\right] + B_2 \qquad (10)$$

where $\eta = u_\tau \delta / \nu$

and in the relative-roughness mode is

$$\sigma = \frac{U}{u_\tau} = A \ln \frac{\delta}{k} + B_r\left[k^*,T\right] + B_2 \qquad (11)$$

The quantity σ is a convenient local coefficient of skin friction given from the definitions by $\sigma = (\tau_w/\rho U^2)^{-1/2}$

The logarithmic laws of friction will be shown to be the basis of indirect roughness drag characterizations.

3. EVALUATION OF OUTER-LAW INTEGRALS

Subsequent analyses require the evaluation of outer-law integrals I_1, I_2, and I_3, where

$$I_1 = \int_0^1 \left(\frac{U-u}{u_\tau}\right) d\left(\frac{y}{\delta}\right) \qquad (12)$$

$$I_2 = \int_0^1 \left(\frac{U-u}{u_\tau}\right)^2 d\left(\frac{y}{\delta}\right) \qquad (13)$$

and

$$I_3 = \int_0^1 \left(\frac{U-u}{u_\tau}\right)\left(\frac{y}{\delta}\right) d\left(\frac{y}{\delta}\right) \qquad (14)$$

I_1, I_2, and I_3, are constants if the outer law is considered a function of only y/δ right up to the wall (y=0).

If the logarithmic relation, Equation (8), is considered applicable also to the wall, then for the whole boundary layer (y=0 to y=δ), the outer law is given by

$$\frac{U-u}{u_\tau} = -A \ln \frac{y}{\delta} + B_2 - B_2 \frac{w}{2} - A q \qquad (15)$$

where w is the Coles wake function and q is the wake modification function.

From Equation (15) the outer-law integrals become

$$I_1 = A + B_2 - B_2 \int_0^1 \frac{w}{2} d\left(\frac{y}{\delta}\right) - A \int_0^1 q\, d\left(\frac{y}{\delta}\right) \qquad (16)$$

$$I_2 = A^2\left[2 + 2\int_0^1 q \ln \frac{y}{\delta} d\left(\frac{y}{\delta}\right) + \int_0^1 q^2 d\left(\frac{y}{\delta}\right)\right] + 2AB_2\left[1 + \int_0^1 \left(\frac{w}{2} \ln \frac{y}{\delta} + \frac{w}{2} q - q\right) d\left(\frac{y}{\delta}\right)\right] + B_2^2\left[1 - 2\int_0^1 \frac{w}{2} d\left(\frac{y}{\delta}\right) + \int_0^1 \left(\frac{w}{2}\right)^2 d\left(\frac{y}{\delta}\right)\right] \qquad (17)$$

and

$$I_3 = A\left[\frac{1}{4} - \int_0^1 q \left(\frac{y}{\delta}\right) d\left(\frac{y}{\delta}\right)\right] + B_2\left[\frac{1}{2} - \int_0^1 \frac{w}{2}\left(\frac{y}{\delta}\right) d\left(\frac{y}{\delta}\right)\right] \qquad (18)$$

Polynomial representations[8] for the Coles wake function and the wake modification function are respectively

$$\frac{w}{2} = 3\left(\frac{y}{\delta}\right)^2 - 2\left(\frac{y}{\delta}\right)^3 \qquad (19)$$

and

$$q = \left(\frac{y}{\delta}\right)^2 - \left(\frac{y}{\delta}\right)^3 \qquad (20)$$

Consequently

$$I_1 = \frac{11}{12} A + \frac{1}{2} B_2 \qquad (21)$$

$$I_2 = \frac{4819}{2520} A^2 + \frac{639}{420} A B_2 + \frac{13}{35} B_2^2 \qquad (22)$$

and

$$I_3 = \frac{2}{10} A + \frac{3}{20} B_2 \qquad (23)$$

4. LOCAL METHOD WITH DISPLACEMENT THICKNESS

Some time ago, Hama[3] developed a method to characterize the drag at a station of a specified rough surface by measuring the velocity profile of the whole boundary layer to obtain the displacement thickness. In this regard the Hama method may be considered now as an indirect method in contrast to the direct method which only measures the velocity profile close to the wall in the logarithmic region.

The displacement thickness and the associated wall shear stress are used to determine the drag characterization as follows. The logarithmic law of friction, Equation (10), is rewritten as

$$\sigma = A \ln\left[\left(\frac{U\delta^*}{\nu}\right)\left(\frac{\delta}{\delta^*}\right)\frac{1}{\sigma}\right] + B_1 + B_2 \qquad (24)$$

where δ^* = displacement thickness.

By definition

$$\frac{\delta^*}{\delta} = \int_0^1 \left(1 - \frac{u}{U}\right) d\left(\frac{y}{\delta}\right) \qquad (25)$$

or

$$\frac{\delta^*}{\delta} = \frac{1}{\sigma}\int_0^1 \left(\frac{U-u}{u_\tau}\right) d\left(\frac{y}{\delta}\right) \qquad (26)$$

and from Equation (12)

$$\frac{\delta^*}{\delta} = \frac{I_1}{\sigma} \qquad (27)$$

Finally, for a rough surface

$$\sigma = \sqrt{\frac{2}{c_f}} = A \ln R_{\delta^*} + B_{1,s} + \Delta B + B_2 - A \ln I_1 \qquad (28)$$

where the coefficient of local skin friction = $c_f = 2\tau_w/\rho U^2$

and the displacement-thickness Reynolds number = $R_{\delta^*} = U\delta^*/\nu$.

For a smooth surface where $\Delta B = 0$

$$\sqrt{\frac{2}{c_f}} = A \ln R_{\delta^*} + B_{1,s} + B_2 - A \ln I_1 \qquad (29)$$

For sufficiently high Reynolds numbers and zero pressure gradient the value of B_2 is the same for smooth or rough surfaces.

At the same value of R_{δ^*}, for smooth and rough surfaces, the drag characterization is given by the difference between Equations (28) and (29) so that

$$\Delta B = \left(\sqrt{\frac{2}{c_f}}\right)_r - \left(\sqrt{\frac{2}{c_f}}\right)_s \qquad (30)$$

where the subscripts r and s refer to appropriate values of the rough and smooth surface. The value of k^* associated with ΔB and R_{δ^*} is

$$k^* = R_{\delta^*}\left(\sqrt{\frac{c_f}{2}}\right)_r \left(\frac{k}{\delta^*}\right) \qquad (31)$$

By using measured values of the smooth surface, the experimental error in determining ΔB tends to be minimized.

A sample plot of $\sqrt{2/c_f}$ against log R_{δ^*} is shown in Figure I for some roughness data from Reference 9 in order to illustrate the method.

5. OVERALL METHOD

The total drag of flat plates uniformly covered with a specified roughness has been measured while being towed at various speeds in water-filled basins. Similar measurements have been made with a stationary flat plate immersed in a uniform flow. Such measurements have been successfully converted to the drag characterization at the trailing edge; thus representing a second indirect method.

An analysis which uses the Reynolds-number mode instead of the relative-roughness mode of Reference 4 proceeds as follows. The drag D of one side of a flat plate of length L and of unit breadth is

$$D = \int_0^L \tau_w \, dx \qquad (32)$$

where x is the streamwise distance from the leading edge. The drag coefficient per unit breadth C_F for both sides is given by

$$C_F = \frac{2D}{\rho U^2 L} \qquad (33)$$

where U is the towing speed.

The von Kármán momentum equation for a two-dimensional boundary layer in a zero pressure gradient on a flat plate is

$$\frac{d\theta}{dx} = \frac{\tau_w}{\rho U^2} = \frac{1}{\sigma^2} \qquad (34)$$

where the momentum thickness $\theta = \int_0^\delta \left(1 - \frac{u}{U}\right)\frac{u}{U}\, dy$

After integrating from x = 0 to x = L,

$$C_F = \frac{2\theta_L}{L} = \frac{2R_{\theta,L}}{R_L} \qquad (35)$$

in terms of the momentum-thickness Reynolds number, $R_\theta = U\theta/\nu$ and the length Reynolds number, $R_L = UL/\nu$. The subscript L refers to conditions at the trailing edge. x=L. Integrating Equation (34) results in

$$R_L = \int_0^{R_{\theta,L}} \sigma^2 \, dR_\theta = \sigma_L^2 R_{\theta,L} - 2\int_0^{\sigma_L} R_\theta \, \sigma \, d\sigma \qquad (36)$$

since $R_\theta = 0$ at $x = 0$.
Now from definitions

$$R_\theta = \eta \left(I_1 - \frac{I_2}{\sigma} \right) \tag{37}$$

Since, from Equation (10),

$$\eta = \exp\left(\frac{\sigma - B_1 - B_2}{A} \right) \tag{38}$$

repeated integrations by parts produce

$$\int_0^{\sigma_L} R_\theta \sigma \, d\sigma = A I_1 \eta_L \sigma_L \left[1 - \left(A + \frac{I_2}{I_1} + B_1' \right) \frac{1}{\sigma_L} + \cdots \right] \tag{39}$$

where $B_1' = \dfrac{dB_1}{d(\ln k^*)} = \dfrac{d(\Delta B)}{d(\ln k^*)}$ at $x = L$.
For smooth surfaces $B_1' = 0$ and for fully developed roughness $B_1' = -A$ from Equation (6). Finally from Equations (36) and (39)

$$R_L = I_1 \sigma_L^2 \eta_L \left[1 - \frac{2A + (I_2/I_1)}{\sigma_L} + \frac{2A(A + \frac{I_2}{I_1} + B_1')}{\sigma_L^2} \right] \tag{40}$$

Substituting for η_L from Equation (38) and taking the logarithm results in

$$\ln R_L = \frac{\sigma_L}{A} + \ln \sigma_L^2 - \frac{B_1}{A} - \frac{B_2}{A} + \ln I_1 - \frac{2A + (I_2/I_1)}{\sigma_L} + \cdots \tag{41}$$

In order to substitute the drag coefficient C_F for the local skin-friction coefficient at the trailing edge, σ_L, the procedure is as follows:

Equations (35) and (36) give

$$\frac{1}{\sigma_L^2} = \frac{C_F}{2} \left(1 - \frac{2 \int_0^{\sigma_L} R_\theta \sigma \, d\sigma}{\sigma_L^2 R_{\theta,L}} \right) \tag{42}$$

Substituting for $R_{\theta,L}$ and $\int_0^{\sigma_L} R_\theta \sigma \, d\sigma$ from Equations (37) and (38) results in

$$\frac{1}{\sigma_L^2} = \frac{C_F}{2} \left[1 - \frac{2A}{\sigma_L} + \frac{2A(A + B_1')}{\sigma_L^2} + \cdots \right] \tag{43}$$

Through reiteration σ_L is replaced by C_F within the brackets so that

$$\frac{1}{\sigma_L^2} = \frac{C_F}{2} \left[1 - 2A \left(\frac{C_F}{2} \right)^{\frac{1}{2}} + 2A \left(2A + B_1' \right) \left(\frac{C_F}{2} \right) + \cdots \right] \tag{44}$$

and by the binomial theorem

$$\frac{1}{\sigma_L} = \sqrt{\frac{C_F}{2}} \left[1 - A \left(\frac{C_F}{2} \right)^{\frac{1}{2}} + A \left(\frac{3}{2} A + B_1' \right) \left(\frac{C_F}{2} \right) + \cdots \right] \tag{45}$$

By inversion

$$\sigma_L = \sqrt{\frac{2}{C_F}} \left[1 + A \left(\frac{C_F}{2} \right)^{\frac{1}{2}} - A \left(\frac{A}{2} + B_1' \right) \left(\frac{C_F}{2} \right) + \cdots \right] \tag{46}$$

Substituting the expressions for $\frac{1}{\sigma_L^2}$, $\frac{1}{\sigma_L}$ and σ_L into Equation (41)

and truncating, result in

$$\sqrt{\frac{2}{C_F}} = A \ln (R_L C_F) + B_1 + B_2 - A - A \ln(2 I_1) + A \left(\frac{A}{2} + \frac{I_2}{I_1} + B_1' \right) \sqrt{\frac{C_F}{2}} \tag{47}$$

For a smooth surface, then,

$$\sqrt{\frac{2}{C_F}} = A \ln (R_L C_F) + B_{1,S} + B_2 - A - A \ln(2 I_1) + A \left(\frac{A}{2} + \frac{I_2}{I_1} \right) \sqrt{\frac{C_F}{2}} \tag{48}$$

This equation has the same form as the well-known Karman-Schoenherr formula[10] for the drag of smooth flat plates (which was originally derived by a less rigorous method)

$$\sqrt{\frac{2}{C_F}} = \alpha \ln (R_L C_F) + \beta \tag{49}$$

where the constants α and β have been adjusted to accommodate the $\sqrt{C_F}$ - term on the right of Equation (48).

The indirect method of drag characterization for a station at the trailing edge is obtained by subtracting the smooth Equation (48) from the rough Equation (47) at the same value of $R_L C_F$ so that

$$\Delta B = \left(\sqrt{\frac{2}{C_F}} \right)_r - \left(\sqrt{\frac{2}{C_F}} \right)_s - A \left(\frac{A}{2} + \frac{I_2}{I_1} \right) \left[\left(\sqrt{\frac{C_F}{2}} \right)_r - \left(\sqrt{\frac{C_F}{2}} \right)_s \right] - A B_1' \left(\sqrt{\frac{C_F}{2}} \right)_r \tag{50}$$

The associated value of k^* for the given value of $R_L C_F$ is then

$$k^* = \left(\frac{R_L C_F}{2} \right) \left(\frac{k}{L} \right) \left(\sqrt{\frac{2}{C_F}} \right)_r \left[1 - A \left(\frac{C_F}{2} \right)_r^{\frac{1}{2}} + A \left(\frac{3}{2} A + B_1' \right) \left(\frac{C_F}{2} \right)_r \right] \tag{51}$$

A sample plot of $\sqrt{2/C_F}$ against $\log(R_L C_F)$ is shown in Figure 2 for for some roughness data from Reference 11.

6. LOCAL METHOD WITHOUT DISPLACEMENT THICKNESS

Karlsson[5] mounted a flat plate with a specified rough surface in a uniform flow and measured the wall shear stress at a station by means of a floating element. In most cases no survey was undertaken of the velocity field of the boundary layer over the floating element. Only the stream velocity and shear stress were measured. Hence the Hama method which involves a measured boundary-layer displacement thickness is not applicable. However, it is still possible to obtain a drag characterization using only the free-stream velocity and shear stress by the following method which is now proposed.

The boundary layer develops from some ori-

gin for a distance x at the location of the floating element. Equation (41) is rewritten as

$$\ln R_x = \frac{\sigma}{A} + \ln \sigma^2 - \frac{B_1}{A} - \frac{B_2}{A} + \ln I_1 - \frac{2A+(I_2/I_1)}{\sigma} + \cdots \quad (52)$$

where $R_x = Ux/\nu$.
With $\sigma = \sqrt{2/c_f}$, Equation (52) becomes

$$\sqrt{\frac{2}{c_f}} = A \ln\left(R_x c_f\right) + B_1 + B_2 - A\ln(2 I_1) + A\left(A + \frac{I_2}{I_1}\right)\sqrt{\frac{c_f}{2}} + \cdots \quad (53)$$

For a smooth surface, then

$$\sqrt{\frac{2}{c_f}} = A \ln\left(R_x c_f\right) + B_{1,s} + B_2 - A\ln(2 I_1) + A\left(A + \frac{I_2}{I_1}\right)\sqrt{\frac{c_f}{2}} + \cdots \quad (54)$$

This equation has the same form of the well-known von Kármán formula[12]

$$\sqrt{\frac{2}{c_f}} = a \ln\left(R_x c_f\right) + b \quad (55)$$

where the constants a and b have absorbed the terms eliminated by truncation. Subtracting Equation (54) from Equation (53) at the same value of $R_x c_f$ results in an indirect method for a drag characterization such that

$$\Delta B = \left(\sqrt{\frac{2}{c_f}}\right)_r - \left(\sqrt{\frac{2}{c_f}}\right)_s - A\left(A + \frac{I_2}{I_1}\right)\left[\left(\sqrt{\frac{c_f}{2}}\right)_r - \left(\sqrt{\frac{c_f}{2}}\right)_s\right] \quad (56)$$

The associated k^* is given by

$$k^* = \left(R_x c_f\right)\left(\frac{k}{2x}\right)\left(\sqrt{\frac{2}{c_f}}\right)_r \quad (57)$$

A sample plot of $\sqrt{2/c_f}$ against log $(R_x c_f)$ is shown in Figure 3 for some roughness data from Reference 5.

7. INDIRECT METHOD FOR PIPES

In order to show a commonality with the methodology of flat plates, the indirect method is now derived for circular pipes coated inside with a specified rough surface. The average velocity of the flow through the pipe is used instead of a velocity survey across the pipe. The average velocity V across a circular pipe is given by

$$\pi r^2 V = 2\pi \int_0^r u\,(r-y)\,dy \quad (58)$$

where r is the inside radius of the pipe. For fully-developed pipe flow, then

$$\frac{V}{u_\tau} = 2 \int_0^1 \frac{u}{u_\tau}\left(1 - \frac{y}{\delta}\right) d\left(\frac{y}{\delta}\right) \quad (59)$$

where $r = \delta$.

Using the outer law, Equation (3), results in

$$\frac{V}{u_\tau} = \sigma - 2\int_0^1 \left(\frac{U-u}{u_\tau}\right) d\left(\frac{y}{\delta}\right) + 2\int_0^1 \left(\frac{U-u}{u_\tau}\right)\left(\frac{y}{\delta}\right) d\left(\frac{y}{\delta}\right) \quad (60)$$

or

$$\frac{V}{u_\tau} = \sigma - 2 I_1 + 2 I_3 \quad (61)$$

Substituting for σ from Equation (10) yields

$$\frac{V}{u_\tau} = A \ln \eta + B_1 + B_2 - 2 I_1 + 2 I_3 \quad (62)$$

The Fanning friction factor f is defined as

$$f = \frac{2\tau_w}{\rho V^2} \quad (63)$$

and pipe Reynolds number R_D as

$$R_D = \frac{2Vr}{\nu} \quad (64)$$

Then

$$\frac{V}{u_\tau} = \sqrt{\frac{2}{f}} \quad (65)$$

and

$$\eta = R_D\sqrt{f} \,/\, \sqrt{8} \quad (66)$$

Equation (62) becomes

$$\sqrt{\frac{2}{f}} = A \ln\left(R_D\sqrt{f}\right) + B_1 + B_2 - A\ln\sqrt{8} - 2\left(I_1 - I_3\right) \quad (67)$$

For a smooth surface then

$$\sqrt{\frac{2}{f}} = A \ln\left(R_D\sqrt{f}\right) + B_{1,s} + B_2 - A\ln\sqrt{8} - 2\left(I_1 - I_3\right) \quad (68)$$

This is the same form as the well-known Prandtl-Karman equation for flow through a smooth pipe. For fully developed pipe flow the value of B_2 is the same for smooth or rough surfaces.

At the same value of $R_D\sqrt{f}$ then

$$\Delta B = \left(\sqrt{\frac{2}{f}}\right)_r - \left(\sqrt{\frac{2}{f}}\right)_s \quad (69)$$

The associated k^* is given by

$$k^* = \frac{\sqrt{2}}{2}\left(R_D\sqrt{f}\right)\left(\frac{k}{2r}\right) \quad (70)$$

The evaluation of ΔB by subtracting smooth results from rough results was originally advocated by Robertson et al.[13] A recent paper by Grigson[14] gives an unnecessarily more complicated procedure for determining ΔB.

A sample plot of $\sqrt{2/f}$ against log $R_D\sqrt{f}$ is shown in Figure 4 for some roughness data from Reference 2.

8. NUMERICAL VALUES

Numerical values are now supplied for the formulas which have need of them.

For values of $A = 2.5$ and $B_2 = 2.4$ for flat plates, it follows from Equations (21) and (22) that $I_1 = 3.49$ and $I_2 = 23.2$. These values give total drags agreeing with the Schoenherr line.

Consequently for the indirect method involving total drag, Equations (50) and (51) become

$$\Delta B = \left(\sqrt{\frac{2}{C_f}}\right)_r - \left(\sqrt{\frac{2}{C_f}}\right)_s - 19.7\left[\left(\sqrt{\frac{C_f}{2}}\right)_r - \left(\sqrt{\frac{C_f}{2}}\right)_s\right] - 2.5\,B_1'\left(\sqrt{\frac{C_f}{2}}\right)_r \tag{71}$$

and

$$k^* = \left(\frac{R_L C_f}{2}\right)\left(\frac{k}{L}\right)\left(\sqrt{\frac{2}{C_f}}\right)_r \times \left[1 - 2.5\left(\frac{C_f}{2}\right)^{\frac{1}{2}} + 2.5\left(3.75 + B_1'\right)\left(\frac{C_f}{2}\right)\right]^{-1} \tag{72}$$

It should be noted that for the fully rough regime, Equation (6) with B_r constant, $B_1{}' = -A = -2.5$. Otherwise $B_1{}'$ may be evaluated by reiteration. Here ΔB and k^* are calculated for $B = 0$. B_1' is determined from the slope of ΔB plotted against k^*. The process may be repeated.

Also, for the local method without displacement thickness, Equation (56) becomes

$$\Delta B = \left(\sqrt{\frac{2}{c_f}}\right)_r - \left(\sqrt{\frac{2}{c_f}}\right)_s - 19.7\left[\left(\sqrt{\frac{c_f}{2}}\right)_r - \left(\sqrt{\frac{c_f}{2}}\right)_s\right] \tag{73}$$

9. CONCLUDING REMARKS

The various indirect methods developed in this paper are summarized in Table 1. There is a basic sameness in all the procedures. An appropriate drag coefficient is plotted against an appropriate Reynolds number combined usually with a drag coefficient. The difference between the rough and smooth curves determines the drag characterization. By using this difference the truncation error in the second and third methods is made negligible, also.

Once a drag characterization has been determined for a particular roughness, it may be used in boundary-layer calculations to determine the drag of bodies: that of a flat plate in Reference 4 by means of a formula unlike the complicated procedure of Grigson[14], that of a two-dimensional body with pressure gradients in Reference 15 by an integral method and that of more general bodies by the mixing lengths given in Reference 1.

REFERENCES

1. Granville, P.S., "Mixing-Length Formulations for Turbulent Boundary Layers over Arbitrarily Rough Surfaces", Journal of Ship Research, Vol. 29, No. 4, pp. 223-233 (Dec. 1985).

2. Nikuradse, J., "Laws of Flow in Rough Pipes," NACA TM 1292 (Nov. 1950) (translation from VDI-Forschungsheft 361, Jul/Aug 1933).

3. Hama, F.R., "Boundary-Layer Characteristics for Smooth and Rough Surfaces," Transactions of the Society of Naval Architects and Marine Engineers, Vol.62, pp. 333-358 (1954).

4. Granville, P.S., "The Frictional Resistance and Turbulent Boundary Layer of Rough Surfaces," Journal of Ship Research, Vol. 2, No. 3, pp. 52-74 (Dec. 1958).

5. Karlsson, R.I., "The Effect of Irregular Surface Roughness on the Frictional Resistance of Ships," Proceedings of International Symposium on Ship Viscous Resistance, L. Larsson, ed., Swedish State Shipbuilding Experimental Tank, (1978).

6. Granville, P.S., "Drag-Characterization Method for Arbitrarily Rough Surfaces by Means of Rotating Disks," Journal of Fluids Engineering (ASME), Vol. 104, pp. 373-377 (Sept. 1982)

7. Granville, P.S., "Drag and Turbulent Boundary Layer of Flat Plates at Low Reynolds Numbers," Journal of Ship Research, Vol. 21, No. 1, pp. 30-39 (March 1977).

8. Granville, P.S., "A Modified Law of the Wake for Turbulent Shear Flows," Journal of Fluids Engineering (ASME) Vol. 98, No. 3, pp. 578-580 Sep. 1976).

9. Karlsson, R.I., "Studies of Skin Friction in Turbulent Boundary Layers on Smooth and Rough Walls; Part 3," Chalmers University of Technology (Sweden), Dept. of Applied Thermo and Fluid Dynamics Publication 80/4 (1980).

10. Schoenherr, K.E., "Resistance of Flat Surfaces Moving Through a Fluid," Transactions of the Society of Naval Architects and Marine Engineers, Vol. 40, pp.279-313 (1932).

11. Couch, R.B., "Preliminary Report of Friction Plane Resistance Tests of Anti-Fouling Ship Bottom Paints," David Taylor Model Basin Report 789 (Aug. 1951).

12. Goldstein, S. ed., "Modern Developments in Fluid Dynamics, Vol. 2" Clarendon Press, Oxford, 1938. (See p. 364).

13. Robertson, J.M., J.D. Martin and T.H. Burkhart, "Turbulent Flow in Rough Pipes," Industrial & Engineering Chemistry Fundamentals, Vol.7, No. 2, pp.253-265 (May 1968).

14. Grigson, C., "The Drag at Ship Scale of Planes Having Any Quality of Roughness," Journal Of Ship Research, Vol. 29, No. 2, pp. 94-104 (June 1985).

15. Granville, P.S., "Similarity-Law Entrainment Method for Two-Dimensional Turbulent Boundary Layers in Pressure Gradients on Smooth or Rough Surfaces," (to be published)

Table I - Summary of Indirect Methods

Method		Measured	Plotted	ΔB	k^+
Flat plate	Displacement thickness	δ^*, U, τ_w	$\sqrt{\frac{2}{c_f}}$ vs. $\log R_{\delta^*}$	Eq. (30)	Eq. (31)
	Overall	U, D	$\sqrt{\frac{2}{C_F}}$ vs. $\log(R_L C_F)$	Eq. (71)	Eq. (72)
	Local Without Displacement Thickness	U, τ_w	$\sqrt{\frac{2}{c_f}}$ vs. $\log(R_x c_f)$	Eq. (73)	Eq. (57)
Pipe		V, τ_w	$\sqrt{\frac{2}{f}}$ vs. $\log(R_D\sqrt{f})$	Eq. (69)	Eq. (70)

Figure 1 - Local Method with Displacement Thickness (Hama, Ref. 3)

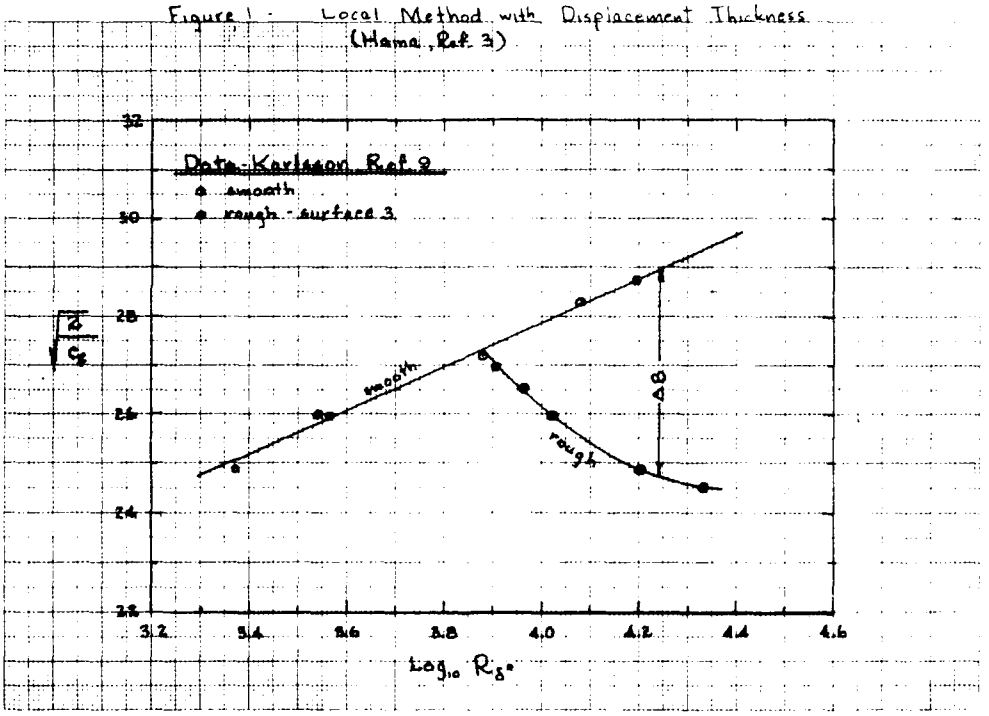

Figure 2 - Overall Method (Granville, Ref 4)

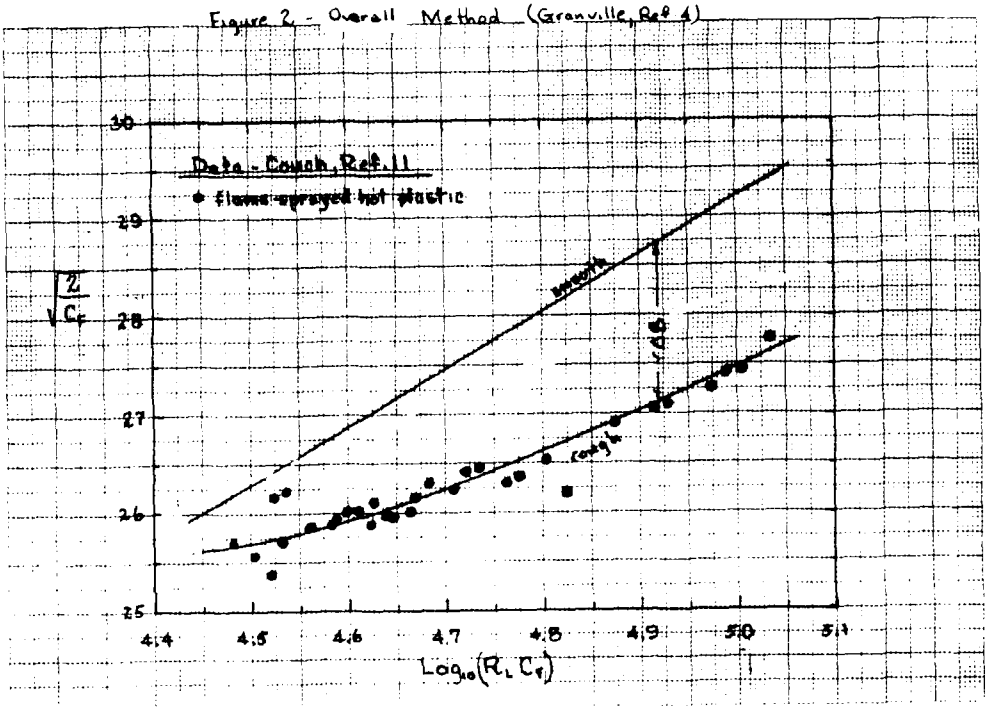

Figure 3 - Local Method without Displacement Thickness (New)

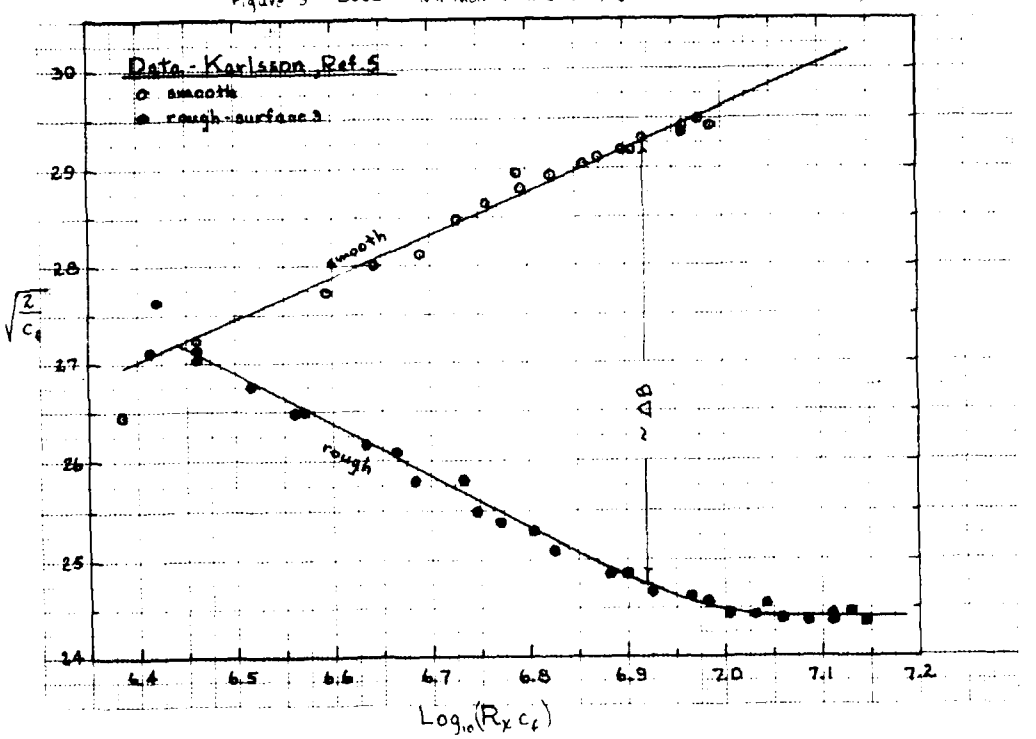

Figure 4 - Indirect Method for Pipe Flow (Nikuradse, Ref 2, Robertson et al Ref 13)

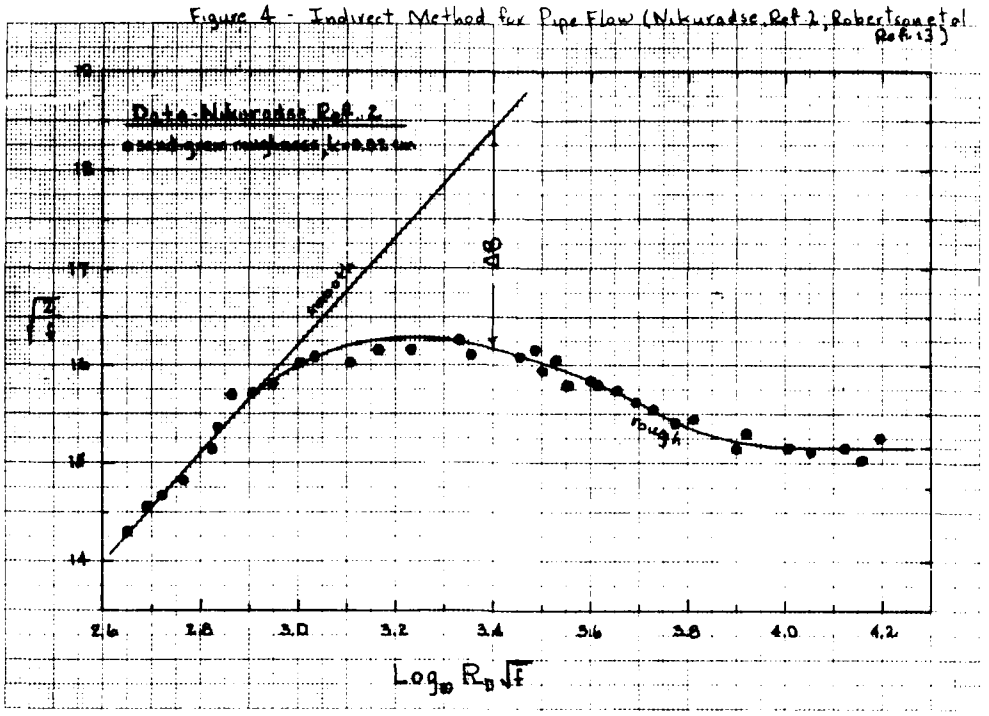

A SEMI-EMPIRICAL APPROACH TO USING FIVE HOLE PITOT TUBES

by John C. Kuhn
Project Engineer
Offshore Technology Corporation
Escondido, California USA

ABSTRACT

The calibration and application of spherical five hole pitot tubes are examined. In particular, calibration data are used to numerically "tune" potential flow solutions, which in turn are used in the application of the pitot tubes to find three dimensional flow fields (e.g. a ship's wake). Pitot tube calibrations based on tuned potential flow solutions result in more accurate velocity resolutions than can be practically obtained from purely empirical approaches. Comparisons are made and examples are given.

1.0 INTRODUCTION

In many areas of fluid mechanics it is desirable to obtain measured flow information. One means of obtaining such information is with pitot tubes, during an experiment or otherwise. To obtain three dimensional data with pitot tubes requires the use of dynamic calibration data to interpret results. In general, this calibration data is nonlinear and reasonably complex. Therefore, some straightforward methods of interpolation (within a "look-up" table of numbers representing the dynamic calibration) may lead to systematic, and perhaps significant errors.

The subject of this paper is the development and application of a technique to accurately interpret pitot tube measurement results with potential flow solutions that are numerically tuned to fit dynamic calibration data. Results contained in this paper are for spherical, five hole pitot tubes that were developed by, and are applied at the Offshore Technology Corporation in Escondido, California. However, the methods contained in this paper are generally applicable to any nearly spherical pitot tubes having five probe holes for obtaining three independent pressure measurements in two orthogonal planes, as is sufficient for the determination of three dimensional flow velocities.[1]

2.0 DYNAMIC CALIBRATION OF PITOT TUBES

Five hole pitot tubes provide their user with five pressure measurements that, upon interpretation with dynamic calibration information, yield a steady state three dimensional flow velocity. The methods presented herein are for steady state applications only.

2.1 METHODS

The dynamic calibration of pitot tubes requires an experimental set-up to acquire pressure measurements for known inflow angles and velocity magnitudes. To develop a complete dynamic calibration requires that pressure measurements be recorded for a matrix of inflow angles that sufficiently envelops the expected region of interest during applications of the instrument. Through the formulation of pressure coefficients that are properly normalized with respect to inflow velocity magnitudes, it usually becomes unnecessary to include a systematic variation of inflow velocity in the dynamic calibration test matrix. Rather, the pitot tubes may be calibrated for one nominal Reynolds number within the expected Reynolds number range during application, as long as the range is not too broad. The effect of varying Reynolds number on the pressure coefficients given in equations (1) through (5) is neglible for reasonable changes in Reynolds number, as shown by Treaster and Yocum.[3] However, if Reynolds number (based on diameter) changes on the order of 2,500 or greater are anticipated, then it may be worth conducting a parametric variation of Reynolds numbers during dynamic calibrations if velocity magnitude accuracies of within 2 percent are desired (flow angle resolution is not significantly affected by Reynolds number variations).[3]

Normalization with respect to the known flow velocity and fluid density (i.e. the known free stream dynamic pressure, $1/2\rho U^2$) is sufficient, but introduces an additional unknown during application. Therefore, it is desirable to normalize with measured pressures, as long as the coefficients thus formed are independent of measured value magnitudes. A suitable coefficient formulation has been developed by Treaster and Yocum[3] using a normalization parameter developed by Krause and Dudzinski[2] and is given in equations (1) through (5).

$$C_{yaw} = \frac{(P_2-P_3)}{(P_1-P_0)} \qquad (1)$$

$$C_{pitch} = \frac{(P_4-P_5)}{(P_1-P_0)} \qquad (2)$$

$$C_{total} = \frac{(P_1-P_{total})}{(P_1-P_0)} \qquad (3)$$

$$C_{static} = \frac{(P_0-P_{static})}{(P_1-P_0)} \qquad (4)$$

John C. Kuhn, 257 Neptune Avenue, Encinitas, California 92024

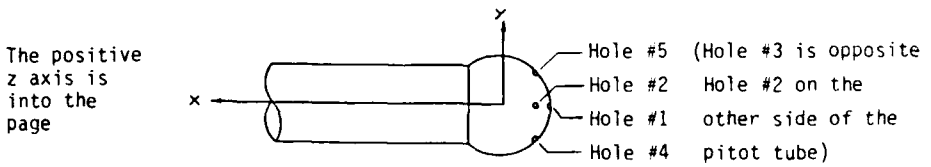

Figure 1: The Pitot Tube Fixed Coordinate System

$$P_0 = \frac{P_2+P_3+P_4+P_5}{4} \qquad (5)$$

where:

P_i = mean measured pressure for hole #i, i=1 to 5

P_{static} = static pressure

$P_{dynamic}$ = dynamic pressure = $(1/2)\rho U^2$

P_{total} = total pressure = $P_{static} + P_{dynamic}$

ρ = fluid density

U = free stream velocity

The numerical subscripts refer to the probe holes on a given pitot tube, as shown in Figure 1. It is convenient at this point to define another coefficient which effectively takes the place of two coefficients (C_{static} and C_{total}), the "velocity coefficient":

$$C_{velocity} = C_{static} - C_{total} \qquad (6)$$

This coefficient, together with "C_{yaw}" and "C_{pitch}" ,completely formulate the dynamic calibration characteristics of a five hole pitot tube for the purpose of determining three dimensional flow velocities.

To conduct calibration tests it is necessary to mount the pitot tube(s) on an apparatus allowing known angular displacements relative to the flow direction. There are basically two classes of devices for this purpose, one that pitches about the yawed position, and one that yaws about the pitched position. Using the pitot tube fixed Cartesian coordinate system in Figure 1, the following relations implicitly define the pitch angle (α) and the yaw angle (β) for the indicated device:

(1) for a device that pitches about the yawed position:

$$\begin{aligned} V_x &= V\cos(\alpha)\cos(\beta) \\ V_y &= V\sin(\alpha)\cos(\beta) \\ V_z &= V\sin(\beta) \end{aligned} \qquad (7)$$

(2) for a device that yaws about the pitched position:

$$\begin{aligned} V_x &= V\cos(\alpha)\cos(\beta) \\ V_y &= V\sin(\alpha) \\ V_z &= V\sin(\beta)\cos(\alpha) \end{aligned} \qquad (8)$$

where:

V = velocity magnitude

V_x = x velocity

V_y = y velocity

V_z = z velocity

α = pitch angle

β = yaw angle

The relations above apply not only for velocity vectors, but for any vectors in the so-defined space. Device one may be termed a "pure yaw" device since vectors in the yaw plane (the x-z plane) are unaffected by pitch, and device two may be termed a "pure pitch" device since vectors in the pitch plane (the x-y plane) are unaffected by yaw.

It is convenient at this point to introduce the location of the stagnation point. Let the following nondimensionalization of spacial coordinates be assumed:

$$\begin{aligned} x &= rX \\ y &= rY \\ z &= rZ \end{aligned} \qquad (9)$$

The nondimensional stagnation point location (X_s,Y_s,Z_s) for flow at pitch angle (α) and yaw angle (β), where the angles are relative to the negative x-axis, follows from equation (7) or (8), whichever is applicable:

(1) for the pure yaw device:

$$\begin{aligned} X_s &= -\cos(\alpha)\cos(\beta) \\ Y_s &= -\sin(\alpha)\cos(\beta) \\ Z_s &= -\sin(\beta) \end{aligned} \qquad (10)$$

(2) for the pure pitch device:

$$\begin{aligned} X_s &= -\cos(\alpha)\cos(\beta) \\ Y_s &= -\sin(\alpha) \\ Z_s &= -\sin(\beta)\cos(\alpha) \end{aligned} \qquad (11)$$

The probe hole locations in the coordinates given in Figure 1 may be summarized as follows:

$$\begin{aligned} x_p &= A_p r \\ y_p &= B_p r \\ z_p &= C_p r \end{aligned} \qquad (12)$$

where:

p = probe hole number = 1,2,3,4, or 5

and the constants A_p, B_p, and C_p define the probe hole locations on a given pitot tube. The pitot tubes used to obtain

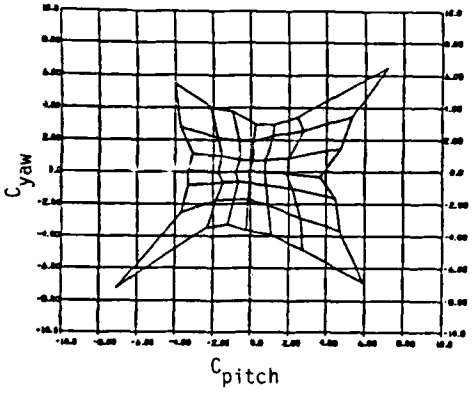

Figure 2: Empirical C_{pitch}/C_{yaw} Grid

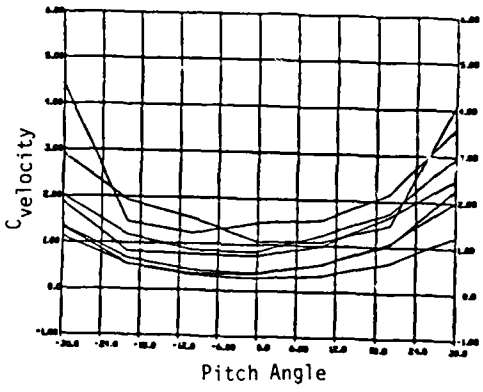

Figure 3: Empirical $C_{velocity}$ Plot

the data presented in this paper have the following probe hole constants:

p	A_p	B_p	C_p
1	-1.0	0	0
2	-cos(45°)	0	-cos(45°)
3	-cos(45°)	0	+cos(45°)
4	-cos(45°)	-cos(45°)	0
5	-cos(45°)	+cos(45°)	0

2.2 RESULTS

Typical calibration results are presented in Figures 2 and 3. This data resulted from a test matrix of +/-30 degrees pitch and yaw in 10 degree increments and a free stream velocity of 4.0 feet per second. The density of the fluid (freshwater) was 1.9362 pound-second^2/feet^4, corresponding to a water temperature of 70 degrees Fahrenheit.

3.0 INTERPRETING MEASUREMENTS WITH CALIBRATION RESULTS

Pressure data collected with pitot tubes placed in unknown flow conditions serves as the input to the computational problem of determining the flow velocity. This velocity is determined by:

1) Computing C_{pitch} and C_{yaw} with mean pressures (see equations 1 and 2).

2) Finding the inflow angle components α(pitch) and β(yaw) with C_{pitch}/C_{yaw} calibration data (see Figure 2).

3) Finding $C_{velocity}$ with the $C_{velocity}$ calibration data (see Figure 3).

4) Computing the velocity magnitude:

$$V = [(2/\rho)(dP_1 - dP_0)(1 + C_{velocity})]^{1/2} \qquad (13)$$

where:

$dP_1 = P_1 - P_{ref}$

$dP_0 = P_0 - P_{ref}$

P_{ref} = a reference pressure that measurements were taken relative to.

ρ = fluid density

5) Computing the velocity components:

a) for calibration data obtained with a pure yaw device:

$$V_x = V\cos(\alpha)\cos(\beta)$$
$$V_y = V\sin(\alpha)\cos(\beta) \qquad (14)$$
$$V_z = V\sin(\beta)$$

b) for calibration data obtained with a pure pitch device:

$$V_x = V\cos(\alpha)\cos(\beta)$$
$$V_y = V\sin(\alpha) \qquad (15)$$
$$V_z = V\sin(\beta)\cos(\alpha)$$

Steps 2 and 3 above require the use of dynamic calibration data. In general, this requires the development of an algorithm to determine relevent characteristics associated with measurement data based on known characteristics associated with neighboring calibration data. Two approaches are considered below. The first approach utilizes interpolation confined to the immediate region within which the measurements lie. The second approach uses numerically tuned functions that are based on potential flow around a sphere.

3.1 INTERPOLATION WITHIN CALIBRATION DATA

A standard approach to dealing with steps 2 and 3 above is to interpolate within the calibration data. Step 2 requires a search through the C_{pitch}/C_{yaw} calibration data based on C_{pitch} and C_{yaw} values. Once the proper region is found, a reverse three point bivariate interpolation[5] may be done, as illustrated in Figure 4 and formulated in Equation 16:

$$d\alpha[(C_{pitch})_{1,0} - (C_{pitch})_{0,0}] + d\beta[(C_{pitch})_{0,1} - (C_{pitch})_{0,0}] =$$
$$= (C_{pitch})_{measured} - (C_{pitch})_{0,0} \qquad (16a)$$

$$d\alpha[(C_{yaw})_{1,0} - (C_{yaw})_{0,0}] + d\beta[(C_{yaw})_{0,1} - (C_{yaw})_{0,0}] =$$
$$= (C_{yaw})_{measured} - (C_{yaw})_{0,0} \qquad (16b)$$

Equation 16 is a two by two system of linear equations that may be solved for $d\alpha$ and $d\beta$; thus, this interpolation is linear.

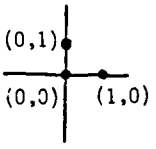

Figure 4: Three Point Bivariate Interpolation Diagram

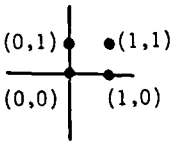

Figure 5: Four Point Bivariate Interpolation Diagram

The pitch and yaw angles are then:

$$\alpha = (\alpha)_{0,0} + (d\alpha)\Delta\alpha$$
$$\beta = (\beta)_{0,0} + (d\beta)\Delta\beta \qquad (17)$$

where:

$\Delta\alpha, \Delta\beta$ = the spacing between dynamic calibration points.

Step 3 also requires a search through the calibration data, but this time the search is conducted within the $C_{velocity}$ data and is based on the α and β values found in equations 17. Upon finding the proper region, a forward four point bivariate interpolation[5] may be done, as illustrated in Figure 5 and formulated in Equation 18:

$$C_{velocity} = (1-d\alpha/\Delta\alpha)(1-d\beta/\Delta\beta)((C_{velocity})_{0,0}]$$
$$+(d\alpha/\Delta\alpha)(1-d\beta/\Delta\beta)((C_{velocity})_{1,0}]$$
$$+(d\beta/\Delta\beta)(1-d\alpha/\Delta\alpha)((C_{velocity})_{0,1}]$$
$$+(d\alpha/\Delta\alpha)(d\beta/\Delta\beta)((C_{velocity})_{1,1}]$$
$$+(C_{velocity})_{0,0} \qquad (18)$$

The four point bivariate interpolation procedure is nonlinear, but is not a true second order procedure (a six point bivariate interpolation would be second order accurate - see Reference 5).

Now the interpolation procedures are complete, and the velocity magnitude may be found with equation 13, and its components with equation 14 or 15, whichever corresponds to the type of calibration apparatus used.

3.2 ITERATION WITHIN NUMERICALLY TUNED POTENTIAL FLOW SOLUTIONS

An alternative to interpolating within dynamic calibration data is to "fit" functions to it, and then use the functions in lieu of the data itself. If it is possible to fit a function to data accurately, then any errors associated with interpolation may be avoided. Additionally, if the data under examination contains any scatter, it may be possible to fit "smooth" functions through the immediate vicinity of the data points, so as to increase the statistical accuracy of the resulting "fit". It is for both of these reasons that the following approach was developed.

3.2.1 THE BASE POTENTIAL FLOW FUNCTION

To fit a function to data it is necessary to:

1) choose a "base" function to start with, and

2) identify parameters associated with the base function that may be systematically varied to fit the function to the data.

For item (1), the potential flow solution derived in Appendix A may be used as a base function:

$$P(X') = (\rho U^2/8)[18X'^2 - 9X'^4 - 9X'^2\sin^2(\cos^{-1}(X')) - 5] \qquad (19)$$

This is the solution for the pressure (P) on the surface of a sphere in an infinite, ideal fluid in a nondimensional, flow fixed coordinate system where the positive X' direction is coincident with the free stream flow direction, and:

$$X' = x'/r \qquad (20)$$

To make use of (19) it is necessary to develop a coordinate transformation between the flow fixed coordinates used above (the X' system) and the pitot tube fixed coordinates given in Figure 1 (the X,Y,Z system). For the purposes of fitting (19) to dynamic calibration data, it is necessary to determine the X' value associated with each probe hole on a given pitot tube for a given angle of attack. Due to the special symmetry of the sphere, the following nondimensional dot product represents a complete transformation for the purposes of evaluating (19):

$$X' = -(A_pX_s + B_pY_s + C_pZ_s) \text{ if } \theta < 90 \text{ degrees} \qquad (21)$$
$$= +(A_pX_s + B_pY_s + C_pZ_s) \text{ if } \theta \geq 90 \text{ degrees}$$

where:

A_p, B_p, C_p = probe hole constants as defined in (12)

X_s, Y_s, Z_s = stagnation point location as defined in (10) and (11)

θ = spatial angle between a given probe hole and the stagnation point

The minus sign in (21) is acceptable as long as the stagnation point location and the probe hole location are not more than 90 degrees apart on the surface of the sphere. In general, spherical (or nearly spherical) pitot tubes become ineffective under such conditions anyway, so the minus sign may be consistently maintained with the addition of a suitable angle of attack constraint for the specific pitot tube design being used.

The theoretical C_{pitch}/C_{yaw} grid resulting from (10), (12), (19), and (21) is shown in Figure 6, and the corresponding $C_{velocity}$ plot is shown in Figure 7. These plots are based on the same inflow matrix as was used to create the empirical plots shown in Figures 2 and 3. A comparison of these results leads to the following observations:

1) the location and spacing of the "constant angle" lines (i.e. the lines representing a constant pitch or yaw angle) in the C_{pitch}/C_{yaw} grids can differ.

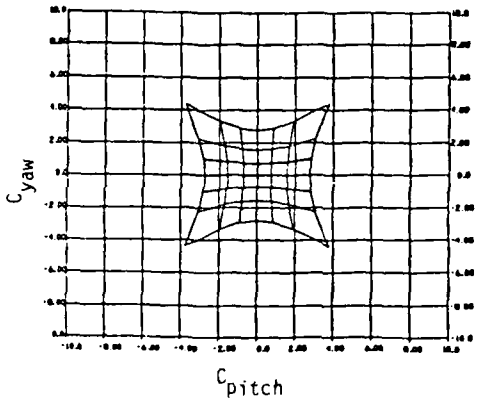

Figure 6: Base Theoretical C_{pitch}/C_{yaw} Grid

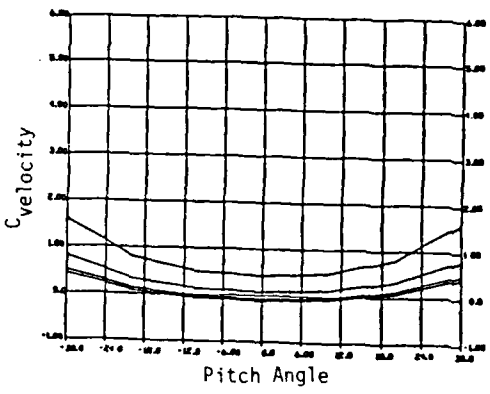

Figure 7: Base Theoretical $C_{velocity}$ Plot

2) the effective probe alignment relative to the flow direction may not be "perfect", as assumed in the theoretical results (thus their symmetry across axes).

3) in general, $(C_{velocity})_{empirical} > (C_{velocity})_{theoretical}$

The observations above are indicative of possible tuning parameters. In addition, the following basic observations may also suggest possible tuning parameters:

4) the empirical data contains the effect of a viscous boundary layer.

5) the pitot tubes are made with a fairly significant cylinder supporting a sphere (see Figure 1).

3.2.2 TUNING PARAMETER SELECTION

Based on the observations made in Section 3.2.1, the following types of tuning parameters are considered:

1) alignment adjustment angles - to correct for apparent discrepencies in alignment. This discrepency is made most apparent in the C_{pitch}/C_{yaw} grid. The error associated with this may be quantified as follows:

$$(E_a)_{pitch} = [\sum_{i=1}^{N} |(C_{pitch})_{empir,i} - (C_{pitch})_{theo,i}|]/N \quad (22a)$$

$$(E_a)_{yaw} = [\sum_{i=1}^{N} |(C_{yaw})_{empir,i} - (C_{yaw})_{theo,i}|]/N \quad (22b)$$

where the sum is done for all flow angles surveyed and N = the number of flow angles

2) an effective probe hole location adjustment - to correct for the presence of a boundary layer and/or the effective overall probe hole locations (especially the outer probe holes) being something other than as described in section 2.1 (see equation (12)). This discrepency is made most apparent in the $C_{velocity}$ plots (the reason for this lies in the fact that the equations used to arrive at $C_{velocity}$, equations (3) and (4), are fairly strong functions of outer hole behaviour, especially equation (4)). The error associated with this may be quantified as follows:

$$E_d = [\sum_{i=1}^{N} |(C_{velocity})_{empir,i} - (C_{velocity})_{theo,i}|]/N \quad (23)$$

where the sum is done only for $-10 <= \alpha,\beta <= +10$ and N = the number of flow angles in the (-10,+10) envelope.

3) a flow angle exponential - to exponentially correct for apparent discrepencies in flow angle. This discrepency is made most apparent in the C_{pitch}/C_{yaw} grid. The error associated with this may be quantified as follows:

$$(E_e)_{pitch} = [\sum_{i=1}^{N} |abs(C_{pitch})_{empir,i} - abs(C_{pitch})_{theo,i}|]/N \quad (24)$$

$$(E_e)_{yaw} = [\sum_{i=1}^{N} |abs(C_{yaw})_{empir,i} - abs(C_{yaw})_{theo,i}|]/N$$

where N = the number of flow angles surveyed.

4) a linear flow angle multiplier - to linearly correct for apparent discrepencies in flow angle. This discrepency is made most apparent in the C_{pitch}/C_{yaw} grid. The error associated with this may be quantified as follows:

$$(E_m)_{pitch} = [\sum_{i=1}^{N} |abs(C_{pitch})_{empir,i} - abs(C_{pitch})_{theo,i}|]/N \quad (25)$$

$$(E_m)_{yaw} = [\sum_{i=1}^{N} |abs(C_{yaw})_{empir,i} - abs(C_{yaw})_{theo,i}|]/N$$

where the sum is done only for $-20 <= \alpha,\beta <= +20$ to distinguish this error from E_e (more on this later) and N = the number of flow angles in the (-20,+20) envelope.

The error functions given in equations 22 through 25 are "polarized" in the sense that they have both positive and negative values associated with them.

Tuning parameter types (1), (3), and (4) may be incorporated by tuning the inflow angles, α and β, which preserves the spherical

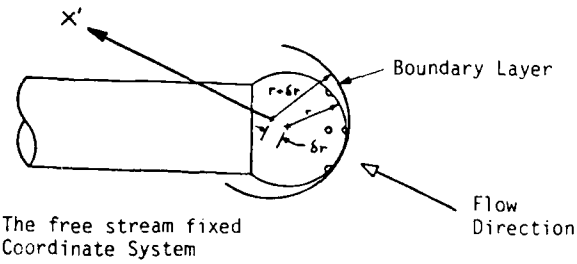

Figure 8: The free stream fixed Coordinate System

symmetry of the problem formulation. To maintain the symmetry, parameter type (2) may be incorprated with the assumption that the boundary layer creates, for the purposes of pressure distribution prior to separation, a roughly spherical shape circumscribing the sphere itself (see Figure 8). Since flow around a "body plus boundary layer" shape that is spherical is equivalent to flow around any sphere (as long as geometrically similar points are considered), "apparent" (or effective) probe hole locations may be found to account for both the presence of a boundary layer and effective shifts in probe hole locations. The entire tuning process may then be achieved by simply modifying the argument (X') of (19), and the type of transformation used in equation (21) is still applicable.

The flow angle exponential and linear multiplier may be incorporated at once as follows:

$$\begin{aligned} \alpha_T &= M_a(\alpha)^{(E_a)} \text{ if } \alpha > 0 \\ &= -M_a(-\alpha)^{(E_a)} \text{ if } \alpha < 0 \\ &= 0 \text{ if } \alpha = 0 \end{aligned} \tag{26}$$

$$\begin{aligned} \beta_T &= M_b(\beta)^{(E_b)} \text{ if } \beta > 0 \\ &= -M_b(-\beta)^{(E_b)} \text{ if } \beta < 0 \\ &= 0 \text{ if } \beta = 0 \end{aligned} \tag{27}$$

where:

M_a = α multiplier
M_b = β multiplier
E_a = α exponential
E_b = β exponential
α_T = tuned pitch angle
β_T = tuned yaw angle

To incorporate the alignment angles and the effective probe hole location adjustment, the stagnation point locations and the probe hole locations are affected as follows (see Figure 8):

(1) for the pure yaw device:

$$\begin{aligned} X_s &= -(1+\delta)\cos(\alpha_T-\alpha_A)\cos(\beta_T-\beta_A) \\ Y_s &= -(1+\delta)\sin(\alpha_T-\alpha_A)\cos(\beta_T-\beta_A) \\ Z_s &= -(1+\delta)\sin(\beta_T-\beta_A) \end{aligned} \tag{28}$$

$$\begin{aligned} X_p &= A_p - \delta\cos(\alpha_T-\alpha_A)\cos(\beta_T-\beta_A) \\ Y_p &= B_p - \delta\sin(\alpha_T-\alpha_A)\cos(\beta_T-\beta_A) \\ Z_p &= C_p - \delta\sin(\beta_T-\beta_A) \end{aligned} \tag{29}$$

(2) for the pure pitch device:

$$\begin{aligned} X_s &= -(1+\delta)\cos(\alpha_T-\alpha_A)\cos(\beta_T-\beta_A) \\ Y_s &= -(1+\delta)\sin(\alpha_T-\alpha_A) \\ Z_s &= -(1+\delta)\sin(\beta_T-\beta_A)\cos(\alpha_T-\alpha_A) \end{aligned} \tag{30}$$

$$\begin{aligned} X_p &= A_p - \delta\cos(\alpha_T-\alpha_A)\cos(\beta_T-\beta_A) \\ Y_p &= B_p - \delta\sin(\alpha_T-\alpha_A) \\ Z_p &= C_p - \delta\sin(\beta_T-\beta_A)\cos(\alpha_T-\alpha_A) \end{aligned} \tag{31}$$

where:

$$\delta = (r_{bl}/r) - 1.0 \tag{32}$$

r_{bl} = radius of body plus boundary layer (see Figure 8)
r = radius of body
α_A = pitch alignment angle
β_A = yaw alignment angle

With the incorporation of the effective probe hole location adjustment the transformation (21) must be modified to account for the non-unit radius sphere that results from nonzero δ values:

$$X' = -(X_pX_s+Y_pY_s+Z_pZ_s)/(X_p^2+Y_p^2+Z_p^2)^{1/2}/(1+\delta) \tag{33}$$

The effects of varying each of the parameter types are shown in Figures 9 through 12. The alignment angles, flow angle exponentials, and flow angle multipliers are each broken into independent α and β components to allow increased flexibility in fitting the solution to the data. However, the effective probe hole location adjustment is a global parameter having the same impact on pitch and yaw oriented values.

3.2.3 TUNING PARAMETER DETERMINATION

The successful execution of a tuning algorithm that finds values for each of the tuning parameters requires that the parameters be constrained. The parameters used here are physically motivated, and so the constraints on them may be arrived at via physical inspection also. Since boundary layers are of a positive thickness, it is required that:

$$\delta > 0 \tag{34}$$

The suspected effect of the cylinder supporting the sphere (see Figures 1 and 8) is to cause an apparent inflow angle of a smaller magnitude than the actual inflow angle (i.e. the cylinder tends to align the flow). The spacing of the "constant angle" lines in the

Figures 9-12: Tuning Parameter Effects for Specific Parameter Values:

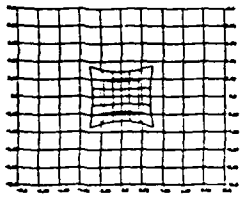

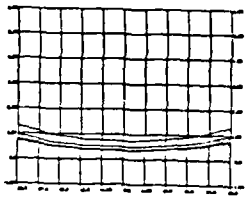

$\delta = 0.3$

$\alpha_A = \beta_A = 0°$

$M_a = M_b = 1$

$E_a = E_b = 1$

Figure 9: Boundary Layer Adjustment

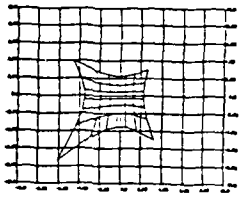

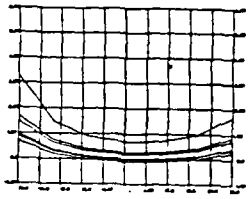

$\delta = 0$

$\alpha_A = \beta_A = 4°$

$M_a = M_b = 1$

$E_a = E_b = 1$

Figure 10: Alignment Adjustment

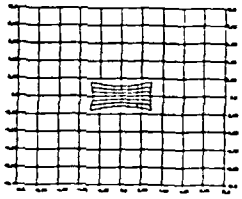

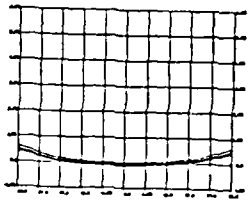

$\delta = 0$

$\alpha_A = \beta_A = 0°$

$M_a = 1, M_b = 0.5$

$E_a = E_b = 1$

Figure 11: Flow Angle Multiplier Adjustment

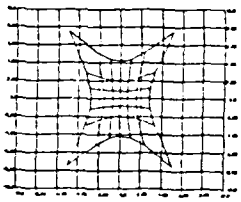

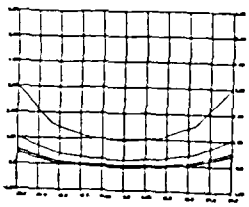

$\delta = 0$

$\alpha_A = \beta_A = 0°$

$M_a = M_b = 1$

$E_a = 1, E_b = 1.06$

Figure 12: Flow Angle Exponential Adjustment

C_{pitch}/C_{yaw} grid for relatively small inflow angles supports this idea. However, the spacing of these lines at relatively large inflow angles suggests that something is acting to increase the magnitude of the apparent inflow angle. This is probably due to the onset of separation. Based on these observations and observations concerning the convergence of the tuning algorithm to be presented shortly, the following flow angle multiplier and exponential constraints are acceptable:

$$0 < M_a, M_b < 1.0 \qquad (35)$$

$$E_a, E_b > 1.0 \qquad (36)$$

The alignment angles are constrained by the quality of the instruments and dynamic calibration apparatus, and the effect of any auxiliary apparatus (e.g. a wake rake, or a device used to hold the pitot tube(s) in place) on the flow "seen" at the pitot tube(s). The following constraints are usually acceptable, but may be broadened as necessary:

$$-5.0 < \alpha_A, \beta_A < 5.0 \qquad (37)$$

It is necessary to find acceptable values for four types of parameters that affect the solution shape in ways which are fairly unique, but are also related (see Figures 9 through 12). That is, a given parameter may primarily affect one solution characteristic while secondarily affecting others. Therefore, independent optimizations for each type of parameter are not sufficient. However, if multiple passes are made through a prioritized sequence of independent optimizations, it may be possible to converge to an acceptable solution with carefully chosen convergence criteria. In particular, it is important to order the independent optimizations in a given pass such that successive optimizations have as little impact on solution characteristics primarily associated with prior optimizations as possible. Consider the following ordering of independent optimizations for the problem at hand:

1) adjust alignment angle
2) adjust effective probe hole locations
3) adjust flow angle exponentials
4) adjust flow angle multipliers

Since the effects of adjustments 2 through 4 on alignment are small

(or perhaps nothing at all), the alignment adjustment made during adjustment 1 will maintain its validity as adjustments 2 through 4 are made. The effects of adjustments 3 and 4 on effective probe hole locations tend to be relatively small, and so the effective probe hole location adjustment made during adjustment 2 will tend to maintain its validity during adjustments 3 and 4. Unfortunately, adjustment 4 can have a significant impact on solution characteristics associated with adjustment 3. However, the regions in which each of these adjustments act strongly are somewhat different. That is, the flow angle exponential has its strongest impact at relatively large flow angle magnitudes, while the flow angle multiplier has a linear impact throughout the envelope of flow angles. The effects of each adjustment may be controlled by restricting the region in which the error function (used to determine the quality of the fit) associated with it is evaluated. As long as the error function is redundant, this approach will not endanger the global quality of the resulting fit. By restricting the error function associated with adjustment 4 (equation 25) to flow angles of a relatively small magnitude, adjustments made will have a smaller impact on solution characteristics associated with flow angles of a relatively large magnitude, and so the flow angle exponential adjustment made during adjustment 3 will tend to maintain its validity (this is why the restricted inflow envelope was used for equation 25). Upon completion of adjustment 4 one pass has been made through the prioritized sequence of optimizations given above. Since the sequence is ordered according to the principles described above, the amount of damage each successive optimization has on prior optimization results is minimized. It is on this basis that multiple passes through the sequence of optimizations will converge to a solution (no proof will be given).

Consider the following standard bisection algorithm:

It is desired to solve $E(x)=0$ where E is a polarized error function (i.e. it has both positive and negative values). Assuming $E(x)$ is continuous and bounds a and b can be found such that $E(a)E(b)<0$, then (by the intermediate value theorem) there exists a root r such that $a<r<b$ and $E(r)=0$. A solution within an average tolerance t of the true solution (based on the error function E) is desired. The bisection algorithm is then:

1) set $a_1=a$ and $b_1=b$
2) set $i=1$
3) set $r_i=0.5(a_i+b_i)$
4) if $abs[E(r_i)]<t$ then STOP
   if $abs[E(r_i)]>0$ then go to step 5
5) if $E(r_i)E(a_i)>0$ then go to step 6
   if $E(r_i)E(a_i)<0$ then go to step 8
6) set $a_{i+1}=r_i$ and $b_{i+1}=b_i$
7) set $i=i+1$ and go to step 3
8) set $a_{i+1}=a_i$ and $b_{i+1}=r_i$
9) set $i=i+1$ and go to step 3

Although the standard bisection algorithm presented above will always converge for continuous functions having a unique root between the bounds imposed,it will fail to converge if the root is outside the bounds. This can happen if sequential optimizations are being done where successive optimizations may effect results associated with prior optimizations. That is, the bounds associated with a given optimization during a given pass through a sequence of optimizations may be inappropriate during later passes as a result of successive optimizations affecting the results of prior optimizations. There are several ways to alleviate this problem. One way is to perform a test within the bisection algorithm to see if the procedure is "stepping" toward the solution with step sizes meeting the following criteria:

$$abs[E(r_i)-E(r_{i-1})] < Ct \qquad (38)$$

where:

C = a constant < 1
t = the average required tolerance

If this criteria is not satisfied, then it means that the bounds must be modified to straddle the root.

This criteria may be incorporated in the bisection algorithm as follows:

1) set $a_1=a$ and $b_1=b$
2) set $i=1$
3) set $r_i=0.5(a_i+b_i)$
4) if $abs[E(r_i)]<t$ then STOP
   if $abs[E(r_i)]>0$ then go to step 5
5) if $E(r_i)E(a_i)>0$ then go to step 6
   if $E(r_i)E(a_i)<0$ then go to step 9
6) set $a_{i+1}=r_i$ and $b_{i+1}=b_i$
7) if $abs[E(r_i)-E(r_{i-1})] < Ct$ then $b_{i+1}=b_i+db$
8) set $i=i+1$ and go to step 3
9) set $a_{i+1}=a_i$ and $b_{i+1}=r_i$
10) if $abs[E(r_i)-E(r_{i-1})] < Ct$ then $a_{i+1}=a_i-da$
11) set $i=i+1$ and go to step 3

Values of da and db depend on the nature of the bounds, but are usually a fraction of the initial difference in bounds a and b. In addition to allowing the bisection algorithm to converge when used within a sequence of optimizations, the above modification also allows the algorithm to "walk" outside its initial bounds.

This modified bisection algorithm may be used within the sequential optimization procedure described earlier to arrive at final tuned potential flow solutions. An acceptable criteria for convergence is that one pass be made through the optimization sequence, from adjustment 1 through adjustment 4, such that no adjustments are made. That is, if the test in step (4) above yields a "STOP" for $i=1$ for each of the adjustments 1 through 4 during a given pass, then convergence has been achieved in the sense that the present tuning parameters have yielded a solution that is within the average tolerances specified.

The values of the bounds (a and b), da, db, and C used in conjunction with the data presented in this paper are as follows:

Parameter Type	Initial Bounds a	Initial Bounds b	Bound Test Constant C	Bound Modifiers da	Bound Modifiers db
Alignment Angles	-5°	+5°	1/10	5°	5°
Probe Hole Location	0	0.6	1/10	0.05	0.05
Flow Angle Exponential	1.0	1.2	1/10	0.03	0.03
Flow Angle Multiplier	0.5	1.0	1/10	0.04	0.04

3.2.4 RESULTS

The tuning algorithm described in section 3.2.3 was used to process dynamic calibration data for five five-hole pitot tubes like those shown in Figure 8. The functions given in equations 22 through 25 were used as error functions during the tuning process. The

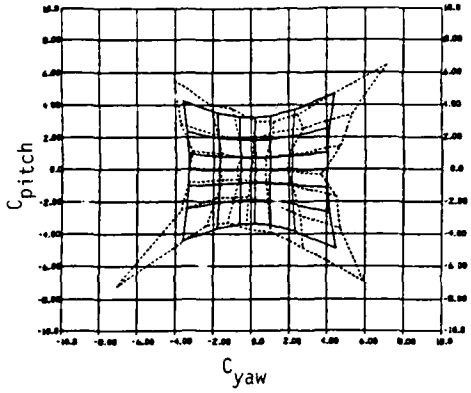

Figure 13(a): Empirical and Tuned Theoretical C_{pitch}/C_{yaw} Grids

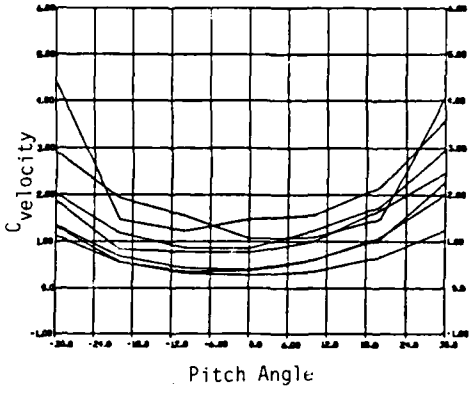

Figure 13(b): Empirical $C_{velocity}$ Plot

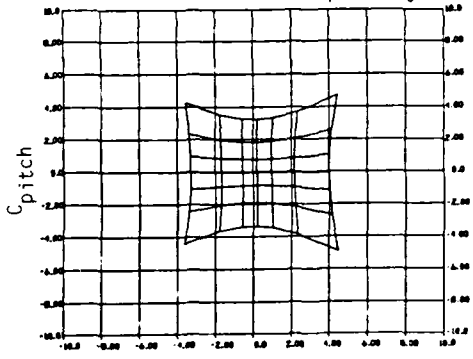

Figure 14(a): Tuned Theoretical C_{pitch}/C_{yaw} Grid

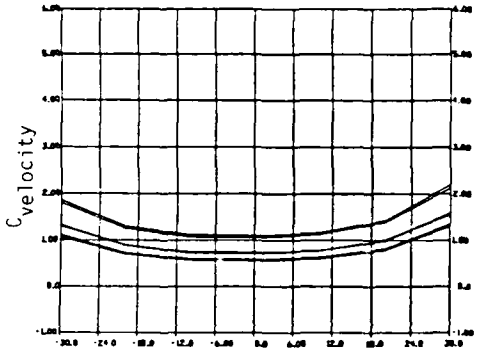

Figure 14(b): Tuned Theoretical $C_{velocity}$ Plot

tolerances with which these error functions were compared are as follows:

Parameter	Error Function	Tolerance
Alignment Angles	Eqn. 22	0.12
Probe Hole Location	Eqn. 23	0.05
Flow Angle Exponentials	Eqn. 24	0.12
Flow Angle Multipliers	Eqn. 25	0.12

After 11 passes (consisting of a total of 142 iterations) per pitot tube, the following tuning parameters were found for each of five pitot tubes.

	Pitot Tube Number				
Parameter	1	2	3	4	5
alignment angles:					
α_A	4.29°	-0.71°	-1.16°	-2.42°	-0.71°
β_A	1.89°	-3.36°	-2.73°	0.54°	1.33°
effective probe hole location:					
δ	0.60	0.37	0.34	0.41	0.34
flow angle exponentials:					
E_a	1.35	1.17	1.24	1.25	1.18
E_b	1.27	1.21	1.24	1.15	1.24
flow angle multipliers:					
M_a	0.39	0.72	0.49	0.52	0.49
M_b	0.60	0.36	0.51	0.69	0.52

The results for pitot tube #4 are shown in Figures 13 and 14. These results are representative of the results obtained for the five spherical, five hole pitot tubes examined.

3.2.5 USING THE TUNED SOLUTIONS

Once tuned solutions have been found, they may be used in lieu of the dynamic calibration data itself to determine three dimensional flow

Table 1: Results with Experimental Data

Actual		via Interpolation				via Iteration			
α (degrees)	β (degrees)	α (degrees)	β (degrees)	Velocity (knots)	Velocity % error	α (degrees)	β (degrees)	Velocity (knots)	Velocity % error
-25	0	22.8	-0.6	1.51	5	-20.6	-0.5	0.94	-6
-15	0	-16.5	-0.8	1.36	36	-12.8	-1.2	1.09	9
-5	0	-4.8	-1.8	1.22	22	-4.2	-2.1	1.06	6
15	0	15.7	-0.7	1.14	14	11.2	-1.9	1.09	9
0	-15	11.0	-12.8	1.30	30	-4.2	-12.0	0.98	-2
0	15	1.2	12.9	1.32	32	-1.2	11.6	1.01	1
-15	-15	6.5	-14.9	1.11	11	-13.8	-12.2	1.05	5
5	-15	16.2	-10.5	1.15	15	9.7.0	-11.6	1.07	7
15	15	12.9	10.3	1.20	20	8.8	9.9	1.01	1
15	15	-14.2	12.0	1.35	35	-14.1	12.7	0.97	-3
15	10	-16.0	9.6	1.40	40	-12.8	8.5	1.03	3
-15	12.5	-16.9	11.3	1.26	26	-16.7	12.9	0.91	-9
-15	17.5	-13.0	14.0	1.40	40	-12.9	14.3	1.01	1
-15	20	-12.1	14.3	1.46	46	-12.0	14.3	1.06	6
-20	-20	-20.9	-16.9	1.17	17	-18.3	-19.6	0.95	-5
20	-20	-24.0	-15.9	1.20	20	22.1	-17.2	0.97	-3
20	20	14.6	19.4	1.26	26	15.9	19.2	1.01	1
20	20	-18.0	18.6	1.31	31	-16.7	19.1	0.99	-1
-10	-10	-10.2	-9.9	1.11	11	-10.0	-9.9	1.06	6
10	-10	9.9	-9.9	1.11	11	8.8	-10.4	1.06	6
-10	10	-10.1	10.1	1.12	12	-9.7	8.9	1.05	5
10	10	9.9	10.1	1.13	13	5.9	9.7	1.04	4

Table 2: Results with Theoretical Data

Actual		via Interpolation				via Iteration			
α (degrees)	β (degrees)	α (degrees)	β (degrees)	Velocity (knots)	Velocity % error	α (degrees)	β (degrees)	Velocity (knots)	Velocity % error
25	0	-24.9	0.0	1.28	28	-25.0	0.2		0
-15	0	-14.7	0.0	1.13	13	-15.0	-0.2		0
-5	0	-4.9	0.0	1.03	3	-4.9	0.2		0
15	0	14.7	0.0	0.98	-2	15.0	-0.2		0
0	-15	0.0	-14.7	1.08	8	0.2	-15.0		0
0	15	0.0	14.7	1.08	8	0.2	15.0		0
-15	-15	-14.8	-14.9	1.27	27	-15.0	-15.0		0
-15	-15	14.4	-14.3	1.07	7	15.0	-15.0		0
15	15	14.6	14.8	1.07	7	15.0	15.0		0
-15	15	-14.5	14.3	1.27	27	-15.0	15.0		0
-15	10	-14.7	9.9	1.10	10	-15.0	10.0		0
-15	12.5	-14.6	12.1	1.24	24	-15.0	12.5		0
-15	17.5	-14.4	16.7	1.19	19	-15.0	17.5		0
-15	20	-15.5	20.3	1.17	17	15.0	20.0		0
-20	-20	20.0	-20.0	1.12	12	-20.0	-20.0		0
20	-20	20.0	-20.0	1.12	12	20.0	-20.0		0
20	20	20.0	20.0	1.12	12	20.0	20.0		0
20	20	-20.0	20.0	1.12	12	-20.0	20.0		0
-10	-10	-10.0	-10.0	0.99	-1	-10.0	-10.0		0
10	-10	10.0	-10.0	0.99	-1	10.0	-10.0		0
-10	10	-10.0	10.0	0.99	-1	-10.0	10.0		0
10	10	10.0	10.0	0.99	-1	10.0	10.0		0

velocities from mean pressures measured with the pitot tubes. This procedure may be accomplished with a modified bisection algorithm functionally identical to the one presented in Section 3.2.3 (the subscript 'e' means empirical, 't' means theoretical, 'L' means lower, and 'U' means upper):

1) compute $(C_{pitch})_e$ and $(C_{yaw})_e$ from measured pressures
2) set lower bounds $\alpha_L=a_L$ and $\beta_L=b_L$
3) set upper bounds $\alpha_U=a_U$ and $\beta_U=b_U$
4) set i=1
5) set $\alpha_i=0.5(\alpha_L + \alpha_U)$
   $\beta_i=0.5(\beta_L + \beta_U)$
6) compute $(C_{pitch})_{t,i}$, $(C_{yaw})_{t,i}$, and $(C_{velocity})_{t,i}$ from the tuned solution
7) if $abs[(C_{pitch})_{t,i}-(C_{pitch})_e] < t_1$ and $abs[(C_{yaw})_{t,i}-(C_{yaw})_e] < t_2$ then STOP; otherwise, continue
8) if $abs[(C_{yaw})_{t,i}-(C_{yaw})_e] < t_2$ then go to step 16
9) if $(C_{yaw})_{t,i} > (C_{yaw})_e$ then go to step 13
10) $\beta_L = \beta_i$
11) if $abs[(C_{yaw})_{t,i-1} - (C_{yaw})_{t,i}] < t_2$ then $\beta_U = \beta_U + 5.0°$
12) go to 15
13) $\beta_U = \beta_i$
14) if $abs[(C_{yaw})_{t,i-1} - (C_{yaw})_{t,i}] < t_2$ then $\beta_L = \beta_L - 5.0°$
15) if $abs[(C_{pitch})_{t,i}-(C_{pitch})_e] < t_1$ then go to step 22
16) if $(C_{pitch})_{t,i} > (C_{pitch})_e$ then go to step 20
17) $\alpha_L = \alpha_i$
18) if $abs[(C_{pitch})_{t,i-1} - (C_{pitch})_{t,i}] < t_1$ then $\alpha_U = \alpha_U + 5.0°$
19) go to 22
20) $\alpha_U = \alpha_i$
21) if $abs[(C_{pitch})_{t,i-1} - (C_{pitch})_{t,i}] < t_1$ then $\alpha_L = \alpha_L - 5.0°$
22) set i=i+1 and go to step 5

4.0 METHOD EVALUATIONS

Two categories of evalutions (one with known inputs and the other with unknown inputs) were conducted. For both of them the resolution tolerances t_1 (pitch) and t_2 (yaw) were set at 0.005.

4.1 WITH KNOWN INPUTS

With known α, β, and velocity values, four types of evaluations were conducted. Results for purely empirical interpolation (as described in Section 3.1) and semi-empirical iteration (as described in Section 3.2.5) were computed for a representative matrix of flow angles for which data was collected during the dynamic calibration testing (as described in Section 2.2). The representative results given in Table 1 are for pitot tube #4. As a means of differentiating between errors associated with experimental scatter and errors associated with the method being used, theoretical solutions corresponding to each flow angle were computed. That is, for each flow angle theoretical pressures were created to serve as "measurements", and velocities were resolved (via interpolation and iteration) using dynamic calibration information (spanning the +/-30 envelope in 10 increments) based on the same theoretical solution as was used to compute the "measurements". These results, which are presented in Table 2, are indicative of errors associated with the method being used (i.e. interpolation or iteration) since no experimental data was involved in their creation.

4.2 WITH SHIP MODEL WAKE DATA

Both the purely empirical interpolation procedure and the semi-empirical iteration procedure were used to process wake survey data for a twin screw vessel with vertical bossings (see Figure 15, 0 degrees is directly "up" in this figure). The plots in Figure 15 correspond to measurements obtained with pitot tube #4.

5.0 CONCLUSIONS

For the most part, the empirical interpolation procedure and the semi-empirical iteration procedure performed equally concerning flow angle determination. However, velocity magnitudes were systematically overpredicted by the interpolation procedure. In comparison, velocity magnitudes were predicted well with the iteration procedure, with a slight tendency toward overprediction. Therefore, attention to nonlinear behaviour is necessary for the accurate prediction of velocity magnitudes from pitot tube pressure data. The semi-empirical iteration procedure appears to be sufficient for this purpose, and may possibly be further improved through the incorporation of different and/or additional tuning parameters.

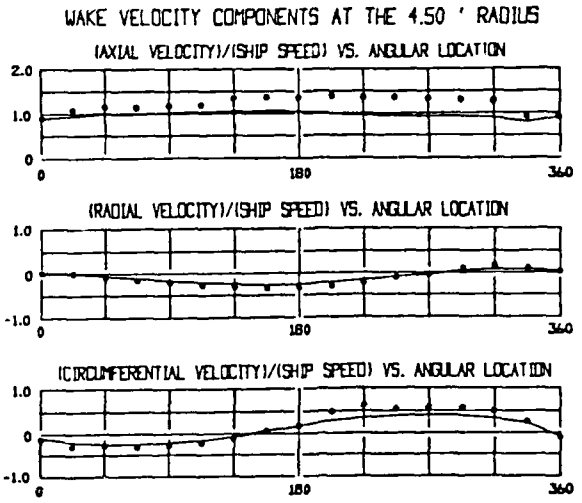

Figure 15: Wake Profile Results (• = interpolated data; ——— = iteration data)

REFERENCES

1) Pien, P. C., "Five Hole Spherical Pitot Tube," David Taylor Model Basin Report 1229, May 1958.
2) Krause, L. N., and Dudzinski, T. J., "Flow-Direction Measurement with Fixed Position Probes in Subsonic Flows over a Range of Reynolds Number," NASA TMX-52576, May 1969
3) Treaster, A. L., and Yocum, A. M., "The Calibration and Application of Five-hole Probes," ISA Transactions, Vol.18, No. 3
4) Kellog, O. D., "Foundations of Potential Theory," Dover Publications, 1953.
5) Abramowitz, M., and Stegun, I. A., "Handbook of Mathematical Functions," Dover Publications, 1970.

APPENDIX A

POTENTIAL FLOW AROUND A SPHERE IN AN INFINITE FLUID IN FREE STREAM ORIENTED COORDINATES

Consider potential flow in the positive x' direction around a sphere of radius "r" in an infinite fluid using the flow fixed Cartesian coordinates shown in Figure 8. Assuming a free stream velocity "U", the velocity potential "ϕ" is:

$$\phi = Ux' + \frac{Ur^3x'}{2(x'^2+y'^2+z'^2)^{3/2}} \qquad (A1)$$

From Bernoulli's equation the dynamic pressure "P" at a point on the surface of the sphere may be found:

$$P(x',y',z') = (1/2)\rho\{U^2-(u^2+v^2+w^2)\} \qquad (A2)$$

where:

ρ = fluid density

and:

$$u = d\phi/dx' = U + U/2\{(r^3-3x'^2r)/r^3\} \qquad (A3)$$
$$v = d\phi/dy' = -(3Ux'y')/(2r^2) \qquad (A4)$$
$$w = d\phi/dz' = -(3Ux'z')/(2r^2) \qquad (A5)$$

on the surface of the sphere:

$$r = (x'^2+y'^2+z'^2)^{1/2} \qquad (A6)$$

From A2, A3, A4, and A5 it is seen that:

$$P(x',y',z') = (\rho U^2/8r^4)\{18r^2x'^2-9x'^4-9x'^2y'^2-9x'^2z'^2-5r^4\} \qquad (A7)$$

Now, letting

$$l^2 = y'^2 + z'^2 \qquad (A8)$$

and

$$x' = rX' \qquad (A9)$$
$$l' = rL' \qquad (A10)$$

yields, upon substitution into A7:

$$P(X',L') = (\rho U^2/8)\{18X'^2-9X'^4-9X'^2L'^2-5\} \qquad (A11)$$

It may be seen from spherical geometry that:

$$L = \sin(\cos^{-1}(X')) \qquad (A12)$$

From A11 and A12 it is seen that:

$$P(X') = (\rho U^2/8)\{18X'^2-9X'^4-9X'^2\sin^2(\cos^{-1}(X'))-5\} \qquad (A13)$$

The one dimensionality of A13 arises from the symmetry of the sphere.

IN OUR EXPERIENCE: SOME NEW METHODS AND TECHNIQUES

Ryan R Young
Naval Architect

United States Coast Guard Research and Development Center
Avery Point, Groton, CT 06320

Abstract

Recent tests in the U.S. Coast Guard Academy's Circulating Water Channel to obtain the pressure field over the hull of a planing hull model at large angles of trim, roll and yaw involved the development of several methods and techniques of "tankery" of interest to ATTC members. Transparent models of a notional patrol boat design were built using acrylic plastic sheet materials. Transparent models facilitate flow visualization and the determination of the dynamic waterlines under planing conditions, but involve certain fabrication problems. A straightforward and relatively economical method for measuring static pressures from a large number of ports was implemented, and Ultra-violet fluorescence was used to aid photographic recording of the surface flow patterns indicated by specially treated tufts.

1.Introduction

A pressure distribution survey is being conducted by the United States Coast Guard Research and Development Center as part of a program of research into the stability characteristics of High-Speed craft under the auspices of the Coast Guard's Advanced Marine Vehicles (AMV) Project. The principle objectives of this program are to develop a better understanding of the operating characteristics of various AMV's, to aid in their design, and to anticipate of the need for new operating techniques and procedures to assure their their safe use in performing Coast Guard missions.

The primary purpose of this set of tests is to obtain pressure distributions and flow patterns for a notional model of a 100 ft, 100 ton displacement hard-chine planing patrol boat. Additionally, this experiment was planned as a complement to a set of rotating arm and towing tank experiments performed at Stevens Institute; key parameters were matched as closely as possible.

Pressure surveys of this type have been performed before, most notable is Kapyran (1955). However, a search of the available literature has failed to turn up any experimental results for deadrise surfaces heeled and yawed. Indeed, there are only a few results presented for calculated distributions in the heeled and yawed condition, although it is felt that the finite element approach of Doctors (1975) or Wellicome (1978) could produce such results, and this will be a subject of future work in the AMV project.

2.Description of Model

2.1 Lines

The model represents a typical 100 ft long, 100 ton displacement, planing patrol boat, with a length to beam ratio of 5, and a 20 degree deadrise vee-bottom hull. A convenient scale of 1/32 was chosen to keep the Froude scale speed within the capability of the channel and to reduce blockage. In order to facilitate computer analysis, the hull shape was kept as simple as possible, which also made fabrication easier. On the other hand, a pure constant deadrise form, the simplest possible, was undesirable due to the perception that real boats don't look like that.

The section plan of the model is presented in figure 1. The model has a constant deadrise prismatic afterbody and a developable forebody. The chine heights and the deadrise distribution of the forebody were taken from PT boat data in Clement (1963), particularly the Huckins data, since that hullform is developable, and was reputed to have good seakeeping. The topsides above the chine are developed using 2 cones, the lower surfaces use evenly spaced generators arranged to merge the flat afterbody sections with a conically developed forefoot, which starts along a generator line which intersects the centerline of the hull around station 3. The shape is very similar to existing single-chine patrol and crew boats. The main difference is the straight buttocks aft of amidships, where most full-scale craft would be rockered for running trim adjustment, and to improve low speed resistance.

2.2 Construction

The desirability of transparent models for planing research stems from the need to record the constantly changing wetted surface. This can be done using underwater photography, but this technique is less suitable for a circulating water channel, since we cannot disturb the flow with underwater cameras, lights, etc. A transparent model makes it much simpler to record the spray root, the area wetted by spray, and the immersed area.

In designing models for transparent sheet materials, their high density and low elastic modulus should be kept in mind. As an example, the specific gravity of Plexiglass UVA, a common acrylic, is 1.19, and the modulus 450,000 psi, as compared to 0.71 and 1,600,000 psi for yellow pine. Attention to structural stiffness prevents heavy, flexible models. Before using any of the transparent plastics for the first time, obtain the manufacturer's design and fabrication data sheets, such as Rohm and Haas (1984), published by the makers of Plexiglass, but applicable to any acrylic material.

For prismatic shapes with no curvature, it is simple to construct models using acrylic (Plexiglass is a common brand name), polycarbonate (LEXAN), or even safety glass panels, probably in that order of difficulty. It is the author's feeling that this is the preferred technique for such simple shapes. If the model is very large, and the skin relatively thin, it may be possible to cold form acrylic, but the minimum bend radius is about 180 times the thickness of the sheet. Heat forming is the best way to form non-prismatic shapes, and the only way to form non-developable hulls. Instantly, the economics of transparent models becomes marginal. At the very least, a male plug must be made to drape the hot sheet over, and such a plug must be at least as fair and smooth as a wooden tow tank model. In this project, it was necessary to use a male and a female mold cast in plaster, as well as the initial wooden plug. Since most of the work was performed by the author, it is difficult to estimate the hours that went into the model (including the first un-satisfactory attempt), but a guess would be 2-3 times the hours needed for a wooden model of comparable quality. Vacuum forming would help speed up the process, as only a female mold is needed, but at a loss of control over thickness and optical clarity. The Rohm and Haas data sheet PL-4N has many valuable details on all aspects of forming sheet acrylics. Polycarbonates can be heat formed as well, but at a higher temperature, and they must be carefully dried first to prevent permanent hazing and fogging.

If a model is constructed from more than one piece, it must be glued together. The changing bevels on a complex model make it hard to use the common solvent cements, which are toxic and produce a weak joint which degrades under long-term exposure to water. There is a type of viscous 2-part cement, known by the trade name Weld-On-40 (see appendix for sources) which can fill substantial gaps, and has good strength and water resistance, and was used for most of the joints on this model. Polycarbonates cannot be solvent welded, and the most satisfactory cements are the isocyanurate or "crazy glue" types. There is at least one such glue which is gap filling, called "Super-T".

A balsa wood model was constructed to use for preliminary experiments in the CWC and to use as a plug.(Incidently, balsa steam bends quite nicely using a small travel steamer) A plaster of paris female mold was then cast from this plug, and the developed shape of the panels was picked off using a sheet of mylar drawing film, avoiding graphical development. A flexible linoleum material the same thickness as the hull plating (1/8 in) was used to line the female mold in order to cast a male mold which allowed for the thickness of the plating.

After several experiments with heat guns and a gas-fired pizza oven, a new door was fabricated for an ordinary household oven, which allowed the partial insertion of the precut bottom plating into the oven. An electric heat gun was used to increase heat transfer by convection, and the oven racks were wrapped in fiberglass cloth to prevent marring of the plexiglass surface. The molds were pre-heated and greased. To keep the afterbody perfectly flat, only the forward section of the plexiglass was heated. Once the plexiglass had reached a surface temperature of at least 290 deg F, it was draped carefully into the female mold and the male mold placed on top of it. The weight of the male mold was sufficient to keep the sheet from warping as it slowly cooled.

An annoying property of acrylic sheet is the lack of control over the bending properties. A 10 deg temperature change will produce an order of magnitude change in the modulus. The material will bend, stretch, neck down in thickness and pick up the pattern of whatever surface it is laid against, and then in less than a minute, it will be rigid.

The formed panels were then cemented to the frames, which had been previously attached to the deck (1/4 inch thick for rigidity). The shape and bevel of the frames was carefully calculated using the method of Morris (1983) to account for the plating thickness. The topside panels had less curvature, and were less critical; they were heat formed using the original balsa model as a male mold. Sharp chines and keels were maintained.

3.Apparatus and Procedures

3.1 Test facility

The investigation was carried out in the Circulating Water Channel (CWC) of the United States Coast Guard Academy. This facility and

it's capabilities are described in Colburn (1981). The facility's 5-axis rudder dynamometer was modified for this experiment by fitting a camera tripod tilt and pan head to the dyno's central shaft. In this series of experiments, the dyno was not energized, and no force or moment data was taken. Hopefully, this data will be obtained in a later series of experiments, so that it can be compared with the rotating arm data. The central shaft is free to heave, and a weight was connected between the shaft and the fixed framework of the apparatus to set the unloading force, the model all-up being slightly over scale weight. Roll and trim angles were set with the aid of a digital level. Yaw angles were set using a vernier indicator on the yaw arm of the dynamometer. A differential pressure sensor monitored the speed of the water flow through the channel's contraction section, and a pitot static tube measured the open-channel velocity. The depth of in the channel was just under 2 ft, so that the flow was slightly supercritical, but there was no evidence of standing waves or a hydraulic jump if the channel inlet lip and the water level were carefully adjusted.

3.2 Pressure scanning

The piezometer orifices on the model's surface were formed by inserting stainless steel tubes into holes drilled perpendicular to the bottom and securing them with iso-cyanurate cement. The model had a total of 91 orifices, 3/64 of an inch diameter. The orifices were arranged along three major buttocks, one of which was 3/32 of an inch in from the chine, another 1/16 of an inch from the keel, and the third midway between the model centerline and the chine. A few auxiliary orifices were placed in buttocks midway between the major buttocks, and the arrangement was altered in the forward sections to account for the dimunition of beam. The general arrangement of these orifices is shown in figure 1. The stainless tubes were plumbed with vinyl tubing and connected to a model J7 Scanivalve. This device, familiar to wind tunnel experimenters, but not common in hydrodynamic testing, acts as a fluid rotary switch, allowing one transducer to scan 48 pressure ports sequentially. In this setup, a modular Scanivalve system was used, with a motor drive, a slide wire position encoder, and 2 scanners, for a total of 96 ports (91 taps, 2 static calibrations, 3 spare). The output from the transducers was fed to an X-Y recorder, along with the position information, to form a "square wave" record of the pressure distribution. The transducers are differential, single crystal silicon pressure sensors. A schematic of the system is shown as figure 2.

This type of pressure scanner has many other possible uses in hydrodynamic testing. Wake testing, using several five-hole pitot tubes could be conducted using only one transducer, and with a dead weight calibrator plumbed to one channel of the scanner, the setup would be self-calibrating. Tidal and estuary models could monitor hundreds of water levels at a time. Scanning speeds can be as high as several ports a second. The manufacturer's literature shows several other applications, other types of analog and digital channel indicators are available, as well as solenoid and stepper motor drives.

3.3 Flow visualization

The flow visualization scheme using fluorescent tufts was first outlined in Crowder (1977), and later expanded in Stineberg (1983). The problem with tufts is one of visibility; if they are large enough to see easily, they disturb the flow. The ultra-violet photography technique outlined in the references solves this problem neatly; by causing the tufts to flouresce, so they appear larger, then filtering out the ultraviolet illumination, the only light hitting the film plane is the visible light emanating from the tufts. This allows the tufts to be small enough that their disturbance to the flow is nil. As Crowder points out, concurrent flow visualization makes the interpretation of pressure distributions much simpler (in extreme cases, possible).

It was found that the available nylon monofilament material (1 lb test fly fishing leader) was too stiff to accurately align itself to the flow at the relatively low speed of this test, and sewing thread treated with flourescent dye (Sandoz Leucophor EFR, 100 to 1 in a half vineger, half water solution) was used instead. At higher speeds, the nylon materials used by Crowder and Stineberg are needed for durability. It was found that the isocyanurate cement used by Stineberg to attach the tufts "wicked" along the tufts when applied to the acrylic, and a nitrocellulose cement used in model airplane construction (Ambroid) was used instead. Normal acrylic sheet materials absorb ultra-violet light, and are themselves slightly flourescent, so the 3/4 in thick windows in the CWC were replaced with Ultra-violet Transparent acrylic, and a bank of "black light" flourescent tubes illuminated the test section. The model was also constructed of UVT acrylic.

3.4 Test Matrix

Using the SNAME recommended right hand rule co-ordinate system, tests will be conducted with -5, 0, 5, and 10 degrees of yaw, 0, 2, 4 and 6 degrees of trim, and -10, 0, 10 and 20 degrees of roll. Eliminating symmetrical redundancies, this means a total of 64 test runs to be completed. At the time of this writing (6-30-86) 2 runs have been completed. All data will be taken at the same speed, 6.73 feet per second, for a speed coefficient of 1.5, and a volumetric Froude number of 1.72. This corresponds to the lowest speed coefficient to be tested at Stevens, and is just at the inception of planing lift.

4. Results and Discussion

4.1 General Behavior

Since the data is but hours old, the discussion of results must be brief. Only two complete, reliable runs have been made, one at zero degrees yaw, 4 degrees trim, and 0 degrees roll, and a run with 10 degrees of roll and yaw at the same trim. Many other trial runs have been made at other angles to observe the system's behavior, but with no data taken.

There have been no surprises with the behavior of the model in the channel. It is definitely gaining dynamic lift at the speed tested, as seen by a rise in the CG. Yaw alone reduces lift considerably for a given trim, leading to drafts below the still water level, but accompanying roll with yaw, as would be seen during a full-scale maneuver, restores the dynamic lift. The model planes with it's chines wet at all attitudes examined so far, although the transom is clear. This wetting of the inside chine (I.E. the starboard chine for a turn to the right) may produce negative pressures in the topsides as the water flows over the chine, unfortunately, there are no ports in the area in question.

The wake of the model at high angles of yaw is deflected off the channel walls less than a boat length behind the model, leading to a suspicion that there may be some disruption of the flow field around the model. A smaller model might alleviate this problem, but the pressures would also be smaller, and the ports harder to accurately locate.

4.2 Flow Visualization

While photographs of the flow patterns observed during the completed tests are not available at the time of this writing, some discussion of the results can be made. The patterns seen during upright running very much resembled those shown in many references on planing flow. The results from the yawed and heeled case were instructive. In general, the flow along the hull aligned itself much more along the buttocks than would be imagined. Restated, there is little evidence of flow across the breadth of the hull when yawed and heeled except in the area near the keel, where there is strong cross flow. No evidence of separation was noted, although further examination might reveal areas of separation.

4.3 Pressure Distributions

A presentation of even the skimpy data collected thus far would be far to lengthy for this paper, however, fig 3 gives a feel for the distributions. The section in question is just forward of amidships, and has very little curvature, as it is just starting the transition from the prismatic afterbody to the developed forebody.

The upright distribution shows qualitative agreement with the results of Kapyran (1955). The heeled and yawed results show the effects of the increased local angle of attack of the port side, and the suction created on the starboard side. It's interesting to note the high positive pressures at the starboard chine, and the difference in pressure between the 2 centerline ports, which seems to reflect the cross-flow noted by the flow visualization tufts. Overall, the pattern on each side seems to follow the same trend as the upright case, I.E. rising roughly parabolicly to a high at the chines.

References

Colburn , W. Simpson, W. and Phelps, V., "**The U.S. Coast Guard Academy Circulating Water Channel**", Marine Technology, Vol. 18, #3, July 1981, pp 253-263.

Clement, Eugene P., "**How to Use the SNAME Small Craft Data Sheets For Design and for Resistance Prediction**", Society of Naval Architects and Marine Engineers, New York, 1963.

Crowder, J.P., "**Fluorescent Mini-Tufts for Non-Intrusive Flow Visualization**", McDonnell Douglas Report MDC J7374, February, 1977.

Doctors, L. J., "**Representation of Three-Dimensional Planing Surfaces by Fiuite Elements**", 1st Conference on Numerical Ship Hydrodynamics, DTNSRDC, Washington, D.C., 1975.

Kapyran, Walter J., and Boyd, George M., **Hydrodynamic Pressure Distributions Obtained During a Planing Investigation of Five Related Prismatic Surfaces,** Technical Note 3477, National Advisory Commitee for Aeronautics, Washington, D.C., September, 1955.

Morris, Ralph, "**Lofting by the Numbers**", WoodenBoat, #52, May/June 1983, pp 69-72.

Rohm and Haas, "**Plexiglass Design and Fabrication Data**", PL-1p, -2k, -4N, -7N, -9h, Philadelphia, PA, 1983-4.

Stineberg, D.R., and Treaster, A.L., "**Water Tunnel Flow Visualization by the use of Fluorescent Mini-Tufts**", Third Int'l Symposium on Flow Visualization, Ann Arbor, MI, September, 1983.

Wellicome, J.F., and Jahanger, J.M., "**The Prediction of Pressure Loads on Planing Hulls in Calm Water**", Transactions, Royal Institute of Naval Architecture, London, 1978, pp 53-70.

Sources of Supply

Aircraft Spruce and Specialty, Box 424, Fullerton, CA 92632 (Super T)

Industrial Polychemical Services, P.O. Box 379, Gardena, CA 92074 (Weld-On-40)

Local Aodak Dealer (Wratten filters for UV Photography)

Local Plastics distributor (plastic sheet)

Sandoz Color and Chemical (Leucophor EFR)

Scanivalve Corporation, P.O. Box 20005, 10222 San Diego Misson Road, San Diego, CA 92120

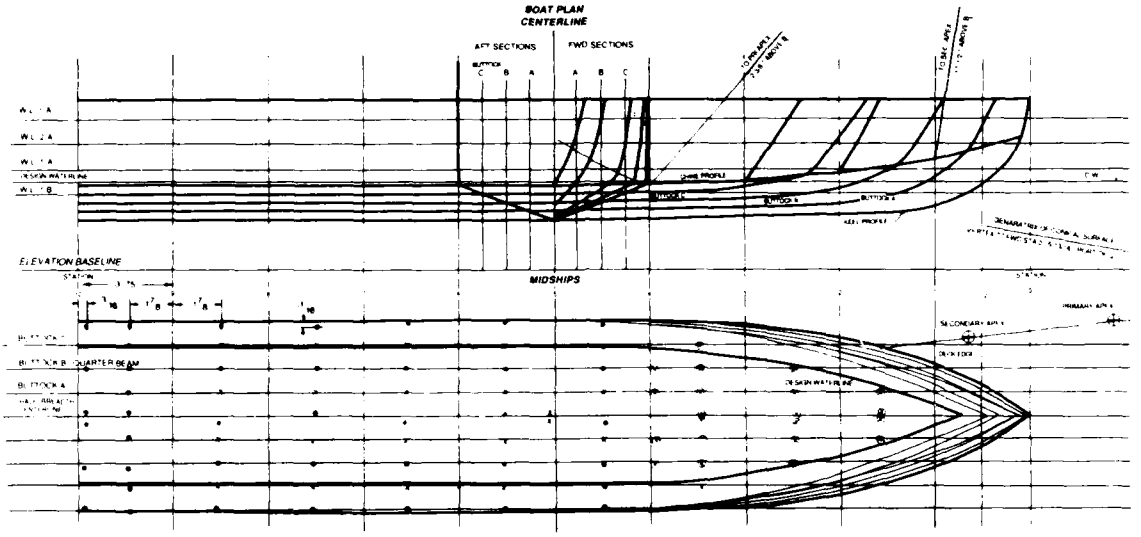

Figure 1. Lines Plan and Port Arrangement

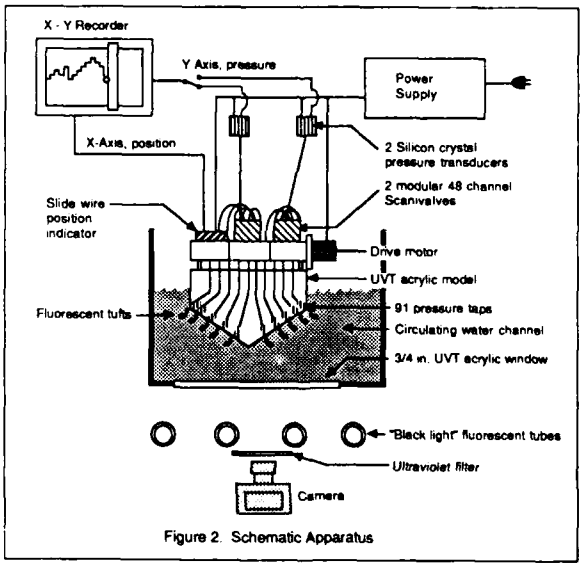

Figure 2. Schematic Apparatus

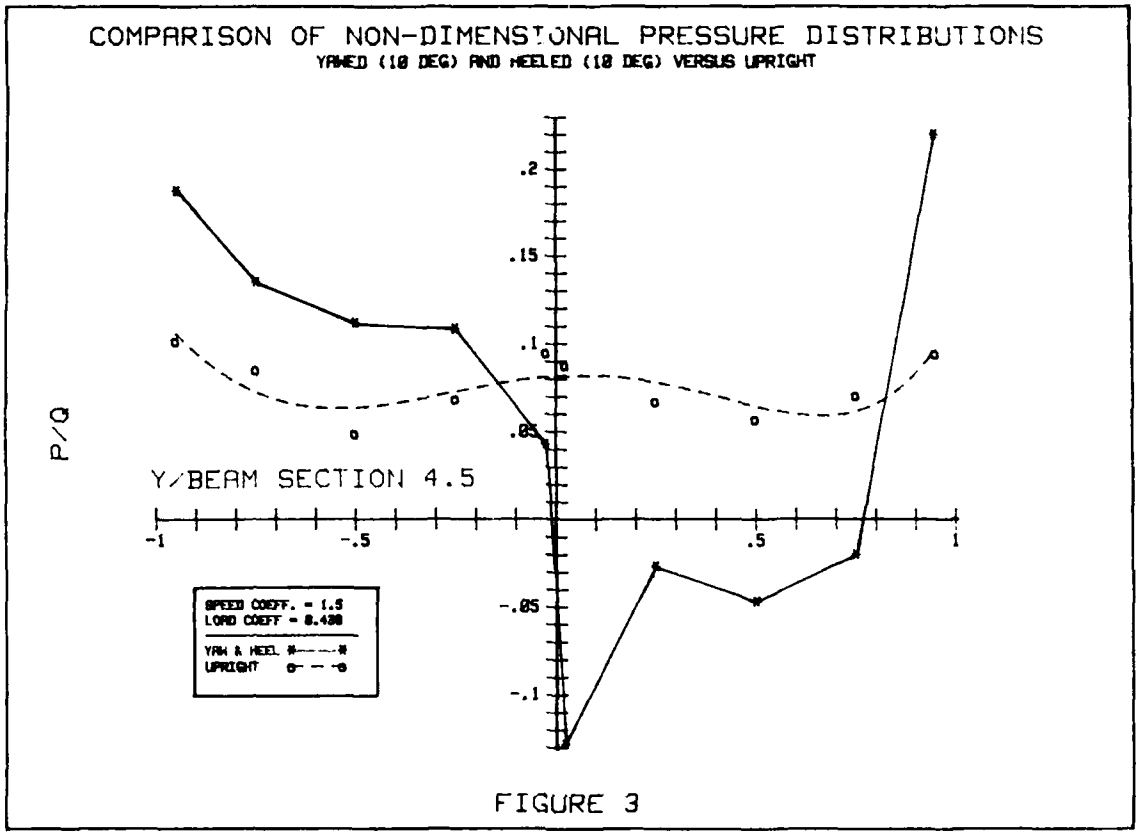
COMPARISON OF NON-DIMENSIONAL PRESSURE DISTRIBUTIONS
YAWED (10 DEG) AND HEELED (10 DEG) VERSUS UPRIGHT
P/Q
Y/BEAM SECTION 4.5
.2
.15
.1
.05
-.05
-.1
-1
-.5
.5
1
SPEED COEFF. = 1.5
LORD COEFF = 0.488
YAW & HEEL
UPRIGHT

FIGURE 3

Measuring Ship-Model Resistance with a "Mini" Towing Tank

C.C. Hsiung*, O. Cochkanoff*, Gui Qianyi**, and Ali Hazzouri**
*Professor **Graduate Student

Department of Mechanical Engineering
Technical University of Nova Scotia
Halifax, Nova Scotia, Canada B3J 2X4

ABSTRACT

A "mini" towing tank was established by installing a towing carriage over an existing wave flume of 1m x 1m x 30m. A mechanical balance system was designed and built to measure ship-model resistance for various speeds. Turbulence stimulation and blockage effect are considered to calibrate the resistance measurement on a standard Series 60 Block 60 model. A procedure will be developed for routine ship-model resistance tests. Instruments for seakeeping experiments and using micro-computers for data acquisition and control are being devised. The tank can be used for class demonstration and research projects for students in the Naval Architecture and Ocean Engineering Program at TUNS.

1. Introduction

With the establishment of a graduate program of Naval Architecture at the Technical University of Nova Scotia (TUNS), a hydrodynamic experimental faciltiy was deemed necessary to support the teaching and research efforts. However, with the limited funding situation, building a towing tank test facility of proper size was impossible at the time. Attention has been turned to the utilization of the existing facilities on campus. In the Hydraulics Laboratory of TUNS, there is a concrete wave flume of 1m x 1m x 30m (Fig. 1). A hinged flap-type wave-maker at one end of the flume (Fig. 2) can generate regular waves of a height up to 0.3 m. It has been used for various test related to waves.

In the past, the second author supervised a group of senior mechanical engineering students to design and construct a towing carriage and rail system (Fig. 3) over the wave flume as a senior design project [1]. The measuring devices were not developed then. Later, a simple strain-gauge resistance dynamometer was installed. A standard 0.61m (2 ft.) Series 60 Block 60 model was built for tests and calibration. However, the electrical recorder picked up an excessive amount of noise. This led to the current design of a mechanical resistance dynamometer (Fig. 4).

2. Towing Facility

The basic structure of the towing facility is the carriage and rail assembly. The carriage provides the support structure for the model, measuring devices and driving unit. The carriage, instead of being towed by a cable system is self-propelled and driven by a 0.25 horsepower DC motor. It can reach a maximum velocity of 2.44 m/sec (8ft/sec), and sustain a maximum model resistance of 9.1 kg. (20 lbs.). The motor control unit permits the carriage to be run in both forward and reverse directions at the same speed with a maximum acceleration or deceleration of 1.22 m/sec^2 ($4ft/sec^2$) to reach the designated operating speed. It has a brake mode, which causes the driving motor to act as a braking generator and to brake itself effectively, thus eliminating the need for mechanical braking. Moreover, a limit-switch is installed at each end of the carriage. The driving motor is switched off automatically at the end of the rail or when an obstacle is encountered by the carriage. The control unit also operates with a feedback sensing system. This permits the operator to select an operating speed and have the carriage speed remain constant even though the load may be fluctuating.

The self-propelled towing carriage requires the installation of a power cable system to provide DC current to the motor. The cable system is mounted, or hung on small trolleys on a track which is parallel to the rails. The cable is towed or pushed by the carriage as it moves in the forward or reverse directions. As shown in Fig. 6, looped flat cables run on small trolleys inside the square tubing. The flat cable has 25 wires containing both power and data transmitting channels.

The rails are standard steel channels, designed to be mounted along one of the

flanges on a double nut arrangement for level adjustment (Fig. 7). The upper flange is the supporting surface for the carriage wheels, and the outside surface of the web is for the guide wheels. The two running surfaces are machined to meet the required smoothness in order to ensure proper operation of the towed model and to reduce unnecessary mechanicl noise while taking measurements. The rails are supported every 0.508 m (20") along its 27.43 m (90') except at the viewing port. The support plates are epoxied to the top of the cement tank walls.

3. Resistance Dynamometer and Resistance Test

A mechanical resistance dynamometer has been designed and constructed to be installed in the carriage as shown in Fig. 4 and Fig. 5. It is a very simple design as suggested in Ref. [2] with a diamond-shaped balance system. The measured resistance is balanced by a calibrated spring and is measured on the recording drum. A balance weight system can be used to adjust for large resistance offsets.

A 0.61 m (2 ft.) Series 60 Block 60 model was build for test and calibration. The model was first run without turbulance stimulation. In the later runs, a 0.3175 cm (1/8 inch) rod was placed about 5.08 cm (2") in front of the model as the turbulance stimulator [3]. The test results are shown in Fig. 8. It has been found that the blockage effect [4] is minimum for the model of such size, and that the dicrepancy between test results will be mainly due to the measurement error and scale effect of the "smallness" of the model.

4. Concluding Remarks

A "mini" towing tank facility has been established at the Technical University of Nova Scotia by installing a self-propelled carriage and rail assembly over the existing wave flume. A 2 ft. Series 60 Block 60 model has been employed to calibrate the resistance measurements of the "home made" mechanical resistance dynamometer. The initial tests (Fig. 8) have shown less than satisfactory results. The next step will be to increase the model size to say 3 ft. (.914 m), to reduce the scale effect. The blockage effect then may have to be included for consideration. Eventually, a reliable test procedure will be implemented for routine ship-model resistance tests.

Instruments for seakeeping tests are being developed, and improvement of the wave-generator is under consideration. Data acquisition and processing will be by micro-computer. The micro-computer will also be employed to control the carriage and the wave-generator. This "mini" towing tank facility can be a very practical and useful tool for class demonstrations and research projects for the Naval Architecture and Ocean Engineering Program at TUNS.

ACKNOWLEDGMENTS

The authors would like to acknowledge the Civil Engineering Department at TUNS for permission to use their Hydraulic Laboratory. Thanks are extended to Messrs. A. MacPherson and G. Richardson for their technical support and to Mrs. Cathy Wood for typing this report.

REFERENCES

1. Forbes, B.M., et at, (1980): Instrumentation of a Tow Tank Facility. Design Project 377 Report, Mechanical Engineering Department, Technical University of Nova Scotia.

2. Barnaby, K,C., (1948): Basic Naval Architecture, Anchor Press.

3. Murray, A.B. (1959): Methods for Inducing Turbulence for Small Models at Davidson Laboratory. Proceedings of 12th ATTC.

4. Scott, J.R., (1966): A Blockage Corrector. TRANS. RINA, Vol. 108.

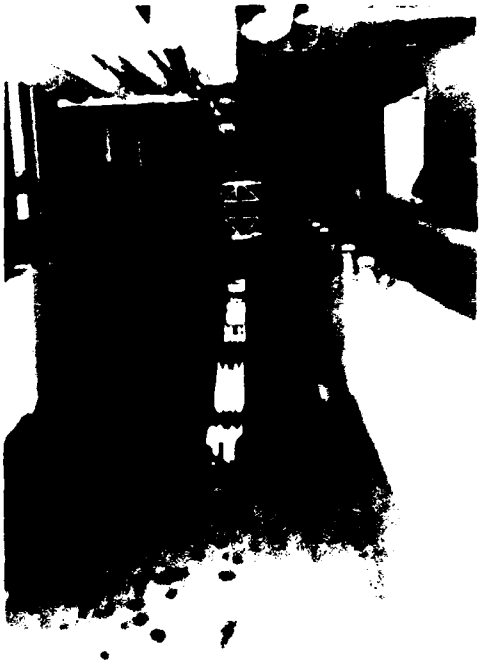

Fig. 1 Side View of the Tank

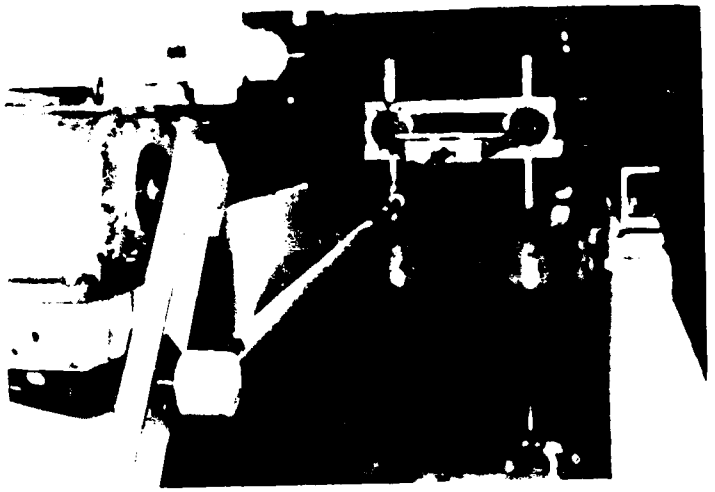

Fig. 2 Wave-Generator

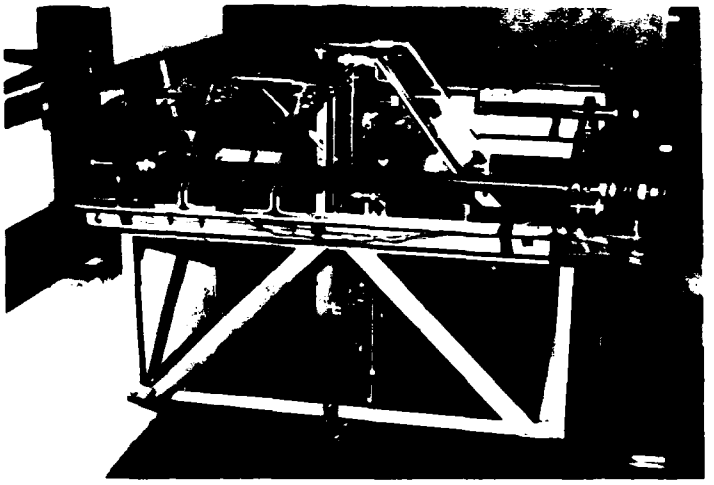

Fig. 3 Towing Carriage

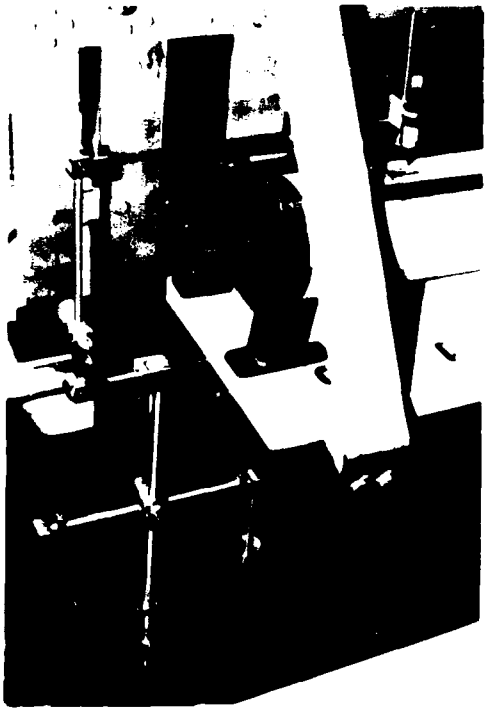

Fig. 4 Resistance Dynamometer

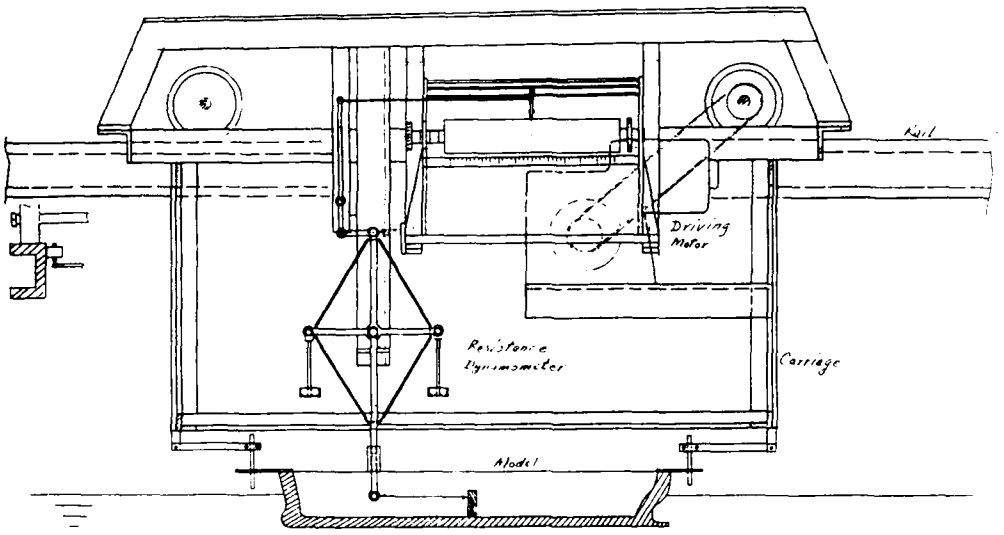

Fig. 5 Carriage/Rail/Dynamometer/ Model Schematic Drawing

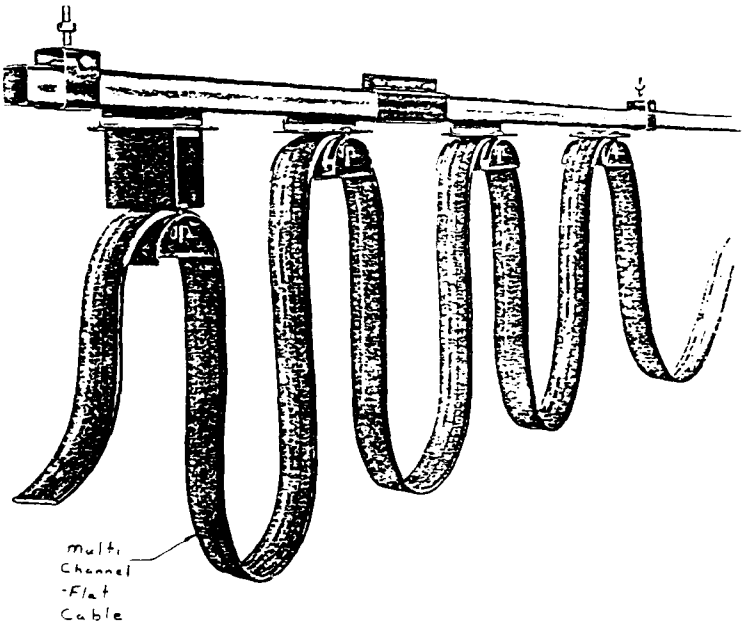

Fig. 6 Looped Flat Cables

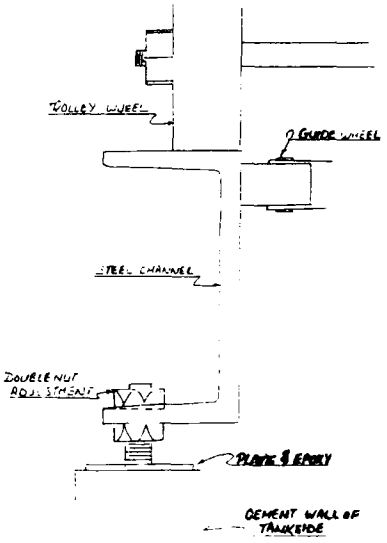

Fig. 7 Rail Schematic Drawing

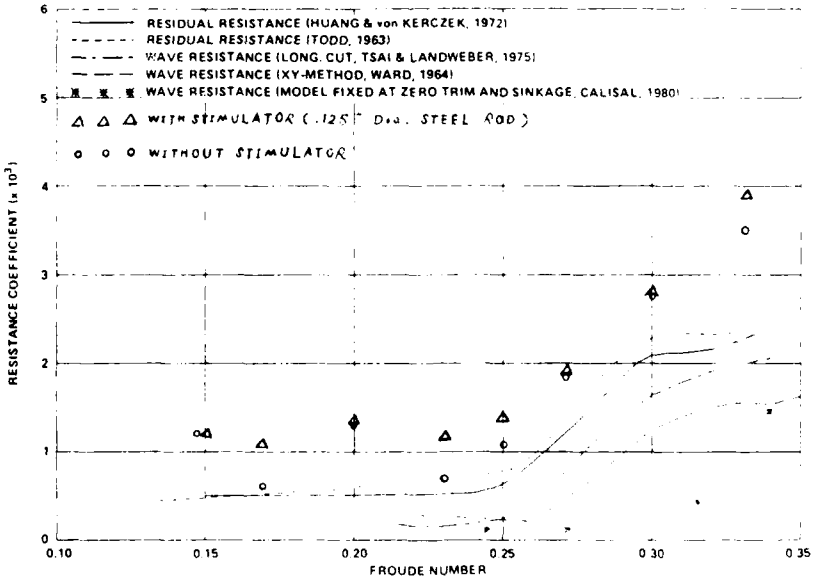

Fig. 8 Series 60 Block 60
Experimental Data

ANALYTICAL APPROXIMATION FOR STEADY SHIP WAVES AT LOW FROUDE NUMBERS

by
Francis Noblesse
David Taylor Naval Ship R&D Center
Bethesda, MD 20084

ABSTRACT

A simple analytical relationship between a ship-hull form and its steady far-field Kelvin wake is obtained by considering the low-Froude number limit of the Neumann-Kelvin theory. In particular, this relationship predicts the occurrence of a sharp peak in the amplitude of the waves in the far-field Kelvin wake at an angle, α, from the ship track that is smaller than the Kelvin-cusp angle of 19°1/2 for a hull form which has a small region of flare and is wall sided elsewhere, if the Froude number is sufficiently small. An explicit relationship between the angle, φ, between the ship track and the tangent to the ship mean waterline in the region of flare and the corresponding "wave-peak" angle α in the Kelvin wake is obtained. For instance, this relationship predicts the occurrence of a sharp peak in wave amplitude at an angle α in the Kelvin wake equal to 14° for a hull having a small region of flare within which the waterline-tangent angle φ is approximately equal to either 30° or 74°. This theoretical result may explain the bright returns that have sometimes been observed in SAR images of ship wakes at angles smaller than the Kelvin-cusp angle. The low-Froude-number asymptotic analysis of the Neumann-Kelvin theory presented in this study also predicts that the wave-resistance coefficient is $O(F^2)$, where F is the Froude number, for a ship form with a region of flare, $O(F^4)$ for a ship form that is wall sided everywhere and has either a bow or a stern (or both) that is neither cusped nor round, and $O(F^6)$ for a wall-sided ship form with both bow and stern that are either cusped or round.

1. INTRODUCTION

It has been observed, see for instance Fu and Holt (1982) and McDonough et. al. (1985), that SAR (Synthetic Aperture Radar) images of ship wakes sometimes reveal bright returns along rays at angles from the track of the ship smaller than the Kelvin-cusp angle of 19°1/2. A plausible explanation for these surprising observations was proposed by Scragg (1983) who considered a simple ship bow form with large flare for which he found that the zeroth-order slender-ship approximation to the far-field wave-amplitude function given in Noblesse (1983) predicted a sharp peak in the value of the amplitude of the divergent waves at an angle from the track of the ship equal to approximately half the bow entrance angle. This numerical result of Scragg was confirmed by Barnell and Noblesse (1986) who also found that the peak in the amplitude of the divergent waves becomes sharper as the value of the Froude number decreases, and thus suggested that the occurrence of a sharp peak in the amplitude of the far-field Kelvin waves was a large-flare low-Froude-number feature.

The numerical studies of Scragg and of Barnell and Noblesse are based on two simple approximations to the far-field wave-amplitude function, namely the Michell thin-ship approximation for which no peak was found and the zeroth-order slender-ship approximation which exhibited a peak as was already noted, so that it is not clear from these studies whether a more realistic mathematical model for the far-field wave-amplitude function, such as that provided by the Neumann-Kelvin theory, would also predict the occurrence of peaks in the

amplitude of the far-field Kelvin waves. Furthermore, the numerical results obtained by Scragg and by Barnell and Noblesse correspond to a particular ship form and thus provide little physical insight into the origin of the predicted peak in the amplitude of the far-field Kelvin waves, specifically the manner in which such a peak is related to the shape of the ship hull.

A complementary analytical study of the low-Froude-number limit of the Neumann-Kelvin theory for an arbitrary ship form is thus presented here. This asymptotic analysis of the Neumann-Kelvin theory provides a simple analytical relationship between a ship-hull form and its steady far-field Kelvin wake. In particular, this relationship predicts the occurrence of a sharp peak in the amplitude of the waves in the far-field Kelvin wake at an angle, α, from the ship track that is smaller than the Kelvin-cusp angle of 19°1/2 for a hull form which has a small region of flare and is wall sided elsewhere, if the value of the Froude number is sufficiently small. A simple explicit relationship between the angle, φ, between the ship track and the tangent to the ship mean waterline in the region of flare and the corresponding wave-peak angle α in the Kelvin wake is given and depicted in Figure 3b. For instance, this figure predicts the occurrence of a sharp peak in the amplitude of the divergent or transverse waves at an angle α in the Kelvin wake equal to 14° for a hull having a small region of flare within which the waterline-tangent angle φ is approximately equal to 30° or 74°, respectively. This analytical result may explain the bright returns that have sometimes been observed in SAR images of ship wakes at angles smaller than the Kelvin-cusp angle.

The low-Froude-number asymptotic analysis of the Neumann-Kelvin theory presented in this study also predicts that the wave-resistance coefficient is $O(F^2)$, where F is the Froude number, for a ship form with a region of flare, $O(F^4)$ for a ship form that is wall sided everywhere and has either a bow or a stern (or both) that are neither cusped nor round, and $O(F^6)$ for a wall-sided ship form with both bow and stern that are either cusped or round.

More precisely, the low-Froude-number asymptotic approximation (50) to the far-field wave-amplitude function K(t) shows that the main contributions to the function K(t) stem from several particular points on the mean waterline. These are the bow and the stern, on one hand, and (usually but not always) one (or several) point(s) of stationary phase. Indeed, the number of these points of stationary phase, and their position on the waterline, depend on the value of t and on the shape of the waterline. The first two terms in the low-Froude-number asymptotic expansions for the contributions $K_{B,S}$ of the bow and stern and the contributions $K_{\pm}$ of the points of stationary phase in equation (50) are given by equations (51)-(55) and (59)-(62), respectively. The second-order terms in these asymptotic expansions are defined by complex expressions. However, the first-order terms provide simple approximations defined explicitly in terms of the geometrical characteristics of the hull and the velocity components in the tangential directions $\vec{t}$ and $\vec{n} \times \vec{t}$ to the hull (see Figure 2). In particular, these low-Froude-number asymptotic expansions show that the contributions K_B and K_S of the bow and stern are O(1) except if the bow or stern is cusped or round, in which case we have $K_{B,S} = O(F^2)$. The contribution of a given point of stationary phase is $O(1/F)$, and thus is dominant, if the hull has flare at this point; otherwise, that is if the hull is wall sided at the point of stationary phase, its contribution is O(F). The low-Froude-number approximation (50) also shows that we have $K(t) = O(1/t^3)$ as $t \to \infty$. In fact, this result is valid for any value of the Froude number.

The latter result implies that the lines along which the steepness of the short divergent waves in the far-field Kelvin wake takes given large values, say 1/7 and 1/15, are parallel to the ship track, as was found in Figure 21 of Barnell and Noblesse (1986) by using the Michell thin-ship approximation for a simple ship form. The Neumann-Kelvin theory therefore predicts that the far-field Kelvin wake contains three distinct regions: (i) a narrow constant-width inner region bordering the track of the ship where no divergent gravity waves can exist, (ii) an outer region where the usual transverse and divergent waves are present, and (iii) an intermediate region at the boundary between the inner and outer regions where short steep divergent waves can be found. In reality, surface tension and possibly also viscosity must evidently be taken into account in the vicinity of the track of the ship.

2. STATIONARY-PHASE APPROXIMATION TO THE FAR-FIELD KELVIN WAKE

The far-field Kelvin wake may be conveniently analyzed in terms of the nondimensional far-field coordinates $(\xi,\eta,\zeta) = (X,Y,Z)\ g/U^2$, where g is the gravitational acceleration, U is the speed of advance of the ship, and (X,Y,Z) are dimensional coordinates. The mean free surface is taken as the plane $\zeta = 0$, with the ζ axis pointing upwards, and the ξ axis is chosen along the track of the ship, that is in the ship centerplane, and pointing towards the bow. The origin of the system of coordinates is placed within the ship.

Equations (4), (3a), (7) and (8) in Barnell and Noblesse (1986) yield the following expression for the elevation ζ of the free surface at a sufficiently large distance behind the ship, such that nonlinearities may be neglected:

$$\pi\zeta(\xi,\eta) = \mathrm{Re}\int_0^\infty (E_- + E_-)\ K(t)\ (1+t^2)^{1/2}\ dt, \tag{1}$$

where K(t) is the far-field wave-amplitude function and $E_\pm$ is the exponential function defined as

$$E_\pm(t;\xi,\sigma) = \exp\ [i\xi\theta_\pm(t;\sigma)], \tag{2}$$

with the phase-function $\theta_\pm$ and the parameter σ defined as

$$\theta_\pm(t;\sigma) = (1\mp\sigma t)(1+t^2)^{1/2}, \tag{3}$$

$$\sigma = \eta/(-\xi). \tag{4}$$

For a ship with port- and starboard-symmetry, as is considered here, the Kelvin wake is symmetric about the ship track $\eta = 0$. We may then restrict the analysis of the Kelvin wake to the quadrant $\eta \geq 0$, $\xi < 0$ and assume $\sigma \geq 0$. Let α be the angle between the track of the ship and the line joining the origin of the system of coordinates to the observation point (ξ,η). We thus have

$$\alpha = \tan^{-1}\sigma. \tag{5}$$

A far-field asymptotic approximation, valid as $\xi \to -\infty$, to the wave integral (1) may be obtained by applying the method of stationary phase, as is well known. The result of this classical asymptotic analysis may be found in Barnell and Noblesse (1986), for instance. Specifically, equations (28), (24a), (20b), (25a-d) and (26a-d) in this reference yield

$$(-\xi)^{1/2}\zeta(\xi,\alpha) \sim \mathrm{Re}\ \{A_-\ K(t_-)\ \exp\ [i(\xi\Theta_- - \pi/4)] + A_+ K(t_+)\ \exp\ [i(\xi\Theta_+ + \pi/4)]\}\ \text{as}\ \xi \to -\infty, \tag{6}$$

with $0 \leq \alpha < \tan^{-1}(2^{-3/2}) \simeq 19°28'$,

where $t_\pm(\alpha)$ are the values of t for which the phase-function $\theta_+(t;\alpha)$ is stationary, $\Theta_\pm(\alpha) = \theta_+(t_\pm;\alpha)$ represents the corresponding values of the phase-function $\theta_+(t;\alpha)$, and $A_\pm(\alpha)$ is the function defined as $A_\pm(\alpha) = (2/\pi)^{1/2}(1+t_\pm^2)^{1/2}/[\mp\theta''_+(t_\pm;\alpha)]^{1/2}$. The functions $t_\pm(\alpha)$, $\Theta_\pm(\alpha)$ and $A_\pm(\alpha)$ are given by

$$t_\pm(\alpha) = [1\pm(1-8\sigma^2)^{1/2}]/4\sigma, \tag{7}$$

$$\Theta_\pm(\alpha) = [3\mp(1-8\sigma^2)^{1/2}]\ [1+4\sigma^2\pm(1-8\sigma^2)^{1/2}]^{1/2}/2^{1/2}8\sigma, \tag{8}$$

$$A_\pm(\alpha) = [1+4\sigma^2\pm(1-8\sigma^2)^{1/2}]^{3/4}2^{1/4}/4\pi^{1/2}\sigma^{3/2}(1-8\sigma^2)^{1/4}, \tag{9}$$

where we have

$$\sigma = \tan\alpha \tag{10}$$

as is given by equation (5).

The far-field asymptotic approximation (6) shows that the wave pattern at any point (ξ,α), with $\xi \ll -1$ and $0 \leq \alpha < 19°28'$, consists in two elementary plane progressive waves, so-called transverse and divergent waves, as is most well known. The wavelengths $\lambda_\pm$ and the directions of propagation $\beta_\pm$, measured from the track of the ship, of the transverse (λ_-,β_-) and divergent (λ_-,β_-) waves at an angle α from the track of the ship are given by

$$\lambda_\pm(\alpha) = 2^{1/2}16\pi\sigma^2/[3\mp(1-8\sigma^2)^{1/2}]\ [1-4\sigma^2\pm(1-8\sigma^2)^{1/2}]^{1/2}, \tag{11}$$

$$\beta_\pm(\alpha) = \cos^{-1}\{2^{1/2}2\sigma/[1+4\sigma^2\pm(1-8\sigma^2)^{1/2}]^{1/2}\}. \tag{12}$$

We have

$$1 \geq \lambda_-/2\pi \geq 2/3 \geq \lambda_-/2\pi \geq 0 \text{ and} \tag{13}$$

$$0 \leq \beta_- \leq \sin^{-1}(1/3^{1/2}) \simeq 35°16' \leq \beta_- \leq 90°. \tag{14}$$

Equation (6) shows that the amplitudes of the transverse and divergent waves in the Kelvin wake are asymptotically equal to $A_\pm K(t_\pm)/(-\xi)^{1/2}$ as $\xi \to -\infty$. The steepnesses, say $s_\pm$, of these waves then are given by $s_\pm = A_\pm|K(t_\pm)|/\lambda_\pm(-\xi)^{1/2}$. We then have

$$(-\xi)^{1/2}s_\pm(\xi,\alpha) \sim S_\pm|K(t_\pm)| \text{ as } \xi \to -\infty, \tag{15}$$

where the functions $S_\pm(\alpha)$ are defined as $S_\pm(\alpha) = A_\pm(\alpha)/\lambda_\pm(\alpha)$. Equations (9) and (11) then yield

$$S_\pm(\alpha) = [3\mp(1-8\sigma^2)^{1/2}]\ [1-4\sigma^2\pm(1-8\sigma^2)^{1/2}]^{1/2}\ [1+4\sigma^2\pm(1-8\sigma^2)^{1/2}]^{3/4}/2^{1/4}64\pi^{3/2}\sigma^{7/2}(1-8\sigma^2)^{1/4}. \tag{16}$$

Equations (7), (8), (9), (10) and (16) show that we have

$$t_- = 0,\ \Theta_- = 1,\ A_- = (2/\pi)^{1/2} \tag{17a,b,c}$$

$$\text{and } S_- = 1/2^{1/2}\pi^{3/2} \text{ for } \alpha = 0, \tag{17d}$$

$$t_+ \sim 1/2\alpha,\ \Theta_+ \sim 1/4\alpha,\ A_+ \sim 1/2\pi^{1/2}\alpha^{3/2} \tag{18a,b,c}$$

$$\text{and } S_+ \sim 1/16\pi^{3/2}\alpha^{7/2} \text{ as } \alpha \to 0, \tag{18d}$$

$$t_\pm = 1/2^{1/2} \text{ and } \Theta_\pm = 3(3/2)^{1/2}/4 \tag{19a,b}$$

$$\text{for } \alpha = \tan^{-1}(1/2^{3/2}) \simeq 19°28',$$

$$A_\pm \sim 3/\pi^{1/2}6^{1/4}(1-8\sigma^2)^{1/4} \text{ and} \tag{19c}$$

$$S_\pm \sim 9/4\pi^{3/2}6^{1/4}(1-8\sigma^2)^{1/4} \tag{19d}$$

$$\text{as } \alpha \to \tan^{-1}(1/2^{3/2}).$$

The stationary-phase values $t_\pm(\alpha)$, the phase-functions $\Theta_\pm(\alpha)$, the amplitude-functions $A_\pm(\alpha)$ and the steepness-functions $S_\pm(\alpha)$ are depicted in Figures 1a and 1b, which correspond to the transverse and divergent waves, respectively.

It may be seen from these figures and from equations (19c) and (19d) that the amplitude-functions $A_\pm(\alpha)$ and the steepness-functions $S_\pm(\alpha)$ are singular at the Kelvin cusp line $\sigma^2 = 1/8$, $\alpha = \tan^{-1}(1/2^{3/2}) \simeq 19°28'$, in accordance with the well-known fact that the asymptotic approximation (6) is not uniformly valid at the boundary of the Kelvin wake. A complementary asymptotic approximation, expressed in terms of Airy functions, valid at and near the Kelvin cusp line is given in Ursell (1960) for the particular case of the Kelvin wave pattern due to a concentrated pressure point at the free surface. However, Ursell's more complex asymptotic approximation will not be considered here because the simple asymptotic approximation (6) is little affected by the weak singularity $(1-8\sigma^2)^{-1/4}$ for points (ξ,α) inside the Kelvin wake and not too near the cusp line $\alpha \simeq 19°28'$, in which we are mostly interested in this study.

Equation (11) yields

$$\lambda_- \sim 8\pi\alpha^2 \text{ as } \alpha \to 0. \tag{20}$$

This approximation and the approximation (18b) show that there are an infinite number of divergent waves with indefinitely shorter wavelength in the vicinity of the track of the ship, as is well known. It may be seen from Figure 1b and equations (18a,c,d) that the stationary-phase value $t_+(\alpha)$, the amplitude-function $A_+(\alpha)$ and the steepness-function $S_+(\alpha)$ are unbounded in the limit $\alpha \to 0$. Equations (18a,c,d) yield

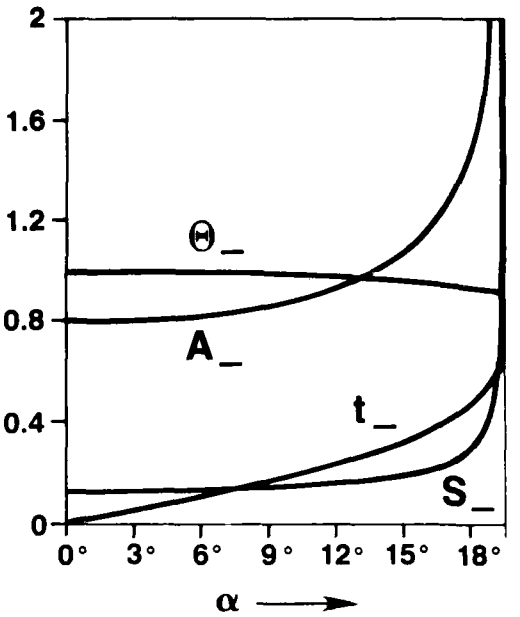

Fig. 1a - The Stationary-Phase Value $t_-(\alpha)$, the Phase-Function $\Theta_-(\alpha)$, the Amplitude-Function $A_-(\alpha)$ and the Steepness-Function $S_-(\alpha)$ Corresponding to the Transverse Waves in the Kelvin Wake

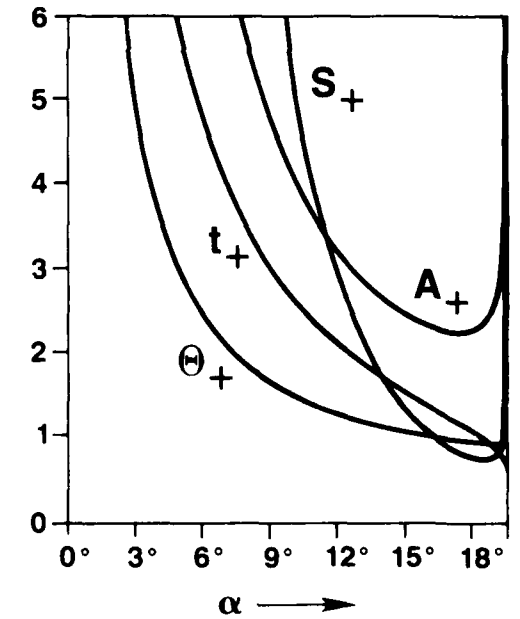

Fig. 1b - The Stationary-Phase Value $t_+(\alpha)$, the Phase-Function $\Theta_+(\alpha)$, the Amplitude-Function $A_+(\alpha)$ and the Steepness-Function $S_+(\alpha)$ Corresponding to the Divergent Waves in the Kelvin Wake

$$A_+ \sim (2/\pi)^{1/2}t_+^{-3/2} \text{ and} \tag{21a}$$

$$S_+ \sim t_+^{-2}/2^{1/2}\pi^{3/2} \text{ as } t_+ \to \infty. \tag{21b}$$

Equations (21a) and (6) show that the amplitude of the divergent waves, given by $A_+|K(t_+)|/(-\xi)^{1/2}$, vanishes at the track of the ship if we have

$$t^{3/2}K(t) \to 0 \text{ as } t \to \infty. \tag{22}$$

Furthermore, it is shown in Barnell and Noblesse (1986) that the asymptotic approximation (6) is uniformly valid at the track of the ship if condition (22) is verified. It may be seen from equations (21b) and (15) that the steepness of the divergent waves, given by $S_+|K(t_+)|/(-\xi)^{1/2}$, is unbounded at the track of the ship if we have

$$t^{7/2}|K(t)| \to \infty \text{ as } t \to \infty. \tag{23}$$

Both conditions (22) and (23) can be satisfied simultaneously if we have

$$K(t) \sim 1/t^{\mu} \text{ as } t \to \infty \text{ with } 3/2 < \mu < 7/2. \tag{24}$$

In summary, the asymptotic approximation (6) expresses the far-field wave pattern of a ship at a point (ξ,α), with $\xi \ll -1$ and $0 \leq \alpha < 19°28'$, as the sum of a transverse wave and a divergent wave. The phase $\xi\Theta_\pm(\alpha)\pm\pi/4$ of these two waves are defined explicitly in terms of ξ and α; and their amplitudes $A_\pm(\alpha)K(t_\pm)/(-\xi)^{1/2}$ are given by the product of the functions $A_\pm(\alpha)/(-\xi)^{1/2}$, which are also defined explicitly in terms of ξ and α, and the far-field wave-amplitude function $K[t_\pm(\alpha)]$, which depends on the speed (Froude number) and the shape of the ship. The far-field wave-amplitude function is now considered.

3. BASIC EXPRESSIONS FOR THE FAR-FIELD WAVE-AMPLITUDE FUNCTION

The far-field wave-amplitude function K(t) may be conveniently defined in terms of the nondimensional near-field coordinates $(x,y,z) = (X,Y,Z)/L$, where L is the length of the ship. In the Neumann-Kelvin theory, the function K(t) is given by the sum of an integral around the mean waterline of the ship and an integral over the mean wetted-hull surface. Specifically, for a ship with port and starboard symmetry, as is considered here, the function K(t) may be expressed in the form

$$K(t) = K_+(t) + K_-(t), \tag{25}$$

where the functions $K_\pm$ are given by

$$F^2K_\pm(t) = \int_C E_\pm(n_x^2 + t_x\phi_t - n_z t_y \phi_d + i\nu^2 p\phi)t_y \, dl + \nu^2 \int_h \exp(\nu^2 p^2 z) E_\pm(n_x + \nu^2 p^2 \phi n_\pm) \, da, \tag{26}$$

as is shown in Noblesse (1983). In this equation, F is the Froude number defined as

$$F = U/(gL)^{1/2}, \tag{27}$$

ν is its inverse, that is

$$\nu = 1/F, \tag{28}$$

p is defined as

$$p = (1+t^2)^{1/2}, \tag{29}$$

and $E_\pm$ represents the exponential function

$$E_\pm = \exp[-i\nu^2 p(x \pm ty). \tag{30}$$

Furthermore, c and h represent the positive halves of the mean waterline and of the mean wetted-hull surface, respectively. The unit vector tangent to c and pointing towards the bow is denoted by $\vec{t}(t_x,t_y,0)$, and $\vec{n}(n_x,n_y,n_z)$ is the unit vector normal to h and pointing into the water, as is indicated in Figure 2. The term $n_\pm$ is defined as

$$n_\pm = -n_y + i(n_x \pm t n_y)/p. \tag{31}$$

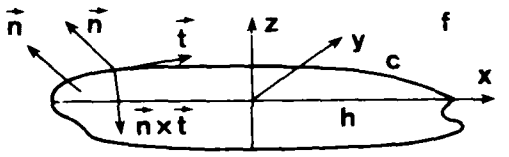

Figure 2 - Definition Sketch for a Single-Hull Ship with Port and Starboard Symmetry

Also, dl and da represent the differential elements of arc length of c and of area of h, respectively. Finally, $\phi = \phi(\vec{x})$ represents the nondimensional disturbance potential $\phi = \Phi/UL$ at the integration point $\vec{x}$ on c or h, ϕ_t represents the derivative of ϕ in the direction of the tangent vector $\vec{t}$ to c, and ϕ_d is the derivative of ϕ in the direction of the vector $\vec{n}\times\vec{t}$, which is tangent to h and pointing downwards as is shown in Figure 2.

Equations (25) and (26) express the far-field wave-amplitude function K(t) in terms of the value of the Froude number and the form of the mean wetted-hull surface, as was noted previously. More precisely, equation (26) expresses the function $K_\pm(t)$ as the sum of a line integral around the mean waterline and a surface integral over the mean wetted-hull surface of the ship. Furthermore, these integrals involve the disturbance velocity potential ϕ in their integrands. The relationship between the far-field wave pattern of a ship and its form

and speed thus is a complex one, which offers little physical insight. However, analytical approximations for the waterline and the hull integrals in equation (26) can be obtained in the limiting case when the value of the Froude number is sufficiently small. This low-Froude-number asymptotic approximation for the function K(t) is now obtained.

4. LOW-FROUDE-NUMBER LAPLACE APPROXIMATION TO THE FAR-FIELD WAVE-AMPLITUDE FUNCTION IN TERMS OF A WATERLINE INTEGRAL

For large values of $\nu = 1/F$, or more generally of νp, the exponential function $\exp(\nu^2 p^2 z)$ in the hull-surface integral in equation (26) vanishes rapidly for negative values of z. Therefore, only the upper part of the mean-wetted hull surface h yields a significant contribution in the low-Froude-number limit. More precisely, the null-surface integral can be approximated by a line integral around the mean waterline c. Furthermore, this integral can be combined with the waterline integral in equation (26). The analysis is presented in detail in Noblesse (1986a) and is briefly summarized below.

The mean waterline is represented by the parametric equations

$$x = x_0(\lambda) \text{ and } y = y_0(\lambda), \tag{32a,b}$$

where the parameter λ varies between its bow and stern values, that is

$$\lambda_B \leqslant \lambda \leqslant \lambda_S. \tag{32c}$$

In the vicinity of the mean free surface, the hull surface is represented by the parametric equations

$$x = x_0(\lambda) + z\, x_1(\lambda) + z^2 x_2(\lambda) + \ldots, \tag{33a}$$

$$y = y_0(\lambda) + z\, y_1(\lambda) + z^2 y_2(\lambda) + \ldots, \tag{33b}$$

$$\text{where } \lambda_B \leqslant \lambda \leqslant \lambda_S \text{ and } z \leqslant 0. \tag{33c}$$

The velocity potential $\phi(\lambda,z)$ on the hull surface in the vicinity of the plane $z = 0$ likewise is expressed in the form

$$\phi = \phi_0(\lambda) + z\, \phi_1(\lambda) + z^2 \phi_2(\lambda) + \ldots. \tag{34}$$

Differentiation of the functions $x_n(\lambda)$, $y_n(\lambda)$, $\phi_n(\lambda)$ with respect to the parameter λ is denoted by the superscript '; thus, we have $x_0' = dx_0(\lambda)/d\lambda$.

By using the foregoing parametric representations for the hull surface and the velocity potential, applying the Laplace method for approximating the hull-surface integral in equation (26), and combining the resulting waterline integral with that already present in equation (26), we may obtain ___ after lengthy algebraic transformations ___ the following low-Froude-number approximation for the function K(t):

$$K(t) \sim \nu^2 q^2 \int_{\lambda_B}^{\lambda_S} (E_0^{+} a_{+} + E_0^{-} a_{-})\, d\lambda \text{ as } F \to 0, \tag{35}$$

where we have

$$q = 1/p = 1/(1+t^2)^{1/2}, \tag{36}$$

$E_0^{\pm}$ is the exponential function

$$E_0^{\pm} = \exp[-i\nu^2 p(x_0 \pm t y_0)], \tag{37}$$

and $a_{\pm}$ is the amplitude function

$$a_{\pm} = u_{\pm} a_1^{\pm} + F^2 q^2 (u_{\pm})^2 a_2^{\pm} + O(F^4), \tag{38}$$

where $u_{\pm}$ is defined as

$$u_{\pm} = 1/[1 - iq(x_1 \pm t y_1)], \tag{39}$$

and the functions $a_1^{\pm}$ and $a_2^{\pm}$ are now defined.

The first-order amplitude function $a_1^{\pm}$ is given by

$$a_1^{\pm} = y_0' A_{\pm}/(1+\varepsilon^2) + 2q(x_0' \pm t y_0')(u_{\pm})^2 B_{\pm}\phi_0 + C_{\pm}\phi_0' + uD_{\pm}\phi_1/(1+\varepsilon^2) + ip(y_1\phi_0' - y_0'\phi_1), \tag{40}$$

where we have

$$\varepsilon = (y_0' x_1 - x_0' y_1)/u, \tag{41}$$

with u defined as

$$u = [(x_0')^2 + (y_0')^2]^{1/2}, \tag{42}$$

and the coefficients $A_{\pm}$, $B_{\pm}$, $C_{\pm}$ and $D_{\pm}$ are defined as

$$A_{\pm} = [(1 + py_0'/u)(1 - py_0'/u) + \varepsilon^2] + i(py_0'/u)[y_1(x_0' \pm t y_0')/u + \varepsilon], \tag{43a}$$

$$B_{\pm} = q(y_2 \mp t x_2) + i(y_1 x_2 - x_1 y_2), \tag{43b}$$

$$C_{\pm} = [(\mp t - p^2 x_0' y_0'/u^2) + (py_0'/u)^2 \varepsilon (x_1 x_0' + y_1 y_0')/u(1+\varepsilon^2)] + i[y_1(x_0' \pm t y_0')/u + \varepsilon] [px_0'/u - (py_0'/u)\varepsilon(x_1 x_0' + y_1 y_0')/u(1+\varepsilon^2)], \tag{43c}$$

$$D_{\pm} = [(x_0' \pm t y_0')/u][(1+\varepsilon^2)(y_1 \pm iqt)u_{\pm} + i(py_0'/u)\varepsilon y_1] - (py_0'/u)\varepsilon(py_0'/u - i\varepsilon). \tag{43d}$$

The second-order amplitude function $a_2^{\pm}$ is given by

$$a_2^{\pm} = -y_1' + 2u_{\pm}(\phi_0 m_2^{\pm} + \phi_1 m_1^{\pm} + \phi_2 m_0^{\pm} - i y_0' \gamma_2^{\pm}) + 6i(u_{\pm})^2[\phi_0(m_1^{\pm}\gamma_2^{\pm} + m_0^{\pm}\gamma_3^{\pm}) + \phi_1 m_0^{\pm}\gamma_2^{\pm}] - 12(u_{\pm})^3 \phi_0 m_0^{\pm}(\gamma_2^{\pm})^2, \tag{44}$$

where we have

$$\gamma_n^{\pm} = q(x_n \pm t y_n), \tag{45}$$

$$m_u^{\pm} = \mu_n + iq(y_n' \mp t x_n'), \tag{46}$$

with

$$\mu_0 = \varepsilon u, \tag{47a}$$

$$\mu_1 = x_1 y_1' - y_1 x_1' + 2(x_2 y_0' - y_2 x_0'), \tag{47b}$$

$$\mu_2 = x_1 y_2' - y_1 x_2' + 2(x_2 y_1' - y_2 x_1') + 3(x_3 y_0' - y_3 x_0'). \tag{47c}$$

In the particular case when the phase of the exponential function $E_0^{\pm}$ is stationary, that is at a point $(x_0, y_0, 0)$ where we have $x_0' \pm t y_0' = 0$, the first-order amplitude function $a_1^{\pm}$ takes the form

$$a_1^{\pm} = \pm \varepsilon [i y_0' + (p y_1 \mp i t)\phi_0' \mp u \phi_1]/(1 \pm i\varepsilon) + ip(y_1 \phi_0' - y_0' \phi_1) \quad \text{if } x_0' \pm t y_0' = 0. \tag{48}$$

Furthermore, if the hull surface intersects the plane $z = 0$ orthogonally at a point of stationary phase we have

$$a_1^{\pm} = i F^2 p y_0' \partial^2 \phi_0 / \partial x^2 \quad \text{if } x_0' \pm t y_0' = 0 \text{ and } n_z = 0, \tag{49}$$

and the amplitude function $a_{\pm}$ then is or order F^2.

The low-Froude-number asymptotic approximation to the far-field wave-amplitude function K(t) given by the waterline integral (35) is considerably simpler than the exact expression (26), which involves both a waterline integral and a hull-surface integral; and the approximate expression (35) is well suited for efficient numerical evaluation. However, expression (35) can be simplified by applying the method of stationary phase, which takes advantage of the rapid oscillations of the exponential function $E_0^{\pm}$ given by equation (37) in the low-Froude-number limit $\nu \to \infty$, or more generally in the limit $\nu p \to \infty$. This stationary-phase approximation is now obtained.

5. LOW-FROUDE-NUMBER STATIONARY-PHASE APPROXIMATION TO THE FAR-FIELD WAVE-AMPLITUDE FUNCTION

The method of stationary phase indicates that the major contributions to the integral (35) in the limit when the exponential functions $E_0^{\pm}$ are rapidly oscillating, that is if $\nu \to \infty$ or more generally $\nu p \to \infty$, stem from points where the phases of these exponential functions are stationary, that is from points where we have $x_0' \pm t y_0' = 0$, and from the end points λ_B and λ_S of the integration range, that is from the bow and the stern. This stationary-phase analysis is presented in detail in Noblesse (1986b) and only its results are given here. We have

$$K(t) \sim iq^3(K_B - K_S + \Sigma K_{\pm}) \text{ as } F \to 0, \tag{50}$$

where K_B and K_S correspond to the contributions of the bow and the stern, respectively, and $K_{\pm}$ corresponds to the contribution of a point where the phase of the exponential function $E_0^{\pm}$ is stationary, that is where we have $y_0'/(-x_0') = \pm 1/t$ or $dy_0/dx_0 = \mp 1/t$; the summation in the asymptotic approximation (50) is extended over all such points of stationary phase on the mean waterline c. The expressions for the contributions of the bow and stern $K_{B,S}$ and of the points of stationary phase $K_{\pm}$ are given below.

The contribution $K_{B,S}$ of the bow or stern may be expressed in the form

$$K_{B,S} = A_{B,S} \exp(-i\nu^2 p x_{B,S}), \tag{51}$$

where $x_{B,S}$ is the abscissa of the bow or stern and the amplitude-function $A_{B,S}$ is given by

$$A_{B,S} = 2n_x A_1 + iF^2 q(A_2^+ + A_2^-) + O(F^4); \tag{52}$$

in this expression, the functions A_1 and $A_2^{\pm}$ are defined by the equations

$$(n_x + iqn_z)A_1 = n_x n_y [1 - ipn_y/(n_x + iqn_z)]/(1 - n_z^2 - p^2 n_x^2)] + t_y \phi_t - ipn_y t_y \phi_d (1 - n_z^2 + ipn_x n_z)/(1 - n_z^2 - p^2 n_x^2) \tag{53}$$

and

$$\theta_{\pm}' A_2^{\pm} = (u_{\pm} a_1^{\pm}/\theta_{\pm}')' + iq(\iota_{\pm})^2 a_2^{\pm}, \tag{54}$$

where the superscript ' denotes differentiation with respect to the parameter λ, the functions $u_{\pm}$, $a_1^{\pm}$ and $a_2^{\pm}$ are defined by equations (39), (40) and (44), respectively, and the function $\theta_{\pm}$ is defined as

$$\theta_{\pm} = x_0 \pm t y_0. \tag{55}$$

Expression (54) for the second-order amplitude-function $A_2^{\pm}$ is a complex one. However, equation (53) defines the first-order amplitude function A_1 explicitly in terms of the value of t, $p = (1+t^2)^{1/2}$ and $q = 1/p$, the geometrical characteristics of the hull at the bow or stern, namely the unit vector $\vec{t}(t_x, t_y, 0)$ tangent to the mean waterline and the unit vector $\vec{n}(n_x, n_y, n_z)$ normal to the hull, and the components ϕ_t and ϕ_d of the velocity vector in the directions of the unit vectors $\vec{t}$ and $\vec{n} \times \vec{t}$ tangent to the hull. Equation (52) shows that the first-order approximation to the amplitude-function $A_{B,S}$,

given by $2n_xA_1$, vanishes if $n_x = 0$, that is if the waterline has a cusp at the bow or stern. Equation (53) shows that the first-order approximation to the function $A_{B,S}$ also vanishes if the bow or stern is round, since we then have $n_y = 0$ and $\phi_t = -\phi_y = 0$ by symmetry. It may thus be seen that the contribution of the bow or stern to the far-field wave-amplitude function K(t) is of order F^2 if $n_x = 0$ or $n_y = 0$ at the bow or stern, respectively; that is, we have

$$K_{B,S} = O(F^2) \quad \text{if } n_x = 0 \text{ or } n_y = 0 \tag{56}$$

at the bow or stern. In the particular case when the hull surface is vertical at the bow or stern we have $n_z = 0$ and equation (53) becomes

$$A_1 = t_x - \phi_t - ipt_x\phi_z/(1 - p^2t_y^2) \quad \text{if } n_z = 0, \tag{57}$$

which yields

$$A_1 = t_x - \phi_t + O(F^2) \quad \text{if } n_z = 0 \tag{58}$$

as is indicated by the free-surface boundary condition $\phi_z = -F^2\phi_{xx} = O(F^2)$.

The contribution $K_\pm$ of a point of the mean waterline c where the phase of the exponential function $E_0^\pm$ is stationary, that is where we have

$$dy_0/dx_0 = \mp 1/t, \tag{59}$$

may be expressed in the form

$$K_\pm = \pm\nu(2\pi r)^{1/2}A_\pm \exp[\mp i\nu^2(y_0t_x - x_0t_y)/t_y^2 + i\varepsilon\pi/4], \tag{60}$$

where r is the radius of curvature of c at the point of stationary phase (x_0,y_0), ε is equal to $+1$ or -1 if the center of curvature of c at the point (x_0,y_0) is upstream or downstream from (x_0,y_0), respectively, and the amplitude-function $A_\pm$ is given by

$$A_\pm = (1 - n_z^2)^{1/2}(n_zt_y + \phi_d) - F^2qA_2^\pm + O(F^4); \tag{61}$$

in this expression, the second-order amplitude-function $A_2^\pm$ is defined by the equation

$$\pm 2[(x_0')^2 + (y_0')^2]^{1/2}A_2^\pm = [(u_\pm a_1^\pm)'/\theta_\pm'']' + u_\pm a_1^\pm[5(\theta_\pm''')^2/3\theta_\pm'' - \theta_\pm^{(4)}]/4(\theta_\pm'')^2 + 2iq(u_\pm)^2a_2^\pm, \tag{62}$$

where the superscript ' denotes differentiation with respect to the parameter λ and the functions $u_\pm$, $a_1^\pm$, $a_2^\pm$ and $\theta_\pm$ are given by equations (39), (40), (44) and (55), respectively.

The expression for the second-order amplitude-function $A_2^\pm$ is a complex one. However, equation (60) and the first-order approximation to the amplitude function, namely

$$A_\pm = (1 - n_z^2)^{1/2}(n_zt_y + \phi_d) + O(F^2), \tag{63}$$

provide a simple explicit expression for the stationary-phase contribution $K_\pm$ in terms of the geometric characteristics of the hull and the downward tangential derivative ϕ_d of the potential at the point of stationary phase. In the particular case when the hull surface is vertical at the point of stationary phase we have $n_z = 0$ and equation (63) becomes

$$A_\pm = -\phi_z + O(F^2) \quad \text{if } n_z = 0, \tag{64}$$

which yields

$$A_\pm = O(F^2) \quad \text{if } n_z = 0. \tag{65}$$

Equation (60) then shows that the stationary-phase contribution at a point (x_0,y_0) of c where the hull is vertical is of order F, that is we have

$$K_\pm = O(F) \quad \text{if } n_z = 0. \tag{66}$$

On the other hand, equations (60) and (63) show that we have

$$K_\pm = O(1/F) \quad \text{if } n_z \neq 0. \tag{67}$$

The stationary-phase contribution at a point where the hull has flare thus is dominant in the zero-Froude-number limit.

The summation in equation (50) is extended to all the points of the mean waterline c where the phase of the exponential function E_0^+ or the function E_0^- is stationary, that is the points where the slope dy_0/dx_0 of c is equal to $-1/t$ or $+1/t$, respectively. The number of stationary points, and their position along the waterline, depend on the value of t and on the shape of c. For instance, for the simple case of a hull with waterline consisting of a sharp-ended parabolic bow region $1/4 \leqslant x \leqslant 1/2$ defined by the equation $y = 4bx(1 - 2x)$, where b denotes the ship's beam/length ratio, a straight parallel midbody region $-1/4 \leqslant x \leqslant 1/4$, and a round-ended elliptic stern region $-1/2 \leqslant x \leqslant -1/4$ defined by the equation $y = b[-2x(1 + 2x)]^{1/2}$, there is one point of stationary phase in the stern region given by $x = -[1 + 1/(1 + 4b^2t^2)^{1/2}]/4$, so that we have $-1/2 \leqslant x \leqslant -1/4$ for $0 \leqslant t \leqslant \infty$ with $x \to -1/2$ as $t \to 0$ and $x \to -1/4$ as $t \to \infty$, and one point of stationary phase in the

bow region given by $x = (1 + 1/4bt)/4$ for $1/4b \leqslant t \leqslant \infty$, so that we have $1/2 \geqslant x \geqslant 1/4$ for $1/4b \leqslant t \leqslant \infty$ with $x \to 1/2$ as $t \to 1/4b$ and $x \to 1/4$ as $t \to \infty$. We thus have one point of stationary phase in the stern region for $0 \leqslant t < 1/4b$ and two points of stationary phase, one in the stern region and one in the bow region, for $1/4b \leqslant t \leqslant \infty$. The two points of stationary phase approach the shoulders $x = \pm 1/4$, where $dy/dx = 0$, as $t \to \infty$.

The asymptotic approximation (50) and equations (51)-(58) and (59)-(67) defining the contributions of the bow and stern and of the stationary-phase point(s) on the waterline, respectively, show that the low-Froude-number behavior of the far-field wave-amplitude function is strongly influenced by the shape of the hull in the vicinity of the waterline. More precisely, for a value of t for which there is one (or more) point of stationary phase on the mean waterline where the hull has flare, the contribution of this stationary-phase point dominates the contribution of the bow and stern and is of order $1/F$, that is we have $K(t) = O(1/F)$. On the other hand, for a value of t for which either there corresponds no point of stationary phase or the hull has no flare at the point(s) of stationary phase, the dominant contribution stems from the bow and stern, and it is of order 1, that is we then have $K(t) = O(1)$. However, if $n_x = 0$ or $n_y = 0$ at both the bow and the stern, that is if the bow and the stern are either cusped or round, their contribution is $O(F^2)$ and the contribution of the stationary-phase point(s), which is $O(F)$ if there is no flare (as is assumed here), is dominant; so that we then have $K(t) = O(F)$.

For a ship form that is everywhere wall sided, the contribution of the bow and stern is dominant for all values of t, and we have $K(t) = O(1)$ for $0 \leqslant t \leqslant \infty$. On the other hand, for a hull form that has flare over a portion of the waterline and is wall sided elsewhere, the contribution of the bow and stern is dominant, and $O(1)$, only for those values of t for which the corresponding points of stationary phase fall outside the range of flare; for the range of values of t for which the corresponding points of stationary phase are within the range of flare, the contribution of these stationary-phase points is dominant, of order $1/F$. In this instance, the function $K(t)$ is $O(1/F)$ for a range of values of t (corresponding to the region of flare) and $O(1)$ for other values to t. If the region of flare is of small extent, and the slope dy/dx of the waterline does not vary widely within that region, the range of values of t for which $K(t) = O(1/F)$ is also small. The far-field wave-amplitude function $K(t)$ can then exhibit a sharp peak for some value of t in the low-Froude-number limit. In fact, several isolated peaks of the function $K(t)$ can exist if the hull form has several distinct regions of flare within which the slope of the waterline varies gradually.

It should be noted that the result $K(t) = O(1/F)$ for values of t for which the hull has flare at the corresponding points of stationary phase does not imply that the corresponding free-surface elevation becomes unbounded in the zero-Froude-number limit $F = 0$. Indeed, the asymptotic approximation (6), where we have $(\xi,\zeta) = (X,Z)g/U^2$, then yields $Zg/U^2 = O[1/F(-\xi)^{1/2}] = O[1/(-X/L)^{1/2}]$ as $F \to 0$ and $-X/L \to \infty$. The free-surface elevation Z thus is of order $(U^2/g)/(-X/L)^{1/2}$ as $F \to 0$ and $-X/L \to \infty$, and equation (15) shows that the corresponding wave steepness s is $O[1/(-X/L)^{1/2}]$. For values of t for which $K(t) = O(1)$ it is seen that Zg/U^2 and s are $O[F/(-X/L)^{1/2}]$ as $F \to 0$ and $-X/L \to \infty$.

It should also be noted that the asymptotic approximation (51)-(55) for the contribution of the bow and stern is not uniformly valid for the values of t for which the bow or the stern is a point of stationary phase, that is for which the waterline slope dy_0/dx_0 at the bow or the stern is equal to $-1/t$ or $1/t$, respectively. Indeed, it may be shown that we have $1 - n_z^2 - p^2 n_x^2 = 0$ at a point of stationary phase, so that the first-order approximation to the amplitude functions $A_{B,S}$ given by equation (53) becomes unbounded. The asymptotic approximation (60)-(62) for the contribution of a point of stationary phase likewise is not uniformly valid at a stationary-phase point where the waterline has an inflexion point. Indeed, the radius of curvature r at such an inflexion point is infinite and equation (60) yields an unbounded contribution $K_{\pm}$. Asymptotic approximations valid for these special cases may easily be obtained and are given in Noblesse (1986b). It will only be noted here that the far-field wave-amplitude function $K(t)$ for a hull form having flare at a point where the waterline has an inflexion may be expected to exhibit a particularly pronounced peak at the value of t corresponding to the inflexion point since we have $K(t) = O(1/F^{4/3})$ as $F \to 0$ for this particular value of t.

6. CONCLUSION: HULL FORM AND KELVIN-WAKE FEATURES

The classical far-field asymptotic approximation to the Kelvin wake, obtained in section 2 by applying the method of stationary phase, and the low-Froude-number asymptotic approximation to the far-field wave-amplitude function, obtained in sections 4 and 5 by successively using the Laplace method and the method of stationary phase, provide a simple analytical relationship between the hull shape, on one hand, and the waves it generates, on the other hand. This explicit relationship between the wavemaker and its waves is summarized below.

The far-field asymptotic approximation to the Kelvin wake (6) shows that at any point (ξ,α), with $\xi = Xg/U^2 \ll -1$ and $0 \leq \alpha < \tan^{-1}(2^{-3/2}) \simeq 19°28'$, the wave field consists in two plane progressive waves —— a transverse wave and a divergent wave —— with wavelengths λ_- and λ_+ propagating at angles β_- and β_+ from the track of the ship, respectively. The wavelengths $\lambda_\pm$ and the propagation angles $\beta_\pm$ depend on the angle from the ship track α alone, that is $\lambda_\pm$ and $\beta_\pm$ are independent of the hull shape and size, as is well known. Specifically, the functions $\lambda_\pm(\alpha)$ and $\beta_\pm(\alpha)$ are defined by equations (10), (11) and (12). At a given downstream distance ξ, the amplitudes of these waves, on the other hand, are given by the product of the functions $A_\pm(\alpha)$, defined by equation (9), and the far-field wave-amplitude function K(t) evaluated at the stationary values $t_\pm(\alpha)$ given by equation (7). The function K(t) depends on the hull shape and the Froude number in a fairly complicated manner via an integral over the mean wetted-hull surface and an integral around the mean waterline, as is indicated by equation (26). A low-Froude-number asymptotic approximation to these integrals is obtained in sections 4 and 5.

The analytical approximation (50) shows that for a given value of t corresponding to a given value of α, as is specified by equation (7), the main contributions to the function K(t) stem from several particular points on the mean waterline. These are the bow and the stern, on one hand, and (usually but not always) one (or several) point(s) of stationary phase. Indeed, the number of these points of stationary phase and their position on the waterline, defined by the condition

$$|dy_0/dx_0| = 1/t, \tag{68}$$

depend on the shape of the waterline and the value of t.

Let φ denote the angle between the tangent to the mean waterline and the track of the ship, that is we have

$$\tan\varphi = |dy_0/dx_0| \text{ and } 0 \leq \varphi \leq \pi/2. \tag{69}$$

Equations (68), (69), (7) and (10) then show that the stationary values $t_+(\alpha)$ and $t_-(\alpha)$ associated with a given value of α are defined by the equation

$$\varphi_\pm(\alpha) = \tan^{-1}\{4\sigma/[1\pm(1-8\sigma^2)^{1/2}]\}, \tag{70}$$

where $\sigma = \tan\alpha$. For a given waterline shape, equation (70) thus defines the number of stationary points and their position on the waterline corresponding to any given angle α inside the Kelvin wake. In particular, equation (70) yields

$$0 \leq \varphi_+ \leq \tan^{-1}(2^{1/2}) \simeq 54°44' \leq \varphi_- \leq 90° \tag{71}$$

and $\varphi_+ \sim 2\alpha$, $\varphi_- \sim \pi/2 - \alpha$ as $\alpha \to 0$. (72a,b)

Points of the waterline with slope between 0 and 54°44' thus contribute mostly to the system of divergent waves while waterline slopes between 54°44' and 90° mostly contribute to the transverse waves.

Equations (10), (11), (12) and (70) define the wavelengths $\lambda_\pm$, the wave-propagation angles $\beta_\pm$ and the waterline-tangent angles $\varphi_\pm$ corresponding to a given angle from the ship track α. The functions $\lambda_\pm(\alpha)$, $\beta_\pm(\alpha)$ and $\varphi_\pm(\alpha)$ are depicted in Figure 3a, where the subscripts T and D are used, instead of $-$ and $+$, to refer to the transverse and divergent waves, respectively. The foregoing relationships between α and λ, β, φ may be used for determining the angle from the ship track α, the wavelength λ and the wave-propagation angle β corresponding to a given waterline-tangent angle φ. Specifically, we may obtain the remarkably simple relations

$$\alpha = \tan^{-1}[\tan\varphi/(2+\tan^2\varphi)], \tag{73}$$

$$\lambda/2\pi = \sin^2\varphi \text{ and } \beta = \pi/2 - \varphi. \tag{74a,b}$$

The functions $\alpha(\varphi)$, $\lambda(\varphi)$ and $\beta(\varphi)$ are depicted in Figure 3b. Alternatively, the foregoing relationships among φ, α, λ and β can be represented in the form of Figures 3c and 3d, which depict the functions $\varphi(\beta)$, $\alpha(\beta)$, $\lambda(\beta)$ and $\varphi(\lambda)$, $\alpha(\lambda)$, $\beta(\lambda)$, respectively. These equivalent graphical representations show that we have

$$0 \leq \varphi_D \leq \tan^{-1}(2^{1/2}) \simeq 54°44' \leq \varphi_T \leq 90°, \tag{75a}$$

$$0 \leq \lambda_D/2\pi \leq 2/3 \leq \lambda_T/2\pi \leq 1, \tag{75b}$$

$$90° \geq \beta_D \geq \tan^{-1}(2^{-1/2}) \simeq 35°16' \geq \beta_T \geq 0, \tag{75c}$$

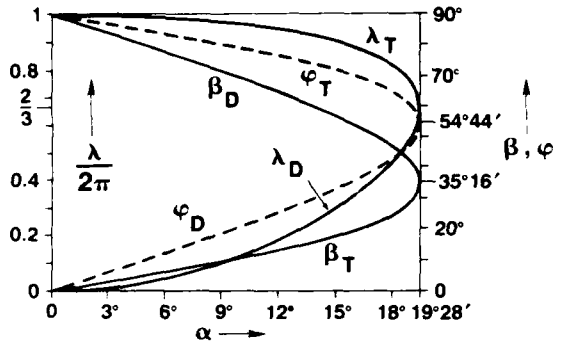

Fig. 3a - The Waterline-Tangent Angle φ, the Wave-Propagation Angle β and the Wavelength λ as Functions of the Angle From the Ship Track α; the Subscripts T and D Refer to the Transverse and Divergent Waves, Respectively.

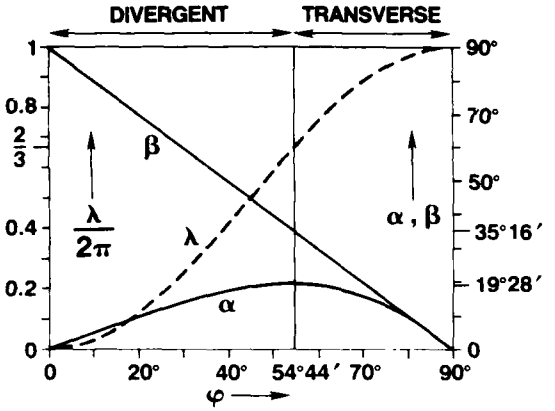

Fig. 3b - The Angle From the Ship Track α, the Wave-Propagation Angle β and the Wavelength λ as Functions of the Waterline-Tangent Angle φ.

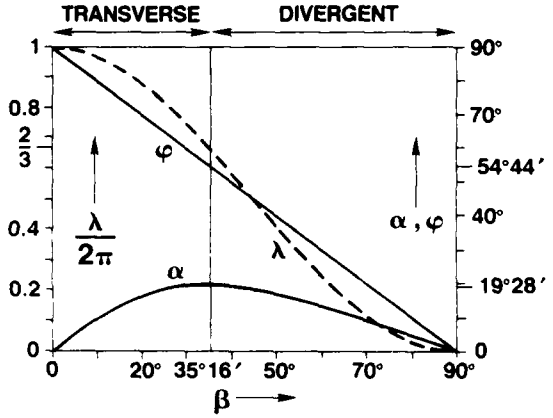

Fig. 3c - The Waterline-Tangent Angle φ, the Angle From the Ship Track α and the Wavelength λ as Functions of the Wave-Propagation Angle β.

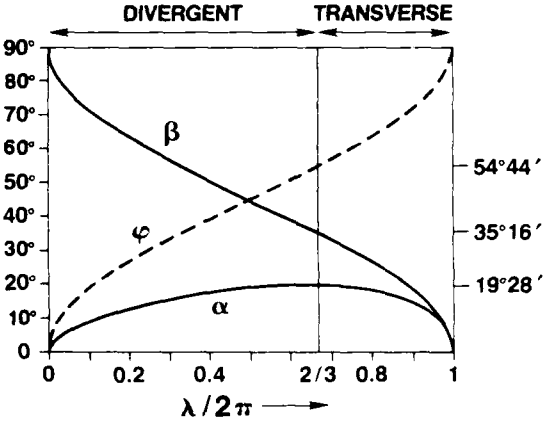

Fig. 3d - The Waterline-Tangent Angle φ, the Angle From the Ship Track α and the Wave-Propagation Angle β as functions of the Wavelength λ.

where the subscripts D and T refer to the divergent and transverse waves, respectively.

The first two terms in the low-Froude-number asymptotic expansions for the contributions $K_{B,S}$ of the bow and stern and the contributions $K_{\pm}$ of the points of stationary phase in equation (50) are given by equations (51)-(55) and (59)-(62), respectively. The second-order terms in these asymptotic expansions are defined by complex expressions. However, the first-order terms provide simple approximations defined explicitly in terms of the geometrical characteristics of the hull and the velocity components in the tangential directions $\vec{t}$ and $\vec{n}\times\vec{t}$ to the hull. In particular, the low-Froude-number asymptotic expansions given in section 5 show that the contributions K_B and K_S of the bow and stern are O(1) except if the bow or stern is cusped or round, in which case we have $K_{B,S} = O(F^2)$. The contribution of a given point of stationary phase is O(1/F), and thus is dominant, if the hull has flare at this point; otherwise, that is if the hull is wall sided at the point of stationary phase, its contribution is O(F).

Thus, for a ship form that is everywhere wall sided, the contributions of the bow and stern are dominant (assuming that they are not both either round or cusped) for all values of the angle α from the ship track, that is everywhere in the far-field Kelvin wake. On the other hand, for a hull that has flare over a portion of the waterline and is wall sided elsewhere, the contributions of the bow and stern are dominant, and O(1), only for those angles α in the Kelvin wake for which the corresponding points of stationary phase on the waterline fall outside the region of flare; for the

range of values of α for which the corresponding points of stationary phase are within the range of flare, the contribution of these stationary-phase points is dominant, of order 1/F. In this instance, the amplitude of the waves in the far-field Kelvin wake is of order $(U^2/g)/(-X/L)^{1/2}$, as $F \to 0$ and $X/L \to -\infty$, for the range of values of α corresponding to the region of flare and of order $F(U^2/g)/(-X/L)^{1/2}$ for values of α outside this range. If the region of flare is of small extent, and the waterline-tangent angle φ does not vary widely within that region, the corresponding range of values of the angle α where the wave amplitude is an order of magnitude larger than elsewhere is also small, and thus appears as a peak for sufficiently small values of the Froude number. This peak is particularly pronounced for a hull with a small region of flare in the vicinity of an inflexion point of the waterline.

The low-Froude-number asymptotic analysis of the Neumann-Kelvin theory presented in this study thus shows that the characteristics of the far-field Kelvin wake strongly depend on the shape of the ship hull, notably the presence of flare and the shape of the waterline at the bow and stern. This analysis also predicts that the nondimensional wave-resistance coefficient $R/\varrho U^2L^2$, where U and L are the speed and the length of the ship and ϱ is the density of water, which is given by the Havelock integral

$$\pi R/\varrho U^2L^2 = F^4 \int_0^\infty K(t)^2(1+t^2)^{1/2}\,dt, \qquad (76)$$

is $O(F^2)$ for a ship form with a region of flare, $O(F^4)$ for a ship form that is wall sided everywhere and has either a bow or a stern (or both) that is neither cusped nor round, and $O(F^6)$ for a wall-sided ship form with both bow and stern that are either cusped or round.

The low-Froude-number asymptotic approximation (50) also shows that we have

$$K(t) = O(1/t^3) \text{ as } t \to \infty. \qquad (77)$$

This result is actually valid for any value of the Froude number; indeed, the asymptotic approximation (50) is valid not only in the low-Froude-number limit $F \to 0$ but more generally in the limit $\nu p = (1+t^2)^{1/2}/F \to \infty$, that is as $F \to 0$ or/and as $t \to \infty$, as may be seen from the exponential functions $\exp(\nu^2 p^2 z)$ and $E_\pm = \exp[-i\nu^2 p(x \pm ty)]$ in equation (26).

Equations (15), (18a), (21b) and (77) then yield

$$(-\xi)^{1/2} s_+(\xi,\alpha) \sim t_+^{1/2} \sim 1/\alpha^{1/2} \text{ as } \alpha \to 0 \qquad (78)$$

for the steepness of the short divergent waves in the vicinity of the track of the ship. By using equations (4) and (5), which yield $\alpha \sim \eta/(-\xi)$ as $\alpha \to 0$, in equation (78) we may obtain

$$s_+(\xi,\eta) \sim 1/\eta^{1/2} \text{ as } \eta \to 0. \qquad (79)$$

Equation (79) thus shows that the lines along which the steepness of the short divergent waves in the far-field Kelvin wake takes given large values, say $s_+ = 1.7$ and 1/15, are parallel to the ship track, as was found in Figure 21 of Barnell and Noblesse (1986) by using the Michell thin-ship approximation for a simple ship form. The Neumann-Kelvin theory therefore predicts that the far-field Kelvin wake contains three distinct regions: (i) a narrow constant-width inner region bordering the track of the ship where no divergent gravity waves can exist, (ii) an outer region where the usual transverse and divergent waves are present, and (iii) an intermediate region at the boundary between the inner and outer regions where short steep divergent waves can be found. In reality, surface tension must evidently be taken into account in the vicinity of the track of the ship.

ACKNOWLEDGMENTS

This study was supported by the Independent Research program and the General Hydrodynamics Research program at the David W. Taylor Naval Ship Research and Development Center. I wish to thank Mr. Alexander Barnell for his help in drawing Figures 1 and 3 and Dr. Arthur Reed for his useful suggestions.

REFERENCES

1. Barnell, A. and F. Noblesse (1986) "Far-Field Features of the Kelvin Wake," 16th Symposium on Naval Hydrodynamics, University of California, Berkeley.

2. Fu, Lee-Lueng and Benjamin Holt (1982) "Seasat Views Oceans and Sea Ice with Synthetic Aperture Radar," JPL Publication 81-120.

3. McDonough, Robert N., Barry E. Raff and Joyce L. Kerr (1985), "Image Formation from Spaceborne Synthetic Aperture Radar Signals," Johns Hopkins APL Technical Digest, Vol. 6, No. 4, pp. 300-312.

4. Noblesse, F. (1983) "A Slender-Ship Theory of Wave Resistance," Journal of Ship Research, Vol. 27, No. 1, pp. 13-33.

5. Noblesse, F. (1986a) "Steady Ship Waves at Low Froude Numbers (Part One)," David Taylor Naval Ship R&D Center Report No. DTNSRDC-86/024, 22 pp.

6. Noblesse, F. (1986b) "Steady Ship Waves at Low Froude Numbers (Part Two)," David Taylor Naval Ship R&D Center Report in preparation.

7. Scragg, Carl A. (1983) "A Numerical Investigation of the Kelvin Wake Generated by a Destroyer Hull Form," Science Applications Report No. SAI-83/1216, 46 pp.

8. Ursell, F. (1960) "On Kelvin's Ship-Wave Pattern," Journal of Fluid Mechanics, Vol. 8, pp. 418-431.

A TECHNIQUE FOR PERFORMING FLUORESCENT DYE FLOW STUDIES ON PROPELLER BLADE SURFACES IN A MODEL BASIN

Frederick H. Ashcroft
Research Associate,
Ship Hydrodynamics Laboratory
University of Michigan
Ann Arbor, Michigan 48109

ABSTRACT

Oil has been used extensively in water tunnels to indicate the flow on the surface of propeller blades. The application of this technique in a model basin is discussed and a specific test is described.

PREFACE

Since very little information is publically available on this technique, both technique and experimental results are presented. The paper is divided into two sections: Technique is discussed in section 1 and the specific experiment is discussed in section 2.

1.0 TECHNIQUE

Test procedures in water tunnels require a carefully controlled spin-up period (which might last several minutes) followed by four to five minutes of steady-state and a reciprocal spin down to maintain constant J during the entire process. Duplicating this procedure in the U of M model basin was not desirable. Even with the relatively low pitch propellers tested for this paper (U of M most commonly tests propellers with P/D<1.1) single run times were limited to ten seconds each for spin-up and spin-down with sixty seconds of steady-state. Rather than building up a pattern using multiple runs, it was desirable to have a flow indicator that would migrate fully during a single run with a duration of sixty seconds or less.

The flow indicator most successful in the water tunnel (SAE 50 oils with lampblack as a pigment) was much too viscous for use in a model basin: full migration could not be achieved even with "built-up" runs. It was necessary to find a new flow indicator mixture and application technique for use in model basins.

The most successful of the tested mixtures were: SAE 10 oil with 1.0 gm of white luminous theatrical makeup or 0.5 gm of Day-Glo orange powder.

The mixtures were applied to the blade surface in small dots (initial diameter not greater than .04 inches), stripes (initial width not greater than 0.25 inches), or whole blade coating. It was important to use different color indicators on opposite sides of the blade to show any cross-flow. Both dots and stripes indicated laminer or turbulent flow, but full coating was a better indicator of possible blade loading problems. All three application methods showed cross-flow. It was important to apply the oil/indicator mixture as thinly as possible. If the oil layer was too thick it effected the flow and yielded no distinguishable pattern. High quality artists' paint brushes were used as applicators. A Winsor & Newton series 233 no. 2 was used to apply the dots and a series 397 no. 3 was used for both striping and coating.

Ultra violet (black) light was used to highlight the flow indicators for observation. Nearly all the flow patterns observed under black light were not visible under either incandescent or fluorescent light. It was possible to photograph the propeller under black light with normal film. All the photographs in this paper were taken using Ektachrome asa 400 slide film and an exposure time of two seconds at f8.

2.0 FLOW OBSERVATION

2.1 The Propeller:

Initial tests were performed with propeller U of M 40 at J=0.50 (operating J). A propeller Reynolds number of 1.28 E 5 at 600 rpm was typical of the operating condition for this model propeller. Spin-up/spin-down times were best at 10 seconds each and a steady-state run duration between 45 and 60 seconds was acceptable. Propeller U of M 40 was chosen for the flow observation test for three reasons.

First, during a preliminary test in 1984 it was observed that there was an anomolous flow pattern on just one blade. The oil/indicator did not migrate, it remained on the blade as an indefinable smear. Second, it is typical of modern merchant ship propellers which the SHL tests fairly often. Third, U of M 40 was manufactured for the SHL by the Ship Research Insitute of Norway (NSFI); U of M 41 was manufactured to the same plans by the China Ship Scientific Research Center (CSSRC) but, due to an error in conversion between inches and centimeters, is twice as thick as it is supposed to be; U of M 42, also manufactured by CSSRC, is supposed to be an exact duplicate of propeller 40. The only other differences between these propellers is in the material and surface finish: the NSFI propeller is made of aluminum and has a matt finish; the CSSRC propellers are made of pot metal and are highly polished. These differences are summarized in Table 1.

Table 1

Prop No.	Manufacturer	Thickness Ratio	Material
40	NSFI	1	Aluminum
41	CSSCR	2	Pot Metal
42	CSSCR	1	Pot Metal

Figure 1 shows the open water curves and Table 2 gives the particulars for all three propeller models.

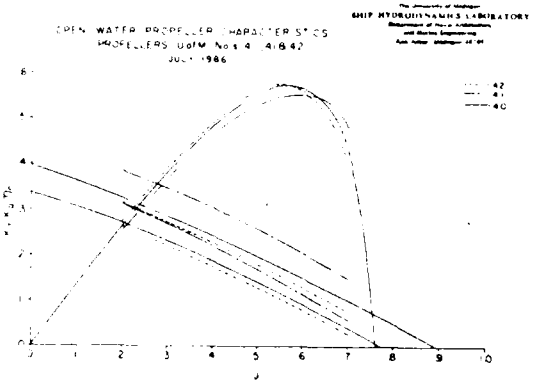

Table 2
Principal Particulars
of
Propellers U of M
40, 41, and 42

Diameter	0.604ft
P/D	0.7105
B.A.R.	0.668
Rake	6.188°
Z	5

2.2 Test Conditions:

The propellers were all tested using white pigment on the pressure surface and orange pigment on the suction surface to allow indication of crossflow. Three application techniques were used: small dots, stripes, and full surface coating.

The smooth surface finish of propellers 41 and 42 required the use of SAE 20 oils with 2.0 gm white and 1.0 gm orange as indicators. No attempt was made to correlate the surface finish with the performance of the flow indicator.

2.3 Test Results

Anomolous flow patterns shown on U of M 40 in the preliminary tests was caused by too thick a coating of oil on the blade surface. However, every blade of this propeller drew white pigment from the pressure side onto the trailing edge of the suction side for about 15° of the chord over most of the length of the blade.

There was one run (No. 6) where there was only migration of the white pigment near the tip of the blade, yet the suction side had white down the entire trailing edge.

The flow patterns appeared similar for all three propellers. The flow was turbulent as shown by the essentially chordwise pattern of the indicator, however at about 65% chord aft on the suction side of the blade the flow moved radially outward. The flow patterns are shown in detail in Figures 2 through 4.

Figure 2 shows the flow patterns found on propeller U of M 40.

Figure 3 shows the flow patterns found on propeller U of M 42 (supposedly identical to 40).

Figure 4 shows the flow patterns found on propeller U of M 41 (double thickness).

2.4 Discussion of Results:

The drawing of indicator fluid from the suction to the pressure side of the blade on all the propellers indicates a large separation of flow on the low pressure side of the blade.

The anomolous flow on run number 6 (prop U of M 40) seems to indicate a flow pattern that moves radially inward along the trailing edge (this defies logic). This was also suprising because the propeller was operating well inside its normal J range.

There are three major possible causes for the separated flow: use of a wake adapted propeller in open water, poor design, and/or poor manufacture. It was not possible to test any of the three propellers in the behind condition and the measuring equipment available could not measure any physical difference between propellers 40 and 42, however with two

propellers of the same design but different manufacture, it was felt that some inferrences could be made. Examination of Figures 2 and 3 shows that Chinese propeller (U of M 42) has significantly less tendency to draw indicator from the pressure to suction side of the blade (it still draws some indicator). The effect of thickness, as shown in Figure 4, is not great. Propeller 41 has somewha more separation, but generally exhibits the same patterns as 42. All the propellers indicated separation on the trailing edge, however the severity of the separation appears dependent on th. construction of the model propeller.

3.0 CONCLUSIONS

The use of fluorescent dyes as flow indicators on propeller blades can be a useful tool in the model basin as well as in the water tunnel. Attention must be paid to maintaining constant J during spin-up/spin-down. The actual oil/indicator mixture will probably vary widely from tank to tank. In general, for test runs of short duration, oil weights not greater than SAE 20 are desirable. The oil viscosity used appears dependent on ambient water temperature (the temperature during our tests was 71! F). Black light and fluorescent dyes make the flow patterns much easier to see. This work should be used as a guide to find the best combination of oil weight and indicator for the local conditions.

Flow patterns on all three propellers indicated separation of flow on the low pressure side of the blade. It is important to note however, that the severe flow anomaly indicated on propeller 40 during the 1984 preliminary tests was due to improper test technique and the severity of the separation patterns exhibited by propeller 40 during the 1986 test appear to be caused by differences in manufacture.

It is clear that this flow observation technique will indicate problems such as separated flow at a fraction of the cost of cavitation tests. Propeller U of M 40 was tested in the cavitation tunnel at MIT and the separation problem was not evident in the results. Based on the results of these flow studies it is apparent that some improvement could be made to these propellers to enhance their overall performance. From the practical standpoint, propellers 40 and 42 have good (and very similar) performance, but how much improvement could be realized by elimination of the separation cannot be easily predicted.

ACKNOWLEDGEMENTS

I would like to thank the University of Michigan Department of Naval Architecture and Marine Engineering for the financial support that made this experiment possible and the following individuals: Terry Brockett for his assistance and guidance in interpreting flow data, John Kooienga for his assistance with the computer program, Frank Dennis for modifying the carriage electronics to suit this control scheme, Marty Mardiros for assisting with the actual experiments, and Margaret Kirschner for editorial and typing services.

a) dot pattern: pressure side.

b) dot pattern: suction side.

c) stripe pattern: pressure side.

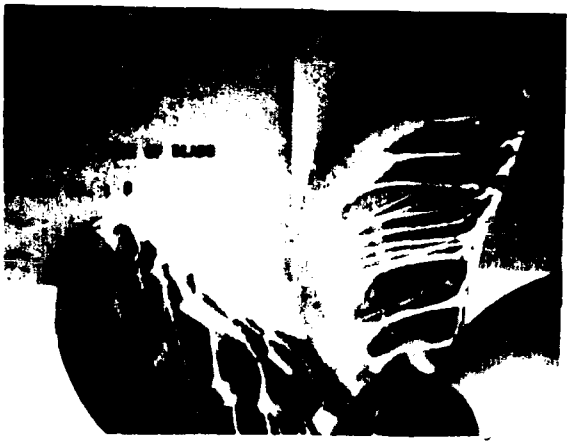

d) stripe pattern: suction side.

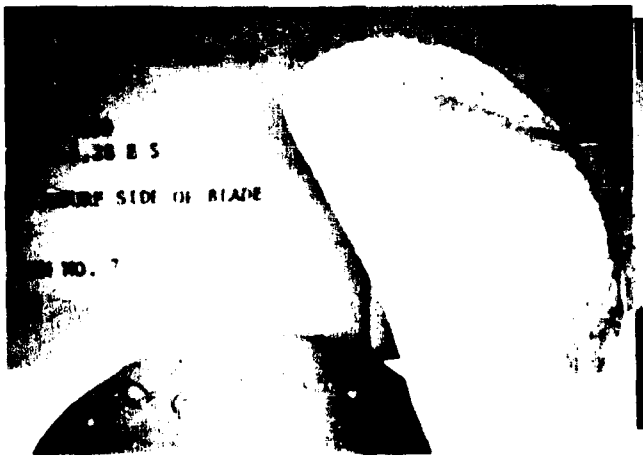

e) coated pattern: pressure side.

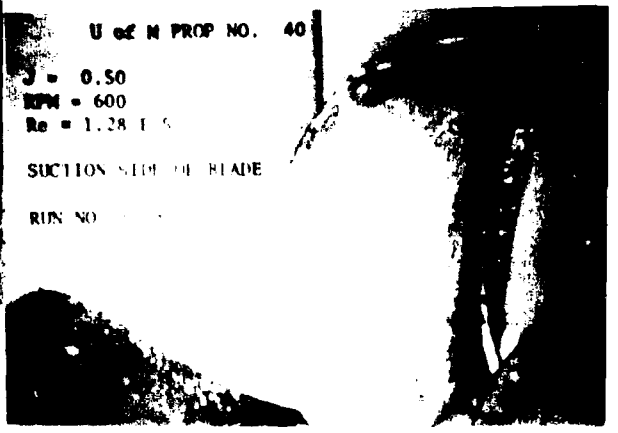

f) coated pattern: suction side.

Figure 2(a)-(f): Flow Patterns on Propeller #40.
Note presence of pressure side fluid on trailing edge of suction side in b,d, and f.

a) dot pattern: pressure side.

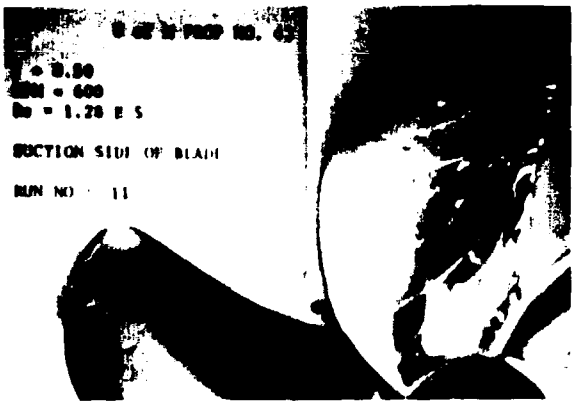

b) dot pattern: suction side.

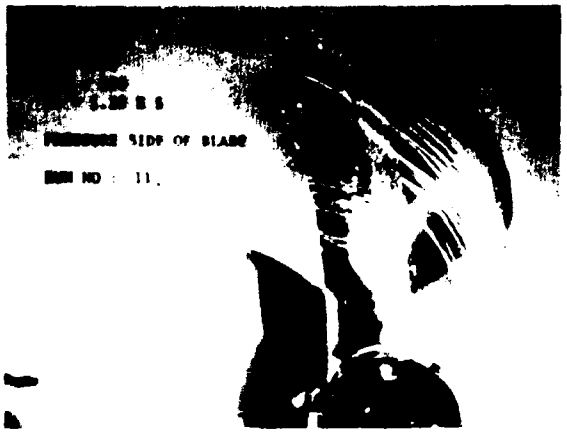

c) stripe pattern: pressure side.

d) stripe pattern: suction side.

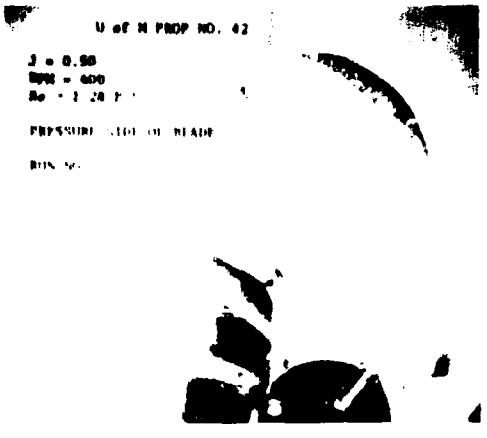

e) coated pattern: pressure side.

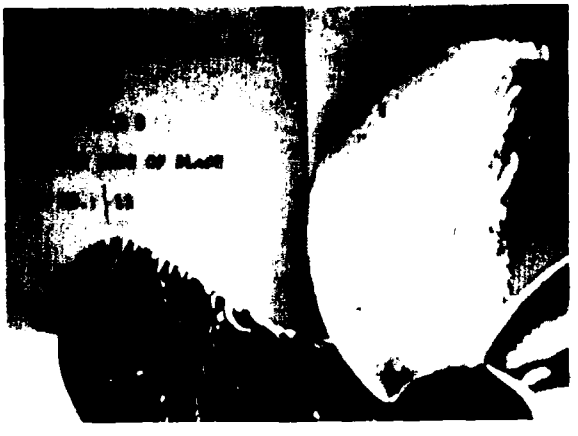

f) coated pattern: suction side.

Figure 3(a)-(f): Flow Patterns on Propeller U of M 42. Note presence of pressure side fluid on trailing edge of suction side in b,d, and f.

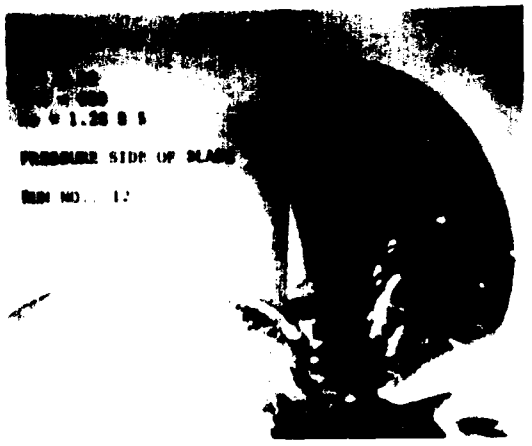

a) dot pattern: pressure side.

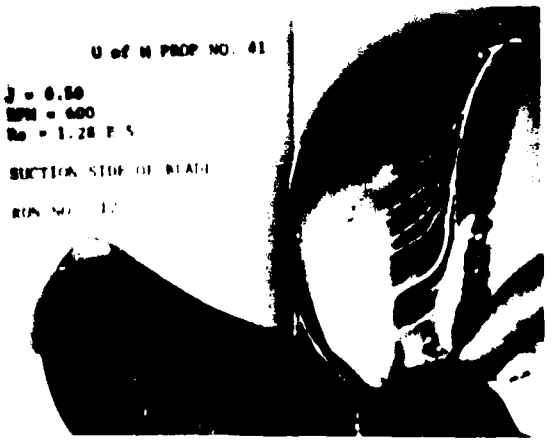

b) dot pattern: suction side.

c) stripe pattern: pressure side.

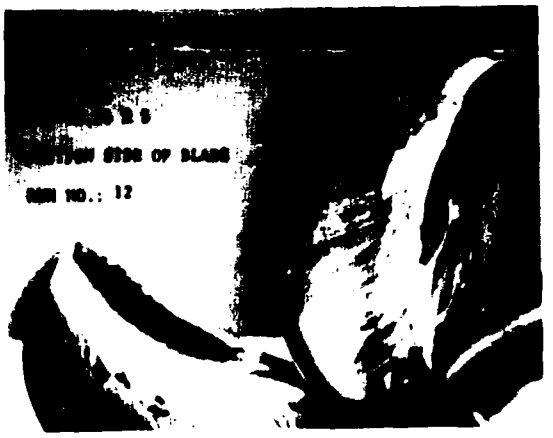

d) stripe pattern: suction side.

e) coated pattern: pressure side.

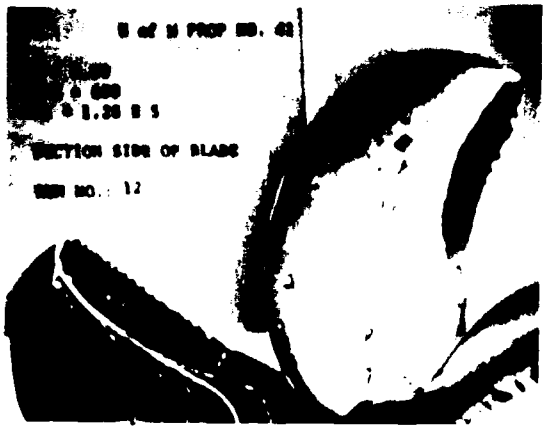

f) coated pattern: suction side.

Figure 4(a)-(f): Flow Patterns on Propeller U of M 41. Note presence of pressure side fluid on trailing edge of suction side in b,d, and f.

SESSION IV
NEW FACILITIES AND TECHNIQUES

TECHNICAL COMMITTEE MEMBERS

Mr. D.C. Murdey (Chairman)	National Research Council/Canada
Mr. Bruce Johnson	U.S. Naval Academy
Dr. Robert Latorre	Univ. of New orleans
Mr. John McDowall	Offshore Technology Corp.
Dr. Richard Rothblum	DTNSRDC
Prof. Armin Troesch	University of Michigan
Mr. Alex Goodman	Tracor Hydronautics

REPORT OF COMMITTEE ON NEW FACILITIES AND TECHNIQUES

David Murdey (Chairman)
National Research Council
Institute for Marine Dynamics
St. John's, Newfoundland
Canada

The New Facilities and Techniques Committee for the 21st ATTC consisted of:

Mr. Alex Goodman
Tracor Hydronautics

Professor Bruce Johnson
U.S. Naval Academy

Professor Bob Latorre
University of New Orleans

Mr. John McDowall
Offshore Technology Corporation

Mr. Richard Rothblum
David Taylor Naval Ship Research and Development Center

Professor Armin Troesch
University of Michigan

As usual, the work of the Committee was accomplished by telephone and correspondence. Contributions to the sessions were solicited through the Committee members, as well as through the general call for papers. The Committee reviewed abstracts of all papers submitted.

There is strong evidence that new demands put on test facilities are resulting in important developments at a time of somewhat smaller requirements for traditional ship model testing. New facilities have been inaugurated specifically directed towards the offshore industry and operations in ice. There have been major developments in the techniques for producing and analyzing waves. The latest computer technology has had an impact on both the hardware and software used in tanks. These various aspects are summarized below.

NEW FACILITIES

The major new facilities of the National Research Council of Canada's Institute for Marine Dynamics (IMD) were officially opened on 5 November 1985. The building houses an ice tank, seakeeping tank and towing tank, together with model making and other support facilities. A general outline of these facilities was given to the 20th ATTC by Gospodnetic and Miles. A detailed description of the ice tank, originally submitted to this Committee, forms part of the Ice Committee report to this Conference. Norris, Gamberg and Thorburn describe the instrumentation and data acquisition systems of IMD. The data acquisition facilities are based on distributed computer approach, in which acquisition at each of the Institute's three tanks is controlled by a separate mini computer connected to a local area network. The network also includes a host computer for long term storage and several dedicated machine control computers. This configuration allows maximum flexibility in terms of distribution of computing power, on-line storage capability and real-time responsiveness.

In February 1986 a major milestone was reached in the construction of the Ship Offshore Laboratory Towing Tank at the University of New Orleans when the concrete was poured. This tank is designed for conventional ship studies in both deep and shallow water and the testing of offshore structures with provision for observation and anchoring. The sizing and specifications of this facility are described in the paper contributed by Latorre.

Detailed design work on the large cavitation channel proposed for the David Taylor Naval Ship Research and Development Center has continued. The demanding design goals placed on flow quality, and specifications for acoustic levels required detailed evaluation of some of the critical components. Both physical model studies and mathematical modelling techniques were used for this as described in the paper by Wetzel, Song and Arndt.

Several developments of existing facilities have taken place. At the Offshore Technology Corporation (OTC), for example, the towing carriage drive system was replaced in order to achieve a maximum carriage speed of 20 ft/sec. This speed was required by the testing of large scale models of 12m yachts. Also at OTC, the plunger wavemaker on the short side of the shallow water basin has been replaced by a modern flap design.

WAVEMAKERS

The most significant developments in facilities and techniques over the past three years have been in relation to wavemaking technology. Major efforts have been made to produce and control even better models of the seaway found in nature. This has led to the development of the computer controlled multi-element wave generators. Two variations on this approach are described in papers by Miles, Laurich, and Funke and by Outlaw, respectively. In the first, the authors describe a system developed at the NRC Hydraulics Laboratory in Ottawa, which uses 64 elements. Design features include variable depth operation, multiple articulation modes (piston, flapper and combination), large amplitude capability and automatic sensor calibration. Outlaw describes the generator installed in the wave basin at the Coastal Engineering Research Center of the U.S. Army Engineer Waterways Experiment Station. This wave generator consists of 60 elements, separated into four modules, which are portable and can be relocated within the wave basin. The elements operate in translational motion (piston mode). It is evident that operation of such complex wavemakers depends very much on the sophistication of the control system and drive signal generation techniques used. Both papers emphasize the need for operational flexibility and scope for future enhancements of the system.

Multi-element systems are expensive to install, and attempts have been made to find alternative ways of producing short-crested waves. A novel, simple solution to this problem is described by Tulin and Kilaini. They attached a three dimensional shape to the end of a vertically oscillating plate, and found this resulted in the propagation of short crested waves. The nature of these waves over a useful frequency range is described in their paper.

Wavemakers for long-crested waves in towing tanks have continued to be developed, and the IMD St. John's facility uses a fully computer controlled, dual flap wavemaker. This can be operated in various flap-motion combinations for both regular and irregular waves. The calibration of the wavemaker, and the determination of the optimum board motion combination to minimize wave profile distortion are described by Datta and Murray.

NOVEL APPLICATIONS

The towing tanks have seen an accelerated change in their main uses and types of work carried out. Recently, much interest has been expressed in ship propeller generated noise, and experiments have been performed in dedicated facilities, such as vacuum tanks and some cavitation tunnels. Other problems of acoustics in oceanography and communication under water exist. Goodman, Silverstein and Gottwald outline measurements made to establish the acoustic signature of a conventional towing tank and make an assessment of the utility of a quiet ship model towing tank as an acoustic test facility.

CONCLUSION

The last three years have seen considerable activity in the development of test facilities. The eight papers following this report give a good cross section of this activity.

CALIBRATION OF TOWING TANK WAVEMAKING SYSTEM AT THE INSTITUTE FOR MARINE DYNAMICS

I. Datta, Associate Research Officer
and
J.J. Murray, Assistant Research Officer
Institute for Marine Dynamics
St. John's, Newfoundland, Canada

ABSTRACT

A 200m x 12m x 8m towing tank has recently been commissioned at the newly-built laboratories of the Institute for Marine Dynamics. The tank is equipped with a dual-flap wavemaker which can be operated in various flap motion combinations and be made to generate both regular and irregular long-crested waves. The maximum height of regular waves is 1m at a water depth of 7m.

A series of tests have been conducted to calibrate the wavemaker and determine its performance in a number of modes of articulation of the two flaps. Measured wavemaker performance has been compared with theoretical predictions calculated from the linear theory. Agreement between the two has been quite good and it is concluded that suitable combination of board articulation will yield very good wavemaker performance over a wide band of wave frequencies.

1. INTRODUCTION

Recently the National Research Council of Canada (NRC) has built new ship and offshore structures research laboratories in St. John's, Newfoundland. These laboratories, named the Institute for Marine Dynamics (IMD), have been described by Gospodnetic and Miles (1983). Among the major facilities built at this site is a 200m long towing tank (generally referred to as the Clearwater Tank), shown in Figure 1. Large ship models up to 12m long can be tested in this tank at speeds up to 10 m/s in both regular and irregular uni-directional long-crested waves. These waves, which may be up to 1m in height, are generated by an articulated dual-flap wavemaker fitted at one end of the tank. The original design work on this wavemaker was carried out by Miles (1984) which was based on the algorithms developed by Dalzell (1975). The theory was in essence an extension of the work by Havelock (1929) and Biesel et al (1951) to cover the case of a dual-flap wavemaker. Ursell, Dean and Yu (1960) conducted some experimental studies to compare with theoretical predictions for a piston type wavemaker.

Tests on the wavemaker have recently been carried out in two parts -- tests with regular waves and those with irregular waves. In the latter case, no effort was made to generate any specific spectrum at this stage of testing. Instead, attention was confined to obtaining the transfer functions between the input signals and the resulting output wave heights. Since the wavemaker can be operated in a number of modes of articulation, performance in each mode as a function of wave frequency was of prime interest. Generation of a range of waves and the measured performance in various modes have been reported in this paper. Wherever possible, design curves for regular and irregular waves calculated by Miles (1984) have been presented for comparison with experimental data.

2. WAVEMAKER AND BEACH DESCRIPTION

The wavemaker, shown in Figure 2, is of dual-flap, dry back construction. These flaps, or waveboards, can be operated independently of each other. Each waveboard is powered by a single actuator at the centre with two additional side actuators providing hydrostatic support as well as dynamic wave load compensation. A watertight seal is maintained along vertical sides by means of pneumatically pressurized sealing gaskets. The power unit, consisting of three pumps, can develop up to 275 kW of hydraulic power, delivering 13.25 L/s at 20.7 MPa.

The drive signals for regular wave generation can be supplied by a function generator which is an integral part of the control system. It generates sinusoidal signals with very low harmonic distortion. In this mode, both boards operate at the same frequency, but they can be made to move either in phase or out of phase with each other. However, the use of linear wave theory for the generation of laboratory waves is known to produce undesired free harmonic components,

see Sand and Mansard (1985). Therefore, an alternative option, where correctly computed time series drive signals can be fed into the board controllers from a remote source, is also available. Both regular and irregular waves can be generated in this manner. In the latter case, pre-computed time series signals of desired spectral bandwidth and energy distribution are fed into the waveboards. Because of inertia limitation, the lower board is designed to operate at up to 1.0Hz maximum, though the upper board can be operated to 1.8 Hz wave frequency.

The beach at the other end of the tank is made of corrugated plates bolted to a rigid framework. The surface has a large circular profile of 30m radius and extends 20m into the tank at the toe. The section of the beach near the water level (from top end to 2m below the mean water level) is topped by transverse wooden slats, 5cm x 5cm cross-section spaced 7cm apart, sitting on the corrugated surface. The bottom 2m of the beach profile is left uncovered. At the top end, about 60cm clearance is provided to facilitate water from long waves to run over the top and flow back into the tank. The segment of the beach in front of the dock area can be lowered to allow models to be floated from and back into the dock.

3. WAVEMAKER CONTROL

3.1 Modes of Articulation

The dual-flap nature of the wavemaker makes it possible to combine the flap motions in four basic modes. These modes are illustrated in Figure 3 and are:

- Mode A - Lower flap only (upper flap locked in zero position in line with the lower flap);
- Mode B - Upper flap only (lower flap locked in the vertical position);
- Mode C - Flaps out of phase (upper flap held vertical);
- Mode D - Flaps in phase.

In the out-of-phase mode, the upper flap angle at any instant is equal and opposite to the lower flap angle and, therefore, it always stays vertical. In the in-phase mode, both flaps reach maximum (or minimum) at the same instant but their amplitudes can be different. In the present experiments, upper and lower flap angles were determined using a model proposed by Dalzell (1975), where the absolute flap angle amplitude ratio at any given frequency (for the upper flap this meant the sum of lower and upper flap angles) was equal to the mean slope (with depth) of the horizontal particle amplitude profiles in the corresponding regions of depth.

In addition, a fifth mode of operation called the least squares apportionment (Mode E) was tested. In this mode the flap angles were chosen such that the least squares difference between a board and the water particle displacements over the depth of the board is minimized. The flaps operate either in phase or out of phase, depending upon the wave frequency, and the board angles are calculated following the method proposed by Clark and Menken (1977).

It must be noted here that at the current stage of development of the wavemaker control system, tests in modes D and E could be performed with regular waves only.

3.2 Regular Wave Generation

It is beyond the scope of this paper to provide a full account of the derivation of the expression for wave elevation from the basic Laplace's equation and the prevailing boundary conditions. It will suffice to give the general expression for wave elevation produced by a dual flap generator of the type illustrated in Figure 2. This expression, as derived by Dalzell (1975), as a function of distance x from the mean waveboard position and time t, is given by:

$$\begin{aligned}\eta(x,t) = {} & [\alpha_o R_o(h_1) + \beta_o R_o(h_2) \cos\varepsilon_2] \sin(k_o x - \omega t) \\ & - [\beta_o R_o(h_2) \sin\varepsilon_2] \cos(k_o x - \omega t) \\ & - [\alpha_o Q(h_1,x) + \beta_o Q(h_2,x) \cos\varepsilon_2] \cos(\omega t) \\ & + [\beta_o Q(h_2,x) \sin\varepsilon_2] \sin(\omega t) \qquad \ldots (1)\end{aligned}$$

where

- α_o = amplitude of lower flap angle motion
- β_o = amplitude of upper flap angle motion
- k_o = wave number given by linear wave dispersion relationship

$$\omega^2 = g\, k_o \tanh(k_o h)$$

- ω = wave frequency (rad/sec)
- g = acceleration due to gravity
- ε_2 = phase lag of upper board motion with respect to the lower board
- h = depth of water in the tank
- h_1 = depth of lower flap hinge below still water level
- h_2 = depth of upper flap hinge below still water level.

$R_o(h_1)$ and $R_o(h_2)$ are essentially the transfer functions between the board angles and the resulting wave amplitudes for the lower and the upper board respectively. $Q(h_1,x)$ and $Q(h_2,x)$ are the near-wavemaker disturbance terms which can be shown to disappear at a distance of over two wave-depths away from the wavemaker. Thus the first two terms of equation (1) will yield the steady state wave amplitude $|\eta|$ and the last two terms contribute to the "evanescent" wave amplitude $|\eta_d|$. Both can easily be derived from equation (1) and are given by the following equations:

$$|\eta| = [\alpha_o^2 R_o^2(h_1) + \beta_o^2 R_o^2(h_2) + 2\alpha_o\beta_o R_o(h_1) R_o(h_2)\cos \varepsilon_2]^{1/2} \quad \ldots (2)$$

and

$$|\eta_d| = [\alpha_o^2 Q^2(h_1,x) + \beta_o^2 Q^2(h_2,x) + 2\alpha_o\beta_o Q(h_1,x)\, Q(h_2,x) \cos \varepsilon_2]^{1/2} \quad \ldots (3)$$

It can also be shown that for modes where upper board operates either in phase or out of phase with the lower board, the envelope of waves as a function of x may be written as:

$$|\eta_e| = |\eta|[1 + |\eta_d/\eta|^2 - 2|\eta_d/\eta| \sin(k_o x)]^{1/2} \quad \ldots (4)$$

As $|\eta_d|$ will vanish far away from the wavemaker, the envelope of wave amplitude will eventually converge to the steady state condition $|\eta|$.

At the wavemaker, where x = 0,

$$|\eta_e/\eta| = [1 + |\eta_d/\eta|^2]^{1/2} \quad \ldots (5)$$

This term has been referred to as the "Figure of Merit" (FOM) and gives a theoretical estimate of the expected distortion in the wave profile that will arise at the wavemaker due to the mismatch between the actual wavemaker motion and the hyperbolic distribution of motion (witn depth) required to produce perfectly regular waves. Since different modes of articulation would produce different board displacements, FOM would be a function of the mode selected. If perfect waves were produced, $|\eta_d|$ would have been zero and FOM = 1. As the wavemaker motion deviates from the required profile, FOM increases, with larger values generally signifying poorer quality of waves near the wavemaker. Theoretically calculated values of FOM for various modes of operation as functions of frequency are given in Figure 4. This Figure suggests that mode B should be used for high frequency waves only, whereas modes A and C are more appropriate for generating lower frequency components. Therefore, a combination of various modes would likely be needed to produce good quality waves over a wide bandwidth.

3.3 Irregular Wave Generation

Assuming that any given irregular wave spectrum $S(\omega)$ can be reproduced in the time domain by the linear summation of N sinusoidal wave components (where N is an arbitrarily large number), the surface elevation at any given location $x = x_R$ can be expressed as:

$$\eta(x_R,t) = \sum_{j=1}^{N} A_j \cos(k_{oj} x_R - \omega_j t - \varepsilon_j)$$

where

$A_j = \sqrt{2\, S(\omega_j)\, \Delta\omega}$

$\Delta\omega = 2\pi\Delta f$ = frequency difference at which discretization is carried out

ω_j and ε_j = frequency and phase associated with j-th component.

In such a case, equation (1) may be re-written as the linear summation of N such discrete components. Assuming sufficient distance from the waveboards, the "evanescent" terms should disappear and the equation then reduces to:

$$\eta(x_R,t) = \sum_{j=1}^{N} [\{\alpha_{oj} R_{oj}(h_1) + \beta_{oj} R_{oj}(h_2) \cos \varepsilon_{2j}\} \sin(\varepsilon_{ij} - \omega_j t) + \{\beta_{oj} R_{oj}(h_2) \sin \varepsilon_{2j}\} \cos(\varepsilon_{ij} - \omega_j t)] \quad \ldots (7)$$

where $\varepsilon_{ij} = k_{oj} x_R - \varepsilon_j$

Here $R_o(h_1)$ and $R_o(h_2)$ are written with suffix j to indicate that they are functions of the frequency component ω_j and can be calculated directly from equations given by Dalzell (1975).

Two of the four unknowns in the above equation ($\alpha_{oj}, \beta_{oj}, \varepsilon_{ij}$, and ε_{2j}) are determined as the mode of operation for a given frequency component ω_j is selected. These can be given as follows:

Mode A : $\beta_{oj} = 0$, $\varepsilon_{2j} = 0$
Mode B : $\alpha_{oj} = 0$, $\varepsilon_{2j} = 0$
Mode C : $\alpha_{oj}/\beta_{oj} = 1$, $\varepsilon_{2j} = \pi$
Mode D : $\alpha_{oj}/\beta_{oj} = (Y_1.h_2)/(Y_2.h_1)$, $\varepsilon_{2j} = 0$
Mode E : $\alpha_{oj}/\beta_{oj} = |(B.E - C.D)/(B.D - A.E)|$, $\varepsilon_{2j} = 0$ or π depending on whether the above ratio is positive or negative.

for j = 1,N.

Here $Y_1 = \frac{h_1}{(h_1 - h_2)} [|\exp(-k_o h_2) - \exp(-k_o h_1)| / \{1 - \exp(-k_o h_1)\}]$

$Y_2 = 1 - Y_1$

$A = \sum_{i=0}^{\frac{h_1}{\Delta h}} (h_1 - y_i)^2$

$B = \sum_{i=0}^{\frac{h_2}{\Delta h}} (h_1 - y_i).(h_2 - y_i)$

$C = \sum_{i=0}^{\frac{h_2}{\Delta h}} (h_2 - y_i)^2$

$D = \sum_{i=0}^{\frac{h_1}{\Delta h}} (h_1 - y_i).X(y_i)$

$E = \sum_{i=0}^{\frac{h_2}{\Delta h}} (h_2 - y_i).X(y_i)$

Δh = short step width in y-direction

$X(y_i)$ = magnitude of water particle displacement in x-direction at a depth y_i

$$= a \frac{\cosh(k_o(h - y_i))}{\sinh(k_o h)}$$

a = wave amplitude.

The remaining two terms are obtained by matching the amplitude and phase of the wave component at location $x = x_R$. It can then be

shown that the lower and the upper board angles in the time domain, that is $\alpha(t)$ and $\beta(t)$ respectively, are given by the Fourier summations:

$$\alpha(t) = \sum_{j=1}^{N} [\, c_j \cos(\omega_j t) + d_j \sin(\omega_j t)]$$

$$\beta(t) = \sum_{j=1}^{N} [\, e_j \cos(\omega_j t) + f_j \sin(\omega_j t)]$$

where

$$c_j = \alpha_{o_j} \cos(\varepsilon_j)$$
$$d_j = -\alpha_{o_j} \sin(\varepsilon_j)$$
$$e_j = \beta_{o_j} \cos(\varepsilon_j + \varepsilon_{2_j})$$
$$f_j = -\beta_{o_j} \sin(\varepsilon_j + \varepsilon_{2_j})$$

4. CALIBRATION

4.1 Data Acquisition and Instrumentation

The measurement of wave elevation time series in the tank was performed using two sets of capacitive wave probes mounted in line with the direction of wave propagation. The first set was located approximately 46.7m from the mean waveboard position (to the first probe in the set) and the second set close to the beach approximately 153.4m from the waveboards. The second set was required to measure data for beach reflection performance, which will be reported in future. Data from the wave probes, as well as from the angular displacement transducers (both lower and upper) which are mounted permanently on the board hinge axes, were sampled at 20 Hz and stored using the data acquisition system located on the towing carriage. The resolution of the wave probe data was less than 0.07mm and that for the board angles was better than 0.001 degree. Each set of wave probes contained 5 to 6 individual probes which were spaced to cover a wide range of frequencies. This technique of measurement of wave data was developed and refined at the NRC Hydraulics Laboratory in Ottawa and has been described by Mansard & Funke (1980) and Mansard, Sand & Funke (1985).

4.2 Regular Wave Testing

The wavemaker has been designed primarily to optimize generation of waves between 2m and 50m wavelength (model scale). Since the scale of models to be tested in the tank is likely to be between 1:10 and 1:50, the range of prototype waves that will be covered will depend upon the choice of scale. However, it should be adequate to include most first order wavelengths that may be of interest in model testing. The required performance curves of the wavemaking system for regular wave generation have been shown in Figure 5.

The test programme was devised so that the performance of the wavemaker in all modes of operation could be tested. Tests were planned at a number of frequencies, and at each frequency the wave slope was to be varied from minimum (wave height/length = 1/100) to maximum (wave breaking). The squares in Figure 5 represent the frequencies and wave heights chosen for testing. Because of some current temporary limitations of the towing tank, tests with longer waves below 0.25 Hz wave frequency and higher waves of 0.8m wave height and above have been deferred.

4.3 Irregular Wave Testing

The wavemaker was subjected to a flat white noise spectrum generated digitally at a Δf of 6.1035×10^{-4} Hz attenuated at both ends to avoid board acceleration, velocity and displacement beyond the maximum capabilities of the wavemaker. The input signal, equivalent to r.m.s. board angle amplitudes of 3.54 degrees, was fed into the board controllers simultaneously. The stage of hardware development at the time of reporting did not provide a way of inputting separate signals to each board for more than one frequency component at a time. Therefore the angle apportionment (modes D and E) described in Section 3.1 was not possible for the irregular wave calibration.

After one repeat period, data acquisition was carried out and transfer functions between the waveboard angular displacement and the resulting wave profile were determined from one data record of duration equal to the repeat period of the input signal.

5. RESULTS AND DISCUSSION

The results of wavemaker tests in regular waves have been plotted in Figures 6 and 7 for the different modes of operation as functions of wave frequency. The transfer functions in Figure 6 are presented in terms of wave amplitude per unit "half-stroke" of the wavemaker at the water level, which is given by the relationship:

$$s = h_1 \alpha_o + h_2 \beta_o .$$

The theoretically computed curves have also been superimposed on the data points. In Figure 7, magnitudes of free second harmonic waves in various modes as ratios of calculated fundamental wave heights have been shown. No attempt has been made here to draw any mean curves through the data points.

From Figure 6(a) to 6(e) it can be seen that for all modes, the correlation between theory and experiment is quite good for frequency up to about 0.5 Hz. Above this, the deviation starts getting larger. One reason for this seems to have been the compromise made in wave probe spacing recommended by Mansard and Funke (1980) so as to cover a wider range of wave frequencies. In fact it was known that the wave probe spacing was not optimum for the correct measurement of waves shorter than 6m wave length (0.51 Hz). This compromise was made to avoid frequent change of wave probe position during the test programme and attention was primarily given to measuring performance in longer waves more accurately. The calculated amplitudes for

both the fundamental and the higher harmonic waves probably had larger margin of error for these shorter waves.

Figures 7(a) and 7(e) indicate the quality of waves produced in terms of harmonic distortion (second harmonic wave height to fundamental wave height ratio). Although there is some scatter, it appears that A, B and D show general trend of lower distortion with higher wave frequencies, whereas modes C and E do not show any specific trend. Instead, the results seem to be confined within a band of 0 to 10% of the fundamental waveheight.

As expected, harmonic distortion in Mode B is particularly high at lower frequencies, confirming that the top flap alone should primarily be used to generate higher frequency components. The relatively high harmonic content in mode D is particularly to be noted. It appears that though mode D maximizes wavemaker response in terms of producing the highest waves per unit board angle as shown by Dalzell (1975), it pays a heavy price in terms of harmonic distortion of the wave profile, particularly for low frequency waves. Mode C, in general, seemed to produce less harmonic distortion than mode E. However, on the whole, possibly either of them could be used quite satisfactorily for generating low frequency waves.

The results of wavemaker testing with random noise spectrum have been plotted in Figures 8 to 10 as flap angles per unit wave-height. Only results for modes A, B and C have been presented since the control programmes for feeding proportioned input signals to the two waveboards were under development at the time of reporting. The theoretically expected transfer functions have also been plotted for comparison.

The results show very good agreement between analytical and experimental results over a wide frequency band. The larger deviation at the very low frequencies were probably due to spurious long waves arising from the discretization of wave frequency. At the higher frequency end, particularly in mode B, some attenuation in waveheight appears to have caused an increase in the transfer function. However, for the primary wave-length range of 2m (0.884 Hz) to 50m (0.149 Hz), the transfer functions in all these modes appear to agree with theoretical curves very well.

6. CONCLUSIONS AND FUTURE WORK

In this paper, only the results of the first set of calibration tests conducted in the IMD Clearwater Tank have been presented. Performance of the wavemaker on the whole has been found to be quite satisfactory. Some deviation from theoretical curves has been noted at the higher frequency end of the wave spectrum. It is believed that the cause for this deviation lies more in the way data were analyzed, rather than in the actual wavemaker performance. Obviously modifications in the data analysis procedures will be required to improve calibration results. Some of the important areas that need additional work have been mentioned below. No doubt refinement of calibration will be an on-going process as the future advances in model scale wavemaking techniques, suppression of higher order waves, measurement and analysis of major wave parameters, etc., are taken advantage of.

(1) Some of the tests at frequencies higher than 0.5 Hz would have to be done with modified wave probe spacing to measure co-existing incident and reflected waves more closely and to obtain the fundamental and higher harmonic wave heights with greater accuracy.

(2) Tests have to be extended to cover longer waves (of frequency below 0.25 Hz) and higher wave heights (0.80m and over) which could not be performed earlier because of temporary limitations.

(3) Tests to investigate waveheight distribution along the length of the tank would be needed to establish whether there is any appreciable attenuation of height as a wave train travels down the tank. If these tests do show any significant attenuation, appropriate booster functions will have to be introduced to obtain correct waveheight at the required locations.

(4) Control programs that will generate proportioned input signals to the two waveboards are being developed. These would be needed for irregular wave generation so that modes D and E could be used.

(5) Lastly, investigation on reflection performance of the beach fitted in the tank is under way at the moment. Results of these investigations will show the efficiency of the beach as a wave absorbing unit and whether any improvements need to be made in its design.

7. REFERENCES

GOSPODNETIC, D. and MILES, M.D. (1983) : "New Model Testing Facilities of the NRC Arctic Vessel and Marine Research Institute". 20th American Towing Tank Conference, Davidson Laboratories, Hoboken, N.J.

MILES, M.D. (1984) : "Computer Programs for Design of Dual-Flap Wavemakers". NRC/IMD Laboratory Technical Report No. LTR-SH-379, June 1984, Ottawa, Ontario.

DALZELL, J.F. (1975) : "Technical Report on Analyses of Articulated Flap Wavemakers". ABA Electromechanical Systems, Inc. Report No. TR75-1, March 1975, Pinellas Park, Florida.

HAVELOCK, T.H. (1929) : "Forced Surface-Waves on Water". Philosophical Magazine

Series 7, Vol.8(51), October 1929.

BIESEL, F. et al (1951) : "Laboratory Wave Generating Apparatus". (In French), La Houille Blanche, No. 2,4,5/1951;6/1952.

URSELL, F., DEAN, R.G. and YU, Y.S. (1960) : "Forced Small-Amplitude Water Waves : A Comparison of Theory and Experiment". J. Fluid Mech., Vol. 7 (1), pp.33-52.

SAND, S.E. and MANSARD, E.P.D. (1985) : "Reproduction of Higher Harmonics in Irregular Waves". NRC Hydraulics in Irregular Waves". NRC Hydraulics Laboratory Technical Report No. TR-HY-012, Ottawa, Ontario.

CLARK, A. and MENKEN, M. (1977) : "Dual Flap Wavemaker Phasing and Motion Apportionment by Linear Regression". 18th American Towing Tank Conference, August 1977, U.S. Naval Academy, Annapolis, MD.

MANSARD, E.P.D. and FUNKE, E.R. (1980) : "The Measurement of Incident and Reflected Spectra Using a Least Squares Method". Proc. 17th Coastal Engineering Conference, Sydney, Australia.

MANSARD, E.P.D., SAND, S.E. and FUNKE, E.R. (1985) : "Reflection Analysis of Non-Linear Regular Waves". NRC Hydraulics Laboratory Technical Report No. TR-HY-011, November 1985, Ottawa, Ontario.

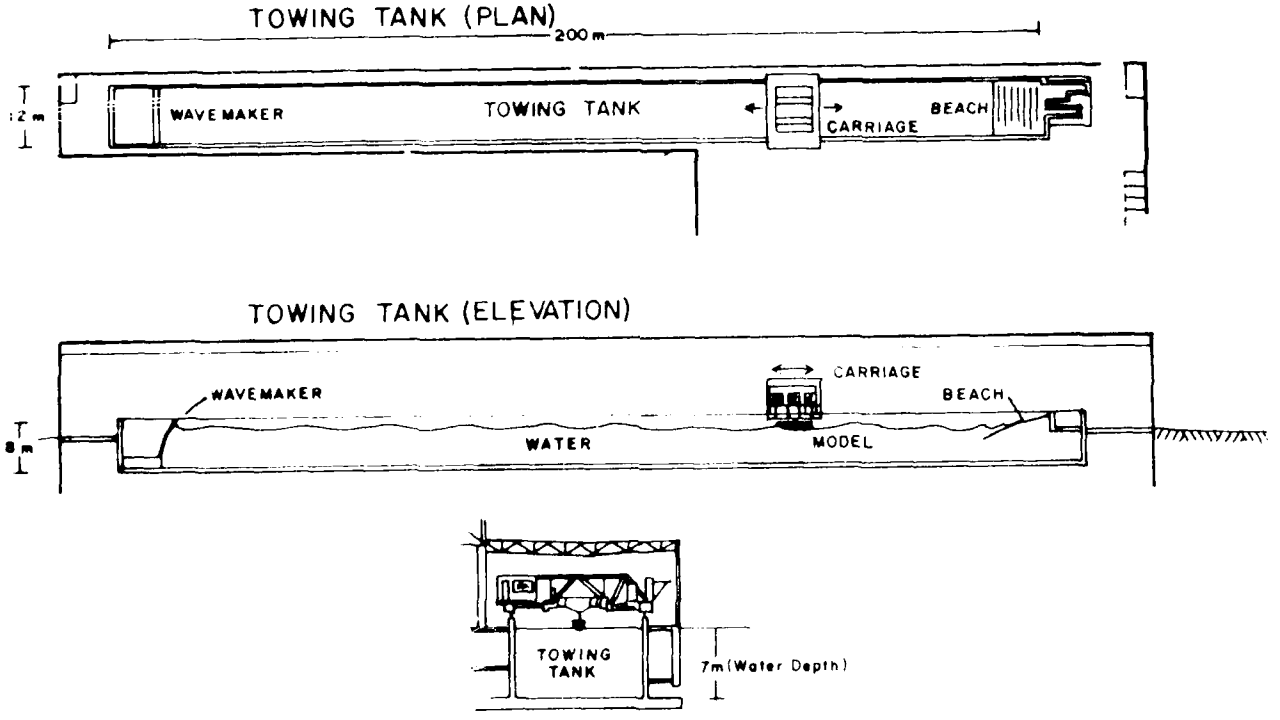

Figure 1 - Clearwater Tank Schematics

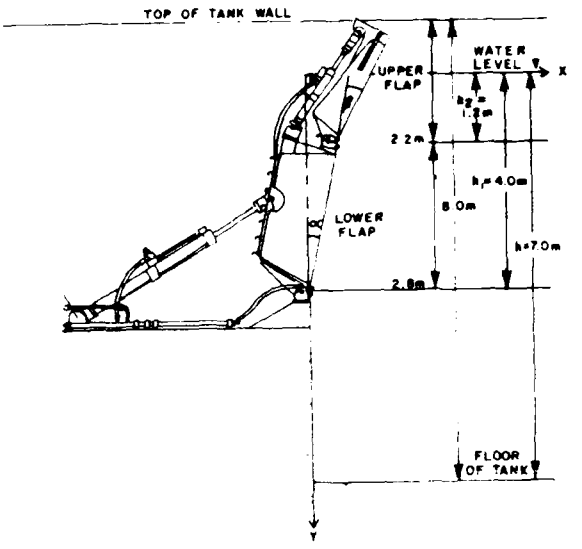

Figure 2 - Dual Flap Wavemaker Dimensions and Schematics

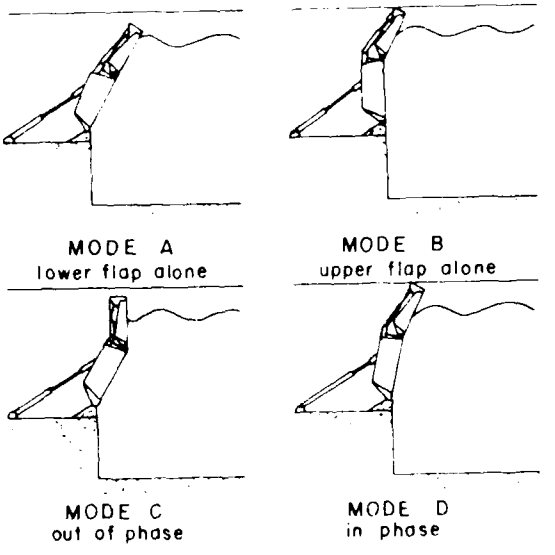

Figure 3 - Main Modes of Wavemaker Articulation

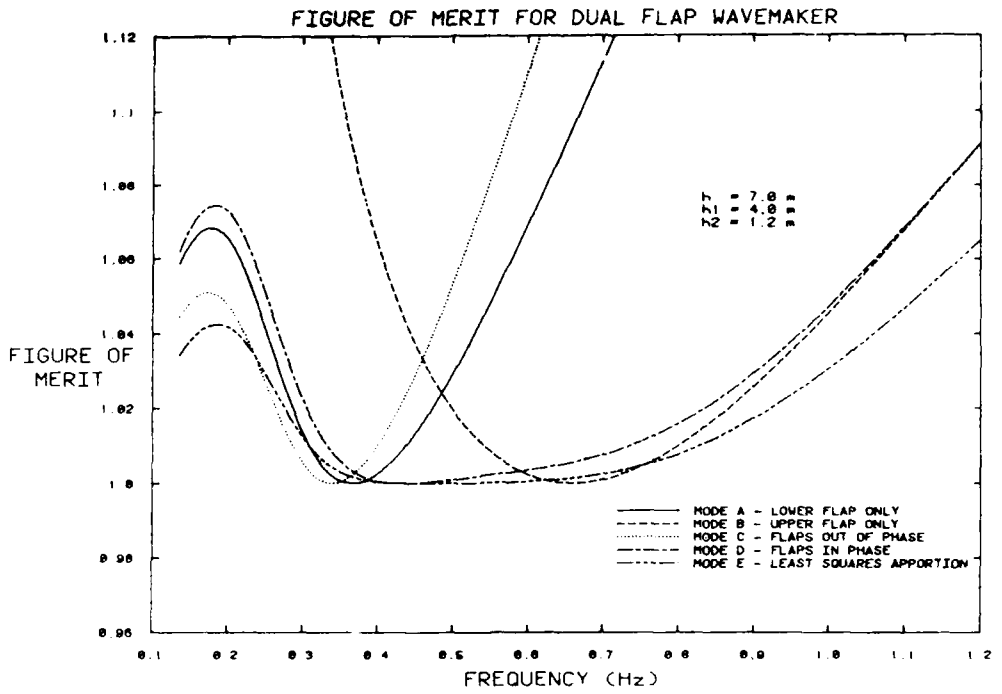

Figure 4 - Figures of Merit at Various Modes

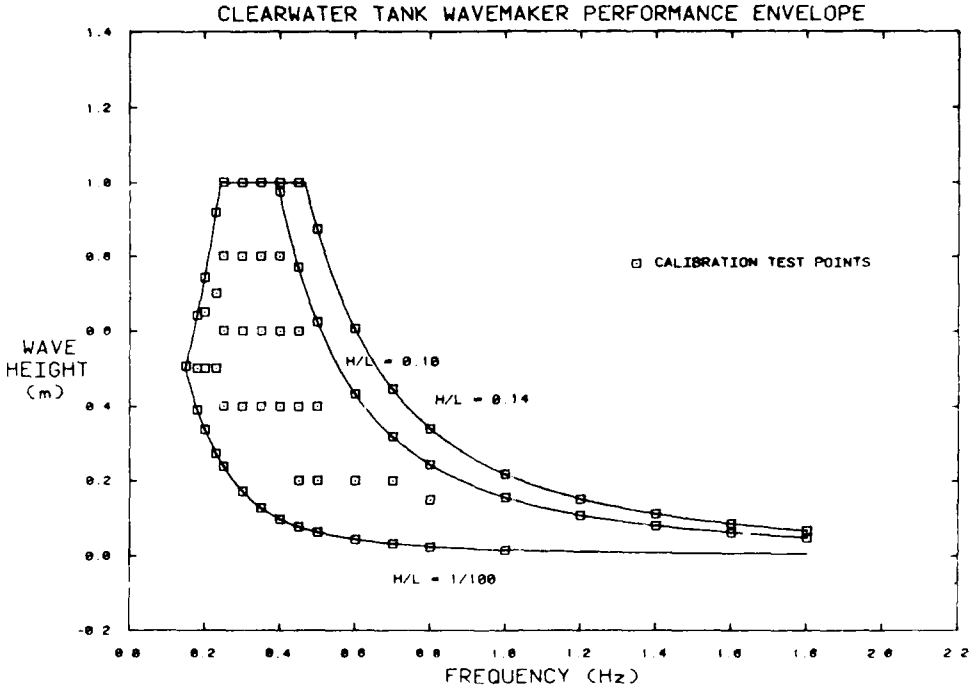

Figure 5 - Wavemaker Performance Envelope

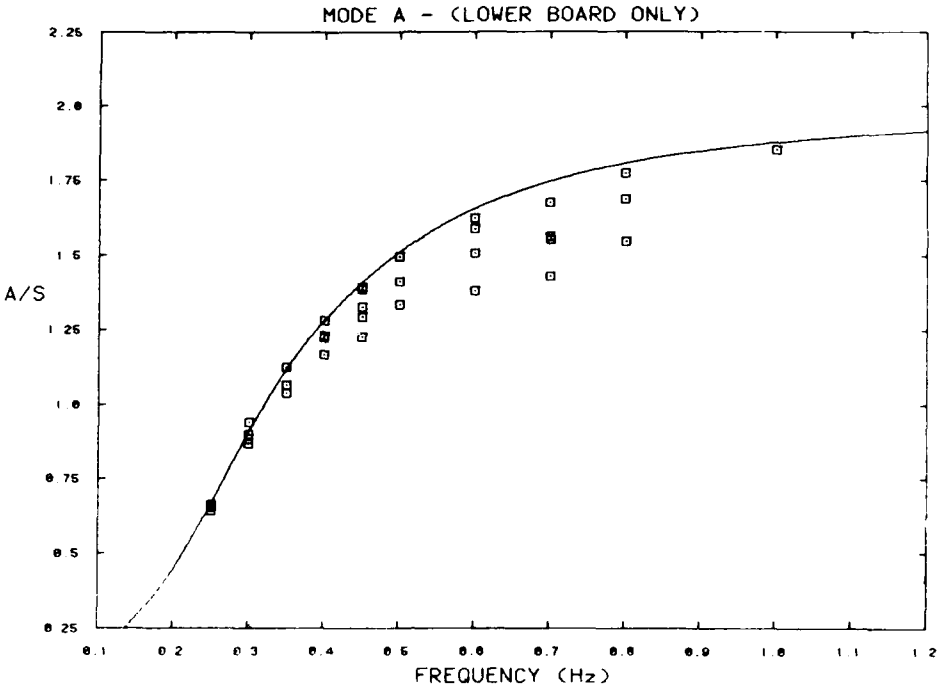

Figure 6(a) - Wavemaker Performance in Regular Waves
(Mode A, Lower Board Only)

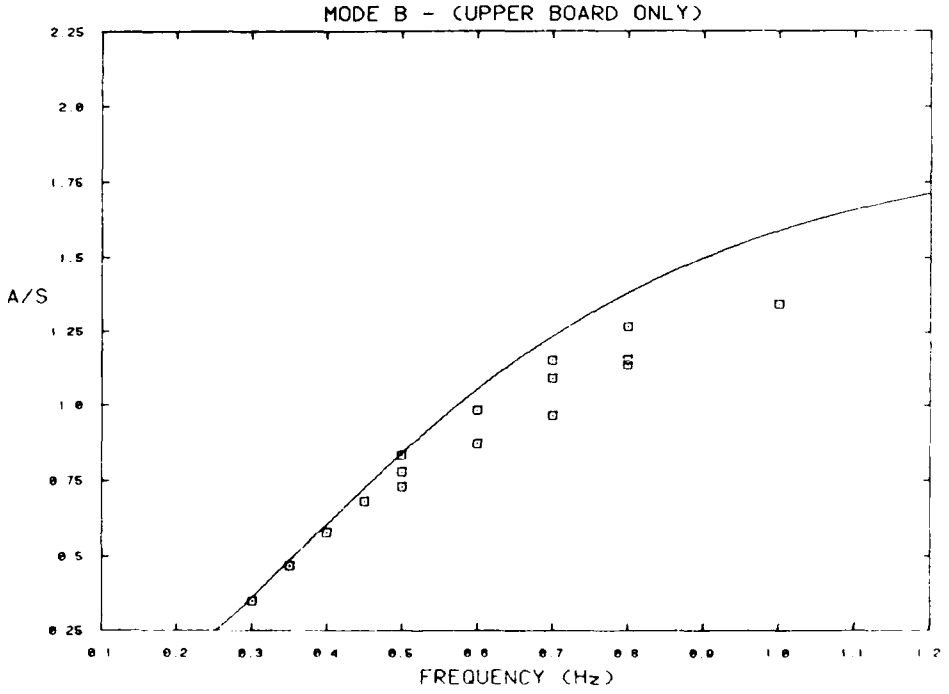

Figure 6(b) - Wavemaker Performance in Regular Waves
(Mode B, Upper Board Only)

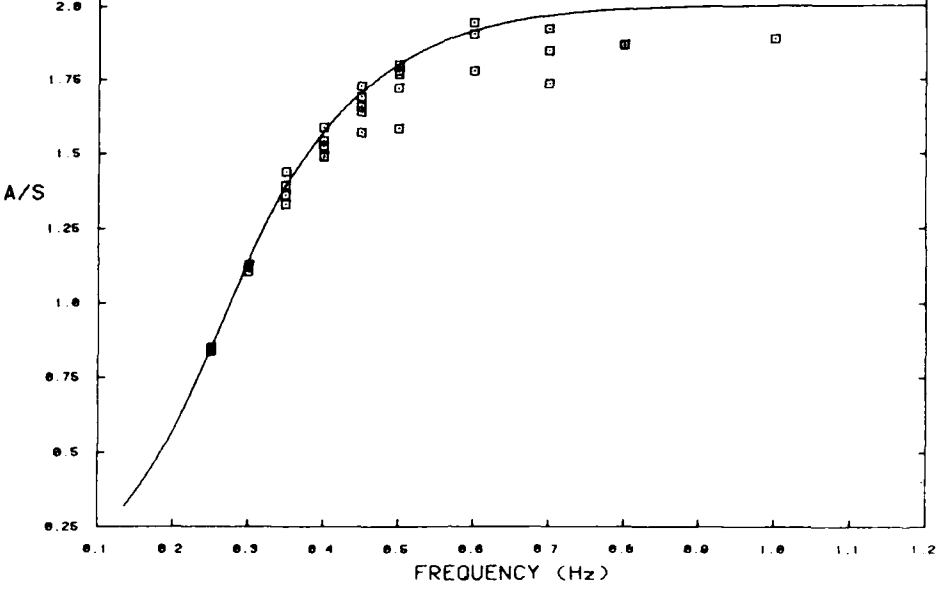

Figure 6(c) - Wavemaker Performance in Regular Waves
(Mode C, Boards out of Phase)

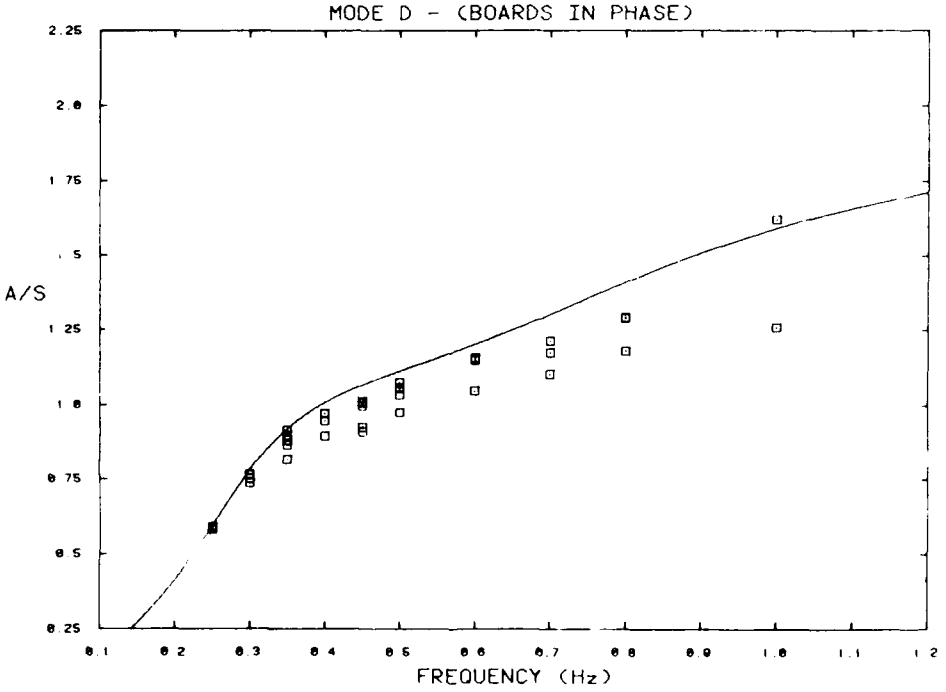

Figure 6(d) - Wavemaker Performance in Regular Waves
(Mode D, Boards in Phase)

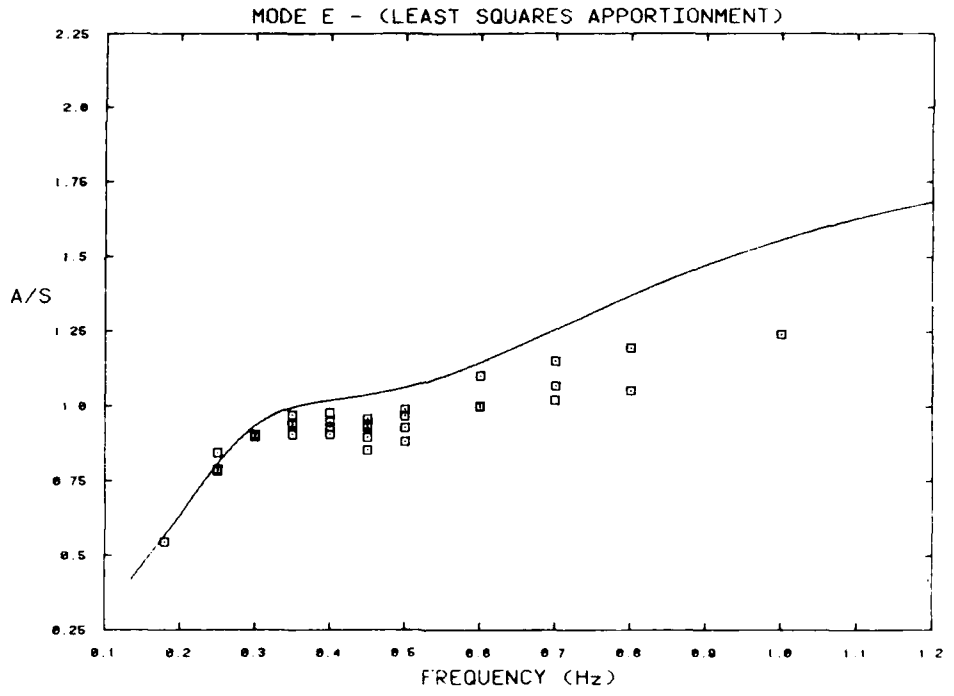

Figure 6(e) - Wavemaker Performance in Regular Waves
(Mode E, Least Squares Apportionment)

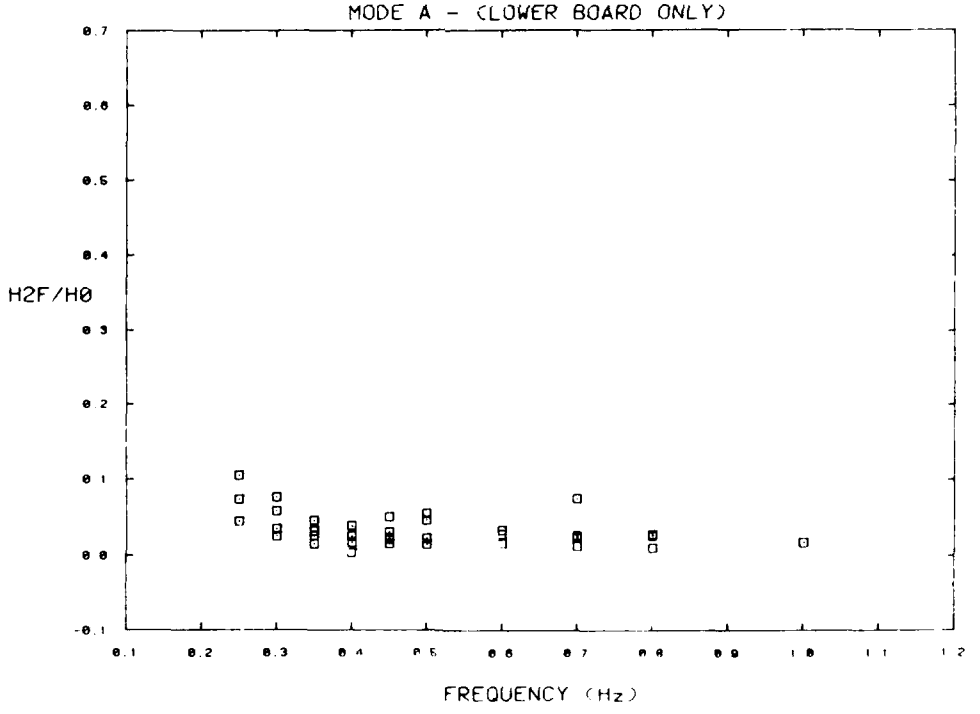

Figure 7(a) - Free Harmonic Content in Regular Waves
(Mode A, Lower Board Only)

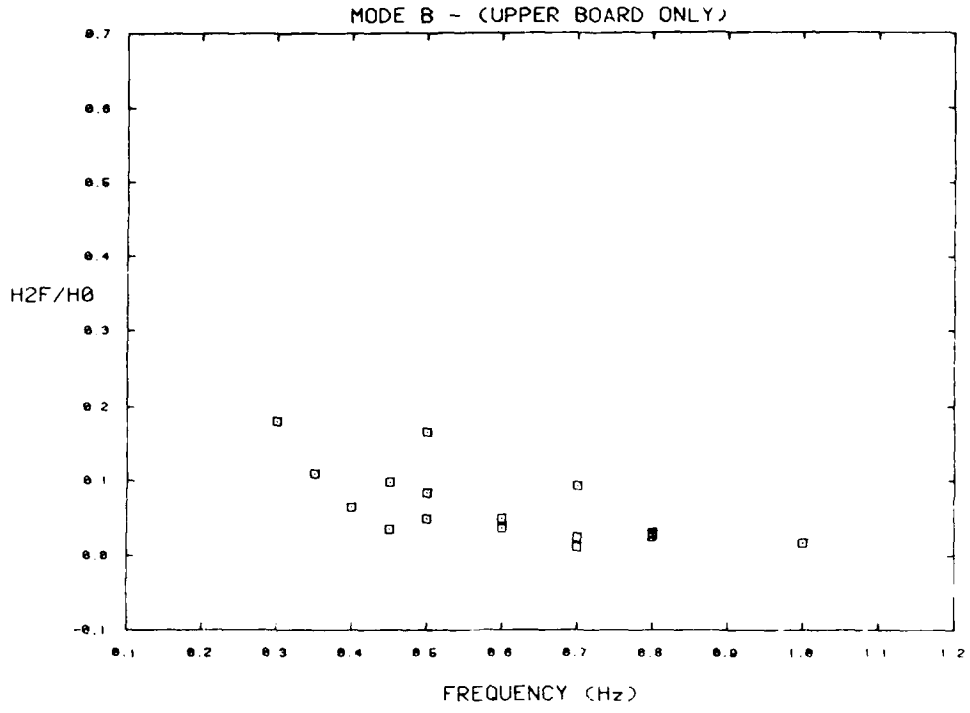

Figure 7(b) - Free Harmonic Content in Regular Waves
(Mode B, Upper Board only)

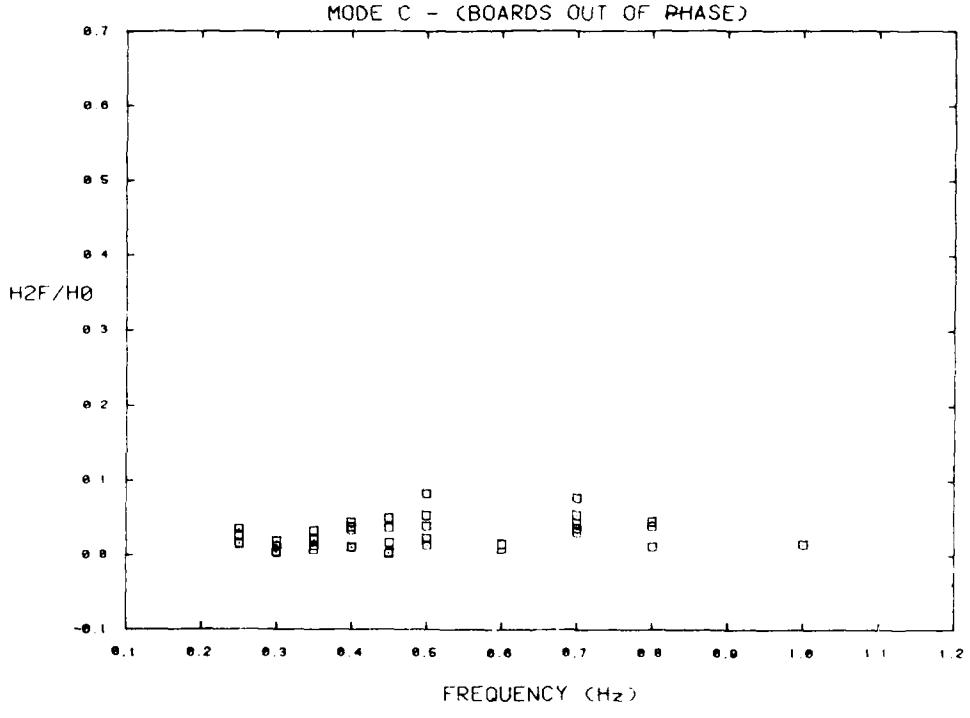

Figure 7(c) - Free Harmonic Content in Regular Waves
(Mode C, Boards out of Phase)

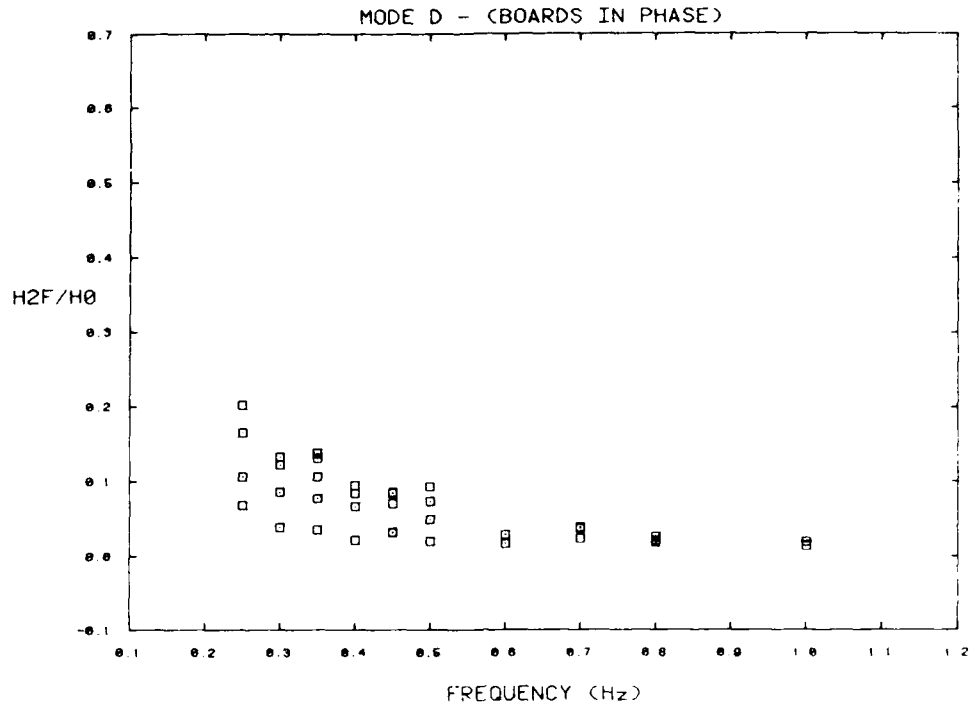

Figure 7(d) - Free Harmonic Content in Regular Waves
(Mode D, Boards in Phase)

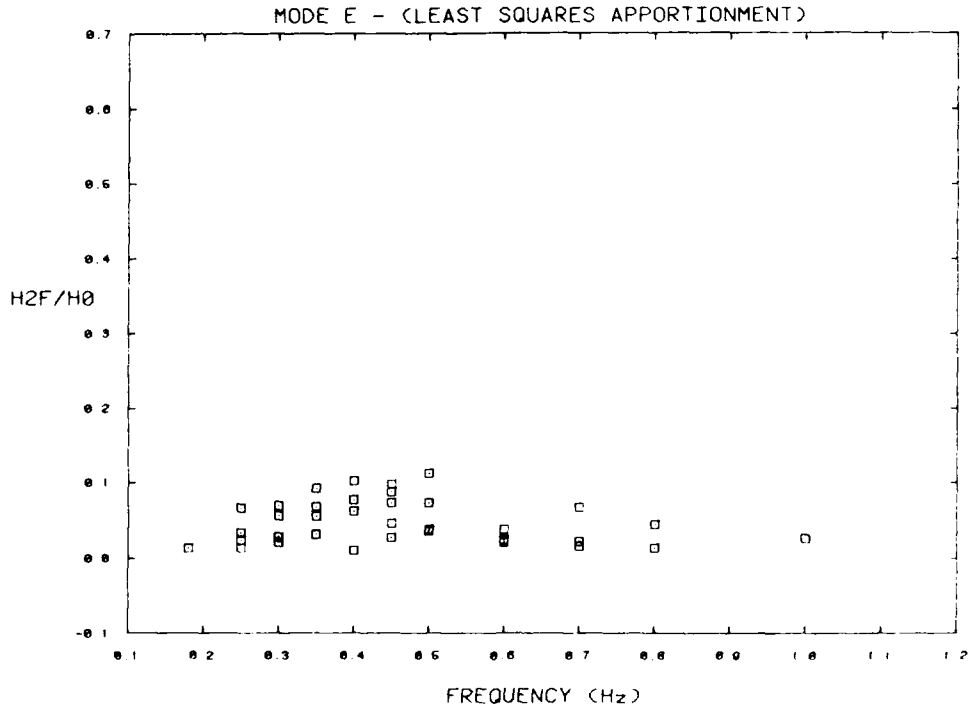

Figure 7(e) - Free Harmonic Content in Regular Waves
(Mode E, Least Squares Apportionment)

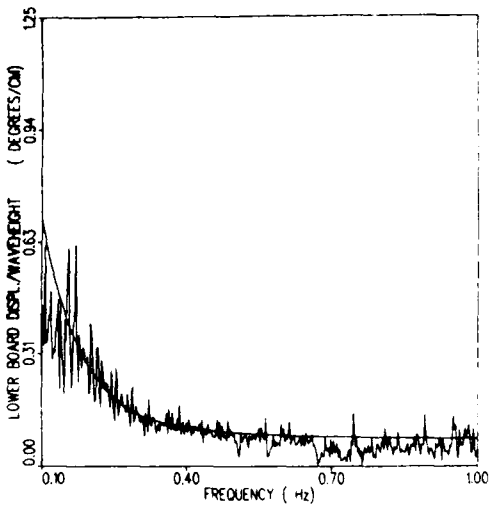

Figure 8 - Wavemaker Transfer Function in Mode A

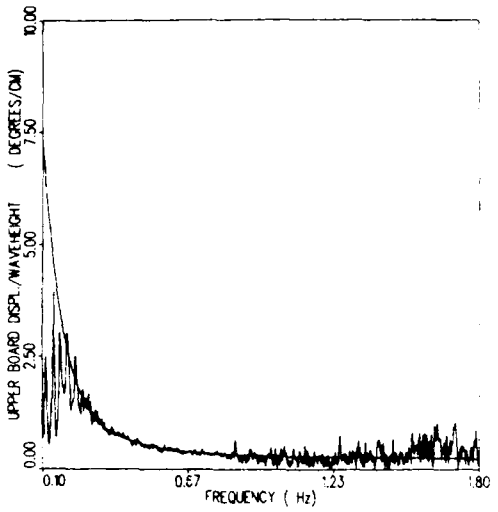

Figure 9 - Wavemaker Transfer Function in Mode B

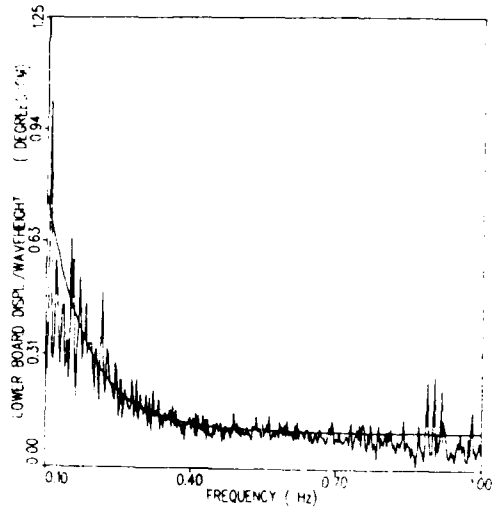

(a)

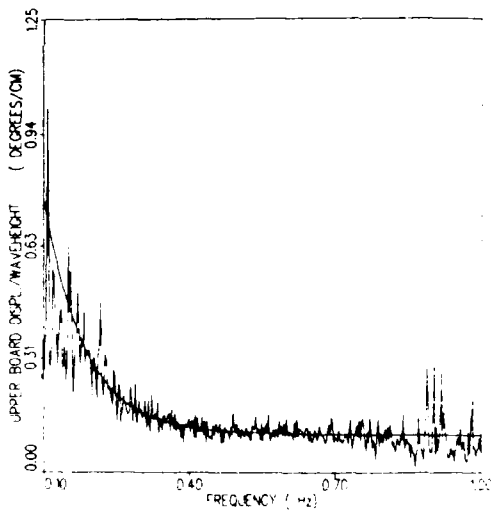

(b)

Figure 10 - Wavemaker Transfer Functions in Mode 1

COMMENT

Mr. John F. Dalzell
David Taylor Naval Ship R&D Center
Bethesda, MD, USA

I am delighted to see a comparison of the calibration results from the IMD articulated flap wave machine with linear theory. Once a machine is built theoretical/experimental correlations are of little benefit to the owner, but are potentially of great value to anyone in the market for a new system. I was somewhat surprised that the correlation with theory was so good for small wave slopes. The experience with the similar but smaller Davidson Laboratory machine described at the last ATTC was different. In the calibration of that machine it was found that linear theory consistently underestimated the wave amplitude for a given stroke, by a margin which would have resulted in about ten percent less regular and irregular wave height capability than had been hoped for had it not been for some compensating conservatism in other aspects of the design. An important difference between the two machines is that the DL machine is wetback and the IMD machine is dryback. With the publication of the IMD dryback experience it appears that leakage due to lack of seals in the wetback system is a primary reason for the discrepancy. As a matter of interest, the DL experience suggests that a wetback system preliminary design using linear theory may yield better results if a virtual hinge depth 93 to 95 percent of the physical depth is used in the theory.

A MULTI MODE SEGMENTED WAVE GENERATOR FOR THE NRC HYDRAULICS LABORATORY

M.D. Miles
P.H. Laurich
E.R. Funke

Hydraulics Laboratory
National Research Council
Ottawa, Canada

ABSTRACT

The offshore wave basin of the NRC Hydraulics Laboratory has dimensions of 50 m by 30 m by 3 m and is used primarily for ocean engineering studies of bottom-founded and moored structures. It has recently been equipped with a new 64-segment, multi-mode, directional wave generator system which incorporates a number of design features which are unusual or unique for a segmented machine. These include variable depth operation, multiple articulation modes (piston, hinged flapper and combination), large wave amplitude capability, automatic sensor calibration and a distributed microprocessor-based direct digital control system.

Various aspects of the design and implementation of this system are described including hydrodynamic performance, selection of actuators and sensors, servo dynamics, control system architecture and drive signal generation techniques. The relative merits of analog and digital control systems for this type of application are also discussed.

1.0 INTRODUCTION

The following describes a 64-segment wave generator system at the Hydraulics Laboratory of the National Research Council (NRCC) in Ottawa, Canada. This machine became operational in April 1986 and is a prototype of a larger 180-segment machine planned for the Institute for Marine Dynamics of NRCC in St. John's, Newfoundland.

A "serpentine" wave generator is a machine which, through the snake-like movement of its wave board, can produce progressive waves that propagate at oblique angles to the front of the wave board. For this purpose, the board is broken up into many small segments. Such a machine was first proposed by Biesel and built at Neyrpic in 1952 [1,2]. The authors know of two other wave generators of this type which were built in Holland about 25 years ago and have been in use extensively. These have a common mechanical drive for all segments but an individual phase adjustment for each. They can therefore produce monochromatic, long-crested, oblique waves. With the availability of faster and cheaper control and digital hardware, it became practical to provide individual articulation of each wave generator segment and, with this, the prospect of generating multi-directional wave spectra became possible.

The concept of individually controlled generator segments was first implemented by Salter and his staff at the University of Edinburgh in 1978 [3,4]. This was followed very soon by similar machines at the Hydraulics Research Station in Wallingford (HRS), U.K. (1980), the National Engineering Laboratories (NEL) in Glasgow, U.K. (1980), Wave Power Ltd. (WPL) in Southampton, U.K. (1981), the Norwegian Hydrodynamics Laboratory (MARINTEK) in 1981, the Offshore Technology Corporation (OTC) in Escondido, U.S.A. (1983), the Danish Hydraulics Institute (DHI) in 1984, the Delft Hydraulics Laboratory (DHL) in 1984, British Maritime Technology (BMT) in Feltham, U.K. (1985), the Coastal Engineering Research Center (CERC) in Vicksburg, U.S.A. (1984) and the University of Aalborg, Denmark in 1986. Installations are also being planned or are under construction in Japan, Spain and China and there may be others which are unknown to the authors.

The art of wave generation has always been an activity which left much scope for individuality. It is therefore not surprising that most of the installations named above are different to some extent. However, all machines are based on the principle of an articulated wave board with the exception of the OTC machine which uses the plunger principle. The CERC and the Aalborg machines operate in the piston mode only and use a principle that was first described by Sand [5,6,7]. It uses variable width wave board sections which are interconnected by vertical hinges. The actuation of the translational movement takes place at the hinge points. In this way the wave board is a straight line approximation of the ideal boundary. All other segmented wave machines may be considered to use a "stair case" approximation to each sine wave component.

Table 1 summarizes the installations with which the authors are acquainted. From this it may be noted that the majority use the flapper (i.e. rotational) mode and that some of the machines are of the "dry back design" while the remainder are of the "wet back design". These concepts will be explained later.

TABLE 1 SEGMENTED WAVE MACHINES

NAME	BASIN		NO. OF SEGMENTS	MODE	SEGMENT		STROKE/2 (±)	ACTN.	DRY/WET	Hmax REGL.	REF.
	SIZE (m)	DEPTH (m)			WIDTH (m)	HEIGHT (m)					
U. Edinburgh	27x11	1.2	80	FL	0.3	0.7	15°	ELEC	DRY	.22	[8]
HRS	30x48	2.0	80	FL	0.31			ELEC	WET	.50	[9,10]
NEL				FL				ELEC	DRY		
WPL	very small		60	FL							[11]
MARINTEK	50x72	0-10.	144	FL	0.5	1.3	16.5°	ELEC	DRY	.40	[12]
DHI	30x20	3.0	60	FL	0.5	1.5	16.7°	HYDR	DRY	.50	[13]
BHT	30x48	2.-3.	90	FL	0.33			HYDR	DRY		see [1]
CERC*	59x111	.76	60	PIST*	0.46	0.76	0.15 m	HYDR	WET	.30	[14]
DHL	variable	1.3	80	VARBL	0.33	1.28	0.40 m	ELEC	WET		[15]
OTC	42x32	1.5	40	PLNGR	0.6	n.a.	n.a.	HYDR	WET	.10	[16]
Aalborg U.*	8.1x12	1.2	9	PIST*	0.9	1.0	0.30	HYDR	WET		[17]
NRCC OTT	30x50	.3-2.9	64	VARBL	0.5	2.00	0.40 m	HYDR	WET	.70	

* With straight line interpolation

[1] Personal communication

Perhaps the most meaningful grouping of these facilities is in terms of their area of application. Because of the water depth of the basins in which they are installed, some of them can only be used for shallow water, coastal zone simulations whereas the others may be used for ocean engineering research. It is therefore presumed that the CERC, the DHL and Aalborg machines were intended primarily for shallow water coastal studies. From the maximum wave heights for regular waves, the total wave board lengths as well as the water depths, as given in Table 1, it appears that some facilities have limited capability for testing at scales greater than 1:50 which is the generally preferred scale for offshore engineering research.

There are two basic approaches to permit testing under variable water depth conditions. One may either arrange for an adjustable basin floor, as was done by MARINTEK, or one may build a wave generator which can be adjusted vertically along the basin wall and then raise or lower the water level in the basin to achieve the specified depth. In the latter case, it is possible to run construction machinery onto the solid basin floor and to build artificial islands and/or other concrete or gravel models which are to be tested. This is the principle which was used in the design of the Offshore Wave Basin of the NRCC Hydraulics Laboratory.

In addition to the unique feature of vertical adjustability, there were other considerations which made the option of a Canadian design and development attractive. Among these were the necessity to produce much higher short crested waves than had been accomplished previously and to produce a machine which was potentially of the highest reliability and provided the greatest convenience for calibration and for control parameter adjustments. It was also anticipated that, at some future date, active absorption of waves obliquely incident on the wave board was to be developed. For this, it was considered necessary to accommodate the feedback of control information from wave boards adjacent to the segment under control. These requirements and cost considerations made the concept of direct digital control by micro-processors attractive.

The wave machine and the control system development was a joint venture between NRCC and W.R. Davis Engineering Ltd. of Ottawa.

2.0 THE OFFSHORE WAVE BASIN

Fig. 1 provides an overview of the Offshore Wave Basin of the Hydraulics Laboratory. It may be noticed that there are only 60 segments of the generator attached to one side wall of the basin. Another submodule equipped with only two segments is mounted in a temporary flume which serves as a test facility for the design of digital control circuits and algorithms. The side flume was also used extensively for the development of a novel wave absorber which is effective at any depth of water. This module will be added to the other 60 segments at a later date. A photograph of the wave generator is shown in Fig. 2.

The basin is 3 m deep. Depending on the wave crest height, tests may therefore be carried out at water depths up to 2.9 m but the maximum depth for larger waves is 2.6 m. There is a pit of 3x3x3 m which allows testing of structures in up to 5.9 m of water.

Wave absorbers are placed all around the main basin. The absorbers which are opposite to the wave machine consist of a removable front section and a fixed, wall mounted section. The reasons for this layout are as follows. The reflective properties of the 3.5 m wave absorber are such that 5% reflection can be expected for waves less than .3 m high. Under these conditions, it is possible to operate the basin with a larger test area. However, if waves between 0.3 and 0.7 m must be produced, a 5% reflection coefficient can only be realized if an additional 2.5 m of movable absorber is deployed at the expense of a reduced test area.

The side absorbers can be shut off by panels. These removable side walls are typically used for the generation of long-crested waves normal to the wave board. They ensure a more uniform distribution of wave heights throughout the basin which is in the order of ±5% from the expected value. It was decided not to use reflecting side walls for short-crested waves in order to avoid undesirable phase locking effects [18].

A relocatable long-crested wave generator is installed in the side basin. It can produce waves up to .3 m high and is intended to be used for research involving the interaction between short-crested locally generated storms and long-crested swells which are typically of smaller wave height. For these studies, the partition, which separates the two basins, and the side absorbers are removed. A removable ramp and gate provide access to the main basin for model construction equipment.

The relocatable wind and current simulators can generate flows of up to 5.5 m/s for wind and 0.5 m/s for current. The wind velocities can also be modulated under computer control to match gustiness charateristics.

External to the main hall is a water storage basin which measures 15 m by 90 m by 5 m deep. This tank is connected by an underground pipe to the test basin. A pumping system is used to transfer water between the two basins. Complete filling can be achieved in approximately three hours. This is an extremely useful feature which allows the operators to construct and service models and mooring arrangements in the dry.

3.0 MECHANICAL DESIGN

3.1 Wave Generation Requirements

In order to meet a wide range of anticipated applications in the fields of both coastal as well as offshore engineering, wave periods ranging from 5 to 20 seconds must be simulated. At scale factors of 1:40 and 1:80, these translate into periods from 0.8 to 3.2 and from 0.56 to 2.2 seconds respectively. With the additional allowance for the presence of higher frequencies in wave spectra or for the control of super harmonics, it must be expected that waves with periods as short as .3 seconds need to be produced. On the other end of the spectrum is the requirement to suppress the emission of spurious long waves which are associated with the generation of irregular waves. In theory, these waves can be extremely long and the corresponding wave board movements for these waves are excessively large. It is therefore necessary to make reasonable compromises in order to maintain a good balance between three factors: the performance of the machine at the dominant frequencies, the extended capability for non-linear wave generation and the overall cost of the equipment.

3.2 Segment Width

The design of multi-directional wave generators poses the question of the appropriate choice of a board segment width. A compromise needs to be made between the quality of the wave profile to be generated, the power limits of commercially available actuators and the overall cost of the equipment. There is no question about the principle that the smaller the segment width, the better is the potential for generating pure wave profiles for oblique waves. The smaller segment width requires less driving power but needs more components for a given overall width of a wave machine. Therefore, the total cost of the equipment goes up. On the other hand, the larger segments require more actuator power and because the loading on the machine frame is more concentrated, the frame design becomes more demanding and more costly.

The dominant wave periods for which the machine was planned range from 0.8 to 3.2 s. At a propagation angle of 45° relative to the wave board, the wavelength along the board is $2.5*\sqrt{2} = 3.5$ m and $7*\sqrt{2} = 10$ m respectively. Therefore, if the segments have a board width of 0.5 m, then the shortest wave length would be approximated by 7 steps and the longest by 20. This is considered adequate. It also allows generation of waves as short as 1.2 m at angles up to 60 degrees without violating the Biesel condition [2] for spurious secondary wave components.

As can be seen from Table 1, segment widths for machines that have been built so far vary from 0.3 m to 0.6 m. The NRCC segment width of 0.5 m is therefore in the range of established practice.

3.3 Variable Depth Capability

To accommodate the range of water depths from .3 m to 2.9 m at which the NRCC Offshore Wave Basin may be operated, the machine was designed to slide up or down an A-frame which is attached to the basin side and floor. The machine frame is then fixed to the A-frame at a selected elevation of

the wave board above the basin floor. This arrangement is indicated in Fig. 3. Closure plates are attached to both the A-frame as well as the bottom of the machine frame. These plates prevent the recirculation of water under the wave board and therefore conserve the energy which is being fed into the progressive wave.

3.4 Articulation Modes

The translational and rotational modes of a flat board offer simple and reliable calculations for wave height generation and for structural loading at any frequency. Nonlinear wave generation theory has also been adapted to these devices. The simplicity of design and proven performance made the articulated board the preferred choice over other types such as plungers. The height of the wave board and the stroke range are calculated from the maximum specified height by assuming that the machine operates in the translational mode of wave board articulation. The resultant stroke is then the maximum required for first order wave generation. If shorter period waves were to be generated with the same translational mode, two problems arise. First, the required translational displacement of the wave board for these is very small, resulting therefore in control inaccuracies. Secondly, because the rigid vertical board moving in a translational mode is a poor approximation of the actual velocity profile of a short period wave, the energy which cannot escape through normal wave propagation will be trapped in front of the wave board and cause cross mode wave activity. For this reason, it is necessary to convert the wave board movement into the rotational mode for shorter period waves. For intermediate conditions, a partial piston, partial flapper mode has advantages.

The wave machine's ability to be converted to different articulation modes greatly extends its dynamic range and usefulness. It allows it to be used both for the shallow water coastal applications and for the deep water ocean engineering situations. This type of mode control can be realized with a dual actuator system. However, to reduce cost, a single actuator together with a simple linkage arrangement can be used to achieve the same purpose although at the expense of time loss during mode change. Fig. 3 illustrates the functioning of the linkage mechanism by showing the wave board in the fully retracted position for the three modes. Fig. 4 shows the performance curves for the three modes at an assumed water depth of 2.6 m. Lower water depths would yield lower wave heights.

Non-linear wave generation, particularly for the suppression of spurious long waves [19], requires excessively large strokes of the wave board. Because of loss of accuracy and an increase in cost, this cannot be adequately realized. Instead, it has been found that an approximately 25% excess in stroke capacity beyond that calculated for the maximum regular wave can be a reasonable compromise.

3.5 Wetback and Dryback Design

The designer of wave generators must consider the advantages and disadvantages of these two options. The dryback design is attractive because the total operational power requirements are nearly one-half of that required for the wetback design. In addition, there is no wave action behind the wave board which must be absorbed.

The dryback requires a seal which keeps the water from entering the space behind the machine. This seal must be able to withstand many cycles of flexing and deformation under significant static pressure. The "rolling" seal, which was used by Salter, has proven an excellent solution to this problem. However, this seal has only been applied to the rotational mode of board articulation. It does not lend itself easily to a multi mode design of board articulation. The seal problem and the associated reliability question is a major reason why the dryback design had to be ruled out for the NRCC design. In addition, there is the technical difficulty which arises from the considerable lift forces which result when the piston mode dryback design is used for a wave machine which can be vertically relocated. These lift forces do not exist when the machine is fixed and the wave board is sealed to the wall. There are also static forces which act on the wave board itself. These also have a cost implication because they must be balanced by appropriate mechanical or hydraulic equipment.

On the other hand, when considering the wetback design, it can be found that the structural steel behind the wave board acts as a good wave absorber which eliminates all splashing and wave overtopping over the basin wall. The second disadvantage of higher operational power cost also becomes of lesser importance if one considers the fact that a typical wave basin is on standby most of the time while models are being installed and prepared for testing. The actual time during which waves are being generated is generally very small, even in the busiest laboratory.

A further argument which has been advanced in support of the dryback design is related to the active absorption of waves incident on the wave board. The method used by Salter measures the wave induced force and the board velocity as a combined feedback quantity. For this, the board inertia must be kept small and there should be no corrupting wave forces acting on the board from behind. Therefore, if the Salter method is used, the dryback design is essential. However, reflection absorption can also be achieved by measuring the board velocity and the water elevation in front of

AD-A196 627 PROCEEDINGS OF THE AMERICAN TOWING TANK CONFERENCE (21ST) HELD IN WASHINGTON DC ON 5-7TH AUGUST 1986(U) NATIONAL RESEARCH COUNCIL WASHINGTON DC R F MESSALLE 3/6

UNCLASSIFIED AUG 87 F/G 13/10 NL

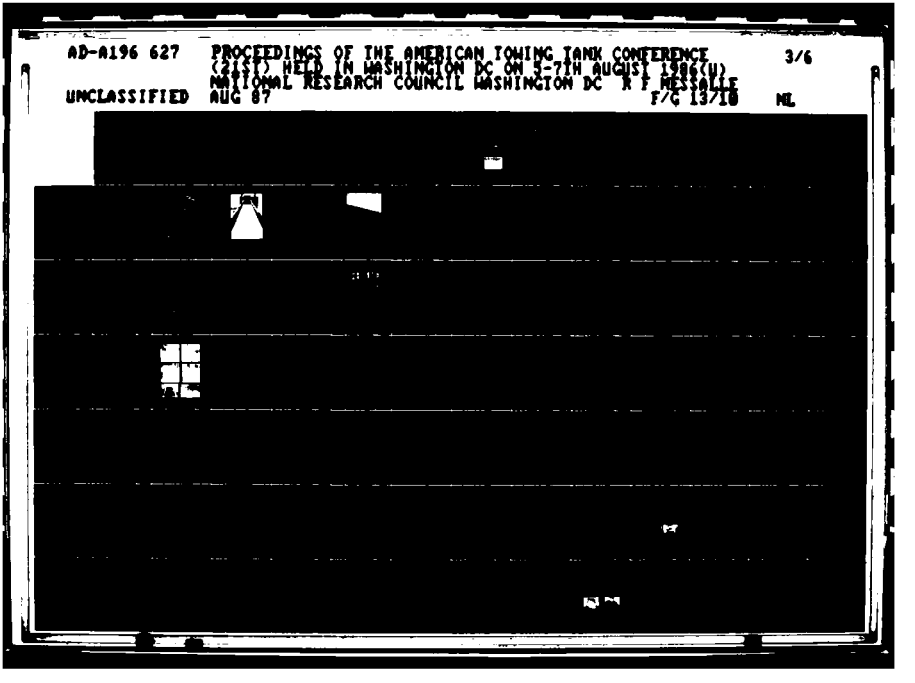

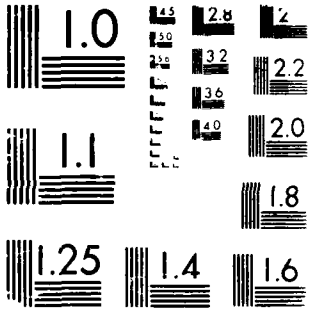

MICROCOPY RESOLUTION TEST CHA

the board. The wetback design may be used for this method without disadvantages.

On balance, because of the multiple articulation mode and variable depth requirements, it was found that the wetback design was cheaper and promised greater reliability.

3.6 Actuator Selection

Dynamic analysis of the wave generator provides information on the resistive and inertial forces acting on the wave board. It also supplies the average and maximum velocities. With this information, suitable actuators may be selected.

The choice is limited to either electrical or hydraulic devices. For larger force requirements and large linear actuation, the hydraulic actuators are cheaper, tend to have a better frequency response and are more reliable. Because standard lengths of hydraulic actuators are cheaper and more readily available, mechanical stroke amplification by means of a lever arm is used. This is also illustrated in Fig. 3.

The oil volume in the cylinder has compliance and acts as a spring attached to the combined mass of the wave board, associated glider and linkages and the entrained water. This oil column must therefore be considered in calculating the natural frequency of the wave board. In order to ensure adequate control of the board, the natural frequency should be in the order of 5 Hz. Therefore, the actuator piston area must be increased until the desired oil column stiffness is achieved. Thus, the sizing of an actuator is not only a function of the dynamic force requirements of the wave board but also a function of the oil column stiffness.

The NRCC system uses Moog actuators with a stroke of 0.2 m, a rated static force of 45 kN, and a hydraulic power supply consisting of six pumps, each rated 50 USGPM and each driven with a motor rated at 75 kW.

4.0 CONTROL SYSTEM

Three basic classes of servo controllers were considered during the preliminary design phase - analog, digital and hybrid. Analog servo controllers have been used on most other 2D and 3D hydraulically actuated wave generators and they have proven to be reasonably reliable on the 2D machines installed at NRC. Although they are a relatively inexpensive component of a 2D machine, their cost is much more significant on a segmented machine, especially when cabling and safety interlocks are considered. Manual operations such as loop optimization and sensor calibration, which are fairly routine on a 2D machine, become rather impractical when 100 or more segments are involved. The number of manual controls can easily become excessive which adversely affects system reliability. Fault detection capabilities are quite limited and the inherent lack of flexibility of analog controllers was also considered a major disadvantage in this application.

Hybrid controllers consist of an analog control loop which can be digitally tuned. This is achieved by replacing the usual potentiometers with multiplying D/A converters which are controlled by a digital processor. Digital control loops can also be cascaded on the analog inner loop for increased functionality. This approach offers considerable flexibility while retaining the speed and high loop integrity advantages of analog controllers. It was found to be the most expensive option, however, due primarily to the amount of custom hardware development required.

Digital servo controllers offer the greatest flexibility since the control loops are implemented entirely in software. Features, such as automatic sensor calibration and automatic loop retuning to compensate for changes in articulation mode or water depth, are easily incorporated. The main disadvantage of digital controllers is the software development cost since the control routines require very careful design to ensure adequate speed, synchronization and reliability. Software development is not a major cost factor when amortized over a large number of segments, however. Hardware cost was similar to that of analog controllers since most of the system could be built using standard microcomputer components. Other advantages of the digital approach are more comprehensive error detection and reporting, simplified cabling between the modular control units and the host computer, and local storage and interpolation of drive signals. It was therefore decided to use digital servo controllers since they offered the greatest potential capabilities at reasonable cost and also provided the most practical growth path for future enhancements such as active wave absorption.

4.1 Architecture

The wave generator control system is designed in a modular fashion so that the number of segments in the generator can be changed without affecting the performance of the controller. Each module consists of all of the hardware and software required for the control of 16 segments. Each module is known as a Module Control Unit (MCU).

The modules form a loosely coupled system with each MCU and the host computer acting as nodes on an Ethernet network as shown in Fig. 5. The HP 1000 cannot access the Ethernet network directly so another node, the Host Communication Computer (HCC), is used to transfer data from the HP's IEEE-488 GPIB bus onto the Ethernet network.

The specifications for digital control of 16 segments at a control rate of 100 Hz indicated that each module would require multiple microprocessors operating in paral-

lel. It was decided that the microprocessor components had to be existing board level products compatible with an established bus standard. The IEEE-796 Multibus standard was selected which offers the capability to have up to 16 bus masters working in parallel. The wide acceptance of the Multibus standard also means that there are many board level products to choose from.

Three main functions can be identified for the computational component of an MCU. They are: interface between the module and the Ethernet network; scheduling real time tasks such as the acquisition of feedback data, calculation of control signals and the output of the control signals; and the calculation of the control signals from the drive signal and the feedback data.

The first function is carried out by an Intel iSBC 186/51 communication computer. This single board computer includes an 80186 CPU, on board RAM and the hardware required for the Ethernet serial interface. This computer, the Module Communication Computer (MCC), is responsible for accepting commands from the Ethernet network, passing the commands to the realtime scheduler and relaying results back to the host via the Ethernet network.

Scheduling of real-time tasks is the heart of the control system. Tasks must be scheduled to execute at the proper time and data must be passed between tasks which may be running on separate processors. The Intel iSBC 286/10 single board computer was selected to provide these functions. This single board computer includes an 80286 CPU, allows the addition of an 80287 numeric coprocessor, has dual ported RAM memory which is necessary to pass data between itself and other computer boards, and has a high speed data bus which can be used to transfer data to and from offboard memory at close to local bus bandwidth. The additional memory is required to store the 16 drive signals of up to 10,000 samples each, as well as any data acquired by the computer. This computer, known as the Module Controller (MC), is responsible for accepting commands passed to it by the MCC, acquiring feedback data, processing drive signals and passing these data on to the computers which calculate the control signals.

The calculation of control signals using the feedback data and desired drive signal data is the most computationally intensive component of the digital controller. This function lends itself extremely well to multiprocessing. Once the control loops have been initialized, only self-contained packets of information need to be sent to the processors. The control task then uses these data to calculate the control signal. No further interaction between the processors are required until the results are ready to be returned. This isolation makes it straightforward to add additional processors to achieve the desired control rate. The Intel iSBC 186/03 single board computer was selected to perform the control calculations. This computer board has an 80186 CPU which provides the required processing power at a reasonable cost. These computers are known as Segment Controllers (SCs) and their only functions are to accept command packets from the MC, execute the command and report back on the results of the execution.

Figure 6 shows a block diagram of the computational component of an MCU. The figure shows the board level products and how they interact with each other and the Ethernet network. In the figure, the external control blocks are digital input/output modules which are required to monitor and control external events. The figure also shows that the parallel port of the MC is connected to each SC. This is necessary to allow the MC to interrupt specific SCs without using the limited number of Multibus interrupt lines. Four analog input cards and two analog output cards are also shown connected to the Multibus.

4.2 Interprocessor Communication

All interprocessor communication within a module control unit takes place over the Multibus, going to and from buffers located in the dual ported RAM area in the MC. Communication between the MC and the MCC uses one buffer for transfers from the MC and another for transfers to the MC. In both cases, the buffers are not re-used until the receiving processor indicates that the transmitted packet has been processed.

Communication between the MC and an SC uses a FIFO buffer capable of stacking 16 commands. The normal procedure is for the MC to write a command into a buffer, interrupt an SC and then for the SC to overwrite the buffer with its response. When the response is ready, the SC interrupts the MC which then instructs the SC to use the command stacked in the next buffer while the MC processes the response. Each SC has a separate buffer area in the MC's dual ported RAM.

4.3 Feedback Sensors

The types of feedback sensors to be used for servo control were determined mainly by testing of a 3-segment prototype machine. The primary feedback variable is actuator displacement and externally mounted RVDT's measuring the lever arm angle were selected on the basis of resolution, linearity, lifetime and accessability. Resolution was of particular importance since it was decided to derive velocity from the displacement signal by means of digital differentiation in order to avoid a separate sensor.

Either acceleration or delta P (differential pressure across the actuator) feedback was also found to be necessary for stability in order to control oil column

resonance effects. Delta P was selected because of somewhat better performance and because it provides the most direct measure of the force exerted by the actuator.

Both force and wave elevation feedback have been used on other wave machines for wave absorption control [3]. Force feedback was not considered practical because of the wet-back design. It also requires phase compensation at higher frequencies where the resistive component of the hydrodynamic force no longer dominates the inertial component. It was therefore decided that wave elevation at the board and horizontal wave board velocity at the mean free surface would be used as the feedback variables for wave absorption with the velocity computed from the measured lever arm angle.

The machine has been fitted with a capacitance wave elevation probe on the front of each wave board in order to allow for future implementation of wave absorption control. This consists of a wire strung in a "W" pattern about 2 cm from the face of the board in order to measure the average water elevation across the width of the board. Software compensation will be used to account for the wave board angle in the flapper and combination modes. Capacitance probes were selected primarily on the basis of previous experience at NRC where similar devices have proven to be very reliable and relatively inexpensive.

4.4 Automatic Calibration

Automatic calibration has been provided for each of the analog feedback sensors. A slotted vane is mounted on the lever arm shaft of each segment and a simple optical switch is used to detect the edge of each slot as the lever arm rotates. This defines ten discrete angles with an accuracy of 0.02 degrees which are used to calibrate the RVDT sensor.

The delta P sensors are DC coupled in hardware to allow static calibration but are high-pass filtered in software when used for feedback control. Each sensor is calibrated by slowly moving to each of the mechanical limits of the actuator and then opening the servo valve so that full supply pressure is applied to the transducer. A third point at zero pressure is obtained by averaging the signal for 30 seconds while the wave board is stopped at the centre position.

One wave board in each group of 16 is equipped with a water elevation step gauge which is used to calibrate the analog capacitance wave probes. This consists of 16 conductivity probes mounted with a vertical spacing of 10 cm. The MC is interrupted each time a probe enters the water which defines a discrete calibration point. The 16 probes are spaced to cover the full range of operating depths but only 3 or 4 are used in a given calibration.

The wave probes can be calibrated in a dynamic mode by running all segments in phase to generate a long-crested wave. Although fast and convenient, this mode is used mainly as an operational check since accuracy is limited by small variations in wave elevation from segment to segment. The primary calibration of the wave probes is done by slowly raising the water level in the basin.

The calibration procedure for each type of sensor is initiated by a host computer command and all segments are usually calibrated simultaneously. Calibration constants are computed by linear regression and checked for validity. All calibration data are stored in a disk file on the host and downloaded automatically each time the machine is started.

4.5 Servo Dynamics

In order to assist in the initial design of the control system, a fairly general computer program was developed to calculate the servo dynamics of hydraulic wave machines in the frequency domain. It can handle analog controllers with position, velocity, error rate and delta P feedback terms. The hydraulic components are essentially modelled as linearized devices using techniques described in [20] but nonlinear compensation is included to account for the pressure dependence of the servo valve flow coefficient. The effective mass and damping seen by the actuator and the delta P feedback signal are calculated on the basis of linear wave theory [21] with extensions for elevated wave boards and multiple articulation modes.

The program can predict closed loop frequency response reasonably well for preliminary design purposes as shown in Fig. 7. It was also extended to provide a simplified model of the digital controller by including transfer functions for the input and output filters and a propagation delay term to account for the computation cycle. This version correctly predicted the 5 Hz instability which occurs when the delta P feedback is too small as well as a higher frequency resonance which occurs when the delta P coefficient is excessively large as shown in Fig. 8.

The program was also used to select the frequencies for the delta P and position sensor input filters and the valve driver output filter. It is common practice in digital signal processing to set input filters at or below the Nyquist frequency to prevent aliasing. In this case, however, it was necessary to set the filters well above the 50 Hz Nyquist frequency in order to avoid excessive phase lag with consequent loss of stability as shown in Fig. 9. The filters were set as low as possible while still maintaining a 6 db gain margin and other methods such as shielded cables and differential input amplifiers were used to minimize noise. In practice, aliasing has not been a significant problem.

4.6 Control Loop Software

A block diagram of the control loop is shown in Figure 10. The control algorithm uses the desired angular position of the lever arm, the actual angular position, the differential pressure across the piston of the hydraulic actuator and any time histories of these variables to compute the drive voltage to the servo valve signal conditioning circuitry. The basic control equation used is:

$$\text{Drive voltage} = K_{loop}*[\,K_{err}*(\theta_d-\theta_a) - K_{\Delta p}*\text{DELP} - K_{vel}*\theta_{vel}]$$

K_{loop}, K_{err}, $K_{\Delta p}$ and K_{vel} are gain constants which can be changed by the host. θ_d is the input desired position, θ_a is the actual position and θ_{vel} is the filtered first derivative of the actual position. DELP is the differential pressure. Any changes to the gain terms in the equations or changes to other parameters in the control loop, such as calibration curves for the transducers, are all ramped over a period of 10 seconds so that the transition is smooth.

The control calculations in the SC all used scaled integer arithmetic with 32 bits of accuracy maintained where required. All of the math routines are coded in assembler to optimize the performance of the controller. The control equation shown above and any checks for error conditons execute in under 2 msec on the 6 Mhz 80186 based SC. This means that 4 SCs can easily handle the control calculations for 16 segments. The software in the MC allows from 1 to 8 SCs to be used. Upon reset, the MC determines the number of SCs in the system and distributes the computational load between the SCs. If 8 SCs are used, the time available for the control calculations for each segment is up to 5 msec so there is ample reserve for future enhancements.

The MC's main responsibilities for control are to start a control loop every 10 msec; acquire feedback data for each segment, calculate the desired position of each segment and pass the data to the appropriate SC; check to ensure that the SCs report the successful control of all segments every control interval; and take any actions necessary in the event of a failure. The MC calculates the desired position by linearily interpolating between points of a stored drive signal which has an intersample spacing of 100 msec.

4.7 Safety Features

Since each actuator can produce more than 4 tonnes of force, it is imperative that the failure of critical components of the wave generator be diagnosed quickly. Once a failure is detected, the system must be disabled before damage can occur. Disabling of the system can be done by either opening the hydraulic interlock loop or by forcing the signal into the servo valve to zero. Opening the hydraulic interlock loop shuts off the pumps, but the residual hydraulic pressure remains high for a few seconds; forcing the drive to the servo valves to zero has an immediate effect which stops the wave board without any mechanical damage.

Possible faults which necessitate emergency shutdown include:

(1) failure of the Module Controller;
(2) failure of a Segment Controller;
(3) failure of the system bus;
(4) failure of a feedback transducer;
(5) failure of a servo valve;
(6) failure of an analog input or output channel.

Under normal operating conditions, the MC generates a 50 Hz square wave under software control, interrupts the MCC at a 10 Hz rate and ensures that 16 control calculations are performed every control interval. The square wave is input to a retriggerable one-shot which will timeout if not reset in 40 msec. This will then cause the hydraulic interlock loop to be opened and the servo valve drive current to be forced to zero. Both the MC and the MCC also have the capability to use these disabling methods directly via digital I/O modules on the computer boards.

If the MC fails, then the 50 Hz square wave will disappear; if an SC fails, then less than 16 control calculations will be carried out successfully in a control interval and thus be detected by the MC. Failure of the system bus will be diagnosed by the MC since there will not be any segments controlled. In all cases, the fault will be detected and the system disabled.

Failure of a feedback transducer can occur in different ways. The signal conditioning circuitry has been designed so that failure of the bridge in the transducer will cause the voltage from the signal conditioning circuitry to exceed the normal operating range. This condition is checked by the SC and, if found, the SC will advise the MC of the failure and instruct the MC to disable the system. If the transducer failure is not detected in this manner, the system will not behave as it should. In this case, at least one of the checks on the limits on the absolute position of the actuator allowed or the limits on the error between the desired and the actual position or exceedance of velocity limits will fail and be detected by the SC controlling the segment. The SC will then advise the MC of the failure and advise the MC to disable the system. The failure of a servo valve may be detected in much the same manner as above.

Failure of an analog input or analog output board will likely either be detected as a failed transducer or the processor accessing the board will not finish the read or write cycle in time causing a timeout violation to occur. This violation will

make the number of segments controlled in 10 msec less than 16 and thus the error will be detected by the MC.

4.8 Other Features

Data acquisition functions have also been included. The control system has the ability to acquire a maximum of 32,000 samples of information from 1 to 20 channels at a rate of up to 100 Hz. These samples are taken from the SCs and may include many intermediate calculations in the control loop. These samples can in turn be used to analyze and optimize control loop performance. The sampled data can be uploaded and stored in host computer files for subsequent plotting or analysis using standard routines.

The MC also accepts a terminal which the user can utilize to interrogate the MC and the SCs during active control. Any error messages normally relayed to the host are also displayed on the terminal. If a terminal is not connected, then the MC automatically queues the error messages until a terminal is connected or the MC is reset.

A local hand-held control box can also be plugged into any MCU. This device gives the user manual control of any three segments and is intended primarily for mechanical maintenance. All commands from the host are disabled while the local controller is plugged in.

5.0 HOST COMPUTER SOFTWARE

The host computer software consists of an on-line control program named SWG and a set of directional wave synthesis programs. SWG allows the user to operate the machine by entering simple commands with menu assistance on request. It also displays and maintains a log of detailed messages for errors detected at any level of the control system. SWG commands include system initialization, calibration, drive signal downloading, starting and stopping of wave generation, data acquisition and control parameter modification (privileged users only - protected by password).

The present wave generation software is based on the snake principle method [2,22]. Although the discrete double summation model has been widely used for directional seas, it is neither ergodic nor spatially homogeneous unless frequency averaging is used [18,23]. The software has therefore been designed to handle both single summation (1 direction per frequency) and double summation (multiple directions per frequency) wave models.

Since a very extensive 2D wave generation package had previously been developed at NRC [24], it was decided to integrate the new 3D software with the existing system as shown in Fig. 11. A standard data file format containing amplitude, phase and direction (APD) matrices has been adopted to define a directional wave system at a given reference point in the basin. The propagation directions can be selected arbitrarily but the components are restricted to equally spaced frequencies in order to facilitate the use of FFT procedures.

Program SYDRP synthesizes directional waves for specified amplitude, spreading index and mean angle spectra using either the random phase spectrum or the random complex spectrum method. Various parametric energy spectra (Pierson-Moskowitz, ITTC, JONSWAP, etc.) as well as measured prototype spectra can be used in conjunction with a Mitsuyasu type spreading function in which both the spreading index s and the mean angle of propagation are functions of frequency. Program SYUD converts time domain wave trains to the APD format. This allows most of the existing 2D programs to be used to generate unidirectional waves with direction of propagation as an added control parameter.

Program DWREP computes the drive signal for each segment which is required to reproduce the wave system defined by the APD matrices. It can handle up to 200 segments located on 1 to 3 basin walls. The wave elevation at each segment and the corresponding wave board displacement are calculated by linear wave theory. Compensation for servo dynamics is applied and the drive signals are checked to ensure they do not exceed the operational limits of the machine. DWREP also checks for spurious waves in the defined test area caused by reflection and diffraction effects as well as secondary propagating waves due to components which violate the Biesel condition [2]. Since all drive signals are pre-computed, there are no real-time constraints on the number of components which can be used to synthesize a wave system. The present software can handle up to 1024 frequencies and 100 angles but these limits can be easily increased.

6.0 REFERENCES

1. Biesel, F. et al., "Laboratory Wave Generating Apparatus", St. Anthony Falls Hydraulic Laboratory Report No. 39 (For DTNSRDC), March, 1954.

2. Biesel, F., "Wave Machines", Proc. First Conference on Ships and Waves, Hoboken, NJ, 1954.

3. Salter, S.H., "Absorbing Wave-makers and Wide Tanks", ASCE Conf. on Directional Wave Spectra Applications, Berkeley, California, 1981.

4. Salter, S.H., "Physical Modelling of Directional Seas", Symp. on Description and Modelling of Directional Seas, Copenhagen, Denmark, 1984.

5. Sand, S.E., "Three-Dimensional Deterministic Structure of Ocean Waves", Series Paper No. 24, Inst. Hydrodyn. and Hydraulic Eng., Tech. Univ. of Denmark, 1979.

6. Sand, S.E. and Lundgren, H., "Three-Dimensional Structure of Ocean Waves", Proc. Second Int. Conf. on Behaviour of Off-Shore Structures, BOSS '79, Vol. 1, London, Aug. 1979, pp. 117-120.

7. Sand, S.E. and Lundgren, H., "Selection and Three-Dimensional Reproduction of Wave Records that Give Maximum Ship Motions", Int. Symp. on Hydrodynamics in Ocean Engineering, Norway, 1981.

8. Edinburgh Wave Power Report, Fourth Year Report, Vol. 3 of 3, July, 1978.

9. Huntington, S.W. and Thompson, D.M., "Forces on Large Vertical Cylinder in Multi-Directional Random Waves", Proc. 8th Offshore Tech. Conf., Houston, Texas, 1976, paper 2539.

10. Publicity pamphlet "The Offshore Sea Basin", Hydraulics Research Ltd., Wallingford, OX10 8BA, England.

11. Jeffreys, E.R. et al., "Measuring Directional Spectra with the MLM", ASCE Conf. on Directional Wave Spectra Applications, Berkeley, 1981.

12. Eggestad, I., "NHL Ocean Laboratory: Engineering and Construction of Building and Sub-Systems", NHL Symp. on Hydrodynamics in Ocean Engineering, Trondheim, 1981.

13. Aage, C. and Sand, S.E. "Design and Construction of the DHI 3-D Wave Basin." Symp. on Description and Modelling of Directional Seas, Copenhagen, Denmark, 1984.

14. Outlaw, D.G., "A Portable Directional Irregular Wave Generator for Wave Basins". Symp. on Description and Modelling of Directional Seas, Copenhagen, Denmark, 1984.

15. Mynett, A.E. et al., "Effects of Directional Seas in Coastal Regions". Symp. on Description and Modelling of Directional Seas, Copenhagen, Denmark, 1984.

16. Biewer F.N. and Dillingham, J.T., "Model Testing in Multidirectional Waves", Marin Technology, Vol. 20, No. 3, July, 1983, pp. 227-229.

17. Burcharth, H.F., "A Three Dimensional Sea Facility for Deep and Shallow Water Waves". Proc. 5th Int. Offshore Mechanics and ARctic Engineering (OMAE) Symposium, Tokyo, Japan, 1986.

18. Jeffreys, E.R., "Directional Seas Should be Ergodic", to be published in Applied Ocean Research.

19. Barthel, V., Mansard, E.P.D., Sand, S.E. and Vis, F.C., "Group Bounded Long Waves in Physical Models", Ocean Engineering Vol. 10, No. 4, 1983.

20. Lewis, E.E. and Stern, H., "Design of Hydraulic Control Systems", McGraw Hill, 1962.

21. Gilbert, G., Thompson, D.M. and Brewer, A.J., "Design Curves for Regular and Random Wave Generators", IHR, Vol. 9, No. 2, 1971.

22. Gilbert, G., "Generation of Oblique Waves", Hydraulics Research Station, Wallingford, Notes 18, pp. 3-4, 1976.

23. Pinkster, J.A., "Numerical Modelling of Directional Seas", Paper C-1, Symp. on Description and Modelling of Directional Seas, Copenhagen, 1984.

24. Funke, E.R. and Mansard, E.P.D., "The NRCC Random Wave Generation Package", NRCC Div. of Mech. Eng. Rpt. TR-HY-002, 1984.

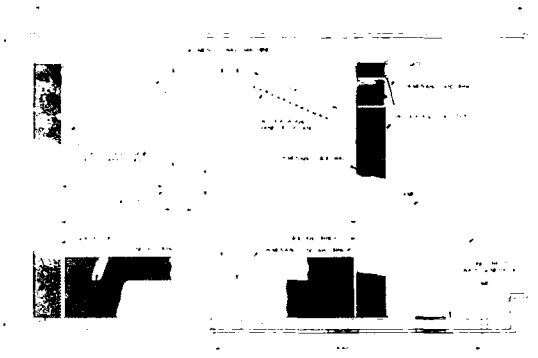

Fig. 1 The Offshore Wave Basin

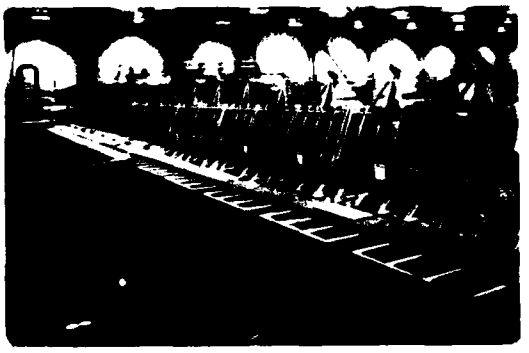

Fig. 2 Photo of Segmented Wave Generator

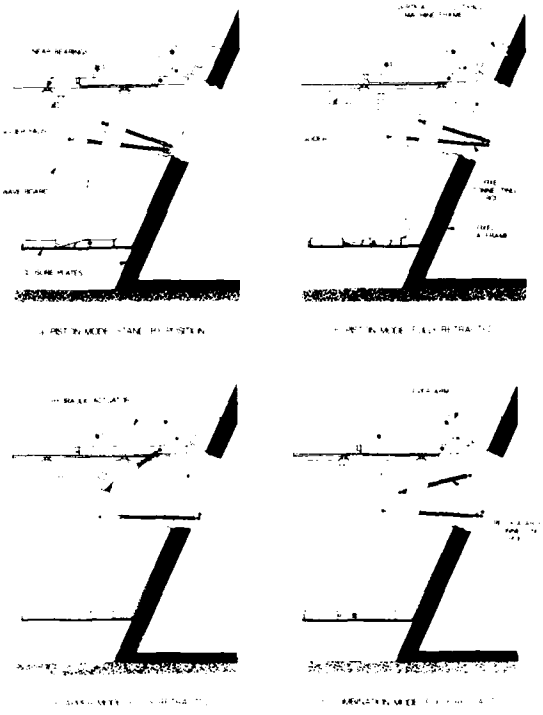

Fig. 3 Kinematics of Segmented Wave Generator

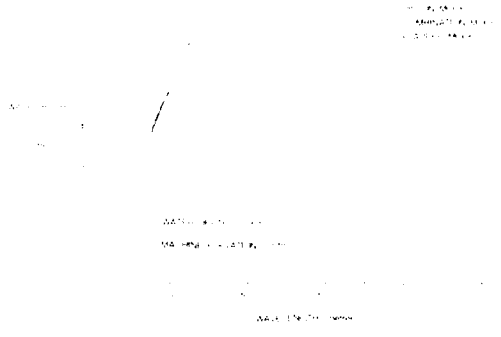

Fig. 4 Regular Wave Performance at 2.6 m Depth

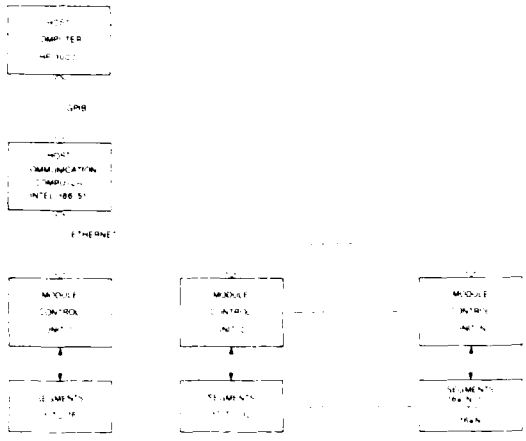

Fig. 5 Control System Network Modules

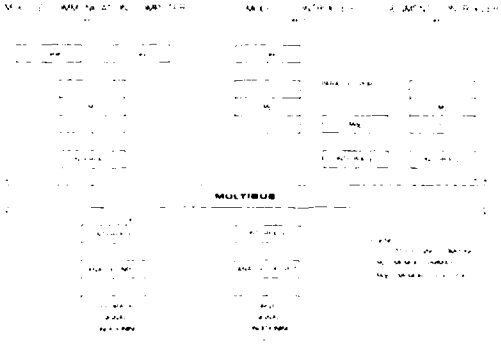

Fig. 6 Block Diagram of Module Control Unit

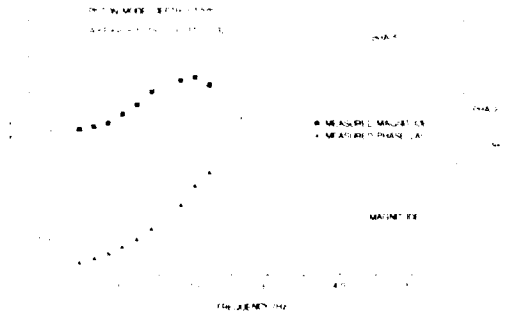

Fig. 7a Closed Loop Response (Piston Mode)

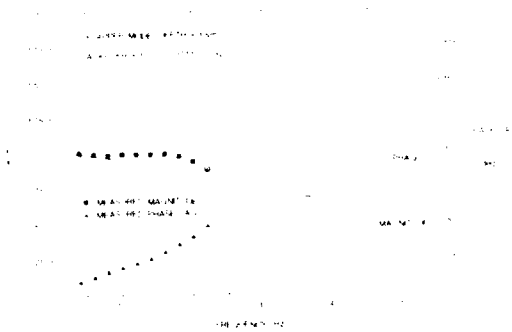

Fig. 7b Closed Loop Response (Flapper Mode)

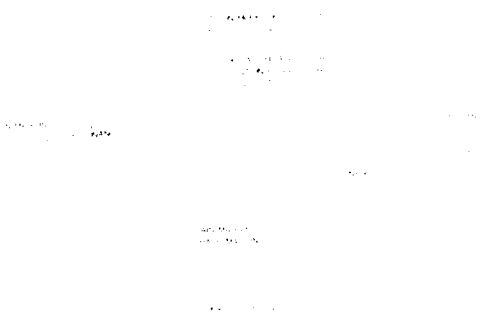

Fig. 8 Effect of ΔP Feedback on Stability

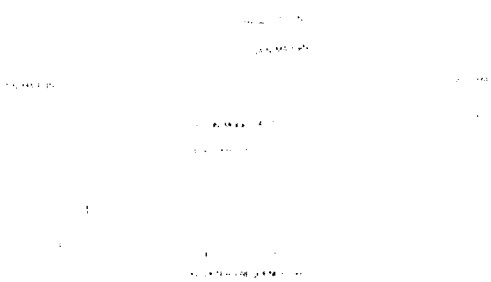

Fig. 9 Effect of ΔP Filter Frequency

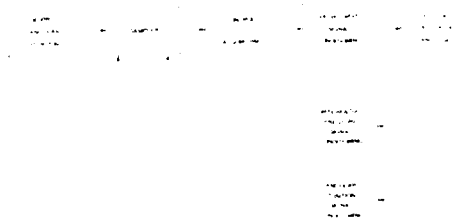

Fig. 10 Block Diagram of Control Loop

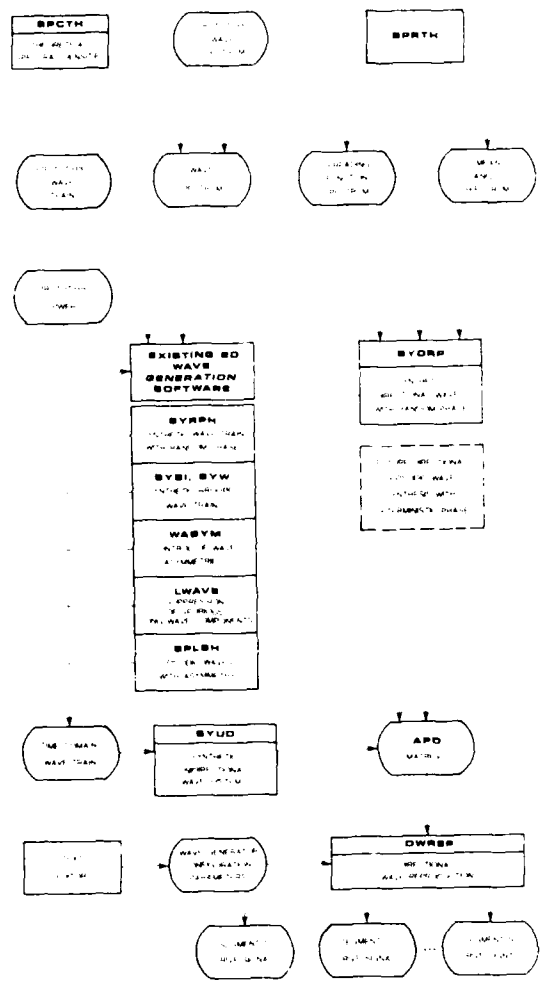

Fig. 11 Directional Wave Generation Software

STEEP SHORT-CRESTED WAVES PRODUCED BY A SIMPLE THREE DIMENSIONAL WAVEMAKER

Professor Marshall P. Tulin and Ali Kolaini

Ocean Engineering Laboratory
University of California
Santa Barbara, CA 93106

ABSTRACT

Steep, short-crested waves, as well as a large variety of three dimensional propagating wave patterns have been created in our laboratory in a novel and simple way, utilizing a plunging half-cone wavemaker. This three dimensional shape attached to a plunging vertical plate at the end of a wave tank (3'x3'x70') creates complex wave patterns dependent upon the wavemaker shape, its frequency, and the tank width. Waves of total height somewhat in excess of the wavemaker stroke have been created for certain frequencies; these were sometimes conical in appearance and broke throughout the length of the wave tank. It is thought that this type of simple wavemaker may be useful in practice.

In this paper, both theory, computer simulation results, and experimental data are presented which predict, explain, and describe these three dimensional waves.

1. INTRODUCTION

Steep waves at sea are often short-crested, and it would therefore be highly desireable to be able simply to produce such waves in experimental tanks for the purpose of testing the response of platforms and ships, as well as for the study of the fundamental properties of short-crested waves, their breaking, etc. At the present time, such waves are sometimes produced in tanks by segmented programmed wavemakers of the Salter type. It occurred to the senior author in 1984 that short-crested waves might be produced very simply through the action of a plunger wavemaker of non-planar form, of conical shape for example, and in the same year some tests were carried out in a small wave tank at UCSB and proved successful. Subsequently we have built a much larger wave tank, 70' in length and 3'x3' in cross section, see Figure 1, and we are continuing these studies. We have, in addition, made theoretica' studies of these waves. This paper represents a preliminary report on the properties of short-crested waves produced in a tank by a plunging semi-cone placed at one end wall. It is presented to the ATTC because of its potential importance for tank testing.

The existence of discrete standing wave modes (resonance) in closed tanks is well known, Lamb (1932), and was understood for semi-infinite channels by Ursell (1952), who was particularly interested in asymmetric wave modes in connection with edge waves on sloping beaches. Subsequently, asymmetric propagating waves produced by a flat plate oscillating about a central vertical hinge were studied close to the first resonance (or cut-off frequency) by Bernard, Mahony, and Pritchard (1977), and the general properties of such asymmetric waves were studied experimentally by Madsen (1973). More recently, experimental and theoretical studies of non-linear effects near the second cut-off frequency have been studied by Kit, Miloh, and Shemer (1986), and over a range of frequencies by Shemer, Kit, and Miloh (1986). These works emphasize asymmetric waves produced by paddle-like wavemakers and may be regarded as complementary to our own work, which emphasizes asymmetric waves produced by a plunging conical shape, and has been particularly motivated by an interest in the practical application of such a wavemaker.

We have carried out theoretical analyses, computer simulation, and experimental studies of monochromatic waves produced by a semi-cone of half angle 36°, mounted on a plunging end wall. The theoretical studies are restricted to the linear regime, but most of our experiments have been carried out with relatively steep short-crested waves, as a central question for us has been whether such waves can be readily produced in this way. In summary, we have found it not difficult to produce steep short-crested waves at frequencies not too close to cut-off. In fact, quite remarkably, we are able to produce such waves which break continuously through the entire length of our wave tank.

2. THEORY

2.1 General Solution

We consider the propagation of small am-

plitude surface gravity waves in a semi-infinite deep channel of width, ℓ, where the waves are being produced by an oscillating wavemaker mounted at one end of the channel. For example, we imagine the wavemaker, of arbitrary shape, is being driven in vertical oscillations (plunging) described by:

$$\eta_w(t) = R \int_{-\infty}^{+\infty} \tilde{\eta}_w(\omega) e^{-i\omega t} d\omega \qquad [1]$$

and produces a wave pattern in the channel, $\eta(x,z;t)$, where x is the distance along the channel parallel to the walls and measured from the wavemaker wall; y is the vertical distance, positive upward; and z is the distance transverse to the channel walls and measured from the near wall. If the wave pattern corresponding to a harmonic oscillation at frequency, ω, and unit wavemaker amplitude is $\eta'(x,z;\omega)e^{-i\omega t}$, then:

$$\eta(x,z;t) = R \int_{-\infty}^{+\infty} \tilde{\eta}_w(\omega)\eta'(x,z;\omega)e^{-i\omega t} d\omega \qquad [2]$$

The wave pattern, $\eta'(x,z;\omega)$ may in principle be found making use of the boundary conditions on the wall ($\phi_n=0$), on the wavemaker [$\phi_n=\phi'_n(o,y,z)$], and on the free surface ($\phi_{tt}+g\phi_y=0$), where ϕ is the velocity potential ($\nabla^2\phi=0$), and where the wave pattern is related to ϕ through the kinematical free surface condition, $\eta_t=\phi_y(y=0)$. Thus if,

$$\phi(x,y,z;t) = R \int_{-\infty}^{+\infty} \tilde{\eta}_w(\omega)\phi'(x,y,z)e^{-i\omega t} d\omega, \qquad [3]$$

then

$$\eta'(x,z;\omega) = -\frac{1}{\omega}\phi'_y(x,o,z) \qquad [4]$$

An appropriate representation for ϕ' is:

$$\phi'(x,y,z;\omega) = \sum_{n=0,1/2,1,3/2,2,\ldots} [A_n(\omega)e^{(\omega^2/g)y} \cos\frac{2\pi nz}{\ell} \cdot e^{ik_n x}] \qquad [5]$$

where,

$$k_n = [(\omega^2/g)^2 - (2\pi n/\ell)^2]^{\frac{1}{2}} \qquad [6]$$

and A_n may be determined from the boundary conditions on the wavemaker wall.

Note that the wave corresponding to n=0 is simply a planar wave. Larger integer values of n correspond to cosine wave patterns across the channel; these are symmetric with ragard to the centerline for n, integer, and asymmetric for n, half integer. A symmetric wavemaker would thus produce a wave pattern for n=0,1,2,etc. For each frequency, ω, there exists a value of n* sufficiently large that $2\pi n^*/\ell > \omega^2/g$, so that k_{n^*} is imaginary. The wave pattern for such modes thus decays as $e^{-k_n^* /x}$ away from the wavemaker. Therefore only a finite number of modes for $n < n^*$ will result in propagating waves; in general, the higher the wave frequency, the greater the number of propagating wave modes.

2.2 The Dispersion Curves

The situation is best appreciated by considering the dispersion curves for free-wave propagation in a channel; i.e., the relation $k_n(\omega)$, or $\lambda_n(\omega)$, where $\lambda_n = 2\pi/k_n$ is the down-tank wavelength of the mode n. This relationship $\lambda_n(\omega)$ follows immediately from [6] and is (see Figure 2):

$$\bar{\lambda}_n^2 = (\bar{\omega}^4 - n^2)^{-1} \qquad [7]$$

where $\bar{\lambda}_n = \lambda_n/\ell$ and $\bar{\omega} = \omega/(2\pi g/\ell)^{\frac{1}{2}}$. It is evident that a series of cut-off frequencies exists, $\bar{\omega}^* = \sqrt{n}$, for integer n (symmetric) and half-integer n (asymmetric). These actually correspond to frequencies for which free waves exist in a purely transverse mode (sloshing mode); they are therefore resonance frequencies near which very large amplitudes may be expected near the wavemaker. At cut-off, it may be shown that the group velocity of the resonant mode disappears, so that wave energy cannot escape from the wavemaker; we have observed this effect both in the computer simulation and experimentally. Nonlinear effects limit the wave amplitude at resonance and also permit some energy to propagate; these are the subject of the work of Bernard, et al. and Kit, Shemer, and Miloh, previously referenced.

As each cut-off frequency is exceeded in turn, a new propagating wave mode contributes to the far field wave pattern, resulting in more complex transverse and down-channel patterns, again as observed.

2.3 The Free-Wave Patterns

For each frequency, the number of waves is determined by the number of propagating modes. The resulting patterns, the sum of a discrete number of waves of different wavelengths, can become complicated, even for a single frequency. The situation for a frequency between the first and second cut-off (note that $\ell/2 < \lambda_0 < \ell$ in this case), resulting in two propagating modes, n=0 and n=1, is readily analyzed (we later compare data). Let,

$$\eta(x,o,t;\omega) = A_0 e^{i(k_0 x-\omega t+\alpha_0)} + A_1 e^{i(k_1 x-\omega t+\alpha_1)} \qquad [8]$$

where $k_0 = \omega^2/g$ and $k_1^2 = k_0^2 - (2\pi/\ell)^2 = (2\pi)^2(1/\lambda_0^2 - 1/\ell^2)$.

It can easily be shown that [8] is equivalent to the sum of two-beat patterns:

$$\eta(x,o,t;\omega) = (A_0+A_1)\cos\left[\left(\frac{k_0+k_1}{2}\right)x - \omega t + \left(\frac{\alpha_0+\alpha_1}{2}\right)\right]\cdot\cos\left[\left(\frac{k_0-k_1}{2}\right)x + \left(\frac{\alpha_0-\alpha_1}{2}\right)\right] -$$

$$(A_0-A_1)\sin\left[\left(\frac{k_0+k_1}{2}\right)x - \omega t + \left(\frac{\alpha_0+\alpha_1}{2}\right)\right]\cdot\sin\left[\left(\frac{k_0-k_1}{2}\right)x + \left(\frac{\alpha_0-\alpha_1}{2}\right)\right]. \qquad [9]$$

This sum is in turn equivalent to an irregular wave with a modulating beat:

$$\eta(x,o,t;\omega) = \underbrace{[(A_0^2+A_1^2) + 2A_1A_0\cos(k_0-k_1)x]^{\frac{1}{2}}}_{\text{beat}}\cdot\underbrace{\cos\left[\left(\frac{k_0+k_1}{2}\right)x + \tan^{-1}\beta(x) - \omega t + \left(\frac{\alpha_0+\alpha_1}{2}\right)\right]}_{\text{irregular wave}} \qquad [10]$$

where $\beta(x) = \left(\frac{A_0-A_1}{A_0+A_1}\right)\tan\left[\left(\frac{k_0-k_1}{2}\right)x + \left(\frac{\alpha_0-\alpha_1}{2}\right)\right]$.

(Only in the case $A_0 = A_1$ does the irregularity disappear.) This irregularity was apparent in experimental observations of waves produced between the first and second cut-off frequency. The beat was also measured, as discussed later.

Additional modes will, of course, increase the complexity of the wave pattern.

2.4 Method of Images

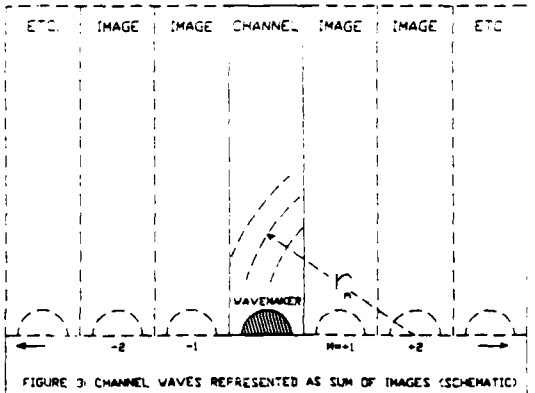

FIGURE 3: CHANNEL WAVES REPRESENTED AS SUM OF IMAGES (SCHEMATIC)

A computational simulation of the wave pattern suggests itself. For this simulation we have made use of the method of images whereby the wavemaker symmetrically placed between walls is replaced by its equivalent, an infinite cascade of identical wavemakers displaced along the plane, x=0, with spacing ℓ, see Figure 3. The propagating, monochromatic wave field due to each of the wavemakers in the cascade is in the far field kinematically simple, corresponding to an outgoing cylindrical wave whose amplitude is decaying as $1/\sqrt{r}$ (where r is the radius from the wavemaker center), and whose wavelength becomes constant (and equal to λ_0) within a radius of a few wavelengths. The wave pattern in the channel is thus simply equal to the sum of the cylindrical waves issuing from the wavemaker cascade, see Figure 3.

For example, the far field potential due to an oscillating source of strength, $qe^{i\omega t}$, located at depth f beneath the free surface is, Havelock (1955)

$$\phi(r_m,t) \sim 2\pi q k_0\left(\frac{2}{\pi k_0 r_m}\right)^{\frac{1}{2}}\sin(\omega t - k_0 r_m + \pi/4)e^{-k_0 f} \qquad [11]$$

where $k_0 = \omega^2/g$, as usual, and r_m is the radial distance from the observation point to the n^{th} wavemaker in the cascade. The total far field wave pattern in the channel (x,z) due to some vertical distribution of source density, q'(f), is therefore:

$$\phi(x,z,t;\omega) = \int_0^\infty e^{-k_0 f} q'(f)df \sum_m 2\pi k_0\left(\frac{2}{\pi k_0 r_m}\right)^{\frac{1}{2}}\sin(\omega t - k_0 r_m + \pi/4) \qquad [12]$$

where $r_n = [x^2 + (m\ell - z)^2]^{\frac{1}{2}}$, for m=0,±1,±2,etc.

2.5 Computational Simulation

In this way a conical wavemaker may readily be simulated. (The relation between q'(f) and the conical shape was determined using a version of slender body theory). In applying [12], the down channel distance within which the calculation is applicable increases with the number of terms m_{max} which are summed. Results are presented in Figure 4 for the values of $\bar{\omega}$ shown in the sequence below; also shown below are the cut-off frequencies, $\bar{\omega}^* = \sqrt{n}$; the wavemaker amplitude was fixed. (The cross-channel and down-channel scales are not identical).

n	1	2	3
$\bar{\omega}^*_n$	1.000	1.414	1.732
$\bar{\omega}$	.769, 1.000, 1.038, 1.154	1.423, 1.538	1.738

These simulations show the appearance of the appropriate new modes each time a cut-off frequency is exceeded. They also reveal that for frequencies at or slightly (less than 1%) in excess of the cut-off frequency, the far field wave amplitudes are relatively low while very large amplitudes appear near the

wavemaker and grow as the frequency is increased just beyond critical. (It must be kept in mind that these calculations involve only the propagating waves and not the local wave). The irregular-wave, see Eq. [10] is also evident in the x-cut created by the wall in the case of operation between the first two cut-off frequencies, $\bar{\omega} = 1.154$. Generally, the simulated and observed wave patterns are very similar. Notice that the waves become increasingly short crested as the frequency is increased across the cut-off frequencies - compare $\bar{\omega} = 1.154$ and $\bar{\omega} = 1.538$. We consider these waves to be adequate for the experimental study of short crested effects.

2.6 The Directional Spectrum

It may be shown that the directional spectrum corresponding to these wave patterns is concentrated at discrete orientations, θ_n, measured from the down-channel direction, where:

$$\sin \theta_n = \frac{n}{\bar{\omega}^2} , \qquad n < n^* \qquad [13]$$

The directional spectra thus involve more components and become more widely spread, for larger n^*. A well spread directional spectrum therefore requires a large value of ℓ/λ_0, i.e., a large tank width. The relative energy of the directional components depends upon the wavemaker shape and may be determined from the theory. In particular the amplitude of each of the propagating free wave modes is directly related to a corresponding Fourier coefficient in an expansion of the cross-channel wavemaker shape. In the case of the conical wavemaker, the higher (cross-channel) modes are quite heavily weighted, leading to waves which are relatively steep in the cross-channel direction (short-crested), as observed experimentally.

3. EXPERIMENTS

Waves were created in the glass walled wave tank shown schematically as Figure 1 utilizing the semi-cone of half angle 36°. The cone was attached to a flat vertical plate, almost spanning the tank and free to ride vertically on vertical rails; it was offset from a fixed vertical false wall by a distance of 0.187 ft. This plate was itself set into plunging oscillations in the range of about 1-2 Hz. An effective beach composed of lightweight honeycomb material was set at a small angle to the mean water level at the far end of the tank. The tank is equipped with a moveable instrument carriage, to which can be attached capacitance wire wave gauges. These gauges are stable and linear, and can be recorded either on a conventional strip chart recorder or digitally in the memory of a mini-computer (IBM PC). The latter mode allows for the subsequent analysis of the data, including spectral analysis.

A series of observations have been made for a fixed and large wavemaker amplitude, 5" total stroke. A photograph of the wave pattern produced at a frequency $\bar{\omega} = 1.154$ ($\omega = 1.5$Hz.), between the first and second cut-off frequencies, is shown as Figure 5. A film of the waves produced through the range of frequencies is available (shown at the meeting), and the wave patterns are seen to be in accord with the computer simulation. The wave height (total) was measured over the range of distances from 15' to 45' down-channel from the wavemaker for the frequency $\bar{\omega} = 1.154$, and is shown in Figure 6. These data are fit by a beat function of the form shown in Eq. [10] but allowing for a linear decay in wave amplitude with distance, and an empirical small phase in the beat. This allows the determination of the ratio A_1/A_0, which is estimated to be 3.2. The agreement between the measured ($0.91 ft^{-1}$) and predicted ($0.95 ft.^{-1}$) values of beat wavemaker $(\frac{k_0 - k_2}{2})$ is satisfactory. The instantaneous wave profile across the tank was measured and found to be approximately of the form $a + b \cos 2\pi z/\ell$, but with a profile steeper near the wall (perhaps due to breaking which occurred there).

Total wave heights of H = 6" were measured (for a 5" total stroke), whereas the lengths of the two basic waves for the frequency $\bar{\omega} = 1.154$ are: $\lambda_0 = 27.33"$; $\lambda_1 = 42.0"$. The corresponding wave slopes are very large: $H/\lambda_0 = .22$; $H/\lambda_1 = .14$. It is not therefore surprising that breaking accompanied these waves. It is, however, somewhat surprising that breaking occurred continuously over the range measured, as observed visually. This is the probable cause of the linear decay in wave height observed, Figure 6. A possible cause of the continual breaking lies in the non linear interaction between the two component waves, each of which is very steep.

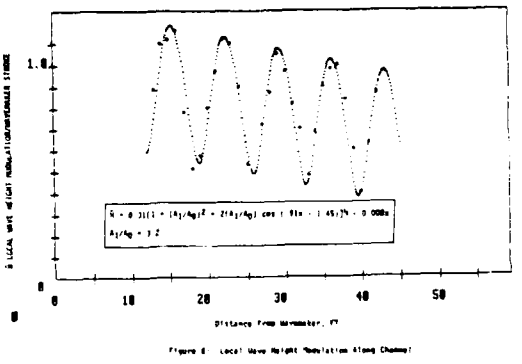

CONCLUSIONS

1. Steep, short-crested waves may easily be generated in a conventional wave tank utilizing a simple plunging semi-cone, or similar three dimensional wavemaker. They should therefore be useful for ocean wave simulation in experimental wave tanks.

2. For a sufficiently large angle cone (half angle 36°), steep almost conical waves can be produced with a wave height somewhat in excess of the wavemaker total stroke, and with wave slopes comparable to or greater than the greatest slopes possible for planar waves ($\bar{\omega} = 1.154$).

3. These steep waves can be produced to break throughout a down channel length of at least 15 tank widths.

4. Even a monochromatic wave pattern exhibits considerable irregularity and complexity, which varies rapidly with changing frequency, especially upon passing cut-off frequencies, which are regularly spaced.

5. These complex wave patterns due to the plunging cone can be reasonably predicted utilizing linear wave theories and computer simulation, except in the very near vicinity of resonance.

REFERENCES

Bernard, B.J.S., Mahony, J.J. and Pritchard, W.G. (1977): The Excitation of Surface Waves Near a Cut-Off Frequency. Phil. Trans. R. Soc. London, Vol. A286, pp. 87-123.

Havelock, T. (1955): Waves Due to a Floating Sphere Making Periodic Heaving Oscillations. Proceedings of the Royal Society, A, Vol. 231, pp. 1-7.

Kit, E., Miloh, T. and Shemer, L. (1986): Non-Linear Wave Maker in a Channel: Theory and Experiments. Presented at the ONR Symposium on Naval Hydrodynamics, Berkeley, July 1986.

Lamb, H. (1932): Hydrodynamics. Dover Press.

Madsen, O.S. (1974): A Three Dimensional Wave Maker, Its Theory and Application. J. of Hydraulic Research, 12, pp. 205-222.

Shemer, L., Kit, E. and Miloh, T. (1986): Measurements of Two- and Three-Dimensional Waves in a Channel, Including the Vicinity of Cut-Off Frequencies. To appear in Experiments in Fluids.

Ursell, F. (1952): Edge Waves on a Sloping Beach. Proc. R. Soc. London, A214, 79.

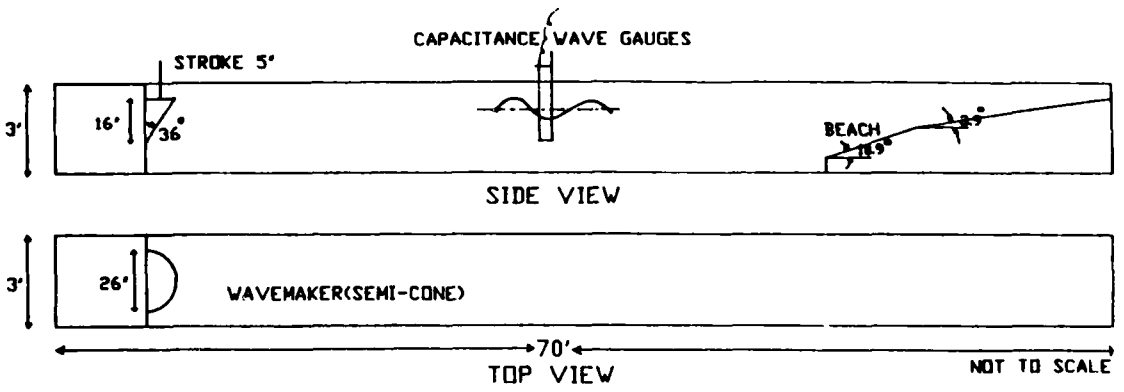

FIGURE 1: UCSB WAVE TANK (SCHEMATIC)

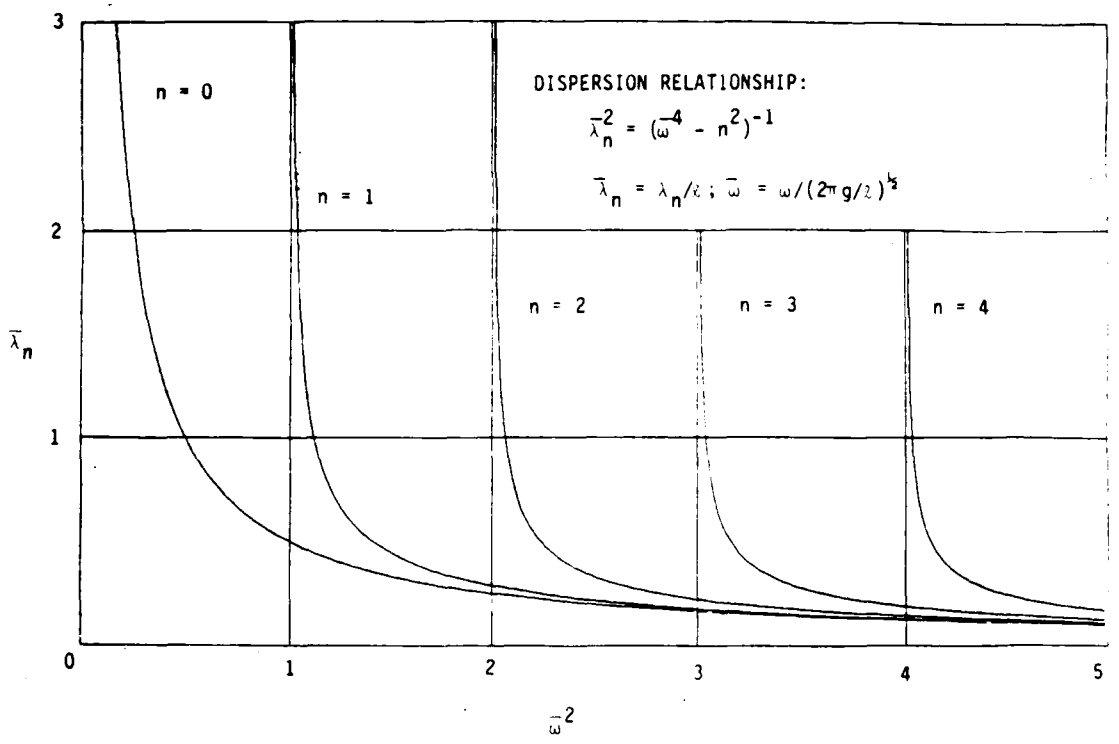

Figure 2: Dispersion Curves (Symmetric Modes) for a Channel, Width ℓ.

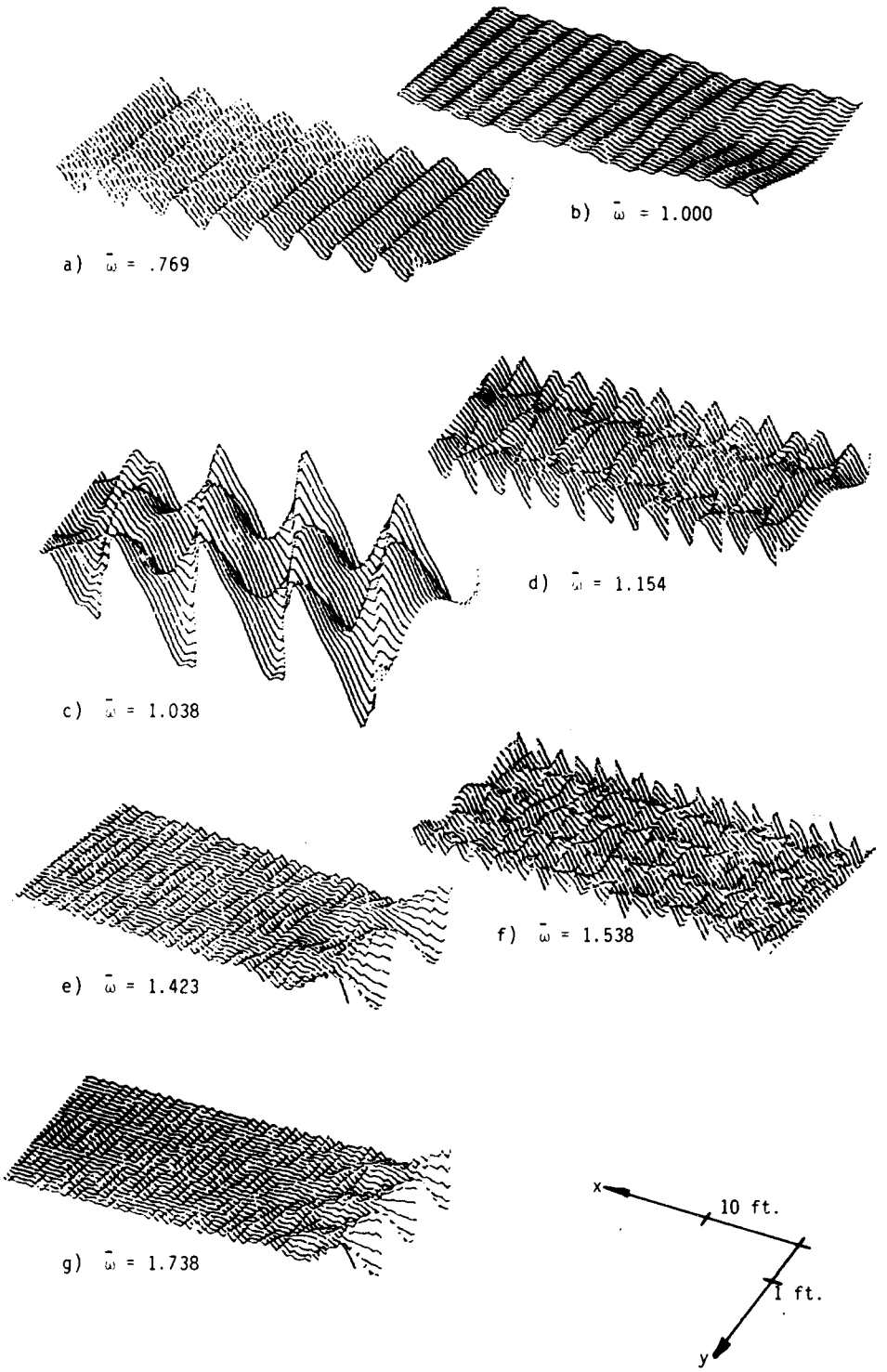

Figure 4: Three Dimensional Wave Patterns Due to Half-Cone Wavemaker in a Channel. Computer Simulations. $\bar{\omega}$ = .769, 1.00, 1.038, 1.154, 1.423, 1.538, 1.738

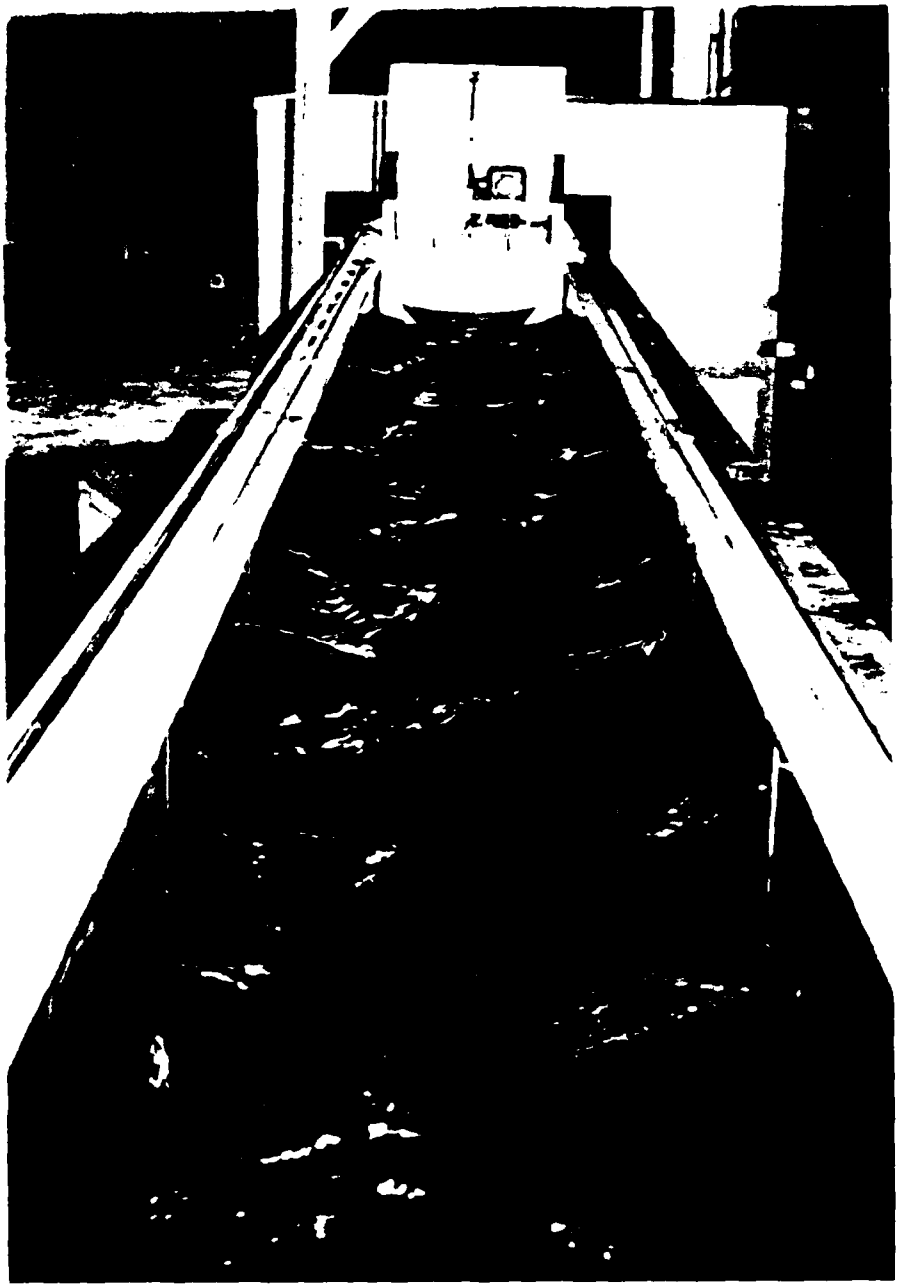

Figure 5: Wave Pattern Produced at a Frequency $\bar{\omega}$ = 1.154 (ω = 1.5H_z)

DIRECTIONAL IRREGULAR WAVE GENERATOR DESIGN FOR SHALLOW WAVE BASINS

D. G. Outlaw
Chief, Wave Processes Branch
and
M. J. Briggs
Research Hydraulic Engineer

Wave Dynamics Division
Coastal Engineering Research Center
U.S. Army Engineer Waterways Experiment Station
P.O. Box 631
Vicksburg, MS 39180-0631

ABSTRACT

A directional irregular wave generator is installed in a wave basin at the U.S. Army Engineer Waterways Experiment Station's Coastal Engineering Research Center (CERC). The unique design provides a wave generator which can simulate local sea and distant swell spectra over a broad range of differing directions of approach and directional distributions.

The wave generator consists of 60 wave paddles, each 1.5 ft in width, separated into four modules. The modules are portable and can be relocated within the test basin. The wave paddles are driven at the paddle joints to reduce generation of parasitic waves. The wave paddle displacement is in translational motion and is designed for water depths up to 2 ft. Displacement of each paddle is independently controlled by an automated data acquisition and control system (ADACS).

Design considerations and performance characteristics of the directional irregular wave generator are presented. The operating software is configured for maximum flexibility during experimental tests. To date the wave generator has been used for nonlinear wave research studies, analysis of irregular directional seas for generalized cases, and site-specific studies.

1. INTRODUCTION

The directional irregular wave generator installed at CERC provides a unique resource for experimental studies of natural sea states in a laboratory environment. Unique features of the wave generator include its size, modular design, portability, wave paddle drive, and joint seal techniques. A portable design for the wave generator was selected in order to:

a. Obtain a directional irregular wave generator which can be used on a study at any location within the wave basin.

b. Allow relocation to simulate principal directions of wave attack while generating a directional wave distribution.

c. Provide for future expansion of the wave generator.

d. Allow operation of the wave generator in an alignment which can be varied module by module.

e. Reduce spurious wave generation at higher frequencies.

The wave generator has been designed for use primarily on coastal projects in intermediate to shallow water depths. The addition of the directional irregular wave generator has enhanced CERC's experimental capability. Significantly improved model data will be obtained for a broad range of coastal engineering site-specific studies and research investigations since the interaction of wave trains from multiple directions and directional spreading of wave energy can be included in future studies.

2. WAVE BASIN

Currently, the wave generator (Fig. 1) is located in a test basin approximately 95 ft long by 114 ft wide. The maximum water depth is 2 ft. Wave absorbers are installed along the basin perimeter and consist of 2-in. layers of rubberized hair installed between two layers of expanded sheet metal. The slope of the wave absorbers is 37 deg along the side walls and front of the basin. Behind the wave generator, the absorber is adjustable. Flume tests (Briggs, ____) show an average reflection coefficient of approximately 12 percent.

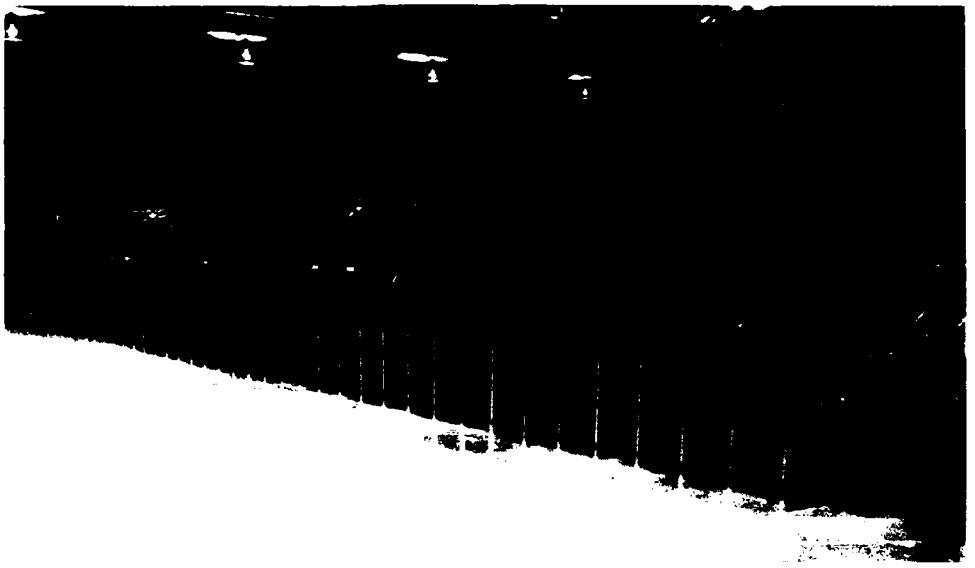

Figure 1. Directional irregular wave generator in model test basin.

The test basin is located inside a concrete wave basin 192 ft wide by 362 ft long with walls 2.5 ft high. The wave generator can be relocated within any part of the wave basin. Headbays, to be used during tidal generation, run along the inside of each of the 362-ft walls and are 4 ft by 4 ft. The wave basin was constructed inside an insulated steel-frame shelter. Posts for roof support extend down the center longitudinal length of the wave basin at 20 ft intervals. Overhead walkways provide an unobstructed view of both sides of the basin and are used for supporting instrumentation cables to the wave generator and model wave gages. A sump pit for use during tidal generation is located outside the shelter.

The office area and control room for the wave generator ADACS are located along the side of the wave basin.

3. DIRECTIONAL IRREGULAR WAVE GENERATOR SYSTEM

3.1 Major Components

The directional irregular wave generator, described previously by Outlaw (1984) and Briggs (____), was designed and constructed by MTS Systems Corporation of Minneapolis, Minnesota. The wave generator is an electronically controlled, electromechanical system and consists of four portable modules, digital to analog (D/A) converters, and an electronic console for 61 wave board control channels.

3.2 Module Design

Each of the four modules, shown schematically in Fig. 2, has a steel frame. The wave boards on each module are 1.5 ft wide and 2.5 ft high. They are driven at the wave board joints with a fixed and a linked wave board hinge and are powered by 0.75-horsepower direct current servo motors. A simplified plan of the articulated joint and seal between each of the wave boards is shown in Fig. 3. Adjacent wave boards are connected by a sliding, flexible-plate seal. The seal slides are in a guide between the front and rear plates of the wave board.

The wave board stroke is $\pm$ 0.5 ft and each wave board can be operated 180 deg out of phase with the adjacent wave board. The wave boards are operated in translational motion and are not sealed at the bottom or at the ends of the generator. Wave board displacement is controlled by the belt-driven carriage assembly shown in Fig. 2.

Each module is equipped with six adjustable mounting pads for leveling. The modules are moved using four dollies at each of four lifting points. Two of the lifting points are in front of the wave board and are raised above the wave boards when the wave generator is in position for testing.

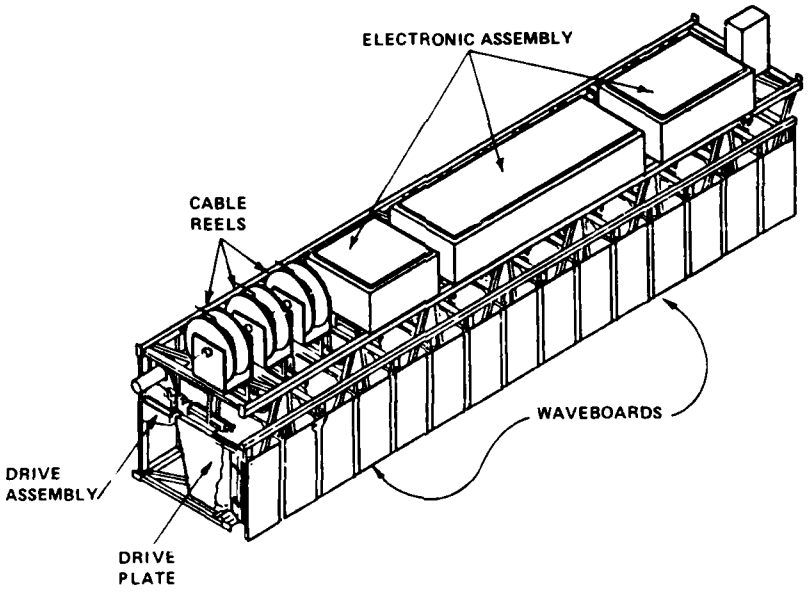

Figure 2. Schematic of wave generator module.

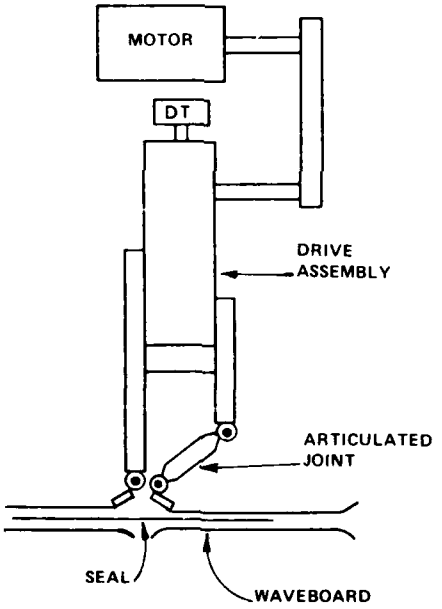

Figure 3. Articulated joint and seal between wave boards.

Wave board position is monitored by a displacement transducer. All motor and transducer power and signal voltages are contained in the enclosures mounted above the module frame along with the six-axis, pulse-width, modulated-drive amplifiers. Three cable reel assemblies mounted alongside the enclosures provide the cables for the wave board command displacement signals, transducer displacement feedback signals, and power.

3.3.1 Wave Generator Console

The wave generator console provides for digital wave board position control data to be input through a D/A converter using an IEEE 488 interface. The D/A

converter output is supplied to the 61 control channels which provide the analog signal for the individual servo controllers. The servo controller modules provide the drive enable/disable and the drive command signals. In addition, signals are provided to the calibration/test indicator for adjustment of the servo controllers.

Wave board position displacement transducer feedback from the generator modules is supplied to the servo controller modules with a displacement readout for control monitoring by the ADACS. The servo controller modules generate stroke-limit and displacement-error detection signals and will halt wave board displacement if stroke or error limits are exceeded.

3.4 Data Acquisition and Control

An ADACS is used to generate and transmit control signals to each of the 61 wave boards, monitor wave board feedback, and collect time-series experimental data from the wave basin. The ADACS consists of a DEC VAX 11/750 central processing unit, 120 multiplexed channels of A/D conversion, IEEE 488 interface for output to 61 channels of D/A, 577 megabyte fixed-disk storage, 10 megabyte removable-disk storage, and two 125 ips, 800/1600 bpi, start/stop tape drives. The VAX system was selected due to the following factors:

a. The powerful operating system (VMS) readily supports multitasking for real-time applications.

b. Extensively used in scientific applications.

c. Flexible capability and expansion potential.

d. Software can be written exclusively in a high-level language (FORTRAN 77).

e. Availability of system drivers for real-time peripherals.

f. The system's performance allows many nonreal-time central processor unit (CPU) intensive applications (such as data analysis and wave board signal generation) to be executed locally. Adequate CPU time is available to incorporate real-time data analysis functions in the future.

4. PERFORMANCE CHARACTERISTICS

4.1 Operational Control

The snake wave generation principle is used to generate directional waves in the test basin. Naeser (1981) and Sand (1979) describe the technique and note that the directional band for waves is limited at higher frequencies due to the number of wave paddles per wavelength needed along the wave generator. The design of the drive system at each of the wave generator joints (Sand, 1979, and Sand and Lundgren, 1981) reduces spurious wave amplitudes at higher frequencies. The spurious waves, which can appear at higher frequencies, propagate at an angle to the principal wave direction. The predicted high-frequency limit above which spurious waves will be generated is 1.52 Hz for a wave direction of 30 deg from the direction normal to the wave generator. For paddles driven at the center of the paddle without a link between the paddles, the predicted high-frequency limit is 1.28 Hz. At the relatively small scales typically used for three-dimensional coastal models, improved capability to generate a directional spectrum of wave energy without spurious waves is significant.

4.2 Directional Wave Characteristics

Calculated and measured wave heights for a 1-ft depth are compared in Fig. 4a and 4b for waves propagating normal to the wave generator and at an angle of 30 deg respectively. The wave heights shown are an average value using data from nine wave gages located in a grid pattern over a 20-ft square measurement area. The measurement area was located parallel to and 10 ft in front of the wave generator and the gages were 10 ft apart. Calculated wave heights were obtained using a two- and three-dimensional wave height transfer function (Biesel, 1954 and Sand, 1979).

The measured wave amplitude is decreased by leakage around and under the generator as shown by Fig. 4 for each wave direction. The ratio of measured wave height to predicted wave height is shown in Table 1 for each test condition.

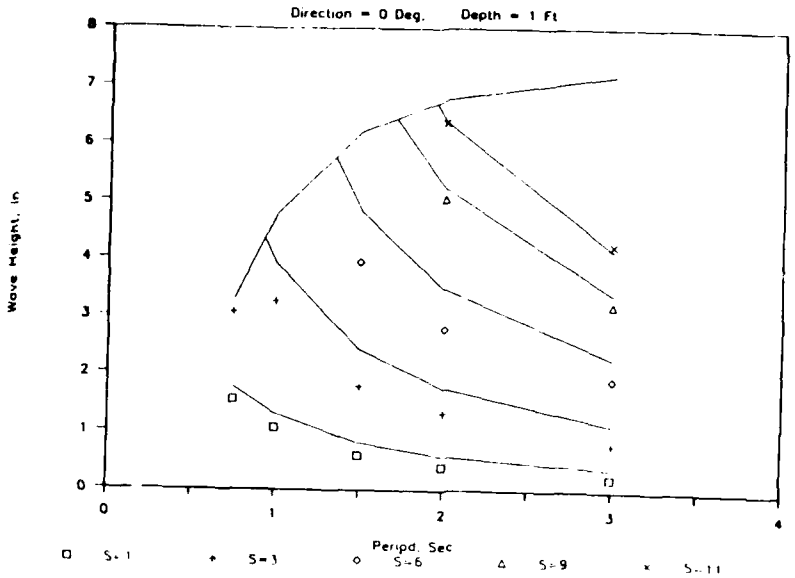

a. Waves of 0 Degrees

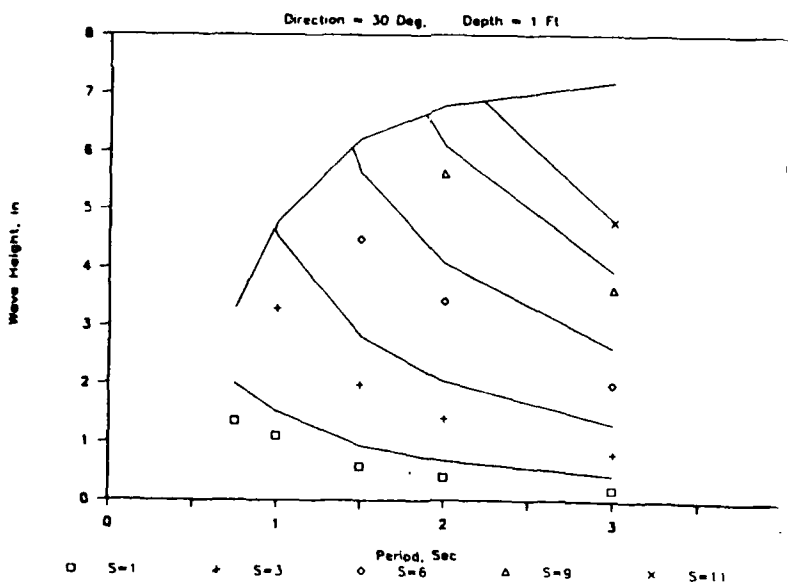

b. Waves of 30 Degrees

Figure 4. Measured Versus Theoretical Wave Heights.

Table 1

Ratio of the Measured Wave Height to the Predicted Wave Height

Direction, deg	Period, sec	Stroke, in 1	3	6	9	11
0	0.75	0.88	0.93	----Breaking limit exceeded---		
	1.00	0.82	0.83	"	"	"
	1.50	0.74	0.73	0.82	"	"
	2.00	0.71	0.76	0.80	0.97	1.00
	3.00	0.60	0.72	0.84	0.95	1.02
30	0.75	0.68	--------Breaking limit exceeded----------			
	1.00	0.73	0.73	"	"	"
	1.50	0.62	0.70	0.80	"	"
	2.00	0.59	0.70	0.84	0.92	"
	3.00	0.45	0.62	0.76	0.93	1.00

Wave height response is lowest for the shorter wave paddle strokes and is particularly noticeable for the 30-deg direction of wave propagation. The wave height attenuation probably is due to leakage around the wave generator. At longer strokes, leakage effects are less significant and the measured wave height agrees well with the calculated theoretical wave heights.

5. TEST APPLICATIONS

The directional irregular wave generator currently is being used on a study of directional wave effects on wave conditions in the lee of a semi-infinite breakwater and in the lee of a shoal. Test wave conditions consisting of monochromatic and unidirectional and directional spectra are being investigated. From the results, the effects of different amounts of frequency and directional spreading on the refraction and diffraction of the waves will be ascertained.

Recently, an exact solution for two-dimensional, nonlinear, shallow-water waves has been proposed. This solution represents a unique solution of the Kadomtsev-Petviashvili (K-P) equation, the direct generalization of the Korteweg-de Vries equation for one-dimensional nonlinear waves (referred to as cnoidal waves). The directional spectral wave generation facility currently is being used to verify that the theory does, in fact, represent these naturally occurring nonlinear wave fields.

6. SUMMARY

The capability to conduct directional irregular experimental wave studies for coastal projects is expected to result in improved and less costly designs. The directional wave generator is a unique resource for study of natural sea states in the laboratory environment.

7. ACKNOWLEDGMENT

The Office, Chief of Engineers, is gratefully acknowledged for authorizing publication of this paper.

REFERENCES

Biesel, Francis 1954. "Chapter 21. Wave Machines," Proceedings of the First Conference on Ships and Waves, Hoboken, New Jersey, pp. 288-304.

Briggs, M.J. ____. "Directional Spectral Wave Generator Basin Response to Monochromatic Waves," Technical Report (in publication), U.S. Army Engineer Waterways Experiment Station, Coastal Engineering Research Center, Vicksburg, Mississippi.

Naeser, H. "Methods for Generation of Short-Crested Sea in a Wave Basin," Prepared for the ITTC Seakeeping Committee, Norwegian Hydrodynamic Laboratories, Trondeim, Norway.

Outlaw, D. G. 1984. "A Portable Directional Irregular Wave Generator for Wave Basins," Symposium on Description and Modeling of Directional Seas, Paper No. B-3, Technical University of Denmark, pp. 1-6.

Sand, Stig E. 1979. "Three-Dimensional Deterministic Structure of Ocean Waves," Series Paper No. 24, Institute of Hydrodynamics and Hydraulic Engineering, Technical University of Denmark, pp. 1-177.

Sand, Stig E. and Lundgren, H. 1981. "Selection and Three-Dimensional Reproduction of Wave Records that Give Maximum Ship Motions," International Symposium on Hydrodynamics in Ocean Engineering, The Norwegian Institute of Technology, pp. 101-120.

ACOUSTIC NOISE LEVELS IN THE HYDRONAUTICS SHIP MODEL BASIN

Alex Goodman, B. L. Silverstein, and J. T. Gottwald

Tracor Hydronautics, Inc.
7210 Pindell School Road
Laurel, Maryland 20707

ABSTRACT

Underwater acoustic noise characteristics of the HSMB are quantified. Tests were conducted and the noise levels associated with carriage operation were measured. The carriages were quieted and the new operational levels are presented. Two examples of the use of the HSMB for underwater acoustical measurements are included.

1. INTRODUCTION

The Hydronautics Ship Model Basin (HSMB®) was placed into operation in January 1969. The tank has been used primarily for the conduct of resistance, powering, seakeeping, static and dynamic stability and control, and wake studies for surface ships, towed bodies, torpedoes, and submarines. In addition, tests to evaluate the hydrodynamic performance of offshore structures have been conducted.

The application of a towing tank for hydroacoustic work was disucssed during SEAHAC meetings which were held at DTNSRDC in May 1981. A literature search revealed that DTMB had investigated the feasiblity of using the towing tank for hydroacoustic work in 1943 and 1946 as described by Chrisler and Lasky (1948). Tests were performed at DTMB to evaluate the noise levels using both Carriage No. 1 and Carriage No. 3. Carriage No. 3 was a wooden structure supported by pneumatic tires. The results were encouraging. We believe that Carriage No. 3 was used for subsequent acoustic testing. The HSMB carriages are supported by pneumatic wheels. Accordingly, in 1982 Hydronautics undertook an inhouse funded study to evaluate and quantify the underwater acoustic characteristics of the HSMB and the HSMB carriages. The study was completed in 1986.

This paper presents the physical characteristics of the HSMB and its carriages with particular emphasis on those characteristics which may affect the underwater acoustical noise levels in the basin, a description of instrumentation used to acquire the underwater acoustic data, the ambient underwater acoustical noise in the basin and its relationship to the basin environment, the noise level generated by the two carriages, and the changes in noise level achieved by modifications to the carriages and basin. Finally, two examples of the use of the basin as an acoustic test facility are described.

1.1 HSMB PHYSICAL DESCRIPTION

The basin is of steel reinforced concrete construction. The internal dimensions are about 420-feet (128 m) long by 25-feet (7.6 m) wide by 13-feet (4 m) deep. There is a deep cylindrical test section located 85 feet (26 m) from the East end of the basin. The cylindrical section is centered in the basin, extends 30 feet (9 m) below the bottom of the basin and is 11 feet (3.4 m) in diameter. The bottom of the basin is 12-inches (30 cm) thick. The sides are 18-inches (46 cm) thick at the bottom and 12-inches (30 cm) thick at the top. The basin sits completely in the ground and the concrete walls and floor are backed with dirt and crushed rock.

1.2 SOUND SPEED IN THE BASIN

The temperature of the water in the basin, which controls the sound speed, is measured before each test since the water temperature influences the Reynolds number. The lowest temperature observed in the basin was 58°F (14.5°C) and the normal winter low is around 60°F (15.6°C). The highest observed temperature was 70°F (21.1°C) and the normal summer high is around 68°F (20°C).

Based upon the work of Leroy (1969), the speed of sound in the basin lies between 4793 ft/sec (1461 meters/sec) and 4859 ft/sec (1481 meters/sec).

1.3 INSTRUMENTATION

Underwater sound pressure levels in the HSMB were measured using a KSP Industries Model HS-111 hydrophone and a Bunker Ramo,

Model 600 hydrophone. The KSP hydrophone consists of a 2.0-inch long, 1.5-inch diameter cylindrical PZT element connected to a +40 dB gain, low noise preamplifier and 75 feet of shielded cable. The manufacturer's stated free field sensitivity for the crystal is -194 dB//1μPa/Volt with a flat response up to 20 KHz. The sensitivity was checked at 4 KHz by reciprocity calibration and found to be within 1 dB of the stated sensitivity.

The Bunker Ramo hydrophone is a 1.0-inch long, 1.0-inch diameter cylindrical PZT element. The sensitivity of the element was measured, using the reciprocity calibration technique, to be -205 dB/μPa/Volt between 10 Hz and 20 KHz.

Two forms of analysis were performed on the hydrophone outputs. In one case the hydrophone output was amplified, bandpass filtered and recorded on a strip chart recorder. In the other case, the hydrophone output was amplified and analyzed using a Nicolet 660B digital spectrum analyzer. The reduced data were recorded on magnetic disc and the spectra were plotted for analysis.

2. BACKGROUND NOISE

The operational definition of underwater acoustic background noise or ambient noise for the basin is that sound pressure level which exists when the basin carriages are not in operation and all other local equipment is secured. As expected, the ambient sound pressure levels and spectra are highly variable in time and the band level is dominated by that portion of the spectrum below 500 Hz.

On the bottom and sides of the basin, the water is in contact with and is contained by concrete, and the surface interface is with air at atmospheric pressure. This rectangular "room" of water is driven by a large variety of external sources. The major acoustic sources external to the water must couple to the water through the concrete since the air-water interface couples relatively little energy into the water from the air as is pointed out by Ross (1976). Sources of acoustic energy which are coupled to the basin through the walls include seismicity, auto and truck traffic, operation of heavy equipment near the basin, people walking in the building, and the wind blowing over the ground and around the building. Seismic energy generally occurs at frequencies below 1 Hertz and will not influence most measurements made in the basin.

2.1 TIME HISTORIES

Temporal records of the broadband noise levels in the basin taken over periods of days reveal a multitude of noise sources. Table 1 lists some typical band levels observed in the basin. Figures 1, 2, and 3 illustrate broad band time histories of the underwater acoustic noise observed in the Basin.

Figure 1 illustrates the broadband noise level recorded between midnight and 0600 on Friday, July 29, 1984. The average background noise level is 97 dB//μPa. The noise spikes which occur at 30 minute intervals are caused by an air compressor. The short noise spikes which are 15 minutes apart are caused by an unknown radio frequency source.

Figure 2 illustrates the background noise levels generated in the basin as a result of the activities during a "typical" workday. The predominant feature of the day is the 10-15 dB increase in noise level associated with the model shop machinery which is located in the building with the HSMB. The increased noise level near the end of the day is caused by the use of the main carriage. It is evident from this figure that ambient noise is not a limiting factor when the carriage is in use.

Figure 3 illustrates the broadband noise level for a weekend night (Friday, July 6, 1984 to Saturday, July 7, 1984). The slight increase in noise level and the increased variability is believed to be caused by the increase in heavy truck traffic which is known to occur on Route 95 during weekends.

One trend noted during the measurement period was a gradual increase in the quietest observable levels from winter (74 dB//μPa) through spring (87 dB//μPa) into summer (97 dB//μPa). This increase is thought to be associated with the increased use of air-conditioning equipment in the area as well as an increase in traffic on the major highways located near the basin.

Table 1

Noise Band Levels in a 10 KHz Band

Source	Level, dB//μPa
Cars in Driveway	103-105
Air Compressor	102-106
High-Speed Fan	108-114
Shop Fans	100-105
Low-Speed Fans	108-111

2.2 SPECTRAL CHARACTERISTICS

The ambient noise spectra were analyzed in a band from 10 Hz to 10 KHZ.

Figure 4 is an example of a noise spectrum collected in the basin on 3 May 1984. At frequencies above 1 KHz the sound pressure levels are below 45 dB//μPa/Hz, dropping to a low of about 28 dB at 8 KHz. Above 500 Hz all of the levels lie below open ocean ambient levels equivalent to a 5 knot wind speed or less than Beaufort 2. Above 2 kHz, the Basin background level is

equivalent to a 1 knot wind speed or about Beaufort 1 (Sea State 0).

Figure 5 illustrates the details of the low frequency portion of the background noise in the Basin. The highest level occurs at 28 Hz. This line correlates with energy generated by the large Clausing Lathe in the model shop. The lathe was operating during the measurements.

3. CARRIAGE GENERATED NOISE

To obtain a basic understanding of the underwater acoustic noise levels generated in the HSMB by the operation of either the main or high speed carriage, the broadband noise level generated by each carriage was measured during the passage of the carriage over the hydrophone. These measurements were made as a function of speed for each carriage. Figure 6 is a graph of band level versus carriage speed for the main carriage. Also illustrated in Figure 6 are levels for the NSMB depressurized towing tank as reported by Vande Kooij and De Bruyn (1984) and levels for carriages 1 and 3 at DTNSRDC as reported by Chrisler and Lasky (1948).

Figure 7 demonstrates the first surprise of the measurements. The main carriage and the high speed carriage generate the same noise level versus speed. The main carriage weighs 32000 lbs and the high speed carriage weighs 8000 lbs. Above 4 feet/second the level generated by the high speed carriage is always lower than the main carriage, but the maximum difference, at 20 feet/second is only 4 dB. Considering the number of differences between the two carriages, this result was surprising. A test program was then undertaken to determine which of the similarities between the carriages was controlling the noise level and what could be done to reduce the levels.

The common characteristics of the two carriages are listed in Table 2. As a first step in the test program, the noise level for each carriage was measured with the carriage coasting and the motor secured. The resulting levels agreed with those obtained with the carriage powered. To confirm these results, the motor, pump, wheel motors, and rails were instrumented with accelerometers and the accelerometer outputs were cross-correlated. The resulting cross-correlation functions never exceeded 10 percent over the band 12.5 Hz to 10 KHz. These measurements eliminated the drive motor, pump, and wheel motors as major sources for the observed underwater acoustic noise levels for either the main carriage or the high speed carriage.

Next a series of tests were conducted using the high speed carriage with mass added. Mass was added to the high speed carriage in 1/2 ton increments up to a total added mass of 4 tons. No change in acoustic noise level was observed.

Table 2
Characteristics Common to Both HSMB Carriages

Characteristic	Note
Drive Motor and Pump	
Wheel Motor	6 on Main Carriage 4 on High Speed Carriage
Tires	8 on Main Carriage 4 on High Speed Carriage
Insul-8-bar	
Tachometer Installation	
Rail Brushes	

The next series of tests involved operating the high speed carriage with various air pressures in the tires. The pressure was varied over the range from 40 psi to 90 psi in 10 psi increments. The normal tire air pressure is 70 psi. The test series was conducted using manpower to propel the carriage at a speed of 4 ft/sec. There was no measurable difference between the noise levels observed at the various air pressures. There was also, no difference between these "hand pushed" levels and the previously observed powered levels, further confirming the conclusion that the power system for the carriages was not the primary source of the measured noise levels.

The next series of tests were conducted to assess the noise generated by the insul-8-bar system. This is the carriages' electrical connection to the rail. For the test, the insul-8-bar on the high speed carriage was removed. The carriage was propelled by pushing it to speed with the main carriage and measuring the noise level as the high speed carriage passed over the hydrophone. Prior to the measurement, the main carriage was stopped and powered down. The measured levels were identical to the levels measured when the high speed carriage passed over the hydrophone under its own power. To insure no contamination from the main carriage, one set of measurements were conducted at 3 ft/sec by hand pushing the high speed carriage. The same levels were measured as when the carriage was powered.

The next set of measurements involved covering a 60 ft section of the rails with a 1/2 inch thick layer of neoprene to isolate the carriage from the rail. The noise level was carefully observed as the carriage proceeded down the rail, moved onto the neoprene, traversed the 60 ft neoprene section, and moved back onto the uncoated rail. With the carriage on the uncoated rail, the noise levels in the basin were as previously observed. When the carriage was on the neoprene, the noise levels were observed to decrease by as much as 6 dB at 1 ft/sec.

Further observation revealed that the steel tachometer wheel was the primary source

of the noise. This conclusion was reached when it was observed that as the main carriage moved from the neoprene back to the steel rail, the noise level did not increase until the tachometer wheel left the neoprene. Figure 8 illustrates the carriage noise band levels with the carriage on the steel rail and on the neoprene coated portion of the rail. The low speed noise levels in both cases were established by the carriage motor. Before each series of runs, the carriage was parked over the hydrophone, the motor was placed in operation and a load placed on the motor. In the case of the steel rail measurements the observed level was 110 dB//μPa and when the carriage was parked on the neoprene, the observed level was 104 dB//μPa. The conclusion then is that isolating the steel tachometer wheel from the steel rail reduces the direct coupling of carriage vibrations by 6 dB. Figure 8 confirms this reduction at 1 ft/sec but the noise reduction at 10 ft/sec is 24 dB. This seems to indicate that in addition to directly coupling vibrations from the carriage to the rails, the tachometer wheel generates additional noise as it rolls on the rail when the carriage is in motion.

Since it is not desirable to cover the rails with neoprene, a tachometer wheel with a reduced diameter was covered with neoprene and tested for noise characteristics. The main carriage, when equipped with the neoprene coated tachometer wheel, exhibited the same noise levels when operating on the steel rail as it exhibited when equipped with the steel tachometer wheel operated on the neoprene coated rails. It should be noted that the original tachometer installation was neoprene coated. This wheel was subsequently replaced by a steel wheel because of excessive wear and the chemical action of oils on the neoprene.

4. ACOUSTIC TESTING

As a result of the quantification of the underwater acoustical characteristics of the HSMB, several experiments have been conducted utilizing the facility. Two of these experiments are now described.

4.1 BUBBLE SWEEPDOWN TEST

Under some environmental conditions certain surface ship sonar systems experience performance degradation which is thought to be caused by air bubbles entrained in the flow field over the hull. The objective of this experiment was to develop and test a means of simulating the bubble sweepdown. The approach consisted of mounting six hydrophones from the centerline to starboard in a small sonar dome. An acoustic projector was mounted on an outrigger. All receiving hydrophone signals were recorded on magnetic tape. Acoustic data was analyzed by recording the hydrophone signal on a B and K Level strip chart recorder. By recording a signal for a run without and then with bubbles, the reduction in signal due to the bubbles could be determined.

Prior to the actual testing, some preliminary work was done to determine what parameters should be used for the acoustic measurements and what configuration the bubble generation apparatus should take.

In order to determine the appropriate parameters for the acoustic measurements, the model was placed in the tank, and a set of background noise measurements was made. Then the signal pulse was turned on and adjusted to give a reasonable baseline level from the receiving hydrophones. The pulse length and repetition rate were adjusted so as to minimize the effect of reflections and to give a reasonable number of pulses per run. The final values used were a pulse length of one msec and a rate of one pulse per second. At this point, a signal frequency of 35 KHz was being used because it was best suited to the available experimental arrangement. The dimensions of the HSMB and the 4 foot offset to starboard from the basin centerline made the starboard side of the basin the nearest acoustic reflector which could generate a direct reflection detectable by the receiving hydrophones. The direct travel time from the projector, in its outboard configuration, to the nearest receiving hydrophone is 0.85 milliseconds. The travel time for the first wall reflected return is 2.82 milliseconds. The leading edge of the wall reflected return arrives approximately one millisecond after the end of a one millisecond direct arrival (1.00 + 0.85 milliseconds). This one millisecond window between the direct arrival and the first wall reflected return is necessary for processing the data. Thus a one millisecond pulse is the longest pulse which can be used. At 35 KHz, a one millisecond pulse allows 35 cycles of the waveform to be transmitted. The combined characteristics of the power amplifier, transformer, projector, and receiving hydrophone impose a rise time on the pulse form which reduces the number of full amplitude cycles from 35 to between 20 and 25 cycles; i.e., a rise time of about 180 microseconds. As the acoustic frequency is reduced, the number of full amplitude cycles is reduced and the processed results begin to show variations attributable to rise time effects. Fewer than about 15 cycles provides unacceptable error bounds on the results. This represents a frequency of about 23 KHz. A test was then conducted to determine if the presence of bubbles would give a significant transmission loss at this frequency of 35 KHz. A bubble generation tube was mounted in front of the sonar dome to assure complete coverage of the dome, and a run was taken both with and without bubbles. The results showed up to a 10 dB loss in signal which was felt to be adequate. A frequency of 35 KHz was used for all testing.

Figure 9 shows one example of the measured data at a full scale speed of 20 knots. The top row are the data from the hydrophones with no bubbles injected. The bottom row are the data from the hydrophones when 200 μm bubbles are injected at the stem 5.8 feet above the base line. Table 3 summarizes the transmission loss for 35 KHz, 1 msec pulses through screens of 200 μm bubbles when the bubbles are injected at seven different points above the baseline.

Table 3

Summary of Relative Transmission Loss Due to Bubble Sweepdown

Ship Condition:	29.5 Foot Draft					
	0.0 Foot Trim					
	20 Knots					
Acoustic Conditions:	35 KHz					
	1 msec pulses					
	1 sec interval					
Relative Transmission Loss, dB						
Air Injection Point	Hydrophone Number 1	2	3	4	5	7
5.6' ABL	6.5	8	11.5	8.5	3.5	1.5
9.1' ABL	5.0	7	11.5	8.5	4.5	2.0
12.4' ABL	4.5	5.5	7.5	4.5	3.5	3.5
15.7' ABL	7.5	8.0	9.5	5.5	3.0	2.0
19.0' ABL	6.0	7.0	5.5	2.5	1.0	1.5
22.3' ABL	3.5	3.5	1.5	0.5	0.5	1.0
25.6' ABL	2.5	2.0	2.5	0.5	0.5	1.0

4.2 SEISMIC STREAMER HYDROMECHANICAL EXCITATION

As part of a hydroacoustic study of seismic streamers, two 50-meter sections of a streamer were suspended in the HSMB. The objective of the experiment was to quantify the acoustic response of the streamer to longitudinal mechanical excitation. Table 4 lists the location of each of the sensors relative to the location of the first triaxial accelerometer in the test section. This accelerometer was attached to the electrical connector housing at the "front" end of the test section.

Data were collected using two forms of longitudinal excitation, continuous sinusoidal excitation and transient excitation. When the test sections were continuously excited, three data sets were collected for each condition of tension (1000, 2000, and 3000 lbs), and frequency (2, 5, 10, 20, 46, 75, and 100Hz). In addition, data sets were collected at specific frequencies where either acoustical or mechanical resonances were noted. Ten data sets were acquired at each tension for transient excitation.

The time history data were acquired in digital form and stored on disk by the computer on the HSMB main carriage. These data were then transferred to the VAX 11/750 for display and analysis. Figure 10 is an example of the time history of the outputs of two hydrophones during test 5024. This figure also illustrates the mechanism which is at the root of the observed signal levels. The two hydrophones, 7 and 8, are on opposite sides of an oil filler bulkhead. It is obvious that the signals from the two hydrophones are exactly out of phase as would be the case if the bulkhead were generating bulge waves.

Table 4
Location of Sensor in Test Section

Sensor	Meters
A1	0
A2	9.38817
A3	12.53817
A4	24.68717
A5	49.29714
HY1	1.21807
HY2	2.95407
HY3	4.68907
HY4	6.42507
HY5	8.16007
HY6	9.89607
HY7	11.63207
HY8	13.36707
HY9	15.10307
HY10	16.83807
HY11	18.57407
HY12	20.31007
HY13	22.04507
HY14	23.78107
HY15	30.72307
HY16	42.87207
HY17	56.42507
HY18	68.57407
HY19	80.72307
HY20	92.87207
ST1	1.21807
ST2	2.95407
ST3	4.68907

A = Accelerometer
HY = Hydrophone
ST = Strain Gauge

5. CONCLUSIONS

On the basis of the extensive acoustical tests performed in the HSMB the following conclusions can be drawn:

- Self and radiated noise tests can be successfully conducted in the HSMB, and

- Carriage generated noise levels are amenable to further reduction.

REFERENCES

Chrisler, V. L. and Lasky, M. L., Levels and Frequency Distribution of Noise in the Test Basins of the David W. Taylor Model Basin, The David W. Taylor Model Basin, Report 643, June 1948.

Leroy, C. C., "Development of Single Equations for Accurate and More Realistic Calculation of the Speed of Sound in Sea Water," J. Acoust. Soc. Am., 46, 216 (1969).

Ross, D., Mechanics of Underwater Noise, Pergamon Press, New York, 1976, pp. 40-41.

van de Kooij, J. and de Bruijn, A., "Acoustic Measurements in the NSMB Depressurized Towing Tank," Int. Shipbuilding Prgress, Vol. 31, No. 353, 1984, pp. 13-25.

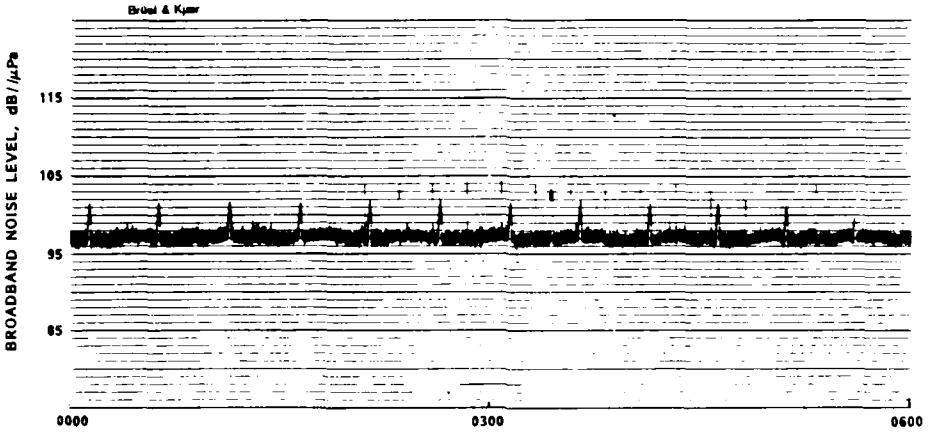

FIGURE 1 - BROADBAND UNDERWATER NOISE LEVEL IN THE HSMB BETWEEN MIDNIGHT AND 0600 ON FRIDAY, JULY 29,1984

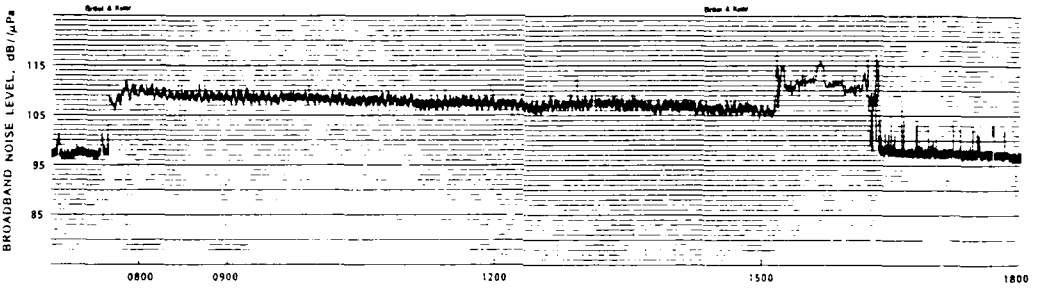

FIGURE 2 - BROADBAND UNDERWATER NOISE LEVELS IN THE HSMB DURING "TYPICAL" WORKDAY, FRIDAY, JULY 29, 1984

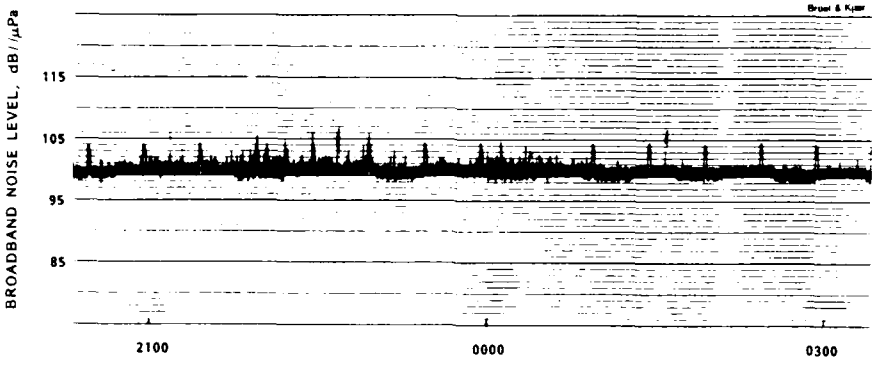

FIGURE 3 - BROADBAND UNDERWATER NOISE LEVELS IN THE HSMB ON A WEEKEND NIGHT, FRIDAY, JULY 6, 1984

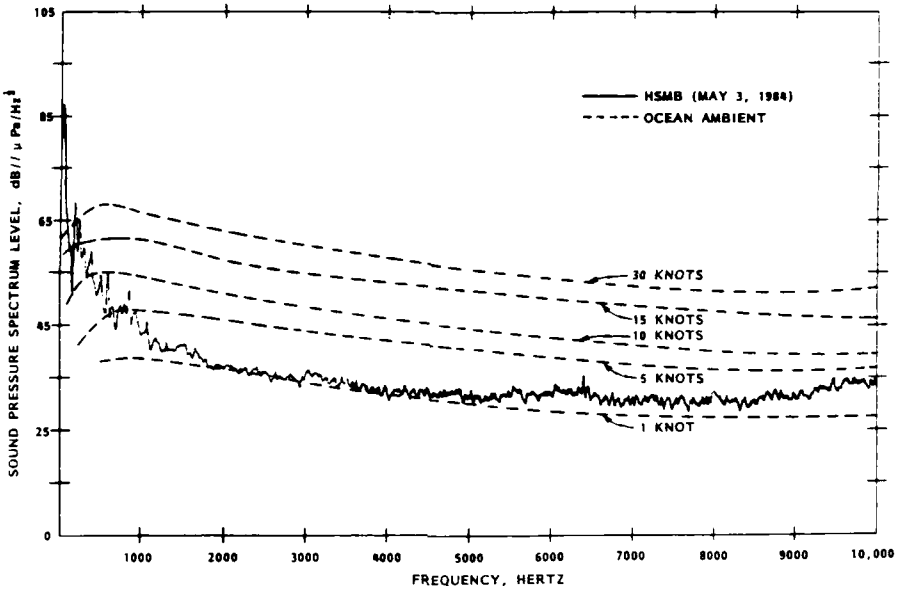

FIGURE 4 - BACKGROUND NOISE SPECTRUM IN THE HSMB WITH COMPARISON TO OCEAN AMBIENT WIND GENERATED NOISE

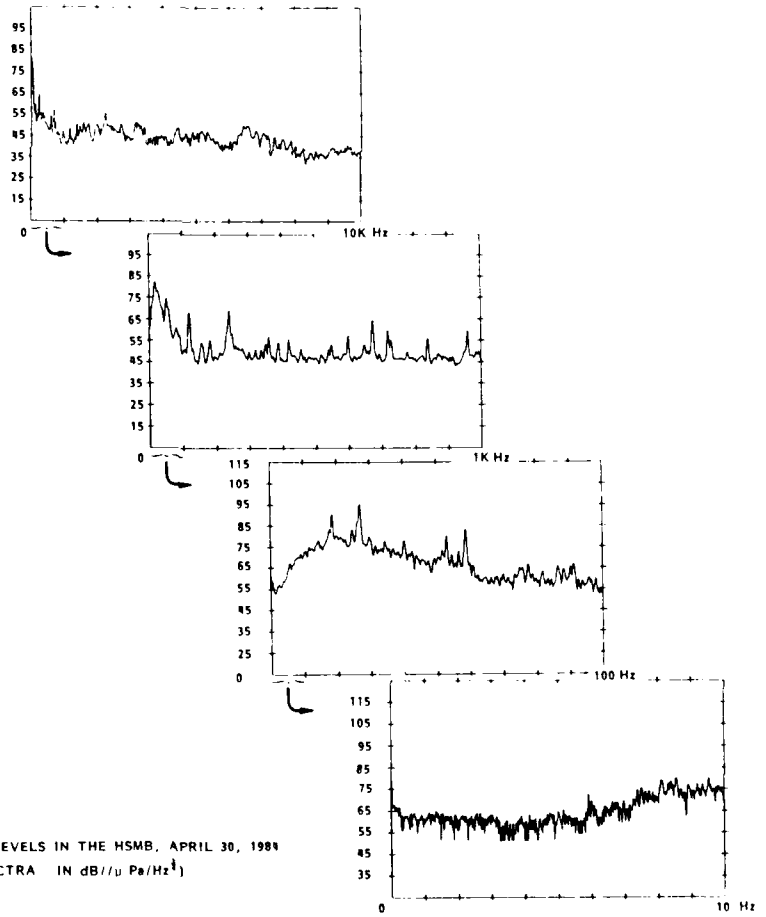

FIGURE 5 - BACKGROUND NOISE LEVELS IN THE HSMB, APRIL 30, 1984
(AVERAGE POWER SPECTRA IN dB// μ Pa/Hz½)

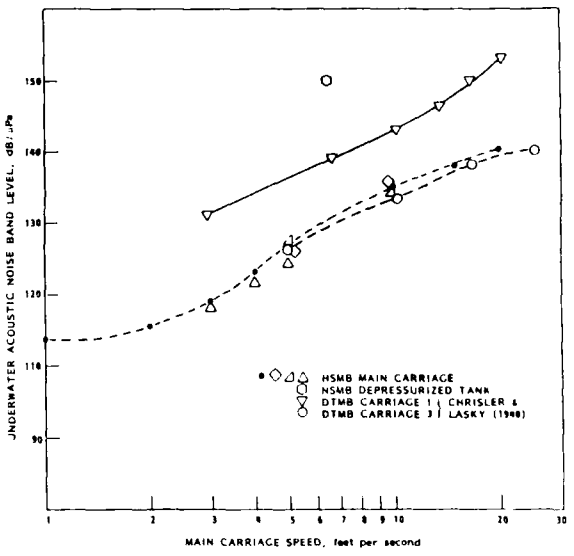

FIGURE 6 - COMPARISON OF THE UNDERWATER ACOUSTIC NOISE BAND LEVELS FOR FOUR CARRIAGES AS A FUNCTION OF CARRIAGE SPEED (10kHz BAND)

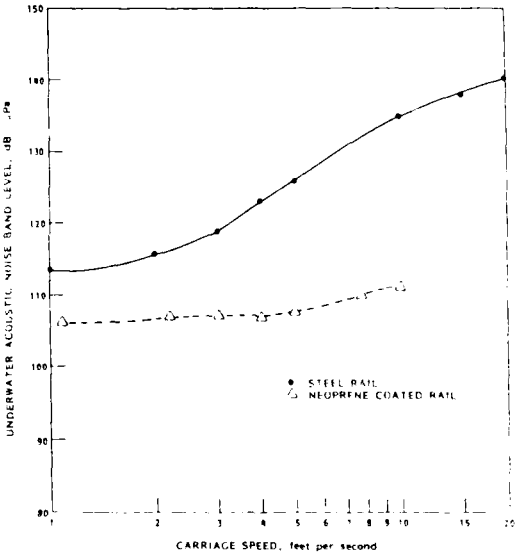

FIGURE 8 - UNDERWATER ACOUSTIC NOISE BAND LEVELS FOR THE HSMB MAIN CARRIAGE AS A FUNCTION OF CARRIAGE SPEED (10 kHz BAND)

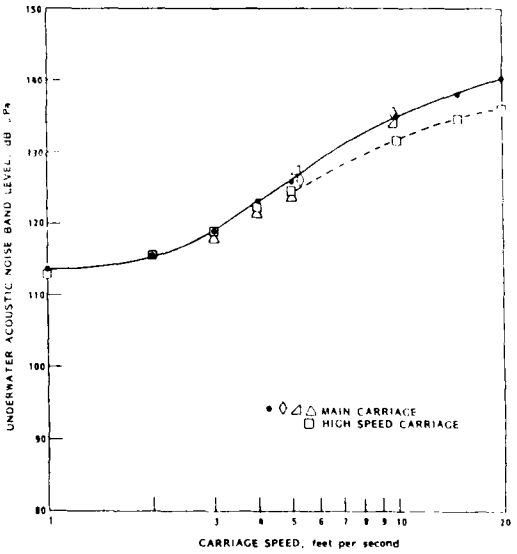

FIGURE 7 - UNDERWATER ACOUSTIC NOISE BAND LEVELS FOR THE THE HSMB MAIN AND HIGH SPEED CARRIAGES AS A FUNCTION OF CARRIAGE SPEED (10 kHz BAND)

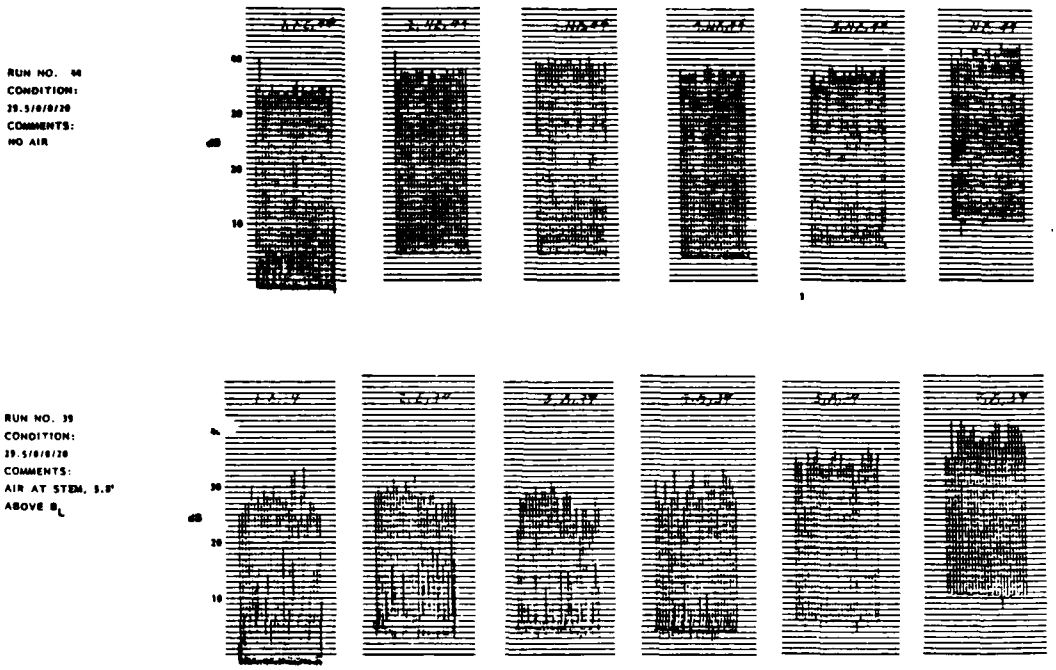

FIGURE 9 - EXAMPLE OF RECEIVED ACOUSTIC LEVELS WITH AND WITHOUT BUBBLES DURING TEST 26

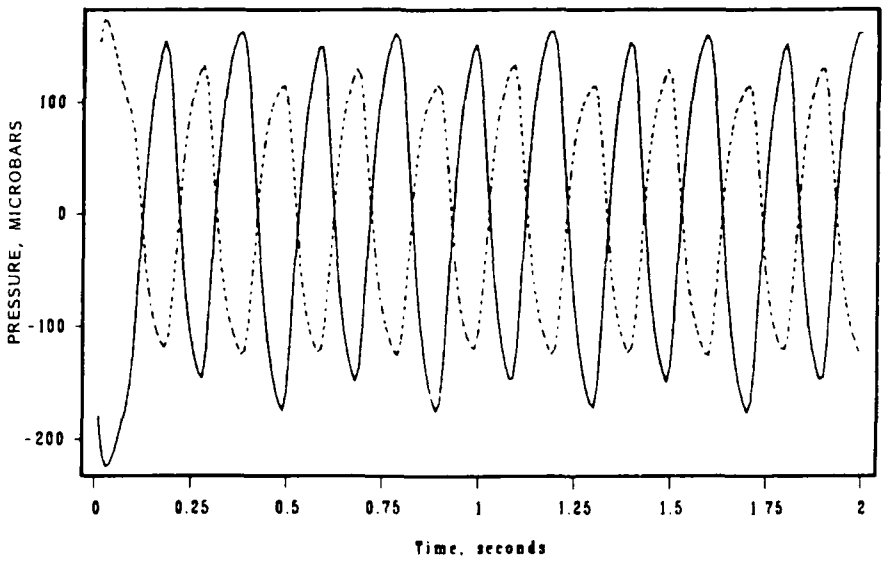

FIGURE 10 - TIME HISTORY OF HYDROPHONES 7 (——) AND 8 (------). DRIVE FREQUENCY = 4.92 Hz, DRIVE AMPLITUDE = 468 μm, TENSION = 4450 NEWTONS, TEST 5024

CONCEPTION OF THE UNIVERSITY OF NEW ORLEANS SHIP OFFSHORE UNIVERSITY LABORATORY

R. LATORRE, ASSOCIATE PROFESSOR
SCHOOL OF NAVAL ARCHITECTURE AND MARINE ENGINEERING
UNIVERSITY OF NEW ORLEANS, P.O. BOX 1098
NEW ORLEANS, LOUISIANA 70148

ABSTRACT

On February 4, 1986 the pouring of the University of New Orleans (UNO) Ship Offshore University Laboratory was begun. This paper covers the initial stages of the design development and summarizes the unique features of the towing tank now under construction.

The Tank is configured for three purposes:

1. Conventional ship reseach in deep water with calm water or waves.
2. Offshore structure testing with provision for observation and anchoring.
3. Shallow water research in calm water, current, and waves.

NOMENCLATURE

A_x	Model cross section area, ft^2
b	Model beam, ft
B	Towing Tank width, ft.
C_b	Block Coefficient of hull
D	Propeller diameter, ft.
F_n	Froude number $F_n = V/\sqrt{gL}$
F_h	Depth Froude number $F_h = V/\sqrt{gH}$
g	Gravity constant
H	Towing Tank water depth, ft or m
L	Towing Tank length, m
L,l	Model length, ft, m
R_H	Tank Hydraluic radius, ft.
R_n	Reynolds number $R_n = VL/\nu$
t	Model draft, ft.
W	Tow Tank width, m.
Subsrcipts	m = model, s = ship.
λ	Scale ratio L_s/L_m
ν	Kinematic viscosity

1. INTRODUCTION

There are typically three stages in the development of an engineering project:

1. Conception and initial performance specification.
2. Finalization of the detail design to meet the specifications.
3. Measurement of operational performance and calibration.

This paper concerns the first stage, namely the conception of the 125 ft 8 in long, 15 ft wide 0 -7 ft deep (38.3 m x 4.57 m x 0-2.134 m) towing tank for the University of New Orleans School of Naval Architecture and Marine Engineering.

2. PROLOGUE

A number of events are listed in Table 1. This table attempts to summarize the starting of the School of Naval Architecture and Marine Engineering at the University of New Orleans.

In the past decade the US Gulf Coast experienced a tremendous boom in its offshore marine business. This led to a manpower shortage, especially in the area of degreed naval architects and marine engineers. During this period a group of concerned persons from the marine industry formed the Committee for the School of Naval Architecture and Marine Engineering and a Model Test Basin at the University of New Orleans. Other groups joined and finally they succeeded in having the State of Louisiana fund a feasibility study for the school of Naval Architecture and Marine Engineering at the University of New Orleans (Hereafter denoted UNO-NAME) The conclusions and recommendations of this study were (Grimball 1979 pp 5-8):

1. UNO-NAME is feasible.
2. UNO-NAME be founded at UNO within the college of engineering.
3. UNO-NAME follow the University of Michigan BSE-NAME Curriculum.
4. A New Engineering Building be built with the Educational Marine Model Testing Facility built'in the foundations'.

TABLE I Events in the Building of the Towing Tank in the New Engineering Building at the University of New Orleans (UNO).

Date	Event
7/77	Mr. Wall and UNO Chancellor H. Hitt discuss the needs for a NAME Program and Model Test Facility while on a Nile River Cruise sponsored by the N.O. International House.
9/77	Committee for the School of Naval Architecture and Marine Engineering and a Model Test Basin at the University of New Orleans (CSNAME-UNO) is formed with Mr. Wall chairman.
8/79	Final Report of the Feasibility Study for the School of Naval Architecture and Marine Engineering at the University of New Orleans completed.
1980	CSNAME-UNO, Louisana Shipbuilders Assoc., Propeller Club, SNAME Section, and UNO are successful in having a 5 year special appropriation passed and the approval for New Engineering Building at UNO bond issue.
1981	Feasibility study for a University Affiliated Marine Model Testing Facility completed. Architect S. Muller & Associates begins New Engineering Building Naval Architecture & Marine Engineering Classes begin at UNO.
1982	Dean Dohse obtains materials from several towing tanks.
8/82	Dr. Munchmeyer hired as Chairman and Mr. A. Suda is hired.
10/82	Visits to tanks at Univ. of Mich., Stevens Inst. of Tech., Webb Inst. of Tech., US Coast Guard Academy, US. Naval Academy, Hydronautics, and DWTNSRDC are made by Dr. Munchmeyer. This leads to initial specification of a 120ft x 10ft x 6 ft deep tank. Feedback results in Level I specifications of a 120 ft x 12 ft x 8 ft deep tank with unmanned carriage pulled by tow wire with wedge wavemaker. Building is designed around these tank dimensions.
5/83	Dr. Latorre is hired as Associate Professor in charge of the towing tank(eff. 1/84) He begins a study to finalize the tank dimensions and determine the tank capabilities. Phase I steel tank is considered for ease in leveling and observation windows/discarded.
8/83-10/83	Phase 2 Finalization of tank dimensions at 125ft 8 in x 15 ft x 0-7 ft depth. Tank envisoned for three tasks: Classicial deep water studies, Ocean Engineering and Shallow water research. Provision for Cavitation tunnel and current maker incorporated in building. Specifications developed by V.A. Phelps and Architect around Dr. Latorre's Dwgs 8/83-10/83.
1984	Building bid documents released. Inputs from Mr. Goodman, Hydronautics, Mr. P. Wahraven MTS, and Dr. Bruce Johnson. J.A. Jones & Co. selected as building contractor, Groundbreaking by Governor E. Edwards. Integrated Engineering Services Corp selected as the subcontractor for the rail-carriage system and wave maker/beach platform. Mr. G. Luthra, Project engineer VBD, Duisburg W Germany meets with Contractor and architect regarding the installation of the level bottom at the Duisburg Tank. Dr. Latorre presents a design and progress report at the SNAME Gulf Section Meeting9/21/84. Initiation of tank foundation isolation, installation of current maker piping, and change from wedge to flap type wave maker with irregular wave generation capability is begun.
1985	Development of flap type specifications for deep and shallow water wave making. Development of Caviation tunnel design.
1986	Pouring of towing Tank slab 2/4/86. Study on the automation of the model making.

As Table 1 indicates the State of Louisiana adopted these resolutions and provided the funds to begin the UNO-NAME program and build a new engineering building. College of Engineering Dean Dohse began to organize the UNO-NAME program which was continued by Professor Munchmeyer.

A university affliated marine model testing facility also evolved out of the UNO-NAME feasibility study. This resulted in a parallel project directed by Mr. J. Cocchira for the State of Louisiana. This study involved site visits to facilities in the US and abroad and resulted in a proposal for a estimated 33.6 million dollar complex including (Grimball, 1981):

200m x 10m x 6m deep towing basin
30 m x 30m x 15m deep seakeeping basin
70 m x 30m x 2m deep maneuvering basin
future cavitation tunnel

Under these circumstances the UNO towing tank was envisioned as primarily a teaching facility with the industrial projects being conducted in the larger complex. As Table 1 indicates the new engineering building Figs. 1 and 2 was initially arranged around a 120 ft x 12 ft x 8 ft tank before the present author joined the project in May, 1983.

3. INITIAL CONCEPTIONAL STUDY 5/83--8/83

To distinguish the UNO-NAME towing tank from the large university affiliated complex, the author begun using the Ship-Offshore University Laboratory to denote the UNO-NAME tank.

Three perceptions of the present and future of the towing tank usage guided the subsequent design of the tank and the inclusion of a number of features. These perceptions are:

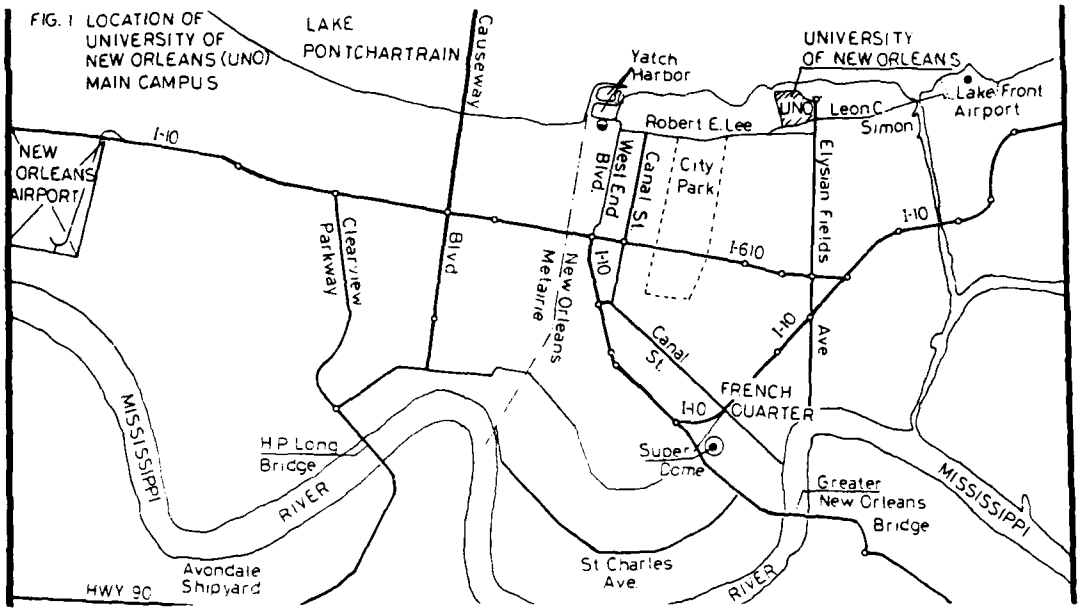

FIG. 1 LOCATION OF UNIVERSITY OF NEW ORLEANS (UNO) MAIN CAMPUS

I. Proximity of Mississippi River and Gulf of Mexico will require tank capability in:
   1. Classical ship EHP, maneuvering, and seakeeping tests
   2. Offshore structure tests
   3. Simulated river tests involving shallow water, current and waves.

II. Budgets for commerical work are small so model size of 7 - 10 ft length will be typical.

III. Tank will evolve into a tool to support numerical hydrodynamics analysis. This will allow correction for similitude problems to be rationally developed.

In essence this tank will be used to develop creative technology as well as estabilishing original scientific achievements. (Inui, 1981).

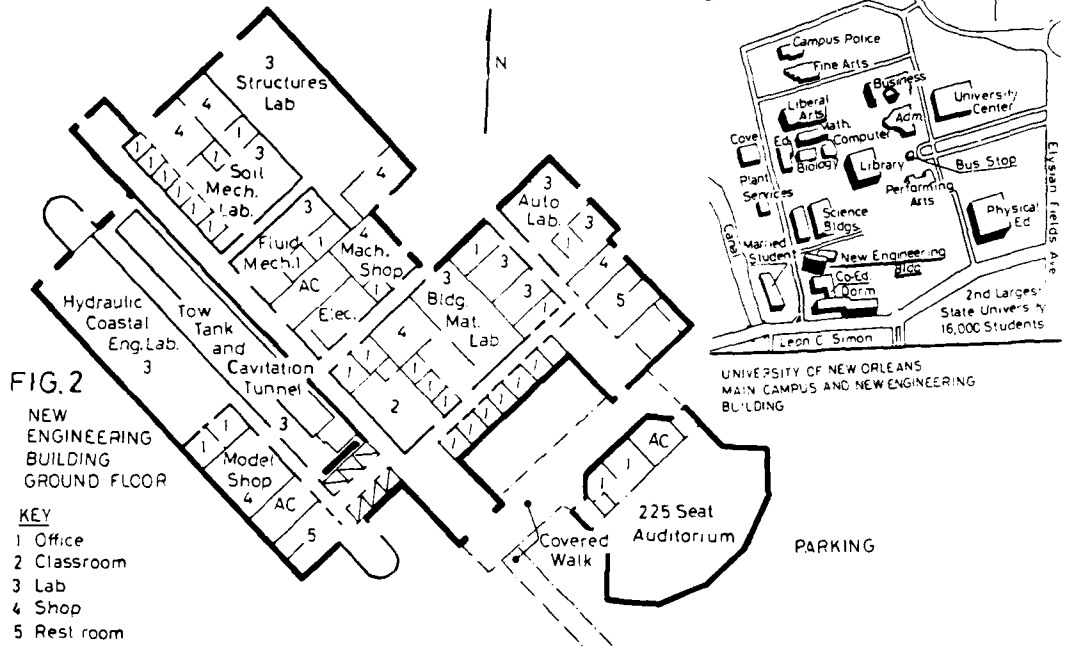

FIG. 2 NEW ENGINEERING BUILDING GROUND FLOOR

UNIVERSITY OF NEW ORLEANS MAIN CAMPUS AND NEW ENGINEERING BUILDING

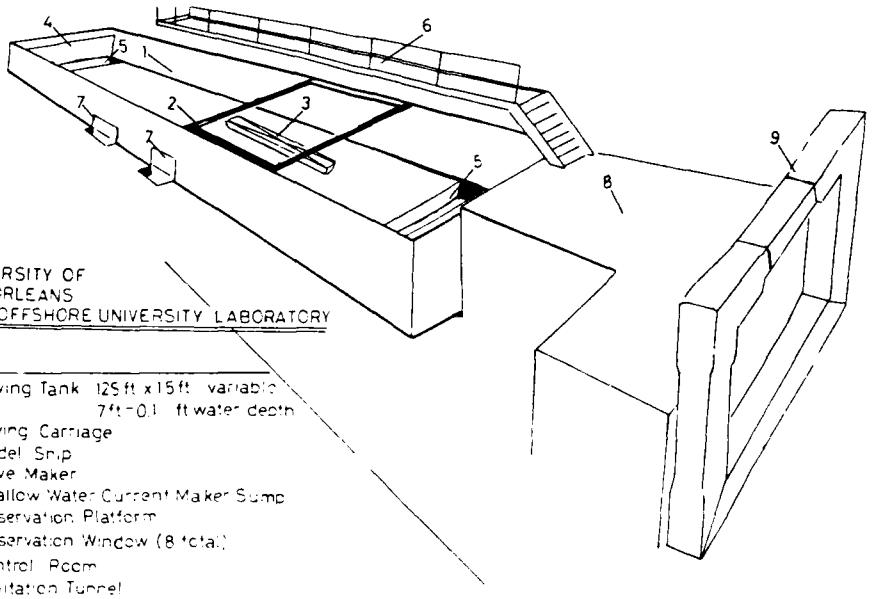

FIG 3 UNIVERSITY OF NEW ORLEANS SHIP OFFSHORE UNIVERSITY LABORATORY

KEY

1 Towing Tank 125 ft x 15 ft variable 7 ft - 0.1 ft water depth
2 Towing Carriage
3 Model Ship
4 Wave Maker
5 Shallow Water Current Maker Sump
6 Observation Platform
7 Observation Window (8 total)
8 Control Room
9 Cavitation Tunnel

3.1 Blockage Considerations and Check

The first task was to study the towing tank cross section dimensions to clarify the appropriate tank width W and water depth H to have minimal blockage when testing 7-10 ft models. A spectrum of typical vessels was selected ranging from a cargo ship to a river towboat (Sketch T-II-0 Appendix I) for study.

Using scale ratios of $30 \leq \lambda \leq 50$ the models were sized and the blockage caused by the tank dimensions checked (Comstock, 1967). As sketch T-II-0 indicates, the tank dimensions of W = 15 ft (4.57 m) and H = 7 ft (2.134 m) resulted in an acceptable value for V'/V_∞ ratio of speed in shallow water to deep water for equivalent ship resistance.

3.2 Location of Observation Windows and Observation Pits

Observation windows in tow tanks are invaluable in observing the complex flow around the ship hull and offshore structures.

Two set of requirments merged in locating the observation windows. The first was the need to make observations near the water surface. The second was to make observations of the bottom during shallow water testing. To accomplish two tiers of windows were evolved. The upper tier consists of 5 windows, 2.5 ft long by 2.67 ft high. The top of the frame is 10 in. below the tank wall upper edge. The second tier consists of 3 windows 1.5 ft wide by 4 ft high. These windows are set so the lower frame is below the tank edge allowing a clear view of the tank bottom from the observation pit.

It is envisioned that a prism similar to the one developed by van Sower (1973) will be used to correct for the air-water distortion.

Table II gives the window centerlines. These values were determined to insure the model would be at steady state conditions using the following equation adopted from Bogdanov(1982):

$$L = \frac{V^2}{2}\left(\frac{1}{a_a}\right) + L_s + L_1 + V\, t_o \quad (3.1)$$

V : model speed
a_a: carriage acceleration
L_s: starting location of model from end
L_1: stabilization length
t_o: measuring time

3.3 Shallow Water Test Requirements

The author was fortunate to visit the Versuchsanstalt fur Binnenschiffbau E.V. in Duisburg, Germany in Novemeber, 1982. This tank conducts shallow water research in support of the development of water transport on the Rhine river and other waterways throughout the world.

While early work in shallow water was done using a movable bottom, it was stressed that conducting tests in a shallow water tank is preferable. This requires that the tank bottom be finished to a high tolerance in levelness. Discussions indicated that a $\pm$ 1mm levelness is appropriate. This is close to the $\pm$0.03 in. Captain Saunders used in his discussion of the MIT towing tank (Saunders, 1953).

Table II UNO towing tank window locations

No.	Tier	Window Centerline to end
1	Eye level	15 ft
2	Eye level	24 ft
3	Bottom level	37 ft
4	Bottom level	48 ft
5	Eye level	48 ft
6	Bottom level	60 ft
7	Eye level	74 ft
8	Eye level	104 ft

These discussions resulted in the specification of a ± 1 mm bottom levelness tolerance as shown in sketch T-I-1 (Appendix I). The shallow water tests envisioned included tests with the model near a wall or simulated bank. Therefore the shallow water extension beam would be able to be moved transversly following sketch T-II-1 (Appendix I).

In addition to these calm water studies research in waves and current was envisioned. For shallow water waves, a wave board moving horizontally is typically employed. Provision was made for the installation of this unit.

In the case of a shallow water current maker a desired current of 0.7 ft/s in 0.7 ft of water was adopted. The current maker consists of troughs set at each end of the tank the connecting piping, a pump and control system. During the tank construction the under ground piping was installed as well as the troughs cast with the tank bottom.

3.4 Ocean Engineering Test Provisions

In addition to the observation windows a special provision was made to have eight imbeded mounts be set flush in the tank bottom. These allow the securing of pallets with an offshore structure model secured or the direct tie down of a structure to the tank bottom.

4. BUILDING INTERFACE 10/83

During the meetings with the architect a number of areas were identified which would require modification. These changes would allow the installation of a vertical loop cavitation tunnel, as well as streamline the transfer of the models from the model shop into the towing tank. Since the author was overseas at that time, a series of skeches UNO/T1-T4 were prepared and sent from France by the author. These sketches are included in Appendix II.

5. EVOLUTION OF DESIGN

At the initial stages in Table 1 a wedge type wave maker generating regular waves was specified. A more elaborate wave maker with irregular wave making capability represented a larger cost which was difficult to cover before the final bidding was completed.

By 1984 when the UNO Engineering Building sealed bids were opened, it was clear that the State of Louisiana was not in a position to sponsor the start up of the university affliated marine model testing facility. This meant that the near term industrial work would focus on the UNO Ship-Offshore University Laboratory. This would require capability to perform tests in regular and irregular waves which required upgrading the wavemaker. A number of inputs were provided by Mr. Luthra, VBD, Duisburg on the appropriate shallow water wavemaker performance as well as from Mr. Walraven, MTS,

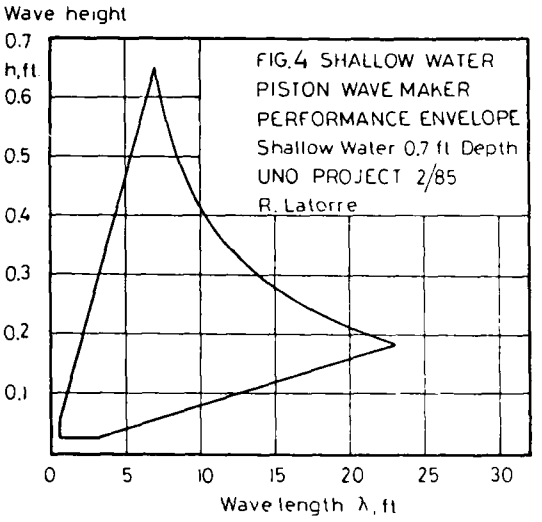

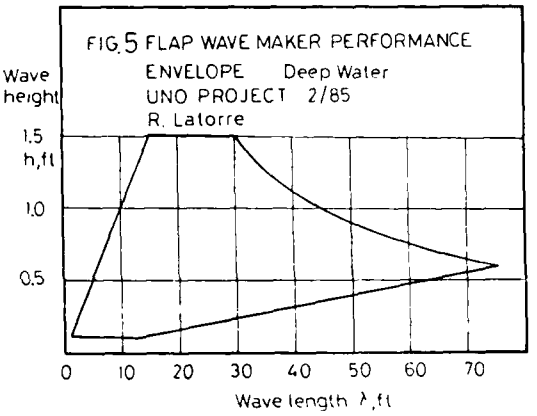

for a deep water flap type wavemaker. In the justification for the change we had the support of Professor Bruce Johnson, US Naval Academy. The resulting deep and shallow water wavemaker performance envelopes are shown in Figs. 4 and 5. At writing this is under action by the State of Louisiana.

While most papers of this type go into detail regarding the rail and carriage system performance, these details will be left for a future ATTC paper. The carriage is pulled by a 7.5 HP electric motor which gives an top carriage speed of 10,4 ft/s turning at 1750 rpm. A photo of the carriage(6/86) is shown in Appendix III in Photo 5.

6. DISCUSSION

In the interim between the studies made in 1983 and the present the author has made a survey of educational towing tanks with length less than 110 m. For the large tank designed for the University of Veracruz (150 m x 11 m x 5.5 m deep) Professor D'Archangelo used a relationship for tank width W to length L:

$$W = 0.9 \sqrt{L} \qquad (6.1)$$

Table III Examples of Educational Towing Tank Dimensions for length L < 110 m Ref. ITTC 1978.

Country	Facility	Date	Notation	Tank L,m	W,m	T,m
US	US Coast Guard Academy	1981	USCG	35	3.04	1.82
	US Naval Academy	1975	USNA	40	2.06	1.8
	University of California	1954	UC	61	2.44	1.52
	Mass. Institute of Technology	1953	MIT	33	2.6	1.25
	University of Michigan	1905/62	UM	109.7	6.7	2.9
	University of Minnesota	1954	UMinn	77	2.74	1.8
	University of New Orleans	1987	UNO	38.3	4.57	2.134
	Stevens Institute of Tech.	1933	SIT-1	41.5	2.8	1.4
			SIT-3	92	3.7	1.7
	Webb Institute of Technology	1954	Webb	28.3	3.0	1.5
JAPAN	Hiroshima University	1967	HU	87	5.0	3.0
	Kobe Univ. of Merchant Marine	1972	KUMM	70	6.0	1.5
	Kyushu University Res. Inst	1956	KU-a	60	1.5	1.2
		1962	KU-b	70	8.0	3.0
	Kyushu University	1933/67	KU-c	36	5.4	5.0
	Matsue Technical School	1972	MTS	33.2	3.0	2.0
	Osaka University	1970	OU	100	7.8	4.35
	University of Tokyo	1937	U Tokyo-1	85	3.5	2.4
		1942	U Tokyo-2	44.8	5.0	3.4
ENGLAND	Glasgow University	1963	UG	76	4.6	2.4
FRANCE	Ecole Nat. Superieure de Mecanque, Nantes		ENSM	70	5.0	3.0
GERMANY	Institute fur Schiffbau, Hamburg		IFSH	34.3	2.1	1.0
ITALY	Universite di Trieste	1966	UDT	50.	3.1	1.6
	Universite di Genova	1947	UDG	49	2.9	1.5
NETHERLANDS	Univeristy of Tech., Delft	1971	Delft	80	2.8	1.3
NORWAY	University of Trondheim	-	SRIN	27	2.5	1.0
POLAND	Technical University Gdansk	1955	TUG	30	5.0	1.6
SPAIN	Escuela Tecnica Superior de Ingenieros Navales, Madrid	1967	ETSM	76	3.5	2.0

and a second relationship for tank water depth H to length L:

$$H = 0.45\sqrt{L} \qquad (6.2)$$

As can be seen from Figs. 6 and 7, eqs. (6.1)&(6.2) represent the upper bound of educational tank width W but grossly overpredict the tank water depth H.

Examining Table III it is clear that the US towing tanks are somewhat narrower in comparison with the Japanese tank dimensions. This is clear in Fig. 6 where the UNO tank width is significantly larger than other US tanks less than L = 90 m.

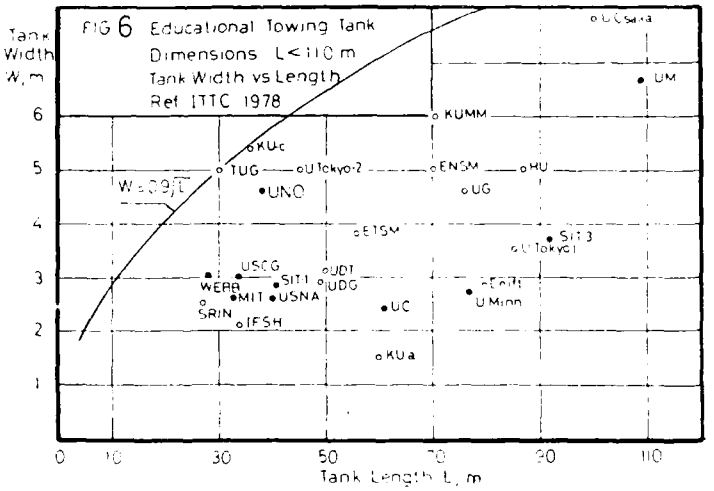

FIG 6 Educational Towing Tank Dimensions L<110 m Tank Width vs Length Ref ITTC 1978

There is less range to the tank depth H shown in Fig. 7. Nevertheless the UNO tank is deeper than the other US tanks less than L = 90 m.

In the course of this survey the author found two papers presented at the SNAME Chesapeake Section meeting of October, 1982, Fireman, 1982 and Fischer, 1982 dealing with the classification of ship model size and the results of using small (5 to 6.6 ft) models for studying hull form improvement. According to this classification the models sized in Sketch T-II-0 (Appendix I) fall into the category of medium size as shown in Fig. 8.

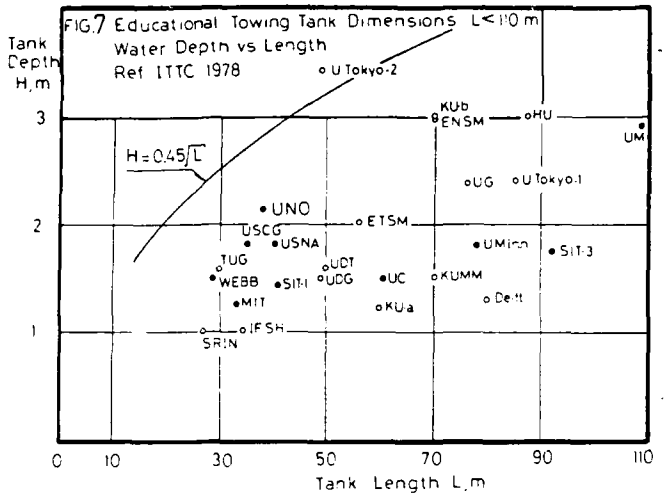

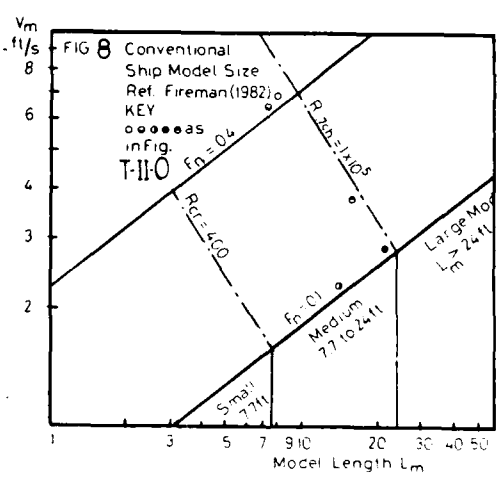

The survey of towing tank costs by Firman et al. (1982) indicated that the model making is a sizable element in the cost of performing a model test. Therefore the author has been involved in the design of an model milling machine which is illustrated in Fig. 9.

The photos in Appendix III give an impression of the UNO Ship-Offshore University Laboratory size as well as the progress towards its completion in 1987.

7. ACKNOWLEDGEMENTS

The author is grateful to a number of persons on the Committee for a School of Naval Architecture and Marine Engineering at UNO, as well as the members of the Louisiana State University Physical Plant Services who are involved with the day to day details of this project. The cooperation of the architect S. Muller & Associates in allowing the modifications described in this paper is gratefully acknowledged. Finally the author is thankful to Prof. Munchmeyer and Dean Mahmoud for their support as well as V.A. Phelps and Fred Phelps for their help.

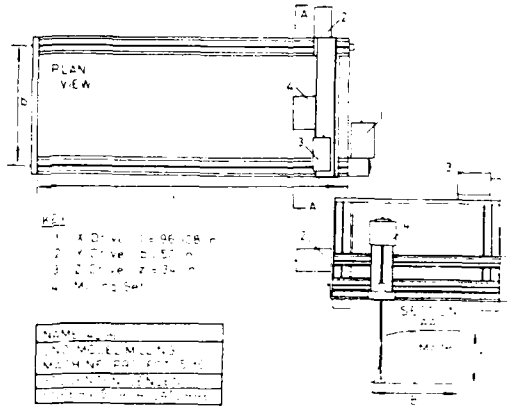

FIG. 9 Model Milling Machine Concept.

8. REFERENCES

Annon. (197) Directory of Facilities, App. V Proceedings, ITTC Meeting, Berlin 1423-45.

Bogdanov, P., et al. (1982) Methods and Means for Complex Hydrodynamic Investigations and Tests at BSHC of Models of Ships and Other Floating Structures in Restricted Water, PROC. 11th Scientific & Method. Seminar, VARNA, Bulgaria, Vol I, pp1-18.

Comstock, J.P.(1967) PRINCIPLES OF NAVAL ARCHITECTURE, SNAME, pp 320-329.

D'Archangelo, A.M.,(1974), Supportive Educational and Research Facilities for a Developing Shipbuilding Industry, Univ. of Michigan Dept. of Naval Arch. & Mar. Eng. Report No. 150, 23 pp.

Grimball, H.G.(1979), Feasibility Study, A School of Naval Architecture and Marine Engineering, University of New Orleans, Triton Teams Ltd., Metairie, Louisiana.

Grimball, H.G.(1981) A Study for a University Affiliated Marine Model Testing Facility, La State Project No. 603 1001, G/G/S Consultants, Ltd., Metairie, Louisiana.

Fireman, H., Hough, J., Hoyt III, J, Lones, A (1982) The Use of Small Models in the Ship Design Process, SNAME Chesapeake Section Meeting.

Fisher, S.C., (1982) An Assessment of the Merit of Using Small Models to Predict Effects of Hull Form Cahnges upon Resistance, SNAME Chesapeake Section Meeting.

Saunders, H.E. (1953) Written discussion on The Ship Model Towing Tank at MIT (Abkowitz M., and Paulling, J.) TRANS. SNAME Vol 61.

Scwer, Van W, (1973) A Correcting Prism for Underwater Viewports, Ocean Engineering, Vol. 2, pp 223-29.

Inui, T., (1981) 3rd Weinblum Lecture, JSR, Vol. 25, No. 3.,p 179.

APPENDIX I

Sketches used to define the UNO towing tank capability for coventional ship testing and shallow water research.

These were prepared for discussions with architect and V. A. Phelps in August, 1983.

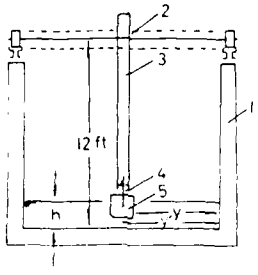

KEY
1—Towing Tank
2—Towing Carriage
3—Shallow Water Extension
4—Dynamometer
5—Ship Model

SHALLOW WATER
Test Geometry
Water Depth h
0.5in≤h≤30 ft
Distance from Tank Wall
0.25in≤y≤8.0 ft
50 in≤y≤80 ft

ARRANGEMENT SKETCH T-II-1 Univ New Orleans Project
Tank Section: Shallow Water Test R Latorre 8/83

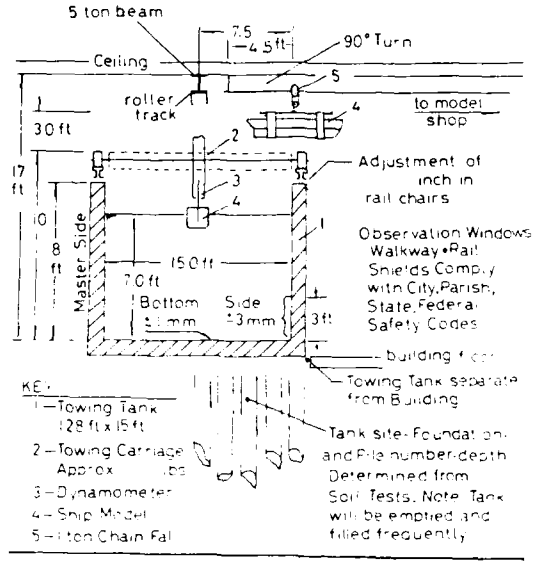

KEY
1—Towing Tank
128 ft x 15 ft
2—Towing Carriage
Approx lbs
3—Dynamometer
4—Ship Model
5—1 ton Chain Fal

ARRANGEMENT SKETCH T-II-1 Univ New Orleans Project
Towing Tank Section R Latorre 8/83

Univ New Orleans Project
R Latorre 8/83
ARRANGEMENT SKETCH T-II-0

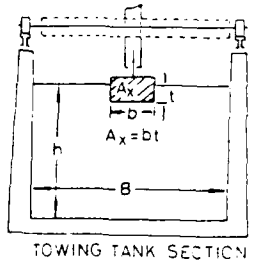

TOWING TANK SECTION

$$R_H = \frac{(Bh - A_x)}{(B + 2h + k(b+2t))}$$

Froude No. $F_n = \frac{V}{\sqrt{gl}}$

Depth Froude No. $F_h = \frac{V}{\sqrt{gh}}$

CALCULATION OF BLOCKAGE EFFECT
REF PNA pp 320-325

Vessel Type	Cargo Series 60	Offshore Supply	Offshore Barge	Towboat & 5x3 Tow	Towboat & 2x3 Tow
Vessel					
Length L ft	400	220	650	1100	545
Speed Vmax	30 kts	20 kts	9 kts	14 mph	14 mph
F_n	0.446	0.40	0.105	0.110	0.155
Model Scale λ	50	30	50	50	30
Length l, ft	8.0	7.3	13.0	22.0	18.2
Beam b, ft	1.25	1.5	2.5	2.1	3.5
Draft t, ft	0.50	0.35	0.5	0.2	0.3
Prop. Dia. D, ft	0.35	0.25	NA	0.25	0.35
Speed $V = V/\sqrt{\lambda}$, ft/s	7.2	6.2	2.15	2.9	3.75
Blockage Effect					
B = 15 ft h = 7 ft					
Check $F_n < 0.5$	0.477	0.410	0.143	0.193	0.249
Hyd. Radius R_H, ft	3.34	3.35	3.19	3.32	3.14
$\sqrt{A_x}/R_H$	0.237	0.216	0.35	0.195	0.326
SYMBOL	○	⊕	⊙	●	⊖
V/V_∞	0.996	0.997	0.992	1.0	0.993

LANDWEBER'S PLOT

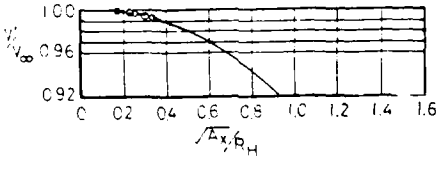

APPENDIX II

Sketches used to delineate the UNO towing tank room and provide space for cavitation tunnel.

These were prepared in October, 1983 using architect supplied drawings as the basis.

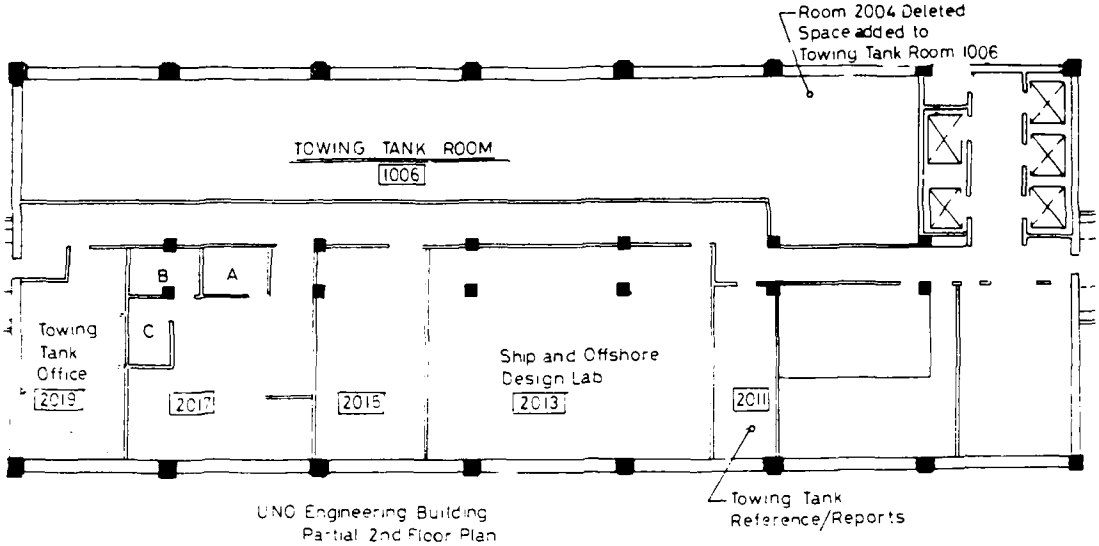

UNO Engineering Building
Partial 2nd Floor Plan

Notes
Changes following Memo (9/20/83) to Vice Chan. D'Agun and discussion with Prof. Munchmeyer 10/83

Univ. of New Orleans Project	
SKETCH: UNO/T1 Second Floor	
Date: 10/83	R.Latorre

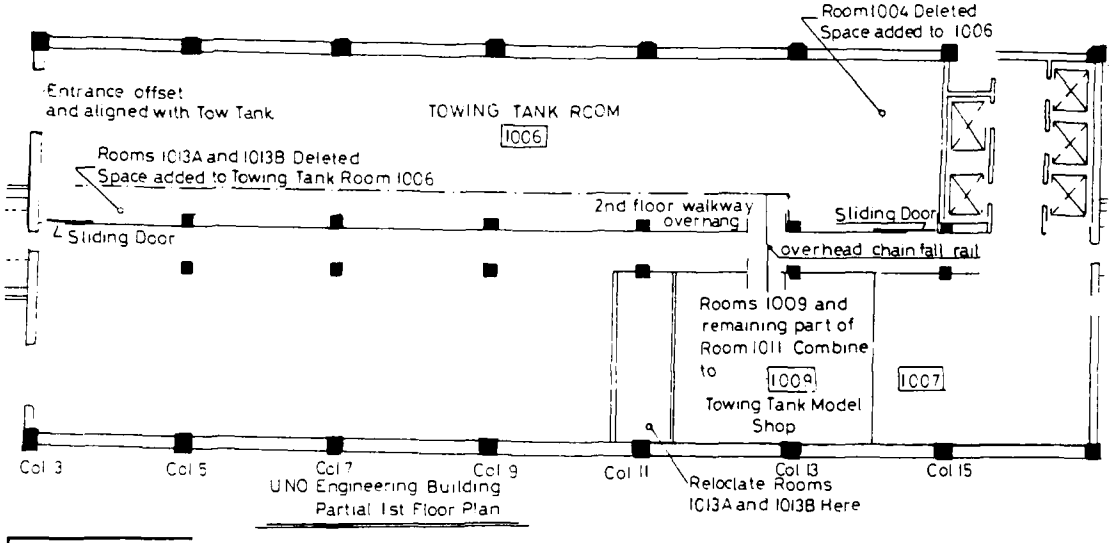

UNO Engineering Building
Partial 1st Floor Plan

Notes
As SKETCH UNO/T1

Univ. of New Orleans Project	
SKETCH: UNO/T2 First Floor	
Date 10/83	R.Latorre

APPENDIX II (Continued)

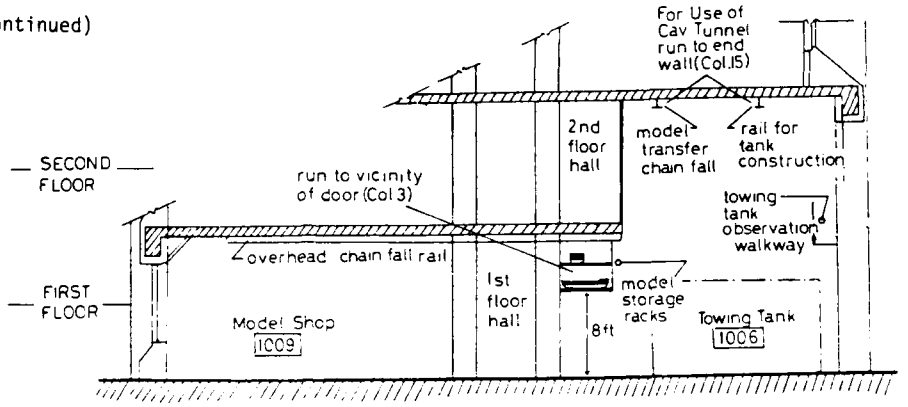

Section at Col.13

Univ. of New Orleans Project	
SKETCH UNO/T3 Section	
Date 10/83	R Latorre

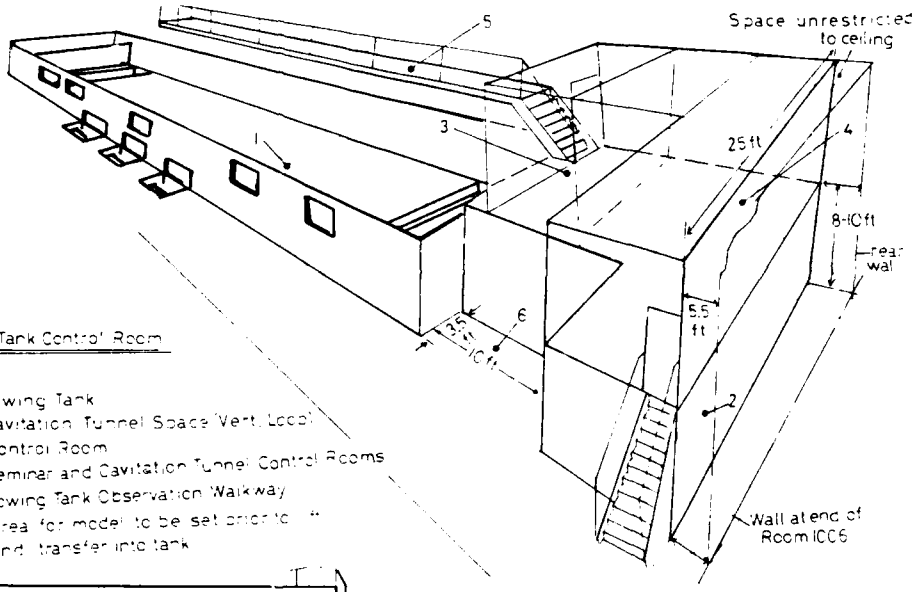

Towing Tank Control Room

KEY

1. Towing Tank
2. Cavitation Tunnel Space (Vert. Loop)
3. Control Room
4. Seminar and Cavitation Tunnel Control Rooms
5. Towing Tank Observation Walkway
6. Area for model to be set prior to [illegible] and transfer into tank

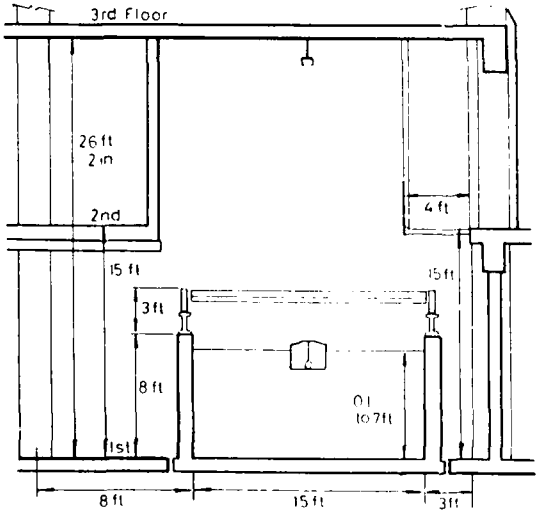

Univ of New Orleans Project	
SKETCH UNO/T4 Control Room	
Date: 10/83	R.Latorre

Section showing the final arrangement of towing tank and observation walkway (1986)

APPENDIX III Photos of UNO Towing Tank Construction (January, 1986)

Photo 1 View of tank from control room end.

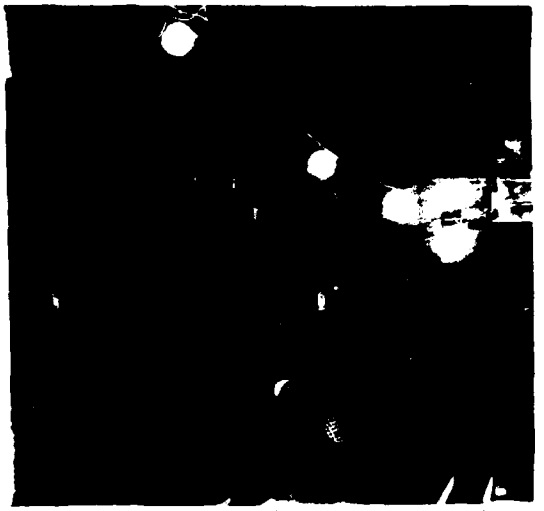

Photo 2 View of control room and cavitation tunnel cavity.

Photo 3 View of tank with bottom rod installed

Photo 4 Detail of observation pits and windows.

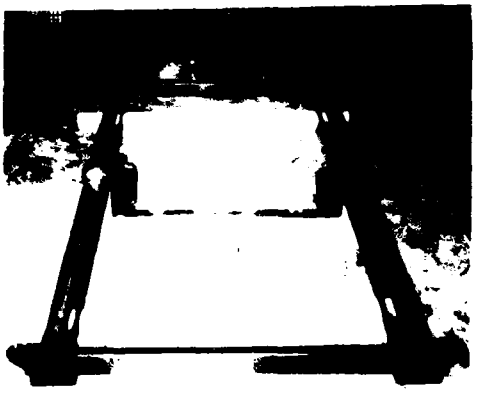

Photo 5 Towing carriage (courtesy W. Iverson)

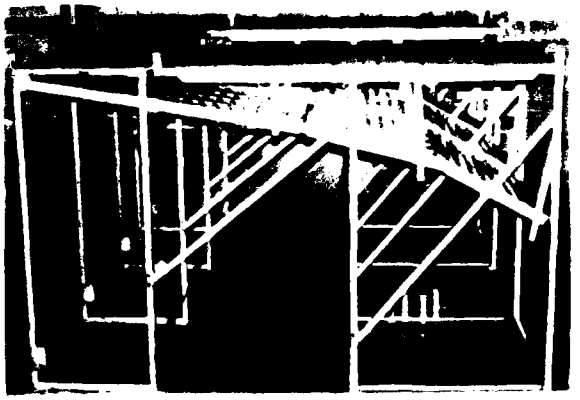

Photo 6 Beach assembly (courtesy W. Iverson)

THE INSTRUMENTATION AND DATA ACQUISITION SYSTEM AT NRC'S NEW MODEL TEST FACILITY

C. Norris, B. Gamberg and P. Thorburn
National Research Council Canada
Institute for Marine Dynamics
St. John's, Newfoundland
Canada
A1B 3T5

ABSTRACT

In November 1985, NRC officially opened its new model test facility at the Institute for Marine Dynamics, St. John's, Newfoundland. This facility consists of a towing tank (200 x 12 x 7m) complete with a double flap wavemaker, a seakeeping basin (75 x 32 x 3.5m) to be fitted with a multisegment wavemaker and the world's largest ice tank (80 x 12 x 3m). The Institute has comprehensive model manufacturing facilities.

A wide scope of work is intended for the Institute including the testing of most surface vessels as well as submarine and offshore structures. The Institute also conducts complementary measurements at full scale and ice field studies.

The present paper outlines and discusses the several aspects of the instrumentation and data acquisition facilities which have been installed to satisfy the general requirements of the Institute.

1. INTRODUCTION

Canada, being bounded by some of the worlds most hostile waters on three sides and with interests in a major inland waterway, has a major interest in marine technology and ocean engineering. With the impetus of the 1973 oil crisis, commercial exploitation of offshore resources is becoming increasingly important and major developments in the Arctic and off the East Coast of Canada are anticipated. Much of the Canadian coastline is affected by ice and hostile seas for most of the year. Thus Canada has a particular interest in ice technology as well as traditional hydrodynamic problems.

Because of the broad marine interest of Canadian Industry a wide scope of work is intended for the Institute. Studies will be carried out in the fields of ocean engineering, ice technology and the more traditional type of work conducted by other facilities. The range of vessels and structures to be tested is comprehensive and will include boats, small and large merchant ships, naval ships, both surface and submarine, and offshore structures. Complementary full scale measurements in ice fields and at sea will be conducted in support of the research program. Model testing will also be carried out on an individual client basis.

Major emphasis has been placed on developing a cost effective instrumentation capability to satisfy the needs of the Institute. The objective of this paper is to discuss the strategy adopted in defining the instrumentation needs and to outline some details of the instrumentation package adopted.

2. GENERAL STRATEGY

Prior to specifying components of the total instrumentation system, a needs analysis was carried out. The types of experiments to be conducted and the quantities to be measured were identified. The operational scenario for the instrumentation was also considered. Particular constraints and requirements were identified and taken into account during the specification and procurement of individual items. Some of these constraints and requirements are discussed below.

2.1 Budgetary Limitations

As with most modern facilities, budget limitations are a perennial problem. Careful planning has avoided redundancy and overlap of equipment. Standard packages have been adopted for all tanks thus minimising the cost of spares and maintenance. The adoption of a standard Data Acquisition System for each tank allows direct interchangeability of software and hardware thus avoiding time consuming software conversions and interfacing problems.

2.2 Flexibility and Reliability

The wide range of test types to be conducted involves frequent changes in test set ups. All equipment has been chosen to be suitable for use in as many experimental arrangements as possible. Dedicated instrumentation has been avoided. Standard connectors and wiring systems have been adopted on each carriage.

2.3 Environmental Adaptation

The approach has been to avoid the need for environmental adaptation as far as possible by housing most equipment in the air conditioned carriage control rooms. Certain equipment, for example, transducers, motors, cameras, etc. are exposed to the tank environment. Careful selection has often been all that was necessary to satisfy the environmental requirements even in the ice tank where temperatures may be as low as -35°C. Specific equipment such as high-speed ciné cameras having been specially adapted and heaters installed.

2.4 Expandability

Throughout, care has been taken to specify only connectors, computer interfaces etc. which are well established in the market place. Wiring harnesses and the DAS have been configured to allow simple expansion.

2.5 Independence of Facilities

Whilst great emphasis has been placed on an integrated approach to the computer system, it is essential that each tank be able to continue testing for a reasonable period without support from other parts of the system. This is particularly important in the ice tank where the test "window" may be only one hour and failure to test will result in up to 48 hours delay.

2.6 Staffing Levels

It is intended that IMD will operate with relatively low staff levels and will supplement permanent staff using external contractors or university staff. To avoid the need for extended training all equipment must be easy to use and be protected against misuse.

3. GENERAL SYSTEMS

3.1 Computer System

The computer system is used for data acquisition, analysis and control functions. The system consists of a host computer (VAX 11/750) linked to six smaller computers in a high-speed local area network. The host computer is fitted with 8 Mbytes of memory, 900 Mbytes of on-line disk storage and 1600/6250 bpi tape drives. Experimental data acquisition is handled by 3 identical systems, each consisting of a microVAX II with 1 Mbyte memory, a 30 Mbyte hard disk, a Tektronix 4106 colour graphics terminal with hardcopy capability, and a NEFF 620 A/D converter/multiplexor. Control functions are handled by 3 identical systems, each consisting of a ruggedized VT103 terminal containing a PDP 11/23 PLUS processor, 0.5 Mbyte memory and a 4 channel D/A convertor. Interconnection between systems is accomplished with DECNET software using ETHERNET cables, with additional RS-232 connections where necessary.

Key features of the system design include:

- The use of common hardware to provide built-in redundancy.
- The use of a common data file format throughout the system to minimise the programming effort.
- The use of common data structures throughout the acquisition/analysis/display system.
- The use of a common user interface where possible.
- The use of the GKS graphics standard as a common graphics interface.
- The use of DECNET software as a communication standard between all computers.

3.1.1 Data Acquisition System

Each of the data acquisition systems is designed to allow collection and preliminary evaluation of experimental data independently of the host computer. In the case of the carriage-mounted data acquisition system, this independence is a necessity, since during carriage movements, the resources of the host computer are unavailable due to the necessary disconnection of all cabling from the carriage.

The software is designed to collect as much information as possible concerning the signals being measured at the time of data acquisition. This information is stored with each channel of data collected, reducing the possibility of operator error. Included are date and time of collection, name of test and run, physical units of data being recorded, filter characteristics, gain, settings, calibration constants or curves, etc.. Extensive use is made of the VAX/VMS hierarchial file structure. In designing the interfaces between the NEFF system and the micro VAX, a decision was made to perform all timing functions at the application program level, in a high level language (FORTRAN-77). This approach limits the maximum throughput of the system, but allows maximum flexibility in control from the high level language. As configured the system can simultaneously digitize 20 channels at 50Hz. In the future when higher sampling rates are required the timing functions will be moved to either the driver of hardware level.

A calibration program is available for

transducers connected to the NEFF A/D converter. N-point calibration data is stored on disk and is automatically associated with the test data during data acquisitions. Additional software for data acquisition includes programs to meter data channels, edit calibration parameters, list, transfer and delete acquired data runs.

3.1.2 Control Computers

The control computers are used in areas where real time control of mechanical devices (such as the wavemaker and the model mill) is required. Each of the control computers is able to operate independently of the host, although each depends on the host for down loading of data. At present the towing tank wavemaker computer is programmed in stand alone PDP11 assembly language with no operating system present. An RS-232 link to the host computer provides a slow down load capability.

A future development will be to connect the wavemaker control computer to the ETHERNET system and program under the RSXII/S operating system. This will allow full network capabilities instead of the limited down loading capabilities which are now available.

3.1.3 Host Computer

The VAX II/750 host computer is used for long term storage and analysis. All test and control signal data are stored in common test directories. Currently this data is stored on conventional disk devices but as optical disk technology develops, it is expected that this information will be transferred to large capacity write-once devices.

Throughout the analysis software intermediate data files are avoided. This allows program codes to be tidier and more efficient.

Wherever possible, standard VAX DCL command format is preferred. A standard forms management system (DEC FMS) is being used for interactive user communication. The GKS graphics standard is being used to allow program portability and device interchangeability.

3.2 Analogue Recorders and Displays

The analogue outputs of transducers can be displayed on a dual beam monitoring oscilloscope and also metered. The analogue signals can be recorded on both Gould chart recorders and a KYOWA RTP-600B 14 channel magnetic tape recorder. This allows both rapid signal validation, back up and analyses of high frequency components of signals.

3.3 Transducers

A wide variety of transducers have been procured. Transducers are available to measure, among other quantities, pressure, motions (servo accelerometers), position (LVDT's, sonic probes), force (load cells), angular displacement (ADT's), wave height (capacitance probes), torque and thrust (dynamometers). Transducers have been selected to adequately cover the dynamic range which is anticipated in models ranging from 1.5m to 12m in length.

As far as possible, in order to allow simple interfacing to the NEFF 620 series 300 signal conditioner, which is best suited to strain gauge types of transducers, DC/DC devices have been selected. This eliminates the need for special power supplies etc and allows standardised connectors and extension cables to be adopted throughout.

3.4 Motors and Motor Controllers

A wide range of DC drive motors ranging from approximately 24 to 3500 watts are available. All motors have servo-controllers available. A special range of lightweight servo-controllers for use in small models has been developed in-house and can be utilised for Z-drives, side thruster, small propellers etc.

3.5 Video Recording

A comprehensive set of video recording equipment has been installed. In general ½"VHS tape has been adopted for convenience although it has limited resolution. 3/4" U-Max tape recording is available where higher resolution is needed.

In normal use, each carriage is fitted with the following:

-4 Genlock colour cameras Panasonic Type WV-CD-120 complete with zoom lens C3/208 (1-6 zoom)

-4 Pan/tilt heads Panasonic WV-7260

-4 Environmental Housings Panasonic WV-7160B

-4 Recorders Panasonic WV-6300, ½" VHS

-1 Pan/tilt and zoom controller Panasonic WV-7490

-1 Special Effects Generator Panasonic WJ 4600

-4 Monitors Panasonic BJ-5702N

-1 Annotator, Genlock, complete with Julian Clock and keyboard and Video Expander Modules - HEI Model 522A

In addition to the above equipment an underwater pan/tilt head and lights are available for use in the ice tank. For special cases a lightweight JVC type camera can be utilised.

The editing and tilting capability consists of:

-1 Sony SMC 70G Computer, titler, time , date generator and appropriate software

-1 Recorder-Panasonic AG6300

-1 Recorder-Panasonic NV8500

-1 Controller-Panasonic NVA500

-2 Colour Monitors-Panasonic BTS 700.

The Genlock feature on all cameras and annotator is particularly useful in many experimental setups. Overlay, mixing and

split screen formats of various images are simple to achieve. Using the Genlock annotators basic test data is simultaneously recorded on all images prior to commencing an experiment. A common time base can also be displayed on all images during the experiment.

3.6 Photographic Equipment

The usual range of 35mm cameras is available. A LOCAM 11 16mm ciné camera capable of operation from 1 to 400 frames/sec is available. The camera is battery powered and is fitted with heaters, timing lights and a reflex viewer and is suitable for use on ice fields at temperatures down to -35°C.

4. SPECIFIC TEST EQUIPMENT

The previous section described instrumentation which is utilised on an Institute wide basis. In addition to this general instrumentation, specific equipment is available in individual tanks.

4.1 Ice Tank

4.1.1 Towing Post

A towing post for ice resistance testing has been designed and constructed in house. The towing post has been designed to have a high natural frequency and to be capable of handling models ranging from a few metres to 12m length. The surge and sway freedoms are fixed and the axial resistance force measured. The towing post allows the other 4 D.O.F. In practice the yaw freedom is restrained using Kempf and Remmers guiders. If required the yaw moment is measured using a load cell at the point of attachment of the guiders.

4.1.2. Underwater Carriage

An underwater carriage has been designed and will be installed in the near future. This carriage is pushed by the main carriage and is guided by a centre rail attached to the bottom of the tank. The carriage uses a modular design concept and is fabricated completely of aluminum, stainless steel and plastics. The carriage is 6m wide and can be extended from approximately 3m length to 12m length depending on the model size to be tested.

Underwater pan/tilt units with feedback angle transducers and lamps are available for mounting on the carriage. Complete viewing of the underside of the ice sheet inway of the main carriage and the model is possible by simple reconfiguration of the camera set up.

4.1.3 Propeller Dynamometer

Ice testing of propellers places stringent requirements on thrust and torque dynamometers due to the high transient loads that can be imparted by the ice. These loads are measured using a Tracor Hydronautics Model HI-TD-750/1500 dynamometer.

4.2 Towing Tank

A towing post and pneumatic model clamp have been designed and constructed in house. These units are modular in concept is as the ice towing post. The units have been designed to take advantage of the automatic test bay elevation features of the carriages and are capable of handling models from 3m to 12m length with either soft or rigid connection. Kempf and Remmers guiders are available for yaw control. A modular unit based on frictionless tables, LVDTs and a servo-accelerometer is used to monitor roll, pitch and heave during testing.

A Kempf and Remmers Model H39 propeller dynamometer is available for open water propeller testing. Wake surveys can be carried out by using the NRC wake rake.

4.3 Seakeeping Tank

4.3.1 Optical Position Tracking

An Eloptopos electro-optical positioning system supplied by Eloptricon AB of Sweden has been installed. This is a non-contact lightweight position measuring system. Infrared diodes (LED's) are attached to the model. Infrared detectors, called cameras, are located around the basin. Sets of cameras are used to determine both horizontal and vertical angles between the target LED and fixed reference LED's. Each camera has an associated camera processor which digitizes the video signal from its charge coupled device (CCD) array. The cameras processors transfer angle data via a RS-232 link to a data concentrator, a dedicated microcomputer. Operation of the system is carried outby a micro VAX II interfaced to the data concentrator with an IEEE-488 bus connection.

These angular measurements and the geometry of the camera deployment are used to determine the three dimensional position of each target LED. By using 3 LED's all 6 degrees of freedom of the model in space can be calculated. Measurements for each LED are made in time sequence with synchronization provided by radio signals. By differentiating the time varying position data the velocity and accelerations of the model can be determined.

The advantagesof the system include low model installation weight, ruggedness, ease of operation, accuracy and ability to measure position, velocity and acceleration in all 6 D.O.F. Data recording is done on shore without radio telemetry from the model. The system operates in reasonable ambient light provided infrared content is low and has provisions to deal with water reflections.

After installation and initial testing

at IMD the system was temporarily transferred to NRC, Ottawa for use in the Hydraulics Laboratory. In view of the relative ease of the transfer, and the reliability of the system, periodic relocation to the clearwater tank carriage for testing of offshore structures etc. will be carried out.

4.3.2. Telemetry and Remote Control

A remote control and telemetry system, both in-house designs, are used with free-floating models. The remote control system is a 5 channel digital radio link at 27.425 MHz with 8 bit resolution. Rudder angle, motor speed, power on/off and reverse/forward direction are controlled from the shore station.

The telemetry system samples 24 channels of analog data at a 100 Hz frame rate. The data is digitized to 12 bits and transmitted on a carrier of 260 MHz.

5. FUTURE DEVELOPMENTS

To date, effort has been concentrated on establishing a strong base capability for essentially routine model testing. In future, considerable expansion is anticipated to cover more specialised types of testing. One particular development that is anticipated is submarine model testing. A planar motion mechanism and associated instrumentation will probably be procured in the near future. The equipment will be utilized for testing other bodies such as ROV's and pipelines.

Other areas where significant developments are anticipated include seakeeping work where a new range of light weight instrumentation will be developed. A particular aspect of seakeeping will be capsizing where the models will be small and where relatively fast digitization rates on many channels of data will be required.

Hydrodynamic Design Aspects of a Large Cavitation Channel

J. M. Wetzel, C.C.S. Song, and R.E.A. Arndt
St. Anthony Falls Hydraulic Laboratory
University of Minnesota
Minneapolis, Minnesota U.S.A. 55414

ABSTRACT

To establish design criteria for a large, recirculating flow, cavitation channel, physical and mathematical modeling was employed for selected components in the upper leg of the flow circuit. These models were used to assess hydrodynamic performance, susceptibility to cavitation, and boundary layer separation. Good agreement was found between calculated and measured quantities.

1. INTRODUCTION

1.1. General

The St. Anthony Falls Hydraulic Laboratory (SAFHL) was part of a team involved in the design of a large cavitation channel to be constructed at the David Taylor Naval Ship Research and Development Center (DTNSRDC). In addition to its large physical size, the specifications for both hydrodynamic and hydroacoustic performance were demanding. The low noise level requirements necessitated the elimination of any local cavitation in the circuit, and strongly influenced the design of internal components, boundary shapes, and the recirculating pump.

The top surface of the upper leg of the proposed channel was horizontal to provide flexibility in model testing over a wide range of velocities and pressures. The resulting configuration differs from conventional water or wind tunnel designs as the contraction and diffuser are non-symmetrical in elevation. The non-symmetry raised questions as to the hydrodynamic performance of these components. To evaluate the performance characteristics of critical components, experiments were carried out in a wind tunnel at a model scale of 1 to 10. These physical model studies were complemented with mathematical modeling of the contraction and turning vanes in the mitered elbows. An unsteady Euler equation model for low Mach number flow was developed and used for the computations.

1.2. Overall Channel Features

Some of the major dimensions of the channel are shown in Fig. 1. Shaded areas represent components modeled. The design is based on a test section 10 ft (3 m) sq with a length of 40 ft (12 m) and a maximum flow velocity of 50 fps (15 m/s). The non-symmetrical

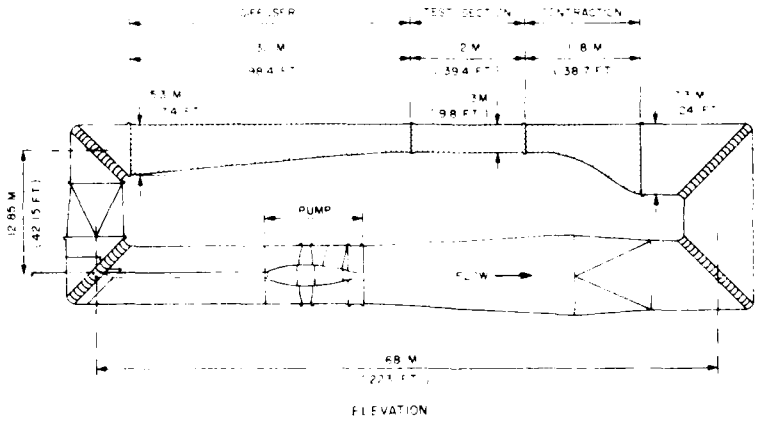

Fig. 1. Proposed configuration of cavitation channel.

contraction has an area ratio of six. A diffuser with an included angle of 5 degrees follows the test section, and its centerline is deflected 2.5 degrees downward from the centerline of the test section. The first vaned elbow turns the flow through 87.5 degrees into a shape transition. The second elbow and most of the lower leg are circular in section. The shape transition back to square is just before the third elbow. A turbulence management system is positioned between the fourth elbow and the entrance to the contraction. This consists of a shallow, coarse honeycomb followed by a deep, fine honeycomb.

The test section flow quality specifications are:

- Velocity uniformity ±1% excluding boundary layer regions
- Turbulence intensity 0.1%
- Pressure range 0.5 to 60 psia

In addition, noise levels were specified for the test section, but these will not be discussed here. The main effort in the hydrodynamic evaluation was to make the flow circuit as cavitation-free as possible. The major noise source in a closed loop circuit is pump cavitation. Chances for a successful pump design are enhanced if the inflow velocity profile to the pump is symmetrical about the centerline. Much effort was expended by the entire design team to arrive at a design leading to a satisfactory inflow profile. It is, therefore, apparent that the hydroacoustic specifications require that the hydrodynamics of the flow in regions other than the test section must be addressed.

2. DISCUSSION OF RESULTS

2.1. Contraction

Several variables are considered in the design of a contraction: area ratio, length, and boundary shape. The selection of a contraction ratio is a compromise between flow quality and economics, as it dictates the physical size of other components. The length should be as short as possible, and is usually related to the inlet size. Boundary shape should be selected to avoid the possibility of boundary layer separation and local cavitation. Severe pressure gradients are to be avoided, and thus the location of the boundary inflection point becomes important.

The preliminary contraction design had an area ratio of 6 and a length of about 39 ft (11.8 m). Two boundary shapes were investigated, expressed in dimensionless form as

$$y = 2x^3 - x^6 \qquad (1)$$

$$y = Ax^3 + Bx^4 + Cx^5 \qquad (2)$$

where $A = 10x_I(Ax_I-3)/D$, $B = -2A+5$, $C = A-4$, and $D = 10x_I^2-12x_I+3$.

The location of the inflection point is x_I, and the origin is at the contraction exit. Coordinates have been made dimensionless by dividing by the contraction length, L, and the total deflection for the abscissa and ordinate, respectively.

Equation 1 is the shape proposed in the preliminary design with the inflection point at 0.737. Equation 2 represents a family of shapes that can be related to x_I for a given length and area ratio. It is well known that as the flow enters a contraction, the wall pressure rises and then decreases as the flow is accelerated. If the magnitude and spatial rate of change are excessive, boundary layer separation can occur. According to Stratford (1959), the criteria for turbulent boundary layer separation can be written as

$$St = C_p\left(x\frac{dC_p}{dx}\right)^{1/2} - 0.35(10^{-6}Re)^{1/10} \qquad (3)$$

and the boundary layer with separate if $St > 0$ and no separation predicted for $St < 0$. C_p is the pressure coefficient and $Re = Ux/\nu$.

Near the exit region of the contraction, the reverse curvature results in an overshoot in velocity with a corresponding decrease in pressure. Sufficiently low pressure can lead to cavitation. The magnitude of the pressure coefficient can be changed by varying the location of the inflection point, x_I.

To illustrate the above effects, the minimum pressure coefficient near the contraction exit has been calculated for various x_I based on test section velocity and pressure as reference values. Equation 3 has been calculated near the contraction entrance with entrance velocity and pressure used for reference. The results are shown in Fig. 2 for full-scale Reynolds numbers. As x_I increases, the magnitude of C_p decreases and St becomes less negative. Thus, for a contraction of given length and area ratio, a compromise must be made as to inflection point location.

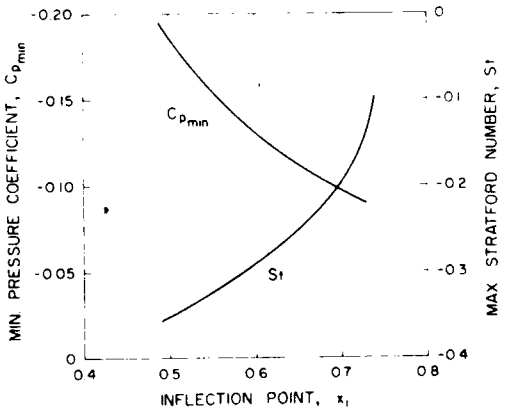

Fig. 2. Effect of inflection point location on Cp_{min} and separation parameter for contours given by Eq. 2.

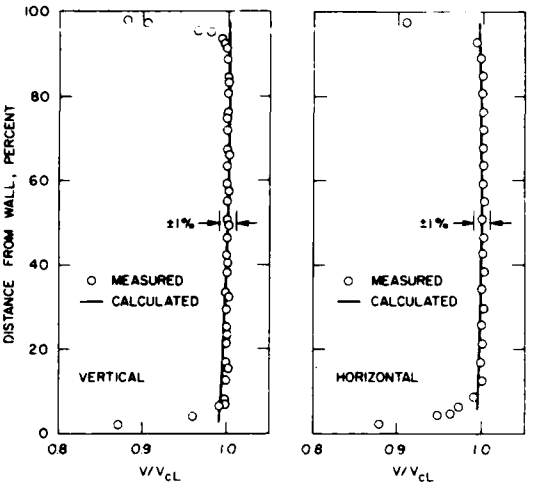

Fig. 3. Comparison of measured and calculated mean test section velocity distribution.

The contraction shape expressed by Eq. (1) was the first to be experimentally evaluated. Although the measured test section velocity distribution was satisfactory, there was a tendency for boundary layer separation at the inlet. This was observed with small tufts attached to the bottom surface. Calculations also indicated that separation should occur at the model Reynolds number.

The contraction shape was changed to that given by Eq. (2) with $x_1 = 0.5$. Experimental data for the velocity distribution along horizontal and vertical centerlines are plotted in Fig. 3. Outside the boundary layer regions, the velocity profiles are flat and agree well with the calculated profiles. These profiles were taken with a uniform velocity profile at the contraction inlet. Skewed inlet profiles were also tried, and the test section profiles were still acceptable.

A comparison of computed and measured wall pressures along the bottom centerline are shown in Fig. 4 where C_p is referenced to test section pressure and velocity. The agreement between the measured and computed values is good. As the math model was sufficiently accurate to predict boundary pressures, another iteration was made to improve the exit pressure conditions. A value of x_1 of 0.7 was chosen to reduce the magnitude of the pressure coefficient and still provide adequate resistance to boundary layer separation.

Cavitation may occur when the local pressure is reduced to near vapor pressure, or in terms of coefficients, $\sigma = -C_p$. The cavitation number, σ , should be greater than $-C_p$ for no cavitation. With vapor pressure at the top of the test section, the cavitation number at the bottom of the test section at a velocity of 50 fps is about 0.26, greater than the calculated minimum C_p of -0.09.

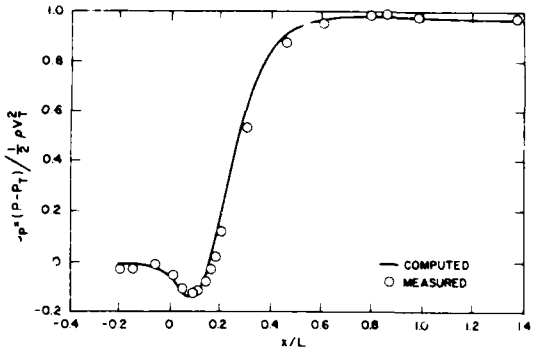

Fig. 4. Comparison of measured and computed contraction wall pressures. Bottom centerline, $x_1 = 0.5$.

2.2. Diffuser

The entrance to the diffuser is subject to the lowest pressure and highest velocity in the circuit. To avoid abrupt changes in slope at the entrance of the diffuser, a two-part curved transition was placed in the first 23 ft (7 m). The first 13.1 ft (4 m) was a quartic curve on the bottom only with the sidewalls parallel. This was followed by a parabolic sidewall curve over the next 9.8 ft (3 m) with the bottom straight. The unusually long transition was employed to encourage a stable flow.

Diffuser losses and turbulence levels are quite high, and exit velocity profiles may be highly non-uniform, even for a bare tunnel. These flow features have a strong influence on the design of downstream components, such as the turning vanes in the first elbow. Furthermore, distortion arising from the diffuser can be reflected in the inlet velocity profile of the pump. Therefore, to evaluate diffuser performance, wall pressures were measured along its entire length. Steady and unsteady velocity measurements were made at the diffuser exit plane.

The measured wall pressures did not indicate any flow separation, and none was visually observed with small tufts of yarn attached to the surfaces. The minimum C_p on the bottom surface of the first transition should not result in local cavitation.

Experimental data for the vertical, mean velocity profile at the centerline of the diffuser exit plane are shown in Fig. 5, normalized with the maximum velocity at the centerline. Comparisons are made with data taken with both a Pitot cylinder and hot wires. Data along the horizontal centerline are similar.

Turbulence intensities of axial and vertical components, u', v', are shown in Figs. 6 and 7 for five stations. Each of the rms values have been normalized with the local mean axial velocity. The lowest intensity occurs near the diffuser centerline, and the

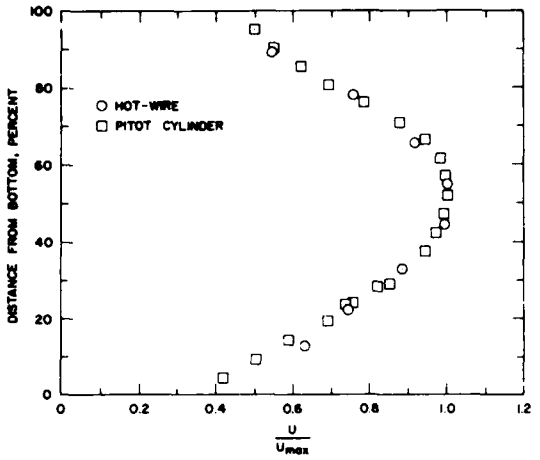

Fig. 5. Comparison of mean velocity profiles at the vertical centerline of diffuser exit.

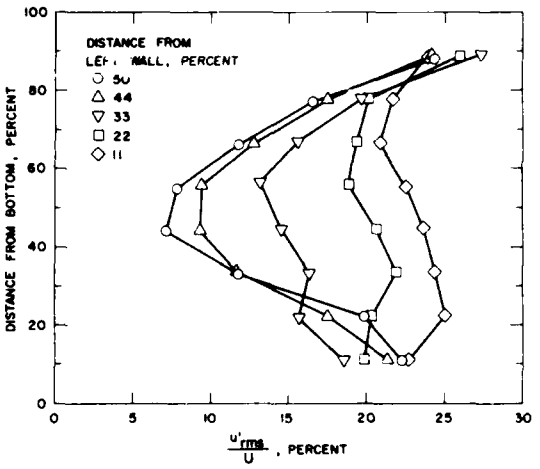

Fig. 6. Turbulence intensity of axial velocity component diffuser exit.

intensity increases near the walls. The arctangent of the vertical velocity component is related to the angle of attack. This angle is about 4 degrees at the center of the diffuser, increasing to about 10 degrees at the top and bottom.

Mean velocity profiles and changes in angle of attack are important in the design of cavitation-free turning vanes. Although there is a pressure rise in the diffuser, the centerline velocity at the diffuser exit is about 1.6 times the average velocity. The turning vanes were selected to have a negative pressure peak of low magnitude to avoid local cavitation. Analysis of the turning vanes is summarized by Song, et al. (1986).

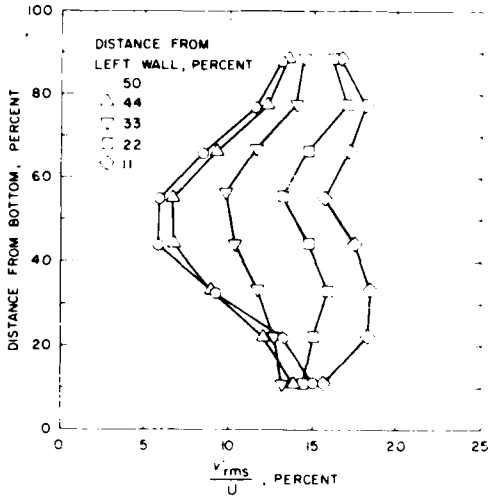

Fig. 7. Turbulence intensity of vertical velocity component diffuser exit.

3. CONCLUSIONS

A three-dimensional mathematical model based on the Euler equations for low Mach number was developed for analysis of a non-symmetrical contraction. Calculations and experimental data were in good agreement for several contraction shapes. A contraction was selected that should be free of flow separation and local cavitation for design flow conditions.

No flow separation was observed in the first diffuser, although the exit velocity profiles were non-uniform with relatively high turbulence levels near the walls. The measured velocity field was used as input, to a mathematical model of the mitered elbow and turning vanes.

ACKNOWLEDGEMENT

Support for this work was provided by SSV&K/DMJM:Joint Venture as part of their design of a large cavitation channel for David Taylor Naval Ship Research and Development Center, Department of the Navy.

REFERENCES

Song, C.S.S., Wetzel, J. M., Yuan, M. and Arndt, R.E.A. (1986): Mathematical Modeling for a Varied, Miter Elbow. Presented at the Conference on Advances in Aerodynamics, Fluid Mechanics and Hydrodynamics, ASCE, Minneapolis, MN.

Stratford, B. S. (1959): The Prediction of Separation of the Turbulent Boundary Layer. Journal of Fluid Mechanics, Vol. 5, Part 1.

SESSION V
STEERING AND MANEUVERING

TECHNICAL COMMITTEE MEMBERS

R. Thomas Waters (Chairman)	DTNSRDC
Dr. Vladimir Akudinov	Tracor Hydronautics
Prof. Rameswar Bhattacharyya	U.S. Naval Academy
Prof. Michael G. Parsons	Univ. of Michigan
Prof. William C. Webster	Univ. of California/Berkeley
Dr. Haruzo Eda	Stevens Inst.

REPORT OF THE STEERING AND MANEUVERING COMMITTEE TO THE 21ST AMERICAN TOWING TANK CONFERENCE

R. Thomas Waters (Chairman)
David W. Taylor Naval Ship R&D Center
Code 1562
Bethesda, Maryland 20084

1. INTRODUCTION

As always, when preparing the State-of-the-Art report, there seems to be little research that could be classified as new in Steering and Maneuvering tank testing. However, if the definition of "tankery" is expanded to include all the research being performed with respect to the prediction maneuvering performance of ships and evaluation of their controlability, then much can be said about the advancements in this field of endeavor since the last American Towing Tank Conference in 1983. This seems to be a valid approach to this report since:

1) The job of the member organizations of the ATTC is to predict the performance of marine vehicles.

2) Much of the research in maneuvering is performed by the members of the ATTC, even if the work does not necessarily happen in the tank or under a towing carriage.

In addition to the research which is being done, there is an effort underway by the Joint International Maneuvering Program (JIMP) and the Society of Naval Architects and Marine Engineers (SNAME) to facilitate the exchange of information and data which comes from the research, so that everyone can benefit and improve their capabilities. All these advancements become even more important given the current trends of the regulatory bodies and the governments which oversee the marine industry, to formulate standards for the maneuverability and control of marine vessels. When these standards take effect, our ability as researchers to the predict performance of a given design will become very important to the owners and the designers of marine vehicles.

2. CURRENT PREDICTION TECHNIQUES

A review of the work in maneuvering since the 20th ATTC indicates that the technology used to quantify the maneuvering performance of marine vehicles has not undergone any radical changes. The horizontal planar motions mechanism (HPMM) and the rotating arm are primarily used to derive the input for the digital computer maneuvering simulations. A more direct measure of maneuvering performance is embodied in the free running radio controlled model testing. This approach, however, has several inherent limitations (such as scale effects) and it will not provide the necessary data to predict the performance of a design that is modified later. One intriguing approach being recently used by the Dutch at the Delft Hydrodynamics Laboratory, de Vries (1984), combines a bit of each of the above techniques to obtain the input for a mathematical simulation model. This forced excitation of a free sailing model offers some very interesting solutions to current maneuvering problems. System Identification (SID) technology has come to the forefront of maneuvering research in the last three years. The various SID techniques are being tested and serious efforts have been taken to make this technique available to the community. The work of being performed at DTNSRDC, presented in preliminary form at the last ATTC, has been formally published Moran and Wemple (1983). A paper on a SID instrument package for full scale trials, which was funded by Maritime Administration (MARAD), has been prepared for this session by Mr. Tom Trankle (1986).

2.1 FORCE EXCITATION ON FREE SAILING MODELS

This approach uses servo-controlled air propellers attached to the bow and stern of the model to force the model to perform some specific maneuver (HPMM or Rotating Arm paths) by imposing an external force. This techniques does not need a towing carriage and allows the measurement of both velocity-coupled and acceleration dependent math model terms with the same test set-up. A computer operated servo-controller generates commands such that the air fans push the ship hull through a predetermined path. The forces acting on the model due to these air fans are measured and analyzed in the same manner that force gage read-outs would be analyzed from a conventional captive model experiment. A schematic of the test set-up is shown in Figure 1. As seen in that figure, the air fans are used to replace the towing carriage of a more conventional model test set-up. However, an experiment such as this may be more sucepable to errors induced by instrumentation inaccuracies. One possible use of this technique is to use these air fans as part of a systems identification procedure to increase the number of inputs and thereby increase the number of identified parameters. This could also be applied in much the same way that Mr. Trankle proposed to use a tug in his discussion of Abkowitz (1980) to identify the acceleration dependant terms.

2.2 SYSTEMS IDENTIFICATION

As previously stated, a number of advancements in the area of SID maneuvering performance prediction have been made since the last ATTC. Systems identification is the process whereby the coefficients if the equations of motion which assume to describe the hydrodynamics of the ship in a turn are obtained by exciting either the ship itself or a free running model of the ship, measuring the response, and then solving for the unknown coefficients in the equations of motion using regression analysis. This differs from the better known approach using captive model data and simulations to predict the ship motions given a measured set of coefficients for an assumed set of equations of motion. The published results of Moran and Wemple state that:

1. A complete set of the coefficients for the non-linear equations of motion can be deduced from model scale free running model experiments using the rudder angle as the excitation mode. For this procedure to work more effectively, prior knowledge of the added mass and added mass moment of inertia is recommended.

2. The existing instrumentation set-up used for submarine SID work at DTNSRDC can be applied for surface ship maneuvering research. This instrumentation is rather precise, but quite expensive.

3. Multi-input procedures (more than just rudder angle) will improve the SID process, but single-input techniques will work. The Delft air fan system may be of use to help solve this problem for single screw, surface ship designs.

4. SID techniques adequately predict the path of the full scale ship under known control inputs.

Tom Trankle's paper gives a progress report on the MARCIS instrumentation package. The MARCIS is a self contained instrument package which has been developed specifically to perform full scale systems indentification trials. To date the MARCIS has been used on the SS KING's POINTER and the USCG TAMPA. This report, along with the work by Moran and Wemple and the work of Abkowitz show the promise of the SID concept as a tool to improve maneuvering prediction, but there are still several technical areas that require further study.

The work presented by Abkowitz (1980) presented the results of systems identification trials on a tanker using only the ship instruments and an accurate yaw rate gyro. There seems to be some question as to what level of instrument sophistication is necessary to carry out this type of experiment.

3.0 PERFORMANCE PREDICTION TECHNIQUES

Once the maneuvering experiments have been conducted, a digital computer simulation is needed to provide the ship owner or operator with the final product which they need: the actual maneuvering performance (tactical diameter, overshoot angle, etc.) including enviromental effects. In this area, much work has been done by

the international community to facilitate the exchange of data between different organizations. The Joint International Maneuvering Program (JIMP) has been working to set up a procedure for transmittal of test data for selected Hull forms by proposing that the raw test data from the experiments be exchanged or that maneuvering simulations be run in a mode to produce pseudo-tank data, i.e. the simulations recreate rotating arm test results and HPMM test results where test data does not exist. This allows the receiving organization to; curve fit the data to their own set of equations of motion, instead of trying to adapt a different set of coefficients and provides for a comparison of analysis techniques. The Society of Naval Architects and Marine Engineers (SNAME) has developed a set of data sheets for transmitting maneuvering coefficients and including the equations of motion which are used with that data. These two efforts should be supported so that the technical community can develop a predictive capability earlier in the design process, before tank testing occurs.

4.0 OTHER TECHNOLOGY AREAS

4.1 ANALYTICAL PREDICTION TECHNIQUES

One of the largest problems in maneuvering research concerns our ability to predict the maneuvering performance of a given ship design in the absents of any tank testing data. The goal then, is to develop tools which are based on some theoretical calculation or consistent data base. Towards this goal, *The U.S. Maritime Administration Systematic Series of Full Form Merchant Ships* will soon published by SNAME. The publication will provide systematic resistance, propulsion and maneuvering data obtained at Tracor Hydronautics, Inc. for large, full-form vessels using the MARAD series models as a basis.

The paper by Asinovsky, Landberg, and Hagen (1986), presented in these proceedings, together with the work presented by Ankudinov (1985) propose a "modular" approach to estimating the hydrodynamic forces actin on the various components of a vessel (hull, propeller, rudder, and appendages) while maneuvering.

4.2 UNCONVENTIONAL DESIGN MANEUVERING PERFORMANCE

Although not one of the mainstream technology areas, research into the maneuvering performance of Small Waterplane Area Twin Hull (SWATH) ship designs has progressed a great deal in the last three years. The paper presented in these proceedings by Nethercote and Molyneux presents an update of work being performed in Canada using radio controlled models. In the United States, the work of Gupta (1986) has been directed towards developing a new rudder concept for the SWATH hull. Specifically, this concept was developed to provide a rudder design for SWATH hulls where the strut does not overhang the lower hull at the propeller. A sketch of this configuration is shown in Figure 2 and a schematic of how the stabilizers are used to control the SWATH ships heading is presented in Figure 3.

One rather fortunate aspect of SWATH maneuvering performance predictions is how well the hull form lends itself to analytical and theoretical predictions of the hydrodynamic maneuvering forces. Hirano (1978) and (1980) published the results of a rather promising study which was done in Japan. Since the original texts are published in Japanese (1978 paper was translated by BSRA) , it has not received the notice that it deserves. This particular work shows a great deal of promise for improving the prediction of maneuvering performance of SWATH ships during early design stages.

4.2 VALIDATION

The validation of prediction techniques is generally performed by comparison of full scale trials results with the predicted performance using general measures of performance such as tactical diameter and overshoot angles from zig-zags. Recently CAORF (Computer Aided Operations Research Facility) undertook a program to validate the math model used in the CAORF simulator. For this validation, the simulation was compared to the actual track of a ship making a transit around the bend in a channel. This comparison, documented by Puglisi et al (1985), used the actual rudder angle and engine activity measured during the full scale trials as the drivers for the mathematic model. The conclusions of this effort were that: the correlation was acceptable; the amount of effort required to perform the validation was considerable; and finally,

the procedure was very sensitive to minor (velocity ± 0.003 meters/sec) differences in the initial conditions between the ship and the simulation.

5.0 REGULATIONS AND MANEUVERING STANDARDS

As stated in the last ATTC Steering and Maneuvering State-of-the-Art report by Webster (1983), the regulatory bodies charged with monitoring the marine industry (International Maritime Organization Marine Safety Committee) are proceeding with efforts to require certain maneuvering information to be posted on the bridge of a ship and to require that the maneuvering performance of the vessel be listed in a "Maneuvering Booklet", Marine Safety Committee of the IMO (1985). The U.S. Coast Guard appears ready to propose national rule making to implement the same rules for new ship construction. The information required for these postings is, perhaps, considerably more detailed than the information which would be obtained from a simple full scale trials agenda. The Tracor Hydronautics study (1981) sponsored by the U.S. Coast Guard indicates that the United States government is considering imposing specific maneuvering performance standards on ships at some point in the future. A regulation like this will require that the technical community be able to predict maneuvering performance during very early design stages without the benefit of model testing in order to assure the owner that his ship will meet the imposed requirements. The technology to make accurate maneuvering predictions without model testing is very limited. Therefore, it seems prudent to direct research efforts towards developing better analytical methods of predicting the maneuvering performance of ship designs when there is no model test information available.

6.0 WORK OF THE ITTC

The 17th International Towing Tank Conference (ITTC) Maneuverability Committee (1984) reported on research being carried out by the international community. Their report covers a great deal of research by many different persons and organizations. The Committee made several recommendations as to the direction of future work. The Committee was most interested in the development of theoretical and analytical methods of predicting maneuvering performance and of quantifying the interactions between the propeller, rudder and hull. The group was also concerned about the direction of regulation and making sure that any indices were appropriate.

7.0 CONCLUSIONS AND RECOMMENDATIONS

Based upon a review of the current research in steering and maneuvering the Committee sees the following areas as requiring further work and increased effort:

a. Develop the analytical capability to predict the maneuvering characteristic and performance of a specific vessel design when no model data is available. This technical tool is needed so that maneuvering requirements can be included in the design process.

b. Continue to develop smaller and less expensive instrumentation packages and associated analysis techniques for the study of the maneuvering behavior of ships.

8.0 REFERENCES

Abkowitz, M.A. (1980):
Measurement of Hydrodynamic Characteristics from Ship Maneuvering Trials by Systems Identification. Transactions SNAME, "80.

Ankudinov, V. (1985)
Ship Maneuvering Simulation Model Including Regimes of Slow Speeds and Large Drift Angles. Report for the First Maritime Simulation International Symposium, Munich, Germany.

Barr, R.A., Miller,E.R., Ankudinov,A. and Lee, F.C. (1981)
Technical Basis for Maneuvering Performance Standards, Department of Transportation, United States Coast Guard Report CG-M-8-81.

Gupta, S.K. and Schmidt (1986):
Developments in SWATH Technology. Naval Engineers Journal, Vol. 98, No. 3.

Hagen, G. (1983):
Mathematical Ship Maneuvering Models and the Society Coefficient Data Sheets (A Primer). 19th American Towing Tank Conference, Hoboken, New Jersey.

Hirano, M. and Fukushima, M. (1978):
A Calculation of Hydrodynamic Forces Acting on a Semi-Submerged Catamaran in Maneuvering Motion. Transactions Western Japan Society of Naval Architects and Marine Engineers, No. 56. BSRA Translation No. 4274

Hirano, M., Fukushima, M. et al (1980):
A Study of Hydrodynamic Forces Acting Upon Wing System Which Consist of Small Aspect Ratio Wings. Mitsui Technical Review No. 106 (in Japanese)

International Maritime Organization (1985):
Revision of Resolution A.209(VII) Annex3, Information to be Included in the Manoeuvering Booklet. Sub-Committee on Ship Design and Equipment, DE 27/W.P.8 Annex 3

International Towing Tank Conference (1984):
Report of the Steering Maneuverability Committee. Proceedings of the 17th ITTC, Goteburg, Sweden.

Moran, T.L. and Wemple, A.B.:
Mariner Surface Ship System Identification. David W.Taylor Naval Ship Research and Development Center Report Number SPD-1041-01.

Puglisi, J.J., Case, J.S. and Hwang, W. (1985):
The Progress of Validation in Simulation Research. 6th CAORF Symposium, Kings Point, New York.

Roseman, D.P. and Seibold (1985):
An Introduction to the U.S. Maritime Administration Systematic Series. Marine Technology, Vol.22, No. 4.

Trankle, T.L. (1986):
Status of MARCIS: The Marine Coefficient Identification System. 20th American Towing Tank Conference, Washington, D.C.

Vries, W.A. de (1984):
Determination of Hydrodynamic Coefficients by Force Excitation on Free Sailing Ship Models. Third International Conference on Marine Simulations, Rotterdam, The Netherlands.

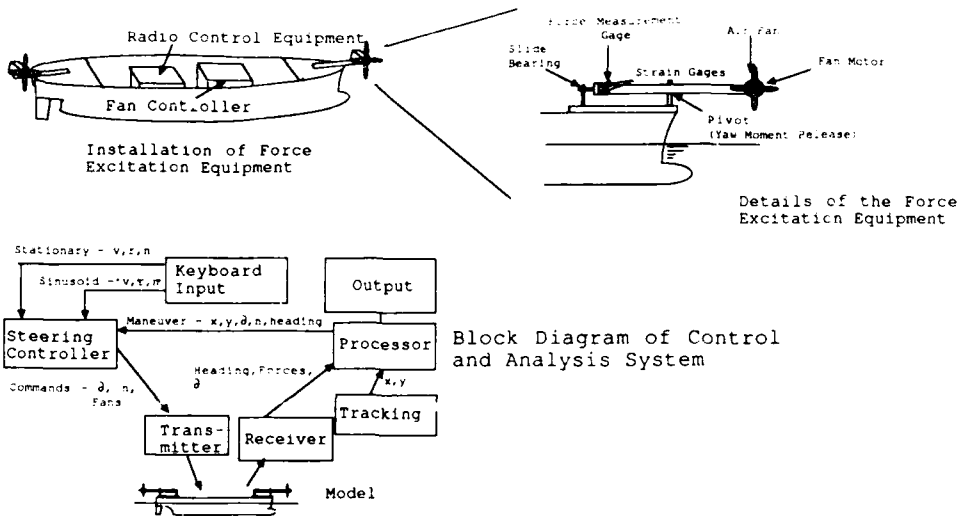

Figure 1 - Schematic of Force Excitation Equipment and System Diagram for Force Excitation on Free Sailing Models

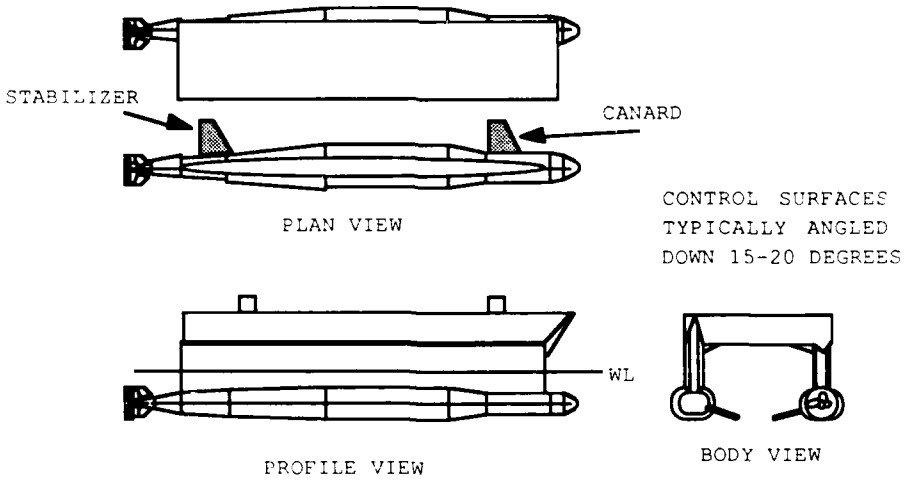

Figure 2 - Sketch of a Stabilizer Steering Configuration

FORCE = SIN(DYHEDRAL ANGLE) * LIFT + FREE SURFACE FORCE + CIRCULATION PRESSURE FOCE

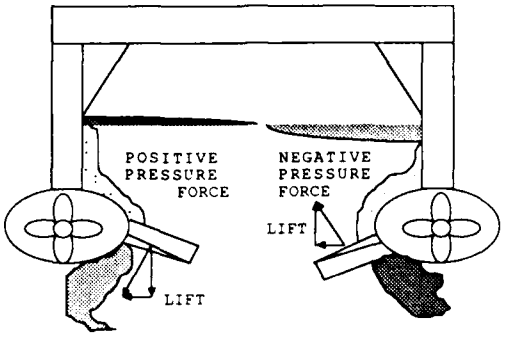

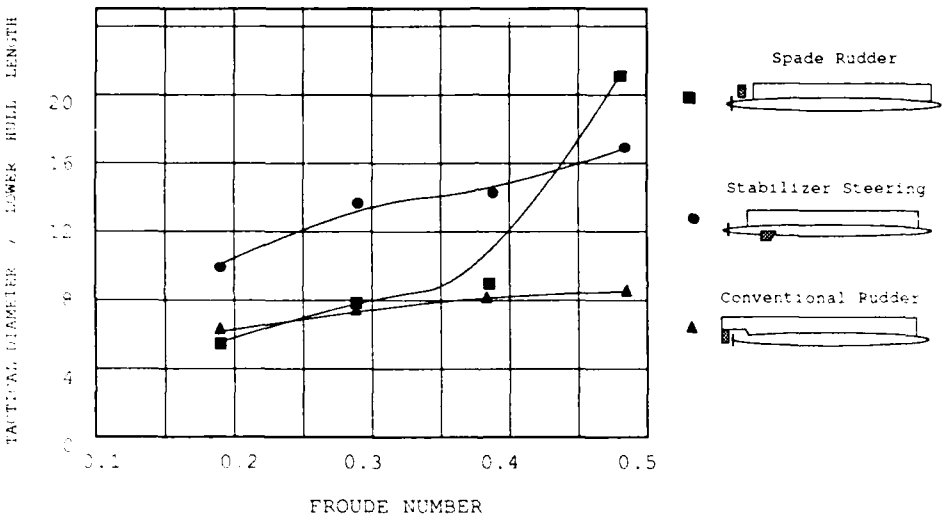

Figure 3 - Schematic of Stabilizer Steering Force Force Generation Mechanism and It's Relative Performance

SWATH MANOEUVRABILITY RUNNING TRIM EFFECTS

W.C.E. Nethercote, Defence Research Establishment Atlantic

and

W.D. Molyneux, Institute for Marine Dynamics

ABSTRACT

SWATH ship model manoeuvring experiments were performed to assess the effect of running trim on turning performance. Canard angles were set for level trim at both entry and steady turning speeds to obtain bow down and level steady turning trims respectively. The results indicate that turning performance is improved with trim control and that, at level trim, correlation between the tests and numerical manoeuvring simulations is improved.

NOMENCLATURE

DWL	Design waterline length
Fn	Froude number
Fn_I	Initial Froude number
GM	Metacentric height
GM_L	Longitudinal metacentric height
GM_T	Transverse metacentric height
L	Demi-hull length
T_Φ	Roll Period
T_Θ	Pitch period
TD	Tactical diameter
$\delta Fn/Fn_I$	Speed loss ratio

1. INTRODUCTION

In a paper to the 20th ATTC, Nethercote, Miles and Molyneux[1] reported the results of manoeuvring tests with a model of SWATH 5A and compared their results with simulations reported by Waters and Fein[2]. Turning circle correlations were not always good; differing running trims were a possible cause. The Defence Research Establishment Atlantic (DREA) sponsored the tests at the Institute of Marine Dynamics (IMD). A radio-controlled free-running model was used for the tests. It had fixed aft fins and adjustable, but fixed, canards which were set to maintain level trim during the approach to the turning manoeuvre. The Waters and Fein simulations were based on rotating arm tests[3] where the model was constrained to level trim.

The work reported herein was undertaken as an extension of Reference 1 to quantify the effects of running trim and, hopefully, to improve correlation.

2. EXPERIMENTS AT IMD

The experiments were carried out in IMD's Ottawa outdoor manoeuvring basin (122m long x 61m wide x 3m deep).

Details of the model are given in Table 1. In all respects the model duplicated its condition for Reference 1.

2.1 Test Procedures

The model was fitted with a high intensity lamp as an aiming point, which was tracked using two automatic photosensitive telescopes. Model velocity and trajectory were established by triangulation. Yaw gyro and telemetry systems were not fitted to the model as the model size, the same as that reported in Reference 1, severely constrained payload.

Turning circles were measured at three nominal Froude numbers, with two rudder angles using canard angles for level trim at both approach and steady turning speeds, as given below:

Nominal Approach Speed, Fn:	0.432	0.480	0.538
Approach Canard Angle, deg:	22.5	7.0	- 5.0
Turning Canard Angle, deg:	29.0	25.0	19.0
Rudder Angles, deg:	25	25	25
	35	35	35

The speeds were restricted to the range in which pitch moment was very Froude number sensitive, as implied in Figure 1.

2.2 Experiment Analysis

The test data were analyzed by first fitting splines to the measured X and Y coordinates of the model trajectory as individual functions of time using a least-squares technique. These splines thus served to define both position and velocity as continuous functions of time. A first-order wind drift correction was then applied by subtracting a

constant wind drift velocity vector from the measured model velocity. Since tests were only conducted when the wind was light, this correction was always small.

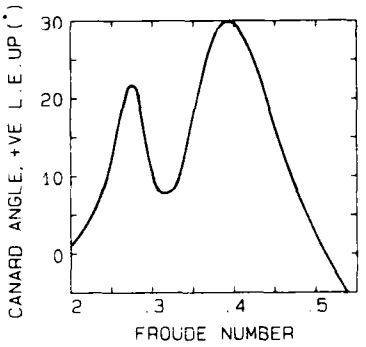

Figure 1: SWATH 6A, Canard Angles for Level Trim

Initial examination of the data proved quite disturbing because results of tests using canard angles for level trim at approach speed were inconsistent with Reference 1. Upon re-examination of the earlier data, differences in cross-fairing techniques were noted, and consequently both the present and the earlier tests were re-faired in a consistent manner. For completeness, Reference 1's SWATH $6A_2$ results were also refaired, and are included in Appendix 1. SWATH $6A_1$ results reported herein represent combined, cross-faired data, where appropriate.

2.3 Discussion of Results

The SWATH $6A_1$ turning results are plotted as non-dimensionalized tactical diameter to a base of steady turning Froude number in Figures 2 and 3, together with the Waters and Fein simulations.

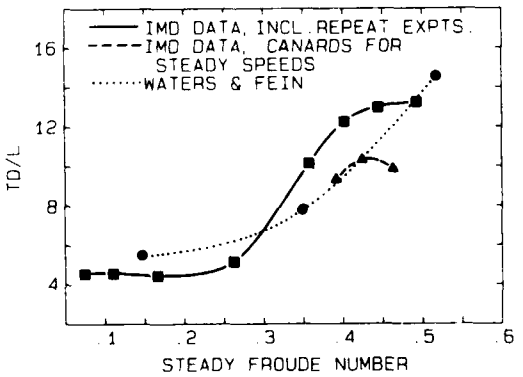

Figure 2: SWATH $6A_1$, Rudder Angle 25 Degrees

The use of canard angles set for level trim in steady turning conditions, rather than for level trim on approach, gives a significant reduction in tactical diameter, of the order of 20 percent. Steady turning canard angle experiments were performed only where trimming moment was heavily Froude number dependent. It was expected that there would be little change in tactical diameter at lower speeds where canard angles vary less with speed and speed loss in turns is less. Both Figures 2 and 3 are of a form which suggests that the steady turning speed canard results could scarf into the original results at lower speeds.

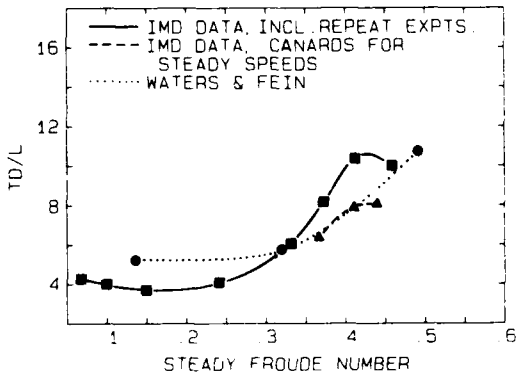

Figure 3: SWATH $6A_1$, Rudder Angle 35 Degrees

4. CORRELATION WITH SIMULATION

The Waters and Fein simulations[2] were based upon rotating arm tests[3] with a fixed trim model. Reference 1 identified trim as an important discrepancy between simulation and free-running model results. The experiments reported herein were undertaken to confirm this supposition.

The tactical diameter reduction achieved by use of steady turning speed level trim canard angles improves agreement between experiment and simulation, both in the sense of reduced error at high speed, and in reducing the tactical diameter jump seen in the earlier results for SWATH $6A_1$, but absent in simulations.

5. CONCLUDING REMARKS

The results of the IMD manoeuvring tests indicate the sensitivity of the SWATH $6A_1$ design's manoeuvrability to running trim. Clearly, for best manoeuvrability an active pitch control system is desirable. This result is not general, because the SWATH $6A_1$ design has an unusually low GM_L, and requires much larger control fin and deflections than does, for example, the SWATH $6A_2$ design.

Finally, it is encouraging that use of steady turning speed canard angles improved the correlation between simulation and free-running model tests. As a result, assuming active pitch control or large GM_L at full scale, it is reasonable to use fixed trim rotating arm stability derivatives in simulating manoeuvring performance.

TABLE 1: PRINCIPAL PARTICULARS

IMD Model 329 λ = 1/22.5

Hull length, m	3.25
Maximum breadth, m	1.22
Reference point, m abaft bow	1.56
Displacement, kg	252
Draft, m	0.365
GM_T, m	0.149
GM_L, m	0.281
T_ϕ, sec	3.58
T_θ, sec	4.15
Rudder Details	
Chord, m	0.241
Span at leading edge, m	0.330
Span at D.W.L. at leading edge, m	0.171
Area to D.W.L., m^2	0.043
Thickness/chord	0.150
Aft Control Fin Details	
Chord, m	0.200
Span at leading edge, m	0.222
Thickness/chord	0.150
Distance 1/4 chord abaft bow, m	2.749
Canard Details	
Chord, m	0.116
Span at leading edge, m	0.129
Thickness/chord	0.150
Distance 1/4 chord abaft bow, m	0.743

APPENDIX 1 - RE-FAIRED SWATH 6A RESULTS

Re-faired SWATH 6A results and comparisons with Waters and Fein simulations are given in Figures A1 to A4, which replace Figures 7, 8 and 9 of Reference 1. The re-fairing has produced differences in minor detail only, and the discussion and conclusions of Reference 1 are unaffected.

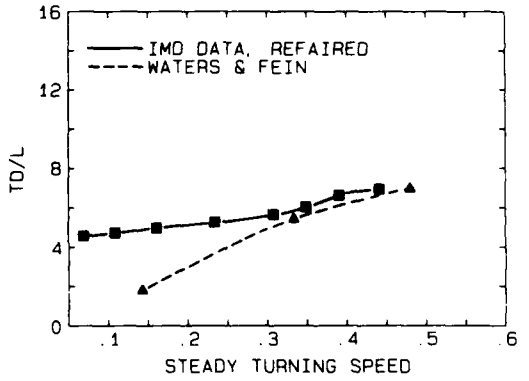

Figure A1: Effect of Speed on Turning, 25 Degree Rudder Angle, SWATH $6A_2$

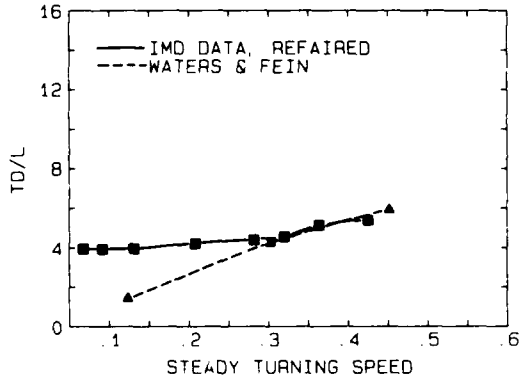

Figure A2: Effect of Speed on Turning, 35 Degree Rudder Angle, SWATH $6A_2$

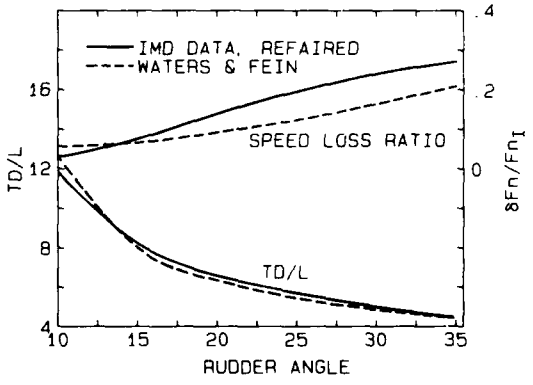

Figure A3: SWATH $6A_2$, Effect of Rudder Angle Turning, Initial Fn = 0.384

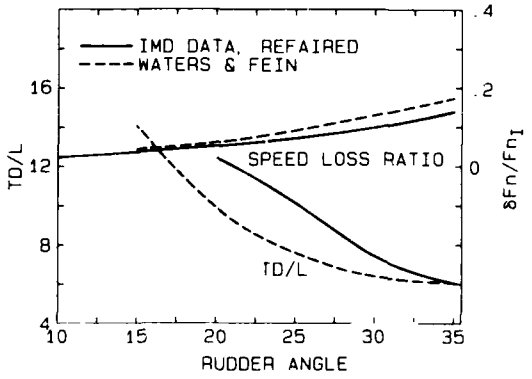

Figure A4: SWATH $6A_1$, Effect of Rudder Angle on Turning, Initial FN = 0.384, Canards set for Approach Speed

REFERENCES

1. Nethercote, W.C.E.; Miles, M.D. and Molyneux, W.D.: Manoeuvring of SWATH Ships, Proc. 20th ATTC, Hoboken, 1983.

2. Waters, R.T. and Fein, J.A.: Manoeuvrability of SWATH Ships, Proc. 19th ATTC, Ann Arbour, 1980.

3. Fein, J.A. and Waters, R.T.: Rotating Arm Experiments for SWATH-6A Manoeuvring Predictions, DTNSRDC SPD698-01, July 1976.

STATUS OF MARCIS: THE MARINE COEFFICIENT IDENTIFICATION SYSTEM

Thomas L. Trankle
Group Manager
Systems Control Technology, Inc.
1801 Page Mill Road
Palo Alto, California 94304 USA

ABSTRACT

The Marine Coefficient Identification System (MARCIS) is an integrated package that can perform very powerful data collection, storage, and processing functions aboard ship. The MARCIS consists of a data collection front end computer system and an analysis workstation back end. The system is housed in two compact and rugged enclosures, making rapid shipping and installation possible. High quality inertial sensors in the front end system provide a method of collecting data on ship motion of much higher quality than is now generally available. Software implemented in the workstation can perform the complete system identification task from data inspection to parameter estimation and final simulation validation. The system has been used to date to estimate maneuvering hydrodynamic models of two ships.

NOMENCLATURE

- $\mathbf{A}$ matrix of independent variables in a regression
- $\underline{a}$ acceleration in ship-fixed coordinates
- $\underline{b}$ vector of unknown hydrodynamic coefficients
- C_x total hydrodynamic coefficient for x force
- C_y total hydrodynamic coefficient for y force
- C_n total hydrodynamic coefficient for yaw moment
- $\underline{h}$ vector of measurement functions
- I_z moment of inertia about vertical axis
- f_x longitudinal force component
- f_y lateral force component
- f_z vertical force component
- m_z yaw moment
- ℓ ship length
- $\mathcal{L}$ output error performance index
- m ship mass
- $\underline{p}$ position vector (3 components)
- q dynamic pressure
- $\underline{q}$ quaternion vector (4 components)
- r yaw rate
- r' dimensionless yaw rate: $r \cdot \ell / u_r$
- t time
- $\mathbf{T}$ transformation matrix from ship to earth coordinates (a 3 × 3 matrix)
- u longitudinal ship-fixed velocity component relative to earth
- u_r longitudinal ship-fixed velocity component relative to water
- $\underline{u}$ input vector
- v lateral ship-fixed velocity component relative to earth
- $\underline{v}$ velocity vector (3 components)
- v_r lateral ship-fixed velocity component relative to water
- v' dimensionless lateral velocity: v_r/u_r
- $\mathbf{W}$ diagonal weighting matrix
- x north coordinate of ship origin
- $\underline{x}$ state vector
- y east coordinate of ship origin
- $\underline{z}$ vector of dependent variables in a regression
- δ rudder angle
- ψ heading angle
- Ψ transformation matrix from level ship to north, east coordinates (a 2 × 2 matrix)
- η propulsion point
- ρ water density
- $\underline{\omega}$ 3 dimensional angular rotation vector
- Ω 4 × 4 matrix representing quaternion dynamics

bold symbols are matrices
underscore symbols are vectors

1. MOTIVATION

The maritime industry has a strong interest in the maneuvering performance of surface ships and in computer simulation of ship maneuvering[1]. Presently, ship equations of motion are determined using captive model tests[2]. Captive model tests require the measurement of the forces and moments on a scale model towed in a water tank. The

fidelity of mathematical models determined in this way may be adversely affected by scale effects. There are not enough full-scale and model test data available over the whole range of ship types and water depths to allow the comprehensive determination of scale effect correction factors. It is desirable to collect full-scale ship maneuvering data and to use system identification processing to identify the hydrodynamic coefficients appearing in the simulation model[3]. These coefficients may be compared to those determined from captive model tests in order to quantify scale effects. A better understanding of scale effects would allow more confident use of captive model data in computer simulation of ship maneuvering.

The Maritime Administration of the U.S. Department of Transportation has developed a portable instrument package designed expressly for the collection of maneuvering sea trial data for identification of ship hydrodynamic models[4]. This MARCIS (MARine Coefficient Identification System) package consists of

- a microcomputer controlled data collection and storage system and
- an analysis workstation.

The data collection system uses high quality inertial sensors to provide ship motion data and has a variety of interfaces for obtaining data from ship's sensors such as rudder angle or Doppler sonar. The analysis workstation implements system identification data processing methods. The use of the workstation onboard the ship allows the validation and processing of collected data while the vessel and test crew are still at the test site and are able to repeat any test maneuvers initially having faults (e. g., maneuver not properly executed or sensor channel not working).

The package has collected maneuvering data on two vessels: an ocean-going tug[5] and a Coast Guard cutter[6].

This paper overviews the data collection hardware used by MARCIS and the multiple stage system identification procedure implemented in the MARCIS workstation used to process raw sensor data in order to determine hydrodynamic coefficient estimates.

2. HISTORY OF THE MARCIS PROGRAM

The roots of the present MARCIS program extend at least to 1977, when the *Esso Osaka* conducted extensive deep and shallow water maneuvering trials in the Gulf of Mexico. To put the present work in perspective, it is worthwhile to review briefly the subsequent efforts.

In 1977, the *Esso Osaka*, a 278,000 ton very large crude carrier (VLCC) conducted extensive deep and shallow water maneuvering trials in the Gulf of Mexico[7]. The on-board instrument system collected velocity, position, and angular rate data. Data were used to identify a nonlinear hydrodynamic model[8]. In 1978, the National Maritime Research Center hosted an industry and government workshop on the topic of the determination and use of the hydrodynamic coefficients of a liquefied natural gas (LNG) carrier. The workshop included a discussion on the use of various types of sensors for the collection of full scale maneuvering data for system identification and about the system identification processing itself. In 1979 a feasibility and accuracy study of possible sensor sets that might be used in a MARCIS instrumentation system highlighted the operational utility of high grade inertial sensors for determination of ship motion during maneuvering. Such sensors would need minimal interfacing with the ship's own sensor set (e.g. Doppler sonar)[9]. The study also indicated the need for a complete six degree of freedom set of inertial sensors because of the extreme sensitivity of the estimation of acceleration in the level plane to tilt errors.

In 1981, MarAd contracted with Systems Control Technology (SCT) for the detailed design and construction of the MARCIS instrumentation console. The data collection and real-time processing were performed by a Data General Eclipse S140 computer. The initial test of the inertial sensors and shipboard sensor interfaces aboard a ship was conducted aboard the *Kings Pointer* in November. The instrument system recorded inertial data at 64 samples per second (SPS) and external tracking and velocity data at 1 SPS but did not do extensive real-time processing. A set of hydrodynamic coefficients was later identified using off-line processing.

A second test of MARCIS was performed aboard the *Bear* class Coast Guard cutter *Tampa* in January of 1984. *Tampa* conducted two days of trials in the Straits of Juan de Fuca, executing 44 maneuvers including z maneuvers conducted in both ahead and astern motion, steady turns in ahead and in astern motion, accelerating turns, a Williamson turn, and a pivot in place using differential thrust. Data collected allowed estimation of nearly all aspects of a

nonlinear hydrodynamic model including linear and nonlinear hull and rudder coefficients for ahead and astern motion and rudder/propeller interaction for ahead motion. The MARCIS computer executed real-time data filtering and display functions that allowed assessment of data quality as the maneuvering trials were being conducted.

The MARCIS computer system is now being upgraded from the 16 bit Eclipse to a 32 bit Digital Equipment Corporation Microvax 2 system. This upgrading will provide enhancements, the need for which become apparent after the *Kings Pointer* and *Tampa* trials. Specifically, the existing system based on the 16 bit computer did not provide enough mass storage capacity and could not perform complete system identification processing of collected data. The Microvax 2 system will use two independent Microvaxes, one for data collection, filtering, and storage and the other for processing. The second Microvax will be able to execute all of the system identification algorithms needed to identify all of the coefficients of the commonly used nonlinear hydrodynamic models (Appendix).

3. KEY MARCIS CONCEPTS

There are four key concepts behind the MARCIS system:

MARCIS uses a *standard, portable package* for data collection. The use of a such a package reduces the cost of collecting data from a large number of ships. Standardization also simplifies the job of comparing results from tests of different ships.

Inertial data provide both lateral and longitudinal axis velocity estimates. These estimates are important to the system identification of hydrodynamic coefficients. Both components of velocity can be measured by some Doppler sonar systems. However the lateral axis measurement is often not available. Measurements that are available may be too noisy to be of use in identification. Inertial measurements allow the estimation of velocity using data from an inertial measurement unit. Such a unit can easily be installed aboard any ship of opportunity and is part of the MARCIS sensor set.

A *microcomputer* having an *industry standard bus architecture* controls data collection and storage. Many sensor interface circuit cards may be plugged into the standard bus with no modification of the microcomputer hardware and little modification of its software. This is important because each new vessel to be tested may have unique interface requirements.

Real-time filtering and off-line system identification processing of data *on board the test vessel* immediately assesses data quality. Experienced system identification analysts recommend an iterative procedure (Figure 1)[10] for data collection and processing. Test maneuvers should be repeated following processing of initial data sets. For the ship identification problem, this requires that the data be processed on board while the instrumentation system and test crew are still available for further data collection.

4. MARCIS DATA COLLECTION SYSTEM

The upgraded MARCIS data collection system uses two Digital Equipment Microvax 2 microcomputers. These operate in a front-end/back-end arrangement. The front-end system controls the data acquisition, drives data collection status displays, and stores the data. The back-end system serves as an analysis workstation. A system identification analyst uses this workstation to process the data collected by the front-end system. This processing is performed during the trials on board the ship. Such processing validates the data and alerts the test director in the case of failed sensors or to the need for additional maneuvers. Data can be transferred between the two systems using either cartridge tapes or the DECNET local area network.

Using two identical computers on board ship gives some protection from failure of critical components, such as of the front-end computer central processing unit (CPU) board. The corresponding component from the back-end computer could be substituted during such an emergency.

Each of the two Microvaxes uses the Q-bus architecture (Figure 2). The front end computer has standard CPU, RAM memory, disk/tape controller, analog-digital converter, and serial port circuit cards installed in the Q-bus. Two custom cards for interfacing with the inertial measurement unit and with synchro signals are also now provided. Both the front end and back end computers have a single 71 megabyte disk drive and a 100 megabyte tape cartridge drive. Each computer has a graphics terminal and a dot matrix, graphics capable printer. The back end computer (analysis work station) is similar in layout to the front end system except that the back end system does not have sensor interface cards. This analysis work station makes heavy use of the graphics terminal and printer during processing of the data.

The front-end computer archives data on a 100 megabyte cartridge tape drive. The sensors produce about 5 megabytes of data

per hour. This is first written to the disk drive. Once every 4 to 8 hours the accumulated data are dumped onto a cartridge. The cartridge can then be hand carried to the back-end workstation for further processing.

Both front and back end computers are mounted in Environmental Container Systems transportable electronics enclosures. Both enclosures are made of molded fiberglass and have eight-point internal shock mounting of their internal equipment racks. The computers and associated electronics can be shipped directly in these enclosures without additional packaging. Figure 3 shows a front view of the front end data collection computer enclosure. The analysis workstation is housed in a smaller enclosure.

The MARCIS front end records 7 or more data channels at a 1 to 1/6 sample per second rate and 6 inertial data channels at a 64 sample per second rate (Table 1). The accuracies of shipboard sensors depend on the particular ship being tested. (The table indicates typical accuracies.)

The inertial sensors are of the strapdown type; they are fixed to the ship frame rather than to a leveled platform. The three accelerometers measure translational acceleration along the orthogonal, right handed, ship-fixed x, y, and z axis (z position down). The three angular rate gyros measure angular rates about the same three axes. Longitudinal and lateral velocity components are measured if Doppler sonar is available. Latitude and longitude are measured using Loran-C. The Loran–C set is a part of the MARCIS system. It is easier to provide one such radio receiver as part of the front end system than it is to interface the Q-bus with whatever set may be on the subject vessel.

5. PROCESSING METHODS

The complete processing procedure implemented in the MARCIS workstation has three steps: filtering, model structure determination, and parameter estimation. Typically the filtering function runs on the data collection front end while model structure determination and parameter estimation run on the workstation. The analyst using the workstation can monitor the data processing (e. g. manipulate data arrays, plot channels) using CTRL-C[11] (CTRL-C[11] is a proprietary program owned by Systems Control Technology.)

5.1 Filtering

Filtering uses an extended Kalman filter to compute estimates of vessel velocity and acceleration, resolved into the level plane used in the ship maneuvering simulation. The most important requirement here is to eliminate components of gravity from the translational accelerometer outputs. The extended Kalman filter acts as an aided inertial navigation system[12].

The extended Kalman filter works with a system of differential equations of the form

$$\underline{\dot{v}} + \underline{\omega} \times \underline{v} = \underline{a} \tag{1}$$

$$\underline{\dot{q}} = \Omega(\underline{\omega}) \cdot \underline{q} \tag{2}$$

$$\underline{\dot{p}} = \mathbf{T}(\underline{q}) \cdot \underline{v} \tag{3}$$

$$\underline{y} = \underline{h}(\underline{v}, \underline{p}, \underline{q}) \tag{4}$$

This set of equations uses a quaternion[13] to represent attitude. (See nomenclature section for definition of terms.) The differential equations in the filter (eqns. 1, 2, 3) represent the process of integrating acceleration and angular rate to estimate position, velocity, and attitude. This integration is done at a 64 sample per second rate. The measurement equations in the filter (eqn. 4) represent shipboard sensors of some of the filter states such as position and velocity. The filter updates these states about once per second as the measurements become available.

Several parameters of the extended Kalman filter cannot be determined *a priori*. These include

- inertial and shipboard sensor biases,
- shipboard Doppler sonar misalignment (The x and y doppler sonar axes may be installed as much as 1 degree away from the ship x and y axes. This causes a bias in estimated sideslip angle.),
- shipboard sensor misalignments, and
- inertial and shipboard sensor noise covariance.

A maximum likelihood method run in a batch (non-real-time) mode in the workstation estimates these parameters. The Kalman filter produces an innovations sequence as a byproduct of state estimation. This sequence can be used to evaluate a likelihood function for any given values of the unknown parameters. A modified Levenberg-Marquardt (LM) method[14,15,16] can then maximize the likelihood function with respect to the unknown parameters. This method is more reliable for this application than a popular alternative, which is to augment the Kalman filter state with the unknown parameters.

The 3 x 3 coordinate transformation matrix **T** is the most important product of the filtering process. **T** relates measured accelerations to the hydrodynamic force components f_x and f_y

$$\begin{bmatrix} & & 0 \\ & \Psi & \\ & & 0 \\ 0 & 0 & 1 \end{bmatrix} \begin{bmatrix} fx/m \\ fy/m \\ fz/m \end{bmatrix} = \mathbf{T} \cdot \underline{a}$$

f_z is primarily buoyancy..

5.2 Model Structure Determination

Model structure determination uses outputs of the filter directly to set up a linear regression for the two hydrodynamic force components f_x and f_y and the hydrodynamic yaw moment m_z. For the f_x term, the regression has the form

$$\min_{\underline{b}} \quad | \ \underline{z} - A \cdot \underline{b} \ |^2 \qquad (6)$$

where $z_i = f_x(t_i)$, $A_{ij} = \partial f_x(t_i)/\partial b_j$ and $\underline{b}$ is a vector of the unknown hydrodynamic coefficients. Regressions for f_y and m_z have similar forms.

The regressions may be analyzed using straightforward linear least squares methods or any of several subset regression methods[17,18]. This is possible because the A_{ij} elements are functions only of the measured or estimated states u, v, and r and are not functions of the unknown hydrodynamics coefficients in $\underline{b}$. This makes possible the application of computationally simple linear least square estimation. This use of a linear estimation method is possible even when the model represents nonlinear hydrodynamics. This method is commonly applied to aircraft aerodynamics estimation[19].

5.3 Parameter Estimation.

Final parameter estimation uses conceptually simple minimization of output error. A fit error performance index can be evaluated for any given parameter values simply by integrating the nonlinear ship equations of motion and computing a performance index $J(\underline{b})$ given by:

$$J(\underline{b}) = \sum_i \left\{ \underline{v}(t_i,\underline{b})' \cdot \mathbf{W} \cdot \underline{v}(t_i,\underline{b}) \right\} \qquad (7)$$

where vector $\underline{v} = (\underline{z}_e(\underline{b}) - \underline{z}_m)$ and $\underline{z} = (f_x \ f_y \ r \ u \ v \ \Psi \ x \ y)'$. $\underline{z}_e$ represents the value of the vector $\underline{z}$ estimated using the ship simulation running with nominal parameters $\underline{b}$. $\underline{z}_m$ represents the value measured by the MARCIS sensors. $\underline{v}$ is thus the error between the estimated and actual sensor outputs. **W** represents a diagonal weighting matrix. Parameters $\underline{b}$ are chosen to minimize this nonlinear least square performance index using the LM method.

6. FUTURE WORK

The upgraded MARCIS having Microvax 2 data collection and workstation computer systems will be tested aboard the *Kings Pointer* in August of 1987. Following this test the package should be available for use aboard ships of opportunity for collection of system identification data. While MARCIS has been optimized for the collection of maneuvering hydrodynamics system identification data, there is the potential for collection of data on seakeeping characteristics as well.

ACKNOWLEDGEMENT

This work was supported by the Maritime Administration Marine Sciences contract number MA–80–SAC–01092, adminsterd by the Office of Advanced Ship Development and Technology.

APPENDIX: HYDRODYNAMIC MODEL

The workstation software can use any of the popular forms for hydrodynamic coefficients, including the square-absolute form[20] used by the United States Coast Guard river tow simulation and the cubic form[21] used by the Computer Aided Operations Research Facility (CAORF) simulator operated by the United States Maritime Administration.

The ship mathematical model represents three of the six possible degrees of freedom of a rigid body. The degrees of freedom are x and y position in the horizontal plane and yaw attitude. Modeling maneuvering in calm water requires the representation of only these three degrees of freedom.

The dynamic equations of the ship now implemented in the workstation simulation are:

$$m(\dot{u} - v \cdot r) = f_x = q \cdot \ell^2 \cdot C_x(v', r', \delta, \eta, u', v', r') \qquad (8)$$

$$m(\dot{v} + u \cdot r) = f_y = q \cdot \ell^2 \cdot C_y(v', r', \delta, \eta, u', v', r') \qquad (9)$$

$$I_z \cdot r = m_z$$

$$= q \cdot \ell^3 \cdot C_n(v', r', \delta, \eta, u', v', r') \quad (10)$$

$$q = \rho \text{¥} u^2/2 \quad (11)$$

$$\begin{bmatrix} \dot{x} \\ \dot{y} \end{bmatrix} = \Psi(\psi) \begin{bmatrix} u \\ v \end{bmatrix} \quad (12)$$

$$\Psi(\psi) = \begin{bmatrix} \cos(\psi) & -\sin(\psi) \\ \sin(\psi) & \cos(\psi) \end{bmatrix} \quad (13)$$

The three dimensionless coefficients C_x, C_y, and C_n are called total hydrodynamic coefficients or, simply, total coefficients. Each total coefficient is a nonlinear function of the dimensionless states v' and r', the rudder angle δ, and of the dimensionless propulsion point η. The identification of the ship hydrodynamic model is equivalent to determining these three nonlinear functions.

The three nonlinear total hydrodynamic coefficients have the following forms:

$$C_x = X_{vv} \cdot v' \cdot v' + X_{rr} \cdot r' \cdot r' \cdot X_{vr} \cdot v' \cdot r' + X_u \cdot u' + X_{vv\eta} \cdot v' \cdot v \cdot \eta_a + X_{\delta\delta} \cdot \delta \cdot \delta + a_i + (b_i \cdot \eta_s + c_i \cdot \eta_s^2 + b_i \cdot \eta_p + c_i \cdot \eta_p^2)/2 \quad (14)$$

$$C_y = Y_* + Y_v \cdot v' + Y_r \cdot r' + Y_v \cdot v' + Y_r \cdot r' + Y_{v|v|} \cdot v'|v'| + Y_{r|v|} \cdot r'|v'| + Y_{r|r|} \cdot r'|r'| + Y_{v|r|} \cdot v'|r'| + (Y_{v\eta} \cdot v' + Y_{r\eta} \cdot r' + Y_{v|v|\eta} \cdot v'|v'|) \cdot \eta_a + K(\eta) \cdot (Y_\delta \cdot \delta' + Y_{\delta|\delta|} \cdot \delta \cdot |\delta|) \quad (15)$$

$$C_n = N_* + N_v \cdot v' + N_r \cdot r' + N_v \cdot v' + N_r \cdot r' + N_{v|v|} \cdot v'|v'| + N_{r|v|} \cdot r'|v'| + N_{r|r|} \cdot r'|r'| + N_{|v|r} \cdot |v'|r' + (N_{v\eta} \cdot v' + N_{r\eta} \cdot r' + N_{v|v|\eta} \cdot v'|v'|) \cdot \eta_a - Y_s \cdot (b_i \cdot \eta_s + c_i \cdot \eta_s^2)/2 + Y_p \cdot (b_i \cdot \eta_p + c_i \cdot \eta_p^2)/2 + K(\eta_s) \cdot (N_\delta \cdot \delta s' + N_{\delta|\delta|} \cdot \delta \cdot |\delta s| \cdot |\delta s|) + K(\eta_p) \cdot (N_\delta \cdot \delta p' + N_{\delta|\delta|} \cdot \delta p \cdot |\delta p|) \quad (16)$$

The dimensionless hydrodynamic coefficients X_{vv}, X_{rr}, . . . , $N_{\delta|\delta|}$ are the elements of the vector $\underline{b}$ in equations 6 and 7. The propulsion ratio η_a is the deviation of the average of the port and starboard propulsion ratios from unity:

$$\eta_a = ((\eta_s + \eta_p)/2 - 1) \quad (17)$$

The rudder/propeller interaction term $K(\eta)$ can be identified as a second degree polynomial:

$$K(\eta) = d + e \cdot D \cdot \eta + f \cdot D^2 \cdot \eta^2 \quad (18)$$

where D is propeller diameter.

REFERENCES

1 Rinehart, V., "Opening Remarks," *Proceedings of the Workshop for Development of an International Joint Ship Maneuvering Program*, Maritime Administration, U.S. Dept. of Transportation, 1981.

2 Mandel, P., "Ship Maneuvering and Control," *Principles of Naval Architecture*, Society of Naval Architecture, New York, 1967.

3 Astrom, K.J., Kallstrom, C.G., "Identification of Ship Steering Dynamics," *Automatica*, Vol. 12, pp 9-22.

4 Trankle, T.L., Karmarkar, J.S., Tyler, J.S., "Instrumentation and Data processing for Identification of Nonlinear Ship Hydrodynamics," *Sixth IFAC Symposium on Identification and System Parameter Estimation Preprints*, McGregor and Werner, Inc, Washington, D.C., 1982, pp 669-674.

5 Trankle, T. L., Akhter, M., "*Kings Pointer* Data Processing Results," Draft of Interim Technical Report to U.'S. Department of Transportation under Contract MA-80-SAC-01092, December 1985.

6 Trankle, T. L., "WMEC *Tampa* Data Processing Results ," Draft of Interim Technical Report to U.'S. Department of Transportation under Contract MA-80-SAC-01092, March 1986.

7 Crane, C. L. Jr., "Maneuvering Trials of a 278,000-DWT Tanker in Shallow and Deep Waters," *SNAME Transactions*, Vol. 87, 1979, pp. 251-283.

8 Abkowitz, M. A., "Measurement of Hydrodynamic Characteristics from Ship Maneuvering Trials by System Identification," *SNAME Annual Meeting*, New York, N. Y., Nov. 13-15, 1980.

9 Trankle, T. L., "A System for Estimation of Hydrodynamic Coefficients for Full-Scale Ship Tests," U. S. Department of Commerce Maritime Administration Final Report NMRC– 207, Jan. 1981.

10 Trankle T. L. "Practical Aspects of System Identification," ASME Paper 79-WA/DSC-23, Winter Annual Meeting, New York, N.Y., August 17, 1979.

11 Little, J. N., Emami-Naeini, A., Bangert, S. N., "CTRL-C and Matrix Environments for the Computer-Aided Design of Control Systems," *Lecture Notes in Control and Information Sciences*, Springer-Verlag, 1984

12 Farrell, J. L., *Integrated Aircraft Navigation*, Academic Press, New York, 1976.

13 Friedlander, B., "Analysis Strapdown Navigation Using Quaternions," *IEEE Trans Aerospace and Electronic Systems*, Vol. AES-14, No. 5, September 1978, pp 764-768.

14 Marquardt, D.W., "An Algorithm for Least Squares Estimation of Nonlinear Parameters," *J. Soc. Indust. Appl. Math.*, Vol. 11, No. 2, 1963, pp 431-441.

15 Trankle, T.L., Rabin, U.H., "Filtering Flight Data Prior to Aerodynamic System Identification," *AIAA Atmospheric Flight Mechanics Conference*, Gatlinberg, Tennessee, August 1983.

16 Brown, K.M., Dennis, J.E. Jr., "Derivative Free Analogues for the Levenberg-Marquardt and Gauss Algorithms for Nonlinear Least Squares Approximation," *Numer. Math.*, Vol. 18, pp 189-207.

17 Draper, N.R., Smith, H., "Selecting the 'Best' Regression," *Applied Regression Analysis*, Wiley and Sons, New York, 1966.

18 Furnival, G.M., Wilson, R.W., "Regression by Leaps and Bounds," *Technometrics*, Vol. 16., No. 4, Nov. 1974, pp 499-511.

19 Gupta, N.K., Hall, W.E., and Trankle, T.L, "Advanced Methods of Model Structure Determination from Test Data," *J. Guidance and Control*, Vol.1, No. 3, May-June 1978, pp 197-204.

20 Miller, E. R., "The Prediction of River Tow Maneuvering Performance," Final Reprot No. CG-D-32-78 for U. S. Coast Guard Office of Research and Development under Contract No. DOT-CG-72701-A, May 1978.

21 Eda, H., "Equations of Motion for the Ship-Handling Simulator and Proposed Program for Acquistion of Hydrodynamic Data," Davison Laboratory, Stevens Institute of Technology, Hoboken, N. J., Report SIT-DL-71-1572, Nov. 1971.

TABLE 1 Data Channels

	Channel	Samples /sec	Accuracy
Inertial	Translational Accel.	32	50 micro g
	Angular Rate	32	0.02 deg/hr
Radio Nav.	Latitude	1/6	0.5 sec
	Longitude	1/6	0.5 sec
Ship Sensors	Heading	1	1/6 deg
	Longitudinal Vel.	1	0.1 m/sec
	Lateral Velocity	1	0.1 m/sec
Ship Controls	Rudder Angle	1	0.5 deg
	Propeller Rate	1	1 RPM

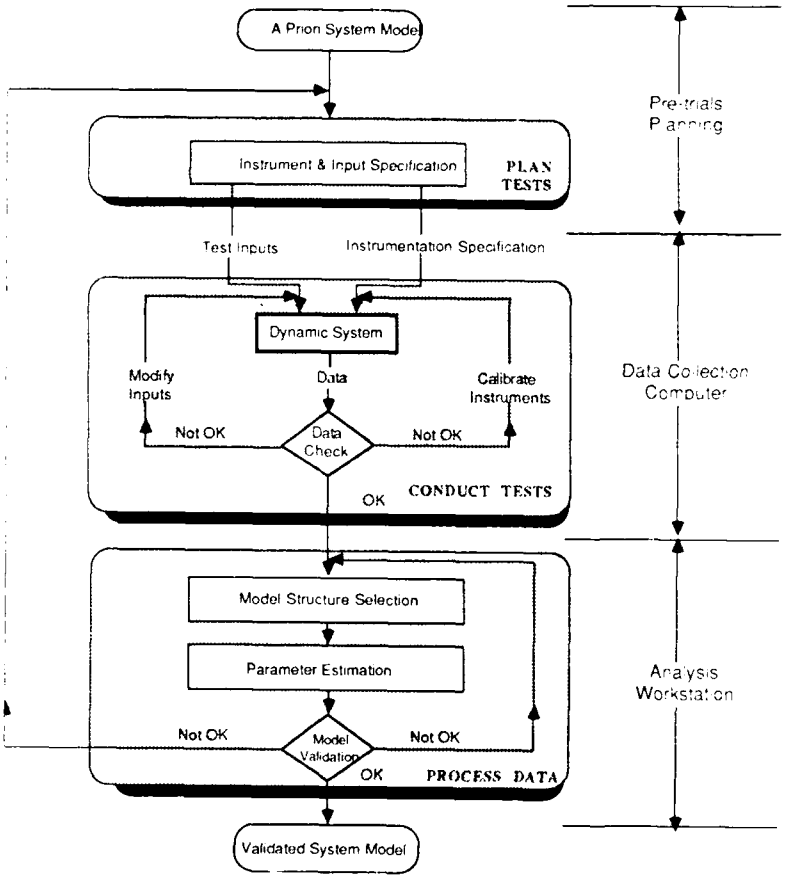

Figure 1: MARCIS System Identification Process

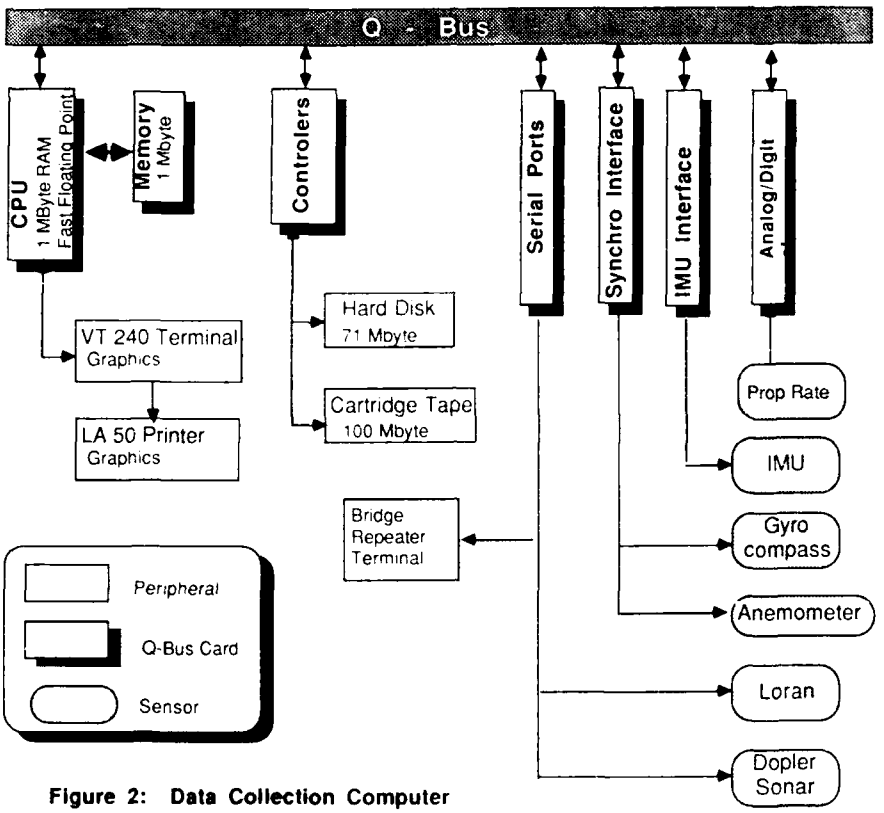

Figure 2: Data Collection Computer

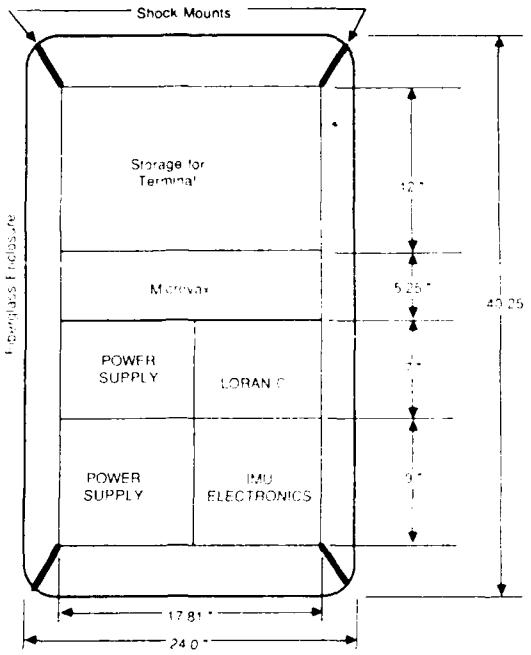

FIGURE 3: FRONT END SYSTEM

A CASE FOR THE SEPARATE DETERMINATION OF HYDRODYNAMIC CHARACTERISTICS OF SHIP'S HULL AND RUDDER[1]

Volf Asinovsky
Senior Project Engineer
J.J. McMullen Associates, Inc.
Suite 715
2341 Jefferson Davis Highway
Arlington, VA 22202

Alexander C. Landsburg
CAORF Liaison
Maritime Administration
MAR-770, Room 7330
Department of Transportation
Washington, D.C. 20590

Grant Hagen
Senior Naval Architect
Designers & Planners, Inc.
Suite 500
2011 Crystal Drive
Arlington, VA 22202

ABSTRACT

A serious methodological problem prevents the collection and use of the experimental data on the ship hydrodynamic characteristics that are necessary for design calculations and studies of the maneuverability of ships. The approach popular among members of the ATTC consists of determining the total hydrodynamic forces and moments acting on a model completely equipped with propeller(s), appendages, and rudder(s). The roles and contributions of the individual components of this sytem are thus not directly considered. This paper provides a discussion of a "differential" approach that is more convenient for the designer. It is based on the separate determination of the hydrodynamic characteristics of the hull, propeller, rudder, and appendages in combination with an investigation of the dynamic and kinematic interactions in the system.

INTRODUCTION

It seems fair to say that, at least in the United States, the acquisition of hydrodynamic data for use in mathematical models for ship maneuvering has relied heavily on experiments using fully-appended captive models. From the outset of the development of mathematical modeling, of course, it was recognized that a vessel could be considered to be comprised of a number of component parts, including at least the bare hull, skeg(s), rudder(s), and propeller(s), each contributing its share to the total (resultant) hydrodynamic force (and moment) acting on the vessel during maneuvering.

Thus the approach to captive-model experiments could be a "differential" one where separate determinations could be made of the hydrodynamic contributions of the various ship components. The separate contributions would then be assembled in a mathematical model, with proper representations being made of the flows about the various components and the hydrodynamic interactions among them.

It was considered, however, that, in general, the quantitative evaluation of the required forces and moments for use in the mathematical model could be accomplished best by performing experiments with completely appended models. In such experiments the interaction effects would be properly included in the measurements of the forces and moments (except for possible scale effects in the total system) and the problem of mathematical modelling would be simplified. This approach is generally in use today by the various establishments which comprise the ATTC.

It is to be understood that it does not necessarily follow that the structure of a mathematical model which incorporates data obtained from tests with fully-appended models is unsuitable for use with hydrodynamic input obtained by different processes. Reference 1, for example, presents procedures for estimating certain hydrodynamic coefficients by means of methods which can be found in the literature of aerodynamics. Undoubtedly, practitioners in the field of ship maneuverability exercise their own ingenuity in providing estimates of the required hydrodynamic coefficients.

While the appended-model approach has much to recommend it, particulary in its application to the evaluation of complete ship designs for which the required hydrodynamic data is available, the overall process lacks the flexibility (to say nothing of the problem of acquiring the necessary hydrodynamic input) required by the designers who must evaluate the course stability and maneuverability of an arbitrary ship design during the phase of design wherein the ship's geometric characteristics are under development. The difficulty of this task probably can be fully appreciated only by the one who has responsibility for performing it, the design naval architect. At this stage of the design little time is available, and many tradeoffs

[1] The opinions expressed in this paper are those of the authors and do not necessarily reflect those of their employers.

to be made with maneuverability usually receive no attention because of the lack of an easy approach to analysis.

While the acquisition of pertinent hydrodynamic data for a mathematical model, whether by specific experiments or other means, is always a problem, it is suggested that the "differential" approach to acquiring the hydrodynamic data and for its inclusion in the mathematical model is superior to what appears to be the process generally used by the community represented in the ATTC.

The use of the methodology involving experiments with fully-appended models is amply presented in many papers, including References [1-7]. The differential approach is used by the technical schools which are credited with development of the method, and is described, in particular, in papers of Inoue [8] and K. Kose [9] on the model of the Japanese Mathematical Modeling Group (MMG). The basic principle in the approach of this school is that it involves the study of the hydrodynamic characteristics of the hull, propellers, and rudders separately, and the study of the interactions among these components of a ship.

Long before the publication of the papers [8] and [9] the approach based on the separate consideration of the hydrodynamic components was used by A. Basin, [10], K. Fediaevsky [11] and several others. This method happened to be very fruitful because of the informal and physical consideration of the hydrodynamic phenomena in the hull/propeller/rudder system. The functional presentation of the hydrodynamic characterics as well as the forms of the equations of motion in the method developed in [10, 11] and in the method of K. Kose [9] are different.

This paper is partly devoted to the consideration of the principal differences in these generally known approaches in the light of the practical applications in ship design.

The results of calculations of the kinematic characteristics of ship motion which have been performed over the years, as well as the results of full scale trials which have been collected up to the present time make it possible to evaluate (and to correct in some cases) the previously established concepts used in the consideration of the kinematics of maneuverability.

Some comments are also made using the results of analyses of the kinematic characteristics of motion.

DETERMINING HYDRODYNAMIC CHARACTERISTICS

The equations of ship motion in the ship coordinate system of Figure 1 have been obtained directly from Lagrange's equations and are as follows:[1]

$$\begin{aligned}
&(m + \lambda_{11})\frac{du_x}{dt} - (m + \lambda_{22})u_y r - \lambda_{26} r^2 = R_x \\
&(m + \lambda_{22})\frac{du_y}{dt} + (m + \lambda_{11})u_x r + \lambda_{26}\frac{dr}{dt} = R_y \\
&(I + \lambda_{66})\frac{dr}{dt} + (\lambda_{22} - \lambda_{11})u_x u_y + \lambda_{26} r u_x + \lambda_{26}\frac{du_y}{dt} = N
\end{aligned} \qquad (1)$$

Values of forces R_x, R_y and moment N in the general case for still water are:

$$R_x = \Sigma T_e - X_h - \Sigma X_r \qquad (2)$$

$$R_y = Y_h - \Sigma Y_r - \Sigma Y_p \qquad (3)$$

$$N = M_h + \Sigma M_r - \Sigma M_p \qquad (4)$$

This system is necessarily used in any study of maneuverability either in its full form or in simplified version. The principal differences mentioned in the introduction are concerned with the determination of the hydrodynamic forces and moments.

In the straightforward application of the methodology which involves experiments with fully-appended models, the hydrodynamic forces are determined for the ship as a whole, and the explicit and detailed consideration of component forces, as is allowed by use of equations (2) - (4), is not necessary. In other words, the methodology does not require that the phenomena inside the hull/propeller/rudder system be studied. Thus in such applications, the hydrodynamic forces acting on the rudder(s), appendage(s), and propeller(s) are not considered separately

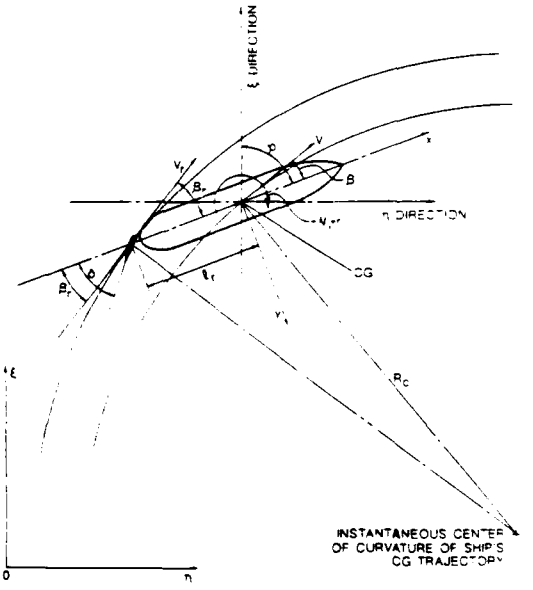

Fig. 1 Systems of coordinates

[1] See nomenclature section at end.

from the forces acting on the hull. Nor are the angle of attack of the rudder and the dynamic and kinematic interaction in the hull/propeller(s)/rudder(s) system studied. With this approach one cannot combine the maneuverability calculations with simultaneous analysis of the hydrodynamic loads on the rudder arrangement. Simultaneous calculations of rudder torque and maneuverability, however, are very desirable for the correct design of the rudder stock and selection of the steering gear. During the phase of early design of a ship when the propellers, rudder(s), appendage(s) (and their location) are modified several times as well as are the hull form and dimensions, the use of the fully appended model analysis requires, at least in principle, a new model test every time that a modification is made.

The obvious disadvantages of the formal approach are realized by many researchers and engineers. As a result the natural physical analysis of the hydrodynamic forces acting on the hull, propeller, and rudder and investigation of the interaction in the hull/propeller/rudder system are conducted by many specialists in the area of maneuverability. Several publications of the last few years have discussed the achievements of the MMG group in Japan.

In some of the works of the MMG group [8, 9] the equations (2) - (4) are studied and analysed. Physically consistent experimental study of hull hydrodynamic characteristics has been described in the paper of S. Inoue, M. Hirano and K. Kijima [8] along with an attempt to approximate the hydrodynamic forces and moments using a simplified mathematical model.

K. Kose [9] has presented a consistent and detailed analysis of hull and propeller hydrodynamic forces as well as a study of the interactions in the hull/propeller/rudder system. The studies of wake fraction of the rudder and the propeller-induced velocity in the wake incoming to the rudder given by K. Kose are of a special interest. The attempt was made to analyze the effective angle of attack of the rudder located behind the hull and behind the hull and propeller. (In doing so K. Kose has approached the physical model considered earlier by the school of Prof. K. Fediaevsky [10,11]). Discussing the influence of the hull on the rudder force and the rudder influence on hull hydrodynamic characteristics, K. Kose has provided a deep physical analysis of the kinematic and dynamic interactions in the hull/rudder system.

However, all the dependencies determining the rudder angle of attack characteristics of interaction, and propeller induced velocities are based in [9] on a series of purely empirical coefficients which limit the application of the Kose data to the range of the tested configurations.

The variables in the equations of motion in the MMG studies (as described, in particular, in [8] and [9]) are the nondimensional angular velocity

$$r_d = r \cdot L/V$$

and the nondimensional value of the components of the speed, V, of the center of gravity of the hull in the x and y directions.

$$u_x = V\cos\beta$$

and $$u_y = -V\sin\beta,$$

Thus, in terms of the selection of variables the MMG model is similar to that used in [1-7 etc.] (See also later comments)

V. Ankudinov has made a comparative analysis of several "mathematical models" and has presented in [12] the consecutive development of a full system of equations of ship motion based on Lagrange's equations as it has been done in the classical works on ship dynamics. However, the hull hydrodynamic characteristics in [12] were also presented in a form of rigid approximations which somewhat limits the applications of the mathematical model. The propeller and rudder forces were also introduced into the equations of motion through approximations. In doing so, the rudder side force was presented as a function of the rudder angle δ. In other words, the physical angle of attack of the rudder $\alpha_r = \delta - \kappa\beta_r$ was replaced by some empirical function of δ, which cannot be universal for a variety of ships, rudders and/or maneuvers. The equations of motion were presented using the same variables as in [1-9].

Equations of motion in the form where the speeds u_x and u_y are two of three kinematic parameters of motion to be determined during solution, are associated with some inconveniences. From the physical standpoint, the coefficients of hydrodynamic forces and moments are functions of r_d and β but not of u_x' and u_y'. The drift angle β is equivalent to the angle of attack of the ship's hull. Studying the distribution of β along the hull one can consider and solve a series of tasks concerned with determination of hull hydrodynamic characteristics, analysis of maneuverability when going astern [13], analysis of the effective angle of attack of the ship's rudder and others.

The drift angle in the area of rudder location β_r (which is the direct function of β and r_d) has to be considered in the calculation of the angle of attack of the rudder $\alpha_r = \delta - \kappa\beta_r$ and, correspondingly, in the rudder torque calculations [14]. The drift angle β is one of two basic parameters investigated in the model tests carried out on the rotating arm. For these reasons a more logical approach for studying flat horizontal motion of a ship would be to consider r_d, β, and V_n as the independent paramaters.

The approach used in [10] and [11] and, later, in different works on maneuverability is based

on the additional transformation of the equations of system (1) in order to consider the direct combination of kinematic parameters in determining the hydrodynamic forces and moments acting on the ship. In other words, the equations of motion are presented in the form, where the unknown parameters are:

- -the drift angle β
- -the nondimensional angular velocity r_n (or r_d)
- -the speed drop $V_n = V/V_o$

In nondimensional form the corresponding system of equations is obtained from (1) - (4) taking into account, that $u_x = V\cos\beta$ and $u_y = -V\sin\beta$ as follows:

$$m_{22} = \frac{m + \lambda_{22}}{\frac{\rho}{2} A_d L} \; ; \quad m_{26} = \frac{\lambda_{26}}{\frac{\rho}{2} A_d L^2} \; ;$$

$$m_{66} = \frac{I + \lambda_{66}}{\frac{\rho}{2} A_d L^3} \; ; \quad \varepsilon = \frac{l_r}{L}$$

The sequence of the solution of the system (5) depends on the form of the presentation of the hydrodynamic characteristics C_{xh}, C_{yh}, and C_{mh} and on the technique used to determine σ_e and correspondingly, V_n.

$$\left.\begin{aligned}
&m_n \frac{dV_n}{d\tau}\cos\beta - m_n V_n \frac{d\beta}{d\tau}\sin\beta + m_{22} r_n V_n \sin\beta - m_{26} r_n^2 = \sigma_e z_p V_{pn}^2 (1-\omega)^2 \frac{A_p}{A_d} - C_{xn} V_n^2 \\
&-m_{22}\frac{dV_n}{d\tau}\sin\beta - m_{22} V_n \frac{d\beta}{d\tau}\cos\beta + m_{11} V_n r_n \cos\beta + m_{26}\frac{dr_n}{d\tau} = C_{yn} V_n^2 - C_{yr} V_{rn}^2 \frac{A_r}{A_d}(1-\omega_r)^2 z_r k_p \\
&m_{66}\frac{dr_n}{d\tau} - m_{26}\frac{dV_n}{d\tau}\sin\beta - m_{26}\left(V_n \frac{d\beta}{d\tau}\cos\beta - V_n r_n \cos\beta\right) + (m_{11} - m_{22}) V_n^2 \cos\beta \cdot \sin\beta = \\
&= C_{mn} V_n^2 + C_{yr} V_{rn}^2 \frac{A_r}{A_d}(1-\omega_r)^2 z_r e k_p
\end{aligned}\right\} (5)$$

(See nomenclature at end)

where

$$\sigma_e = \frac{T_e}{\frac{\rho V_p^2}{2}(1-\omega)^2 A_p} \qquad (6)$$

= propeller pull loading coefficient

$$C_{yr} = \frac{Y_r}{\frac{\rho V_r^2}{2}(1-\omega_r)^2 A_r k_p} \qquad (7)$$

= rudder side force coefficient (in the ship coordinate system)

$$V_r = V \frac{\cos\beta}{\cos\beta_r} \qquad (8)$$

= flow velocity in the region of propeller-rudder system location without the hull influence correction

$$(V_{rn} = \frac{V_r}{V_o})$$

$$C_{xn} = \frac{X_n}{\frac{\rho V^2}{2} A_d} \; ; \quad C_{yn} = \frac{Y_n}{\frac{\rho V^2}{2} A_d} \; ;$$

$$C_{mn} = \frac{M_n}{\frac{\rho V^2}{2} A_d L} \; ; \quad m_n = \frac{m + \lambda_{11}}{\frac{\rho}{2} A_d L} \; ;$$

Numerous approximate techniques have been used before the introduction of computers into maneuverability calculations. In doing so, usually the speed drop was ignored (V_n was accepted as constant and equal to 1.0) and the experimental data on the hydrodynamic characteristics of the hull were approximated by simple polynomials (usually not higher than the second degree).

The drift angle β was assumed to be small. The significant difference between the speed of the rudder, V_r, and at the ship's CG, V, was ignored. Sometimes, additional assumptions were used regarding the rudder function $\delta(t)$ which helped to simplify the solution of the equations of motion, but did not reflect the real character of the rudder angle change in time t.

Current high speed numerical techniques allow dropping the simplifications and assumptions used before. In [15] the solution based on the system (5) was combined with consideration of changes in propulsion characteristics in the process of maneuvering in order to determine the $V_n(\tau)$ function in the most accurate way. To achieve this objective the changes in propeller and propulsion plant characteristics versus time were considered.

The combined system of equations of motion (5) and the equations of the propeller shaft turning can be presented in a Cauchy form suitable for application of numerical methods

as follows [15-17]:

$$\left.\begin{aligned}
\frac{dn_n}{d\tau} &= \frac{V_n^2}{1-\frac{m_{26}^2}{m_{66}m_{22}}}\frac{1}{m_{66}}\left[x_r\left(\frac{m_{26}}{m_{22}}+\varepsilon\right)C_{yr}-\frac{m_{26}}{m_{22}}\bar{C}_{yn}+\bar{C}_{mn}\right]\\
\frac{d\beta}{d\tau} &= \frac{1}{V_n}\left\{\frac{\cos\beta}{m_{22}}\left[m_{26}\frac{dn_n}{d\tau}+V_n^2\left(x_r C_{yr}-\bar{C}_{yn}\right)\right]+\right.\\
&\quad\left.+V_n^2\frac{\sin\beta}{m_{11}}\left[\bar{C}_{xn}-x_p\frac{n_n^2}{V_n^2}K_T\right]\right\} \qquad (9)\\
\frac{dV_n}{d\tau} &= \frac{\sin\beta}{m_{22}}\left[m_{26}\frac{dn_n}{d\tau}+V_n^2\left(x_r C_{yr}-\bar{C}_{yn}\right)\right]+\\
&\quad+V_n^2\frac{\cos\beta}{m_{11}}\left[x_p\frac{n_n^2}{V_n^2}K_T-\bar{C}_{xn}\right]\\
\frac{dn_n}{d\tau} &= \mu^{*}-\mu^{**}K_Q n_n^2
\end{aligned}\right]$$

where

$$K_T = K_T(j, \times\beta_r) \qquad (10)$$

$$K_Q = K_Q(j, \times\beta_r) \qquad (11)$$

$$x_r = z_r\frac{\cos^2\beta}{\cos^2\beta_r}\frac{A_r}{A_d}(1-w_r)^2 k_p \qquad (12)$$

$$x_p = \frac{\delta z_p}{\pi j_0^2}\frac{A_p}{A_d}(1-\theta) \qquad (13)$$

$$\mu^{*}=\frac{\rho n_0 D^5}{2\pi I_e}\frac{L}{V_0}\;;\quad \mu^{**}=\frac{M_e}{2\pi I_e}\frac{L}{V_0 n_0}$$

$$\bar{C}_{xn} = m_{22}\frac{n_n}{V_n}\sin\beta - m_{26}\frac{n_n^2}{V_n^2}+C_{xn} \qquad (14)$$

$$\bar{C}_{yn} = C_{yn} - m_{11}\frac{n_n}{V_n}\cos\beta \qquad (15)$$

$$\bar{C}_{mn} = C_{mn} - (m_{11}-m_{22})\cos\beta\cdot\sin\beta - m_{26}\frac{n_n}{V_n}\cos\beta \qquad (16)$$

When the hydrodynamic characteristics of a hull are obtained from the model tests on the rotating arm, the values of C_{xh}, C_{yh}, and C_{mh} are as follows:

$$\bar{C}_{xn} = C_{xn} + m_0\frac{n_n}{V_n}\sin\beta \qquad (14a)$$

$$\bar{C}_{yn} = C_{yn} - m_0\frac{n_n}{V_n}\cos\beta \qquad (15a)$$

$$\bar{C}_{mn} = C_{mn} \qquad (16a)$$

where

$$m_0 = \frac{m}{\frac{\rho}{2}A_d L}$$

The rudder side force coefficient C_{yr}, which is a function of its angle of attack

$$\alpha_r = \delta - \kappa\beta_r$$

is calculated on the basis of the open water characteristics of the rudder and the values of δ and β_r determined on the considered step of the solution. The coefficient of hull influence on the flow direction in the rudder area "κ" was introduced by K. K. Fediaevsky (see [11], in particular) to take into account the kinematic influence of the ship's hull on the angle of attack of the ship's rudder. The second coefficient w_r reflects the hull influence on the average speed in the wake incoming to the rudder installed behind the hull. These two coefficients take into account the kinematic interaction between the hull and the rudder.

The calculations with the use of the system of equations (9) are performed numerically. In doing so, all functions (C_{yh}, C_{xh}, C_{mh}, C_{yr}, K_T, K_Q, etc.) are given numerically. At each step of the solution these functions are determined by the interpolation depending on the corresponding arguments (r_n, β, $\kappa\beta_r$, V_n etc.). The solution is performed by modifications of the Runge-Kutta method of the fourth order [19].

The important feature of this method is also that any assumptions or simplications are not used here. Calculations are performed directly with the use of the full system of equations determining the physics of the phenomenon. This is very important for the analysis of maneuverability of merchant ships especially for ships with good steering qualities. For such ships the accuracy of all motion elements depends highly on the accuracy of determining V and n.

SOME RESULTS OF KINEMATIC ANALYSIS

Series of calculations using the differential method have been performed in the course of the few last years. The results of these calculations and full scale trials data enables the consideration of some of the characteristics of the kinematics of ship maneuvering as discussed before in the literature on maneuverability. Here we consider some of these results, which should be taken into account in the process of analysis and simulation of maneuverability.

1. The trajectory of the ship center of gravity when the ship is entering the turn is not always as described in the traditional literature [1,10,11, etc.]. A displacement of the CG in the first part of a turn to the side opposite of the turn was not found in the studied cases. As calculations and trials have generally indicated, ships may enter the turn without such a displacement. On the other hand, this opposite side displacement obviously takes place in the trajectory of ship's stern, and, because of that, is always visible in the wake behind the ship.

2. The dependencies of angular velocities r (or r_n, but not r_d) from time t when the ship is entering the turn, always have the typical maximum (Figure 2). The maximum corresponds to the value of τ, when the speed drop V_n starts to decrease from Vn = 1.0.

Such a maximum is also typical for the dependencies $r_n(\tau)$ when the ship is changing the turn direction (Figure 3). However, in these cases the maximum is not as significant as in the case of entering a turn.

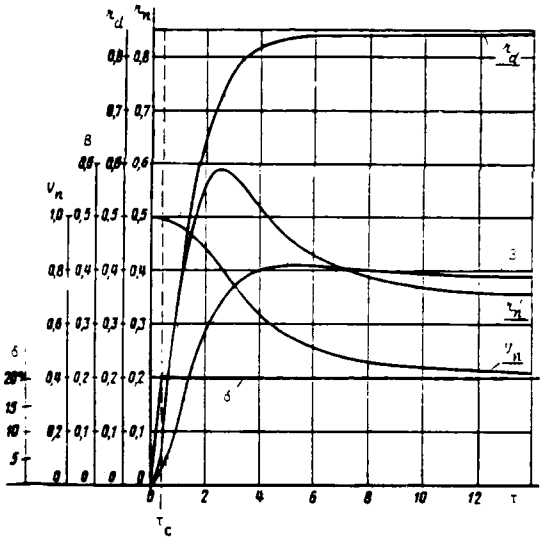

Fig. 2 Dependencies $r_d(\tau)$; $r_n(\tau)$; (τ); $V_n(\tau)$ and (τ) for entering the turn at δ_o = 20 (Calculation example)

3. The rate of change of the derivatives,

$$\frac{dr_n}{d\tau}(\tau);\quad \frac{d\beta}{d\tau}(\tau);\quad \frac{dV_n}{d\tau}(\tau)\quad \text{and}\quad \frac{dn_n}{d\tau}(\tau)$$

is different during maneuvering. The angular acceleration $dr_n/d\tau$ in entering the steady turning motion is approaching zero much faster than

$$\frac{d\beta}{d\tau}\ ;\quad {}^{dV_n}/_{d\tau}\ ,\ \text{and}\ {}^{dn_n}/_{d\tau}\ \text{[See 15]}$$

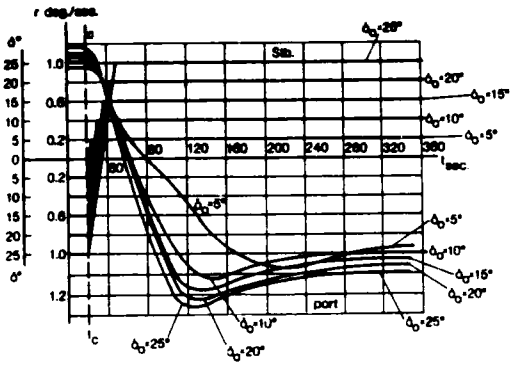

Fig. 3 Experimental dependencies $r(\tau)$ obtained in meeting rudder maneuvers with different δ (from [15]).

In the meeting rudder process the acceleration $dr_n/d\tau$ is also changing much faster, than $d\beta/d\tau$ As a result, the angular velocity r_n (and r_d, correspondingly) changes sign earlier, than the drift angle β (Figures 4 - 5).

The fact, that r_n and β do not change sign simultaneously in the meeting rudder process is a very important indicator that the linear theory of maneuverability is inapplicable to the analysis of maneuverability of merchant ships.

4. The dependencies $V_n(\tau)$ and $n_n(\tau)$ are very important in the process of the formation of the trajectory of center of gravity as well as all of the kinematic parameters of motion. Thus, accurate methods of calculating $V_n(\tau)$ and $n_n(\tau)$ are necessary in any method of maneuverability calculation.

5. An important observation is associated with the dependencies determining the hydrodynamic forces and moments acting on the ship's rudder. It was found, that the drift angle in the rudder area β_r, can be of very significant value and, usually, is much greater, than the drift angle in the area of the center of gravity, β ,(See Figure 6, for example).

The speed of rudder motion

$$V_r = V\frac{\cos\beta}{\cos\beta_r}$$

is much greater than the speed of the center of gravity V when the ship is performing a "strong" maneuver. As a result, $V_{rn} = V_r/V_o$ can be equal to 1.0, when $V_n = V/V_o$ has already dropped substantially (see Figure 6). In the case where the rudder is reversed to recover from a turn, the angle of attack α_r is

$$\alpha_r = \delta + \kappa\beta_r$$

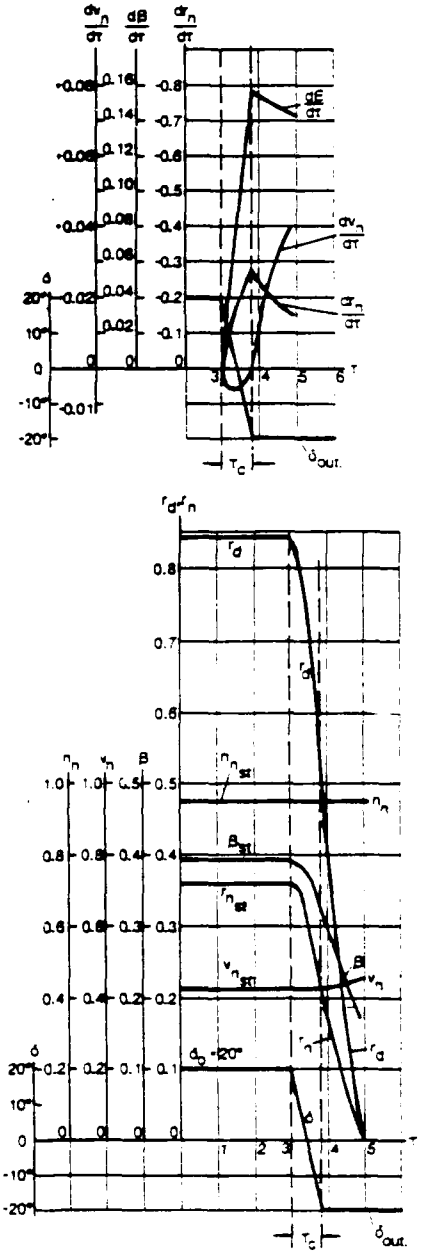

Fig. 4 Calculation example of change of the elements of motion during meeting rudder from the steady turning motion at $\delta_o = 20°$ by applying of the opposite rudder.

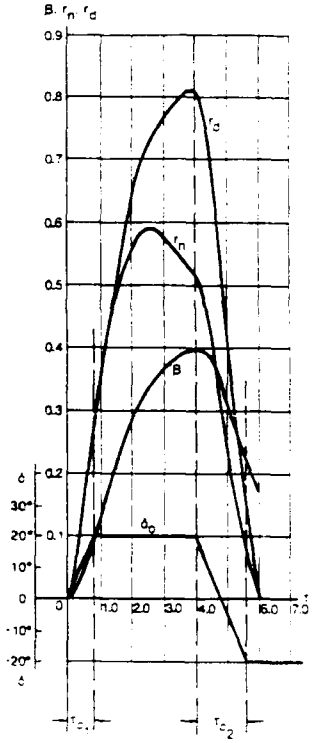

Fig. 5 Meeting rudder in evolutional period.

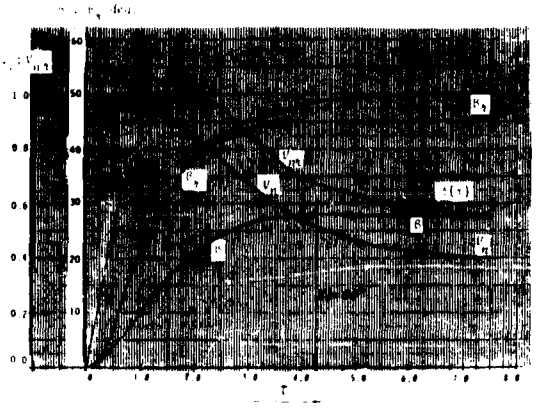

Fig. 6 [illegible] of changing the steady turning motion at δ_o = [illegible]

The noted situation is possible in such a maneuver, when $x_n > 5$ and V_r is not smaller than $V = V_o$ on a straight course.

Such conditions do not confirm the basic assumptions used in some of the contemporary methods for calculations of the hydrodynamic load in the design of the steering arrangement. The differential approach in the analysis of maneuverability permits combining the hydrodynamic calculations of the steering arrangement (rudder torque and force calculations) with the calculations of the kinematics of motion. Such an approach in rudder design seems to be the most logical for the cases when maneuverability analysis is

performed in the course of the design. If the maneuverability analysis is not made, the calculation of maximum hydrodynamic loads acting on the rudder arrangement can be performed on the basis of considering the possible range of the angles of attack [14] and assuming $V_{rn} \approx V_n \approx 1.0$.

SERIES TEST PROPOSAL

To develop a minimum body of data that would be useful for the designer utilizing the differential approach, a modest series of model tests would be required. While the series is certainly much more expensive than a single test of a specific ship, the results are a powerful design tool that is general and can be used on many designs to relatively quickly and easily study the effects of different hull shapes, rudders, and propellers.

It is thought that a single screw series could be quite broad but involve only nine models with three variations of block, L/B, B/H, and stern undercut. Eight of the models would be bare hull tests and the ninth or base model would be fully appended. The bare hull models could be tested in a rotating arm at six radii with about nine different drift angles. Runs in the towing tank would also be required at similar drift angles.

The base model would require similar tests but in addition the tests would be repeated after removing first the propeller and again after removing the rudder.

In order to determine the values of κ, a flap can be installed at the rudder location on the bare hull models. The angle between this flap and the center plane created by the flow in the stern area in the course of a run gives the value of the angle, $\kappa\beta_r$. Comparing this angle with the calculated value of β_r,

$$\beta_r = \beta + \arctan \frac{\varepsilon \cos\beta}{\frac{x_c}{L} + \varepsilon \sin\beta}$$

yields the value of the coefficient of hull influence, κ. The wake fraction for the rudder is determined simultaneously with the bare hull tests using a pitot tube installed in the area of the rudder location.

With this general introduction to the tests required, an estimate of the cost can be roughly determined. There are a total of up to 600 runs to be made and nine models to be constructed, one with full appendages. A sum of from a low of $25,000 (assuming all the models already exist) to a high of about $300,000 (where large models must be constructed and other contingencies must be met) is estimated to support this minimum series. Consideration to using small models for the bare hull tests could save some cost.

CONCLUSION

The comparative analysis of the contemporary approaches used for maneuverability simulation and calculations shows that the separate consideration of the hull and rudder hydrodynamic characteristics and the characteristics of interaction in the hull/propeller/rudder(s) system (differential approach) provides the most universal and flexible technique for maneuverability studies. Such an approach is based on consideration of the hydrodynamic phenomena without unnecessary formalization of the calculations. It also allows combining the maneuverability analysis with the appropriate and economical design of the steering arrangement.

The test of a systematic series of hull models can provide a substantial economic effect in comparison with the equal number of tests of the completely equipped models when looking at the longer term usage of the data. Iterative calculations of maneuverability during both the early and later stages of design can minimize maneuverability problems and optimize a design's capability.

REFERENCES:

1. Mandel P., "Ship Maneuvering and Control" in "Principles of Naval Architecture", SNAME, 1967.

2. Eda, M., Falls, R., Walden D.A., "Ship Maneuvering Safety Studies", SNAME Transactions, Vol. 87, 1979, pp. 229-250.

3. Hsao-Hsin Chen, "Some Aspects of Ship Maneuverability", Journal of Ship Research, June 1969.

4. Brown, S.H. and Alvestad, R., "Simulation of Maneuvering Charateristics of a Destroyer Study Ship Using a Modified Nonlinear Model", Journal of Ship Research, Vol. 19, No. 4, December 1975, pp. 254-265.

5. Abkowitz, M. A., "Measurement of Hydrodynamic Characteristics From Ship Maneuvering Trials by System Identification", SNAME Transactions, 1980, pp 283-318.

6. Chislett M.S. and Strom-Tysen, J., "Planar Motion Mechanism Tests and Full Scale Steering and Maneuvering Prediction for a Mariner Class Vessel", International Shipbuilding Progress, Vol. 12, May 1965, No. 129, pp. 201-224.

7. Hagen, G. R., "A Catalog of Existing Mathematical Models for Maneuvering", Presented to The Twentieth American Towing Tank Conference (Stevens Institute of Technology), 2-4 August 1983.

8. Inoue, S., Hirano, M., Kijima, K., "Hydrodynamic Derivatives on Ship Maneuvering" International Shipbuilding Progress, May 1981.

9. Kose, K., "On a New Mathematical Model on Maneuvering Motion of a Ship and Its Applications," International Shipbuilding Progress, August 1982.

10. Basin, A. M., "Propulsion and Maneuverability of Ships", Publishing House "Transport", 1968 (in Russian).

11. Fediaevsky, K. K., Sobolev, G. V., "Maneuverability of Ships", Publishing House "Sudpromgiz", 1963, (Translated by the U.S. Department of Commerce as "Control and Stability in Ship Design," 1964).

12. Ankudinov, V., "Ship Maneuvering Simulation Model Including Regimes of Slow Speeds and Large Drift Angles" Report for the First Maritime Simulation International Symposium, Munich, Germany, June 1985.

13. Asinovsky, V., "Simplified Approches for Evaluation of Maneuverability of Ships", Naval Engineers Journal, 1986, Vol. 98, No. 3, pp. 189-198.

14. Asinovsky, V., "Consideration of Maneuverability Characteristics in the Rudder Design Process", Presented to Los Angeles Metropolitan Section of The Society of Naval Architects and Marine Engineers, 14 March 1985.

15. Asinovsky, V., Videtsky, A., "Maneuverability", Part 3 in "Technical-Operating Properties of Combined Navigation Capability Ships", Publishing House "Transport", 1974 (NAVSEA translation, 1983).

16. Asinovsky, V., "Features of Maneuverability of Ships with Steering Nozzles", Marine Technology, Vol. 23, No. 1, January 1986, pp. 23-34.

17. Asinovsky, V., "On Maneuverability Criterion for Determining Ship Response to Rudder Angle Change," Presented to Chesapeake Section of the Society of Naval Architects and Marine Engineers, 17 May 1983.

18. Landsburg, A. C., Card, J.C., Crane, Jr., L.C., Alman, P.R., Bertsche, R., Boylston, J.W., Eda, H., Keith, V.F., McCallum, I.R., Miller, Jr., E.R. and Taplin, A., "Design and Verification for Adequate Ship Maneuverability", SNAME Transactions, Vol. 91, 1983.

19. Milne, W.E., "Numerical Solution of Differential Equations", Dover Publications, Inc., New York, N.Y.

NOMENCLATURE

A_d = area of center plane, limited by middle buttock

A_p = propeller's disk area

A_r = area of rudder

C_{xh}, C_{yh} = coefficients of longitudinal and lateral components of hydrodynamic resultant, acting on a ship's hull (in the ship coordinate system)

C_{mh} = coefficient of hydrodynamic moment acting on the ship's hull

C_{yr} = rudder side force coefficient (in the ship coordinate system)

D = diameter of propeller

I = mass moment of inertia about the vertical axis through the center of gravity (CG) of a ship

I_e = moment of inertia of rotating masses of engine and propulsion shafting

K_Q = propeller torque coefficient

K_T = propeller thrust coefficient

k_p = coefficient of propeller influence on rudder side force [11,14, and 17]

L = ship length

l_r = distance between the rudder center of pressure and the ship's CG

m = mass of the ship

M_e = moving moment of the engine

n = instantaneous value of propeller revolutions

$n_n = n/n_o$ = relative revolutions drop

n_o = propeller revolutions on a straight course

r = angular velocity of ship turning about the vertical axis through the center of gravity

$r_d = r \cdot L/V = r_n/V_n$ = dimensionless angular velocity related to the instantaneous value of ship speed, V

$r_n = r \cdot L/V_o$ = dimensionless angular velocity related to the speed on a straight course, V_o

T_e = pull of propeller

t = time

u_x, u_y = projections of the vector of velocity of the ship's CG, V, on the axes (X and Y ship coordinate system)

V = instantaneous value of the speed of the ship's center of gravity

V_o = ship speed on a straight course

$V_n = V/V_o$ = relative speed drop

V_r = flow velocity in the region of propeller-rudder system location without the hull influence correction

w = wake fraction for propeller

w_r = wake fraction for rudder

z_p = number of propellers

z_r = number of rudders

α_r = angle of attack of rudder

β = drift angle at the CG

β_r = drift angle at the rudder location

δ = rudder angle

δ_o = constant value of rudder angle

ε = relative distance between the rudder stock and the center of gravity of the ship, $= L_r/L$

ξ, η = coordinates of the absolute coordinate system

κ = coefficient of hull influence on the flow direction in the region of the rudder

λ_{11} = longitudinal added mass

λ_{22} = lateral added mass

λ_{26} = added static moment

λ_{66} = added moment of inertia

θ_e = thrust deduction fraction

σ_e = propeller pull loading coefficient

$\tau = t \cdot V_o/L$ = nondimensional time

φ = course angle

COMMENTS

Lewis Motter
David Taylor Naval Ship R&D Center
Bethesda, MD

This is a very interesting paper. We need to be reminded that there are more rigorous ways of evaluating ship maneuvering performance and that there are research programs that would help this effort. Most often, time and funding constraints limit the approach to ship maneuvering evaluations.

In 1979, the David Taylor Ship R&D Center embarked on a test program similar to the one recommended in the paper. The work was initiated by B. Cieslowski under the Ship, Subs and Boats Technology Development Program. The original plans called for testing one fully appended hull form each year with an ultimate goal of obtaining a data base of information that could be used to develop analytical ship maneuvering simulations in early design from ship lines. Dr. A. Strumpf of Davidson Laboratory, the project manager for the tests, immediately recognized the need for what he called appendage strip tests to identify the individual effects of each appendage. Over the next 3 years, the appendage strip tests were conducted on only 2 hulls with the funding for 3 fully appended hulls. Appendage strip tests did cost about 5 percent more than conventional tests.

Over the same 3 years, DTNSRDC research funds were cut, "Data Base" was dubbed "dirty words," and upper management concluded that ship maneuvering was not high priority for the Navy. The project died in spite of Dr. Strumpf's enthusiastic efforts to sell the project to the Maritime Administration, and I believe the first hull

The [illegible] proposal in this report is [illegible] of tests, but the idea has not been [illegible] the original [illegible] project for [illegible].

[illegible]

[illegible]
[illegible]
[illegible], MD

The paper [illegible] [illegible]
[illegible] ship [illegible] [illegible]
[illegible] [illegible]
[illegible] [illegible]
[

tion particularly for large propeller loads and speed/RPM reversals.

Figures 2 and 3 showing typical results of the captive model testing for the MARINER and ESSO OSAKA VLCC ship hulls conducted in the wide range of the rudder and drift angles variation (self-propulsion conditions in both tests). The remarkable feature of these results is that the slope of the side forces due to the rudder is practically independent of drift angle, and thus it does not support the concept of the effective rudder angle. The hydrodynamic analysis of the flow in the vicinity of the rudder indicates a complicated hydrodynamic interaction of the unsteady propulsion wake, shear viscous flow at ship stern, vortices due to the ship lateral motions and undisturbed flow acting on the different parts of the rudder profile. Because of the strong interaction of the rudder with the propeller race (in ahead motion, the rudder effectiveness typically increases from two to three times compared with no propeller conditions), these forces are dependent on the propeller load and ship speed/RPM ratios. Perhaps, a more detailed investigation of the dynamic interaction of the rudder with the propeller and hull is required.

(3) In regard to the proposed ship maneuvering model test series the authors make a strong emphasis on using bare hull models to systematically examine ship hull variations. Considering the strong hydrodynamic interaction of all three elements (hull/rudder/propeller) and practical orientation of these tests it is proposed to do just the opposite: to conduct a majority of the tests with the fully appended models and only some of them systematically stripped of appendages, and to study interaction effects in depth by measuring the forces on the appendages separately and with the model and examining the flow in their vicinity. The models should be as large as possible in order to provide meaningful measurements of the small forces on the appendages and to avoid significant scale effects. Tests should provide data on surge, sway, yaw, and roll forces and moments in the widest range of the speeds and propeller variations, perhaps, covering the complete four quadrants operations. Moreover, these data will serve as a basis not only for ship designers but also for the hydrodynamicist in further development of the math models and understanding a dynamic mechanism of ship-fluid interaction.

REFERENCES

1. Oltmann, P. and Sharma, S., "Simulation of Combined Engine and Rudder Maneuvers Using an Improved Model of Hull-Propeller-Rudder Interactions," 15th Symposium on Naval Hydrodynamics, Hamburg, September 1984.
2. Smitt, L., Chislett, M., "Large Amplitude PMM Tests and Maneuvering Predictions for a Mariner Class Vessel," 11th ONR Symposium on Naval Hydrodynamics, London, 1976.
3. "Model Test and Simulation Correlation Study Based on the Full-Scale 'Esso Osaka' Maneuvering Data," Report for MARAD MA-79-SAC-0097, Tracor Hydronautics, October 1980.

AUTHORS' REPLY

We wish to thank Mr. Motter for his supportive comments. It is indeed a tragedy that support is so difficult to obtain for running of maneuvering series. The availability of such series would permit the practical analysis of maneuvering capability on a more analytical basis (as done with ship powering). This more analytical approach would also permit analysis at the early stages of design. These are the stages where major dimensions are selected and maneuvering analysis should be performed but isn't because the current approach requires model testing of each variation!

Dr. Ankudinov also strongly embraces the approach where hull, propeller, and rudder changes are considered separately for the advantages of not only assisting with ship design analyses but also for the wide applications in the maneuvering simulation, pilot training, and port design areas and for the eventual contribution (after gathering of test data) to the further development and understanding of the dynamic mechanism of ship-fluid interaction.

Regarding his more critical comments, each of his three remarks has been discussed to some degree in the paper. The following additional rationale addressing each of his items in turn may help clarify the approach being advocated:

Item 1. In addition to the paper's arguments favoring use of the drift angle β we note that the speed projections u and v used in "conventional ship maneuvering equations" are not "clearly identified" with "the well-defined damping and inertia forces." From the standpoint of physics, the forces are not functions of u and v, but of β and r_d. It is true that in stability analyses which involve responses to small perturbations about equilibrium conditions the velocity terms are damping terms, and in oscillation experiments they occur as forces which are out of phase with, and oppose, the motion. On the other hand, in turning motions the velocity component v (which is functionally related to drift angle β) is responsible for the side force which forces the ship into the turn - it does not oppose the motion, and thus does not provide damping of the motion. The use of β and V in lieu of u and v provides for the correct sense of the force in either case.

Dr. Ankudinov discusses the artificial concept of derivatives as though they really exist in nature. The obvious difference between our approach and that described by Dr. Ankudinov is that his method is based on the mathematical model outlined in (1), combined with the separate determination of forces acting on the hull and the rudder. Our model is different in principle. We do not consider

any "derivatives." We are analyzing just physical forces and moments, introduced numerically as functions of and r_d, upon which they depend.

Item 2. It seems strange to see any objections to use of the angle of attack as a parameter for determining the hydrodynamic forces and moments acting on a wing. The structure of the formula for the angle of attack of the rudder

$$\alpha_r = \delta - K\beta_r$$

where

δ = rudder angle,
β_r = drift angle in the rudder vicinity,

has long been used and is derived from the direct consideration of the kinematics of rudder motion in the process of a maneuver. The coefficient K is not unknown. This coefficient was experimentally and theoretically investigated by several researchers. Nobody assumes that this coefficient is always constant. The nature of this coefficient should be better investigated. However, the use of such a coefficient is normal in similar hydrodynamic studies and is in full accordance with the physical phenomenon.

It is necessary to understand that in Figures 2 and 3 of Dr. Ankudinov's comments the curves N'and Y' are from experiments with models having rudders in place, and are thus associated with the "combined" approach to testing. This being the case, the effects of the rudder at zero rudder setting are already included in the forces and moments which are attributed to drift angle. The "effective" rudder angle for zero rudder setting will, in general, be different from zero. The coefficient takes account of this situation when the "differential" approach that is advocated in the paper is used.

Item 3. Nobody is arguing against tests using large models. Experimental studies, however, have demonstrated (see the additional reference (1), for example) that the scale effects in rotating arm tests are not significant. At the same time, the use of small facilities permits saving a substantial part of the cost of the tests.

Nor is anyone arguing against the use of stripping tests. However, the sequence of tests is not important. At the same time, the bare hull characteristics are basic and the bulk of information on these characteristics is the most limited. This is the reason why we suggest starting with the bare hull tests. The important interactions must be studied, but from our practice we know that the impact of possible discrepancies in interactions is not comparable with impact of wrong data on bare hull characteristics.

We thank our discussers for their contributions and appreciate the opportunity to clarify further the approach being advocated. We feel it is critically important to test a series of models and thus provide the data necessary to perform useful studies of maneuvering at the early stages of design.

Additional Reference:

1. Strumpf, A., "Analysis and Correlation of Captive Model Rotating Arm Tests Results of a Destroyer," Stevens Institute of Technology, Davidson Laboratory, Report SIT-DL-82-9-2264, February 1982.

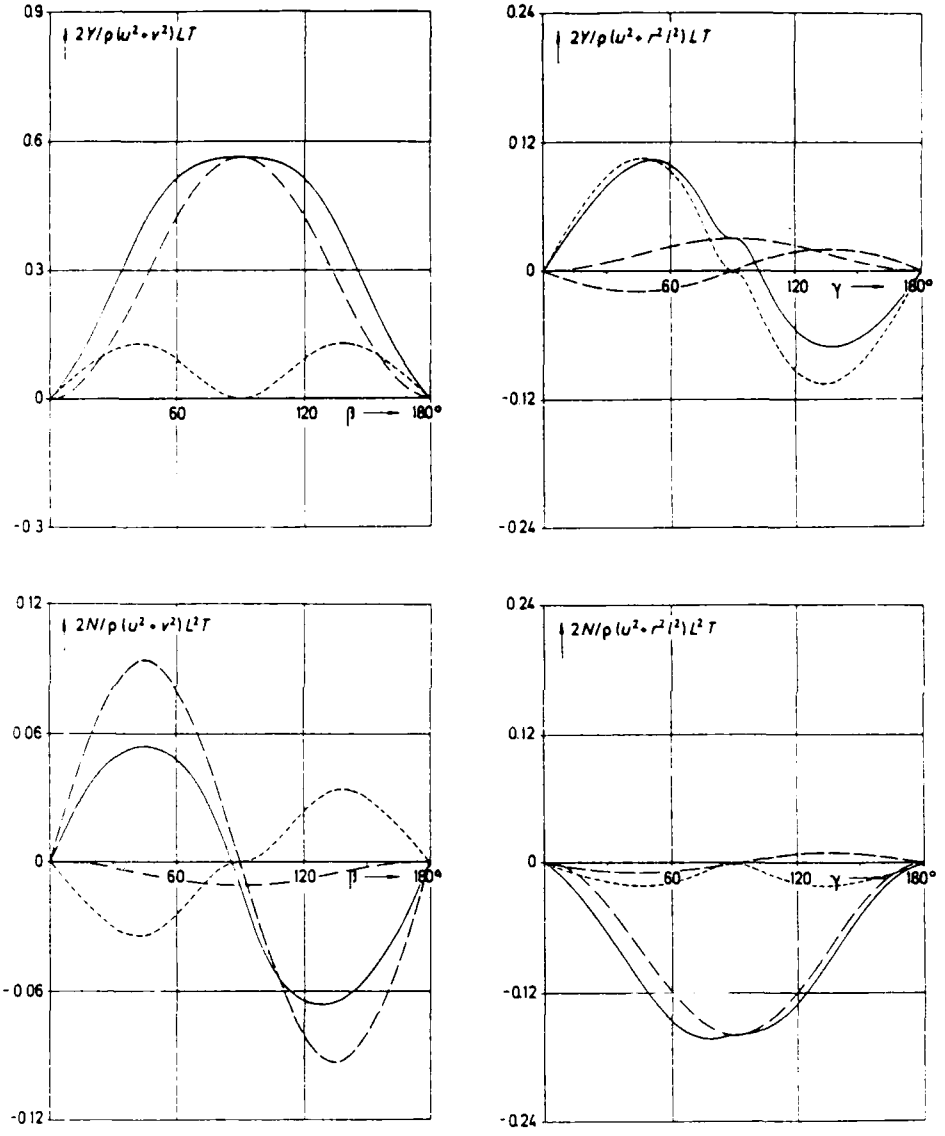

Side force (top) and yaw moment (bottom) on the tanker resulting from pure drift

Side force (top) and yaw moment (bottom) on the tanker resulting from pure yaw

Common legend
- Ideal fluid effects
- Lifting effects
- Cross flow effects
- Total

FIGURE 1 - LATERAL FORCES AND MOMENTS ON THE TANKER, REFERENCE 1

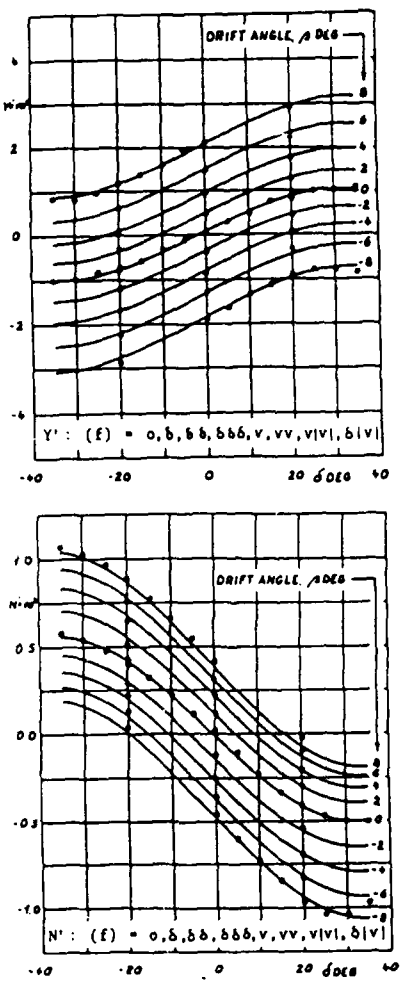

FIGURE 2 - STATIC DRIFT AND RUDDER ANGLE TEST. SIDE-FORCE AND TURNING-MOMENT VERSUS RUDDER ANGLE FOR VARIOUS DRIFT ANGLES, MARINER MODEL, REFERENCE 2

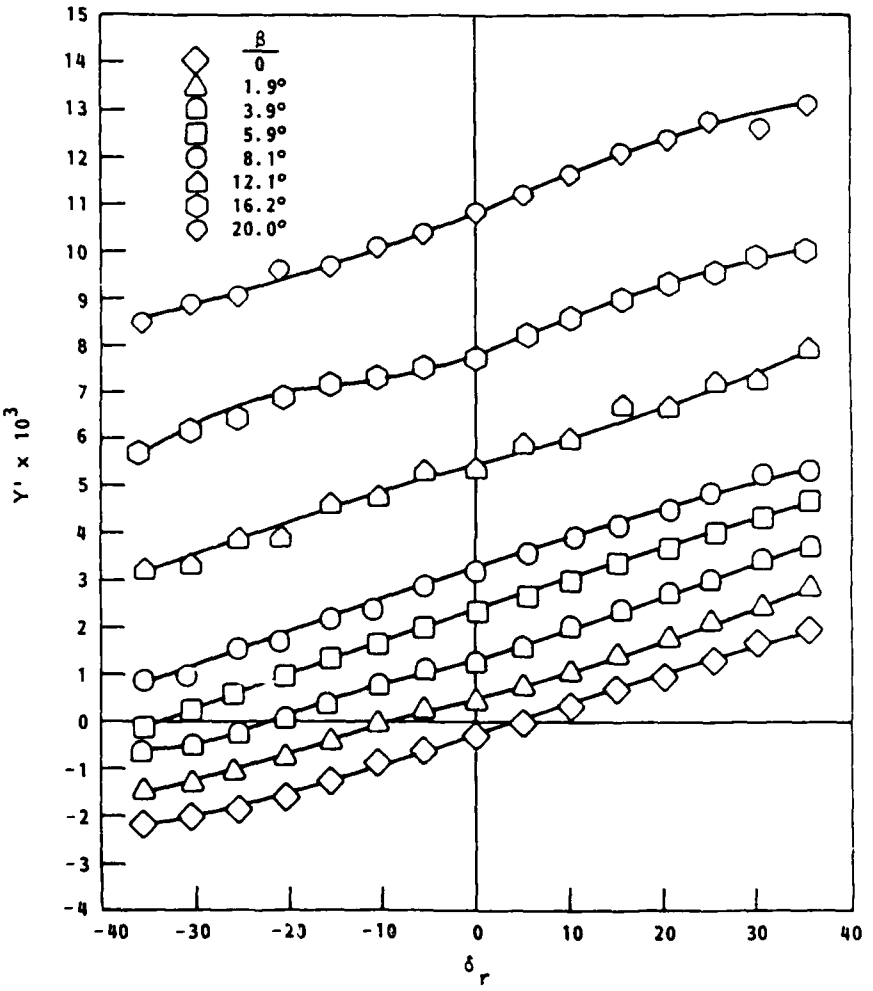

FIGURE 3 - LATERAL FORCE COEFFICIENT DUE TO THE RUDDER. DEEP WATER, ESSO OSAKA VLCC SHIP MODEL, REFERENCE 3

SESSION VI
ICE TESTING

TECHNICAL COMMITTEE MEMBERS

Dr. Stephen J. Jones (Chairman)	National Research Council of Canada
Mr. J.C. Tatinclaux	U.S. Army Cold Regions Research and Engineering Lab.
Dr. G.W. Timco	National Research Council of Canada
Dr. R. Ettema	Univ. of Iowa
Mr. A. Keinonen	Valmet Arctic Canada Ltd.
Mr. David N. Baker	Melville Shipping Ltd.
Mr. T.V. Kotras	Arctec Engineering Inc.
Mr. I. Glen	Arctec Canada Ltd.
CDR D.H. Humphreys	U.S.C.G

REPORT OF ICE TESTING COMMITTEE

Dr. Stephen J. Jones
National Research Council
Institute for Marine Dynamics
St. John's, Newfoundland, Canada

The Ice Testing Committee for the 21 ATTC consisted of:

Stephen J. Jones (Chairman) - National Research Council Canada
David Baker - Melville Shipping Ltd.
Rob Ettema - University of Iowa
Ian Glen - Arctec Canada Ltd.
David Humphreys - U.S.C.G.
Arno Keinonen - Valmet Arctic Canada Ltd.
Tom Kotras - Arctec Engineering Inc.
J-C Tatinclaux - C.R.R.E.L.
Gary Timco - National Research Council Canada

We held 3 meetings during the last 3 years:
24 September 1984 at NRC in Ottawa
7 May 1985 at CRREL in Hanover, N.H.
7 November 1985 at NRC in St. John's, Nfld. which included a brief joint meeting with ITTC Ice Committee.

At the CRREL meeting it was decided to enlarge the committee to its present membership to include not only ice tank operators, but also some members of the client community who had demonstrated their interest in ice tank technology over the years.

The committee reviewed all 8 abstracts submitted. They will be presented by their authors so I will only review them briefly. One paper, "Full Scale & Model Scale Correlations of the Ice Resistance of the R Class Icebreaker" by Howard et al has been withdrawn.

Piece Size Distribution

The piece size distribution in the broken channel left by an icebreaker was a major area of interest to the committee and three papers are presented under this general title. Tatinclaux will present data on the effect of ice-floe size on propeller torque in ship model tests; Kotras, Humphreys and Ettema will present results of both full scale and model scale tests of icebreaking patterns; and Comfort, Glen, Keinonen and Grinstead will discuss piece size distribution in model ice tests with the Kigoriak and compare with full scale data.

Ice Indexer

Baker will give a paper explaining the design and development of a model ice indexer, which, when fully developed, will allow the automatic measurement of the model ice properties. Tests which we have done at NRC are encouraging.

New Ice Tank

Jones will describe the National Research Council Canada's new ice tank in St. John's, Newfoundland. Originally submitted to the Committee on New Facilities and Technology, it was later decided to include it with the Ice Testing Committee.

Other Matters

Many other topics of interest were discussed at our meetings. It was felt that the committee could identify areas for which techniques have not been developed, and recommend areas where research should be done. It was as a result of the committee's desire to see some work done on propeller/ice interaction that the three papers on piece size distribution were developed.

A development in model ice technology which occurred in the last 3 years and which should be mentioned, is Timco's development of (another) new model ice. This is his B2/AD/3 ice - a mixture of ethylene glycol, aliphatic detergent and sugar. We at IMD are using it, and it will be interesting to see if other tanks switch to it. Details of it have been described in the literature. Its main advantage is a lower fracture toughness than urea ice which may help to more correctly model the piece size distribution.

EFFECT OF ICE-FLOE SIZE ON PROPELLER TORQUE IN SHIP-MODEL TESTS

Jean-Claude Tatinclaux
Research Hydraulic Engineer
U. S. Army Cold Regions Research
and Engineering Laboratory
Hanover, NH 03755-1290

ABSTRACT

Results of a laboratory study on ice-propeller interaction conducted with a model icebreaker are presented. The tests were made in ice-free water, precut channels with regularly shaped ice floes of different sizes, and brash-filled ice channels. The test results showed that the propeller torque and its standard deviation increased with both ice floe size and ship speed. The dominant frequency in the torque fluctuations was found to be related to either the propeller speed or the ratio of ship speed to floe width. The effect of ice ingestion on propeller thrust could not be determined because of malfunction of the thrust component of the propeller dynamometer.

The results suggest that difference in ice density and in ice-hull friction coefficient between model tests and full scale trials may be at least partially responsible for the lack of agreement between torque and powering requirements predicted from model propulsion test results and those measured during full-scale trials.

1. INTRODUCTION

1.1 Background

Unrealistically high power requirements for ships operating in level ice are often predicted from direct extrapolation of model propulsion test results, unless some empirical scale-effect factor is introduced. The lack of agreement between model test results and full-scale trial measurements was attributed by Keinonen (1983) to the fact that the ice floes broken by a ship model were relatively larger than full-scale floe size for corresponding test conditions. It was conjectured that the larger the ice floes passing through the propeller disk(s), the higher the torque exerted on and the lower the thrust delivered by the propeller(s), and, consequently, the higher the shaft power required to propel the ship at a given speed through level ice.

A previous laboratory study (Tatinclaux 1985, 1986) investigated the size distribution of ice floes created by a simple wedge towed through level ice as a function of ice properties (thickness h, bending strength, characteristic length) and towing speed V. The test results indicated that the floe size distribution followed a log-normal probability density function, as found from field observations (McKindra and Lutton, 1981), and that the mean floe size, adimensionalized with respect to ice thickness, was only a function of the parameter $\frac{\sigma}{\gamma_w h}$ (γ_w = specific weight of water). Field confirmation of this latter result could not be ascertained because of the lack of reliable field measurements of floe size and ice properties during full-scale trials.

1.2 Current study

A second approach to the problem of ice-propeller interaction and possible corresponding scale effects in model tests was attempted by performing propulsion tests in presawn channels in level ice with known ice floe dimensions. This study, the results of which are summarized in this paper, was conducted with a 1:9.273 scale model of the U.S. Coast Guard Great Lakes icebreaker "Katmai Bay." This 2500-hp, 140-ft-long icebreaker was designed to break 18 in. (45 cm) of level ice at a continuous speed of 3 knots (1.54 m/s).

2. TEST CONDITIONS AND PROCEDURES

2.1 Ice conditions

All tests were made in about 5-cm-thick ice. Three sawcuts, one along the towing tank centerline and one 60 cm (2 ft) on each side of the center cut, were made in the level ice sheet. The resulting ice channel was then cut into ice floes of regular size or broken up manually into pieces one to two ice thicknesses in plan dimensions to simulate brash ice channels. In a first series of tests, three floe sizes were evaluated, namely 20x20 cm (8x8 in.), 30x30 cm (12x12

in.), and 60x40 cm (24x16 in.). In a second series of tests, only the 60x40-cm floes and the brash ice conditions were investigated. Photographs of channels with 60x40-cm floes and with brash ice are shown in Figure 1.

2.2 Test procedure

The icebreaker model was attached to the towing carriage by means of a tow post and was therefore totally restrained in surge and sway. It was, however, free to heave, pitch and roll, and was restricted in yaw. A 1.5-hp, variable speed DC motor was used to power the four-bladed model propeller, which was 11 in (28 cm) in diameter. A dynamometer mounted between the motor and the propeller shaft measured the propeller thrust and torque. A magnetic pick-up over a 60-tooth gear mounted on the propeller shaft was used to measure the propeller speed of rotation. Finally, a force block mounted between the tow post and the ship model to measure the net propeller pull completed the instrumentation.

In the first test series, the carriage speed was kept constant at 50 cm/s (20 ips) which corresponded to a full-scale speed of 3 knots, and three nominal propeller speeds of 725, 775 and 825 rpm were used. Each test followed the same procedure: the propeller speed was set at the lowest rpm to be investigated, and the carriage was set in motion at the prescribed speed once the data acquisition system had been checked. At about one-third of the tank length the propeller speed was switched to the intermediate value, and at two-thirds of the tank length the propeller speed was changed to its third and final value. Each test section was thus performed over a distance of 14 to 11.5 m (46 to 38 ft), or about 2.7 ship lengths.

In the second series of tests three carriage speeds were investigated, namely 16.7 cm/s (6.5 ips), 33.4 cm/s (13 ips) and 50 cm/s (20 ips), corresponding to full-scale ship velocities of 1, 2, and 3 knots, respectively. The three propeller speeds tested were changed to 525, 575, and 625 rpm, because initial analysis of the first test results indicated that the rated torque capacity of the dynamometer (100 in.-lb or 11.3 Nm) and the rated power of the driving motor were exceeded at times for propeller speeds greater than 700 rpm. In addition the test procedure was slightly modified: once the ice channel had been prepared, the propeller speed was set at a particular value and the carriage set in motion at a prescribed speed V. At one-third of the tank length, the carriage was stopped, the model was backed a few meters, a second propeller speed was set and the carriage was restarted at the same speed as before. This second

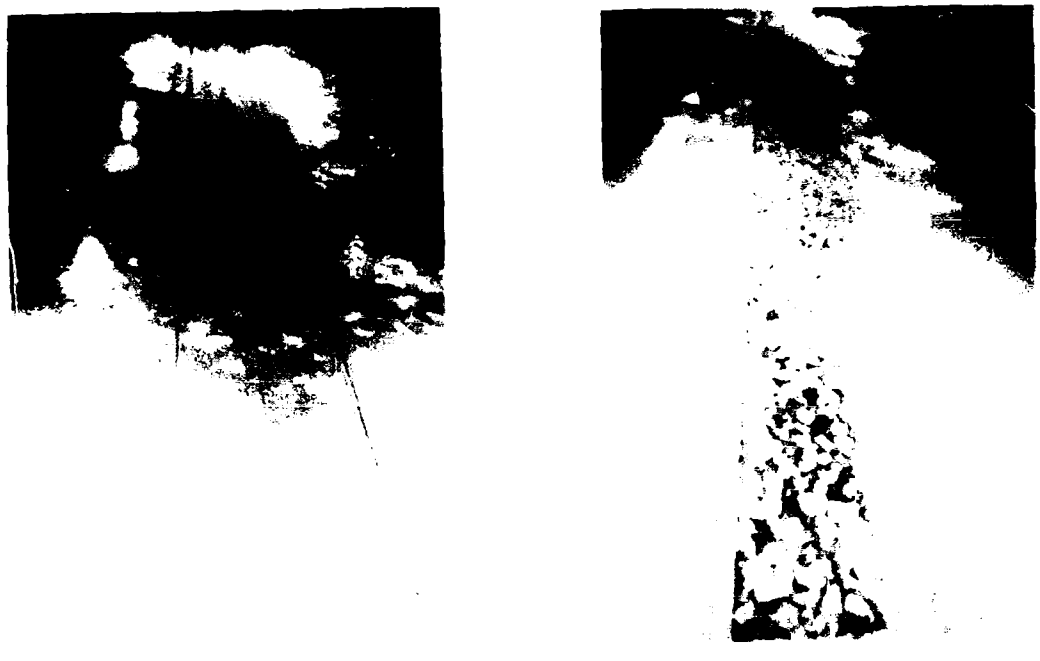

a. 60 x 40 cms floes

b. brash ice

Figure 1. Views of ice channels

test was performed over the second third of the tank length. The procedure was then repeated over the last third of the tank length for the third propeller speed to be investigated. In backing the model, the channel was usually cleared of nearly all ice. Therefore, the initial part of each run was made in an ice-free channel, which allowed direct comparison between propeller performance in ice free water and in the ice-filled channel.

2.3 Data acquisition

During the tests, five data channels were constantly monitored: carriage speed, propeller speed, propeller thrust and torque, and net pull between ship model and towing post. The analog signals were digitized and sampled at a rate of either 40 or 50 Hz, i.e. the sampling interval was 25 or 20 ms. The analog signals also were monitored graphically on chart recorders as a visual means of checking the proper functioning of the instrumentation.

3. EXPERIMENTAL RESULTS

3.1 Data presentation

After the first series of tests was completed, it was found that the thrust output of the dynamometer had developed problems and was giving erratic signals. The effect of ice-propeller interaction on propeller thrust could not be ascertained and the data analysis was therefore limited to propeller torque. The torque average and standard deviation were calculated for each test condition. In addition the dominant frequency f of the torque signal was determined from a fast Fourier transform of the digitized data. The test data are tabulated in Table 1 for the first series of experiments. The results of the second test series obtained with the 60x40 cm floes are listed in Table 2a, and those obtained in brash ice are listed in Table 2b. Examples of the traces of propeller speed, propeller torque and carriage speed are shown in Figure 2a for the case of large ice floes (60x40 cm) and in Figure 2b for the case of brash ice.

3.2 Data analysis

Figure 3 presents the torque Q and its standard deviation S_Q versus velocity V for the cases of ice-free run, brash ice, and 60x40-cm ice floes, respectively, for three values of propeller speed, namely n = 8.6 rps (Fig. 3a), n = 9.6 rps (Fig 3b), and n = 10.4 rps (Fig. 3c). For the case of ice-free water, the torque decreased with velocity as was expected while the standard deviation remained constant with velocity. In the case of large ice floes, both the torque Q and standard deviation S_Q increased significantly with increasing velocity. Finally, for the brash ice case Q and S_Q also increased with V but at a much smaller rate. It can also be observed from Figs 3a to 3c that while Q in-

Table I. Results of First Series of Tests

Test #	Ice Conditions	h (cm)	V (cm/s)	n (rps)	Q (Nm)	S_Q (Nm)	V/W (s^{-1})	f (Hz)
111	No Ice	-	50.9	12.2	7.2	0.3	-	-
		5	50.7	12.1	9.5	2.2	1.7	1.7
	30x30 cm	5	50.4	12.7	10.7	2.2	1.7	1.7
	Ice Floes	5	50.4	13.0	11.2	2.1	1.7	1.7
121	No Ice	-	50.8	12.4	7.5	0.2	-	-
	20x20 cm	4.5	50.7	12.3	9.1	1.5	2.5	2.7
	Ice Floes	4.5	50.3	12.9	9.6	1.6	2.5	2.7
		4.5	50.2	13.7	11.0	1.5	2.5	2.7
131	No Ice	-	50.3	12.4	7.6	0.4	-	-
		4.5	50.1	12.4	8.7	0.8	-	1.4
	Brash Ice	4.5	49.7	12.9	9.5	0.8	-	6.3
		4.5	49.5	13.9	11.1	0.7	-	6.1
141	No Ice	-	50.5	12.1	7.2	0.2	-	-
		4.7	50.3	12.1	8.5	1.5	1.3	1.7
	60x40 cm	4.7	50.1	12.6	9.5	1.6	1.3	1.3
	Ice Floes	4.7	49.8	13.3	11.2	1.4	1.3	1.3
151	No Ice	-	51.1	12.1	7.3	0.4	-	-
		4.7	50.9	12.1	8.4	0.9	-	5.5
	Brash Ice	4.7	50.5	12.6	9.7	1.1	-	3.9
		4.7	50.3	13.6	10.7	0.8	-	-

Table II. Results of Second Series of Tests

a. 60x40 cms Ice Floes

Test #	Ice Conditions	h (cm)	V (cm/s)	n (rps)	Q (Nm)	S_Q (Nm)	V/W (s^{-1})	f (Hz)
201	No Ice	-	50.4	8.7	3.9	0.6	-	8.4
	60x40 cms floes	5	50.4	8.7	7.0	2.5	1.26	1.2
202	No Ice	-	50.3	9.6	4.4	0.8	-	18.9
	60x40 cms floes	5	50.3	9.6	8.1	2.5	1.26	1.25
203	No Ice	-	50.1	10.5	5.7	1.0	-	19.5
	60x40 cms floes	5	49.8	10.4	8.0	2.3	1.25	1.25
221	No Ice	-	33.4	8.7	4.2	0.7	-	8.6
	60x40 cms floes	5	33.3	8.7	5.1	1.5	0.83	1.17
222	No Ice	-	33.3	9.6	5.1	0.8	-	9.50
	60x40 cms floes	5	33.2	9.5	6.6	1.9	0.83	1.23
223	No Ice	-	33.1	10.3	6.0	0.9	-	9.50
	60x40 cms floes	5	33.0	10.3	7.2	1.7	0.83	0.85
261	No Ice	-	16.3	8.6	4.2	0.6	-	8.6
	60x40 cms floes	5	16.3	8.6	4.7	1.2	0.41	0.40
262	No Ice	-	16.3	9.5	5.0	0.8	-	19.0
	60x40 cms floes	5	16.2	9.5	5.7	1.4	0.41	0.44
263	No Ice	-	16.2	10.3	5.9	0.9	-	20.60
	60x40 cms floes	5	16.2	10.3	6.6	1.5	0.41	0.44

b. Brash Ice

Test #	Ice Conditions	h (cm)	V (cm/s)	n (rps)	Q (Nm)	S_Q (Nm)	V/W (s^{-1})	f (Hz)
211	No Ice	-	50.5	8.8	3.7	0.6	-	17.2
	Brash Ice	5	50.5	8.8	5.3	1.6	-	8.6
212	No Ice	-	50.3	9.8	4.7	0.8	-	19.0
	Brash Ice	5	50.1	9.7	6.4	1.5	-	19.0
213	No Ice	-	50.1	10.5	6.4	1.0	-	19.4
	Brash Ice	5	49.9	10.5	8.1	1.8	-	19.4
235	No Ice	-	33.6	8.7	4.0	0.7	-	16.2
	Brash Ice	5	33.6	8.7	4.9	1.3	-	8.6
236	No Ice	-	33.5	9.5	4.8	0.8	-	9.4
	Brash Ice	5	33.3	9.5	5.4	1.1	-	9.4
237	No Ice	-	33.3	10.3	5.6	1.0	-	12.8
	Brash Ice	5	33.2	10.3	6.0	1.1	-	12.8
231	No Ice	-	32.9	11.4	7.6	1.1	-	10.7
	Brash Ice	5	33.0	11.4	8.2	1.5	-	10.7
232	No Ice	-	33.0	12.6	9.2	1.0	-	8.3
	Brash Ice	5	32.8	12.6	10.2	1.6	-	8.3
233	No Ice	-	33.4	13.4	10.3	0.9	-	13.3
	Brash Ice	5	33.2	13.3	11.0	1.4	-	13.3
271	No Ice	-	16.9	8.6	4.4	0.8	-	17.2
	Brash Ice	5	16.8	8.6	5.0	1.2	-	8.6
272	No Ice	-	16.8	9.5	5.1	0.8	-	19.0
	Brash Ice	5	16.7	9.5	5.7	1.2	-	19.0
273	No Ice	-	16.7	10.3	6.0	0.9	-	20.7
	Brash Ice	5	16.6	10.3	6.5	1.2	-	20.7

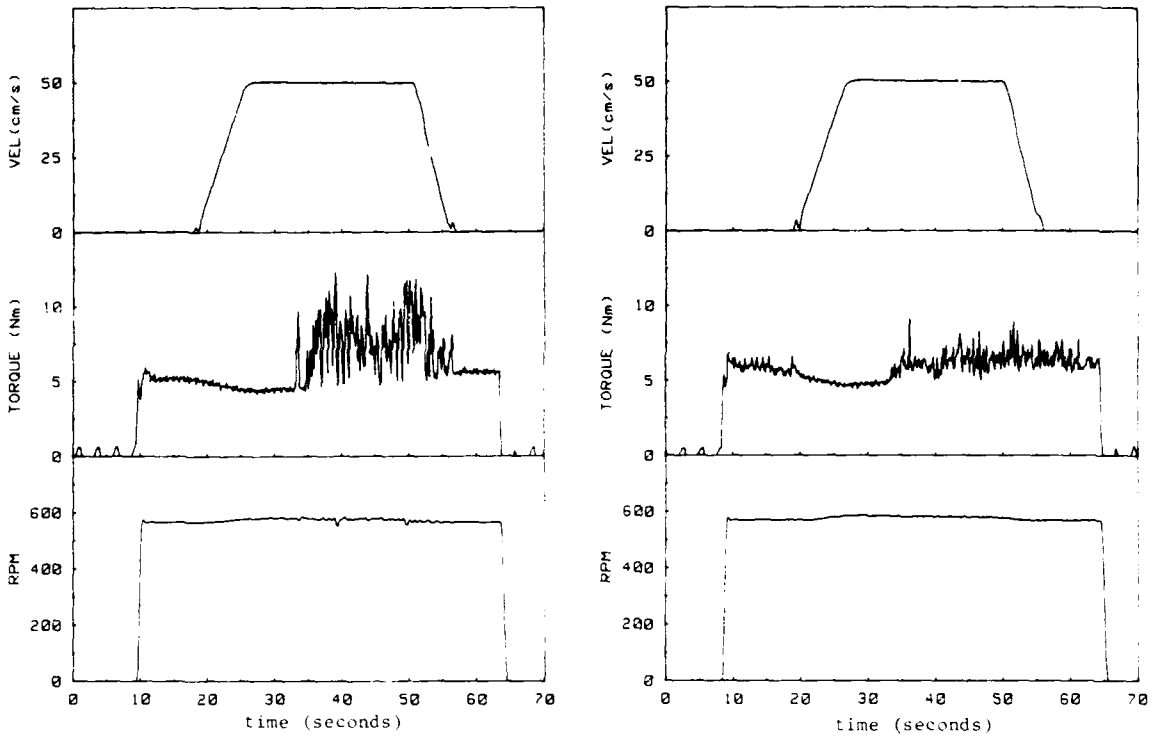

a. Test No. 202 - 60 x 40 cms floes

b. Test No. 212 - brash ice

Figure 2. Examples of data signals (n=575 rpm, v=50 cm/s)

creased with increasing propeller speed, as was to be expected, the standard deviation S_Q was practically independent of n.

The torque measurements for all the tests run with large ice floes and brash ice, and under ice-free conditions are presented in non-dimensional form in Figure 4 as torque coefficient $K_Q = Q/\rho n^2 D^5$, where ρ = water density and D = propeller diameter, versus advance coefficient J = V/nD. It can be seen that while K_Q decreased with J for ice-free conditions, it increased rapidly with J for the tests in large ice floes, and either remained nearly constant or increased only slowly with J for the brash ice case. Comparison of the results obtained at a common value of J of about 0.135 (Fig. 5) showed that K_Q increased approximately linearly with floe width, at least within the range of floe sizes investigated here.

The variations of S_Q with velocity V are shown on Figure 6. For ice-free conditions, S_Q was independent of V and reflected minor imbalance of the propeller and friction on or slight misalignment of the propeller shaft. The results of the tests with large ice floes showed a rapid increase of S_Q with V, indicating an increase in ice ingestion and ice-propeller interaction as the ship velocity increased. The results obtained with brash ice fall within the two extreme cases of ice-free and large ice floes conditions, with S_Q remaining approximately constant for V up to 33 cm/s and increasing significantly for V = 50 cm/s. The effect of floe size on S_Q is further illustrated in Figure 7, where the results obtained at the same ship speed of 50 cm/s plotted versus floe width show S_Q increasing rapidly with floe size.

Examination of the values of the dominant frequency of the torque signal listed in Tables 1 and 2 shows that, for the case of ice-free tests, the dominant frequency f was equal to the propeller speed n or to a multiple of n. For the tests run in a channel filled with discrete ice floes, f was found to be equal to the ratio V/W, where W is the width of the ice floes, or to a multiple of this ratio.

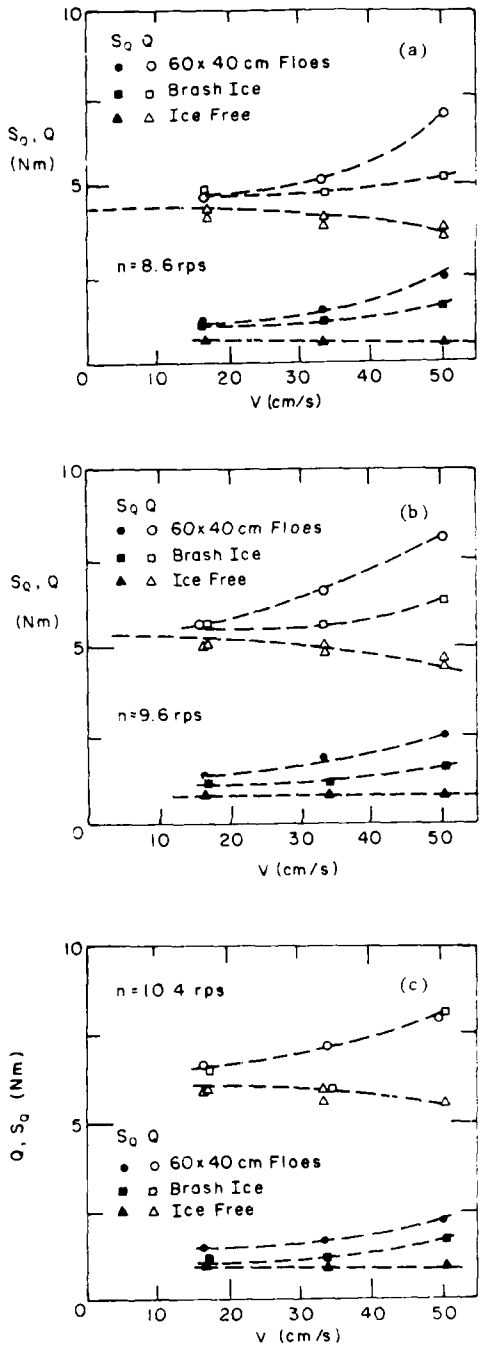

Figure 3. Variation of torque average and standard deviation with model speed

a. n=8.6 rps
b. n=9.6 rps
c. n=10.4 rps

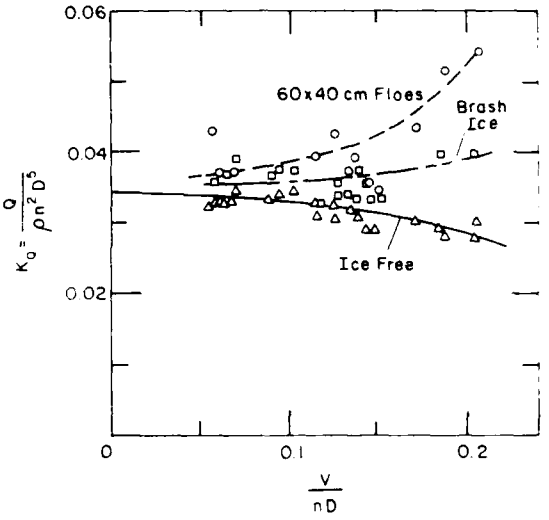

Figure 4. Variation of torque coefficient with advance coefficient

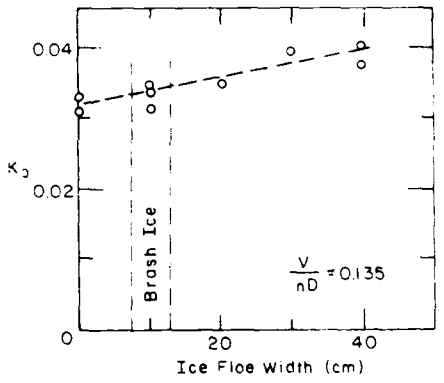

Figure 5. Variation of torque coefficient with model floe width (v=50 cm/s)

4. DISCUSSION OF RESULTS AND FUTURE STUDIES

The results of the present study do indicate that propeller torque increases with increasing floe size. Therefore, if inceed the model ice used in propulsion model tests breaks in relatively larger floes than real ice, the torque and corresponding power requirements predicted from model test results would be excessive. The effect might be further exaggerated if the propeller thrust does decrease with floe size as can be expected. Additional tests need to be conducted to investigate the effect of floe size on propeller thrust.

AD-A196 627 PROCEEDINGS OF THE AMERICAN TOWING TANK CONFERENCE (21ST) HELD IN WASHINGTON DC ON 5-7TH AUGUST 1986(U) NATIONAL RESEARCH COUNCIL WASHINGTON DC R F MESSALLE 4/6

UNCLASSIFIED AUG 87 F/G 13/10 NL

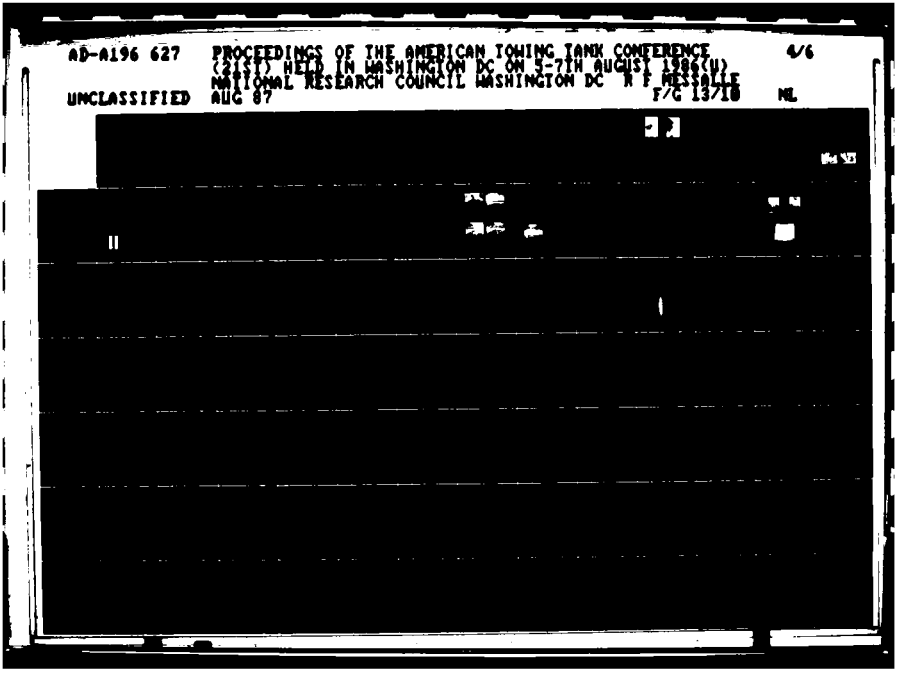

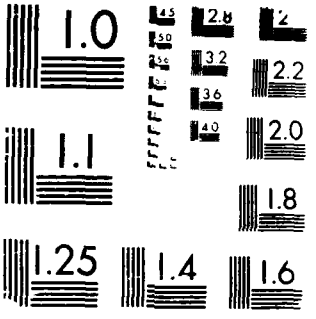

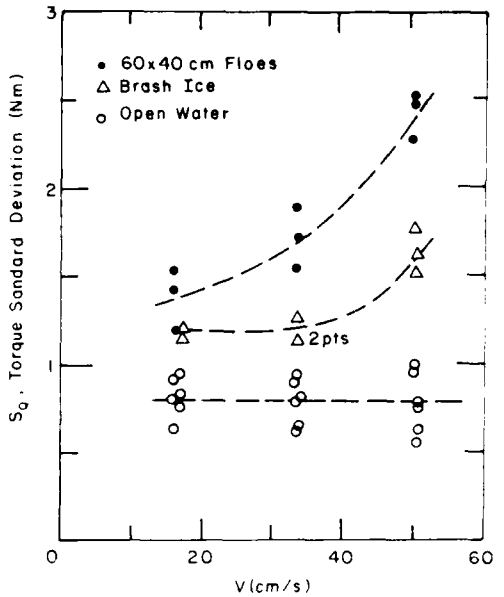

Figure 6. Variation of torque standard deviation with model speed

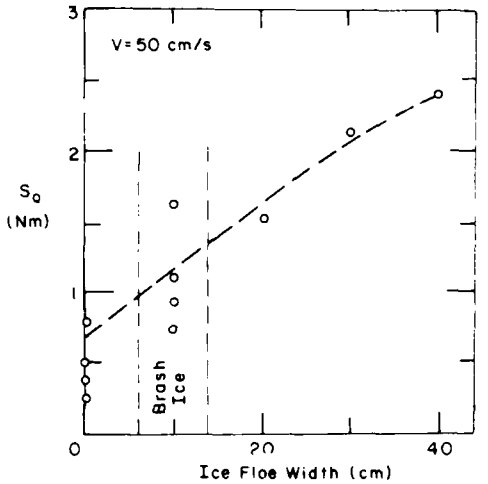

Figure 7. Variation of torque standard deviation with floe width

The detrimental effect of ice ingestion on propeller torque was also seen to increase rapidly with ship velocity. An ice floe broken by the ship bow is first submerged and then rises to the free surface as the vessel moves by. The rise velocity of the ice floe, w_i, and therefore its rise time, t_i, are functions of the ice specific gravity, s_i, the ice-hull friction coefficient, and possibly the floe shape and dimensions. The time required for the ship to travel one ship length is $t_s = L_{WL}/V$, where L_{WL} is the ship length at the water line. As long as t_s is greater than t_i, i.e. at low ship speed, it can be expected that most of the broken ice floes will reach the water surface before they enter the propeller area. Little or minor ice-propeller interaction can then be expected. However, as V increases and t_s decreases to a value nearly equal to t_i or below, the ice floes may reach the propeller area before they can reach the free surface. They become entrained into the propeller disc, resulting in significant ice-propeller interaction. Model ice such as the urea-doped ice used in the current study has a specific gravity of about 0.93, greater than the specific gravity of either freshwater ice or sea ice. It can thus be expected that the corresponding rise velocity of urea-ice model floes is relatively lower than that of sea-ice floes. Ice ingestion in the propeller and corresponding detrimental ice-propeller interaction can thus be expected to occur at a lower ship speed and to be more pronounced at the model scale than at full scale. It can also be conjectured that variations in ice hull friction coefficient will affect the floes rise velocity and, therefore, ice ingestion by the propeller(s). An analytico-numerical study of the effect of ice specific gravity and ice-hull friction on ice floe trajectory along an idealized hull is underway at CRREL.

5. SUMMARY AND CONCLUSIONS

The current experimental laboratory study on ice-propeller interaction during model propulsion tests has shown that the propeller torque and its standard deviation increased with both ice floe size and ship velocity. The torque coefficient K_Q was found to increase rapidly with the advance factor J for ice floes with plan dimensions of the order of 10 times the ice thickness, while it remained constant or increased only slightly with J for brash ice, i.e. for ice floes of plan dimensions of one to two ice thicknesses.

Additional tests are planned to confirm the above results, and to investigate the effect of floe size and ship velocity on the propeller thrust, which could not be ascertained in this study because of a malfunction of the thrust component of the dynamometer.

It is suspected that model ice specific gravity and ice-hull friction coefficient may significantly affect propeller performance in ice during model tests. An analytical study is underway to address these questions.

The overall goal of the current and future research efforts by the author is to develop model testing procedures and data analysis methods that will allow the full-scale performance of ships in ice to be predicted more reliably.

ACKNOWLEDGMENTS

This study was funded by CRREL's In-House Laboratory Independent Research Program. The author gratefully acknowledges the help that he received from his colleagues at CRREL in one capacity or another. In particular many thanks are due Mr. Carl Martinson, Mechanical Engineering Technician, who was in charge of setting up the tests and driving the test carriage, and who, together with Mr. Gordon Gooch, had the task of sawing the ice channel in the requested piece sizes.

REFERENCES

Keinonen, A. (1983): Major Scaling Problems with Ice Model Testing of Ships. Proceedings, 20th American Towing Tank Conference, vol. II, Hoboken, N.J.

McKindra, C.D. and Lutton, T.C. (1981): Statistical Analysis of Broken Ice Dimensions Generated during 140-ft WTGB Icebreaker Trials. Proceedings, 6th International Conference on Port and Ocean Engineering under Arctic Conditions (POAC 81), vol. 1, Quebec, Canada.

Tatinclaux, J.C. (1985): Level Ice Breaking by a Simple Wedge. U.S. Army Cold Regions Research and Engineering Laboratory, CRREL Report 85-22.

Tatinclaux, J.C. (1986): Ice Floe Distribution in the Wake of a Simple Wedge. Proceedings, 5th International Symposium and Exhibit on Offshore Mechanics and Arctic Engineering (OMAE), vol. IV, Tokyo, Japan.

COMPARISON OF USCG POLAR CLASS ICEBREAKING PATTERNS: FULL SCALE TRIALS, PHYSICAL MODEL TESTS AND ANALYTICAL PREDICTIONS

T. KOTRAS, D. HUMPHREYS
R. ETTEMA AND A. FREE
USA

ABSTRACT

One of the areas which have been of continuing interest to investigators involved in the field of ice engineering has been concerned with the icebreaking pattern around an icebreaker. More specifically, this concern has been related to: What is the true icebreaking pattern around a ship as it proceeds through the ice? What is the true initial broken ice piece size? What is the influence of this icebreaking pattern and size on ice resistance? How do full scale tests, model scale tests, and analytical prediction techniques compare? The objective of this paper is to attempt to answer these questions, in part, by comparing the results of full scale ice performance trials, physical model tests, and analytical predictions for the USCG's POLAR Class icebreakers. The full scale ice performance trials were conducted in the Bering Sea and in McMurdo Sound, Antarctica. The physical model tests were conducted at the University of Iowa's ice tank. The analytical model predictions were developed as part of the USCG Naval Engineering's ongoing efforts to develop predictive tools for estimating performance of icebreaking ships to operate in ice covered waters.

1. INTRODUCTION

As an icebreaking ship proceeds through an ice field, the ice breaks under the forces imposed by the ship's bow. The shape and size of the broken pieces are a direct result of the ship's bow form and speed, and the ice thickness and strength. In both physical and analytical modeling of icebreaking ship performance, assumptions about the icebreaking pattern and broken piece size are necessary.

Full scale measurements are time consuming and usually receive a low priority during full scale test planning. For accurate and careful measurements, it is necessary to stop the ship and back down so that the region just under the bow may be examined and the pieces measured. This sometimes dangerous and always time consuming activity is usually left undone because of the time constraints and testing priorities. Occasionally, estimates of piece size and geometry can be made on the move. A technique to estimate piece size on the move was applied and these full scale results are reported.

Extensive model scale tests are continuing at the University of Iowa, Institute of Hydraulic Research. The results of these tests include underwater video observations of icebreaking patterns, in addition to investigation of hull motions and level ice resistance.

This paper is an attempt to present both the model scale and the sparse full scale icebreaking pattern and piece size data, obtained with the U.S. Coast Guard's POLAR Class icebreakers.

2. ANALYTICAL PREDICTION

As part of the development of computer model for predicting ship performance in level ice (SPLICE MODEL), developed for the U.S. Coast Guard's Design Branch of Naval Engineering), a mathematical representation for the icebreaking pattern for an icebreaking hull form was developed [1]*. In defining the icebreaking pattern, it is assumed that the ice breaks in a consistent and predictable manner, in order that a steady-state resistance might be achieved. In its simplest form, this breaking pattern can be viewed as a series of cusps, modeled as semi-ellipses, running from the stem of the ship along the hull as shown in Figure 1.

Utilizing ice cusp data obtained aboard the USCGC STATEN ISLAND, JELPARRM, and FINCARRIER depicted in Figure 2, the SPLICE MODEL used an optimization routine to obtain

* Numbers in brackets denotes References at end of paper.

the best fit for full-scale ice trials data for the following five icebreaking ships: KATMAI BAY, MACKINAW, PIERRE RADISSON, STATEN ISLAND and SS MANHATTAN. These five ships ranged in size and hull shape from an icebreaking tug to an icebreaking tanker. The results of this optimization procedure resulted in the following expression:

$$\frac{D_c}{K_1 \ell_c} = \frac{1}{2.4 + 6.0\,\overline{V}} \qquad (1)$$

where

D_c = Cusp depth

$k_1^c = 50.7\,N_3^2 - 64.5\,N_3 + 21.3$

N_3 = Average direction cosine over forward 20% of ship's length (0.712 for USCG POLAR STAR and POLAR SEA)

ℓ_c = Ice characteristic length

$$= \left(\frac{Eh^3}{12(1-\nu^2)\rho g}\right)^{1/4} \qquad (2)$$

$$\overline{V} = (\sin\alpha/\tan\beta') \bullet (V/\sqrt{g\ell_c}) \qquad (3)$$

α = Hull waterline angle at center of cusp

β' = Normal flare angle at center of cusp

E = Young's modulus for ice

h = Ice thickness

ν = Poisson's ratio for ice

g = Acceleration due to gravity

V = Ship's forward speed

ρ = Mass density of water

3. FULL SCALE RESULTS

As part of the 1985 Antarctic deployment of USCGC POLAR STAR, icebreaking pattern data was gathered in ice thicknesses of 3.0, 3.7, and 4.9 feet at ship speeds of approximately 2 knots. A summary of the cusp depth observed during these tests is presented in Table I [2]. Additional data was gathered aboard the USCGC POLAR SEA during the 1985 Bering Sea Deployment as illustrated by Figure 3 [3].

In Figure 4, the estimated cusp depth using Equation (1) is shown as a function of ice thickness. Superimposed on this figure is the average cusp depth distribution for the three measured ice thicknesses. Based on this plot and realizing the limited data and methodology used to gather it, the following conclusions were drawn:

1. The cusp depth prediction given by Equation (1) appears to give a reasonable estimate of the averge depth of icebreaking cusps as function of ice thickness for POLAR Class vessels.

2. There is a broad range of cusp sizes for a given set of similar ice thickness, ship speed, and hull location conditions.

3. The basic icebreaking pattern of "cusp failure" was observed to be the primary ice failure process.

TABLE 1. SUMMARY OF ICE CUSP DEPTH DATA

	ICE THICKNESS (ft)		
	3.0	4.0	5.0
Ship speed (knots	2	2	2
Equation (1) Cusp Depth (ft)	11	15	18
Prediction (ft)			
Observed Data			
Mean Cusp Depth (ft)	12	16	17
50% Range of Cusp Depth (ft)	± 2	± 3	± 3
90% Range of Cusp Depth (ft)	± 4	± 4	± 5

4. PHYSICAL MODEL SCALE TESTS

A series of model scale tests were conducted with the aim of determining the relationships between icebreaking, hull motions, and level ice resistance. The tests were conducted at the Iowa model ice tank (20 meters long, 5 meters wide) and involved the use of a 1:48 scale, 3 meter long, model of a POLAR Class icebreaker hull. The test hull was towed the full length of the tank so that time histories of resistance together with pitch, heave, and roll motions (displacements as well as accelerations) would be sufficiently long to facilitate accurate time series analyses. The tests were divided into two companion parts: in one, the hull was free to pitch, heave, yaw, and roll; in the other, the hull was restrained from moving. The results from the two sets of tests were compared to reveal the interrelationships between hull motions, icebreaking, and resistance. At the time of presentation of this paper, tests (involving stronger ice) were still underway. The test results presented here are limited to hull speeds ranging from 0.05 to 0.9 m/s (about 0.2 to 3.2 kts prototype speed) and flexural strengths of about 18 to 25 KPa (about 860 to 1200 KPa prototype strength). For each test, icebreaking was viewed and recorded using an underwater video camera. A clock, with 0.01 second precision, synchronized the video to the time histories of resistance and motions.

4.1 Observations of Model Scale Icebreaking

Two processes characterized the way by which a POLAR Class hull broke sheets of urea ice: shearing and crushing of ice at the bow's stem, and flexure of ice depressed by the bow's flared faces. The interaction and relative importance of these breaking

processes varied with hull speed, thickness of ice sheet, hull motions, and were influenced by the comparative plasticity of urea ice tempered to flexural strengths of about 20 KPa or less. Although the effect on icebreaking of ice sheet strength has yet to be examined in the tests, they have inadvertently shown (when the test hull struck a stray, stronger patch in an ice sheet) that it plays a significant role, especially through modifying hull motions. Hull motions influenced icebreaking by altering the geometry and rate by which the bow loaded the ice sheet and made the cyclic icebreaking processes more broad-banded then they were when the hull was restrained from moving. Even for steady towing speeds, icebreaking patterns were often observed to vary along the track broken by the hull.

Although some major variations of icebreaking patterns were observed, Figure 5 is an attempt to depict schematically icebreaking as was observed through the underwater video camera. Space here precludes a full, well-illustrated, discussion of the observed variations in icebreaking.

When the test hull moved through a sheet of urea ice, (its bow depressed the ice sheet, simultaneously crushing and shearing the ice at the bow's stem and, after a brief interval, flexurally broke a cusp on each side of the bow. The circumferential crack produced by flexure appeared first at the center of the cusp then propagated toward the bow's stem and its shoulder. For relatively higher speeds and thinner ice, the breaking length associated with the cusp was shorter (see Figure 6) causing the circumferential cracks to align more parallel to the bow's waterline, forming a strip-like cusp. However, for lower speeds and thicker ice, the loading geometry varied during the propogation of the circumferential crack because the larger pitch motions of the bow increased the pitch angle. The cusps were more curved, and were somewhat wider near the bow's stem because of shearing/crushing in the contact zone during the flexural failure of the cusp. It is likely that the plasticity of urea ice, by reducing the speed of flexural crack propagation compared to the rate of shearing/crushing at the bow, may have affected to the form and size of the cusps.

In all cases, the cusps were further fractured when overriden by the hull. Smaller cusps were more readily deflected downwards and passed beneath the bow. However, relatively large cusps, especially for thicker ice, were confined by the bordering ice sheet such that the bow's stem was forced to continue shearing/crushing through the cusps before they were deflected beneath the hull.

Viewed from above the hull, all that could be seen of icebreaking was the formation of a sequence of semi-circular cusps lodged around the perimeter of the bow's shoulder.

4.2 Geometry of Broken Ice

Generally, the length of the circumferential crack leading to the formation of a cusp each side of the bow was approximately equal to the waterline distance from the bow's stem to its shoulder, for the condition of trim that the crack formed. The length of this crack varied slightly with ice sheet thickness and hull speed. Once the hull overrode a cusp freshly broken from an ice sheet, the cusp was broken to smaller fragments, as schematically depicted in Figure 5.

Measured values of initial cusp depth, D_6, plotted in Figure 7 show that cusp depth width increased with increasing ice sheet thickness, h, and decreased with increasing hull speed, V. The values of D_c are average widths measured for several cusps beneath the bow, not in the track behind it. The ratio of cusp width to ice sheet thickness, D_c/h, ranged from about 3 to 5, for hull speeds of 0.5 m/s and above, to about 7 for creeping speeds of 0.05 m/s. The variation of D_c/h with V can be attributed, in part, to the hydrodynamics of water displacement during ice sheet deflection, and in part to altered geometry of loading associated with the simultaneous shearing and flexing of the ice sheet.

After passing beneath the hull, the ice cusps were broken to form smaller cusps and wedges which were arrayed in rows, whose regularity was affected by hull speed. For the thicker ice sheets (20 mm and thicker), increasing hull speed resulted in less ice remaining in the track, while the reverse appeared to hold for thinner ice sheets. This trend is likely due to the influences of hull motions and the confining action of the bordering ice sheet. The additional breaking of ice beneath the hull somewhat masked the variation of initial cusp size with hull speed, for the same thickness of ice sheet, the influence of hull speed on the average size of broken ice was considerably less clear than that for the width of initial cusps.

4.3 Comparison With Analytical Predictions

An overview of the comparison of the physical model tests with Equation (1) is given in Figure 8. Based on this figure, the following observations can be made:

1. The cusps observed in the ice model tests were larger than those predicted by Equation (1) by a factor of 2 to 7.

2. The analytical predictions show a lesser dependence of cusp size upon both ice thickness and velocity than was observed in the model tests.

5. CONCLUSIONS

Based on the level of comparison between Equation (1) and the full scale results and the model scale results, the following overall conclusions and recommendations can be drawn:

1. Using the analytical model for predicting ice piece size given by Equation (1) as the basis for comparision, model tests in thin, weak urea doped ice result in ice pieces which when scaled to prototype dimension are significantly larger than those observed in the field.

2. The analytical model presented in Equation (1) agreed well with the limited full scale data from the USCGC POLAR SEA and POLAR STAR.

3. Cusp size tends to increase with ice thickness and decrease with ship velocity.

6. RECOMMENDATION

While the reesults of this paper indicate that thin weak urea doped ice does not currently model piece size, no conclusion can be made concerning the effects of size on the usefulness of model tests to predict resistance and powering requirements of icebreakers. It has been documented in the literature that model self-propulsion tests in ice tend to overpredict prototype powering requirements, however, it has not been conclusively determined that piece size is the cause for the discrepancy. There is limited full scale towed resistance data, but ice model tests do appear to accureately predict icebreaking resistance despite the inaccurately scale piece sizes. It is recommended, therefore, that the next step is to determine the effect of ice piece size on icebreaking resistance, ice movement along the hull, propeller ice interaction, and powering requirements in an effort to determine if improperly scaled prototype ice piece size in model tests is the cause for overpredicting power requirements, and if so, how should ice modeling materials be improved to better predict powering requirements.

7. REFERENCES

1. Kotras, T.V., et al, "Predicting Ship Performance in Level Ice", Presented at SNAME Annual Meeting, New York, NY, 1983.

2. Voelker, R.P., et al, "Ship Icebreaking Dynamic and Maneuvering Testing Aboard POLAR STAR in Antarctica, ARCTEC, Incorporated Report 1060C-2, Columbia, MD, April 1985.

3. St. John, J., et al, "Navarin Basin and Ice Edge Data Collection Aboard USCGC POLAR SEA, March-April 1985, ARCTEC ENGINEERING, Incorporated Report No. 1070C, Columbia, MD, June 1986.

4. Mueller, A. and R. Ettem, "Dynamic Response of an Icebreaker Hull to Icebreaking", *IIHR Report No. 273*, Iowa City, Iowa, February 1984.

8. ACKNOWLEDGEMENTS

The authors wish to thank the U.S. Coast Guard's Design Branch of Naval Engineering which funded the development of the analytical model; the Maritime Administration which funded the model tests; and the U.S. Coast Guard, Maritime Administration, Canadian Ministry of Transport for funding the field tests.

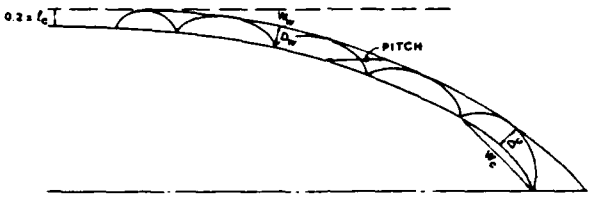

Figure 1

BREAKING PATTERN REPRESENTATION

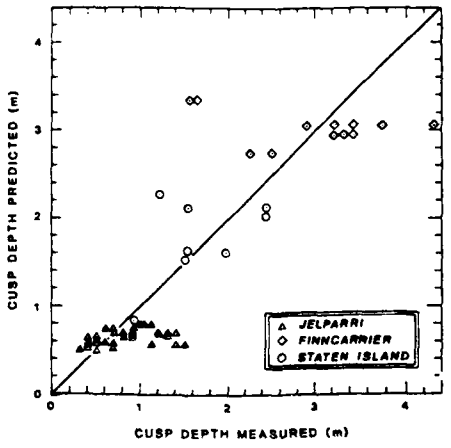

Figure 2

COMPARISON BETWEEN CUSP DEPTH PREDICTED
AND MEASURED DATA

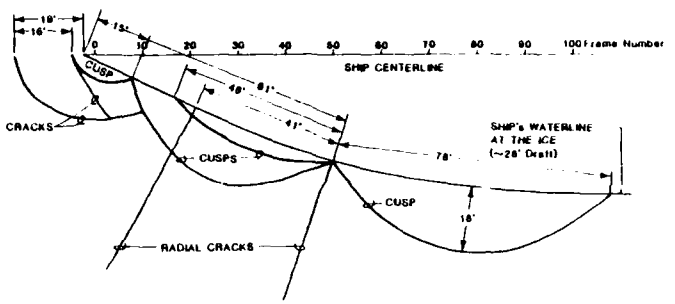

Figure 3
DOCUMENTATION OF CUSP FORMED BY ICE BREAKING
IN 30 INCH THICK LEVEL ICE
USCGC POLAR SEA - April 3, 1985 - Bering Sea

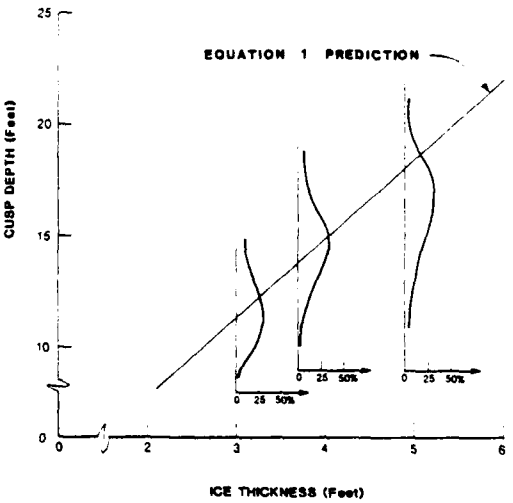

Figure 4
COMPARISON OF OBSERVED CUSP DEPTH SIZE
WITH EQUATION 1 PREDICTION

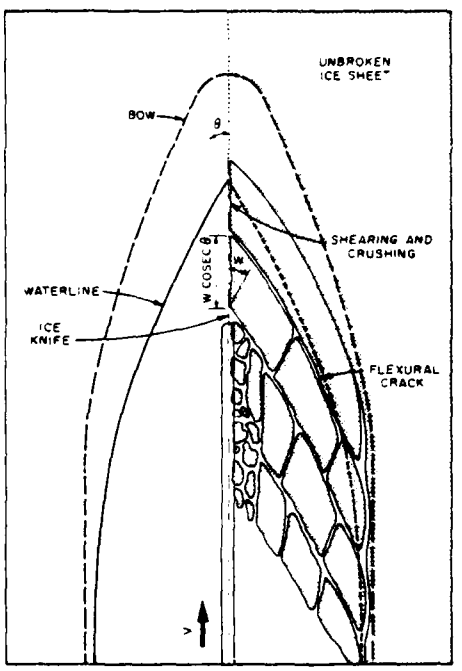

Figure 5
SCHEMATIC DEPICTION OF ICE-BREAKING BENEATH THE BOW
OF A POLAR CLASS HULL

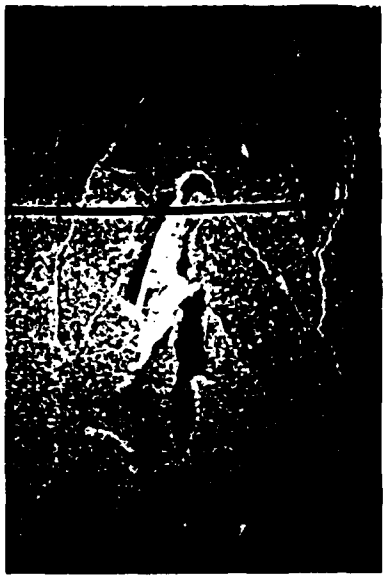

Figure 6a

ICEBREAKING PATTERN FOR
30 mm THICK ICE AT 0.1 m/s

Figure 6b

PATTERN OF BROKEN ICE:
h = 10 mm, V = 0.5 m/s

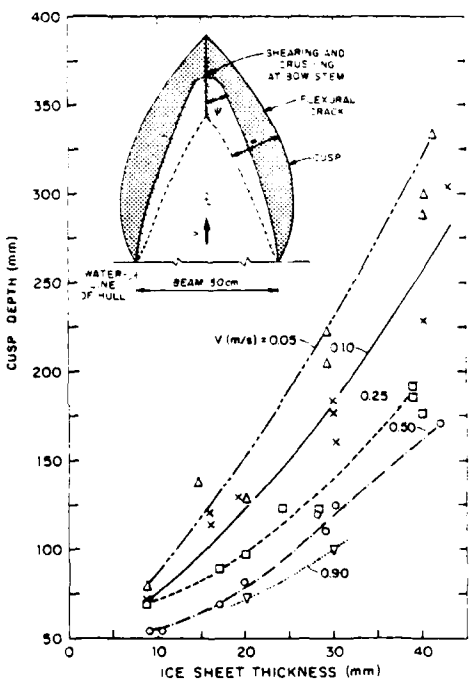

Figure 7

INITIAL CUSP DEPTH, D_c, vs. ICE SHEET THICKNESS AND HULL SPEED

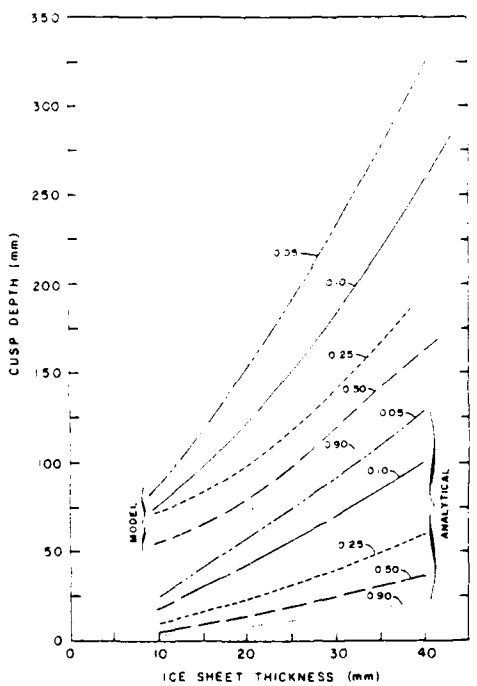

Figure 8

COMPARISON OF CUSP SIZE PREDICTIONS BY EQUATION 1
WITH MODEL TEST RESULTS

- A STRENGTH INDEXER FOR MODEL ICE -

D. N. Baker
Melville Shipping Ltd.
Ottawa, Ontario

G.W. Timco
National Research Council
Of Canada
Ottawa, Ontario

C.C. Nowicki
Transportation
Development Centre
Montreal, Quebec

ABSTRACT

The mechanical properties of model ice, are usually represented by manual cantilever beam tests. Additional ice property calibration is not feasible with existing testing equipment because of the model ice properties change with time. This report describes the design, development and preliminary testing of an instrument, the Indexer, which monitors the primary mechanical properties of the model ice, simultaneously with the model test.

The Indexer consist of three instrumented plates which are arranged to monitor the flexural, shearing and crushing strength of the model ice. The model tests were conducted at the National Research Centre (NRC) Hydraulics Laboratory in Ottawa, Canada.

The results of the tests indicate that the Indexer is capable of monitoring the three ice fracturing mechanisms and that the device will be of significant benefit to model ice testing tanks.

1. INTRODUCTION

During the last three years, Melville Shipping Ltd. (Melville) has been actively involved in an extensive series of model ice tests on an existing icebreaking cargo ship (Baker 1984, Melville 1984, Melville 1985). The tests were conducted in three of the major ice tanks in Europe and North America with simulated ice thicknesses of up to 2.2 m.

One aspect of the test programme was to review the procedures adopted by each tank to monitor the model ice characteristics. Although the methods used in each tank were different, in general it was concluded that:

- The present methods for measuring model ice properties are difficult and time consuming.
- Usually only the flexural strength and elastic modulus were measured, which made it difficult to compare results from different tanks using different types of model ice.
- Considering some of the scaling problems associated with model ice, it would be appropriate to measure other properties such as the compressive and shear strength.

Responding to these conclusions, Melville has developed a device called an Indexer. The work was carried out under the sponsorship of the Transportation Development Centre (TDC) of Transport Canada, and with technical input from both the National Research Council (NRC) Hydraulics Laboratory in Ottawa and the Institute for Marine Dynamics (IMD) in St John's. The objective of the Indexer is to monitor the mechanical properties of the ice continuously along the length of the tank simultaneously with the ship model test.

This paper describes the initial design and model testing of the Indexer at the NRC Hydraulics Laboratory and presents some of the preliminary correlation between the Indexer output and manual ice strength measurements.

2. BACKGROUND

Physical modelling has been used for a number of years to predict the performance of ice transiting ships. With this technique, an instrumented model transits through an ice field which is reduced in strength and thickness to model scale values. The technology involved in creating the model ice for these simulations has developed rapidly. Improved dopents, ice formation techniques and more control of the ambient conditions in the ice tank have been the key to these improvements (Timco 1984).

It is general practice to use Froude scaling to define the model ice properties. The scale factor selected will be based on the ship, the characteristics of the full scale ice being simulated, and any constraints imposed by the physical size of the model test tank.

The model ice can be duplicated quite accurately over a wide range of thicknesses from less than one centimeter up to over six centimeters (at model scale). Unfortunately, the mechanical properties of the ice are more difficult to reproduce. This is in part due to the nature of the model ice and the growing techniques which cause the mechanical properties to change with time. Usually there is a limited time period when conditions are suitable for the test. To obtain an accurate representation of the model ice mechanical properties during the test, they must be recorded as close to the test time as possible.

The mechanical properties of the ice sheet are usually represented by measuring the elastic modulus directly before and the flexural strength directly after the model test. Both of these procedures are time consuming and tedious, particularly with respect to the cantilever tests. The data collected from these tests consist of one or two elastic modulus data points and flexural strength data about every 5 m along the tank. This does not adequately represent the characteristics of the model ice sheet since the flexural strength measurements are too widely spaced and there is no attempt to monitor the shear or crushing strength.

To address this problem, a device is required that will quickly and accurately characterise an ice sheet so that more confidence can be placed in the performance prediction of ship models in ice tanks.

3. DESIGN AND CONSTRUCTION

The objective was to design a device that could be mounted on the towing carriage and used as standard equipment for model tests. To achieve this objective the design criteria were;

- The device must be capable of monitoring the mechanical properties of the model ice continuously, over the entire ice sheet, simultaneously with the model test.
- The device should not influence the model test.
- The device must be simple to deploy requiring minimal maintenance.
- The configuration of the prototype should be flexible to permit as many adjustments as possible during the design development.

From the preliminary design stage it was recognized that it would not be possible to develop a simple device that could measure mechanical properties directly comparable with model or full scale ice. The information gathered from the device would be an "index" of the ice sheet properties and would have to be correlated with conventional techniques. Once the correlation was established, the conventional techniques would only be used to monitor the ice during the growing and tempering stages and possibly after the model test for checking purposes.

Three mechanical properties were targeted for the prototype device; flexural strength, shear strength and crushing strength. The device was designed using flat plates orientated so that they would fail the ice predominantly in these three modes. The forces necessary to produce these breaking mechanisms could then be recorded continuously and would represent the ice sheet strength.

The device which was developed, known as the Indexer, is shown in Figure 1. Plates 1 and 2 show the Indexer prior to mounting on the carriage and in operation, respectively. The motors on the forward frame cut parallel lines in the model ice directly in front of three instrumented plates which load the ice in either bending, shearing or compression. The bending plate is located directly behind and between the two cutters, inclined in the vertical plane, and is intended to fail the ice in a predominantly flexural mode. The shear plate, located adjacent to the bending plate, is also inclined in the vertical plane with one edge behind a cutter and is intended to fail the ice in a predominantly shear mode. The crushing plate is oriented vertically behind and to the side of the bending plate and is intended to fail the ice in a predominently crushing mode.

FIGURE 1

EXPLODED DIAGRAMMATIC VIEW
OF THE INDEXER

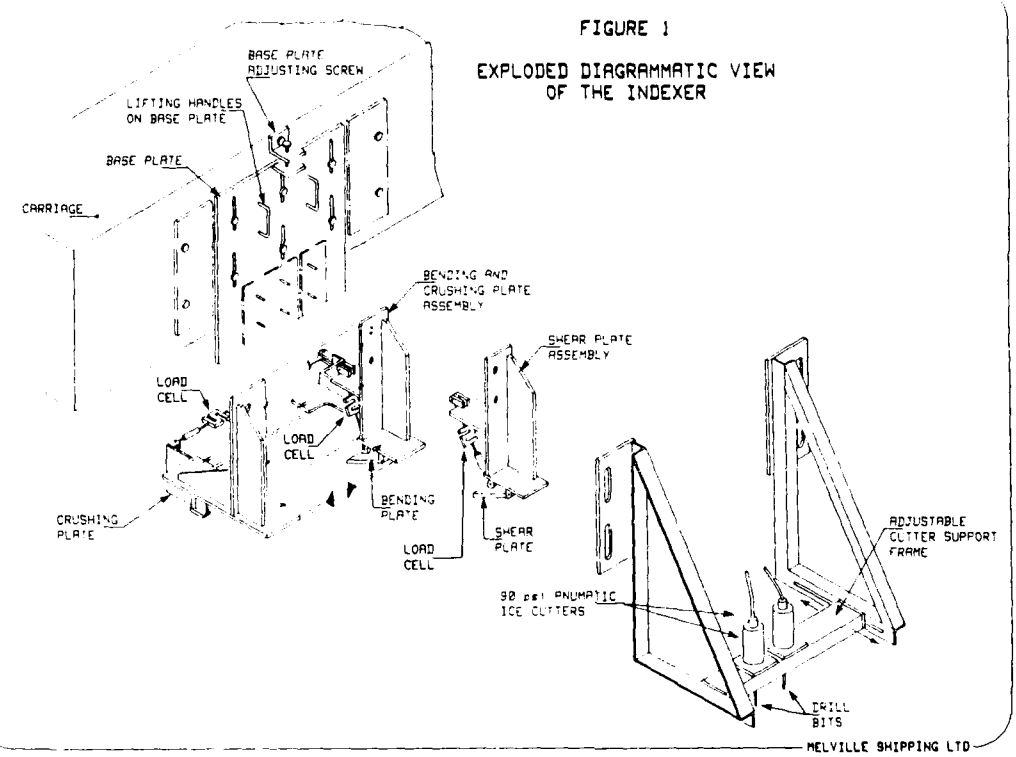

MELVILLE SHIPPING LTD

PLATE 1

INDEXER PRIOR TO MOUNTING ON THE TOWING CARRIAGE

MELVILLE SHIPPING LTD

PLATE 2

INDEXER IN OPERATION ON THE TOWING CARRIAGE

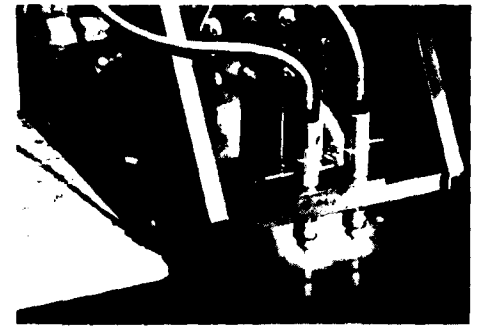

MELVILLE SHIPPING LTD

Considerable time and effort was invested in the initial configuration of the Indexer. Particular aspects of the design which are considered to be important are:

- The Indexer is constructed of 1/2 inch (12.7 mm) and 3/8 (9.5 mm) mild steel plate to obtain a high natural frequency (about 60 Hz).

- The ice cutters are high speed phneumatic drills which are capable of cutting 40 mm ice at 0.5 m/sec. The cutters have left hand screws to direct tailings and any entrained water down. This prevents wetting the ice surface which may influence the test results.

- The drills are mounted on a separate frame from the instrumented plates to minimise vibration effects.

- The plates are hinged to the main assembly using stainless steel machined bushings and pins to minimise corrosion effects and plate movement.

- The plates are instrumented using axial 'S' type water proof load cells, rated at 50 lb (222 N) for the bending and shear plates and 250 lb. (1,112 N) for the crushing plate.

- The plates may be fitted with different surfaces to monitor the effect of friction.

- The plates are adjustable through a range of angles.

- The Indexer may be adjusted longitudinally, to change the plates relative position to the cutters, and vertically, to move the Indexer relative to the ice surface.

- The shear and bending plates are mounted separately to allow relative adjustment in the longitudinal direction.

- The Indexer is built in a number of sections which are easy to handle and move from one location to another.

4. MODEL TESTS

Two series of model tests have been scheduled with the Indexer.

The first series, conducted from December 1985 to February 1986, consisted of five ice sheets at the National Research Council's hydraulics ice tank in Ottawa, Ontario (Pratte 1981). Table 1 presents the test programme and illustrates the range of ice conditions, speeds and Indexer configurations that were tested. The second series of tests which are ongoing at IMD include a broader range of ice strengths, thicknesses and Indexer configurations. These will be reported at a later date.

TABLE 1

SUMMARY OF TEST PROGRAMME

Test #	Ice Sheet #	Indexer Speed cm/sec	Ice Thickness [mm]	Ice Strength (kPa)	Comments
1	1	2.0	35	40	
2	1	5.0	35	40	- December 17, 1985 - Only nominal ice strength and thickness values recorded
3	1	20.0	35	40	
4	1	50.0	35	40	
5	1	1.2	35	40	
6	2	10.0	32 - 36	35 - 42	- December 19, 1985 - Single run over length of tank
		- INDEXER MODIFIED -			
7	3	10.0	35 - 38	26 - 38	- February 13, 1986 - Cutters in forward position - Indexer in low position
8	3	10.0	36 - 40	32 - 42	- February 13, 1986 - Cutters in aft position - Indexer in low position
9	4	10.0	37 - 43	28 - 35	- February 18, 1986 - Cutters in aft position - Indexer in high position
10	4	10.0	37 - 42	32 - 41	- February 18, 1986 - Cutters in aft position - Indexer in low position
11	5	10.0	38 - 42	29 - 48	- February 20, 1986 - Cutters in aft position - Indexer in high position
12	5	10.0	36 - 43	5 - 7	- February 20, 1986 - Cutters in aft position - Indexer in high position

MELVILLE SHIPPING LTD

During the preliminary tests at the NRC Hydraulics Laboratory, ice thickness was recorded every half meter along the track left by the Indexer. The flexural strength was recorded by cantilevers about 3 m from the Indexer track (to prevent the Indexer from influencing the cantilevers) every 0.5 or 1 m down the tank depending on the test. Each cantilever location consisted of three beams tested manually with a calibrated spring loading gauge.

Manual crushing and shearing tests have not yet been conducted to correlate those force outputs with the measured ice sheet strengths, these will be part of the ongoing work at IMD.

5. RESULTS

5.1 Behaviour Of The Indexer In Ice

The main objective of the preliminary test series was to ensure qualitatively that the Indexer would fail the ice consistently with minimal influence on the surrounding ice cover. This objective was achieved. Plate 3 shows a typical track of the Indexer and illustrates the consistent fashion with which it breaks the ice. Minor disturbances of the ice sheet did occur on the crushing side of the Indexer, but are not considered significant.

Figure 2 presents typical load time histories obtained from the flexure, shearing and crushing plate instrumentation. In general each of the time series is consistent with the breaking mode of the ice.

- Bending Plate, Figure 2a. The load output from the bending plate is typical of the failure which would be obtained from a conventional cantilever beam test. In this case the load increases until there is an abrupt failure of the cantilever beam with the load dropping quickly. This cycle is then continuously repeated as the Indexer moves through the ice. Between the peaks, however, there appears to be a high frequency cyclic loading. The reason for this is not clear, but could be associated with the buoyancy forces of the broken beam on the plate. More work is required to identify the source of this load.

- Shearing Plate, Figure 2b. The load output from the shearing plate is difficult to interpret unambiguously since the shearing action of the plate includes a component of flexural failure in the form of a series of load peaks. It is anticipated that this will be modified in the next phase of ice tests at IMD by decreasing the width of the shear plate to reduce the bending component in the failure process.

- Crushing Plate, Figure 2c. The output from the crushing plate is cyclic at a much higher frequency than either the bending or shear plate output. This represents crushing and the elastic buckling of the ice as the Indexer moves through it. During the tests, the latter failures can be seen in the form of waves radiating away from the Indexer. To prevent them from influencing the model being tested, the crushing plate must be directed away from the model being tested.

PLATE 3

TYPICAL TRACK BROKEN BY THE INDEXER

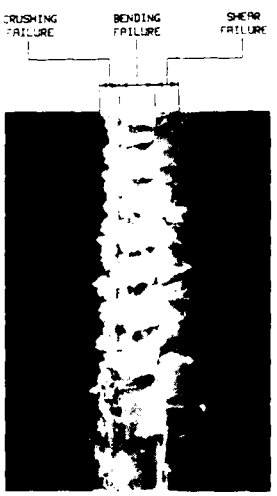

FIGURE 2

TYPICAL TIME HISTORIES OBTAINED FROM THE INDEXER

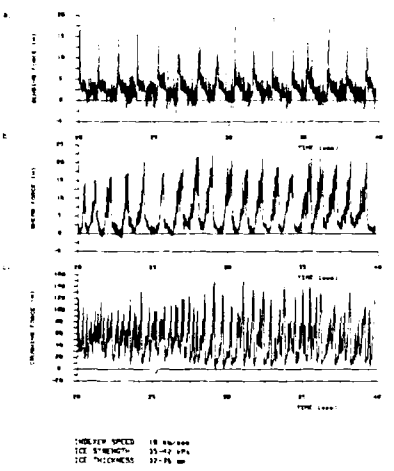

5.2 Initial Correlations

Having established the good qualitative behaviour of the Indexer, a procedure must be developed that will permit the correlation between the Indexer load cell outputs and the measured strength of the ice sheet. Although this is a major task, the limited results of these preliminary tests indicate that it will be possible. The only mechanical property measured during the tests was the flexural strength. Figure 3 illustrates the procedure used to deduce the "index" of flexural strength from a typical load output. Figure 4 presents the typical correlation that was achieved between the Indexer and the measured ice strength using manual cantilever beam techniques. In general, the correlation is good and demonstrates the capability of the technique. It is important to note that the "absolute" values of flexural strength, calculated from the Indexer output, will not be identical to the manual values because of the different type of loading technique. The trends of increasing/decreasing ice strength are important and this is illustrated in Figures 4.

6. CONCLUSIONS

A limited range of ice tests have been conducted on the Indexer with preliminary results indicating that it will be a valuable tool in monitoring the mechanical properties of model ice. The test programme on the Indexer is ongoing at the IMD ice tank and after a number of additional structural alterations will be used in conjunction with a series of model tests of an ice-capable cargo ship.

7. ACKNOWLEDGEMENTS

The authors wish to acknowledge the help and guidance of those individuals who have contributed to the success of this project, in particular; Dr. Mary Williams of the Institute for Marine Dynamics in St. John's and; Rob Bowen and Dan Pelletier of the Hydraulics Laboratory in Ottawa, and Ian Gilbert of Melville Shipping Ltd.

FIGURE 3

PROCEDURE USED TO DEDUCE INDEX OF FLEXURAL STRENGTH

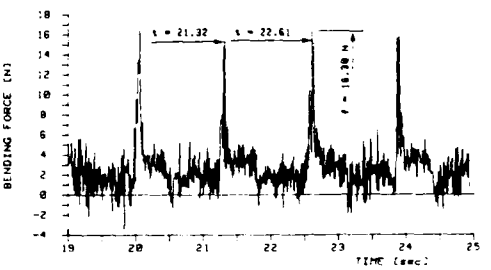

- FORCE VS. TIME DATA
  - Vertical Force Recorded at 13 Seconds, F = 16.30 N
  - Angle of Load Cell to Vertical = 22.5°
  - Vertical Component of Force, F = F x (cos 22.5) = 15.06 N
- FROM POSITION VS. TIME DATA:
  - Location of Indexer at 22.63 sec = 6 m
  - Ice Thickness at 6 m = 3.3 cm
- FROM SPEED VS. TIME DATA:
  - Speed of Indexer = 10 cm/sec
  - Time Span Over Cantilever Fracture = 1:29 sec
  - Length of Cantilever, L = 12.9 cm
  - Width of Cantilever, W = 18 cm
  - Bending Stress at Failure = $\frac{6 \times F \times L}{W \times t^2}$ = 59 kPa

MELVILLE SHIPPING LTD

FIGURE 4

TYPICAL CORRELATION BETWEEN MANUAL CANTILEVER TEST RESULTS AND INDEXER TEST RESULTS

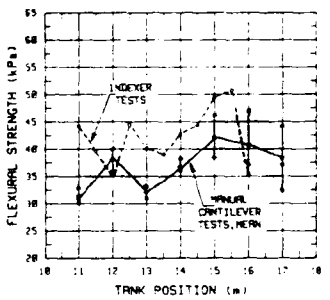

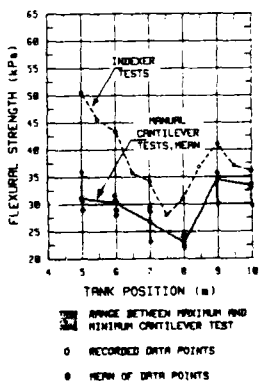

REFERENCES

Baker, D.N. and Nishizaki, R. (1984): A New Bow for M.V. ARCTIC. Paper presented at the 1984. IAHR Ice Symposium, Hamburg, West Germany, Vol. III, pp. 325-341.

Melville (1984): Redesign of the M.V. ARCTIC Bow - Design and Model Testing. Report for the Transportation Development Centre - TP5456E.

Melville (1985): Redesign of the M.V. ARCTIC Bow - Additional Model Tests at HSVA and WARC. Report for the Transportation Development Centre - TP5812E.

Timco (1984): Ice Forces on Structures: Physical Modelling Techniques. State-of-the-art report on Ice Forces on Structures, special volume proceedings of the IAHR Symposium on Ice, Hamburg, West Germany, Vol. IV, pp. 117-150.

Pratte, B.D. and Timco, G. (1981): New Model Basin for the Testing of Ice Structure Interactions. 6th International Conference on Ports and Ocean Engineering Under Arctic Condition (POAC), Vol. II, pp. B57-B66.

CANADA'S NEW ICE TANK

Stephen J. Jones
Head, Arctic Vessel Research Section
Institute for Marine Dynamics
St. John's, Newfoundland
Canada
A1B 3T5

ABSTRACT

The new refrigerated model basin, or ice tank, at the National Research Council of Canada's Institute for Marine Dynamics is described. Brief mention is made of the first projects to be conducted.

1. INTRODUCTION

On 5 November 1985 the National Research Council of Canada inaugurated its new Institute for Marine Dynamics (IMD) in St John's, Newfoundland. While this event marked the beginning of a new era of research into marine dynamics in Canada, the Institute itself is not new, but rather it is an outgrowth of the Marine Dynamics and Ship Laboratory which had existed in Ottawa since 1933. However, this paper will describe only the refrigerated model basin, or ice tank. Two other papers (Jeffrey and Murdey, 1986; Jeffrey and Jones,1986) give descriptions of the whole institute, its structure and organization, and its mandate for research and industrial collaboration.

2. THE ICE TANK

2.1 General

With a usable ice sheet length of 76m, width of 12m and a depth of 3m, the IMD ice model basin is the largest in the world, see Fig. 1. The 12m width allows large scale models to be tested and also permits limited manoeuvring studies on smaller models. Typical model lengths will be 6 to 8m, but models up to 12m in length can be accommodated.

An additional 15m long setting up area is located at one end of the ice tank and is separated from it by a large thermal barrier door, as shown in Fig. 2. The opposite end of the tank has a sloped ramp leading into a melt pit (Fig. 3) which has an insulated cover to enable the next ice sheet to be grown while the remains of the previous one are melting.

The tank is constructed of 0.6m thick steel reinforced concrete with a glass fibre reinforced epoxy liner and external polythurethane foam insulation, 0.113m thick. The tank is supported on four rows of concrete columns with teflon pads to allow for thermal expansion. The basin has sufficient corrosion resistance to handle saline ice but other dopants, such as the new EGADS ice, (Timco 1986) will be used, since studies at NRC have shown that this provides more accurately scaled model ice properties. Section 2.6 below describes this ice in more detail. The laboratory in which the tank is housed is 105 metres long by 18 metres wide by 10 metres nigh. The walls and ceiling of the room are constructed with prefabricated, steel-clad, urethane foam panels, using special techniques to reduce air infiltration from the outside.

2.2 Refrigeration System

The refrigeration system uses two-stage mechanical compression and utilizes ammonia (R-717) as the working fluid. The rejected heat is reclaimed for ice melting, domestic water preheat, and tank wall perimeter heating, via embedded pipes fed with glycol, for ice sheet release. The ammonia refrigerant is delivered to 24 ceiling hung evaporators in the main tank plus two similar units in the setting up area. Compressor capacity, evaporating pressure and fan speed are computer controlled in order to obtain a uniform temperature distribution near the water surface. The aim is to provide a cold air supply over the upper part of the basin with heat transfer near the ice sheet/air interface by natural convection, and this is achieved because of the height of 10m between the ice surface and the evaporators. Air temperature is measured with a system of 12 control thermocouples positioned along the centre of the tank and held about 30mm above the water surface. Water temperature is measured by 3 thermocouples submerged in the tank. The air temperature can be controlled from -30°C

to +15°C, and ice growth rates of 3.5mm/hour at -25°C have been obtained with a maximum thickness of 15cm. A separate chiller system is used initially to cool the water to +0.2°C.

2.3 Towing Carriage

The ice tank towing carriage, shown in Fig. 4, is an 80,000 kg. steel structure with the following dimensions: 15m long, 14.2m wide, and 3.95m high. This carriage is mounted on four sets of bogie wheels and two sets of rack drive wheels.

The carriage is driven by 4 high speed motors and two low speed motors. The high speed motors drive the carriage at speeds ranging from 0.02 to 4.0 m/s with an accuracy of 1 part in 1000. The low speed operating range is from 0.0002 m/s to 0.04 m/s with an accuracy of 1 part in 200. The high speed drive control consists of a tight loop with a motor mounted tachometer and a reset signal from one or both of the two separately mounted wheel driven pulse generators. These two units are used to compensate for the carriage twist that may be caused by offset loads. The low speed drive range is controlled by a motor mounted tachometer.

The carriage control room is 14m long, 2m wide and is thermally insulated. The control room houses the computer equipment for the drive control and the instrumentation racks for the model test frames.

The model test frame itself is capable of handling up to a 12m long model with a displacment of 12000 kg. The distortion for a model of this size would be ±2mm with a 0.1 degree rotation. The test frame can locate the model on the tank centreline or on either of the quarter points of the tank width. The beams of the test frame can be set from 1 to 3m apart and raised from water level to over a meter above water level. The test frame is designed for the following ice forces: 60 kN on the centreline, and 30 kN on the 3m offset points.

The carriage can be operated in either friction drive or rack drive. In the friction drive mode, the carriage top speed is 2m/s, while in the rack drive mode the top speed is 4 m/s. There are 4 methods of controlling the carriage drive speed. These are: jog control, joy stick control, manual control and automatic control. All of these methods except the joy stick have both high and low speed control. The jog control is used for inching the carriage into position, and can be operated from either the control desk or a remote on the front of the carriage. Under jog control, the high speed is 0.20 m/s and the low speed is 0.005 m/s. The joystick control is an override control with a forward/reverse control stick located behind the carriage control desk panel. This control is used in the event of a failure in the other three systems. The manual control has a coarse and fine control setting with the ability to change the settings as the carriage is moving. This type of control is useful for following self-propelled models. The automatic control program can set up to 8 different test speeds in the one run. With the automatic control the following parameters are programmed in before the run starts: speed, acceleration and constant speed run distance. For both the manual and automatic control, the acceleration/deceleration is set by a switch on the control board. This switch allows any of 6 possible accelerations from 0.2 m/s^2 to 1.18 m/s^2 with a step size of 0.2 m/s^2. The acceleration curve can also be set in the automatic mode, as either an S curve or a linear curve.

The carriage has a maximum test distance of 52.1m at the top speed of 4 m/s. The carriage uses regenerative brakes for stopping under normal circumstances. There are also emergency brakes that can cause a 0.3g deceleration and an oil buffer system capable of 1.0g decleration, located at the end of the rails. In addition to these breaking features, there are six limit switches incorporated into the design. These switches control an automatic deceleration point, an emergency stop point, and a travel end point at both ends of the tank.

The power for the carriage drive system is supplied by a 480 volt 3 phase 4 wire bus bar system which supplies DC drive panels and provides 208/120 volt, 3 phase for service power. A clean power supply for instrumentation is supplied by a single phase 2 wire bus bar system feeding into an onboard isolating transformer. In addition to these there are also two grounds supplied through the bus bar system: a code ground for normal use and an isolated ground for instrumentation.

2.4 Data Acquisition

The ice tank data acquisition system is mounted in the towing carriage operators' room and is connected to appropriate transducers mounted on the model and towing frame via cables passing under the floor. The transducers' outputs are digitized by a NEFF system 620 series 100 amplifier/multiplexer and the (digital) data stored in a DEC micro VAX II micro-computer running under micro VAX/VMS v 4.1 operating system, see Fig. 5. The micro VAX also controls the operation of the NEFF. The analogue outputs of the transducers are recorded on tape by a KYOWA RTP-600B 14 channel data recorder. This is done primarily as a back-up, but also allows analyses of the high frequency components of the signals if deemed necessary. The current digitizing performance is 20 channels at 50 Hz per channel for about 7 minutes. User communication with the system is through a Tektronix 4106 colour raster graphics terminal. Data collected are

downloaded to the lab's VAX 11/750 via ETHERNET. Excitation for the transducers is provided by a NEFF System 620 series 300 signal conditioner.

2.5 Service Carriage

A separate service carriage is used for ice control and measurement work. It is a 4 wheel, 24 ton, hydraulically driven carriage and is shown in Fig. 6. Manual control permits speeds of up to .4 m/s in either direction. The carriage is fitted with a 3 section working platform which can be raised or lowered to any convenient height from the ice. The sections can be operated individually or in unison. A 3 section ice boom is installed in front of the carriage and these sections can also be raised or lowered together or separately. The boom can be tilted from horizontal to vertical for ice pushing and cleaning operations. The combined tilting and lifting effects are used to build pressure ridges, and the boom is capable of lifting 1800 kg. The boom can withstand thrust forces of 60 kN, though for such work the carriage is attached to the main towing carriage. The carriage is fitted with a hydraulically operated, folding, sea crane and winch, to aid in the installation of bottom mounted test structures. A bucket extension is provided for maintenance of ceiling mounted fixtures in the laboratory.

An underwater carriage is being constructed to carry video, and high speed ciné, cameras for making visual records of, for example, the interaction of ice pieces with a model and its propellers.

2.6 The EG/AD/S Ice

This model ice has been described in detail by Timco (1986). It is a dilute aqueous solution of ethylene glycol (EG), aliphatic detergent (AD) and sugar(S) in the approximate ratio 0.4/0.03/0.04%. Its advantages are summarized by Timco (1986):- "EG/AD/S ice maintains the ability to scale correctly the flexural strength over a wide range of scale factors while maintaining a good E/σ ratio similar to urea ice, and it has the added features of being single-layered, columnar in structure with better overall scaling of the flexural properties, uni-axial and confined compressive strengths, failure envelope and fracture toughness. In total, it appears to be a significant improvement in model ice technology." Its only disadvantage is its initial cost, approximately twice that of urea.

Our own experience confirms Timco's findings, and we are now optimizing the concentrations of the three chemicals for our tank.

3. PROJECTS FOR 1986 IN THE ICE TANK

3.1 Friction Coefficient to Improve Performance Prediction.

This is our first outside client for ice tank work, namely Melville Shipping and the Transportation Development Centre. The part of the project that involves IMD will test a 1:30 model of the MV Arctic with different friction coefficients on the bow and mid-section.

3.2 R-Class Icebreaker Testing

We have already tested this model in Ottawa at scales of 1:20 and 1:40, as have many other ice tanks (Newbury and Williams, 1986). We will repeat the tests for comparison in the new ice and, possibly, build and test a larger model of the ship.

3.3 Semi-submersible in Pack Ice

As part of our contract with NORDCO, we are just completing the testing of a model semi-submersible in pack ice. GVA Canada have also contributed funds to this project.

3.4 Joint Projects with MUN

We have 5 projects in hand which originated with faculty and students at Memorial University of Newfoundland.

4. REFERENCES

JEFFREY N.E. and JONES, S.J. 1986 Canada's New Institute for Marine Dynamics: Opportunity for improved polar transportation. International Polar Transportation Conference, Vancouver, 4-8 May 1986 (in press).

JEFFREY, N.E. and MURDEY, D.C. 1986. NRC Institute for Marine Dynamics - Your new national facility. Proceedings of the 38th annual technical conference, Canadian Shipbuilding and Ship Repairing Association, Ottawa, Ontario, Canada, p. 53-82.

NEWBURY, G.S. and WILLIAMS, F.M. 1986. R-Class icebreaker model experiment results. Proceedings International Conference on Ice Technology, M.I.T., Cambridge, U.S.A. 10-12 June 1986.

TIMCO, G.W. 1986. EG/AD/S: A new type of model ice for refrigerated towing tanks. Cold Regions Science and Technology, Vol. 12, p. 175-95.

Fig. 1 A general view of the ice tank at IMD looking from the melt pit to the thermal door.

Fig. 3 The melt pit shown with its lid open.

Fig. 2 The thermal barrier door shown partly open with the carriage beyond just visible.

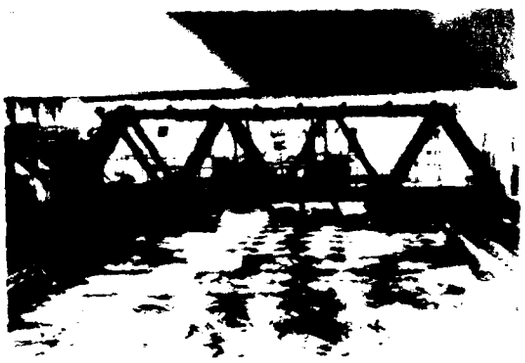

Fig. 4 The main carriage of the ice tank.

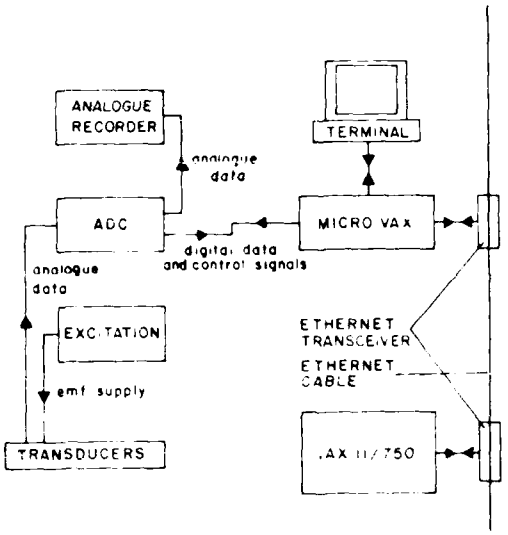

Fig. [illegible] Diagram showing layout of the data acquisition system on the main carriage.

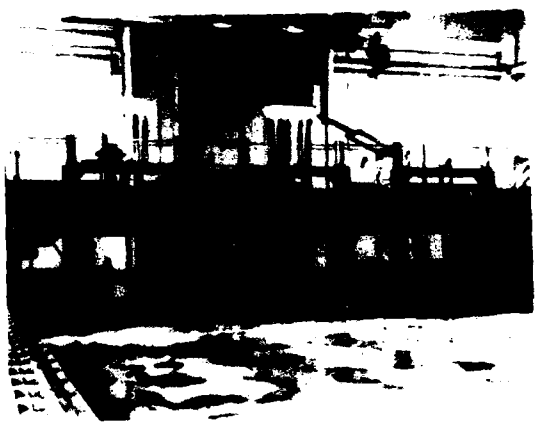

Fig. 6 The service carriage, used for testing the ice sheets.

MODELLING THE BROKEN CHANNEL

G. COMFORT,
Principal Engineer,
Arctec Canada Limited,
311 Legget Drive,
Kanata, Ontario.

I.F. GLEN,
President,
Arctec Canada Ltd.
311 Legget Drive,
Kanata, Ontario

A. KEINONEN
Vice President,
Valmet Arctic Canada Ltd.,
402 600 6th Ave. SW.
Calgary, Alta.

J. GRINSTEAD
Canadian Coast
Guard,
Ottawa, Ontario

ABSTRACT:

Model tests were carried out in urea-doped ice and synthetic mod-ice to investigate techniques for modelling full scale icebreaking patterns. Preliminary full scale data were collected for the MV CANMAR KIGORIAK during an early winter deployment. Model tests were conducted over a range of flexural strengths, elastic moduli and ship velocities. Model scale icebreaking patterns at the bow were not observed to vary significantly with these parameters.

Ice piece sizes were typically smaller for the tests carried out in synthetic ice as compared to urea-doped ice. A definitive full scale versus model scale comparison is not possible as the field data is incomplete; however, model scale ice pieces appear to be significantly larger than the field data for both types of modelling materials. Preliminary model ice fracture toughness measurements were made for each ice sheet tested. These data indicate that model ice is too fracture tough. This may be one factor contributing to the observed piece size tendencies. Further research is recommended to investigate model ice testing and scaling techniques for accurate modelling of icebreaking patterns.

1.0 INTRODUCTION

Over the past decade, physical modelling has been used as a tool to predict the behaviour of ships in level ice and broken ice conditions. Geometric and dynamic similarity have been sought and in general ice model testing laboratories have based their full scale resistance predictions on Froude scaling laws. It is recognized that currently available modelling techniques do not allow simultaneous scaling of all significant parameters and characteristics over the full range of prototype conditions.

One area which has received scant attention but which is of great importance to the designer is that of modelling the geometric aspects of the ice as it breaks and passes under the hull of an advancing ship into the broken channel astern. Correct modelling of the broken ice piece geometry has great significance in terms of predicting the interaction of ice pieces with propellers and other hull appendages. Misrepresentation by model tests of this critical area may result in incorrect decisions at the design stage which may adversely affect the performance of the ship.

The process of modelling this phenomenon is difficult for the following reasons:

a) The parameters governing ice piece size are not well understood.

b) Modelling techniques do not scale all significant properties simultaneously.

c) the geometry of the broken ice pattern for a given set of ice conditions is not well-documented in full scale.

This paper described a study [1] which was commissioned by the Canadian Coast Guard to observe icebreaking patterns in both full scale and model scale for the M.V. CANMAR KIGORIAK.

2.0 STUDY APPROACH

The study was comprised of two parts:

1. Collection and analysis of limited full scale ice piece size data for the M.V. CANMAR KIGORIAK during an early winter arctic deployment.

2. Conduct of a series of ice model tests in two modelling media which attempted to duplicate the field conditions and which parametrically varied the ice model properties.

3.0 FIELD PROGRAM

Full scale data collected during the December 1983 voyage of the M.V. CANMAR KIGORIAK from Kogyuk to McKinley Bay in the Canadian Beaufort Sea was analyzed to determine the size of the broken ice pieces and to document field icebreaking patterns. This data was collected in 0.49 to 0.74 m thick ice conditions. Air temperatures were below -30°C during the trip. A light snow cover of approximately 0.02 m was present.

The field data was collected by backing the vessel about one ship length out of the ice. Piece sizes forward of the ship were scaled from photographs.

The elastic modulus and the flexural strength of the ice were estimated as 6 gpa and 0.9 gpa, respectively.

From the field data collected, the following main observations were made.

1. Piece size - the vast majority of ice blocks had dimensions which were less than the ice thickness. Ice pieces which were larger than this only represented 1 to 20% of the total channel coverage. Figure 1 shows a typical ice piece size area histogram.

2. Icebreaking Pattern - larger ice pieces were, in general, found close to the edges of the channel. The centre portion was typically covered by a densely-packed mass of small ice pieces.

From the layout of the pieces, it is suspected that initially large cusps were broken from the level ice. This area where initial ice failures occurred was termed the **"primary breaking"** zone. Subsequently, ice pieces were refractured as they passed aft along the hulls. This refracturing was termed **"secondary breaking"** and is believed to be responsible for the large number of small ice pieces which were observed in the channel.

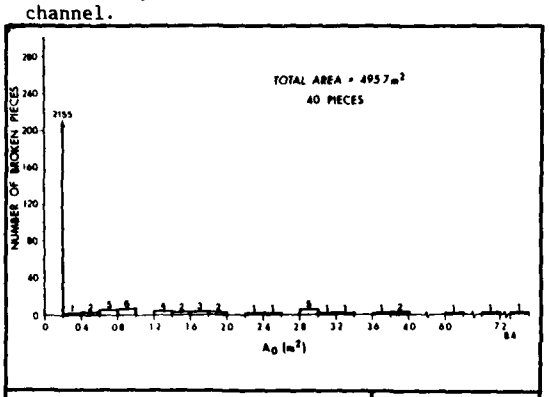

HISTOGRAM OF ICE PIECE AREA DISTRIBUTION — FIGURE NO. 1

4.0 MODEL TEST PROGRAM

4.1 Model Test Program Scope

Physical model tests were conducted using a 1:22.5 scale model of the M.V. CANMAR KIGORIAK in both urea - doped ice at Arctec's ice model basin in Kanata, and in Arctec's proprietary synthetic ice material MOD-ICE at the Polar Engineering Laboratory in Calgary.

Table 1 summarizes the test matrix that was carried out. The test plan was aimed at investigating the dependence of the icebreaking pattern on:

a) ice thickness
b) ice elastic modulus
c) ship velocity

Table 2 describes the model which was used for testing. For all tests, the model was fixed rigidly to the carriage. This was done to avoid excessive model motions during the tests, which were likely to occur as a result of the high strength model ice used for several of the tests.

For each run, the model was penetrated into the ice sheet at least one ship length after being accelerated to the required speed. The carriage was then stopped which resulted in an almost instantaneous deceleration of the model. The model was then slowly backed down the channel so that the breaking pattern at the bow became visible. The breaking pattern was documented photographically using a 35 mm camera and a calibrated 1.2 m x 1.2 m grid for reference.

Runs were repeated two or three times as allowed within the length confines of the basin, for a particular set of test conditions.

Ice piece sizes were measured from the available photographs for each test run. The same conventions used to characterize the full scale ice piece sizes, were used for the model scale data.

TABLE 1

MODEL TEST MATRIX SUMMARY

MODELLING MATERIAL	ICE SHEET #	RUN #	ICE THICK. (mm)	SHIP VEL. (m/s)	ICE ELAST. MOD. (mpa)	ICE FLEX STRENGTH (kPa)
Urea-doped refrigerated ice	1	1-3	67	0.2	394	47
		4-6	70	0.2	160	54
	2	7-9	79	0.2	337	122
		10-12	74	0.2	176	85
	3	13-15	30	0.2	64	59
		16-18	29	0.2	27	51
Synthetic Mod-ice	1	1-2	56	0.2	305	142
		3-4	57	0.6	305	142
	2	5-6	30	0.2	242	115
		7-8	31	0.6	242	115
	3	9-10	56	0.2	242	115
		11-12	47	0.6	242	115

TABLE 1

MODEL CHARACTERISTICS

MODEL:	M.V. KIGORIAK
MODEL SCALE:	1:5
DISPLACEMENT OF MODEL TESTED:	2700 N
DRAFT OF MODEL TESTED:	0.54 M
ICE MODEL KINETIC FRICTION FACTOR:	UREA-DOPED ICE: 0.12 ± 0.02
	SYNTHETIC ICE: BOTTOM SURFACE OF ICE: 0.11 ± 0.01
	TOP SURFACE OF ICE: 0.25 ± 0.05

4.2 Model Scale Results

Plates 1 and 2 show typical breaking patterns observed at the bow during the urea-doped ice tests. The broken ice pieces were all relatively large and consisted of "scimitar-shaped" ice pieces in rings which were somewhat concentric. These pieces were formed during initial contact of the bow with the ice sheet. Typically, these pieces remained intact in passing along the hull although secondary breaking did occur in some cases.

A different icebreaking pattern occurred during the synthetic mod-ice tests. The icebreaking pattern typically consisted of an outer ring of relatively large pieces formed around the bow to the reamers with radial and circumferential cracks. (See Plate 3). Inside and further aft from this primary breaking zone, piece sizes were generally smaller and more varied.

As may be seen from these photos, model scale ice piece sizes varied greatly within each run and were dependent upon their location in the broken channel. This made simple quantitative piece size analyses difficult to apply. Typically, piece sizes were observed to be greatest at the periphery of the channel in the primary breaking zone. As the ice pieces moved aft and towards the centre of the channel, they were refractured and hence were typically smaller in size.

For both modelling materials, there did not appear to be signiticant variations in icebreaking patterns over the range of ice elastic moduli, ice thicknesses and ship velocities tested. Ice piece sizes were measured, grouped and plotted to further investigate the influence of these parameters. Figures 2 to 4 show typical plots. These figures appear to show that the ice piece size is not strongly related to these parameters.

The reader is cautioned that these plots are based on all piece size data measured within 11 m (full scale) of the leading edge of the channel. Consequently data from both the primary and the secondary breaking zones are included. This may have obscured possible trends in the data as different icebreaking mechanisms occur within each of these zones.

FIGURE 2

PIECE LENGTH VS. ELASTIC MODULUS FOR UREA-DOPED ICE MODEL TESTS

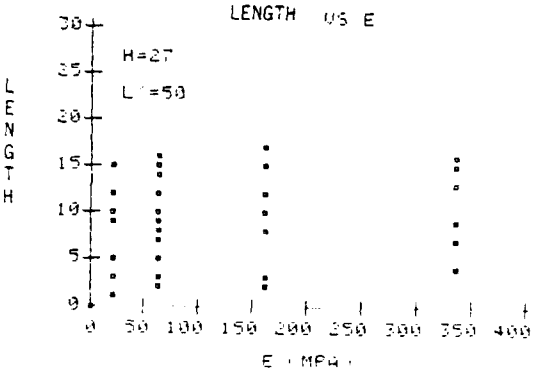

NOTES: 1. Ice Thickness = 27 mm
2. Ice pieces within 0.5 m of channel leading edge

FIGURE 3

PIECE LENGTH VS. ICE THICKNESS FOR MOD-ICE TESTS

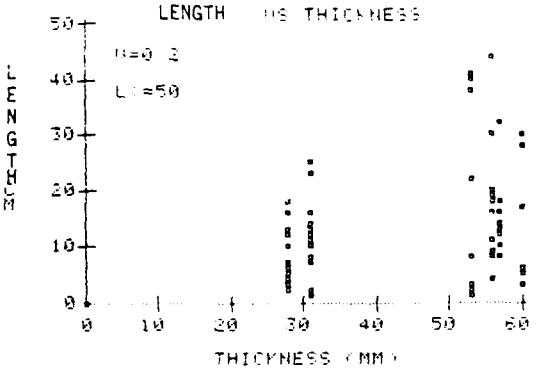

NOTES: 1. Ship Velocity = 0.2 m/s
2. Ice Pieces within 0.5 m of channel leading edge

PLATE 1

TYPICAL ICEBREAKING PATTERN AT BOW FOR
UREA-DOPED ICE MODEL TESTS
RUN #9

PLATE 2

TYPICAL ICEBREAKING PATTERN AT BOW FOR
UREA-DOPED ICE MODEL TESTS
RUN # 16

PLATE 3

TYPICAL ICEBREAKING PATTERN AT BOW
FOR SYNTHETIC ICE MODEL TESTS
RUN #7

FIGURE 4

PIECE LENGTH VS. SHIP VELOCITY FOR MOD-ICE TESTS

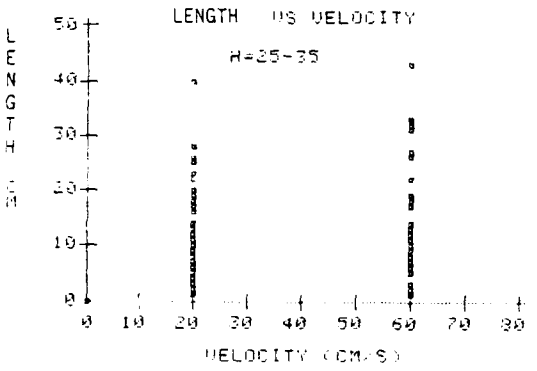

NOTES: 1. Ice Thickness: 25-35 mm

5.0 DISCUSSION

5.1 Comparison of Full Scale and Model Scale Icebreaking Patterns

Only preliminary statements can be made with the available data. This is due to a number of uncertainties. Much of the field data was collected in conditions of darkness which made resolution of individual ice pieces in the broken channel difficult and somewhat imprecise. Also, field ice properties could not be measured during the field deployment and hence it was necessary to use estimated values for establishing the model test matrix.

The model test piece size data was typically measured within 20 m (full scale value) of the leading edge of the channel whereas the field data were often measured beyond this point in the channel. Thus, ice pieces in the field case typically passed over a longer section of the hull than did those in the model basin. This may have resulted in a greater number of fractures for the field ice pieces as compared to the model scale ice pieces.

Finally, the field data was collected over a range of velocities (as the ship was decelerated) whereas the model scale data was collected at a near constant velocity.

Notwithstanding the above uncertainties, ice piece sizes in the model basin appear to be significantly larger than the observed full scale data. Also, the field ice pieces appear to be more uniform in size and more densely packed than the model scale ice pieces.

It is clear that secondary breaking is an important process influencing the sizes of the broken ice pieces. Significantly less secondary breaking occurred at model scale.

The program has also shown that an elastic flexural bending analysis is unable to characterize the size of the broken ice pieces. Table 3 summarizes the observed relationships between the ice breaking length and the characteristic length. These ice breaking lengths are significantly, less than that predicted by elastic theory, eg. [5], [6].

TABLE 3

ICE BREAKING LENGTH

	MAXIMUM PIECE LENGTH / ICE CHAR. LENGTH	MEAN PIECE LENGTH / ICE CHAR. LENGTH
Field Data	0.25	0.1
Urea-Doped Model Ice Tests	0.38	0.17
Mod-Ice Tests	0.50	0.23

Note: It should be noted that only the larger field ice pieces were measured and consequently the above field mean piece length/characteristic length ratio is overestimated.

5.2 Modelling Distortions

The program investigated a number of ice modelling approaches. For the urea-doped ice tests, some runs were made using model ice which approximately scaled the estimated field ice flexural strength. Other runs were made which approximately scaled the estimated field ice elastic modulus and the elastic modulus/flexural strength ratio. (Urea-doped ice materials properties do not allow simultaneous scaling of flexural strength and elastic modulus).

Icebreaking patterns did not appear significantly different for any of the urea-doped ice tests, and so it seems that other parameters are of more significance. It was decided to investigate the fracture toughness of the model ice.

A number of notched beam fracture toughness tests were carried out on each ice sheet. Table 4 summarizes this data along with the other measured model ice mechanical properties.

Using Froude scaling laws, the fracture toughness should scale as $\lambda^{1.5}$, where λ is the geometric model scale factor. Since the scale of the M.V. KIGORIAK MODEL used was 1:22.5, a target model scale K_{IC} value of 0.9 kN/m$^{3/2}$ is implied by this relation. However since some tests were based on sheets which targeted on elastic modulus, the flexural strength of the model ice sheets was often too high. Consequently, K_{IC} was also distorted since it is related to the ice flexural strength by the following general relation:

$$K_{IC} = \sqrt{\pi a}\ \sigma_{failure}$$

TABLE 4

MODEL ICE MATERIAL PROPERTIES

MODEL ICE MATERIAL	SHEET NO.	RUN NO.	AVG. MODEL SCALE ICE FLEX. STR. (σ_f) (kPa)	AVG. MODEL SCALE ELASTIC MOD (E) (MPa)	AVG. MODEL SCALE CRIT. STRESS INTENSITY (k_{IC}) FACTOR ($kN/m^{3/2}$)	E/σ_F	FULL SCALE FLEX. STR [1] / MODEL SCALE FLEX. STR.	EXTRAPOLATED FULL SCALE K_{IC} ($kN/m^{3/2}$) VALUE USING FLEX. STRENGTH AS AS A BASIS [2]
Urea Doped	1	1-3	47	394	33.7	8380	10.6	1163
Ice*		4-6	54	160	12.4	2960	9.3	352
	2	7-9	122	337	35.4	2760	4.1	294
		10-12	95	176	28.7	2070	5.9	411
	3	13-15	59	64	14.3	1080	8.5	354
		16-18	51	27	19.7	530	9.8	604
Synthetic	1	1-2	142	305	42.5	2150	3.5	278
Ice		3-4	142	305	42.5	2150	3.5	278
	2	5-6	115	242	33.1	2100	4.3	295
		7-8	115	242	33.1	2100	4.3	295
	3	9-10	115	242	33.1	2100	4.3	295
		11-12	115	242	33.1	2100	4.3	295

Notes : 1 Full scale ice flex. strength taken as 0.5 mpa.

2 Extrapolated full scale K_{IC} value taken as:

$$(\text{Model Scale } K_{IC}) \times \left(\frac{\text{Full Scale Flex. Str.}}{\text{Model Scale Flex. Str.}} \right)^{1.5}$$

1. A typical full scale K_{IC} value is 100 $kN/m^{1.5}$ [2].

where $\sigma_{failure}$ = stress at failure, which is highly dependent upon the ice flexural strength in this case.

a = crack length

Table 4 summarizes the relationship of the measured K_{IC} values to other model ice properties and the scale factor for each test run.

This table shows that the model ice fracture toughness was too high in relation to the other elastic ice properties. If flexural strength is adopted as a scaling basis then this table shows that the model ice fracture toughness was too high by factors of approximately 3 and 3 to 12 for the synthetic mod-ice and the urea-doped ice respectively.

The broken ice pieces did not refracture as easily at model scale as observed in the field. Consequently less secondary breaking occurred at model scale. The measured model ice fracture toughness support the observed ice piece size trends as they indicate that model ice is too fracture tough in relation to the other scaled ice elastic properties.

The reader is cautioned that other factors such as the relative distribution of cracks and inhomogeneities in model scale and full scale may also have contributed to the observed discrepancies. Also, techniques for model ice fracture toughness measurement are still in their infancy and require further development.

Nevertheless, it is suspected by the authors that an improvement in the brittle properties of model ice materials and their scaling will result in greatly improved ice piece size modelling. This is a necessary prerequisite for the effective prediction of critical hull appendage - ice interactions such as the interaction of ice with ship propellers. We of course note that since this work was performed, several new model ice materials have been announced [3], [4], that appear to show an improvement in this area.

6.0 CONCLUSIONS AND RECOMMENDATIONS

a) The preliminary results obtained in this test program indicate that model scale ice pieces are significantly larger than full scale piece sizes. The full scale ice pieces are also more uniform in size. This is due to massive secondary breaking of the broken ice pieces in the field, which is not reproduced in model tests.

b) The elastic modulus and flexural strength of the model ice used during the test programs were varied over a wide range. As significant differences in icebreaking patterns were not observed between various test sheets, it is suspected by the authors that the model ice brittle properties may be of more significance for piece size modelling.

c) Preliminary measurements of model ice fracture toughness indicate that the model ice sheets were several times too fracture tough in relation to the other scaled elastic ice properties.

d) Further research towards the improved modelling of full scale ice brittle properties is recommended as the next step towards improved piece size modelling.

REFERENCES:

[1] Arctec Canada Limited, Dome Petroleum Limited, 1984, Modelling the Broken Channel, Transport Canada Report TP5373E, Ottawa, Ontario.

[2] Mellor, M., 1983, Mechanical Behaviour of Sea Ice, CRREL Monograph 83-1.

[3] Enkvist, E. and Makinen, S., 1984, Experience With a New Type of Model Ice, proc. Ice Tech '84, Society Naval Architects and Marine Engineers.

[4] Timco, 1985, EG/AD/S: A New Type of Model Ice for Refrigerated Towing Tanks, Cold Regions Science and Technology, October.

[5] Hetenyi, M., 1946, "Beam on an Elastic Foundation", University of Michigan Press.

[6] Nevel, D., 1968, "Bearing Capacity of Floating Ice Sheets", CRREL Research Report No. 21.

ACKNOWLEDGEMENTS:

The authors wish to acknowledge the efforts of Vlodek Laskov, of Arctic Research and Development, who was part of the project study team. Also contributions to the original study effort were made by Gary Timco, and Mary Williams of the National Research Council.

SESSION VII
SEAKEEPING

TECHNICAL COMMITTEE MEMBERS

Prof. Jeffrey T. Dillingham (Chairman)	Univ. of Michigan
Mr. Frank DeBord	Offshore Technology Corp.
Dr. Stefan Grochawalski	Institute for Marine Dynamics
Mr. Geoffrey G. Cox	DTNSRDC
Prof. Bruce Johnson	U.S. Naval Academy
Prof. William C. Webster	Univ. of California/Berkeley
Dr. Bent Jacobsen	Tracor Hydronautics
Dr. Subrata Chakrabarti	Chicago Bridge and Iron Co.

REPORT OF THE SEAKEEPING COMMITTEE

Dr. Jeffrey T. Dillingham
Chairman
Naval Architecture & Marine Engineering
University of Michigan

The Seakeeping Committee for the Twenty-first American Towing Tank Conference is composed of the following members:

Prof. Jeffrey T. Dillingham
Committee Chairman
The University of Michigan

Mr. Frank DeBord
Offshore Technology Corporation

Dr. Geoffrey G. Cox
David W. Taylor Naval Ship Research and Development Center

Dr. Stephen Grochowalski
National Research Council Canada

Dr. Bent Jakobsen
Tracor Hydronautics

Dr. Subrata Chakrabarti
CBI Industries

Dr. Bruce Johnson
Naval Academy Hydromechanics Laboratory

Prof. William C. Webster
University of California, Berkeley

The function of the committee was to review the abstracts of offered papers and to select those for presentation at the conference. In addition, the committee members have submitted short reports on recent work which has been undertaken at their respective laboratories. In some cases these reports have been written by the committee members themselves, while in other cases the reports have been written by other members of their organizations. Following this section are all of the individual reports. The remainder of this section is a brief summary of activities.

The following topics have received considerable attention since the last ATTC.

1. IMPROVED WAVE GENERATION AND ANALYSIS

As the methods and tools available for analyzing model test data from random wave tests with conventional spectra become almost routine, attention is being focused on more realistic and complicated types of waves. At DTNSRDC and OTC work continues on improving methods for measuring, generating and characterizing multi-directional waves. At the Naval Academy, work is being done on describing and generating waves with bimodal spectra. At the University of Michigan a detailed study of the effect of side-wall reflections of waves in a towing tank is nearing completion.

2. CAPSIZING AND STABILITY

Four institutions (NRC, Hydronautics, Naval Academy, University of Michigan) have either completed or are in the process of conducting research related to stability of small vessels. This work takes the forms of both experimental and numerical investigations. Attention has been focused on fishing vessels and the response of vessels to large amplitude or steep breaking waves.

3. SLAMMING

NRC and The University of Michigan have both conducted experiments aimed at understanding slamming or impact loads of bow shaped bodies.

4. COMPUTER MODELING

Most organizations who reported mentioned the development of improved computer programs for modeling of waves and for predicting seakeeping behavior of various types of vessels and offshore structures.

5. NOVEL STRUCTURES

Participating organizations reported the usual broad spectrum of projects related to

innovative offshore structures. In the area of energy production, CBI reports that they have conducted experiments related to OTEC, and the University of Michigan has conducted laboratory tests of a new type of wave power absorption device. The latter will be field-tested in Lake Michigan in the summer of 1987. In the offshore area, CBI has conducted tests on a tension leg platform design and a conical drilling structure.

6. YACHT TESTING

In an ongoing program OTC has tested models of America's Cup yachts for five different syndicates. Results are not public information for obvious reasons.

Seakeeping and Related Research at the U.S. Naval Academy 1984-86

by Bruce Johnson and Louise Wallendorf
Naval Academy Hydromechanics Laboratory

1. DEVELOPMENT OF BI-MODAL SPECTRA GENERATION CAPABILITY.

The Hydro Lab has incorporated the work of John Dalzell while he was NAVSEA Research Professor into a capability to generate specified bi-modal wave spectra in either of the two towing tanks. The sea and swell spectral forms (Bretschneider, Jonswap, Ochi-6 parameter, etc.) and the peak frequencies are inputs to the program which then iterates the generated waves until the desired bi-modal spectrum is achieved. The laboratory recently completed a unidirectional verification of the assumption that the total significant wave height equals the square root of the sum of the squares of the sea and swell significant heights. This assumption is used in ship response prediction programs.

2. SEAKEEPING STUDIES ON NAVAL FRIGATES.

A Trident Scholar, Jeffery Hoyle, performed a series of seakeeping studies on a FFG-7 hull form, appended with five different bow bulbs and tested in periodic irregular encountered waves. The visual studies as recorded on a slow motion video analyzer proved to be quite useful, but the motions analysis proved to be less periodic than was hoped, so considerable data scatter was present. This was a disappointment for the attempts to develop a "single-pass seakeeping analysis" technique reported in previous ATTC Reports and discussed at the 17th ITTC. There appears to be no substitute for long record runs in irregular waves or single runs in regular waves. This study will be presented at the SNAME annual meeting in November 1986.

3. EXTREME BREAKING WAVES AND CAPSIZING STUDIES.

Extensive studies on capsizing of both yachts and small boats have been performed in the Naval Academy 120 foot towing tank. John Zseleczky and other members of the Hydro Lab staff contributed much of the experimental data for the final report of the USYRU/SNAME Joint Committee on Safety from Capsizing issued in June 1985. A series of two-dimensional ship models have also been studied with respect to their capsizing characteristics for the U.S. Coast Guard.

A continuing problem in capsizing studies is that of characterizing the capsizing wave, either a spilling or plunging breaker. Extensive studies of breaking waves with the goal of determining the most significant characteristics common to such extreme waves is underway under Coast Guard sponsorship. Jim Duncan of Flow Research Inc. is working with the authors in this project. As part of the characterization study, a modified computer generation program has been developed which enables the investigator to locate the capsizing wave anywhere in either of the two towing tanks. The final goal is to make a capsize resistance evaluation of a Coast Guard rescue boat and a UDT support boat.

The USNA Hydro Lab is maintaining a collection of published literature on capsizing. Investigators are encouraged to send any reports they generate on this subject to either of the authors of this report.

Marine Research Activities
CBI Industries, Inc.
by Keith Melvin

The CBI Industries Marine Research Department has conducted many hydrodynamic model tests of various types in the 18 years since the Wave Tank Facility began operation. Model testing programs have included the analysis of bottom mounted structures, mooring systems, towing tests, submergence tests, scour tests and riser studies. The facility includes a wave tank 250 ft. long, 33 ft. wide and 18 ft. deep. It is equipped with a movable floor so that any depth of water can be simulated with a practical scale factor. A deep pit has been installed in the center of the wave tank to accommodate testing of deepwater structures, providing an overall testing depth of 30 ft. Waves are generated pneumatically to simulate any regular wave or random wave spectrum required. Regular waves up to two feet in height with periods ranging from one to eight seconds can be generated. The tank is equipped with current generators for producing uniform profiles up to one foot per second either with the waves or against the waves. Portable current generators may be installed to introduce current at any angle to the waves. Wind and wind generated waves are simulated with fans.

The facility can be used for towing tests through use of the bridge, which can travel at speeds up to four feet per second. The bridge is also the control center for tank operations, instrumentation controls, and data acquisition.

A full inventory of standard instruments and signal conditioners are available, including a Selspot motion measuring system. In addition, our machine shop, electronics laboratory and materials testing facilities are available for in-house development of special instrumentation to satisfy unusual test requirements.

The data acquisition system consists of a 64 channel analog-to-digital converter, a PDP 11/70 computer with 64 K of core storage. The data collection is completely automated at a rate of up to 1,000 samples per second on all 64 channels with on-line display terminals and two printer-plotters. Data reduction and analysis on the in-house IBM 3033 and the DEC System 20 includes a complete wave theory package, a statistical analysis program, a spectral analysis program, a variety of wave force and motion analysis programs, structural analysis programs and fatigue analysis programs. Reduced data are available minutes after completion of a test run so that results can be used for planning subsequent runs.

The facility is also equipped with above water and underwater high speed photographic equipment for documenting real time model motions. This equipment can be operated remotely or manually by the wave tank diving crew. A video recording system is available for continuous monitoring of tests.

The total services of the Marine Research Facility include model design and construction in the completely equipped model shop. With the support of our machine shop, these facilities allow the test designer to specify very sophisticated models built from wood, plastic, fiberglass, aluminum, steel or other media. Several models of tankers and radio controlled tugs are available for use.

Some examples of the various types of testing performed recently are discussed in the following sections.

1. TOWING, SEAKEEPING AND SUBMERGENCE OF ARCTIC STRUCTURES

A gravity based Conical Drilling Structure has been tested at the CBI Industries wave tank facility. The test consisted of towing and seakeeping of the model in various waves both in shallow and deepwater, and the installation of the structure in shallow water. The model tests provided towing loads and motion response of the model in waves and during the submergence of the structure.

The results of the study showed that the natural period of the structure appeared to be out of the range of most ocean waves, and the motion response seemed to be fairly linear for the level trim, design draft position. The deepwater towing resistance of the structure was not affected by waves in a JONSWAP sea of 5 ft. or less. It also appeared that seafloor contact was unlikely when towing the structure at the design draft, however, contact would be expected for an alternate design draft under consideration. The submergence sequence tested by compartmental ballasting demonstrated system stability.

2. OCEAN THERMAL ENERGY CONVERSION (OTEC) MODEL TESTING

Model tests of a shelf-mounted Ocean Thermal Energy Conversion (OTEC) platform and a slope-mounted cold water pipe have been performed in the CBI Industries wave tank. The work leading to the model testing program was sponsored by the National Oceanic and Atmospheric Administration (NOAA).

3. OTEC PLATFORM TESTS

The purpose of the test was to investigate the effect of the submerged OTEC power modules on the platform structure. The submerged modules supported by the platform provide a significant blockage to waves and current, which increases the loads imposed on the structure. In this testing program, the parameters of module size, type and location were varied to determine their effect on the platform forces and pressures under controlled waves and current conditions.

The basic platform model consisted of four vertical steel columns placed in a square configuration. A Froude scale of 1:25.75 was selected, resulting in a model with overall dimensions of 8.5 ft. x 8.5 ft. x 14 ft. tall, which was fabricated in-house in our model

building facility. Variation of the model configuration included blockage of different segments of the platform to represent the submerged power modules mounted on an OTEC structure. These modules were modeled using solid or uniformly perforated panels. The structure was instrumented so that the global forces and pressure profiles at critical points on the platform could be measured. The specialty instrumentation required for this test was developed in-house in our machine shop and electronics laboratory.

The tests showed that the module type is an important parameter affecting the magnitude of the wave forces. For example, the wave loads on a perforated module with 80% blockage were considerably lower than the corresponding wave loads on a solid module with 57% blockage.

4. OTEC COLD WATER PIPE TESTS

The purpose of these tests was to collect and reduce data that can be used to calibrate or verify existing pipe load prediction techniques. The test setup was chosen to simulate an at-sea test of a section of cold water pipe at Keahole Point, Hawaii. The cold water pipe model was fabricated from a tubular aluminum section specially machined to accommodate several flush-mounted pressure transducers. The model was supported by load cells mounted on a foundation sloped at 40° from the horizontal plane. It was subjected to various environmental conditions involving waves and currents.

The variations of the test condition included four wave angles of attack, three elevations of the pipe off the bottom and three bottom slopes. Pipe load, water surface elevations, dynamic pressures around the circumference of the pipe and local water particle velocities were recorded.

CBI is currently performing extensive analysis of the data which was obtained under this testing program. Coefficients related to the tested variable will be determined to improve theoretical prediction techniques.

5. TENNSION LEG PLATFORM MODEL TESTING

Tension Leg Platforms (TLPs) are receiving increasing attention as a solution for deepwater oil production. As the water depth increases, the cost of constructing a stationary frame type structure increases prohibitively. TLPs are a good compromise between these frame structures and dynamically positioned vessels which require large crews and consume large quantities of fuel.

A TLP consists of a floating platform whose legs are moored to the seafloor by cylindrical steel tendons. The structure is permitted to move in response to wave forces, but its range of motion, particularly in heave and pitch, is restricted to prevent damage to the drill string.

A TLP experiences two types of forces: a primary exciting force at the wave period and a secondary nonlinear exciting force having steady and oscillating components outside the range of typical wave periods. In particular, a high frequency springing force develops in the tendon in the pitch natural period. A model test was performed in the CBI wave tank to investigate this tendon force.

For this purpose a large scale model of a TLP was built and tested in the wave tank. The platform consisted of four columns, arranged in a square configuration. The corner columns were interconnected with smaller pontoon members. The TLP was held in place by four tendons, one under each corner column.

The second order springing loads in the tendons were clearly evident during the test runs with regular waves and wave groups as well as with random waves. The testing in the tank was demonstrated to the Hydrodynamic Committee of the American Petroleum Institute.

Review of Seakeeping Activities at
Tracor Hydronautics, Inc., 1983 - 1986
by Dr. Vladimir Ankudinov

Much of the seakeeping work on conventional ship types have been based on the analytic prediction methods and experimental verification in the model basin (HSMB) for several new naval designs.

Seakeeping studies primarily involved investigations of hull form modifications, (such as, different loading conditions, variation of the stabilizing devices, etc.) on seakeeping performance in typical ocean environment and operational range.

Typical example is presented on the Figure 1 for pitch motion response of the fine form vessel in Sea States 4, 5, and 6. Solid lines are SMP-81 ship motion predictions, and dotted lines are results of the time domain calculations described in Reference 1. Both predictions methods are based on Bretschneider spectrum distribution for specified significant wave heights and wave modal periods (period of maximum energy). It appears calculations and experiments to be in good agreement. Some differences are partially due to the difficulties to reproduce accurately the theoretical spectrum in our model basin and due to the scatter errors for small speeds of advance.

1. MULTIHULL VESSELS RESPONSE IN A SEAWAY

Many open sea or offshore operations involve two or more vessels closely positioned so that their motions in waves are hydrodynamically interdependent. Examples of operations of this type are:

- cargo/liquid transfer operations
- deep-ocean mining operations
- military operations, like ship replenishment, wave protection by larger vessels, etc.
- operation of an OTEC platform and its supportive systems at sea.

In regard to the last item, Tracor Hydronautics conducted an extensive seakeeping test of two candidate OTEC platform and their multipoint moorings, Reference 2. Two platforms, a barge-like hull and a semi-submersible, were tested with an elastically scaled Cold Water Pipe (CWP) and four rigid discharge pipes modeled. Tests were conducted with the CWPs and the transition platform at the top of the CWP attached to, and disconnected from, the platform. Measurements included surface platform motions and accelerations, mooring line forces, transition platform motions and interaction forces between the hull and CWP transition platform.

Recently, Tracor Hydronautics has developed the computer program to predict the motions of two closely spaced bodies of arbitrary geometry, Reference 3. These bodies may be connected to each other and/or to the ocean bottom. The calculated results are presented in Figure 3 for a representative problem of lightering from a ship to a closely spaced, parallel barge in water of finite depth (50 feet). The ship and barge are parallel and are connected by six mooring lines and two cylindrical fenders, see Figure 2.

2. DETERMINISTIC AND LARGE AMPLITUDE SHIP MOTIONS

In recent years Tracor Hydronautics have been developing a computer capability for time-domain simulation analysis of ship motions in waves, specifically for assessments of stability and overall mission performance in high seas, References 1 and 4. The non-linear mathematical model includes terms of both, viscous and potential nature in six degrees of motion, non-linear wave and ship motion amplitude terms, and terms representing interaction between the ship hull, propeller and rudder in wave flow. So called "memory" effects (associated with the wave effects of the hull on the free surface, and vorticity which is shed from the oscillating hull) are included through the use of higher order differential equations with the constant coefficients.

The last procedure is an engineering alternative to computing the convolution integrals, which typically require knowledge of the kernel function for all frequencies from zero to infinity. Tracor Hydronautics simulations are carried out in the frequency range of practical interest, and the required constant coefficients are determined by curve-fitting from the existing test or calculated data.

The ability of the vessel to maintain effective control in a seaway is a critical item in numerous vessels operations and in certain circumstances it determines its survivability.

Figure 4, taken from Reference 1, shows that in irregular waves larger 11 feet of the significant waves ($H_{1/3} > 10$ ft), a turning ship lost its directional stability and behaves quite erratically unless stabilizing and autopilot control devices are employed.

Tracor Hydronautics has been involved for some time in assessment of the ultimate stability and possible capsizing of small vessels such as fishing boats, sailing yachts and naval vessels. Figure 5, taken from Reference 4, shows time domain simulation results for extreme rolling in combined wind and waves ($H_{1/3} \approx 65$ ft).

Time-domain simulations of random events must be great enough to insure that a significant number of events have occurred to insure statistical validity of the results. It appears from Figure 5 that wave and roll parameters do not show any significant variations for times greater than 20 minutes, and though roll motion exceeds 30 degrees there has been no capsizing.

REFERENCES

Ankudinov, V., "Simulation Analysis of Ship Motion in Waves," International Workshop on Ship and Platform Motions, University of California, October, 1983.

Ankudinov, V. and Barr, R. A., "Simulation of Large Amplitude Rolling Motions of Naval Vessels," Tracor Hydronautics Technical Report 7925.66-2, 1983.

Duncan, J., Barr, R., and Liu, Y. Z., "Computations of the Coupled Response of Two Bodies in a Seaway, International Workshop on Ship and Platform Motions, Univ. of California, October, 1983.

Koetzli, J. and Zseleszky, J., "Model Test Report for Two Configurations of a Moored Pipe/Mobile Platform OTEC Plant, Hydronautics,

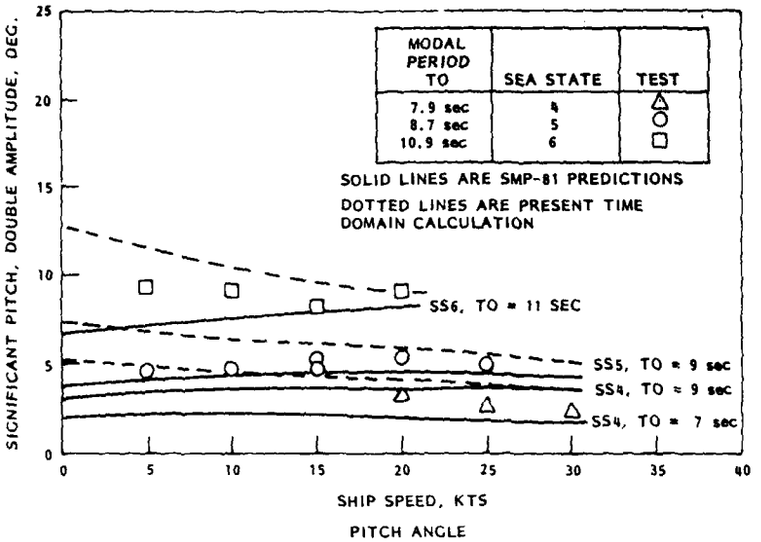

FIGURE 1 - MOTION OF FINE HULL SHIP (C_B = 0.50) IN LONG-CRESTED SEAS

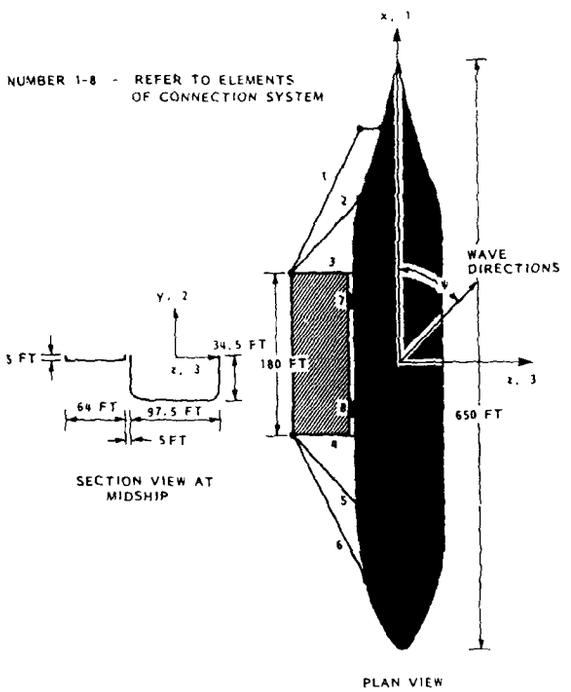

FIGURE 2 - SCHEMATIC OF SHIP AND BARGE CONFIGURATION

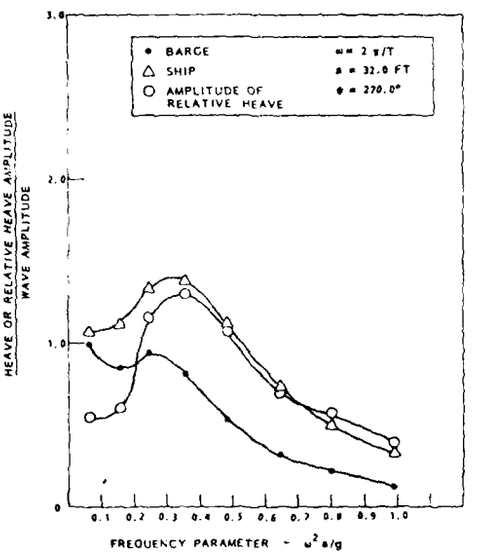

FIGURE 3 - NON-DIMENSIONAL HEAVE AMPLITUDES IN BEAM SEAS BARGE IN LEE OF SHIP

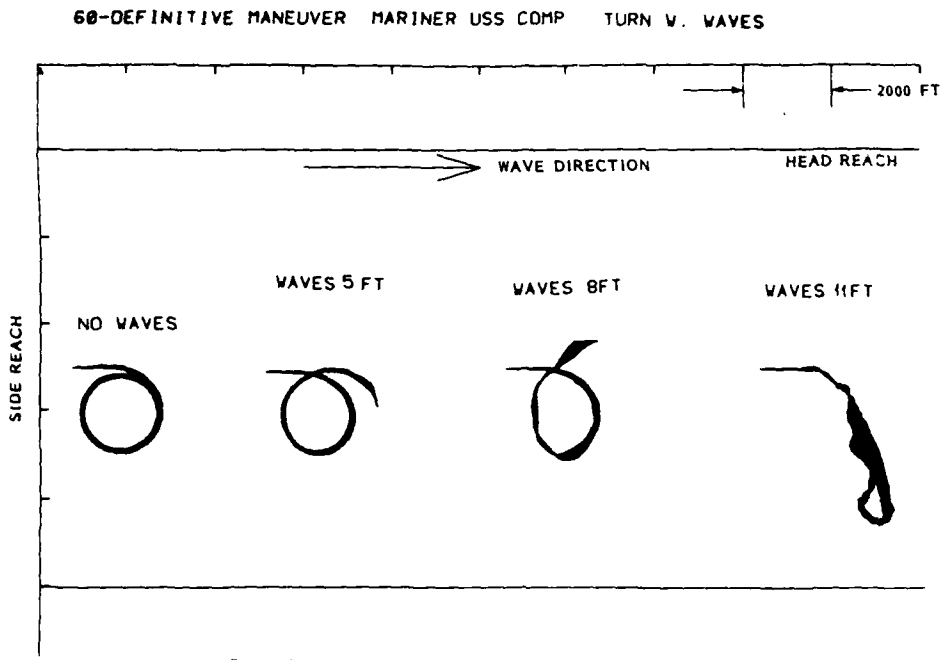

FIGURE 4 - COMPUTER SIMULATED TRAJECTORIES FOR 35 DEGREES RIGHT TURNS OF THE MARINER IN IRREGULAR WAVES. APPROACH SPEED OF 15 KNOTS. BRETSCHNEIDER SPECTRA. WAVES HEIGHTS ARE OF SIGNIFICANT VALUES.

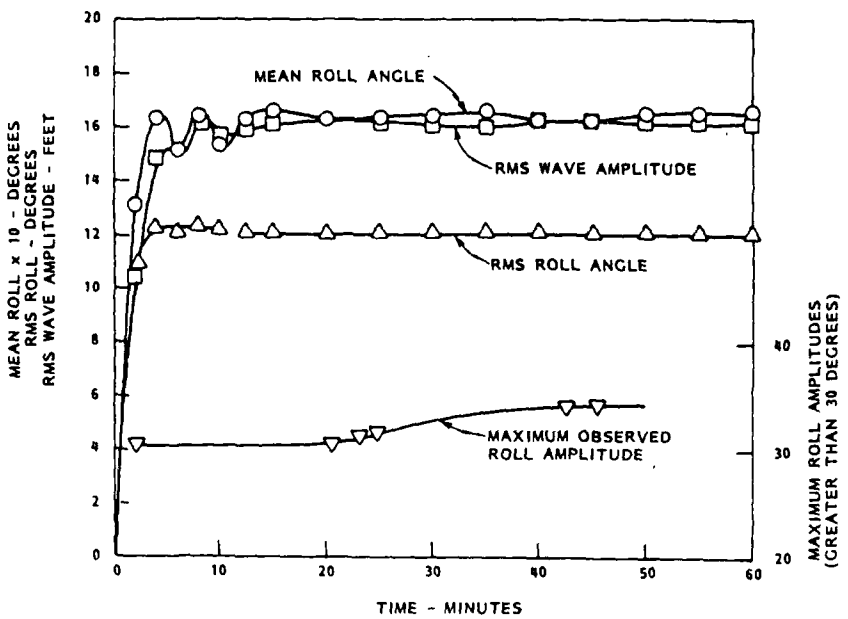

FIGURE 5 - VARIATION OF CALCULATED STATISTICS OF WAVES AND ROLL MOTION WITH TIME FOR SALVAGE VESSEL

Activities in Seakeeping Research at Institute for Marine Dynamics, National Research Council, Canada.
by Stefan Grochowalski

The relocation of the Institute to the new facilities in St. John's was the major factor affecting the activities during the last three years. Much effort has been spent on specification of required features for the measuring equipment, acquiring and commissioning it. This process is still being done. However, the scientific activities have continued during this period. The main areas of research in seakeeping were the following:

1. CAPSIZING OF SMALL FISHING VESSELS IN BREAKING WAVES

The objective of this program has been defined as:

- To investigate the physics of capsize phenomena in the general case;
- To define a mathematical model suitable for the prediction of capsizing in heavy seas;
- To establish a basis for intact stability regulations for small fishing vessels.

Extensive model tests with the model of a typical Canadian small fishing vessel have been carried out at SSPA in Sweden. To enable analysis of mechanism of capsize phenomena three different model attitudes were investigated:

1. Free-running model, both self-propelled and remote controlled during which all six components of the motion were measured.

2. Full captive model tests for the same conditions as 1 during which the acting forces and moments were red and recorded.

3. Semi-captive model tests, with freedom to heave and pitch, during which the forces and moments of the captive modes and the characteristics of heave and pitch were measured.

The tests were carried out in quartering, regular and irregular breaking waves for different model speeds, different headings and different angles of heel. All the runs were video-recorded. The time bases in the recorded time histories and on the video-records were synchronized. This enables detailed and precise comparative analysis of the model behavior in conjunction with the results of measured forces and moments in captive tests.

The analysis of the results is not yet completed.

2. SLAMMING

The influence of the bow shape on the slamming performance of a fast ship in head seas was studied. Three defferent bows were tested and bottom slam force on the bow, relative motion and logitudinal body motions were measured. Additionally some tests with prismatic models have been carried out to investigate the correlation between the relative velocity of a bow section, pressure distribution on the model surface and the total impact force.

3. SEAKEEPING OF FISHING VESSELS DESIGNED FOR OPERATING IN ICE

A Study is being made of the design of large and middle distance fishing vessels to investigate possible improvements to the capability of operating in ice infested waters. This study includes intensive model tests in clear water and ice. In particular, the seakeeping qualities of the various designs will be determined so that the need for trade-offs against performance in ice can be identified.

4. OTHER SEAPKEEPING ACTIVITIES

Besides the above projects some small routing seakeeping tests, sea trails and theoretical predictions of seakeeping by using the standard computer programs have been performed.

A considerable effort has been spent on the development of a computer model of ship dynamics in extreme waves. Computer software for time domain analysis and simulation is still not completed.

Seakeeping at the University of Michigan
by Armin W. Troesch

Since the previous ATTC meeting, The University of Michigan's SHip Hydrodynamics Laboratory (SHL) has expanded its seakeeping capabilities in both research and education. Concurrent with this expansion, commercial projects involving ocean-going and coast-wise barges, offshore terminal structures, tugs, and amphibious vehicles were also undertaken. The commercial test programs involved the more traditional measurements of added resistance, heave, pitch, roll, vertical accelerations, and video recording. This report will concentrate on the new and unique aspects of the projects in the past three years.

RESEARCH

1. TANK WALL REFLECTIONS:

In a project supported by the University of Michigan/Sea Grant Program, Stuart Cohen has investigated the effects on tank boundaries on zero speed model tests. Both theoretical and experimental investigations were conducted. In the analysis of the phenomenon, it was determined that even tanks with large dimensions can experience wall effects. In general, the proximity of the tank walls were the limiting factor in the length of time a test could be conducted before errors were introduced. This implies that zero speed tests involving long run times, such as slow drift experiments, may be susceptible data distortion caused by wall reflection.

2. THREE DEGREES OF FREEDOM MOTION DYNAMOMETER

Through support from the Office of Naval Research and The University of Michigan, the SHL has acquired a new motions dynamometer. The instrument is attached to the model through means of a heave staff. The heave, pitch, and surge motions are unrestrained while surge, roll, and yaw are restricted. A constant torque clutch applies a predetermined tow force to the model. In this way the added resistance in waves or calm water is measured. The dynamometer has already performed satisfactorily in a joint UM/STNSRDC ship-motions-comparison project. Future work will involve self propulsion tests in waves. The constant tow force will be selected to match the proper propeller loading condition.

3. BOW FLARE IMPACT

In work sponsored by the Maritime Administration, a series of experiments investigating the impact force on three dimensional bodies were conducted. Two shapes, a sphere and a cusped body, were dropped from various heights and the time histories of the impact force was recorded. The cusped body was axisymmetric and resembled the bow profile of a ship with flare. The sphere was subjected to both vertical and oblique impact angles while the cusped body experienced only vertical motion. A theoretical model using three dimensional, normal dipole distributions was formulated and compared to the experiments. Results indicate that depending upon body shape, theoretical estimates of the maximum impact force may be smaller or larger than the experimental values.

4. WAVE ENERGY RESEARCH

A model tandem-flap wave energy device was designed, constructed, and evaluated by the SHL. The work was jointly supported by DOE and Q Corporation, Troy, Michigan. The project produced a Ph.D. thesis. Based upon these results, a moderate-sized twin flap device will be designed and constructed for deployment in Lake Michigan in Summer, 1986. Preliminary estimates indicate that the 2.44m flaps will be able to recover up to 10kw in one meter seas.

5. COMPARATIVE SEAKEEPING MODEL EXPERIMENTS

The question of experimental accuracy in seakeeping experiments was addressed in a joint project between The University of Michigan and David Taylor Naval Ship Research and Development Center. Using an ITTC recommended hull form, a model was constructed and tested at both facilities. Studies on the variability of the results were made. Even though both organizations used substantially different test techniques (self propelled vs heave staff) and defferent data reduction methods, the results of the project indicate that carefully conducted seakeeping experiments can reduce the scatter to less than 5%.

6. ACADEMIC PROJECTS

The SHL has supported a graduate level course in experimental hydrodynamics. The intent of the course is to give students a chance to organize and design experiments in seakeeping, ocean engineering, and propulsion.

The seakeeping experiments involved a full scale ship motions experience on the RV LAURENTIAN, The University of Michigan's 24.4m research vessel. Experiments included heave, pitch, and roll motions, maneuvering characteristics, forward speed effects on roll damping.

Experiments conducted in the SHL included wall reflection experiments, cable strumming, relative motion, added resistance, and measurement of wave diffraction forces on a vertical column.

Significant Areas of Progress for Seakeeping at DTNSRDC

by Geoffrey G. Cox

Seakeeping remains an area of vigorous activity since the last conference. Basically, progress has consisted of improvements to the significant changes in emphasis outlined in the committee report to the last conference.[1]

A source document of wave and wind statistical data has been published for the North Pacific Ocean.[2] The data presented are the result of Spectral Ocean Wave Model (SOWM) hindcasts based on 17 years of six hourly archived pressure field data for about 1500 grid point locations. Bales gives a description of SOWM and related technology developed and used by the Navy in Reference 3. Efforts continue for the practical measurement, from a ship, of multidirectional wave spectra at sea. This effort is based on the lightweight ENDECO Wave-Track buoy and a data analysis program has been developed for the buoy data.[4]

The DTNSRDC Ship Motion Prediction Program for monohulls, SMP81,[5] has been enhanced by improvements to the accuracy of roll motion predictions, and inclusion of (i) antiroll fin systems with known controller gain values, (ii) wave induced vertical loads, and (iii) a set of tables of severe ship responses.[6] The DTNSRDC Small Waterplane Area Twin Hull (SWATH) Seakeeping Evaluation Program (SSEP) was modified to provide an assessment for the effects of stabilizing fins on the vertical motions (contouring and platforming) and/or roll motion.[7] The method employs linear quadratic theory of optimal control to determine the fin control law or optimal gains for controlling th vertical plane or roll motions of the SWATH ship.

Since the pioneering work of N.K, Bales on destroyer hull geometry for superior seakeeping,[1] considerable development and refinement has taken place. In particular, attention is drawn to References 8 to 11 for recent work on the topic.

Applications of the new developments for the ocean environment, ship motion prediction programs and superior seakeeping hulls; together with new tools for the presentation of performance assessment data developed at the Center, are given in References 12 and 13.

Development work on a Ship Motion Recorder, SMR, has been ongoing for several years, with an initial version fitted to two USCG cutters to indicate the effectiveness of the Rudder Roll Stabilization as an assist for helicopter operations. This version provided digital displays of roll and pitch motions, i.e., RMS and peak values. An improved version has now been developed with up to 16 channels of sensor information processed, analyzed, and logged on an IBM personal computer. Research on some statatistical aspects of seakeeping, and modeling of nearshore shallow water multidirectional waves is being carried out.[14,15]

Three papers from the Ship Performance Department at DTNSRDC are presented in the committee report. One, in cooperation with the University of Michigan, deals with comparative seakeeping model experiments, and two dealing with the measurement and analysis of multidirectional waves in basins and at sea.

REFERENCES

1. Cox, G. G., "Significant Areas of Progress for Seakeeping at DTNSRDC," Seakeeping Committee Report, Proc., 20th ATTC, August 1983.

2. Lee, W.T. et al., "Wave and Wind Environments for the North Pacific Operational Areas," Report DTNSRDC/SPD-0919-02, July 1985.

3. Bales, S. L., "Development and Application of a Deep Water Hindcast Wave and Wind Climatology," Internnat. Symposium on Wave and Wind Climate Worldwide. Royal Institution of Naval Architects, London, April 1984.

4. Lai, R. J. and R. J. Bachman, "Directional Wave Measurement and Analysis," Report DTNSRDC/SPD-1167-01, September 1985.

5. Meyers, W.G. and A. E. Baitis, "SMP84" Improvements to Capability and Prediction Accuracy of the Standard Ship Motion Program SMP81," Report DTNSRDC/SPD-0936-04, September 1985.

6. Meyers, W. G. et al., "User's Manual for the Standard Ship Motion Program, SMP81," Report DTNSRDC/SPD-0936-01, September 1981.

7. Gore, J. L., "Modern Ships and Craft, Chapter II: SWATH Ships," Nav. Eng. Journal, Special Edition, Vol. 97, No. 2, February 1985.

8. McCreight, W. R., "Estimating the Seakeeping Qualities of Destroyer Type Hulls," Report DTNSRDC 1074-01, January 1984.

9. Walden, D. A., "Practical Methods for Assessing Seakeeping Performance," Report DTNSRDC/SPD-1089-01, August 1983.

10. Walden, D. A. and P. Grundmann, "A Study of Methods for Designing Hull Forms with Reduced Motions and Dry Decks," Naval Eng. Journal, Vol. 97, No. 4, May 1985.

11. Walden, D. A. et al., "Optimization of Hull Form for Seakeeping and Resistance," Workshop on Developments in Hull Form Design, published by MARIN, The Netherlands, October 1985.

12. McCreight, K. K. and R. G. Stahl, "Recent Advances in the Seakeeping Assessment of Ships," Naval Eng. Journal, Vol. 97, No. 4, May 1985.

13. Kennel, C. G. et al., "Innovative Naval Designs for North Atlantic Operations," trans. SNAME, Vol. 95, 1985.

14. Dalzell, J. F., "Effect of Short Crested Seas on Quadratic Response," Report DTNSRDC 85/102, January 1986.

15. Lai, R. J. et al., "Wave Statistics in Nearshore Zones," Proc. Ocean Structural Dynamics Symp. 1984, Oregon State University, September 1984.

NOTE: References 5 and 6 are limited distribution documents.

MEASUREMENT AND ANALYSIS OF MODEL EXPERIMENT DATA ON BOTTOM SLAMMING

I. Datta, Associate Research Officer
National Research Council Canada
Institute for Marine Dynamics
St. John's, Newfoundland

ABSTRACT

The design, instrumentation and analysis of bottom slamming experiments on a number of slender ship models conducted at the IMD have been described in this paper. The main measurements considered were vertical hydrodynamic force on the bow, pressure at the keel level at various forward positions, relative motion at the forefoot and the motions at the body center of gravity. The data were reduced to conduct peak analysis of the force and motion data. The results demonstrate viability and some of the limitations of these techniques. Possible areas of improvement in instrumentation for future research have also been recommended.

1. INTRODUCTION

Over the past several years, the Institute for Marine Dynamics (IMD) has conducted a number of experimental projects to study the effect of bottom slamming on seakeeping performance of slender ship forms of high L/B ratio. A majority of these tests have been on fast frigate designs, but in one case they were carried out to make comparative bow design studies on a bulk carrier. These experiments have helped to develop and test an instrumentation and data analysis package primarily for bottom slamming tests in a towing tank.

Historically, experimental as well as theoretical quantification of bottom slamming has devoted attention to the measurement and calculation of pressure on the keel at the forward body and correlation of this pressure with the amplitude of impact velocity at the moment of re-entry of the bow in water. Tests in IMD were primarily done to compare the performance between a number of alternative bow designs for the same basic hull. Comparison of pressure data between the bows would be difficult without using an overwhelmingly large number of pressure transducers. Measurement of the total vertical force on the bow was considered simpler and more relevant for such comparison. The design developed was similar to the "segmented model" concept for flare slamming described by Bales and Jones [1], where the bow was cut as a separate wedge and reattached to the main hull through a force transducer so that the vertical impact force on the bow could be measured.

In order to measure impact velocity between the forefoot and the water surface at the instant of impact, a "digital" pin type relative motion probe was developed. Data from this probe was later differentiated to compute the impact velocity.

Description of the above-mentioned pieces of equipment and some typical results are presented in this paper. The problems that were encountered in developing these techniques have been described and possible future improvements that can be made to them are also suggested.

2. INSTRUMENTATION

The basic set up used in slamming experiments was essentially same as the one used for head seas seakeeping test in the IMD towing tank. In previous tests the waves generated were sinusoidal, but the new towing tank in St. John's now incorporates irregular wave generation facility.

The model was usually made of wood and was self-propelled without any external tow force. The only restraint on the model was provided by guiders consisting of vertical poles fore and aft sliding between horizontal rollers mounted on the tank carriage, thereby compelling the model to maintain a straight course down the center of the tank but allowing it the freedom to pitch, heave and surge.

The parameters studied in these test programs were the Froude number, wave frequency and the wave steepness. Froude number was varied from 0.15 upwards, depending upon the hull form and the design speed of the prototype. Non-dimensional frequency ($\omega_E \sqrt{L/g}$, where ω_E is wave encounter frequency in rad/s, L is model length on waterline and g is acceleration due to gravity) was varied about the mean value of 2.5 where slamming was most likely to occur.

Wave steepness (H/λ, where H is wave height and λ is wave length) was varied from a relatively mild 0.02 to higher values up to 0.06.

In slamming test programs at the IMD, four different forms of data were usually measured -

(1) bow impact force on the forefoot,
(2) relative motion at the forefoot between the bow and the adjacent water surface,
(3) rigid body motion of the model at its center of gravity, from which motions at other points could be derived, and
(4) in addition, a few pressure transducers were located at keel level in the bow section and the fore body.

The requirements for measurement, analysis, interpretation, etc. of each of these data types were fairly different. The biggest problem arose from the vast difference in required sampling rates. The trade-offs made in solving these problems and the techniques used for accurate measurement of the afore-mentioned data are described briefly in the following paragraphs.

2.1 Bow Impact Force Measurement

The technique used for the measurement of vertical impact force is illustrated in Figure 1. It utilized a detachable bow wedge cut horizontally at the load water line and at a longitudinal position corresponding to Station 18. This wedge, made of fiberglass to keep its weight as low as possible, was re-attached to the hull through a single cantilever type force transducer. This transducer was mounted close to the longitudinal position of the centroid of the bow segment so that the effect of bending moment could be minimized. Additional precaution for eliminating the bending moment component was taken by cutting two orthogonal notches on the rod connecting the bow segment to the force transducer mounted on the main hull. A uniform gap of about 2 mm all round was left between the two so that the only connection between them would be the force measuring system. The model was made watertight by cementing 40 mm wide latex strips all round the gaps. Any loss of peak force due to stretching of the latex was considered to be negligible.

Signal output from this transducer gave the time history of the total force on the bow. As has been pointed out by Bales and Jones [1], this measured vertical force time history contained several components in addition to that arising from pure vertical impact loading. Most prominent of this was the regular exciting force component at the wave encounter frequency. This force was responsible for the quasi-sinusoidal nature of the recorded data. In addition there was a quasi-static upward force arising from the change of mean trim of the hull and the rise of bow waves. An entirely non-representative inertial force component due to acceleration of the bow segment by the motion of the model was anticipated. Moreover the impact loading on the bow was likely to induce vibrations that could be large enough to be noticeable. Lastly small electrical noise from the data recording instrumentation could also be present.

Obviously it would be desirable to filter these non-impact type force components before statistics of impact force could be computed. The approach taken to resolve the recorded force data have been described in Section 5.1.

2.2 Relative Motion Measurement

For the measurement of relative motion, a prototype 16 pin digital device, as shown in Figures 1 and 2, was developed. The reason for choosing this device over traditional capacitance or resistance wire method was that this technique was considered to be less susceptible to the effect of splash that inevitably accompanies slamming since this could be eliminated from the recorded data while post-processing using programming logic.

The pin sensors were mounted on a vertical strut close to the centroid of the bow section (or alternatively at the forward perpendicular) and a little away from the model so that the strut and the pins could be extended down below the keel level without seriously disturbing the water surface. Extension of the strut below keel helped to obtain a more accurate estimate of impact velocity at the instant of re-entry of the bow into the water. The pins were electrically excited and checked at regular intervals. When a sensor registered a change of state (from wet to dry or dry to wet) an event was recorded. This yielded a record of pin emergence/re-entry time history which, when converted to distance from the keel, gave the relative bow motion as a function of time. By fitting a cubic curve to this data near the keel level and then differentiating with respect to time, bow impact velocity at the moment of bow submergence could be computed.

2.3 Rigid Body Motion and Wave Data Measurement

The model motions were obtained from four accelerometers fixed rigidly to the model and aligned with the model axes. Three accelerometers at the bow, stern and the LCB measured vertical accelerations and the fourth measured longitudinal acceleration with respect to the body axis system of the model. The surge translation of the model relative to the carriage was measured by means of a sonic probe fitted on the carriage and a target fitted near the rear end of the model. A pitch gyro was used for direct measurement of pitch motion.

In addition, the carriage speed and the incident wave elevation were also recorded. The latter was recorded using a sonic wave

probe fixed to the carriage at a known distance away from the nominal mean position of the model with respect to the carriage.

2.4 Pressure Measurement

In order to obtain some correlation between the vertical force on the bow and corresponding rise in vertical impact pressure at the forward bottom, pressure transducers were mounted in a few cases at the keel level at suitable positions. The miniature piezo-resistive transducers used for this purpose had very thin diaphragms of the order of 2.54 mm in diameter and natural frequency of about 45 kHz. These transducers, which operated on resistance-bridge principle, were flush-mounted with the outside surface of the model. Data from these transducers were passed through signal conditioners and recorded on magnetic tapes. A brief description of the data acquisition system is given in Section 3.

3. DATA ACQUISITION SYSTEM

Typical rise time for a pressure peak was likely to be of the order of 100 μs, requiring a sampling rate of at least 20,000 samples per second to define properly. On the other hand, optimum sampling rate for force data was found to be around 500 samples per second. Apart from being vastly different from each other, these two sampling rates were much higher than the highest rate which the carriage-based data acquisition system could handle. Moreover a typical test run of approximately 30 seconds in duration could involve about 30 wave encounters. If each of these encounters produced a slam, just one run would generate some 600,000 data points from one pressure transducer alone. It is obviously impractical to record so much of data directly on a computer without some prior processing and data reduction.

The solution devised at the IMD was to record the force and pressure signals as analog data onto a tape recorder and digitize them afterwards with suitable trigger levels to retain the impulse time history only and eliminate rest of the unnecessary data. An 8-channel HP-3968A FM tape recorder was used for this purpose. The model motions, wave elevation and carriage speed, on the other hand, were digitized in real time at 20 samples per second and recorded directly on a standard IMD data acquisition system (DAS) driven by the carriage computer. Data from the 16-pin relative motion probe was also recorded on the DAS system in an encoded form and later decoded separately to extract the relative motion information.

In order that the two types of data (force/pressure data on the tape and the motion data on the computer hard disc) could be correlated, one channel on the FM tape was used to record a time synchronization signal. A second channel was usually reserved for voice recording to label the runs, record run descriptions and operator's comment on each run. Therefore a maximum of 6 channels were available to record force and pressure data on this machine. A higher speed 14 channel tape recorder is being developed to provide the option to record larger number of channels in future tests.

A single channel transient recorder/oscilloscope was also used to monitor and visually examine the force and pressure signals during each run.

4. DIGITIZATION OF FORCE AND PRESSURE DATA

Different digitization processes were used for the force and the pressure signals. Since frequency and, to a certain extent, time domain analyses were carried out on the force data, it was digitized simply as a continuous time series at 500 samples per second. This rate was found to give good definition of the force signal.

For the digitization of pressure, the process was quite different. To start with, the maximum sampling rate on the PDP 11/34 computer used with the DAS system in the IMD Ottawa laboratories was 10,000 samples per second for one channel. Therefore in order to obtain an effective sampling rate of 20,000 samples per second, the tape recorder had to be played back at half speed and digitized one channel at a time. However since this required one playback/rewind cycle to digitize one channel, it was a very time consuming process and had to be automated. Since the 8 channel HP-3968A tape recorder had a HP-IB interface, it could be computer controlled to make it start, stop, advance and rewind automatically. A special program was written to drive the FM tape recorder, locate runs by sampling the timing signal on the synchronization channel and then digitize the pressure channels one at a time. The program emulated a digital transient recorder with a record length of 500 samples per transient event. Only when the pressure exceeded a user-defined trigger level (usually of the order of 5 kPa) was the signal digitized, with the process extending from 100 samples (5 ms) before to 400 samples (20 ms) after the trigger point. This process continued until all the peaks from one channel that exceeded the trigger level were digitized. When all channel were completed, data from the whole run was copied into a master file and the program commenced sampling a new run.

5. ANALYSIS

The analysis of test results were conducted in a number of stages to reflect the specific needs for the different types of data recorded. The force data had to be corrected for the inertia force associated with the fiberglass part of the bow, filtered and the statistics of the time series records could then be determined. The digitized transient pressure records were scanned to eliminate spurious peaks and statistical analysis was performed. The encoded data from the relative motion probe was converted to relative motion

time series from which relative velocity could be computed. The measured accelerations and displacements were converted to heave and pitch amplitudes and phases and presented in standard non-dimensional forms. A brief description of the first three are presented in the following paragraphs. Since the analysis of motion data followed standard seakeeping data presentation practice, this has not been separately discussed here.

In order to analyze the data, a large volume of computer software was developed in-house. Description of these computer programs has been given in detail by Koniecki [2]. A flow chart of data recording and analysis procedure is shown in Figure 3.

5.1 Force Data

As has been described in Section 2.1, measured vertical force time history was a superposition of a number of components, from which the non-impact type force would have to be eliminated before computing the slamming data. As a first step, the inertia force component was eliminated from the record. This was easily done by first computing, from the recorded acceleration data, vertical acceleration at the location of centroid of the bow segment as a function of time and then multiplying by its mass. Figure 4 illustrates the process. Channel 1 gives a typical recorded time history, Channel 2 shows corresponding vertical inertia force and Channel 3 the resultant signal containing only the hydrodynamic force component.

The forces due to bow wave and trim change were quasi-static in nature and were interpreted as zero shift for the purpose of data analysis. They could easily have been removed by making calm water runs at the same Froude numbers and measuring the average force on the bow. However in the tests described here, these calm water runs were not needed for reasons explained later.

Attempts had been made to use a mathematical filtering technique to eliminate the remaining non-slamming forces. Difficulties immediately arose in using this technique. Since the slam force was transient in nature spaced approximately at the encounter frequency interval, Fourier decomposition of the time history failed to preserve these transients faithfully. Any attempts to filter out the encounter frequency component seriously attenuated the slam force peaks.

In view of the afore-mentioned problem, the encounter frequency force component was not eliminated from the data. Instead the force data was treated primarily as total vertical hydrodynamic force rather than purely slam force. This approach was acceptable because, as has been explained earlier, the tests were primarily for the comparison between alternative bows. For each individual slam, the peak force was defined as the difference between the peak and the mean base level of the record just prior to the peak. Attention to this difference in level helped to ignore the quasi-static components arising from bow wave and trim change and so calm water runs were not needed.

In spite of the above difficulties, it was still possible to filter out the vibration and electrical noise components from the records by applying bandstop and low pass filters respectively. Approximate calculations were made to estimate the natural frequency of the bow arrangement and the actual band was found by trials. Attenuation of the hydrodynamic force signal due to filtering out of these high frequencies was usually minimal. The Channel 4 in Figure 4 shows a typical filtered force time history.

In most tests, a small number of repeat runs were also made to assess the variability and repeatability of the computed force data. For each run in nominally identical test condition, peak hydrodynamic force and the corresponding rise time were calculated for each wave encounter. Rise time was measured as the time taken by the force to rise from 10% to 90% of its peak value. These individual peak forces and rise times were combined to form two large sample groups. From these the usual sample statistics like the mean, standard deviation, the maximum and the minimum values were computed and histograms plotted. In Figures 5(a) and 5(b), typical probability densities of peak bow force and corresponding rise time are shown.

5.2 Pressure Data

Figure 6 shows an example of the time history of pressure peak corresponding to the largest slam recorded in a typical run. Contrary to the force signals which were digitized on a continuous basis, pressure signals were digitized as transients only when the signal exceeded a pre-defined trigger value. The trigger point in the above-mentioned Figure is located 5 ms after the start of the transient record. To is the time at which trigger occurred relative to the start of the run and is shown in the plot.

5.3 Relative Motion Data

From the time series records of relative displacement, it was possible to compute relative velocities between keel and wave surface at the moment of re-entry for each encounter where the keel emerged prior to impacting on the incident wave. The average value of relative velocity at re-entry in each run was computed and plotted against corresponding average of peak hydrodynamic force. A typical result is given in Figure 7. From this plot, a positive correlation between average peak force and relative velocity is apparent, even though there is significant amount of scatter. It was thought that the high scatter might be explained by investigating the other parameters, namely

the Froude number, wave encounter frequency and wave steepness. However with relatively limited number of data points per each parameter, such parametric study did not yield any meaningful trend. This, however, should not overrule the possibility of these parameters influencing the results.

6. CONCLUDING REMARKS AND FUTURE AREAS OF WORK

In this paper the techniques used for the measurement and analysis of slamming experiment data that have been developed in IMD are presented. While some of these techniques proved very useful in evaluating the slamming characteristics of a given hull form, others were troubled by both design as well as hardware problems. It is quite evident that new techniques now available can perform some of these measurements and analysis more accurately and efficiently. Following areas of future improvement have been suggested here, some of them already being developed for implementation in a new series of slamming experiments currently scheduled at the IMD.

(1) The biggest problem was faced in isolating the slam force from the regular quasi-sinusoidal hydrodynamic force component. It was evident that frequency domain analysis was of limited value in this case. It may be worthwhile to employ more of time domain analysis by fitting the best sinusoid to the recorded time history and then subtracting it from the force data to obtain the predominantly transient time history. Algorithms for fitting such an optimum sine wave form to a periodic record has been developed for quite a different application in the Hydraulics Laboratory of the National Research Council in Ottawa [3,4]. It may be possible to use the same algorithms in this case. However the so-called hydrodynamic force component, even in the absence of slamming, is non-linear in nature and therefore problems may occur in fitting simply the best sinusoid. This and other methods are to be investigated.

(2) The effect of various parameters like model speed, wave encounter frequency and wave steepness on impact force vs. vertical relative velocity relationship will certainly need to be studied in more detail in future tests.

(3) Problems were encountered during model testing due to the use of a single cantilever type force measuring transducer. Even though the bending moment was effectively eliminated from the force data, the fiberglass bow did flex under dynamic loading, in some cases causing physical contact between the two bodies. The peak bow force was found to be clipped as a result. This problem was temporarily eliminated by shaving more wood off the forward end of the main model so that the horizontal gap between it and the bow segment was increased. However, this has now been changed to a three point mounting, similar to the one used by Bales and Jones [1] for flare slamming. This will not only make the bow rigid and eliminate the problem arising from flexing of the bow segment, but the center of application of bow force as a function of time may also be computed.

(4) The relative motion probe developed in the earlier stages of experiments sampled at fixed intervals and therefore suffered from small loss of resolution as to exactly when a change of state (from wet to dry or vice versa) for a pin took place. An improved device recently developed uses a real time clock which, instead of sampling at fixed intervals, samples only when a change of state takes place. The possibility of using an intelligent device which can compute the impact velocity directly from pin data and output it to the data acquisition system is being investigated.

(5) The larger than desirable variations in bow force and pressure data in nominally regular waves was of some concern. It was anticipated that small variation in wave profile, combined with some variation in the model attitude from one wave to another, would give rise to some scatter in the data. It is being expected that the new wave-making system in St. John's will be able to provide uniform wave train and at least one source of this variation could be eliminated.

(6) Lastly, tests in the past have only been conducted in regular waves. It will be of interest to extend this to testing in irregular waves and obtain statistical results to be compared with the predictions using the stochastic theory developed by Ochi and Motter [5].

REFERENCES

1. Bales, N.K. and Jones, H.D. (1980) : "Measurement and Reduction of Model-Scale Data on Flare Slamming and Deck Wetness". Proc. 19th American Towing Tank Conference, Ann Arbor, Michigan, July 1980, pp. 209-226.

2. Koniecki, M. (1984) : "Software for M.V. Arctic Slamming Experiments". NRC/IMD internal report no. MTB-156, Ottawa, Ont., October 1984.

3. Mansard, E.P.D. and Funke, E.R. (1980) : "The Measurement of Incident and Reflected Spectra Using a Least Squares Method". Proc. 17th Coastal Engineering Conf., Sydney, Australia.

4. Mansard, E.P.D., Sand, S.E. and Funke, E.R. (1985) : "Reflection Analysis of Non-linear Regular Waves". NRC Hydraulics Laboratory technical report no. TR-HY-011, Ottawa, Ont., Nov. 1985.

5. Ochi, M.K. and Motter, L.E. (1973) : "Prediction of Slamming Characteristics and Hull Responses for Ship Design". Trans. SNAME, Vol. 81, 1973, pp. 144-176.

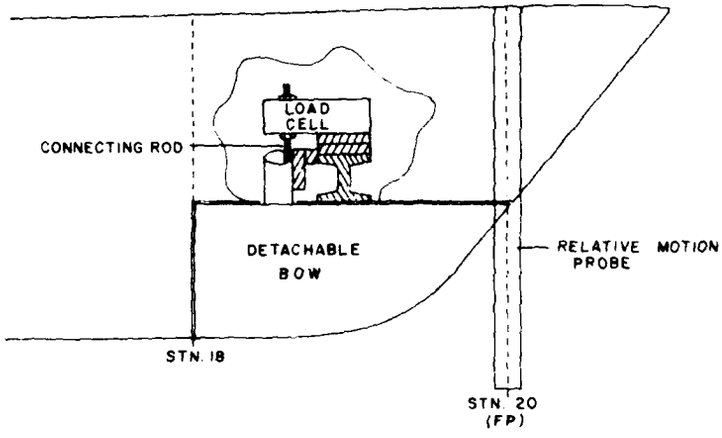

FIGURE 1 Bow Bottom Slamming Measurement Instrumentation Scheme

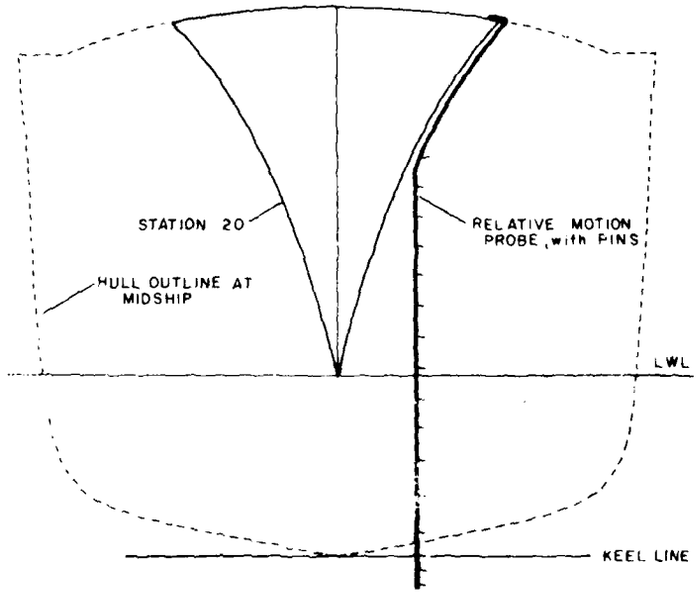

FIGURE 2 The Pin-Type Relative Motion Probe Concept

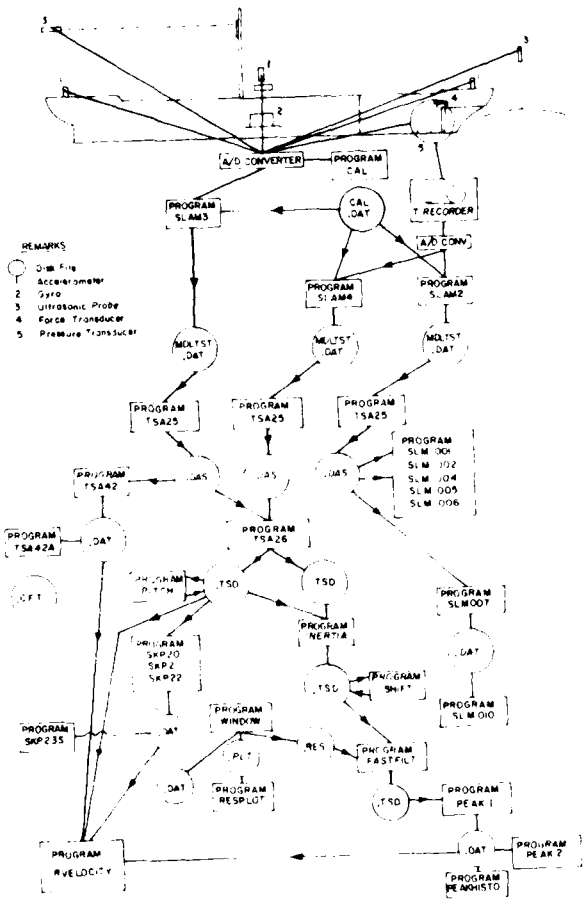

FIGURE 3 Flowchart of Software for Slamming Experiments.

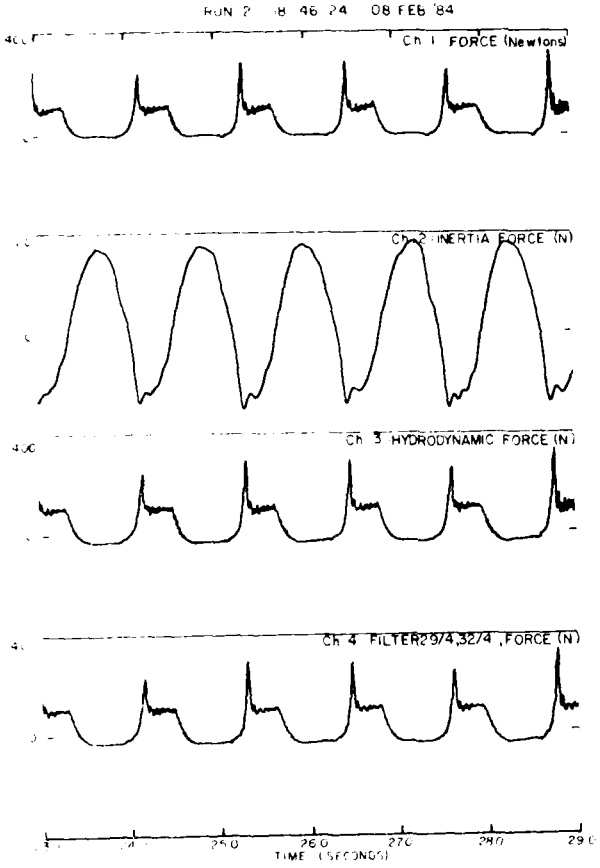

FIGURE 4 Force Measurement Time History

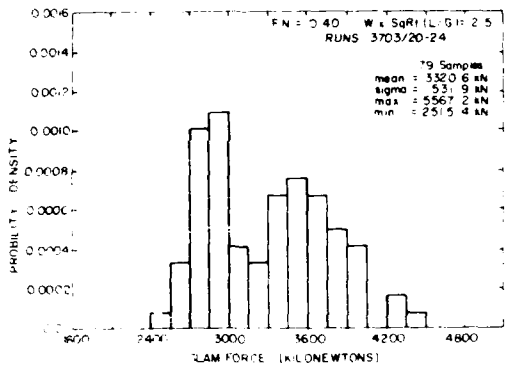

FIGURE 5a Histogram of Force Data

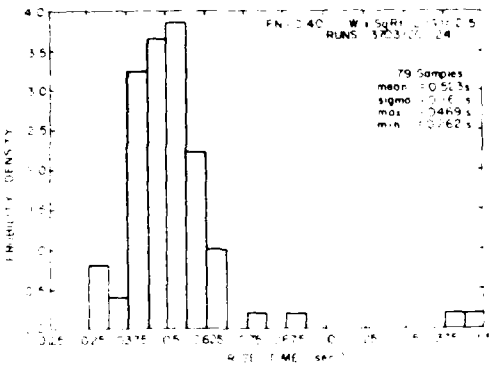

FIGURE 5b Histogram of Rise Time Data

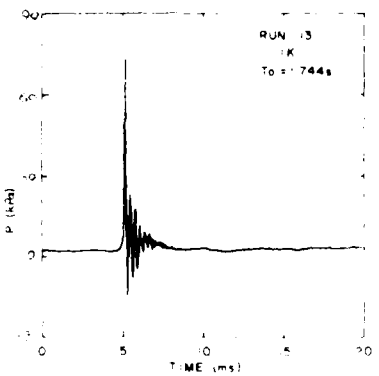

FIGURE 6 Pressure Time History at Keel

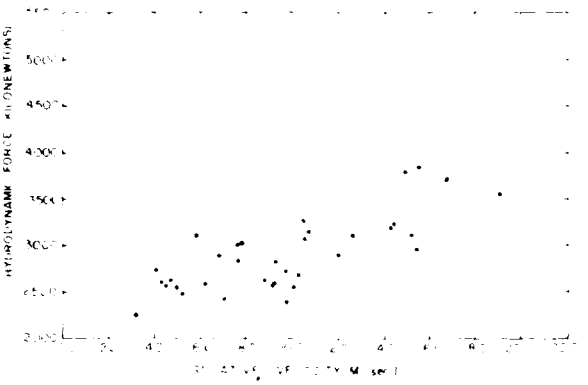

FIGURE 7 Hydrodynamic Force vs. Relative Velocity

ERRORS DUE TO INTERACTIONS IN SEAKEEPING MODEL TESTS

Stuart B. Cohen
Research Associate
Department of Naval Architecture
and Marine Engineering
The University of Michigan
Ann Arbor, Michigan 48109

ABSTRACT

Towing tank model testing of ships at slow speeds and oil platforms at zero speed may exhibit large experimental scatter due to wall interaction effects. An investigation of one class of interactions (an infinite row of identical bodies) indicates that the usual frequency domain analysis is unattainable in principle in finite sized tanks. A time domain approach is offered in which the error of predicting an unbounded water heave RAO and added mass by using a finite tank is quantified. Some preliminary results showing the maximum experimental error are presented.

1. INTRODUCTION

Model testing of ships at low speed and ocean platforms at zero speed in narrow towing tanks have shown large experimental scatter due to tank wall effects. These effects have been demonstrated for both deep and shallow water by Tasai et al [1978] among others. The Seakeeping Committee Report of the 17th ITTC [1984] discusses problems in head and following seas for model speeds below V_{int}, the minimum speeds below which interference can occur for a given λ/L range. (The values of V_{int} are obtained from the Tank Wall Interference Diagram from Goodrich [1969]). These problems include changes in the longitudinal drift force, peaks in measured response data for all directions of motion, and two-dimensional transverse standing waves generated between the model and tank walls. In addition, when the wave encounter frequency is close to one of these transverse slosh modes of the model, large time varying responses can occur.

The wide variety of time varying effects in tank testing have been a concern since the last ITTC Report. For analysis purposes, the general problem of time varying tests measurements can be separated into three classes:

1) forced motion: the circular, radiating waves generated by a body can reflect off flat tank walls and return to interact with the model,

2) fixed bodies: along with the diffraction problem for a single body between walls (similar to the radiation problem), there are diffraction effects for a one-dimensional row of bodies (such as a line of wave energy absorbers) or between a fixed and floating body (a moored ship) in incident waves which can be strongly influenced by the tank wall effect. Even in the absence of walls (i.e., unbounded water), Takaki et al [1984] have shown that a 2-dimensional analysis of a moored ship shows strong transients and time varying results are obtained in this case.

3) internal motion: resonant frequencies between two rows of an array of bodies (such as the struts of a semi-submersible) generated either by incident or radiated waves are in a different range of interest from the usual frequencies of ship motions, but these interactions can be time varying even without tank walls. Because of so much generality, this paper will be restricted to the cases that include flat tank walls.

During an investigation of the second class of interactions (the frequency domain diffraction effects of an infinite row of identical bodies) a method was found to estimate the time varying effects when the time record is short and steady conditions have not been reached. This indicates that with walls, the usual frequency domain representation of model response cannot be attained in principle for some frequency values no matter how large the testing tank is. To investigate these frequencies, a time domain approach was used to determine the maximum error in predicting an unbounded heave response aplitude operator (RAO) of a floating sphere when using results from tests in a finite size tank.

2. PROCEDURE

The procedure follows the impulse response function (IRF) method as described by Cummins [1962]. The response in heave $\eta(t)$ is due to the convolution of the IRF, $H(t)$, with an arbitrary forcing function $F(t)$:

$$\eta(t) = \int_{-\infty}^{t} H(t-\tau)\, F(\tau)\, d\tau$$

An example for a 0.61 m diameter sphere in unbounded water (Figure 1) shows that after four or five waves have passed, the motion reaches steady-state. Compare this to Figure 2, the response in a tank of width 6.71 m. (This width corresponds to the towing tank of the University of Michigan's Ship Hydrodynamics Laboratory). For the input frequency chosen, each reflection arrived from the wall delaying the growth to full steady-state values. The choice of frequency determines the steady-state value since some nearby frequencies will reinforce the motion.

This effect is best seen on the steady state (frequency domain) plots of the RAO due to seven spheres as in Figure 3, where the partial reinforcement and cancellations show as small oscillations, and the reinforcement of all seven images shows as a major peak. The method of images (See Newman [1980]) allows a mathematical replacement of the tank walls by an infinite number of identical bodies.

However, the actual test typically takes less than 60 seconds, so the effects of the outlying spheres are diminished, since the higher frequency waves generated by the images never arrive in time to be measured. Note, for instance, that if the IRF is truncated to 60 seconds, we can see that for a fixed wall separation, W = 6.71 m, there are 4 images. Increasing the number of spheres does not effectively change the truncated IRF (theoretically, the zero-frequency components move instantaneously, but their amplitude is negligible). Since the value of the IRF outside the truncation limits is zero, the convolution integral obtains no contribution outside these limits. Therefore, when considering a finite time interval, the effect of the walls can be represented in the time domain by an integer number of images.

Figure 4 shows the corresponding seven-sphere added mass and damping coefficients. For the lower frequencies, that is, frequencies below the first major peak in the added mass graph, two observations can be made: 1) for the RAO, the interaction effects are small, 2) for the added mass, they are small below the first transverse resonant frequency. At still lower frequencies, wall effects are expected to be minimal. A graph of tank width required to be below the first transverse frequency is shown in Figure 5. This is based on the deepwater, frequency domain observation that when the sphere is on the tank centerline, a wave equal to the tank width has a frequency $f_w = \sqrt{g/2\pi(W-2A)}$. Thus, if the measured record contains frequencies above that value, there should be some detectable error.

To gain a measure of the error and how long it takes to build up, we can look at the added mass and damping coefficients at the first resonant frequency. Preliminary observations indicate that the percentage error of the added mass is largest at the first slosh frequency, and that value is approximately the same as the error of the RAO at the spheres natural frequency in heave. Although these are broad assumptions, they give an upper limit to the error and are expected to be useful for guidance.

3. ADDED MASS IN HEAVE

The basic illustration uses a sphere of .61 m (A=.305m) diameter. The added mass coefficient, A_{33} and frequency parameter, κA, have been non-dimensionalized in the usual way. The peak error is defined as the difference between the value of the single (unbounded water) sphere (Figure 6) compared to the value of a particular number of multiple spheres at the first transverse slosh frequency. Figure 7 shows a family of curves relating the percentage error to the test time duration for various tank widths. From this graph, it can be seen that for heave added mass at each of the slosh frequencies, and for heave RAO at the body's natural frequency, there will be some error no matter how large the tank, but the error diminishes rapidly with increased tank width and inversely with frequency of interest. These curves have been substantially smoothed: the error varies as rapidly as the multiple sphere added mass does. The points of peak error have been connected to give a fair curve. Times have been defined as the period until the last image has less than 1% amplitude compared to the first image. For frequencies of interest at higher harmonics, the time to reach the error level indicated on the graph is $\sqrt{n}$ times the value at the first harmonic, where $n \cdot f_w$ is the higher frequency. For example, a 33 m tank has a first resonant peak at 0.23 Hz. This gives an error of 9.7% after 100 sec. At 1.13 Hz, it will take $\sqrt{5}$ times longer or 224 secs.

4. OBTAINING THE IRF

For completeness, a brief description of the method of obtaining the multiple sphere IRF will be given. Using a multipole expansion of the 3-dimensional, free surface velocity potential as described by Greenhow [1980], frequency domain results were obtained. The discrete inverse Fourier Transform of these results yields the IRF. For small enough separations, each body's contribution to the total IRF can be seen individually, so the length of time for that body (and therefore for that image) to reach the center sphere is known. The error is determined from the frequency domain results such as Figure 3. Both these results can be checked by actually performing the convolution which confirms the time and amplitude values.

5. CONCLUSIONS

Preliminary results are given for the error induced by testing floating bodies in narrow towing tanks. These are preliminary because they are restricted to spheres, operating in heave, floating in an ideal fluid, excited by a single, linear frequency, and are maximum values due to the assumption that the

error is at the first slosh frequency and holds for all the other transverse resonant frequencies. However, the method appears to give a first-order measure of the errors expected to be encountered in tanks of all sizes.

6. ACKNOWLEDGEMENTS

These results are from part of a thesis dissertation, supported by the Michigan Sea Grant Program (Project number R/T-16, Grant number NA-80AA-D-00072), which is expected to be published in the near future.

7. NOTATION

A = body radius or half-beam (m)
A_{33} = added mass coefficient
$= a_{33}/\rho\nabla$
f_w = frequency (Hz)
$F(t)$ = arbitrary forcing function
g = gravity (m/sec^2)
$H(t)$ = impulse response function
L = ship model length (m)
t = time (sec)
V_{int} = minimum speed for which there is no interaction effect (m/sec)
W = tank width (m)
$\eta(t)$ = heave response (m)
ρ = mass density (kg/m^3)
λ = wave length (m)
κ = wave number
$= \omega^2/g$ (m^{-1})
ω = frequency (rad/sec)
∇ = underwater volume (m^3)
IRF = impulse response function
RAO = response amplitude operator

REFERENCES

17th ITTC [1984], International Towing Tank Conference Proceedings, Swedish Maritime Research Center SSPA, Goteborg, Sweden, p 478.

Cummins, W. E. [1962], "The Impulse Response Function and Ship Motions," Shiffstechnik, Vol. 9, Number 47, p 101.

Goodrich, G. [1969],"Proposed Standards for Seakeeping Experiments in Head and Following Seas," Report of the Seakeeping Committee, 12th International Towing Tank Conference Proceedings, Rome, 1969, p 675.

Greenhow, M.J.L., [1980], "The Hydrodynamic Interactions of Spherical Wave Power Devices in Surface Waves," Power from Sea Waves, edited by B. Count, Academic Press.

Newman, J. N. [1980], Marine Hydrodynamics, MIT Press, Cambridge, Mass., p. 152.

Takaki, M., Saito, K., & Nakamura, S. [1984], "Comparisons of Simulation Methods for Motions of a Moored Body in Waves," Proceedings of ASME 3rd Int'l Offshore Mechanics & Arctic Engineering Symposium, New Orleans.

Tasai, F., Takaki, M., Ohkusu, M. [1978], "Ship Motions in Restricted Waters-Tank Tests," Research Institute for Applied Mechanics Report, Kyushu University, Vol XXVI, Number 81, July 1978.

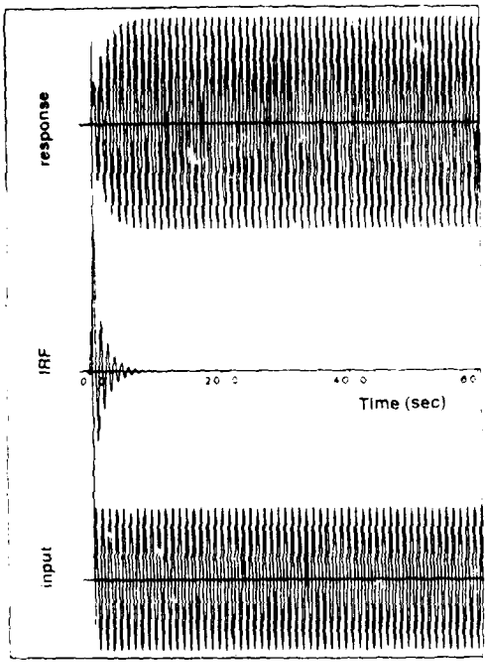

Figure 1. Heave response of one sphere to sinusoidal waves in unbounded water.

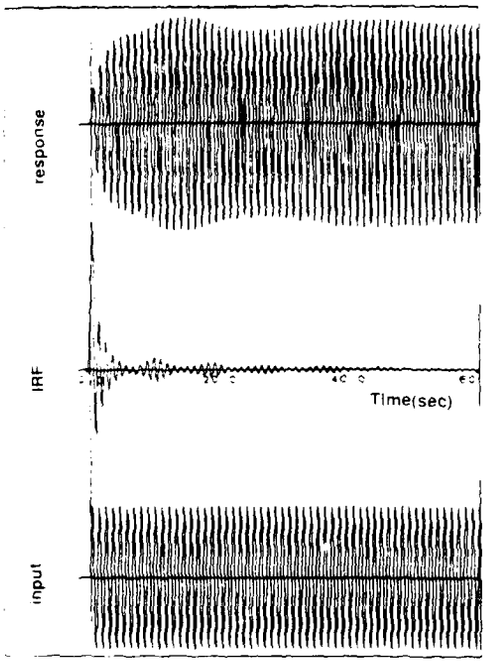

Figure 2. Heave response of 7 spheres to sinusoidal waves with separation distance of 6.71 m.

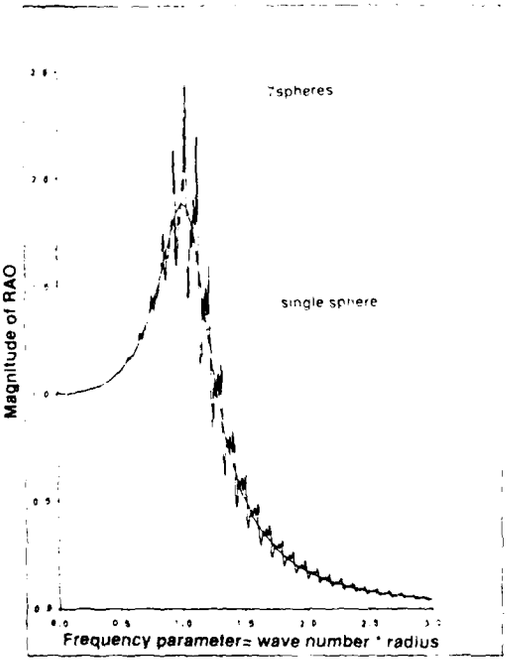

Figure 3. Magnitude of RAO for 1sphere and for 7 spheres with separation distance of 20.1 m.

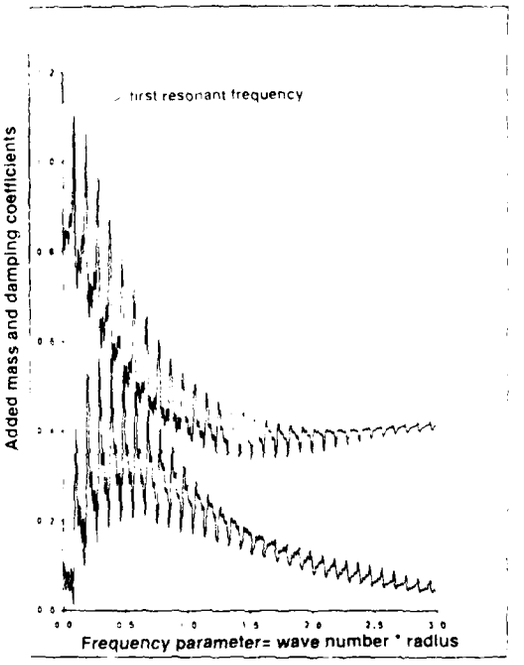

Figure 4. Added mass and damping coefficients for 7 spheres with separation distance of 20.1 m.

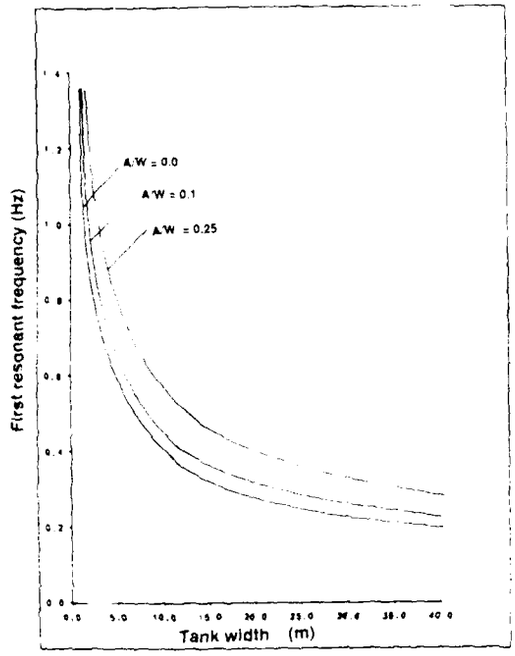

Figure 5. Tank width required to have no transverse resonant frequency.

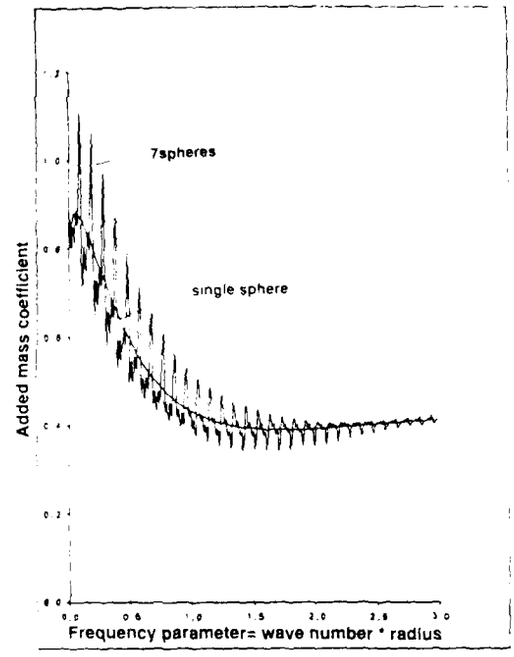

Figure 6. Added mass coefficient for 1 sphere and for 7 spheres with separation distance of 20.1 m.

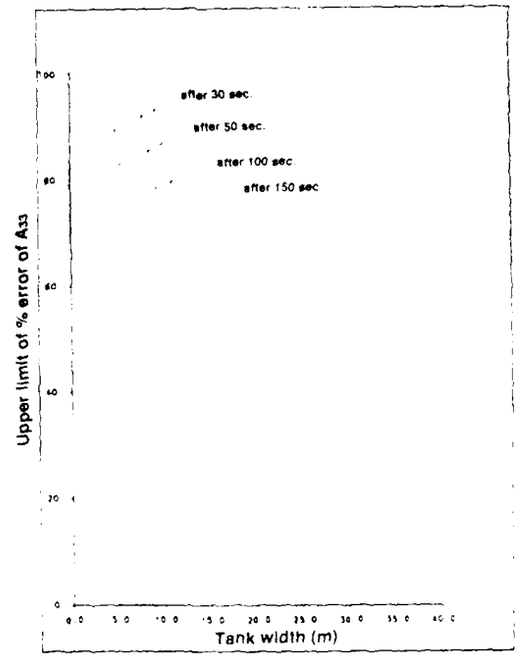

Figure 7. Upper limit to error of A_{33} at first resonant frequency for various tank widths.

COMPARATIVE SEAKEEPING MODEL EXPERIMENTS

John P. O'Dea
David W. Taylor Naval Ship Research and Development Center
Bethesda, Maryland
and
Armin W. Troesch
The University of Michigan
Ann Arbor, Michigan

ABSTRACT

As part of a continuing International Towing Tank Conference (ITTC) effort to investigate methods of predicting and measuring ship responses to waves, comparative seakeeping experiments were performed at The University of Michigan and at David W. Taylor Naval Ship Research and Development Center using a model of the SL-1/5 hull form. Experiments were done in regular waves with measurements of heave, pitch, and bow acceleration. The results have been analyzed to provide an estimate both of variability of results within an experiment and differences in results between experiments and between different laboratories. Differences in experimental techniques and their influence on measured differences are discussed.

1. INTRODUCTION

The prediction of ship responses in a seaway rests primarily on the theory of linear systems by which the response to a wide range of inputs can be determined if the transfer functions of the vehicle are known. Thus, the determination of these transfer functions is one of the fundamental objectives of seakeeping research. The development of improved theoretical/numerical techniques for predicting these functions is a continuing process. Various versions of strip theory are used today in designing and evaluating new ships, and improvements such as three-dimensional panel methods are reaching the stage of practical application. However, the ultimate criterion in evaluating the accuracy of any of these prediction methods is a comparison to actual measurements either on a full scale ship or on a scale model. The comparison is made more difficult by uncertainties regarding the accuracy of the physical measurements. In fact, because of the expense involved in model testing, experiments are rarely carried out expressly for the purpose of determining experimental accuracy, and there is little quantitative information published by which the degree of correlation between seakeeping theory and experiment can be assessed. In the case of full scale experimental measurements, the problem is further compounded by the random and uncontrolled nature of the prevailing natural environment.

This paper addresses the question of experimental accuracy in seakeeping model experiments. The impetus for the work has been a project promoted by the International Towing Tank Conference (ITTC), in which member organizations have been encouraged to perform seakeeping experiments on a standardized hull form. In the United States, these experiments have been performed at The University of Michigan (UM) and at the David W. Taylor Naval Ship Research and Development Center (DTNSRDC). The same model was used by the two organizations, eliminating any of the variations associated with model construction and scale ratio. However, there remain many other factors which are different in the two experiments, including tank size, instrumentation, and methods of testing and data analysis, which may affect the outcome of the experiments. The experiments have been analyzed for the purpose of assessing the variability of results, both within each experiment or laboratory and between laboratories, and several sources of the variations are discussed.

2. EXPERIMENTAL ACCURACY

In other engineering fields, there have been attempts to develop a rigorous approach to analyzing experimental accuracy. The purpose is to emphasize that all experiments are subject to uncontrolled variations in the relevant physical parameters or their measurement, and that bounds on the possible variation in reported results should be stated and substantiated. In the Fluids Engineering Division of the American Society of Mechanical Engineers (ASME), this approach has been defined as "uncertainty analysis," and a symposium has recently been held on the subject (Abernathy et al. (1985)). In uncertainty analysis, several contributions to the total uncertainty of results are identified. The first, and most difficult to quantify, is bias in the experiment. Bias is defined as any effect which is held constant throughout the duration of the experiment, and which leads to

a constant variation of results from the true value. Examples of bias include calibration errors and differences in test technique or facility. The second type of uncertainty source, which is familiar to any experimenter, is defined as the precision error and is the random scatter of results seen when experiments are repeated under nominally identical conditions. Other aspects of uncertainty analysis emphasized by the ASME are the importance of assessing the sensitivity of results to changes in test conditions and the need to distinguish different types of experiments in which accuracy requirements may be quite different. Ideally, the quantification of uncertainty in this approach is substantiated by statistical measures with a large body of repeated data. In most seakeeping experiments, this is not done because of obvious time and cost restraints. The work reported herein is merely a first step in the direction of obtaining such a data base. The discussion of the results will be in the context of these uncertainty analysis definitions, and an attempt will be made to quantify some of the identifiable sources of uncertainty.

3. THE MODEL

The hull form chosen for the ITTC comparative seakeeping study is a single-screw merchant hull form designated as hull S7-175. The scale ratio may be chosen by participating organizations to suit individual towing basin or instrumentation standards and requirements. The model used in the present study was constructed of wood by DTMB (model serial number 1561) to a linear scale ratio of 2%.3%. A list of principal particulars is shown in Table 1, and a body plan is shown in Figure 1. Measurements included heave at the center of gravity, pitch, and vertical acceleration at a point equal to 15 percent of the length (defined as length between perpendiculars) aft of the fore perpendicular. In the case of rigid body motion, the vertical acceleration at any point could, of course, be calculated from combined heave and pitch motions. Thus the acceleration measurement was redundant but provided a means of checking the accuracy of measurement of all three quantities.

The mean waterline (9.6 m full scale) was marked at four locations on the model, two forward (port and starboard) and two aft. At DTMB, the model was ballasted to the draft marks and the weight recorded and compared with hydrostatic calculations. The vertical center of gravity was measured through an inclining experiment, and the radius of gyration was set on a swing table. At DTNSRDC, the model was ballasted to a calculated displacement, which resulted in a slight variation from the marked waterline. The vertical center of gravity was measured by an inclining experiment, and the radius of gyration was measured by swinging the model in yaw (pitch radius of gyration was assumed equal to yaw radius of gyration) and measuring the natural period in air.

4. EXPERIMENTAL PROCEDURES

The experiments were conducted in regular head waves at two nominal speeds corresponding to Froude number 0.200 and 0.275. Regular wave periods corresponding to full scale periods in the range 6 to 14 seconds, in one second increments, were initially chosen. Additional intermediate periods were added to the test program as a result of some unexpected preliminary results. The model was free to surge in both experiments; however, the details of towing arrangements varied as explained below.

The first set of experiments were conducted at the Ship Hydrodynamics Laboratory at DTMB. In the DTMB experiment, the model was attached to a new motions dynamometer developed at DTMB through support from the Office of Naval Research. The dynamometer provided a constant predetermined tow force to the model while allowing the model to be free to surge. Two carriages, a lightweight one from which the heave and pitch motions were recorded, and a relatively heavy, rigid one which carried the control electronics and a constant torque motor, traveled on rails attached to the main towing carriage of the tank (see Figure 2). The heave displacement was measured from the motion of the heave staff which was attached at the center of gravity of the model. The pitch motions were recorded from a RVDT located at the base of the heave staff. Surge amplitudes were determined by combining the motions of the lightweight and rigid carriages relative to the main carriage. Yaw and, to a lesser extent, roll were restrained by the heave staff. The constant tow force was measured from a load cell attached to the lightweight carriage. The incident wave elevation was measured from a capacitance wave probe attached to the main carriage. The probe was located one hull length forward of the bow off the centerline of the tank. The heave and surge transducers, the wave probe, and the tow force load cell were mechanically calibrated in place each day. These gains were then used in the data collection and reduction. The pitch RVDT was bench calibrated before the start of the test program and verified on a daily basis. The analog signals from the various transducers were filtered at a cutoff frequency of approximately 25 Hz and digitized in a TRANCEPA 12 bit A/D converter connected to a TEKTRONIX 4052 computer.

Before the start of a typical run, all the transducers were checked and zeroed for drift. An estimated tow force for the test speed, incident wave period and wave amplitude was dialed into the control panel. The period of the wavemaker was then set and the plunger started. For the tests described in this paper, wave height to wavelength ratio at DTMB had a nominal value of 1/37. When the waves reached the end of the tank where the carriage was waiting, the carriage would accelerate to the preset speed, the model would be unclamped, the constant tow force applied, and

data recorded. Unless the initial estimate of the tow force was exact, the model would experience some small net movement relative to the main carriage. In a limited number of cases, the model would accelerate towards the front or back of the carriage, depending on whether the initial tow force estimate was either high or low, and the run would be terminated. When the data collection was completed, the model was clamped, the carriage stopped, and the process repeated. The time between runs averaged about 25 minutes. This allowed for the tank to sufficiently settle down and for the data reduction to be completed.

At DTNSRDC, the model was tested in the Harold E. Saunders Maneuvering and Seakeeping Basin (MASK). A schematic arrangement of the equipment is shown in Figure 3. The model was rigged to be self-propelled under the MASK carriage, with a towing force applied only during the acceleration phase of each run. During a run, propeller RPM was adjusted manually to keep the model centered axially under the carriage with the towline slack. Steering was accomplished automatically by a servo system which sensed sway and yaw error relative to the carriage. Propulsion power and rudder control signals were carried to the model, and transducer signals carried back to the carriage by means of an umbilical cable. On the carriage, the measurement signals were recorded on a DEC MXC-11/23 computer through a 12-bit analog-to-digital converter.

Wave elevation was measured by a probe attached to the carriage, extending approximately one ship length ahead of the model center of gravity, in order to avoid interference from model generated waves. The waves were generated by the pneumatic wavemakers installed in the MASK, using a sinusoidal function generator as the control signal. Both wave elevation and heave motion were measured by ultrasonic displacement transducers. In the case of heave, the transducer was mounted in the hull, aimed upward at a horizontal planar target fixed to the carriage (see Figure 3). Pitch and bow acceleration were measured by a gyroscope and linear accelerometer. Sway, roll, and yaw were also monitored by an ultrasonic probe and gyroscopes, respectively, since the model could move in all degrees of freedom. The usual wave height to wavelength ratio in the DTNSRDC experiments was 1/50, with additional steepness values included at certain conditions to assess linearity of response.

On a typical run, the model was accelerated by means of the towline. After steady carriage speed was attained, the towline was released and the model continued under its own power. Data collection was then begun, continuing until the carriage was required to stop at the end of the basin, where a restraint line attached to the stern was used to decelerate the model. During the run, small amounts of rudder action were automatically introduced as the model deviated from a straight path under the carriage, and this in turn caused a small oscillatory roll motion to occur in many runs. The time between runs was typically 15 to 20 minutes. Onboard data analysis consisted of harmonic analysis of the entire run length. This was followed up by reanalysis to determine if the data was corrupted by such things as unsteady speed, poor wave quality, or loss of data signals. In such a case, only the acceptable part of a run was used for final analysis.

5. ANALYSIS PROCEDURES

Since all data was nominally periodic, the basic procedure was to perform harmonic analysis on all data channels in order to extract the fundamental harmonics and determine the transfer functions between the wave input and motion response outputs. However, there were various differences in the details of the procedures employed at UM and DTNSRDC, which are discussed below.

In the UM experiments, the analog signals were filtered at 25 Hz and digitized at a nominal sample rate of 100 samples per second. To aid in Fast Fourier Transform (FFT) analysis, the actual sampling rate was varied from run to run, so that a 1024 point sample size for each channel corresponded to an integer number of wave encounter cycles. This was intended to reduce the truncation effects associated with the FFT analysis.

Each record for the incident wave, heave, pitch, and vertical acceleration was analyzed both in the time and frequency domains. The time domain analysis consisted of finding the mean value of the record, locating zero crossings, and indexing the peak and trough amplitudes. From these indexed amplitudes, the average of all the amplitudes, and the average of the one-third and one-tenth highest peaks and troughs were calculated. The frequency domain analysis consisted of Fourier analyzing the records with a FFT. The spectral density function, spectral moments of order one through four, and the complex amplitudes of the harmonics were printed out. The data were saved on tape for further analysis and quantification of results.

The wave slopes were determined from the measured wave height and the calculated wavelength. The wavemaker period was recorded to an accuracy of 0.01 second. With this value the linear wave infinite depth dispersion relationship was used to find the wavelength. The wave height was determined from the time history records of the wave analysis, and was taken as the sum of the average peak and trough amplitudes.

The magnitude of the various transfer functions was found using the results of the frequency domain analysis. For pure harmonic data with no noise or truncation effects, the spectral values would be delta functions. In practice, the incident wave resembled a delta function with large values occurring at only two or three frequencies centered around the wave frequency of encounter. The frequency resolution of the FFT for a 10 second record

is approximately 0.1 Hz.) However, since the model was free to move relative to the main carriage and incident wave probe, there was a slight shift and broadening of the different response spectra. To get the response functions, the mean square of the process for both incident wave and the response was found in the immediate region of the incident wave frequency of encounter. Specifically, the following steps were taken:

1. Locate the nominal frequency of encounter from the incident wave spectrum
2. Sum the five spectral ordinates centered around the frequency of encounter for both wave and response
3. Take the ratio of the root mean square of the response to that of the wave as the magnitude of the transfer function

Since the wave probe was attached to the carriage and the model was moving relative to the probe, the phase relationships between the response and incident wave could only be approximated.

In the DTNSRDC experiments, data was digitized at a rate of 20 samples per second on each channel. The total number of encounter cycles collected on each run was typically between 5 and 10, as determined by model speed, wave period, and available run length. The initial step in analysis was to determine the actual period of encounter by searching for zero-crossings on the measured wave record. The average encounter period over the available run length was then used to determine the fundamental frequency, and harmonic analysis of all the data channels followed using the same fundamental. Essentially, a Fourier series was fit to the data, with the first few harmonics being printed out. The goodness of this fit was monitored by comparing the energy of the estimated first harmonic to the total energy of the signal. In most of the runs, this ratio amounted to 95 percent or better, indicating that the data was close to a pure sinusoid and that the first harmonic had been correctly captured. Finally, the transfer functions of the responses were determined by assuming that the first harmonics of responses represented the linear response. Thus, the ratio of the magnitude of a response first harmonic to the magnitude of the wave first harmonic defined the magnitude of the transfer function. For phase, the shift in phase of a response first harmonic, relative to the phase of the wave first harmonic, defined the transfer function phase. In this case, an adjustment was made to the phase to compensate for the wave probe location by using the usual frequency-wave number relationship of linear free-surface wave theory. Therefore, the phase angles represent the phase lead of the response relative to maximum wave elevation at the center of gravity of the hull.

6. RESULTS

6.1 Presentation of Results

The primary results of the experiments are presented in Figures 4 and 5, as transfer functions of heave, pitch, and bow acceleration. All symbols follow ITTC standard definitions. The results are plotted against a nondimensional wave frequency, $\omega\sqrt{L/g}$. Magnitudes have been made nondimensional as follows: heave divided by wave amplitude, pitch divided by wave slope, and acceleration divided by wave amplitude multiplied by the quantity (length/gravity). Positive values of wave elevation, heave and acceleration are upward, while positive pitch is bow down. Phases are defined as leads with respect to maximum positive wave elevation at the ship ship center of gravity. For example, for waves and heave response:

$$\zeta(t) = \zeta_a \cos(\omega t) \tag{1}$$

$$Z(t) = Z_a \cos(\omega t + \epsilon_{z\zeta}) \tag{2}$$

Phase results are presented only from the DTNSRDC experiments, since variations in the motion of the UM subcarriage were found to cause unacceptable phase estimation.

Emphasis was placed on repeatability of results, as well as a close definition of the shape of the response functions. Furthermore, as the experiments progressed, it became apparent that the hull exhibited some unexpected behavior in heave at the lower of the two speeds tested and in a narrow range of frequency. Therefore, a relatively large number of data points was obtained near the peak responses at $F_n = 0.200$. In order to more clearly show the results of the two sets of results in this region, the magnitude of the transfer functions has been plotted on an expanded scale in Figure 6. In this figure, the results are plotted against a nondimensional frequency of encounter, rather than wave frequency. The reason for this is to illustrate that the encountered wave frequency actually experienced by the model is subject to a certain degree of scatter, as well as the responses themselves, and variations in this frequency can have a very strong effect on the results. In particular, the variability in period of generated waves in the DTNSRDC experiments causes the most fluctuation, while the variability in model speed (as opposed to carriage speed) in the UM experiments was the primary source of encounter frequency fluctuation.

6.2 Discussion

An initial comparison of the results of the two sets of data shown in the figures shows close agreement in pitch at both speeds. In terms of nondimensional pitch/(wave slope), the mean difference or bias between the two experiments was typically less than 0.03, and the scatter within each experiment was approximately 0.03 also.

The heave results in Figures 4 and 6 appear to have considerably more scatter, especially at $F_n = 0.200$, and the UM results

are somewhat smaller than the DTNSRDC results. However, close examination of the data has revealed a dependence of the data on wave steepness, as illustrated in Figure 7. When the heave data at a particular combination of speed and wave frequency (F_n = 0.200, $\omega\sqrt{L/g}$ = 2.4) are plotted against ($2\zeta_a/\lambda$), the trend becomes apparent and the random scatter of results is reduced. Similar effects occur for pitch and vertical bow acceleration. In fact, a linear regression of the data produces a correlation coefficient near 0.9 for the regression lines shown in Figure 7 for heave and acceleration, while the dependence of pitch on steepness is much weaker.

The results at other frequencies near the peak heave response, at both Froude numbers, are consistent with Figure 7. That is, the smaller magnitudes of responses in the UM experiments were obtained using somewhat steeper waves than were used in the DTNSRDC experiments. Thus, the motions of this hull at this particular condition display a significant degree of nonlinear behavior. The source of this behavior may be viscous damping, which would be expected to have a most noticeable effect at heave resonance. A considerable amount of green water was observed to come over the bow in the steeper waves, and this could also have an effect.

The bow acceleration results of Figure 4 show the UM results to be somewhat smaller than the DTNSRDC results, and the scatter in each experiment was less than for heave but more than for pitch. This is not surprising, since the total rigid body motion and acceleration at a point is a combination of the heave and pitch motions. Also, as shown in Figure 5, most of the differences in the data are explained by the nonlinear behavior. Since the hull is a rigid body, a calculation of acceleration can be made from the heave and pitch motions, and compared to the measured value. This has been done for both sets of data. In the DTNSRDC data, calculated and measured results agreed within $L\ddot{z}/g = \pm 0.6$, or about 2 percent of the peak values. At UM, the measured values came out consistently lower than calculated, i.e., by approximately 5 percent. This may be an indication of a bias or drift in the accelerometer calibration. This result, combined with the observed nonlinear behavior, largely accounts for the differences in the two sets of acceleration data.

The phase measurements from the DTNSRDC data show approximately a ±10 degree scatter, with a greater range near heave resonance. This latter result may be associated with the nonlinear behavior noted in the magnitudes of the responses, although no trend was found in examining the phase data. It is possible that it is merely a result of the larger number of repeated runs in this range, which, if the results include a random component, are more likely to include larger scatter. It is believed that the limiting factor on phase measurements in these experiments was the variation of model location with respect to the wave probe location.

6.3 Sensitivity of Results

The variability of results both within the individual experiments and between the two laboratories is shown qualitatively in the figures. In order to more quantitatively define the sources of experimental variability, the following lists a number of identified physical parameters, the estimated accuracy with which they can be controlled and/or measured in each facility, and the sensitivity of results to variations in them.

6.3.1 Measurements

a. Speed - The two Froude numbers used in the experiments correspond to 2.71 and 3.73 knots. At DTNSRDC, the carriage speed is accurate to ±0.004 knots, and it is estimated that model surge freedom resulted in an additional uncertainty of ± 0.01 knots. At UM the slow drift motion of the subcarriage resulted in a speed variation of ±0.1 knots. In both cases, it is estimated that the most important effect of this variation is in the resulting variation of encounter frequency, which may be affected as much as 1.5 percent at $\omega\sqrt{L/g}$ = 2.4.

b. Wave generation and measurement - At DTNSRDC, waves are generated by pneumatic wavemakers which are difficult to control. The period of generated waves can usually be set to 0.01 sec, but the amplitude of the waves sometimes fluctuates noticeably during a run. The sampling rate used in the experiments also limited the ability to estimate encounter period to approximately ±2 percent. The wavemaker period in the UM experiments was controlled to within 0.001 second.

c. Instrument calibration - The deviation of measured instrument values from an assumed linear calibration, as found from repeated static calibration points, was ±0.2 mm for heave and wave transducers, ±0.03 degrees for pitch, and ±0.002 g for acceleration. For typical magnitudes of measured responses, these values represent approximately 0.5 to 1 percent of the measurements. Discretization in the A/D converters accounts for an additional uncertainty of 0.25 to 0.5 percent.

6.3.2 Analysis

In addition to the uncertainty introduced into the experimental results by the various measurements discussed above, other errors may be introduced by the method of harmonically analyzing the data. In particular, the estimation of the encounter period is affected by fluctuations in model speed and by the discretization in time, which produces errors in amplitude estimation because the harmonic analysis is not carried out over an integer number of cycles. It can be shown that if a signal is a pure sine wave,

$$F(t) = \sin\left(\frac{2\pi t}{T_0}\right) \qquad (3)$$

and the sampled record length is αT_o where α is a parameter (not necessarily an integer), then the Fourier series estimate is

$$f(t) = C_o + \sum_{n=1}^{\infty} C_n \sin\left(\frac{n2\pi t}{T_o} + \phi_n\right) \qquad (4)$$

where $C_n = \sqrt{A_n^2 + B_n^2}$ and $\phi_n = \tan^{-1}(B_n/A_n)$,

$$A_n = \frac{1}{\pi}\left(\frac{n}{\alpha^2-n^2}\right) \sin(2\pi\alpha)$$

$$B_n = \frac{1}{\pi}\left(\frac{\alpha}{\alpha^2-n^2}\right) \left(1-\cos\ (2\pi\alpha)\right) \qquad (5)$$

For example, if the desired record was selected to include three complete cycles, but the actual record was 0.05" too long (n = 3, α = 3.05), then C_1 = 0.9881 and ϕ_1 = 9.1 degrees. For a longer record with the same error in sample length (n = 10, α = 10.05), the error is reduced to C_1 = 0.9935, ϕ_1 = 9.0 degrees.

7. CONCLUSIONS

Good agreement has been found between experimental seakeeping results obtained at the two laboratories, particularly when careful attention is paid to subtle differences in experimental procedures and analysis techniques. In the experiments reported here, an unexpected dependence of the responses on wave steepness was found, and the results from the two experiments correlated closely when this was taken into account. In terms of bias and precision error, the following conclusions are made:

1. The scatter (or precision error) in either of the two sets of results is approximately 3 to 5 percent of the maximum magnitude of the transfer functions.
2. The bias between the two laboratories is of the same order of magnitude as the scatter. Differences between the results are due to a combination of measurement and analysis procedures.

It must be cautioned that the results reported herein reflect what may be possible in terms of repeatability and agreement between different towing tanks when care is taken to obtain reliable results. In many cases, it is not practical to take the extra time (and expense) to make repeated carriage runs to assess repeatability and to closely examine the results for subtle effects. It is also likely that different hull forms may be more or less sensitive than the present one to test conditions such as frequency of encounter or wave steepness. It is desirable to identify two distinct types of seakeeping experiments, with clearly different goals. One is a rather qualitative one (and certainly the more common type carried out today), in which a rough confirmation of expected seakeeping performance is needed. This is often a random wave experiment in which accurate resolution of results is sacrificed due to the inherent statistical variability of this type of experiment; however, the wave environment is a more realistic approximation to the real world. Another type of experiment, of which the currently reported work is an example, is one in which the goal is to verify, as accurately as possible, the underlying assumptions on which many practical seakeeping applications rest. This type of experiment requires carefully controlled conditions, and is more costly to carry out; however, it is necessary if a realistic estimate of the reliability, that it is possible to obtain when maximum accuracy is required, is the goal.

ACKNOWLEDGMENTS

These experiments were carried out using in-house funds at both UM and DTNSRDC. Funding for the construction of the model was provided by the Office of Naval Research under Contract N00014-85-K-0118. The experiments at UM were carried out by Ship Hydrodynamics Laboratory personnel and students of Course NA 621, Experimental Hydrodynamics. The experiments at DTNSRDC were carried out by Richard Bishop and Robert Stanko.

REFERENCE

Abernathy, R.B., R.P. Benedict and R.B. Dowdell (1985): ASME Measurement Uncertainty. Journal of Fluids Engineering, Vol. 107, pp. 161-164.

TABLE 1 - PRINCIPAL HULL PARTICULARS

	Ship	Model
Length (L_{pp})	175.0 m	4.957 m
Length (LWL)	179.2 m	5.048 m
Beam (B)	25.4 m	0.719 m
Draft (T)	9.5 m	0.269 m
GM	1.0 m	0.028 m
L_{pp}/B	6.89	
B/T	2.67	
LCB (% L_{pp} aft)	1.4	
C_t	0.572	
C_p	0.589	
C_m	0.970	
R_{yy}/L_{pp}	0.24	

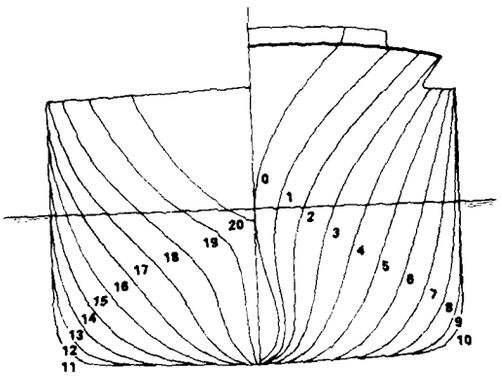

Figure 1 - Body Plan

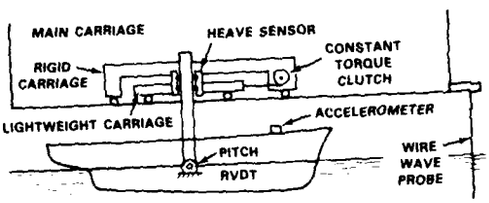

Figure 2 - UM Schematic

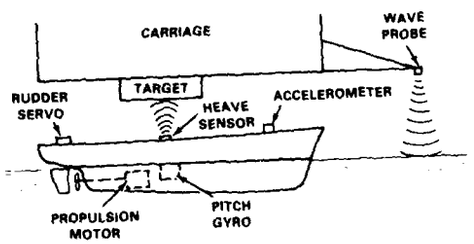

Figure 3 - DTNSRDC Schematic

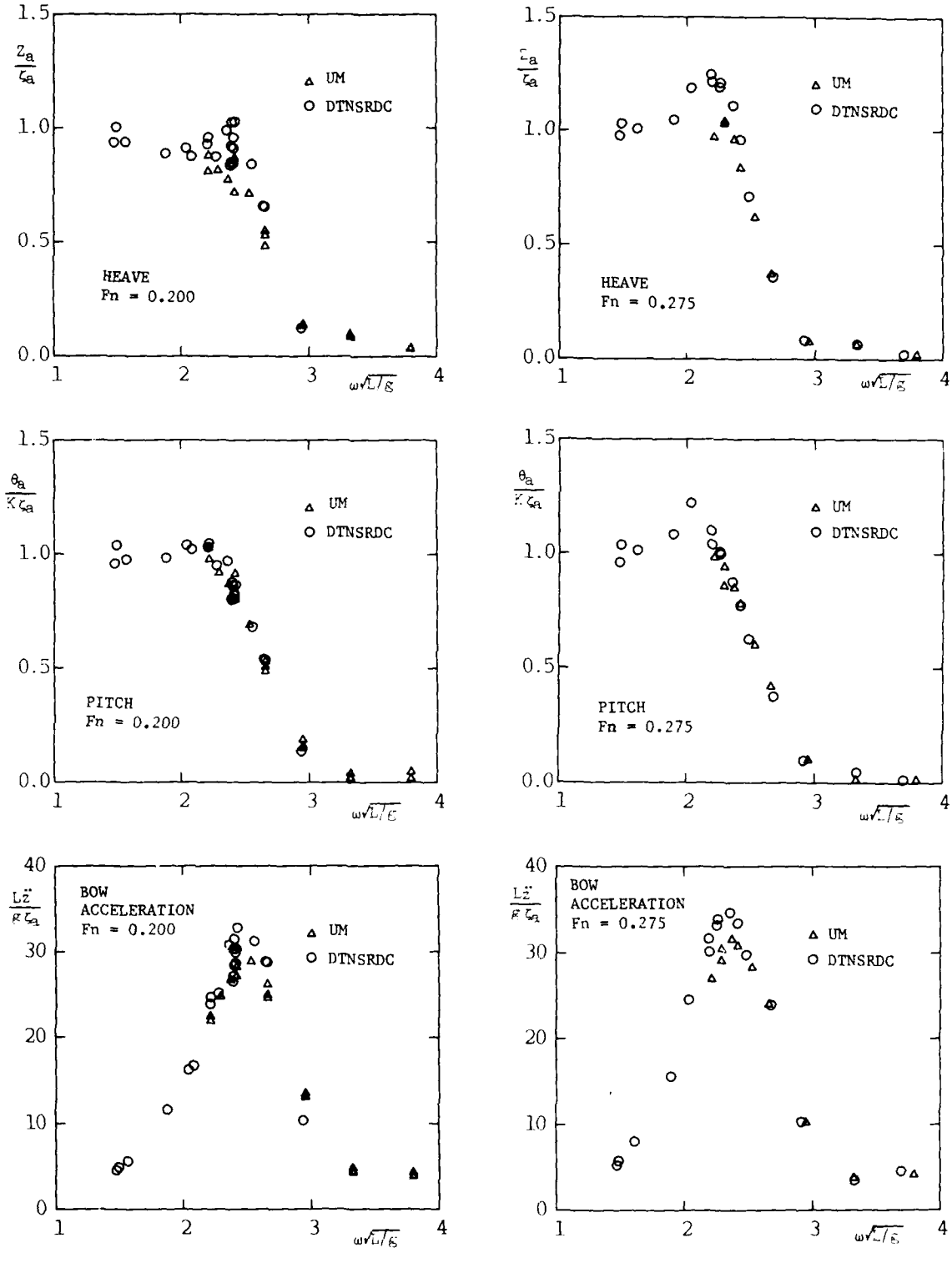

Figure 4 - Magnitude of Transfer Functions

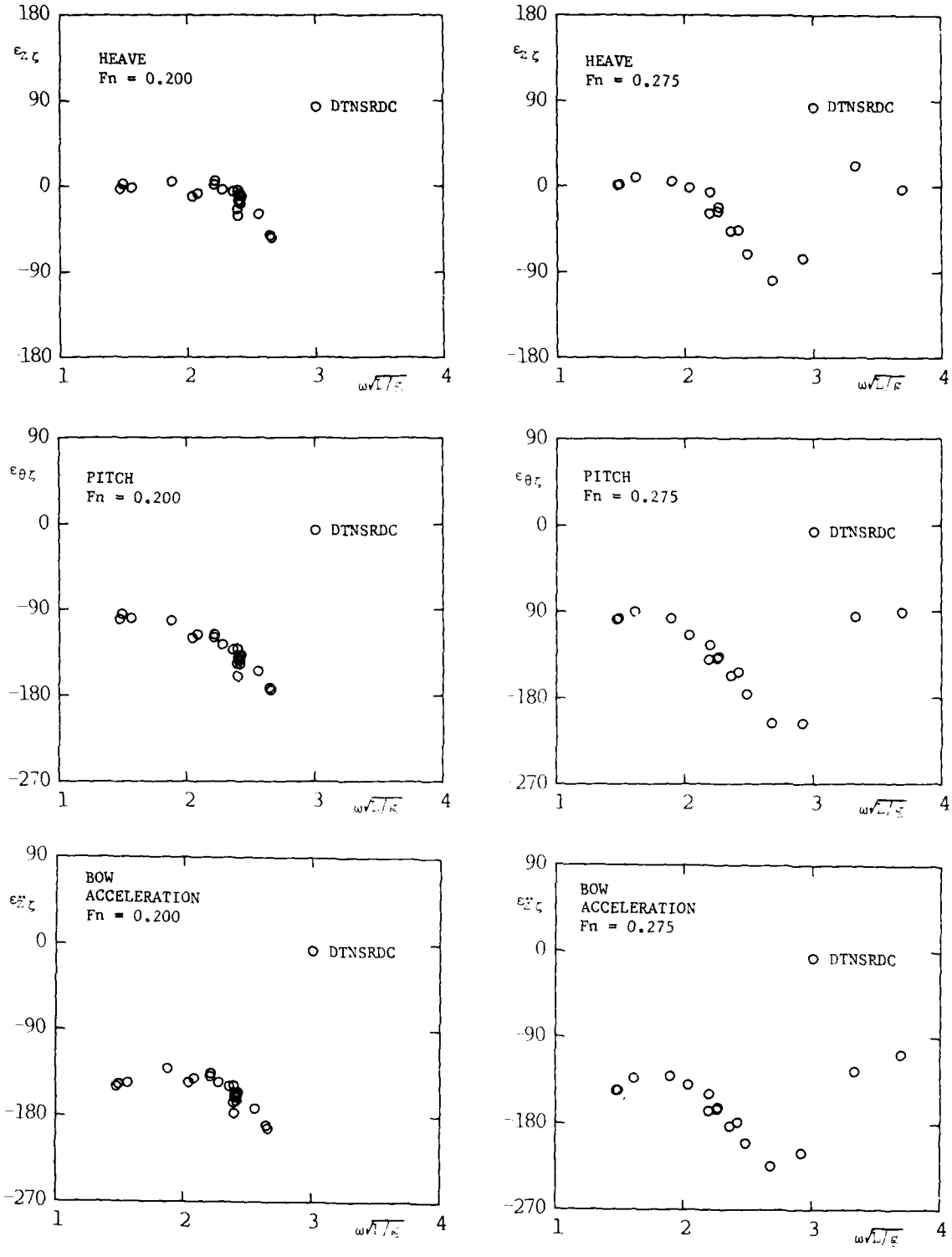

Figure 5 - Phase of Transfer Functions

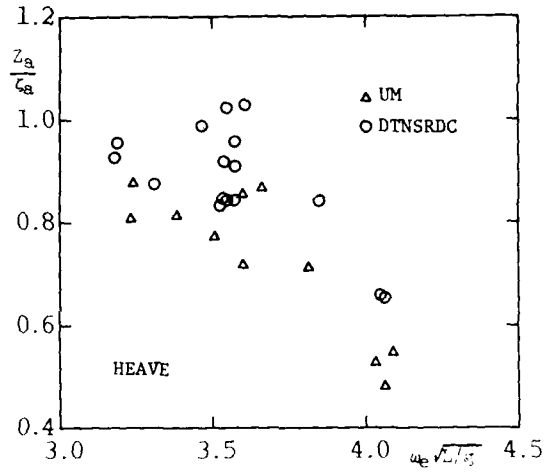

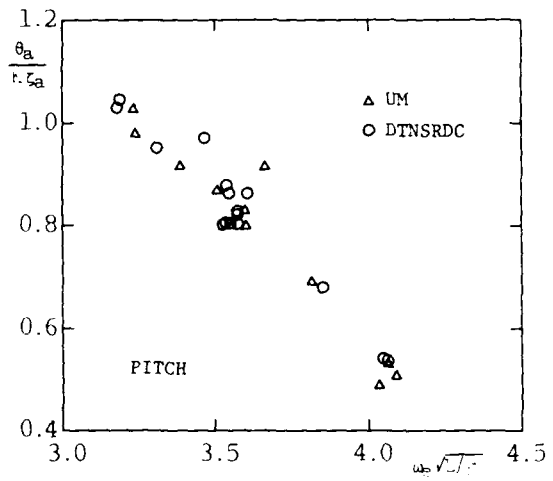

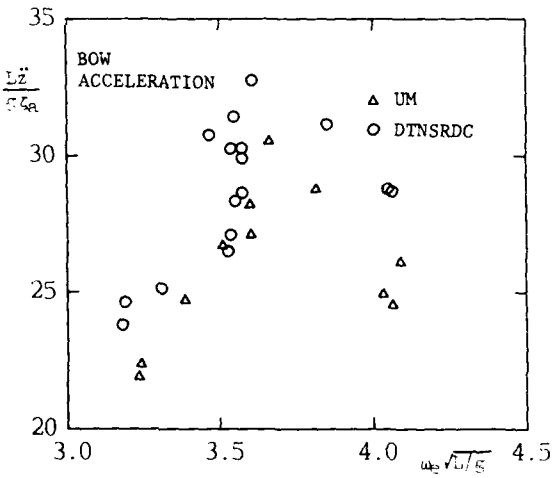

Figure 6 - Detail of Transfer Functions, Fn = 0.200

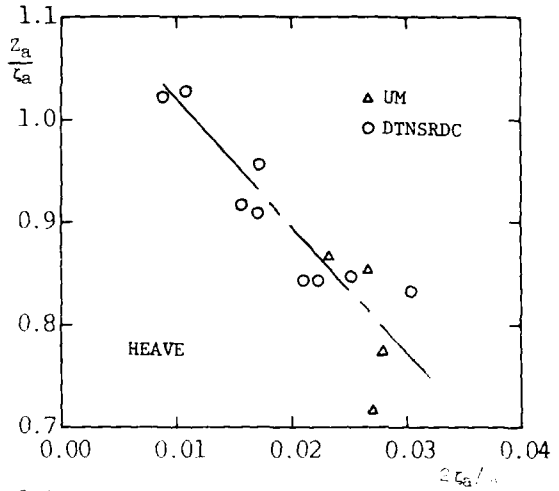

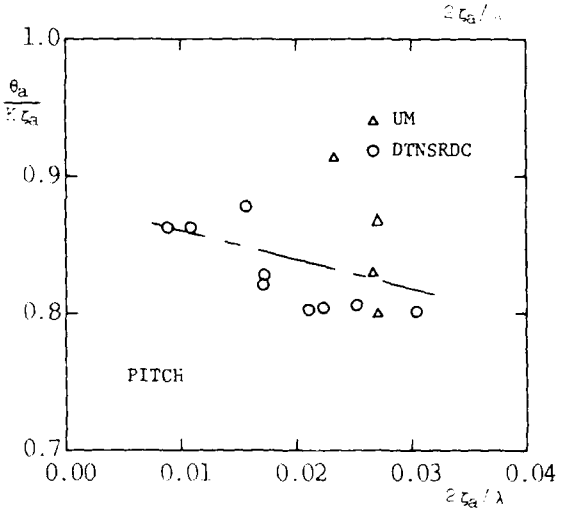

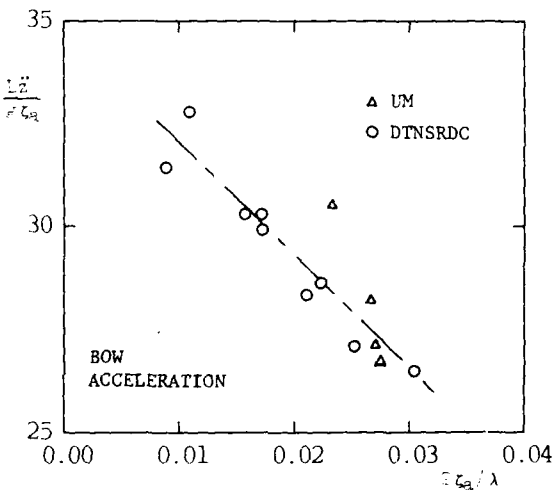

Figure 7 - Variation of Response Magnitude with Wave Steepness at Fn =0.200, $\omega\sqrt{L/g}$ = 2.4

MEASUREMENT OF SIX DEGREE OF FREEDOM MODEL MOTIONS USING STRAPDOWN ACCELEROMETERS

M.D. Miles

Hydraulics Laboratory
National Research Council
Ottawa, Canada

ABSTRACT

A method for the measurement of ship model motions in oblique seas using seven strapdown accelerometers is described which provides a light, reliable and inexpensive alternative to other systems such as gyro-stabilized platforms or optical tracking devices. Although linearized analysis is satisfactory for roll, pitch and heave motions at angles up to 15 degrees, significant errors can occur in yaw, surge and sway displacements at roll and pitch angles as low as 5 degrees due to residual gravity terms, nonlinear cross-coupling and convolution of energy to lower frequencies.

An alternative iterative analysis procedure is described which uses an FFT-based integration technique to solve the full nonlinear differential equations for the displacement motions. The average roll and pitch angles are also determined by resolving the mean direction of the gravity field. Numerical simulations using typical motion spectra have shown that the nonlinear procedure converges at angular motions up to 60 degrees and reduces errors by an order of magnitude compared to linearized analysis. Model test results for a prototype of the strapdown system are also presented.

1.0 INTRODUCTION

A variety of methods have been used in ship model basins to measure vessel motions during seakeeping tests. These include instrumented linkages to carriages, angular position and rate gyros, fixed and gyro-stabilized accelerometers, ultrasonic ranging devices and, more recently, optical tracking systems [1]. Since the NRC seakeeping basins are not equipped with carriages, inertial sensors have generally been preferred and gyro-stabilized platforms have been used extensively for both model tests and full scale trials. Although gyro systems provide sufficient accuracy, their initial cost is fairly high and they also tend to require frequent and expensive maintenance. Their relatively high weight and power requirements also preclude their use in smaller radio-controlled models.

Gyro-stabilized platforms have also been widely used in inertial navigation systems for aircraft but are now being superseded by strapdown systems which have become practical with the advent of microprocessors and improved sensor technology to cope with the wider dynamic range requirements. The strapdown systems employ rate gyros and accelerometers which are fixed to the vehicle frame and offer advantages of increased reliability and lower cost, weight and power consumption compared to gimballed systems.

A system of 3 fixed accelerometers had previously been used at NRC to measure heave, pitch and surge in regular head seas with performance comparable to that of a gyro platform. It was therefore decided to develop a strapdown system to measure oscillatory motion in 6 degrees of freedom in irregular waves. Although ring laser gyros provide a technically attractive alternative to mechanical rate gyros for strapdown systems, currently available models were found to be prohibitively expensive. Since this application is less demanding than inertial navigation, it was decided to eliminate the rate gyros and use only accelerometers. This approach requires an additional level of integration for the angular motions but allows the use of more reliable and less expensive instrumentation.

Although 6 accelerometers are sufficient to measure 6 degree of freedom motion, it was decided to use 7 instead so that they could all be located in one plane in order to simplify installation and to minimize the effect on the vertical mass distribution of the model. The proposed system was first evaluated by computer simulation and model tests were subsequently carried out on a prototype unit with an optical tracking system for comparison.

2.0 EQUATIONS OF MOTION

In order to utilize a strapdown system, it is first necessary to derive equations of motion which define the fundamental motions of the rigid body in terms of the measured accelerations. Consider a vessel oscillating in 6 degrees of freedom about an equilibrium position which moves at constant velocity relative to the earth. Acceleration effects due to earth rotation, such as Coriolis force, may be neglected in this application. Using standard ITTC and SNAME [2] notation, let (x_0, y_0, z_0) denote an inertial frame which moves relative to the earth at the average velocity of the vessel. The z_0 axis is vertically downwards and the x_0 axis is aligned with the average heading of the vessel. Let (x,y,z) denote the body axes of the vessel. The 7 accelerometers are mounted in the x-y plane as shown in Fig. 1 where C is an arbitrary reference point. Accelerometers 1,2,5 & 6 are sensitive in the z direction, 3 & 4 are sensitive in the y direction and 7 is sensitive in the x direction. Let $\vec{x}_0(Q)$ be the vector to some arbitrary point Q on the vessel and let $\vec{x}(CQ)$ be the vector from C to Q. Since $\vec{x}(CQ)$ is constant,

$$\ddot{\vec{x}}_0(Q) = \ddot{\vec{x}}_0(C) + \ddot{A}\,\vec{x}(CQ) \qquad (1)$$

where A is the rotation matrix given by

$$\begin{pmatrix} \cos\theta\cos\psi & \sin\theta\sin\phi\cos\psi - \cos\phi\sin\psi & \sin\theta\cos\phi\cos\psi + \sin\phi\sin\psi \\ \cos\theta\sin\psi & \sin\theta\sin\phi\sin\psi + \cos\phi\cos\psi & \sin\theta\cos\phi\sin\psi - \sin\phi\cos\psi \\ -\sin\theta & \cos\theta\sin\phi & \cos\theta\cos\phi \end{pmatrix}$$

Applying (1) at each accelerometer location and taking the dot product with the unit vector of the sensitive axis, it follows that

$$\ddot{\vec{x}}_0(C) = A\,\vec{P} + g\hat{k}_0 \qquad (2)$$

where

$\hat{k}_0$ = unit vector in the z_0 direction,

$P_1(t) = a_7$,

$P_2(t) = (R_4 a_3 + R_3 a_4)/(R_3 + R_4)$,

$P_3(t) = (R_2 a_1 + R_1 a_2)/(R_1 + R_2)$,

a_j = acceleration measured by accelerometer j and

R_j = the radial distance from point C to accelerometer j.

Equation 2 gives the translatory acceleration at point C in terms of the measured vector $\vec{P}$ and the rotation matrix A. Once A has been determined as a function of time, each component of (2) can be integrated separately to obtain the surge, sway and heave velocities and displacements.

FIGURE 1 CONFIGURATION OF STRAPDOWN ACCELEROMETERS

The angular accelerations are obtained by subtracting the signals from each pair of accelerometers. For example, applying (1) at accelerometers 5 and 6,

$$a_5 = \hat{k}\cdot[A^{-1}\,(\ddot{\vec{x}}_0(C) - g\hat{k}_0)] + R_5\hat{k}\cdot[A^{-1}\,\ddot{A}\,\hat{j}] \qquad (3)$$

and $$a_6 = \hat{k}\cdot[A^{-1}\,(\ddot{\vec{x}}_0(C) - g\hat{k}_0)] - R_6\hat{k}\cdot[A^{-1}\,\ddot{A}\,\hat{j}] \qquad (4)$$

where $\hat{i},\hat{j},\hat{k}$ are unit vectors in the x,y,z directions.

Let $F_1(t) = (a_5 - a_6)/(R_5 + R_6)$.

$$\therefore\quad F_1 = \hat{k}\cdot[A^{-1}\,\ddot{A}\,\hat{j}]\ . \qquad (5)$$

It is shown in ref. 3 that

$$\dot{A} = A\,\Omega \qquad (6)$$

where $\Omega = \begin{pmatrix} 0 & -\omega_z & \omega_y \\ \omega_z & 0 & -\omega_x \\ -\omega_y & \omega_x & 0 \end{pmatrix}$

and ω_x, ω_y and ω_z are the components of the angular velocity vector resolved along the body axes. It can be shown, by considering the small angle rotations which occur over a time interval Δt, that these are related to the SNAME Euler angles as follows:

$$\omega_x = \dot{\phi} - \dot{\psi}\sin\theta$$

$$\omega_y = \dot{\theta}\cos\phi + \dot{\psi}\cos\theta\sin\phi \qquad (7)$$

$$\omega_z = -\dot{\theta}\sin\phi + \dot{\psi}\cos\theta\cos\phi$$

It follows from (6) that $\ddot{A} = A\,B$ where $B = \Omega^2 + \dot{\Omega}$ and hence $F_1 = B_{32}$. Defining similar functions for the other accelerometers, we obtain

$$\dot{\omega}_x = F_1(t) - \omega_y \omega_z \qquad (8)$$

$$\dot{\omega}_y = F_2(t) + \omega_x \omega_z \qquad (9)$$

and $$\dot{\omega}_z = F_3(t) - \omega_x \omega_y \qquad (10)$$

where $F_2(t) = (a_2 - a_1)/(R_1 + R_2)$

and $F_3(t) = (a_3 - a_4)/(R_3 + R_4)$.

Equations 8-10 are the fundamental relations defining the rotation rates in terms of the measured quantities F_1, F_2 and F_3. The Euler angles are then defined by

$$\dot{\phi} = \omega_x + \tan\theta\,(\omega_y \sin\phi + \omega_z \cos\phi) \qquad (11)$$

$$\dot{\theta} = \omega_y \cos\phi - \omega_z \sin\phi \qquad (12)$$

$$\dot{\psi} = (\omega_y \sin\phi + \omega_z \cos\phi)/\cos\theta \qquad (13)$$

which follow from (7).

Equations 8-10 must first be solved numerically to obtain ω_x, ω_y and ω_z. Equations 11 and 12 are then solved for ϕ and θ and ψ is obtained by integrating (13). The rotation matrix is then defined so (2) can be integrated to obtain surge, sway and heave.

3.0 ANALYSIS PROCEDURE

If the motions are sufficiently small, the linearized form of the equations can be used. In this case, $\ddot{\phi} = F_1(t)$, $\ddot{\theta} = F_2(t)$ and $\ddot{\psi} = F_3(t)$ so the angular motions are obtained by direct numerical integration. Similarly, $\ddot{x}_0(C) = P_1(t) - g\theta$, $\ddot{y}_0(C) = P_2(t) + g\phi$ and $\ddot{z}_0(t) = P_3(t) + g$ so surge, sway and heave are also obtained by double integration. The linearized equations are not sufficiently accurate for most practical applications, however.

The following iterative technique was found to be very effective in solving the full nonlinear equations of motion. Initial estimates of the average roll and pitch angles are first computed from

$$\phi_0 = -\overline{P_2(t)}/g \quad \text{and} \quad \theta_0 = \overline{P_1(t)}/g$$

which follow from imposing the condition of zero average surge and sway acceleration on the linearized form of (2). The angular velocities are then computed using the following iteration equations:

$$\dot{\omega}_x(n+1,t) = F_1(t) - \omega_y(n,t) * \omega_z(n,t)$$

$$\dot{\omega}_y(n+1,t) = F_2(t) + \omega_x(n,t) * \omega_z(n,t)$$

$$\dot{\omega}_z(n+1,t) = F_3(t) - \omega_x(n,t) * \omega_y(n,t)$$

An FFT-based integration routine incorporating a high pass filter is used at each step of the iteration process. The filter cut-off point, FC, is selected to prevent excessive amplification of low frequency noise. The integration constants are obtained by imposing the condition that the average angular velocities are zero for oscillatory motion. After the ω's have been computed, the following iteration equations are used to calculate roll and pitch:

$$\dot{\phi}(n+1,t) = \omega_x + \tan(\theta(n,t)) * (\omega_y \sin\phi(n,t) + \omega_z \cos\phi(n,t))$$

$$\dot{\theta}(n+1,t) = \omega_y \cos\phi(n,t) - \omega_z \sin\phi(n,t)$$

Yaw is then computed by direct integration of (13) and final estimates of the average roll and pitch angles are obtained by adding constant perturbations to satisfy the condition that the average surge and sway accelerations from (2) are zero. The average roll and pitch angles are thus determined by measuring the mean direction of the gravity vector relative to the vessel frame. Finally, surge, sway and heave at any arbitrary point Q are obtained by integrating each component of

$$\ddot{\vec{x}}_0(Q) = A\,[\vec{P} + B\,\vec{x}(CQ)] + g\hat{k}_0 \qquad (14)$$

which follows from (1) and (2).

4.0 NUMERICAL SIMULATION

Two different methods were used to synthesize signals for the numerical simulations which were used to evaluate the proposed system. In the first method, time series for each degree of freedom were synthesized using a random phase method such that all motions had the same spectral shape but the time series were uncorrelated. The linear and nonlinear analysis procedures were then used to estimate the fundamental motions from the synthesized accelerometer signals. The simulation results were compared mainly on the basis of the Normalized RMS Error or NRE which is defined as follows:

NRE = 100 * RMS[X1(t)-X2(t)]/(4*RMS[X2(t)]), %

where X1(t) is the motion estimated from the accelerometer signals and X2(t) is the actual motion. The NRE was calculated for accelerations, velocities and displacements but the largest errors usually occurred in displacements.

The relative performance of the linear and nonlinear analysis procedures for angular motions is shown in Fig. 2. The nonlinear iterative procedure is far superior with NRE's of less than 2 percent for simultaneous roll, pitch and yaw motions up to 15

degrees rms (45 degrees peak). The NRE's of the linear procedure are an order of magnitude larger and it would not be useful at amplitudes much above 3 degrees rms. It should be noted, however, that the linear procedure will work better in planar motion cases where one angle dominates because the product terms in equations 8-10 are then small.

The linear procedure also has poor low frequency performance, even at fairly small amplitudes, as shown in Fig. 3. In this case, the actual motion spectra do not contain any significant energy at frequencies below 0.25 Hz. As the analysis cut-off frequency is reduced below this point, the nonlinear procedure errors stabilize at small values whereas the linear procedure errors grow rapidly. These errors are caused by low frequency components in F_1, F_2 and F_3 due to convolution of the roll, pitch and yaw spectra by the nonlinear centripetal acceleration terms. This appears as low frequency noise to the linear procedure which is amplified by integration.

In the second simulation method, an irregular encountered wave train was first synthesized and the time series for the fundamental motions were then computed using strip theory transfer functions. This method produced more realistic correlated ship motions with proper relative phasing. The simulations were done using a frigate hull form and a typical result using the iterative procedure is shown in Fig. 4. The NRE's for all motions are less than 2 percent for H_S up to 15 m which produced peak roll and pitch angles of 30 degrees and 12 degrees respectively.

The NRE is also significantly smaller for roll, pitch and heave than for surge, and sway. This effect showed up in all simulations and is caused mainly by the fact that the vertical accelerometers are weakly coupled to the gravity field through the cosines of roll and pitch. Consequently, roll and pitch errors have a much smaller effect on heave than on surge and sway which are strongly coupled to gravity by the sines of roll and pitch. Roll and pitch must therefore be measured very accurately for good surge and sway results since a 1 percent roll error can easily generate a 10 percent sway error.

The range of convergence of the iterative procedure was also checked by simulation. In both the correlated and uncorrelated motion cases, the procedure never failed to converge until the peak angles exceeded 60 degrees, which should be adequate for most seakeeping work with the exception of extreme situations such as capsizing. The procedure normally converges in about 6 iterations at peak angles up to 20 degrees but 30 to 40 iterations may be required at larger angles.

The effect of measurement noise was investigated by adding Gaussian white noise to each of the synthesized accelerometer signals. As shown in Fig. 5, rms measurement noise up to 2 percent is tolerable for roll, pitch and heave but it must be kept below 0.2 percent for good surge, sway and yaw accuracy.

Since the analysis procedure uses an FFT integrator, the number of points in each time series must be a power of 2 and all signals must be cyclic. The first condition is easily satisfied by resampling at a smaller time step using simple parabolic interpolation. The measured signals must also be forced to be cyclic in order to prevent large surge and sway errors which otherwise result from Gibbs phenomenon. Tapering the signals to zero at each end greatly reduces these errors but a technique called cyclic merging was found to be more effective as shown in Fig. 6. This consists of overlapping the tapered zones to form a continuous cyclic splice without reducing signal amplitude. The effect of cyclic merge length is shown in Fig. 7. A merge length of 5 percent is usually satisfactory so the original record length will normally be reduced by about 10 percent during analysis. Cyclic merging is not necessary in regular waves since a cyclic segment can be selected for processing.

As noted previously, it is necessary to use a low frequency cut-off, FC, during the integration process. The effect of this parameter was also investigated by simulation and a typical result is shown in Fig. 8. The choice of FC is not critical for roll, pitch, yaw and heave but low frequency surge and sway errors will result if FC is set too low. The optimum value for FC is generally about 0.8*f1 where f1 is defined as the frequency such that 99 percent of the energy of the encountered wave spectrum lies above f1.

5.0 MODEL TESTS

A prototype strapdown accelerometer system was built and tested on 1:40 scale models of an offshore supply vessel and a semisubmersible platform. The models were tested in both regular and irregular waves in the Offshore Wave Basin of the NRC Hydraulics Laboratory. Sundstrand QA-1400 servo accelerometers were selected since they are specifically designed for inertial navigation applications having a resolution of 1 μg and a linearity error of less than 20 μg/g. They were mounted on a rigid aluminum frame with a roll separation of 30 cm, a pitch separation of 84 cm and a yaw separation of 95 cm.

An OPTOPOS optical tracking system [4] was used to make independent measurements of the model motions for comparison. This system uses 5 cameras to measure the (x,y,z) positions of 3 infra-red light emitting diodes (LED's) mounted on the model. The position of each LED is measured with a specified accuracy of about 1 mm and the 6 degree of freedom mode motions are then computed geometrically by means of a software package supplied with the system.

A typical example of the roll, pitch and yaw motions measured by the two systems on the offshore supply vessel is shown in Fig. 9. The overall agreement is very good, even at roll angles up to 20 degrees. Localized differences, such as pitch and yaw at 57 seconds, were probably caused by occasional false readings in the OPTOPOS due to reflected light. In later tests on the semisubmersible, most of these false readings were eliminated by mounting the LED's higher on the model.

The accelerometer data were also used to compute surge, sway and heave at one of the LED positions for direct comparison with the raw OPTOPOS measurements. As shown in Fig. 10, the general agreement is quite good, especially in sway, but small differences tend to occur near the minima and maxima of the signals. Since this effect is indicative of undersampling, these differences are probably a consequence of the OPTOPOS sampling rate which had to be set at 5 Hz instead of the normal 10 Hz because of software constraints in the data acquisition system.

The roll, pitch and heave motions from one of the moored semisubmersible tests are shown in Fig. 11. In this case, the mooring lines were adjusted to produce average roll and pitch angles of -5 and +4 degrees. Roll and pitch agree very well and their mean values have also been accurately determined. Heave agreement is excellent in the lower frequency waves used in this test which supports the theory that the small differences observed at higher wave frequencies were caused mainly by the limited OPTOPOS sampling rate.

6.0 CONCLUSIONS

It has been demonstrated by numerical simulations and model tests that a strapdown system of 7 accelerometers can provide accurate acceleration, velocity and displacement measurements in 6 degrees of freedom for most types of seakeeping tests in both regular and irregular waves. The system has the advantages of high reliability, light weight, low power consumption and relatively low cost (approx. $15,000 U.S.).

The linearized analysis procedure is inadequate at peak angles above 10 degrees and at low frequencies. The nonlinear iterative analysis procedure was found to be much more accurate and can be used at peak angles up to 60 degrees. It also has better low frequency performance.

The most demanding motions for the strapdown system are surge and sway displacements and the accelerations must be measured very accurately in order to determine these motions with reasonable precision. This necessitates the use of inertial navigation grade accelerometers and a data acquisition system with at least 0.1 percent accuracy.

The strapdown system is not suitable for measuring surge and sway at very low frequencies. For example, it could not be used at low encounter frequencies in following seas or to measure moored platform surge due to second order long waves. A displacement measuring device, such as an optical tracking system, must be used in these situations. It should be noted that this is not a limitation of the strapdown approach per se, however, since any inertial system will have difficulties at very low frequencies.

Although optical tracking systems have excellent low frequency performance, velocities and accelerations computed from their displacement measurements tend to be somewhat noisy due to spatial resolution and sampling rate limitations. Thus, even when an optical system is available, it may be useful to supplement it with a strapdown accelerometer system for more accurate measurement of the higher frequency motions.

7.0 REFERENCES

(1) Report of the Seakeeping Committee, Section II.3, 15th ITTC, 1978.

(2) "Nomenclature for Treating the Motion of a Submerged Body Through a Fluid", SNAME T&R Bulletin 1-5, 1952.

(3) Britting, K.R., "Inertial Navigation System Analysis", Wiley-Interscience, 1971, pp. 11-17.

(4) Abelseth, L. and Rotvold, O., "A 3-Dimensional Position Measuring System", 16th ITTC, Vol. 1, 1981, pp. 507-516.

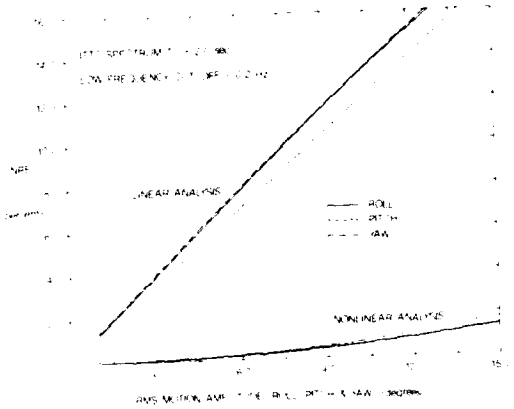

FIGURE 2 NORMALIZED RMS ERROR OF UNCORRELATED ROLL, PITCH AND YAW MOTIONS

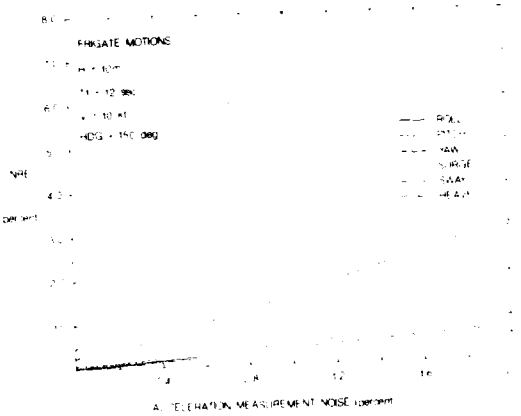

FIGURE 5 EFFECT OF MEASUREMENT NOISE ON COMPUTED DISPLACEMENTS

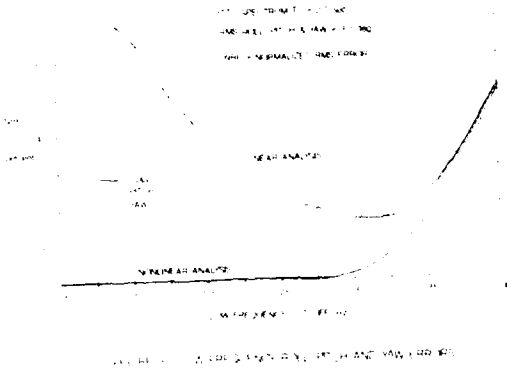

FIGURE 3 NONLINEAR ITERATIVE ANALYSIS OF SIMULATED FRIGATE MOTIONS

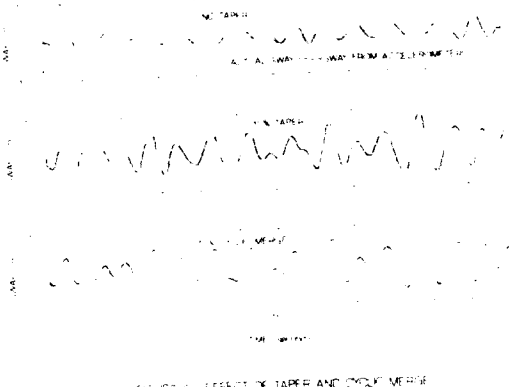

FIGURE 6 EFFECT OF TAPER AND CYCLIC MERGE ON FRIGATE SWAY MOTION, SCALE 1:4

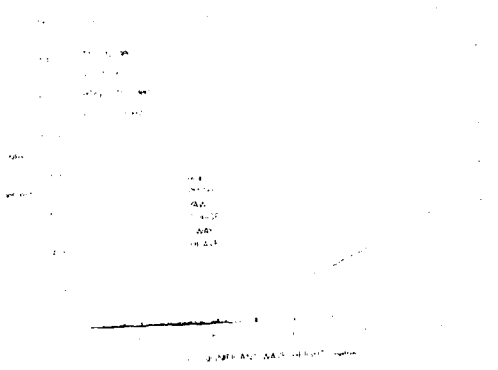

FIGURE 4 NONLINEAR ITERATIVE ANALYSIS OF SIMULATED FRIGATE MOTIONS

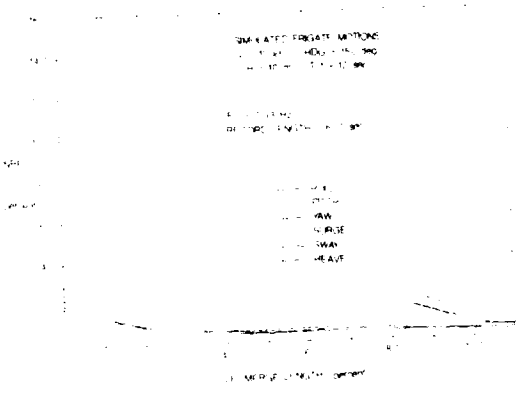

FIGURE 7 EFFECT OF CYCLIC MERGE LENGTH ON DISPLACEMENT ERRORS

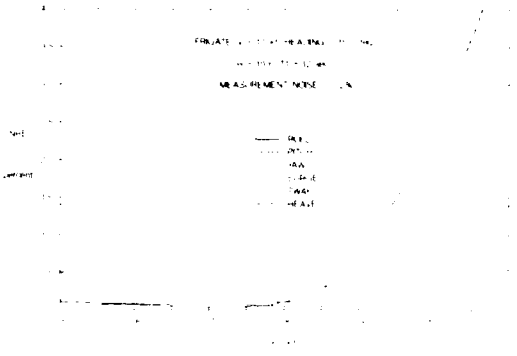

FIGURE 6 EFFECT OF [illegible] FREQUENCY ON DISPLACEMENT ERRORS

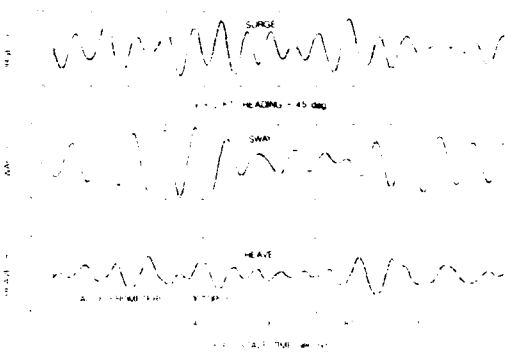

TRANSLATORY MOTION AT TRANSMITTER OF OFFSHORE SUPPLY VESSEL

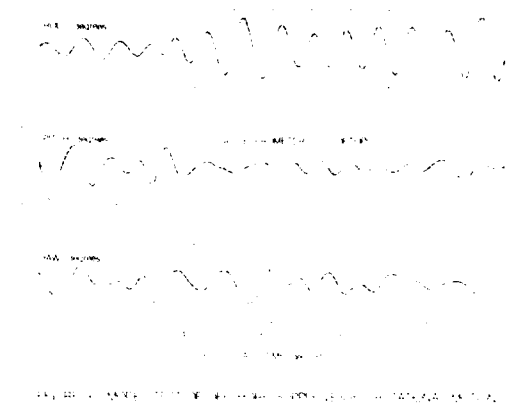

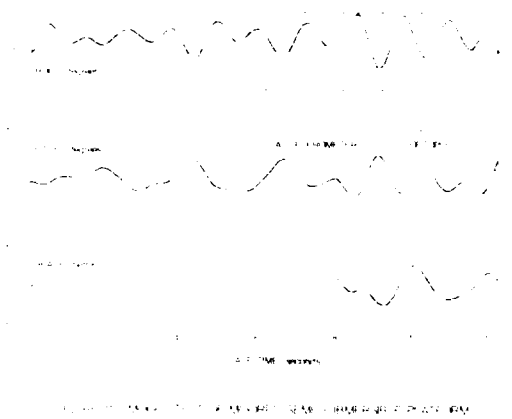

WAVE FORCE TESTING OF LARGE BASED STRUCTURES

ERIK E. BROGREN AND SUBRATA K. CHAKRABARTI
CBI INDUSTRIES, INC.
1501 N. DIVISION ST.
PLAINFIELD, ILLINOIS 60544

ABSTRACT

Many offshore structures are designed and constructed on the basis of using the seafloor as a sealed foundation. The effect of a gap between the seafloor and the structure on the horizontal wave force is small. However, the vertical force and overturning moment on a structure, having even a small gap separating the underside of the structure from the sea floor, are substantially different from those having no gap. Wave force testing of gravity structures is typically done by mounting the structure on load cells and positioning the model as close to the model seafloor as possible.

It is generally recognized that this testing method will result in erroneous measurement for a bottom seated gravity structure resulting in much higher vertical forces, and thus, influencing the overturning moments. Measurements of the true horizontal and vertical loads on a sealed gravity structure can be done with a gas filled hydrodynamic seal method of testing. This paper describes the theory and technique of hydrodynamic sea testing of bottom mounted structures. Measurements of pressures underneath the structure in the presence of a gap as well as a seal were made under separate testings of the same setup. Examples of actual recorded data, and examples of recorded data computations are shown.

INTRODUCTION

The wave forces on an offshore structure model are often determined in a wave tank to confirm calculated wave loads. The determination of horizontal (X) and vertical (Z) forces on the offshore model is usually a rather simple task to accomplish at a hydrodynamic testing facility. This is normally true for those structures which are fastened to the seafloor by some mechanical means. A piled, jacket type, platform would be an example of this kind of structure. Wave force tests on a model of this type would be done by merely mounting the model on three load cells. Data taken from the load cells, during a wave run, can then be translated into total horizontal and vertical forces and overturning moment.

Although a test program of this type is quite straightforward, difficulties can arise. Often, it is difficult to mount the model on load cells, because of small model member sizes or because the model is not stiff enough to be supported on three points. However, most of these problems can be overcome by clever model construction.

The determination of wave forces on a gravity type offshore structure presents the hydrodynamic testing facility with a complex task. A gravity type offshore structure can be defined as a structure that resides and is supported by the surface of the seafloor. The structure is also considered or designed to be sealed to the seafloor. Large arctic conical drilling and production platforms or mat supported jack-up drill rigs are examples of gravity type structures. In either case, the seafloor is an integral part of the structure wherein wave pressure does not appear beneath the structure footprint. Thus, the experimenter must install the model in the wave tank in such a manner, as to exclude wave pressures from underneath the model and yet instrument the model so as to record the horizontal and vertical force components of waves passing by the model. This paper describes a method whereby this can be accomplished with accurate results.

LARGE-BASED GRAVITY STRUCTURES

Two examples of gravity type structures are shown in Figs. 1 and 2. Figure 1 is a conically shaped, arctic drilling structure. Figure 2 is an example of a mobile drilling structure. Accurate wave force data on models of these types is extremely important, because little or no movement of the structure can be tolerated without affecting drilling operations.

The usual method of testing a gravity-based structure is to mount the model on load cells with the flat underside of the model spaced as close as possible to the tank floor. The small gap between the model and the tank floor is a result of having to mount the model on force transducers. Most force transducers operate on the basis of the measurement of a small movement. If a strain gage is the measuring instrument the surface to which the gage is applied must deform before a force can be measured. A force cell using an LVDT (Linear Variable Differential Transformer) must also deflect before a force can be measured. In all cases, where the model is mounted on a set of force transducers, the model must be free to move in all directions, albeit a small amount. The model is usually supported on three load cells at the bottom. This arrangement of transducers is commonly used to measure the two-component loads at three points of model support. The horizontal and vertical loads, and the overturning moment, due to waves, are derived from the load cell readings.

When a gravity type structure is tested in this manner, the vertical loads will not be valid [Chakrabarti (1986)] since there is a gap beneath the model. This gap, however small, is necessary so as to allow free movement of the horizontal and vertical load cells. Thus, wave pressures have free access to the bottom of the model, for some distance, and therefore directly affects the uplift forces and overturning moments experienced by the model. These forces on the bottom may not be present on the prototype structure since it has been installed and embedded or sealed to the seafloor.

FOUNDATION SEAL FOR GRAVITY STRUCTURE MODEL

A method of testing gravity type structures with more accurate force measurements is to use a rolling hydrodynamic seal [Brogren and Chakrabarti (1986)] between the tank floor and the model. The hydrodynamic seal, or gas bag, is made by cutting two thin, soft, plastic sheets in the exact shape of the footprint of the model. Internal cutouts where wave pressure is present can be made as would a seal bag for the model shown in Fig. 2. Typically, 6 mil. thick PVC (polyvinyl chloride) plastic sheeting, such as used for a backyard swimming pool, is a suitable material to fabricate a seal. The edges of the plastic sheeting may then be welded or glued together and provisions made for the attachment of hoses. Welding of the plastic sheets is easily done with a hot iron or by using a hot air welding torch. Hose fittings for attachment to sheet plastic are available from sheet plastic fabricators.

The seal is placed in the gap beneath the model and the tank floor and inflated with air to a pressure greater than the combination of the static water pressure and the dynamic wave pressure. Additional pressure is necessary since water at wave pressure can penetrate between the gas seal bag and the tank floor or between the seal bag and the underside of the model. This effect is quite obvious as it appears as a zero-offset in the vertical force gages. The large uplift forces generated by the pressure of the gas seal bag must be offset by the addition of weight to the model. The additional weights must be placed symmetrically on the model, so as not to upset the mass distribution of the model. The pressure in the gas seal bag is recorded by a sensitive pressure gage, along with all of the other force data, and wave profiles. It is obvious, a priori, that because of Pascal's Law, the pressure within the gas seal bag is spatially constant at any given instant in time. Thus, the vertical loads on the model can be computed and considered valid, since spatially variable wave pressure is not present under the model. Horizontal forces are unaffected, since the model is free to move on the rolling gas seal bag.

GRAVITY STRUCTURE MODEL TEST

A model of the arctic drilling structure shown in Fig. 1 was constructed at a Froude scale of 1:50 resulting in a model 11 ft. in diameter and over 4 ft. high. The model was constructed of steel and weighed approximately 1700 lbs. The model was made watertight so as to prevent any flow of water in and out of the model. Three mounting saddles for the load cells were attached to the model at 120 degree spacings with bolts.

In order to verify the bottom pressures underneath the gravity structure and the effect of the seal to the overall loads as well as the bottom pressures, the test was conducted in two phases. In the first series of tests the gap between the model and the tank floor was left open and the pressures and loads were recorded. In the second phase the gap was sealed by a bag and the test was repeated.

FACILITY DESCRIPTION

The model tests were performed in the CBI Industries wave tank located at Plainfield, Illinois. The tank measures 250 ft. long by 33 ft. wide by 18 ft. deep. A deep pit is located in the center of the tank which measures 8 ft. in diameter and 13.5 ft. deep thereby increasing the local depth in the pit to over 30 ft. Figure 3 presents both a plan and elevation view of the wave tank.

The desired water depth in the tank is not achieved by adding or withdrawing water. The water depth is completely variable within the 18 ft. depth range by moving floor sections which make up the intermediate floor. These floor sections can be adjusted to simulate bottom shoaling and thus breaking wave effects. One of the floor sections is made out of steel which allows fastening the model to the floor easily and is generally used as the test section. The water depth for this test was in the neighborhood of 2 ft.

The wave generator is a pneumatic type, consisting of an open bottom plenum chamber partially immersed in water, and a blower with a low pressure head. The blower is connected to the plenum chamber by a valve which alternately connects the discharge and the intake of the blower with the plenum chamber. The system draws water up into the plenum chamber and then pushes down to produce the wave form. A hydraulic servo control system actuates the pneumatic valve on the wave generator. Baffles in the plenum chamber minimize the formation of transverse waves.

The tank's wave generator is controlled by a dedicated microcomputer. Waves are formed in the tank in response to the computer's control signal representing the required instantaneous wave elevation. A digital time series for single period regular waves is generated and output sequentially to the wave generator in real time. Random wave time series are calculated prior to testing using the laboratory's DECSystem 20 computer. Random waves can be generated with any number of frequency components (typically about 100) and are designed to have no repeating wave patterns. The use of stored digital time series for the generation of random waves makes possible increased wave control and repeatability. Identical waves can be generated for different test setups with digital control of the wavemaking system.

The wave absorbing beach is made up of graded stone in a rack covered with a plastic mesh. The rack is inclined at an angle of 15° to the still water surface and extends 10 ft. below the surface. The wave energy absorbing efficiency is 90-98% depending on wave period.

INSTRUMENTATION AND TEST SETUP

The instruments used in these types of tests are capacitance-type wave probes, pressure transducers and two component (X-Z) load cells. The incident waves are measured by a wave probe located without the model in-place but where the center of the model would lie. This was done to determine the incident wave height without any diffraction effects caused by the presence of the model. Then, in the presence of the model the same waves are repeated and the phase information between waves and responses is obtained by a phase wave probe placed on the model centerline but alongside the model.

In this particular test, pressure transducers were used to measure the pressure under the model and in the airbag as the waves passed over the model. Each pressure transducer was calibrated by raising and lowering it 18 inches in still water while maintaining a back pressure on the transducer equal to the operating water depth. Three pressure transducers were used underneath the model - one at its center and two on horizontal center lines and 2 ft. from the edge of the model. In addition, a pressure transducer was connected to the bag to monitor the bag pressure.

The vertical and down-tank horizontal forces were measured with X-Z load cells. The overturning moment about the model center is then calculated using the values obtained from the load cells and the distance from each load cell to the center of the model.

Typically, each component of a load cell is machined from a block of 6061-T6 aluminum and operates on a bending beam principle. The resulting deflection of the beam is measured with an LVDT which produces an output voltage proportional to the deflection of the beam. Although these deflections are quite small, in the order of ten thousandths of an inch (±0.010 ins.), it is for these deflections that a model must be free to move horizontally and vertically and therefore must have a slight gap from the tank floor.

The model, as mounted in the tank, is shown in Fig. 4 and is supported by three X-Z load cells. Figure 5 shows a typical two component load cell assembly. Figure 6 shows a load cell located in a recessed pocket in the wave tank floor and supporting a model with the gap underneath the model filled by a gas bag. A gap of 1/8 to 1/2 in. is normally adequate to allow the seal to roll with the slight movement of the model.

Two hoses were connected to the bag. One was attached to a high pressure air line and was used for inflation. The other was connected to the previously mentioned pressure transducer and a U-type manometer via a "T" section. The manometer was used as a convenient means for monitoring the bag pressure during inflation.

The model was filled with water to compensate for its buoyancy. The typical

initial loads on the vertical load cells were approximately +500 lbs. (tension) with the air bag and -500 lbs. (compression) without the bag.

Increasing the bag pressure also increased the vertical force on the model. The model had an 11 ft. diameter and consequently one inch of pressure in the bag resulted in 494 lbs. of lift on the model. Thus when the bag was fully inflated, each vertical load cell had a pre-load of roughly 900 lbs. Because the load cells were calibrated to measure 1000 lbs. it was necessary to remove some of this pre-load by placing lead weights on top of the model. A total of 1590 lbs. of lead was used and this reduced the pre-load to an acceptable level.

TEST RESULTS

The test results are summarized in Figs. 7 and 8. Figure 7 shows the pressures at three points under the model when a gap existed between the model and the tank floor. The gap was of the order of 1/4 ins. The pressures are due to a shallow water regular wave of 3.25 sec. period and about 4 1/4 in. height. Note that both the magnitudes and phases of the pressures at different points under the model are different. Thus, it is not possible to correct for the pressures under the model in the measured vertical loads and overturning moments.

Figure 8 shows the pressures from the north and west transducers, as well as the bag pressure when the air bag was used to seal the underside. This plot shows that the pressure at different points under the model is in-phase. It also shows that the pressure at each point has about the same magnitude; the small difference being attributed to the elasticity of the bag interfering with the pressure transducers under the model. These results are typical. It is then a straight forward task to correct for the vertical loads and overturning moment by considering the uniform bag pressure. For example, the total vertical load on the corresponding sealed model may be obtained by adding this pressure times the area of the bottom of the model in appropriate phase. The resulting vertical load corresponds to diffraction theory results [Garrison (1978)].

CONCLUDING REMARKS

The testing of large based offshore structures in a wave basin is complex because of the small gap demanded by the load cells between the model bottom and the tank floor. A device consisting of an air bag to seal the bottom is described which overcomes this problem. The suitability of this device is demonstrated through pressure measurements with and without the bag in a wave tank test of a typical gravity structure model.

The hydrodynamic rolling seal provides the hydrodynamist with a new tool to more accurately determine the forces acting on gravity based ocean structures. The method, and required apparatus, is simple and data reduction is straight forward.

REFERENCES

Brogren, E.E. and Chakrabarti, S.K., "Hydrodynamic Test Apparatus with Offshore Structure Model Using Gas Bag Seal at Model Bottom," U.S. Patent No. 4,559,187, December 24, 1985.

Chakrabarti, S.K., "Wave Forces on an Offshore Gravity Platform," Journal of Waterway, Port, Coastal and Ocean Engineering, Vol. 112, No. 2, March 1986, pp. 269-283.

Garrison, C.J., "Hydrodynamic Loading of Large Offshore Structures, Three-Dimensional Source Distribution Methods," Numerical Methods in Offshore Engineering, John Wiley & Sons, Great Britain, 1978, pp. 87-140.

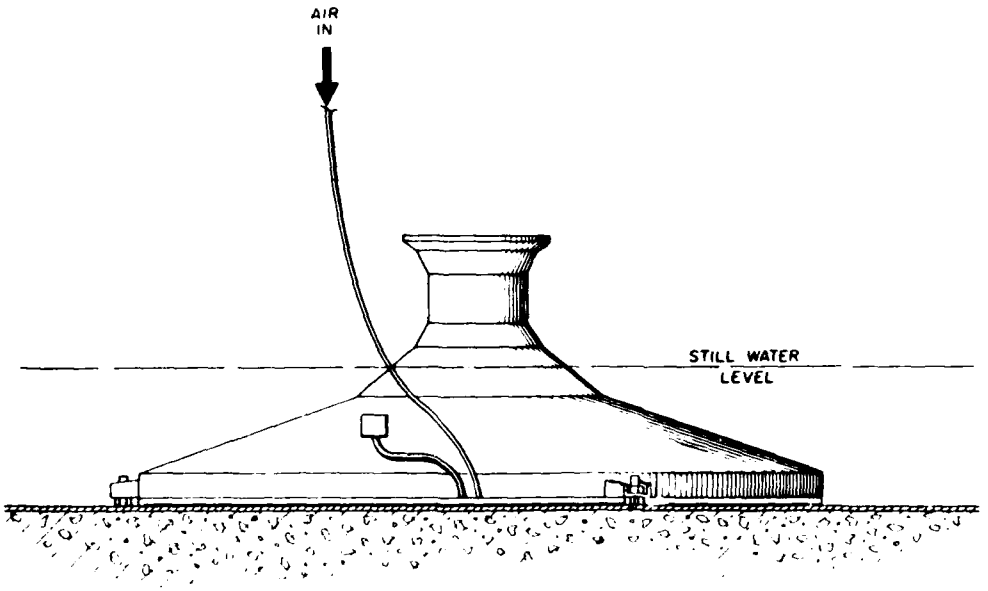

FIGURE 1

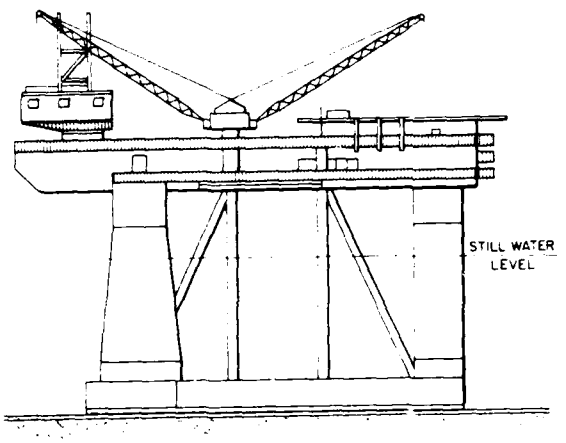

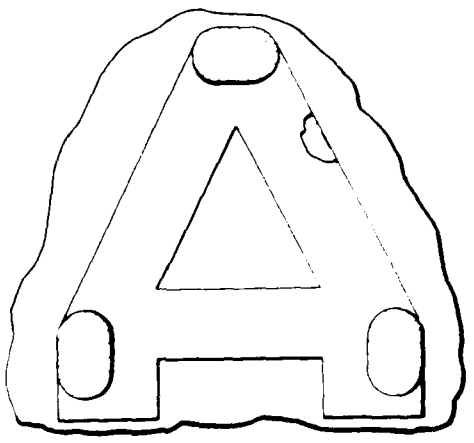

FIGURE 2

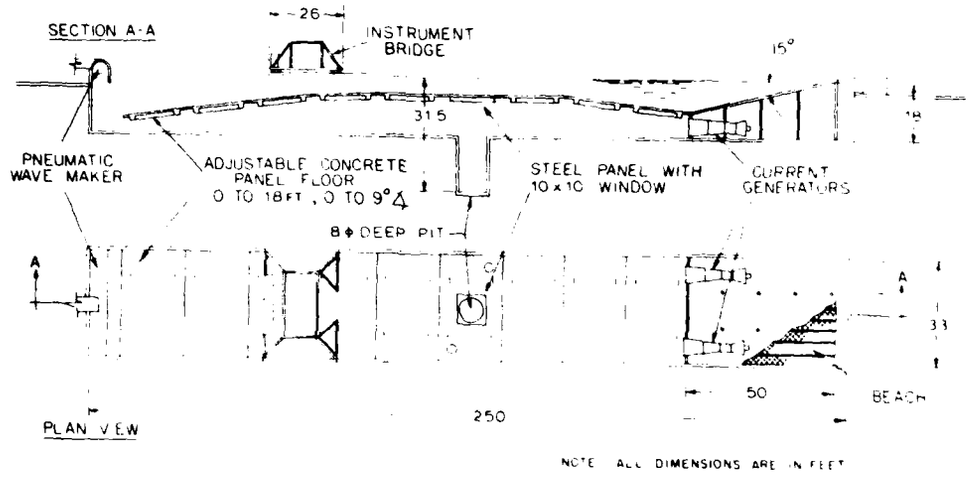

FIGURE 3

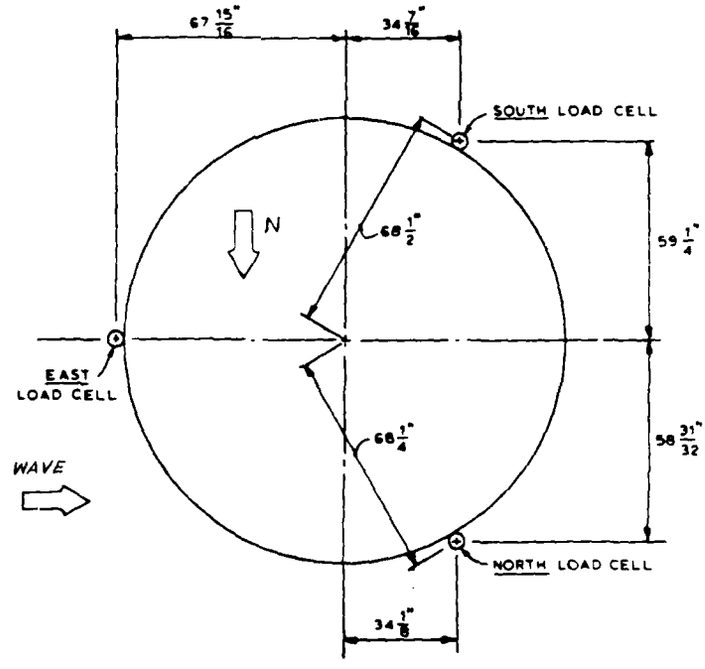

FIGURE 4

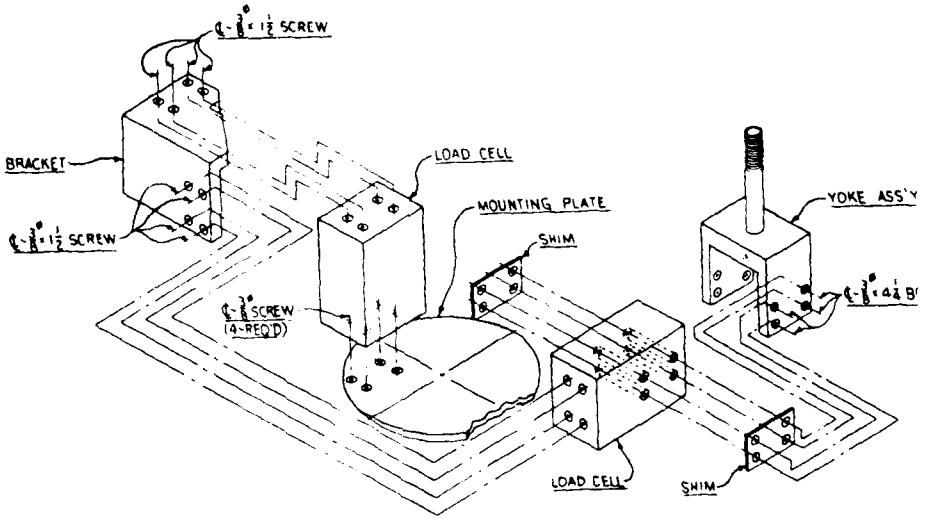

FIGURE 5

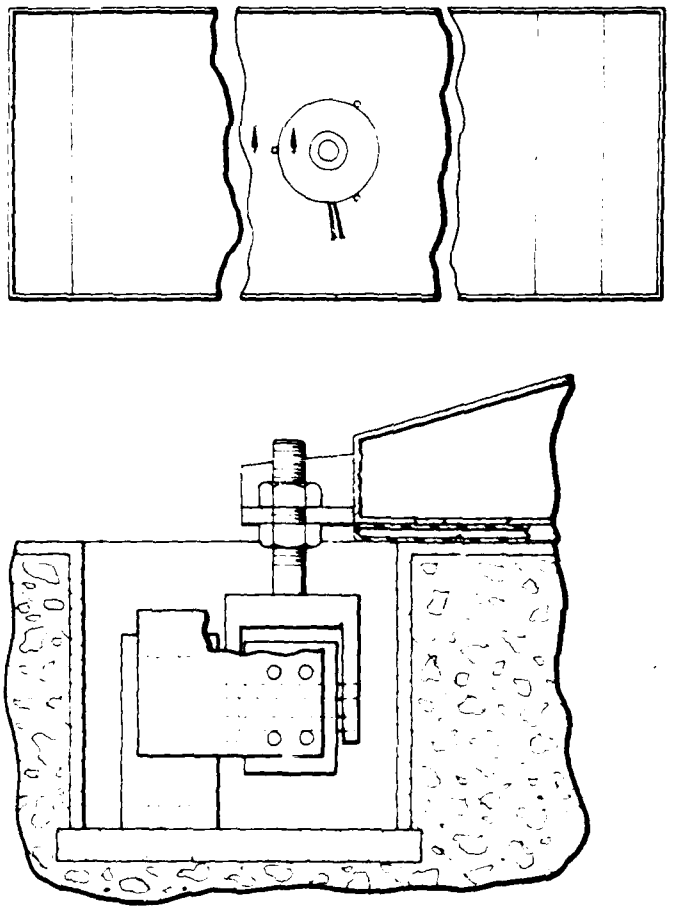

FIGURE 6

FIGURE 7

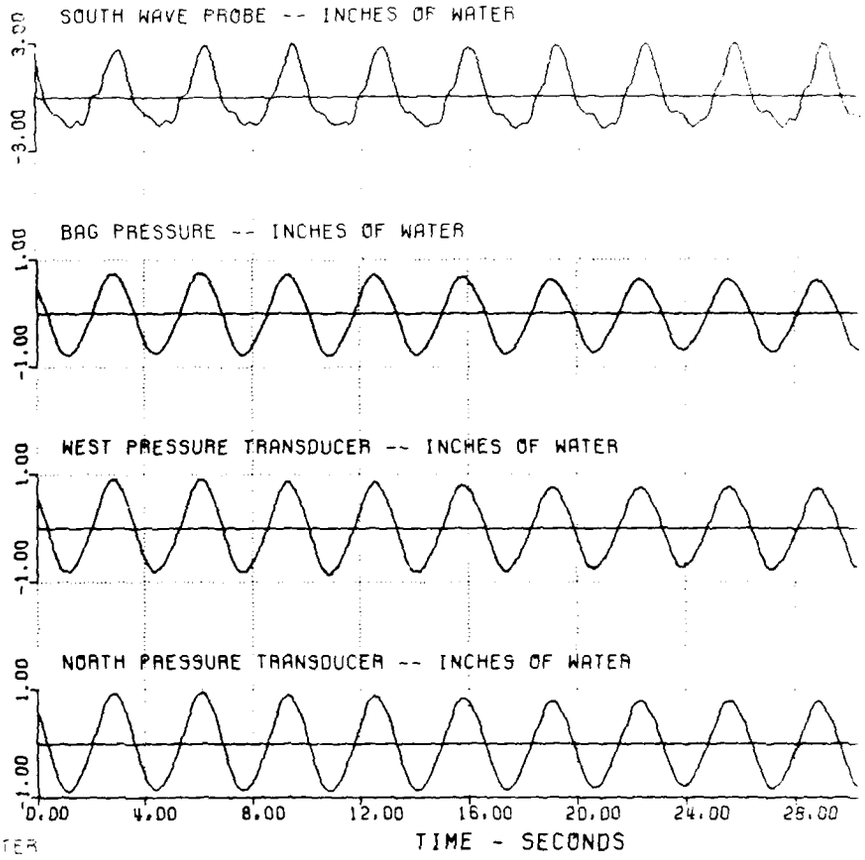

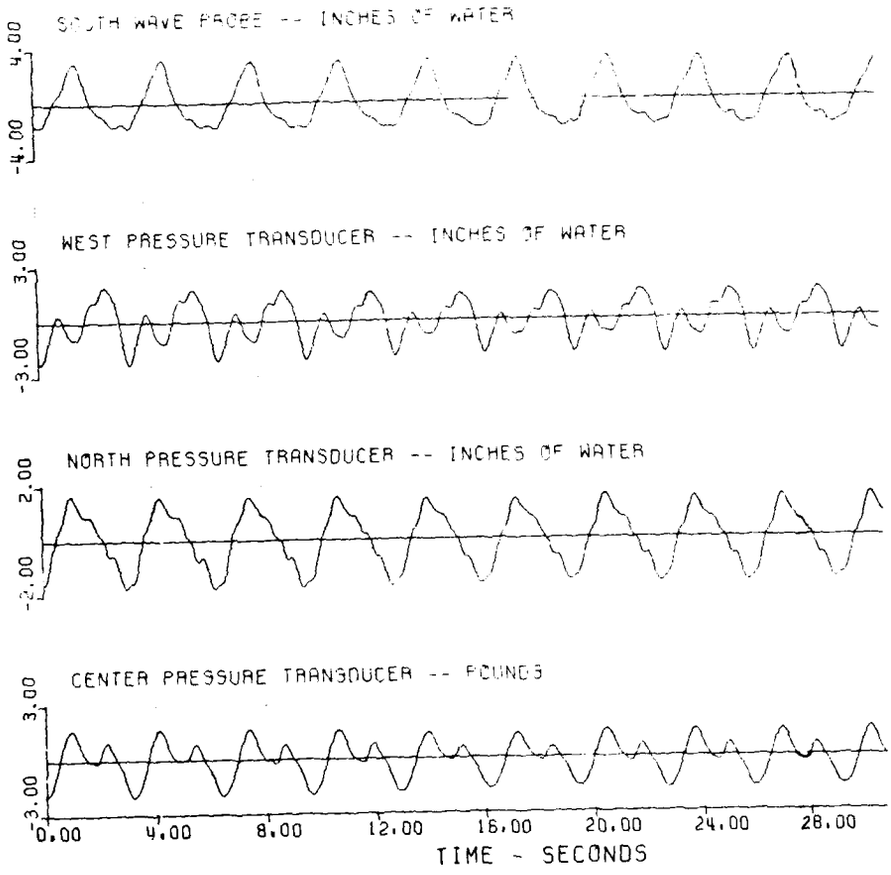

FIGURE 8

TECHNIQUES IN DIRECTIONAL WAVE SPECTRAL ANALYSIS WITH APPLICATIONS FOR THE SEAKEEPING BASIN

Martin J. Dipper Jr.
Naval Architect
David W. Taylor Naval Ship Research And Development Center
Code 1562, Special Ship And Ocean Systems Dynamics Branch

ABSTRACT

Methods to accurately estimate the directional components of ocean and basin waves have been evaluated at the David W. Taylor Naval Ship Research and Development Center (DTNSRDC). Use of multidirectional seaways in the Maneuvering and Seakeeping (MASK) facility at DTNSRDC requires application of a precise method for analyzing the direction of these waves.

This paper examines the techniques developed to estimate directional wave spectra through an application of the Maximum Likelihood Method (MLM). The Maximum Likelihood Method was chosen because it is capable of estimates optimized for resolution of wave direction for wave probe arrays with arbitrary spacing, thereby allowing flexibility in probe installation in both full and model scale applications.

Graphics techniques are applied to the directional wave spectrum presentation allowing the display and interpretation of the large amount of data produced in this analysis as a single three dimensional graph. Limiting characteristics of the MLM as well as confidence ranges for the application of the MLM to the directional seaway analysis are explored. Confidence limits associated with wave probe spacing and the resultant directional spectrum have been quantified and are presented as a single three dimensional graph. These three dimensional graphs and the associated two dimensional projected contour graphs are well suited to direct interpretation by engineers and scientists.

Results from MASK facility tests are presented demonstrating the techniques developed in this application of the MLM through directional analysis of seaways with controlled directionality. Data from deployment of wave probe arrays with both highly optimized and poorly optimized spacings relative to the basin generated seaways are examined.

INTRODUCTION

Methods to accurately estimate the directional components of ocean and basin waves have been evaluated at DTNSRDC. In full scale seakeeping trials, this information is necessary for characterizing the directionality aspects of the seaway. The future use of multidirectional seaways in the Maneuvering and Seakeeping (MASK) facility at DTNSRDC requires the understanding and practical application of a precise method for analyzing the direction of these waves. Definition of a wave height power density spectrum as a function of both frequency and direction can be a useful tool in seakeeping experiments. In a previous effort [1] different methods were surveyed for estimating directional wave spectra applicable to full scale and model scale environments. The method chosen for development was an application of the Maximum Likelihood Method (MLM) [2]. This method is capable of estimates optimized for resolution of wave direction for wave probe arrays with arbitrary spacing allowing flexibility in probe installation in both full and model scale applications.

Past efforts at DTNSRDC resulted in the development of the computer algorithms necessary for implementing the MLM for estimating directional wave spectra. Cross spectral modeling techniques were used to verify these algorithms. Applications of these algorithms raised questions about the factors that influence the accuracies of this method.

This paper presents the techniques developed to enhance capabilities in the analysis and interpretation of directional seaways through an application of the MLM. Results from a three probe wire capacitance transducer array and a three probe sonic transducer array are presented for basin generated unidirectional and bidirectional seaways. Graphics techniques applied to the directional wave spectrum presentation allow the display of the large amount of data produced in this analysis as a single three dimensional graph. These graphics techniques are employed here to demonstrate an ability to also identify results of the analysis which may fall outside the confidence ranges for application of the MLM. Application of these directional analysis techniques to MASK facility testing illustrates these points best, by example, in deployment of both highly optimized and poorly optimized wave probe arrays in similar seaways. The tests were run in mid 1986 using the MASK wavemakers, prior to the wavemaker upgrade.

BACKGROUND

The MLM directional analysis is a direct approach dependent upon measurement of wave height time histories at several spatially defined points in an array. The auto and cross spectra characteristics of the wave height time histories from the array are determined directly for each combination of probe pairs. The autospectrum analysis method uses overlapped Fast Fourier Transform processing of windowed data segments. A 50-percent segment overlap and a raised cosine data window are the reduction parameters specified for this method [1]. Methods for determining optimum resolution in the autospectra and confidence in the cross spectra (by measure of coherency) were utilized.

The inverse of the cross spectral matrix, as associated with the array geometry, is used in the MLM to estimate the directional spectrum. The MLM is a data adaptive technique in which the wave number window used in the directional spectrum estimate changes its shape, giving higher resolution, and is a function of the wave number at which the directional estimate is being made [3]. The method produces directional wave spectrum estimates with an optimally small beamwidth; the size of this beamwidth depends on the characteristics of the wave height time histories in that measurement noise and mismatch (non-parallel wave fronts, for example) will automatically increase this beamwidth [4].

The ability of the MLM to resolve the true directional spectrum depends upon many factors such as the array size and geometry, wave front curvature, and measurement noise. An array geometry must be tuned spatially with respect to the frequency content characteristic of the seaway for which a directional spectrum is to be estimated. Should wavelengths encountered become too long or too short relative to the probe spacing within an array, directional resolution degenerates, and the MLM estimated directional spectrum may indicate wave energy at directions not present in the true spectrum. The effects of array geometry, particularly in gage pair spacing, on directional resolving capability are investigated in this paper.

DEFINITION OF THE TUNING FACTOR

A tuning factor has been developed which is used as a first pass in obtaining a spatial arrangement of probes in an array which is well suited for high directional resolution of a seaway of specific frequency content. The tuning factor is derived from an average of a ratio of wavelength to effective probe spacings in an array. The effective probe spacing is the distance between two probes along a line perpendicular to the wave front. A ratio is calculated for each probe pair at one direction of propagation; and the average of these ratios is recorded as the unmodified tuning factor value at that direction and frequency. An unmodified tuning factor is calculated at each frequency and direction analyzed.

The tuning factor presented graphically is derived from the unmodified tuning factor. This factor is modified to yield values between zero and one over the entire frequency and directional analysis domain. Zero represents the lowest confidence and one the highest. For ratios of less than one (the short wavelength limit), the tuning factor is presented unmodified. However, for wavelength to average effective probe spacing ratios between one and ten the tuning factor is set to one. Further, for wavelength to effective probe spacing ratios greater than ten (the long wavelength limit), the modified tuning factor is ten divided by the unmodified factor. Use of the factor ten in modifying the ratio for the long wavelength region is a conservative value. As the wavelengths become long relative to the probe spacing, instrument noise becomes more dominant in influencing resolving power [4]. These modifications yield tuning factors of one or less at both ends of the frequency range, identifying regions of low spatial confidence for the directional analysis.

A well tuned array will have a tuning factor surface of one in the regions of interest for the associated directional spectrum. Should values of less than one result for a configuration in regions of interest for seaways with a frequency content different than expected, a change in array probe spacing may be required. Spatial aliasing is a possibility at tuning factors of less than one in the high frequency regions. This results from waves of length less than the average effective probe spacing, resulting in loss of wave phase agreement among the probes. Spurious directional results may be seen in the estimated spectrum. An analogy to this would be frequency aliasing associated with the nyquist frequency in sampling problems. In the low frequency regions, directional scatter in the estimated directional spectrum may occur should the wavelengths become long relative to the average probe spacing. In the limiting case for relatively low frequencies, the array is effectively reduced to a point sensor losing directional resolving capability.

In past research [3] the RMS of the gage pair spacings was used to obtain an initial estimate for probe arrangement. The average effective probe spacing used in the tuning factor is similar in approach. The three dimensional tuning factor surface however, lends itself to direct interpretation in qualifying the probe arrangement with the resultant directional spectrum. A more conservative tuning factor limit for the higher frequencies can be set by replacing the average of the effective probe spacings with the spacing associated with the broadest pair (i.e. the worst case pair as the limiting distance).

The tuning factor surface is used as a first past to qualify gage pair spacings of an array geometry, identifying regions of high or low spatial confidence at the high and low frequency limits of the MLM in estimating the directional spectrum. In the data adaptive MLM, an effective beam pattern exists for each frequency analyzed, defining in detail the resolving capability of an array geometry [4]. A large amount of data is contained in the presentation of the effective beam pattern at a single frequency. The tuning factor surface can be used to identify those frequencies which require determination of an effective beam pattern to more accurately qualify the resolving capability of the array configuration.

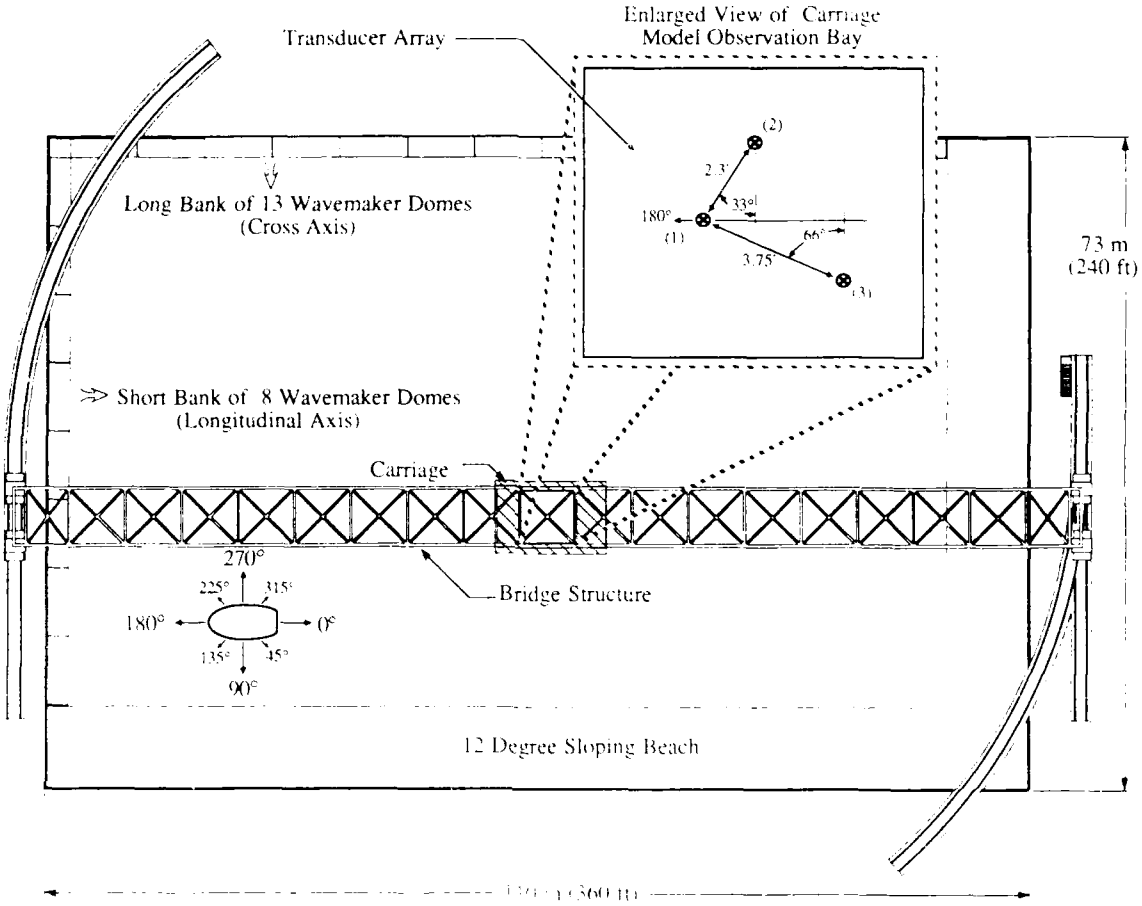

Figure 1. Plan view of the Maneuvering and Seakeeping Basin illustrating the wave probe geometry of the closely spaced wire capacitance transducer array (average gage pair spacing 3.4 feet).

MASK FACILITY TEST WITH A HIGHLY OPTIMIZED ARRAY

Results from the MASK facility tests are presented in the following sections. The techniques developed in this application of the MLM are demonstrated through analysis of directionally controlled basin seaways. In this first example, a closely spaced wave probe array consisting of three wire capacitance transducers was deployed in the configuration shown in Figure 1. The characteristics of the wire capacitance transducers are ideally suited for measurement of the shorter wavelengths encountered in model basin wave work [5]. The wire probes can be deployed in an array at close spacing to each other without contaminating individual signals through transducer cross talk. The directional reference frame assigned to the MASK basin in the tests is also indicated in Figure 1. Waves generated by the Short Bank Wavemaker are viewed as coming from 180 degrees. Waves generated by the Long Bank Wavemaker are viewed as coming from 270 degrees.

A unidirectional random seaway was generated by the combination of wavemaker drives with the spectral characteristics shown graphically in Figure 2. There is good agreement among the three probes in terms of spectral shape. (The coherency associated with the cross spectra is high through the frequency range 0.5 - 8.0 rad/s.)

The MLM directional analysis of this unidirectional seaway is presented graphically in Figure 3 as a three dimensional directional wave height spectrum. The curves plotted on the vertical sides are projections (or shadows) of the directional spectrum surface as seen by looking along the orthogonal lines of direction and frequency. Figure 4 is a two dimensional projected contour plot of the same directional spectrum (Figure 3), where curves of constant power density are shown. Presentation of the directional spectrum surface using this cartesian coordinate system rather than a polar coordinate system is preferred when examining a directional spectrum plot to determine directional spreading in a seaway. Polar presentations with frequency plotted as increasing with radius can give a graphic illusion of increased directional spreading of the power in a seaway at the higher frequencies (outer radius) of a polar plot.

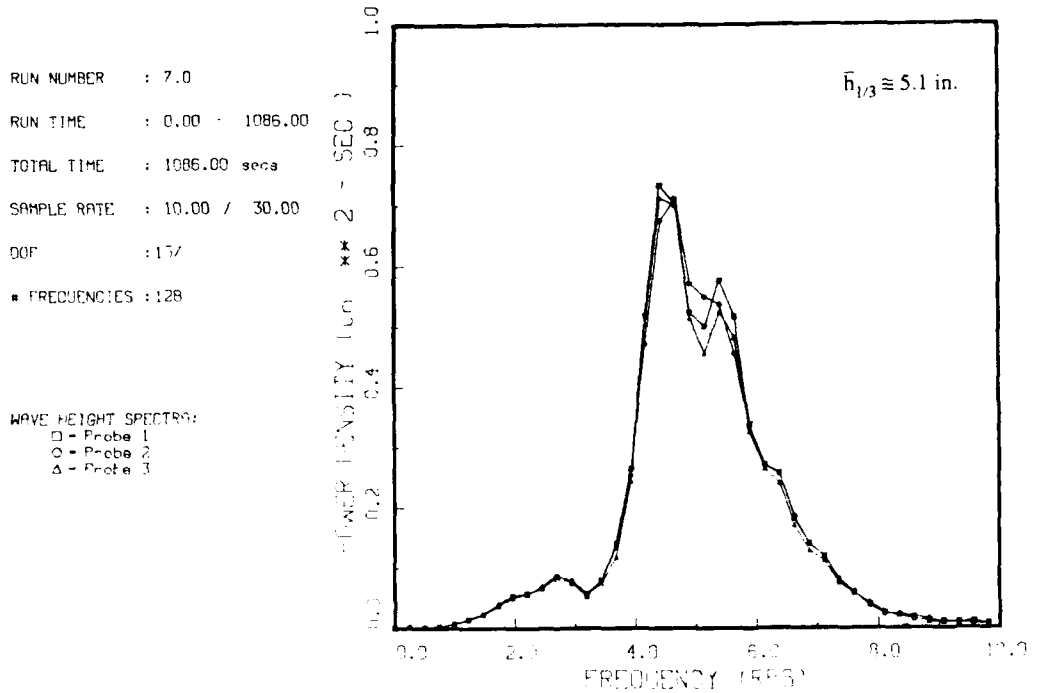

Figure 2. Wave Height Spectra of a unidirectional random seaway generated in the MASK basin by the Short Bank wavemaker. Measurements were made with wire capacitance transducers in a closely spaced array.

The directional spectra plots depict predominant energy coming from 180 degrees with a frequency of maximum energy of 4.5 rad/s. The estimated directional spectrum shows good agreement with the expected characteristics of this controlled basin seaway. (There is a small high frequency energy spike indicated in the estimated directional spectrum at 65 degrees which was not expected. This occurrence is discussed in a later section of this paper.)

The tuning factor directional pattern was calculated for the geometry of the three probe array used in directional measurement of this seaway and is shown in Figure 5 as a three dimensional surface. The frequency and direction axes of the tuning factor directional pattern plot are identical to those of the associated directional spectrum plot, thereby allowing a direct comparison. Figure 6 is a two dimensional projected contour plot of the tuning factor directional pattern shown in Figure 5. Comparison of the contour plots for both the directional spectrum (Figure 4) and the tuning factor directional pattern (Figure 6) indicates good optimization in gage pair spacing of the array for this seaway. Predominant energy for the directional spectrum occurs where the associated tuning factor surface is one.

MASK FACILITY TEST WITH A POORLY OPTIMIZED ARRAY

As the second example, a broadly spaced wave probe array consisting of three surface reflecting ultrasonic transducers was deployed in the configuration shown in Figure 7. The characteristics of the sonic transducers used here required a broader probe spacing in comparison to the wire capacitance transducers to avoid error from transducer cross talk. The gage pair separation used here is somewhat broader than the minimum separation required (approximately four feet minimum). A characterization of free surface measurements by ultrasonic displacement sensors is given in reference [5].

A unidirectional random seaway was again generated by the short bank of wavemaker domes with characteristics similar in frequency content to that of the first example (Figure 2). The same wavemaker program was run, with the seaway in this second example having approximately half the peak power. The autospectra for the probes in this sparse array are shown in Figure 8. There is bad agreement between the seaway observed by Probe 3 with that observed by Probes 1 and 2, particularly at the frequency of maximum energy. The broad spacing of this array, and the position of the MASK carriage, resulted in the array spanning across a seam of two Short Bank wavemaker domes. Poor optimization in gage pair spacing of the array for this seaway is indicated here by poor agreement of the autospectra (Figure 8.). (The coherency associated with the cross spectra is low for frequencies above 3.0 rad/s.)

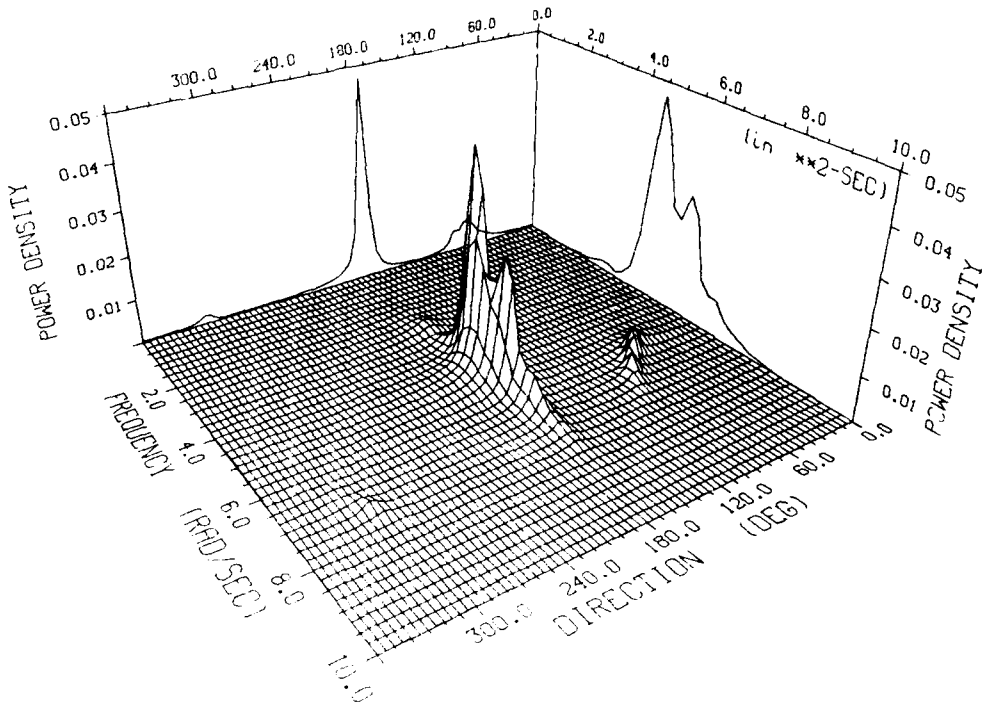

Figure 3. Directional Wave Height Spectrum of a unidirectional random seaway generated in the MASK basin by the Short Bank wavemaker. Measurements were made with wire capacitance transducers in a closely spaced array.

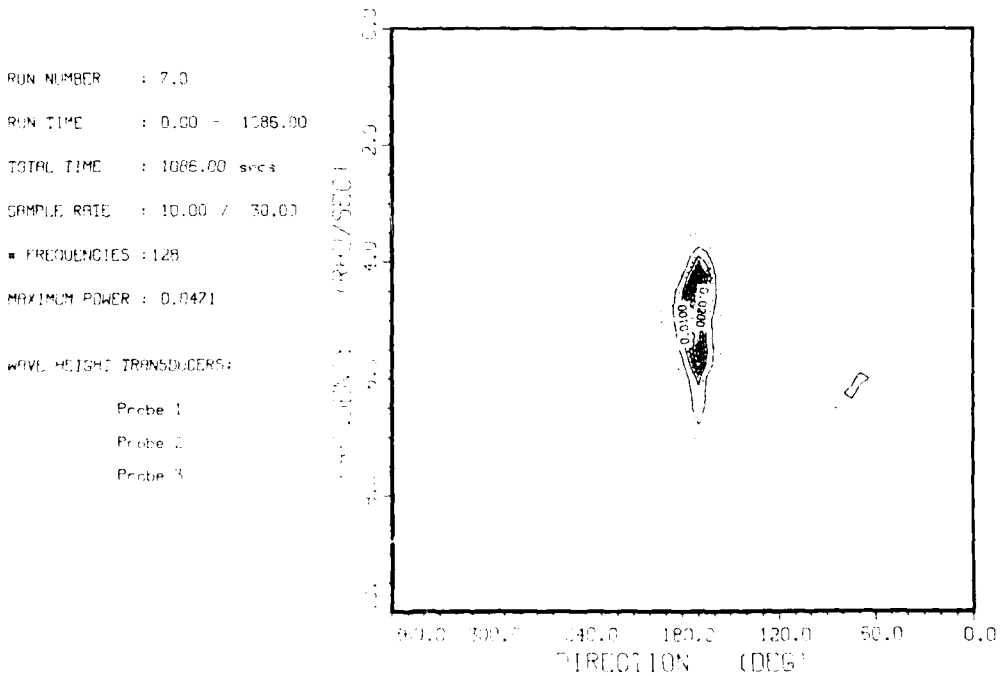

Figure 4. Directional Wave Height Spectrum of a unidirectional random seaway generated in the MASK basin by the Short Bank wavemaker (Curves of constant Power Density).

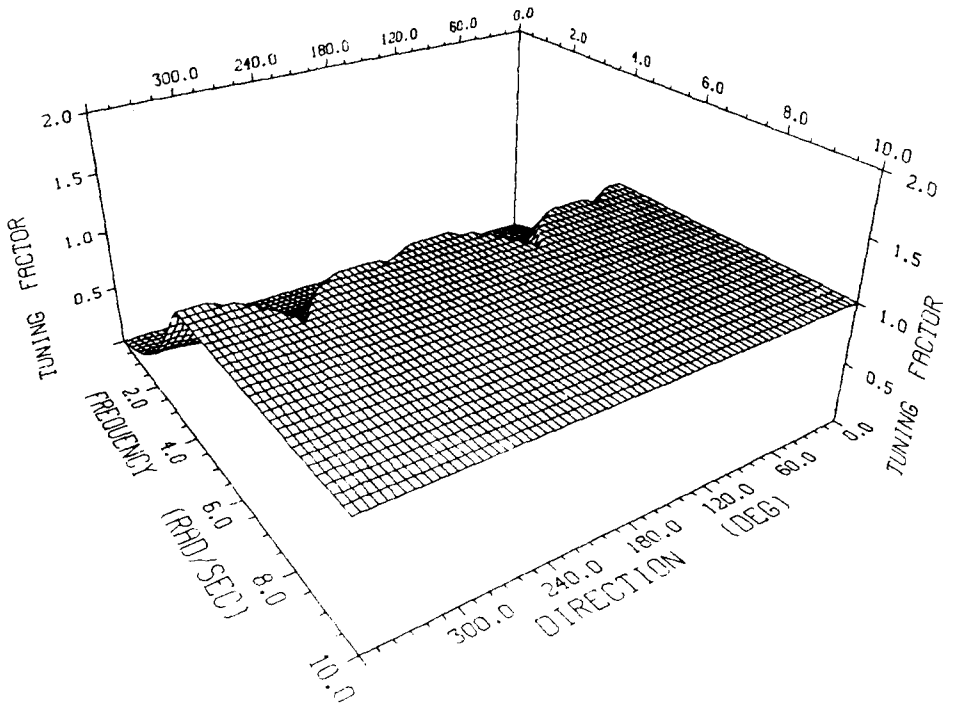

Figure 5. Tuning Factor Directional Pattern determined for the wave probe geometry of the spaced wire capacitance transducer array.

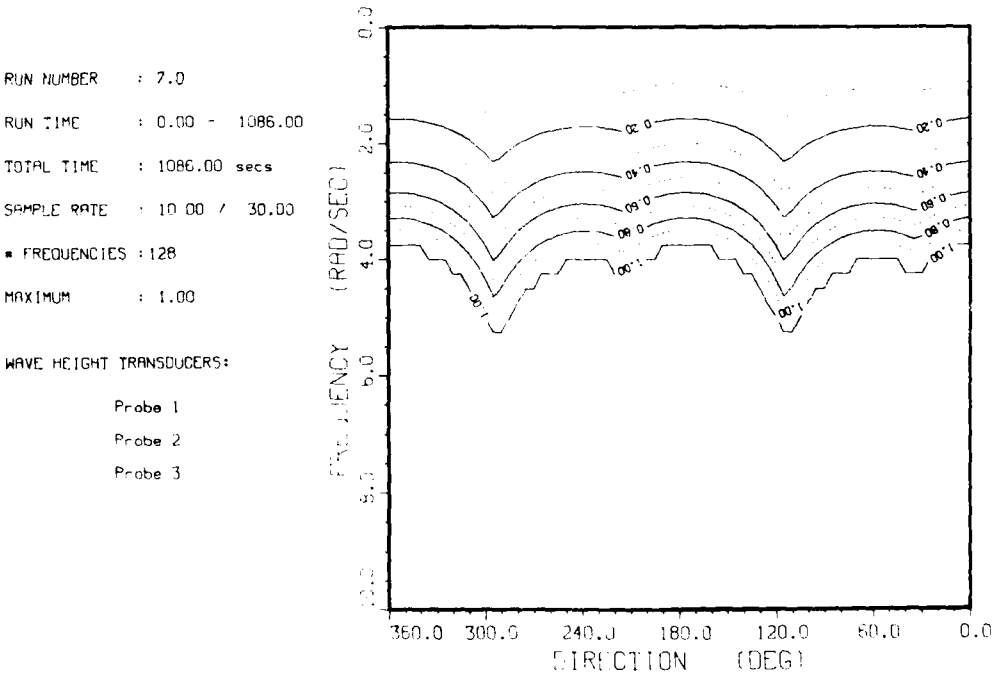

Figure 6. Tuning Factor Directional Pattern projected contours for the wave probe geometry of the closely spaced wire capacitance transducer array.

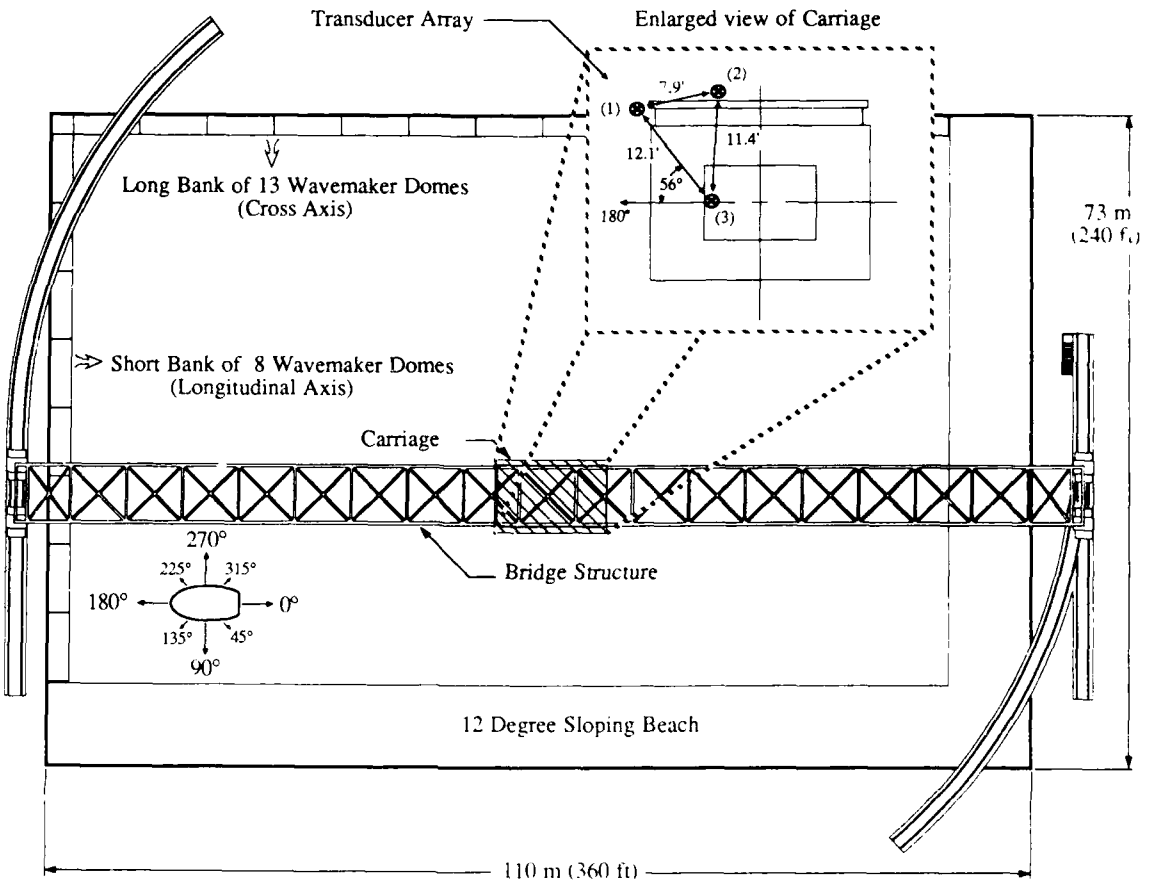

Figure 7. Plan view of the Maneuvering and Seakeeping Basin illustrating the wave probe geometry of the broadly spaced sonic transducer array (average gage pair spacing 10.5 feet).

The estimated directional wave height spectrum obtained from the three probe sonic transducer array is shown in Figure 9. A projected contour plot of this estimated directional spectrum is shown in Figure 10, featuring curves of constant power density. The random seaway was generated with predominant energy coming from 180 degrees with a frequency of maximum energy of 4.5 rad/s. Review of the estimated spectrum (Figures 9 and 10) indicates that accurate directional definition is limited at frequencies above 3.0 rad/s; some directional spreading occurs in the estimated spectrum at lower frequencies.

In the low frequency region of this seaway, 1.5 to 3.0 rad/s, there is fair agreement among the autospectra (Figure 8). Looking at this same frequency range in the directional spectrum contour plot (Figure 10), the expected characteristics of the controlled seaway from 180 degrees are evident. There is some directional spreading in this region. The tuning factor directional pattern for this array geometry, shown in Figures 11 and 12, indicates tuning factors of less than one for frequencies below 2.5 rad/s at 180 degrees.

In the frequency range of 3.0 to 6.0 rad/s the method breaks down for the probe spacing in this array as matched to this seaway. There is very poor agreement among the autospectra (Figure 8) in this range. The directional scatter in the estimated directional spectrum is likely due to a mismatch of the encountered wave to the expected math model wave (from non-parallel or bent wave fronts). The MLM requires parallel wave fronts and long crest lengths relative to the probe spacing. Variations in wave fronts along crest lengths which appear short relative to gage pair distances can result in spatial aliasing at lower frequencies than expected.

At frequencies higher than 6.0 rad/s there is also energy indicated in the estimated spectrum at directions other than 180 degrees. Spatial aliasing occurs here as the wavelengths become short relative to the gage pair spacings in this array geometry. The tuning factor at 180 degrees is less than one at these frequencies.

In the two tests presented above, the short bank wavemaker was run with only the five center segments of the eight segment front active. Operation of the wavemaker was similar for both test cases, generating a seaway similar in direction and frequency content.

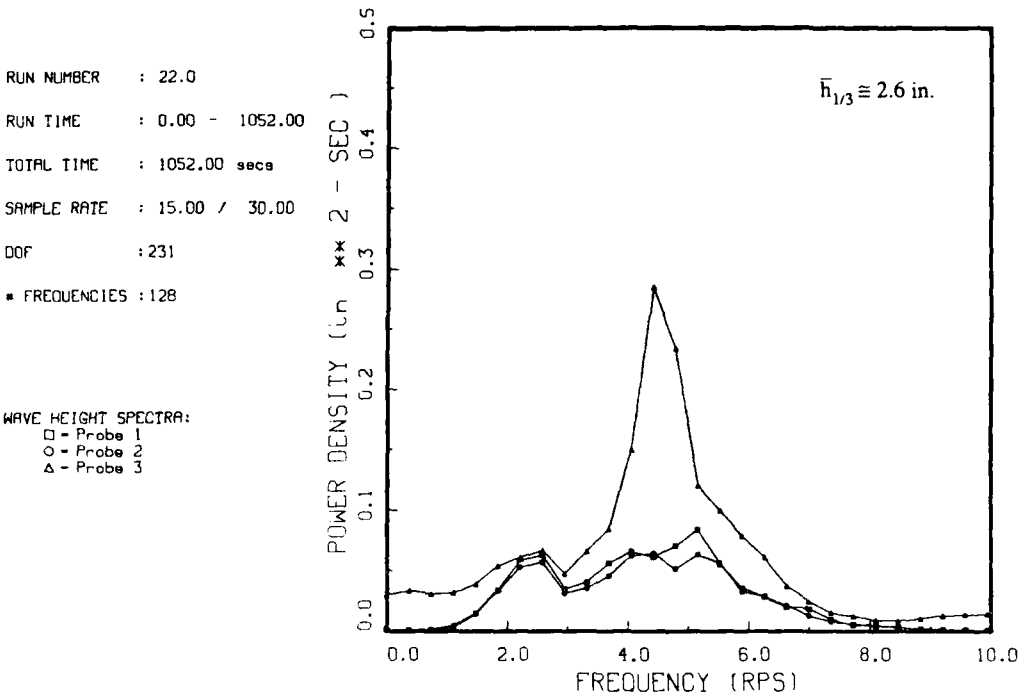

Figure 8. Wave Height Spectra of a unidirectional random seaway generated in the MASK basin by the Short Bank wavemaker. Measurements were made with sonic transducers in a broadly spaced array.

Although the type of transducer used in each test was different, the major difference in directional resolving capability was a function of array geometry. The closely spaced array used in the first test case is able to resolve the directional components of the seaway more accurately. The broadly spaced probe configuration employed in the second example represented a limiting case for this application of the MLM. The graphics techniques developed demonstrate an ability to identify results which fall outside acceptable limits of accurate directional resolution.

A MASK FACILITY BI-DIRECTIONAL SEAWAY

A bi-directional seaway was generated in the MASK basin with a random seaway component from the Short Bank of wavemakers and a regular swell component from the Long Bank of wavemakers. The random seaway was generated by the same wavemaker program run in the first example (Figure 2), and is identical in power and spectral shape. The regular swell has a frequency of maximum energy of 3.9 rad/s. The closely spaced wave probe array consisting of three wire capacitance transducers was used again as shown in Figure 1. The autospectra for this bi-directional seaway are shown graphically in Figure 13. The MLM directional analysis of this seaway is presented in Figure 14 as a three dimensional directional wave height spectrum. In the estimated directional spectrum, a random seaway coming from 180 degrees, and a swell coming from 270 degrees are resolved.

A unidirectional seaway consisting of only the regular swell component from the Long Bank of wavemakers was generated and analyzed for comparison. The autospectra are shown in Figure 15. The estimated directional spectrum is shown in Figure 16.

Note the absence of the energy spike at 65 degrees in this unidirectional Long Bank seaway. The unexpected energy at 65 degrees which is evident in Figures 3 and 14 is associated with this array configuration as matched to this seaway generated by the short bank wavemaker. Further analysis of parameters which also affect directional resolution, such as measurement noise, number of probes in an array, and mismatch due to wave front curvature, is required to better qualify this energy spike in the estimated spectrum.

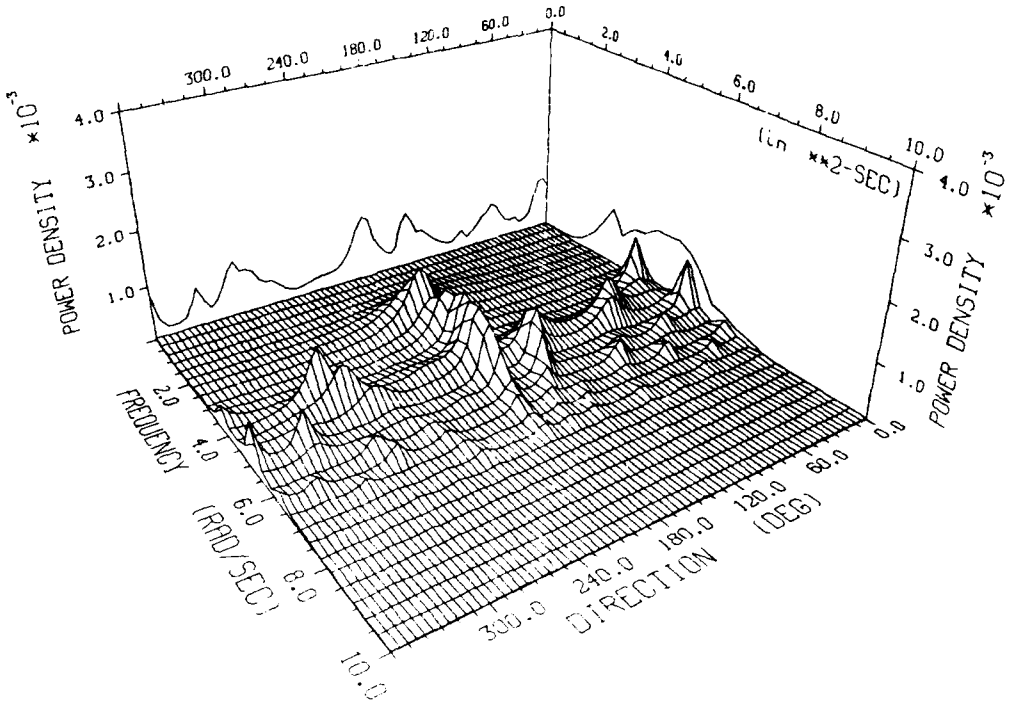

Figure 9. Directional Wave Height Spectrum of a unidirectional random seaway generated in the MASK basin by the Short Bank wavemaker. Measurements were made with sonic transducers in a broadly spaced array.

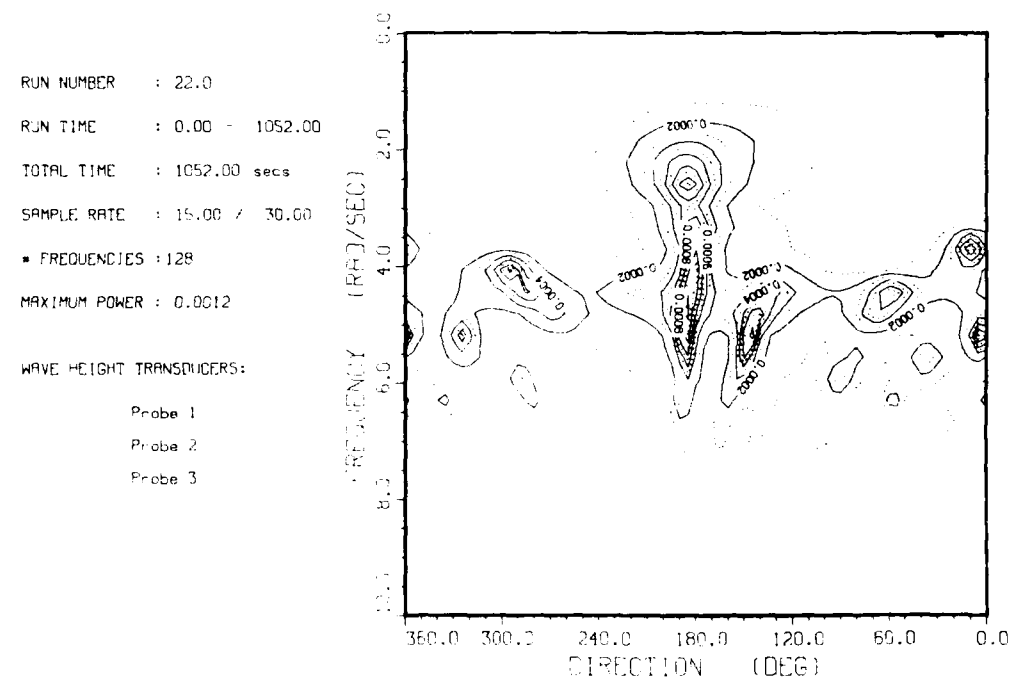

Figure 10. Directional Wave Height Spectrum of a unidirectional random seaway generated in the MASK basin by the Short Bank wavemaker (Curves of constant Power Density).

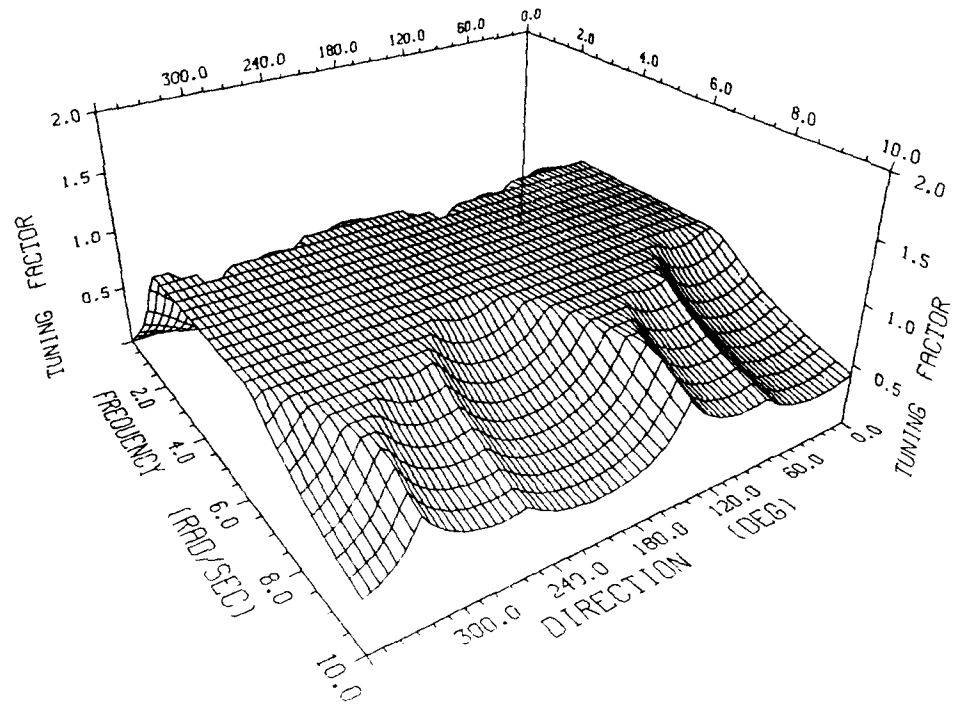

Figure 11. Tuning Factor Directional Pattern determined for the wave probe geometry of the broadly spaced sonic transducer array.

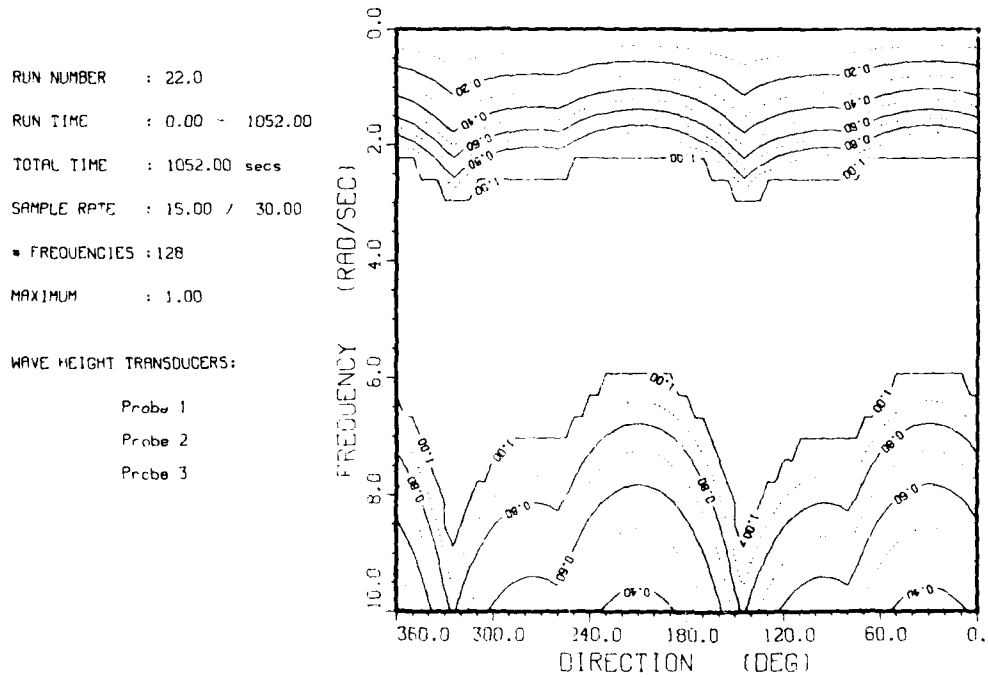

Figure 12. Tuning Factor Directional Pattern projected contours for the wave probe geometry of the broadly spaced sonic transducer array.

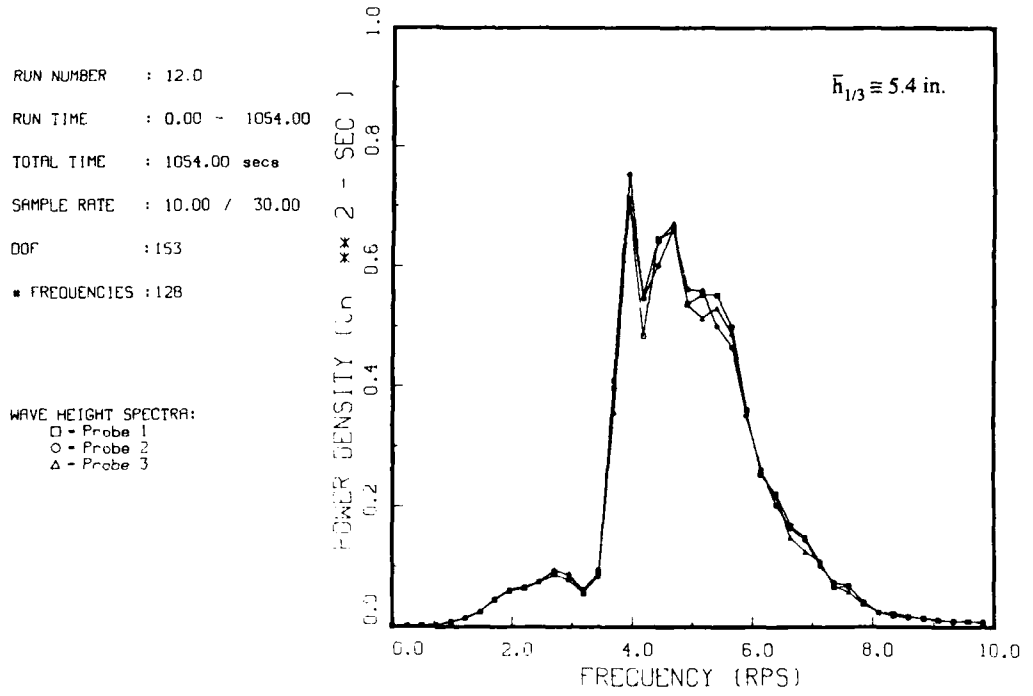

Figure 13. Wave Height Spectra of a bi-directional random seaway with swell generated in MASK basin by simultaneous operation of the Short Bank and Long Bank wavemakers. Measurements were made with a closely spaced array.

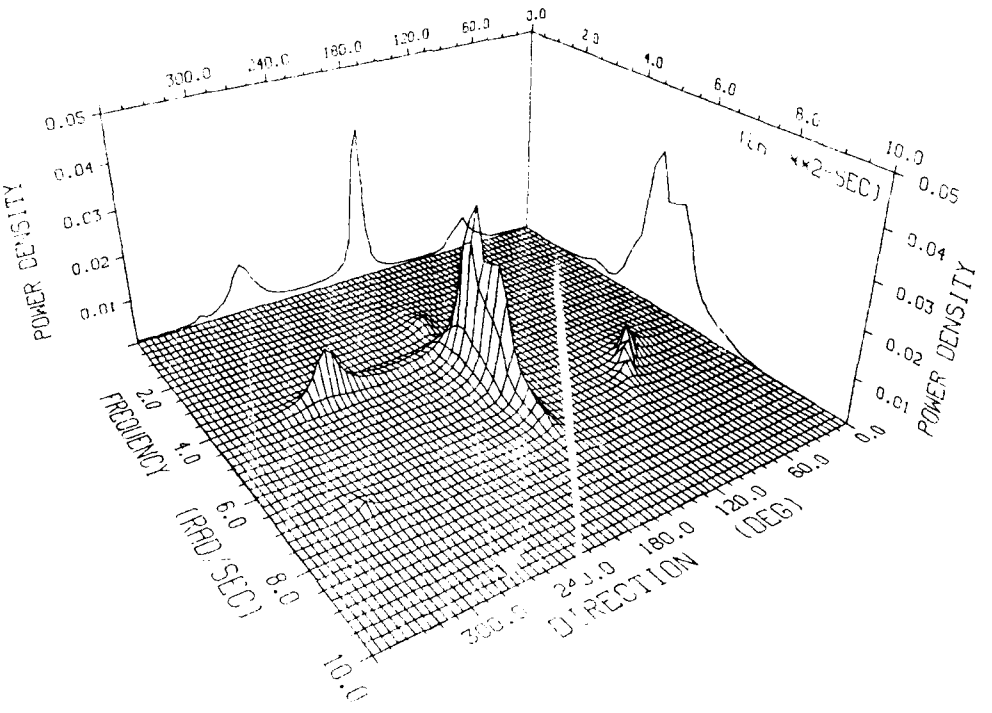

Figure 14. Directional Wave Height Spectrum of a bi-directional random seaway with swell generated in the MASK basin by simultaneous operation of the Short Bank and Long Bank wavemakers. Measurements were made with a closely spaced array.

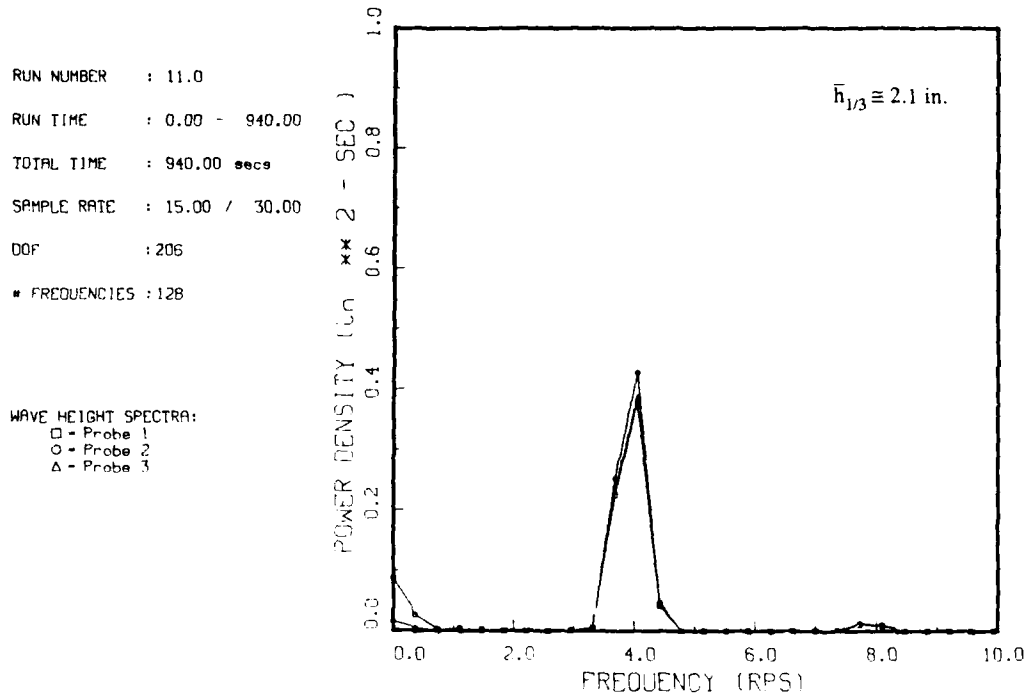

Figure 15. Wave Height Spectra of a unidirectional regular seaway generated in the MASK basin by the Long Bank wavemaker. Measurements were made with a closely spaced array.

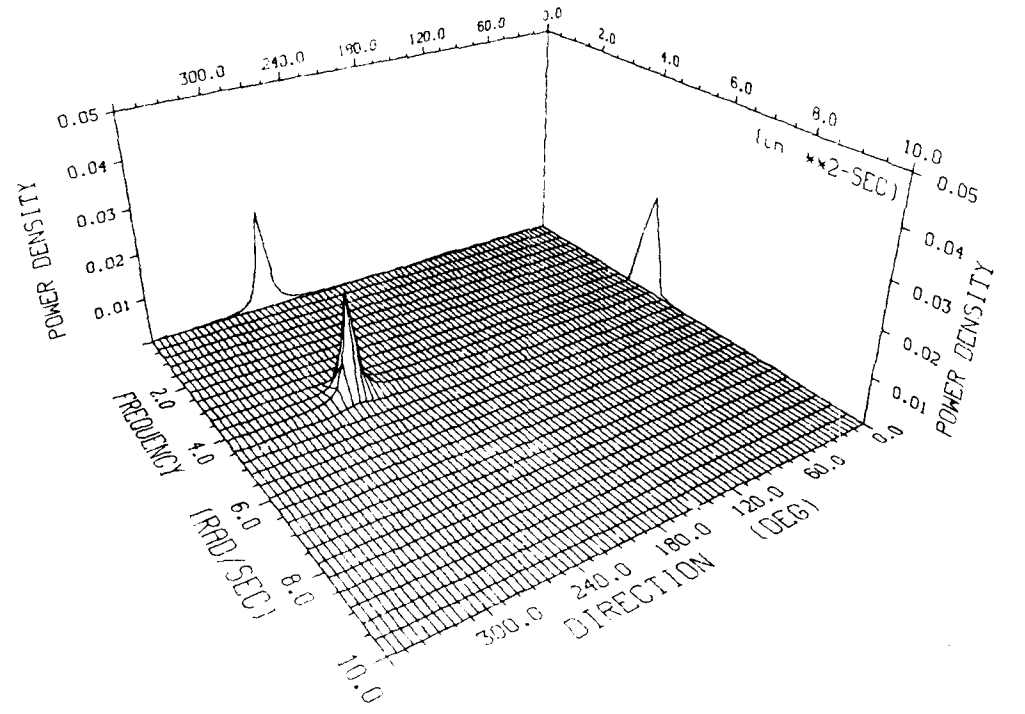

Figure 16. Directional Wave Height Spectrum of a unidirectional regular seaway generated in the MASK basin by the Long Bank wavemaker. Measurements were made with a closely spaced array.

VARIABLES INTRODUCED BY THE WAVEMAKER

In basin work, array geometries can be tuned in shape and spacing (for a fixed number of probes) with respect to the expected direction and frequency ranges of the generated seaway. However, unplanned imbalance in phasing or power along the generating front of a segmented, or sparsely segmented, wavemaker may introduce such factors as bent wave fronts, non-parallel wave fronts or short wave crest lengths (short relative to the probe spacing). Such anomalies seen in basin generated waves can result in a breakdown of the method seen as directional scatter in the estimated spectrum due to mismatch. The occurrence of non-parallel or bent wave fronts becomes significant as the array gage pair distances appear large relative to changes along a crest length. A probe spacing closer than anticipated is needed to reduce the significance of these events in the basin generated seaways.

In this application, the MLM requires parallel wave fronts and crest lengths which are long relative to the probe spacing. Deviation from this model can result in the method estimating energy at directions which are not present in the true directional spectrum. Identification of such events in the results of the analysis warrants a change in array geometry to better resolve the existing seaway or a change in wavemaker segment balance to produce the seaway first anticipated.

SUMMARY AND CONCLUSIONS

The techniques developed to enhance capabilities in the analysis and interpretation of directional seaways through an application of the MLM have been presented through example. The closely spaced wire capacitance transducer array used in the MLM to obtain a directional spectrum estimate of a random unidirectional basin seaway produced an estimated spectrum in good agreement with the known characteristics of this controlled seaway. Employment of a broadly spaced sonic transducer array to a similar random unidirectional basin seaway showed poor agreement between the estimated spectrum and the known characteristics of the seaway. The broadly spaced array was poorly optimized for this seaway as seen in poor agreement among probes shown in the auto and cross spectra estimates. Poor array optimization was also indicated by declining values of the tuning factor at high and low frequencies of interest. The tuning factor represents a quantification of the spatial confidence limits associated with array wave probe geometry. An ability to resolve basin generated bi-directional seaways was demonstrated. The MLM directional analysis can be sensitive to anomalies seen in basin generated waves, such as bent or non-parallel wave fronts which can appear extreme relative to particular gage pair spacings.

The graphics techniques applied to the directional spectrum presentation allows the display and interpretation of the large amount of data produced in this analysis as a single three dimensional graph. The three dimensional graphs and the associated two dimensional projected contour graphs are well suited to direct interpretation.

REFERENCES

1. Davis, M.J., Turner, C.R., Peters, J.B., and McGuigan, S.H., "Amphibious Assault Landing Crafts JEFF A and JEFF B: Seakeeping Full-Scale Trials", Proceedings Society of Naval Architects and Marine Engineers STAR Symposium, April 1982.

2. Capon, J., "High-Resolution Frequency Wave number Spectrum Analysis", Proceedings Institute of Electrical and Electronic Engineers, Vol. 57, August, 1969.

3. Paniker, N., "Review of Techniques for Wave Spectra", Proceedings International Symposium on Ocean Wave Measurement and Analysis, American Society of Civil Engineers, September 1974.

4. Oakley, O.H., Lozow, J.B., "The Resolution of Directional Wave Spectra Using the Maximum Likelihood Method", Department of Ocean Engineering, Massachusetts Institute of Technology, Ocean Engineering Report 77-1, May 1977.

5. Pierce, R.D., "The Characterization of Off Vertical Return Error in Free Surface Measurements by Ultrasonic Displacement Sensors", Central Instrumentation Department, David W. Taylor Naval Ship Research and Development Center, Research and Development Report DTNSRDC-86/060, September 1986.

DIRECTIONAL WAVE MEASUREMENTS FOR APPLICATION TO SHIP TRIAL ANALYSIS

Robert J. Bachman, Ronald J. Lai and Edward W. Foley
David W. Taylor Naval Ship Research and Development Center
Bethesda, Maryland 20084-5000

ABSTRACT

Directional wave measurement is in the process of replacing conventional wave measurement in support of ship trials. Frequency-energy distribution is no longer sufficient to define the wave energy, rather, the directional distribution of wave energy of each frequency component is required for determining ship response.

To measure wave directionality, David W. Taylor Naval Ship Research and Development Center (DTNSRDC) has chosen a lightweight, easy to handle, directional wave sensing buoy, known as an ENDECO Wave-Track buoy. Software has been developed at the Center to analyze the data obtained from the buoy. Included in the analysis are effects of local current. The existence of currents modify the wave directionality. Interpretation of the directional data is dependent on the method of buoy deployment, moored, free drifting or tethered to a ship. Consequently, the measured wave directionality should be adjusted before being applied to ship response calculations.

The buoy has been used during several trials and compared with other directional wave sensing buoys, such as a discus buoy and a cloverleaf buoy. The results generally agreed well.

1. INTRODUCTION

The quantification of waves has always been important to full-scale seakeeping trials. During a trial, the measurement of the wave forcing function allows the naval architect to validate relationships between sea conditions and resulting ship motions or loadings. These relationships, or ship response amplitude operators (RAOs), define the seakeeping characteristics of a given ship design and can be used for various purposes including providing operator guidance through the generation of safe operating envelopes (Jones and Foley, 1979).

Over the last couple of decades, the naval ship community has used wave height and period measuring buoys, i.e., point spectra buoys, to determine the sea conditions in which the ship operates. This method defined the energy spectrum of the sea but gave no indication of wave direction and spreading characteristics. In addition, wave measurements were obtained from a buoy that either free drifted with the wind and current or was tethered to a ship, which also may have moved with the wind and current. When the ship was underway performing trial legs, it was obvious that the ship and the wave measuring buoy encountered different waves, due to the ship's speed and heading. It has thus become necessary to transform the stationary, or fixed frequency, measured wave information to the frequency of encounter. Owing to the relationship of wave direction relative to the ship heading in the frequency transformation, an estimate of the wave direction at appropriate frequencies must be performed.

A directional sensing wave buoy is one method of providing the naval architect with the capability to measure wave directionality. From this he can determine the relative direction of travel between ship and waves in addition to the standard wave height and period information. Many types of directional sensing wave buoys have been developed over the years. Discus shaped buoys, cloverleaf buoys, spiral following buoys and spar buoys between designs have all found their way into routine use. The size of the buoy and its principle of operation determine deployment and analysis methods. The David W. Taylor Naval Ship Research and Development Center (DTNSRDC) chose an ENDECO Wave Track buoy for trial use, as it can be easily deployed using minimal deck equipment while still providing sufficient resolution of wave directionality. The Wave Track buoy relies on a different principle to measure the wave directionality than does a conventional slope following buoy (see figure 1). Consequently, the analysis of the Wave Track data requires a modification of the conventional slope analysis. The analysis procedure of the Wave Track data, developed and used by DTNSRDC, has been reported earlier, by Lai and Bachman (1980).

As mentioned above, buoys do not necessarily measure waves in the same frame of reference as the ship encounters. Buoys may be moored, free drifted, or tethered to a

ship. When moored, buoys measure waves in the fixed frequency domain. If the wave data is to be used in the ship's frame of reference, i.e., the encountered frequency domain, a transformation of the data must be performed. Furthermore, if the wave buoy is measuring waves while free drifting, it is necessary to first transform the data from the drifting, moving coordinate system to the fixed coordinate system, i.e., encountered to fixed frequency. The data then can be transformed to the wave frequency domain encountered by the ship.

A brief review of past applications of the buoy and analysis will be covered, followed by computation of wave transformations to the ship encounter domain. Relevant equations and derivations will be presented in a future publication.

3. APPLICATION OF BUOY

The measurement of directional waves with a buoy during ship trials was first performed by DTNSRDC in May 1982. During these trials aboard the Hr. Ms. TYDEMAN, waves and their directions were measured by a WAVEC buoy, built by Datawell, and the Wave Track buoy, built by ENDECO and owner operated by DTNSRDC. A third buoy, measuring just the energy spectra was also deployed. The Wave Track data was analyzed by DTNSRDC using the analysis technique developed at the Center. The Department of Hydro-Instrumentation of the Ministry of Public Works in the Netherlands analyzed the WAVEC data (Gerritsma, 1983). Though two different instruments and analysis techniques were used, the results of the two directional sensing wave buoys generally agreed (Bachman and Foley, 1985). One comparison of the results is shown in Figure 2. The energy spectra are comparable, as are the mean directions. The erratic directions for the Wave Track buoy data below 0.1 hertz in this case, occur at low levels of energy and so the buoy may not have enough resolution to correctly determine wave directions. Most of the comparisons showed similar oscillation of the directions at low frequencies containing insignificant levels of energy. However, in a few cases at low frequencies containing reasonable amounts of energy, the directions shifted more than would be expected. At the high end of the frequency spectrum, the mean wave directions are steady at low energy levels. It is not certain whether the effect of the erratic wave directions containing some energy is due to the analysis technique or the response of the buoy. One possible cause of the varying directions at the lower end of the spectrum is the large frequency response corrections used for the low frequencies in this analysis.

The Wave Track buoy was next used in a field experiment, known as the Surface Expression of Bathymetry Experiment (SEABEX), (Lai and Bachman, 1983) along with a cloverleaf directional wave sensing buoy from the Institute of Oceanographic Sciences (IOS) in England. The Wave Track buoy was allowed to free drift with a current over the Phelp's Bank in the Nantucket Shoals, while the cloverleaf buoy was tethered to the ship. The ship maintained minimum headway such that it and the buoy slowly drifted with the current over Phelp's Bank.

DTNSRDC analyzed the data from the Wave Track buoy and IOS analyzed the data from the cloverleaf buoy. The results for one case can be seen in Figure 3. Prior to the transformation of the drifting Wave Track buoy data, the spectral density shapes of the Wave Track data and the cloverleaf data are similar, however, the peak densities occur at different frequencies and the magnitudes are different due to the existence of the current. The secondary peaks at the lower frequencies are also similar, but at slightly different frequencies and magnitudes. The mean wave directions of the two buoys are also comparable at their respective peaks.

Once the drifting buoy data has been transformed to a fixed coordinate system to account for the current effects, the spectra of the two buoys more closely agree in shape and frequency, with the peak frequencies in closer alignment. The transformed drifting buoy data now shows a narrower frequency band, with a greater peak value, than for the tethered buoy data at the peak frequency. The mean wave directions at the peak of the transformed data and the tethered buoy data are essentially identical. An overall better agreement in directions occur above 0.133 hertz after the transformation.

In the low frequency range, the transformation causes the secondary peak frequency of the drifting buoy data to shift into agreement with the tethered buoy. The transformed energy densities in this range decrease for a slightly better agreement with the tethered buoy, while the directions remain about the same or slightly decrease in agreement.

There are two ranges of frequency where the results of the mean wave directions oscillate. The first occurs at the low frequency end for both buoys. A drastic change in direction can be seen, but this occurs at such low energy levels as to be insignificant. The second noticeable effect in direction can be seen to occur between frequencies 0.11 and 0.12 hertz for the Wave Track buoy. This effect occurs at a frequency between two peaks of wave energy with a relative direction of 90 degrees between them. The transformation of the drifting buoy data does not effectively improve the wave directions, though they do shift. One possible cause for this region of oscillating directions is that the DTNSRDC analysis is unable to handle the data at this interface of two distinct directions. It is also possible that the subsurface stem of the Wave Track buoy is responding to an eddy or other subsurface effect at this location due to the rapidly changing topography near Phelp's Bank.

Having made comparisons of the wave spectra and mean directions between the Wave

Track buoy and two different directional wave sensing buoys, the authors found generally good agreement. Transforming wave data from a moving coordinate system to a fixed coordinate system was then found to be effective and important to account for the effects of current in interpreting the results of the SEBEX data. Subsequent deployments further demonstrated the value of measured directional wave data during ship trials. The next step was then to examine the transformation of wave data to a reference frame, or coordinate system, as encountered by a ship underway.

3. RESULTS OF WAVE TRANSFORMATION

Transforming directional wave data measured by a buoy drifting with a current, to that as encountered by a ship consists of two transformations, from moving to fixed coordinate and from fixed to moving coordinate. The transformation of wave energy is straightforward and computed to the second order approximation. The transformation of wave directional spreading requires the truncated Fourier coefficients to follow a different set of equations. Details of these derivations will be published elsewhere.

The combination of these methods will be used here to examine their validity with the results shown in Figures 4 and 5. The wave data used in the computation were obtained near the western edge of the Gulf Stream off the coast of Port Canaveral, Florida. The buoy was deployed in a free drift mode with the assumption that there was no appreciable current (Lai, Pachman, and Foley, 1984). The first step in validating the methodology is to introduce the buoy to an ocean current, such as the Gulf Stream, heading north (θ = 0 deg) with a speed of 4.0 ft/s. The waves encountering the buoy are heading southwest and are measured in the moving coordinate system by the buoy as shown by the solid line in Figure 4. The measured data are transformed to the fixed coordinate as represented by the dashed line in Figure 4. The whole spectrum shifts to the lower frequency range, implying that these waves measured in the moving coordinate system are actually shorter than those that would be measured in the fixed coordinate system. The changes in mean wave directions after the transformation are small but follow predictions of ray theory (Phillips, 1977). The Root Mean Square (RMS) spreading angles shown in Figure 4 are reduced following transformation to the fixed coordinate system.

The computed wave data in the fixed coordinate system are then transformed to the moving coordinate system, using the same current speed of 4.0 ft/s through an inverse of the Jacobian and a new set of equations for the truncated Fourier coefficients. The results, shown in Figure 4, indicate that this data is transformed back to its original form. The dotted line in Figure 4 coincides with the solid line except for some deviations at higher frequencies.

Similar computational results, but with the assumed current of 4.0 ft/s heading south (θ = 180 deg) are shown in Figure 5. In this case, the measured waves are propagating in the same direction as the drifting buoy. The measured wave data are first transformed to the fixed coordinate system and are represented by the dashed line in Figure 5. Here, the wave spectral density shifts to the higher frequency range implying that the waves measured from the drifting buoy are longer than the waves that would be measured from a moored buoy. The mean wave directions become larger, bend further to the west and agree with predictions by linear ray theory. The values of RMS spreading angles also become larger when transformed to the fixed coordinate.

The computed wave data are then transformed back to the original moving coordinate system as shown by the dotted line in Figure 5. The agreement between solid and dotted lines is again very good except for the data at frequencies greater than 0.22 Hz. In this range, the mean wave directions started to fluctuate and consequently change the wave spectral density values. Thus, with few exceptions at the high end of the frequency spectrum, the transformation methods have been proved valid.

The transformation methods developed for drifting buoy data can also be applied to the computation of ship motion. The computed results of these applications are shown in Figures 6 and 7. In Figure 6, the wave data represented by the solid line are measured by a moored Wave Track buoy in a fixed coordinate system. These data are transformed to the moving coordinate system according to the ship speed and heading. The waves encountered by a ship transiting at a speed of 4.0 ft/s and a heading of 0 deg are represented by the dotted lines. If the ship heading was 180 deg, the waves encountered by the ship are then represented by the dashed lines. The values of the spectral densities, mean directions, and RMS spreading angles thus change corresponding to the speed and heading of the ship.

If a wave buoy follows a current heading one direction, while a ship travels in the opposite direction, an extreme case of differences in encountered waves for spectral densities, mean directions, and RMS spreading develops. Two such cases can be seen in Figure 7. In the first case, the assumption is made that the buoy drifts with a current heading north (0 deg) at 4.0 ft/s and the ship travels south (180 deg) at 4.0 ft/s. The ship speed is the same as the current speed in order to best show the direction effect. The waves measured by the buoy are indicated by the solid line, while the computed waves encountered by the ship are represented by the dashed line. The peak of the spectral densities changed significantly, from 0.094 Hz measured by the buoy to 0.078 Hz as encountered by the ship. The change in the mean directions is small, but the RMS spreading, at

AD-A196 627 PROCEEDINGS OF THE AMERICAN TOWING TANK CONFERENCE (21ST) HELD IN WASHINGTON DC ON 5-7TH AUGUST 1986(U) NATIONAL RESEARCH COUNCIL WASHINGTON DC R F RESSALLE 5/6

UNCLASSIFIED AUG 87 F/G 13/10 NL

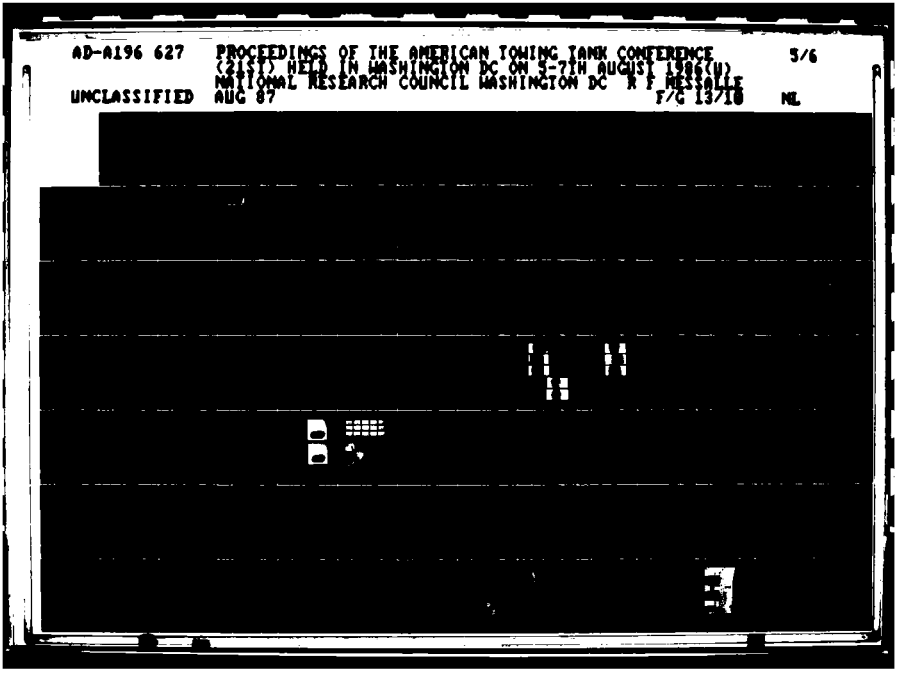

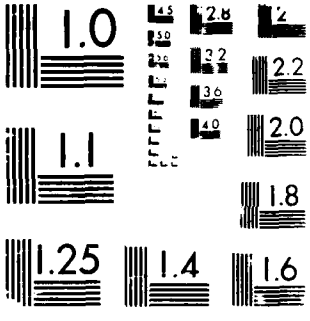

MICROCOPY RESOLUTION TEST CHAR

Track buoy and two different directional wave sensing buoys, the authors found generally good agreement. Transforming wave data from a moving coordinate system to a fixed coordinate system was then found to be effective and important to account for the effects of current in interpreting the results of the SEBEX data. Subsequent deployments further demonstrated the value of measured directional wave data during ship trials. The next step was then to examine the transformation of wave data to a reference frame, or coordinate system, as encountered by a ship underway.

3. RESULTS OF WAVE TRANSFORMATION

Transforming directional wave data measured by a buoy drifting with a current, to that as encountered by a ship consists of two transformations, from moving to fixed coordinate and from fixed to moving coordinate. The transformation of wave energy is straightforward and computed to the second order approximation. The transformation of wave directional spreading requires the truncated Fourier coefficients to follow a different set of equations. Details of these derivations will be published elsewhere.

The combination of these methods will be used here to examine their validity with the results shown in Figures 4 and 5. The wave data used in the computation were obtained near the western edge of the Gulf Stream off the coast of Port Canaveral, Florida. The buoy was deployed in a free drift mode with the assumption that there was no appreciable current (Lai, Bachman, and Foley, 1984). The first step in validating the methodology is to introduce the buoy to an ocean current, such as the Gulf Stream, heading north (θ = 0 deg) with a speed of 4.0 ft/s. The waves encountering the buoy are heading southwest and are measured in the moving coordinate system by the buoy as shown by the solid line in Figure 4. The measured data are transformed to the fixed coordinate as represented by the dashed line in Figure 4. The whole spectrum shifts to the lower frequency range, implying that these waves measured in the moving coordinate system are actually shorter than those that would be measured in the fixed coordinate system. The changes in mean wave directions after the transformation are small but follow predictions of ray theory (Phillips, 1977). The Root Mean Square (RMS) spreading angles shown in Figure 4 are reduced following transformation to the fixed coordinate system.

The computed wave data in the fixed coordinate system are then transformed to the moving coordinate system, using the same current speed of 4.0 ft/s through an inverse of the Jacobian and a new set of equations for the truncated Fourier coefficients. The results, shown in Figure 4, indicate that this data is transformed back to its original form. The dotted line in Figure 4 coincides with the solid line except for some deviations at higher frequencies.

Similar computational results, but with the assumed current of 4.0 ft/s heading south (θ = 180 deg) are shown in Figure 5. In this case, the measured waves are propagating in the same direction as the drifting buoy. The measured wave data are first transformed to the fixed coordinate system and are represented by the dashed line in Figure 5. Here, the wave spectral density shifts to the higher frequency range implying that the waves measured from the drifting buoy are longer than the waves that would be measured from a moored buoy. The mean wave directions become larger, bend further to the west and agree with predictions by linear ray theory. The values of RMS spreading angles also become larger when transformed to the fixed coordinate.

The computed wave data are then transformed back to the original moving coordinate system as shown by the dotted line in Figure 5. The agreement between solid and dotted lines is again very good except for the data at frequencies greater than 0.22 Hz. In this range, the mean wave directions started to fluctuate and consequently change the wave spectral density values. Thus, with few exceptions at the high end of the frequency spectrum, the transformation methods have been proved valid.

The transformation methods developed for drifting buoy data can also be applied to the computation of ship motion. The computed results of these applications are shown in Figures 6 and 7. In Figure 6, the wave data represented by the solid line are measured by a moored Wave Track buoy in a fixed coordinate system. These data are transformed to the moving coordinate system according to the ship speed and heading. The waves encountered by a ship transiting at a speed of 4.0 ft/s and a heading of 0 deg are represented by the dotted lines. If the ship heading was 180 deg, the waves encountered by the ship are then represented by the dashed lines. The values of the spectral densities, mean directions, and RMS spreading angles thus change corresponding to the speed and heading of the ship.

If a wave buoy follows a current heading one direction, while a ship travels in the opposite direction, an extreme case of differences in encountered waves for spectral densities, mean directions, and RMS spreading develops. Two such cases can be seen in Figure 7. In the first case, the assumption is made that the buoy drifts with a current heading north (0 deg) at 4.0 ft/s and the ship travels south (180 deg) at 4.0 ft/s. The ship speed is the same as the current speed in order to best show the direction effect. The waves measured by the buoy are indicated by the solid line, while the computed waves encountered by the ship are represented by the dashed line. The peak of the spectral densities changed significantly, from 0.094 Hz measured by the buoy to 0.078 Hz as encountered by the ship. The change in the mean directions is small, but the RMS spreading, at

Lai, R.J., R.J. Bachman and E.W. Foley (1984): Measurement of Directional Waves in Finite Water Depths. Conference Record Oceans 84.

LeBlanc, L.R. and F.H. Middleton: Pitch Roll Buoy Wave Directional Spectral Analysis, University of Rhode Island, unpublished manuscript.

Phillips, O.M. (1977): The Dynamics of the Upper Ocean, 2nd edition Cambridge Univ. Press.

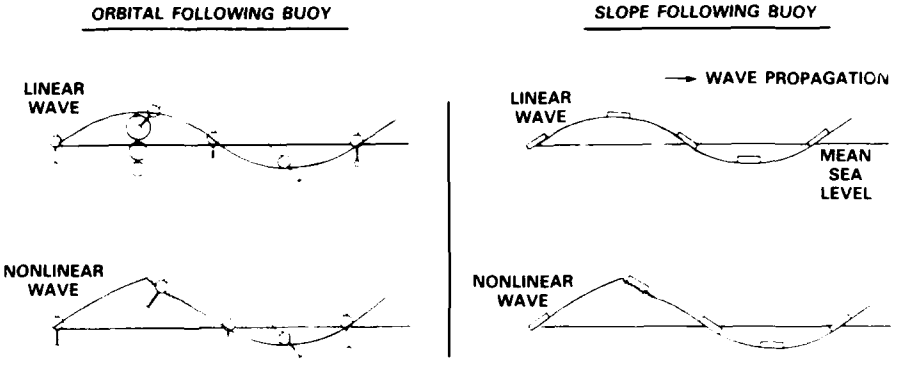

Figure 1 - Principle of the Orbital Following Wave Track Buoy (After LeBlanc and Middleton)

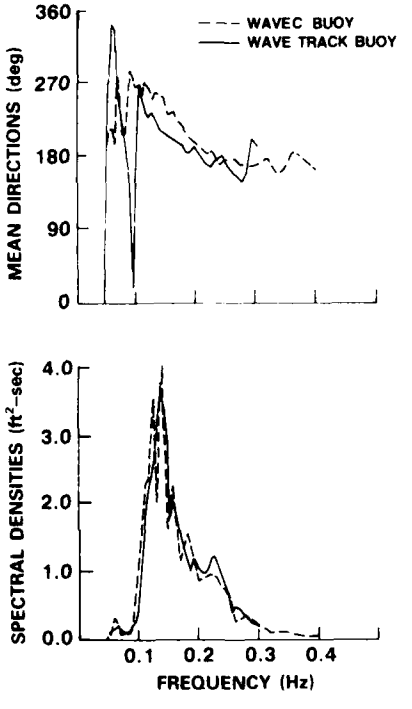

Figure 2 - Spectral Densities and Mean Directions from the WAVEC and Wave Track Buoys

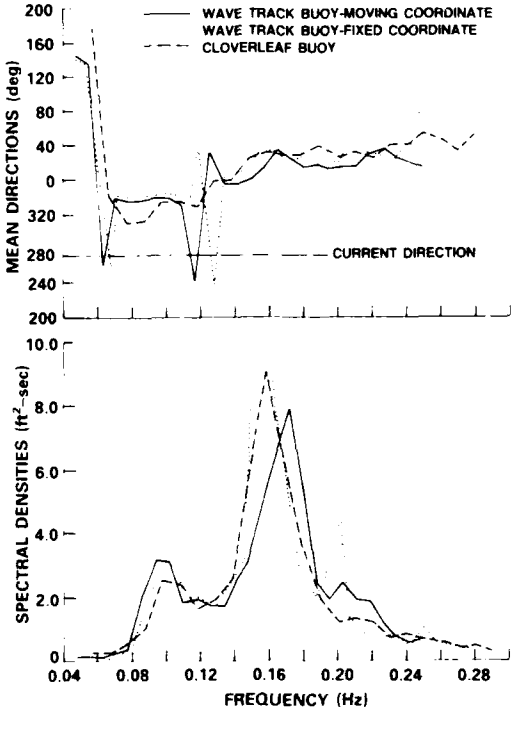

Figure 3 - Spectral Densities and Mean Directions from the Cloverleaf and Wave Track Buoys, including Current Effects on the Drifting Wave Track Buoy

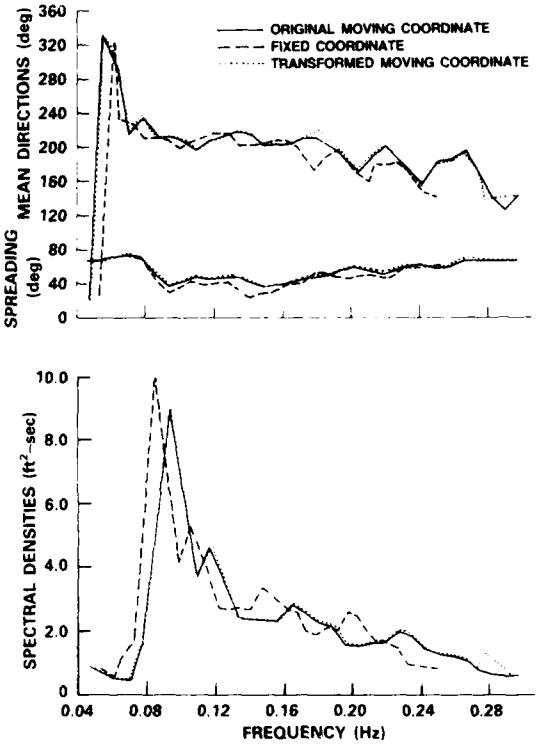

Figure 4 - Spectral Densities, Mean Directions and RMS Spreading of Drifting Buoy in the Moving Coordinate, of Results Transformed to the Fixed Coordinate and Back to the Moving Coordinate for a Current Velocity of 4.0 ft/s Heading 0 deg

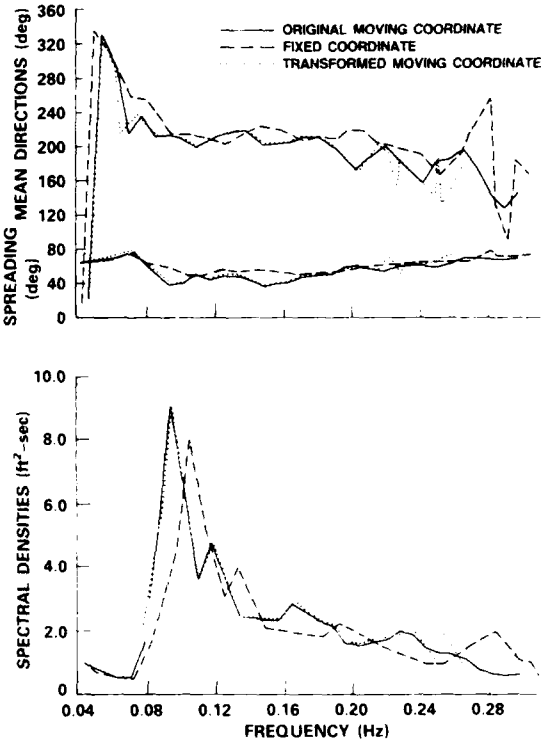

Figure 5 - Spectral Densities, Mean Directions and RMS Spreading of Drifting Buoy in the Moving Coordinate, of Results Transformed to the Fixed Coordinate and Back to the Moving Coordinate for a Current Velocity of 4.0 ft/s Heading 180 deg

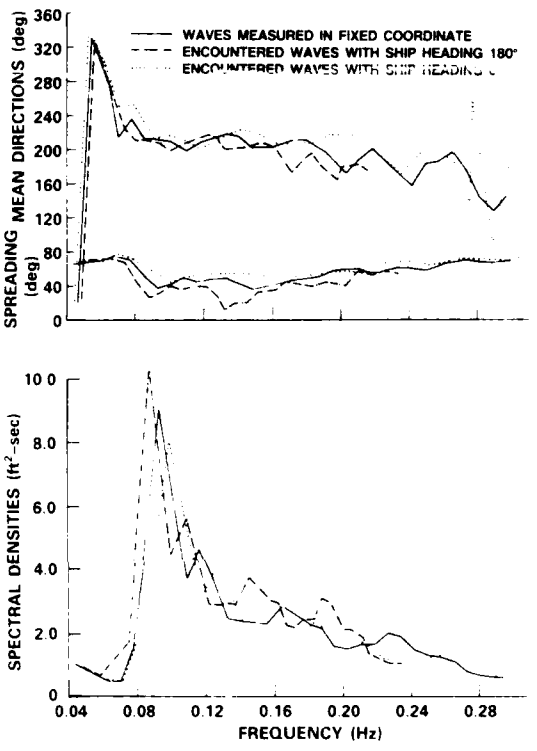

Figure 6 Spectral Densities, Mean Directions and RMS Spreading of Waves Measured in the Fixed Coordinate and Waves as Encountered by a Ship with Velocity of 4.0 ft/s Heading 0 deg and 180 deg

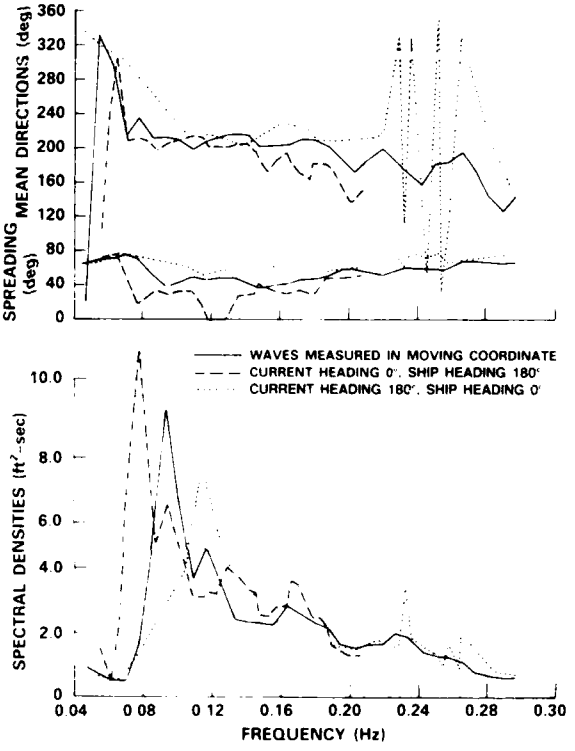

Figure 7 Spectral Densities, Mean Directions and RMS Spreading, as Encountered by a Ship Heading 180 deg at 4.0 ft/s, with Waves Measured in a Current Heading 0 deg at 4.0 ft/s, and as Encountered by a Ship Heading 0 deg at 4.0 ft/s, with Waves Measured in a Current Heading 180 deg at 4.0 ft/s

SESSION VIII
CAVITATION

TECHNICAL COMMITTEE MEMBERS

Mr. Michael Billet (Chairman)	ARL/Penn State Univ.
Dr. Allan J. Acosta	California Inst. of Tech.
Dr. Joseph Katz	Purdue Univ.
Dr. Young T. Shen	DTNSRDC
Dr. R.E.A. Arndt	St. Anthony Falls Hydraulic Lab. Univ. of Minnesota
Dr. Georges L. Chahine	Tracor Hydronautics
Dr. L.J. Leggat	Defense Research Establishment Atlantic
Dr. Blaine R. Parkin	ARL/Penn State Univ.
Dr. Vijay H. Arakeri	Indian Inst. of Science
Mr. Scott Gowing	DTNSRDC
Mr. D.J. Noble	DREA/CANADA
Mr. N.C. Sponagle	DREA/CANADA
Dr. H. Higuchi	St. Anthonly Falls Hydraulic Lab. Univ. of Minnesota
Mr. Timothy J. O'Hern	California Inst. of Tech.
Mr. H. Lin	Purdue Univ.

CAVITATION COMMITTEE REPORT

21st American Towing Tank Conference
Washington, D.C.

by

Michael L. Billet, Chairman

In many ways, the progress made in cavitation research can be found by reviewing the many journal articles and symposia on cavitation published since the 20th American Towing Tank Conference held at The Stevens Institute of Technology in 1783. Of particular importance are the many recent cavitation symposia and a partial list follows:

1. International Symposium on Cavitation Inception, New Orleans, Louisiana, December 9-14, 1984, ASME;
2. Cavitation in Hydraulic Structures and Turbomachinery, Albuquerque, New Mexico, June 24-26, 1985, ASME;
3. Cavitation and Multiphase Flow Forum - 1985 (20th Anniversary issue), Albuquerque, New Mexico, June 24-26, 1985 ASME;
4. The International Symposium on Propeller and Cavitation, Wuxi, China, April 8-12, 1986;
5. International Symposium on Cavitation, Sendai, Japan, April 16-19, 1986;

and

6. International Symposium on Cavitation and Multiphase Flow Noise, Anaheim, California, December 7-12, 1986, ASME.

Approximately 180 papers on cavitation are represented by the above symposia and less than one out of every five papers originates from the ATTC community. It is felt that this is representative of the low priority given to cavitation research by the sponsors of the ATTC community. A brief summary of the China and Japan symposia written by Blaine Parkin is included.

These symposia papers represent many areas of cavitation research both basic and applied. Since the ITTC standard cavitation tests conducted in 1966 and the subsequent work by Acosta and Arakeri on viscous effects, a great deal of research has been directed toward cavitation inception, modelling and scaling. As an example, instrumentation has been developed to measure the cavitation nuclei in the model and prototype environments. Much work is being done on quantifying the importance of these nuclei on inception. Statistical models of cavitation inception are being developed. Particularly important is the work on cavitation in shear flows including the tip vortex. Also, models of bubble dynamics are being coupled with fluid mechanics to correlate many observations. All of these areas are well represented by the specific contributions of the committee members to this report. These are:

1. "Cloud Cavitation Dynamics and Bubble Interaction", G. L. Chahine of Tracor Hydronautics Inc.
2. "DREA Propeller Cavitation Research", D. J. Noble, N. C. Sponagle and L. J. Leggat of Defense Research Establishment Atlantic/Canada
3. "Analysis of Recent Tip Vortex Cavitation Inception Data," V. H. Arakeri, H. Higuchi, and R. E. A. Arndt of St. Anthony Falls HydraulicsLaboratory, University of Minnesota
4. "Cavitation Susceptibility of Ocean, Lake and Laboratory Waters", Y. Shen and S. Gowing of David W. Taylor Naval Ship R&D Center
5. "Cavitation Phenomena in Jets", H. Lin and J. Katz of Purdue University
6. "Cavitation Observations in a Turbulent Shear Flow", T. O'Hern and A. J. Acosta of California Institute of Technology.

Although limited in number, these contributions represent well the state-of-the-art in areas of importance to the membership of the American Towing Tank Conference. Finally, a summary of the ITTC cavitation committee work is included.

CAVITATION SYMPOSIA ON CHINA AND JAPAN -- BRIEF IMPRESSIONS by Blaine R. Parkin

Wuxi, China

Three major classifications for papers at Wuxi were PROPELLERS [25 papers], CAVITATION [28 papers] and CAVITY FLOWS [4 papers]. Four of the papers in the first category concerned cavitation as such. These dealt with cavitation and excitation forces on tandem propellers in a non-uniform inflow; turbulence stimulation and cavitation scale effect reduction; hull pressure fluctuations due to a cavitating propeller; and on cavity characteristics and pressure fluctuations induced by a cavitating propeller.

The many worthwhile papers in the CAVITATION category can not all be reviewed here. We can at least classify the papers by topics treated, however. For example, three papers dealt with acoustics and cavitation -- either as cavitation due to acoustic radiation, acoustic detection or cavitation noise. The topic of inception included papers on nuclei; cavitation "indicators" or "susceptibility meters"; inception related to surface irregularities; inception and pressure fluctuations due to irregularities; inception in turbulent shear flows; and cavitation similitude. Papers on trailing vortex cavitation were well represented. Two papers presented data on cavitation in hydraulic machines and one paper dealt with a new facility for the study of cavitation mechanics. A number of papers on bubble dynamics were given and several of these concerned air-bubble oscillations rather than vaporous cavitation.

The four papers on cavity flow involved noise reduction on a cavitating swept foil, inverse cavity flow theory, cavity flows in a compressible fluid and a new theory for a partially cavitating foil under a free surface.

Sendai, Japan

This meeting was devoted to cavitation experiments and theory covering nearly every sub specialty in the field. Consequently, many of the topics treated by the authors in Wuxi also found their way into this meeting. The same can be said of quite a few authors. Therefore, it would be repetitious if we were to report a detailed list of topics as already given. This meeting was more narrowly focused on cavitation than the Wuxi symposium, however. It also was marked by a keynote address and special lectures which was one of its important distinguishing features. As one expects, the symposium topics consisted of bubble dynamics including collapse and the statistics surrounding dynamics, cavitation on bodies including fluids machinery; propellers and foils, and cavitation in trailing vortices was given its share of attenton. Nuclei and inception attracted a goodly amount of work and cavitation noise and erosion were also covered extensively. Those sessions dealing with bubble dynamics often treated air-bubble mechanics but collapsing vaporous bubbles were important considerations of the sessions. Considerable impressive experimental work on bubble collapse near a wall and the subsequent material response were reported.

Retrospective

From the foregoing, it is certainly apparent that those who attended both meetings were "well cavitated" when the final gavel was heard. In my view, both meetings were of a generally high standard, but not without some controversy. This latter feature is evidence of an active international community of investigators. As indicated above, there was a healthy mix of both traditional and more innovative approaches to cavitation research. As was expected, the papers on cavity flows were much fewer than those dealing with other aspects of cavitation research probably because we already have obtained solutions to most of the practical problems in this specialty and the application of results already available are no longer fashionable in most nations. Cavitation damage on marine propellers and in other hydraulic machinery is still an important topic if the attention of the research community given to this topic at the meetings is an indicator. The complexities of the many manifestations of the inception and early development of cavitation on hydraulic machines and on propellers bedevils us still.

In this last regard, it was refreshing to see some papers by young Chinese investigators on statistical aspects of inception. This is an idea that has been in the background for many years and its time is still to come in my view because we have not yet solved those aspects of inception processes which can be seen as deterministic or almost deterministic.

More needs to be done along these lines in order to establish the arena in which statistical methods will be most fruitful. I believe that the young investigators who are starting out on various statistical approaches should be encouraged in their research because their day is certainly coming. Their work needs to mature before it will be truly useful.

Another aspect of the symposium which I found stimulating was the ultra high speed photographic work being carried out at the Institute of High Speed Mechanics on cavitation bubble dynamics -- particularly bubble collapse and multiple-bubble dynamics. This group is also studying interactions between transparent solid walls and bubble collapse. These are the first photographs of this phenomenon which I view as showing both P- and S-wave fronts in the solid. The flavor of their work is strongly reminiscent of pioneering efforts by Al Ellis at the Caltech Hydro Lab about 30 years ago. In those days, Ellis had to design and build everything he needed for his research, which was no mean achievement at that time. Today, due to the advances in this technology, one can purchase well engineered ultra high-speed photographic systems which out perform the homemade equipment of Ellis and results not attained by him can now be obtained.

Now we turn to some facts instead of opinion: How to obtain copies of the Proceedings of the Symposia. Eventually there will be two volumes from each of these meetings.

Proceedings of the International Symposium on Propeller and Cavitation, Wuxi, China, April 1986, is distributed by:

China International Book Trading Corporation
Post Office Box 399
Beijing, China
[Price approximately $28.00 plus postage]

Proceedings of the International Symposiun on Cavitation, Sendai, Japan,
April 1986, is distributed by:

Institute of High Speed Mechanics
Tohoku University
Sendai, Japan
[Price approximately $86.00 plus postage]

ITTC CAVITATION COMMITTEE by Blaine R. Parkin

As many ATTC members know, the ITTC is more strongly focused on towing tank questions relating to "standard" test procedures and expected outcomes in different facilities than is the ATTC. The ITTC emphasis is not that of a research organization. Consequently, the work of its several technical committees is concerned with a review of recent world literature in their specialties in order that they may put a conference report together which emphasizes those aspects of ship-research progress of most use to towing tank superintendents for the acquisition, reduction and communicton of test results to ship owners and firms in the related fields of naval architecture and off-shore engineering.

ITTC member organizations are encouraged to contribute new findings of their own as they apply to the goals of the ITTC. The ATTC provides a forum for all the Americas to contribute to this process of the ITTC. Thus, the ATTC brings together new research findings of interest to its membership with the idea that some of the ATTC papers also might be of interest to the ITTC Technical Committees and can be brought to the attention of "tankery" people around the world.

Of course, the strong research atmosphere of the ATTC suggests that many papers are given at the ATTC because of their intrinsic value to our field. Therefore, we tend to think of the interests of the ITTC as being somewhat peripheral. But even so it may interest our members as to just what the ITTC Cavitation Committee has been trying to do since its most recent directions were established by the ITTC Executive Committee in Goteborg in 1984. The topics being addressed by the Committee involve the influence of cavitation on the design and construction of ships. And since many of the important aspects of this phenomenon are related to marine propellers and high-speed craft, the ITTC Cavitation Committee must coordinate its work closely with those two technical committees to ensure that there is not duplication of effort and that there is no conflict between the findings and recommendations of all three committees. It is too soon to report the outcome of the present Cavitation Committee's deliberations in behalf of the ITTC. These will be published at the time of the 18th ITTC in Japan

next year. We can indicate the kinds of things that are being considered, however. These are

- Cavitation Scale Effects
- Practical Aspects of Cavitation Testing
- Cavitation and Leading Edge Roughness
- Cavitation Noise
- Cavitation and Hull Pressure Fluctuations
- Cavitation Erosion
- Sydney Express Cavitation -- Testing of Model Propellers
- Cavitation on Propellers for High-Speed Craft
- Tunnel Wall Effects for Partially Cavitating Hydrofoils

Naturally, any light that can be shed on any of these topics by contributors to the present ATTC report will be greeted with enthusiasm by the 18th ITTC CAVITATION COMMITTEE.

CLOUD CAVITATION AND BUBBLE INTERACTION

Georges L. Chahine
Tracor Hydronautics, Inc.
7210 Pindell School Road
Laurel, MD 20707

INTRODUCTION

A propeller when operating in the wake of a ship will, at least intermittently, cavitate, inducing erosion of the blades, loss of efficiency, noise, and occasionally structural failure of nearby plating. These harmful effects are mainly due to the collapse of cavities. These include individual bubbles as well as sheet cavities and bubble clouds. Cloud bubbles are especially known to be associated with erosion. These clouds are either detached from the frothy mixture at the trailing end of an unsteady sheet cavity, or generated in a finite region of the liquid downstream of the unsteady sheet where significant fluctuating pressures exist. The study of cloud cavitation has recently received accrued attention (Mørch, 1982; Chahine, 1981-1986; D'Agostino and Brennen, 1983). In this paper we summarize the singular perturbation theory we have developed to study the collective behavior of a multibubble system, and the interaction between bubbles. A general theory including mass and heat transfer is first presented, then particular examples are shown. Codes for a system of N equi-sized symmetrically distributed bubbles as well as a code for any given distribution of bubbles were developed and extensively used.

GENERAL FORMULATION OF THE PROBLEM

As a first step to study the general problem of a bubble cloud in a flow field and near solid boundaries, we consider a cloud of bubbles in an unbounded medium of uniform pressure, P_∞, concentration of dissolved gas, C_∞, and temperature, T_∞. This corresponds to the case where the size of the cloud is small compared to the flow field characteristic length scale. P_∞, C_∞, and T_∞ are then the local values of the pressure, the concentration, and the temperature in the flow field in the absence of the cloud. We further assume the liquid to be inviscid and incompressible and the flow irrotational. The bubble cloud behavior is sought when the ambient pressure, $P_\infty(t)$, is time dependent.

In order to determine the flow field in the bubble liquid medium and to obtain the motion and deformation of any bubble in the cloud, one must solve the Laplace equation for the velocity potential, Φ

$$\Delta\Phi = 0 \ , \tag{1}$$

subjected to kinematic and dynamic conditions on the bubbles' surfaces. The equation of a bubble surface in a coordinate system moving with velocity $\dot{b}^i$ in the direction e_z, is $r = R^i(\theta,\phi,t)$. $\mathscr{C}^i$ and n^i are respectively the local curvature of the surface of bubble B^i and its unit normal vector at the point $M(r,\theta,\phi)$. γ and T_R are respectively the surface tension of the liquid and its temperature at the bubble wall. P_g and P_v are the partial pressures of the noncondensible gas and the vapor inside the bubble. The boundary conditions at the bubble walls can then be written in the moving coordinates system:

$$\nabla\Phi \cdot \underline{n}^i = \left[\dot{R}^i \underline{e}_r + \dot{b}^i \underline{e}_z\right] \underline{n}^i \ , \tag{2}$$

$$\rho\left[\dot{\Phi} - \dot{b}^i \underline{e}_z \cdot \nabla\Phi + \frac{1}{2}\left|\nabla\Phi\right|^2\right] = P_\infty(t) - P_v^i(T_R) - P_g^i(t) + 2\,\gamma_i(T_R)\,\mathscr{C}_i(\theta,\phi,t) \ , \tag{3}$$

Due to the relatively very short time of vaporization compared to bubble dynamics and gas diffusion characteristic times, the vapor is considered to instantaneously flow in and out of the bubble, and P_v is taken equal to the value of the equilibrium vapor pressure of the liquid at the bubble wall temperature. The concentration of dissolved gas, C, at the bubble surface is related by Henry's law to the partial pressure of the gas within the bubble and to Henry's constant, H,

$$P_g = H\,C(R^i) \ , \tag{4}$$

The value of P_g constitutes the coupling between the dynamic and gas diffusion problems. Similarly the values of the equilibrium vapor pressure P_v and of the surface tension γ constitute the coupling between the dynamic and the heat problems.

To determine the temperature at the bubble wall, $T_R(\theta,\phi,t)$, one needs to solve the energy equation in the liquid,

$$\dot{T} + \underline{\nabla}\phi \cdot \underline{\nabla}T = D \cdot \Delta T, \qquad (5)$$

where D is the thermal diffusivity of the liquid. Equation (5) is subjected to a boundary condition on the bubble wall stating that the heat locally lost at any point of the interface is used to vaporize an amount of liquid determined by the local bubble volume expansion rate. If ρ_v is the vapor density, L the latent heat of the liquid, and K its thermal conductivity, the heat balance can be written locally at the bubble surface:

$$\left.\frac{\partial T}{\partial n^i}\right|_{r=R^i(\theta,\phi,t)} = \frac{\rho_v L}{K} \dot{R}^i \qquad (6)$$

The concentration of gas in the liquid, $C(r,\theta,\phi,t)$, is determined by the equation

$$\dot{C} + \underline{\nabla}\phi \cdot \underline{\nabla}C = D_g \cdot \Delta C \quad , \qquad (7)$$

where D_g is the molar diffusivity of the gas in the liquid. This equation is subjected at the bubble wall to the condition that the concentration at the interface is given by Henry's law, (4). The molar rate of transport of gas across the interface, $\dot{n}_g$, is related to the gradient of gas concentration in the liquid at the bubble wall by

$$\dot{n}_g = D_g \iint \frac{\partial C}{\partial n^i} \, dS^i \qquad (8)$$

Time integration of (8) determines at every instant the total number of moles of gas, n_g, in the bubble.

The gas and vapor within the bubble are taken to comprise an ideal gas mixture obeying the equation of state

$$(P_g + P_v) V_b = (n_g + n_v) R_u T_g \quad , \qquad (9)$$

where V_b is the volume of bubble, n_g and n_v are the number of moles of gas and vapor within the bubble, R_u is the Universal gas constant, and T_g is the absolute temperature of the gas and vapor mixture within the bubble.

The only remaining variable needed to apply this perfect gas law is the temperature inside the bubble. The application of the first law energy balance for the bubble interior relates this temperature to the boundary work due to volume change, the enthalpy transfer due to transport of gas and vapor across the bubble wall, and the change in internal energy of the bubble content. This can be written:

$$d U = - d W + \sum_i \dot{n}_i h_i \, dt \quad , \qquad (10)$$

where for the control volume over a period of time dt, dU is the change in internal energy, dW is the work done, $\dot{n}_i$ is the net molar rate of mass transfer of component i, and h_i is the specific enthalpy of component i. In (10), we have neglected changes in kinetic and potential energies of the bubble and any heat exchange between gas and liquid. n_v and n_g will change as the bubble volume changes and vapor will condense or liquid vaporize at the bubble wall and gas will diffuse in and out of it. This results in a form of heat or energy exchange between the bubble and the liquid that is accounted for by the enthalpy change.

With these assumptions we can write

$$dU = c_v^v \, d(n_v T_g) + c_v^g \, d(n_g T_g) \quad , \qquad (11)$$

$$\sum_i \dot{n}_i h_i = (\dot{n}_v c_p^v + \dot{n}_g c_p^g) T_l \quad . \qquad (12)$$

where c_v and c_p are respectivly the specific heats of the vapor (superscript v) and the gas (superscript g) at constant volume and constant pressure. The work term in (10) can be expressed as the boundary work in moving the bubble surface

$$dW = (P_v + P_g) \, dV_b \quad . \qquad (13)$$

Equations (1) to (13) form, with the bubble energy equation and the initial and at infinity conditions a complete set of equations which must be solved to determine the flow, concentration, and temperature fields.

CLOUD DYNAMICS SINGULAR-PERTURBATION THEORY

The following approach is applicable to a cloud of bubbles of low void fraction. Provided that the characteristic size of a bubble in the cloud, r_{b_o}, is small compared to the characteristic distance between bubbles, ℓ_o, we can assume, in the absence of an initial relative velocity between the bubble and the surrounding fluid, that each of the individual bubbles reacts, in first approximation, to the local pressure variations spherically as if isolated. To the following orders of approximation, interactions between bubbles induce bubble motion and deformation that are taken into account.

Since the problem possesses two different length scales, ℓ_o and r_{b_o}, we can consider two subproblems. The "outer problem" is that considered when the reference length is set to be ℓ_o. This problem addresses the macrobehavior of the cloud, and the bubbles appear in it only as singularities. The "inner problem' is that considered when the lengths are normalized by r_{b_o} and its solution applies to the vicinity of the considered individual bubble of center B^i. The presence of the other bubbles, all located

at infinity in the "inner problem", is sensed only by means of the matching condition with the "outer problem". That is to say, physically the boundary conditions at infinity for the "inner problem" are obtained, at each order of approximation, by the asymptotic behavior of the outer solution in the vicinity of B^i.

The determination of the flow field and the dynamics of any of the individual bubbles, B^i, is accessible once the boundary conditions at infinity in the corresponding "inner region" are known. Here we impose the restrictive assumption that the void fraction is low enough so that the information about the variation of the ambient pressure around the cloud, $P_\infty(t)$, is transmitted to the microscale in a time scale much shorter than the bubble collapse time. Therefore, in the absence of a slip velocity between the considered bubble and the surrounding fluid and when interactions are neglected, the only boundary condition at infinity is the imposed pressure variation $P_\infty(t)$. When a finite value of the sound speed in the cloud medium must be accounted for, $P_\infty(t)$ can be approximated by $P_\infty(t')$ where $t' = t - x/c$ and x represents the minimum thickness of the cloud shell at the bubble location. To address the problem more rigourously one must solve the two-phase medium flow equation. The "inner problem" is therefore spherically symmetric and its solution is given by the well known Rayleigh-Plesset equation. With the assumption that the liquid is inviscid and incompressible, this equation can be written as follows neglecting the superscripts i:

$$a_o \ddot{a}_o + \frac{3}{2}\dot{a}_o^2 = -\bar{P}_\infty(t) + \pi(t) - \mathscr{P} - P_g(t) - W_e^{-1}\gamma/a_o . \quad (14)$$

In this equation, $a_o(t)$ is the radius of bubble B^i normalized by r_{b_o}. The times are normalized by the Rayleigh time, T_o, based on r_{b_o} and a characteristic value of the pressure varation, ΔP. All pressures are normalized by ΔP.

$$\begin{aligned} \mathscr{P} &= (P_o - P_v(o))/\Delta P , \\ \bar{P}_\infty(t) &= (P_\infty(t) - P_o)/(\Delta P) , \\ \pi(t) &= (P_v(t) - P_v(o)/\Delta P . \end{aligned} \quad (15)$$

The Weber number is related to the surface tension, γ, ΔP, and r_{b_o} by:

$$W_e = r_{b_o} \cdot \Delta P / 2\gamma . \quad (16)$$

For a given $P_\infty(t)$, Equation (14) can be solved for the variation of the bubble radius, $a_o(t)$. This allows the subsequent determination of the pressure field around the bubble of center B^i.

When interactions cannot be neglected, but an "inner region" enclosing the bubble B^i can still be defined, the boundary conditions at infinity can be much more complex. First, the macroscale pressure in the cloud at B^i can be very different from the imposed far field pressure. Second, a relative velocity between the bubble and the surrounding fluid can exist causing the bubble to be nonspherical. The matching condition between the velocity potential in the inner problem, ϕ^i, and the velocity potential in the outer problem, ϕ, expresses the at-infinity conditions for ϕ^i. This condition once expanded in powers of $\varepsilon = r_{b_o}/\ell_o$ states in physical terms that the first order correction, to the nonperturbed spherical behavior of the bubble, $a_o(t)$, is due to a modification of the collapse driving pressure. This introduces a spherical correction $a_1(t)$. At the following order, (ε^2), a second correction of the uniform pressure appears, as well as a uniform velocity field accounting for a slip velocity between the bubble and the surrounding fluid. This induces a spherical correction, $a_2(t)$, and a nonspherical correction $f_2(t)\cos\theta^{ig}$, where θ^{ig} is a direction between the bubble B^i and the cloud "center". Things become more complex at the order of expansion ε^3, where in addition to the uniform pressure and velocity corrections, $a_3(t)$ and $f_3(t)\cos\theta^{ig}$, a velocity gradient is to be accounted for to generate a nonspherical correction, $g_3(t)\ (3\cos^2\theta^{ig}-1)/2$.

As a result, the equation of the surface of the bubble B^i can be written in the form:

$$R(\theta^{ij},t) = a_o^i(t) + \varepsilon a_1^i(t) + \varepsilon^2\left[a_2^i(t) + f_2^i(t)\cdot\cos\theta^{ij}\right] + \varepsilon^3\left[a_3^i(t) + f_3^i(t)\cos\theta^{ij} + g_3^i(t)\,\mathscr{P}_2(\cos\theta^{ij})\right] + \ldots , \quad (17)$$

The successive corrections are obtained by solving similar differential equations as for a_o (Equation 14) (see Chahine, 1982).

A general, detailed solution of heat and gas diffusion equations would likely involve a time consuming numerical approach, such as a space and time dependent finite difference scheme, and is not necessary for many cases of interest. Plesset and Zwick (1952) obtained a solution to (5) or (7) for the case of an isolated spherical bubble for which appreciable concentration gradients are confined to a boundary layer of thickness δ which is small compared to the bubble radius:

$$T = T_\infty - \left[\frac{D}{\pi}\right]^{1/2} \int_o^t \frac{L\rho_v\, a_o^2\, \dot{a}_o}{K\left[\int_x^t a_o^4(y)dy\right]^{1/2}}\, dx. \quad (18)$$

$$C = C_\infty - \left[\frac{1}{\pi D_g}\right]^{1/2} \int_o^t \frac{\dot{n}_g/4\pi}{\left[\int_x^t a_o^4(y)dy\right]^{1/2}}\, dx. \quad (19)$$

These expressions were applied to the spherical part of the bubble radius, $R(\theta,t)$.

NUMERICAL STUDY AND RESULTS

It is helpful, in order to understand the various numerical results, to consider the pressure field generated by the collapse of an individual bubble. Let us consider the pressure history at a point M at a distance ℓ_0 from an isolated bubble when the ambient pressure is submitted to a sudden pressure jump. As we can see from Figure 1, the resulting perturbation pressure, i.e., the difference between the pressure at ℓ_0 and the far field pressure, is negative for $t<0.75$ for the considered case. Later, for $t>0.75$, the pressure at ℓ_0 increases rapidly to 2.3 times the imposed pressure at the end of the bubble collapse. This observation is a key to the understanding of multibubble behavior in a sudden pressure increase. Indeed, if a fictitious bubble which does not influence the process is centered in M, it will first sense a less important and more gradual increase in the surrounding pressure at the beginning of the collapse. In the case considered instead of a nondimensional surge of the pressure from 0 to 1, P jumps only to 0.84 then rises slowly, not attaining 1 until t=0.75. This induces a relative decrease in the intensity of the first phase of the bubble collapse and affects the bubble radius variation with time exactly as seen later in Figure 3. Later, the sharp rise in the pressure field makes the subsequent end of the collapse much more violent.

Figure 2 considers two different bubbles. This figure is intended to explain both cumulative effects due to a multibubble system and modification due to different bubble size, bubble interdistance, and delay times (compressibility) effects. Had the two bubbles been of the same size and at equal distance from M, the two corresponding pressure time profiles would have superimposed. In this case, both effects described above (initial relative pressure reduction and subsequent dramatic pressure increase) will be doubled (without any additional consideration of the interaction such as modification of the pressure histories). The interaction between bubbles A and B would amplify the phenomena described above. Now, if bubbles A and B are either at a different distance from M or are not of equal size, the pressure profiles will not overlap. If they are of equal size but at different distances from M, the pressure peaks would occur simultaneously unless compressibility effects are included. A delay time corresponding to the difference in the travel paths will then occur between the two peaks. From the above discussion it is evident that the behavior of a fictitious bubble located at M will strongly depend on both the sizes of the other interacting bubbles and their space distribution. Compressibility would have the same effect as a nonsymmetric bubble distribution in addition to its influence on the collapse intensity and amplitude of the generated pressures. It would therefore tend to reduce the collective effect expected from the incompressible symmetrical case.

Various spherically symmetrical cloud configurations were investigated numerically. Figure 3 shows the results of five different computations for a sudden jump in the imposed ambient pressure. The cases of two, three, and twelve bubbles are presented together with that of an isolated bubble. In each case the variation with time of the distance, B^1E^1, between the extreme point on a bubble E^1, and its initial center, B^1, is chosen to represent the bubble dynamics. Taking the bubble collapse in an unbounded fluid as reference, it is easy to see from Figure 3 how increasing the number of bubbles changes the dynamics of the one studied. During the early slow phase of the implosion process, the collapse is significantly delayed. At any given nondimensionsal time the distance B^1E^1 (and simultaneously the bubble characteristic size) is greater when the number, N, of interacting bubbles increases. Then, in the final phase of the implosion the tendency is reversed: the phenomenon speeds up and the final velocities of the motion are higher when N increases. This is explained by accounting for the modification of the driving pressure of the collapse of any bubble due to the dynamics of the other bubbles as described above.

Figure 4 is a collection of results obtained in absence of gas and heat diffusion from several cases studied. The maximum nondimensional pressures generated during the cloud collapse are represented versus the number of bubbles in the cloud. The cumulative effect is obvious since the values obtained vary over a range of several orders of magnitude. These theoretical numbers give an indication of how tremendous pressures can be generated with an increasing number of interacting bubbles. In this figure, the maximum pressures are presented at the cloud center, C, at B^1 when it is removed and at a distance r_{b_0} from the center of one of the bubbles in the cloud. These results show the important role played by the gas content of the bubbles. Increasing P_{g_0} has dramatically reduced the generated pressures. This is mainly due to the cushioning effect of the gas which significantly reduces the velocities attained at the end of the implosion.

Another very interesting observation from Figure 5 is that a pressure drop of finite duration followed by a recompression (case B) gives lower values for maximum pressures generated at the end of the collapse than the pressure jump case A. This effect is not due to the apparent higher gas content in this case. The value of P_{g_0} to consider for comparison purposes should be for all cases that at the start of the collapse which is smaller in case B. The pressure attenuation observed can be explained as follows. In the

classical pressure jump case the initial cumulative effect is to cause the bubble size to be larger at the start of the collapse pressure surge. Conversely, the initial cumulative effect for a pressure drop of finite duration followed by a pressure recovery (case B) is to reduce the size of the bubble when the collapse pressure surge occurs. As a result the potential energy for collapse in case B is relatively smaller.

The above results show that even for very low void fractions, collective bubble collapse can generate pressures orders of magnitude higher than those produced by single bubble collapse. This would tend to explain the observed high erosion intensities and the bending of trailing edges. The cumulative effect comes from the fact that the interaction increases the driving pressure of collapse of each individual bubble. This augments the violence of its implosion and thus the interaction with the other bubbles. Thus, each bubble ends its collapse not under the effect of a pressure of the same order as the ambient, but orders of magnitude higher.

The method described above was used to study the dynamic behavior of a multibubble system in a cavitation susceptibility meter and to compare the behavior of an isolated spherical bubble with that of a bubble in a cloud. Both sets of cases were considered for the NSRDC venturi (see Chahine and Shen, 1986). The bubble wall motion during its traverse through the venturi is illustrated in Figure 5. A typical bubble radius history can be described as follows. Near the throat entrance the bubble radius oscillates for a certain number of cycles which decreases with bubble size and increasing flow velocity. Then, if this velocity is large enough a continual growth is observed until the bubble reaches the venturi expansion area. This is followed by a more or less violent bubble implosion which may be detected acoustically. Figure 5 shows the influence of the initial size of a bubble on its dynamics and the modification of the behavior by interbubble and mean flow interactions. All cases are considered for the same ambient pressure and throat velocity. The larger bubbles achieve their maximum size further downstream inside the venturi diffusion section. When interactions are considered the bubble of initial radius R_0 = 5 μm has its behavior moderately modified. However, for the 20 μm bubble the modification of the behavior is dramatic. Large oscillations are induced through interactions and an early collapse occurs inside the venturi throat. Such a bubble cloud would not be detected optically and probably not acoustically if the intensity of the collapse is not strong enough.

For the present user of the Venturi Cavitation Susceptibility Meter, the curves relating the initial radius of a detectable bubble to the critical velocity at the throat are the most useful. Any bubble of initial radius larger than that given by these static predictions would grow explosively at the corresponding velocity. The problem is more complex when dynamics and interactions are taken into account. This fact can be illustrated, as in Figure 6, by comparing R_0 versus V_t obtained by both static and dynamic considerations. Here one can observe significant differences at the larger bubble radii and also at the higher velocities. These theoretical differences are relatively small when expressed in terms of V_t but reflect very large differences in the critical pressures. The most interesting results seems to be the presence of a minimum in the dynamic curve. This implies that at a given velocity above a minimal value (25.1 m/s in the case of Figure 6) only a finite range of bubble radii are excited. Compare this prediction with the conclusion from statics that all bubbles above a critical radius become active. This may explain the experimentally observed lower number of detected bubbles in the venturi CSM as opposed to the scattering method.

Figures 7 to 9 illustrate the influence of gas diffusion on multibubble dynamics. bubble growth has been considered following a sudden ambient pressure drop. Figure 7 shows a collection of cases of bubble radii, versus times. The isolated bubble cases are presented for reference. When mass transfer is neglected at the bubble/liquid interface a polytropic compression law is adopted. For an isolated bubble comparisons are made between the two extreme cases of no-gas diffusion: isothermal behavior and adiabatic behavior, and the case where the mass transfer and the energy balance equations are solved. The adiabatic assumption in the absence of gas diffusion gives closer results to the solution of the diffusion problem. Based on the perfect gas law, this result is to be expected when during the bubble growth the increase in the number of moles of gas entering the bubble overcomes the decrease in gas temperature in the product $n_g T_g$. As seen in the example in Figure 8 the temperature drops in the initial phase of the growth but recovers rapidly to maintain its value later in the bubble growth history. In a multibubble system interactions become very significant when the bubble sizes approach the interbubble distance. This is reflected by an oscillation in the bubble radius similar to that obtained in the heat transfer problem. Initially during the bubble growth the modification of the imposed pressure field by the presence of the other bubbles in the cloud reduces the bubble size achieved. At any instant the bubble radius is smaller than that of an isolated bubble. Two such radii are shown in Figure 7. R_2 is the measurement of the bubble radius along the cloud center direction, while R_3 is measured in the opposite direction. Figure 7 shows the variation of these two dimensions as functions of time for a set of values of the spacing parameter ε. It is

obvious from this figure that bubble interaction and deformation increase when the spacing between bubbles is reduced. The presence of multiple bubbles introduces a flattening of the bubble on its side closer to the cloud center. This side has a slower growth than the other side. The computed shrinking and oscillation of the bubble shape in the latter stage of the growth needs to be investigated to assure it does not result from a failure of the asymptotic approach.

Figure 8 shows for various conditions the time variations of the effective gas polytropic coefficients when gas diffusion is taken into account. The two effective coefficients used in these figures are defined as follows. The total effective polytropic coefficient, K is computed at each time step using

$$K = (\text{Log } P_g/P_{g_o})/(\text{Log } V/V_o) \quad . \qquad (20)$$

The local effective polytropic coefficient, K_ℓ, is based on a compression law which applies locally between two computation steps, and it is therefore computed using the relation

$$K_\ell = (\text{Log } P_{g_i}/P_{g_{i+1}})/(\text{Log } V_i/V_{i+1}) \quad . \qquad (21)$$

Figure 9 shows that the total effective polytropic coefficient drops rapidly, at the beginning of the growth from the value 1.4 to a minimum value which depends on the initial gas concentration, C_o. As seen in the figures this value can become significantly smaller than one. Since at these later times the gas temperature becomes practically constant, the lower is the minimum value of K the stronger is the relationship between the number of moles of gas diffusing into the bubble and the bubble volume change. The local effective coefficient of compression, K_ℓ decreases much more significantly than K. From the initial value of 1.4, K_ℓ decreases practically to 0 later during the growth expressing the fact that P_g and T_g become practically constant during the growth.

The variation of both K and K_ℓ are much more sensitive to the initial conditions, (such as initial gas concentration, C_o, and initial bubble size, R_o), than the actual bubble radius history. This is probably due to the fact that K and K_ℓ express only the gas thermodynamic behavior while the bubble radius behavior includes gas and vapor thermodynamic and dynamic phenoma (pressure drop). Figure 8 presents the temperature histories for two initial bubble radii. This figure is typical of all temperature versus time curves. Initially, the temperature drops significantly and attains a minimum. Later, the temperature inside the bubble recovers to reach the initial temperature and remains practically constant. The minimum temperature achieved and the time to achieve this minimum are functions of the initial conditions. This result is related to the variations of K and K_ℓ.

The above results should be extended to actual pressure fields where the pressure variations are more realistic than a sudden pressure drop and, more importantly, to longer computation times where gas diffusion effects become more significant. For such more practical situations the influence of the magnitude of the pressure drop, $P_o - P_{inf}$, should be investigated carefully.

ACKNOWLEDGEMENTS

The study described in this report was supported by the Naval Sea Systems Command, General Hydrodynamics Research Program administered by the David Taylor Naval Ship Research and Development Center under Contract No. N00014-83-C-0244. I would like to extend my sincere appreciation to the many colleagues at Tracor Hydronautics for their encouragement and direct support, particularly to Dr. K. M. Kalumuck for his direct contribution to the gas diffusion study.

REFERENCES

Chahine, G. L. (1981), "Asymptotic Theory of Collective Bubble Growth and Collapse," Proc. 5th International Symp. on Water Column Separation, IAHR, Obernach, Germany.

Chahine, G. L. (1982), "Cloud Cavitation - Theory," Proceedings, 14th Symposium on Naval Hydrodynamics, Ann Arbor.

Chahine, G. L. and Liu, H. L. (1985), "A Singular Perturbation Theory of the Growth of a Bubble Cluster in a Super-heated Liquid," Journal of Fluid Mechanics, 156, pp. 257-274.

Chahine, G. L., Kalumuck, K. M., and Perdue, T. O., (1986), "Cloud Cavitation and Collective Bubble Dynamics," Tracor Hydronautics Technical Report 83017-1.

Chahine, G. L. and Shen, Y. (1985), "Bubble Dynamics and Cavitation Inception in Cavitation Susceptibility Meters," ASME, Intn'l Symp. Fundamental Aspects of Gas Fluid Flows, Miami Beach, Florida, Nov. 17-22, pp. 137-146.

D'Agostino, L. and Acosta, A. J., (1983) "On the Design of Cavitation Susceptibility Meters," 20th American Towing Tank Conference.

Mørch, K. A. (1982), "Energy Considerations on the Collapse of Cavity Clusters," Appl. Sci. Res. 38, 313.

Plesset, M. S. and Zwick, S. A., (1952), "A Nonsteady Heat Diffusion Problem with Spherical Symmetry," Journal of Applied Physics, Vol. 23, No. 1, pp. 95-98.

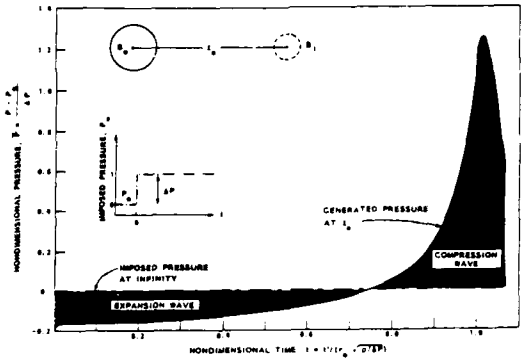

FIGURE 1 - PRESSURE VARIATION VERSUS TIME AT A DISTANCE L_o FROM AN ISOLATED SPHERICAL BUBBLE $P_{g_o} = 0.1$, $W_o = 100$, $\epsilon = r_o/L_o = 0.33$

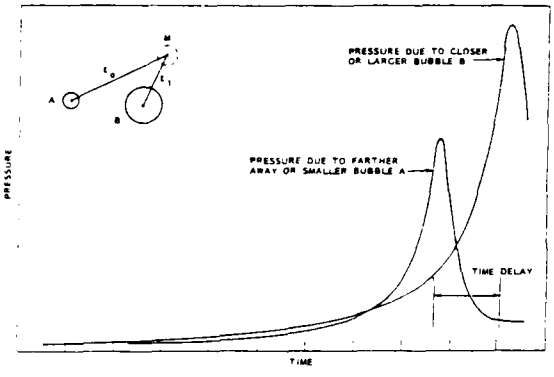

FIGURE 2 - PRESSURES GENERATED AT A POINT M BY TWO COLLAPSING BUBBLES, BUBBLE A SMALLER OR FARTHER AWAY, BUBBLE B LARGER OR CLOSER

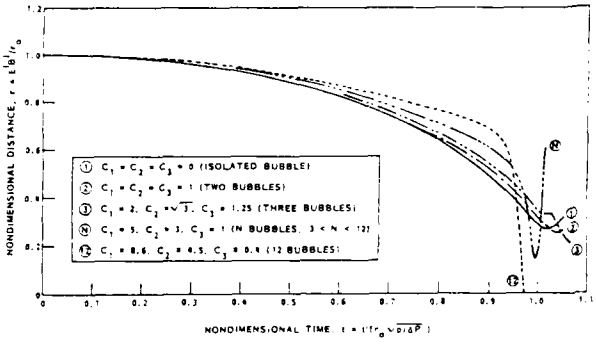

FIGURE 3 - MOTION OF THE BUBBLE WALL TOWARD THE CLOUD $\epsilon = 0.05$, $P_{g_o} = 0.1$, $K = 1.4$, POSITIVE PRESSURE STEP

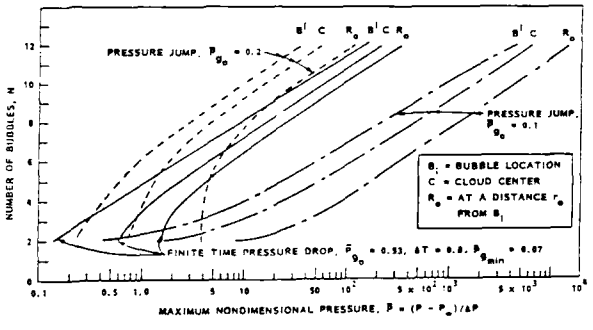

FIGURE 4 - VARIATION WITH THE NUMBER OF BUBBLES OF THE MAXIMUM PRESSURES GENERATED, $W_o = 100$, $\epsilon = 0.1$

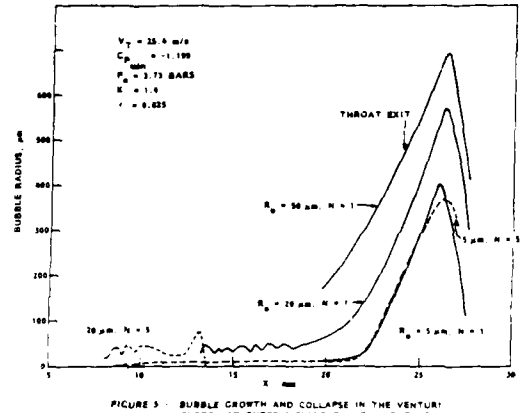

FIGURE 5 - BUBBLE GROWTH AND COLLAPSE IN THE VENTURI SYSTEM AT THREE DIFFERENT INITIAL BUBBLE SIZES

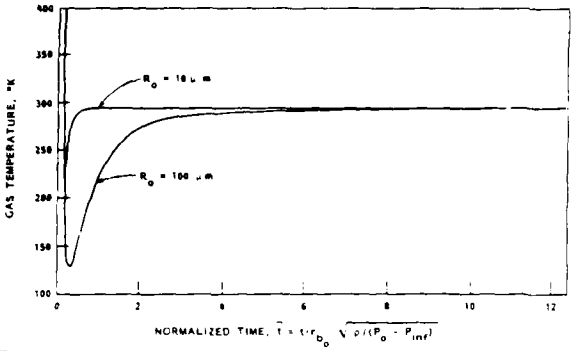

FIGURE 8 - NONCONDENSIBLE GAS TEMPERATURE VERSUS TIME. INFLUENCE OF INITIAL GAS SIZE. (P_o = 5 atm, P_{inf} = 0.01 atm, R_{b_o} = 10 R_o, C_o = 0.1)

VENTURI BUBBLE DYNAMICS

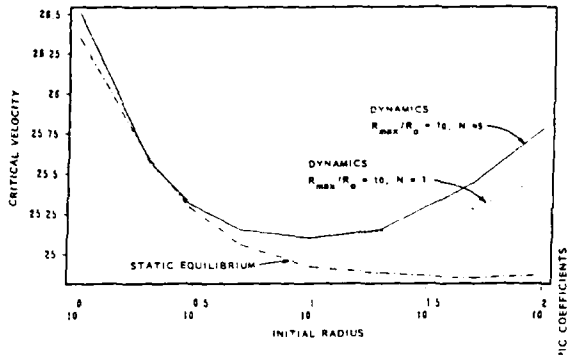

FIGURE 6 - COMPARISON BETWEEN DYNAMICS AND STATIC CRITICAL VELOCITY AT VENTURI THROAT AS A FUNCTION OF INITIAL BUBBLE RADIUS

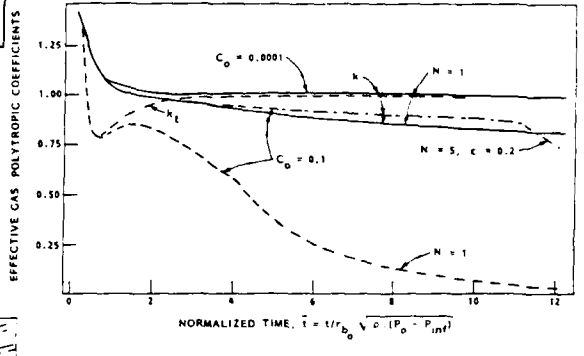

FIGURE 9 - VARIATION OF EFFECTIVE GAS POLYTROPIC COEFFICIENT DURING BUBBLE GROWTH FOLLOWING A SUDDEN DEPRESSURIZATION (P_o = 5 atm, P_{inf} = 0.01 atm, R_{b_o} = 1 mm, R_o = 0.1 mm)

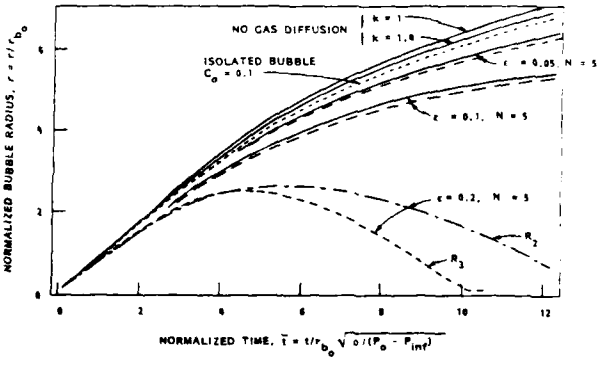

FIGURE 7 - BUBBLE GROWTH FOLLOWING A SUDDEN DEPRESSURIZATION (P_o = 5 atm, P_{inf} = 0.01 atm, R_{b_o} = 1 mm, R_o = 0.1 mm). INFLUENCE OF BUBBLE SPACING PARAMETER ε, $\varepsilon = r_{b_o}/L_o$.

DREA PROPELLER CAVITATION RESEARCH

D.J. Noble, N.C. Sponagle and L.J. Leggat

Defence Research Establishment Atlantic
P.O. Box 1012
Dartmouth, Nova Scotia, Canada

ABSTRACT

Two aspects of cavitation research at the Defence Research Establishment Atlantic are reported. The first applies to numerical prediction of sheet cavitation extents on propellers using a modified version of PUF-2. The singularity methods used to predict the extents of sheet cavitation are described, and evaluated through comparisons with model test data. Techniques for expanding the methods to enable prediction of acoustic pressures are described.

The second area of research is in the investigation of cavitation noise produced by tip vortex and bubble cavitation. Cavitation is developed on two-bladed propellers which are operated in a bollard-pull condition in a near anechoic environment. Results of experiments with fully developed and incipient cavitation are described.

1. INTRODUCTION

The first part of this paper is concerned with the development of numerical prediction capabilities at the Defence Research Establishment Atlantic (DREA) for periodic sheet cavitation on marine propellers and the resulting blade rate harmonics of far-field noise. Although model testing of propellers in depressurized tanks and tunnels can provide reliable data for propeller performance and cavitation development, the measurement of low frequency noise is hampered by the highly reverberant nature of model test facilities. A reliable theory for low frequency noise prediction is an important asset for preliminary acoustic evaluation of novel design concepts for propellers.

Since the rapid growth and collapse of cavitation is a predominant propeller noise generating mechanism, prediction of cavitation volume variations is an essential first step of the numerical method. The sheet cavitation prediction program recently developed at DREA is based on procedures formulated by Lee (1980) and Van Houten (1982) and included in the review of cavitation research at the Massachusetts Institute of Technology (MIT) by Van Houten, Kerwin and Uhlman (1983). Lee's method is an extension of the lifting-surface analysis code PUF-2 developed by Kerwin and Lee (1978) for predicting unsteady forces and moments on propellers operating in a ship's wake. In the DREA code, Lee's chordwise distribution of singularity segments and control points is replaced by a slightly modified distribution suggested by Van Houten in an effort to improve the prediction of cavity development close to the leading edges of the blades. Additionally, the model for radial contraction and roll up of the downstream wake sheets used in PUF-2, but removed in Lee's cavitation prediction method, is retained to improve predictions of cavity development at more heavily loaded or off design operating conditions.

After integrating cavity extent and thickness distributions over the blade, the resulting periodic cavity volume variations are used to define an effective acoustic source strength for determining far-field noise levels at harmonics of the blade rate frequency. The expressions developed for far-field noise include the effect of a finite sound speed that appears as a retarded time difference in the acoustic relations. This finite time delay for acoustic signals to travel between the source and observer is usually neglected when evaluating propeller induced hull pressures in the relative near-field, but is an important consideration for radiated noise. A Lloyd's mirror effect due to the free surface is important in surface ship applications and is also included in the noise prediction method. This part of the paper describes theoretical procedures and presents comparisons between theory and experiment for propeller back sheet cavitation extents and blade rate noise levels.

A second component of cavitation research at DREA is directed at providing a better understanding of the basic nature of the noise generation mechanisms of propeller cavitation. An improved understanding is sought of the micro-scale behavior of cavitation, which controls the emission of broadband noise at medium to high frequencies as opposed to the macro-scale behavior, that is thought to control the emission of low frequency narrow band noise. In the long term, it is hoped that this research will lead

to the development of reliable methods to predict cavitation noise based on appropriate input from propeller analysis and ship wake calculations. Improved understanding of cavitation noise mechanisms will allow the development of better noise scaling procedures and experimental techniques. However, for the foreseeable future, scale model tests also will be required either to predict cavitation noise for full-scale ships, or to confirm the results of other prediction techniques.

The second part of this paper deals with this aspect of cavitation research at DREA. An experimental facility is described where various types of measurements can be made of cavitation noise produced by specialized propellers. Measurements have been made of the level, spectral content, and directivity of the far-field noise. Also, a technique is described for measurement of the location, strength, and spectral content of the acoustic sources in the flow near cavitating propellers, which is used to reveal details about the noise source mechanisms of cavitation that could not be studied using far-field measurements alone. Finally, the results of measurements with three propellers which produce vortex and bubble cavitation are presented. Due to the limited space, this discussion will emphasize the philosophy and special advantages of the facility. Further details about the facility and results for these propellers are provided by Leggat (1982) and Sponagle and Leggat (1984, 1985).

PART 1

NUMERICAL PREDICTION OF PROPELLER SHEET CAVITATION AND NOISE

2. BACK SHEET CAVITATION PREDICTION

2.1 Basic Assumptions

In the lifting-surface procedures developed at MIT, propeller blades are assumed to be thin, rigid, equally-spaced identical surfaces of otherwise arbitrary shape. All sections of the blade operate at small angle of attack. The inflow to the propeller consists of three spatially varying components of the ship's wake which are assumed to have negligible time dependence and variation in the propeller axial coordinate relative to a ship fixed reference frame.

Since reliability of the cavitation prediction method depends on the accuracy of this ship wake, much effort has been directed towards developing scaling methods and effective wake corrections for the measured nominal wake data obtained in model test facilities. Reynolds number scaling procedures attempt to correct for hull boundary layer differences between model and full scale ships. Huang and Groves (1980) have developed propeller-wake interaction corrections for the inviscid, rotational flow effects that the propeller has on the incoming wake vorticity distribution. These types of corrections would be most significant for single propeller vessels where the major portion of each blade encounters a large wake deficit region near the centre plane of the ship. For twin propeller configurations where only the outer extremities of this deficit region are cut by the blade tips, the effects of these corrections should be quite small.

In Lee's cavitation prediction method, the sheet cavity is assumed to be a thin, continuous layer forming on the back surfaces of the blades, starting from the blade leading edges and remaining attached to the blades. Diffusion of gas or vapour into or out of the cavity, blade surface tension and roughness are not treated, and the cavity is assumed to remain at a constant pressure; the vapour pressure of water.

2.2 Governing Equations

The velocities induced by a cavitating propeller are solutions of the equation of mass conservation for an incompressible, potential flow. In the lifting-surface problem, the potential flow and sheet cavity development are required to satisfy three major boundary conditions:

1) Flow Tangency: The normal component of the total velocity vanishes on the blade mean surfaces.
2) Cavity Dynamic Condition: A linear version of the unsteady Bernoulli equation in blade fixed coordinates is used to instantaneously enforce a constant vapour pressure condition at the cavity/water interface.
3) Cavity Closure: Cavity thickness vanishes at its outer extremities.

In addition, flow disturbances must vanish far upstream of the propeller, a Kutta condition of tangential flow at the blade trailing edges is enforced and Kelvin's theorems on circulation and vorticity conservation are applied using the procedures that Kerwin and Lee developed for PUF-2. Vortex distributions are used on the blade mean surfaces and downstream wake sheets to represent a jump discontinuity in tangential velocity and to generate circulatory flow and lift on blade sections. Source distributions are also used on these surfaces to represent jump discontinuities in normal velocity and to provide blade and cavity thickness contributions to the induced flow.

2.3 Singularity Discretization and Control Points

The grids of vortex line segments used on the blade mean surface and near wake sheet, as well as the vortex arrangement used for a rolled-up ultimate wake are illustrated in Figures 1a and 1b. The blade grid is essentially the one defined by Lee except for a slight modification in the chordwise distribution of segment end points. The DREA program uses a chordwise spacing suggested by Van Houten for prediction of hydrofoil

cavitation which is shifted one quarter of the chordwise intervals between bound vortex segments towards the leading edge compared with Lee's grid.

The downstream wake grid is identical to the model used by Kerwin and Lee in the original PUF-2 code. Reasonable estimates of the roll-up radius and wake pitch angle required to define grid geometry can be obtained by applying actuator disk theory and momentum conservation to the mean flow in a contracting stream tube. This process ensures variation of near wake geometry with thrust loading coefficient, and can improve numerical predictions at more heavily loaded operating conditions.

Figure 2 depicts the relative placement of source and vortex segments, as well as the position of boundary condition control points, in a typical chordwise strip between two fixed radius arcs on the blade mean surface and extending into the near wake. As in PUF-2, blade thickness source segments are made coincident with bound vortex segments, and are assigned known constant strengths obtained from thin wing theory. The dashed lines oriented in a spanwise sense represent cavity thickness source segments. These are positioned between successive bound vortex segments using Van Houten's chord spacing with leading edge concentration. If the sheet cavity should extend beyond the trailing edge, additional cavity source segments are placed midway between successive shed vortex segments in the near wake.

The circular symbols in Figure 2 at the midpoints of cavity source segments on the blade are control points at which the flow tangency condition is enforced. The 'X' symbols at bound and shed vortex midpoints are control points for enforcing a constant vapour pressure requirement using the cavity dynamic condition over the instantaneous extent.

2.4 Solution Procedures

The details of the equations established to solve for the instantaneous bound vortex and cavity source segment strengths in a single strip, as well as the time-stepping, iterative solution procedures, are fully described by Lee, and so are not repeated here. However, the system of linear equations solved by the DREA code is a slightly modified version of Lee's system.

With Lee's singularity grid, it is necessary to interchange the chordwise locations of the first cavity source segment and pressure control point in each strip in order to simulate the proper source strength behaviour at the leading edge. However, by placing the first bound vortex segment right at the leading edge, Van Houten finds that the cavity source and vortex chordwise strength distributions near the leading edge obey a common quarter-root singularity behaviour. Van Houten's relation between the leading edge segment strengths is used in the DREA program to eliminate the first cavity source strength and pressure control point from the solution process. The number of unknowns and equations solved in each strip is thus reduced by one.

2.5 Cavity Extent Correlation with Experiment

Back sheet cavitation chordwise extent predictions were compared to experimentally observed extents for two propeller models tested at the Netherlands Ship Model Basin (NSMB). Geometry descriptions of the model propellers NSMB 5349 and 5268 are included in a related paper by Kennedy, Noble and Casgrain (1986).

Figure 3 compares calculated and model test data for back sheet cavitation extents on the five-bladed propeller model 5349. The figure shows the projected view of a blade looking downstream into the rotation plane for various angular positions between - 180° and 180° with 0° corresponding to the top vertical position. The blade turns outward through the 0° position, and just before reaching it, passes through a large axial velocity deficit region produced by the shaft bossing and hull boundary layer. The numerical predictions were obtained using axial, radial and tangential components of the measured nominal wake. As the figure shows, numerical extents correlate well with model test data for this unskewed, high aspect ratio blade.

An example having cavitation extending into the downstream wake is shown for a more typical low aspect ratio blade in Figure 4. Here, numerical and model test extents on five-bladed propeller model 5268 are compared. Although not correlating quite as well as the narrow blade results, the predictions provide a reasonable estimate of model cavitation extent time history including the cavity extent beyond the trailing edge at the 60° position. These twin propellers rotate inward over the top and develop maximum back sheet cavitation extents as the blades move down through the wake deficit. Again the three orthogonal components of the measured nominal wake are used for the predictions.

3. NOISE PREDICTION

3.1 Fundamental Relations

The equation for sound pressure radiated from a region of acoustic source strength density, f, can be found in standard texts on theoretical acoustics such as Morse and Ingard (1968). Assuming a constant sound speed, c, the sound pressure as a function of time at a fixed field location can be formally expressed in terms of the following integrals over source volume and time.

$$p(t) = \frac{1}{4\pi} \int_{V_o} \int_{t_o} \frac{f}{R} \delta(t_o - t + \frac{R}{c}) \, dV_o \, dt_o \qquad (1)$$

Here R is the distance from an element of the source volume to the field location and δ is a Dirac delta function, which through the time

integral, evaluates the source time variable t_o at the retarded time t - R/c. A more convenient formulation when source coordinates are in motion relative to the observer is obtained by Fourier time transforming equation (1) to the frequency domain.

$$P(\omega) = \frac{1}{8\pi^2}\int_{V_o}\int_{t_o}\frac{f}{R}\exp(-ikR)\exp(-i\omega t_o)\,dV_o\,dt_o$$
$$k = \frac{\omega}{c} \qquad (2)$$

3.2 Rotating Point Sources for Cavity Volume

At large distances from the propeller, a source distribution over the blades can be replaced by a single point source on each blade rotating at shaft rate Ω at an effective radius in the plane of rotation as depicted in Figure 5. As described by Ross (1976), a small coherently pulsating volume has a time derivative of volume flux equal to the fluid density times the second time derivative of volume. Locating point sources on each of B blades at source position vectors $\vec{r}_o = \vec{r}_n$, n = 1, 2, ..., B, the source strength density, f, for cavity volume fluctuations becomes:

$$f = \sum_{n=1}^{B}\rho\ddot{V}_n\,\delta(\vec{r}_o - \vec{r}_n) \qquad (3)$$

Here ρ is water density and $\ddot{V}_n$ is the second time derivative of cavity volume on blade n. In terms of cylindrical coordinates $\vec{r}_o = (x_o, r_o, \theta_o)$ at the propeller centre, the components of $\vec{r}_n$ are $x_o = 0$, $r_o = a$ and $\theta_o = 2\pi(n-1)/B - \Omega t_c$.

Assuming identical cavity volume time histories on each blade that are periodic at the shaft rate, the volume V_n has the following time delayed Fourier series representation.

$$V_n = \sum_{q=-\infty}^{\infty} C_q \exp\left(iq\Omega\left[t_o - \frac{2\pi(n-1)}{B\Omega}\right]\right) \qquad (4)$$
$$C_q = |C_q|\exp(i\alpha_q)$$

3.3 Far-Field Relations

Substituting equation (3) into (2), the source volume integration simply evaluates source coordinates at components of $\vec{r}_n$. The rather complicated source time integral remaining can be simplified by making the following far-field approximation for the source to observer distance.

$$R \simeq \bar{r} + \frac{a^2}{2\bar{r}} - \frac{ar}{\bar{r}}\cos\psi, \text{ in phase}$$
$$R \simeq \bar{r}, \text{ in amplitude} \qquad (5)$$
$$\psi = \theta + \Omega t_o - \frac{2\pi(n-1)}{B}, \quad \bar{r} = \sqrt{x^2 + r^2}$$

Here $\bar{r}$ is the spherical radial coordinate of the field point from the propeller centre and x, r and θ are observer cylindrical coordinates.

After introducing the approximations of equation (5) into equation (2), the time transform of acoustic pressure contains a time dependent phase factor that has a Bessel function series expansion.

$$\exp(is\cos\psi) = \sum_{p=-\infty}^{\infty} J_p(s)\exp\left(ip\left(\psi + \frac{\pi}{2}\right)\right) \qquad (6)$$
$$s = \frac{kar}{\bar{r}}$$

On substituting equation (6) and the Fourier series, equation (4), for cavity volume into equation (2), the sum over the blades leads to a cancellation of shaft rate harmonics that are not multiples of the blade rate frequency BΩ. The source time integration can now be performed and the Fourier time transform inverted to give a series representation of the far-field sound pressure in terms of blade rate harmonics.

3.4 Free Surface Effect

The theory presented so far assumes that acoustic pressures are radiated in an unbounded medium. To account for the effects of a free water surface, the method of negative images can be used to model a Lloyd's mirror phenomenon. Assuming that characteristic wavelengths of the surface waves are large compared to acoustic wavelengths of interest, image sources for cavitation are positioned symmetrically above the waterline as shown in Figure 6. The net acoustic pressure will then vanish at the waterline and be significantly reduced at certain observer locations below the free surface.

3.5 Noise Correlation with Experiment

To indicate how back sheet cavitation noise predictions correlate with overall measured levels at blade rate harmonics, the difference in far-field sound pressure levels obtained for theory relative to experiment on full scale sea trials of one propeller is summarized in Table 1.

Blade Rate Harmonic	ΔSPL [dB]
1	7.3
2	5.9
3	-9.2
4	-2.6
5	-5.7

Table 1: Noise Level Differences for CFAV QUEST - Theory Relative to Experiment

For the Canadian Forces Auxiliary Vessel (CFAV) QUEST with propellers corresponding to NSMB model 5349, the theory predicts levels that range from 2 to 9 dB on either side of the measured levels at the 11.2 knot operating speed. At this speed both back sheet and tip vortex cavitation are present to contribute to the measured levels. In addition, levels were obtained with a bottom mounted hydrophone. The larger differences at lower harmonics may in part be due to effects of the sea bottom as well as the proximity of the propeller to the hull surface.

PART II

EXPERIMENTAL STUDIES OF CAVITATION NOISE

4 BACKGROUND

Typically, the power spectral density of cavitation dominated ship noise contains a series of low frequency, narrow bandwidth lines that are superimposed on broad-band noise spread over a large frequency range. The low frequency lines are associated with periodic macroscopic variations in the total volume of cavitation which are induced by periodic variations in the propeller operating conditions. In the far-field, this component of the noise is not greatly affected by the microscopic details of the cavity dynamics. The broadband component of cavitation noise is very different in nature. In this case, although the periodic variations in the propeller operating conditions play a part, they are not the dominant consideration. Instead, the microscopic detail of the collapse of the cavitation bubbles dominates.

Accurate estimates of this broadband component of noise from ship propeller cavitation, as measured in the far-field, requires estimates of all of the following parameters:

1. acoustic source strength:
   a. quantity and types of cavitation caused by the propeller.
   b. details of the sound emission mechanisms of each type of cavitation.
2. propagation of the sound from the source to the receiver:
   a. increased dissipation and changes in spectral shape due to shock formation.
   b. effect of multiple sound transmission paths including reflections from solid boundaries.
   c. acoustic transmission properties of the water.

This forms a convenient way to break up the cavitation noise problem for study since each of these topics can be studied independently. It is typical of acoustic problems to study the acoustic sources separately from the propagated noise field. The implicit assumption made is that the energy removed by the radiated noise is a small part of the total energy of the source, and this is usually true for cavitation (except during the final stages of collapse of a cavitation bubble containing very little uncondensible gas). Also, it is assumed that the types and amounts of cavitation present on the propeller can be calculated from purely hydrodynamic considerations. However, each form of cavitation is assumed to produce noise by a separate mechanism. It is the detail of these noise mechanisms that is under study here.

5. EXPERIMENTAL SETUP

Typically, propeller cavitation noise is measured either by full-scale ship trials on a sound range or by scale model tests in a cavitation tunnel or towing tank. Full-scale trials are very costly and are difficult to control since a host of extraneous factors must be considered such as the wind, sea state, tidal current, ship operating conditions, depth of water, experience of crew, etc. On the other hand scale model tests are convenient to perform, but meaningful acoustic data are often difficult to obtain since the measurement chambers may be highly reverberant, may have resonant modes of excitation, and may have high ambient noise levels due to associated machinery or flow noise. This necessitates the use of complex calibration procedures that depend on frequency and the locations of the source and receiver. Also, unless the facility is very large, it will be impossible to make measurements in the acoustic far-field except at high frequencies.

DREA has put into operation a somewhat different cavitation noise research facility which allows the investigation of the mechanisms and sources of cavitation noise in a nearly anechoic environment. This facility is located at the DREA Acoustics Barge described by McMahon (1961). This is a floating laboratory that is located in a large salt water estuary. The water beneath the barge is approximately 50 m deep and the bottom is covered with several meters of soft mud with good acoustic absorption properties. This provides a non-reverberant, quiet environment for acoustic measurements.

A complete description of the cavitation noise facility was given by Leggat (1982), and a drawing of the setup is shown in Figure 7. The apparatus is suspended, in open water, below the barge. The propellers are powered by a stationary, variable speed electric drive system that is attached to the barge. Up to 30 kW of power can be delivered at shaft speeds up to 2500 rpm. Visual cavitation observations and photography are carried out from the surface through a periscope, with lighting provided by a system of strobe lights which are synchronized to the rotation of the propeller. Measurements of the torque delivered by the propeller also can be obtained.

Far-field measurements have been performed to examine the level, spectral content, and directivity of cavitation noise using omnidirectional hydrophones spaced at least 25 m from the cavitating noise source.

Several methods are available to perform the free field corrections. If the source is compact and the locations of the source and receiver are well defined, then a computer model of sound propagation at the facility can be used. Also, echo removal techniques based on auto-correlation and cepstrum analysis have been used to analyse wide-band signals. Since the environment is nearly non-reverberant and the source and receiver can be well separated, the geometry of the facility imposes virtually no limits on the frequency range of the measurements. Also measurements of the spacial distribution of acoustic sources in the flow around the cavitating propellers is made using the technique described in the next section.

The following characteristics of the facility allow accurate acoustic measurements to be made over a wide frequency range.

1. The environment is almost non-reverberant; therefore, spectral measurements can be corrected to free field conditions over a wide frequency range and analysis of the pressure time history data is possible.
2. The measurements can be carried out at sufficient distance from the source to ensure far-field conditions even at low frequencies and for large distributed sources.
3. Acoustic directivity measurements can easily be carried out.
4. There is low ambient noise.

It should be noted that the cavitation noise experiments that are performed at this facility are designed to provide a better understanding of the basic nature of the noise generation mechanisms of propeller cavitation. However, realistic simulation of full-scale conditions cannot be carried out with this facility due to two limiting constraints.

1. The propeller drive system is fastened directly to the barge which is securely moored. Therefore, the test propellers must operate at zero advance coefficient.
2. Environmental conditions such as pressure, nuclei content, and temperature cannot be controlled, but should remain steady due to the unlimited quantity of water and stable temperature.

6. MEASUREMENT OF ACOUSTIC SOURCE DISTRIBUTIONS

In this section the basis for the experimental method used to obtain information about the spacial distribution of acoustic sources in the flow about a cavitating propeller is described. This method provides a way to estimate the mean squared pressure level and power spectral density of the components of the far-field sound that originates at various locations. Also, it is shown that the effect of multiple sound transmission paths may be eliminated so that true free field estimates can be made.

It can be shown, either from approximate simplifications of Curle's solution to the Lighthill equation or from consideration of the Helmholtz-Kirchoff integral solution to the wave equation, that the mean squared far-field pressure level, $\langle P^2 \rangle$ (relative to a range of 1 m), can be written as a surface integral over any arbitrary surface, S, that completely surrounds the source:

$$\langle P^2 \rangle = \int_S \frac{d\langle P^2 \rangle}{dS}\, dS \qquad (7)$$

For a distribution of uncorrelated monopole sources the integrand is

$$\frac{d\langle P^2 \rangle}{dS} = -\frac{x}{4\pi}\,[\nabla P_n\, P]_{x/c} \qquad (8)$$

Here, ∇P_n is the component of the pressure gradient normal to the surface S, P is the far-field pressure, x is the distance from the surface point to the far-field point, and the square brackets indicate the unnormalized cross-correlation function evaluated at the transit time of sound from the near-field point to the far-field point. This integrand is interpreted as a surface acoustic source distribution which is measured directly over the surface S. Information about the actual volume acoustic source distribution is then inferred from the structure of the measured surface distribution.

The flow into the propeller is axisymmetric; therefore, the surface S was chosen to be a cylinder with a radius 25 mm greater than the propeller radius and which was long enough to include all of the cavitation. Because of the axial symmetry, $d\langle P^2 \rangle/ds$ can be determined over the whole cylinder by scanning the pressure gradient hydrophone once axially along the surface. In the text that follows, this is referred to as a wake scan, and the abscissa of the source distribution plots refers to this axial position. Positive numbers indicate positions downstream of the propeller and negative numbers refer to positions upstream.

A distinct advantage of this cross-correlation technique is that it can be used to take advantage of the non-reverberant environment at the DREA Acoustics Barge to produce results that do not require further free field correction. Noise from cavitation is typically quite broadband, and so the cross-correlation function due to noise that travels to the far-field point via the direct path will peak at the appropriate time delay and die rapidly to zero away from the peak. Noise that travels via other discrete paths will produce similar peaks centered at later time delays. At the Acoustics Barge, with appropriate choice of the far-field measurement point, the difference in time delay between the direct path and all reflections may be made large enough so the the cross-correlation peaks do not overlap; thus the effect of multiple transmission paths is automatically removed.

7. PROPELLERS

In the remainder of this paper the results obtained for three different propellers will be summarized. These were two bladed, 250 mm diameter propellers that were designed to produce specific forms of cavitation in the experimental conditions. Each of these propellers had a NACA 16 thickness distribution and a NACA 65 mean camber line. However, the radial distributions of pitch, chord length, maximum thickness, and maximum camber were different. The circulation distribution of these propellers is shown in Figure 8.

The first propeller, called Tip Vortex Propeller No. 1, had a circulation distribution that peaked relatively near the blade tip (at approximately 0.75 radius fraction), and therefore produced a strong tip vortex. The only form of cavitation produced by this propeller, at any speed, was tip vortex cavitation. Both of the other two propellers, called Tip Vortex Propeller No. 2 and Back Bubble Propeller, had circulation distributions that peaked nearer center span (near 0.6 radius fraction), and so produced weaker tip vortices and stronger hub vortices. Tip Vortex Propeller No. 2 produced only tip vortex and hub vortex cavitation. The Back Bubble Propeller produced tip vortex and hub vortex cavitation, as well as mid-chord bubble cavitation on the suction side at high speeds. The inception speed of each type of cavitation for the propellers is shown in Table 2.

Type of Cavitation	TV1 Prop	TV2 Prop	BB Prop
tip vortex	605	670	520
hub vortex		890	1295
back bubble			1430

Table 2: Cavitation Inception Speeds (rpm)

8. FAR-FIELD NOISE MEASUREMENTS

Measurements of the far-field radiated noise have been carried out at distances of at least 25 m from the cavitating source. The Tip Vortex Propeller No. 1 was the most noisy propeller at speeds between 1000 and 2000 rpm, exceeding the levels of the other propellers by as much as 19 dB in some frequency and speed ranges. The Tip Vortex Propeller No. 2 and the Back Bubble Propeller produced nearly the same noise levels at speeds below the inception of bubble cavitation on the Back Bubble Propeller. In these speed ranges the noise produced by all three of the propellers is dominated by tip vortex cavitation noise and seems to be more related to the strength of the tip vortices than to the relative inception speeds. The propeller with the strongest circulation in the blade tip region (and the strongest tip vortices) produced the most noise, while both propellers with lower (but equal) circulation in the tip region produced lower (but approximately equal) noise levels. Also, both propellers for which tip vortex cavitation noise continued to dominate at high speeds were observed to produce maximum noise near 2000 rpm followed by a significant reduction in noise emission above this rotation rate. Only the Back Bubble Propeller did not show this decrease and this appears to be due to the formation of bubble cavitation.

9. CAVITATION NOISE DIRECTIVITY

The directional characteristics of the propeller cavitation noise were measured by positioning the far-field hydrophone at various angles in the vertical plane containing the propeller axis. The directivity of the 1 kHz frequency noise produced by the three propellers at 1880 rpm is shown in Figure 9. These data have been corrected to remove the effect of multiple sound transmission paths using the computer model of sound propagation at the Acoustic Barge. Both the Tip Vortex Propeller No. 2 and Back Bubble Propeller were omni-directional to within 1 dB over the angles tested, suggesting that noise is produced by a distribution of uncorrelated monopole sources. However, the Tip Vortex Propeller No. 1 was somewhat directional, showing an increase of 5 to 6 dB within an angle of 10 degrees of the downstream propeller axis. This suggests the existence of an additional source mechanism for this propeller; quite possibly a dipole.

10. ACOUSTIC SOURCE DISTRIBUTIONS

Figures 10, 11, and 12 show the measured acoustic source distributions for the three propellers at different rpm. The source distribution of each of the propellers evolved differently as the rpm was increased above the cavitation inception speed, leading to the conclusion that several different mechanisms are involved in cavitation noise production.

All of the propellers produced tip vortex cavitation first, and so the characteristics of the source distributions due to this form of cavitation can be determined with the greatest confidence. Three distinct cases can be seen:

1. At high propeller rotation rates, where the tip vortex cavitation was well developed, most of the noise originated from a position 300 to 400 mm downstream from the propeller, which corresponds with the observed location of breakup of the tip vortex cavities.
2. At rotation rates of several hundred rpm above visual tip vortex cavitation inception, noise was produced both at the location of the propeller and at the downstream position of breakup of the cavities. At axial positions downstream from this breakup location, the source strength dropped off at a steady rate of 22 dB per meter, much slower than in the other

cases.

3. At rotation rates near tip vortex cavitation inception, the Tip Vortex Propeller No. 1 developed a localized noise source at a location 300 mm downstream from the propeller, at the same location where the well developed tip vortex cavities were observed to collapse. However, the other two propellers produced noise near the location of the propeller.

The effect of hub vortex cavitation on the source distributions is not as clear since hub vortex cavitation was always present with tip vortex cavitation. For both the Tip Vortex Propeller No. 2 and the Back Bubble Propeller the downstream peak in the source distribution became much broader when the hub vortex cavitation became well developed. No corresponding broadening of the downstream source peak occurred for the Tip Vortex Propeller No. 1 which did not produce hub vortex cavitation. This behavior suggests that the hub vortex cavitation was radiating sound along its length. This behavior may be due to the observed intermittent nature of the hub vortex cavities.

Finally, the development of bubble cavitation on the Back Bubble Propeller caused a significant sound source to develop at the location of the propeller. It appears that the bubble cavitation noise source region is confined to the propeller plane as the source strength distribution did not change appreciably downstream of the propeller as rpm increased from 1430 to 1670.

11. CONCLUDING REMARKS

A computer code has been developed at DREA based on MIT lifting-surface procedures, which provides good correlation with model test back sheet cavitation extents. A linear acoustic theory to predict blade rate levels was presented, which included retarded time differences and a Lloyd's mirror, free surface effect. The method requires periodic cavity volume estimates from the back sheet cavitation code. Predicted far-field sound pressure levels generally fall within 10 dB of the overall measured noise levels for the low frequency blade rate harmonics. To help improve noise correlations with experiment, the acoustic theory should be extended to include the influence of the hull surface and sea bottom, as well as noise generated by other types of cavitation besides back sheet.

In the second part of this paper an acoustic measurement facility was described where the far-field level, spectral content and directivity of propeller cavitation noise can be measured. Also, a technique was described for measurement of the spatial distribution of acoustic sources due to propeller cavitation.

The results of application of these techniques to three propellers that produce vortex and bubble cavitation were presented. The directivity measurements showed that well developed tip vortex cavitation can produce directional noise that is strongest on the downstream propeller axis. Bubble cavitation noise showed no directional nature.

The source distribution measurements suggest that different noise generation mechanisms are responsible for noise from well developed, incipient, and intermediate tip vortex cavitation. Also, the source localization technique was useful in discriminating bubble cavitation noise sources from those of well developed tip vortex cavitation.

REFERENCES

Huang, T.T. and Groves, N.C. (1980): Effective Wake : Theory and Experiment, 13th Symposium on Naval Hydrodynamics, Tokyo, Japan.

Kennedy, J.L., Noble, D.J. and Casgrain, C.M. (1986): Evaluation of Some Propeller Analysis Methods, 21st American Towing Tank Conference, Washington, D.C.

Kerwin, J.E. and Lee, C.S. (1978): Prediction of Steady and Unsteady Marine Propeller Performance by Numerical Lifting-Surface Theory, Trans. SNAME, Vol. 86.

Lee, C.S. (1980): Prediction of the Transient Cavitation on Marine Propellers by Numerical Lifting-Surface Theory, 13th Symposium on Naval Hydrodynamics, Tokyo, Japan.

Leggat, L.J., (1982): Propeller Cavitation Noise Investigations in a Free-Field Environment", Presented at the NATO DRG Seminar on Advanced Hydrodynamic Testing Facilities, The Hague

Leggat, L.J. and Sponagle, N.C., (1985): The Study of Propeller Cavitation Noise Using Cross-Correlation Methods, ASME Journal of Fluids Engineering, Vol. 107, pp. 127-133.

McMahon, G.W., (1961): New Floating Laboratory Facilitates Underwater Acoustic Measurements, Canadian Electronics Engineering.

Morse, P.M. and Ingard, K.U. (1968): Theoretical Acoustics, McGraw-Hill.

Ross, D. (1976): Mechanics of Underwater Noise, Pergamon Press.

Sponagle, N.C. and Leggat, L.J., (1984): The Spacial Distribution of Acoustic Sources at Propeller Vortex Cavitation Inception, ASME International Symposium on Cavitation Inception, New Orleans, Dec. 1984.

Van Houten, R.J. (1982): The Numerical Prediction of Unsteady Sheet Cavitation on High Aspect Ratio Hydrofoils, 14th Symposium on Naval Hydrodynamics, Ann Arbor, Michigan.

Van Houten, R.J., Kerwin, J.E. and Uhlman, J.S. (1983): Numerical Solutions of Lifting Surface Sheet Cavitation - A Review of Research at MIT, 20th American Towing Tank Conference, Hoboken, New Jersey.

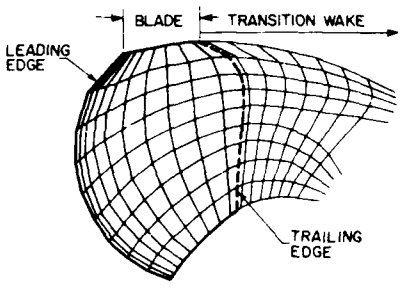

Figure 1a. Vortex Grid - Blade and Near Wake

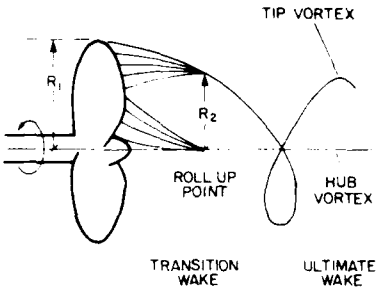

Figure 1b. Vortex Modelling - Roll-up and Ultimate Wake

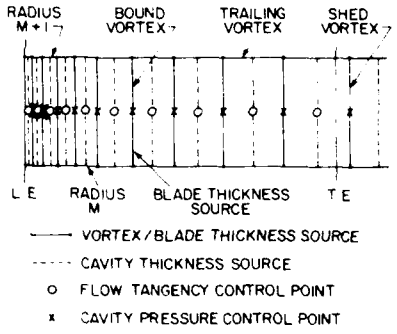

Figure 2: Singularity and Control Point Locations

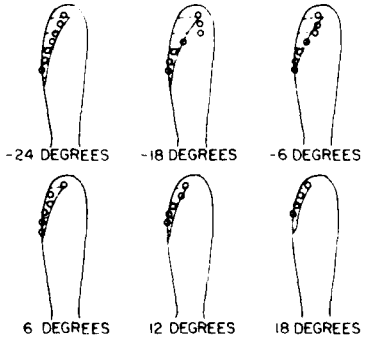

Figure 3: Cavitation Extent Correlation - Model 5349

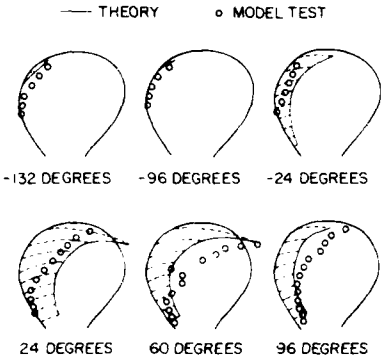

Figure 4: Cavitation Extent Correlation - Model 5268

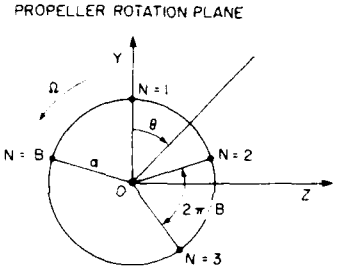

Figure 5: B Rotating Point Sources

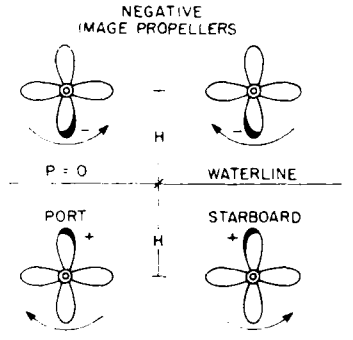

Figure 6: Free Surface Effect

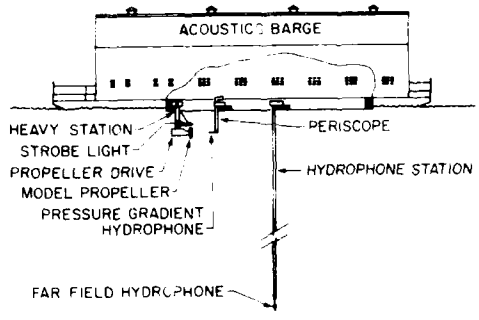

Figure 7: Experimental Setup at DREA Acoustics Barge

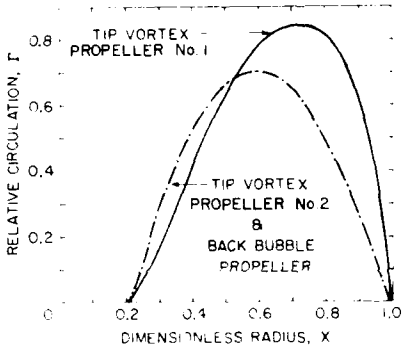

Figure 8: Propeller Circulation Distributions

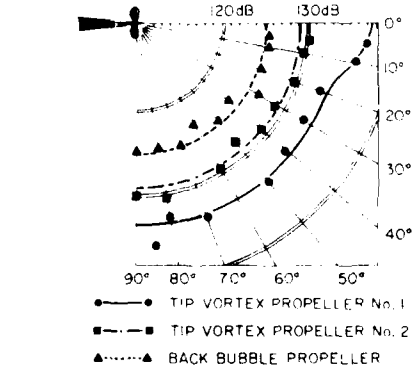

Figure 9: Noise Directivity

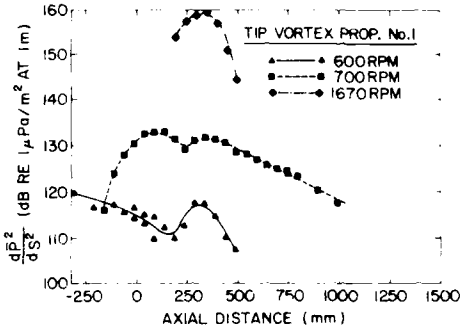

Figure 10: Source Strength Distribution - Tip Vortex Propeller No. 1

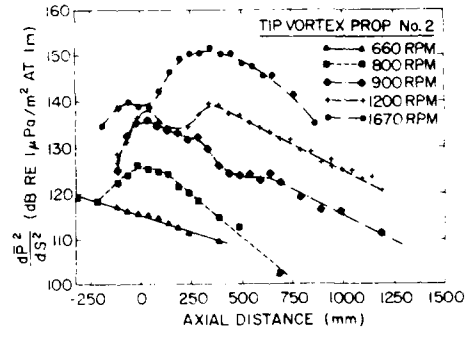

Figure 11: Source Strength Distribution - Tip Vortex Propeller No. 2

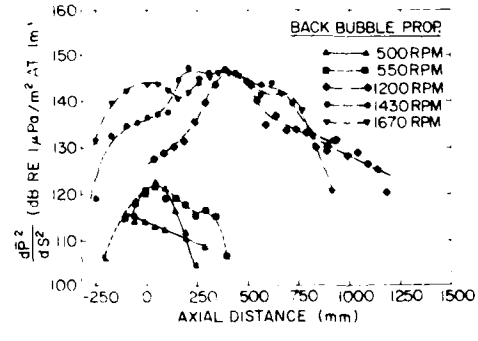

Figure 12: Source Strength Distribution - Back Bubble Propeller

Analysis of Recent Tip Vortex Cavitation Inception Data

V. H. Arakeri, H. Higuchi, and R.E.A. Arndt
St. Anthony Falls Hydraulic Laboratory
University of Minnesota, Minneapolis, Minnesota 55414

ABSTRACT

An analysis of the recently obtained σ_i values for tip vortex cavitation inception from an elliptical planform hydrofoil is presented. This includes the estimation of critical σ values for nuclei supply from the facility and separated regions on the foil. When measured σ_i values are compared to these critical σ values, certain obvious trends are noted. These have been used to estimate the dominant nuclei size at inception and are found to be surprisingly small. Thus, it is found that their role should be carefully examined in analyzing present inception data.

NOMENCLATURE

c	local chord length
C_g	gas content parameter, $\beta\gamma/1/2\rho U^2$
C_o	base chord of the hydrofoil
$C_{p_{min}}$	minimum pressure coefficient, $(P_{min}-P_\infty)/1/2\rho U^2$
C_{p_s}	Pressure coefficient at separation, $(P_s-P_\infty)/1/2\rho U^2$
P_{init}	initial test section pressure before start of inception tests
P_{min}	minimum static pressure in the flow
P_s	static pressure in the separated region
P_{sat}	saturation pressure corresponding to the dissolved gas content, $\beta\gamma$
P_v	vapor pressure of water
P_∞	free stream reference pressure
Re	Reynolds number based on base chord, UC_o/ν
R_o	dominant nuclei size at inception
T	coefficient of surface tension
U	free stream reference velocity
x	axial distance from the leading edge
α	geometric angle of attack
α_o	zero lift angle
β	Henry's constant
γ	dissolved gas content in ppm (mole basis)
ν	kinematic viscosity
ρ	water density
σ	cavitation number $(P_\infty-P_v)/1/2\rho U^2$
σ_{cr}	critical cavitation number for nuclei supply
σ_i	cavitation number at inception
σ_{init}	cavitation number based on initial pressure $(P_{init}-P_v)/1/2\rho U^2$

1. INTRODUCTION

One normally associates the inception cavitation number or index, σ_i with the minimum pressure coefficient in the flow, $-C_{p_{min}}$. However, a close relationship between the two is expected and observed only if a copious supply of nuclei with size typically exceeding 100 μm is assured. Strictly speaking, it is necessary to modify the first statement by stating that the minimum pressures of interest are in the regions of the flow where nuclei supply is likely to occur. The best example to illustrate this is by studying the inception characteristics of the hemispherical nose. In this case, in many facilities, the nuclei supply is from the separated region and thus the minimum pressures of consequence are the ones downstream of separation and not the theoretical minimum pressure coefficient. The latter, would, however, be significant in facilities where nuclei supply is assured within the test section itself. Therefore, following Holl (1969), it is useful to characterize nuclei as either "free stream" nuclei or "body" nuclei. Free stream nuclei are the ones available in the flow upstream of the body susceptible to cavitation. The concept of body nuclei is new and replaces the term "surface" nuclei used by Holl. Surface nuclei are the ones generated from the surface of the body; however, they are rarely found to be important in the inception process. The body nuclei are the nuclei generated within the separated, transitional or turbulent boundary layer regions of the flow over the body. It is now well established through the work of Katz (1984) that separated regions are definitely crucial sources of body nuclei. The role of the other two is to be still firmly established. It is to be emphasized that the original source of the body nuclei is still the free stream nuclei or surface nuclei. To quantify these ideas, it would be worthwhile to introduce the critical cavitation numbers associated with nuclei supply and designated by

$$\sigma_f^{(50)} \quad \text{or} \quad \sigma_b^{(25)}$$

The subscript here indicates the source, namely "f," for free stream or "b" for body, and the superscript number in the parenthesis indicates the largest dominant nuclei size (μm) available at that cavitation number. We expect the magnitude of σ_f to be dependent on the facility characteristics, like whether equipped with a resorber or not, dissolved gas content, etc. Whereas, the magnitude of σ_b would be dependent on whether the body possesses laminar separation or not, the dissolved gas content, etc. Further work is necessary to quantitatively estimate the values for the critical cavitation numbers introduced. However, it is not beyond the scope of present capabilities to at least estimate the values of σ_f and σ_b at which the local critical pressures would be greater or smaller than the partial pressure of the dissolved gas in the liquid.

The next question to be addressed is how to utilize the known information about $-C_{p_{min}}$, $\sigma_b^{(50)}$, $\sigma_f^{(25)}$, etc. to predict the magnitude of σ_i. For this, a hypothetical situation shown in Fig. 1 will be used. On this curve hypothetical values are shown for $\sigma_b^{(2)}$, $\sigma_b^{(10)}$, $\sigma_b^{(50)}$ and $\sigma_f^{(10)}$; thus body nuclei are likely to be the dominant source of nuclei for inception. The shape of these curves are like $C/1/2\rho U^2$, where C is proportional to the partial pressure of dissolved gas. The magnitude of $-C_{p_{min}}$ is assumed to be constant. During inception tests it is normal practice to lower the pressure at a fixed velocity, thus, proceeding along the arrow marked as A or B in the figure. Now consider the case of 20 ft/sec, as we proceed along the direction indicated by A, before approaching the condition of $\sigma = -C_{p_{min}}$, we cross the condition $\sigma = \sigma_b^{(10)}$. Thus, when conditions are just favorable for vaporous cavitation, that is $\sigma < -C_{p_{min}}$, we have a supply of nuclei having a dominant size of 10 μm. However, we do not expect inception under these conditions,

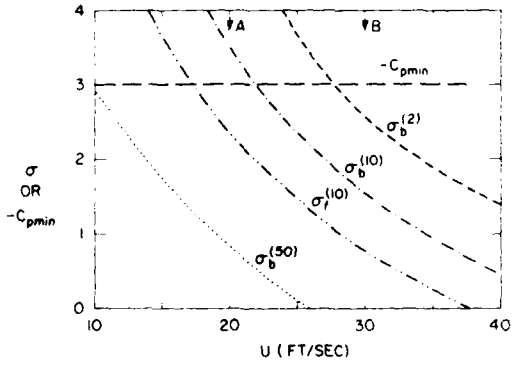

Fig. 1. Hypothetical dependence of critical σ and $-C_{p_{min}}$ on velocity.

since the tension required for a R_o = 10 μm nuclei is (see Katz, 1984)

$$\Delta\sigma^{(10)} = \frac{4}{3}\frac{T}{R_o \times 1/2\rho U^2}$$

with appropriate units for the other quantities. Assuming that as we go to lower σ values the dominant size of nuclei does not change, then

$$\sigma_i \cong (-C_{p_{min}}) - \Delta\sigma^{(10)}.$$

Similarly, at 30 ft/sec, along B, we expect

$$\sigma_i \cong (-C_{p_{min}}) - \Delta\sigma^{(2)}.$$

If nuclei size does change, let us say for the case A, then σ_i is predicted from the condition that available tension is equal to the required tension corresponding to the available dominant nuclei size.

In the present article we use these ideas to analyze recently obtained tip vortex cavitation inception data from an elliptical planform hydrofoil over a range of Reynolds number (velocity), angle of attack and dissolved gas content. Details of the experiments and extensive results are available in Rogers (1986). However, these are presented briefly here first. Then the method of estimating critical σ for nuclei supply is outlined. This is followed by the analysis of the results and finally a summary is provided.

2. EXPERIMENTAL METHODS AND RESULTS

The experiments were conducted in the 7.5"x7.5" (0.19 m x 0.19 m) square test section of the SAFHL, high speed water tunnel facility. Tip vortex cavitation inception data was obtained for an elliptical planform hydrofoil having a base chord of 3.15" (81 mm) and a semispan of 3.74" (95 mm) giving a full span aspect ratio of three. The cross section of the hydrofoil had a NACA 66_2-415 shape with a=0.8 mean line. The design lift coefficient, all due to camber, was 0.4. The zero lift angle, α_o for the profile is - 2.5°. The hydrofoil was mounted on a calibrated base plate, such that its geometric angle of attack, α could be varied. In addition, the free stream velocity, U and the dissolved gas content, γ was also varied.

The procedure for inception observations was as follows. At a given geometric angle of attack and free stream velocity, the tunnel was run at high pressures (for example corresponding to test section σ value of about 12 at a velocity of 22 ft/sec (6.71 m/s)) for ten minutes and then the test section pressure was slowly lowered until inception of cavitation was detected visually. The corresponding test section pressure etc. were recorded for the computation of σ_i, Re and

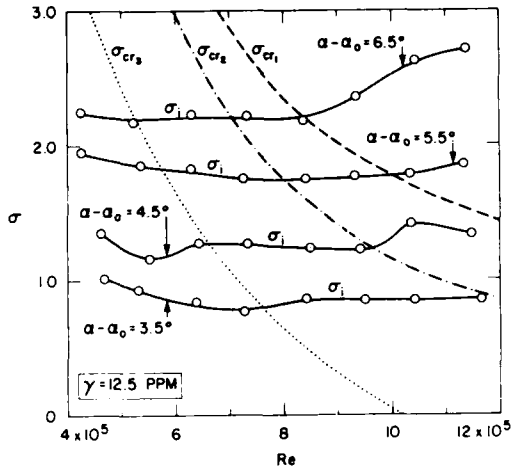

Fig. 2. σ_i dependence on Reynolds number and angle of attack. Also shown are critical σ's for nuclei supply. γ = 12.5 ppm.

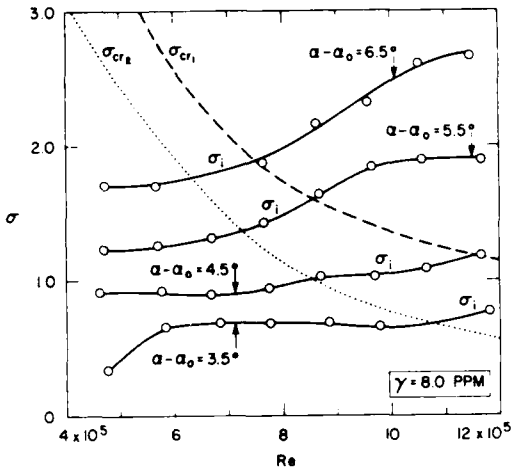

Fig. 3. σ_i dependence on Reynolds number and angle of attack. Also shown are critical σ's for nuclei supply. γ = 8 ppm.

other required parameters. Some video recording of the inception process was also made. This procedure was repeated for a range of test section velocities, angle of attack and dissolved gas content. In the present analysis, the data used covers a range of $\alpha-\alpha_o$ values of 3.5° to 6.5°, U values of 20 ft/sec to 50 ft/sec (6.1 m/s to 15.24 m/s) and three dissolved gas content, γ values of 12.5 ppm, 8 ppm and 4 ppm. The mean temperature for the tests was 67.5°F (19.7°C) and hence the following values were used for reducing the data.

$$\nu = 1.08\times10^{-5}\ ft^2/sec\ (1\times10^{-6}\ m^2/s)$$

$$p_v = 0.34\ psia\ (2313\ Pa)$$

$$\beta = 0.976\ psia/ppm\ (6640\ Pa/ppm)$$

The mean dependence of σ_i on the Reynolds number at $\alpha-\alpha_o$ values of 3.5°, 4.5°, 5.5°, and 6.5° is shown in Fig. 2 for a dissolved gas content value of γ of 12.5 ppm. Similar results for γ values of 8 ppm and 4 ppm are shown in Figs. 3 and 4, respectively. These results will be used for present analysis.

3. ESTIMATION OF CRITICAL σ FOR NUCLEI SUPPLY

3.1. Body Nuclei

As indicated, the conditions for the supply of body nuclei are strongly dependent on the viscous flow characteristics of the body. Boundary layer computations were made on both the suction and pressure side of the particular hydrofoil under consideration. The theoretical pressure distribution at a given angle of attack was computed using the method described in Abbott and Von Doenhoff

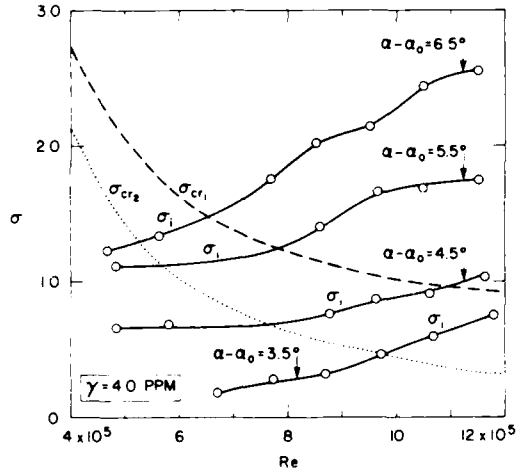

Fig. 4. σ_i dependence on Reynolds number and angle of attack. Also shown are critical σ's for nuclei supply. γ = 4 ppm.

(1959). These do not include any three-dimensional effects which are likely to be important in the tip region. Next the boundary layer growth calculations were made using the Thwaites method, and the separation bubble, if existing, was decided to be either short or long based on the results of Gaster (1967), also used by Huang and Peterson (1976). One set of computed results on the suction side at an angle of attack of $\alpha-\alpha_o$= 5.5° is shown in Fig. 5. A laminar separation bubble is predicted as indicated. Since on an elliptic planform the local Reynolds number towards the tip decreases sharply, a long separation bubble is predicted near this

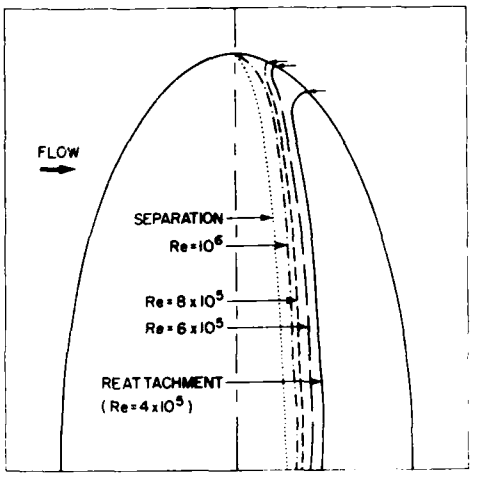

Fig. 5. A schematic of the predicted viscous flow pattern on the suction side at $\alpha-\alpha_o = 5.5°$.

region. The point of changeover from short to long separation bubble shifts towards the tip as Reynolds number is increased, indicated by a small arrow mark. Only at a Reynolds number of 10^6, a short separation bubble is predicted to exist almost all the way to the tip. Approximate stability estimates were also made to predict the transition location within the attached boundary layer. Flat plate results were used, since the pressure distribution showed a flat region almost from 5 percent of chord to 60 percent of chord, the location of minimum pressure point. Separation is predicted just downstream of this at about 63 percent chord. Using the maximum spatial amplification factor for the flat plate, it was predicted that laminar separation would prevail up to a Reynolds number of $2x10^6$.

On this foil, separation is also predicted on the pressure side at the angles of attack of present interest. In addition, the location of separation and pressure coefficient at separation were not found to be a strong function of angle of attack as indicated below for the suction side.

TABLE 1. Suction Side Separation Properties

$\alpha-\alpha_o$	4.2°	5.5°	7.5°
$(x/c)_s$	0.628	0.634	0.634
$-Cp_s$	0.66	0.70	0.74

On the pressure side, at an angle of attack of $\alpha-\alpha_o = 5.5°$, the $(x/c)_s$ and $-Cp_s$ values are 0.823 and 0.11, respectively. We may point out here that the gross viscous flow features predicted have been confirmed at a Re of $5.3x10^5$ through flow visualization studies as described in Higuchi et al. (1986a, 1986b). The important result from the above computations is the magnitude of $-Cp_s$, which will be required to predict the critical σ for nuclei supply as indicated below.

On the suction side, the critical condition for nuclei supply was taken to be

$$p_s = p_{sat} = \beta\gamma$$

Here, p_s is the static pressure in the suction side separated region and p_{sat} is the saturation pressure corresponding to the dissolved gas content. In terms of $-Cp_s$ and σ the above can be written as

$$\beta\gamma = (\sigma_{cr_1} + Cp_s)\frac{1}{2}\rho U^2 + p_v$$

σ_{cr_1} here designates the σ value when the above condition is satisfied. To a good approximation we can neglect p_v to give

$$\sigma_{cr_1} = \frac{\beta\gamma}{\frac{1}{2}\rho U^2} - Cp_s$$

or introducing the gas content parameter, $Cg = \beta\gamma/1/2\ \rho U^2$,

$$\sigma_{cr_1} = Cg - Cp_s$$

or using the average value for $-Cp_s$ from Table 1, we get

$$\sigma_{cr_1} = Cg + 0.7 .$$

The above value of σ is critical in the sense that if $\sigma < \sigma_{cr_1}$, locally in the suction side separated region, the liquid is supersaturated and if $\sigma > \sigma_{cr_1}$, it is undersaturated. Similar arguments for the pressure side give

$$\sigma_{cr_2} = Cg + 0.11.$$

We are deviating from our earlier convention in designating these as σ_{cr_1} or σ_{cr_2} and not as $\sigma_b^{(50)}$ etc. since we have no method at present of estimating the nuclei size for the prevailing super- or undersaturation. The magnitude of σ_{cr_1} and σ_{cr_2} as a function of Re (or velocity) are shown in Figs. 2, 3, and 4 at the coresponding γ values.

3.2. Free Stream Nuclei

The lowest pressures in a tunnel circuit are in the test section. Thus, a critical σ for the supply of free stream nuclei would be associated with the condition,

$$p_\infty = \beta\gamma$$

and again ignoring p_v, we interpret that this critical σ is in fact the value of Cg and hence is not too different from σ_{cr_2}. Next, one should ask whether the test section is able to generate nuclei even if $p_\infty < \beta\gamma$, since the velocities are maximum there, and hence low residence times. Therefore, a more viable critical σ for the free stream nuclei could be associated with separated regions in the turning vane regions of the bend after the diffuser. Such separations are predicted in the theoretical work of Song et al. (1986). Similarly, the stagnation region upstream of the contraction could also be a viable candidate for free stream nuclei supply due to long residence times there. These possibilities were examined in detail, and it was found that the critical σ, designated by σ_{cr_3} for either the turning vanes or the stagnation region, is given to the same approximations as before, by

$$\sigma_{cr_3} = Cg - 1$$

The magnitude of σ_{cr_3} was found to be of interest only for the case of γ = 12.5 ppm and is shown in Fig. 2. For other γ values, σ_{cr_3} is found to be mostly much lower than the σ_i values and hence are not shown. We might note that if $\sigma < \sigma_{cr_3}$, liquid in the entire upper leg of the tunnel circuit is supersaturated.

4. ANALYSIS OF INCEPTION DATA

4.1. General Trends

Close examination of the inception data in Figs. 2, 3, and 4 shows certain interesting general trends when compared with the behavior of critical σ's for nuclei supply. One of the clear trends from all the three figures is that if $\sigma > \sigma_{cr_1}$, then σ_i is a strong function of Re with σ_i increasing with an increase in Re. The second trend which is also apparent is that in the Reynolds number range for which $\sigma_{cr_3} < \sigma_i < \sigma_{cr_2}$, σ_i is almost independent of Re and finally from Fig. 2, we note that if $\sigma_i < \sigma_{cr_3}$, then σ_i is again dependent on Re but with σ_i increasing with decrease in Re. It is not obvious here that this trend is due to gaseous cavitation normaly observed since we do not know the precise magnitude of $-Cp_{min}$. It is of interest to speculate on the possible source of nuclei when $\sigma_i > \sigma_{cr_1}$ in which case obviously no region either on the body or in the facility has liquid which is supersaturated. However, it is likely that certain sized nuclei are still sustained and available due to the existence of strong pressure fluctuations in the reattachment zone of the separated region.

4.2. Estimation of Dominant Nuclei Size

Now consider the specific case of inception data for $\alpha - \alpha_o = 6.5°$ and γ = 4 ppm in Fig. 4.5. We note that, at a Re of the order of 5.25×10^5 σ_i is significantly lower than the σ_i for example at a Re of 1.15×10^6. If the latter is a measure of $-Cp_{min}$, then at inception with Re of 5.25×10^5, the liquid in the minimum pressure region must have been under significant tension. This aspect is used to predict the dominant nuclei size at inception. The existence of tensions was supported from video observations which indicated that under these conditions inception was sudden and when it appeared was developed with a twisted rope type of tip vortex cavity. Whereas, at higher Reynolds numbers with the same conditions, inception was still sudden but the cavity which appeared was much less developed.

For dominant nuclei size estimation a good estimate for $-Cp_{min}$ is required and this was obtained as follows. It would be expected that the observed tensions or the difference between σ_i and $-Cp_{min}$ would be reduced if the

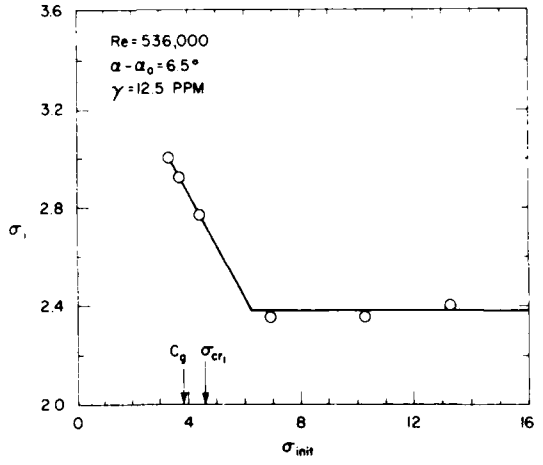

Fig. 6. Dependence of σ_i on the initial cavitation number at the start of the inception tank.

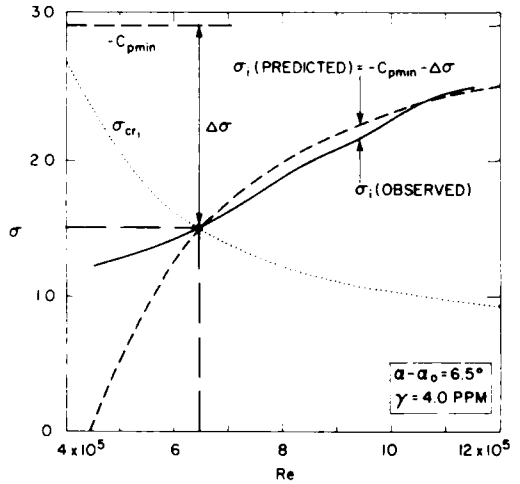

Fig. 7. Conditions used for estimating dominant nuclei size and predicted behavior of σ_i . γ = 4 ppm.

inception tests were started with initial pressure lower and lower. The results of such a study for γ = 12.5 ppm, Re = 5.36×10^5 and $\alpha-\alpha_o$ = 6.5° are shown in Fig. 6. The corresponding values of σ_{cr_1} and Cg are also shown. It is clear that there seems to be a cut-off condition which is given by $\sigma_{init} \cong 6$. It is tempting to associate this with σ_{cr_1}, but one thing is apparent that if $\sigma_i < \sigma_{cr_1}$, then the nuclei growing to larger sizes than when $\sigma > \sigma_{cr_1}$ is a possibility, thus reducing the required tension. From Fig. 6, we can estimate the $-Cp_{min}$ for $\alpha-\alpha_o$ = 6.5° as equal to three. Now the dominant nuclei size at inception was estimated for $\alpha-\alpha_o$ = 6.5° and γ = 4 ppm by making the following assumptions.

(i) $-Cp_{min}$ = 3 and does not change with Re

(ii) the dominant nuclei size R_o is associated with the conditions at the crossing point of σ_i and σ_{cr_1}.

Thus, from Fig. 7 and the expression

$$\Delta\sigma = \frac{4T}{3R_o} \frac{1}{\frac{1}{2}\rho U^2}$$

we get

$$R_o = \frac{4 \times 0.004935 \times 2}{3\times(3 - 1.5)\times 1.98\times(26.33)^2} = 6.3\times10^{-6} \text{ ft}$$

$$= (1.9\ \mu\text{m}).$$

Similar estimates with $\alpha-\alpha_o$ = 6.5° give R_o values of 6.0×10^{-6} ft (1.83 μm) and 7.22×10^{-6} ft (2.2 μm) for γ values of 8 ppm and 4 ppm, respectively. The dominant nuclei size in the regions $\sigma_i > \sigma_{cr_1}$ are surprisingly small and uniform in size. A lower value is predicted for γ = 8 ppm than 4 ppm probably because of data scatter.

4.3. Predicted Behavior of σ_i

Now assuming the dominant nuclei size remains the same over the Reynolds number range, we can predict the behavior of σ_i from

$$\sigma_i = -Cp_{min} - \Delta\sigma$$

$$= -Cp_{min} - \frac{4T}{3R_o} \frac{1}{\frac{1}{2}\rho U^2}$$

With the use of appropriate $-Cp_{min}$ and R_o values. This has been done for the case of $\alpha-\alpha_o$ = 6.5° and γ = 4 ppm with the results shown in Fig. 7. In this case, $R_o = 6.3\times10^{-6}$ (1.9 μm) and $-Cp_{min}$ = 3 values were used. For Re > 6.4×10^5, the observed σ_i dependence with Re can be explained solely on the basis of tension effects. For this Reynolds number range also, there is no obvious source of

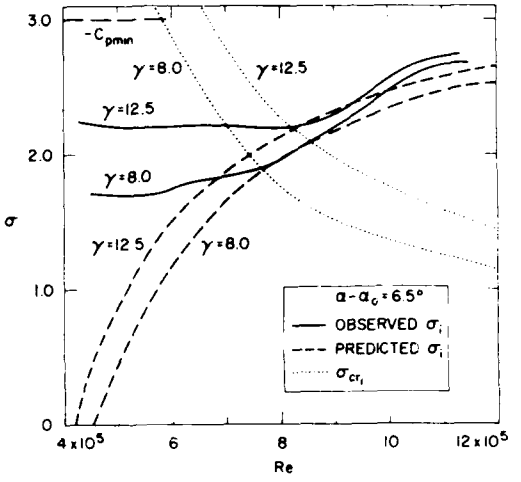

Fig. 8. Predicted behavior of σ_i. γ = 8 ppm and 12.5 ppm

nuclei based on static pressure considerations, and hence the assumption that R_o remains constant may be a valid one.

For Re < 6.4×10^5, observed σ_i follows a different trend from the predicted one. In this region, at inception, the extent of supersaturation being proportional to $\sigma_{cr_1} - \sigma_i$ increases with decrease in Re or velocity. Thus we may not expect R_o to remain constant here but to increase roughly in proportion to $(\sigma_{cr_1} - \sigma_i) \sim 1/1/2\ \rho U^2$. In the same Reynolds number range $\Delta\sigma$ required for inception increase like $1/2\rho U^2$ and the two effects may cancel giving a constant σ_i value. This is roughly in agreement with the observations.

The predictions of σ_i for γ of 8 ppm and 12.5 ppm along the same lines as for the case of 4 ppm are shown in Fig. 8. The general trends observed are similar to the ones discussed for the case of 8 = 4 ppm. Based on the analysis presented, we can reach the following broad conclusions.

5. SUMMARY

There is definite evidence that the observed complex behavior of σ_i for tip vortex cavitation inception with Reynolds number (actually velocity since body size was not varied), angle of attack and dissolved gas content are related to the critical conditions for nuclei supply. It is necessary to examine the latter for both the free stream and separated regions that may exist on the foil. In the regions of Reynolds numbers (velocities) where there is no obvious source for nuclei supply, the σ_i value is a strong function of Reynolds number and is almost independent of the dissolved gas content value. From the measured σ_i values, it was

possible to estimate the dominant nuclei size responsible for inception and these are found to be surprisingly small being of the order of 2 μm. Thus, some of the Reynolds number dependence on σ_i can be ascribed to the tension effects. It appears that in dealing with inception characteristics of flows with high $-Cp_{min}$ values, it is necessary to carefully examine the nuclei supply conditions. For flows with lower $-Cp_{min}$ values like axisymmetric bodies, the nuclei supply conditions may not be as critical. The above conclusions are valid for inception conditions.

REFERENCES

Abbot, I. H. and Von Doenhoff, A. E. (1959): Theory of Wing Sections. Dover Publication. pp. 75-79.

Gaster, M. (1967): The Structure and Behavior of Laminar Separation Bubbles. NPL Aero Rept. 1181 (revised), National Physical Laboratory, Great Britain.

Higuchi, H., Quadrelli, J. C. and Farell, C. (1986a): Vortex Roll-Up for an Elliptically Loaded Wing at Moderately Low Reynolds Numbers. AIAA Paper No. AIAA-86-0562. Presented at AIAA 24th Aerospace Science Meeting, Reno, Nevada.

Higuchi, H., Arakeri, V. H. and Arndt, R.E.A. (1986b): Further Studies of Tip Vortex Cavitation. Cavitation and Multiphase Flow Forum, ASME, New York.

Holl, J. W. (1969): Limited Cavitation. Article in "Cavitation State of Knowledge," ASME. J. Robertson and G. F. Wislicenus (eds.).

Huang, T. T. and Peterson, F. (1976): Influence of Viscous Effects on Model Full-Scale Cavitation Scaling. J. of Ship Research, Vol. 20, No. 4, pp. 215-223.

Katz, J. (1984): Cavitation Phenomena Within Regions of Flow Separation. J. Fluid Mech., Vol. 140, pp. 397-436.

Rogers, M. F. (1986): Experiments in Tip Vortex Cavitation and Associated Noise, M.S. Thesis, St. Anthony Falls Hydraulic Laboratory, Univ. of Minnesota.

Song, C.C.S., Wetzel, J. M. Yuan, M. and Arndt, R.E.A. (1986): Mathematical Modeling for a Vaned, Miter Elbow, Advancements in Aerodynamics, Fluid Mechanics and Hydraulics. ASCE Conference, Minneapolis, Minnesota, pp. 385-392.

CAVITATION SUSCEPTIBILITY OF OCEAN AND LABORATORY WATER

Y.T. Shen and S. Gowing
David W. Taylor Naval Ship R&D Center
Bethesda, Maryland

ABSTRACT

Experiments have been carried out in laboratories to relate cavitation inception and nuclei distributions. The existence of a strong relationship between cavitation and nuclei has been documented for laboratory waters, but little information is available about ocean waters. Towards this end, ocean measurements were carried out in Exuma Sound and the Gulf Stream off the coast of Florida to provide comparative results in different bodies of water. The test program included cavitation susceptibility masurements by a venturi system, nuclei population measurements by a light scattering device, and a series of standard oceanographic measurements. The depths ranged from 10 to 200 meters, deeper than ever before for these types of measurements. To provide a reference for comparison between laboratory and natural waters, the same measuring devices were used in the DTNSRDC 12-inch variable pressure water tunnel.

There was no difficulty inducing cavitation throughout the test matrix. At depths less than 100 meters, the water in the Gulf Stream cavitated more easily than the water in Exuma Sound. At deeper depths, the opposite trend was found. The bubble concentrations and tensile strengths at cavitation inception were compared with data obtained by other investigators in other parts of the ocean. Bubble instability theory and the Rayleigh-Plesset dynamic equation provide good explanations of many of the observed phenomena. The postulate of a critical bubble radius is used to explain the unexpected phenomenon that the concentration of bubbles that may cavitate could increase with depth.

INTRODUCTION

Most hydrofoils or propellers will develop tip vortex and surface cavitation at high speeds. The occurrence of cavitation leads to undesirable changes in hydrodynamic performance, noise generation, and physical damage from vibration and erosion. Therefore, the ability to predict the occurrence of cavitation is an important subject. The prediction of cavitation inception relies heavily on model experiments and extrapolation of their results to full scale because of the complexity of physical processes involved. Full-scale evaluations are often conducted and correlated with the model data.

Present knowledge is inadequate to always accurately predict cavitation performance in laboratories or in oceans. In laboratories, cavitation takes a variety of forms which may differ from facility to facility with similar models or even the same model. The International Towing Tank Conference (ITTC) headform is a good example of this. Cavitation inception indices on this headform ranged from 0.3 to 0.6. Even the appearance of the cavitation varied, some forms looking totally dissimilar from others. It was pointed out by Acosta and Parkin[1] that boundary layer characteristics and free stream nuclei are responsible for producing the varied appearances of cavitation on a single test model. Due to the lack of nuclei, difficulty in producing propeller cavitation in a depressurized towing tank has been observed[2]. With the introduction of bubbles by electrolysis ahead of the propeller, the occurrence of tip-vortex cavitation was significantly enhanced. This fact raises the question "Which nuclei concentration should be used in model tests to predict the prototype inception?"

In the ocean, propeller cavitation inception values within the same class of ships can exhibit a wide range of scatter. The causes are many. Laboratory studies suggest that environmental effects may contribute partly to the scatter. The understanding of the influence of cavitation nuclei on cavitation becomes important for the propeller designer to avoid cavitation.

The effect of free stream nuclei on cavitation has been studied extensively in laboratory water. Also, ocean measurements were conducted at several locations in the early spring of 1983 near the Bahamas and in the Gulf Stream off the coast of Florida. Laboratory measurements were made in the DTNSRDC 12-inch water tunnel to provide a reference for comparison between ocean and laboratory waters.

The variance in the ocean of cavitation susceptibility was measured by a cavitation susceptibility meter consisting of a venturi, a hydrophone, a pressure transducer, and a flow rate sensor. These experiments were conducted *in situ*. Nuclei concentrations and size

distributions were indicated by a microbubble light detector. Water samples examined by the microbubble detector were obtained from a sample collector which maintained the sample at *in situ* pressure. The depths ranged from 10 to 200 m. A complement of other oceanographic data was also collected. Related holographic measurements of cavitation nuclei in the ocean have been reported by Acosta, O'Hern and J. Katz[3] and cavitation susceptibility measurements have been made by Ligneul and Bovis.[4]

A summary of the important findings from the cavitation and nuclei measurements at the 10 and 25 meter depths were given in Reference 5. Since then, the data from deeper depths (to 200 m) have been analyzed. These new results are in this paper. Also, numerical calculations are used to interpret the results. These calculations have been extended from static bubble instability theory to include bubble dynamic instability[6] and multibubble interaction.[7]

TEST EQUIPMENTS

CAVITATION SUSCEPTIBILITY MEASURING SYSTEM

The cavitation susceptibility measuring system used in the sea has two major components: an underwater unit, which causes cavitation by a venturi and detects cavitation by a hydrophone, and a shipboard sub system which controls the underwater unit and conditions data signals for recording and display. The two components are connected by a multiconductor cable. The underwater unit is deployed vertically to a desired depth. Sea water flows through a screen which filters out particles larger than 1 mm that can damage the venturi. The flow then passes through the venturi, the pump, a flow straightener, and finally the flow meter before exhausting to the outside.

The flow rate is regulated by a motor-speed controller in the shipboard subsystem. The cavitation signals are detected by a wideband high frequency hydrophone and then band-pass filtered between 10 and 100 kHz. The acoustic signal is multiplexed with the engineering-sensor data of flow rate and ambient pressure, and together they are transmitted to the shipboard electronics via an electromechanical cable. The signals are then processed on board for display and recording by the shipboard electronics. Further discussions of this system are given in Reference 8.

In the 12-in. water tunnel, the same venturi unit was used but the pressure sensors were replaced by mercury and water manometers. A pipe parallel to the water tunnel flow was used to transfer water from the center of the test section to the venturi. A major difference between the ocean and the 12-in. water tunnel set-up is that the light-scattering microbubble detector was in-line with the venturi system in the 12-in. water-tunnel experiments, whereas the microbubble detecting system and venturi systems were deployed separately in the ocean.

MICROBUBBLE MEASURING SYSTEM

The nuclei measuring system consists of two major components: an underwater sample collector and a shipboard light scattering bubble detector. In the water tunnel experiments, only the bubble detector was used. In the ocean, nuclei were measured by examining the microbubbles retrieved from depth in a large sampler. The retrieval device is a 100-L pressure tank with an internal bladder and a large valve at the bottom. After pressurizing the bladder with shipboard nitrogen to the pressure at which the water sample is to be collected, the tank is lowered to the desired depth. The nitrogen in the bladder bubbles out from a top hose while the ocean water slowly fills the tank through the bottom valve as the bladder collapses. The exit of the top hose is over 2 m above the water intake. The filling is stopped with a residual amount of nitrogen left in the bladder to act as a pressure reservoir and the bottom valve is closed[5].

Upon retrieval to shipboard, the microbubble detector is connected to the bottom valve of the tank and a pressurized nitrogen supply line is connected to the bladder. The 76 to 95 L water sample then exhausts through the detector as the bottom valve is opened and the bladder expands inside the tank. The entire process maintains the ocean water sample at *in situ* pressure until the water sample passes downstream of the detector.

The microbubble detector uses focused white light beams to illuminate bubbles flowing through a pipe and the reflected signals yield the bubbles sizes. Further discussion on the bubble detector is given by Ling, Gowing and Shen[9]. To evaluate the reliability of the device for bubble measurements, a comparison test of this device with an in-line holographic camera was carried out in a California Institute of Technology (CIT) water tunnel and reported in a paper by Katz et al[10].

OCEANOGRAPHIC DATA MEASURING SYSTEM

Standard oceanographic data were collected on the sea trip as continuous water column measurements made with a Neil Brown conductivity-temperature-depth probe equipped with a transmissometer. A General Oceanics Rosette sampling device collected water samples from discrete depths. The temperature, water density, oxygen content, etc., were mapped throughout the ocean tests. Further discussion of the data is given by Zsolney, et al.[11]

OCEAN MEASUREMENTS

Measurements were carried out in Exuma Sound and the Gulf Stream near the coast of Florida to provide comparable susceptibility results in different bodies of water. To investigate the effect of depth on susceptibility, measurements were made at depths from 10 to 200 m. The cruise track and station locations are shown on the map of Figure 1.

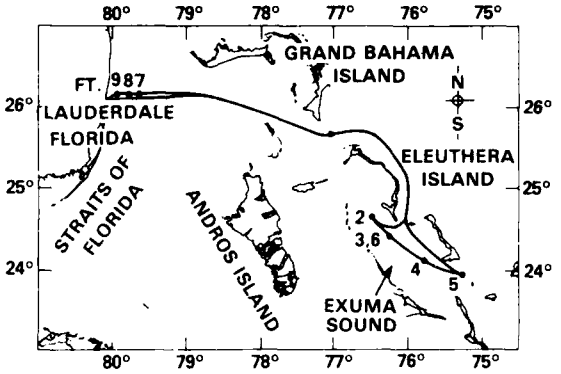

Figure 1 — Ocean Test Stations

Susceptibility measurements covered Stations 3 to 6 in Exuma Sound, and 7 to 9 in the Gulf Stream in the Straits of Florida. Station 6 was the same location as Station 3 but 4 days later. Because of the strong currents and ship drift in the Gulf Stream, deep depth measurements there were difficult. However, with good weather throughout the whole test program, the fluctuations in surface elevation were relatively small and the ambient pressures seen by the pressure sensors were almost constant at a given depth.

The sequence of data collection follows. Once on station, the Neil Brown conductivity-temperature-depth probe equipped with a transmissometer was used to collect standard oceanographic data. This was followed by the deployment of the General Oceanics Rosette sampling device to collect water samples from discrete depths. Immediately after the completion of the oceanographic tests, the cavitation susceptibility meter was deployed.

The underwater venturi unit was deployed to a specific depth while monitoring the pressure on the transducers. Cable markers provided general guidance on the overall depth. Once at depth, the flow rate was set just below the critical speed such that no acoustic signals were detected for 3 to 5 min. The flow was then gradually increased until high amplitude acoustic signals were detected, and then tuned to attain a specific frequency of cavitation events. The flow rate, ambient pressure, and acoustic signals were recorded on tape and displayed on the shipboard readout unit for 3 to 5 min, with a few 10 min runs.

OCEANOGRAPHIC DATA

The temperature, water density, and dissolved oxygen distributions relative to atmospheric pressure are given in Figures 2, 3 and 4 as a function of depth. The other important oceanographic data such as nitrogen, salinity, carbon, and biological parameters etc. are given and discussed in Reference 11. In Exuma Sound the temperature profiles did not vary much with location or depth. The temperature dropped only 3°C going from the surface to 200 m, with a weak thermocline occurring at 125 to 150 m. The Gulf Stream had stronger thermoclines, around 75 to 100 m deep, and the temperature

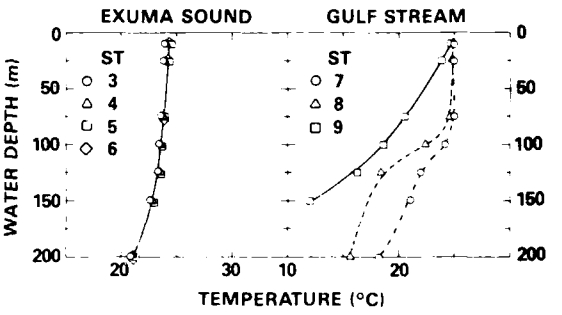

Figure 2 — Temperature Distribution in Ocean

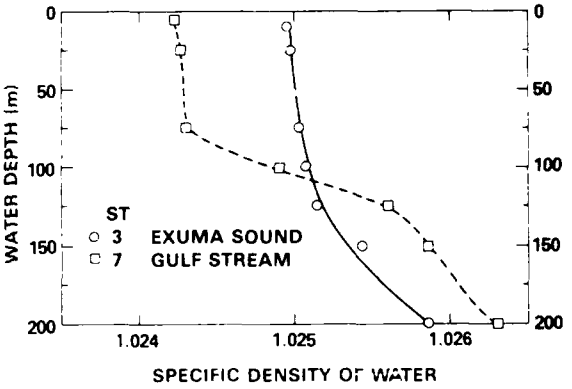

Figure 3 — Water Density Distribution in Ocean

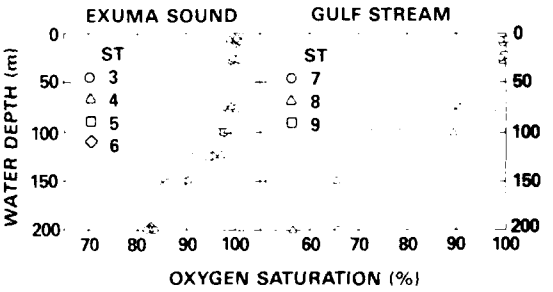

Figure 4 — Oxygen Saturation in Ocean at Standard Temperature and Atmospheric Pressure

dropped 10°C between the surface and 200 m. The temperature profiles in the Gulf Stream also varied with location. See Figure 2.

The dissolved oxygen distribution in Exuma Sound was relatively insensitive to geographic location (Figure 4). Furthermore, the percent of oxygen saturation dropped very gradually with increases in water depth. At the surface, the water was about 100% saturated with oxygen. Even at 200 m, 83% saturation was measured in Exuma Sound. On the other hand, the oxygen saturation distribution in the Gulf Stream was very different. The percent of saturation decreased markedly at depths greater than 100 m, down to 50% saturation at 200 m.

The significance of this parameter, "dissolved oxygen", is that quite often biological activity is related to oxygen balances and microbubble distributions may well be a consequence of biological activity.

In summary, the water in Exuma Sound was very homogenous and contained little biological activity.[11] The sound is surrounded by the Bahama Islands and is consequently sheltered from much flushing action. The Gulf Stream, however, had much more biological activity and movement. It was hoped that these environmental differences would show up in the cavitation susceptibility measurements.

MICROBUBBLE DATA

Nuclei measurements in the 12-inch water tunnel are presented first. The ocean data follow. Six test results, denoted as WT1 through WT6, are presented in this report. The measured numbers of bubbles per cubic centimeter, N/cm^3, for these runs are shown in Table 1. The symbol α_{ST} denotes the dissolved air saturation relative to 20°C and atmosphere pressure measured by a Van Slyke device. The symbol α_E denotes the same air content but relative to the actual pressure in the tunnel. The symbol R_0 denotes the bubble radius in microns.

Consider the test series consisting of runs WT2, WT4, WT5 and WT6. These four test runs were conducted at the same test pressure. The bubble concentrations in terms of air contents are plotted in Figure 5 where $N(\bar{R})$ is defined as

$$N(\bar{R}) = \frac{\text{Number of nuclei per unit volume with radii between } R_1 \text{ and } R_2}{R_2 - R_1}$$

and $\bar{R}$ is the mean of R_1 and R_2.

Looking at Figure 5, the density distribution function $N(\bar{R})$ is approximately a power function of the bubble size. Next, consider the ocean data. The ocean microbubble spectra were measured by examining the microbubbles retrieved from depth in the large water sampler, and the measurements were then carried out on shipboard. However, it is important to point out that the entire sampling process maintained the ocean water sample at *in situ* pressure until the sample passed downstream of the bubble detector. The measured number density distribution functions $N(\bar{R})$ versus depth and geographic location are given in Figure 6. The bubble concentrations in the radius range of 10 to 25 μm are given in Table 2.

For the purpose of comparison with the water tunnel data, the ocean microbubble measurements at the 10-m depth are given in Figure 5. The ocean bubble concentrations fall between those corresponding to supersaturation and medium air content conditions for the water tunnel. Note that these laboratory bubble measurements were at 1.17 bars ambient pressure while the ocean data were measured at 2.09 bars. The difference in bubble size because of these pressure differences would be only about 21%. Because of the significant effect of ambient

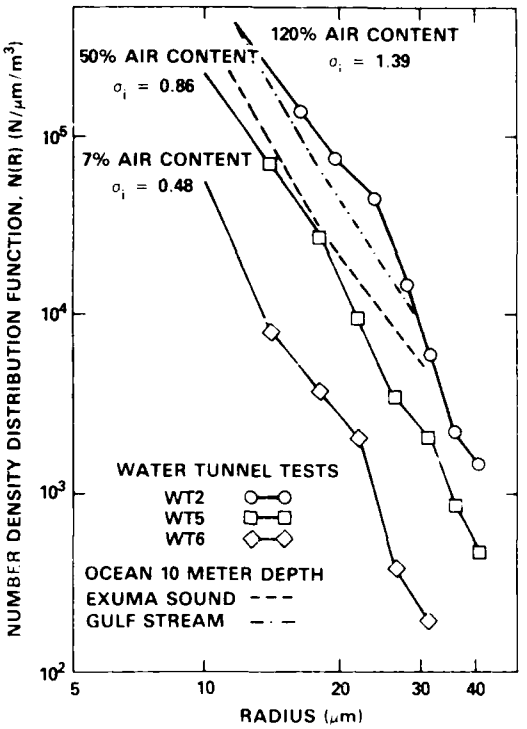

Figure 5 — Water Tunnel Microbubble Spectra, P_0 = 1.17 bars

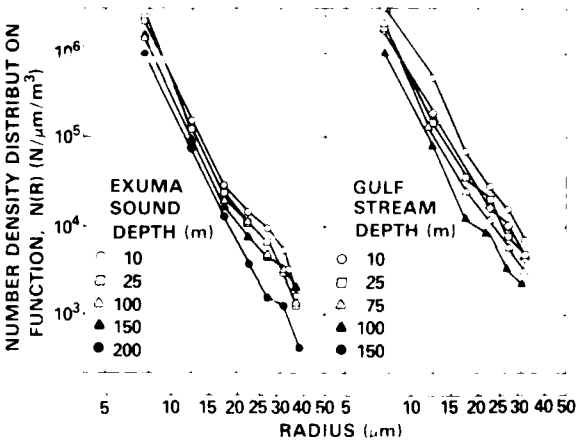

Figure 6 — Nuclei Spectra Measured in Ocean

pressure on microbubble instability, however, the comparison given in Figure 5 can only be interpreted qualitatively.

In the shallow depths the nuclei concentrations in the Gulf Stream are greater than those in Exuma Sound (see Figures 5, 6). This correlates with biological activity which also was greater in the Gulf Stream than in Exuma Sound.[11] In both bodies of water, the nuclei concentration for a given bubble size decreased with deeper depths. However, the rate of decrease seems steeper in

the Gulf Stream than in Exuma Sound. For example, at 150 m, the measured nuclei concentrations in Exuma Sound are greater than those in the Gulf Stream. This observation is consistent with the oceanographic measurements, namely that the oxygen saturation measurements given in Figure 4 show a similar trend. The slope of the density distribution function in terms of bubble size is similar to the size-concentration distributions found by other investigators for bubbles in water tunnels or in the ocean. This consistency of the shape of the bubble distributions at various sites has been previously noted.[12]

No attempt is made here to rationalize why nuclei populations are different at the two ocean locations. In the next section, however, an attempt will be made to correlate the measured nuclei and the cavitation measurements.

The present measurements given in Table 3 will now be compared with the ocean data measured by Acosta et al[13, 14] using a holocamera and Medwin[15], using photographic techniques. For simplicity, only the bubble sizes in the range of 10 to 25 μm in radius are presented. At 10 m the bubble concentration around the Catalina Island measured by Acosta et al is about the same as that measured in the Gulf Stream and higher than in Exuma Sound. The bubble concentrations dropped as the depths increased from 10 to 25 m in Exuma Sound and in the Gulf Stream. The same trend is also observed in Acosta et al's measurements from the surface to 15 m. However, they report a large increase in bubble concentration at 30 m. The thermoclines at Catalina Island occurred between 18 m and about 30 m. At the bottom of thermoclines strong biological activity may occur and this may account for the higher number density.

As shown in Table 2, the bubble concentrations generally decreased with depth in the Gulf Stream and in Exuma Sound. At 75 m in the Gulf Stream and 150 m in Exuma Sound, however, the concentrations seem high. This fact coincides with the thermoclines which occurred around 75 to 100 m in the Gulf Stream and 125 to 150 m in Exuma Sound. Figure 4 also shows the correlation of thermoclines and oxygen saturation. More work is needed to relate biological activity, nuclei concentrations and dissolved gas levels.

The existence of gas bubbles near the ocean surface down to 30 m has been documented by various people using different techniques (in Table 3). But, the existence of gas bubbles at 200 m has not been previously reported. Gas absorption physics would predict rapid absorption of bubbles at these depths and low relative air saturation levels. The absorption rates of rising gas bubbles in seawater were visually measured in the laboratory. Oxygen bubbles were electrolytically generated in a vertical pressurized glass tube filled with seawater, and the sizes were determined by their terminal velocity as they rose in the tube. The dissolving rates were then measured for different pressures to represent different depths. Some results are shown in Figure 7. Based on these results which were recalculated for air bubbles, even at 10 meters deep with an atmosphere - saturated ocean, bubbles less than 50 μmm in radius would dissolve in less than 2 minutes. But during the ocean measurements, about 5 to 10 minutes elapsed between recovery of the sampling device and actual bubble measurements. All the bubbles captured should therefore have dissolved. Hence absorption would predict the extinction of bubbles less than 50 μm at 10 meters deep even with whatever surfactants are present in seawater. At deeper depths the absorption would be even greater.

Despite these absorption results, bubbles as deep as 30 meters have been visually identified using holography. These results are very concrete. The venturi cavitation results certainly establish the existence of pressure-responsive nuclei in the ocean as deep as 200 meters. These nuclei exhibit behavior similar to a bubble as well. It may be premature to conclude that these cavitation nuclei are all microbubbles without more thorough testing of Harvey model nuclei and organic particulate matter that may contain metabolic bubbles. The latter types of nuclei are more plentiful in the ocean. The word "nuclei" may be more proper than the word bubble to describe the light scatterers detected at the deep depths. Further work should be carried out to clarify it, perhaps by a holographic or a photographic device in parallel with the present set-up.

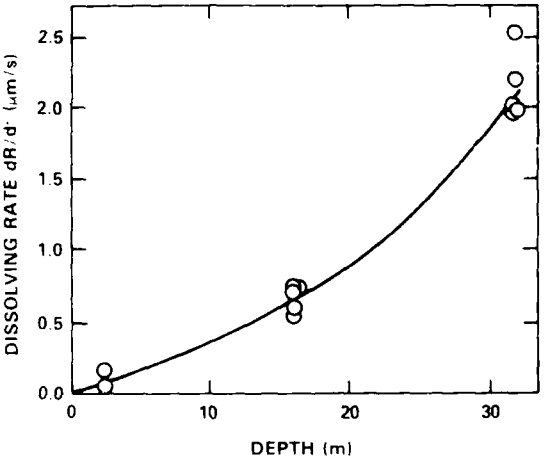

Figure 7 -- Dissolving Rate of Air Bubbles Rising in Seawater as a Function of Depth

CAVITATION INCEPTION DATA

For the cavitation susceptibility study, only cavitation from a single bubble or multi-bubble bursting was of interest. Surface sheet cavitation did occur in the venturi occasionally but it was easily removed by reducing the throat velocity. Increasing the throat velocity again usually did not restart the surface cavitation. The bursting noise of a cavitation bubble was at least 10 times greater (+20 dB) than the background level. As a result, it was not difficult to detect cavitation bursting acoustically. To

determine the frequency of cavitation events, a threshold was set to count cavitation bursting in a counter. The oscilloscope trace indicated that the bubble bursting signal decayed in about 1 ms. To avoid counting the rebound signals of a single bubble as multiple bubbles, a time lapse of 1.5 ms was set to trigger the counting of another event. Typical acoustic signals of a single bubble bursting are shown in Figure 8.

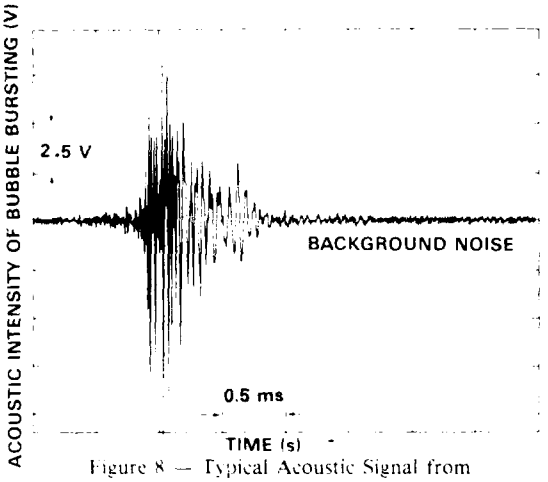

Figure 8 — Typical Acoustic Signal from Single Bubble Bursting

The nuclei measurements in the 12-inch water tunnel are presented in Table 1. The measured cavitation data will now be presented. Let σ_i denote the cavitation inception index defined by

$$\sigma_i = \frac{P_0 - P_v}{\frac{1}{2}\rho V_i^2}$$

where P_0 and P_v denote the reference and vapor pressure, V_i denotes the mean throat velocity at cavitation inception and ρ is the fluid density.

The flow characteristics at cavitation inception, as "called" by a hydrophone, are given in Table 4. The corresponding Reynolds number (based on the throat diameter) Re, the minimum throat pressure coefficient $-C_{pmin}$, and the throat pressure P_T at inception are listed here. The negative sign with the throat pressure P_T denotes a compression and a positive sign denotes tension. The first three test runs correspond to supersaturated air content conditions at standard temperature and pressure, and the last three test runs correspond to medium and low air content conditions.

As reported in Table 1 the bubble concentrations change significantly with air content, and the cavitation changes also. The measured cavitation inception index σ_i varies from 0.48 at an extremely low air content to 1.39 at the supersaturated conditions. The measured water tensile strength of 0.3 to 1.7 bars is compatible with the values measured by Knapp[16]. With the water samples not pressurized, Knapp et al also reported compression at cavitation inception.

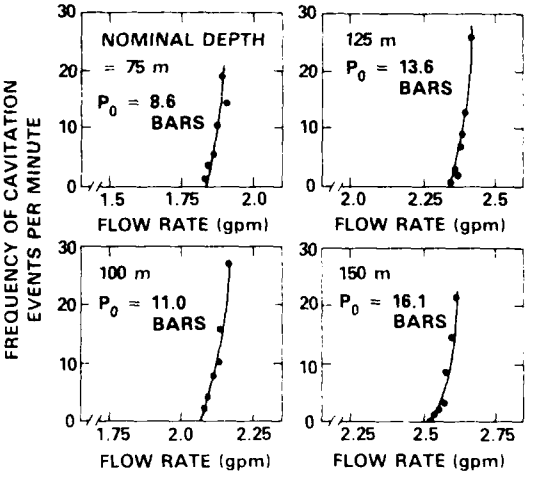

Figure 9 — Cavitation Event Frequency Versus Flow Rate at Exuma Sound Station 6

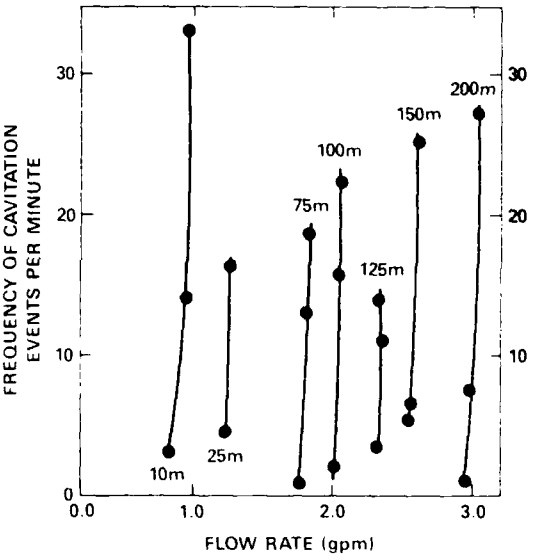

Figure 10 — Gulf Stream Station 7

The cavitation data from the ocean are now presented. The test matrix at Station 6 was more extensive than at other stations. The measured frequency of cavitation events and flow rates at Station 6 are shown in Figure 9 at four depths. The vertical axis shows the averaged frequency of measured cavitation events per minute for a typical test run of 3 to 5 min. The horizontal axis gives the corresponding flow rate meaured in the middle of the test run. Plots are shown for water depths of 75, 100, 125 and 150 m, respectively. Note that as the ambient pressure increases with depth so does the required flow rate to induce cavitation. As another example the cavitation measurements in the Gulf Stream are shown in Figure 10. The measurements show that at a given depth or ambient pressure, there exists a critical flow rate

below which no cavitation occurs. For a flow rate greater than this value, a slight increase in flow rate results in a significant increase in the frequency of cavitation events.

As mentioned previously, the existence of gas bubbles down to 30 m has been well documented. Bubble dynamic theory should be applicable to investigation of cavitation events at least down to a 30 m depth. Based on the Rayleigh equation, bubble static instability curves have been constructed and are given in Figure 11. The effect of the pressure drop due to viscous losses in the venturi throat has been included. The horizontal axis corresponds to bubble size. The vertical axis corresponds to the critical velocity at which the bubble becomes unstable. The curves are referred to as static bubble instability curves. Further discussions are given in Reference 5.

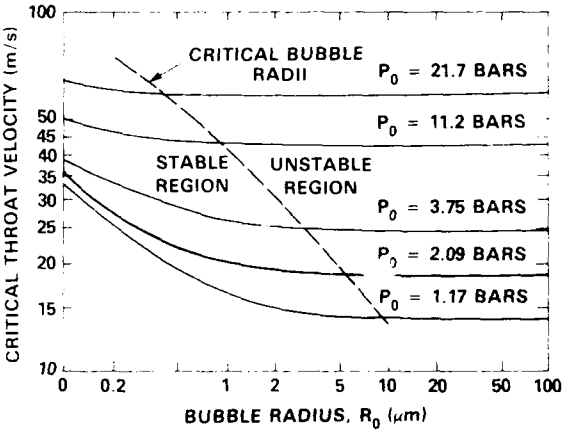

Figure 11 — Critical Bubble Radius Versus Throat Velocity

Figure 11 shows that at a given depth or ambient pressure there exists a critical velocity below which all the bubbles are stable and bubble cavitation would not be anticipated. When the critical velocity is reached, all the bubbles greater than the critical size become unstable and a large number of bubbles should burst. In the case of the present venturi system, the dynamic effect on bubble growth is given in Figure 12. The cavitation inception is assumed to occur when the bubble grows to 10 times its original size. It is seen that the required critical throat velocity is higher for dynamic than for static instability. Furthermore, because of the inertia effect, the large bubbles may not have enough time to grow to the critical size; namely the relative importance between bubble dynamic characteristic time and time the bubble takes to cross the low pressure throat region. The critical velocity versus initial bubble radius curve thus shows a minimum. This implies that the present venturi system excites only a part of the nuclei spectrum. Nevertheless, the difference between dynamic and static instability curves is small. This instability theory still supports the idea that the sudden increase in cavitation frequency with flow rate is a consequence of bubbles becoming unstable. Reference 7 discusses the multibubble interaction and cavitation inception. Even though the existence of microbubbles at deep depths has not been proved conclusively, the same cavitation frequency trends observed in Figure 9 and 10 occurred at the deep depths, which supports the possible existence of bubbles.

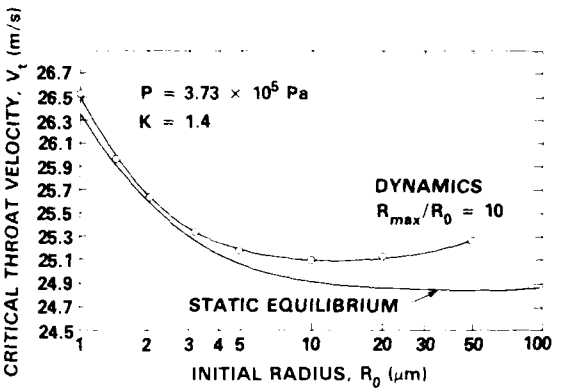

Figure 12 — Comparison Between Dynamic and Static Critical Velocity at Venturi Throat as a Function of Initial Bubble Radius

The measured cavitation inception indices in Exuma Sound and the Gulf Stream are given in Figures 13 and 14, respectively. The corresponding geographic stations have been given in Figure 1. Cavitation inception must be defined here. Although the definition of cavitation inception is subjective, it is simply assumed in this report that cavitation inception occurs when the bursting signals are detected at an average frequency of 10 events per minute. (0.17 events per second.) The corresponding flow rate is called the critical flow rate Q_i and the mean throat velocity V_i is called the critical throat velocity. The curve denoted by $-C_{pmin}$ in Figures 13 and 14 corresponds to the measured minimum pressure coefficient on the venturi surface at different Reynolds numbers.

From Figures 6, 12, and 13, the following observations can be made:

1. At 10 m, the values of σ_i exhibit a large variation with geographic location. They range from 0.92 to 1.16 in Exuma Sound among 4 stations and 1.13 to 1.24 in

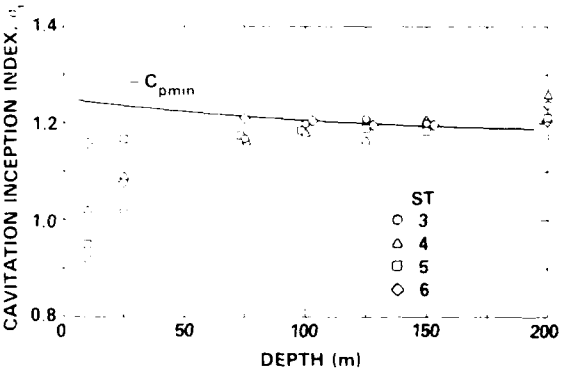

Figure 13 — Measured Cavitation Inception Indices in Exuma Sound

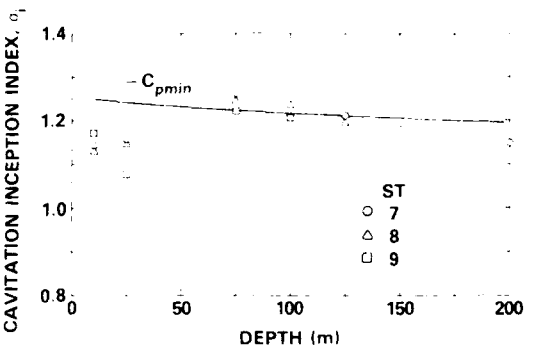

Figure 14 — Measured Cavitation Inception Indices in the Gulf Stream

the Gulf Stream among 3 stations. A relatively large variation in σ_i was also observed at 25 m. At these shallow depths and low ambient pressures, the critical bubble sizes that become unstable, as computed from instability theory, are relatively large and the corresponding bubbles are less abundant in the natural waters. This fact may explain the large variation of σ_i at the shallow depths. These cavitation measurements are supported by the measured bubble concentrations which are higher in the Gulf Stream than in Exuma Sound.

2. At 75 and 100 m in the Gulf Stream, the measured inception indices are surprisingly higher than $-C_{pmin}$ in the venturi throat. These depths coincide with the thermoclines which occurred in the Gulf Stream and the bubble concentrations at these depths seemed high also. (See Table 2). An increase in σ_i at the bottom of thermoclines was not observed in Exuma Sound. In view of Figure 2, however, it is possible that the thermocline there was too weak to create a strong biologically active layer.

3. There was no difficulty to induce in situ cavitation throughout the test matrix, even down to 200 m; hence, deep ocean water cavitates readily. The bubble instability theory shows the critical radius is around 0.4 μm at 200 m deep. Bubbles greater than 0.4 μm would be candidates there for cavitation bursting. Recall that the bubble concentration increases almost linearly with decreasing bubble size on a logarithmic scale. Consequently, the concentration of bubbles eligible to cavitate might increase with depth if the plots in Figure 6 can be extrapolated to smaller sizes. This may explain the fact that σ_i increases with depth as it did in Exuma Sound. Because the relatively large bubbles measured by the detector only form a small fraction of the total bubbles eligible for cavitation if the plots in Figure 6 were extrapolated, this hypothesis may not be proved, as the direct measurement of bubble sizes less than 5 μm has not successfully been made.

4. A comparison of σ_i measured between the ocean and the 12-in. water tunnel indicates that high air contents are needed in the laboratory to reproduce the same cavitation susceptibility as the ocean at deep depths.

5. At deep depths the present measurements support the classic cavitation scaling law that σ_i approaches $-C_{pmin}$ at high pressures and velocities. In these measurements, σ_i came within $\pm 8\%$ of $-C_{pmin}$.

TENSILE STRENGTH DERIVED FROM VENTURI MEASUREMENTS

At a given depth the flow rate required to induce cavitation may differ between ocean and laboratory waters. No direct measurements were made to determine the corresponding tensile strength at cavitation inception. Nevertheless, it may be estimated by the following indirect method. The tensile strength P_i is computed by

$$P_i = -P_0 + K \frac{\rho}{2} V_i^2$$

The negative sign on the right hand side is used to yield positive values for tension and negative values for compression. The symbol K includes the loss coefficient due to viscosity. The actual value of K depends on the venturi geometry and the friction coefficient. In this study, it is approximated by the measured value of $-C_{pmin}$.

The computed tensile strengths of laboratory water at different air contents are given in Table 4. At supersaturation conditions, compression was sometimes measured at the state of cavitation inception. At lower air contents and bubble populations, the tunnel water showed tension at inception. A tensile strength of 1.69 bars, corresponding to 24.5 psi was computed at the 7% air content. As shown in Table 4, the range of tensile strengths computed for the 12-in. water tunnel is in the same range as those measured by Knapp at the California Institute of Technology.[16]

The computed tensile strengths of ocean waters are given in Table 5. A slight difference between this table and the one given in Reference 5 is due to the recomputation of the critical flow rate. Except at 150 and 200 m, the water in Exuma Sound could sustain a higher tensile strength before cavitating than the Gulf Stream. According to bubble instability theory the critical bubble size should be smaller at deeper depths. The compression values measured at the 200 m depth in Exuma Sound and 75 to 100 m depths in the Gulf Stream were not expected.

The tensile strength computed by the above equation does account for the energy loss due to viscosity by using the measured $-C_{pmin}$ value as the value of K. However, the influence of boundary layer growth and potential core acceleration in the throat are not considered. Hopefully, this correction is not large. Further refinements of the theoretical analysis are needed to improve values given in Tables 4 and 5.

Cavitation susceptibility measurements at sea were also carried out by Ligneul and Bovis using a venturi device on the French Mediteranean coast and the Brittany coast[4]. The measured tensile strengths at various depths are given in Table 6. At 10 m, the tensile strengths of 0.50 bar on the French coast and 0.30 in Winter and 0.69 bar in Spring off the Britton coast are compatible with the range of tensile strengths measured in Exuma

Sound and the Gulf Stream at 10 m. The same trend is also observed for the present and Ligneul's measurements at 25 m. However, higher tensile strengths are reported at 65 m by Ligneul and Bovis than the present measurement at 75 m.

Akulichev and Ilyichev[17], using an acoustic device, measured the tensile strength of ocean waters at 10 m in various parts of the world. They report higher values of tensile strength at cavitation than the values given in Tables 5 and 6 using the venturi measurements. This may be a result of using different cavitation generating techniques.

CONCLUSIONS

For the first time, cavitation susceptibility, nuclei distributions, and oceanographic data were measured in the ocean down to 200 meters. To provide a reference for comparison, the water in the 12-in. water tunnel was also measured with the same devices.

The important results obtained from the ocean measurements can be summarized as follows:

1. At shallow depths the bubble concentrations measured off California by Acosta et al using holography are similar to those measured in the Gulf Stream near Florida using light scattering. Even Medwin's bubble concentrations measured with photograph techniques are similar to these results. The consistency of ocean bubble concentrations measured by different people with different techniques in different locations is surprising, especially in view of the vast range of concentrations previously measured in water tunnels.

2. For depths shallower than 100 m, the Gulf Stream water contained more bubbles and cavitated more easily than the Exuma Sound water. This trend is similar to water tunnel behavior in which, given the same pressure, more bubbly water cavitates more easily.

3. For a given bubble size, the nuclei concentrations generally decrease with deeper depths. Also the measured number density distribution functions N(R) have approximately the same slope as those measured in the 12-inch water tunnel. The consistency of the shape of the number density function between ocean and laboratory waters is interesting. Whatever factors stabilize water tunnel bubble concentrations must behave similarly in the ocean.

4. The cavitation inception index and bubble concentration showed local high values near the top of the thermocline in the Gulf Stream. The thermocline can trap sinking microscopic debris to form a biologically active layer; hence, this activity may increase the water's cavitation susceptibility.

5. There was no difficulty to induce in situ cavitation throughout the test matrix, even down to 200 m; hence deep ocean water cavitates readily. According to the bubble instability theory, the concentration of bubbles eligible to cavitate can theoretically increase with depth if the number density distribution function can be extrapolated to smaller sizes.

6. At deep depths the present venturi measurements seem to support the classic cavitation scaling law that σ_i approaches $-C_{pmin}$ to within $\pm$ 8 percen..

7. At 10 m, the tensile strengths measured in Exuma Sound and the Gulf Stream compare favorably with Ligneul and Bovis' measurements off the French coast and the Brittany coast.

8. At 200 m, compression was measured in the venturi throat at cavitation inception in Exuma Sound. This result was a surprise. Further studies are underway to identify the cause.

9. The present conclusions are based on very limited data. As shown by Akulichev and Ilyichev, the measured ocean tensile strengths at 10 m show great variation with different regions of the world.

ACKNOWLEDGEMENTS

The authors express their appreciation to Dr. A. Zsolnay at NORDA for his support of the sea cruise. The continuous support and encouragement of Mr. J.H. McCarthy and Dr. F.B. Peterson throughout the course of this project are greatly appreciated. Finally, the benefits of technical discussions with Dr. T.T. Huang are greatly appreciated. This project was supported by the Office of Naval Technology's Ship and Submarine Technology Program, Element 62543, Propulsor Subproject SF 43-434.

REFERENCES

1. Acosta, A.J. and Parkin, B.R., "Cavitation Inception — A Selective Review," 17th American Towing Tank Conference (1974).

2. Kuiper, G., "Cavitation Inception on Ship Propeller Models," Ph.D. dissertation, Netherlands Ship Model Basin (1981).

3. Acosta, A.J., O'Hern, T., and Katz, J., "Some Recent Trends in Cavitation Research," International Symposium on Cavitation, Sendai, Japan, April 1986.

4. Ligneul P. and Bovis, A., "The Use and Limitation's of the Venturi Tube as a Cavitation Susceptibility Meter," International Symposium on Cavitation, Sendai, Japan, April 1986.

5. Shen, Y.T., Gowing, S., and Pierce, R., "Cavitation Susceptibility Measurements by a Venturi," International Symposium on Cavitation Inception — 1984, ASME (1984).

6. Shen, Y.T. and Gowing S., "Scale Effect on Bubble Growth and Cavitation Inception in Cavitation Susceptiblity Meters," Cavitation and Multiphase Flow Forum, Albuouerque, NM (1985).

7. Chahine G., and Shen, Y.T. "Bubble Dynamics and Inception in Cavitation Susceptibility Meters," ASME 1985 winter meeting Miami (1985).

8. Shen, Y.T., Gowing, S., and Eckstein, B., "Cavitation Susceptibility Measurements of Ocean, Lake and Laboratory Waters," DTNSRDC Report 86/019, May 1968.

9. Ling, S.C., Gowing, S., and Shen, Y.T., "The Role of Microbubbles on Cavitation on Headforms," 14th Symposium on Naval Hydrodynamics (1985).

10. Katz, J., Gowing, S., O'Hern, T. and Acosta, T., "A Comparative Study Between Holographic and Light Scattering Techniques of Microbubble Detection," IUTAM Symposium - Measuring Technique in Gas-Liquid Two-Phase Flows, Nancy, France 1983.
11. Zsolnay, A., Lavoie, D.M., Wiesenburg, D.A. and Reid, D., "Environmental parameters in Exuma Sound and the Straits of Florida," Naval Ocean Research and Development Activity, Technical Note 252 (1984).
12. Billet, M.L., "Cavitation Nuclei Measurements — A Review," ASME Caviation and Multiphase Forum (1985).
13. Acosta, A., T. O'Hern, and J. Katz, "Some Recent Trends in Cavitation Research," International Symposium on Cavitation, Sendai, Japan, 1986.
14. O'Hern, T.J., Katz, J., and Acosta, A.J., (1985), "Holographic Measurement of Cavitation Nuclei in the Sea", ASME Cavitation and Multiphase Flow Forum, Albuquerque, N.M.
15. Medwin, H., (1970), "In Situ Acoustic Measurements of Bubble Populations in Coastal Ocean Waters", J. Geophysical Research, 75, 3, 599-611
16. Knapp, R.T., Daily, J.W., and Hammitt, F.G., "Cavitation," McGraw-Hill (1970).
17. Akulichev, V.A. and Ilyichev, V.I.," Acoustic Cavitation in Sea Water," International Symposium on Propeller and Cavitation, Wuxi, China (1986).

TABLE 1 — 12-INCH WATER TUNNEL BUBBLE CONCENTRATIONS

Test No.	α_{ST}	P_0 (bar)	α_E	Bubble Concentration N/cm^3			
				$R_0 > 10$ μm	$R_0 > 15$ μm	$R_0 > 20$ μm	$R_0 > 30$ μm
WT1	1.05	0.5	2.10	3.6	1.0	0.32	0.08
WT2	1.20	1.17	1.02	2.8	1.0	0.52	0.10
WT3	1.20	1.87	0.65	1.4	0.36	0.14	0.028
WT4	0.60	1.17	0.53	—	—	—	—
WT5	0.50	1.17	0.42	0.39	0.18	0.10	0.020
WT6	0.07	1.16	0.06	0.15	0.028	0.0085	0.0011

TABLE 2 — OCEAN BUBBLE CONCENTRATIONS
(10 μm < R_0 < 25 μm)

Depth	P_0	Bubble Concentrations N/cm^3	
(m)	(bar)	Exuma Sound	Gulf Stream
10	2.0	1.26	2.54
25	3.5	1.05	1.33
75	8.4	—	1.43
100	10.9	0.77	1.16
150	15.9	0.73	0.52
200	20.8	0.53	—

TABLE 3 — OCEAN BUBBLE CONCENTRATIONS AT SHALLOW DEPTHS
(10 μm < R_0 <25 μm)

Source	Location	Technique	Wind (m/s)	Depth (m)	Bubble Concentration (number/cc)
Present Results	Gulf Stream	Light Scattering	Calm	10.0 25.0	2.54 1.33
	Exuma Sound	Light Scattering	Calm	10.0 25.0	1.26 1.05
Acosta et al [13, 14]	Catalina	Holography	Calm	3.05 6.10 15.24 30.48	14.98 3.29 1.59 8.55
Medwin (1970) [15]	Monterey Marina	Photography	Calm	Surface 3.05	2.64 3.29

TABLE 4 — MEASURED CRITICAL THROAT SPEEDS AND CAVITATION INCEPTION INDICES IN THE 12-INCH WATER TUNNEL

Test No.	α_{ST}	P_0 (bar)	α_E	V_0 (m/s)	σ_i	R_e	$-C_{pmin}$	Tensile Strength (bar)
WT1	1.05	0.5	2.10	8.47	1.31	1.8×10^4	1.28	−0.04
WT2	1.20	1.17	1.02	13.0	1.39	2.6×10^4	1.25	−0.11
WT3	1.20	1.87	0.65	19.1	1.02	3.8×10^4	1.23	0.37
WT4	0.60	1.17	0.53	15.3	0.96	3.0×10^4	1.24	0.28
WT5	0.50	1.17	0.42	16.3	0.86	3.3×10^4	1.23	0.47
WT6	0.07	1.16	0.06	21.6	0.48	4.3×10^4	1.22	1.69

TABLE 5 — TENSILE STENGTH OF OCEAN WATER
Tensile Strength (bar)

Station \ Depth		10 m	25 m	75 m	100 m	125 m	150 m	200 m
Exuma Sound	3	0.73	0.76	0.37	0.08	0.01	0.06	−0.58
	4	0.46	0.47	0.44	0.27	0.43	−0.08	−1.11
	5	0.64	0.17	0.36	0.28	0.32	0.51	−0.28
	6	0.11	0.55	0.07	0.02	0.19	0.21	0.07
Gulf Stream	7	0.21	0.20	−0.43	−0.90	0	0.35	1.04
	8	0.19	0.54	0	0.10	—	—	—
	9	0.23	0.24	−0.37	−0.29	0.11	—	—

TABLE 6 — TENSILE STRENGTH MEASURED AT SEA BY VENTURI METHOD (Ref. 4)

Station	Season	Depth (m)	P_0 (bar)	P_c (bar)	R_0 (μm) equivalent
French Mediterranean Coast	Summer	10	2.12	0.50	0.79
		25	3.40	1.47	0.31
		30	4.17	1.33	0.32
Britton Coast	Winter	10	2.00	0.30	1.16
		25	3.50	0.13	1.75
		35	4.43	0.19	1.28
	Spring	10	1.97	0.69	0.62
		20	2.96	0.50	0.73
		30	3.90	0.10	1.97
		50	5.94	1.87	0.23
		65	7.30	2.10	0.20

CAVITATION PHENOMENA IN JETS

H.J. Lin and J. Katz

School of Civil Engineering
Purdue University
West Lafayette, Indiana 47907

Abstract

Cavitation phenomena in water jets are being studied in a specially designed test facility. Of particular interest are the relationships between the jet's coherent turbulent structures, the physical appearance and the conditions for the onset of cavitation. The experiments are being carried out with jets up to one inch in diameter, exit velocity up to 60 ft/sec, and with nozzle geometries ranging from a sharp edge orifice to a long and smooth contraction. Special care has been taken to the control of free stream turbulence and filtering of external disturbances. The experiments consists, firstly, on measurements of the cavitation inception indices with various levels of dissolved air content, different free stream turbulence level, and acoustic excitation and secondly, on observations of the location and physical appearance of cavitation. Results demonstrate that free stream velocity, free stream turbulence, air content and background noise play dominant roles in the generation of turbulent structures and the resulting cavitation. The report includes also comparison between the present observations and other studies of jet cavitation.

Introduction

In spite of the efforts made by many investigators to determine the conditions for cavitation inception in submerged water jets, the available literature contains only conflicting results without any clear scaling trends. Some investigators, for example, reported that the cavitation inception index, σ_i (defined as $(P - P_v)/(0.5\ \rho V^2)$, where P is a characteristic pressure, chosen almost arbitrarily, P_v is the vapor pressure, and V is the jet velocity) increased with the Reynolds number (Johnson et al (1982)), others did not observe any clear trend with the velocity (Ooi (1981,)) Numachi et al (1960)), and some (Kobayashi (1967)) reported a reduction in σ_i when the velocity was increased. The relationship between the nozzle diameter, the inception indices, and the dimensions of the test facility was also a subject for an unresolved debate. Lienhard and Stephenson (1966), Lienhard and Goss (1971) and Lienhard (1984) combined the results of their own observations with other measurements to demonstrate that the values of σ_i increased with both the jet's diameter and the ratio, $\beta = d/D$ (d and D are the diameters of the nozzle and the pipe in which nozzle is inserted, respectively). Based on the combined results they formulated an empirical relationship between the inception index and the jet's size. Similar trends, but with substantially different values of σ_i, were also observed by Ball (1960), Ooi (1985), and Kobayashi (1967). However, due to the large scatter in the data, some of which are summarized in Figure 1, it is impossible to make any conclusive statement. For example the values of σ_i for a 0.125 inch (.32 cm) diameter jet vary between 0.1 and almost 0.6, for a 0.25 inch (1.27 cm) jet the inception indices range between 0.2 and almost 0.7, and for 2 inch (5.08 cm) jets the results vary between 0.6 and 1.6. Thus, the inception indices measured by Baker et al. (1976) with a 2 inch (5.08 cm) nozzle are not different from the values measured by Lienhard and Goss (1971) on a 0.25 inch (.64 cm) jet. Actually, even the definitions of σ_i vary from one study to the other. For example, when cavitation phenomena are studied in a jet created by an orifice in a pipe, the location of the pressure sensor downstream of the aperture affects the value of the inception index. Some investigators (Numachi et al. (1960), Kobayashi (1967), Lienhard and Goss (1971)) measured the pressure just downstream of the aperture, that is close to the vena contracta, whereas others (Ball (1960)) measured it several diameters downstream. Obviously, their results for σ_i would be different.

Attempts to explain the large variations in the results focused mainly on the differences in the population of cavitation nuclei in the various test facilities. Baker et al. (1976) and Ooi (1985)) noticed

that σ_i increased with the amount of air dissolved in the water, and when Ooi (1981) generated freestream bubbles by electrolysis, his results for a 0.25 inch (one cm) jet changed from about 0.22 to more than 0.5. These observations led Ooi (1985) and Franklin and McMillan (1980) to develop theories for predicting the occurrance of cavitation based on the nuclei population, the distribution of turbulent pressure fluctuations, and the size of the region prone to cavitation inception. One of the problems related to this work are the difficulties in measuring the freestream pressure fluctuations which Ooi tried to resolve by utilizing microscopic bubbles as sensors.

The location of inception in the jet and the role of its coherent turbulent structure has also been a subject for discussions. Arndt (1981) claimed that jet cavitation appearing in jets was observed to occur in ring-like bursts; whereas, Johnson et al. (1982) and Geneoux and Chahine (1984) observed the same phenomena only when the jet was excited either by an external transducer or by creating a resonence chamber upstream of the nozzle.

These observations led Geneoux and Chahine (1984) to model the flow field as a series of ring vortices and to neglect the effect of the secondary turbulent structures. This approach was motivated also by the work of Grow and Champagne (1971) and Kibens (1979) that studied the effects of acoustic excitation on the coherent vortex structures in jets. They observed that when the Strouhal number (defined as fd/V, f being the frequency) of the excitation signal was about 0.3, the jet's flow structure transformed into a series of ring vortices. As will be shown later (figures 4(b) and 5(c)), this tendency was also noticed during the present study. In unexcited orifice flows Numachi et al (1960) and Kobayashi (1967) observed that inception occured in the jet's shear layer but did not notice a particular location or ring-like structures. Ooi (1985) claimed that careful studies of hundreds of photographs and holograms of his jets showed clearly that the cavities appeared in the distance from six to sixteen diameters downstream of the exit, but favoring no particular radial position. As will be shown later, these observations are also confirmed by the present measurements, even in excited jets.

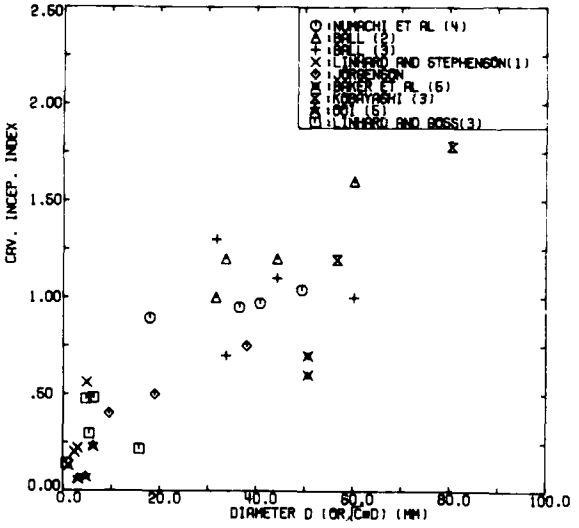

Fig. 1. A collection of measured cavitation inception indices of water jets.
(1). Orifice in pipe, based on the pressure and velocity in the vena contracta
(2). Orifice in pipe, based on exit velocity, and pressure downstream
(3). orifice in a pipe, based on the velocity in the vena contracta, and the pressure for downstream
(4). Orifice in a pipe, based on the pressure and velocity in the vena contracta
(5). nozzle in a large container

This puzzling state of knowledge motivated the current research program whose primary objectives are to determine the flow parameters affecting the onset of cavitation in water jets. Of special interest are the role of the nozzle geometry, the free stream turbulence level, the jet coherent vortex structures, the free stream velocity, and the diameter of the jet. This program is currently in progress and the present report contains the results of the initial series of observations.

Experimental Facility

A special test facility has been designed and constructed for the present project. As shown in figure 2, the water was injected into a 1.5 x 2.5 x 6.5 ft (0.69 x 0.76 x 1.98 m) chamber whose pressure could be controlled either by a vaccum pump or with a source of high pressurized air. The current set of experiments has been conducted with a free surface, that is the chamber was filled to a height of about 2 ft (.61 m). The recirculating pump was located about 15 ft (4.57 m) below the test section to prevent the occurrance of cavitation there, and the velocity has been measured with a turbine flow-meter. The pressure has been determined with a transducer connected to two pressure taps located on the chamber's wall at the same height as the center of the nozzle. Cavitation has been observed under stroloscopic light and inception has been determined by maintaining the jet at a constant velocity and gradually lowering the pressure. When inception occurred, the readings of the flow meter and the transducer were frozen and recorded.

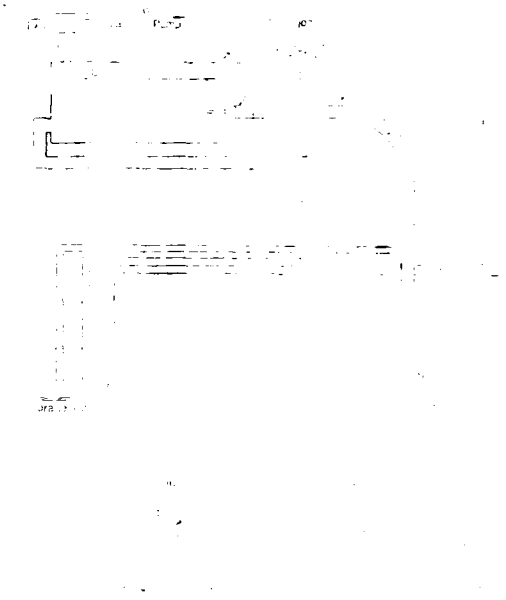

Fig. 2. A schematic description of the test facility

Reduction in the amount of air dissolved in the water was achieved by recirculating the flow at a low pressure and high speed for about half an hour. An oxygen meter was used to monitor the air content, which was kept during the entire set of experiments at a level of about 35-50 percent of the saturation level at room temperature and pressure.

In order to reduce the effect of pump vibrations and background noise the facility was mounted on vibration isolators, the connections to the pump were made with flexible tubing, and the pump itself was isolated from the floor. The jet was externally excited by mounting a large speaker on its inlet pipe, and with the help of a function generator it was possible to vibrate the pipe at any desired frequency in the range of 20-2500 HZ.

Four different nozzles were tested during the present phase of the project. Two had a gradual and smooth contraction from the inlet pipe (which had a diameter of 4 inches (10.16 cm)) to the 1 inch (2.54 cm) diameter exit. Both nozzles had a cosine contour, but with different length; 3 inches (7.62 cm) and 6 inches (15.24 cm). The other two were sharp edge orifices, with diameters of 1 inch (2.54 cm) and 0.5 inch (1.27 cm). A honeycomb and two screens could be installed in the pipe upstream of the nozzle, and the experiments were carried out both with and without these flow straighteners.

Results

The location and the physical appearance of cavitation inception in the various jets are presented in Figure 3. As is evident from these photographs, the first cavities appeared in the range starting from about six diameters downstream of the nozzle. Even the addition of background noise did not alter this location (Figure 3(c)). When the pressure was lowered beyond the inception level the cavities became larger and appeared closer to the inspection point. At these advanced stages, as is evident from the photographs in Figure 4, the occurence of cavitation is closely related to the coherent vortex structures of the jet. In figure 4(a) a series of odd-shape cavities appear mostly in discrete locations, suggesting that the jet's ring-like vortices play a role in creating conditions favorable for cavitation. However, the shape of the bubbles in this photograph , some of them appearing in string-like form, demonstrate that secondary turbulent structures are also major contributors to the occurence of cavitation in this flow. Vibrating the inlet pipe with the speaker had a major effect on the appearance of cavitation, especially when the Strouhal number was kept between 0.3 and 0.5. As shown in Figure 4(b), the rings appear more distinctly, and much less evidence of the secondary structures is visible. However, the region containing the clearly organized structures extends to about 5 diameters downstream of the nozzle. The bubbles beyond this region still appear in various odd shapes without any noticable orientation. Note that figure 3(c) demonstrates that inception of cavitation occurs within this region of "disarray". These observations are in agreement with the studies of the effects of external excitation on a jet performed by Zaman and Hussain (1980) and Hussain and Zaman (1981). They also observed that the region mostly affected by the noise extended to about 6 to 8 diameters downstream of the injection point. Vibrating the pipe had the same effect on the flow through the orifice, as is evident from comparing figures 5(a), (b), and (c). Actually, without the external excitation the flow through the orifice appeared sometimes in complete disarray (fig.(5a)), and in other times there were some traces of the ring-like structures (Fig. (5b)). The external excitation transformed this flow to a series of distinct rings which extended only to a few diameters downstream of the nozzle.

In order to determine whether variations in the boundary layer play any role in the conditions of inception, the internal surface of the smooth 6 inch (15.24 cm) long nozzle was coated with roughness elements made of fine sand particles. Unfortunately, these elements became the sites of cavitation inception within the nozzle prior to

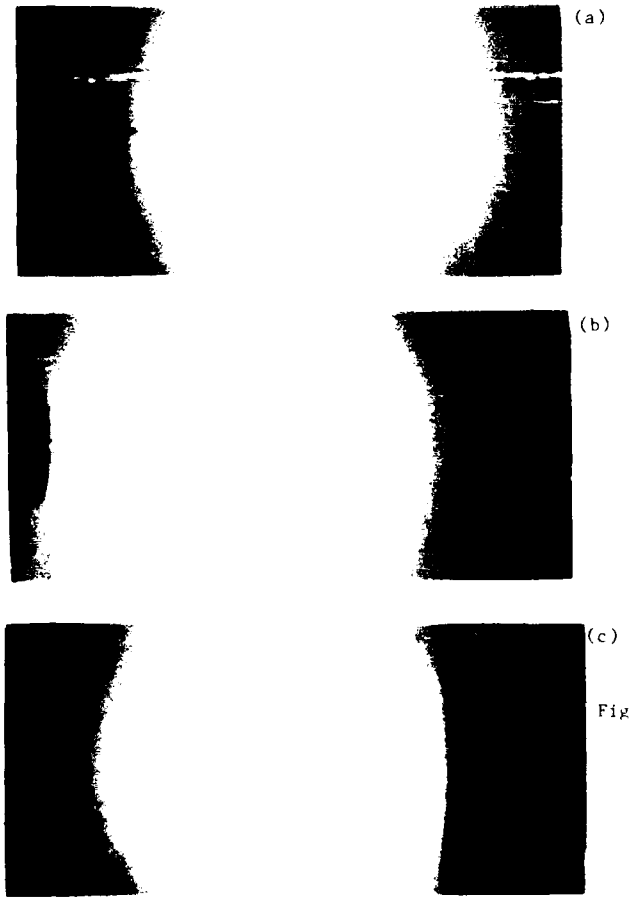

Fig. 3. Cavitation inception in a jet injected from a
(a) (1.27 cm) diameter orifice, σ = 0.155, v = 20.5 m/s
(b) 2.54 diameter smooth nozzle, σ = 0.388, v = 5.9 m/s
(c) 2.54 diameter nozzle with external excitation σ = 0.552, v = 11.9 m/s St = 0.30

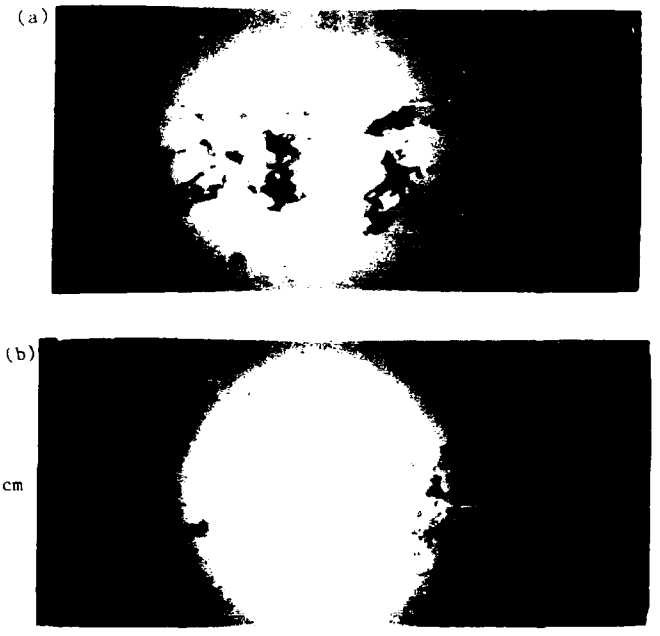

Fig. 4. Cavitation downstream of the 2.54 cm diameter
(a) without external excitation; σ=0.177; V=8.75 m/s
(b) with external excitation; σ=0.257; V=9.8 m/s; St=0.29

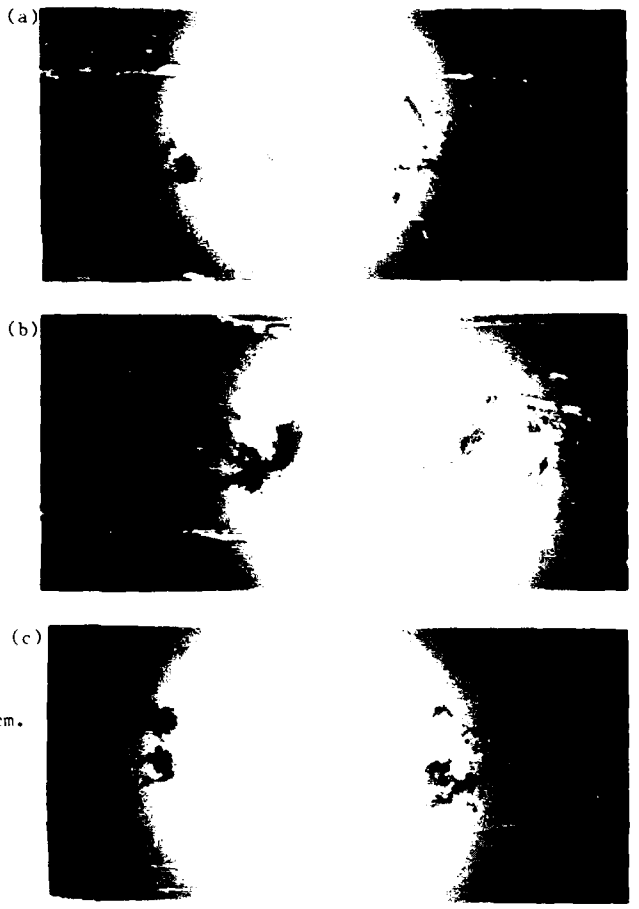

Fig. 5. Cavitation downstream of the 2.54 cm. orifice
(a) without external excitation; σ=0.136; V=15.6 m/s
(b) without external excitation; σ=0.215; V=11.4 m/s
(c) with external excitation; σ=0.35; V=10.0 m/s St=0.39

the appearance of the external cavities. The same phenomenon occured even when the coated region extended only up to about 1 inch (2.54 cm) upstream of the injection point. Thus, the effect of surface roughness on jet cavitation could not be determined. This problem will be corrected in the future by constructing a new nozzle with a carefully roughened internal surface. Figures 6-9 present the values of σ_i measured during the present study. Note that figures 6 and 9 (b) contain 2 scales, one based on the speed at the exit and the other on the velocity at the vena contracta. Before discussing these results, note that inception indices ranging from 0.35 to almost 2.0 were measured in a 1 inch (2.54 cm) diameter jet. Thus, the empirical relationship suggested by Lienhard (1984), that uses the diameter as the only scaling parameter, seems unrealistic. Several trends can be observed from the results. Firstly, the inception indices displayed a general trend of becoming smaller when the jet velocity was increased. In some cases (the short, 3 inch (7.62 cm) long, nozzle and the orifice) σ_i reached a minimum on intermediate speeds at about 28 ft/sec (8.53 m/s) for the nozzle (Figure 7) and at 30 ft/sec (9.14 m/s) for the orifice (Figure 6). Secondly, figure 7 demonstrates that the inception indices of the 6 inch (15.24 cm) long smooth nozzle are much higher than the values measured with the shorter, 3 inch (7.62 cm) long nozzle. Thus, the contour of the injector affected the conditions for cavitation inception. Thirdly, when based on the injection speed, the orifice results are much higher than the values of σ_i of either nozzle. However, when the vena contracta speed is used, the orifice results become comparale, in some cases (without flow straighteners) they are higher and in some (with honeycomb and screens) they are lower. The effect of the flow straighteners (a honeycomb and 2 screens) is visible in all nozzles, but with conflicting trends. They caused a small increase in the inception indices of the short nozzle, a reduction in σ_i of the 1 inch (2.54 cm) orifice and the long nozzle, and had very little effect on the results of the 0.5 inch (1.27 cm) orifice.

The effects of external excitation on

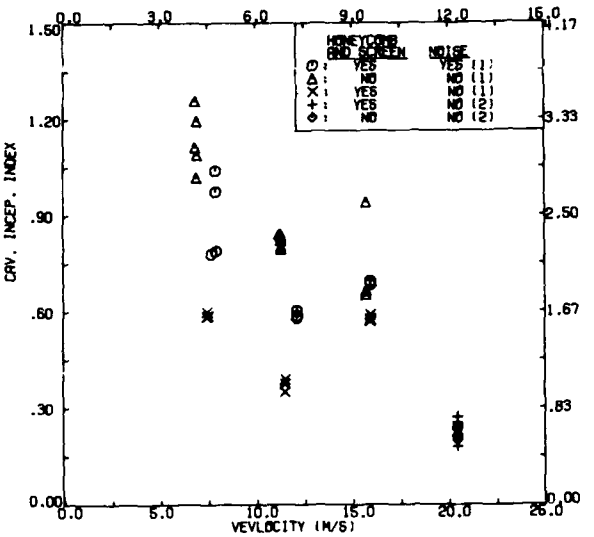

Fig. 6. Cavitation inception indices of the orifice jet. The scales with the higher speeds (lower) and lower σ (left hand side) are based on the velocity at the vena contracta. The scales with lower speed (upper) and higher σ (right hand side) are based on the velocity at the orifice.

the inception indices of the orifice and the nozzle are presented in figures 6 and 8, respectively. Vibrating the pipe upstream of the orifice containing screens and a honeycomb resulted in a substantial increase in the values of σi. These results are in agreement with the trends reported by Johnson et al. (1982), even though the present changes in σi are much more moderate. This trend is not evident in the inception indices of the smooth nozzle (figure 8). Here, the values of σi of an excited jet (with and without flow straighteners) are very close to the results of an unexcited jet with flow straighteners, and lower than the inception indices measured when the screens and the honeycomb are removed.

The effects of varying the concentration of dissolved air in the water are demonstrated in figures 9(a) and 9(b). The inception indices of the nozzle increased substantially in saturated water to more than 2. at low velocities and to about 0.9 at high speeds. These results are in agreement with the trends described by Baker et al. (1976). The orifice results, however, showed much less dependence on the air content, and the values of σi for a concentration of 90 percent of saturation are close to the inception indices measured when the dissolved air content was only 35 percent of the saturation level.

Summary and Conclusions

Several trends, some of them conflicting, were observed during the present study. Firstly, an increase in the free stream

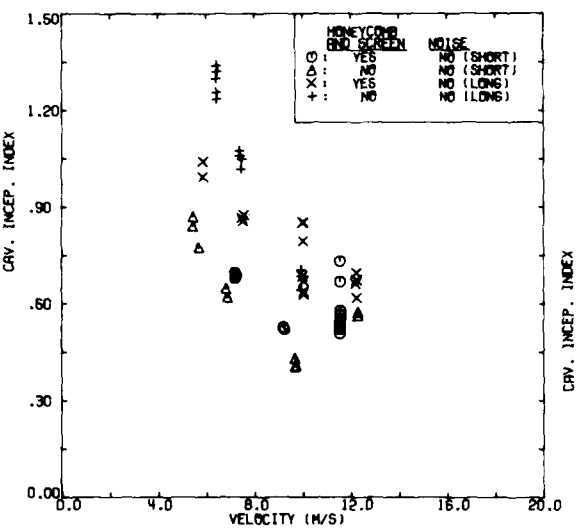

Fig. 7. Cavitation inception indices of the smooth nozzle

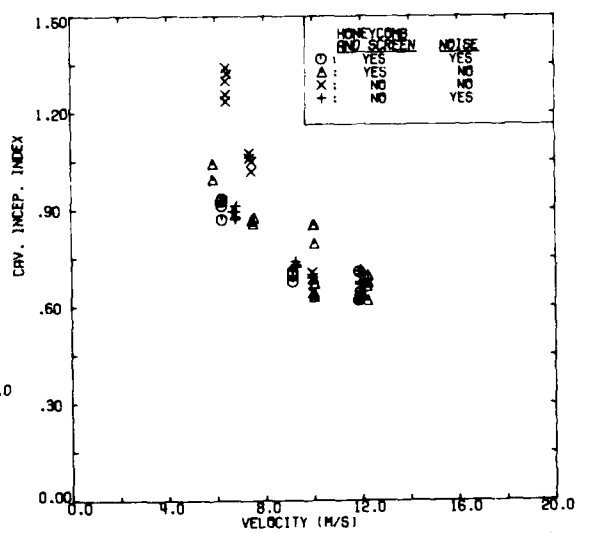

Fig. 8. The Effect of external excitation on the inception indices of the smooth nozzle

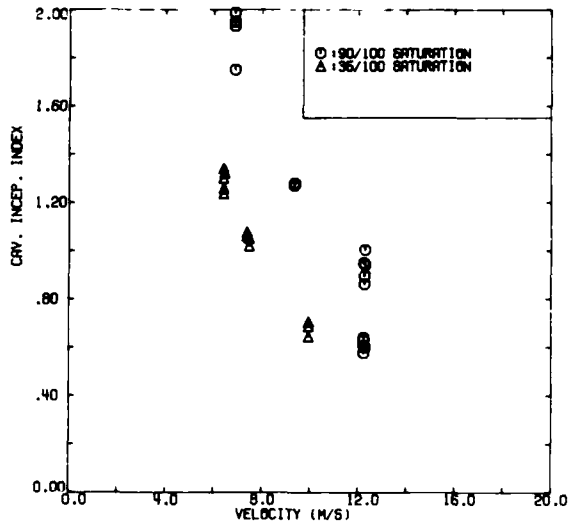

(a)

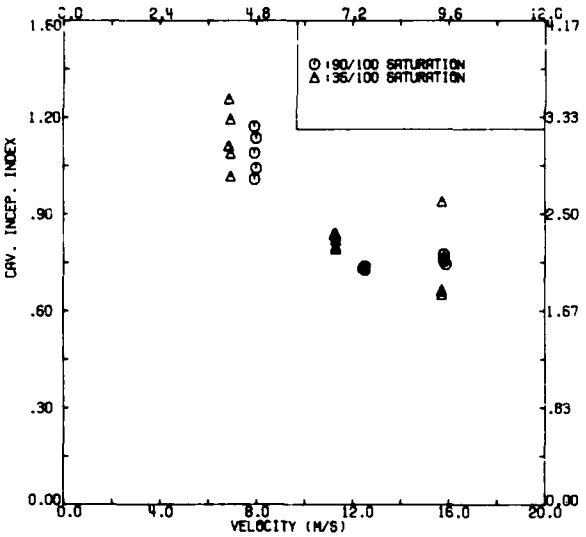

(b)

Fig. 9. The effect of dissoled air content on the inception indices of the
(a) smooth nozzle
(b) orifice (the two different scales are described in figure 6)

velocity resulted in a decrease in the values of σi. Secondly, the nozzle geometry does affect the conditions for cavitation inception, a conclusion that contradicts the results of Baker et al. (1976), but agrees with the measurements of Kobayashi (1967). Thirdly, external excitation of the pipe upstream of the nozzle helped in organizing the jet vortex structures into a series of discrete rings and altered the inception indices. Moreover, changes in the free stream turbulence level (created with the additions of the screen and the honeycomb in the pipe) also affected the values of σi. Finally, an increase in the amount of dissolved air in the water resulted in a substantial increase in the inception indices in some cases and in very little changes in others. These results demonstrate clearly that jet flows are susceptible to background noise, to minor disturbances occuring in the pipes leading to the nozzle (free stream turbulence), to geometrical parameters (nozzle size and shape), as well as to the free stream velocity. The effect of these parameters on the turbulent pressure field in the jet must be determined in order to understand their role in the onset of cavitation.

Acknowledgement

Part of the work described in this report was supported by NSF under contract No. MSM-8451065. The authors would also like to thank the lab technician, T. Cooper, for his dedication and support while constructing the test facility.

REFERENCES

1. Arndt, R. E. A., (1981), "Cavitation In Fluid Machinery and Hydraulic Structures, Annual Review of Fluid Mechanics", Vol. 13, pp. 273-328.

2. Baker, C. B., Holl, J. W., Arndt, R. E. A., (1976), "Influence of Gas Content and Polyethylene Oxide Additives Upon Confined Jet Cavitation in Water", ASME, Cavitation and Polyphase Flow Forum - 1976, pp. 6-8.

3. Ball, J. W., (1960), Discussion to Reference 15, J. Fluid Eng. Vol. 84, No. 1, pp. 6-11.

4. Crow, S. C., Champagne, F. H., (1971), "Orderly Structure in Jet Turbulence", J. Fluid Mechanics, Vol. 48, Part 3, pp. 547-591.

5. Franklin, R. E., McMillan, J., (1980), "Noise Generation in Cavitation Flows. The Submerged Water Jet I", Oxford University, OUEL Report No. 1312/80.

6. Geneoux, P. F., Chahine, G. L., (1984), "Simulation of the Pressure Field Due

to a Submerged Oscillating Jet Impacting on a Solid Wall", J. Fluid Engineering, Vol. 106, December, pp. 491-495.

7. Hussain, A. K. M. F., Zaman, K. B. M., (1981), "The Preferred Mode of the Axisymmetric Jet", J. Fluid Mechanics, Vol. 110, pp. 39-71.

8. Johnson, J. E., Chahine, G. L., Lindermuth, W. T., Conn, A. F., Frederick, G. S., Giacchino, G. L., (1982), "Cavitating and Structures Jets for Mechanical Bits to Increase Drilling Rate", ASME paper No. 82-Pet-13.

9. Jorgenson, D. W., "Noise from Cavitation Submerged Water Jets", J. Acoustical Society of America, Vol. 33, No. 10, pp. 1334-8.

10. Kibens, V.,(1979), "Discrete Noise Spectrum Generated by an Acoustically Excited Jet", AIAA paper 75-0592.

11. Kobayashi, R., (1967), "Effect of Cavitation on the Discharge Coefficient of Standard Flow Nozzles", ASME J. Basic Engineering, Vol. 89, No. 3, pp. 677-685.

12. Lienhard, J. H., (1984), "Cavitation Incipience in Submerged Orifice Flows", J. Fluid Engineering, Vol. 106, December, pp. 496-497.

13. Lienhard, J. H., Goss, C. D., (1970), "Influences of Size and Configuration on Cavitation in Submerged Orifice", ASME paper No. 71-FE-39.

14. Lienhard, J. H., Stephenson, J. M., (1966), "Temperature and Scale Effects Upon Cavitation and Flashing in Free and Submerged Jerts", ASME J. of Basic Engineering, Vol. 88, Series D, pp. 525-532.

15. Numachi, F., Yamabe, M., Oba, R., (1960), "Cavitation Effect on the Discharge Coefficient of the Sharp-Edged Orifice Plate", ASME J. Basic Engineering, Vol. 84, No. 1, pp. 1-6.

16. Ooi, K. K., (1981), "Scale Effects on Cavitation Inception in Submerged Jets", Ph.D. dissertation, Cal. Inst. of Tech., Rep. No. ENG. 183-6.

17. Ooi, K. K., (1985), Scale Effects on Cavitation Inception in Submerged Water Jets: A New Look", J. Fluid Mechanics, Vol. 151, pp. 367-390.

18. Rouse, H., 193, "Cavitation in the Mixing Lane of a Submerged Jet", La Hoiville Blanche, Vol. 8, No. 1, pp. 9-19.

19. Zaman, K. B. M., Hussain, A. K. M. F., (1980), "Vortex Pairing in a Circular Jet Under Controlled Excitation, Part 1. Generai Jet Response", J. Fluid Mechanics, Vol. 101, part 3, pp. 449-491.

CAVITATION OBSERVATIONS IN A TURBULENT SHEAR FLOW

T.J. O'Hern and A.J. Acosta
Department of Engineering and Applied Sciences
California Institute of Technology
Pasadena, California 91125

ABSTRACT

Unlike steady flows past smooth bodies, the chief mechanisms of cavitation inception are not well known in shear flows such as that outside the potential core of a jet, or in the flow past a bluff body with a large separation region. An experimental study of cavitation inception in the turbulent shear layer downstream of a sharp-edged plate is described. Inception takes place in the low pressure cores of streamwise oriented vortices, the secondary vortices of the free shear layer. The role of the secondary vortices may be vital to such shear layer inception phenomena as the commonly observed dependence of the inception index on the body Reynolds number.

NOMENCLATURE

l	spanwise core spacing
P_b	base pressure
P_c	vortex core pressure
P_L	local pressure
P_v	water vapor pressure
P_∞	reference pressure
r_c	vortex core radius
S	distance between sharp edge and stagnation line
U_L	local velocity above shear layer
U_∞	reference velocity far from test body
x	downstream distance from the sharp edge
C_{pb}	base pressure coefficient, given by $C_{pb} = (P_b-P_\infty)/(\frac{1}{2}\rho U_\infty^2)$
Re_S	Reynolds number based on U_L and 2S, given by $Re_S = U_L X 2S/\nu$
ρ	density of water
ν	kinematic viscosity of water
σ_i	cavitation inception index, given by $\sigma_i = (P_\infty-P_v)/(\frac{1}{2}\rho U_\infty^2)$
σ_L	local cavitation inception index, given by $\sigma_L = (P_L-P_v)/(\frac{1}{2}\rho U_L^2)$
Γ_p	circulation of primary vortex
Γ_s	circulation of secondary vortex

1. INTRODUCTION

Shear flows are commonly encountered in many engineering applications, for example in flows past valves and internal flows in piping systems generally, past hydrofoils or in separated flow in the wake of a bluff body. Cavitation inception in such flows is of great practical interest due to the harmful effects of noise, erosion and vibration associated with cavitation. For these reasons, several investigators have undertaken experimental studies of cavitation phenomena in various types of turbulent shear flows. Understanding of cavitation in these flows is complicated by several factors. First, the controlling features of the single phase flow have yet to be determined and are still a topic of much basic research. Second, cavitation phenomena in these flows are ill-suited to laboratory examination because of the commonly observed strong scaling effect. Unlike cavitation in flows around streamlined bodies, inception in shear flows occurs in the freestream, usually far from the test body, due to intense fluctuating pressure peaks in the free shear layer. Measurement of the peak intensity of these pressure fluctuations is needed, but these measurements are very difficult to achieve without disrupting the basic flow.

Pioneering work on cavitation inception and scaling in turbulent shear flows was done by Kermeen and Parkin (1957) in their study of cavitation in the wake of sharp-edged disks. They consistently observed inception in the turbulent shear layer of the disk wake, and a steady increase of inception index with increasing Reynolds number. A coherent vortex structure was visible in the shear layer and they speculated that inception occurred in the vortex cores. Arndt (1978) also conducted cavitation experiments in the wake of a sharp-edged disk with similar results. Cavitation phenomena in the flow past hydrofoils at various angles of incidence were studied by van der Muelen (1980), who also found an increase in inception index with Reynolds number in the high incidence cases when gross flow separation took place. Katz (1984) conducted a study of cavitating flows around several axisymmetric bodies including blunt circular cylinders, and found that inception in the flows around these cylinders occurred in the turbulent separated shear layer, and that pressure fluctuations measured on the surface of the cylinder could not explain

either the large numerical values of the inception index or their Reynolds number dependence. Clearly an investigation of the turbulent shear layer is needed to explain inception in each of these situations.

This close relation between cavitation phenomena and the turbulent flow field leads one to make a closer examination of the single phase case in order to gain insight into the basic flow physics. Turbulent shear flows have been a topic of great interest in the international turbulence community over the past decade; these flows clearly demonstrate the existence of coherent vortical structures, allowing the turbulent flows to be described in a more deterministic manner. Experimental investigations by Bernal (1981) and Jimenez (1983) have provided some insight into the mechanisms of the turbulent structure in plane mixing layer shear flows. The structure is seen to consist of the primary two-dimensional vortices resulting from the Kelvin-Helmholtz instability and containing the basic component of vorticity, while three- dimensional secondary vortices introduce the other two components of vorticity into the flow (Roshko (1980)). Experimental investigations such as those listed above indicate a clear, orderly vortex structure even in high Reynolds number, fully turbulent flows.

This paper presents results of an experimental investigation of the shear flow in the wake of a sharp-edged plate. The goals of this study are to investigate the relation between the turbulent flow field and some of the cavitation phenomena first observed by such investigators as Arndt and Kermeen and Parkin previously mentioned. In particular, the location and appearance of inception will be examined under a variety of flow conditions. The role of Reynolds number scaling will be examined at higher values of the Reynolds number than those of previous investigations. Finally, the effect of changes in cavitation nuclei availability on inception will be examined.

2. EXPERIMENTAL APPARATUS AND PROCEDURES

The facility used was the Caltech Low Turbulence Water Tunnel (LTWT). This tunnel has been specially adapted for cavitation testing through addition of a deaeration system and pressure control using a vacuum pump. Figure 1 is a schematic diagram of the test body used in these experiments, consisting of a sharp-edged plate extending vertically into the freestream and spanning the 12 inch test section. The plate blocks approximately half of the oncoming flow, giving a maximum "local" velocity of about 39 ft/s (12 m/s).

The LTWT test section is enclosed by glass side windows and plexiglass top windows. Inception observations were made under stroboscopic light, maintaining a constant velocity then lowering the pressure until the first traces of cavitation became visible. The pressure transducer reading was then frozen and recorded together with the tunnel velocity to allow calculation of the inception index. The location of the tap for making velocity and pressure measurements (defined as the "local" values) is shown in Figure 1. After inception, the water was recirculated at atmospheric pressure for at least ten minutes in order to maintain a steady population of freestream bubbles, see Katz (1984).

Use of clear test section windows also allows photographic examinations especially useful in capturing random events in fairly high speed flows. Simultaneous top and side photographs were made using a high speed (8 microsecond) flash unit which was fired in the middle of the cameras' shutter opening period. The side view photographs record back lit cavitation bubbles which appear dark against the bright background of the light sources diffused by an opal glass, while the top view sees bright side illuminated cavitation against the dark background of the black anodized test body (see Figure 2). Flow conditions in the photographic studies cover several free stream velocities, cavitation numbers and air content levels. High speed movies were recorded using an Eastman Kodak High Speed motion picture camera at framing rates up to 2500 frames/sec. Top, side and simultaneous views were filmed. Figure 3 shows several individual frames from one of the top view motion pictures. High speed movies were recorded under the same flow conditions as the simultaneous photographs.

A holographic camera system has been developed and used extensively for various water tunnel measurements, including flow visualization (Katz (1984)), measurement of cavitation nuclei distributions and pressure fluctuation measurements using injected air bubbles as pressure sensors (Ooi (1985)). This "holocamera" is used for three-dimensional velocity measurements in the present investigation. A pulsed ruby laser is used as the light source because its short (20-50 nanosecond) pulses are needed to freeze images of small objects passing through the region of interest at high speeds. A Pockels Cell electro-optical Q-switch is used to control the numer and timing of the laser pulses.

The holographic technique in these experiments is the in-line or Fraunhofer technique, in which a single laser beam is used as both reference and subject beam in the holographic recording. This is accomplished by illuminating the sample volume with a collimated coherent light beam, part of which is scattered by objects in the liquid sample volume, while the remainder passes through the volume undiffracted. The hologram is formed by recording the interference of these two beam components on a high resolution film.

Holograms are reconstructed and examined using a reconstruction system, in which a 5 mW He-Ne laser beam illuminates the hologram, which acts as a diffraction grating to form two three-dimensional images of the original sample volume, the real and virtual images. The hologram mount is on a three- dimensional translating carriage allowing examination of the real image in all three dimensions at magnifications up to 220X with the aid of a microscope objective lens and a closed circuit vidicon and monitor. The useful resolution of

the present holographic and reconstruction systems is about 10 microns diameter.

The holocamera is used to measure local three-dimensional velocities by operating the ruby laser in a double-pulsed mode in which two Pockels Cell pulses are applied opening the laser cavity twice. Two laser pulses are then emitted with a precisely determined pulse separation period of from 20 to 500 microseconds. The two laser pulses form two holograms superimposed on a single frame of film, so that the reconstructed image displays three-dimensional displacements of flow tracing particles and bubbles in the flow. These displacements can then be accurately measured, allowing direct calculation of the local three-dimensional velocities in the region of interest. Determination of the relative strength of the two laser pulses is needed in order to determine the direction of motion and therefore of the velocity vector. Double-pulsed holography records three-dimensional motions of objects in a fairly large volume (1.4 liters in the present case), and so is particularly useful in flows in which the region of interest is not well defined and therefore not well suited to such point measuring techniques as Laser Doppler Velocimetry. Figure 4 presents examples of the type of images seen in such holograms.

3. RESULTS AND DISCUSSION

3.1 Flow Field and Turbulent Structure

Examination of a large number of simultaneous top and side photographs of various stages of cavitation, such as those in Figure 2, have clarified several key features of cavitation in this flow. Inception is consistently observed to occur in the form of long, thin "strings" oriented in the streamwise direction as seen from above, and at 45 degrees to the mean flow direction as seen from the side (Figure 2a). These are the cavitating low pressure cores of the streamwise oriented secondary vortices of the free shear layer, occurring in the high strain "braid" region between adjacent spanwise or primary vortex cores. Inception is not observed in the primary vortex cores. At lower cavitation indices, more developed cavitation can be seen in both the primary and secondary structures of the free shear layer (Figure 2b). In each case, cavities act to visualize the flow, allowing examination of the pattern of the coherent vortex structure. The photographs at inception do not indicate either a downstream or a spanwise location of most probable occurrence of inception. Rather, inception is seen to occur at random points throughout the shear layer, although it typically occurs at least one plate height downstream, rather than near the sharp edge in the region of high streamline curvature.

Analysis of the high speed motion pictures allows one to determine the evolution of the flow structures seen in the simultaneous still photos. The same general phenomena are visible in the movies as in the still photos; that is, inceptio.. consistently occurs in the streamwise cores and more extensive cavitation is seen in both these streamwise cores and the cores of the spanwise vortices. , Figure 3 is a sequence of frames taken from one of the high speed movies at inception. Note that this sequence provides evidence of the vortex nature of inception; in the 4 milliseconds between frames (iii) and (v) two distinct cavities grow together to fill in the low pressure vortex core region. As in the still photos, no clear site of most probable occurrence of inception has been seen. Inception events occur at random throughout the shear layer, except that they are generally absent within the first plate height downstream. This random occurrence indicates that the secondary vortices are not determined by such constant factors as possible imperfections of the sharp edge (although every effort was made to protect this) or mean flow non-uniformities. The appearance of cavitation did not noticeably change after cleaning and rearranging the order of the flow conditioning screens, or after removing, re-anodizing and reinstalling the test body.

Preliminary analysis of the motion picture frames shows that in general the streamwise oriented cavities occurring at inception are convected some distance downstream before collapsing, but very few move all the way out of the field of view before this occurs. At low cavitation indices, the spanwise vortex cores become visible very close to the separating edge, appearing as straight linear cavities spanning the test section. The spanwise cores generally lose this sharp definition by the time they have moved about 6 inches downstream (x/S = 1.7), by which time the braid region is often filled with thin, streamwise oriented cavities. Beyond about 8 inches downstream (x/S = 2.3), the spanwise cores have grown considerably, and have lost the clear cavities filling their cores, now appearing as large rotating masses of individual bubbles.

Cavitation cannot be considered as a purely passive visualization technique. Franc and Michel (1983) found a change in vortex spacing and in Strouhal number behind wedges due to changes in cavitation index (20 % change in St for decrease in sigma from 2.0 to 1.1). Detailed study of vortex shedding frequency, or in particular dependence of Strouhal number on cavitation index, have not yet been performed in the present experiment.

The dependence of inception on the secondary vortex structure, with inception consistently occurring in the streamwise oriented vortex cores, is not unique to the present flow. van der Muelen (1980) noted the "irregular threadlike appearance of cavitation" in the separated flow past NACA 16-012 hydrofoils at 16 degree angle of incidence. Franc and Michel (1983) studied the flow around wedges, in which vortices of alternating sign of vorticity are shed off either side. Cavitation in this flow visualized both the large shed vortices as well as thin "three-dimensional rotational filaments" connecting the large vortices, as noted by the authors and clearly visible in their figures. Cavitation in the

separated shear layer around the flat-faced circular cylinders studied by Katz (1984) clearly shows inception occurring in the thin, axially oriented vortices, which remain visible even when more intense cavitation fills in the primary circumferential vortices. Although not mentioned in their paper, close examination of photographs of shear layer cavitation in Kermeen and Parkin (1957) provides evidence that cavitation is present in a similar thin, streamwise oriented structure.

These observations indicate that the secondary vortices appear to control cavitation inception in several types of shear flows. However, very little is known about the strength of these secondary vortices or their dependence on flow conditions. The secondary vortices seem to arise from an instability mechanism, either of the primary vortex structure or due to amplification of upstream disturbances (Bernal (1981)). The secondary vortices are superimposed on the primary structure in such a way that the basic coherence of the spanwise vortices is maintained. Bernal (1981) presents a model of the secondary structure as being composed of organized pairs of counter-rotating vortices. His high speed movies using laser sheet illumination of fluorescent dye in one of the two streams of a plane mixing layer clearly show the existence of streamwise vortices consistent with this model. Bernal found that the pattern and the downstream position of first visibility of the streamwise vortices could be adjusted by changing the velocity for a fixed mixing layer velocity ratio. This velocity dependence may be a key to explaining Reynolds number dependence in shear flows. The random appearance of cavitation in the present investigation, particularly near inception, limits its usefulness as a visualization technique, so that such factors as spacing and pattern of the streamwise vortices measured by Bernal cannot be corroborated with any certainty in the present results.

Estimates of the strength (circulation) of the streamwise vortices were made by modelling them as Rankine vortices. Use of this simple model and several important assumptions allows the vortex strength to be determined from tunnel measurements at inception.

The core pressure of a Rankine vortex is:

$$P_c = P_\infty - \rho[\frac{\Gamma_s}{2\pi r_c}]^2$$

If we assume that the core pressure is equal to the vapor pressure at the time of inception, this expression can be rearranged to:

$$\Gamma_s = 2\pi r_c U_\infty [\frac{\sigma_i}{2}]^{1/2}$$

We further assume that the vortex core radius, r_c, is equal to the radius of the visible cavity at inception. The strength of the vortex core can then be determined by measuring this core radius from photographs or movies at inception, along with the inception index and freestream velocity measurements from inception tests. Results of this analysis are presented in Table I. Also listed are estimates of the strength that a primary core would have if it were located at the same downstream position as the streamwise vortices used in Table I. An estimate of this strength is made using the approximate relation:

$$\Gamma_p = \Delta U \cdot f$$

Determination of the spanwise vortex spacing f as a function of downstream position is made from the high speed motion picture frames, defining the vortex spacing as the measured distance between adjacent braid/x-axis intersections (after Bernal (1981)). Flow conditions were $U_L = 10.8 m/s$, $Re_S = 2.1X10^6$ and $\sigma = 0.4$; typical values for a case of heavy cavitation. The expression for the average vortex spacing using a straight line fit to the measured data points is:

$$f/S = 0.50(x/S + 0.20)$$

This growth rate of vortex spacing is considerably higher than that found by Bernal. This may be due to some vortices not being visualized by cavitation, thus indicating a larger spacing between their neighbors. This seems unlikely as only cases in which the spanwise vortices and adjacent braid regions were clearly marked by cavitation were chosen for measurement. A more plausible explanation is simply the basic differences between the two flows. Bernal's measurements were made in a plane gas mixing layer with Reynolds numbers (based on the vorticity thickness and velocity difference across the layer) of $4.6X10^3$ and $2.5X10^4$, for the two cases studied, with the high and low speed gas stream velocities 10 m/s and 3.8 m/s respectively.

Several important assumptions were made in estimating the strength values in Table I. As mentioned, it was necessary to assume that the vortex core pressure at inception is equal to the liquid vapor pressure. It was also assumed that the vortex core size was given by the measured cavity size, which should be accurate within a proportionality factor and so suitable for order of magnitude estimates. In determining the spanwise strength it was necessary to use the freestream velocity U_L as a measure of the velocity difference across the shear layer, since the velocity of the recirculating region beneath the shear layer is very small and is not measured. Again, this assumption should be acceptable for order of magnitude analysis.

Jimenez et al (1985) estimated the relative strengths of spanwise and streamwise vorticity to obtain:

$$\Gamma_s/\Gamma_p = 0.61 \pm 0.79$$

The scatter is very large, but the mean value shows much stronger relative values of streamwise vorticity than that found using the Rankine vortex model.

The strength of the secondary vortices by the present estimates is on the order of less than 10 percent of the spanwise strength, yet inception is consistently seen to occur in the streamwise rather than in the larger and

stronger spanwise structure, due no doubt to the smaller diameter of these vortices. We attempted to measure the vorticity field by the double-pulsed holographic technique. Figure 4 shows a double-pulsed hologram from such a test along with photographs of reconstructed images showing displacements over the 200 microsecond pulse separation period. Typical results of such measurements are shown in Table II.

While these velocity components demonstrate the three- dimensionality of the turbulent flow, the velocities near the small streamwise cores do not seem high enough to explain inception occurring in these cores rather than the stronger, larger primary cores. Part of the difficulty in making these measurements is the lack of natural tracer particles very close to the cavitating cores, so peak velocities are not captured. Higher tracer concentrations are needed in order to determine such important factors as the tangential velocity as a function of radial distance from the core. Increasing the data rate for these velocity measurements is difficult, however, first because particle addition affects the concentration of available cavitation nuclei, and also because the presence of too many tracers complicates the task of matching up the two images seen in reconstruction.

3.2 Cavitation Inception

Local cavitation inception indices are plotted against the body Reynolds number in Figure 5. The length scale in the Reynolds number is taken to be twice the distance between the knife edge stagnation and separation points in order to allow direct comparison to axisymmetric body results. The present results do not show any clear Reynolds number dependence, although their scatter, and the narrow range of velocities available in the tunnel, prevent determination of any universal trend. A clear dependence of the inception index on the dissolved air content is shown by the present data. The concentration of freestream bubbles in the test facility has been shown to be dependent on the dissolved air content in several previous studies, see Katz (1984) and Ooi (1985).

Figure 6 compares the present results at high air content to those of Kermeen and Parkin (1957) and Arndt (1978) behind sharp-edged disks and those of Katz (1984) in the flow around two different size flat-faced circular cylinders. The present results extend the upper Reynolds number bound of this plot. The present results are of the local cavitation inception indices while the values of the inception index in the other cases are based on the pressure and velocity at infinity, so the axes of Figure 6 are adjusted according to the relation $\sigma_L = (\sigma_i + C_{pp})/(1 - C_{pp})$. Here C_{pp} is the minimum base pressure coefficient which was measured by both Kermeen and Parkin (1957) and Katz (1984) and the average of these is taken to be -0.6. The values of the Reynolds number were also adjusted to the local velocity. Figure 6 indicates that although the present results do not, by themselves, display a clear trend with the velocity, they are in the range of data of previous bluff body observations.

A large scatter is seen in the data obtained in the present tests plotted in Figures 5 and 6. Discussion of possible error sources is given in Katz and O'Hern (1986). The major contribution to the data scatter is the inherent variability of the inception process, requiring the presence of a suitable cavitation nucleus at an instantaneously occurring low pressure point in the flow.

4. SUMMARY AND CONCLUSIONS

It has been made clear by many workers that bluff body shear flows are characterized by a primary spanwise rolled-up vortex and a secondary streamwise vortex structure. The present results show that cavitation is initiated in these secondary vorticies. Holographic measurements reveal strong three-dimensionality of these flows although accurate estimates of the circulation of the streamwise vortices could not be made by this means due to the few tracer particles near them. However, photographic estimates of these core diameters permitted one to make estimates of the primary and secondary circulation intensity for the two vortices; the secondary streamwise vorticity appears to be about 10% of the primary. The inception of cavitation in the secondary vortex is attributed to its much smaller size. There is a wide range of inception index and a strong effect of air content. Over the present range of speed no Reynolds number effect could be deduced although the present results are within the range of previous shear flow results.

This phenomena of shear flow cavitation occurring in streamwise vortices is seen to be widespread and may be expected to occur in many applications of naval hydrodynamics.

5. ACKNOWLEDGEMENTS

This work was supported by the Naval Sea Systems Command General Hydromechanics Research Program administered by the David Taylor Naval Ship Research and Development Center under Contract N00014-75-C-0378. This support is gratefully acknowledged. Thanks are also due to Professor Joseph Katz.

6. REFERENCES

Arndt, R.E.A., (1978), "Investigation of the Effects of Dissolved Gas and Free Nuclei on Cavitation and Noise in the Wake of a Sharp-Edged Disk", Joint IAHR/ASME/ASCE Symposium on Fluid Machinery, Fort Collins, Colorado

Bernal, L.P., (1981), "The Coherent Structure of Turbulent Mixing Layers", Graduate Aeronautical Laboratories, Calif. Inst. of Tech.

Franc, J.P. and Michel, J.M., (1983), "Two- and Three-Dimensional Rotational Structures in

the Cavitating Turbulent Wake of a Wedge", submitted to the Fourth Symposium on Turbulent Shear Flows, Karlsruhe, Germany

Jimenez, J., (1983), "A Spanwise Structure in the Plane Shear Layer", J. Fluid Mechanics, 132, 319-336

Jimenez, J., Cogollos, M., Bernal, L., (1985), "A Perspective View of the Plane Mixing Layer", J. Fluid Mechanics, 152, 125-143

Katz, J., (1984), "Cavitation Phenomena Within Regions of Flow Separation", J. Fluid Mechanics, 140, 397-436

Katz, J. and O'Hern, T.J., (1986), "Cavitation in Large Scale Shear Flows", to appear in ASME J. Fluids Engineering, originally presented as ASME Paper Number 83-FE-33, at ASME Fluids Engineering Conference. Houston, TX, June, 1983

Kermeen, R.W. and Parkin, B.R., (1957), "Incipient Cavitation and Wake Flow Behind Sharp-Edged Disks", California Institute of Technology, Hydrodynamics Lab Report No. 85-4

Ooi, K.K., (1985), "Scale Effects of Cavitation Inception in Submerged Water Jets: A New Look", J. Fluid Mechanics, 151, 367-390

Roshko, A., (1980), "The Plane Mixing Layer, Flow Visualization Results and Three Dimensional Effects", in The Role of Coherent Structures in Modelling Turbulence and Mixing, Lecture Notes in Physics, 136, 208-217, Springer-Verlag

van der Muelen, J.H.J., (1980), "Boundary Layer and Cavitation Studies of NACA 16-012 and NACA 4412 Hydrofoils", 13th Symposium on Naval Hydrodynamics, Tokyo, Japan

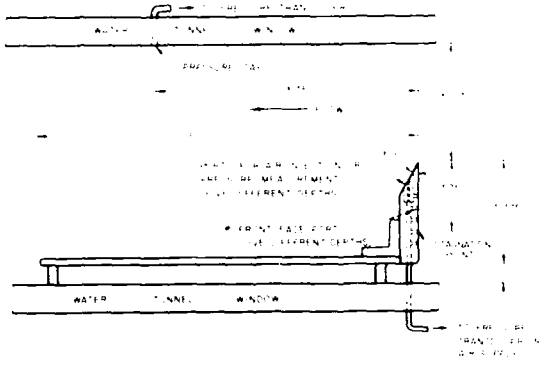

Figure 1. Diagram of sharp-edged plate installed in the Low Turbulence Water Tunnel.

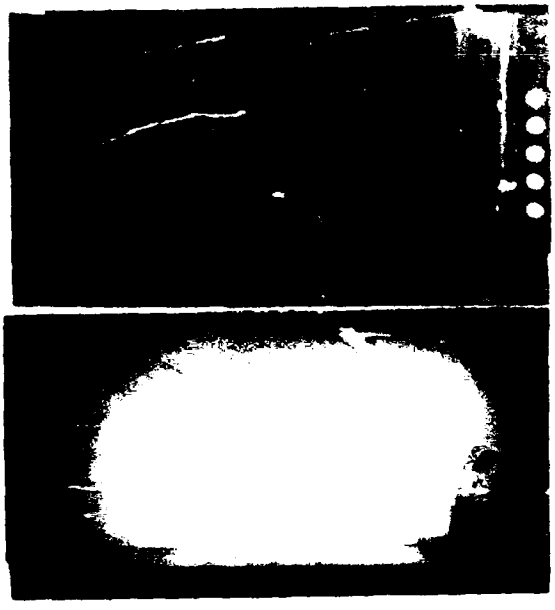

(a)

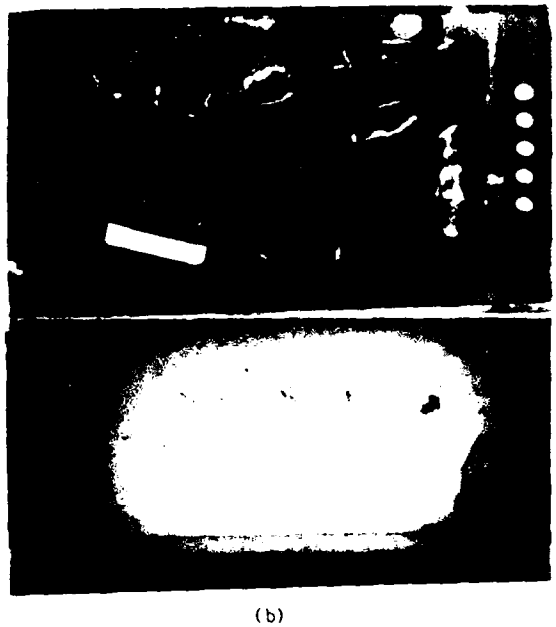

(b)

Figure 2. Simultaneous top and side photographs of free shear layer cavitation
(a) Cavitation inception U_L = 9.4 m/s, σ_L = 1.47 Re_S = 1.84 X 10^6, α = 10.14 ppm

(b) Heavier cavitation U_L = 11.7m/s, σ_L = 0.65 Re_S = 2.2 X 10^6, α = 4.24 ppm

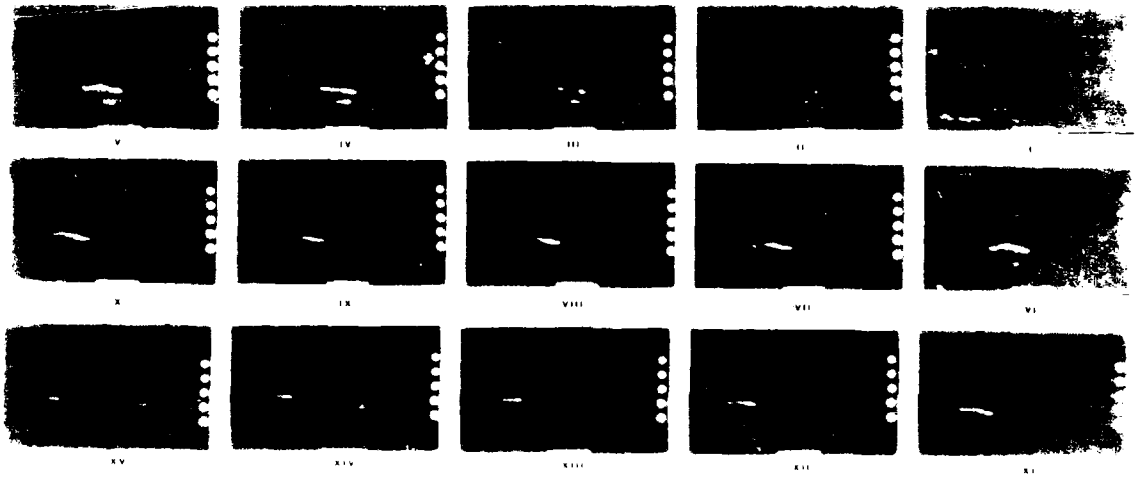

Figure 3. High speed movie sequence showing top view of inception, growth and collapse of an axial cavity. Flow direction is right to left. Note cavity "fills in" vortex core in frames (iii) to (v). Elapsed time between frames is 2 milliseconds. Exposure time is approximately 200 microseconds. Velocity above shear layer is 9.5 m/s, σ_L = 0.88, Re_S = 1.84 X 10^6, α = 4.70 ppm.

Figure 4. Determination of three-dimensional velocity components from double-pulsed holographic images. Center is print of hologram itself, upper photo shows reconstructed image demonstrating translation of 1.7 mm long vortex core, lower photo shows translation of 100 micron diameter bubble. Time separation between laser pulses was 200 microseconds.

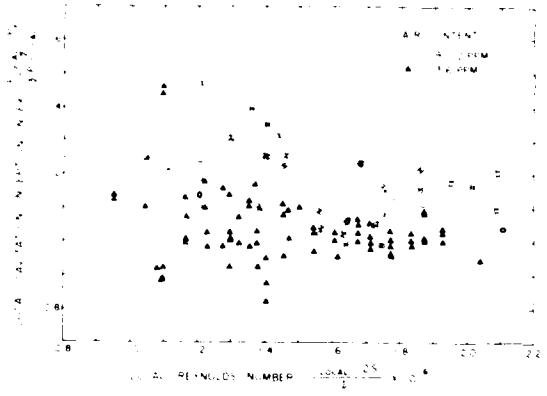

Figure 5. Cavitation inception indices in the free shear layer behind the sharp-edged plate.

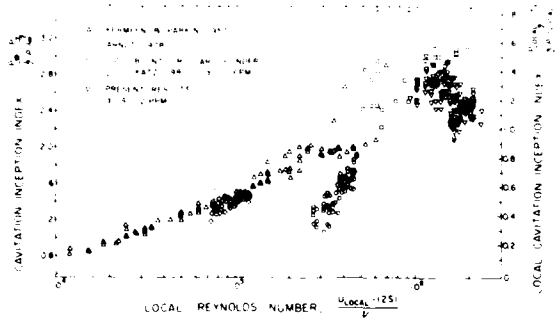

Figure 6. Present cavitation inception indices compared with those of Kermeen and Parkin (1957) and Arndt (1978) for sharp-edged disks, and those of Katz (1981) for two different diameter blunt circular cylinders.

Data pt	U_L (m/s)	Reynolds No. Re_S	Inception Index σ_i	core r_c (in.)	Normalized Downstream Position X/S	Γ_s (m^2/s)	Γ_p (m^2/s)	Γ_s/Γ_p
1	10.4	1.85×10^6	1.02	0.036	4.17	0.04	2.00	0.02
2	10.4	1.85×10^6	1.02	0.019	3.16	0.02	1.54	0.01
3	7.8	1.39×10^6	1.52	0.031	4.58	0.03	1.64	0.02
4	7.8	1.39×10^6	1.52	0.106	3.33	0.12	1.22	0.09
5	9.5	1.68×10^6	1.47	0.056	2.84	0.09	1.27	0.07
6	9.5	1.68×10^6	1.47	0.040	3.07	0.05	1.36	0.04

Table I. Relative strength of spanwise and streamwise vortices. Strength of axial vortices determined using Rankine vortex model and measurements from photographs taken near inception.

Object	Vx(m/s)	Vy(m/s)	Vz(m/s)
125 μm bubble	-0.44	0.44	-2.55
150 μm bubble	3.46	-1.71	-0.86
85 μm bubble	1.68	-0.13	-0.04
145 × 165 μm sheared bubble	2.70	-2.54	-2.70
90 μm bubble	-0.28	0.10	-0.86
110 μm bubble	-0.82	-0.54	-1.98
80 μm bubble	1.08	-0.36	0.55
90 μm bubble	-0.40	-0.49	0.72
140 μm bubble	1.10	-0.21	0.81
160 μm bubble	0	0.54	1.35
vortex core 230 μm long	1.33	0.83	0.60

Table II. Some measured velocity components near one of the streamwise vortex cores. The freestream speed is nominally 7 m/s. Vx is the measured velocity in the direction of flow, Vy is normal (up) and Vz is the spanwise direction. The cavitation index is about 0.5. The three dimensional nature of the flow is clear from various holograms.

SESSION IX
HIGH SPEED VEHICLES AND SAILING

TECHNICAL COMMITTEE MEMBERS

Peter W. Brown (Chairman) Stevens Institute of Technology

A RE-ANALYSIS OF PLANING BOAT PORPOISING STABILITY DATA

P. Ward Brown
Davidson Laboratory
Stevens Institute of Technology
Hoboken, NJ 07030

INTRODUCTION

Towing tank tests of high speed planing craft sometimes result in porpoising and when this happens the tank staff is called on to define the problem and help find a cure. A simple means of checking for the possibility of porpoising would be useful in planning the experimental program. The available experimental data is analyzed in order to develop such a test.

BACKGROUND

The usual method of displaying the porpoising stability characteristics of planing boats is shown on Figure 1. This figure shows the stability trim limit as a function of speed: at high speed the trim must be low enough to avoid porpoising instability. Porpoising is defined as an oscillation in pitch and heave, at a given speed, such that the sustained pitch amplitude is at least one degree.

The usual remedy for power boat porpoising is to decrease the trim by moving the CG forward. However this may not be easy if porpoising is discovered late in the design process, consequently there have been some attempts to provide guidance for the designer and research worker.

Although a number of studies of the porpoising stability of seaplanes have been made there has only been one experimental study of the porpoising of power boats. Day and Haag (1952) at Webb Institute made a systematic study of constant deadrise prismating planing surfaces "to provide the boat designer with useful data on the trim at which porpoising occurs and its dependent variable, the center of gravity..." They succeeded in their primary aim of determining porpoising limits and their results have been presented by Savitsky (1964). The dependence of porpoising on the position of the center of gravity did not yield to their analysis, however, so that it may be of interest to re-examine their data in the light of present knowledge.

ANALYSIS

Day and Haag are to be commended for tabulating their data, thereby fulfilling one of their obligations as responsible scientists to make their results available for others to analyze. For each planing surface (having deadrise angles of 0°, 10.6° and 20.5°) the speed, load and the trim at which porpoising occurs is tabulated. The lift of a planing surface is related to the speed, trim and mean wetted length, therefore if three of these four quantities are known the other may be calculated.

The relationship between planing lift, speed, trim and mean wetted length is referred to as a 'planing equation' and the planing equation developed by Brown (1971) is used: this equation has been shown to give close agreement with dynamic lift data reported by such investigators as Sottorf, Sambraus, Locke, Wadlin, Weinstein, Kapryan, Chambliss, Farshing and Springston. This agreement covers a range of trim angles from 2° to 30° wetted lengths from 1 to 7 beams and deadrise angles from 0° to 50° with provision for transverse curvature.

The most general form of this lifting equation is:

$$C_{L_b} = (\pi/4)\sin 2\tau\cos\tau\left[(1-\sin\beta)\lambda/(1+\lambda) + (C_{D_c}/\pi)\lambda\sin 2\tau\cos\beta + 0.4\sec\tau(\lambda/C_V)^2\right] \quad (1$$

where:
Cross-flow drag coefficient, $C_{D_c} = 1.33$ and

$C_{L_b} = L/\frac{1}{2}\rho V^2 b^2$
$C_V = V/\sqrt{gb}$
λ = mean wetted length-beam ratio
b = beam
τ = trim
β = deadrise

Therefore the mean wetted can be calculated for each entry in the Day and Haag data base. Moreover, given the mean wetted length and speed it is possible to calculate the position of the center of pressure from the formula given by Savitsky (1964), which can be re-stated in the following form:

$$x/y = (54 + 11y^2)/(72 + 33y^2) \quad (2$$

where:

$x = (LCP/Beam)/C_V$

$y = \lambda/C_V$

LCP = longitudinal center of pressure, measured along the keel from the transom.

When this procedure is applied to the Day and Haag data it appears that generally the stability limits correspond to one center of pressure position given by:

$$LCP = 0.65 \text{ (beam)}$$

This finding implies that in order to avoid porpoising the LCG must be at least 65% of the beam ahead of the transom.

In order to test this 65% rule it was assumed to hold and the corresponding trim was calculated from Equations 1 and 2 for each of the loads and speeds tested by Day and Haag, with the result shown on Figures 2 and 3. This process can be illustrated by a worked example.

To calculate the trim corresponding to LCP beam = 0.65 at C_V = 3.0 for a deadrise of β = 10.0° at λ_L = 0.45:

$$x = \frac{LCP \text{ from } C_V}{\text{Beam}} = 0.65/3.0 = 0.233$$

This value of x is used in Equation 2 and the cubic relation is solved to give:

$$y = 1.643$$

$$\lambda = 1.643 \times 3.0 = 4.93$$

Since:

$$\lambda_L = \tau - \frac{\tau^2}{2}$$

$$\tau = \lambda_L + \frac{\tau^2}{2} = 0.45 + \frac{4.93^2}{2}$$

$$= 12.57$$

These values of λ_L, τ and β are substituted in Equation 1 which is solved for trim to give:

$$\tau = 12.57°$$

This process is repeated for each speed and load to generate the stability limits.

The agreement between the experimental data and the stability limits based on the assumption that LCP from Beam = 0.65 seems quite satisfactory. The trend is for the observed [illegible] to be [illegible] than the [illegible] stability limit. [illegible] attempting a particular value of trim for a [illegible] boat, one should err on the [illegible] trim of the boat.

CONCLUSIONS

It is concluded that [illegible] at least 65% of the beam forward [illegible], a power boat may be expected to [illegible].

This applies to planing [illegible] and 30°, for speeds at [illegible] and trim [illegible] of C_V = 2.0 to 5.0.

RECOMMENDATIONS

It is surprising that 30 years have passed since the last experimental study of the coupled heave and pitch motion of planing craft and there remain a certain number of topics yet to be investigated bearing on porpoising instability. These include the effect of moment of inertia, of trim flaps, of deadrise-warping and perhaps of bow shape at low trim.

The early work on porpoising was concerned with seaplane hulls and some similarities have been noted between the forebody of a seaplane and the planing boat. However a seaplane planing on the forebody encounters porpoising at trims less than the stability limit: exactly the opposite is true of the planing hull which porpoises at trims greater than the stability limit. These contradictory experimental findings have yet to be elucidated.

REFERENCES

Day and Haag (1952): "Planing Boat Porpoising" by J.P. Day and R.J. Haag, Thesis presented to Webb Institute of Naval Architecture.

Brown [illegible]: "An Experimental and Theoretical Study of Planing Surface with Trim Flaps," by P. Ward Brown, Davidson Laboratory Report [illegible], April [illegible].

Davitsky (1964): "Hydrodynamic Design of Planing Hulls," by D. Davitsky, Marine Technology, Vol. 1, No. 1, October 1964, pp. 11-95.

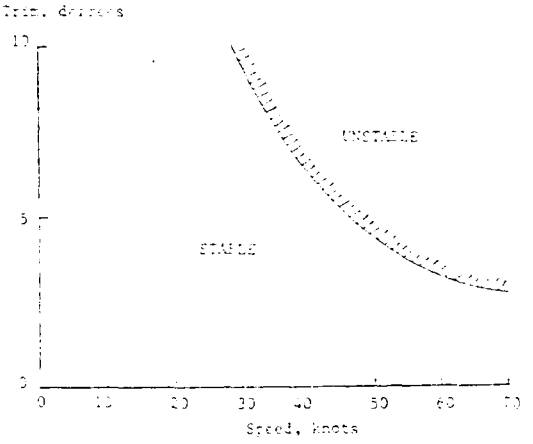

FIGURE 1 TYPICAL PLANING BOAT PORPOISING STABILITY DIAGRAM

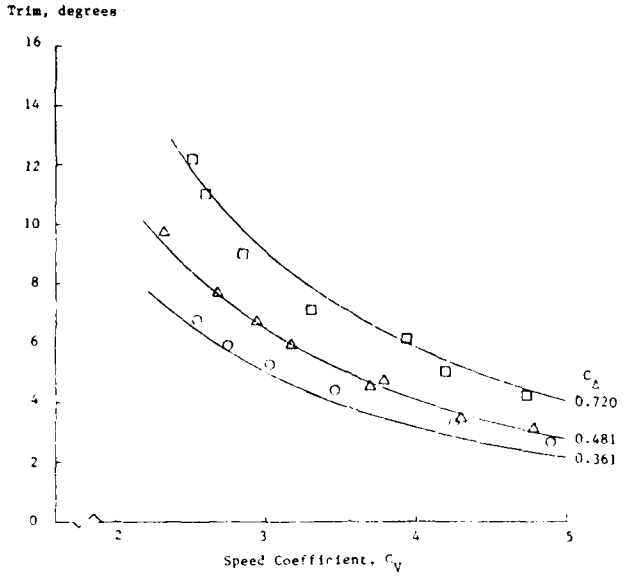

FIGURE 2 COMPARISON BETWEEN CALCULATED TRIM AND PORPOISING DATA, 10.6° DEADRISE

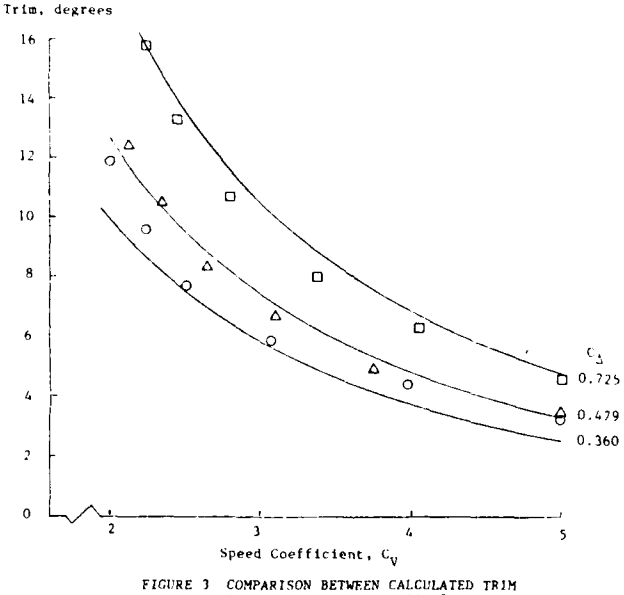

FIGURE 3 COMPARISON BETWEEN CALCULATED TRIM AND PORPOISING DATA, 20.5° DEADRISE

INTERFERENCE EFFECTS BETWEEN PARALLEL PLANING SURFACES AT HIGH SPEED

Daniel Savitsky
Director, Davidson Laboratory
Stevens Institute of Technology
Hoboken, NJ 07030

ABSTRACT

A brief series of tests were conducted to investigate the hydrodynamic interference effects between parallel planing surfaces at high speed. The effect of lateral spacing on the planing area and lift coefficient are presented.

INTRODUCTION

There appears to be a growing world-wide interest in the development of high speed catamaran ferries, yet the open literature contains relatively few references to guide the designer in estimating the hydrodynamic performance of these craft. Many years ago, the Davidson Laboratory conducted a brief study of the interference effects between flat parallel planing surfaces operating at high speeds. This study was then of interest only to the designers of twin-float supported seaplanes and the results were presented in a reader's forum section of the no-longer published Journal of the Aeronautical Sciences (June 1954).

It was considered appropriate to re-examine these data and to present the results to the American Towing Tank Conference whose membership is showing increased interest in high speed planing catamarans. The data presented in this brief report were obtained at very high speed coefficients where the buoyant contribution to lift is small. Nevertheless, the results are quite interesting and can be used as an end-point in eventually developing planing formulations applicable over a wide speed range.

DESCRIPTION OF EXPERIMENTAL STUDIES

In the course of experimental planing investigations conducted at the Davidson Laboratory some 30 years ago, some data were collected on the change in lift and wetted area experienced by a flat planing surface when operating parallel to, and at various lateral distances from another similar surface at identical planing conditions. These data were collected over a limited range of test conditions and hence were not intended to represent a comprehensive study of the interference effects between parallel-running planing surfaces. Nevertheless, it is believed that a presentation of the results will be useful to indicate the type and order of magnitude of the effects to be expected, and the lateral spacing between surfaces for which these effects are important.

A similar interference phenomenon has been considered by the aerodynamicist in the case of two or more wings of high aspect ratio in flight side by side. It can be demonstrated that a resultant upwash velocity is induced by the trailing vortices of one wing on the other giving each wing a larger effective incidence angle, relative to the free stream, than would exist if the two wings were infinitely far apart. This effect naturally results in an increased lift efficiency for each wing.

Tests were made on two 4 inch beam flat surfaces at the planing conditions given in Table 1, with the lateral distances (d) between surfaces varying from 0 to 5 beams. In order to establish an end point a single planing surface was also tested.

Table 1
Test Conditions

C_V*	τ	h	λ_1**
7.50	8°	0.32b	2.60
7.50	8°	0.59b	4.23
7.50	12°	0.25b	1.20
7.50	12°	0.50b	2.40

*$C_V = V/\sqrt{gb}$
**$\lambda_1 = h/b \sin \tau$

The tests were made at a relative high speed coefficients ($C_V = 7.50$), where the buoyant contribution to lift is small. The test procedure was to measure the lift and photograph the wetted bottom area of a single planing surface running alone at a fixed heave and then, keeping all conditions the same, to measure the lift and wetted area when another identical surface was located parallel to and at various lateral distances from the first surface.

RESULTS

Interference Effect on Mean Wetted Length-Beam Ratio

In the case of flat planing surfaces, the mean wetted length-beam ratio (λ) is defined as the distance, *in beams, from* the trailing edge to the stagnation line intersection with the bottom. Reference 1 shows that the running mean wetted length-beam ratio (λ) is 0.30 larger than the mean wetted length-beam ratio measured to the level water intersection with the planing surface (λ_1). This so-called wave rise relation, $\delta\lambda=\lambda-\lambda_1=0.30$, has been found to be generally applicable for $\lambda_1 \geq 1$ over a wide range off trim angles and speed coefficients and includes the test conditions reported herein. The effects of the upwash velocities, resulting from the interference phenomena, on the wave rise can be seen in Figure 1, where the quantity $\delta\lambda$ is plotted against separation distance. In this plot, the beam (b) of one surface is used as the non-dimensionalizing factor. The data for the test trims and wetted lengths collapse on a single curve fairly well and indicate a wave rise variation starting from a value $\delta\lambda = 0.30$ at about three beams spacing and increasing to $\delta\lambda = 0.60$ at zero beam spacing. At this zero spacing end point, the wave rise is in agreement with the original relation $\delta\lambda = 0.30$ if, in this case, the wave rise is expressed in terms of the geometric beam of the combination of surfaces, 2b.

Interference Effect on Lift Coefficient

A plot illustrating the experimental variation in lift with lateral distance between two flat surfaces planing side by side is given in Figure 2. The ordinate of this plot is the ratio of the actual measured lift (Δ_1) for one flat plate running parallel to another flat plate at identical conditions of trim, speed, and depth of immersion, to the lift (Δ) for one surface planing alone at the same trim, speed, and depth of immersion. It is seen that Δ_1 is always greater than Δ. This fact may be attributed, essentially, to two interference phenomena--one is the influence on lift of the change in upwash velocity, while the second is the influence on lift which results from the wetted length change, as discussed in the previous section.

The collected test data collapse on a single curve very well and, similar to the wetted length variation, there is a lift increase on each surface, due to proximity effects, for separation distances between zero and three beams. At spacings greater than three beams between surfaces, the interaction effects are negligible. When both surfaces are in contact with each other (zero beam spacing), the test data show the lift increase to be approximately 47 percent. This end point is in agreement with the results that would be obtained by substituting the present test parameters into empirical planing lift equations given in Reference 1. For values of λ outside the present test range some change in the lift interference curve of Figure 2 is expected. The ratio Δ_1/Δ at the end point d = 0 can be calculated for these values of λ by using the lift equations of Reference 1.

It is not expected that the curve of Figure 2 will be applicable for low speed coefficients, where the buoyant contribution to lift is appreciable, since, at zero velocity, where the entire load is supported by buoyant forces, there is obviously no variation of lift with lateral spacing between the surfaces.

As stated above, one contribution to the lift on a planing body in proximity to another results from a wetted length change. It was found that, for the conditions tested, consideration of the effect of increased wetted length alone could accounts for approximately 15 percent of the total lift increase at any lateral spacing of the surfaces. Thus, the change in upwash velocities is of primary importance in affecting the lift on planing surfaces operating side by side.

REFERENCES

Savitsky, Daniel: Hydrodynamic Design of Planing Hulls. Marine Technology, Vol. 1, No. 1, October 1964.

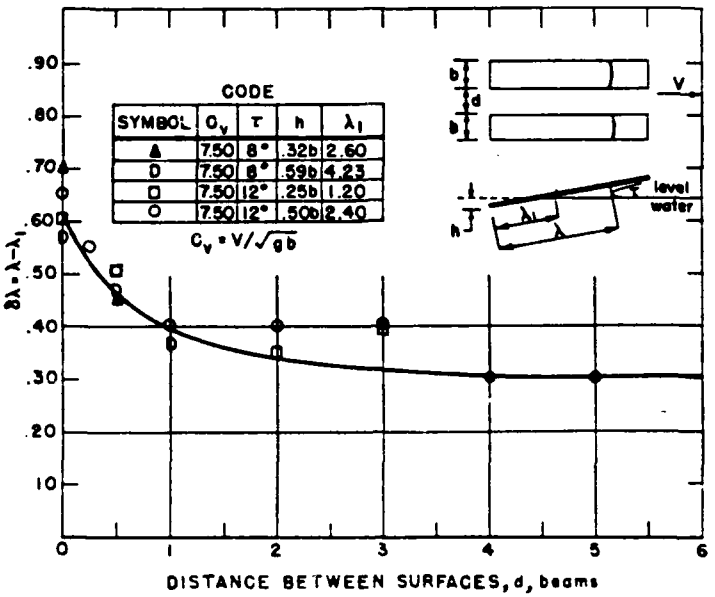

FIG. 1 WAVE RISE INTERFERENCE BETWEEN TWO FLAT SURFACES PLANING PARALLEL TO EACH OTHER

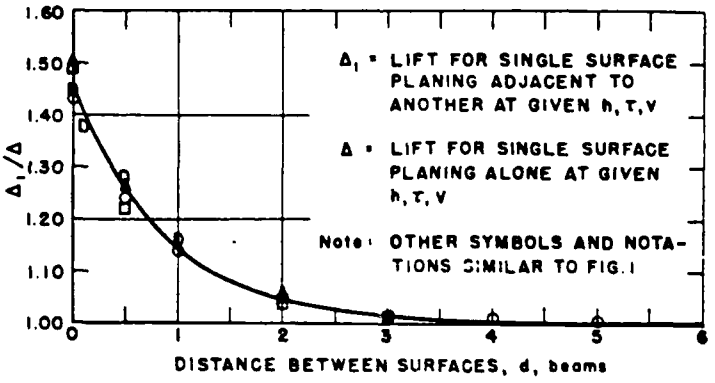

FIG. 2 LIFT INTERFERENCE BETWEEN TWO FLAT SURFACES PLANING PARALLEL TO EACH OTHER

DEVELOPMENT OF THE UNO-SEAKEEP P.C. PROGRAM FOR PLANING HULL SEAKEEPING ESTIMINATION

BY

J. R. BROUSSARD, C. WAGNER, and R. LATORRE

SCHOOL OF NAVAL ARCHITECTURE AND MARINE ENGINEERING
UNIVERSITY OF NEW ORLEANS, P.O. BOX 1098
NEW ORLEANS, LOUISIANA 70148

ABSTRACT

The requirement for planing hulls with both speed and good behavior in the seaway require continual evaluation of the planing hull during the design. While this can be done using graphical aids and empirical equations, it is useful to develop a computer program to perform these evaluations. This paper describes the background, development, and verification of the UNO-SEAKEEP P.C. program for estimating planing hull added resistance, heave, pitch, and acceleration at the center of gravity and bow. For the prismatic hull test data the program gives close prediction of the model test data. However, the evaluation using data from two planing hull models indicate the prismatic hull form estimates are twice the value for the added resistance, heave and pitch motions. Further measurements are recommended to clarify this point.

NOMENCLATURE

b = average beam (ft)

β = average deadrise angle (deg)

C_Δ = displacement coefficient

Δ = displacement (lbs)

E = added resistance correction factor

F = heave and pitch trim correction factor

G = heave and pitch deadrise correction factor

$h_{1/10}$ = 1/10 highest heave amplitude (ft)

$H_{1/3}$ = significant wave height (ft)

ℓ = length of bow section (inches)

L = overall length (ft)

n_{bow} = bow acceleration (g)

n_{CG} = center of gravity acceleration (g)

R_{AW} = added resistance (lbs)

τ = trim angle (deg)

V = speed (kts)

Δ = displacement (lbs)

γ = specific weight of water, 64 lbs/Ft^3 for salt water; 62.4 lbs/Ft^3 for fresh water.

$\phi_{1/10}$ = 1/10 highest pitch amplitude (deg)

1. INTRODUCTION

In response to the need for planing craft with good speed and seakeeping capabilities, a number of experimental studies in both regular and irregular waves were reported by Fridsma (1969, 1970), van den Bosch (1974) and Long-Wen (1985). Fridsma (1970) and Savitsky (1971) presented a graphical design aid based on the irregular wave tests which is denoted here as Method I and later Savitsky and Brown (1976) published empirical formulas which are denoted here as Method II. The test data regular wave test were used by Zarnick (1978) in the development of his computer program for estimating the behavior of a prismatic hull in regular waves.

These and other studies have focused the need for obtaining a balanced planing hull design with good speed and good seakeeping capabilities. Savitsky (1968, 1972) and Payne (1984). This evaluation can be done in two steps:

Step 1. Calm Water Planing Resistance Estimation
For example Blount and Fox (1976)
Given Speed V, displacement Δ, beam b, hull deadline β, longitudinal center of gravity from transom LCG, and vertical location from keel VCG, as well as shaft line location and angle ϵ.

Determine

i) Trim angle τ
ii) Towing resistance R_T

Step II. Response in Irregular Seaway
Assume: Irregular seaway described by the Pierson-Moskowitz Spectrum for long crested waves.

Given 1/3 highest wave height, $H_{1/3}$, data and results from Step I.

Determine (Fig. 1)

II-1 Added resistance in waves, R_{aw}

II-2 Average acceleration at vessel C.G., $\eta_{C.G.}$

II-3 Average acceleration at vessel bow, η_{bow}

II-4 1/10 highest heave amplitude, $h_{1/10}$

II-5 1/10 highest pitch amplitude, $\phi_{1/10}$

Method I can be used to determine the values II-1 through II-5. Method II allows the evaluation of II-1 within ± 20% as well as II-2 and II-3 within ± 0.2g. Since it is necessary that the designer have experience in evaluating both the resistance and seakeeping behavior, a 1 semester student project for developing a P.C. program for planing craft seakeeping evaluation was initiated in NAME 4151 Small Craft Design (Fall 1985). The purpose of this project was to develop a P.C. program for teaching planing craft seakeeping as well as providing a basis for future project work.

The resulting program called UNO-SEAKEEP is the subject of this paper. The program is based on Method I with the graphical aids being approximated by files and read by interpolation routines. Additional routines are provided to calculate the corresponding value of II-1, II-2 and II-3 using the equations of Method II.

This paper covers the following:

1. Brief introduction of Method I and II for planing hull seakeeping estimation
2. Organization of UNO-SEAKEEP Program and
3. Verification of the UNO-SEAKEEP Program
   - 3-a. Verification with hand calculations of program calculations
   - 3-b. Comparison of computer predictions with prismatic model test data
4. Comparison of computer prediction with typical planing craft hull test data.

2. METHOD I AND METHOD II

The basis for Methods I and II are the systematic model studies of the prismatic planing hull in Fig. 1 with the mathematical defined bow (and later a conventional bow) Fridsma (1969). The tests were made at V/ L = 2 through 6; beam loading coefficient $C_\Delta = \Delta / \gamma b^3 = 0.38 - 0.72$; with LCG = 0.54 to 0.68 L aft of the bow stem. The responses were measured during tests in Pierson-Moslowitz sea spectra having significant wave heights of 0.22, 0.44 and 0.66 of the beam.

TABLE I. Range of Applicability of Prediction of Planing Hull Behavior in Irregular Seaway.

Calculation Parameter	Method I	Method II	SEA-KEEP
$\Delta/(L/100)^3$	--	100-250	--
$C_\Delta = \frac{\Delta}{\gamma b^3}$	0.3-0.9	--	0.4-1.00
L/b	3-6	3-5	3-6
τ Deg	3-7	3-7	3-7
β Deg	10-30	10-30	10-30
$H_{1/3}/b$	0-0.8	0.2-0.7	0.2-0.6
$V_k/\sqrt{L}$	0 -6	2-6	2-6

Seven Design Parameters Required:
Displacement Δ, Overall length L, Average beam b, Average deadrise β, Speed V_k, Smooth water trim τ, Significant wave height (1/3 higher of wave height using a long crested Pierson-Moskowitz Spectrum) $H_{1/3}$

The prismatic hulls tested had deadrise angles $\beta = 10^o$, 20^o, 30^o and L/B = 4 and 5.

The tests were conducted at constant speed rather than constant thrust and the tests were arranged to assure at least 75 individual wave encounters to provide a satisfactory data sample for statistical analysis.

2.1 Method I Fridsma (1970) and Savitsky (1971)

Method I is a calculation scheme for determining the added resistance R_{aw}, average acceleration at the vessel C.G. and bow, $\eta_{C.G.}$, η_{bow}, as well as the 1/10 highest heave and pitch amplitudes, $h_{1/10}$ and $\phi_{1/10}$ for a planing hull in irregular waves. They are characterized by the significant wave height denoted by $H_{1/3}$. The design aids consist of 24 charts and appropriate correction equations.

Seven design parameters are required to use the charts which are summarized in Table I (refer Fig. 1) along with the valid range for the calculation parameters used in each method. In Method I the displacement and overall length are the design values, while the average values for the beam, and deadrise angle are taken over the aft 80% of the planing hull. This enables the estimation of the various parameters given below.

2.1.1 Added resistance in waves R_{aw}

The results of the added resistance in waves (R_{aw}) are summarized in charts giving:

$$\frac{R_{aw}}{\gamma b^3} = f_1 (\tau, \beta, H_{1/3}/b, C_\Delta = 0.60 \text{ and } L/b = 5)$$

$$\left(\frac{V}{\sqrt{L}}\right)_{max} = f_2(t, s, H_{1/3}/b, C_\Delta = 0.60 \text{ and } L/b = 5)$$

$$\left(\frac{R_{aw}}{R_{aw}}\right)_{max} = f_3(H_{1/3}/b, V/V_{max}, C_\Delta = 0.60 \text{ and } L/b = 5)$$

where $V/V_{max} = \left(\frac{V}{\sqrt{L}}\right) : \left(\frac{V}{\sqrt{L}}\right)_{max}$

Corrections are then introduced for the case of $C_\Delta \neq 0.6$ and $L/b \neq 5$

$$\frac{R_{aw}}{\rho b^3} = \left(\frac{R_{aw}}{R_{aw}}\right)_{max} \times \left(\frac{R_{aw}}{\rho b^3}\right)_1 \times$$

$$L/V\sqrt{L}, C_\Delta, L/b, H_{1/3}/b) \quad (2.1)$$

where

for $L/\sqrt{L} = 2.0$

$$E = 1 + \frac{(1.6b)^2}{75} - 1)(1 + 0.895 H_{1/3}/b - 0.6) \quad (2.2)$$

for $L/\sqrt{L} = 4.0$

$$E = 1 + 10 H_{1/3}/b)(C_\Delta/0.6 - 0.3) \quad (2.3)$$

for $L/\sqrt{L} = 6.0$

$$E = 1 + 2 H_{1/3}/b)(0.6 - 0.6/0.7)(C_\Delta - 0.6)^2) \quad (2.4)$$

2.1.2 Heave and Pitch $H_{1/3}$ and $\theta_{1/3}$

The results of the heave and pitch measurements are also utilized in charts giving

$$\eta_{1/3} = f_4(L/\sqrt{L}, H_{1/3}/b, L/b = 4, L/b = 5,$$

$$\tau = 0°, \beta = 20°)$$

$$\theta_{1/3} = f_5(L/\sqrt{L}, H_{1/3}/b, L/b = 4, L/b = 5,$$

$$\tau = 0°, \beta = 20°)$$

Corrections are then introduced for the case when $\tau \neq 0°$ and $\beta \neq 20°$

$$\eta_{1/3} = \eta_{1/3}(\beta = 20°) \times \eta_{1/3}(\beta = \text{actual}) \times$$

$$\tau, V/\sqrt{L} \text{ and } L/\sqrt{L}) \quad (2.5)$$

where

$$F = 1 + \frac{\tau^2\sqrt{L}}{24} \quad (\tau = 4°) \quad (2.6)$$

$$G = 0.56 + 0.11 \tau\sqrt{L} + 0.11\left(\frac{\tau}{10}\right)^2(1 - \frac{V/\sqrt{L}}{4}) \quad (2.7)$$

for $V/\sqrt{L} = 0$

for $V/\sqrt{L} \geq 4$

2.1.3 Accelerations at Bow and Center of Gravity η_{bow} and η_{CG}

The results of the acceleration measurements at the center of gravity η_{CG} and η_{bow} are also utilized in charts giving

Table II. Sample File Organization for $x = f(y)$ type graph (Fig. 2)

Counter	$H_{1/3}/b$	$x = V/\sqrt{L}_{max}$	$y = R_{aw}/R_{aw}$
1	0.2	0	0
2	0.2	0.16	0.11
3	0.2	0.36	0.38
4	0.2	0.48	0.43
5	0.2	0.60	0.66

$$\eta_{CG} = f_6(H_{1/3}/b, L/\sqrt{L}, \frac{V}{\sqrt{L}}, L/b = 4, L/b = 5,$$

$$\tau = 4°, \beta = 20°)$$

$$\eta_{bow} = f_7(H_{1/3}/b, L/\sqrt{L}, L/b = 4,$$

$$L/b = 5, \tau = 4°, \beta = 20°)$$

Corrections are then introduced for the case when $\tau \neq 4°$, $\beta \neq 20°$

$$\eta_{CG} = \eta_{CG}(\tau = 4°, \beta = 20°) \times \frac{\tau}{4} \times \frac{\beta}{20} \quad (2.8)$$

For vessels with increased deadrise aft at the bow, the ratio $\eta_{bow}/\eta_{CG} = 1.85$ is adopted.

2.2 Motions of Sea Keeping and Brown (1976)

As explained in the introduction, Salvesen and Brown (1976) published empirical formulae for vertical R_{aw} and η_{bow} which I also tested here. The data is compiled from model tests carried out in the towing tank of the Institut für Schiffbau der Universität Hamburg. The data is compiled in such a way that the added resistance in waves at the ship's bow is given as a function of draft and the bow ordinate of the waterline. The following parameters are used:

Δ = displacement

R_{aw} = added resistance in waves

ρ = density of water

g = acceleration of gravity

ζ_a = wave amplitude

ω = circular frequency of encounter

B = ship's breadth

L = ship's length

C_B = block coefficient

∇ = displacement volume

α = angle between the bow contour line and the centerline plane

y = ordinate of the waterline at the bow

T_F = draft at the forward perpendicular

T_A = draft at the aft perpendicular

T = mean draft

λ = wavelength

ω_e = circular frequency of encounter

$$\omega_e = \omega + \frac{\omega^2}{g} V \cos\beta \quad (2.9)$$

β = angle between the ship's course and the direction of wave propagation

V = ship's speed

ω = circular frequency of the waves

$$\omega = \sqrt{\frac{2\pi g}{\lambda}} \quad (2.10)$$

For head seas ($\beta = 180°$) and $\lambda/L = 1.0$

$$\omega_e = \sqrt{\frac{2\pi g}{L}} + \frac{2\pi}{L} V \quad (2.11)$$

For $\lambda/L = 0$

$$\omega_e = \frac{2\pi}{L} V \quad (2.12)$$

$$\frac{R_{aw}}{\rho g \zeta_a^2 B^2/L} = \frac{1}{2}\left(\frac{\omega_e V}{g}\right)^2 \sqrt{\frac{B}{L}} \left(\frac{T_F}{B}\right)^{1/2} \left(\frac{T_A}{B}\right)^{1/2} \left(\frac{\nabla}{B^3}\right)^{1/3} \left(\frac{\rho g B^3}{\Delta}\right)^{2/3} \left(\frac{L}{B}\right)^{1/2} \left(\frac{y}{B}\right)^2 \sin^2\alpha \quad (2.13)$$

For $\lambda/L = 1.0$ and $\beta = 180°$ (head seas)

$$\frac{R_{aw}}{\rho g \zeta_a^2 B^2/L} = \frac{1}{2}\left(\sqrt{\frac{2\pi g}{L}} + \frac{2\pi}{L} V\right)^2 \sqrt{\frac{B}{L}} \left(\frac{T_F}{B}\right)^{1/2} \left(\frac{T_A}{B}\right)^{1/2} \left(\frac{\nabla}{B^3}\right)^{1/3} \left(\frac{\rho g B^3}{\Delta}\right)^{2/3} \left(\frac{L}{B}\right)^{1/2} \left(\frac{y}{B}\right)^2 \sin^2\alpha \quad (2.14)$$

Equation (2.14) is plotted in Fig. 3.

Table III. Sample File Organization for Two Input Type Graph (Fig. 3)

Parameter $H_{1/3}/b$			X^*	$(R_{aw}/\gamma b^3) = Y$
#1	0.6	5	10	2.14	0.0491
#2	0.6	5	15	3.07	0.0484
#3	0.6	5	20	3.97	0.0469
#4	0.6	5	25	4.99	0.0435
#5	0.6	5	30	5.98	0.0367
#6	0.6	4	10	3.08	0.0539
#7	0.6	4	15	4.02	0.0526
#8	0.6	4	20	5.01	0.0506
#9	0.6	4	25	5.97	0.0476
#10	0.6	4	30	6.99	0.0414

X^* is a dummy variable for interpolation routine.

... the acceleration of Center of Gravity ... and ...

... were obtained for average ... at aw and center of gravity. ... in units ...

... (2.12)

... precision ± 0.2):

$$\ldots \frac{5.2}{\ldots} \frac{\ldots - 2.85}{\sqrt{L}} \quad (2.13)$$

... Precision ± 20 percent ... Impact Accelerations: ... highest acceleration, ... to the average acceleration ...

$$\ldots + \log_2 N_0 \quad (2.14)$$

... 10-highest ... 10-highest ... 2.1 and 3.5 times the ... acceleration.

... SEAKEEP P.C. PROGRAM

... initialize the project the desired ... stated as a P.C. program which ... the planing hull behavior to be ... using both Method I and Method II. ... set in a user-friendly program ...

... Single calculations with Method I ... Parametric calculations with Method I ... Single calculations with Method II ... Parametric calculations with Method II

... Method I, the main task became the conversion ... Parts 5 through 7 into files ... interpolation. These charts can ... categorized as:

... fixed type as in Fig. 2 ... Y = ... as in Fig. 3.

... Organization for Y=fixed Charts

... Y = fixed type is straight-... or ... In this case straight ... were used such that $X_1 < X_0 < X_2$ the ... value of Y_0 is obtained by

$$Y_0 = \frac{(X_0 - X_1)(Y_2 - Y_1)}{X_2 - X_1} + Y_1$$

To enable this interpolation the files were arranged as in Table II which corresponds to Fig. 2:

$$\left(\frac{R_{aw}}{R_{aw\,max}}\right) = f_3(H_{1/3}/b = 0.6, \ldots, L = \ldots)$$

L/b = 5) ... $y = f_3(x - x^*_{max})$ ...

3.2 File Organization for Two Input Y-fixed Charts

An example of the two input ... chart is shown in Fig. 3-a. In order to ... this graph a dummy variable ... each point is defined by ... obtained when digitizing the graph. ... resulted in the file organization in Table ... which corresponds to Fig. 3-b.

3.3 Program Organization/Instructions

To use the SEA-KEEP the following sequence is to be followed:

1. Turn on P.C. and enter ...
2. Depress Caps key.
3. Insert the SEAKEEP diskette.
4. Obtain the A> prompt, type ... hit ENTER_↵.
5. Type SEAKEEP, hit return, ... main menu.
6. Select the desired option, ... the following key:
   1 = Method I single calculation
   2 = Method I parametric calculation
   3 = Method II single calculation
   4 = Method II parametric calculation
   5 = Return to DOS
7. Input data as follows:
   A. Displacement (lbs) ? 525_↵
   B. Length overall (ft) ? ---_↵
   C. Average Beam (ft) ? 11.5_↵
   D. LCG Average aft draft(ft) ? ---_↵
   E. Speed (kts) ? ---_↵
   F. Sig. ht. water running trim and ? ---_↵
   G. Significant wave height (ft) ? 3.0_↵
      Fresh or salt water (F=Fresh, S=Salt) ? S_↵
8. If activity ... read in Step 6 was ... 4 'do method repeats the with ... parameter:
   Parameter you want to vary (4 - 6) ? ---_↵
   Lower ... ? ---_↵
   Upper ... ? ---_↵
9. If activity selected in step 6 ...
   #1 Expect to wait 1.5 min.
   #2 Expect to wait 30 min.
   #3 Expect to wait 2 seconds
   #4 Expect to wait 30 seconds

Note: Program is not ... compiled and ... with Zenith 100 P.C. ... hardware.

TABLE IV
SUMMARY OF DATABASE

Model Test No.	Disp. Lbs.	L ft	b ft	V kts	β Degrees	τ Degrees	H 1/3 ft
3	15.795	3.75	0.75	7.669	10	4.00	0.1667
4	15.795	3.75	0.75	7.746	10	4.00	0.3333
6	15.795	3.75	0.75	11.580	10	4.00	0.1667
18	15.795	3.75	0.75	7.27	10	6.00	0.3333
21	15.795	3.75	0.75	7.746	20	4.00	0.3333
22	15.795	3.75	0.75	7.785	20	4.00	0.1667
28	12.636	3.75	0.75	7.669	20	4.00	0.1667
30	15.795	3.75	0.75	11.561	20	4.00	0.3333
31	15.795	3.75	0.75	11.560	20	4.00	0.1667
34	15.795	3.75	0.75	7.707	20	4.00	0.1667
35	15.795	3.75	0.75	7.785	20	6.00	0.3333
39	15.795	3.75	0.75	3.912	20	6.00	0.1667
40	18.954	3.75	0.75	7.727	20	4.00	0.1667
41	18.954	3.75	0.75	7.765	20	4.00	0.3333
44	18.954	3.75	0.75	11.580	20	4.00	0.1667
45	12.636	3.00	0.75	6.894	20	4.00	0.1667
46	12.636	3.00	0.75	6.946	20	4.00	0.3333
51	12.636	3.00	0.75	10.340	20	4.00	0.1667
52	12.636	3.00	0.75	10.392	20	4.00	0.3333
* 60	12.636	3.00	0.75	10.392	20	4.00	0.1667
* 65	12.636	3.00	0.75	6.911	20	4.00	0.3333
Hull 114A	102.520	7.09	1.42	8.763	24	4.20	0.6463
Hull 114B	134.561	7.09	1.42	12.226	24	4.80	0.6463
Hull 115A	102.520	7.09	1.42	8.763	24	3.60	0.6463
Hull 115B	134.561	7.09	1.42	12.226	24	3.83	0.6463

* Note: Hulls with conventional bow.

The flow chart of the program is shown in Fig. 4. This illustrates how the input data is used in the calculations. The upper and lower range in 8 become the indices for the do-loop which controls the parametric calculations for activity number 2 and 4.

The output is also driven by a menu. The possible outputs are:

A. View output on screen
B. Print output
C. Save output in a file
D. Return to main menu

Sample Output:

Input parameters

Displacement (lbs)	55000
Length (ft)	52
Beam (ft)	11.2
Deadrise (deg)	18
Speed (kts)	30
Trim angle (deg)	5.2
Significant wave height (ft)	3.8
Salt water	

Output parameters

Added resistance (lbs)	2949
Heave (ft)	2.4
Pitch (deg)	4.8
CG accelerations (G's)	0.81
Bow accelerations (G's)	2.23

4.0 UNO-SEAKEEP VERIFICATION

For the verification of the UNO-SEAKEEP the following comparisons were made for activity 1, 2 (Method I):

1. Comparisons with prismatic model test-data Fridsma (1969-1971)
2. Comparisons with manual calculations
3. Comparisons with model planing hull test data vonden Bosch (1974).

The following briefly summarizes the results of this verification.

4.1 Data Base for Comparisons

Fridsma (1971) presents the data for more than 60 prismatic planing tests in irregular waves. After discarding the tests which fell outside the limits of the UNO-SEAKEEP, a data base of 21 tests given in Table IV was established. The tests are identified by their original designation from Fridsma (1971). This table includes tests No. 60 and 65 where the model is fitted with a conventional bow as well as four planing hull tests denoted by hull 114A, B and hull 115A,B from van den Bosch (1974). Models 114 and 115 are shown in Fig. 5.

4.2 R_{aw} Comparisons

Table 5 presents a comparison of the R_{aw} values obtained from model tests with a prismatic hull, UNO-SEAKEEP-METHOD I and METHOD II as well as a limited number of hand checks using method I. Fig. 6 shows a scatter plot to help visualize the agreement between the model data and the program using Method I. Approximately half the

TABLE V. Comparison of R_{aw} Values

Model Test No.	Model Data	Method 1 Programmed*	Method 1 Handcheck	Method 2 Programmed
3	0.73	0.76	0.73	0.78
4	1.20	1.21		
6	0.79	0.72	0.75	0.74
18	0.89	0.89	0.90	0.83
21	1.17	1.16		
22	0.77	0.78		
28	0.57	0.74		
30	0.84	0.87	0.86	0.91
31	0.55	0.56		
34	0.49	0.78		
35	0.93	0.83	0.81	0.74
39	0.47	0.45		
40	0.66	0.83	0.74	0.87
41	1.29	1.29		
44	0.70	0.59		
45	0.59	0.78	0.71	0.58
46	0.96	1.16		
51	0.72	0.53		
52	1.18	0.77		
60	0.62	0.53		
65	1.28	1.16	1.14	0.89

*Notes: Max error wrt model data -59.18
Avg. error 2.57
Correlation coeff. wrt Data 0.82

TABLE VI. Comparison of Heave $H_{1/10}$ Values

Model Test No.	Model Data	Method 1 Programmed*	Method 1 Handcheck
3	0.07	0.07	0.06
4	0.22	0.20	
6	0.08	0.09	0.08
18	0.28	0.27	0.27
21	0.21	0.20	
22	0.06	0.07	
28	0.07	0.08	
30	0.36	0.34	0.34
31	0.07	0.08	
34	0.08	0.07	
35	0.34	0.27	0.28
39	0.08	0.08	
40	0.05	0.06	0.05
41	0.17	0.17	
44	0.06	0.06	
45	0.07	0.08	0.08
46	0.22	0.21	
51	0.09	0.09	
52	0.33	0.31	
60	0.09	0.09	
65	0.20	0.21	0.20

*Note: Max error wrt model data 20.59
Average error 1.45
Correlation coeff. wrt model data 0.99

TABLE VII. Comparison of Pitch $\emptyset_{10}$ Values

Model Test No.	Model Data	Method[1] Programmed*	Method[1] Handcheck
3	2.79	2.54	2.57
4	5.11	5.13	
6	3.03	2.77	2.40
18	7.39	6.85	6.78
21	5.69	5.13	
22	2.72	2.52	
28	2.82	3.02	
30	6.72	6.40	6.20
31	2.60	2.39	
34	3.24	2.53	
35	8.49	6.87	6.82
39	4.26	4.06	
40	2.29	2.17	2.20
41	5.16	4.60	
44	1.19	1.89	
45	3.14	3.03	3.10
46	6.16	5.74	
51	3.22	2.87	
52	6.54	6.68	
60	3.60	2.87	
65	6.04	5.74	5.80

*Notes: Max error wrt model data 58.8
Avg. error 4.51
Correlation coeff. wrt Data 0.98

TABLE VIII. Comparison of Center of Gravity Accelerations n_{CG}

Model Test No.	Model Data	Method 1 Programmed*	Method 1 Handcheck	Method 2 Programmed
3	0.67	0.55	0.55	0.56
4	1.04	0.94		
6	1.01	0.98	0.97	1.27
18	1.70	1.53	1.44	1.46
21	0.71	0.71		
22	0.45	0.42		
28	0.55	0.57		
30	1.77	1.88	1.83	1.63
31	0.68	0.73		
34	0.57	0.42		
35	1.22	1.32	1.14	1.11
39	0.22	0.22		
40	0.34	0.31	0.31	0.35
41	0.43	0.53		
44	0.58	0.54		
45	0.29	0.37	0.37	0.42
46	0.62	0.58		
51	0.83	0.83		
52	1.88	1.75		
60	0.69	0.84		
65	0.35	0.57	0.57	0.73

*Note: Max error wrt model data 62.86
Average error 2.78
Correlation coefficient wrt model data 0.98

TABLE IX. Comparison of Bow Accelerations n_{bow}

Model Test No.	Model Data	Method 1 Programmed[1]	Method 1 Handcheck	Method 2 Programmed
3	2.06	1.72	1.72	2.03
4	3.44	2.54		
6	3.56	2.60	2.59	3.48
18	5.57	4.30	4.10	5.28
21	2.35	1.99		
22	1.65	1.31		
28	2.10	1.72		
30	5.33	4.34	4.47	4.49
31	2.10	1.95		
34	2.09	1.30		
35	4.00	3.69	3.13	4.00
39	1.30	1.13		
40	1.17	0.97	0.99	1.27
41	1.73	1.46		
44	1.72	1.40		
45	1.06	0.93	0.94	1.12
46	1.93	1.53		
51	2.35	1.94		
52	4.08	3.45		
60	1.98	1.96		
65	1.04	1.52	1.53	1.94

[1]Note: Max error wrt model data 46.15%
Average error 14.27%
Correlation coefficient wrt model data 0.98

sample falls inside the dashed lines indicating ± 10%. In Table I the correlation coefficient with the data is 0.82. For reference some results from Method II are included.

4.3 Heave $h_{1/10}$ and Pitch $\emptyset_{1/10}$ Comparisons

Table VI presents comparisons of the heave amplitude $h_{1/10}$ with the prismatic planing hull data. The close values are confirmed by the negligible scatter in Fig. 7 within ± 10% limits. The correlation factor is also high = 0.89. There is also excellent agreement with the hand calculations.

Table VII presents comparisons of the pitch amplitude $\emptyset_{1/10}$ with the prismatic planing hull data. While it is not so clear from Table VII, there is a small basis for the UNO-SEAKEEP to underestimate the pitch amplitude by 10% as shown in Fig. 8. The correlation factor is 0.98. There is again excellent agreement between the program and hand check calculations. Method II is not able to predict heave and pitch and is omitted.

4.4 Bow Center of Gravity Accelerations n_{bow} and n_{CG}

Tables VIII and IX present comparisons of the bow and center of gravity accelerations. Examining Figures 9 and 10, the acceleration of the center of gravity n_{CG} is within the 10% limits. The correlation factor high =0.98

TABLE X. Comparisons of Model Planing Hull Test Results with UNO-SEAKEEP Calculations.

Planing Model	Hull 114A	Hull 114B	Hull 115A	Hull 115B
Model Data	2.28	3.94	2.65	5.13
R_{aw} UNO-PC	6.53	6.72	5.17	8.45
Model Data	0.15	0.19	0.19	0.23
$H_{1/10}$ UNO-OC	0.41	0.42	0.37	0.35
Model Data	2.52	2.76	2.85	3.09
$\emptyset_{1/10}$ UNO-PC	5.98	5.18	5.50	4.34
Model Data	0.61	1.06	0.56	1.16
A_{CG} UNO-PC	0.56	0.87	0.42	0.58
Model Data	1.60	2.66	1.75	2.60
A_{bow} UNO-PC	1.70	2.15	1.25	1.43

in Table VIII, UNO-SEAKEEP. It should be noted that in each evaluation the value underpredicts the value of n_{bow}, the average error is 14% in Table IX. The Method I was multiplied by 0.85 following Section 2.1.3.

4.5 Comparison with Model Planing Hull Test Data of van den Bosch (1971)

The question arises as to how reasonable the estimates of a typical planing hull motion will be using the program. This is difficult to answer since there is relatively little model data available for comparison. The four tests using the models in Table IV and shown in Fig. 5 are summarized in Table X. The results in Table X indicate the success of the designer in reducing R_{AW}, $h_{1/10}$, $\emptyset_{1/10}$ to values up to half those predicted by the program. The estimation of n_{cg} and n_{bow} are more reasonable. From the view of tank testing and design work there appears a need to extend the earlier work to study the influence of the waterplane distribution on the behavior in irregular seas.

5.0 Discussion and Conclusions

The paer discusses two main areas:
1) Development of the UNO SEAKEEP program.
2) Verification using hand checks, as well as model tests with prismatic and regular planing hulls.

Regarding the program development: The planned extension of the work is to link it with a planing hull resistance calculation. In order to do this the UNO-SEAKEEP will need to be streamlined by substituting equations for the data files which should reduce the running time.

Regarding the verification: The conclusions are:

1)The hand check calculations by in large confirmed the fidelity of the program estimates with Method I estimates.

2) The comparison of the prismatic model test data with the program estimates indicates good agreement for the heave, pitch, acceleration at c.g. and bow . The error is reasonably small and there is a high correlation factor. The added resistance in waves appears to be less accurate with a large scatter and lower correlation).84.

3) The comparison of the program estimates with the planing hull test data indicates that the program gives reasonable values for the acceleration at the bow and cg. The limited comparison indicates that the program overpredicts the added resistance in waves, as well as heave and pitch.

In conclusion it is recommended that additional experiments be conducted to provide the data to extend the present method usefulness.

6.0 Acknowledgements

The authors are grateful to Mrs. Latapie for typing the manuscript.

7.0 References

Blount, D, and Fox, D. (1976): Small Craft Power Prediction, Marine Technology Vol. 13, No. 1.

Fridsma, G., (1969): A Systematic Study of the Rough Water Performance of Planing Boats, Davidson Lab. Report 1275, Stevens Inst. of Technology.

Fridsma, G. (1971): A Systematic Study of the Rough Water Performance of Planing Boats in Irregular Waves, Part II, Davidson Lab. Report 1495, Stevens Inst. Tech.

Long-Wen, W. (1985): A Study on Motions of High Speed Planing Boats with Controllable Flaps in Regular Waves, International Shipbuilding Progress, Vol. 32.

Payne, P.R. (1984):Supercritical Planing Hulls Ocean Engineering, Vol. 11, No. 2.

Savitsky, D. (1968): On the Seakeeping of Planing Hulls, Marine Technology, Vol. 5, No. 2.

Savitsky, D. (1970): Behavior in a Seaway Proceedings Small Craft Enginnering, Department of Naval Architecture and Marine Engineering Report 120, Univ. of Michigan.

Savitsky, D. Roper, J. and Benen, L (1972): Hydrodynamic Development of High Speed Planing Hull for Rough Water, Proc. 9th ONR Symposium on Naval Hydrodynamics Paris.

Savitsky, D. and Brown P. (1976): Procedures for Hydrodynamic Evaluation of Planing Hulls in Smooth and Rough Water, Marine Technology, Vol. 13, No. 4.

van den Bosch, J. (1974):Comparative Tests of Four Fast Motor Boat Models in Calm Water and in Irregular Head Waves, Netherlands Ship Research Centre TNO Report 196S.

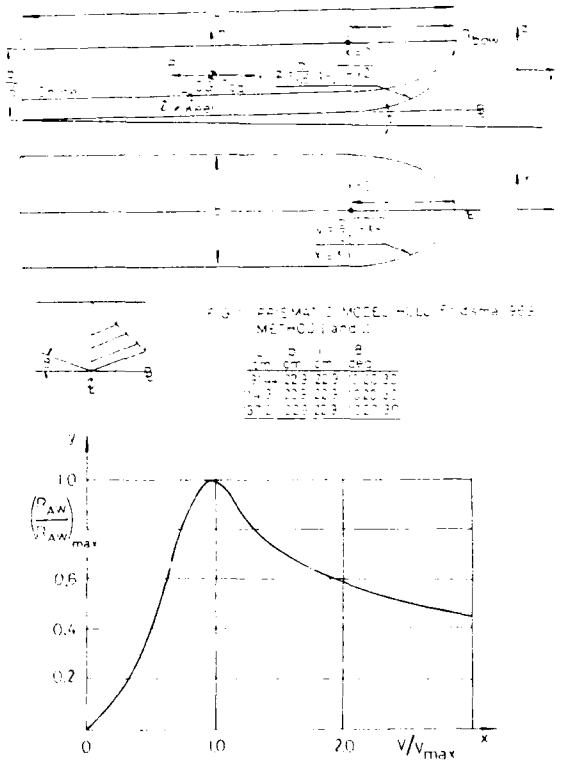

FIG. 2 Example of $\frac{y}{} = f_3(x)$

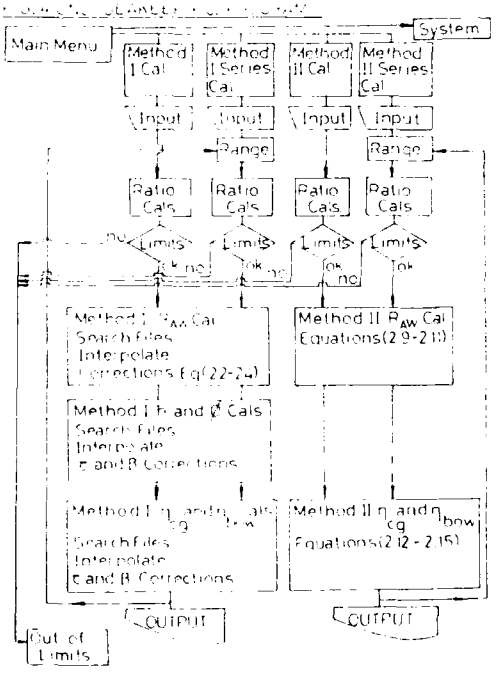

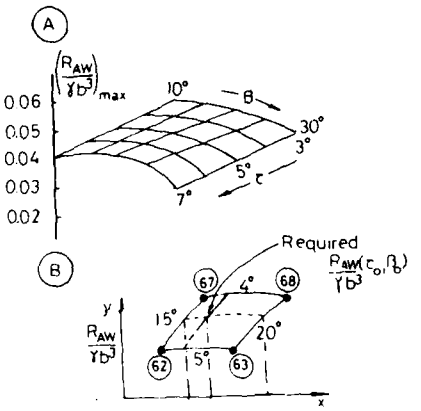

FIG. 3 Example of 2 input chart

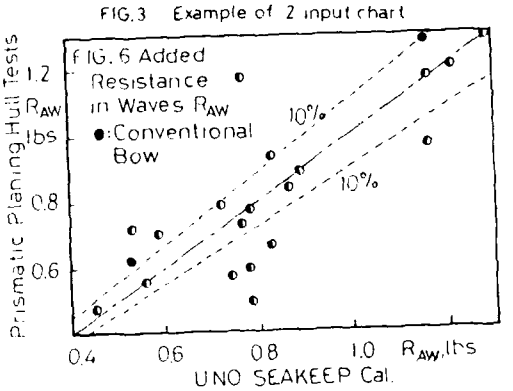

FIG. 5 Planing Model Hull Lines, Van der Bosch (1974)

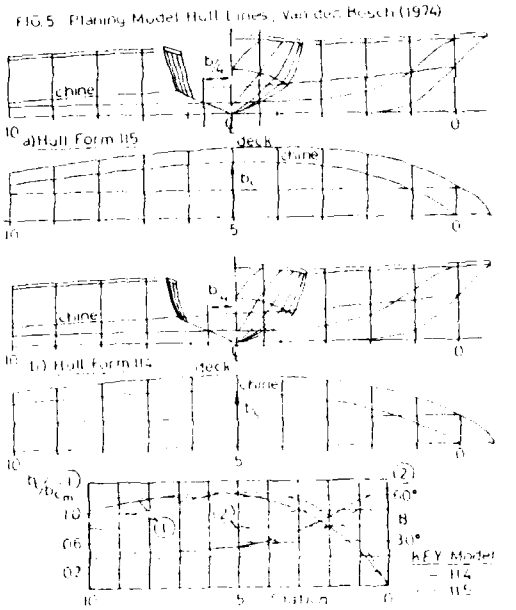

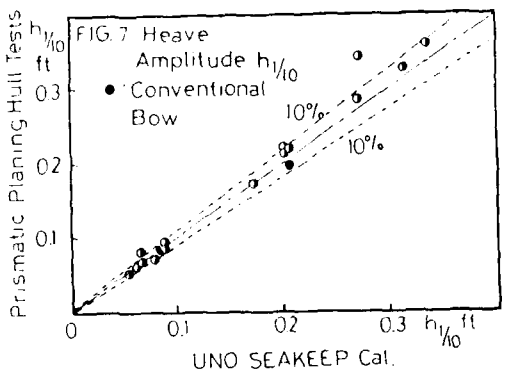

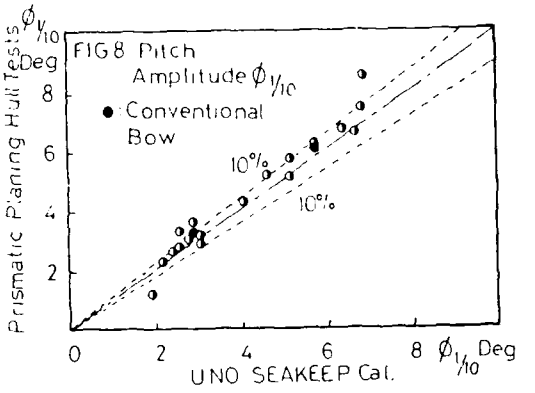

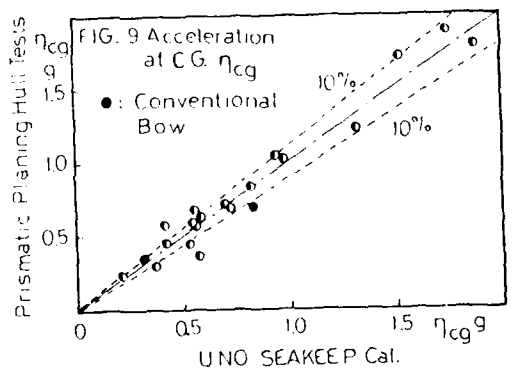

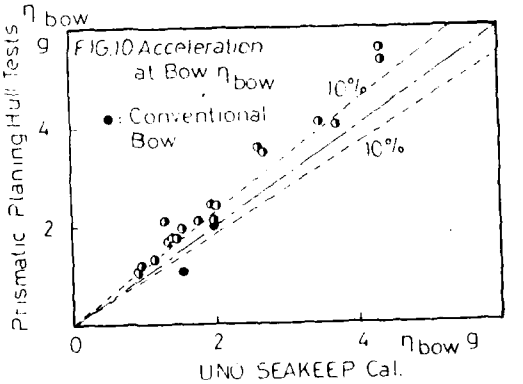

SAILBOAT DRAG PREDICTION BASED ON REGRESSION OF A LARGE DATABASE

ALEXANDER WARRICK
DESIGN SYSTEMS AND SERVICES
ANNAPOLIS, MD

Abstract

Linear and nonlinear regression analysis of sailboat model data is used to develop a full scale drag formula more accurate than those currently available such as the MHS (IMS) or Holtrop's. In this study theoretical and empirical drag components (the independent variables) are correlated with measured model drag (the dependent variable) to develop a formula accurately predicting full scale drag. Suggestions to improve the range and accuracy of the formula include augmentation of the database and use of independent variables which are more related to ship wavamaking drag theory.

I Introduction

Despite the recent enormous investment in theoretical and empirical yacht performance analysis, yacht designers need a general purpose simple yet accurate formula to predict drag as a function of speed, hull geometry and attidude. This study was undertaken to produce a theoretically based formula with empirical corrections. This required modelling the various drag components, building databases and using regression to tune the coefficients of the model.

The linear regression package was put together from pieces of the old IBM SSP (Scientific Subroutine Package) with some modernization of I/O and coding style. It is in the public domain and is available to pursue further studies of this sort. The databases and database processor are similarly available. The nonlinear package is part of the IMSL library of functions found on the Cray X-MP/48 at the San Diego Supercomputer Center.

Nomenclature

Rho - Density of water
V - Speed, length/time
B - Effective beam, length
L - Effective length, length
z - distance below the free surface

II Regression

Regression generally implies least square multiple linear regression. Linear regression includes stepwise regression orthogonal and normal polynomial regression, logarithmic regression. There are several "canned programs" which need only to be supplied with an array for the dependent and each of the independent variables.

Nonlinear regression is an iterative process related to multivariable optimization. It is harder to use than linear regressioni because the user must link to the regression package a computer procedure evaluating the dependent variable as a function of the independent variables. Since nonlinear regression is considerably more extravagant in its use of analyst and computer time, it is best used only when it is necessary to design independent variables to be further refined with linear analysis.

Linear regression can be used to mimic nonlinear regression by regressing several small ranges of the database using a small, consistent set of independent variables. The regression coefficients themselves are then regressed to create an independent variable modeling the behavior over the entire range.

III Statistical Significance

The t statistic is a figure of merit for a independent variable, it is the ratio of the regression coefficient to the standard error associated with that variable. The reciprocal of the 't statistic' can is the "one standard deviation plus or minus" band of confidence for that coefficient. If a 't statistic' is above a certain value, it is considered statistically significant.

A 't statistic' of 2.0 generally implies statistical significance to an economist. This implies that the regression coefficient is known to within plus or minus 50%, which is one reaon why economics is called the dismal science. Physical scientists generally use between 5.0 and 100.0 as threshold of statistical significance, indicating an uncertainty in the regression coefficient between 1 and 20 percent.

The value considered to be statistically significant depends on the experiment design, data quality, the size of the database and the collinearity of the independent variables. Because the effect of collinear variables can not be separated statistically, the usual reason why a variable (other than the effect is simply not present in the data) has a low 't statistics' or a regression coefficient different from that anticipated is that it is collinear with another (or a linear combination of several) independent variable.

Two variables or combinations of variables are considered collinear when they have a high intercorrelation, perhaps above 0.70. Unfortunately many of the independent variables used to predict drag have high intercorrelation and care must be taken to specifiy and select independent variables which both capture the physics of the phenomenon and are sufficiently orthogonal to produce reasonable results.

Orthogonal variables have no intercorrelation, the effect of orthogonal independent variables is accurately separated with regression. Over a suitable period, sine/cosines and Chebechev polynomials are orthogonal, therefore both functions are often used even when there is no overwhelming theoretical basis for it.

IV Residual Analysis

An important part of any regression study is examination of the residuals and elimination of outliers. Residual analysis compares the measured value with the predicted value for each data point. This identifies "outliers", points for which the difference between the predicted value and the observed value is greater than a certain threshold. Since the residuals tend to a normal distribution, points with a residual error greater than 2 standard deviations are candidates for close scrutiny, and those with a residual error greater than 3 should usually not be included because the least squared technique heavily weights the influence of outliers.

Graphical presentation is the best form of residual analysis: this is done by comparing the curve that best fits the data with a scatter plot of the points with all but one independent variable held constant. In this study this was done by making a scatter plot for each model upright with zero yaw and comparing it with the drag versus speed prediction curve.

V Description of the Database

This study used a database consisting of available model data and a second data base containing geometrical descriptions for each model. Most of the database consists of the models tested in Holland as part of the MIT Pratt series, which has the following deficiencies.

1. There is no long, slender and deep hull similar to a 12 meter.

2. There is no long, slender and shallow hull similar to a ULDB or catamaran hull.

3. Some moderately light boats have a higher beam to draft ratio than any models in the Pratt series.

4. All the models are the same scale, so there is not a wide range in Reynolds number.

5. The water temperature of each model series was not recorded in the model test reports.

To alleviate some of these deficiencies the database was augmented with a few additional model tests. Since the lines for these models were generally not available, the hydrodynamic parameters were estimated for these models.

The characteristics of the models used in this analysis are shown in Table 1. The quantities for the most part are self explanatory but those that might be somewhat unfamiliar are described in the analysis.The geometric data required for each model consisted of the following.

1. Length of the tested waterline.
2. Effective length at 0 and 25 degrees heel.
3. Displacement
4. Effective beam
5. Canoe body and total draft
6. Prismatic coefficient
7. Total wetted surface
8. Keel thickness at root, midspan and tip
9. Drag coefficient related to turbulence stimulation
10. Water Temperature

The following characteristics of the database help assure a reasonable level of accuracy.

1. The sheer size of the data base, (over 2200 points)

2. Without keel and half keel data for Pratt hull #1.

3. Base keel and draft data for models 2 and 3.

4. Hull only larger scale geosims for models Pratt models 1, 2, 3 (Murdey [1981])

5. Geosim data for full and 1.6 scale Antiope (Letcher [1974])

6. 1.8 and 1.3 scale 12 meter data (Intrepid [1973] DeBord [1985])

VI Dependent Variable

The dependent variable in this study is the residual drag which is the difference between total drag and form and friction and interference drag. It is supposed to be equal to the total wavemaking and induced drag plus any interference between the wavemaking of the hull and the vortex caused by the side force on the hull keel. One way to improve regression accuracy is to

TABLE 1
MODEL GEOMETRY

FM

Model	LWL	WSURF	Draft	Weight	L/LWL	LH/L	B/LWL	B/T	Cp	L/Tc	LCB	Rchrd	Rthck	Rspan	Rchrd	Rthck	Ctrurb	Temp
Int100	5.97	10.82	1.146	126.70	0.970	1.000	0.240	3.000	0.530	9.600	0.520	2.070	0.165	0.000	0.000	0.000	0.00000	69.0
Int101	6.02	10.82	1.146	127.00	0.970	1.000	0.240	3.000	0.550	9.600	0.520	2.070	0.165	0.000	0.000	0.000	0.00000	70.0
Int102	5.97	10.82	1.146	126.70	0.970	1.000	0.240	3.000	0.550	9.600	0.520	2.070	0.165	0.000	0.000	0.000	0.00000	70.0
Freedom	15.83	70.88	3.028	2248.30	0.970	1.000	0.240	3.000	0.550	9.600	0.520	5.460	0.352	1.500	1.500	0.150	0.00000	70.0
Antiope	24.30	160.0	4.640	5650.0	0.970	0.990	0.226	3.350	0.540	14.800	0.535	7.500	0.530	0.000	0.000	0.000	0.00000	71.0
Antmodel	4.05	4.444	0.770	26.15	0.970	0.990	0.226	3.350	0.540	14.800	0.535	1.250	0.088	0.000	0.000	0.000	0.00000	66.0
Can1	9.04	20.20	0.708	416.34	0.981	0.976	0.309	3.600	0.573	12.510	0.521	0.000	0.000	0.000	0.000	0.000	0.00044	59.0
Can2	9.04	22.46	0.616	416.34	0.981	0.989	0.271	2.910	0.573	12.510	0.521	0.000	0.000	0.000	0.000	0.000	0.00047	60.0
Can3	9.04	19.61	0.822	416.34	0.981	0.965	0.356	4.580	0.573	12.510	0.521	0.000	0.000	0.000	0.000	0.000	0.00047	61.0
Pratt1a	5.25	9.137	1.135	89.20	0.981	0.976	0.309	3.600	0.573	12.510	0.521	1.114	0.167	0.708	0.367	0.085	0.00053	71.0
Pratt1b	5.25	9.137	1.135	89.20	0.981	0.976	0.309	3.600	0.573	12.510	0.521	1.114	0.167	0.708	0.367	0.085	0.00041	71.0
Pratt1c	5.25	9.137	1.135	89.20	0.981	0.976	0.309	3.600	0.573	12.510	0.521	0.000	0.000	0.000	0.000	0.000	0.00048	71.0
Pratt1h	5.25	8.327	0.774	86.92	0.981	0.976	0.309	3.600	0.573	12.510	0.521	1.239	0.186	0.708	0.367	0.085	0.00049	71.0
Pratt2a	5.25	8.772	1.196	89.34	0.982	0.989	0.271	2.910	0.573	10.950	0.521	1.114	0.167	0.708	0.367	0.085	0.00054	71.0
Pratt2a'	5.25	8.772	1.196	89.34	0.982	0.989	0.271	2.910	0.573	10.950	0.521	1.114	0.167	0.708	0.367	0.085	0.00054	71.0
Pratt2b	5.25	8.660	1.135	89.03	0.981	0.989	0.271	2.910	0.573	10.950	0.521	1.155	0.173	0.708	0.367	0.085	0.00055	71.0
Pratt3a	5.25	9.759	1.086	88.99	0.982	0.965	0.356	4.580	0.573	14.470	0.521	1.114	0.167	0.708	0.367	0.085	0.00044	71.0
Pratt3b	5.25	9.856	1.135	89.30	0.982	0.965	0.356	4.580	0.573	14.470	0.521	1.059	0.159	0.708	0.367	0.085	0.00043	71.0
Pratt4	5.25	8.484	1.105	74.46	0.979	0.976	0.278	3.420	0.573	13.790	0.521	1.114	0.167	0.708	0.367	0.085	0.00037	71.0
Pratt5	5.25	10.22	1.211	115.52	0.984	0.976	0.360	3.890	0.573	10.810	0.521	1.114	0.167	0.708	0.367	0.085	0.00067	71.0
Pratt6	5.25	9.769	1.248	116.76	0.984	0.984	0.313	3.100	0.573	9.380	0.521	1.114	0.167	0.708	0.367	0.085	0.00039	71.0
Pratt7	5.25	8.817	1.047	72.64	0.978	0.968	0.306	4.080	0.573	15.630	0.521	1.114	0.167	0.708	0.367	0.085	0.00037	71.0
Pratt8	5.25	9.198	1.135	89.20	0.994	0.989	0.303	3.580	0.595	12.510	0.521	1.114	0.167	0.708	0.367	0.085	0.00045	71.0
Pratt9	5.25	9.073	1.135	89.20	0.967	0.966	0.316	3.650	0.551	12.510	0.521	1.114	0.167	0.708	0.367	0.085	0.00034	71.0
Pratt10	5.47	9.351	1.135	89.20	0.993	0.977	0.307	3.542	0.565	12.648	0.521	1.114	0.167	0.708	0.367	0.085	0.00033	71.0
Pratt11	5.47	9.269	1.135	89.26	0.998	0.964	0.306	3.720	0.565	12.609	0.521	1.114	0.167	0.708	0.367	0.085	0.00044	71.0
Pratt12	5.48	8.635	1.099	74.21	0.994	0.978	0.276	3.318	0.565	13.853	0.521	1.114	0.167	0.708	0.367	0.085	0.00046	71.0
Pratt13	5.48	8.580	1.099	74.21	0.997	0.965	0.273	3.462	0.565	13.853	0.521	1.114	0.167	0.708	0.367	0.085	0.00047	71.0
Pratt14	5.51	8.469	1.122	74.20	0.966	0.977	0.273	3.225	0.530	13.067	0.521	1.114	0.167	0.708	0.367	0.085	0.00045	71.0

normalize the dependent variable by the most powerful causative term, yielding more mutual orthogonal independent variables. The product of dynamic pressure and effective beam squared is used to nondimensionalize the dependent variable. This more evenly weights model weight and speed.

VII Regression Intercept

The first independent variable is the intercept; the statistical technique which forces the intercept to be 0.0 was not used for this run. The value of the intercept indicates whether most of the cause and effect relation effects have been identified by the independent variables. Since it is small compared with the other drag components, most of the variance is explained by the independent variables and not the normalization process.

VIII Frictional Drag

Frictional drag is assumed to as calcualated from the wetted surface, the coefficient from the ITTC frictional drag extrapolation curve, the dynamic pressure and a form factor which depends on the slimness of the body. The form factor implies that the friction extrapolator underpredicts the drag due to separation for full hulls and that form drag decreases with Reynolds number at the same rate as the extrapolation curve. For this study, the hull, keel and rudder were assumed to be operating at separate Reynolds numbers, with a characteristic length of 80% of the LWL for the canoe body and the midchord for the appendages.

Holtrop's [1985](which is statistically derived from Prohaska's [1966] method for extrapolating the form factor to zero Froude number) form factor was used for the hull and Hoerner's [1985] form factor was used for the keel and rudder, as was done by van Oossanen [1985].

IX Interference Drag

Interference drag is assumed proportional to the square of the keel or rudder thickness at the keel hull juncture, as proposed by Hoerner [1960]. Interference drag is generally less than 5% of the total drag, and can be affected by keel hull filleting. By subtracting interference drag, the correlation of the dependent variable with the wavemaking drag is increased.

X Induced Drag

If all forces are considered in the plane of the keel, then heel effects on induced drag are found to be negligible, as in the case for wave drag.

Lifting theory indicates that induced drag is proportional to product of lift squared and the reciprocal of the effective aspect ratio. It is possible to redefine the reference area and aspect ratio such that induced drag is inversely proportional to the square of the span of the lifting surface. For a hull the span is defined as the effective draft.

Effective draft is less than the total draft but greater than the span of the keel. The expression developed by George Clemmer [1978] can be used to estimate the effective draft of a conventional hull keel combination. A more sophisticated model was developed by Letcher for MHS by mapping the hull section in way of the keel to an ellipse in the Trefftz plane. Regression coefficient 9, which is about 1.00, represents this term.

A yet more sophisticated boundary condition solves for the pressure at the free surface in the presence of the wave generated by the hull, leading to a coupling between wave drag and induced drag. Sloof [1985] uses such a boundary for his analysis of the effect of winglets and the optimal spanwise distribution of lift.

In order to model the interaction between the lifting surface of the keel hull and the wavemaking of the hull, terms 31 and 32 were created; they are is proportional to the absolute value of side force and hence proportional to the vorticity of the keel.

Regression coefficients 31 and 32 are relatively small but not negligible. This drag increases with heel angle since term 32 has the cosine of heel angle in the denominator, which represents the fact that the keel vortex approaches the free surface as the boat heels.

XI Wavemaking Drag

At typical sailing speeds wavemaking is the largest drag component and since it is sensitive to hull shape it is of most interest to yacht designers and handicappers. Wave making drag is difficult to calculate theoretically and it is hard to find statistically since it is collinear with both form and friction drag.

Regression analysis was used by Holtrop and van Ootemrsen to estimate the wave drag using a database of conventional ship models. Their formula for predicting wave drag is an exponential relation of Froude number and prismatic coefficient based on Havelock's [19 ' 1934] wave drag analysis with coefficients d ined by regression. Unfortunately in these s ies there is no indication of the statistical nificance of each term, so it is difficult to determine the importance of the various effects.

Representations based on slender body wavemaking developed from Mitchell's integral and updated by Havelock and Lunde typically show more oscillation at low Froude number than observed in model data. However the thery is still useful for designing independent variables to statistically predict wavemaking drag. Representations for wave drag used in this study include one which closely followed the van Ootmersen fit and one which used Chebechev polynomials over the span of 0 to 0.5 Froude number.

XII Effective Beam and Length

Accurate estimation of effective length and beam as a function of hull shape, speed and heel angle has considerable promise. This is because the

effect of weight on wave drag decreases exponentially with distance below free surface, with the following relation to Froude number.

$e^{Z\ lf^2}$

The MHS formula calculates to measure B, the effective wavemaking beam of the boat, at a Froude number of 0.30. The MHS estimates B by integrating the gyradius of the beam over the entire below water hull. A modification to B to account for the effect of heel is discussed below.

The length used to calculate the Froude number is also that used by MHS, modified to model the effect of heel. Duncan [1979] calculated L using the same rate of exponential decrease with draft as for B. This did not improve the comparison of the residual drag for a model with full and half keel. Subsequent investigation confirms that form drag is responsible for this anomaly.

Use of the exponential decrease of volume with distance below the free surface is a more realistic method to estimate the wavemaking length, but since the length as calculated by this method is not available, the MHS method was retained.

XIII Effect of Heel on Length and Beam

Drag is affected by heel due to a change in hydrostatic properties. For boats with low prismatic coefficent and low volume overhangs the effective length decreases considerably with heel, increasing drag as heel angle increases. Conversely, several hull shapes (especially those with hard chines) the effective length increases or stays constant with heel.

The effective beam is corrected for heel by assuming that the product of beam and length is constant, therefore the decrease in L predicted by the hydrostatic program at high heel angles is results in a similar increase in B with heel angle. In between linear interpolation is used.

The results of several different attempt to model drag due to heel show that the wavemaking drag increase with heel angle is best explained by the change in effective length and beam with heel.

XIV Effect of Speed

Theory indicates wavemaking drag is heavily influenced by the *fourth power* of speed. Terms 12 through 17 all have the fourth power (Froude number squared multiplied by dynamic pressure).

The effects of interference between transverse and divergent wave patterns oscillate with speed and are dependent on hull geometry but it is very difficult to find the amplitude and period of these oscillations statistically as a function of hull shapes.

Van Oortmerson's analysis indicated that the interference effects constisted of a two effects, one related to the sine of the reciprocal of Froude number squared and the other orthogonal (cosine) to it. In this analysis the terms were multiplied by the the fourth power of speed to damp out the low speed oscillation.

Terms 13 and 14 show that of the two oscillatory effects, the sine term is stronger. This is at variance from Holtrop's latest analysis in which the sine term is neglected. it is possible that more accurate representation of length will improve the fit of these terms since a slight error in length will considerable alter the period of these oscillatory terms. However the 't statistics' for these terms are sufficiently high to inspire reasonable confidence.

Term 15 includes the volumetric coefficient to represent the relatively low drag/weight ratios of light displacement boats and the corresponding high drag to weight ratio of heavy displacement boats at high Froude numbers.

Term 16 includes the eighth root of t/b, the exponent was estimated by nonlinear regression.

More extensive use of nonlinear regression and more sophisticated modelling to estimate the effective hydrodynamic length, beam and prismatic coefficient will eventually replace terms 15 and 16 with more theroetically based variables.

XV Effect of Prismatic Coefficient

A great deal of the effect of prismatic coefficient is captured by the way in which MHS measures length, which increases with prismatic. However, the MHS formula can not estimate the prismatic *coefficient which minimizes* total drag or wave drag, since the length as measured by MHS increases monotonically as a function of prismatic.

Minimum drag prismatic coefficient increases with Froude number. The minimum drag prismatic increases less than 0.50 at low speed to over 0.60 at Froude numbers of 0.40. A typical prismatic for a sailboat is about 0.57, which is the prismatic for the bulk of the Pratt data. This prismatic is optimal for medium air sailing for boats with typical sail area to weight and wetted surface ratios.

Gerritsma [1977] performed a piecewise regression of the Pratt data, which used a second order fit of prismatic coefficient to residual drag. This fit was then used to calculate the optimum prismatic by setting the derivative of the regression quadratic to zero by ratioing the first and second order regression coefficients and dividing by 2. The minimum drag prismatic was regressed against Froude number to create the expression used to model the drag due to nonoptimal prismatic.

The optimal prismatic as indicated by the Gerritsma analysis is somewhat higher than that appropriate because in his analysis Froude number was calculated by using the load water line, while this analysis uses the MHS derived effective length, which increse with prismatic.

Term 17 was developed using a fit to the minimum drag prismatic coefficient as identified by

Gerritsma's analysis as the initial position for a nonlinear regression identifying the effect of prismatic on drag as shown below

$$\text{Drag} \quad cp \quad cp_{opt} \times q \times b^2 \times \text{Froude2}$$

$$cpopt = a + b \times \text{Froude}^c$$

$$a = 0.06$$
$$b = 0.90$$
$$c = 0.50$$

Term 17 has a high 't statistic indicating that a high level of confidence in the model for the effect of prismatic coefficient on wavemaking drag as a function of Froude number

XVI Dummy Variables

Dummy variables are very simple to use when the dependent variable is properly normalized

Term 24 is a dummy set to 1 0 for all the Pratt series models and 0 otherwise It has a relatively small but non negligible t statistic which indicates that the drag of the Pratt series either due to the tank or technique of turbulence stimulation This term should be neglected for full scale extrapolation

Term 25 is models the induced drag for the model with no keel 25 is included because it is not easy to estimate the effective draft for a hull with no keel Although the ability to predict the drag sail force relation of a hull with no keel is of limited practical importance The inclusion of the upwind and leeward data for the hull with no keel removes variable interrelationship by allowing the effect of the leeward tests to appear in model with no keel

Term 26 estimates the correction to drag to be the average based on the fit of the mirrors at the base of the appendages It is included since the data for the first model of the Light series which was tested in a towing tank is worse than the small tank or wind tunnel data for small models with keels

Term 27 represents the SAMS data which was tested for Antiope Its inclusion in the regression model was necessary to isolate the effect of this term from the [illegible] simulations which [illegible] the model [illegible] Antiope [illegible] model [illegible] was [illegible]

[illegible]

[illegible]

[illegible]

[illegible]

additions to the data base

1 Parametric 12 meter data tested by Milgram in 1982 This would significantly improve the quality of the data base since the models were a systematic series tested at a much larger scale than the bulk current database

2 Maxi boats tested by Milgram in 1985 The reasons to include his 12 meter model are valid for these data as well since these models are of much lower displacement than the bulk of the database

3 Hydronautics (and other) geosim series for Antiope Inclusion of a geosim series isolates the effect of Reynolds number and therefore decreases the intercorrelation between friction and wavemaking drag allowing more accurate statistical separation

4 Delft variable keel series [Gerritsma 1985, 1986] Several keels tested on one hull will improve the estimation of effective draft as a function of keel design

5 Series 64 and catamaran hulls will help improve the formula so that it will behave well in the high L B limit

6 Dinghy hulls with a representation of planing induced drag and wave drag reduction at high speed

7 Wind or water tunnel hull and appendage data which will accurately measure form and friction drag and induced drag in the absence of the free surface

8 More general independent variables better related to wavemaking drag theory The following improvements in modeling form parameters will [illegible] independent variables which have more relation to the physical sense of hull drag than [illegible]

9 Update of the [illegible] processing program to [illegible] effective draft beam and prismatic using [illegible] to assess the effect of displacement [illegible] free surface [illegible] top of keel angle [illegible]

10 [illegible] test method to predict [illegible] hull free surface

11 [illegible] level of theoretical [illegible] independent [illegible]

12 [illegible]

13 [illegible] systematic series [illegible]

14 [illegible]

15 [illegible]

Gerritsma, "Test Results of a Systematic Yacht Hull Series", Hiswa, 1977

Gerritsma, "Test Results of a Systematic Yacht Hull", Tampa Bay Sailing Yacht Symposium 1986

Havelock, T. "Wave Resistance", Proc Royal Society, London 1928

Havelock, T. "The Calculation of Wave Resistance", Proc Royal Society, London 1934

Hoerner, "Fluid Dynamic Drag", Hoerner Fluid Dynamics

Holtrop, J. and Menne, G. "A Statistical Power Prediction Method", ISP, Oct. 1978.

Holtrop, J. and Menne, G. "A Statistical Power Prediction Method", ISP, Oct. 1978.

Holtrop, J. and Menne, G. "A Statistical Reanalysis of Resistance and Propulsion"

Jenkins, D. S. "Analysis of a Systematic Series of Sailing Yacht Models", MS MIT 1977

Kerwin VPP, Pratt reports 1975 - 1978

Kirkman, K and Pedrick, D "Scale Effects in Sailing Yacht Hydrodynamic Testing" Transactions SNAME 1974

Letcher, "Sailing Hull Hydrodynamics, with Reanalysis of the Antiope Data", Transactions SNAME 1975

Lunde, J "Linearized Theory of Wave Resistance", Published by SNAME

Milgram, J "An Experimental Investigation of SAilcloth", HISWA, 1973

Mitchell, J. H, "the Wave Resistance of a Ship", Philcsophy Magazine, 1898

Murdey and Harrison "Systematic TestSEries ... Models 335B, 342 and 343",LTR Report SH 353, Arctic Vessel and Maritime Research Institute of Canada

Prohaska "A method for Estimating Form Drag", ITTC Conference, 1966

Sloof, Joop, "On Wing and Keels", Ancient Interface 1985

Vacanti, D. "Wing Keels Facts and Fallacies", Ancient Interface 1985

van Oosanen, P "Theoretical Estimation of the Influence of Some Main Design Factors on the Performance of International Twelve Meter ClassYachts", Chesapeake Sailing Yacht Symposium, 1977

van Oosanen, P "Theoretical Estimation of the Influence of Some Main Design Factors on the Performance of International Twelve Meter ClassYachts", Chesapeake Sailing YachtSymposium, 1977

van Ootmersen, A Power Prediction Method and its Application to Small Ships", International Shipbuilding Progress (ISP), Nov. 1971.

Table 2.0

REGRESSION OF SAILBOAT MODEL DRAG

Dependent Variable - 8 - Residual Drag (q * beff^2)

Variable Number	Variable Name	Regression Coefficient	T Statistic
	Intercept	0079	
9	Induced drag (q*B^2)	9591	35 9
12	Froude^2	8871	23 9
13	Froude^2* sin(Froude ^{2})	0223	22 3
14	Froude^2* cos(Froude ^{2})	0074	6 0
15	Froude^2* (t b)$^{0.125}$	1 1335	26 3
16	Froude^2* volumetric coefficient	5 0935	13 0
17	Froude^2* abs(cp - cpopt)	0 9190	9 7
25	DUMMY FOR Pratt Series	0002	3 6
26	DUMMY FOR INDUCED DRAG - NO KEEL	2 2675	2 7
27	DUMMY VARIABLE LARGE TANK	0103	4 7
28	DUMMY VARIABLE FOR IOR ANTIOPE	0 0006	7 2
31	Cb * Froude^2	0 2834	0 8
32	Cb * Froude^2 cosphi	0 4707	1 7

STATUS OF THE WATER-PISTON PROPULSOR

R. A. Swanek - Mechanical Engineer, David Taylor
Naval Ship Research and Development
Center, Code 1240, Carderock, MD 20084

V. E. Johnson, Jr. - Chief Engineer, Tracor Hydronautics, Inc.
7210 Pindell School Road, Laurel,
Laurel, MD 20707

ABSTRACT

Preliminary design and performance analyses have shown that the concept of a water piston propulsor system is well suited to propel a 20 ton Marine Corps amphibious vehicle at a speed of over 20 miles per hours over water. Four 16 inch diameter propulsors located in a transom flap on the vehicle will provide the required in-water propulsive thrust to achieve this speed. The propulsion system offers large weight and volume savings because of the elimination of a large diesel or gas turbine engine with its associated drive train. Of primary concern to the viability of the concept to date, is the gas water interface of 3000 degree F gas and 70 degree F water. The water piston design described has the potential for greatly reducing the volume and weight required to propel an amphibian (as well as other marine craft) for the same fuel efficiency as conventional propulsion if heat loss and leakage in the propulsor are not excessive and if the gas-water interface is nearly piston-like. Based on full scale single channel water piston propulsor testing at 800°F, nothing to date has indicated that this interface will yield an unacceptable efficiency or that the concept is not viable.

1. INTRODUCTION

1.1 GENERAL

The mission of future Marine Corps amphibious vehicles may include transits from ship to shore, shore to shore, and shore to ship. If an assault is made on a fortified shore, it may be necessary that the ships launching the amphibians remain well offshore to achieve an over the horizon launch. Long transits in water at slow speeds can seriously reduce the combat effectiveness of the vehicle occupants. For this reason, technologies required to increase the speed in water of future Marine Corps amphibious vehicles are being explored. The effort in this paper is focused on applying the water-piston propulsor to a 20 ton vehicle with a speed of 20 miles per hour in water.

Marine Corps amphibious vehicles are designed to spend only 20 percent of their operating life cycle in the water. During the remaining 80 percent of the running hours, the vehicle must provide an overland capability that will meet the projected threat. The two operating modes have power requirements that are quite different. The overland power for a 20 ton amphibian varies from idle to approximately 400 HP. The required power in water is constant at 1500 HP if 20 plus miles per hour speeds are to be sustained.

Various engine options to meet the two power levels associated with the land and water operations are as follows:

1. A single engine capable of operating in two power regimes,
2. A combination of engines, one of which may be secured when operating ashore, or
3. A land propulsion engine augmented by an in-water propulsor that may not meet the conventional description of an engine.

This paper focuses on the third option.

The ideal source of in-water propulsive thrust for a Marine Corps amphibious vehicle is one that converts a high energy density fuel into hydrodynamic thrust within a minimum volume and weight, with reduced complexity and with reasonable overall efficiency. The water piston propulsor, an unconventional propulsive device, is shown to meet this objective.

This paper describes briefly the working of the water piston propulsor and the tests that have been conducted during the past few years to determine its operating characteristics (References 1-5). These experimental and analytical results were used to design four 16 inch diameter propulsors that can propel a 20 ton tracked amphibious

vehicle at a speed of 20 plus mph in water (References 6-8). In these design studies the power required of the prime mover (air compressor) varies from 625 to 750 HP depending on the gas pressure and temperature values selected for the propulsors. The propulsion system offers large weight and volume savings because of the elimination of a large diesel or gas turbine engine with their associated water drive trains.

1.2 WATER PISTON PROPULSOR DESCRIPTION

The water piston propulsor was originally conceived to propel underwater weapons at high speeds. The device eliminates the majority of the propulsion hardware by discarding most of the process steps that occur between the generation of the working fluid and the production of thrust. In a conventional propulsion system, the hot, high pressure gas is expanded in a piston or a turbine engine. The shaft power produced is conditioned in a gear box and transmitted to the propeller which produces thrust by imparting momentum to a stream of sea water. The same effect is accomplished in the water piston propulsor by having the gas expand directly against columns of sea water entrained in helical channels.

The complete water piston propulsor system shown in Figure 1 consists of an air compressor and its drive which supplies high pressure air to a combustion chamber where heat is added. The resulting hot gas is then expanded through the propulsor. Thus the total heat energy delivered to the system is the sum of that delivered to the compressor prime mover and the combustion chamber. In a typical design the energy supplied to the compressor is substantially less than half the total energy and since the combustion chamber is small and light and the propulsors are similar to water jet systems in volume and weight; the volume and weight of the complete system is much less than for a conventional water jet system.

The propulsor consists of a cylindrical thruster which has many helical channels. When the thruster rotates about a shaft, the channels are blocked and unblocked alternately. As shown in Figure 1, water enters through the open face of the rotor, into the channels. The closed face has a gas port connected to the high pressure, hot gas source. As the channel passes the gas port, the gas imparts momentum to the mass of water as it enters and completes it expansion after the port closes. Because the interfacial area between the gas and the water is small, energy loss is kept to a minimum; thus, a large mass of water is accelerated by a small quantity of gas. After expulsion of the water, the channel is filled with water again when its opening has passed the closed face. The incoming water scavenges the expanded gas. The cycle is repeated for each channel, each time it passes the gas port. Each cycle produces an axial and a tangential impulse because of the change in momentum between the exiting and the incoming flow in two directions. The total thrust in the axial direction equals the product of the number of cycles per second and the axial impulse; the number of cycles per second is the product of numbers of channels and the thruster revolutions per second. The device can produce thrust and tangential force (torque) at the same time, if needed. If the device is used solely to produce thrust, the exit angle is set so as to produce the necessary torque to provide the required rpm (against seal and bearing friction, and external hydrodynamic friction) for the most critical operating condition. Fine control of the rpm at other conditions may then be provided by a control brake.

2.1 WATER PISTON PROPULSOR TESTS

Limited tests conducted on a water piston propulsor model some years ago (References 1 and 2) showed that the propulsor was self starting, and it produced thrust by accelerating a stream of water. But the thrust predicted by the theory was not obtained in those tests because of gas leaks through the space between the rotating thruster and the stationary closed face. The leaked gas mixed with the incoming water and the low density, gas-water mixture entered the channel. Further, flow separation occured at the inlet to the propulsor resulting in poor ingestion of water and therefore, incomplete filling of the helical channels of the thruster. These problems could not be solved at that time because of funding limitations.

A modified propulsor model was constructed to help solve the problems that arose in previous tests (Reference 4). The model was tested in the Tracor Hydronautics Free Surface Water Channel. To prevent gas leakage into the incoming water, a new seal system was designed such that the gas from the inlet to the moving channel was admitted through openings farther inboard than in the previous model. Cold nitrogen, the pressure of which could be varied over a wide range, was used as the propellant in the tests. The thrust and gas flow rate of the propulsor were measured over a wide range of tests conditions.

The following conclusions were reached from the test data analysis, described in detail in Reference 4:

1. The new seal system designed for the propulsor was effective and eliminated the gas leakage into the incoming water, which was serious problem in the tests conducted previously.

2. The water flow through the inlet was nearly uniform without any separation.

3. Despite the wide variation of test parameter values (free stream velocity, gas supply pressure, thruster revolutions per second) the results correlate well in terms of thrust coefficient, advance ratio, and gas pressure ratio for the design condition. These results were of much interest because the dimensionless parameters could be used to predict the performance of a full scale propulsor (cold gas) from model tests. It was further inferred from the excellent correlation of the test data with theory that the water enters the helical channels smoothly and the interface between the gas and water is stable.

Still some fundamental questions remained to be answered, concerning the effects of hot gas and channel height to the width ratio on interface stability and the magnitude of heat loss from the gas to the water. It was decided to proceed with a less expensive single channel, full-scale, non-rotating tests before a commitment was made to fabricating a full scale water piston propulsor. This investigation is reported in Reference 5.

The single channel test apparatus consisted of a gas heater, a trapezoidal channel, an accumulator and a piston drive to vary the sliding valve which approximated the rotation of the rotor against the combustor seal. A high speed movie camera was used for flow visualization and to aid in data analysis. The test setup is shown in Figures 2 and 3.

The trapezoidal channel was used to simulate a single passage of a full-scale water piston rotor. The channel was 32 inches long, 4 inches high, and 2 inches wide. Two transparent vertical walls were made of 1 inch thick bullet proof glass to withstand the gas pressure and temperatures expected and the upper and lower parallel walls were constructed of 1 inch thick aluminum. The glass/metal interface was sealed to prevent any leakage of flow during the expansion phase. The water in the channel, prior to gas injection was contained by means of a thin, brittle diaphagm inserted between flanges at the channel exit. Pressure-time records and high speed movies of cold and hot gas tests were analyzed to evaluate the effect of temperature on the performance of the propulsor.

The two prime objectives of conducting cold and hot gas test in the single channel test apparatus were: (a) establish whether a stable gas-water interface exists at relatively high gas temperatures and (b) determine the effect of heat on the propulsor performance.

The key finding of these tests was that the gas-water interface during the entire cycle of operation remains stable and intact at temperatures up to the maximum value of 685 degrees F tested. The observed interface was stable for all hot and cold tests. Due to leakage problems and anomalies in the two comparative measurement techniques employed, (pressure time histories in the channel vs photographic data on the interface location) results as to the effect of heat on the water piston propulsor performance proved inconclusive.

Additional tests of the single channel propulsor are underway with improved seals and improved instrumentation and photographic techniques; however, results are not yet available.

In summary, of the three obvious potential problems with the water piston propulsor, seal leakage, interface stability, and heat loss, tests to date have been encouraging on the first two of these and no conclusion has yet been reached as to whether the heat loss will be excessive.

The following section describes the application of the water piston propulsor to the 20 ton Marine Corps assault vehicle with the assumption that an adequate seal can be developed and that the heat loss will not greatly exceed the loss to be expected if the water surface area exposed to the hot gas does not greatly exceed the passage surface area. (Reference 7 and 8).

2.2 WATER PISTON PROPULSOR DESIGN

A design was performed for the existing water piston propulsor technology as applied to a nominally 20 ton Marine Corps assault amphibian vehicle to assess the potential benefits of this technology. Given that this concept is being applied to an existing set of requirements it is worthwhile to look at these requirements in light of the fact that the concept under evaluation is applicable to numerous other types of craft and can be tailored to suit many propulsive needs. Based on existing thrust and drag data for the craft under consideration, the following criteria would need to be met to achieve a minimum 20 mph water speed capability:

1. The minimum velocity of the 20-ton tracked amphibious vehicle in water is 20 mph. The thrust required to assume this velocity is 12,000 pounds (lump being approximately 16 mph for the planning hull configuration considered).

2. The propulsors shall be physically located in an external transom flaps of the vehicle. A conceptual sketch of the vehicle is given in Figure 4. This flap folds down

behind the cargo/troop door in the rear of the vehicle. The dimensions of the transom flap are 20 inches high, 58 inches long and 64 inches wide.

3. The geometry of the propulsors is constrained to 16 inches outside diameter.

4. The total weight of a conventional water propulsion system is 5,780 pounds which includes the weight differential between the water drive train/engine and the land drive train/engine. The system weight of the new design is approximately 4,000 pounds or less. In calculating the system weight, the following items were included:

a) the equipment necessary to convert potential chemical energy into an appropriate form of power,
b) the equipment necessary to transmit the power to the propulsor,
c) the propulsor and its housing required to produce the thrust and
d) the fuel required for two hours of operation.

6. The fuel for the propulsion system is No. 2 diesel fuel oil with a heat capacity of 19,000 BTU/lb.

7. The overall thermal efficiency (thrust energy/potential fuel energy) of the system is expected to be at least 10 percent.

8. The propulsion system design exhibited consideration of the safety aspects of the vehicle occupants.

9. The propulsors were equipped with buckets to vector the thrust for steering and reversing. Directional control of the vehicle in the surf is essential to prevent broaching in the surf.

As detailed in Reference 3, the thermal efficiency of the water piston propulsor is far greater than that of a rocket and more nearly that of conventional water jet propulsion. The overall weight and volume of such a water piston propulsor is expected to be less than that of a comparable water jet system; however, whether such a weight and volume advantage actually exits depends on detailed analysis of a specific application. Table 1 compares the expected advantages of the water piston propulsion concept versus an electric drive/water jet conventional design for a 20 ton amphibian.

Table 1

	Diesel Electric	Water Piston Propulsor
Thrust Horsepower	655 HP	655 HP
Fuel Rate	740 lbs./hr	781 lbs/hr
Engine Rating	1800 HP	685 HP
Overall Efficiency	11.2%	10.6%
System Weight	7780 lbs.	5400 lbs
System Volume	110 cu. ft	53 cu. ft

The methods used in the analysis were those presented in References 1 - 4, and computer programs using both these methods have been developed for a VAX 11/750 computer. It is worth reiterating that the main area of uncertainty in actually realizing the performance predicted by these theoretical methods is that the gas expansion in the water piston passages is assumed to be adiabatic, as it is critical to the efficiency of the system. Assuming a planar gas-water interface (not broken into many droplets) the heat loss has been estimated to be about 5% at a gas temperature of 3000°F. A heat loss several times this may be accepted for the present application.

As was demonstrated in the analysis presented in Reference 8, very good performance of the water piston propulsor is achieved at an operating temperature of 2250 degrees F typical of the temperature in a gas turbine. However, the efficiency, weight, and volume of the propulsion system become very attractive if the operating temperature is increased to 3400 degrees F or higher (Figures 5-7). Such temperatures are not allowable in gas turbines because of material structural problems. However, the water piston is continually water cooled and the rotor material temperatures are therefore expected to remain low during operation. Thus, the final operating temperature of an optimum design is likely to be selected on the basis of heat loss rather than material structural problems.

3. CONCLUDING REMARKS

Although the water piston propulsor was invented by Zovko in 1965 (Reference 1), very little was done to develop the concept until only a few years ago. The reasons for this may be that it's one of those things that just "obviously" will end up with an efficiency much less that it ideally could achieve. The seal between the rotor and gas supply must not leak and must have a long life, the gas-water interface must be almost piston-like with no channeling of gas through the water and there must not be excessive heat transfer to the cold water from the hot gas. None of these problems can be adequately treated by anlaysis and so very little was done until 1982.

However, since 1982, some progress has been made in determining the feasibility and characteristics of the water piston propulsor. This paper has briefly described the work done with particular attention given to its possible application to a high-speed (20 mph), 20 ton Marine Corps Amphibian.

The water piston propulsor is so attractive for the Marine Corp Amphibian application that plans for proceeding with full scale tests of one 16 inch diameter unit are underway. A combustor and seal unit has been developed by SOLAR TURBINES INCORPORATED for use in the test system. Barring evidence of excessive heat loss (from single channel tests now underway at Tracor Hydronautics, Incorporated) a complete full scale system test and evaluation may be carried out soon.

REFERENCES

1. Zovko, C.T. "The Water Piston Propulsor", NOL Technical Note 66-222, January 1967.
2. Zovko, C.T. "The Water Piston Propulsor", NL Technical Report 69-130, August 1969
3. Zovko, C.T. "Several Unusual Propulsion Systems", Naval Engrs Journal December 1980, page 43.
4. Krishnamoorthy, V. and Johnson, Jr., V. E., "Invesitgation of a Water Piston Propulsor Powered by Compressed Gas". Tracor Hydronautics, Inc. Technical Report 8201-1. May 1983.
5. Krishnamoorthy,V. and Johnson, Jr., V. E., "Single Channel Tests of the Water Piston Propulsor". Tracor Hydronautics, Inc. Technical Report 82010.50-1. March 1985.
6. Krishnamoorthy, V. and Johnson, Jr., V. E., "Application of Water Piston Propulsor for Amphibious Vehicle Propulsion", Tracor Technical Report 82010.24-1. May 1983.
7. Krishnamoorthy, V., "Water Piston Propulsor for Marine Corps Amphibious Assault Vehicle: An Exploratory Development Test Plan," Tracor Hydronautics Technical Report 82010.36-1, April 1984.
8. Krishnamoorthy, V. and Johnson, Jr., V.E., "Conceptual Design Study of Water Piston Propulsion System for Marine Corps Tracked Amphibians," Tracor Hydronautics Technical Report 83029-1, February 1984.
9. Krishnamoorthy, V., "Water Piston Propulsor for Marine Corps Amphibious Assault Vehicle: An Exploratory Development Test Plan," Tracor Hydronautics Technical Report 82010.36-1, April 1984.

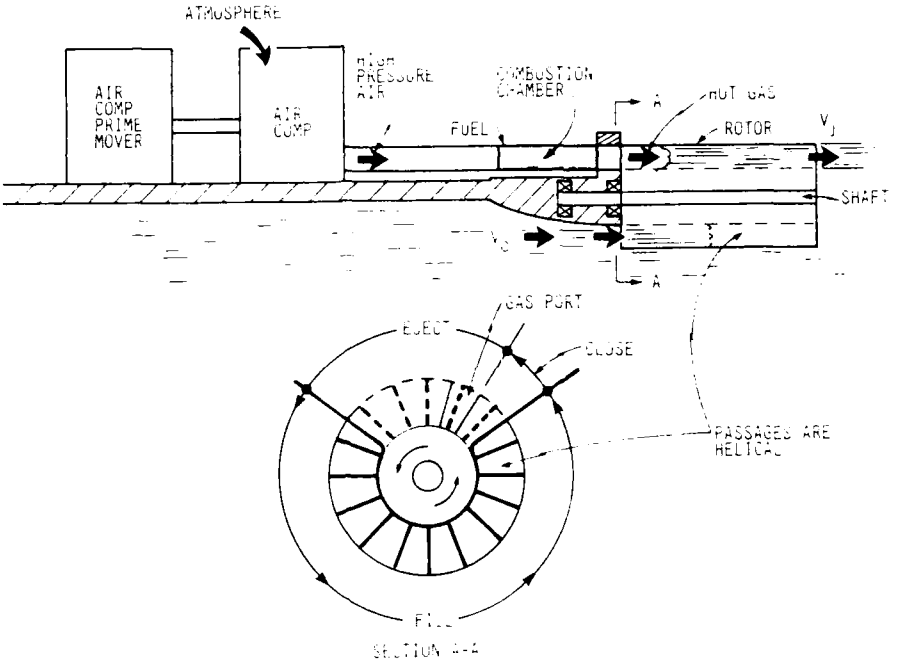

FIGURE 1 - WATER PISTON PROPULSOR CONCEPT

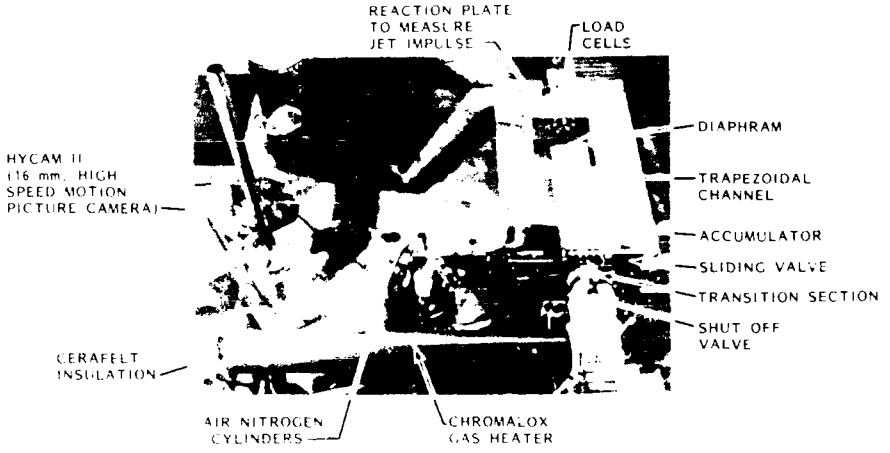

FIGURE 2 - VIEW OF SINGLE CHANNEL TEST APPARATUS

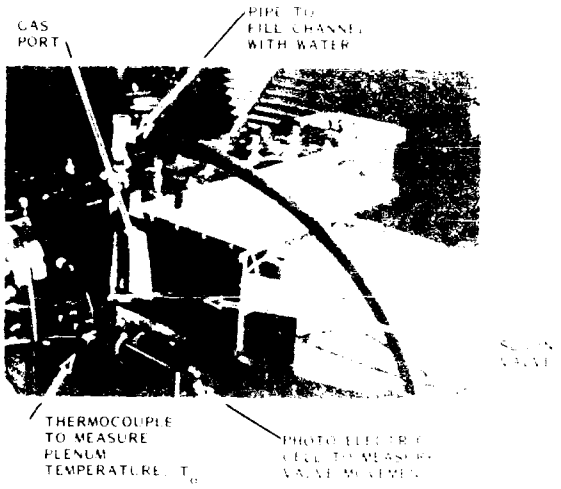

FIGURE 3 - VIEW OF SINGLE CHANNEL TEST APPARATUS
SLIDING VALVE

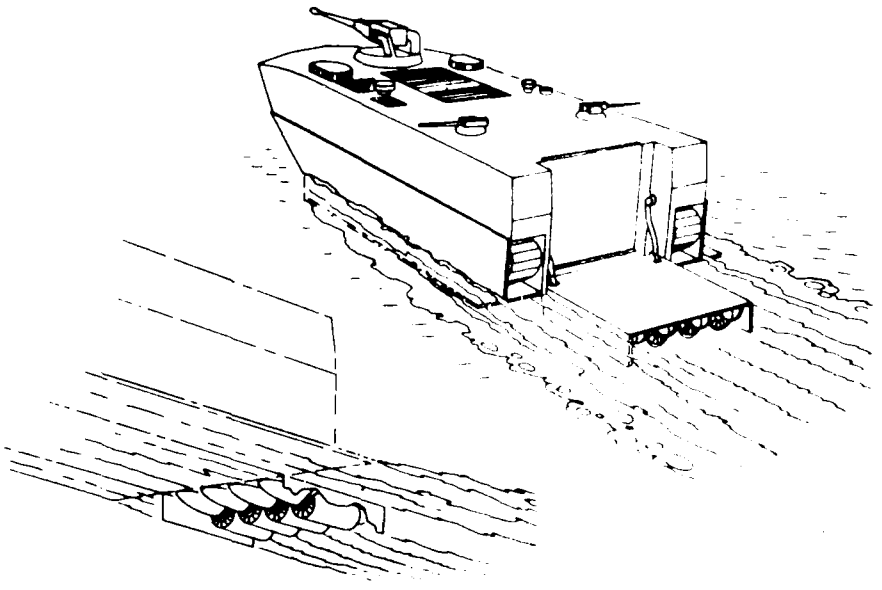

Figure 4 - Application of Water Piston Propulsor on Marine Type Amphibious Vehicle

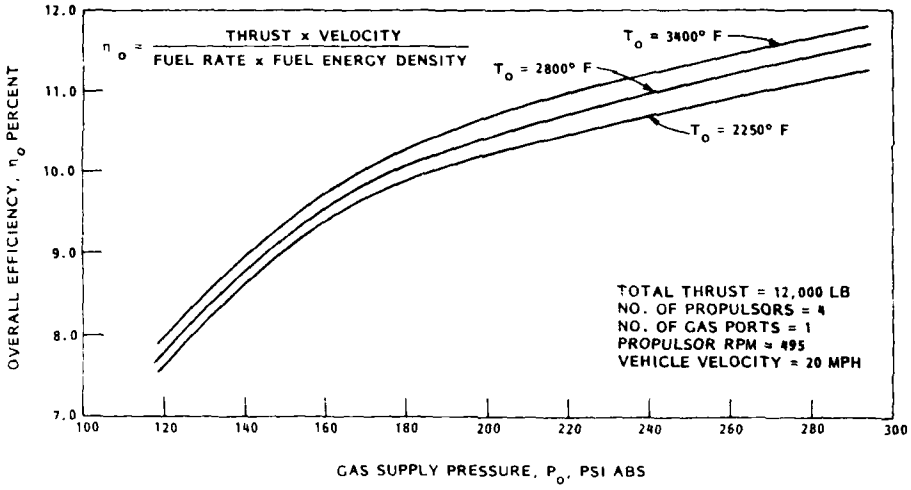

FIGURE 5 - VARIATION OF OVERALL EFFICIENCY OF THE SYSTEM WITH GAS PRESSURE AND GAS TEMPERATURE

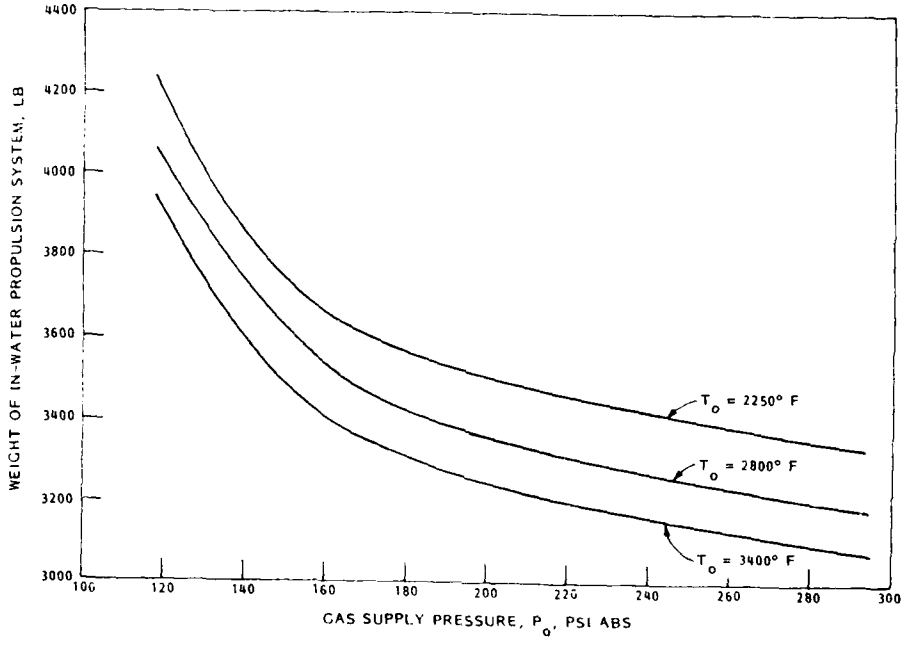

FIGURE 6 - VARIATION OF IN-WATER PROPULSION SYSTEM WEIGHT WITH GAS SUPPLY PRESSURE AND TEMPERATURE

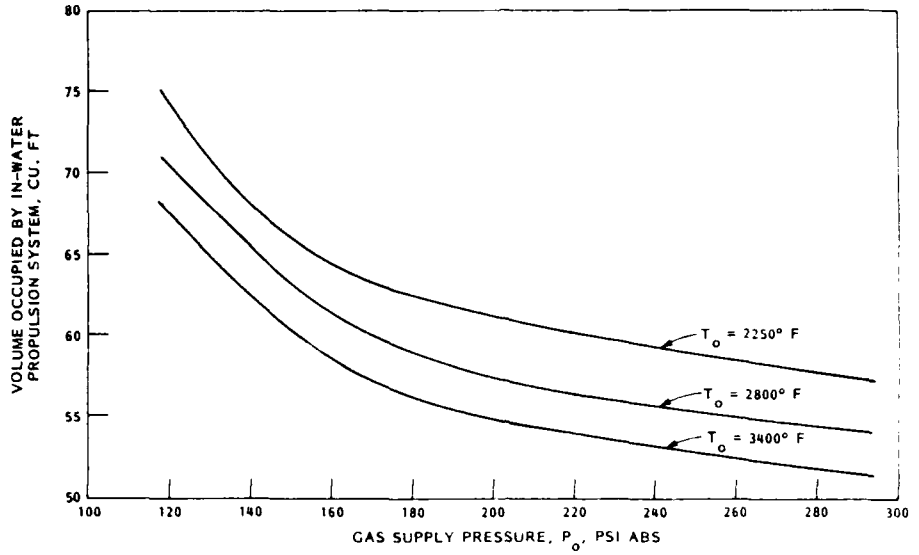

FIGURE 7 - VARIATION OF IN-WATER PROPULSION SYSTEM VOLUME WITH GAS SUPPLY PRESSURE AND TEMPERATURE

Group Photograph of Attendees at the 21st American Towing Tank Conference (taken at noon, 4 Aug 1986)

PARTICIPANTS OF THE 21st AMERICAN TOWING TANK CONFERENCE
5, 6, 7 AUGUST 1986

ABKOWITZ, M., Massachusetts Institute of Technology, Cambridge, MA U.S.A

ALAEZ, J.A., Canal De Experiencias Hydrodinamicas, Madrid, SPAIN

ANDERSON, K., David Taylor Naval Ship R&D Center, Bethesda, MD U.S.A.

ANDREWS, M.D., Naval Research Laboratory, Washington, D.C. U.S.A

ANTHONY, D., David Taylor Naval Ship R&D Center, Bethesda, MD U.S.A.

ARAKERI, V., St. Anthony Falls Hydraulics Lab., Minneapolis, MN U.S.A.

ASHBY, R., David Taylor Naval Ship R&D Center, Bethesda, MD U.S.A.

ASHCROFT, F.H., University of Michigan, Ann Arbor, MI U.S.A.

ASINOVSKY, V., John J. McMullen Assoc., Inc., Arlington, VA U.S.A.

BACHMAN, R., David Taylor Naval Ship R&D Center, Bethesda, MD U.S.A.

BAGNELL, D. G., 12213 Maycheck Lane, Bowie, MD U.S.A.

BAILOR, J., David Taylor Naval Ship R&D Center, Bethesda, MD U.S.A.

BAKER, D., Melville Shipping, Ltd., Ottawa, Ontario, K1R 7S8 CANADA

BARNELL, A., David Taylor Naval Ship R&D Center, Bethesda, MD U.S.A.

BARUSCO, P., PETROBRAS, Rio De Janeiro, BRAZIL

BELL, R., David Taylor Naval Ship R&D Center, Bethesda, MD U.S.A.

BHATTACHARYYA, R., U.S. Naval Academy, Annapolis, MD U.S.A.

BILLET, M., Applied Research Laboratory/Penn State U, State College, PA U.S.A.

BLAKE, W., David Taylor Naval Ship R&D Center, Bethesda, MD U.S.A.

BLANTON, J., David Taylor Naval Ship R&D Center, Bethesda, MD U.S.A.

BRESLIN, J., Stevens Institute of Technology, Hoboken, NJ U.S.A.

BROCKETT, T.E., University of Michigan, Ann Arbor, MI U.S.A.

BROGREN, E., Chicago Bridge and Iron Industries, Inc. Plainfield, IL U.S.A.

BROWN, E.M., U.S. Coast Guard Academy, New London, CT U.S.A.

BROWN, J., David Taylor Naval Ship R&D Center, Bethesda, MD U.S.A.

BROWN, P. W., Stevens Institute of Technology, Davidson Lab. Hoboken, NJ U.S.A.

CALLANEN, S., David Taylor Naval Ship R&D Center, Bethesda, MD U.S.A.

CHANG, Peter, David Taylor Naval Ship R&D Center, Bethesda, MD U.S.A.

CHEN, B., David Taylor Naval Ship R&D Center, Bethesda, MD U.S.A.

CHORNEY, S.J., David Taylor Naval Ship R&D Center, Bethesda, MD U.S.A.

CIESLOWSKI, D., David Taylor Naval Ship R&D Center, Bethesda, MD U.S.A.

COAKLEY, S., David Taylor Naval Ship R&D Center, Bethesda, MD U.S.A.

CODER, D., David Taylor Naval Ship R&D Center, Bethesda, MD U.S.A.

CONRAD, R., Naval Sea Systems Command, Washington, D.C. U.S.A.

COUCH, R.B., University of Michigan, Ann Arbor, MI U.S.A.

COX, B., Hydrodynamics Research Associates, Rockville, MD U.S.A.

COX, G., David Taylor Naval Ship R&D Center, Bethesda, MD U.S.A.

CUMMING, R.A., David Taylor Naval Ship R&D Center, Bethesda, MD U.S.A.

CURPHEY, R., David Taylor Naval Ship R&D Center, Bethesda, MD U.S.A.

CUSANELLI, D., David Taylor Naval Ship R&D Center, Bethesda, U.S.A.

DAI, C., David Taylor Naval Ship R&D Center, Bethesda, MD U.S.A.

DALZELL, J., David Taylor Naval Ship R&D Center, Bethesda, MD U.S.A.

DATTA, I., National Research Council, Institute for Marine Dynamics, St.John's, NF, CANADA

DAY, W., David Taylor Naval Ship R&D Center, Bethesda, MD U.S.A.

DEBORD, F., Offshore Technology Corporation, Escondida, CA U.S.A.

DEMPSEY, E., David Taylor Naval Ship R&D Center, Bethesda, MD U.S.A.

DEVONES, R., SAAB Systems, Inc., Seattle, WA U.S.A.

DIPPER, M., David Taylor Naval Ship R&D Center, Bethesda, MD U.S.A.

DOBAY, G., David Taylor Naval Ship R&D Center, Bethesda, MD U.S.A.

DUNCAN, J., Flow Research, Silver Spring, MD U.S.A.

DURKIN, J.M., David Taylor Naval Ship R&D Center, Bethesda, MD U.S.A.

EDA, H., Stevens Institute of Technology, Davidson Laboratory, Hoboken, NJ U.S.A.

ENGLE, A., Naval Sea Systems Command, Washington, D.C. U.S.A.

ETTER, R.J., David Taylor Naval Ship R&D Center, Bethesda, MD U.S.A.

FEIN, J. A., David Taylor Naval Ship R&D Center, Bethesda, MD U.S.A.

FELDMAN, J., David Taylor Naval Ship R&D Center, Bethesda, MD U.S.A.

FERNANDES, A.C., Instituto de Pesquisas Technologicas, Cidade Universitaria, Sao Paulo, BRAZIL

FIREMAN, H., Naval Sea System Command, Washington, D.C. U.S.A.

FISH, S., David Taylor Naval Ship R&D Center, Bethesda, MD U.S.A.

FISHER, S., David Taylor Naval Ship R&D Center, Bethesda, MD U.S.A.

FOLEY, E., David Taylor Naval Ship R&D Center, Bethesda, MD U.S.A.

FREE, A., ARCTEC, Inc., Columbia, MD U.S.A.

FUHS, D., David Taylor Naval Ship R&D Center, Bethesda, MD U.S.A.

GEARHART, W., Applied Research Laboratory/Penn State U, State College, PA U.S.A.

AD-A196 627 PROCEEDINGS OF THE AMERICAN TOWING TANK CONFERENCE (21ST) HELD IN WASHINGTON DC ON 5-7TH AUGUST 1986(U) NATIONAL RESEARCH COUNCIL WASHINGTON DC R F MESSALLE

6/6

UNCLASSIFIED AUG 87 F/G 13/10 NL

END
DATE FILMED
9 88

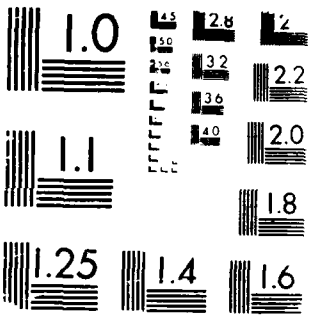

MICROCOPY RESOLUTION TEST CHA

GERSTEN, A., David Taylor Naval Ship R&D Center, Bethesda, MD U.S.A.

GOODMAN, A., Tracor Hydronautics, Inc., Laurel, MD U.S.A.

GORDON, J., David Taylor Naval Ship R&D Center, Bethesda, MD U.S.A.

GOSPODNETIC, D., Dominis Graphis, Ltd.,Vanier, Ontario K1L 7H8 CANADA

GOTTWALD, J.T., Tracor Hydronautics, Laurel, MD U.S.A.

GRANVILLE, P., David Taylor Naval Ship R&D Center, Bethesda, MD U.S.A.

GROVES, N., David Taylor Naval Ship R&D Center, Bethesda, MD U.S.A.

HAGEN, G., Designers & Planners, Arlington, VA U.S.A.

HARPER, H.D., David Taylor Naval Ship R&D Center, Bethesda, MD U.S.A.

HAWKINS, S., David Taylor Naval Ship R&D Center, Bethesda, MD U.S.A.

HENDRIX, D., David Taylor Naval Ship R&D Center, Bethesda, MD U.S.A.

HETTCHE, L.R., Applied Research Laboratory/Penn State U,State College, PA U.S.A.

HILL, J., U.S. Naval Academy, Annapolis, MD U.S.A.

HODGES, S., University of California, Berkeley, CA U.S.A.

HONG, Y., David Taylor Naval Ship R&D Center, Bethesda, MD U.S.A.

HOUGH, J., Naval Sea Systems Command, Washington, D.C. U.S.A.

HOYT, J., San Diego State University, San Diego, CA U.S.A.

HOYT, J., David Taylor Naval Ship R&D Center, Bethesda, MD U.S.A.

HSIUNG, C.C., Technical University of Nova Scotia, Halifax, N.S. CANADA

HSU, C.C., David Taylor Naval Ship R&D Center, Bethesda, MD U.S.A.

HUANG, T.T., David Taylor Naval Ship R&D Center, Bethesda, MD U.S.A.

HUNT, L., Naval Studies Board, National Academy of Sciences, Wash., D.C. U.S.A.

JESSUP, S., David Taylor Naval Ship R&D Center, Bethesda, MD U.S.A.

JOBST, W., David Taylor Naval Ship R&D Center, Bethesda, MD U.S.A.

JOHNSON, B., U.S. Naval Academy, Annapolis, MD U.S.A.

JOHNSON, R.A., Applied Research Laboratory/Penn State U,State College, PA U.S.A.

JONES, S.J., National Research Council, Institute for Marine Dynamics,
St. John's NF CANADA

KAPLAN, P., Virginia Polytechnic Institute and State University, Blacksburg,
VA U.S.A.

KARAFIATH, G., David Taylor Naval Ship R&D Center, Bethesda, MD U.S.A.

KATZ, J., Purdue University, West Lafayette, IN U.S.A.

KELLER, J.C., U.S. Coast Guard, Washington, D.C. U.S.A.

KIM, K.H., David Taylor Naval Ship R&D Center, Bethesda, MD U.S.A.

KIM, S. H., David Taylor Naval Ship R&D Center, Bethesda, MD U.S.A.

KIRKMAN, K., Naval Architects & Marine Engineers, Arlington, VA U.S.A.

KOLAINI, A., University of California, Santa Barbara, CA U.S.A.

KOPP, P., David Taylor Naval Ship R&D Center, Bethesda, MD U.S.A.

KRESIC, M., John J. McMullen Associates, Inc., New York, NY U.S.A.

KUHN, J.C., Offshore Technology Corp., Escondido, CA U.S.A.

LANGE, W., MTS Sytems Corp., Minneapolis, MN U.S.A.

LATORRE, R., University of New Orleans, New Orleans, LA U.S.A.

LAURICH, P.H., National Research Council, Ottawa, Ontario CANADA

LEE, C., Office of Naval Research, Arlington, VA U.S.A

LEE, D., Newport News Shipbuilding, Newport News, VA U.S.A.

LEE, H.C., U.S. Coast Guard, Washington, D.C. U.S.A.

LEE, J., David Taylor Naval Ship R&D Center, Bethesda, MD U.S.A.

LEE, W.T., David Taylor Naval Ship R&D Center, Bethesda, MD U.S.A

LEE, Y.T., David Taylor Naval Ship R&D Center, Bethesda, MD U.S.A.

LIN, W-C., David Taylor Naval Ship R&D Center, Bethesda, MD U.S.A.

LINCOLN, W., U.S. Coast Guard R&D Center, Avery Point, Groton, CT U.S.A.

LINDENMUTH, W., David Taylor Naval Ship R&D Center, Bethesda, MD U.S.A

LIU, H.L., David Taylor Naval Ship R&D Center, Bethesda, MD U.S.A.

LUNDY, W., U.S. Coast Guard, Washington, D.C. U.S.A.

MARTIN, M., David Taylor Naval Ship R&D Center, Bethesda, MD U.S.A.

MCCARTHY, J.H., David Taylor Naval Ship R&D Center, Bethesda, MD U.S.A.

McCREADY, J., David Taylor Naval Ship R&D Center, Bethesda, MD U.S.A.

MCCREIGHT, W.R., David Taylor Naval Ship R&D Center, Bethesda, MD U.S.A.

MELLISH, R., David Taylor Naval Ship R&D Center, Bethesda, MD U.S.A.

MESSALLE, R., David Taylor Naval Ship R&D Center, Bethesda, MD U.S.A.

MEYER, J.R., David Taylor Naval Ship R&D Center, Bethesda, MD U.S.A.

MILES, M. D., National Research Council, Ottawa, Ontario CANADA

MORGAN, W.B., David Taylor Naval Ship R&D Center, Bethesda, MD U.S.A.

MOTTER, L., David Taylor Naval Ship R&D Center, Bethesda, MD U.S.A.

MURDEY, D.C., National Research Council, Institute for Marine Dynamics,
St. John's, NF CANADA

NAGLE, T., David Taylor Naval Ship R&D Center, Bethesda, MD U.S.A.

NGUYEN, P., David Taylor Naval Ship R&D Center, Bethesda, MD U.S.A.

NOBLE, D.J., Defense Research Establishment Atlantic, Dartmouth, N.S. CANADA

NOBLE, P., Arctec, Columbia, MD U.S.A.

NOBLESSE, F., David Taylor Naval Ship R&D Center, Bethesda, MD U.S.A.

NORRIS, C., National Research Council, Institute for Marine Dynamics,
St. John's, NF CANADA

OAKES, M., J.J. McMullen Associates, Arlington, VA U.S.A.

O'DEA, J., David Taylor Naval Ship R&D Center, Bethesda, MD U.S.A.

OUTLAW, D.G., Dept. of the Army, Corps of Engineers, Vicksburg, MS U.S.A.

PARASKEVAS, N.M., The David Taylor Naval Ship R&D Center, Bethesdsa, MD U.S.A.

PIRRONE, M., David Taylor Naval Ship R&D Center, Bethesda, MD U.S.A.

PLATZER, G.P., Naval Sea Systems Command, Washington, D.C. U.S.A.

REED, A., David Taylor Naval Ship R&D Center, Bethesda, MD U.S.A.

RODDAN, G., B.C. Research, Vancouver, B.C. CANADA

ROOD, E., David Taylor Naval Ship R&D Center, Bethesda, MD U.S.A.

SANDBERG, W., Naval Sea Systems Command, Washington, D.C. U.S.A.

SANTORE, G.L., ORI, Inc., Arlington, VA U.S.A.

SAVITSKY, D., Stevens Institute of Technology, Davidson Lab., Hoboken, NJ U.S.A.

SCHWARZENBERG, D., David Taylor Naval Ship R&D Center, Bethesda, MD U.S.A.

SCHOTT, C., David Taylor Naval Ship R&D Center, Bethesda, MD U.S.A.

SEIBOLD, F., Maritime Administration, Washington, D.C. U.S.A.

SELLERS, F., MPR Associates, Washington, D.C. U.S.A.

SHEN, Y.T., David Taylor Naval Ship R&D Center, Bethesda, MD U.S.A.

SHERMAN, P.M., John J. McMullen Assoc., Arlington, VA U.S.A.

SILVER, A., David Taylor Naval Ship R&D Center, Bethesda, MD U.S.A.

SILVERSTEEN, B., Tracor Hydronautics, Inc., Laurel, MD U.S.A.

SMITH, S., U.S. Coast Guard, Washington, D.C. U.S.A.

SMITH, W., ORI, Inc., Rockville, MD U.S.A.

SOUDERS, W., David Taylor Naval Ship R&D Center, Bethesda, MD U.S.A.

SPONAGLE, N.C., Defense Research Establishment Atlantic, Dartmouth, NS, CANADA

STENSGAARD, G., B.C. Research, Vancouver, BC, CANADA

STENSON, R.J., David Taylor Naval Ship R&D Center, Bethesda, MD U.S.A.

SUHOKE, R., DANTEC Electronics, Allendale, NJ 07401 U.S.A.

TATINCLAUX, J.C., Cold Regions Res. & Eng. Lab. Hanover, NH U.S.A.

THOMPSON, E., U.S. Coast Guard Academy, New London, CT U.S.A.

TROESCH, A., University of Michigan, Ann Arbor, MI U.S.A.

TULIN, M., University of California, Santa Barbara, CA U.S.A.

ULMER, E., David Taylor Naval Ship R&D Center, Bethesda, MD U.S.A.

VILLIGER, C., David Taylor Naval Ship R&D Center, Bethesda, MD U.S.A.

VISNESKI, D., U.S. Coast Guard Academy, New London, CT U.S.A.

VORUS, Wm., University of Michigan, Ann Arbor, MI U.S.A.

WALDEN, D.A., David Taylor Naval Ship R&D Center, Bethesda, MD U.S.A.

WALLENDORF, L., U.S. Naval Academy, Annapolis, MD U.S.A.

WARD, L.W., Webb Institute of Naval Architecture, Glen Cove, NY U.S.A.

WARRICK, A., 4331 Corral Canyon Rd., Bonita, CA U.S.A.

WATERS, R.T., David Taylor Naval Ship R&D Center, Bethesda, MD U.S.A.

WETZEL, J.M., St. Anthony Falls Hydraulic Lab., Minneapolis, MN U.S.A.

WHITE, J.A., U.S. Coast Guard, Washington, D.C. U.S.A.

WILSON, M., David Taylor Naval Ship R&D Center, Bethesda, MD U.S.A.

WILSON, R.A., David Taylor Naval Ship R&D Center, Bethesdsa, MD U.S.A.

WISLER, B., David Taylor Naval Ship R&D Center, Bethesda, MD U.S.A.

WOOD, J., David Taylor Naval Ship R&D Center, Bethesda, MD U.S.A.

YANG, C., David Taylor Naval Ship R&D Center, Bethesda, MD U.S.A.

YIM, B., David Taylor Naval Ship R&D Center, Bethesda, MD U.S.A.

YOUNG, R., U.S. Coast Guard R&D Center, Avery Point, Groton, CT U.S.A.

ZARNICK, E., David Taylor Naval Ship R&D Center, Bethesda, MD U.S.A.

ZSELECZKY, J., U.S. Naval Academy, Annapolis, MD U.S.A.

MINUTES OF THE 21ST ATTC BUSINESS SESSION

The business session was called to order by Dr. William B. Morgan, Chairman, at 11:20 AM on Thursday, August 5, 1986.

Since the chairman of the ATTC is the North and South America Area Representative to the ITTC, business items relating to the ITTC were conducted first. Dr. Morgan made the following announcements:

1. Invitations for the Oct 1987 ITTC meeting in Kobe, Japan had been sent out.
2. Volunteers are needed for the technical committees.
3. The ITTC Executive Committee requested that the 1993 meeting be held in Brazil. The ATTC would have to support this endeavor although it is not clear now exactly what this support means.

Antonio Fernandes from Instituto de Pesquisas Technologicas (IPT) in Sao Paulo, Brazil said he feels they can host the 20th ITTC in 1993.

It was moved and unanimously approved that the ATTC will support IPT at the 1993 ITTC meeting in Brazil.

The Chair was turned over to Dr. Daniel Savitsy for the election of the North and South America Area Representative to the ITTC. Normally the representative serves for two terms. The nominating committee nominated Dr. Morgan since he has only served one term. There were no other nominations from the floor. Dr. Morgan was unanimously re-elected as the North and South America Area Representative to the ITTC for a three year term ending in 1989. Dr. Savitsky then expressed thanks to Dr. Morgan and his staff for a great conference.

The ATTC Executive Committee received an invitation for the next meeting from the Institute for Marine Dynamics (IMD) in St. John's, Newfoundland. There were no other invitations from the floor and the invitation was unanimously accepted. Mr. David Murdey from IMD is the Chairman of the 22nd ATTC and will form a new executive committee to prepare for the next conference in 1989.

PAST MEETINGS OF THE AMERICAN TOWING TANK CONFERENCE

1st	14-15 April 1938	Experimental Towing Tank Hoboken, New Jersey
2nd	19-20 Sep 1939	1st day - Receiving Ship Building Navy Yard, Washington, D.C. 2nd day - David Taylor Model Basin
3rd	14th Nov 1940	Waldorf Astoria New York, NY
4th	14th Nov 1941	Waldorf Astoria New York, NY
5th	29-30 Sep 1943	David Taylor Model Basin Washington, D.C.
6th	12-13 Nov 1946	Experimental Towing Tank Hoboken, New Jersey
7th	7-8 Oct 1947	Newport News Shipbuilding & Dry Dock Co., Newport News, Virginia
8th	11-13 Oct 1948	The University of Michigan Ann Arbor, Michigan
9th	11-14 Sep 1950	National Research Council of Canada Ottawa, Canada
10th	4-6 May 1953	Massachusetts Institute of Technology Cambridge, Massachusetts
11th	12-14 Sep 1956	David Taylor Model Basin Washington, D.C.
12th	31 Aug-2 Sep 1959	The University of California Berkeley, California
13th	5-7 Sep 1962	The University of Michigan Ann Arbor, Michigan
14th	9-11 Sep 1965	Webb Institute of Naval Architecture Glen Cove, New York
15th	25-28 June 1968	National Research Council of Canada Ottawa, Canada
16th	9-13 Aug 1971	Instituto de Pesquisas Tecnologicas Sao Paulo, Brazil
17th	18-20 June 1974	California Institute of Technology Naval Undersea Center Pasadena, California
18th	23-25 Aug 1977	U.S. Naval Academy Annapolis, Maryland
19th	9-11 July 1980	The University of Michigan Ann Arbor, Michigan
20th	2-4 Aug 1983	Davidson Laboratory Hoboken, New Jersey
21st	5-7 Aug 1986	National Academy of Sciences Washington, D.C.

AIMS AND ORGANIZATION OF THE AMERICAN TOWING TANK CONFERENCE

The American Towing Tank Conference is a voluntary association of establishments having a responsibility in the prediction of hydromechanic performance of ships and other waterborne craft and their appendages from tests on scaled models.

The objective of the Conference is to promote exchange of knowledge between tank staffs for the purpose of improving methods and techniques. This includes an exchange of knowledge on the design of facilities, equipment and instrumentation, on experimental and construction techniques, and on scaling laws. As a means to this end, the Conference seeks to correlate testing among the various member establishments in order to facilitate the interpretation of experiments, and to issue standards.

The Conference seeks to attain its objective by holding formal triennial meetings and through the encouragement of informal working relationships among the member establishments.

Membership in the Conference is by establishment and is open, upon invitation, to all establishments in the Western Hemisphere. All the member establishments agree to the free and full exchange of all information on the foregoing subjects which is neither proprietary nor of a classified military nature. (To that end mutual agreements on exchange of publications and data of interest will be entered into.)

The members or delegates will be persons holding positions of primary responsibility in Towing Tanks or Water Tunnels, Shipbuilding Research Associations or Departments of Naval Architecture of a University in which prominence is given to the subjects pertaining to the objectives of the Conference. A few delegates can be invited who were not qualified as above but who have rendered services to the aim of the Conference, as well as observers.

The Conference assembles from time to time in different countries of the American Continent. Since 1950 it has assembled at three year intervals.

The details of organization of any particular Conference is the responsibility of the host establishment.

The Conference is a purely communicative body; it has no authority of financial sponsorship; its membership is voluntary and self-supporting.

Each establishment may be represented by one or more members at triennial formal meetings of the Conference.

Although representation is not limited, it is the intent that it be kept reasonably small so that fruitful discussions can be obtained at the working level. The Conference intends to meet formally at each of the member establishments in rotation, the sequence being decided by the membership.

The scope of the Conference is set by the Executive Committee, based on the recommendations of the previous general meetings.

The Executive Committee shall comprise the nominated representatives of the Institutions at which the last three Conferences were held plus Chairman of the SNAME Hydrodynamics Committee, plus the representative of the Institution at which the next Conference is to be held.

In the event that the Chairman of the Hydrodynamics Committee of SNAME does not serve as a member of the Executive Committee of the ATTC, the Executive Committee may invite another official to serve on the Executive Committee.

If a member of the Executive Committee resigns, a replacement shall be selected by his institution.

In addition the United States of America's representative on the ITTC Standing Committee shall, ex officio, be a member of the ATTC Executive Committee.

The ATTC membership of the Standing Committee of the ITTC will be rotated. The representative will normally serve through two

ITTC Conferences.

The ATTC representative on the ITTC Standing Committee shall:

a. hold a senior position in a model basin;
b. be acquainted with the operation of the ITTC; and
c. have means for financing attendance at an annual meeting of the ITTC Executive Committee

A newly appointed ATTC representative on the ITTC Standing Committee shall take office after the ITTC Conference subsequent to the ATTC Conference at which he is appointed.

The Chairman of the Executive Committee shall be the nominated representative of the Institution at which the next Conference is to be, viz, he is the Chairman of the next Conference.

The Secretary of the ATTC shall be any person so nominated by the Conference Chairman.

The Executive Committee shall appoint Chairmen of such Technical Committees as are felt necessary for the effective conduct of the Conference.

The Chairmen of such Technical Committees will appoint such persons as they consider necessary for the effective conduct of such Committees, and further will be responsible for the production of the State-of-the-Art reports and the soliciting of papers to be presented to the Conference.

The reports accepted by the staff of the Conference are discussed in the Technical Sessions during the meetings, first formally then informally. To this end, those reports are previously forwarded, well in advance of the dates of the Conference, to the Chairmen of the Conference Organizing Committee, who arranges for copies to be transmitted to each member. The same applies to the formal contributions which any member may make to the Conference. If the Chairman of the Technical Committee considers that any contribution is unacceptable in view of the objectives of the Conference, he should reject it.

The Chairman of each Technical Session, in association with the Chairman of the Technical Committee concerned, formulate decisions and recommendations arising from the Session. The decisions and recommendations will then be considered and agreed upon at the concluding Session of the Conference.

The Chairman of the Conference Organizing Committee will arrange for the publication of the Proceedings of the Conference.

The venue of the next Conference is subject to the invitation of an Institution, and such invitation shall be accepted by the Executive Committee after a vote of the delegates present at the Business Meeting.

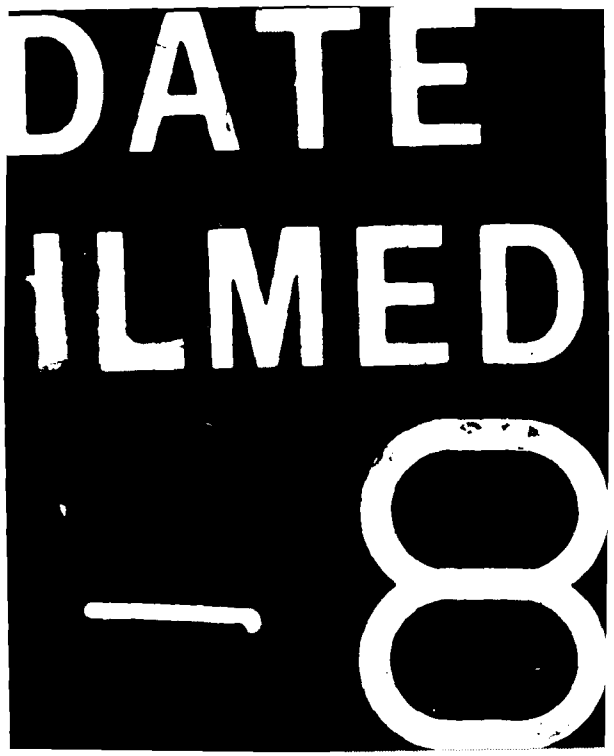
DATE
ILMED
8